Lecture Notes in Electrical Engineering 477

Pengfei Zhao
Yun Ouyang
Min Xu
Li Yang
Yuhui Ren *Editors*

Applied Sciences in Graphic Communication and Packaging

Proceedings of 2017 49th Conference of the International Circle of Educational Institutes for Graphic Arts Technology and Management & 8th China Academic Conference on Printing and Packaging

Springer

Lecture Notes in Electrical Engineering

Volume 477

"Lecture Notes in Electrical Engineering (LNEE)" is a book series which reports the latest research and developments in Electrical Engineering, namely:

- Communication, Networks, and Information Theory
- Computer Engineering
- Signal, Image, Speech and Information Processing
- Circuits and Systems
- Bioengineering

LNEE publishes authored monographs and contributed volumes which present cutting edge research information as well as new perspectives on classical fields, while maintaining Springer's high standards of academic excellence. Also considered for publication are lecture materials, proceedings, and other related materials of exceptionally high quality and interest. The subject matter should be original and timely, reporting the latest research and developments in all areas of electrical engineering.

The audience for the books in LNEE consists of advanced level students, researchers, and industry professionals working at the forefront of their fields. Much like Springer's other Lecture Notes series, LNEE will be distributed through Springer's print and electronic publishing channels.

More information about this series at http://www.springer.com/series/7818

Pengfei Zhao · Yun Ouyang
Min Xu · Li Yang · Yuhui Ren
Editors

Applied Sciences in Graphic Communication and Packaging

Proceedings of 2017 49th Conference of the International Circle of Educational Institutes for Graphic Arts Technology and Management & 8th China Academic Conference on Printing and Packaging

Springer

Editors
Pengfei Zhao
China Academy of Printing Technology
Beijing
China

Li Yang
China Academy of Printing Technology
Beijing
China

Yun Ouyang
China Academy of Printing Technology
Beijing
China

Yuhui Ren
China Academy of Printing Technology
Beijing
China

Min Xu
China Academy of Printing Technology
Beijing
China

ISSN 1876-1100 ISSN 1876-1119 (electronic)
Lecture Notes in Electrical Engineering
ISBN 978-981-10-7628-2 ISBN 978-981-10-7629-9 (eBook)
https://doi.org/10.1007/978-981-10-7629-9

Library of Congress Control Number: 2017961097

Printed on acid-free paper

This Springer imprint is published by Springer Nature
The registered company is Springer Nature Singapore Pte Ltd.
The registered company address is: 152 Beach Road, #21-01/04 Gateway East, Singapore 189721, Singapore

Preface

"2017 49th Conference of the International Circle of Education Institutes for Graphic Arts Technology and Management (IC) & 8th China Academic Conference on Printing and Packaging", one of the series "China Academic Conference on Printing and Packaging" which is mainly hosted by China Academy of Printing Technology, was held on May 14–16, 2017, in Beijing. The conference is co-hosted by Beijing Institute of Graphic Communication, China Academy of Printing Technology, International Circle of Educational Institutes for Graphic Arts, Technology and Management and the Printing Technology Association of China, and co-organized by School of Printing and Packaging Engineering, Beijing Institute of Graphic Communication, Beijing Key Laboratory of New Technology of Packaging and Printing, China Academy of Printing Technology and Printing Technology Professional Committee, Chinese Society for Imaging Science and Technology.

By far, "China Academic Conference on Printing and Packaging (CACPP)" and its series of events have been held for eight sessions since the first session in 2010, and have already become the most influential academic exchange activity in printing and packing fields in China. This time, CACPP was held together with 49th Conference of the International Circle of Education Institutes for Graphic Arts Technology and Management (IC) with more than 60 years history, which made CACPP more international, promoted the exchange and innovation of academic research in the field of international printing and packaging.

In recent years, the printing and packaging industry of China has been keeping a stable growth; in 2016, the total output value of China printing industry has topped to RMB 1271.16 billion, increasing by 3.8%. Up to November 2016, the total output value of China packaging industry reached 1700 billion. Research innovation is becoming more and more important in state and enterprise development, technological content of printing and packaging is becoming much higher, and the demand of printing and packaging high-tech talents is also changing accordingly; hereto, colleges and universities in the world which have printing and packaging majors are doing revolution and innovation of education mode, professional content, and education method.

Except keeping paying close attention to latest digital technology, environmental material technology, and advanced information technology, "2017 49th Conference of the International Circle of Education Institutes for Graphic Arts Technology and Management (IC) & 8th China Academic Conference on Printing and Packaging" also had discussion about research trends of print and packaging education. The conference invited President LUO Xueke from Beijing Institute of Graphic Communication, Vice President ZHAO Pengfei from China Academy of Printing Technology, Prof. Alexander ROOS from Stuttgart Media University, Vice President Prof. Pierre Pienaar from WPO, Prof. Alexander Tsyganenko from Media Industry Academy, Prof. HSIEH Yungcheng from Taiwan University of Arts, Prof. LUO M. Ronnier from Zhejiang University, and Prof. Kamal Chopra from All India Federation of Master Printers to make keynote speeches "Development Prospect of Printing Education", "Pan-printing Discover the Future of Printing in China", "Business Models, Innovation and Strategy Finding for Printing Industry", "Latest Research Achievements in Smart Packaging", "Professional Standards for Printing Industry in Russia", "Printing Media's New Blue Ocean-from Print E-commerce to Me-Commerce (Customized Web-to-Print)", "Study of White Appearance and its New Applications", and "Innovative Packaging Design", respectively. At the same time, the participants had oral presentations, academic exchanges, and latest research achievement on color science, image processing, digital media, printing engineering, packaging engineering, mechanical engineering and intelligence, film, ink, paper, and other functional material technology on nine panel discussion meetings.

The conference received 246 papers this year, among which 120 were selected to be published on Lecture Notes in Electrical Engineering (LNEE) (ISSN: 1876-1100) by Springer.

Here, we greatly acknowledge all the organizations that offered great support for the conference and they are the Printing Technology Association of China; Chinese Society for Imaging Science and Technology; Stuttgart Media University; WPO; Media Industry Academy; All India Federation of Master Printers; College of Light Industry and Engineering of South China University of Technology; College of Packaging and Printing Engineering of Tianjin University of Science and Technology; Faculty of Printing, Packaging Engineering and Digital Media Technology of Xi'an University of Technology; School of Media and Design of Hangzhou Dianzi University; School of Printing and Packaging of Wuhan University; Zhengzhou Institute of Surveying and Mapping; State Key Laboratory of Modern Optical Instrumentation of Zhejiang University; Light Industry College of Harbin University of Commerce; College of Printing and Packaging Engineering of Qilu University of Technology; College of Materials Science and Engineering of Beijing University of Chemical Technology; School of Biological and Chemical Engineering/School of Light Industry of Zhejiang University of Science and Technology; College of Communication and Art Design of University of Shanghai for Science and Technology; College of Bioresources Chemical and Materials Engineering of Shaanxi University of Science and Technology; School of Light Industry and Chemical Engineering of Dalian Polytechnic University;

College of Light Industry Science and Engineering of Nanjing Forestry University; School of Food and Chemical Engineering of Beijing Technology and Business University; School of Mechanical Engineering of Tianjin University of Commerce; School of Materials and Chemical Engineering of Henan University of Engineering; College of Engineering of Qufu Normal University; School of Packaging and Material Engineering of Hunan University of Technology; College of Material Science and Engineering of Zhengzhou University; Food Science and Engineering College of Beijing University of Agriculture; School of Mechanical Engineering, Jiangnan University; Shanghai Publishing and Printing College; School of Media and Communication of Shenzhen Polytechnic; and College of Communications of National Taiwan University of Arts and Beijing Keyin Media and Culture Co., Ltd.

We would like to express our gratitude to the 41 experts from China, Germany, Britain, American, and Japan for reviewing and recommending papers for the conference with strict standards.

We also thank Springer for offering us an international platform for publishing.

We look forward to our reunion at 2018 9th China Academic Conference on Printing and Packaging.

Beijing, China
July 2017

Edited by
China Academy of Printing Technology

2017 49th Conference of the International Circle of Educational Institutes for Graphic Arts, Technology and Management & 8th China Academic Conference on Printing and Packaging

Date May 14–16, 2017
Location Beijing, China

Sponsors

Beijing Institute of Graphic Communication
China Academy of Printing Technology
International Circle of Educational Institutes for Graphic Arts, Technology and Management
The Printing Technology Association of China

Support

Chinese Society for Imaging Science and Technology

Organizers

School of Printing and Packaging Engineering, Beijing Institute of Graphic Communication
Beijing Key Laboratory of Packaging and Printing New Technology, China Academy of Printing Technology
Printing Technology Professional Committee, Chinese Society for Imaging Science and Technology

Co-Sponsors

College of Packaging and Printing Engineering, Tianjin University of Science and Technology
College of Light Industry and Engineering, South China University of Technology
Faculty of Printing, Packaging Engineering and Digital Media Technology, Xi'an University of Technology
School of Media and Design, Hangzhou Dianzi University
College of Printing and Packaging Engineering, Qilu University of Technology
School of Printing and Packaging, Wuhan University
Zhengzhou Institute of Surveying and Mapping
Light Industry College, Harbin University of Commerce
School of Light Industry and Chemical Engineering, Dalian Polytechnic University
College of Light Industry Science and Engineering, Nanjing Forestry University
College of Engineering, Qufu Normal University
School of Packaging and Material Engineering, Hunan University of Technology
College of Material Science and Engineering, Zhengzhou University
Food Science and Engineering College, Beijing University of Agriculture
College of Communication and Art Design, University of Shanghai for Science and Technology
State Key Laboratory of Modern Optical Instrumentation, Zhejiang University
School of Biological and Chemical Engineering/School of Light Industry, Zhejiang University of Science and Technology
College of Bioresources Chemical and Materials Engineering, Shaanxi University of Science and Technology
College of Materials Science and Engineering, Beijing University of Chemical Technology
School of Food and Chemical Engineering, Beijing Technology and Business University
School of Mechanical Engineering, Tianjin University of Commerce
School of Materials and Chemical Engineering, Henan University of Engineering
School of Mechanical Engineering, Jiangnan University
Shanghai Publishing and Printing College
School of Media and Communication, Shenzhen Polytechnic
Department of Graphic Communication Arts, College of Communications, National Taiwan University of Arts

Conference Executive Committee

Chairman

Yanbin Wang, Chairman of The Printing Technology Association of China
Xueke Luo, President of Beijing Institute of Graphic Communication, Vice Chairman of Printing and Printing Equipment Industries Association of China

Tingliang Chu, President of China Academy of Printing Technology, Vice Chairman of the Printing Technology Association of China
Luk Bouters, Chairman of the International Circle of Educational Institutes for Graphic Arts, Technology and Management

Vice Chairman
Wencai Xu, Vice President of Beijing Institute of Graphic Communication, Vice Chairman of the Printing Technology Association of China
Pengfei Zhao, Vice President of China Academy of Printing Technology
Yangzhi Zhang, President Assistant of Beijing Institute of Graphic Communication

Honorary Chairman
Desen Qu, Former President of Beijing Institute of Graphic Communication
Jialing Pu, Chairman of Chinese Society for Imaging Science and Technology

Secretary-general
Xianfu Wei, Dean of School of Printing and Packaging Engineering, Beijing Institute of Graphic Communication
Yun Ouyang, Chief Engineer of China Academy of Printing Technology

Conference Academic Committee

Chairman
Deren Li, Academician of Chinese Academy of Sciences, Academician of China Engineering Academy, Professor of Wuhan University, Director of State Key Laboratory of Information Engineering in Surveying, Mapping and Remote

Vice Chairman
Guangnan Ni, Academician of China Engineering Academy, Researcher of Institute of Computing Technology Chinese Academy of Sciences, Board Chairperson of Chinese Information Processing Society of China
Kefu Chen, Academician of China Engineering Academy, Professor of South China University of Technology, Director of Academic Committee of State Key Laboratory of Pulp and Paper Engineering
Songlin Zhuang, Academician of China Engineering Academy, Director and Professor of School of Optical-Electrical and Computer Engineering of University of Shanghai for Science and Technology, Optical Expert
Bingheng Lu, Academician of Chinese Academy of Engineering, Professor of Xi'an Jiaotong University, Director of the National Engineering Research Center of Rapid Manufacturing

Commissioners
Yuri Andreev, Head of Moscow State University of Printing Arts
Stephen W. Bigger, Doctor, Professor, Vice President of Faculty of Engineering and Science of Victoria University

Congjun Cao, Doctor, Professor of Xi'an University of Technology, Master student supervisor
Guorong Cao, Professor of Beijing Institute of Graphic Communication, Master student supervisor
Guangxue Chen, Doctor, Professor of South China University of Technology, Doctoral supervisor
Hong Chen, Professor of Beijing Institute of Graphic Communication
Ping Chen, Doctor, Doctoral supervisor
Yunzhi Chen, Doctor, Professor of Tianjin University of Science and Technology, Doctoral supervisor
Kamal Chopra, Professor, President of All India Federation of Master Printers
Fuqiang Chu, Doctor, Professor of Qilu University of Technology, Master student supervisor
Tingliang Chu, Professor of China Academy of Printing Technology, Master student supervisor
Changqing Fang, Doctor, Professor of Xi'an University of Technology, Doctoral supervisor
Patrick Gane, Doctor, Professor of Printing Technology at the School of Chemical Technology, Aalto University
De Gao, Professor of Ningbo Institute of Technology, Zhejiang University, Master student supervisor
Phil Green, Professor of Colour Imaging, London College of Communication
Jon Yngve Hardeberg, Doctor, Professor of Norwegian University of Science and Technology
Roger D. Hersch, Doctor, Professor of Computer Science and Head of the Peripheral Systems Laboratory at the Ecole Polytechnique Fédérale de Lausanne, EPFL
Mathias Hinkelmann, Doctor, Professor of Stuttgart Media University
Thomas Hoffmann-Walbeck, Professor of the Faculty of Print and Media Technology, Stuttgart University of Media
Yungcheng Hsieh, Doctor, Professor of National Taiwan University of Arts
Guobin jin, Professor of Shanghai University, Vice Director of China Packaging Education Committee
Takashi Kitamura, Doctor, Professor of Graduate School of Advanced Integration Science, Chiba University
Shijun Kuang, Consultant Engineer of China National Pulp and Paper Research Institute, Chief Engineer
Jose Maria Lagaron, Doctor, Professor, Leader and Founder of the Group Novel Materials and Nanotechnology for Food Related Applications at the Institute of Agrochemistry and Food Technology of the Spanish Council for Scientific Research
Benjamin Lee, Professor, Director of Department of Technology, California State University
Houbin Li, Doctor, Professor of Wuhan University, Doctoral supervisor

Luhai Li, Doctor, Professor of Beijing Institute of Graphic Communication, Master student supervisor
Zhijian Li, Doctor, Professor of Shanxi University of Science and Technology, Doctoral supervisor
Haoxue Liu, Doctor, Professor of Beijing Institute of Graphic Communication, Master student supervisor
Zhen Liu, Professor of University of Shanghai for Science and Technology, Doctoral supervisor
Dongming Lu, Doctor, Professor of Zhejiang University, Doctoral supervisor
M. Ronnier Luo, Professor of Zhejiang University
Xueke Luo, Professor of Beijing Institute of Graphic Communication
Xiufeng Ma, Professor of Qufu Normal University, Master student supervisor
Pierre Pienaar, Professor, Vice President of the World Packaging Organisation
Luciano Piergiovanni, Professor of the Department of Food, Environmental and Nutritional Sciences, Faculty of Agricultural and Food Sciences, University of Milan
Ngamtip Poovarodom, Doctor, Associate Professor of Department of Packaging and Materials Technology of Faculty of Agro-Industry, Kasetsart University
Jialing Pu, Doctor, Professor of Beijing Institute of Graphic Communication, Doctoral supervisor
Penggang Ren, Doctor, Professor of Xi'an University of Technology, Master student supervisor
Alexander Roos, Professor of Stuttgart Media University
Ruizhi Shi, Doctor, Professor of Zhengzhou Institute of Surveying and Mapping, Doctoral supervisor
Zhihui Sun, Professor of Harbin University of Commerce, Doctoral supervisor
Shaoyan Tang, Professor of Hunan University of Technology, Master student supervisor
Zhengning Tang, Doctor, Professor of Jiangnan University, Master student supervisor
Anita Teleman, Doctor, Research Manager of Printing Solutions at the Research Institute Innventia, Sweden
Yuemin Teng, Professor of Shanghai Publishing and Printing College
Alexander Tsyganenko, Professor of Media Industry Academy
Philipp Urban, Head of Emmy-Noether Research Group, Institute of Printing Science and Technology, Technische Universität Darmstadt
Howard E. Vogl, Visiting Professor of Rochester Institute of Technology
Xiaoxia Wan, Doctor, Professor of Wuhan University, Doctoral supervisor
Haiqiao Wang, Doctor, Professor of Beijing University of Chemical Technology, Doctoral supervisor
Jianqing Wang, Professor of Tianjin University of Science and Technology, Doctoral supervisor
Lijie Wang, Professor of Shenzhen Polytechnic
Qiang Wang, Doctor, Professor of Hangzhou Dianzi University, Doctoral supervisor

Yiqing Wang, Doctor, Professor of Xi'an Jiaotong University
Xianfu Wei, Doctor, Professor of Beijing Institute of Graphic Communication, Doctoral supervisor
Yuhchang Wei, Professor of Chinese Culture University
Jimei Wu, Doctor, Professor of Xi'an University of Technology, Doctoral supervisor
Punan Xie, Professor of Beijing Institute of Graphic Communication
Xiulan Xin, Doctor, Professor of Beijing Technology and Business University, Master student supervisor
Jinlin Xu, Professor of Xi'an University of Technology
Wencai Xu, Professor of Beijing Institute of Graphic Communication, Doctoral supervisor
Bin Yang, Doctor, Researcher of Peking University
Haigen Yao, Professor of Shanghai Publishing and Printing College
Yadong Yin, Doctor, Professor of University of California, Riverside
Haiyan Zhang, Professor of Xi'an University of Technology, Master student supervisor
Xiuping Zhao, Professor of Tianjin University of Science and Technology, Master student supervisor
Pengfei Zhao, Senior Engineer of China Academy of Printing Technology
Shisheng Zhou, Doctor, Professor of Xi'an University of Technology, Doctoral supervisor
Yingquan Zou, Doctor, Professor of Beijing Normal University, Doctoral supervisor

Reviewers

Li An, Doctor, Teacher of Beijing Institute of Graphic Communication
Congjun Cao, Doctor, Professor of Xi'an University of Technology
Guorong Cao, Doctor, Professor of Beijing Institute of Graphic Communication
Shaozhong Cao, Doctor, Professor of Beijing Institute of Graphic Communication
Shengyan Cai, Doctor, Associate Professor of Tianjin University of Science and Technology
Guangxue Chen, Doctor, Professor of South China University of Technology
Yunzhi Chen, Doctor, Professor of Tianjin University of Science and Technology
Fuqiang Chu, Doctor, Professor of Qilu University of Technology
Tingliang Chu, Professor, President of China Academy of Printing Technology
Yi Fang, Doctor, Teacher of Beijing Institute of Graphic Communication
Yabo Fu, Doctor, Associate Professor of Beijing Institute of Graphic Communication
Shanshan Gao, Doctor, Associate Professor of Qingdao University of Science and Technology
Minghui He, Doctor of South China University of Technology
Beiqing Huang, Associate Professor of Beijing Institute of Graphic Communication
Zhen Huang, Doctor, Professor of Tianjin University of Commerce
Lijiang Huo, Professor of Dalian Polytechnic University

Yang Jin, Doctor, Professor of Beijing Institute of Graphic Communication
JIANG Xiaoshan, Doctor, Associate Professor of Beijing Institute of Graphic Communication
Xue'e Li, Doctor, Engineer of China Academy of Printing Technology
Zhijiang Li, Doctor, Associate Professor of Wuhan University
Haoxue Liu, Doctor, Professor of Beijing Institute of Graphic Communication
Guodong Liu, Doctor, Associate Professor of Shaanxi University of Science and Technology
Yanan Liu, Doctor, Engineer of China Academy of Printing Technology
Zhuang Liu, Doctor, Associate Professor of Harbin University of Commerce
Maohai Lin, Associate Professor of Qilu University of Technology
Lixin Lu, Doctor, Professor of Jiangnan University
M. Ronnier Luo, Doctor, Professor of University of Leeds
Yalin Miu, Associate Professor of Xi'an University of Technology
Lixin Mo, Doctor, Associate Professor of Beijing Institute of Graphic Communication
Yun Ouyang, Chief Engineer of China Academy of Printing Technology
Ruizhi Shi, Doctor, Professor of Zhengzhou Institute of Surveying and Mapping
Bangyong Sun, Doctor, Associate Professor of Xi'an University of Technology
Haiqiao Wang, Doctor, Professor of Beijing University of Chemical Technology
Qiang Wang, Doctor, Professor of Hangzhou Dianzi University
Dehong Xie, Doctor, Teacher of Nanjing Forestry University
Xiulan Xin, Doctor, Professor of Beijing Technology and Business University
Hongwei Xu, Doctor, Professor of Xi'an University of Technology
Zhuofei Xu, Doctor, Teacher of Xi'an University of Technology
Pengfei Zhao, Associate President of China Academy of Printing Technology
Erhu zhang, Doctor, Professor of Xi'an University of Technology
Fazhong Zhang, Doctor, Engineer of China Academy of Printing Technology
Hanyue Zhang, Professor of Tianjin University of Science and Technology
Yuanlin Zheng, Doctor, Associate Professor of Xi'an University of Technology
Ming Zhu, Doctor, Associate Professor of Henan Institute of Engineering

Contents

Part II Image Processing Technology

Part VII Paper and Related Technology

Part VIII Ink and Related Technology

Part X Novel Functional Material Technology

Part I
Color Science and Technology

Correlation Between Color Quality Metric and Color Preference of Light Source

Rui Peng, Yanfen Zhang, Qiang Liu, Qi Wang and Guo Cao

Abstract Existing studies have shown that a linear combination of some color quality metrics can be used to characterize observers' color preference of light source. In order to study the correlation between metrics and color preference, nine kinds of LED light sources with different correlated color temperature were selected, and the subjective evaluation of color preference for three object scenes under different lighting conditions was obtained by psychophysical experiments. Based on the previous study, the combination of the metrics is optimized by a variety of fitting models. The results show that the Full Spectrum Color Index (FSCI) and its combinations with other metrics can predict the subjective preference well. The results will provide theoretical and methodological reference for the LED light quality evaluation.

Keywords LED · Color preference · Color quality metric · Correlated color temperature

1 Introduction

How to accurately assess the color quality of LED light sources is still a debatable issue [1]. The Commission Internationale de l'Eclairage (CIE) proposed the general color rendering index (CRI *Ra*) in 1965 [2]. However, many studies based on psychophysical experiments have shown that this traditional metric has some defects, especially for the LED luminaries [3–6].

R. Peng · Q. Liu (✉) · Q. Wang · G. Cao
School of Printing and Packaging, Wuhan University, Wuhan 430079, China
e-mail: liuqiang@whu.edu.cn

Y. Zhang
Media Communication System, Dongguan Polytechnic, Dongguan 523808, China

Q. Liu
Shen Zhen Research Institute, Wuhan University, Shenzhen 518000, China

P. Zhao et al. (eds.), *Applied Sciences in Graphic Communication and Packaging*, Lecture Notes in Electrical Engineering 477,
https://doi.org/10.1007/978-981-10-7629-9_1

For general lighting, many people are more interested in the color quality of the light source in terms of visual preference. As a result, metrics related to the subjective color preference are important [5, 7, 8]. However, preference is a complex issue and no single metric could characterize the color preference of light source perfectly [5, 9, 10]. According to some studies, combining two or more color quality metrics is a better method to explain observers' preference evaluations [8, 11–14]. For example, Khanh in his study combined pairs of existing color quality metrics linearly to increase the correlation between color quality metrics and color preference [11].

In this study, observers' evaluations of color preference were obtained in psychophysical experiments. Three groups of objects were illuminated in the light booth or simulated cave. Five or nine spectral power distributions (SPDs) were generated with CCT (correlated color temperature) values ranging from 2500 to 6500 K. We selected observers aged between 18 and 30 years old from Wuhan University. In the experiment, observers scaled the visual color preference by a 7-level rating method on three object scenes under different light sources respectively. The aims of the study are as follows:

(1) To verify the results of previous experiments and continue studying the correlation between color preference and existing color quality metrics;
(2) To combine pairs or triads of metrics to characterize the color preference more accurately and reasonably.

2 Experiment

The experiments were approved by the Ethics Committee of Wuhan University. All procedures followed were in accordance with the ethical standards of the responsible committee on human experimentation (institutional and national) and with the Helsinki Declaration of 1975, as revised in 2008 [5]. Informed consent was obtained from all observers for being included in the study.

Three objects were selected for experiments, which include oil painting, multicolor flowers and mural painting, as shown in Fig. 1.

Philips Hue was used as experimental light source. Five or nine SPDs were generated with CCT values ranging from 2500 to 6500 K. A calibrated spectroradiometer (Photo Research PR 705) together with a standard white board was used to measure the SPDs in a 45/0 optical configuration. Figure 2 shows the measured relative spectral power distributions of nine light sources. In addition, an illuminometer (Testo 540) was used to measure the illuminance. In this study, the average illuminance of the light booth was exclusively set as 200 lx while the mural painting experiment was set to 50 lx, which is the recommended illuminance level in the real caves of Dunhuang. Moreover, only five light sources (2500, 3500, 4500, 5500 and 6500 K) were used when viewing mural painting.

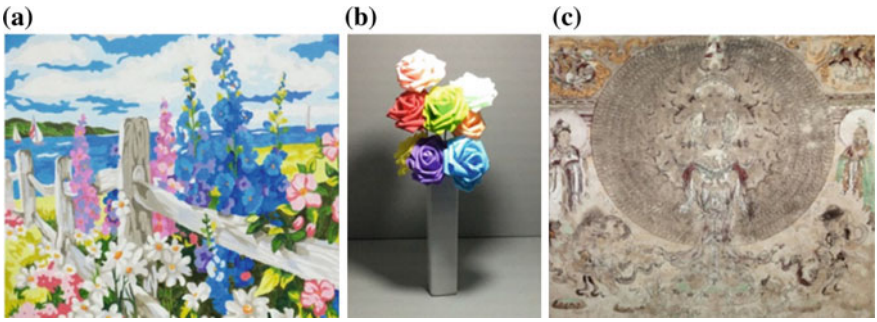

Fig. 1 Different objects adopted in the psychophysical experiments. **a** Oil painting, **b** multicolor flowers, **c** fine art reproduction of Dunhuang mural painting

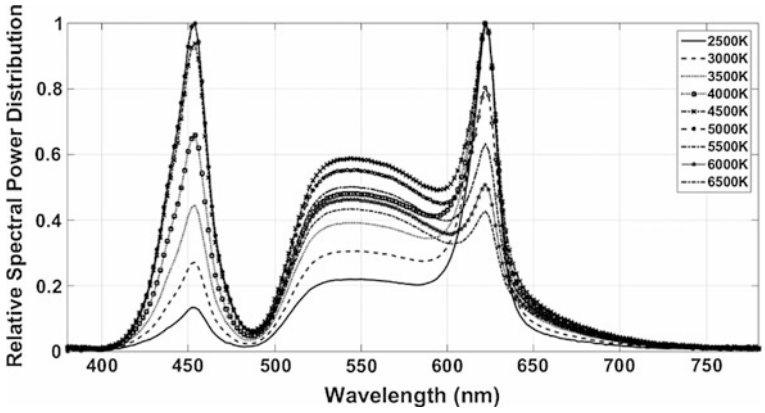

Fig. 2 Relative spectral power distributions of the experimental light sources

In this study, multicolor flowers and oil painting were observed in a light booth while the mural painting was observed in a simulated cave of a museum (Wan Lin Museum of Wuhan University, China), as shown in Fig. 3.

The light booth experiments were carried out in a darkroom. The light source was installed in the inner top of a standard light booth. The surrounding and bottom surfaces of the booth were coated with medium gray matt paint (Munsell N5). A chair was set in front of the booth with a distance around 40 cm. The height of the chair was adjustable to ensure that participants could observe the object at an angle of 45°. The experimental geometry of the simulated cave was different. The same chair was set in front of the center of the mural painting. Two identical lights were used to illuminate the mural painting from both sides of the observer at 45°. Figure 4 shows the geometric observation condition of both experiments.

Altogether 36 observers participated in the light booth experiment, including 17 men and 19 women between 18 and 25 years old. And a total of 20 observers were

Fig. 3 The experimental scenes. Left: light booth, Right: museum (in a simulated cave)

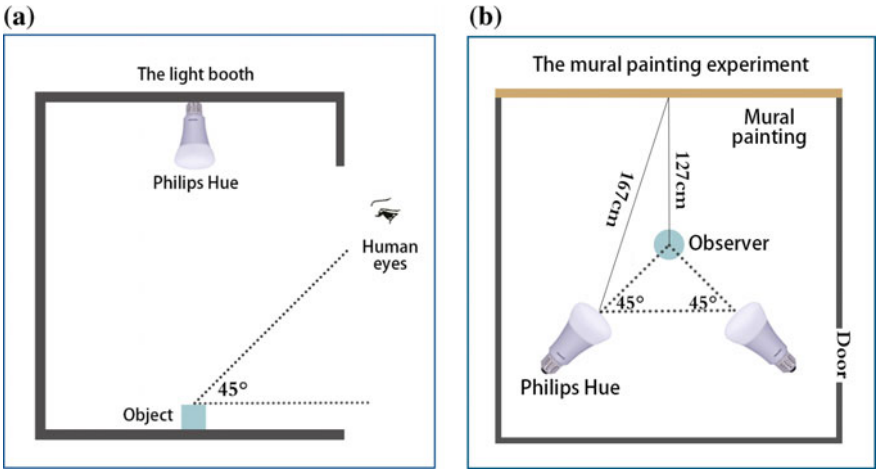

Fig. 4 The geometric observation condition of the light booth experiment (**a**) and the mural painting experiment (**b**)

invited to observe the mural painting, including 14 women and 6 men, between 18 and 30 years old. All observers had good visual acuity and normal color vision. In addition, observers were required to wear neutral gray clothing during the experiment to avoid the influence of other color information. Before the experiment began, the observers were asked to complete the questionnaire about personal information and remove shiny objects like phones.

During the experiment, all the room lights were closed except the light source in the light booth and simulated cave. Observers could scale the color preference using seven values (−3, −2, −1, 0, 1, 2, 3), which respectively represented strongly dislike, moderately dislike, slightly dislike, neural, slightly like, moderately like and strongly like. In each group trial, the order of light sources was randomized. There was a training phase before the formal experiment for observers assessing one light source and one object. In the formal experiment, when the experimenter changed the light, the participant was asked to close his eyes. After that, the participant could

open the eyes and observe the object for about 10 s. Besides, the participant was required to respond orally and the experimenter was responsible for asking questions and recording answers.

3 Results and Discussion

3.1 Pearson's Correlation Coefficient Analysis

In this study, correlation coefficient method was carried out to analyse the relationship between color preference and assorted color quality metrics. Pearson's correlation coefficient r reflects the degree of linear correlation between two variables. In general, the greater the absolute value of r, the stronger the correlation. Table 1 shows the correlation coefficients between the dependent variable (color preference) and the independent variables (color quality metrics plus the CCTs).

As can be seen from Table 1, the color preference of multicolor flowers performs a strong positive correlation with GAI, FSCI, CDI and CSA. FSCI exhibits the best correlation among the independent variables. As expected, the CIE CRI is not a good prediction of subjective color preferences for three object scenes. Besides, the Color Quality Scale, CRI2012 and CAM02UCS CRI do not correlate well with the visual color preference. Different from previous studies [11], MCRI is

Table 1 Correlation coefficients between the color preference and the color quality metrics

	Multicolor flowers	Oil painting	Mural painting
CCT	0.57	0.63	0.24
CRI	−0.59	−0.67	−0.22
GAI	0.88**	0.91**	0.62
FSCI	0.92**	0.94**	0.69
Qa	−0.12	−0.14	0.35
Qf	−0.17	−0.20	0.28
Qp	−0.34	−0.37	0.07
Qg	−0.71*	−0.77*	−0.42
FCI	−0.55	−0.61	−0.21
CDI	0.87**	0.90**	0.62
CSA	0.88**	0.91**	0.63
CPI	−0.59	−0.67	−0.21
CAM02UCS	−0.49	−0.53	−0.10
CRI2012	−0.33	−0.38	0.12
MCRI	−0.59	−0.67	−0.22

**Correlation coefficient significant at the $p < 0.01$ level
*Significant at the $p < 0.05$ level

proved to have no significant effect on visual color preference, at least in the condition of this work.

3.2 Combinations of Color Quality Metrics

According to previous research [8, 11–14], one single metric is not sufficient to describe the color preference of a light source. This study combined pairs or triads of metrics to characterize the color preference more completely. The combined color quality metric predictions should exhibit very strong correlation with perceived color preference ($r > 0.9$).

As the independent variable FSCI had the best correlation, this variable was considered to be combined with other metrics. In addition, to verify previous results, MCRI and CCT also took into account [11–13]. Meanwhile, stepwise regression was used to remove variables that cause multiple collinearity.

Table 2 shows linear combinations of the independent variables and correlation coefficient (r) with color preference for three objects. Khanh's results showed that the combination of CCT and another suitable metric could characterize color preference more efficiently than a single metric [11]. However, from the results in Table 2, the correlation coefficient of the combination of CCT and FSCI is lower than the correlation of color preference with FSCI alone. As a result, it seems that CCT makes no sense to be combined with other metrics.

Many researchers proposed a method of combining color fidelity metric with a gamut-based metric [15–19]. As can be seen from Table 2, the combination (Ra + GAI)/2 didn't exhibit a very strong correlation with preference. However, the results showed that the combination (a Ra + b GAI) with the optimized parameter a and b correlated with color preference well. Furthermore, other gamut area based metrics, like FCI and CSA, and the color fidelity scale CQS Qf also took this effect into account. The results demonstrated that combining color fidelity metric together with a gamut-based metric was useful to describe the color preference of a light source.

Combinations of FSCI and other metrics correlate with color preference better. For multicolor flowers, the best correlation ($r = 0.985$) was achieved by combining FSCI with CDI and CSA. Obviously, from the present results, FSCI has a more significant influence on predicting visual preference. The correlation coefficient resulting from parameter optimization ($r = 0.985$; 0.994; 1.000) is higher than that of FSCI ($r = 0.92$; 0.94; 0.69, see Table 1) alone.

FSCI is a color quality metric based fully on the shape of light source spectrum. Jost-Boissard et al. came up with an idea to evaluate the color rendering properties of a light source by considering four metrics (CQS, FSCI, GAI and CRI) [5]. However, in terms of color preference, there are very few conclusions about the correlation between FSCI and preference. Therefore, further research about the impact of FSCI on color preference needs to be carried out in the next step.

Table 2 Selected linear combinations of the independent variables with parameter values and correlation coefficient (r) with color preference for three objects

	Multicolor flowers				Oil painting				Mural painting			
	a	b	c	r	a	b	c	r	a	b	c	r
a MCR1 + b CCT	−0.01	0		0.62	−0.01	0		0.836*	−0.02	0		0.614
a FSC1 + b CCT	0.02	0		0.512	0.03	0		0.844*	0.04	0		0.88
a CSA + b CCT	−0.58	0		0.501	−0.35	0		0.810*	0.3	0		0.639
a FSCI + b Qe	0.03	−0.02		0.904*	0.04	−0.02		0.964**	0.02	−0.01		0.794
a FSCI + b FCI	0.03	−0.02		0.861*	0.04	−0.02		0.949**	0.01	−0.01		0.767
a FSCI + b FC1 + c Q_E	0.05	0.07	−0.1	0.983**	0.06	0.07	−0.1	0.994**	0.04	0.09	−0.1	0.983
a FSCI + b GA1	0.19	−0.13		0.979**	0.19	−0.13		0.992**	0.09	−0.06		0.902
a FSCI + b GAI + c CSA	0.18	−0.12	−0.22	0.979**	0.19	−0.12	−0.12	0.992**	0.22	−0.22	4.11	1.000**
a FSCI + b CDI + c CSA	0.18	−0.18	−0.09	0.985**	0.18	−0.08	−0.4	0.991**	0.22	−0.15	4.13	0.989*
a FSCl + b GAI + e MCRI	0.18	−0.13		0.979**	0.19	−0.13	0	0.992**	0.2	−0.16	0.02	0.999*
(GAI + CRI)/2				0.332				0.746				0.722
a GAI + b CRI	0.03	−0.02		0.844**	0.03	−0.03		0.939**	0.01	−0.01		0.741
a CSA + b CRI	2.38	−0.04		0.821*	3.06	−0.04		0.930**	1.06	−0.01		0.725
a FCI + b CRI	−0.08	0.09		0.532	−0.1	0.12		0.786*	−0.02	0.03		0.602
a GAI + b Qf	0.02	−0.03		0.773*	0.03	−0.03		0.908*	0.01	−0.01		0.704
a CSA + b Qf	1.9	−0.04		0.695	2.48	−0.04		0.871*	0.65	−0.01		0.662
a FC1 + b Qf	−0.12	0.17		0.878**	−0.16	0.22		0.966**	−0.07	0.11		0.899

**Correlation coefficient significant at the $p < 0.01$ level

*Significant at the $p < 0.05$ level

4 Conclusions

The results showed that combinations of color quality metrics correlated better with color preference than a single metric. As a result, two or three metrics system can be used to predict people's visual preference of light source. FSCI, GAI, CDI and CSA turned out to be significant for observers' color preference. Among them, FSCI and combinations of FSCI with some other metrics mentioned in Sect. 3.2 performed extremely strong correlation. In addition, the method of combining a color fidelity metric (CRI, Qf) together with a gamut-based metric (GAI, FCI, CSA) was proved to be significant to characterize the color preference. However, different from previous studies, CCT and MCRI make no difference in terms of combining color quality metrics. Therefore, in the future work, we will further study the cause of the strong correlation between FSCI and perceived color preference of light source.

The results of this work are intended to contribute to a more precise method to predict observers' color preference. The eventual aim is to provide theoretical and methodological reference for the color quality evaluation of LED luminaries.

Acknowledgements The authors acknowledge the support of the Shenzhen basic research project (grant No. JCYJ20150422150029093), Young Talent Project of Wuhan City of China (Project No. 2016070204010111) and National Natural Science Foundation of China (grant No. 61505149).

References

1. Commission Internationale de l'Eclairage, TC 1–62 (2007) Color rendering of white led light sources. CIE Publication 177: 2007. CIE, Vienna
2. Nickerson D, Jerome CW (1965) Color rendering of light sources: CIE method of specification and its application. Illum Eng 60(4):262
3. Smet K et al (2011) Correlation between color quality metric predictions and visual appreciation of light sources. Opt Express 19(9):8151–8166
4. Tarczali T, Bodrogi P, Schanda J (2001) Color rendering properties of LED sources. In: Proceedings of CIE 2nd LED measurement symposium (Gaithersburg)
5. Jost-Boissard S, Fontoynont M, Blanc-Gonnet J (2009) Perceived lighting quality of LED sources for the presentation of fruit and vegetables. J Mod Opt 56(13):1420–1432
6. Bodrogi P, Csuti P, Hotváth P, Schanda J (2004) Why does the CIE color rendering index fail for white RGB LED light sources? In: Proceedings of CIE expert symposium on LED light sources: physical measurement and visual and photobiological assessment (Tokyo, Japan)
7. Smet KAG et al (2010) Memory colors and color quality evaluation of conventional and solid-state lamps. Opt Express 18(25):26229–26244
8. Islam M et al (2013) User preferences for LED lighting in terms of light spectrum. Light Res Technol 45(6):641–665
9. Wei M et al (2014) Color preference under LEDs with diminished yellow emission. LEUKOS 10(3):119–131
10. Lin Y et al (2015) Color preference varies with lighting application. Light Res Technol. https://doi.org/10.1177/1477153515611458
11. Khanh T et al (2015) Color preference, naturalness, vividness and color quality metrics, Part 1: Experiments in a room. Light Res Technol. https://doi.org/10.1177/1477153516643359

12. Khanh T et al (2016) Color preference, naturalness, vividness and color quality metrics, Part 2: Experiments in a viewing booth and analysis of the combined dataset. Light Res Technol. https://doi.org/10.1177/1477153516643570
13. Khanh T, Bodrogi P (2016) Color preference, naturalness, vividness and color quality metrics, Part 3: Experiments with makeup products and analysis of the complete warm white dataset. Light Res Technol. https://doi.org/10.1177/1477153516669558
14. Dangol R, Islam M, Hyvarinen M, Bhusal P, Puolakka M, Halonen L (2013) Subjective preferences and color quality metrics of LED light sources. Light Res Technol 45:666–688
15. Smet KAG, Ryckaert WR, Pointer MR, Deconinck G, Hanselaer P (2011) Correlation between color quality metric predictions and visual appreciation of light sources. Opt Express 19:8151–8166
16. Houser KW, Wei M, David A, Krames MR, Shen XS (2013) Review of measures for light source color rendition and considerations for a two-measure system for characterizing color rendition. Opt Express 21:10393–10411
17. Hashimoto K et al (2007) New method for specifying color-rendering properties of light sources based on feeling of contrast. Color Res Appl 32(5):361–371
18. Guo X, Houser KW (2004) A review of color rendering indices and their application to commercial light sources. Light Res Technol 36(3):183–197
19. Rea MS, Freyssinier-Nova JP (2008) Color rendering: a tale of two metrics. Color Res Appl 33:192–202

Comparison Between Models, Measurement Instruments, and Testing Datasets for Display Characterization

Lihao Xu and Ming Ronnier Luo

Abstract This paper mainly investigated the performances between different display characterization methods, between different measurement instruments and between different testing datasets. It was found that a hybrid characterization method performed in the linear RGB space gave the highest accuracy while demanded less testing colors. Besides, no significant difference was found by using different measurement instruments on building models, indicating a limited instrumental accuracy is sufficient for characterization of a traditional LCD display. Moreover, a comprehensive dataset including 4096 test colors, i.e. 16 by 16 by 16 nodes was established. MCCC test chart was found to give a similar evaluation accuracy compared to it.

Keywords Display characterization · Instrumental comparison
Model comparison · Dataset comparison

1 Introduction

Displays are everywhere in the daily life, severing as an interaction window between human beings and computers. However, different displays have their own color characteristics and thus result in an inconsistency among them. To solve this issue, methods for display characterization were proposed and they all aimed to achieve the highest fidelity for color reproductions.

In this paper, three aspects are mainly focused on: (1) how various characterization methods perform on a traditional LCD display, (2) how different measurement instruments affect the model performance and (3) how different testing datasets influence the characterization results.

L. Xu · M. R. Luo (✉)
State Key Laboratory of Modern Optical Instrumentation,
Zhejiang University, Hangzhou, China
e-mail: m.r.luo@leeds.ac.uk

P. Zhao et al. (eds.), *Applied Sciences in Graphic Communication and Packaging*, Lecture Notes in Electrical Engineering 477,
https://doi.org/10.1007/978-981-10-7629-9_2

2 Method

2.1 Measurement Conditions

The display tested in this study was a NEC PA272 W 27″ LCD monitor having a size of 640.4 by 378.26 by 85 mm^3 and a spatial resolution of 2560 pixel by 1440 pixel. It can achieve a luminance up to 340 cd/m^2 and a maximum contrast ratio of 1000:1. However, in order to make a right black level, its white was fixed at 144 cd/m^2, with a CCT at around 6500 K.

The total measurement was implemented in a darkened room using two tele-spectradiometer (TSR), a JETI Specbos 1211uv (referred as JETI later) and a Konica minolta CS-2000 Spectroradiometer (referred as CS2000 later). JETI had a luminance range of 0.1–2500 cd/m^2 with its accuracy within 2% when measuring illuminant A of 100 cd/m^2. In comparison, CS2000 had a larger range from 0.003 to 5000 cd/m^2, giving an excellent accuracy in dark colors.

2.2 Color Characteristics

A series of color characteristics was studied. Stability was investigated by displaying a full-screen white on the screen and measured by JETI every 10 s from turn-on the display to 18 h. This display showed a luminance increase of 2.5% at the first 6 h, equaling to a color difference of about 0.89 ΔE^*_{ab}, which can be considered to be acceptable for developing a display characterization model. Note that a one unit DE*ab is considered to be acceptable.

Spatial uniformity was then evaluated by dividing the display into 3 by 3 segments. The MCDM (mean color difference from the mean) was 0.95 ΔE^*_{ab}, and the maximum value was 1.51 ΔE^*_{ab}, again indicating an acceptable performance for this type of display.

Spatial dependency was measured by fixing the center color patch as a middle grey, i.e. $L^*a^*b^*$ value of [50, 0, 0], and changing the background colors from red, green, blue to yellow, magenta and cyan. Again, MCDM was calculated and was 0.63 ΔE^*_{ab}.

And for additivity, a ramp for each channel from 0 to 255 digital inputs with an interval of 15 was measured. The agreement of XYZ values for grey channel with the sum of that for R-, G- and B- channels were evaluated. A color difference of 0.6 ΔE^*_{ab} could be obtained by doing so, implying a good additivity capability of this display.

The colorant consistency is evaluated as how the output color shifts when its luminance increases for a particular primary. As shown in Fig. 1a, color coordinates of the primaries remains unchanged. Figure 1b shows the color gamut of the LCD display. One can find that its gamut is slighter larger (6.6%) than DCI-P3, and covers the whole sRGB gamut (33% larger than sRGB).

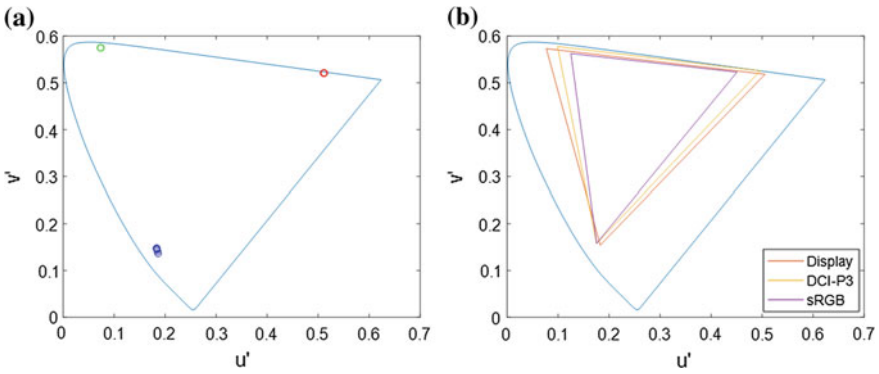

Fig. 1 **a** Colorant consistency in u'v' diagram and **b** color gamut of the LCD display (Color figure online)

3 Display Characterizations

During the last few decades, methods for display characterization have been extensively investigated and they can be divided into 3 categories, 1D (one dimension), 3D and hybrid methods, respectively.

3.1 1D Methods

Usually, 1D based method includes 2 steps. The first step is to transform the digital inputs into luminance domain. In this step, tone reproduction curves are developed for each channel and a mapping will be performed between the luminance and its corresponding digital input. In the second step, luminance values for each channel will be converted to XYZ values and then they will be summed up to produce the total XYZ response for a certain input.

The most classical method in this category is GoG (Gain-Offset-Gamma) [1], which was developed by Bern et al. and was recommended by CIE as a standard characterization method for CRT displays. This method considers the physical properties of a CRT display and uses equations to simulate the inner current-light conversion procedure. Another commonly used method is called PLCC [2] (Piecewise Linear interpolation assuming Constant Chromaticity coordinates) or 1D-LUT, which assumes a linear relationship for inputs that between 2 nodes. In this method, linear interpolations will be adopted piecewise. Both of these two methods will be investigated comprehensively in this study.

3.2 3D Methods

Unlike 1D based method, 3D methods ignore the two fundamental assumptions, i.e. consistent chromaticity coordinates of primaries and perfect additivity property of the display. The key for accuracy of this method is the number of data to build the model. In this category, interpolation method [3] are commonly used, including cubic interpolation [4] (8 points), triangular prism interpolation [5] (6 points), tetrahedral interpolation [6] (4 points) and so on. Usually, distances (or volumes) between the point to be mapped and the known nodes will serve as weighting factors. The principle is assuming that position relationship in RGB space among various points remains the same in the XYZ space.

This study will involve both the cubic interpolation and tetrahedral interpolation methods. Cubic interpolation could be a most commonly used one in this field. In this method, a cube can be found that encompasses the point to be mapped. Then it can be divided into 8 sub-cubes by the point to be mapped. Thus, eight vertexes will have their weights according to the volume of its corresponding cube. While for the tetrahedral interpolation, the cube is divided into six tetrahedrons. The first step is to determine which tetrahedron the point to be mapped is in and then using the 4 vertexes within a same tetrahedron to interpolate. There are more than one possible divisions and the one used in this study is shown below. Both of these 2 division methods are illustrated in Fig. 2a, b.

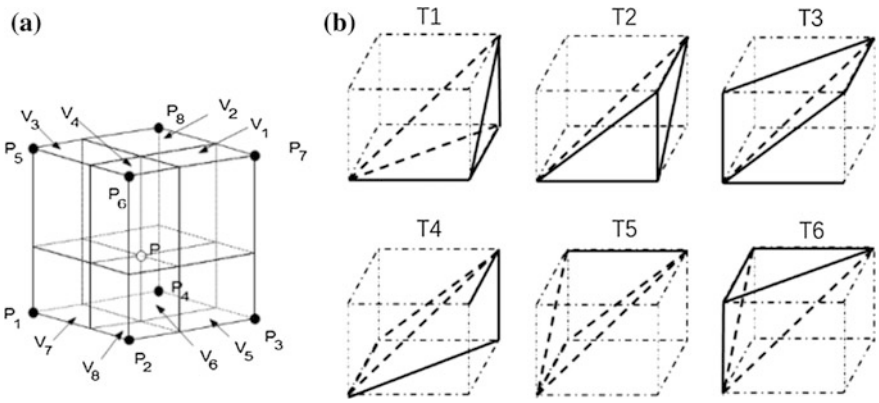

Fig. 2 **a** Cube division and **b** tetrahedron division

3.3 Hybrid Method

As is discussed above, 1D based method transformed digital inputs into luminance domain while 3D based method ignore the inner color characteristics of a display and just consider the position relation between nodes and the point to be mapped. Hence, to take full advantage of these 2 types of method, a hybrid method was proposed.

Initially, each channel of testing samples (red, green and blue) was transformed into luminance domain, called as the linear RGB space, according to their tone reproduction curves. In this step, the non-linear RGB space was converted into a linear one where distance in XYZ space can be more accurately represented. Afterwards, same interpolation method as described in Sect. 3.2 shall be implemented and their XYZ values can be finally derived.

4 Evaluations

4.1 Model Performance

In Sect. 3, five methods, i.e. GoG, PLCC, cube interpolation, tetrahedral interpolation and a hybrid method, for display characterization are introduced. In this section, they were evaluated using the MCCC test chart and their performances were presented in terms of color differences. All the data were measured using CS2000.

For 1D method, digital inputs ranging from 0 to 255 with an interval of 15 were measured using CS2000 as training samples, resulting in 18 XYZ values for each R-, G- and B- channel. In total, 54 measurement values could be obtained. For 3D methods, four sets of training data, i.e. 4 by 4 by 4 nodes, 8 by 8 by 8 nodes, 12 by 12 by 12 nodes and 16 by 16 by 16 nodes were measured. They produced 4 datasets consisting of 64, 512, 1728 and 4096 training colors, respectively.

Figure 3a shows the performance of PLCC and GoG models. It could be seen that both methods can produce a good result. However, when decreasing the number of nodes, accuracy for PLCC dropped swiftly while that for GoG model remained. This mainly lies in excellent performance of GoG model in describing tone reproduction behaviors. A node number of 10–12 was needed for PLCC model to give a similar model performance for that of GoG.

Figure 3b shows the performances for 3D-LUT methods and the hybrid method. It depicted that both 3D-LUT methods gave almost the same result. With the increase of nodes, ΔE^*_{ab} descended quickly at first and then become stable when nodes were over 12. In comparison with 1D methods, a number of 10 or 11 gave an equal performance as GoG's. This figure also shows the excellence of the hybrid method when the number of nodes is limited. A number of nodes at 9 was needed

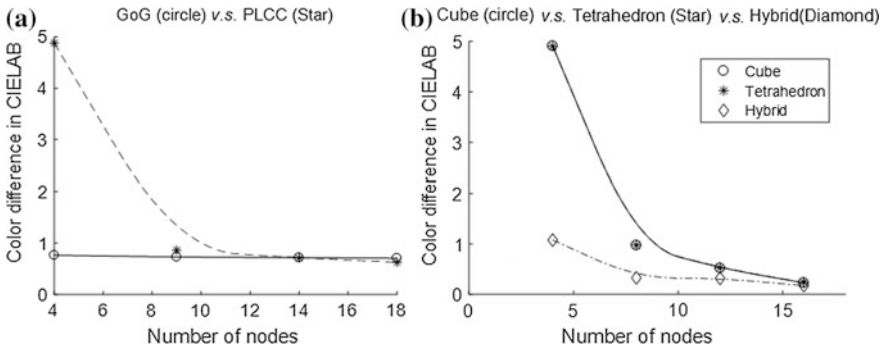

Fig. 3 Performances of different methods for display characterization

for the 3D-LUT methods to give a similar performance of the hybrid method having nodes of 4.

4.2 Instrumental Performance

As mentioned in Sect. 2.1, there were 2 TSRs included in this study. In this section, their performances were compared using 3 different models, i.e. GoG, tetrahedral interpolation and the hybrid methods, and the MCCC test chart.

The performance difference between JETI and CS2000 can be found in Fig. 4 in terms of ΔE^*_{ab} unit. It was obvious that CS2000 had a great accuracy in measuring dark colors, thus led to its excellent performance in model accuracy. However, the current display was set at a black level at 0.41 cd/m^2, which is within the range of both these two instruments. Meanwhile, when fixing the luminance of white patch from MCCC at 100 cd/m^2, the luminance for black patch was set at around 5 cd/m^2. This relatively high luminance was surely within the capability of both

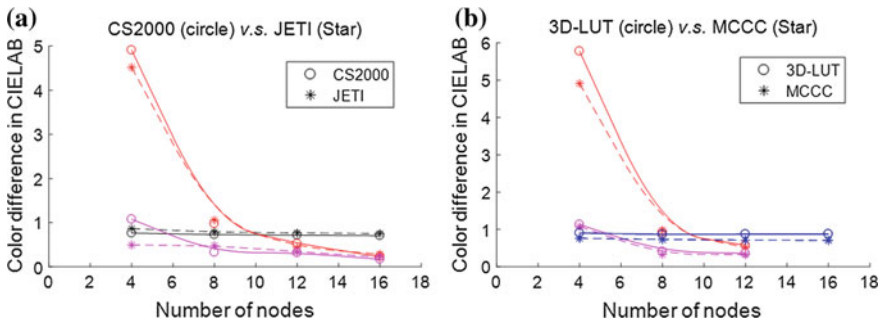

Fig. 4 **a** Comparison between JETI and CS2000, and **b** between testing datasets using GoG (red), tetrahedral interpolation (blue) and hybrid (magenta) methods (Color figure online)

JETI and CS2000. Thus from the figure, no obvious advantage could be observed by using CS2000, i.e. both instruments gave very similar results.

To be more specific, CS2000 showed a consistent advantage over JETI for GoG model, giving a small prediction color difference. For the tetrahedral interpolation method and the hybrid method, JETI performed better at first but was surpassed by CS2000 when the number of nodes increased. However, their difference was not significant.

4.3 Testing Dataset Performance

In this study, two sets of testing datasets were included. The first was Macbeth Color Checker Chart (MCCC) consisting of 24 colors. In addition to MCCC, a comprehensive dataset including 4096 test colors, i.e. 16 by 16 by 16 nodes was also established. Their digital inputs were equally spaced in R-, G- and B- channels from 0 to 255 with an interval of 17. This was to give a better evaluation of each model and was also to test whether MCCC is sufficient as a testing dataset. Their performances were compared using 3 different models, i.e. GoG, tetrahedral interpolation and the hybrid methods. Data measured by CS2000 were adopted.

Figure 4b shows how different sets of testing data would affect the testing results. It can be seen that a large number of data certainly increased ΔE^*_{ab} value, especially when less nodes were used. However, as the number of nodes increased, no obvious difference was observed, indicating MCCC was reliable to evaluate the performance of a display model.

5 Conclusions

This paper concludes typical method for display characterization. For a well calibrated LCD display, 1D method such as GoG model and PLCC model can give an acceptable characterization performance. A comprehensive 3D based method can surely improve the model accuracy but needs a tremendous amount of data, which may be not suitable for a well-behaved display. And the hybrid method takes full advantages of these 2 methods, giving an excellent performance while no further demand for testing samples.

As for different instruments, no obvious difference was found in this study, indicating the accuracy of JETI is sufficient in display characterization for such a traditional monitor. This mainly lies in the black level of display.

And for testing datasets, no significant difference was observed when using MCCC and a full dataset consisting of 4096 colors. This implies MCCC performs well and can give a good evaluation of characterization models.

References

1. Berns RS (1996) Methods for characterizing CRT displays. Displays 16(4):173–182
2. Post DL, Calhoun CS (2000) An evaluation of methods for producing desired colors on CRT monitors. Color Res Appl 25(2):90–104
3. Hung PC (1993) Colorimetric calibration in electronic imaging devices using a look-up-table model and interpolations. J Electron Imaging 2(1):53–61
4. Kang HR (1995) Comparisons of three-dimensional interpolation techniques by simulations. In: Proceedings of SPIE—the international society for optical engineering, pp 104–114
5. Motomura H, Fumoto T, Yamada O, Kanamori K, Kotera H (1994) CIELAB to CMYK color conversion by prism and slant prism interpolation. In: Proceedings of method color and imaging conference, pp 156–158
6. Kasson JM, Plouffe W, Nin SI (1993) Tetrahedral interpolation technique for color space conversion. In: Proceedings of SPIE—the international society for optical engineering, 1909, pp 127–138

Study on the Relation Between Smartphone Icons with Negative Emotion and Color Influence Factors

Yanjun Song, Qiang Wang and Yan Shi

Abstract Emotion design for the user interface, especially the user interface of smartphones, directly affects user interaction, and is influencing the future of design development. Negative emotions are negative emotional experience in psychology, such as fear, sadness and anger. However, few researches on smartphone icons with negative emotion are proposed. In this study, questionnaire, frequency analysis and multiple regression analysis were utilized to analyze the relation between smartphone icons with negative emotion and the specific role of four color influence factors: memory color, visual comfort, color saturation and color image, on emotional arousal. The outcome suggests the particular design focus and design principle on smartphone icons with different types of negative emotion.

Keywords Icon design · Negative emotion · Color

1 Introduction

Smartphones and user interface has gradually penetrated into the public life. The information conveyed by smartphone icons and the expressed content and emotion directly affect user's acceptance of the product. Based on emotion cognition, emotion design dose not only ensure the basic function of design objects, but also arouse user's various emotion by conveying required information, which set its sights on satisfying user's inner affection needs and creating affective experience. Currently, most scholars prefer the study of affective design, which can provide user with positive products to arouse positive emotion making them feel pleasure [1].

In fact, Ekman's research findings claimed that negative emotion predominates among five basic human emotions [2]. The research of Steven Fokkinga and Pieter Desmet investigated negative emotions' role in product experience [3]. And

Y. Song (✉) · Q. Wang · Y. Shi
School of Media and Design, Hangzhou Dianzi University, Zhejiang, China
e-mail: 262407337@qq.com

P. Zhao et al. (eds.), *Applied Sciences in Graphic Communication and Packaging*, Lecture Notes in Electrical Engineering 477,
https://doi.org/10.1007/978-981-10-7629-9_3

Fig. 1 Smartphone icons expressed various emotion

negative emotions can not only provide users with a narrower field of attention so as to make users experience a much slower time, but also improve user's visual contrast sensitivity. Negative stimulus allows user to focus longer on the products and enhance motivations of user's behavior [4]. Furthermore, scholars put forward a method which negative emotions help enrich product experiences and improves user's experience effectively [5]. As the icons show in Fig. 1, icons can express various emotions, while information from smartphone icons may be influenced by colors [6]. However, few related studies have been conducted in this field. It's important to aim at arousing negative emotions, discuss various color influence factors at the same time, provide reliable reference for designer on smartphone icons with negative emotions through reasonable modeling, which is worth study.

2 Choice of Color Preference Factors

Recently scholars at home and abroad have studied the effect of color influence factors on negative emotion and the method of choosing appropriate factors systemically. P. S. Hong from Taiwan discussed the relation between emotional imageries of commercial images and color preference factors [7], Hong's team chose six color influence factors by integrating them in experiment on user's preference, and then obtained highly reliable outcome, which verified that color has fulfilled some of our needs, while we always do not consciously realize this [6]. As research in emotion design demonstrated that many color factors influence the products' emotional expression as well as reflects these factors had an effect on negative emotion to a great extent. Color design that can convey emotions accurately is generally based on good interaction design work.

Color design is an interdisciplinary field of chromatics and design science and this study took the experience of Hong's team on choosing appropriate color influence factors for reference. After dissecting the relation between color design and user's negative emotions, how interaction design was affected by color-guided consciousness, combining features of smartphone icons, this study chose four color influence factors: memory color, visual comfort, color saturation, color image.

Memory color comes from impression of colors deepened in human's long term practice, which lead to the formation of inherent cognition of these colors. Yendrikhovskij proved that human prefer imageries with memory color familiar to them, rather than actual colorimetrical content [8]. Images with memory color makes people feel more natural, which exert effect on user's emotional response

and conduct association with individual emotion factor. Thus, we could infer memory color could be an influence factor of negative emotion.

Visual comfort is the subjective perceptions when people face images. Scholar Sagawa intensively studied whether visual comfort can influence user's preference of color [9] and developed a factor in interdisciplinary field of psychology and visual research which can evaluate user's psychological perception. Visual comfort therefore became an influence factor.

Color saturation is the colorfulness of a color relative to its own purity in chromatics. This general concept is a more objective evaluation standard compared with other factors. User's sensibility of color saturation related to individual color preference, Sagawa studied how average colorfulness of image affects user's visual experience [9]. Hence this factor made the study more comprehensive.

Color image comes from user's psychological perception, when observing colors, as part of the user's perception caused by the association of objects linked to color. Different individuals have various associations, which may arouse negative emotion through reflex. Thus, color image could be one of the color influence factors of user's negative emotion.

3 Experiment Design and Data Analysis

In order to verify the effects of four color influence factors previously proposed on arousing users' various negative emotions, this study did an experimental method design, which contained hypothetical descriptive statistic, and a questionnaire design. Then it reported the qualitative analyses of the relative impacts of four influence factors through frequency analysis and multiple regression analysis based on experimental data.

3.1 Experimental Method Design

Three groups of application icons separately indicating negative emotions: fear, sadness, anger, set by three graduate students who studied user interface design of mobile devices, with each group had a total of 80 icons in use. These icons that had duplicate content, odd shapes, disturbance items or familiar to public were removed and leave a total of 30 icons each group. In the pretest, 5 most powerful icons arousing negative emotion were picked up from each group by subjects. As shown in Fig. 2, each type of negative emotions is represented by 5 application icons. Then, based on three groups of icons, an investigation was conducted for four color influence factors through the questionnaire.

In this study, areas of Jiangsu and Zhejiang provinces and Shanghai district are taken as a gathering place to collect test data. 92.3% subjects are adult aged between 20 and 30. Before filled out the questionnaire, a simple color test was set

Fig. 2 Test icons with three negative emotions

for subjects. None of subjects suffered color perception loss. All procedures performed in studies involving human participants were in accordance with the ethical standards of the institutional and national research committee and with the 1975 Helsinki declaration and its later amendments or comparable ethical standards. Informed consent was obtained from all individual participants included in the study. Research set a 5-point scale of 1–5 to test the degrees of subjects' approval on icons with three negative emotions, two 5-point scales of 1–5 to test the degree of significance on icons with three negative emotions for every color influence factor.

3.2 Data Analysis and Results

In this research, four color influence factors were used as independent variables, degree of negative emotional arousal was used as dependent variable, which evaluated the contributions of each factors on emotional arousal. Mathematical models for test were developed by multiple regression analysis. With satisfying determination condition and substitution of independent variable into model, the predictive value was calculated, consequently infer the predictive model that could predict the degree of negative emotional arousal. Multiple regression analysis model of negative emotional experience, obtained by software Statistical Product and Service Solution, is used as algorithm model. The results of data analysis were as follows (Fig. 3):

(1) Coefficient of determination R^2 is defined as the sum of regression square divided by the sum of variation, employed for inspection of reliability of questionnaire. In statistics, with greater than 0.8 of R^2 coefficient of determination, model has good reliability and validity. In this research, with 0.989 of

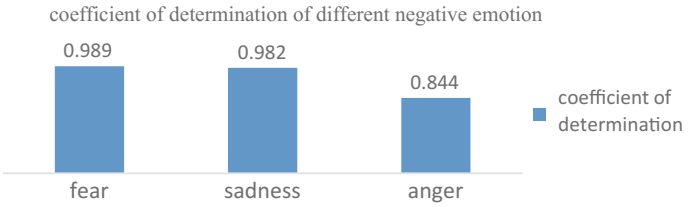

Fig. 3 Coefficient of determination of different negative emotion

R^2 is fear model, 0.982 of R^2 is sadness model, 0.844 of R^2 is anger model, which confirmed that the regression reached statistical significance and the models had highly fitting and forecasting precision.

(2) Every two scales as pair to investigate one color influence factor, the average of two scores was taken as one independent variable, which enhances the accuracy of analysis. Standardized coefficients Beta from result of analysis was used to compare four color influence factors' relative impact on various negative emotions.

According to standardized coefficients Beta of each negative emotion (Tables 1, 2 and 3), four color influence factors were sorted by their significance of the regression on arousing different negative emotion (Table 4).

Table 1 Results of multiple regression analysis for fear icons

Fear icons	Unstandardized coefficients		Standardized coefficients	t	Sig.
	B	Std. Error	Beta		
Constant	−2.139	0.052		−41.237	0
Memory color	0.489	0.015	0.381	32.995	0
Visual comfort	0.47	0.012	0.42	39.163	0
Color saturation	0.452	0.012	0.369	36.649	0
Color image	0.452	0.011	0.437	42.949	0

Table 2 Results of multiple regression analysis for sadness icons

Sadness icons	Unstandardized coefficients		Standardized coefficients	t	Sig.
	B	Std. Error	Beta		
Constant	−2.06	0.067		−30.867	0
Memory color	0.49	0.025	0.313	19.899	0
Visual comfort	0.473	0.022	0.352	21.611	0
Color saturation	0.421	0.023	0.275	18.678	0
Color image	0.419	0.02	0.31	20.485	0

Table 3 Results of multiple regression analysis for anger icons

Angry icons	Unstandardized coefficients		Standardized coefficients	t	Sig.
	B	Std. Error	Beta		
Constant	1.187	0.13		9.105	0
Memory color	0.482	0.056	0.404	8.646	0
Visual comfort	0.135	0.052	0.134	2.599	0.01
Color saturation	0.453	0.05	0.412	9.002	0
Color image	0.179	0.046	0.184	3.889	0

Table 4 Factors' rank on impact of negative emotional arousal

Factors	Emotion			
	Memory color	Color comfort	Color saturation	Color image
Fear	2	3	1	4
Sadness	2	4	1	2
Anger	3	1	4	2

Note figures represent the degree of influence, '4' is most significant

Table 5 Multiple regression equation of three negative emotions

Emotion	Multiple regression equation
Fear	$Y = 0.381X_1 + 0.42X_2 + 0.369X_3 + 0.437X_4 - 2.139$
Sadness	$Y = 0.313X_1 + 0.352X_2 + 0.275X_3 + 0.31X_4 - 2.06$
Anger	$Y = 0.404X_1 + 0.134X_2 + 0.412X_3 + 0.184X_4 - 1.187$

X_1 = memory color, X_2 = visual comfort, X_3 = color saturation, X_4 = color image

The results showed that four factors' relative impacts had obvious difference effects in three negative emotions. In order to create fear icons, color image should be paid more attention, which arouses user's association of horror and meanwhile good visual comfort was crucial. For sadness icons, color comfort had highest significance on emotional arousal. When designing anger icons, color saturation was most important. And the memory color should not be ignored since its significance is only 0.08 lower than color saturation, more dependent than others.

(3) The regression analysis was used to identify a more specific relationship among four color influence factors and icons' performance. For the degree of negative emotional arousal, the following multiple regression equation (Table 5) is obtained. These equations can be used to describe a quadratic curve.

4 Conclusions

This study investigated the relation between four color influence factors: memory color, color comfort, color saturation, color image and common negative emotions in icon design. It took universal mobile devices for instance, with statistics and evaluation conducted via questionnaires and multiple regression analysis, whose results of the analysis are applied to the adults aged 20–30. The more important influence factors should be handled with priority based on different negative emotion, when icon designers expect to get good user evaluation of emotion arousal. The design solutions obtained in this study will greatly aid designers in emotion design and color design of icons for smartphones. The results could be readily employed by designers to create appropriate icons and improve the user emotional experience. Evaluation method used in this study can be applied in other influence factors as well.

Acknowledgements This research was supported by the Zhejiang Provincial Natural Science Foundation of China (Grant No. LQ14E050010), and the Social Science and Humanity on Young Fund of the Ministry of Education (Grant No.16YJC760047).

References

1. Rou W (2014) Review on contemporary emotion design study. Design 06:25–26
2. Ekman P (1999) Basic emotions. John Wiley & Sons, Ltd., U.K
3. Fokkinga SF, Desmet PMA (2012) Darker shades of joy: the role of negative emotion in rich product experiences. Des Issues 28(4):42–56
4. Rucker Derek D, Petty Richard E (2004) Emotion specificity and consumer behavior: anger, sadness, and preference for activity. Motiv Emot 28:3–21
5. Fokkinga SF, Desmet PMA (2013) Ten ways to design for disgust, sadness, and other enjoyments: A design approach to enrich product experiences with negative emotions. Int J Des 7(1):19–36
6. Norman D (2005) Emotion design. Basic books
7. Hong BS (2009) The relation between emotional imageries of commercial images and color preference factors. J Des 14(4)
8. Yendrikhovskij SN, Blommaert FJJ, de Ridder H (1998) Optimizing color reproduction of natural images. In: The sixth color imaging conference: color science, systems, and applications. Society for Imaging Science and Technology, pp 140–145
9. Sagawa K (1999) Visual comfort to colored images evaluated by saturation distribution. Color Res Appl 24(5):313–321

Relationship of Different Scales for Evaluating the Quality of LED Lighting

Ke Liu, Yanfen Zhang, Qiang Liu, Guo Cao, Qingming Li and Zheng Huang

Abstract Existing studies used different scales to evaluate the quality of LED lighting by psychophysics experiments, which viewed specific objects. It is believed that for universal lighting, diverse objects are needed to evaluate color quality. In order to produce a suitable factors space to evaluate the quality of universal lighting, a psychophysics experiment was conducted, which used objects of different color or attribute. The experiments were carried out in darkrooms. In total, 44 observers viewed seven groups of objects to evaluate lighting quality. In this paper, factor analysis was used to reduce the large number of scales into fewer underlying independent factors. The results showed that objects of different color or attribute had an impact on visual perception, and three factors dominate visual perceptions: Attraction, Vividness and Warmth. Basing on this finding, a three-factor space was defined. The work was intended to set up a three-factor space as the help for the construction of LED lighting evaluation and application methods.

Keywords Scale · Factor analysis · LED lighting quality

1 Introduction

The LED technology was gradually accepted and applied in many lighting scenes. However, its specific radiation distribution pattern over the visual spectrum differed from those of standard sources raised questions about conventional CIE colorimetry

K. Liu · Q. Liu (✉) · Q. Li · Z. Huang
School of Printing and Packaging, Wuhan University, Wuhan 430079, China
e-mail: liuqiang@whu.edu.cn

Y. Zhang
Media Communication System, Dongguan Polytechnic, Dongguan 523808, China

Q. Liu
Shen Zhen Research Institute, Wuhan University, Shenzhen 518000, China

G. Cao
Shen Zhen Fu Tian N1 Digital Building Studio, Shenzhen 518000, China

P. Zhao et al. (eds.), *Applied Sciences in Graphic Communication and Packaging*, Lecture Notes in Electrical Engineering 477,
https://doi.org/10.1007/978-981-10-7629-9_4

and CRI calculation methods [1]. As some studies showed, CRI metric was not always provide a reliable description of visual perception of color rendering, especially in the case of white LEDs [2–4]. In order to evaluate lighting quality better, existing studies used different scales by psychophysics experiments and showed scales played an important role [5–10].

For example, Zhai [5] clarified three dominating visual factors including Comfort, Vividness and Definition determine the quality of LED lighting for observing fine art paintings; Jost-Boissard [6] suggested that it should be possible to find LED blendings that perform better than halogen or fluorescent in terms of suitability and, in many cases, more attractive in color rendering (i.e. preferred). However, each study used specific objects in order to clarify the relationship of scales, for instance, paintings as objects by Zhai [5], color samples by Ou [8], and fruits and vegetables by Jost-Boissard [6]. In this case, the factors space for specific objects did not work well for universal LED lighting. It is believed that for the universal lighting, diverse objects are needed to evaluate lighting quality.

Starting out from the above considerations, we used objects of different color or attribute and conducted a psychophysics experiment. This aims to produce a suitable factors space to evaluate the quality of universal lighting. The experiment was carried out in darkrooms. Philips Hue intelligent LED was used as the light source in the experiment. One environment was in a standard laboratory suitable for observation and another was in a museum (Wanlin Art Museum, Wuhan University). In total, 44 observers viewed seven groups of objects to evaluate lighting quality. Besides, a variety of objects were selected because the subjective need in color quality of illumination depended on the character of the illuminated object and its familiarity to the observer [11, 12]. Therefore, the aims of the study are as follows: (1) To verify the results of previous experiments and continue studying the relationship of scales; (2) To produce factors space in order to provide help for the construction of LED lighting evaluation and application methods.

2 Experiment

The experiments were approved by the Ethics Committee of Wuhan University. All procedures followed were in accordance with the ethical standards of the responsible committee on human experimentation (institutional and national) and with the Helsinki Declaration of 1975, as revised in 2008 (5). Informed consent was obtained from all observers for being included in the study.

2.1 Environment

In the laboratory, the light source was installed at the top of a light box, with a size of 60 cm × 65 cm × 89 cm. The surrounding and bottom surfaces of the booth were coated with medium gray matt paint (Munsell N5). Figure 1 shows the viewing conditions.

The experiment set the LED light source correlated color temperature (CCT) to 3500 K in the laboratory and 3500 and 6500 K in the museum. The illuminance was set for 200 lx. 6500 K as a higher CCT was selected, in order to form a validation with Zhai [5].

2.2 Objects and Observers

Objects were divided into familiar and unfamiliar in the experiment. Familiar objects included yellow, red, green, multicolored fruit and vegetables, and flowers. Unfamiliar objects included the yellow-white paper of the calligraphy work and three Dunhuang murals copied. There were four gray and non-reflective discs with the same size to contain fruits and vegetables. Most of them kept consistent with the studies by Jost-Boissard [6], Zhai [5], and Liu [7].

Forty-four Chinese observers aged 18–24 participated in the experiment. In the laboratory, there were fifteen male and fifteen female observers. There were seven male and seven female in the museum. It was intended to be able to compare the results between genders. They were from school of the Printing and Packaging, Wuhan University, and each observer was first tested for their color vision by the Ishihara test.

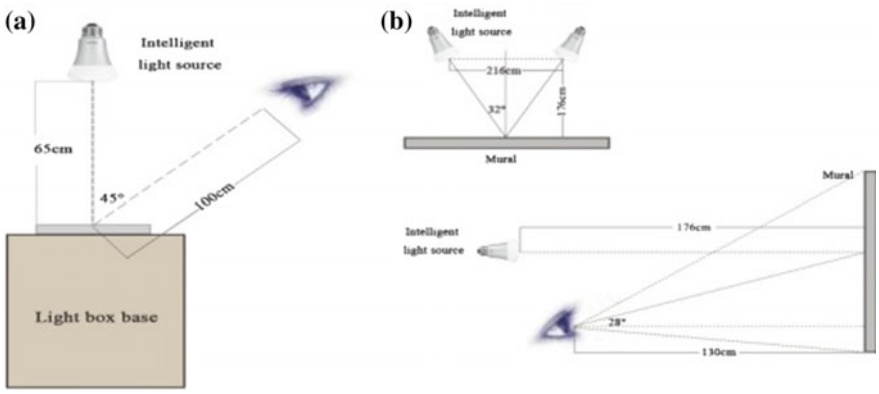

Fig. 1 The viewing condition **a** of the laboratory **b** of the museum

2.3 Scales

12 pairs of scales were used in the experiment. Four of them were associated with the appearance of the objects (Warm/Cool, Fresh/Stale, Bright/Dark, Colorful/Dull), and the others were associated with the atmosphere of the space (Active/Negative, Pleasant/Unpleasant, Attractive/Repel, Soft/Hard, Lively/Boring, Relaxed/Tense, Artistic/Business, Polite/Vulgar), introduced by Zhai [5]. The present study investigated the scales that have been frequently used in early studies [4–7]. Each was scored using a seven-point rating method [13]. Scores 1–3 and −3–1 stood for the range of the positive and negative perceptions, while score 0 stood for there was without positive and negative perceptions.

2.4 Procedure

The experiment was carried out by the experimenter reading out questions that were answered orally by the observers. We did not ask the observers to write an answer for each question. This was to avoid the incomplete chromatic adaption likely to be caused by the observer staring at a questionnaire printed on white paper. In the laboratory, 30 observers evaluated a total of six groups of fruits and vegetables, flowers and calligraphy work using 12 scales under the lighting source with 3500 K. In the museum, 14 observers evaluated three murals using the same 12 scales under the lighting source with 3500 and 6500 K. The orders of the objects in each lighting condition and of the scales for assessing each object were all randomized.

3 Result and Discussion

3.1 Gender Difference

The Pearson product–moment correlation coefficient was used in this study as a measure of gender difference in among 12 scales, based on all objects data under 3500 K, where 3500 K data showed a normal distribution. The coefficients range from −1 to 1, where −1 represents a perfectly negative correlation and 1 a perfect positive correlation. The coefficient of zero indicates a completely nonlinear relationship between two variables.

Active/Negative and Relaxed/Tense scales have low correlation coefficients, 0.47 and 0.40. This suggests that gender difference seem to exist in the two scales Active/Negative and Relaxed/Tense. It is found that the most deviate object on Relaxed/Tense is the red fruits and vegetables, which has a score for male −0.6 and female 1.34. The green fruits and vegetables are most deviate object on Active/

Negative for male −0.27 and female 1.07. Whereas, Most of the correlation coefficients are fairly high with the mean value of 0.7, showing that there is a little gender difference in most scales, consistent with Ou [8].

3.2 Impact of CCT in the Museum

For each scale, the mean rating is calculated. The larger the number is, the stronger the perception to the positive word. When CCT increases, the Warm perception decreases sharply and the Bright perception increases the fastest. In other words, the most obvious impact is that an increase of CCT would lead to a cooler perception, which agrees with our earlier findings [5]. Besides, an increase of CCT would make the environment brighter.

By using the principal component analysis method, three factors are extracted from the 3500 K data, accounting for 70% of the total variance. They are labeled Components 1, 2, and 3. From the 6500 K data three factors are extracted which account for 76% of the total variance. Both the result of 3500 and 6500 K have Pleasant, Lively, Polite and Fresh in Component 1; Artistic in Component 2; Colorful in Component 3. This indicates that 3500 and 6500 K have similar underlying factors of visual perceptions, although several scales are found to fall into different categories such as Active, Relaxed and Warm. Therefore, 6500 K doesn't require analyzed separately.

3.3 Factor Analysis

The next analysis applied to the data in 3500 K is factor analysis, which is intended to reduce the large number of scales into fewer underlying independent dimensions. These could be used as the control parameters for lighting. Principal component analysis and orthogonal rotation were applied in the factor analysis.

3.3.1 Object Difference

To investigate the differences between familiar and unfamiliar objects, the factor analysis is conducted by combining five familiar objects data and two unfamiliar objects data. Three factors are extracted separately from the familiar and unfamiliar objects data, labeled Components 1, 2 and 3. There was one thing to point that Relaxed falls into another factor except three Components for familiar objects, whereas, in Component 2 for unfamiliar objects. When subjects are unfamiliar such as murals and paintings, Relaxed is different from when subjects are familiar including color samples, fruits and vegetables, also noticed by Zhai [5] and Ou [8]

According to the above study, three factors plots are established from the extraction data. The three axes are determined by three factors. In Figs. 2 and 3 present the factor plots for the familiar and unfamiliar objects, respectively.

As shown in these diagrams, most scales, except Colorful, Pleasant and Artistic, are found at similar locations in the two plots. In the familiar objects plot, Colorful is located near Attractive, Lively and Polite, whereas in the unfamiliar objects plot Colorful is located far from all the other scales. This suggests more "colorful" objects of familiar show more "attractive", "lively" and "polite". The familiar objects plot shows that Pleasant is near Fresh and Polite, whereas in the unfamiliar objects plot Pleasant is far from all the other scales except Relaxed. This shows "fresh" and "polite" objects of familiar are more "pleasant", while "relaxed" objects of unfamiliar are more "pleasant". Artistic is near Relaxed and Polite in the familiar objects plot, whereas near Soft in the unfamiliar objects plot. This suggests that "relaxed" or "polite" objects of familiar give an "artistic" perception, whereas "soft" objects of unfamiliar give an "artistic" perception.

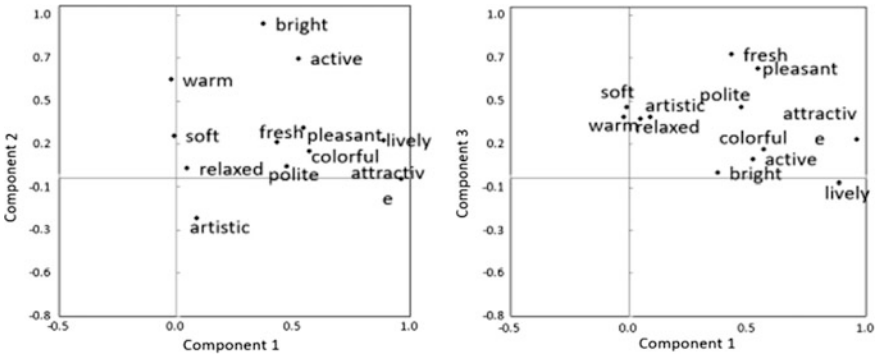

Fig. 2 Three-factor plot of the 12 emotional scales for familiar objects

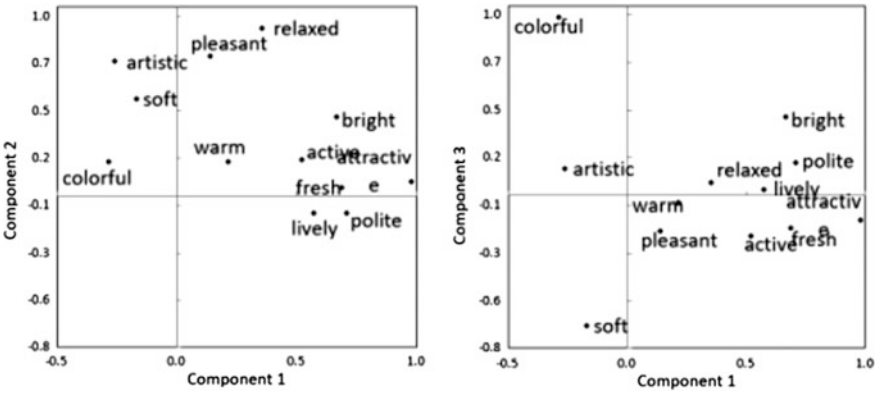

Fig. 3 Three-factor plot of the 12 emotional scales for unfamiliar objects

3.3.2 Factor Extraction

This process excludes four scales, including Colorful/Dull, Pleasant/Unpleasant, Artistic/Business, and Relaxed/Tense. The reason is that Colorful/Dull, Pleasant/Unpleasant, Artistic/Business and Relaxed/Tense produce object difference between familiar and unfamiliar objects, as indicated in the previous section. Besides, Relaxed/Tense produces gender difference.

Three factors are extracted from the remaining color emotions. The names of each factor are based on the word pairs closely related, and they are named Attraction, Vividness and Warmth, respectively. They explain about 60% of the variance, as summarized in Table 1.

The results in Table 1 show that the Attraction factor is more related to the atmosphere perception of the lighting, while Vividness and Warmth factors are more related to the appearance of the objects. Vividness is an important factor about contrast information of objects used in the experiment such as brighter and fresher, which agrees well with Zhai [5]. Warmth factor has been one of the most important scales in early studies [8, 10]. Another factor is Soft and is on its own having a low-variance contribution.

3.3.3 Coordinate Determination

The three factors Attraction, Vividness and Warmth are used to define the three axes in the space. Coordinates of three factors are determined by factor scores. Figure 4 plotted the seven objects along the three factors. The objects at the central area evoke only a small amount of scales and those located at the outer layer evoked strong scales.

At a later stage, the data relating to each individual object are used to conduct factor analysis. The result shows a consistence with most scales among red, multicolored fruits and vegetables and flowers, because the red components of the multicolored object have a considerable influence [6]. Besides, it is found that

Table 1 Factor matrix of scales excluding Colorful/Dull, Pleasant/Unpleasant, Artistic/Business, and Relaxed/Tense

Factor meaning (60%)	1(25%) Attraction	2(19%) Vividness	3(16%) Warmth
Attractive	0.754	0.322	0.270
Polite	0.709	0.037	0.117
Lively	0.683	0.443	0.149
Bright	0.050	0.770	0.067
Active	0.440	0.556	0.318
Fresh	0.423	0.516	0.059
Warm	0.052	0.226	0.970
Soft	0.239	−0.005	0.378

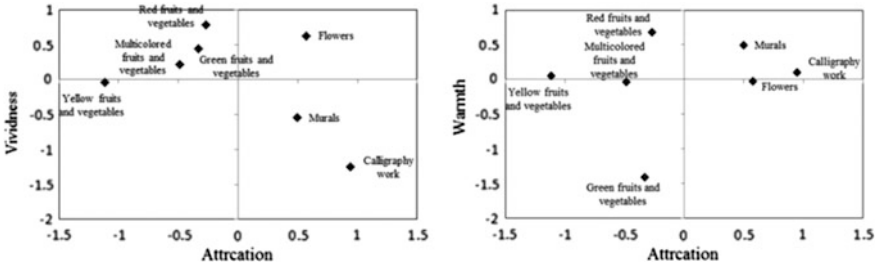

Fig. 4 The three-factor space developed in this study, where the seven objects are plotted along the three factors: Attraction, Vividness and Warmth

objects of different color or attribute had an impact on visual perception. This can be due to the fact that color or attribute for each object is different, and observers evaluate color quality on the basis of color or attribute.

4 Conclusions

A psychophysics experiment was carried out to evaluate color quality of familiar and unfamiliar objects, through which aimed to study the inner relationship of scales and to produce factors space.

It was found that gender difference seem to exist in Active/Negative and Relaxed/Tense perceptions, while not exist in most scales. Also, most scales were consistent in 3500 and 6500 K data, suggesting that there were similar underlying factors of visual perceptions in 3500 and 6500 K.

12 scales were compared between three-factor plot for familiar objects and three-factor plot for unfamiliar objects. Most scales were found at similar locations in the two plots, except Colorful, Pleasant and Artistic.

(a) Colorful: more "colorful" objects of familiar showed more "attractive", "lively" and "polite" while this tendency did not occur to unfamiliar objects.
(b) Pleasant: "fresh" and "polite" objects of familiar were more "pleasant", while "relaxed" objects of unfamiliar were more "pleasant".
(c) Artistic: "relaxed" or "polite" objects of familiar gave an "artistic" perception, whereas "soft" objects of unfamiliar gave an "artistic" perception.

The above three scales and Relaxed were excluded in factor extraction due to the fact that they produce object difference and Relaxed produce gender difference. Then factor extraction revealed three dominating visual factors: Attraction, Vividness and Warmth. These three determine the quality of universal LED lighting. Besides, the three-factor space was defined, which three axes were based on the three factors Attraction, Vividness and Warmth. In later stage, the data relating to each individual object were used to conduct factor analysis. The result

showed a consistence with most scales among red, multicolored fruits and vegetables and flowers. And, the inconsistence between the factors for each individual object and the factors for all the objects verified that objects containing different color or attribute are suitably used to evaluate the quality of universal lighting. The work was intended to set up a three-factor space as the help for the construction of LED lighting evaluation and application methods. In fact, it is believed that lighting quality can be impacted by many other factors including CCT, illuminance level and the observers' characteristics (cultural background). The next step is to focus on existing experimental methods into the actual lighting environment, with hope to enhance the level of theoretical analysis on the basis of improve the data.

Acknowledgements The authors acknowledge the support of the Shenzhen basic research project (grant No. JCYJ20150422150029093) and the Young Talent Project of Wuhan City of China (Project No. 2016070204010111).

References

1. International Commission on Illumination (1995) Method of measuring and specifying colour rendering properties of light sources. CIE No. 13.3-1995, vi, p 16. http://doi.org/10.1002/col.5080200313
2. Bodrogi P, Csuti P, Szabo F, Schanda J (2004) Presented at CIE expert symposium on led light sources: physical measurement and visual and photobiological assessment. In: CIE expert symposium on LED, pp 0–16. http://doi.org/10.1002/col.10242
3. Cie TC (2007) TC 1-62: colour rendering of white LED light sources. CIE 177:2007
4. Schanda J, Sandor N (2003) Presented at international lighting and colour conference. Cape Town, South Africa, pp 76–85
5. Zhai QY, Luo MR, Liu XY (2015) The impact of illuminance and colour temperature on viewing fine art paintings under LED lighting. Light Res Technol 47(7):795–809
6. Jost-Boissard S, Fontoynont M, Blanc-Gonnet J (2009) Perceived lighting quality of LED sources for the presentation of fruit and vegetables. J Mod Opt 56(13):1420–1432
7. Liu Q, Tang MH (2017) Influence of light source and paper color on the exhibiting preference of traditional calligraphy, 0593 (November 2016). http://doi.org/10.3964/j.issn.1000-0593(2016)11-3664-07
8. Ou LC, Luo MR, Woodcock A, Wright A (2004) A study of colour emotion and colour preference. part i: colour emotions for single colours. Color Res Appl 29(5):381–389
9. Osgood CE, Suci GJ, Tannenbaum PH (1958) The measurement of meaning. Am Sociol Rev 23(2):227–228
10. Kobayashi S (1981) The aim and method of the color image scale shigenobu kobayashi. 6 (2):2–3
11. Mizokami Y, Kamesaki C, Ito N, Sakaibara S, Yaguchi H (2012) Effect of spatial structure on colorfulness adaptation for natural images. J Opt Soc Am A 29(2):A118–127
12. Liu A, Tuzikas A, Žukauskas A, Vaicekauskas R, Vitta P, Shur M (2012) Cultural preferences to color quality of illumination of different objects
13. Watson D, Clark LA, Tellegen A (1988) Development and validation of brief measures of positive and negative affect: the panas scales. J Pers Soc Psychol 54(6):1063–1070

Performance Comparison of Uniform Color Spaces by Integrating into a Tone Mapping Operator

Muhammad Usman Khan, Muhammad Safdar, Muhammad Farhan Mughal and Ming Ronnier Luo

Abstract Typically, tone mapping operators are used to map luminance of high dynamic range (HDR) scenes to that of a displayable range. The goal of this study was to compare the performance of different uniform color spaces (CIELAB, IC_TC_P, and Ja_zb_z) by integrating them into a tone mapping operator. The Contrast Limited Adaptive Histogram Equalization-based Tone Mapping Operator (CLAHE-TMO) was used here. For this purpose, the HDR radiance map of a given scene was first constructed from multiple exposures of the scene captured by using an ordinary RGB camera. The radiance map was then transformed to a uniform color space for the application of TMO on its lightness channel. A psychophysical experiment was conducted using pair comparison method to compare performance of different uniform color spaces. Tone mapped images were compared in four different contexts: preference, naturalness, contrast, and texture details. The experimental results are reported here.

Keywords High dynamic range · Adaptive histogram equalization
Uniform color spaces · Tone mapping

1 Introduction

High dynamic range (HDR) imaging is typically used to capture scenes with wide-range of luminance. A human eye, at a single adaptation time, can perceive a dynamic range of up to 5 orders of magnitude (difference in powers of 10 between highest and lowest luminance level) [1]. Currently available consumer cameras can capture a dynamic range of up to 3 orders of magnitude of luminance however this

M. U. Khan · M. Safdar · M. F. Mughal · M. R. Luo (✉)
State Key Laboratory of Modern Optical Instrumentation,
Zhejiang University, Hangzhou, China
e-mail: m.r.luo@zju.edu.cn

M. R. Luo
School of Design, University of Leeds, Leeds, UK

P. Zhao et al. (eds.), *Applied Sciences in Graphic Communication and Packaging*, Lecture Notes in Electrical Engineering 477,
https://doi.org/10.1007/978-981-10-7629-9_5

range can be increased by capturing multiple images with different exposure times, this technique is called temporal bracketing [1, 2]. But the currently available displays can only display 2–3 orders of magnitudes of luminance i.e., not capable of displaying large range of luminance [1].

Tone mapping provides a solution for the problem to display contents with high dynamic range of luminance. A number of tone mapping operators (TMOs) have been proposed for this purpose categorized into local and global tone mapping operators [3]. Yoshida et al. [3] evaluated the performance of different local and global TMOs and describe their pros and cons e.g., tone mapping by using global operators reproduce brighter images and they have better overall contrast compared with local operators, whereas, local operators can reproduce more details in dark regions. Naturalness was another important aspect of tone reproduction in which local operators and a histogram equalization base global operator by Ward et al. [4] performed best. Global operators have an additional advantage of low computational cost compared with local ones. In this study, Contrast Limited Adaptive Histogram Equalization-based Tone Mapping Operator (CLAHE-TMO) was used by applying histogram equalization on Lightness channel [5]. Design procedure of CLAHE-TMO provides us a flexibility to test other uniform color spaces such as IC_TC_P [6] and Ja_zb_z [7] which were developed for HDR imaging applications. The IC_TC_P is a proposal by Dolby Vision and Ja_zb_z was recently proposed by Safdar et al. [7] for HDR and wide gamut imaging applications.

Before tone mapping, RGB radiance map was first transformed to XYZ tristimulus values and then to ISO/CIE standard uniform color space named CIELAB. The CLAHE-TMO then was applied for adaptive histogram equalization on the lightness channel and then tone maps it to a low luminance range [5, 8]. The tone-mapped image is then transformed back to displayable RGB space.

The next section explains the method used to perform tone mapping followed by experimental results and discussions. The conclusions are drawn in the end.

2 Method

The aim of the study was to compare performance of different uniform color spaces which were integrated into a tone mapping operator named CLAHE-TMO where HDR images were used as input. These HDR images were created by using multiple exposures of the same scene. Fairchild [9] did an HDR photographic capturing and provided a database of multi-exposure images of the scenes (nine exposures captured with different exposure times) along with their radiometric measurements at different locations in the scenes. Three of them i.e., a true exposure, an under exposed, and an over exposed exposure were chosen. Both under exposed and over exposed exposures were two stops apart from the true exposure. Selected three exposures can cover mostly used dynamic range of luminance of the real scene along with the additional benefit of less computational cost. Furthermore, image registration problem can be avoided which may occur in case of using more number of exposures.

Safdar et al. [10] developed a method to obtain HDR radiance map of the scene from multiple exposures of an ordinary RGB camera. This method was used in the current study which uses selected three exposures to convert them to HDR radiance map. Figure 1a shows the workflow. The HDR radiance map of the image was then converted to absolute XYZ tristimulus space using method proposed by Safdar et al. [10] and spatial chromatic adaptation transform (used in iCAM06 [11]) was then applied to transform the XYZ tristimulus space to the white point of the CIE standard illuminant D65. Then image in XYZ_{D65} space was transformed to the selected uniform color spaces (CIELAB, IC_TC_P and Ja_zb_z). Subsequently, the Contrast Limited Adaptive Histogram Equalization-based Tone Mapping Operator (CLAHE-TMO) was used where different color spaces were integrated into the operator. This operator applies adaptive histogram equalization on the lightness channel by first computing a transfer function for sub-regions of image lightness channel then interpolate transfer functions of neighboring regions to obtain output values for a central region, it then tone map this lightness channel to a desired low luminance range. After tone mapping, lightness channel is combined with chrominance channels of the corresponding color space to convert them back to XYZ tristimulus space and finally to displayable-RGB.

Tone-mapped images for the three selected color spaces obtained by aforementioned method are shown in Fig. 2. Figure 2a shows that when using CIELAB

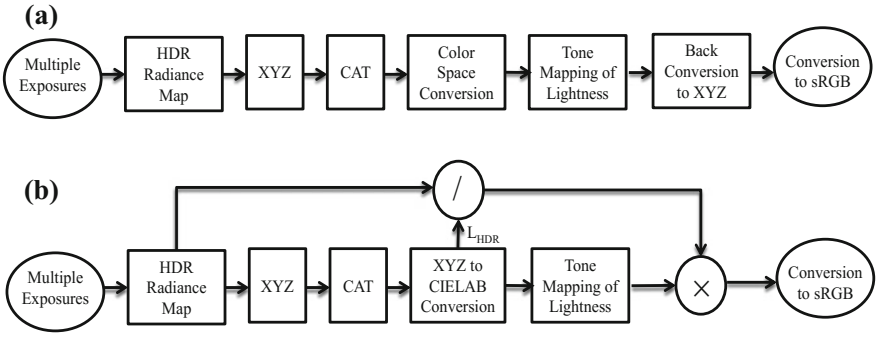

Fig. 1 **a** Workflow of the model for tone mapping, and **b** shows the workflow of the modified model (for CIELAB only)

Fig. 2 Tone mapped images obtained by process of Fig. 1a for three color spaces: **a** CIELAB **b** IC_TC_P and **c** Ja_zb_z (Color figure online)

color space with the model, colors in the tone mapped images were washed out. This problem was not observed for other two color spaces which were intended to be used for HDR applications. So, the model was modified for CIELAB color space (as depicted in Fig. 1b where we normalized the radiance map with the HDR lightness (L*) and then remapped it to a desired luminance range) to reproduce the colors in the tone mapped image. These tone-mapped images were used in the experiments along with the tone mapped images of IC_TC_P and Ja_zb_z color spaces obtained for the model shown in Fig. 1a. Tone-mapped images for CIELAB using both models are shown in Fig. 3 which clearly suggests the use of modified model for CIELAB.

3 Results and Discussions

A psychophysical experiment was conducted to compare performance of selected three color spaces. A calibrated monitor was used to display the tone-mapped images for assessment. Pair comparison method was used where observers were asked to select the best tone-mapped image, out of the two images displayed once, on the basis of preference, naturalness, contrast and texture details. A total of 10 different observers participated in the experiment. Seven different images were used which create 21 pair of images for the three color spaces. Each observer performed 84 (21×4) assessments for all four test criteria. In total 840 assessments were performed by all 10 observers.

Subject scores were transformed to Z-score (higher the better) and the test results are plotted in Fig. 4. The results clearly showed that Ja_zb_z color space outperformed CIELAB and IC_TC_P for all four criteria investigated. Two different scenes produced are shown in Fig. 5. Results showed that for the images having a white object in the scene, Ja_zb_z produced clear details in the shadow regions and also the objects were more colorful and brighter than the other two color spaces (see Fig. 5c). However,

Fig. 3 Tone mapped images for CIELAB color space following: **a** flow chart shown in Fig. 1a, **b** modified flow chart shown in Fig. 1b

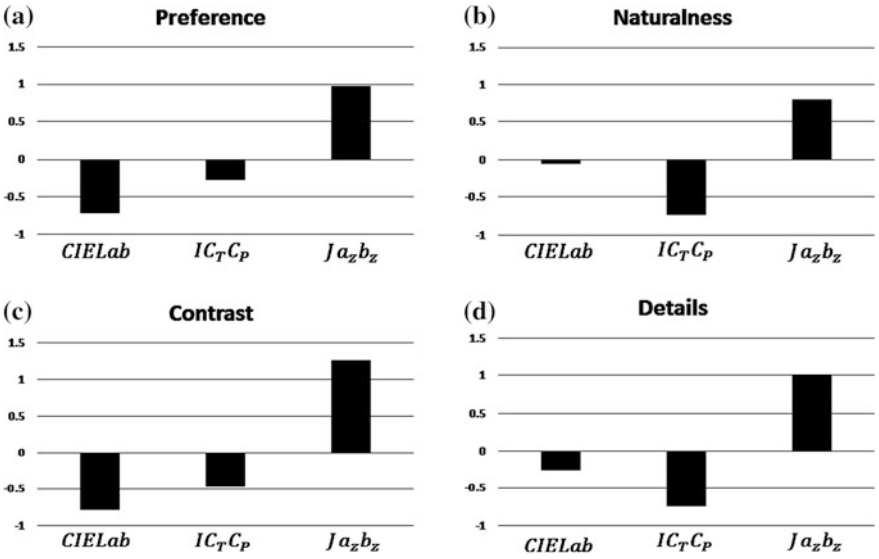

Fig. 4 Z-scores of three color spaces for: **a** Preference, **b** Naturalness, **c** Contrast and **d** Details, in the tone-mapped images

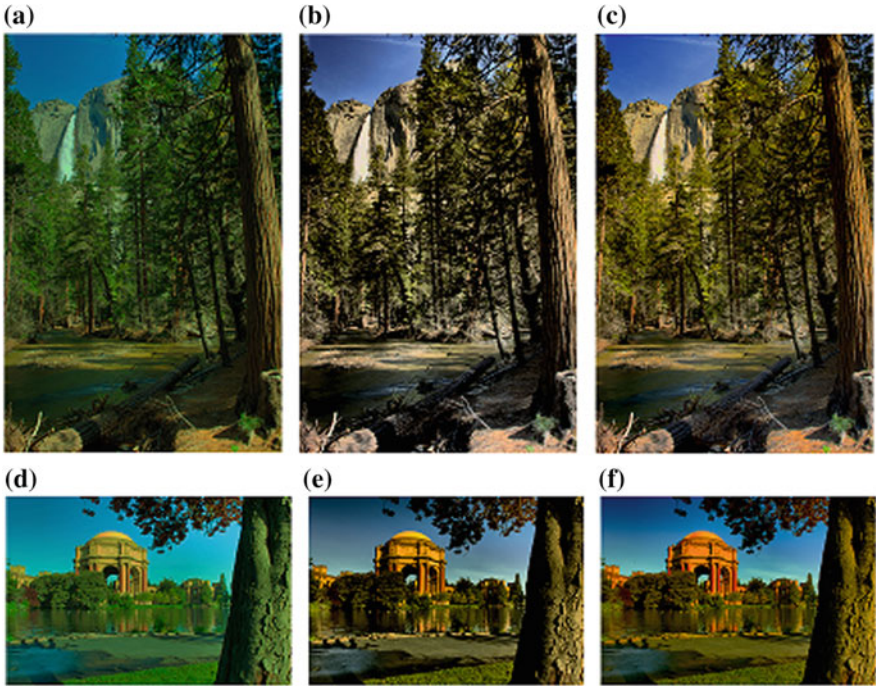

Fig. 5 Tone mapped results for **a** and **d** CIELAB, **b** and **e** IC_TC_P, **c** and **f** Ja_zb_z (Color figure online)

for the images which do not have a white object in the scene, Ja_zb_z struggled to produce true colors of the objects and also the details in the bright regions of the images were not well preserved (see Fig. 5f). The CIELAB performed consistently using the modified algorithm for different kind of scenes. Details were well produced in the bright as well as in the dark regions. Colors of the objects were also preserved to some extent, however the overall brightness and contrast in the images was low which causes the hazing effect in the images and hence reducing the quality of the results. On the other hand, performance of IC_TC_P was also affected due to an absence of a reference white object in the scene similar to Ja_zb_z, furthermore, IC_TC_P produced de-saturated colors and un-natural contrast which resulted in a loss of details in the dark regions (see Fig. 5b, e).

4 Conclusions

Performance of three different uniform color spaces was investigated by integrating them into a tone mapping operator for HDR imaging application. A psychophysical experiment was conducted and results showed that CIELAB and IC_TC_P gave reasonable performance along with their pros and cons but Ja_zb_z performed comparatively better based on four different contexts: preference, naturalness, contrast and details. Current results proved that a more perceptually uniform color space gives better performance for HDR tone mapping compared with a less perceptually uniform color space. Further, CIELAB was ranked second for naturalness and details while IC_TC_P was ranked second for preference and contrast. Hence Ja_zb_z performed best overall and should confidently be used for HDR tone mapping.

References

1. Boitard R, Pourazad MT, Nasiopoulos P, Slevinsky J (2015) Demystifying high-dynamic-range technology: a new evolution in digital media. IEEE Consum Electron Mag 4(4):72–86
2. Debevec PE, Malik J (2008) Recovering high dynamic range radiance maps from photographs. In: Proceedings of ACM SIGGRAPH (ACM), p 31
3. Yoshida A, Blanz V, Myszkowski K, Seidel HP (2005) Perceptual evaluation of tone mapping operators with real-world scenes. In: Electronic imaging, international society for optics and photonics, pp 192–203
4. Larson GW, Rushmeier H, Piatko C (1997) A visibility matching tone reproduction operator for high dynamic range scenes. IEEE Trans Visual Comput Graphics 3(4):291–306
5. Zuiderveld K (1994) Contrast limited adaptive histogram equalization. In: Graphics gems IV, Academic Press Professional Inc., pp 474–485
6. Dolby (2016) What is IC_TC_P—Introduction? White paper, version 7.1, Dolby, United States
7. Safdar M, Cui G, Kim YJ, Luo MR (2017) Perceptually uniform color space for image signals including high dynamic range and wide gamut. Opt Express 25(13):15131–15151

8. International Commission on Illumination (CIE) (2004) Colorimetry, CIE Publication No. 15, CIE Central Bureau, Vienna, Austria
9. Fairchild MZD (2007) The HDR photographic survey. In: Color and imaging conference, Society for Imaging Science and Technology. pp 233–238
10. Safdar M, Luo MR, Zhu Y, Liu XY (2016) Obtaining absolute scene luminance using HDR imaging. In: Ouyang Y et al (eds) Advanced graphic communications, packaging technology and materials, Lecture Notes in Electrical Engineering 369. Doi:https://doi.org/10.1007/978-981-10-0072-0_18
11. Kuang J, Johnson GM, Fairchild MD (2007) iCAM06: a refined image appearance model for HDR image rendering. J Vis Commun Image Represent 18(5):406–414

Spectral Image Color Separation Algorithm Based on Cellular Yule-Nielson Spectral Neugebauer Model

Shiwei Liu, Quanhui Tian, Ming Zhu and Zhen Liu

Abstract Spectral Neugebauer has become a focus because the model has specific physical meaning among all the spectral characteristic model of output devices. In order to improve the precision of the model, Spectral Neugebauer was modified by cell-element and Yule-Nielson exponent, which is called the Cellular Yule-Nielson Spectral Neugebauer (abbreviated as CYNSN). Although CYNSN forward model accuracy is high, but the precision and the efficiency of reverse model (that is, spectral image color separation model) is low. Arming to CYNSN reverse model (spectral image color separation), an adaptive CYNSN reverse model was proposed in this article. Compared with the existing model, the experimental results show that the proposed adaptive spectral color separation model has the same accuracy with the existing model, but efficiency has a great improvement, can achieve about 12.83 times as many of the existing model.

Keywords Spectral image separation · CYNSN · Adaptive · Reverse model

S. Liu (✉)
Department of Printing and Packaging Engineering, Henan University of Animal Husbandry and Economy, Zhengzhou, Henan, China
e-mail: hnzzlsw@163.com

Q. Tian
Department of Printing and Packaging Engineering, Shanghai Publishing and Printing College, Shanghai, China

M. Zhu
Department of Materials and Chemical Engineering, Henan Institute of Engineering, Zhengzhou, Henan, China

Z. Liu
College of Communication and Art Design, University of Shanghai for Science and Technology, Shanghai, China

P. Zhao et al. (eds.), *Applied Sciences in Graphic Communication and Packaging*, Lecture Notes in Electrical Engineering 477,
https://doi.org/10.1007/978-981-10-7629-9_6

1 Introduction

Yule-Nielson Spectral Neugebauer model (YNSN) is a common model for the characterization of printer, in order to improve the precision, the printer color space is divided into several cell, within each cell use YNSN equation to predict the forward model and reverse model, called cell Yule-Nielson Spectral Neugebauer model (CYNSN) model. This method has high prediction accuracy, and can effectively eliminate the phenomenon of metamerism. However, the target color can't be judged simply in which cell in the reverse model. This process may need to solve many times through reverse YNSN model in maybe cells, this has caused a large amount of calculation and CYNSN model computation efficiency is low. As a result, proposing a new high efficiency, high precision cell search algorithm is very necessary [1–5].

Urban was put forward a cell search algorithm based on the linear iteration [6, 7], but the calculation is large and the model accuracy is not high. GUO Jin-yi proposed a cell search algorithm, according the color-difference between each cell center and the target, choose 2k + 1 (k is printer color number) basic cell, then choose the optimal cell [8]. This algorithm has high accuracy, but the amount of calculation is too large, and can't be used in practical application.

Arming to CYNSN reverse model (spectral image color separation), an adaptive CYNSN reverse model was proposed in this article. Compared with the existing model, the experimental results show that the proposed adaptive spectral color separation model has the same accuracy with the existing model, but efficiency has a great improvement, can achieve about nine times as many of the existing model.

2 The CYNSN Forward Model

CMYK four-color YNSN model as:

$$R(\lambda) = \left\{ \sum_{i=1}^{16} w_i * R_i(\lambda)^{1/n} \right\}^n \tag{1}$$

Equation (1), $R(\lambda)$ is the spectral reflectance which is predicted by the ink coverage, λ is wavelength; $R_i(\lambda)$ is the spectral reflectance of the ith color element; w_i depends on the printing color C, M, Y, K ink coverage; n is Yule Nielson-power exponent [9, 10].

Forward CYNSN model can predict the spectral reflectance based on the ink coverage and spectral reflectance of training sample; the optimal CMYK ink coverage can be calculated by reverse CYNSN model through finding the optimal cell.

3 The Adaptive Cell Search Algorithm

The adaptive cell search algorithm steps of backward CYNSN model as shown in Fig. 1. Using the target spectral reflectance and training samples reflectance to determine the initial cell, the initial may be composed one or several basic cell, then search the optimal dynamic cell and the corresponding optimal C, M, Y, K ink coverage. If the error is in a acceptable range, then output the optimal C, M, Y, K ink coverage; On the other hand, the initial cell need to be expanded again to search the optimal cell.

3.1 Searching Initial Cell

In the training sample, choose several samples whose spectral reflectance is closest with target samples, framed a four-dimensional cell called it the original cell, Specific steps as shown in Fig. 2.

The method of judging whether the selected test samples (Ri) can be framed a cell is as follows: in the training sample, find the two samples whose spectral reflectance is closest with target samples and the corresponding CMYK ink coverage. If the equation

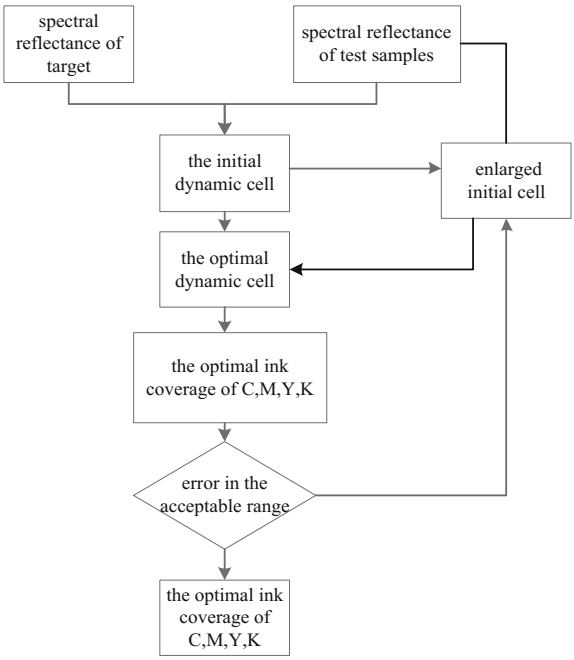

Fig. 1 The adaptive cell search algorithm backward CYNSN model

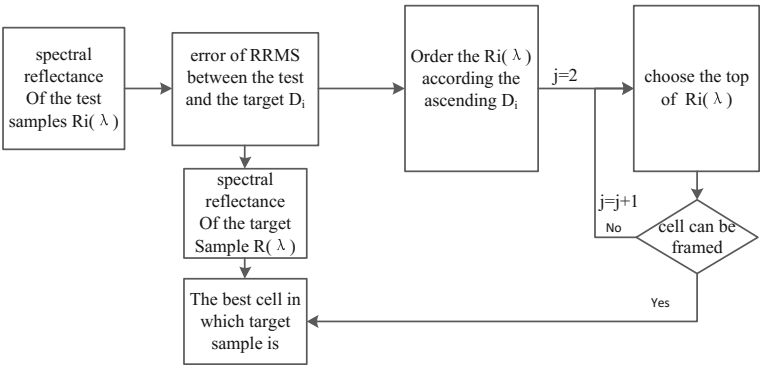

Fig. 2 Searching initial cell

$$(C_{\max} - C_{min}) * (M_{max} - M_{min}) * (Y_{max} - Y_{min}) * (K_{max} - K_{min}) = 0 \qquad (2)$$

test samples can be framed a cell, otherwise, it can't, $C_{\max}$, M_{max}, Y_{max}, K_{max} is the max CMYK ink coverage of the corresponding selected test samples; C_{min}, M_{min}, Y_{min}, K_{min} is the min CMYK ink coverage of the corresponding selected test samples;

3.2 Searching the Optimal Cell

The specific steps of searching the optimal cell is as follows: if the initial cell is a basic cell or the error of backward YNSN model in this initial cell is acceptable, the error threshold is the RRMS average error of forward CYNSN model, then the initial cell is the optimal cell; If not, use a plane to cut the initial cell into two sub cell, choose a better sub cell and judge whether the precision meet the error threshold, or continue cutting the sub cell until its precision meet the error threshold or the sub cell is a basic cell.

3.3 Expanding the Initial Cell

If the target spectral reflectance is not in the on initial cell, and the prediction error is beyond acceptable limits. The initial cell needs to be expanded again.

The specific method of initial cell to be expanded is: in the 2.1 section of searching initial cell, choose j + 1 samples whose spectral reflectance is closest with target samples to frame a four-dimensional cell, if the samples can frame a bigger cell more than the original cell, the bigger cell became the initial cell, conversely, j + 1, repeat the steps.

4 Experiments and Analysis

Selecting HP Designjet Z3200 (24 in.) HT (CMYKRGBmkk) printer as printing equipment choose, all samples were printed after linearization using EFI Colorproof XF, and measured under the condition of (D50, 2°) by spectrophotometer equipment of Gretagmacbeth i1iO.

4.1 The Optimal Value of N-Factor

Literature [9, 10] showed that the CYNSN model can achieve the best prediction accuracy when the cell is divided into 5 levels, so choose 1296 patches as training sample according to the C, M, Y, K ink coverage [0, 0.2, 0.4, 0.6, 0.8, 1], and choose 625 patches color as test samples which C, M, Y, K ink Coverage is [0, 0.25, 0.5, 0.75, 1].

The n-factor of Yule-Nielsen is related to specific experimental environment (printers, ink, paper, etc.), it is difficult to use simple mathematical model to predict, so the optimal n-factor are determined using iteration method with changing n value from 1 to 5, 0.3 interval.

The experimental results show that, when n is 1, the RRMS between the estimated spectral reflectance and the actual measured value of test samples is minimum, so the value of n is 1.

The precision of the CYNSN model was evaluated through RRMS error, CIELAB and CIEDE2000 between the estimated spectral reflectance and the actual measured value of test samples, the experimental data are shown in Table 1.

The Table 1 shows that forward CYNSN model has high prediction accuracy, so the predicted spectral reflectance data by forward CYNSN model used in backward CYNSN models is accurate and credible.

4.2 Backward CYNSN Model and Model Evaluation

Using the measured spectral reflectance of test samples as the target spectral reflectance, predict ink coverage by backward CYNSN model, then print it and measure the duplication of test samples.

Table 1 The forward CYNSN model precision

	Max	Mean	Median
RRMS	0.0189	0.0038	0.0021
ΔE * ab	2.68	1.09	0.93
ΔE * 00	2.42	0.82	0.62

Table 2 Computation efficiency and calculation accuracy of backward model

Operation times		RRMS		ΔE (D50, 2°)	
	Mean	Mean	Max	Mean	Max
Proposed algorithm in this paper	1.3252	0.0304	0.0767	3.5654	10.3765
Proposed algorithm in literature [8]	17	0.0313	0.0765	3.3575	10.2672

Calculate the RRMS error and the D50 light chromaticity error between the test samples' spectral reflectance and the duplicate spectral reflectance. Evaluation operational efficiency of backward CYNSN model by calculating the number of cell involved in the process of reverse solution. At the same time, the RRMS error, chromaticity error and operational efficiency of cell search algorithm are compared with the literature [8] CYNSN model; the results are shown in Table 2.

The Table 2 shows that it need only 1.3252 cell-research times to solve C, M, Y, K ink coverage by backward CYNSN model if using the algorithm proposed in this paper, but need 17 times if using the algorithm proposed in literature [8].

The Table 2 also shows that compared with the literature [8] backward CYNSN model, using the cell-search algorithm proposed in this paper and in literature [8], the RRMS error and the D50 light chromaticity error precision is about the same. Thus, for the human eye, the accuracy is the same, but the former has obvious advantages in operational efficiency.

5 Conclusions

An adaptive cell-search algorithm used in backward CYNSN model is proposed in this paper. Experimental results proved that the proposed cell-search algorithm can achieve high precision replication about the chromaticity and spectral reflectance compared with the existing CYNSN model in literature [8], but the efficiency increased 12.83 times.

Acknowledgements This study was supported by the National Natural Science Foundation of China (no. 61301231).

References

1. Guo J (2010) Novel spectral characterization method for color printer based on the cellular Neugebauer model. Chin Opt Lett 8(11):1106–1109
2. Sun B, Liu H, Zhou S et al (2015) Modified Spectral Neugebauer Model for Printer Characterization. Spectrosc Lett 48(9):660–668
3. Tsutsumi S, Rosen MR, Berns RS (2008) Spectral color management using interim connection spaces based on spectral decomposition. Col Res Appl 33(4):282–299

4. Li CJ, Luo MR (2008) Further accelerating the inversion of the yule-nielson modified neugebauer model. In: Final Program and Proceedings - IS and T/SID Color Imaging Conference, pp 84– 88
5. Zhang Y (2013) Analysis on color configuration of plants in landscape design. Appl Mech Mater 57–360:2122–2125
6. Urban P, Grigat RR (2006) Spectral-based color separation using linear regression iteration. Color Res Appl 31(3):229–238
7. Urban P (2007) Accelerating spectral-based color separation within the Neugebauer subspace. J Electron Imaging 16(4):043014
8. Wang B (2012) Color separation criteria for spectral multi-ink printer characterization. Chin Opt Lett 10(1):013301
9. Zhu M, Liu Z, Chen G (2011) Research on six-color separation model based on subarea neugebauer e-quations. Acta Optica Sinica 31(7):288–297
10. Jin C, Shen H, Shao S et al (2011) Color characterization method for colorful inkjet printers. Acta Optica Sinica 31(12):316–320

The Spectral Characterizing Model Based on Optimized RBF Neural Network for Digital Textile Printing

Zhihong Liu and Yongjun Liang

Abstract Digital textile printing was appeared in 1980s, which printed directly onto the surface of fabric with digital original by ink-jet printer and got high quality color printing textile. The spectral characterization of printer is the key technology for the textile printing. This paper presented a spectral characterizing model based on RBF neural network, which optimized the RBF neural network by extending the input variables of neural network. Experimental results showed that the 90% spectral errors of testing color samples are less than 0.04, the average spectral error is 0.025, the maximum spectral error is 0.066; while the 90% color differences (ΔE_{2000}) of testing color samples are less than 2.8, the average value is 1.89, the maximum value is 8.5. That means the model could effectively improve the characterization chromaticity and spectral precision.

Keyword Spectral characterization · Spectral model · Optimized neural network Digital textile printing

1 Introduction

With the development of color inkjet printing technology and color ink, digital inkjet printing is used for direct printing onto the surface of the fabric to produce high quality color printed textile [1–5].

Studying on the characterization of technology for color reproduction of the inkjet equipment as early as the beginning from 1980s, a large number of researches have focused on inkjet printing inks [6] and substrate [7, 8]. However, there are few researches on the color characterization techniques of inkjet devices in textile

Z. Liu (✉)
School of Media & Communication, Shenzhen Polytechnic, Shenzhen, China

Y. Liang
Group Technology Center, Shenzhen Yuto Packaging Technology Co., Ltd, Shenzhen, China
e-mail: yongliang@szyuto.com

P. Zhao et al. (eds.), *Applied Sciences in Graphic Communication and Packaging*, Lecture Notes in Electrical Engineering 477,
https://doi.org/10.1007/978-981-10-7629-9_7

industry. In this paper, we propose a new algorithm based on the characterization of color printing ink jet equipment to improve the quality of digital ink-jet textile printing.

2 Algorithm Principles

2.1 RBF Neural Network

Ink jet printing system is a typical nonlinear system [9]. In this particular case, an Artificial Neural Network (ANN) is capable to acknowledge nonlinear relationship of input variables, by extracting intrinsic information with learning process based on data for training [10]. A Radial Basis Function Neural Network (RBF-NN) is a particular case of ANNs, which is consisting of three layers. The suitable definition of parameters vectors is the main problem faced by RBF-NN, which will reach advantageous results [11].

2.2 The Optimal Input

Polynomial regression model [12] is a polynomial equation to fit the nonlinear relationship between the two data sets of regression model. The color reproduction of the printer by polynomial regression model is essentially a set of polynomial equations to establish the corresponding relationship between the driving value of the printer and the spectral reflectance of the color sample.

The printer driver vector is extendible (such as Eq. (1) is extended to 11 terms), commonly extending with the expansion of higher order terms and cross terms, such as cm, c^2, cm^2, c^3. Extending the different items gets different influence on the accuracy of the model. The model should be selected according to the optimal number of combination of the actual situation.

$$\begin{aligned}
p_0 &= [cmy] \\
p_1 &= [1 cmy p_0] \\
p_2 &= [cmcymyp_0] \\
p_3 &= [1 cmy p_2] \\
p_4 &= \left[c^2 m^2 y^2 p_0\right] \\
p_5 &= \left[1 cmy p_0^4\right] \\
p_6 &= \left[\mathrm{c}^2\mathrm{m}^2\mathrm{y}^2 p_0^2\right] \\
p_7 &= \left[1 cmy p_0^6\right] \\
p_8 &= \left[c^3 m^3 y^3 p_7\right] \\
p_9 &= \left[cm^2 cy^2 mc^2 my^2 yc^2 ym^2 p_7\right] \\
p_{10} &= \left[cm^2 cy^2 mc^2 my^2 yc^2 ym^2 c^3 m^3 y^3 p_6\right] \\
p_{11} &= [1 cmy p_{10}]
\end{aligned} \tag{1}$$

2.3 *Spectral Characterizing Model*

The structure of the model based on the RBF-NN is shown in Fig. 1. With the training sample and optimizing RBF neural network, the optimal input values of neural network are inputted to predict the spectral reflectance of color reproduction. The sRMS and color difference are used to evaluate the model's accuracy.

3 Experiments

Digital ink-jet printer use CMYK four color separation principle to color process. This paper did experiment to test the model with Neostamp a software which is a Spain digital textile printing software, and EPSON70680 ink-jet printer to print out samples, and Satin 16MM as textile substrate.

First, the maximum ink quantity is measured by the output of the maximum ink test target (as shown in Fig. 2(1)), and then combined with subjective evaluation to determine the maximum ink limit. By observing if the maximum ink output limit test version of the document was printed ink, or pattern edges in the test version of the output of the emergence of ink infiltration open look, the amount of ink overrun.

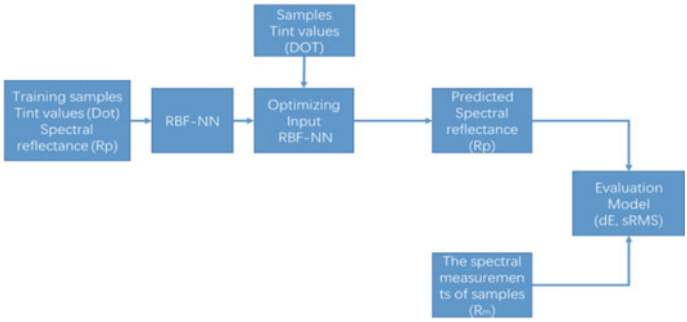

Fig. 1 The structure of optimized RBF neural network model

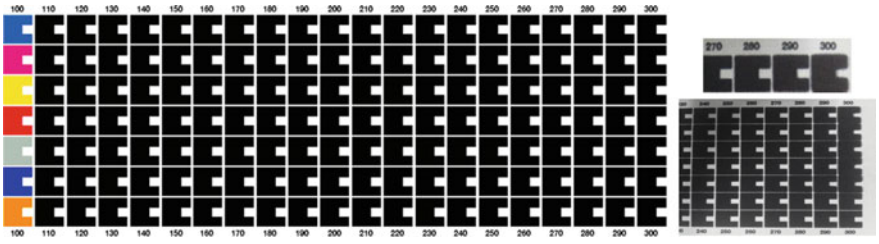

Fig. 2 (1) The maximum ink test target, (2) the output maximum ink test target

Figure 2(2) is the output of the sample effect of the experiment, when the ink is more than 280, the burr edge of the ink appears, and the outline of the figure is not clear.

Second, IT8.7/4 target was printed out and measured with i1 spectrophotometer. The measured results were 50% for model training, and the other was used in the model testing. Comparing the color difference and sRMS to analyze the color reproduction accuracy through the error probability distribution curve.

4 Results and Discussion

4.1 The Chroma Characteristics

The tone of picture is the key point of reproduction. The correct and full of tone reproduction is important for color picture reproduction. Figure 4 is the chroma distribution of 20 steps of cyan, magenta, yellow and black in L-ab coordinate system. From Fig. 3, the distribution of different color, the linear relationship of yellow and black is better than that of green and magenta.

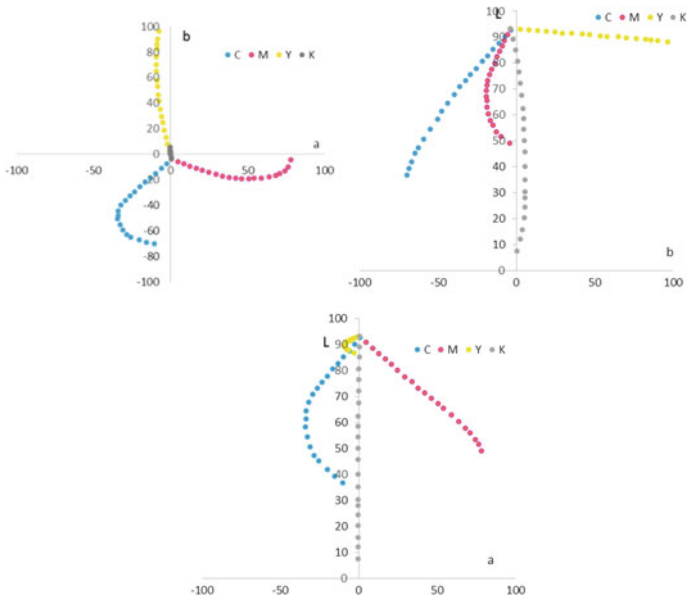

Fig. 3 The tone distribution of Cyan, Magenta, Yellow, Black in L-ab coordinate system (Color figure online)

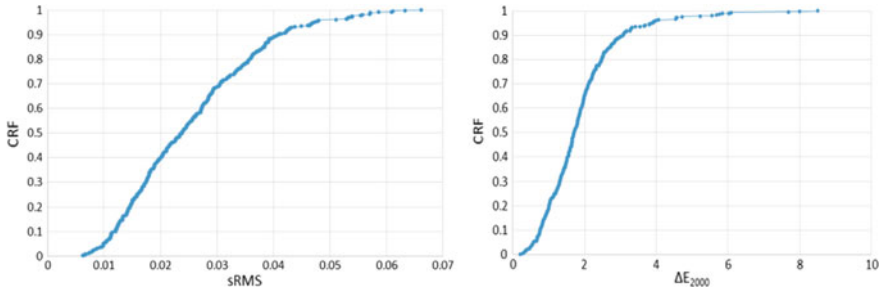

Fig. 4 Cumulative relative frequency (CRF) of sRMS and ΔE_{2000} of the reconstructed color

4.2 Spectral Error and Color Error Characteristics

Compared with the original input variables, the different expansion input terms has an impact on the prediction accuracy of the model. Compared p_4–p_{11} with p_0, p_1, p_2, p_3 respectively, the expansion of quadratic term [c^2 m^2 y^2] and three term [cm^2 cy^2 my^2 yc^2 ym^2], [c^3 m^3 y^3] led to reducing of both the prediction accuracy and generalization ability of the network, and getting extremal point. But the expansion of cross term [1 *cmy*] and [*cm cy my*] for input achieved the accurate result and optimized generalization ability with experiment. So the accuracy of the model is related to the type of the extended term, but nothing to do with the number of extensions.

Figure 4 is cumulative relative frequency (CRF) of the sRMS and ΔE_{2000} of the reconstructed color. From Fig. 4(1), the 90% sRMS of samples is less than 0.04. The average sRMS is 0.025 and the maximum sRMS is 0.066.

At the same time, the 90% color difference (ΔE_{2000}) of samples is less than 2.8. The average ΔE_{2000} is 1.89 and the maximum ΔE_{2000} is 8.5.

From the analysis of physical factors, the using of halftone color printing performance exists single cyan, magenta and yellow, as well as the overprinting of secondary and tertiary of cyan, magenta and yellow at same time. So the expansion of cross term [1 cmy] and [cm cy my] for input achieved the accurate result.

5 Conclusions

We presented a spectral characterizing model based on RBF neural network, which optimized the RBF neural network by extending the input variables of neural network. The extending the input variables of neural network is extend of printer driver vector with the expansion of higher order terms and cross terms. Experimental results showed that the 90% spectral errors of testing color samples are less than 0.04, the average spectral error is 0.025, the maximum spectral error is 0.066; while the 90% color differences of testing color samples are less than 2.8, the

average value is 1.89, the maximum value is 8.5. The model could effectively improve the characterization chromaticity and spectral precision and could be used in the production practice of textile printing well.

References

1. Ujiie H (2006) Digital printing of textiles. Woodhead Publishing, Boca Raton, pp 201–288
2. Zhou R, Yu Z (2010) Unscrambling the development status-quo of international nonwoven equipment. China Text Leader 9:70–72
3. Aehwal WB (2002) Textile chemical principles of digital textile printing (DTP). Colour ge 12:33–34
4. Tyler DJ (2005) Textile digital printing technologies. Text Prog 37(4):1–65
5. Calvert P (2001) Inkjet printing for materials and devices. Chem Mater 13(10):3299–3305
6. Mikuz M, Turk SS, Tavcer PF (2010) Properties of ink-jet printed ultraviolet-cured pigment prints in comparison with screen-printed, thermos-cured pigment prints. Color Technol 126 (5):249–255
7. Daplyn S, Lin L (2003) Evaluation of pigmented ink formulations for jet printing onto textile fabrics. Pogment Resin Technol 32(5):307–318
8. Huang Y, Cao B, Xu C et al (2015) Synthesis process control and property evaluation of a low-viscosity urethane acrylate oligomer for blue light curable ink of textile digital printing. Text Res J 8597:759–767
9. Wan XX, Liu Q (2014) Review of spectral printer characterization. J Image Graph 19(7): 985–997
10. Sarimveis H, Doagnis P, Alexandridis A (2006) A classification technique based on radial basis function neural networks. Adv Eng Softw 37(4):218–221
11. da Cruz LF, Freire RZ, Reynoso-Meza G et al (2016) RBF neural network combined with self-adaptive mode and genetic algorithm to identify velocity profile of swimmers. In: Proceedings of 2016 IEEE Symposium Series on Computational Intelligence (SSCI), pp 1 – 7
12. Rutemiller H, Bowers D (1968) Estimation in a heteroscedastic regression model. J Am Stat Assoc 63:552–557

A Novel Halftone Dot Prediction Model Based on BP Neural Network

Mengying Liu, Yuanlin Zheng, Ziwei Tang and Wei Wang

Abstract The purpose of this study is to reduce the ready time of offset printing by establishing a halftone dot prediction model (HDPM) based on BP neural network. The input data of HDPM is spectral reflectance data and the output data is dot area percentage of monochrome inks. To make sure the Mean Square Error (MSE) between the trained output data and the original data negligible, some experiments are performed. We obtained a set of results for dot area percentage of monochrome inks. The HDPM has stable performance, but it doesn't work well under some special conditions, such as ink with black and dark tone. To improve the precision of HDPM, we increase the training samples of the corresponding area. Therefore, the prediction performance of HDPM has improved, and it does increase the efficiency of printing production in some levels.

Keywords BP neural network · Halftone dot printing · Color matching

1 Introduction

With the rapid development of social economy and quality of life, people have higher requirement for printing. On account of the high-speed growth of personalized printing, people raised new requirements on the speed of printing. Nowadays, offset printing is one of the printing modes which have the widest uses in our country. In this printing mode, the printing color consists of dots with different colors and sizes. Our aim is to develop a prediction model which can predict halftone dot area rate through target color spectrum data, if the prediction

M. Liu · Y. Zheng (✉) · Z. Tang · W. Wang
Faculty of Printing, Packing Engineering and Digital Media Technology,
Xi'an University of Technology, Xi'an, China
e-mail: zhengyuanlin@xaut.edu.cn

Y. Zheng
Shaanxi Provincial Key Laboratory of Printing and Packaging Engineering, Xi'an, China

P. Zhao et al. (eds.), *Applied Sciences in Graphic Communication and Packaging*, Lecture Notes in Electrical Engineering 477,
https://doi.org/10.1007/978-981-10-7629-9_8

model works well, it will play a key role in improving printing efficiency. In our paper, we put forward a new pattern which combined halftone dot prediction model with BP neural network, and it is feasible.

Many researches on color science are based on spectral reflectance data. Based on the Kubelka-Munk equation, Zurita Ares et al. [1] have proposed a simple method for estimating the concentration of mineral dyes. An algorithm [2] is put forward to minimize the spectral difference between the reflectance of a standard sample and that of a match formed sample from a mixture of scattering colorants. Cooper et al. [3] introduce an application based on Kubelka-Munk equation and evolutionary computing, this method obtained appropriate coefficients for the paint set without any prior determination of the scattering and absorption of the colorants on standard white or black backings. In recently years, Kubelka-Munk theory get promoted and expanded. Simplified Kubelka-Munk model [4] can be used to predict the color of Fe_2O_3–$ZrSiO_4$ in glazes.

BP neural network is also widely used in the prediction of color among various subjects. Li et al. [5] improved BP neural network algorithm, which is proposed to correct the color of the traditional Chinese medicine tongue images. In printing industry, Zhang et al. [6] bring forward a method based on BP neural network for Spot color matching in flexographic printing.

2 Our Approach

We propose a halftone dot prediction model (HDPM) based on BP neural network. In this model, input spectral reflectance data of target color, we will get the output data, which are a set of data including dot area percentage of monochrome inks. The goal of training the prediction model is to find out the optimum number of hidden layer numbers and hidden layer nodes and improve the stability and accuracy of the prediction model.

2.1 Preparation

The spectral reflectance data of four-color standard collection [7] was measured under the CIE 1931 standard observer conditions. The viewing angle is 2° and the illuminant is 5000 K). The total samples are four-color dot area rates and spectral reflectance data. We rearrange the total samples order by monochrome to multicolor combination, as is shown in the Table 1.

The training data of HDPM is composed of paper data, monochrome inks data and 1051 groups of data selected from the other data averagely.

As is shown in the Fig. 1, we make plot points of total samples data and selected training samples data in L*a*b* color space. The total samples distributed

Table 1 The combination of total samples

The combination of basis ink	The number of group
Paper + Basis ink	45
C + M	101
C + Y	101
M + Y	101
C + M + Y	1001
C + K	101
M + K	101
Y + K	101
C + M + Y + K (0.1 & 0.3)	2000
C + M + Y + K (0.5 & 0.7 & 0.9)	2700
(C + M + K) & (C + Y + K) & (M + Y + K)	0

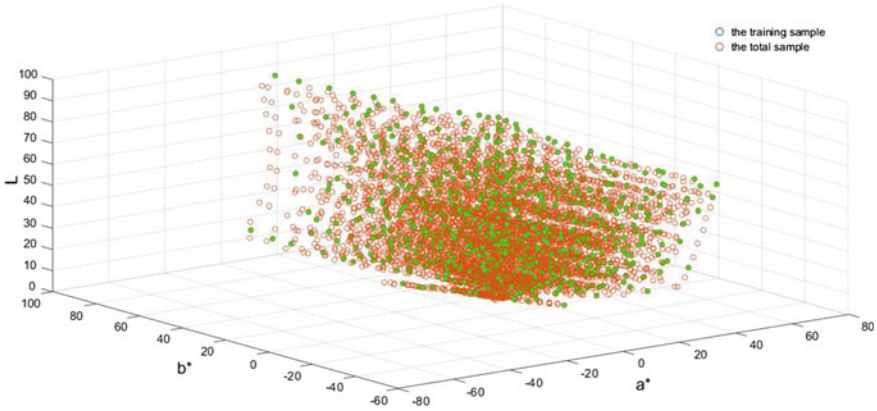

Fig. 1 Distribution of the training sample in the total samples (Color figure online)

uniformly in the L*a*b* color space, and training samples distributed uniformly in total samples.

200 group simulation samples were selected randomly from total samples except for training samples, which is used to test the predictive ability of HDPM. In addition, in order to test the local performance of HDPM, 10% of total samples were taken out from Table 1 uniformly.

2.2 Experiments

This experiment consists of three parts. Firstly, HDPM was established based on BP neural network and training the HDPM, so we can find out the optimal number of

hidden layer and hidden layer node about the prediction model. Then, test the local performance of HDPM. The purpose of these tests is to check out the local prediction performance. Finally, some experiments were conducted to optimize HDPM.

2.2.1 Establish HDPM Based on BP Neural Network

Establish a new forward neural network. The input data is spectrum reflectance data and the corresponding output data is the four-color (C: cyan, M: magenta, Y: yellow, K: black) dot area rates. Bayesian regularization algorithm was used to train the neural networks and the range of training parameters were set, if any training parameters exceed the range, the train process will be terminated. Adjusting the number of hidden layer neural network and hidden layer nodes could change the performance of the network. We can judge the prediction performance of the network based on the MSE which between output value of network and the original data, the smaller the MSE is, the higher the prediction precision of the network is (Fig. 2).

2.2.2 Local Testing the Prediction Model

It assumes that HDPM have different predicting abilities in each color area. HDPM was tested in different color areas. According to the results, find out those color areas which the MSE are high. High value of MSE means HDPM has poor prediction performance in those areas. The local tests were conducted as follows: 10% samples were selected from each group according to Table 1, and then test their predicting performance respectively.

2.2.3 Optimize the HDPM by Increase the Training Samples in the Specific Area

The prediction performance of HDPM is unbalanced in different color areas. The values as shown in Table 3, MSE are less than 9 which means HDPM obtain the good accuracy and stability in these areas. However, t HDPM has some areas where prediction performances are not well, which MSE of these areas are more than 11. HDPM needed to optimize in these specific areas. Increase extra 10% of total samples in specific areas to optimize HDPM, and retest HDPM.

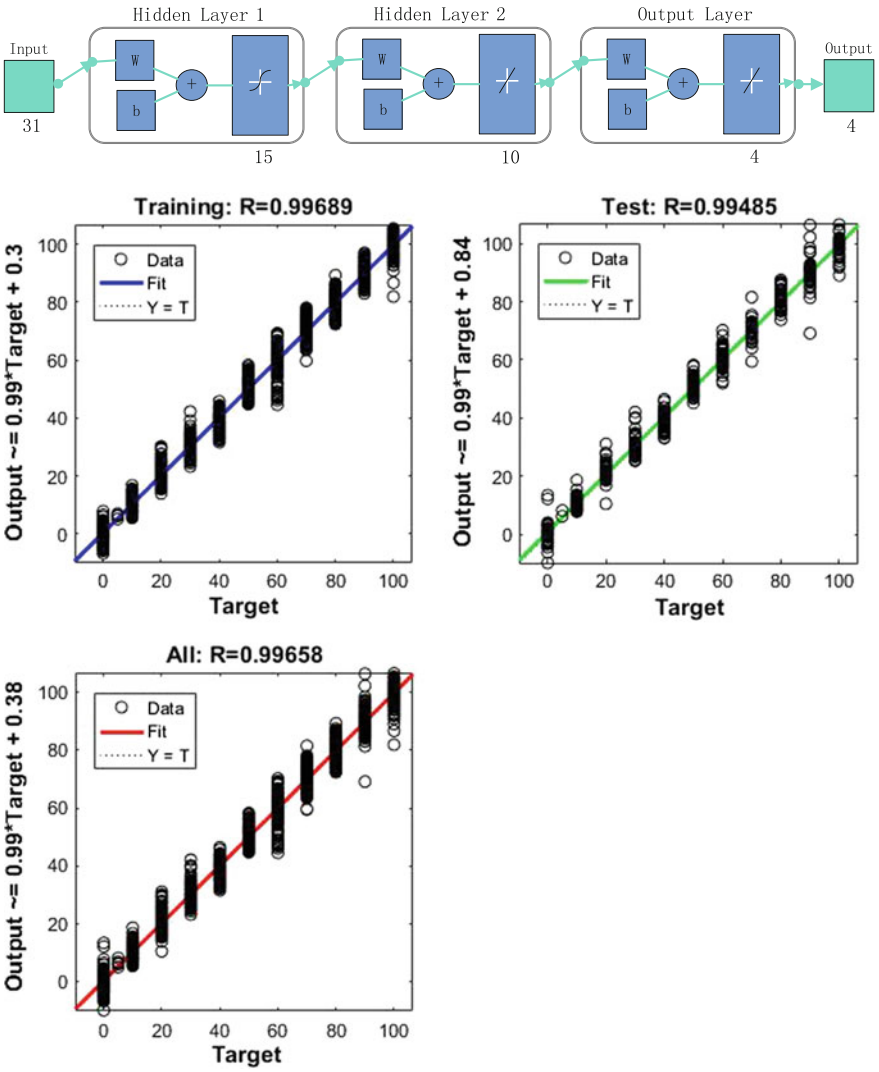

Fig. 2 Neural network

3 Results and Discussion

We can draw conclusion from Sect. 2.2.1 that the best number of hidden Layer is 2, and the hidden layer nodes are 15 and 10, respectively. Under this condition, HDPM have the best stability. The MSE which between the output of the training samples and original data is 6.4389, and the MSE1 which between the output of the simulation samples and original data is 8.3453 (Table 2).

Table 2 The training results

Parameters	Results
Epoch	1294
Regression	0.99658
Gradient	0.019614
MSE	6.4389
MSE1	8.3453

According to the results of the 2.2.1, we can conclude that it is feasible to establish a halftone prediction model based on BP neural network. However, the prediction performance is poor without optimization. Hence, some experiments need to conduct to improve the prediction model.

The result of the 2.2.2 demonstrates that the smaller (even zero) ratio of black ink is, the higher HDPM prediction accuracy of halftone dot area is. With the increasing of black area ratio, the prediction accuracy of HDPM reduced. The HDPM based on BP network, has lower prediction accuracy when the dot area ratio is high in black color or deep tone.

Optimize HDPM by increasing training samples locally. The local training samples are shown in Table 3. It can be seen that the MSE is decreased obviously. Compared with the model before optimization, the prediction performance increased more than 40%.

Table 3 The testing results

The combination of basis ink	The number of groups	The number of detection groups	MSE1	MSE1
CM	84	9	4.9971	–
CY	84	8	15.6925	9.5316
MY	84	8	3.2180	–
CMY	835	84	5.2005	–
CK	84	8	31.9637	13.2085
MK	84	8	8.8709	–
YK	84	8	17.4935	10.1351
CM/CY/MY + K	0	–	–	
CMY + K (K: 0.1 & 0.3)	1667	160	5.8048	–
CMY + K (K: 0.5 & 0.7 & 0.9)	2169	200	11.2617	7.6602

4 Conclusions

Through the above experiments, we can get that it's reasonable to apply the BP neural network to the prediction of the halftone dot area rates. In some areas with light tone or none black dots, MSE value of these areas is less than 9, which means prediction performance of HDPM are excellent. It can be used for printing production directly. But the accuracy of HDPM is limited in some areas, such as the deep tone area and including black dots etc., the prediction performance of HDPM is poor in these areas. By increase the training samples in these areas, the accuracy of HDPM obtains some improvement. Compared with the model before optimization, the prediction performance increased more than 40%. The optimized HDPM has a stable and high-precision predictive ability to predict the areas of the halftone dots. Normally, the spectral reflectance data can be used to compute the ratio combination of halftone dot. This study can reduce the ready time of offset printing and improve the efficiency of printing production.

In the follow-up study, we will try different approach to find the appropriate method to optimize the BP neural network. Then, use the optimized BP neural network to enhance the performance of the halftone dot prediction model.

Acknowledgements This study is funded by Shaanxi Provincial Key Laboratory of project-Printing image quality assessment based on human visual features (13JS082).

References

1. Zurita Ares MC, Villa González E, Torres Gómez AI, Fernández JM (2014) An easy method to estimate the concentration of mineral pigments in colored mortars. Dyes Pigm 101:329–337. https://doi.org/10.1016/j.dyepig.2013.10.001
2. Walowit E, Mccarthy CJ, Berns RS (1988) Spectrophotometric color matching based on two-constant kubelka-munk theory. Color Res Appl 13:358–362
3. Cooper EW, Sakakura Y, Ohta Y, Furukawa K, Shinoda H, Hachimura K (2006) Evolutionary computation with habitats for finding Kubelka-Munk coefficients in metallic and pearlescent paints. In: Systems, Man and Cybernetics, 2006. SMC '06. IEEE International Conference on, pp 5280–5284
4. Schabbach LM, Bondioli F, Fredel MC (2013) Color prediction with simplified Kubelka-Munk model in glazes containing Fe2O3–ZrSiO4 coral pink pigments. Dyes Pigm 99:1029–1035. https://doi.org/10.1016/j.dyepig.2013.08.009
5. Zhuo L, Zhang J, Dong P, Zhao Y, Peng B (2014) An SA–GA–BP neural network-based color correction algorithm for TCM tongue images. Neurocomputing 134:111–116. https://doi.org/10.1016/j.neucom.2012.12.080
6. Zhang YN, Lin M, Gao X (2016) The model of flexographic spot-color matching based on the improved Kubelka–Munk theory 369: 65–71
7. Qian YN (2004) New collection of four-color matching on printing process. Shanghai scientific and technological literature press. ISBN:9787543924001

Research on Spectral Reconstruction Accuracy of Color Reproduction Based on PAC

Yumei Li, Chuanjie Liu, Songhua He, Haojie Chen and Qiao Chen

Abstract The key of spectrum color reproduction is to study the spectral information of original images, and reconstruct the spectral curve of the target color. The accuracy of reconstructed spectra is influenced by many factors. In order to study the influence factors of reconstruction accuracy, two kinds of color cards Munsell Color Matt and Color Checker Classic were selected as the spectral reflectance data samples, two kinds of linear dimension reduction models of PCA were established and different number basis vectors were selected to separately reconstruct the spectrum. Then the influence of the different models and the basis vector numbers on the reconstruction accuracy was evaluated. The experimental results showed that the accuracy by model one was better than that of model two in RMSE GFC and color difference. In two kinds of color cards, when the number of basis vectors obtained by model one reached 6, the color difference was less than 1, the RMSE was less than 0.01; the GFC was up to 0.999. So the optimal scheme of reconstructing spectral images is to select spectral dimension reduction model one and 6 basis vectors.

Keywords Principal component analysis · Covariance matrix diagonalization Image spectrum information · Spectral reconstruction

1 Introduction

The color reproduction technology based on color matching has been very mature and widely used [1, 2]. However, this is the metamerism reproduction technology under the conditions of the specific light source and the standard colorimetric observers [3]. In order to realize the consistency of color reproduction under the

Y. Li · C. Liu · H. Chen
Engineering College, QuFu Normal University, Rizhao, Shandong Province, China

S. He (✉) · Q. Chen
Communication Engineering College, Shenzhen Polytechnic, Shenzhen, China

P. Zhao et al. (eds.), *Applied Sciences in Graphic Communication and Packaging*, Lecture Notes in Electrical Engineering 477,
https://doi.org/10.1007/978-981-10-7629-9_9

condition of changing observation environment [4], the accuracy of spectral reflectance reconstruction should be studied. The constructing method of the reconstruction models and the base vector numbers in low dimensional space need to be studied. This is to ensure that the low dimensional space can accurately contain the spectral information of the original image [5].

2 A Spectral Reconstruction Model

2.1 Principles of Different Spectral Reconstruction Models

The spectral reflectance of the object surface is a continuous smooth curve, so it can use a finite dimensional linear model to reconstruct [6]. As, a spectral data set of R_{m*n}, m said the number of samples, n said the spectral dimension, it can be expressed as a linear combination of several base vectors and principal component coefficients, when the freedom degree of R is less than n, its approximate value R can be regarded as the linear combination of the following ($1 \leq i \leq n$):

$$\widetilde{R}_{m*n} = \sum_{i=1}^{p} c_i e_i = CV^T \tag{1}$$

In order to improve the reconstruction accuracy, the R matrix should be firstly processed by the central processing:

$$\tilde{r}_j = \frac{1}{m}\sum_{i=1}^{m} r_{ij} \quad A = r_{ij} - \overline{r_j} \tag{2}$$

Matrix dimensionality reduction is to reduce the noise and redundant data between dimensions. Covariance matrix can be used to measure the relationship between dimensions:

$$Z = \frac{1}{m-1}(A^T A) \tag{3}$$

The covariance matrix Z_{n*n} is a symmetric matrix. Diagonalization processing is to find an orthogonal matrix V satisfying ZV = DV, where Dn*n is the eigenvalues of Z and its off diagonal elements are zero, Vn*n is the eigenvectors of Z corresponding to eigenvalues:

$$[V, D] = \text{eig}(Z) \tag{4}$$

Determining the number of basis vectors by calculating the cumulative contribution rate of eigenvalues:

$$a_j = \frac{Di}{\sum D} \quad Aa_j = \sum_{i=1}^{j} \left(D_i / \sum D \right) \tag{5}$$

The principal component which is the coefficient of the reconstruction matrix is obtained from the base vector V_{n*p}:

$$C1 = A_{m*n} * V_{n*p} \tag{6}$$

$$C2 = R_{m*n} * V_{n*p} \tag{7}$$

Two different spectral reconstruction models were respectively constructed by C1 and C2:

$$\widetilde{R}_{m*n} = C1 * (V_{n*p})^T + \overline{r_j} \text{ (Model one)} \tag{8}$$

$$\widetilde{R}_{m*n} = C2 * (V_{n*p})^T \text{ (Model two)} \tag{9}$$

2.2 The Evaluation Method of Spectral Accuracy

The accuracy evaluation of spectral reconstruction is mainly from two aspects, color accuracy and spectral accuracy [7]. In this paper, the CIE1976 color difference, DE, is used to evaluate the color accuracy, and the root mean square error, RMSE, and fitting coefficient, GFC, are used to evaluate the spectral accuracy.

$$\Delta E = \sqrt{(\Delta L^2 + \Delta a^2 + \Delta b^2)} \tag{10}$$

$$RMSE = \sqrt{(\sum (R - \widetilde{R})^2 / n)} \tag{11}$$

$$GFC = \frac{\left| \sum (R. * \widetilde{R}) \right|}{\sqrt{\sum (R^2)} \sqrt{\sum (\widetilde{R}^2)}} \tag{12}$$

3 Experiments

3.1 Experimental Environment

In the experiment, Color Checker Classic card and Munsell Color Matt were chosen as the experimental samples and measured the spectral reflectance of each color

block. Gretag Macbeth I1 was used to measure the spectral reflectance of color cards in the conditions of 2 degree field of view and D50 light source. The spectral wavelength is in the range of 400–700 nm at intervals of 10 nm [8]. The 31 dimensional spectral image data matrix was obtained. Then the matrixes were analyzed by PCA.

3.2 The Selection of Eigenvectors

The PCA was used to obtain the eigenvalues, the contribution rates and the cumulative contribution rates as well as the eigenvectors of the matrix. Then the contribution rates and cumulative contribution rates of the first 15 eigenvalues were expressed by a broken line graph.

From Fig. 1, with the increasing number of basis vectors, the corresponding contribution rates decrease, the cumulative contribution rates increase but the increase speed is slow. After sixth eigenvectors, the contribution rate increase could be ignored. The cumulative contribution rate tended to be stable.

The Fig. 2 is the spectral curves of the first six eigenvectors and the average spectral of two kinds of color cards. The curves change trend of two color cards is similar. The curve trend of the first base vector and the average spectral is gentle, which indicates the black and white change in the spectrum. Other base vectors represent other spectral colors range.

4 Results Analysis and Discussion

The following two kinds of reconstruction models and the first 15 base vectors are used to respectively reconstruct the spectrum of two kinds of cards. Then the reconstructed spectrum is compared with the original spectrum in chromaticity accuracy and spectral accuracy.

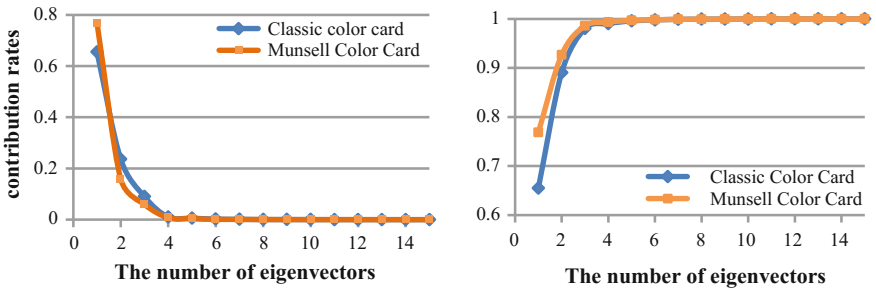

Fig. 1 Contribution rate and cumulative contribution rate

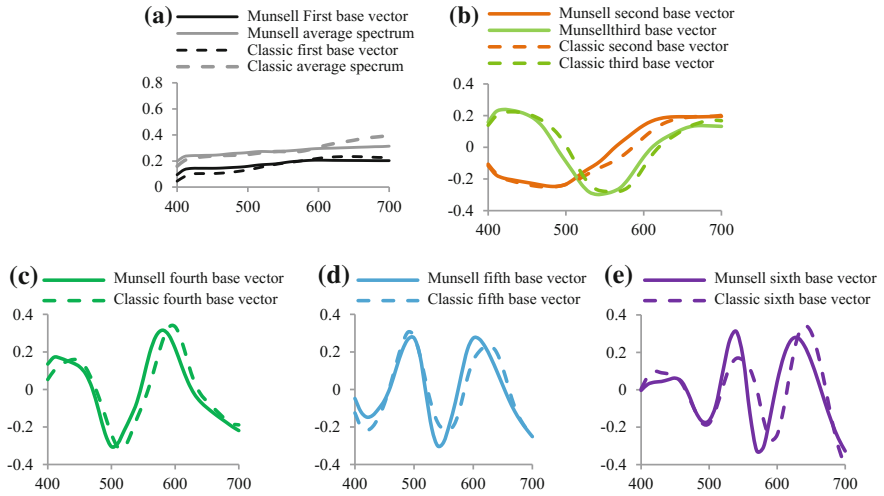

Fig. 2 The spectral curves corresponding to first 6 characteristic roots (Color figure online)

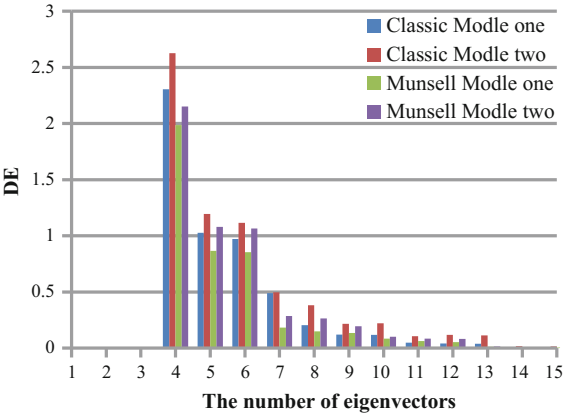

Fig. 3 The mean color-difference (Color figure online)

In Fig. 3, CIE1976 color difference formula is used to measure the chromaticity accuracy of the reconstructed spectrum and the original spectrum. It can be seen that, with the increasing of the eigenvectors number, the average color difference of the reconstructed spectra and the original spectra of the two kinds of color cards with the two models is reduced. When the number of eigenvectors reaches 13, the color difference is almost the same. The color difference of the reconstruction model one is less than that of the model two. If 1 color difference unit is the demarcation point. When the eigenvectors number of Munsell card is 5, the color difference of model one is less than 1, however, the eigenvectors number of the model two is 7, the color difference was less than 1. When the eigenvectors number of Classic card

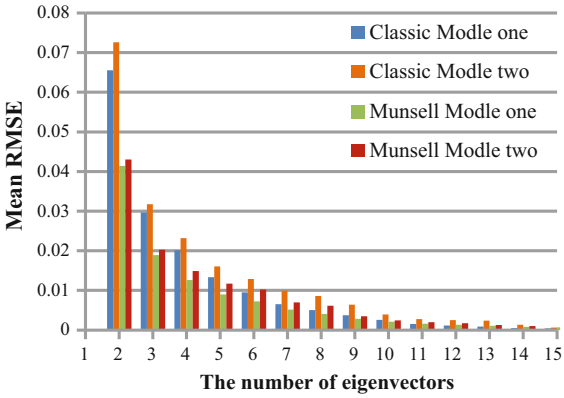

Fig. 4 The mean RMSE (Color figure online)

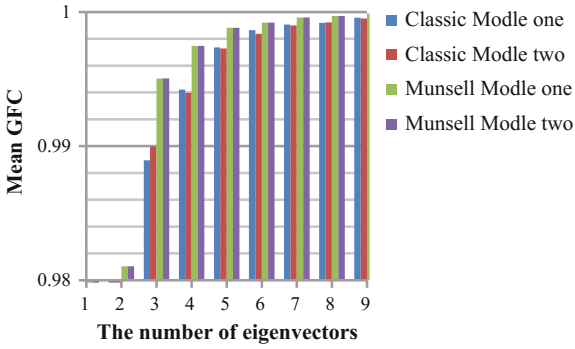

Fig. 5 The mean GFC (Color figure online)

is 6, the color difference of model one is less than 1. From the perspective of color difference and a small number of eigenvectors, model one and 6 eigenvectors are selected to reconstruct the spectrum, the accuracy of reconstruction results will be better.

In Fig. 4, the RMSE is used to measure the spectrum accuracy of the reconstructed spectrum and the original spectrum. It is obvious that, with the increasing of the eigenvectors number, the average RMSE of the reconstructed spectra and the original spectra of the two kinds of color cards with the two models is reduced. The more the number of color blocks, the lower the RMSE after reconstruction. The accuracy of the reconstruction model one is better than the model two. When the reconstruction model one is used, the eigenvectors number of Munsell card reaches 5 and the eigenvectors number of Classic card reaches 6, the RMSE will be less than 0.01. However, using the model two, the eigenvectors number of the two kinds color cards is 7; the RMSE will be less than 1. Therefore, from the perspective of RMSE, model one and 6 eigenvectors are selected to reconstruct the spectrum, which will be more appropriate.

In Fig. 5, the GFC is used to measure the spectrum accuracy of the reconstructed spectrum and the original spectrum. It is obvious that, with the increasing of the eigenvectors number, the average GFC of the reconstructed spectrum and the original spectrum of the two kinds of color cards with the two models is on the increase. The GFC of Munsell card is higher than that of Classic card. When the reconstruction model one is used, the eigenvectors number of the two cards reaches 6, the GFC will be up to 0.999. The two models which is better are not obvious in GFC. Yet, the reconstruction model one is little higher than that of the model two. Therefore, from the perspective of GFC, model one and 6 eigenvectors selected to reconstruct the spectrum will be better.

5 Conclusions

Through the experiment and data analysis, the conclusions are as follows. With the increase of the eigenvectors number, the RMSE, GFC and DE of Color Checker Classic card and Munsell Color Matt spectrum reconstructed by the two reconstruction models are all reduced, and the reconstruction accuracy is increasing. With the same number of basis vectors, Munsell color reconstruction accuracy is better than that of the Classic card, the reconstruction model one is more accurate than the reconstruction model two. When 6 basis vectors and the reconstruction model one were elected to reconstruct the spectra, the RMSE is less than 0.01, the DE is less than 1, the GFC is greater than 0.999, the three evaluation indexes are better. Therefore, the PCA spectral reconstruction model one mentioned in the paper and the 6 basis vectors to be the best solution for the reconstructed spectrum.

Acknowledgements This study is funded by National Natural Science Foundation of China (61108087).

References

1. Ying W (2010) A study of key technology in multi-spectral image color reproduction. Xidian University, Xi'an
2. Ding GH, Zhu YH, Li B et al (2012) Comparison of spectrum reconstruction on different number of color block. Packag Eng 03:14–18
3. Liang D, Zhang LH, Li B (2016) Multi spectral image reconstruction based on optimal wiener estimation algorithm for. Packag Eng 11:164–170
4. Yu HQ, Liu Z, Zhang LH et al (2014) Effects of sample characteristics on spectral image recon-struction. Packag Eng 35(13):144–149
5. Zhang XD (2013) Research on the key technologies of spectrum color management system. China Printing Packag Study 5(1):10–17
6. Songhua H, Qiao C, Jiang D (2015) The research of spectral dimension reduction method based on human visual characteristics. Spectrosc Spectral Anal 35(6):1459–1463

7. Wang HW, Chen GX, Li J (2012) Study on spectral image fusion technology based on high–fidelity reproduction. J Comput Inf Syst 8(5):2107–2115
8. Tzeng D, Berns RS (2004) A review of principal component analysis and its applications to color technology. Color Res Appl 29(2):104–110

The Influence of Individual Color Preference on LED Lighting Preference

Yang Tang, Dan Lu, Yijing Xun, Qiang Liu, Yanfen Zhang and Guo Cao

Abstract The individual color preference plays an important role in visual experience. Therefore, a rigorous psychophysical experiment was carried out to investigate the influence of the individual color preference on lighting preference. 45 observers (age from 19–25) were selected from 318 valid questionnaires including three categories of people (15 students categorically preferred blue, 15 students categorically preferred green and 15 students categorically preferred red). The observers made corresponding subjective preference scores with 7-level rating scale on five experimental objects severally illuminated by five spectral power distributions (SPDs) of LED light with different correlated color temperatures (CCTs). Afterwards we used various statistical methods on 1125 sets of data and it was found that the individual color preference had a significant influence on lighting preference but it was not the crucial factor. Compared with this, the results emphasized the dominate influence of the light of CCTs on lighting preference.

Keywords Individual color preference · LED lighting · Lighting preference

Y. Tang · Y. Xun · Q. Liu (✉)
School of Printing and Packaging, Wuhan University, Wuhan, China
e-mail: liuqiang@whu.edu.cn

D. Lu
School of Printing and Packaging Engineering, Wuhan Vocational College of Communication and Publishing, Wuhan, China

Q. Liu
Shen Zhen Research Institute, Wuhan University, Shenzhen, China

Y. Zhang
Media Communication System, Dongguan Polytechnic, Dongguan, China

G. Cao
Shen Zhen Fu Tian N1 Digital Building Studio, Shenzhen, China

P. Zhao et al. (eds.), *Applied Sciences in Graphic Communication and Packaging*, Lecture Notes in Electrical Engineering 477,
https://doi.org/10.1007/978-981-10-7629-9_10

1 Introduction

Nowadays, numerous influential factors on lighting preference have been explored by researchers, which contain the light source SPD [1–7], experimental object or environment [2, 3, 5, 6], cultural difference [5], gender difference [5, 7] and age difference [7, 8]. For instance, Lin and colleague used three lights with different spectral power distributions (SPDs) illuminating three scenes to discuss the influence of light source SPD and lighting application [1]; Bodrogi et al. investigated four factors on lighting preference including CCT of light, scene, gender and culture [5]; and Dangol et al. studied the factors on office environment [7]. These works have made great contributions to subjective and objective evaluations under LED lighting environment, but we found that although previous studies had taken the individual objective factors such as gender, age and cultural difference into consideration, they ignored the individual subjective difference: color preference. And according to what we knew, there were no previous works studying on the influence of individual color preference on lighting preference.

Therefore, a question emerged that how the individual color preference have its impact on lighting preference. In this experiment, 45 observers with different individual color preference were selected by questionnaire, which included 15 observers categorically preferring color blue (blue individuals), 15 observers categorically preferring green (green individuals), and 15 observers categorically preferring red (red individuals). Five kinds of spectral power distributions of different CCTs (2500, 3500, 4500, 5500, and 6500 K) produced by a tunable white LED light were used to illuminate five experimental objects containing red, green, yellow, multicolored fruit or vegetables and multicolored flowers. These three groups of observers made corresponding subjective preference ratings on these 25 combinations of lights-objects.

The purpose of this work is to investigate the influence of individual color preference and other two influencing factors (CCT and experimental object) on lighting preference. Based on some theories and discussion, a bridge could be preliminarily built between the individual subjective visual experience and lighting preference judgments.

2 Experiments

2.1 Observers Selection

We adopted the form of questionnaire to select observers in order to ensure the uniqueness and purity of the observers participating in the experiments which meant every observer had a certain favorite color. Based on the previous analogous questionnaire about color preference [9, 10], we only presented colors by mentioning the names of these color rather than show the specific color to avoid the

effect of ambient lighting and the degree of value and chroma of colors. A 7-level rating scale was used in the investigation (seven ratings included −3, −2, −1, 0, 1, 2, 3 which respectively represented strongly dislike, moderately dislike, slightly dislike, neural, slightly like, moderately like and strongly like) and when selecting the qualified observer, we ensured that ideal observer should only prefer one color (e.g. with a score no lower than 2) and dislike other colors (e.g. with a score no higher than 0).

323 copies of questionnaires were distributed to the students in two schools of Wuhan University and totally 318 valid questionnaires were recycled. Significant consistency between the two schools was found using the Kruskal-Wallis ANOVA —only the *p*-value of yellow (0.03) less than 0.05 while 0.94 *p*-value for blue, 0.17 for green, and 0.22 for red. 73 blue individuals, 26 red individuals, and 30 green individuals (the number of yellow individuals was only 3, so this group had been given up) who had normal color vision were selected from questionnaires. The order of the favorite color was consistent with the previous conclusions [9–11].

2.2 *Experimental Setup*

The experiment was carried out in the darkroom painted with a spectrally neutral paint. A color-tunable light source (Philips Hue) was installed in the inner top of a standard viewing booth (width 89 cm × depth 60 cm × height 51 cm). A height-adjustable chair was placed about 40 cm away from the edge of the viewing booth to roughly ensure the observers could observe the objects at 45° (for fruit and vegetables) or 60° (for flowers) angle (Fig. 1).

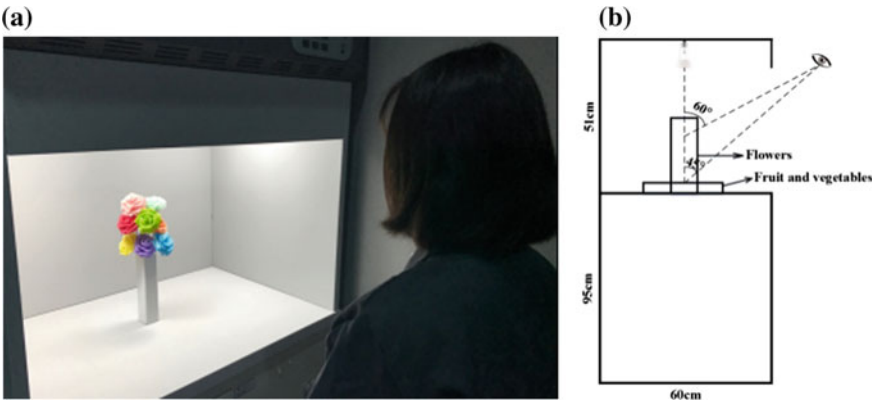

Fig. 1 **a** The experimental scene. **b** The viewing geometry of observers

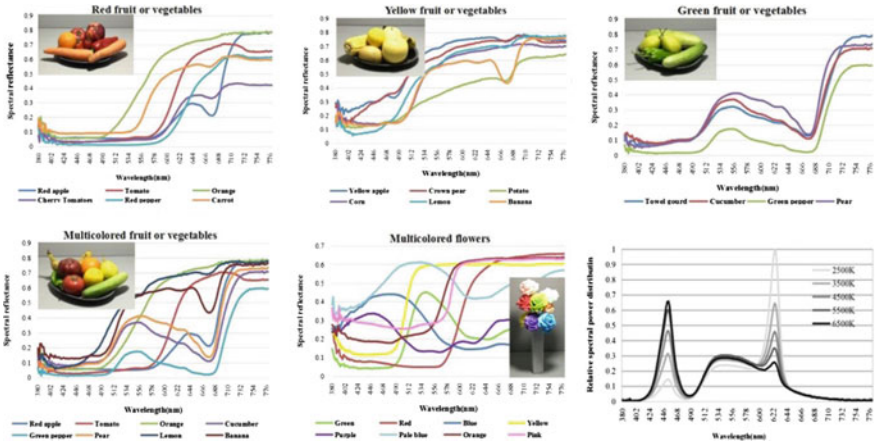

Fig. 2 Five spectral reflectance factors for objects and five relative spectral power distributions of the multi-LED light sources adopted in the experiment (Color figure online)

Boust et al. stated that people don't mind very much about the unfamiliar objects of original color, but have precise thoughts about familiar objects [12]. Therefore, three experimental objects with familiar dominant colors (red, green, yellow fruit and vegetables) and two multicolored objects (multicolored fruit and vegetables and multicolored artificial flowers) were respectively placed in four gray plates with no reflectance and a 20 cm height flower vase.

The illuminometer Testo 545 was used to measure the illuminance in the center of object which was kept on 200 lx. The spectral radiometer PR-705 with 0°/45° geometrical condition was used to measure the spectral reflectance factors for five objects and five relative spectral power distributions of the light sources (Fig. 2).

2.3 Experimental Procedure

When entering the darkroom, the observer was required to put on a grey experimental suit to avoid the effects of the reflectance of clothes. Prior to the start of the experiment, he/her was given about 2 min to accommodate to the darkroom and observe the lighting environment. In the meantime, he/she was enquired some basic information including his/her favorite color once again to ensure the accuracy of the questionnaires, and he/she listened to a changeless oral description of the experimental process and noteworthy matters. Besides, it must be noted that in order to avoid the effects of reflectance from paper, the questions were read out from experimenter.

After finishing relevant introductions and accommodations, the formal experiment began. The observer was required to close the eyes and the experimenter began to change the experimental CCT of light (The order was in random aiming to

remove the impacts of the prior lighting condition caused by short-term memory effect). After that, the observer was asked to open eyes to observe the lighting environment for about 10 s and this procedure was repeated (10–15 s interval between each of the CCTs). The whole procedure was aimed to give an elementary impression to the observer.

Then, we placed the random objects on the platform, taking care to maintain the arrangement of the objects as similar as possible. The procedure was same as the above-mentioned except that when the observer was asked to open the eyes, he/she needed to assess the combination of lights-objects based on their personal preference using the 7-level rating scale. The aforementioned steps were repeated to the last object and the total time taken turned out to be about 25 min. This experiment was finished in two days in order to prevent deterioration of the fruit and vegetables, and the relative positions of each fruit and vegetable were fixed.

The experiments were approved by the Ethics Committee of Wuhan University. All procedures followed were in accordance with the ethical standards of the responsible committee on human experimentation (institutional and national) and with the Helsinki Declaration of 1975, as revised in 2008 (5). Informed consent was obtained from all observers for being included in the study.

3 Results and Discussion

The significance of the effect of the independent variables individual color preference (blue, green, red), CCT (five CCTs between 2500 and 6500 K), and experimental objects (red, green, yellow, multicolored fruit or vegetables and multicolored flowers) on the dependent variable (preference rating) was analyzed by Multiple Analysis of Variance (MANOVA), shown in Table 1.

As can be seen from Table 1, the effects of individual color preference and CCT are statistically significant at the 5% significance level ($p < 0.05$) and the impact of CCT on lighting preference is significantly stronger than other variables. Meanwhile, compared to CCT and individual color preference, the influence of

Table 1 Significance of the effect of the independent variables (individual color preference, CCT, experimental object) on the dependent variable (preference rating) analyzed by MANOVA

Independent variable or interaction	SS	df	MS	F	p
Individual color preference	13.61	2	6.80	3.28	0.037
CCT	717.37	4	179.34	86.34	<0.01
Experimental object	16.45	4	4.11	1.98	0.094
Individual color preference × CCT	4.22	8	0.53	0.26	0.98
Individual color preference × Experimental object	11.51	8	1.44	0.7	0.69
CCT × Experimental object	65.01	16	4.06	1.97	0.013

experimental object is quite limited, but a significant effect of experimental object occurs in interactions with CCT.

3.1 *Influence of Individual Color Preference*

In Fig. 3, it can be seen from the figure that among three kinds of individuals the highest rating score normally belongs to blue individual, the second rating is green individual (except observing green objects), and the last rating is red individual. So we use Mann-Whitney U test for further verification. The results are as follows: Only the *p*-value of blue–red individual (0.025) is lower than 0.05 while the *p*-values of blue–green individual (0.234) and green–red individual (0.287) are both higher than 0.05. Therefore, we can say that color preference significantly affect lighting preference and is more notable between blue–red individual.

In 1969, Luscher thought that personality traits could be described based on one's choice of color, so he conducted the Luscher Color Test (LCT) [13] in which subjects were shown eight different colored cards and asked to place them in order of preference. The conclusion he got was that the individuals who have identical color preference will be inclined to have same personality and we can call it the color-personality relationship. For instance, red individuals tend to be more active, aggressive and initiative. Accordingly, they will straight give expressions to their viewpoint. On the contrary, blue individuals are inclined to be calm, gentle and passive, so they won't express themselves directly.

Therefore, when put into the judgment of light preference, the color-personality relationship might have impact on the process of making judgment. For red individuals, when they notice the object which they don't really like or dislike (just as green objects), they will tend to emerge a relatively repugnant sense and speak out the rating scores in a short period of time so there will relatively raise more negative ratings. Compared with red individuals, the blue individuals may not make the

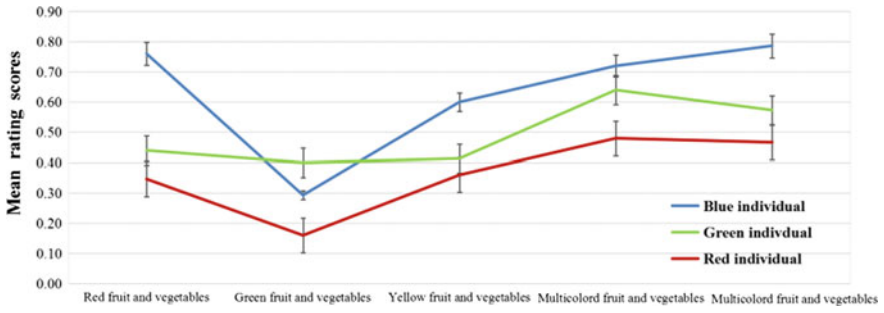

Fig. 3 The mean subjective preference rating scores of three categories of individuals observing five different experimental objects and their 95% confidence intervals for all observers independent of CCT (Color figure online)

negative scores immediately when they realize they dislike this object but make positive or zero score after a brief thought, so it could be the reason why there is an increase in the average rating scores. In addition, for green individuals, their personality is incline to be more stable and has stronger control ability. They are neither passive and gentle like blue individuals nor initiative and direct like red individuals. Therefore, their ratings on lighting preference are also more neutral and the mean rating score is between the other two. Such results have a good consistency with the results in the Luscher Color Test.

As is shown in Fig. 3, an interesting phenomenon happened in green objects, which indicates that the highest mean rating score belongs to green individual. Such phenomenon may be explained with two theories which are both used to explain the origin of individual color preference, the first is ecological valence theory (EVT) theory proposed by Palmer and Schloss in 2010 [14]. As was stated in their works, human color preference is strongly associated with objects they like (e.g. greens with trees and fresh vegetables). The second is color-emotion theory proposed by Ou et al. [15] in 2004. They stated that if people preferred a color to a high level they would emerge positive emotion when seeing it, and the color probably come from observational target. Therefore, both two theories have emphasized that the observers who have different color preference may have different preference degree in observational target. In this paper, perhaps we can call it the effect of target-preference. Another effect is the color-personality as mentioned above. These two effects are mutually restricted. For the lower rated green objects, the effect of target-preference becomes the main factor while the effect of color-personality is relatively weaker so the green individuals have the highest mean ratings. As for higher rated red objects, the effect of color-personality becomes the main factor so the blue individuals still have the highest mean ratings instead of red individuals.

3.2 Influence of CCTs

As can be seen from Table 2, there is a big difference of mean rating scores on different CCTs. For 2500 K the mean value of observer rating is always low, while for 4500, 5500 and 6500 K the mean values are universally high. Besides, Fig. 4 shows us the color gamut of multicolor fruit and vegetables in CIELAB. Under 2500 K the gamut distortion is the most serious and the mean value is the lowest while under high CCTs the gamut area becomes larger and more consistent and the mean values are generally high.

A similar result was concluded by Judd [16], who indicated that the larger color gamut area, the more colors can be displayed and the more likely people would prefer. Meanwhile, in order to get more direct expressions, we used the gamut area index (GAI) to represent the color gamut area under five CCTs. Under 2500 K the value is 6.37, while under 3500, 4500, 5500 and 6500 K the values are 14.99, 22.11, 27.16, and 30.48 respectively. As is mentioned above, such results have proved that the effect of CCT on lighting preference should be attributed to color

Table 2 The mean value (MV) and standard deviation (SD) of observer rating for different experimental objects under different light sources

CCT	Stat	Red	Green	Yellow	Multicolor FV	Multicolor Fl	Avg
2500 K	MV	−0.44	−1.53	−1.38	−1.09	−0.47	−0.98
	SD	1.97	1.6	1.76	1.86	2.08	1.85
3500 K	MV	0.36	−0.22	0.22	0.8	0.44	0.32
	SD	1.26	1.36	1.36	1.29	1.18	1.29
4500 K	MV	1	1.22	1.27	1.31	1.13	1.19
	SD	1.17	1.24	1.16	1.02	1.16	1.15
5500 K	MV	1.02	1.02	1.31	1.22	0.93	1.1
	SD	1.29	1.2	1.4	1.17	1.3	1.27
6500 K	MV	0.64	0.93	0.87	0.82	1	0.85
	SD	1.69	1.29	1.32	1.56	1.51	1.47
Avg	MV	0.51	0.28	0.46	0.61	0.61	–
	SD	1.48	1.34	1.4	1.38	1.45	

The first three objects "Red, Green, Yellow" are red, green, yellow fruit and vegetables. Multicolor FV: multicolor fruit and vegetables. Multicolor Fl: Multicolor flowers. Avg: the average rating of CCTs and objects

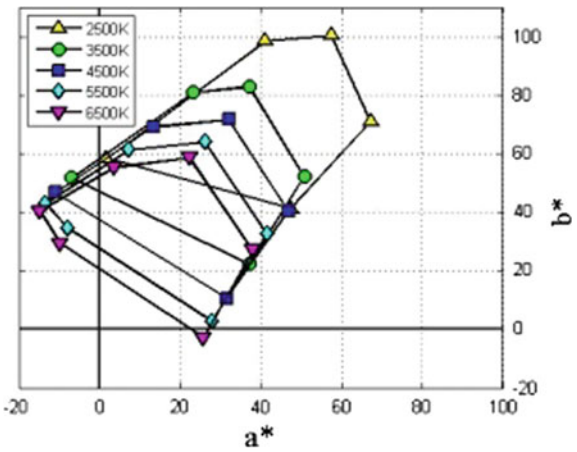

Fig. 4 The color gamut of multicolor fruit and vegetables (containing eight kinds of fruit and vegetables) under different CCTs in CIELAB color space (Color figure online)

gamut area. And some past studies [3, 4, 17, 18] have also stated that GAI is a good predictor on lighting preference.

Table 2 also shows us the stability of 45 observers rating for different objects under different CCTs using the standard deviation. The lower the standard deviation is, the greater the stability of observer rating is. It has the greatest stability under 4500 K while the worst under 2500 K. It's close for the standard deviation of different observational objects which locates around 1.4.

Meanwhile, an interesting conclusion was found that there is a negative correlation ($r = -0.74$) between the mean value and the standard deviation of 25

combination of objects and light sources. It means that if the observers universally prefer a certain combination, their ratings will be concentrated, while if the observers universally dislike a certain combination, their ratings will be decentralized. The result like this has also been mentioned in previous study [17].

3.3 *Influence of Experimental Objects*

As is shown in Table 2, for different objects the mean value has obvious difference. The order of mean values is: green objects (0.28) < yellow objects (0.46) < red objects (0.51) < multicolor fruit and vegetables (0.61) = multicolor flowers (0.61). Such result is consistent with the work of Jost-Boissard et al. [19], who used four colors of fruit and vegetables which was same with us.

Besides, for green objects, its mean value of observer rating is lower than the average value of three other fruit and vegetables by 0.56 under 2500 K, and under 3500 K the value is lower by 0.68. However, under high CCTs (4500, 5500 and 6500 K) the difference is small (0.03, −0.16 and −0.15 respectively). That is to say, the reason of the low value in green objects should be put down to its low values under low CCTs (2500, 3500 K). According to the view of chromatics, light sources rich in red light have a low CCT. When the green objects are lighted by red light it will produce strong stimulus and comfortlessness to the human eyes because in Practical Color coordinate System (PCCS), red–green is a group of contrast color (about 135° distribution). Compared with the green objects, the comfortlessness of yellow objects will decrease under low CCTs owing to the closer distribution (about 90°) of red–yellow in PCCS. Moreover, for red objects the degree of comfortlessness is the lowest so the mean value will be the highest among the three kinds of fruit and vegetables.

For multicolor objects, these two objects have the same mean value which is higher than other three monochrome objects. The color differences may explain it. For the multicolor flowers, the mean color difference (calculated in CIELAB) for the different components was greatest (Delta E = 38.8) in comparison with the multicolor fruit and vegetables (Delta E = 31.4), the red (Delta E = 23.8), the green (Delta E = 13.9) and the yellow (Delta E = 8.8). For multicolor objects with high color difference, they have greater color diversity, and observers feel more natural and comfortable, which leads to high mean value. Furthermore, we calculated the Pearson correlation coefficient between the mean value and color differences in CIELAB. It showed a strong positive correlation (r = 0.79), which meant the greater color difference was, the higher the mean value of observer rating was. This interpretation was also mentioned in the work of Jost-Boissard et al. [19]. Therefore, although it showed limited impact of observational objects in MANOVA, some exceptional conditions are actually existent and need attention.

4 Conclusions

Three kinds of observers with different color preference assessed the preference of the color appearance of arrangements of different color objects with identical illuminance, at five different CCTs. It was found that the color preference has a significant influence on lighting preference and the highest rating currently belongs to the blue individuals, while the second is the green individuals, the last is red individuals. Compared with this, the results emphasize the dominant influence of the light on lighting preference.

Some especial results include that there is the highest preference for green individuals observing green objects while for the other objects they are the second; the observers generally prefer the lights with relatively higher CCTs, while the lowest rating almost appears in 2500 K; and for experimental objects the two multicolored objects have the highest rating whereas the lowest rating generally appears in green fruit and vegetables. The results of this work could make a contribution to a more conscious application of adjustable LED lighting products to different applications depending on the color preference of every certain individual. Besides, in numerous current LED lighting environments, it has provided certain theoretical basis and reference for the users of LED products.

Acknowledgements The authors acknowledge the support of the Shenzhen basic research project (grant No JCYJ20150422150029093), the Open Fund of the State Key Laboratory of Pulp and Paper Engineering (grant No 201528) and National Natural Science Foundation of China (grant No 61505149).

References

1. Lin Y et al (2015) Colour preference varies with lighting application. Lighting Res Technol. https://doi.org/10.1177/1477153515611458
2. Wei M et al (2014) Color preference under LEDs with diminished yellow emission. Leukos 10(3):119–131
3. Khanh T et al (2015) Colour preference, naturalness, vividness and colour quality metrics, Part 1: experiments in a room. Lighting Res Technol. https://doi.org/10.1177/1477153516643359
4. Khanh T et al Colour preference, naturalness, vividness and colour quality metrics, Part 2: experiments in a viewing booth and analysis of the combined dataset. Lighting Res Technol. https://doi.org/10.1177/1477153516643570
5. Bodrogi P et al (2015) Intercultural observer preference for perceived illumination chromaticity for different coloured object scenes. Lighting Res Technol. https://doi.org/10.1177/1477153515616435
6. Dangol R et al (2013) Subjective preferences and colour quality metrics of LED light sources. Lighting Res Technol 45(6):666–688
7. Dangol R et al (2015) User acceptance studies for LED office lighting: preference, naturalness and colourfulness. Lighting Res Technol 47(1):36–53
8. O'Connor DA, Davis RG (2005) Lighting for the elderly: the effects of light source spectrum and illuminance on color discrimination and preference. Leukos 2(2):123–132

9. Bakker I et al (2015) Color preferences for different topics in connection to personal characteristics. Color Res Appl 40(1):62–71
10. Dittmar M (2001) Changing colour preferences with ageing: a comparative study on younger and older native Germans aged 19–90 years. Gerontology 47(4):219–226
11. Valdez P, Mehrabian A (1994) Effects of color on emotions. J Exp Psychol Gen 123(4):394
12. Boust C et al (2006) Color enhancement of digital images by experts and preference judgments by observers. J Imaging Sci Technol 50(1):1–11
13. Lüscher M (1990) The Luscher color test. Simon and Schuster
14. Palmer SE, Schloss KB (2010) An ecological valence theory of human color preference. Proc Nat Acad Sci. 107(19):8877–8882
15. Ou LC et al (2004) A study of colour emotion and colour preference, Part III: colour preference modeling. Color Res Appl 29(5):381–389
16. Judd DB (1967) A flattery index for artificial illuminants. Illum Eng 62(10):593
17. Islam M et al (2013) User preferences for LED lighting in terms of light spectrum. Lighting Res Technol 45(6):641–665
18. Khanh T, Bodrogi P (2016) Colour preference, naturalness, vividness and colour quality metrics, Part 3: experiments with makeup products and analysis of the complete warm white dataset. Lighting Res Technol. https://doi.org/10.1177/1477153516669558
19. Jost-Boissard S, Fontoynont M, Blanc-Gonnet J (2009) Perceived lighting quality of LED sources for the presentation of fruit and vegetables. J Mod Opt 56(13):1420–1432

A Novel Approach to Skin Coloration on Displays

Muhammad Farhan Mughal, Mengmeng Wang and Ming Ronnier Luo

Abstract Cosmetics are used as makeup to enhance the impact of appearance. Individuals like to make strong impression on others from their appearance. Current study is based on facial make-up in two color colorimetric attributes "whiteness" and "hue composition" in CIELAB color space. A workflow was implemented to achieve the facial makeup based on color image processing. From facial images against a fixed gray background, skin colors were extracted and transformed to tristimulus XYZ values via a camera characterization model. The XYZ values were used to calculate CIELAB L*, a*, b* color coordinates. They were then converted to L*, D^*_{ab}, h_{ab} color attributes to render whiteness and hue. Using the workflow, the images based on different facial whiteness level and hue angle were successfully rendered.

Keywords Facial makeup · Whiteness · Hue · Method · Skin detection Color rendering

1 Introduction

The facial makeups are playing a strong part to make the appearance of face according to the requirements of individuals. Swami et al. [1] studied the factors affecting the individual to undergo cosmetic surgeries, with attractive being very strong factor. Individuals undergoing cosmetic surgeries may or may not be satisfy with the outcomes [2]. Most importantly for permanent makeups where there are many complications in the process such as dissatisfaction about color and shape [3]. The theme of the current study is to show the facial changes in terms of whiteness

M. F. Mughal · M. R. Luo (✉)
State Key Laboratory of Modern Optical Instrumentation,
Zhejiang University, Hangzhou, China
e-mail: m.r.luo@zju.edu.cn

M. Wang · M. R. Luo
School of Design, University of Leeds, Leeds, UK

P. Zhao et al. (eds.), *Applied Sciences in Graphic Communication and Packaging*, Lecture Notes in Electrical Engineering 477,
https://doi.org/10.1007/978-981-10-7629-9_11

and hue changes so that individual going through makeup can select one from different color rendering most nearer to the desire.

2 Method

Wang et al. [4, 5] studied the skin color distribution between different locations and skin groups Chinese (O), Caucasian (C), South Asian (SA) and African (A), each having 4 locations forehead (FH), cheekbone (CB), cheek (CH) and neck. Altogether, about 180 subjects were measured. They concluded that the most effective ways to describe the skin colors are whiteness and hue angle. Figure 1a shows the scatter of all skin color groups. There are two clear trends, one is whiteness which is close to the white (see the black vector) and the other is the departure from the black (see the red vector). The former trend represents all skin colors except the African skin group. The latter trend only applies to African skin group. For each skin group, Fig. 1b shows the spread of hue angles for different locations for each skin group. They are ranged between 30° and 60°.

The facial makeup simulations workflow is shown in Fig. 2. From the camera captured facial images with gray background (non-skin color) the skin colors were first extracted [6]. The RGB skin colors were then transformed to tristimulus XYZ values via camera characterization model [7]. The XYZ values were then transformed to CIELAB color space [10]. The L*, a*, b* coordinates were converted to L*, D^*_{ab}, h_{ab} coordinates [8] where L*, D^*_{ab} and h_{ab} represent lightness, depth and hue angle respectively. Depth is defined as "an attribute to represent degree of departure from the neutral white color" by Berns [8]. This implies that depth analysis can be treated as whiteness analysis in opposite direction. The whiteness and hues were rendered separately after each rendering the new L*, D^*_{ab}, h_{ab} color

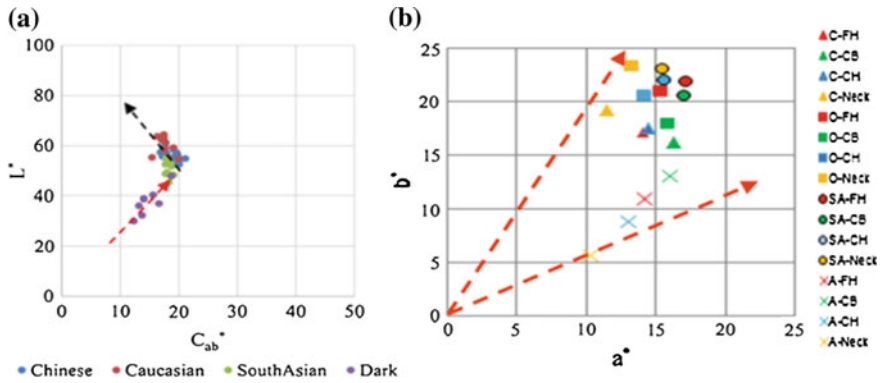

Fig. 1 **a** Plots of data points for four skin color group plus trend lines (represented by red and black dotted lines), **b** spread of hue angles for different location for each skin group (Color figure online)

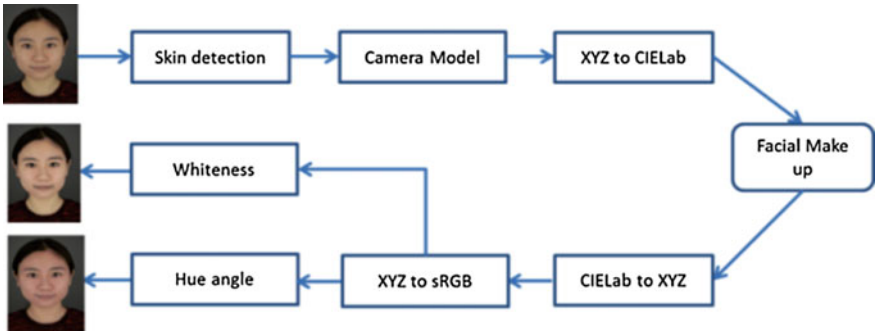

Fig. 2 Workflow for the proposed method to render skin images

space was converted back to CIELAB L*, a*, b* coordinates and from CIELAB to XYZ to standard RGB [9] (sRGB) to view the final output. The details are explained below.

2.1 Skin Detection

Kovac et al. [6] proposed a method to detect skin colors from RGB images. Figure 3 shows the result that skin colors are clearly separated from non-skin colors. The computer generated image in Fig. 3 is created by FaceGen Modeller software.

2.2 Camera Characterization Model

The method to transform RGB to tristimulus XYZ color space was based on polynomial modeling [7]. The RGB to XYZ transformation equation is written as:

$$H = PM \tag{1}$$

In Eq. 1 P represents RGB values, H represents corresponding XYZ values, and M is the transformation matrix. Equation 1 can also take the form

$$M = \left(P^T P\right)^{-1} P^T H \tag{2}$$

Equation 2 was solved to obtain transformation matrix M. In the current study P was extended to n × 11 to achieve better accuracy [7]. The XYZ values were then transformed to CIELAB color space [10].

Fig. 3 Detection of skin region from RGB image

2.3 *Facial Make Up*

Berns [8] explained the conversion of L*, a*, b* coordinates into L^*, D^*_{ab}, h_{ab} coordinates. The mathematical formulas to obtain Depth and hue angle from L*, a*, b* color coordinates are given below in Eqs. 3 and 4.

$$D^*_{ab} = \sqrt{(100 - L^*)^2 + C^*_{ab}} \tag{3}$$

$$h_{ab} = \arctan\left(\frac{b}{a}\right) \tag{4}$$

The whiteness (depth) was calculated as a function of L^* and was used to change a person's whiteness-darkness impression. The hue angle h_{ab} was used as an offset to change a person's hue impression from the range of red to yellow. After the adjustments of whiteness and hue L^*, D^*_{ab}, h_{ab} color coordinates were converted to L*, a*, b* and then CIE XYZ color coordinates and finally they were transformed to sRGB [9] values for display. The final stage can be a monitor model for more accurate presentation on a display.

3 Results and Discussions

The facial images obtained from the Leeds Liverpool Skin Color Database (LLSC) [11], were adjusted by whiteness and hue attributes. Figure 4 shows the simulation of facial renderings for whitening from L* of −15 to L* of +15 with original in the middle. Figure 5 shows the facial skin colors rendered at different h_{ab} angles from original angle minus 15 to original angle plus 15 with each interval of 5°.

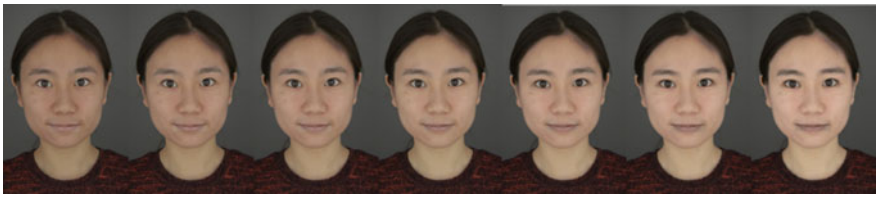

Fig. 4 Images of subject's skin colors at different whiteness levels from more depth to white with the original image in the middle (Color figure online)

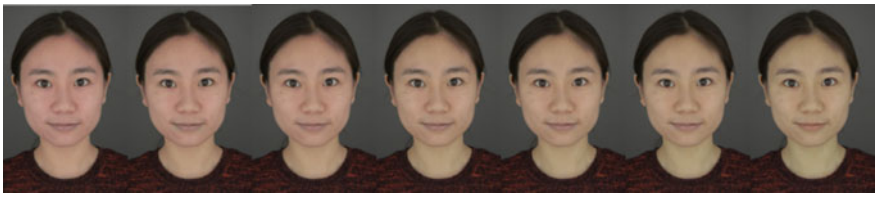

Fig. 5 Images of subject's skin colors at different hue levels from reddish to yellowish with the original image in the middle (Color figure online)

4 Conclusions

A workflow was developed to render skin impression. It successfully achieved the target of facial makeups based on whiteness and hue angle renderings. The method was successfully implemented on many faces including Chinese and South Asian faces. Based on this method, a software demonstrator was developed. The results showed that skin color rendering for different makeup scales can be successfully achieved.

References

1. Swami V, Arteche A, Chamorro-Premuzic T, Furnham A, Stieger S, Haubner T, Voracek M (2008) Looking good: factors affecting the likelihood of having cosmetic surgery. Eur J Plast Surg 30(5):211–218
2. Honigman RJ, Phillips KA, Castle DJ (2004) A review of psychosocial outcomes for patients seeking cosmetic surgery. Plast Reconstr Surg 113(4):1229
3. De Cuyper C (2008) Permanent makeup: indications and complications. Clin Dermatol 26 (1):30–34
4. Wang M, Luo MR, Xiao K, Wurger S, Wang Y, Wei M (2016a) New spectral data for skin colors. In: Proceedings of twenty-fourth CIC, San Diego, CA, pp 266–270
5. Wang M, Xiao K, Wuerger S, Liu HX, Huang M, Luo MR (2016b) Skin color measurement by using non-contact methods. In: Proceedings of CIE 2016 lighting quality and energy efficiency, Melbourne, Australia, pp 487–492

6. Kovac J, Peer P, Solina F (2003) Human skin color clustering for face detection, vol 2. IEEE, pp 144–148
7. Hong G, Luo MR, Rhodes PA (2001) A study of digital camera colorimetric characterization based on polynomial modeling. Color Res Appl 26(1):76–84
8. Berns RS (2014) Extending CIELAB: vividness, Vab*, depth, Dab*, and clarity, Tab. Color Res Appl 39(4):322–330
9. Anderson M, Motta R, Chandrasekar S, Stokes M (1996) Proposal for a standard default color space for the internet—srgb. In: Color and imaging conference, vol 1996(1). Society for Imaging Science and Technology, pp 238–245
10. CIE (2004) Colorimetry. CIE Publication, No. 15, CIE, Central Bureau Vienna, Austria
11. Wang M, Luo MR, Xiao K, Wuerger S, Wang W Wei M (2016) New spectral data for skin colours. In: Proceedings of CIC 2016 conference, pp 266–270

Performance Analysis of Color Measurement System Based on Spectrometer

Xiaochun Wang, Guangxue Chen, Guhong Liu and Kaili Zhang

Abstract Spectral measurement tools are the most widely used color measurement instrument, its various advantages will affect the operator to distinguish colors directly. Although instruments are tested before products come on to the market, but in the using process, instrument will change over time, the instrument will aging gradually, leads to the deviation of color measurement. In order to ensure the accuracy of the measurement, it is very important to calibrate instruments after using a long time. The Lab value of 14 BCRA samples was measured using a marine optical USB4000 spectrometer, a marine optical HL-2000 light source, an optical fiber and a reflective probe, a reflection measurement support, and a standard whiteboard. Using the color difference formula, CIE1976 color difference formula, XYZ value and the mean difference to evaluate the repeatability, reproducibility, accuracy and indication error of the color measurement system. Finally, the conclusions were drawn good overall performance of the spectrometer.

Keywords Spectrometer · Measure error · Repeatability

1 Introduction

Precision is one of the most important performance parameters for the evaluation of color measuring instrument [1]. According to the stability, color measurement system Repeated, reproducibility, error of indication and other performance parameters to test, according to the experimental data to analyze whether each performance index of color measurement system standard, and puts forward the corresponding improvement, in order to obtain accurate color data in the actual production.

X. Wang · G. Chen (✉) · G. Liu · K. Zhang
South China University of Technology, Guangzhou, China
e-mail: chengx@scut.edu.cn

P. Zhao et al. (eds.), *Applied Sciences in Graphic Communication and Packaging*, Lecture Notes in Electrical Engineering 477,
https://doi.org/10.1007/978-981-10-7629-9_12

1.1 Evaluation Index of Indication Error and Accuracy

The value of the indication error of the color measuring equipment is generally expressed as the difference between the measured results and the standard values. If the error of indication error is bigger, the accuracy is lower, and the error is small, the accuracy is high.

$$\begin{cases} \Delta Y = \left|\overline{Y} - Y_0\right| \\ \Delta x = \left|\overline{x} - x_0\right| \\ \Delta y = \left|\overline{y} - y_0\right| \end{cases} \tag{1}$$

$Y_0\, x_0\, y_0$ Standard chroma value of Standard Color Plate
$\overline{Y}\,\overline{x}\,\overline{y}$ The average value of the standard color measuring instrument

National standards for color aberration, for color printing, ΔE^*_{ab} less than 5 in General color printing products, ΔE^*_{ab} less than 4 in Exquisite printing products.

1.2 Evaluation Index of Repeated

Repeatability of the instrument, under the same measuring conditions, Consistency between the results obtained of Continuous and multiple measurements of the same quantity [2].

$$MCDM = \frac{\sum_{i=1}^{N}\left[(L_i - \overline{L_i})^2 + (a_i - \overline{a_i})^2 + (b_i - \overline{b_i})^2\right]^{\frac{1}{2}}}{N} \tag{2}$$

L_i, a_i, b_i ith time measured value,
$\overline{L_i}, \overline{a_i}, \overline{b_i}$ Average of measurement,
N Total number of measurements.

1.3 Evaluation Index of Reproducibility

The reproducibility is an index to express comprehensive ability of reproduction of Instrument and whiteboard [3].

$$\Delta l(u) = \left|u_i - \overline{u}\right|_{\max} \quad (\text{u = 1,2,3,4,5,6,7,8}) \tag{3}$$

u_i ith time measured value,
$\overline{u}$ Average of measurement.

2 Experiments

2.1 Experimental Instruments and Materials

Marine optics USB4000-UV-VIS spectrograph, RPH-1 probe holder, R400-7 Probe and optical fiber, marine optics HL-2000 halogen light source, lab sphere certified reflectance standard white board, 14 pieces BCRA standard ceramic plate, spectrasuite Color measurement software.

2.2 Methods

2.2.1 Selection of Measurement Conditions

Comparison of two angles measured values and standard values, Select a small set of color as the experimental measurement of the geometric conditions.

2.2.2 Uniformity Measurement of Standard Ceramic Plate

Each block was randomly measured at two points, and each point was measured 3 times. The uniformity of color difference is analyzed.

2.2.3 Measurement Reproducibility

8 measurements on BCRA whiteboard, after each measurement, turn 45°.

2.2.4 Repeated Measurement

Short term repeatability for the selection of ten time periods, each time interval 30 s. Each time the color values of 14 BCRA were measured and recorded for short term repeatability. The median repeatability is to select 25 time periods within one day, and the interval is 10 min. The color values of 14 BCRA were measured, and the repeatability of the analysis, the error of indication, the accuracy of the analysis were recorded. Long term reproducibility is within two weeks, after calibration of the instrument, 5 sets of data were measured every day. Each group was divided into 1H.

3 Results and Discussion

3.1 Evaluation of Indication Error and Accuracy of Color Measurement System

The evaluation index of the indication error is the difference between the average value and the standard value, while ΔY is less than 1.5, Δx and Δy are less than 0.02 indicates that the instrument indication error meets the first grade standard, while ΔY is not more than 3, Δx and Δy are not more than 0.02 indicates that the instrument indication error meets the second degree. As we often use the chromatic contrast, it is suitable for testing the color measurement precision of the instrument [4]. And when ΔE is less than 1.6, there is no different between the color, 1.6–3.2, people will think they are the same color, 3.2–6, we can tell the difference and it can be accepted; but while it is more than 6, it will be hard to accepted the difference [5].

The color measurement system based on spectrometer can basically meet the two grade standard; part of the reason the bright color palette is the geometric conditions and measurements between the standard value differences (Figs. 1, 2 and 3).

3.2 Repeatability of Color Measurement System

The repeatability is evaluated by the difference in color difference between the color difference and the standard deviation. If the value is less than or equal to 0.2, it indicates that the instrument reproducibility reaches the primary standard. If the ratio is less than or equal to 0.4, the secondary standard is reached [4]. At the same time, the smaller the value, the data of the small degree of dispersion, data stability

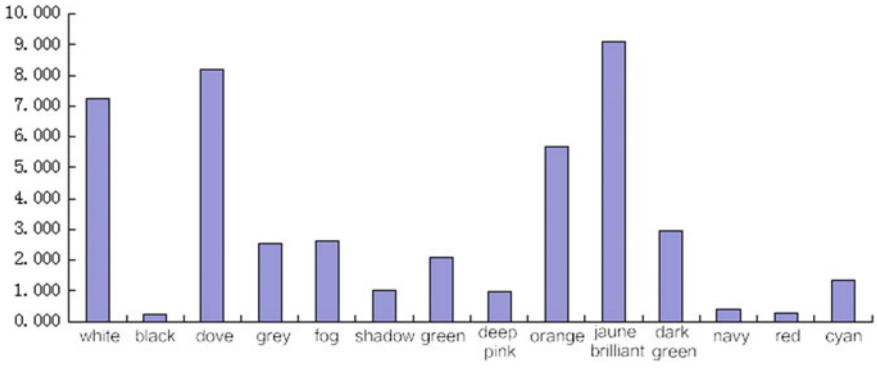

Fig. 1 Error of indication—difference of luminance factor

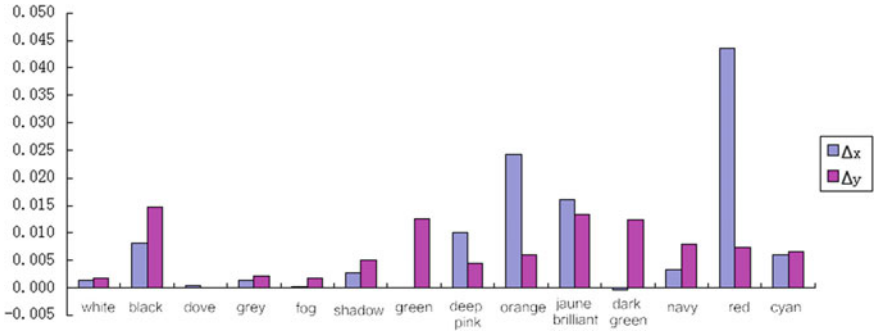

Fig. 2 Error of indication—difference of chromaticity coordinates (Color figure online)

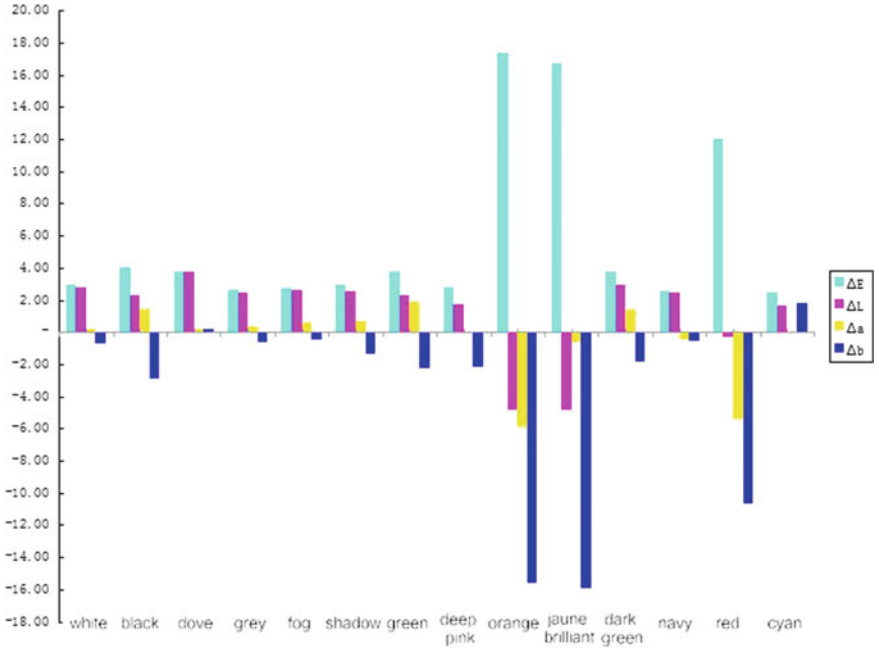

Fig. 3 Difference of between measured value and standard value (Color figure online)

and small fluctuations, good repeatability, the other hand, the greater the value that the data instability, volatility, repeatability worse.

In the repetitive study, short-term repeatability due to the relatively stable light source in the short term, to achieve a standard (Fig. 4), medium-term repeatability due to light source for a long period of time caused by instability in the medium-term repeatability (Fig. 5). Long-term repeatability Since the measurement process as a whole is longer than the mid-term repeatability, the number of system

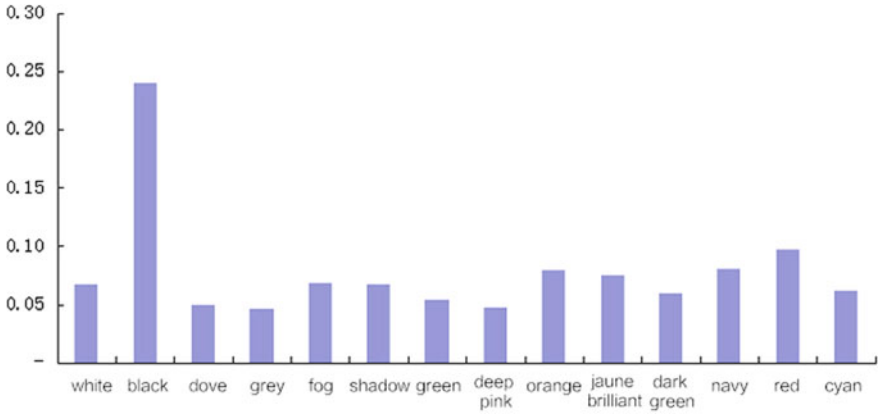

Fig. 4 BCRA color plate short-term repeatability MCDM value

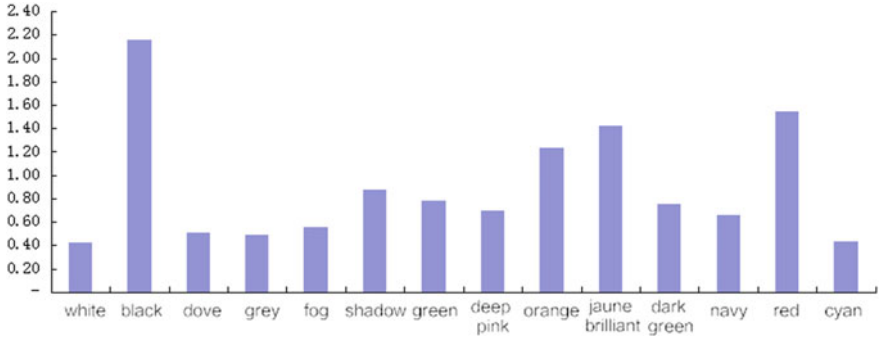

Fig. 5 BCRA color plate medium-term repeatability MCDM value

connections and corrections is also increased, but the long-term repetition of the MCDM value is not much different from the mid-range color difference, so the connection and correction result in subtle deviation (Fig. 6). All in all, the instability of the light source is the main cause of poor instrument reproducibility.

3.3 Reproducibility Analysis

Based on the measured color values, the chromaticity coordinate Δx, Δy is less than zero. As can be seen from the graph, $\Delta Y < 1$, That the instrument repeatability meet the first grade standard (Fig. 7).

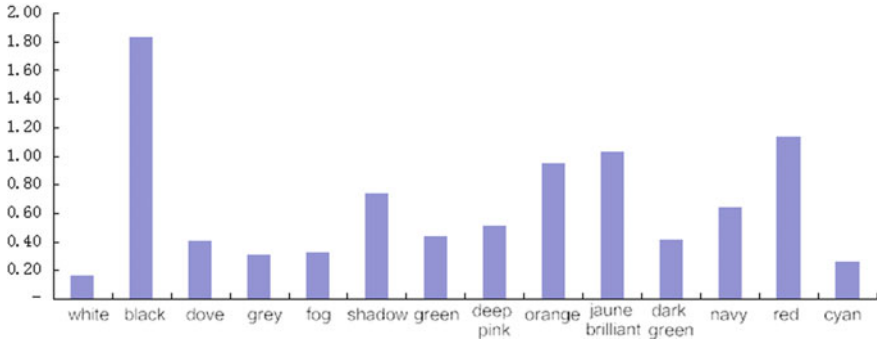

Fig. 6 BCRA color plate long-term repeatability MCDM value

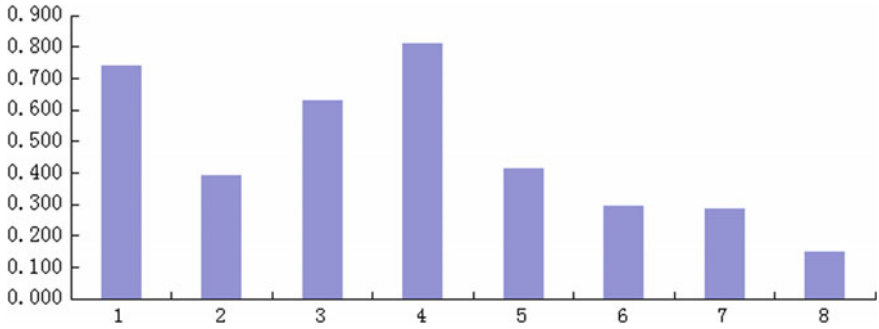

Fig. 7 Brightness difference ΔY

4 Conclusion

In the study of Indication Error and Accuracy, the color measurement system based on the spectrometer basically accords with the secondary standard. Part of the bright color plate produce color difference is due to the difference between the standard value and the measured value of the geometric conditions.

In the study of repeatability, the light source is relatively stable in the short term, so short-term repeatability achieve primary standard. The instability of the light source over a longer period of time results in a greater medium repeatability. In the study of long-term repeatability, since the measurement process is longer than the mid-term repeatability, the number of system connections and corrections is also increased. However, the MCDM values of the long-term repeatability do not differ from the mid-range color difference, so the connection and correction result in slight deviations. All in all, the instability of the light source is the main cause of poor instrument repeatability.

Acknowledgements This research was financially supported by the Guangdong Provincial Science and Technology Project (2017B090901064).

References

1. Wang Y (2011) Research on color difference evaluation method based on color difference formula. Beijing Institute of Graphic Communication
2. Li DH (2009) Repeatability and stability of measurement instruments in calibration laboratory proficiency testing. Chin Measur 4:41–42
3. Song C (2014) Research on recovery technology of color display based on image quality assessment. Doctoral dissertation, Graduate University of Chinese Academy of Sciences, Changchun Institute of Optics, Fine Mechanics and Physics
4. Wang C (2013) Study on portable spectrophotometer system. Doctoral dissertation, China Measures the Institute
5. Sun XR, Lin ZD, Zhang JY, Lin ZX, Jingand QC, Guo SQ (1996) Experimental study on Chinese eye color discrimination. J Psychol 28(1):9–15

A Color Prediction Model for Halftone Print Based on Light Scattering Effect

Tingli Liu and Guangxue Chen

Abstract Considering the translucency of paper and the non-optical contact between the paper and the backing, this study aims at modeling light scattering in order to improve the prediction of the reflection spectra of photoengraving prints, to fetch the explicit expression around the empty space between the printing materials, and to determine the reflectance of the dot parts and photoengraving printing materials in accordance with measure the MTF of paper and calculate point spread function of paper. Furthermore, a new algorithm for color prediction is established. Compared with the practically checked spectral reflectivity of the photoengraving printing materials proof by using spectrophotometer, the precision of the model shown in this paper is greatly verified.

Keywords Light scattering effect · Color prediction · Point spread function Photoengraving prints

1 Introduction

Y. Azuma and M. Inui created a model for predicting the spectra of photoengraving prints. They used one kind of half-tone dot structure model to demonstrate the result of light scattering and then reckoned the colorimetric features of single dot photoengraving print. This model presumes that a half-tone dot contains 2 domains: core and fringe. Rahaman GM Atiqur and Norberg. Ole has a same report about core and fringe of half-tone dot. All the models have the same "lineage" as the prototype Murray–Davies model. However, nowadays not only the data collection but also the model fitting are getting harder and harder, as under certain circumstances they only count on the parameters in theory instead of the practical ones.

T. Liu · G. Chen (✉)
State Key Laboratory of Pulp and Paper Engineering, South China University of Technology, Guangzhou, Guangdong, China
e-mail: chengx@scut.edu.cn

P. Zhao et al. (eds.), *Applied Sciences in Graphic Communication and Packaging*, Lecture Notes in Electrical Engineering 477,
https://doi.org/10.1007/978-981-10-7629-9_13

Regardless of the Yule–Nielsen [1] parameter n, this thesis brings about one theoretical method to observe the halftone spectral prediction [2]. We involve the following parts in the thesis: firstly, we analyze the light scattering effect for monochrome prints and deduce the explicit expression of empty space of printing material, and determine the reflectivity of the dot part and photoengraving printing materials in accordance with measuring the MTF [3] of paper and calculate point spread function [4] of paper. Afterward, this information will be used by our color prediction model in order to compute precisely the spectra of photoengraving prints. Eventually, the color variation of the predicted value and the measured value of the model is going to be checked by us in the thesis.

2 Analyzing Scattering and Reflectance for Halftone Prints

The paper substrate is highly scattering media, and has a low penetrability. However, it is not fully opaque, fewer light could enter through the prints and reflect from the backing of paper, in other words, the backing of paper will influence prints color (Fig. 1). So, the prints backing cannot be neglected for photoengraving spectral prediction.

Due to illumination, the dot part penetrate into the ink layer, the light enter from the ink layer and exit from the ink layer (Fig. 2), the transfer equations of light fluxes traveling between different layers were listed as below,

$$j(b) = R_b i(b) \tag{1}$$

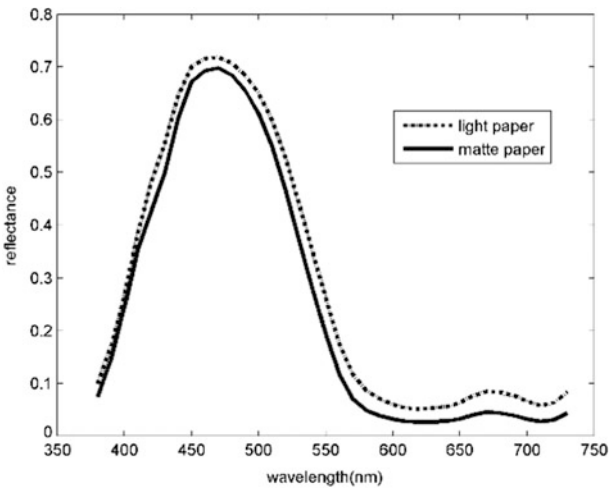

Fig. 1 Spectral reflectance of the cyan solid print with different opaque backgrounds

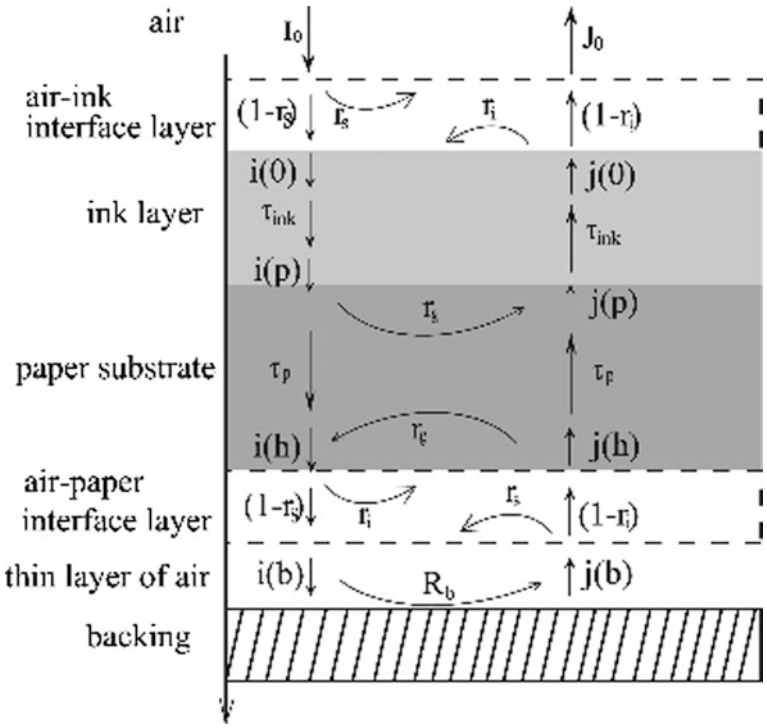

Fig. 2 The entrance and departure of light from the ink layer

$$i(0) = I_0(1 - r_s) + j(0)r_i \tag{2}$$

$$j(0) = j(p)\tau_{ink} \tag{3}$$

$$i(p) = i(0)\tau_{ink} \tag{4}$$

$$j(p) = i(p)r_g + j(h)r_p \tag{5}$$

$$i(h) = i(p)\tau_p + j(h)r_g \tag{6}$$

$$j(h) = i(h)r_i + j(b)(1 - r_s) \tag{7}$$

$$i(b) = i(h)(1 - r_i) + j(b)r_s \tag{8}$$

$$J_0 = I_0 r_s + j(0)(1 - r_i) \tag{9}$$

As mentioned above,

$$R_{S1-S1} = \frac{J_0}{I_0} = r_s + \frac{(1-r_s)(1-r_i)Z_1}{1-r_i Z_1} \tag{10}$$

Among,

$$z_1 = r_g \tau_{ink}^2 + \frac{(1-R_b r_s) r_i \tau_{ink}^2 \tau_p^2 + (1-r_s)(1-r_i) R_b \tau_{ink}^2 \tau_p^2}{(1-R_b r_s)\left(1-r_i r_g\right) - (1-r_s)(1-r_i) R_b r_g} \tag{11}$$

In this formula, I_0 shows the incident ray strength of the whole system, J_0 indicates the emergent ray strength of the entire system, R_{S1-S1} indicates the reflectance of entrance and departure from S_1, r_s represents the specular reflection, r_i represents ink internal reflectance, r_g represents paper internal reflectance, R_P indicates the reflectance of paper-base, τ_{ink} represents ink transmittance, τ_p represents paper-based transmittance, R_b indicates the reflectance of backing. The parameters $\tau_p, r_s, r_i, r_g, \tau_{ink}$ cannot be obtained by direct measurement methods.

To obtain the necessary parameters for predictive expression, the equations system is established by altering the backing, and the reflectance of specimens are measured. Then, we use nonlinear least squares data fitting method. Besides, printing by using magenta ink on paper-base, and calculate the necessary parameters (Fig. 3).

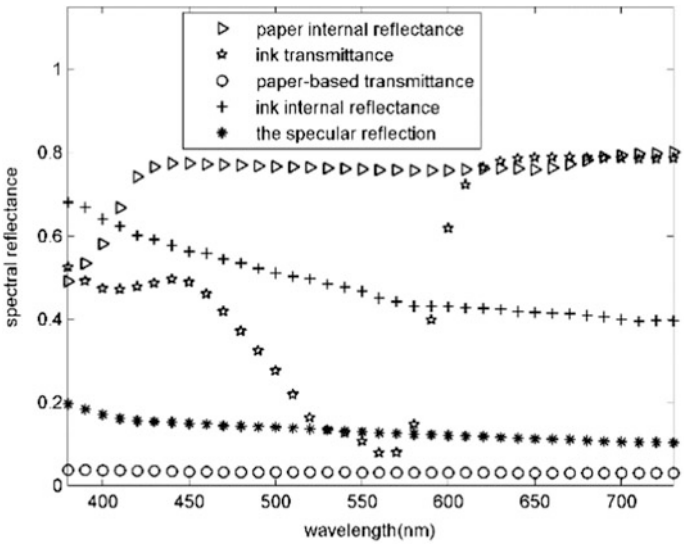

Fig. 3 The parameters of the solid print using magenta ink on paper-base

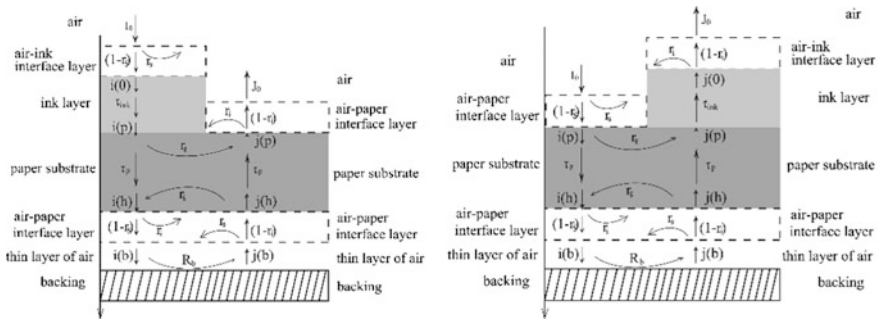

Fig. 4 The ray enters from the paper base and the departure from the ink layer (vice versa)

The fact that ray enters from the paper base and the departure from the ink layer (vice versa) shares the same scattering (Fig. 4), in accordance with the beam path reversal principle, this formula can all be written as below,

$$R_{S1-S2} = R_{S2-21} = r_s + \frac{\tau_{ink}(1-r_s)(1-r_i)\left(r_g + Z_2\right)}{1 - r_i\tau_{ink}r_g - r_i\tau_{ink}Z_2} \tag{12}$$

Among,

$$Z_2 = \frac{r_i\tau_p(1-r_sR_b) + \tau_pR_b(1-r_s)(1-r_i)}{1 - r_sR_b - r_gr_i(1-r_sR_b) - R_br_g(1-r_s)(1-r_i)} \tag{13}$$

R_{S1-S2} indicates the scattering light reflectance from regions S_1 to S_2, R_{S2-S1} indicates the scattering light reflectance from regions S2 to S1.

The light entrance and departure from the paper base as shown in Fig. 5. We obtain:

$$R_{S2-S2} = \frac{(1-r_s)(1-r_i)\left(r_g + Z_2\right)}{1 - r_i\left(r_g + Z_2\right)} \tag{14}$$

R_{S2-S2} indicates the reflectance from regions S2 to S2.

3 Application of the Model

We have tested the reflectance prediction model on photoengraving patches, using the SpectroEye spectrophotometer for measurement [5], the gauge's spectrum region ranges from 380 to 730 nm, whose time interval is 10 nm. The color patches

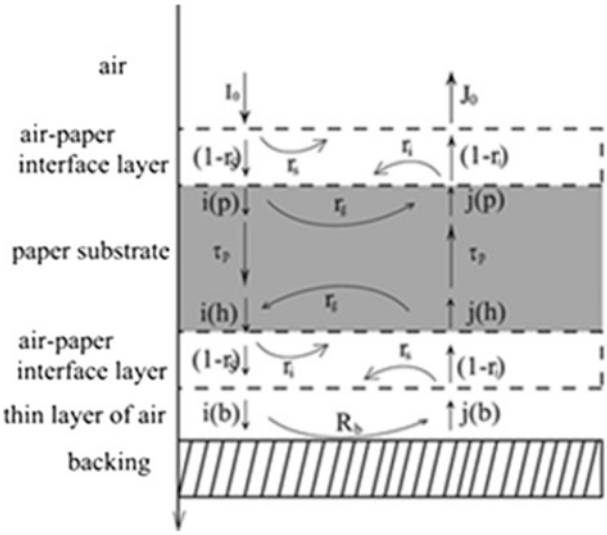

Fig. 5 The light entrance and departure from the paper base

are printed by Heidelberg. The point deducted above spread, probabilistic model and computation formula of halftone spectral prediction was programmed by MATLAB software, and the spectral reflectance of the printing material was calculated. The consequences had been contrasted with the ones checked in reality.

On account of the constrained space, we could only utilize the e observational data of top tone dot wedges (30, 50, 70, 90% cyan, magenta, yellow and black). The explicit expressions deducted in the model, as it has been checked and examined, also apply to various dot wedge specimen pages of cyan, magenta, yellow and black printing inks, the consequences could be checked during the entire experiments.

We calculated the color difference [6] to evaluate the error between the predicted spectral reflectance of photoengraving presswork and the values measured in actual. The findings are presented in Table 1.

Table 1 Difference in ΔE_{94} between predicted and measured reflectance spectra

	Sample	ΔE_{94}		Sample	ΔE_{94}
Cyan	30%	0.69	Magenta	30%	1.02
	50%	1.12		50%	0.95
	70%	0.72		70%	0.92
	90%	1.06		90%	0.81
Yellow	30%	0.72	Cyan + Magenta + Yellow	C50% + M50% + Y50%	1.36
	50%	0.88		C20% + M30% + Y50%	1.61
	70%	0.62		C30% + M60% + Y80%	1.68
	90%	0.75		C40% + M50% + Y60%	1.59

4 Conclusions

The relation formulas among the halftone spectrum and the dot area, the transparency [7] of the ink layer; the point spread function, and the spectral reflection of the paper backing have been acquired by us during the experiments. During the research, we acquire favorable consequences in the spectral reflection prediction with the formula, showing that the accuracy of the recommended halftone spectral prediction model. The thesis merely emphasized on the homochromatic photoengraving presswork. The penetration effect of the printing ink was not considered. When it comes to the multicolor over-print, the punch-through effect of the printing ink requires further study.

Acknowledgements This research was funded by State Key Laboratory of Pulp and Paper Engineering Funded Project (2016c01) and Science and Technology Program of Guangzhou (201607020045).

References

1. Hébert M, Hersch RD (2011) Yule–Nielsen based recto–verso color halftone transmittance prediction model. Appl Opt 50(4):519–525
2. Hersch RD, Crete F (2005) Spectral reflection and dot surface prediction models for color halftone prints. Electron Imaging 14(3):545–554
3. Mourad S (2007) Improved calibration of optical characteristics of paper by an adapted paper-mtf model. J Imaging Sci Technol 51(4):283–292
4. Rossmann K (1969) Point spread-function, line spread-function, and modulation transfer function. tools for the study of imaging systems. Radiology 93(2):257–272
5. Liu Y, Tian Q, Mou X (2016) The experimental research of color measurements with spectrophotometer. Advanced graphic communications, packaging technology and materials. Springer, Singapore
6. Mcdonald R, Smith KJ (1995) Cie94-a new colour-difference formula*. Color Technol 111 (12):376–379
7. Gueymard CA (2001) Parameterized transmittance model for direct beam and circumsolar spectral irradiance. Sol Energy 71(5):325–346

Analysis of the Color Appearance Model of CIECAM02 Based on OSA-UCS Data

Wenbing Yang and Xiaoxia Wan

Abstract The visual uniformity of color space has an important influence on the color difference calculation and color gamut mapping algorithm, so it is necessary to make a qualitative and ration evaluation of the spatial visual uniformity of the CIECAM02 color appearance model. On the basis of known CIECAM02 can predict the color appearance in different environments, OSA-UCS data set was used to analyze the degree of uniformity of CIECAM02 color appearance space. Through the experimental samples, select the data set of 13 color samples with the center color sample, and 12 adjacent color samples with equal visual difference. Each quadrant contains five sets of data, a total of forty sets of group data. T after examination and analysis, the uniformity of the fourth quadrant and the eighth quadrant of the yellow and red color space is better than the other color space, while the third and the seventh quadrant of the blue and red color space uniformity is the worst. Therefore, the overall uniformity of the CIECAM02 color space is not good and needs to be optimized.

Keywords Color appearance space · Date · Optimized · OSA-UCS

1 Introduction

One of the criteria to evaluate the quality of a color space is the visual uniformity of the color space, from the initial CIERGB to CIELAB, It can be said that color and chromaticity have been developing in the direction of uniformity [1, 2]. As the latest theoretical development of color and chromaticity, CIECAM02 has two characteristics, one is the color prediction ability in cross media environment, and

W. Yang (✉)
Yiwu Industrial and Commercial College, No.2, Xueyuan Road,
Yiwu, Zhejiang, China

X. Wan
School of Printing and Packaging, Wuhan University, Wuhan, China

P. Zhao et al. (eds.), *Applied Sciences in Graphic Communication and Packaging*, Lecture Notes in Electrical Engineering 477,
https://doi.org/10.1007/978-981-10-7629-9_14

the other is the visual uniformity of color space [3, 4]. The visual uniformity of color space has an important influence on the calculation of color difference and the quality of gamut mapping algorithm [5], so it is necessary to make a qualitative and ration evaluation of the spatial visual uniformity of CIECAM02 color appearance model.

In this paper, the experimental principle of the uniformity analysis of CIECAM02 color space is the color sample pair of equal visual difference (equal color appearance difference) in the 0SA-UCS (Uniform color scale system of the American Optical Society) uniform color ruler system [6, 7]. After the color sample input data is converted to the color appearance property values in the color space, the color differences in the color space between the color samples of these equal visual differences should be equal, that is the Euclidean distance indicating the color difference should be equal [8]. Therefore, in this paper, based on the experimental principle, the uniformity analysis is carried out.

2 CIECAM02 Color Space J Uniformity Analyses

Based on color appearance space J uniformity analysis, is in the OSA-UCS uniform color scales in selected hue is zero [(J, g) = (0, 0)] of the different brightness of the neutral gray color samples and eight different colors, different brightness color samples are uniformly distributed in the hue plane, consist of nine group of different brightness color samples [9, 10]. Testing the linear relationship between lightness J and lightness L that are converted into CIECAM02 color space. If the brightness J in the CIECAM02 color space is uniform [11, 12], the brightness J and L should be linearly proportional to each other. That is, in the OSA-UCS uniform color scale system, the L values between the color samples have the same change, and the corresponding J values in the color appearance space should also have the same change [13]. The coordinates of the selected nine sets of samples of different brightness colors are listed in Table 1 for reference.

From the nine sets of data, choose 2 sets of different brightness color samples L value and CIECAM02 color appearance space corresponding brightness J relationship, the picture in Fig. 1.

According to Fig. 1, it can be concluded that when the L value of different brightness neutral gray increases uniformly, the corresponding color appearance property lightness value J does not increase uniformly. When the L value is less than zero, the increment of the J value is more uniform, the L value is greater than zero, and the increment of the J value increases. That is to say, the color appearance space has better linear uniformity in the low brightness region, and the linear uniformity in the region of high brightness needs to be further improved.

According to Fig. 2, it can be concluded that the increments of J values are large and small when the L values of samples with different brightness partial yellow are increasing uniformly, which indicates that the uniformity of J value of color appearance space in partial yellow region needs to be improved.

Table 1 The coordinates of nine groups of different hue of different brightness color samples

Color samples	Color sample coordinates
Different brightness neutral gray	(−6, 0, 0); (−4, 0, 0); (−2, 0, 0); (0, 0, 0); (2, 0, 0); (4, 0, 0)
Different brightness partial red	(−6, 0, 2); (−4, 0, 2); (−2, 0, 2); −1, 0, 2); (0, 0, 2); (1, 0, 2); (2, 0, 2); (4, 0, 2)
Different brightness partial yellow	(−6, 2, 0); (−4, 2, 0); (−2, 2, 0); (−1, 2, 0); (0, 2, 0); (1, 2, 0); (2, 2, 0); (4, 2, 0)
Different brightness partial green	(−6, 0, −2); (−4, 0, −2); (−2, 0, −2); (−1, 0, −2); (0, 0, −2); (1, 0, −2); (2, 0, −2); (4, 0, −2)
Different brightness partial yellow and green	(−7, 1, 1); (−5, 1, 1); (−3, 1, 1); (−1, 1, 1); (0, 1, 1); (1, 1, 1); (3, 1, 1); (5, 1, 1)
Different brightness partial yellow and red	(−7, 1, −1); (−5, 1, −1); (−3, 1, −1); (−1, 1, −1); (0, 1, −1); (−1, 1, −1); (−3, 1, −1); (−5, 1, −1)
Different brightness partial blue and red	(−7, −1, −1); (−5, −1, −1); (−3, −1, −1); (−1, −1, −1); (0, −1, −1); (1, −1, −1); (3, −1, −1); (5, −1, −1)
Different brightness partial blue and green	(−7, −1, 1); (−5, −1, 1); (−3, −1, 1); (−1, −1, 1); (0, −1, 1); (1, −1, 1); (3, −1, 1); (5, −1, 1)

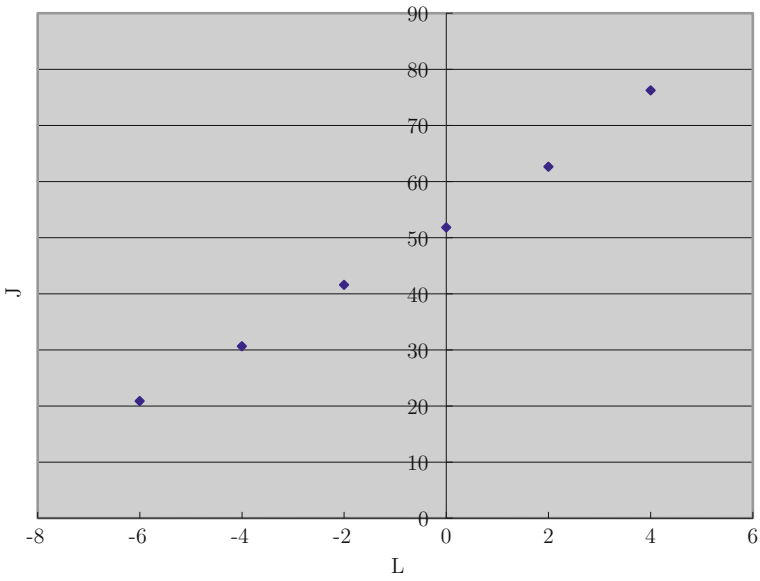

Fig. 1 The linear relationship between neutral grey L and corresponding J different brightness

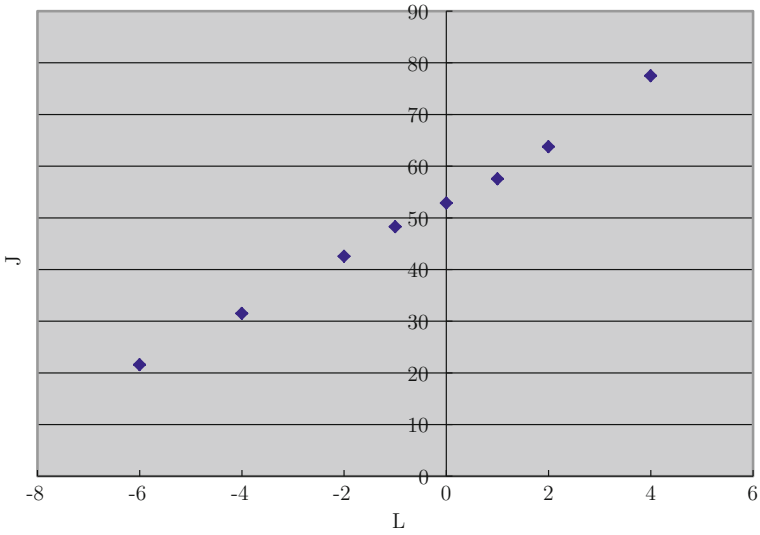

Fig. 2 The diagram of different brightness of partial yellow color samples L and corresponding

3 Selections and Processing of Experimental Data

OSA-UCS uniform color scales system 558 sets of data are uniformly distributed in the OSA-UCS uniform color scales of the L system, J, G in three-dimensional space, form an orthogonal coordinate system [14]. Therefore, the coordinate system can be divided into eight quadrants in space, with (L, J, g) = (0, 0, 0) as the coordinate origin, each quadrant of five sets of data, a total of forty sets of data. The first coordinate samples of the 5 centers were (0, 0, 0), (1, 1, 1), (2, 2, 4), (2, 4, 4), (3, 1, 3), Second quadrant coordinates are (1, −1, 1), (1, −3, 1), (2, −2, 2), (3, −1, 1), (4, −2, 2); The third quadrant coordinates are (1, −1, −1), (2, −2, −2), (2, −2, −4), (3, −1, −3), (4, −2, −2); Fourth quadrant coordinates are (0, 2, and 4), (1, 1, and 3), (2, 4, and 4), (3, 3, and 3), (4, 6, and 2); Fifth quadrant coordinates are (−1, 1, 1), (−2, 2, 2), (−2, 4, 4), (−3, 1, 1), (−4, 2, 2); Sixth quadrant coordinates are (−1, −1, 1), (−2, −2, 2), (−2, −4, 4), (−3, −1, 1), (−4, −2, 2); Seventh quadrant coordinates are (−1, −1, −1), (−2, −2, −2), (−3, −1, −1), (−4, −2, −2), (−5, −1, −1); eighth quadrant coordinate are (−1, 1, −1), (−2, 4, −4), (−3, 3, −1), (−3, 1, −1), (−5, 1, −1). The forty group of OSA-UCS color sample data of the Yxy value, to convert the input data of XYZ CIECAM02 color appearance space, and then converts the color appearance of the color space to the red and green a, yellow and blue b, tonal h and H, brightness J, lightness Q, saturation S, chroma C, colorfulness M. Among them, lightness J, red and green a, yellow and blue b together form the initial color appearance space Jab.

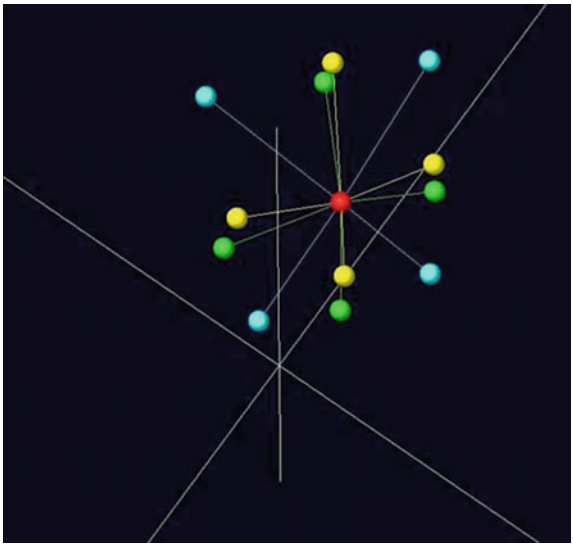

Fig. 3 The spatial relation between the center sample (2, 2, 4) and the surrounding samples

As shown in Fig. 3, a set of color sample spatial relationships is shown in the first quadrant of the center point (2, 2, 4). Figure 3 vertical space coordinate system is the J value, the a value of the horizontal axis is the horizontal plane, the vertical axis is b, 12 points near the center point and is connected to the 12 line, the center point is indicated by a red ball, and said four near the point of center point of the same level with the blue ball, In the direction of the J value, it is higher than the center point, and the four adjacent points on one level are represented by yellow balls, In the direction of the J value, it is lower than the center point, and the four adjacent points on one level are represented by green balls. As you can see from Fig. 3, the spatial distance between the adjacent 12 color samples and the intermediate color sample is not the same. That is to say, the green and yellow (Partial green) region of the color appearance space Jab is not uniform.

Finally, the standard deviation of the chromatic aberration is calculated as shown in Eq. (1) [15].

$$S = \sqrt{\frac{\sum_{i=1}^{n} \left(\Delta E_i - \overline{\Delta E}\right)^2}{n}} \tag{1}$$

Among them, ΔE_i represents the color difference between the surrounding color samples and the central color samples, I represents the first I color samples around the 12 surrounding colors; ΔE Represents the average value of the 12 colors of the set of data; N indicates how many of the data center color samples actually have a number of adjacent points in the OSA-UCS uniform color scale system; the value of n is less than or equal to 12.

The standard deviation can indicate the uniformity of the color appearance space in this region. The smaller the standard difference, the higher the degree of equality of the 12 colors, the better the spatial uniformity; on the contrary, the greater the standard difference, the lower the degree of uniformity of the 12 color differences, the lower the uniformity.

4 Analysis of Spatial Homogeneity of CIECAM02 Color Appearance

After the data selection and processing of OSA-UCS color samples, A total of 40 lattice framework structures in eight quadrants are obtained, namely, the color difference values of forty sets of color samples in the CIECAM02 color space, The standard deviation of the forty sets is calculated according to the color difference of forty sets of color samples, are shown in Table 2.

Through the analysis of the experimental data of Table 2, the following conclusions are obtained, Fifth quadrant low brightness yellow and green hue space uniformity is better than the first quadrant yellow and green with high brightness; Second quadrant high brightness blue and green hue space uniformity is better than the sixth quadrant blue and green with low brightness; Third quadrant high brightness blue and red hue space uniformity is better than the seventh quadrant blue and red with low brightness; Fourth quadrant high brightness red and yellow hue space uniformity is better than the eighth quadrant red and yellow with low brightness; By comparing the standard deviation data of the eight quadrants, it can be seen that fourth quadrant high brightness red and yellow hue space uniformity is better than that of the other quadrants; The five sets of standard deviation in the seventh quadrant are greater than 2, so seventh quadrant low brightness blue and red hue space uniformity is the worst. Fourth quadrant high brightness red and yellow hue space uniformity is optimal.

Table 2 Standard deviation of color difference value of forty groups of color samples

Quadrant	Standard deviation				
	Group 1	Group 2	Group 3	Group 4	Group 5
First quadrant	2.2112	0.92564	1.6143	1.3049	2.1583
Beta quadrant	1.3711	1.3556	1.5562	1.2534	1.7444
Third quadrant	2.1643	0.78694	0.73424	1.9568	1.7170
Delta quadrant	1.2500	0.25211	0.93786	0.49257	1.2332
Fifth quadrant	1.5258	1.9209	1.5946	1.8751	1.7506
Sixth quadrant	1.4236	2.1188	1.7850	2.0374	1.9540
Seventh quadrant	2.4158	2.0992	2.3311	2.2262	2.4582
Eighth quadrant	1.4432	1.3168	1.4958	1.4410	1.7196

5 Conclusions

From the above experimental results, we can conclude that the uniformity of the four color spaces can be investigated by combining eight quadrants, Including the degree of uniformity of yellow and blue color space, blue and green color space, blue and red color space, yellow and red color space, whether it is the uniformity of the fourth quadrant or the eighth quadrant of the yellow and red color space is better than the other color space, while the third and the seventh quadrant of the blue and red color space uniformity is the worst. Therefore, the overall uniformity of CIECAM02 color space is not good, in which the uniformity of yellow and red color space is better, and the uniformity of blue and red color space is poor, the uniformity of CIECAM02 needs to be optimized further.

Acknowledgements This study is funded by School and enterprise cooperation projects in Higher Education (FG2016129), this work is also supported by Project of the National Natural Science Foundation of China (61275172).

References

1. Zhu SY, Luo MR, Cui GH, Rigg B (2002) Comparing different color discrimination data sets. In: Proceeding of the tenth color imaging conference. Color science systems and applications, pp 51–54
2. Li CJ, Luo MR, Rigg B, Hunt RWG (2002) CMC 2000 chromatic adaptation transform CMCCAT2000. Color Res Appl 27:49–58
3. Cai B (2006) Research on some problems of color appearance model CIECAM02. Beijing Institute of Technology, Beijing
4. Luo MR, Cui G, Li C (2006) Uniform color spaces based on CIECAM02 colour appearance model. Color Res Appl 8:320–330
5. Juan LG, Luo MR (2000) New magnitude estimation data for evaluating colour appearance models. Colour Vis Scales NPL, UK 4:3–5
6. Indow TA (2003) Test of uniformities in the OSA-UCS and the NCS. Color Res Appl 28:277–283
7. Macadam DL (1978) Colorimetric data for samples of OSA uniform color scales. J. Opt Soc Am 68(1):121–130
8. Nickerson D (1979) Munsellrenotations for samples of OSA uniform color scales. J Opt Soc Am 69(3):1343–1347
9. Deng Q, Wang N (2012) Color management of digital camera based on CIECAM02 color appearance model. Packag Eng 5:115–118
10. Liu Z, Meng FY, Xie XT (2009) Visual-Uniformity analysis of CIECAM02 color appearance model optimization. Imaging Sci Photochem. 27(2):128–134
11. Lv X, Zhao M (2002) Uniformity of CIELAB color space. J Zhengzhou Univ 34(1):69–73

12. Jin XS, Wang HL (2011) From CIELAB color space to the development of CIECAM02 color appearance model. Printing Dyeing 37(12)
13. Xie D, Zhu W, Li R (2014) Color image evaluation algorithm based on optimal color space and visual masking. Packag Eng 35(21):86–90, 112
14. Dong W, Shi-sheng Z (2008) Application of OSA-UCS model in color space detection. J Wuhan Univ 54(3):321–324
15. Li J, Liu Z (2009) Research progress of CIECAM02 color appearance model. Photogr Sci Photochem 27(5):391–398

Reliability of MacAdam Color Discrimination Ellipses

Jing Liang, Ming Ronnier Luo and Guihua Cui

Abstract The goal of this paper is to investigate reliability of the MacAdam color discrimination ellipses. 1176 pairs of chromatic color difference that was presented on a display. Sampling was done in CIELAB color space. 20 observers assessed the differences using the ratio method. Each pair was assessed against two different backgrounds (a black background and a grey background). Various existing color spaces were tested by the results. It was found that CAM02-UCS performed the best to predict color difference against a grey background. The performance of the CIELAB color space performed the best to predict color difference against a black background. The current experimental ellipses were compared with the original MacAdam ellipses. Both sets had quite different patterns.

Keywords MacAdam color discrimination ellipse · Ratio method
CIELAB color space · Predict color difference

J. Liang · M. R. Luo (✉)
State Key Laboratory of Modern Optical Instrumentation,
Zhejiang University, Hangzhou, China
e-mail: m.r.luo@leeds.ac.uk

J. Liang
School of Information Science and Engineering,
Dalian Polytechnic University, Dalian, China

M. R. Luo
School of Design, University of Leeds, Leeds, UK

G. Cui
School of Physics and Electronics Information Engineering,
Wenzhou University, Wenzhou, China

P. Zhao et al. (eds.), *Applied Sciences in Graphic Communication and Packaging*, Lecture Notes in Electrical Engineering 477,
https://doi.org/10.1007/978-981-10-7629-9_15

1 Introduction

For the lighting industry, MacAdam color discrimination ellipses have been used to define the color tolerance for lighting products. However, the MacAdam experiment was carried out using at a constant luminance level and only assessed by an observer via a visual colorimeter, which had a viewing conditions quite different from the normal binocular vision [1, 2]. With the above in mind, the main goal of this work is: to test the reliability of the MacAdam color discrimination ellipses. The results were also used to investigate the parametric effects of different luminance levels, two backgrounds, and color spaces of sampling and to test various color models' performance.

2 Experimental

A software was developed to present the stimuli on an Eizo color Edge CG220 display. All colorimetric values had been consistently monitored though the experiments so as to maintain accuracy of reproduction. In this study, 18 color centres from the MacAdam dataset and 8 neutral centres from the ANSI C78.377 standard [3] were the experimental color centres. Sampling was performed in a*b* plane, where 21 points were sampled surrounding each color centre ranging from 0° to 180°. Equal difference of ΔE*ab of 5 units was applied to all color centres. The difference between the color centre and samples was defined in terms of Euclidean distance in CIEa*b* plane.

Figure 1 shows all the Macadam ellipses and the 11 color centres studied in the present experiment (those with cross symbol), which are within the color gamut of the display (the blue triangle). In order to determine the influence of different luminance levels, the color centres had two luminance levels, 18.5 and 48 cd/m^2. Two backgrounds were used, a light grey and black corresponding to 24 and 0 cd/m^2. Note that the former corresponds to the original luminance level used in the MacAdam experiment, while 0 cd/m^2 was chosen to have an L* value close to zero to simulate the viewing of street lights in the dark night.

The experimental arrangement of the stimuli is illustrated in Fig. 2. In the display, a scroll bar was provided in the software interface so as to record each assessment. Observers were asked to evaluate color difference of each pair using the ratio method, i.e. each test pair against a fixed reference green pair which was assigned to have a color-difference of one unit. The reference green pair had a lightness difference (ΔL*) of 6 units. The location of the two pairs was randomly interchanged in both dimensions.

In total, 23,520 assessments were made, i.e. (26 centres + 2 repeats) × 21 pairs × 2 backgrounds × 20 observers.

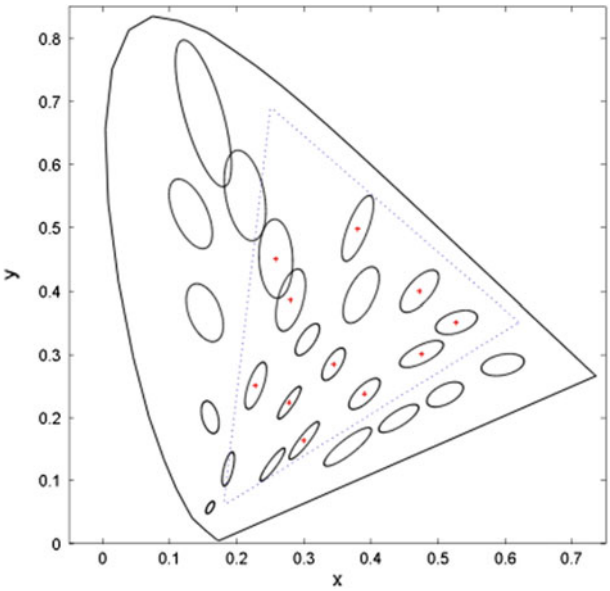

Fig. 1 MacAdam discrimination ellipses along with the selected color centers for the current study marked by the cross symbol; display gamut by blue dash triangle (color figure online)

Fig. 2 Experimental stimuli arrangement for both background

3 Comparing Results and Data Analysis

3.1 Observer Variation

A group of 20 (10 male/10 female) Chinese observers took part in the experiment. Observers had a mean age of 23 ranged between 22 and 26. All observers passed the Ishihara color vision test. And they were informed of the content of the consent experiment. All procedures followed were in accordance with the ethical standards

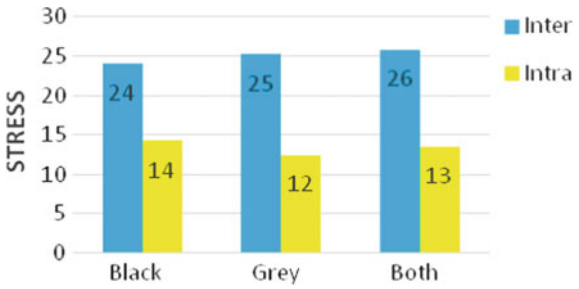

Fig. 3 Results for inter-observer and intra-observer variation

of the responsible committee on human experimentation (institutional and national) and with the Helsinki Declaration of 1975, as revised in 2008 (5). Informed consent was obtained from all patients for being included in the study.

The STRESS (standardized residual sum of squares) measure has been used widely in the color-difference research field [4]. Figure 3 shows the inter-observer and intra-observer variation for the black and grey backgrounds together with the overall data. It can be seen that observer inter-variation had a bigger STRESS value than that of intra-observer variation. The inter-observer variation was about twice of the intra-observer variation. The results of the present study are very similar to the results of the other studies [5–7].

3.2 *Comparing Visual Results Due to Parametric Difference*

Figure 4a, b show the parametric effects of background and luminance, respectively. Figure 4a plots the visual differences for grey background against those for black background. It can be seen that visual differences of black background are larger than those of grey background. In Fig. 4b, the majority of the visual differences of high luminance level (48 cd/m^2) are smaller than those of high luminance level (18.5 cd/m^2).

3.3 *Comparing Experimental Ellipses with the MacAdam Ellipses*

The visual differences for each color centre were used to fit experimental ellipses. The grey background results had the same viewing conditions as the MacAdam experiment. They were used to compare with the MacAdam ellipses. The current experimental ellipses were scaled to have the scale as the MacAdam ellipses by means of ellipse area, (πAB). Thus the purpose of meaningful comparison.

Figure 5 shows three sets of ellipses, MacAdam, the present high luminance and the present low luminance, plotted in black, red and green colors respectively. It can

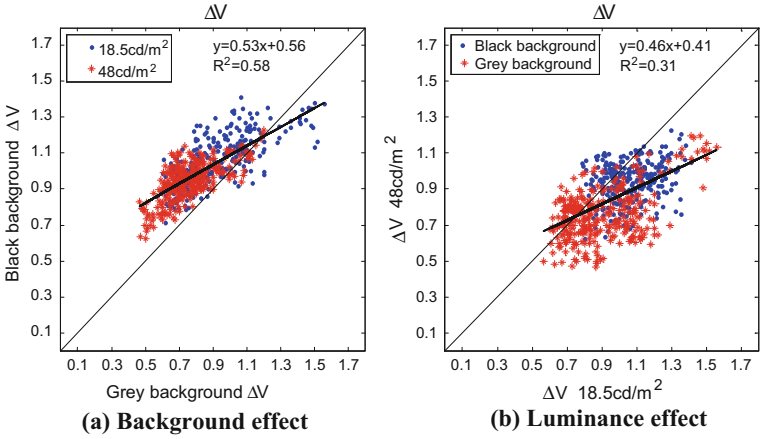

Fig. 4 Plot of ΔV values **a** between grey and black backgrounds, and **b** between the high and low luminance

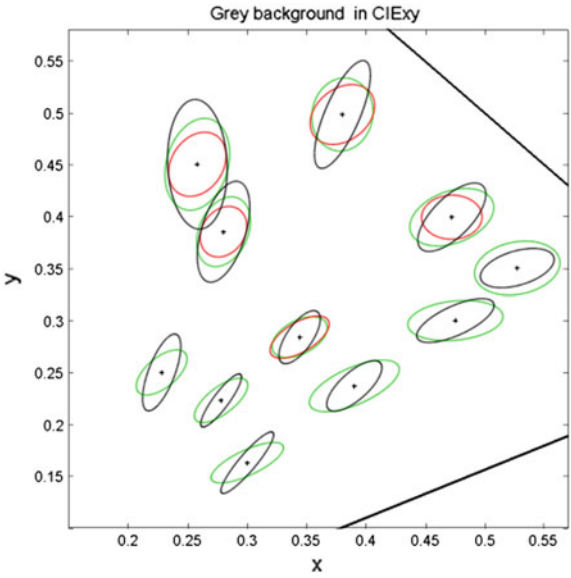

Fig. 5 Experimental ellipses plotted against MacAdam ellipses (color figure online)

be seen that there seems to be a great similarity for all three sets in ellipse orientation. There is a distinct pattern for MacAdam ellipses, i.e. all ellipses increase size from the smallest blue in bottom left to the largest green and also to the saturated yellow, red. However, the sizes of the present ellipses showed a different pattern, i.e. the smallest ellipse in the neutral grey area and gradually increase towards the

Table 1 The performance of color models in STRESS units

Background	CIELAB	CIEDE2000	CIECAM02	CAM02-UCS	CIELUV	xy	FMC-1
Black	16	32	17	22	24	23	32
Grey	24	26	21	15	28	28	32

saturated colors. Overall, from the pattern of ellipses, we can conclude that Macadam data are quite different from the present data.

3.4 Testing the Performance of Color Models

Various color models were tested using the present dataset. They were selected to represent different types of color models. They included two CIE uniform color spaces (CIELAB and CIELUV), CIEDE2000 color difference formula, xy chromaticity diagram, CIECAM02 color appearance model and its color space, CAM02-UCS, and FMC-1 equation, which designed to fit the MacAdam data.

Again, STRESS was often used to indicate the agreement between the visual and predicted color differences. It was found that CIELAB significantly outperformed the other models for the black background condition. The black background was used to simulate the lights in the dark night. Furthermore, it was also found that CAM02-UCS color model gave the best agreement (smallest STRESS) for the current grey background condition. The grey background was used to simulate the surface colors. From the earlier research [7], CAM02-UCS was developed from the surface colors. Finally, FMC-1 equation performed badly to predict both present datasets. Most of the equations were developed to fit different datasets. Table 1 showed that all gave bad prediction to the MaAdam ellipses. This implies a large disagreement between the MacAdam and all the available datasets.

4 Conclusions

An experiment was carried out to assess chromatic color differences and to investigate reliability of the MacAdam color discrimination ellipses. It was used to test various color models. It was found that CIELAB and CAM02-UCS outperformed the others to predict the black and grey background results, respectively. Most importantly, by comparing the present and MacAdam ellipses, their patterns are quite different.

References

1. MacAdam DL (1942) Visual sensitivities to color differences in daylight. J Opt Soc Am 32 (5):247–274
2. MacAdam DL (1943) Specification of small chromaticity differences. J Opt Soc Am 33(1): 18–26
3. ANSI, C78.377-2008 (2008) In specifications for the chromaticity of solid state lighting products. ANSI, United States of America
4. Berns RS (1991) Color tolerance feasibility study comparing crt generated stimuli with an acrylic-lacquer coating. Color Res Appl 16(4):232–242
5. Cui G, Luo MR, Rigg B, Li W (2001) Color-difference evaluation using CRT colors. Part I: data gathering and testing color difference formulae. Color Res Appl 26(5):394–402
6. Cui G, Luo MR, Rigg B, Li W (2001) Color-difference evaluation using CRT colors. Part II: parametric effects. Color Res Appl 26(5):403–412
7. Luo MR, Rigg B (1986) Chromaticity-discrimination ellipses for surface colors. Color Res Appl 11(1):25–42

The Method for Distinguishing the Holographic Master Masks with Different Micro-structures

Bingjie Shi, Min Huang, Zeyang Li, Xiaohui He, Ruili He and Yusheng Lian

Abstract In order to distinguish the holographic master masks from different micro-structures, the X-Rite MA68 II multi-angle spectrophotometer was selected to measure the colorimetric values and spectral power distributions of the same point with different angles on the holographic master masks. They started angles of different holographic master masks were adjusted by the colorimetric values L^*, and then the micro-structures can be detected by the shape and location of the peak value of the measured spectral power distribution with the theory of grating equation.

Keywords Micro-structure · Holographic master mask · Chromaticity measurement · Spectral measurement

1 Introduction

Holographic paper shows dazzling light and are widely used in printing and packaging industries [1]. Holographic papers are manufactured from the gratings with different micro-structures [2], but we cannot distinguish the color differences amongst the holographic papers from different micro-structures. Huang et al. [3], Zheng et al. [4] and Huang et al. [5] have proposed the measuring method with the integrating sphere spectrophotometer. But the color difference is not obvious between the papers with different micro-structures. Huang et al. [6] has proposed a method to measure the constant of the gratings of the light pillar holographic paper.

B. Shi · M. Huang (✉) · X. He · R. He · Y. Lian
School of Printing and Packaging Engineering, Beijing Institute of Graphic Communication, Beijing, China
e-mail: huangmin@bigc.edu.cn

Z. Li
Department of Mechanical and Electrical Engineering, Guangdong Institute of Arts and Science, Guangdong, China

P. Zhao et al. (eds.), *Applied Sciences in Graphic Communication and Packaging*, Lecture Notes in Electrical Engineering 477,
https://doi.org/10.1007/978-981-10-7629-9_16

But the grating of holographic master mask is two-dimension, the light pillar holographic paper is one-dimension. The method cannot be universally used.

In this paper, the X-Rite MA68 II multi-angle spectrophotometer was selected to measure the colorimetric values and spectral power distributions of the same point with different angles on the holographic master masks. The micro-structures can be detected by the shape and location of the peak value of the measured spectral power distribution with the theory of grating equation.

2 The Characteristic of Micro-structure and Spectral Power Distribution

2.1 Micro-structure of the Master Mask

The holographic master mask A, B, C and D were selected as the tested samples, and the micro-structures were measured by 3D laser scanning microscope with the enlargement of 24,000 times (shown in Fig. 1).

As shown in Fig. 1, the micro-structures of sample A and sample B are quite similar, and are different with sample C and sample D. The micro-structures of these samples are regular and symmetrical in the range of [0°, 180°] with the axis of 90°, anyway the initial measured point.

2.2 Spectral Power Distribution of the Master Mask

The spectral power distributions of the master masks were measured by the instrument of the X-Rite MA68 II multi-angle spectrophotometer. The same positions with the interval of 5° from 0° to 180° were measured. The measurement

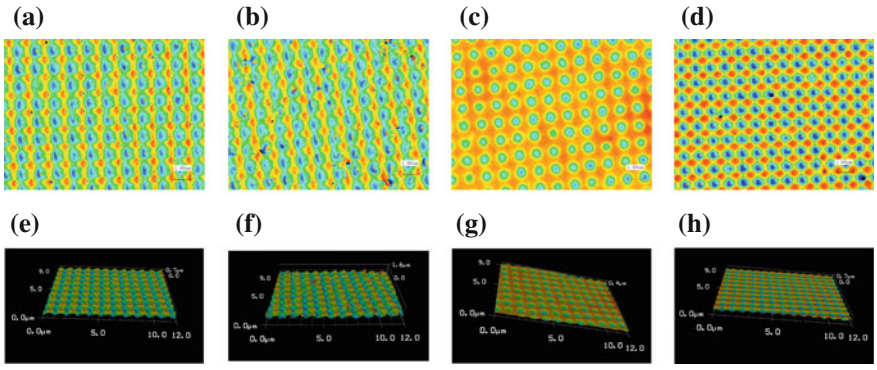

Fig. 1 The micro-structures of the gratings **a** Sample A. **b** Sample B. **c** Sample C. **d** Sample D. **e** Sample A 3D graph. **f** Sample B 3D graph. **g** Sample C 3D graph. **h** Sample D 3D graph

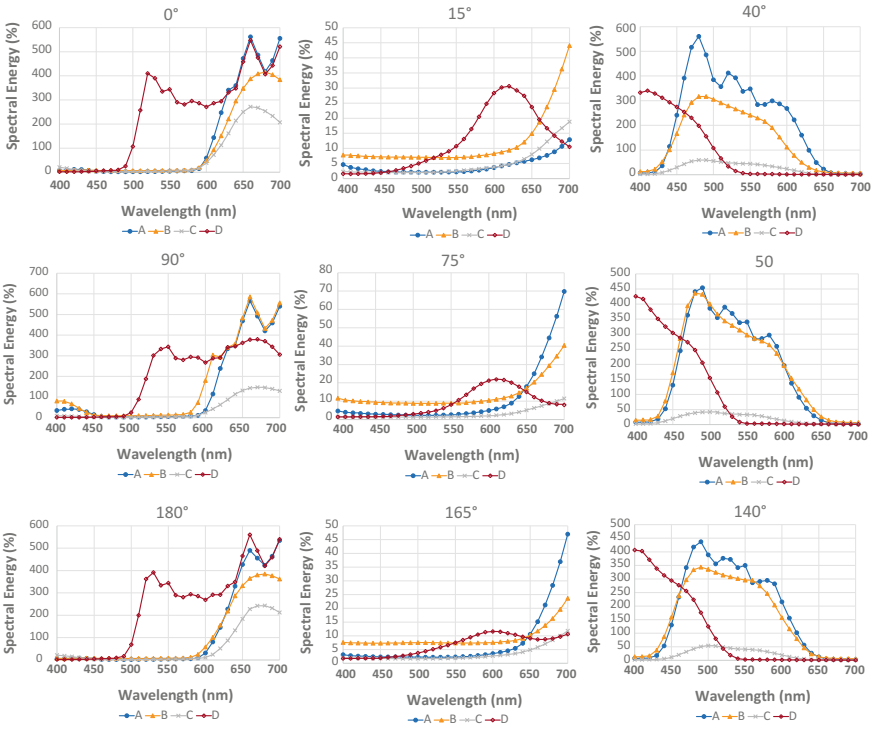

Fig. 2 The spectra of samples with different angles

condition of multi-angle spectrophotometer was set as CIE standard illuminant D65. There are 5 angles of the instrument, which are 15°, 25°, 45°, 75° and 110°. The spectral power distributions of the samples obtained by 45° of the instrument were showed in Fig. 2.

As shown in Fig. 2, the spectral power distributions of the position 15° and 75° and 165°, 0° and 90° and 180°, 40° and 50° and 140° have the similar tendencies for A, B, C and D four master masks, which indicated that the spectral power distributions are symmetrical in the range of [0°, 90°] and [180°, 90°], and are also symmetrical in the range of [0°, 45°] and [45°, 90°]. The phenomena can be explained by the micro-structures of the grating shown in Fig. 1. So, the spectral power distributions in the range of [0°, 45°] of one point can be expanded to the range of [0°, 360°] assumed the uniform distribution of the grating.

3 Experimental Measurements

3.1 Chromaticity Measurements

According to the analysis of the spectral power distributions in Sect. 2.2, the colorimetric values were measured by the instrument of the X-Rite MA68 II multi-angle spectrophotometer on the fixed position with the interval of 5° from 0° to 45°. The initial measured angle was random and the measuring conditions were set as CIE standard illuminant D65 and CIE 1964 10° observer. The colorimetric values of the A, B, C and D four master masks obtained from the 45° of the instrument are shown in Tables 1, 2, 3 and 4.

The maximum L^* values in sample A, B, C and D occurred at different measured angles (see Tables 1, 2, 3 and 4), which are 45°, 35°, 40° and 0° respectively. In order to adjust the initial measured angles of the four masks, sample D was selected

Table 1 The colorimetric values of sample A

	0°	5°	10°	15°	20°	25°	30°	35°	40°	45°
L^*	69.24	56.85	27.85	18.96	20.02	25.13	45.08	136.78	154.94	155.84
a^*	111.74	96.17	41.1	10.95	2.15	−2.98	−33.61	−84.55	−65.84	−61.49
b^*	70.35	57.82	17.71	1.7	−1.69	−2.44	18.5	48.47	16.85	5.31

Table 2 The colorimetric values of sample B

	0°	5°	10°	15°	20°	25°	30°	35°	40°	45°
L^*	41.97	33.31	33.19	34.98	37.8	79.26	133.41	148.65	144.52	114.15
a^*	44.31	7.22	0.45	−2.73	−4.7	−61.29	−77.76	−57.58	−69.28	−74.39
b^*	17.17	1.76	−0.77	−2.27	−2.6	21.32	15.95	−15.03	−1.47	39.46

Table 3 The colorimetric values of sample C

	0°	5°	10°	15°	20°	25°	30°	35°	40°	45°
L^*	46.55	30.12	19.83	15.35	15.06	17.48	51.42	68.6	68.73	59.65
a^*	69.89	38.28	10.85	2.48	−1.17	−7.54	−44.01	−41.29	−34.53	−42.93
b^*	44.29	22.04	7.09	−0.06	−2.04	−0.21	22.88	9.11	−0.59	11.05

Table 4 The colorimetric values of sample D

	0°	5°	10°	15°	20°	25°	30°	35°	40°	45°
L^*	147.17	143.56	126.29	44.18	25.86	18.88	17.12	36.52	67.5	78.73
a^*	−21.51	−8.05	40.92	23.27	−2.03	3.31	1.9	48.35	51.12	34.41
b^*	177.73	181.94	175.19	46.71	17.14	−0.3	−18.71	−90.19	−131.81	−133.48

to be the standard sample, and other samples are adjusted to obtain the same initial measured angle with sample D.

3.2 Spectral Measurements

After adjustment, the four samples were measured at the same position with the angle of 0° and 45° and the spectral power distributions were gathered at the measuring angle of 25° and 45° of the instrument (see Fig. 3).

In Fig. 3, the peak wavelengths of sample A and sample B have the similar position. In Fig. 3c, the position of the peak wavelength of sample A is at 480 nm and for the sample C is at 400 nm, the spectral power distributions of sample A, C and D are different. In Fig. 3d, the position of the peak wavelength of sample A is at 660 nm and for the sample D is at 400 nm, the spectral power distributions of the two samples are different.

According to the grating equation, as Eq. (1) shown

$$d(\sin i + \sin j) = m\lambda \tag{1}$$

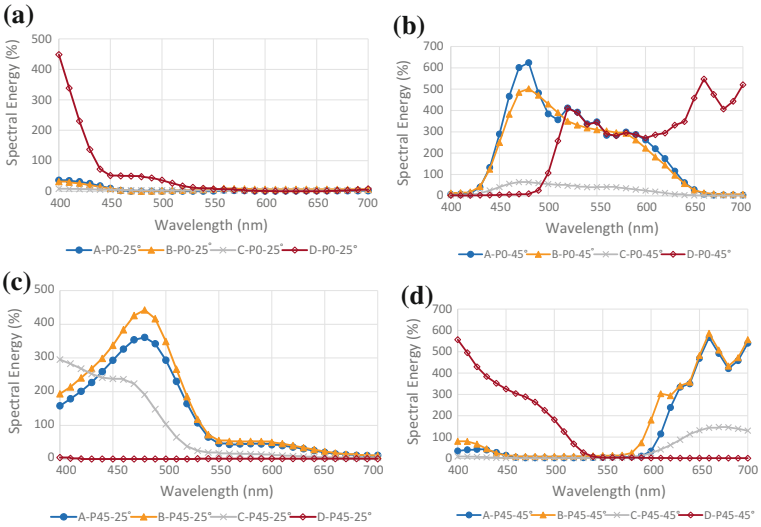

Fig. 3 The spectral power distributions of samples **a** Position: 0°, receiving angle: 25°; **b** position: 0°, receiving angle: 45°; **c** position: 45°, receiving angle: 25°; **d** position: 45°; receiving angle: 45°

where, d is the constant of the grating, i is the incident angle, j is the diffractive angle, λ is the wavelength, m is the diffraction order and it can be ±1, ±2, ±3…. The incident angle and diffractive angle of the instrument are fixed. When the micro-structures of the grating, especially the constants of the grating are different from the master masks, the measured spectral power distributions will be different.

It can be concluded that sample A and sample B have the similar micro-structures, which are quite different from sample C and D. The results can be verified by the measurement of 3D laser scanning microscope (see Fig. 1).

4 Conclusions

The method of distinguishing the holographic master masks with different micro-structures was studied in this paper. Firstly, the colorimetric values of the holographic master mask were measured at the same position with different rotation angles to adjust the initial measured angle according to maximum L^* values, then the spectral power distributions of the master mask at the rotation position angle of 0° and 45° are measured by the multi-angle spectrophotometer. The spectral power distributions obtained at 25° and 45° of the detector were analyzed with the grating equation to distinguish the different micro-structures of the master masks. This method can be used in anti-fake of holographic master masks.

Acknowledgements This research was supported by Beijing Nova Program (NO. Z151100000315076) and Science and Technology Innovation and Service Capacity Building Program (NO. PXM2017_014223_000061) and National Natural Science Foundation of China (Grant No. 61605012).

References

1. Wang Y (2013) From defect detection to quality control—a visual inspection scheme for the quality defects of cigarette package. Printing Technol 16:60–61
2. Ma H (2014) The research and application of super laser paper. MA thesis, South China University of Technology
3. Huang X, Wan X et al (2003) Optimization of the method for color measurement of printing on holographic paper. Color Res Appl 38(2):130–138
4. Zheng Y, Yang S et al (2006) Research on the color characteristic of holographic materials without image and grain based on X-Rite MA68 II. Packag Eng 06:155–156
5. Huang M, Wang L et al (2014) Measurement and analysis of spectral and chromaticity values of pillars of light pattern holographic paper. Acta Optica Sinica 34(6):338–346
6. Huang M, Wang L et al (2016) A method for measurement grating constant of light pillar holographic paper by integrating sphere spectrophotometer: China, CN 104330240 B[P], 31 Aug 2016

Comparison of Two Methods for Color-Normal Observer Variability in Color Discrimination

Ruili He, Min Huang, Chunjie Shi, Bingjie Shi, Peipei Ran and Yusheng Lian

Abstract In order to compare the validation of different methods for observers' color discrimination, 53 observers with normal color vision were organized to carry out two experiments including the Farnsworth Munsell 100 Hue test and the color matching experiment which have been used widely. Four dominant colors (red, yellowish green, turquoise green and bluish purple) in the FM 100 Hue test were selected as the reference colors in color matching experiment. The results were expressed by the total error scores, the mean CIE DE2000 color difference values and the colorimetric ellipses, which indicated that the results of two experiments were not accorded completely for a given color normal observer. The obtained data and three indexes are useful to understand the relationship between these two tests.

Keywords Observer variability · Color matching experiment
Color discrimination · Color normal vision

1 Introduction

Three active photoreceptors, sensitive to long, medium and short wavelengths (L-cone, M-cone, and S-cone) enable color vision for humans under photopic conditions. The light entering our eyes is integrated by these three sensors and color perception occurs. However, not all people possess these three active photoreceptors, so people can be categorized as color-normal or color deficient. Ruiqing et al. [1] have done some works on the detection and classification of color deficiency before visual experiments. The Farnsworth Munsell 100 Hue test is suggested for the test of

R. He · M. Huang (✉) · B. Shi · P. Ran · Y. Lian
School of Printing and Packaging Engineering, Beijing Institute of Graphic Communication, Beijing, China
e-mail: huangmin@bigc.edu.cn

C. Shi
College of Network Communication, Zhejiang YueXiu University of Foreign Languages, Zhengjiang, China

P. Zhao et al. (eds.), *Applied Sciences in Graphic Communication and Packaging*, Lecture Notes in Electrical Engineering 477,
https://doi.org/10.1007/978-981-10-7629-9_17

color-normal observer variability in color discrimination. Large individual variability exits not only when color deficiencies occur but also within "color-normal" people. Asano et al. [2], Shi et al. [3] have studied the observer variability of color perception.

The authors intended to compare the validation of different methods for observers' color discrimination. Two experiments including the Farnsworth Munsell 100 Hue test and the color matching experiment were carried out by 53 observers with normal color vision. Assumed that this two methods could test color normal observer's color discrimination well. Then the results were compared by the traditional indexes, such as error scores, color difference values and chromatic ellipses.

2 Experimental

2.1 Farnsworth Munsell 100 Hue Test

The Farnsworth Munsell 100 Hue test [4] was invented to test human color discrimination quantitatively which consists of 85 movable color samples arranged in four boxes and there is sequence number in the bottom of each color samples. As is shown in Fig. 1, these color samples represent perceptually equal steps of hue and form a natural hue circle.

The test was conducted in a dark room. Observers were asked to sit down in the front of the viewing cabinet which is provided the illuminant with a correlated temperature of 6500 K and illuminance of 947 lx. Figure 2 illustrates the process of the test. First, all the movable color samples in each box were taken out and put in a random order. Second, subjects compared the adjacent colors and arranged them in the sequence of color gradual change. When the color samples of four boxes were arranged, the sequence will be recorded in the matching computer scoring software shown in Fig. 3, the corresponding total error score will be obtained.

53 color-normal observers were organized to participate in the experiment. All of them are the students of Beijing Institute of Graphic Communication and the average age is 20. 31 observers were female while 22 observers were male.

Fig. 1 The color samples in four boxes (Color figure online)

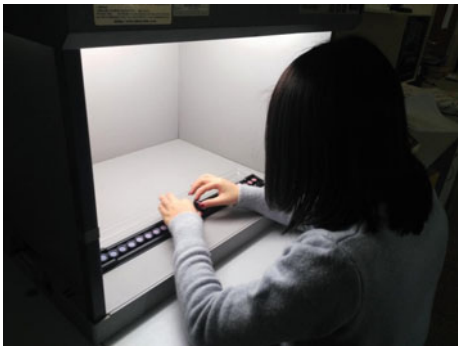

Fig. 2 The process of the FM 100 Hue test (Color figure online)

Fig. 3 Interface of FMT scoring software (Color figure online)

2.2 Color Matching Experiment

The color matching experiments with the NEC MultiSync PA242W LED monitor were designed and conducted in a dark room. Four dominant colors (red, yellowish green, turquoise green and bluish purple) in the FM100 Hue test were selected as the reference colors in order to make a comparison of the results from the two experiments. The experimental interface of color matching is illustrated in Fig. 4. Each of the reference color was randomly displayed on the left or right of the circle and the same stimulus was shown on the corresponding half circle.

The same group of 53 observers was organized to participate in the experiment. They were asked to reduce or add the R, G, B three channels in turn with a distance

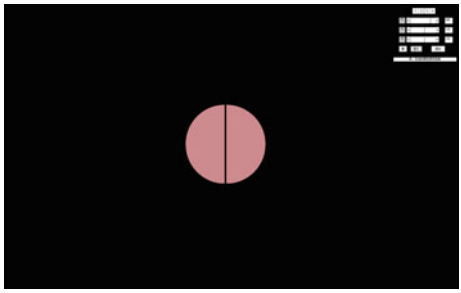

Fig. 4 Experimental interface

of approximately 55 cm until they can detect the color difference of bipartite field. Once a color matching experiment has been finished, the spectral power distribution will be measured by PR670 spectroradiometer. Each color will be adjusted in six orientations (±R, ±G, ±B). In total, there are 1272 (=6 orientations × 4 reference colors × 53 observers) assessments in the experiment.

3 Results and Discussions

3.1 Error Scores

The obtained Total Error Scores (TES) from the matching computer scoring software are shown in Table 1. The higher error scores represent lower ability of color discrimination. All observers were classified into different grades according to the total error scores. Then the average error score of each box obtained by all observers was calculated and the results are summarized in Table 2, which shows the average error score of first box varied from red to yellowish green is the smallest while the second box varied from yellowish green to turquoise green is the largest. Therefore, observers participating in this test are the most sensitive to red while the least sensitive to yellowish green. In addition, People have different ability of color discrimination for different colors.

Table 1 The obtained total error scores

	Superior discrimination					Average discrimination							
Total error scores	0	4	8	12	16	20	24	28	36	40	44	48	64
Number of observers	5	9	10	7	2	5	4	4	1	1	2	2	1

Table 2 The average error score of each box obtained by all observers

Box of samples	1	2	3	4
Average score	1.75	5.62	4.34	4.58

3.2 CIE DE2000 Color Difference Values

The spectral power distributions of target color and matched colors were measured during the color matching experiment and the CIE DE2000 values were calculated in CIE1964 CMF with the obtained data. Table 3 shows the mean CIE DE2000 values of all observers for each color stimuli. The mean CIE DE2000 value of bluish purple is the largest while the value of yellowish green is the smallest, which is not consistent with the result of FM 100 Hue test. Moreover, the individual values of four colors were ordered from small to large and divided into three grades: less than 1.5, between 1.5 and 2.5 and larger than 2.5. The error scores were also compared in Table 4.

Take red for example, there are 12 observers whose CIE DE2000 values smaller than 1.5 and only one person's error score greater than 4, which indicated that the result of color matching is consistent with the result of FM100 Hue test. However, there is just one observers' error score greater than 4 among the 5 people whose color difference values greater than 2.5. Similar result occurs in other three colors. The majority of observers who matched colors with smaller CIE DE2000 values had lower error scores, but the people with lower error scores are not supposed to have small color difference values.

Table 3 The mean CIEDE2000 values of four colors for 1964 CMFs

Color samples	Red	Yellowish green	Turquoise green	Bluish purple
Mean ΔE_{00}	1.88	1.81	1.93	2.12

Table 4 The distribution of the observer in the two experiments

	<1.5		>2.5	
	Total number	Number of ES >4	Total number	Number of ES >4
Red	12	1	5	1
Yellowish green	12	1	6	1
Turquoise green	12	3	6	2
Bluish purple	3	0	9	2

3.3 Chromatic Ellipse

According to six critical values for each color stimuli and the L*a*b* values of matched colors, the chromatic ellipses [5] of four colors are drawn in Fig. 5, the color tolerance ellipses have the regular orientation and size but there is a special individual different from most people in the orientation or size of four color ellipses. The chromatic ellipse area of obs25, obs08, and obs20 and obs53 observer is the respectively maximum of four colors, and the chromatic ellipse orientation of obs13, obs50 and obs06 observer deviates from the average farthest in red, yellowish green and bluish purple. Three index values of observers with abnormal performance are shown in Table 5.

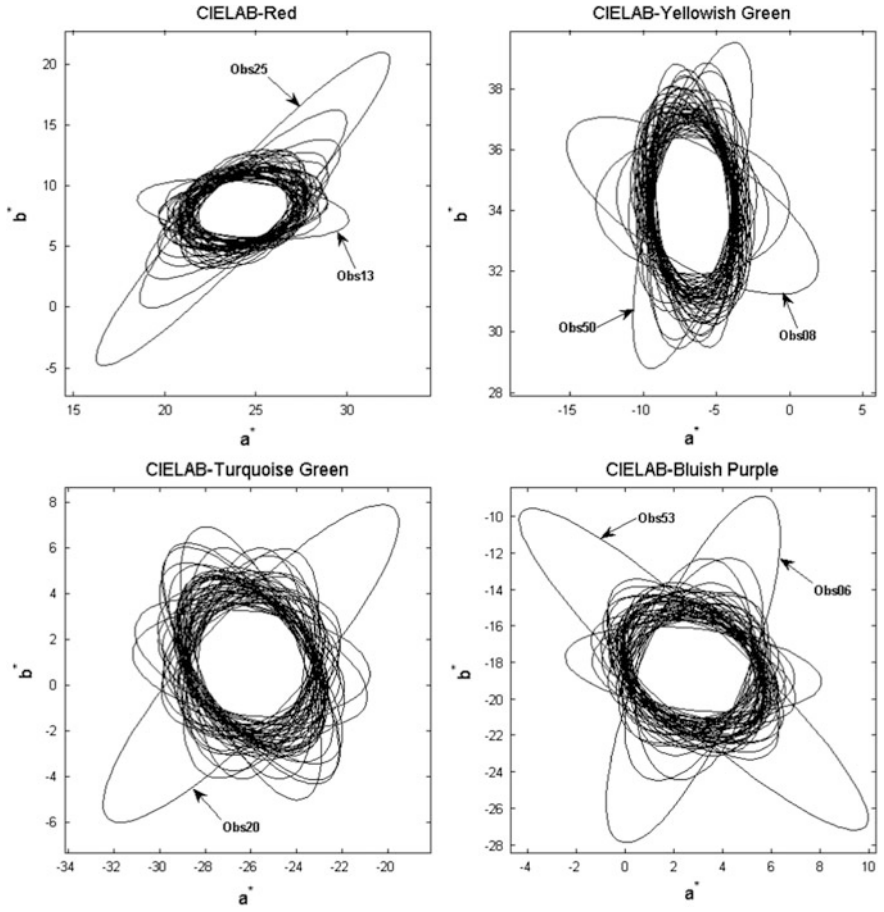

Fig. 5 The chromatic ellipses of four colors for 53 subjects

Table 5 Three index values of observers with abnormal performance

	R (1.97)		Y (1.91)		G (1.95)	P (1.96)	
	Obs25	Obs13	Obs08	Obs50	Obs20	Obs53	Obs06
ES	0	0	4	15	4	12	0
DE2000	1.5	1.75	1.69	1.31	2.88	2.45	2.39
S	3.38	2.16	2.52	2.33	2.71	1.93	1.83

In Table 5, S is the square root of ellipse area and the figures in parentheses are the average S of all observers for each color. In practice, both of high color matching performance and low FM error score represent the better ability of color discrimination. The error scores of observers with abnormal performance in Table 5 are not the largest, even zero, and the CIEDE2000 values have different sizes, which indicates that the results of two experiments are not consistent. In general, the three indexes obtained from these two methods are useful to understand the relationship between these two tests.

4 Conclusions

The Farnsworth Munsell 100 Hue test and color matching experiment with four color matches were designed and conducted by 53 human observers with normal color vision. The observer variability in color discrimination among color-normal people from the obtained data was analyzed. The results from the FM 100 Hue test are not exactly the same with the results of color matching experiment. To quantify the observers' variability, the color matching experiment was preferred. The FM 100 Hue test could distinguish human color discrimination rapidly. So when testing the observer variability in color discrimination, the corresponding experimental method can be selected according to different requirements.

Acknowledgements This research was supported by National Natural Science Foundation of China (grant 61675029, 61308081) and the Science and Technology Project of Beijing Educational Committee of China (Grant No. SQKM201610015005). Thanks for every observer participating in our experiments.

Statement This study follows the Committee on Publication Ethics guidelines. And informed consent was obtained from all individual participants included in the study.

References

1. Ma R, Liao N, Shinomori K (2016) Detection and classification of color deficiency before vision experiment. Acta Optica Sinica 36(6):0633001
2. Asano Y, Fairchild MD, Blondé L et al (2016) Color matching experiment for highlighting interobserver variability. Color Res Appl 41(5):530–539
3. Shi C, Huang M, Liu H (2016) Evaluation of color perception among different aged observers based on color matching experiments. Lecture Notes in Electrical Engineering. https://doi.org/10.1007/978-981-10-0072-0_19, pp 139–145
4. Farnsworth D (1943) The Farnsworth-munsell 100-hue and dichotomous tests for color vision. J Opt Soc Am 33(10):568–574
5. Min H, Haoxue L, Ningfang L (2009) Study on Just-noticeable color difference discrimination threshold by using printed samplesI: analysis of visual evaluation experimental data. Acta Optica Sinica 29:1431–1435

Characterization and Evaluation of Color Gamut Boundary Description Algorithm for Output Equipment

Meiqi Lin, Maohai Lin, Ben Liu and Guichun Hu

Abstract The color gamut boundary description algorithm is used to describe the size of the color gamut boundary and ensure the accurate prerequisite for the conversion of the color gamut mapping. With the development of the research, the application scope and content of the color gamut boundary description are becoming more and more extensive. Firstly, the paper summarizes the development of the color gamut boundary extraction algorithm, characterizes the realization principle of the color gamut boundary description algorithm and predicts the color transfer range which can be achieved by a given color reproduction medium. And then the method of color boundary description algorithm and color gamut mapping algorithm was studied. Finally the paper put forward the views and assumptions in allusion to the problems in the practical application.

Keywords Color gamut · Color gamut mapping · Color gamut boundary description algorithm

1 Introduction

The color gamut boundary is a color surface determined by the extreme color gamut, and the color gamut boundary description is a method of approximating the color gamut boundary. There are two main ways to describe the color gamut boundary: one is the specific media description method and the other is the general class description method. The specific media description method is suitable for describing the color gamut boundary of the medium. This method has a charac-

M. Lin · M. Lin (✉) · B. Liu · G. Hu
School of Printing and Packing Engineering, Qilu University of Technology, Jinan, China
e-mail: imhlin@163.com

M. Lin · G. Hu
State Key Laboratory of Pulp and Paper Engineering, South China University of Technology, Guangzhou, China

P. Zhao et al. (eds.), *Applied Sciences in Graphic Communication and Packaging*, Lecture Notes in Electrical Engineering 477,
https://doi.org/10.1007/978-981-10-7629-9_18

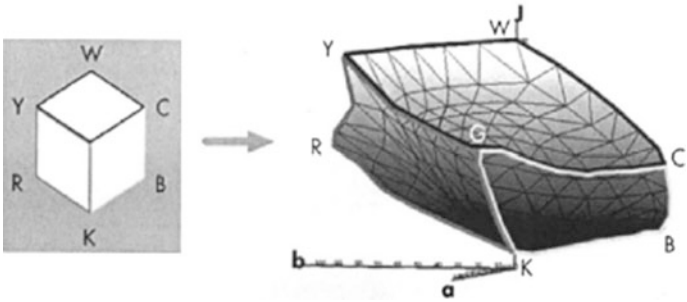

Fig. 1 Herzog cube deformation color gamut

terization model based on the Kubelka-Munk equation, the Newbank equation, the Inui algorithm using the partial differential equation. The method of the gamut model is proposed by Herzog [1] in 1998, this method assumes that most of the media gamut is a deformed cube whose vertices are black, white, red, green, blue, yellow, and green, as shown in Fig. 1.

The specific media gamut description method describes the gamut boundaries of the media device with few parameters, but this method is not suitable for describing the color gamut of the image or the color gamut boundary formed by some patches.

In recent years, there are many researches on the algorithm of color gamut boundary description. In 1997, Bala and Dalal [2] proposed color gamut boundary description algorithm based on the sample measurement of convex hull "inflatable" and "deflated", which is more accurate. But its principle and algorithm is more complex, the implementation is more difficult, the calculation is large, time-consuming; Marc Mahy used the formal inversion to generate the bright contours in the color space, and then obtained the specific surface of the color gamut by splicing the contours, and established the three-dimensional Neugebauer equation to describe the printing model. Since 2000, JanMorovic and Luo M. Ronnier proposed the regional segmentation method for the first time, using the regional segmentation method to calculate the equipment gamut boundary under given observation conditions. Photon, Rolf-Rainer Griga and Ratio Entwicklungen GmbH describe the image gamut boundary by region segmentation. Hiroaki Kotera and Ryoichi Saito describe the image color gamut by region segmentation, and proposed the concept of singe-centre and mutie-centre, which is used in the color gamut boundary description algorithm [3]. Xu proposed the principle that the color gamut boundary description algorithm should be followed [4], the factors that how to choose the color space need to be considered, and on this basis, a color gamut boundary triangle description method is proposed. Hong Guodun introduced the regional segmentation algorithm, proposed a display device and image real measurement of color data points and the sampling method is to establish color data points by virtual methods, and the region was segmented to uniform and non-uniform area, to observe the change of the speed and accuracy. Huang and

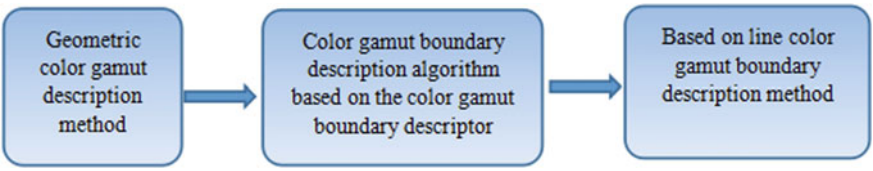

Fig. 2 Development of the algorithm for color gamut boundary description

Zhao [5] proposed a color gamut mapping based on the Zerniker polynomial representation of the color gamut boundary.

With the widespread use of color management in digital processes, the gamut boundary description plays an increasingly important role in the process of print reproduction. In this paper, we can see that the color gamut boundary description algorithm has experienced several stages of development (Fig. 2).

2 Evaluation and Research on Color Gamut Boundary Description Algorithm

2.1 Color Gamut Boundary Evaluation Algorithm

Because of the lack of research on the algorithm of color gamut boundary description, and the lack of a unified standard for the evaluation of color gamut boundary description algorithm, the evaluation method is also mixed, which makes it difficult to choose, and the accuracy of the evaluation is also difficult to assess. Even if the existing evaluation is only for a certain model, it can contain all the points in the characteristic model for all larger color gamut and inaccurate gamut boundary, so this evaluation scores are often high; Secondly, it is difficult to accurately generate points in the gamut boundary through the existing color gamut boundary when constructing the color gamut model, and it is also difficult to judge whether it belongs to the color gamut.

For the constructed color gamut, Morovic [6] proposed to evaluate the advantage of the color gamut by color gamut volume, gamut cross and color gamut smoothness, However, due to the irregularity of the color gamut boundary, it is difficult to calculate the cross volume of the boundary between a certain color gamut and another color gamut, and the color gamut volume is also different obtained by different algorithms. Although the size is the same and the shape is also very different, it is difficult to accurately evaluate the merits of an algorithm. Braun and Green [7, 8] use the known color gamut boundary points to make the comparison with the obtained color gamut boundary points, the accuracy of the color gamut boundary description algorithm is expressed by the difference between the known points and the construction points, but the premise of the algorithm had be known as the color gamut boundary, it has a great limitation on the unknown color gamut.

In summary, the development of color gamut evaluation technology has three stages; the first generation of color gamut evaluation technology is the two-dimensional color gamut boundary description. It is mainly based on the area of the two-dimensional color gamut to achieve the comparison between devices or different device gamut, but the two-dimensional color gamut construction method is relatively more simple, it was often observed the difference by intuition between the different color gamut, so the studies on color gamut evaluation techniques is relatively few; The second generation evaluation technique is accompanied by the generation of three-dimensional color gamut boundary description technology. Since the three-dimensional color gamut boundary description algorithm can reproduce the information of the lightness axis when constructing the color gamut, which can accurately show the color rang in the three-dimensional color gamut of $L * a * b *$ Space. With the further development of the three-dimensional color gamut boundary description technology, it has been found that it is difficult to accurately evaluate the true situation of a gamut boundary description algorithm only by the size of the color gamut and the color gamut cross volume. And thus the color gamut evaluation model is introduced to evaluate the accuracy of the color gamut description algorithm.

2.2 Color Gamut Evaluation Algorithm Theory Model

Because the model can take into account the various factors that are related to the accuracy of the color gamut in the construction process, the evaluation of the color gamut boundary description algorithm has high accuracy, and the color gamut evaluation model is the mainly developing direction. The shape of the real color gamut and the constructed color gamut are often irregular, not just a simple overestimated or underestimated relationship, and sometimes the volume of the color gamut is same, but the shape is different, and the color gamut description algorithms are often different, so for the different color gamut, the final effect may also be different, which make the relationship between the real gamut and the constructed color gamut are more complex [9]. When constructed the color gamut evaluation model, it should be fully taken into account the following three cases:

(1) When the actual color gamut and the constructed color gamut cannot completely contain the other side and cross, then the cross section shape is difficult to determine, the corresponding volume calculation is more complex, so in this case it is difficult to evaluate.
(2) When the actual color gamut is completely contained in the constructed gamut, the cross section of the volume is relatively simpler to determine, and the convex hull algorithm is often the case, the use of convex hull algorithm to build the color gamut boundary is often greater than the actual color gamut 10%.

(3) When the actual gamut is completely contained in the construction of the color gamut, the actual color gamut and the constructed gamut are completely included, and the color gamut volume and the cross gamut volume are relatively simple. The color gamut using the alpha-shape structure often belongs to this situation.

3 Research on Color Domain Mapping Algorithm

Gamut mapping is an important technique for color reproduction in digital printing and also plays a key role in color management processes. The most basic role of the gamut mapping algorithm is to handle the difference between the input gamut and the output gamut, which could promise to keep the original appearance of image in the output process. With the emergence of more gamut mapping algorithms, the evaluation technique of color gamut mapping algorithm has also become an important problem. There are two main types of evaluation for color gamut mapping. One is the subjective evaluation which is based on human sensation and the other is objective evaluation which is based on physical measurement.

Subjective evaluation evaluates the conversion effect through the psychological physics experiment. And the new proposed color gamut mapping is generally experimented by the psychological and physical way, it needs to find a set of visually normal observers to evaluate the images which are produced by several gamut mapping algorithms. The objective evaluation often use the image quality measurement method which use the color difference formula to calculate, this method could make the comparison of the different two images.

Because the subjective nature of the evaluation method is too strong and the objective evaluation method is relatively simple, so based on the objective evaluation method, in this paper, it is proposed to set up a systematic evaluation method about the anti-push according to the purpose of the gamut mapping. This method is independent of the device color, and it mainly makes an objective evaluation combined with an accurate color gamut boundary description algorithm and according to the operation speed and the accuracy of the mapping algorithm and the size of the color gamut after color gamut mapping.

4 Conclusions

In the emergence and application of a new color gamut boundary algorithm, it is very important to evaluate the algorithm of different color gamut boundary description. At present, the evaluation of the development of the color gamble boundary description algorithm is lagging behind the gamut boundary description algorithm, and there is no accepted model which can be used for all color gamut

boundary algorithm evaluation. Therefore, Matching the evaluation model is particularly important, The model can solve the problem that the color gamut saturation region and the unsaturated region existed in the traditional partition type color gamut boundary algorithm, at the same time the accuracy of the color gamut boundary description is improved during the hierarchical processing, which plays an important role in high fidelity reproduction.

Acknowledgements This work was supported by State Key Laboratory of Pulp and Paper Engineering (201606 and 201609).

References

1. Morovic J (2008) Color gamut mapping. Wiley, Chichester, England
2. Bala R, Dalal EA (1997) Method for quantifying the color gamut of an output device. In: Proceedings of SPIE, vol 3018, pp 110–116
3. Morovic J, Luo MR (2002) Calculating medium and image gamut boundaries for gamut mapping. Color Res Appl 25(6):394–401
4. Xu Y (2004) Research on color control technology of digital color output equipment. Tianjin University, Tianjin
5. Huang Q, Zhao D (2003) Color gamut mapping based on Zernike polynomials for color gamut boundaries. Opt Technol 29(2):168–171
6. Morovic J (2008) Color gamut k mapping. Wiley, Chichester, England; Hoboken, NJ
7. Braun GJ, Fairchild MD (1997) Techniques for gamut surface definition and visualization. In: Color and imaging conference, pp 147–152
8. Green P (2000) Defining color gamut boundaries with a test target. Color Imaging Group
9. Lin M, Wen J (2013) Gamut boundary determination using an uneven segmentation algorithm. APCIIT2013

An Evaluation Method for the Color Quality of Digital Hardcopy Output SRGB Image

Shuai Shao, Yanfang Xu, Zhongyue Da, Xinggen Qian, Shun Pan, Yan Li, Bingjie Shi, Peipei Ran and Ruili He

Abstract Aim at evaluating effectively the color quality of digital hardcopy output sRGB images, the assessment method for color quality of digital hardcopy output sRGB images is established. It focuses on the memory color, which designs the assessment color targets to reflect the chroma characteristics of typical memory color (skin color, sky blue color, grass green and cole flower yellow color), it combines the subjective evaluation experiment to ensure the compared scale for chromatic value of color targets of each typical memory color. It carries out the compared analysis for the assessment color lump and chromatic value of actual output and the compared scale, gives out the evaluation of the color quality of hardcopy output sRGB images from three aspects of lightness, chroma and hue. The established method not only can evaluate effectively the color quality of digital hardcopy output sRGB images, but also can provide the technical support for improving and optimizing the color quality of hardcopy output.

Keywords Digital hardcopy · Memory color · Color quality evaluation

1 Introduction

With all kinds of hardcopy output technology become mature constantly, the equipment and material have had a great variety. In the actual production and practice, the color quality of output is different although the normal color management technology is implemented [1].

S. Shao (✉) · Y. Xu · Z. Da · X. Qian · S. Pan · Y. Li · B. Shi · P. Ran · R. He
School of Printing & Packaging Engineering, Beijing Institute of Graphic Communication, Beijing, China
e-mail: shaoshuai920411@qq.com

P. Zhao et al. (eds.), *Applied Sciences in Graphic Communication and Packaging*, Lecture Notes in Electrical Engineering 477,
https://doi.org/10.1007/978-981-10-7629-9_19

At present, the research of the evaluation of print color quality to obtain the electronic image mainly by the scanner or CCD devices, to statistical analysis the chromatic difference of the exports electronic image and all the manuscript pixels, it carries out the evaluation for the color quality of color image by using the mean square error (MSE), peak signal to noise ratio (PSNR), structural similarity (SSIM) and other models [2], but this kind of evaluation belong to the comprehensive evaluation for the accuracy of the overall color of image, it cannot carry out the specific representation and analysis for the copy quality, in addition, this method is on the base of image pixel-level comparison, it acquires the duplicates to form the electronic images by the scanner or scanning devices, and the color management technology has a complex process, and it need the high technical requirements. Therefore, this method cannot be popularized and used in the actual production.

The most of the commercial images give priority to the human portrait and natural landscape and scenery, and human eyes are sensitive to the skin color, sky blue color, grass green color and typical plant color (such as the cole flower yellow color), these colors are become the key of the copy quality of the whole image [3]. Therefore, in this article, the research of the copy quality of these typical memory colors as the assessment content of color quality of image output, combines with the objective measurement and subjective evaluation technology, the assessment method of color quality which is suitable for the production and actual application had given.

In addition, in view of most of the commercial images are sRGB images, this article researches on the images of sRGB space [4].

In this article, the research takes the memory color as the key of the measurement and evaluation of color quality, it extracts the color targets which can reflect the chroma characteristics of memory color, it carries out the objective evaluation experiments for the test patterns which are composed by several pieces of sRGB images and characteristic color targets on the standard of L*, C_{ab}* and h_{ab}*, and the exports samples of various increased and decreased L*, C_{ab}* and h_{ab}* on the base of them, then ensures the best test pattern specimen pages of the changed limit of the L*, C_{ab}* and h_{ab}* and color visual evaluation which can be accepted by the vision, then the L*, C_{ab}* and h_{ab}*chroma values of the color code and color targets in the corresponding test patterns are drew and generated the compared scale curves of each typical memory color, which can be used for the evaluation of color quality of digital hardcopy output sRGB images.

2 The Establishment of Assessment Method of Color Quality

2.1 Extraction of the Chroma Values of the Typical Memory Color Assessment Color Targets

(a) Collect the sRGB images from each ink-jet RIP software company which can be used for the output evaluation, and select the images which include the typical memory color (contain 25 pieces of portrait images, 12 pieces of sky landscape images, 10 pieces of green grassland landscape images and 9 pieces of cole flower images) from them, as shown in Fig. 1.

(b) Analyze separately all kinds of memory color single image, and select the key color homogeneous areas in the memory color images, the Fig. 2 is shown that the selected color homogeneous areas of one piece of portrait image, sky landscape image, grassland landscape image and cole flower image, which contains 900 homogeneous areas of portrait image, 512 homogeneous areas of sky landscape image, 498 homogeneous areas of grassland landscape image and 138 homogeneous areas of cole flower image, calculate and record the

Fig. 1 The typical memory color images (Color figure online)

Fig. 2 The instance of the selection of typical memory color image color homogeneous areas (Color figure online)

average value of sRGB numerical value of image in each area and the chroma values which are changed to the corresponding L*a*b*, L*, C_{ab}*, h_{ab}*.

(c) The distributive scopes of brightness of all kinds of typical memory color image are obtained by analyzing the chroma value data of the obtained L*, C_{ab}*, h_{ab}* on the above process, which are shown in Fig. 3: select separately the skin color L* = 25, sky blue L* = 30, grass green color L* = 30 and rapeseed color L* = 70 as the original brightness, and take the $\Delta L = 5$ as the interval of brightness, draw the a*b* areal chart under the corresponding brightness L* of all kinds of typical memory color, make sure the a*b* boundary range under the corresponding brightness L*, select evenly the characteristic points of the corresponding brightness and record the L*a*b* values in the area of the boundary, the Fig. 4 is shown the selected instance of the characteristic points of portrait image L* = 65, sky landscape image L* = 60, grassland landscape image L* = 50 and rape flower image L* = 85, in total, 178 characteristic color points of skin color, 102 characteristic color points of sky, 112 characteristic color points of grassland and 47 characteristic color points of cole flower.

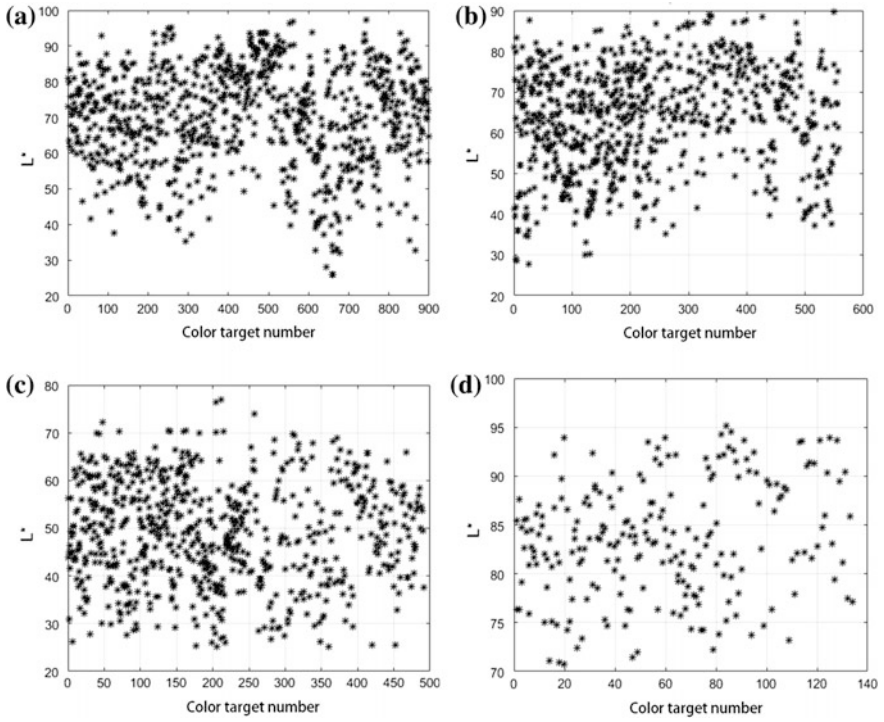

Fig. 3 The distributive scopes of brightness of selected color lumps of all kinds of typical memory color image. **a** Skin color, **b** sky blue color **c** grass green color **d** cole flower color

(d) Carry out the calculation and screening of chromatic aberration between all kinds of extracted memory color characteristic color by using the formula of chromatic aberration, if the chromatic aberration $\Delta E_{ab}^* < 2$ between two adjacent characteristic color, then only one characteristic color point can be reserved, by the screening of chromatic aberration, it can be obtained that 120 chroma values of skin color characteristic color lump, 45 chroma values of sky blue color characteristic color lump, 50 chroma values of grass green color characteristic color lump and 15 chroma values of cole flower yellow characteristic color lump.

2.2 Confirmation of the Compared Scale of the Color Quality of All Kinds of Typical Memory Color

(a) Take 120 chroma values of skin color characteristic color lump, 45 chroma values of sky blue color characteristic color lump, 50 chroma values of grass

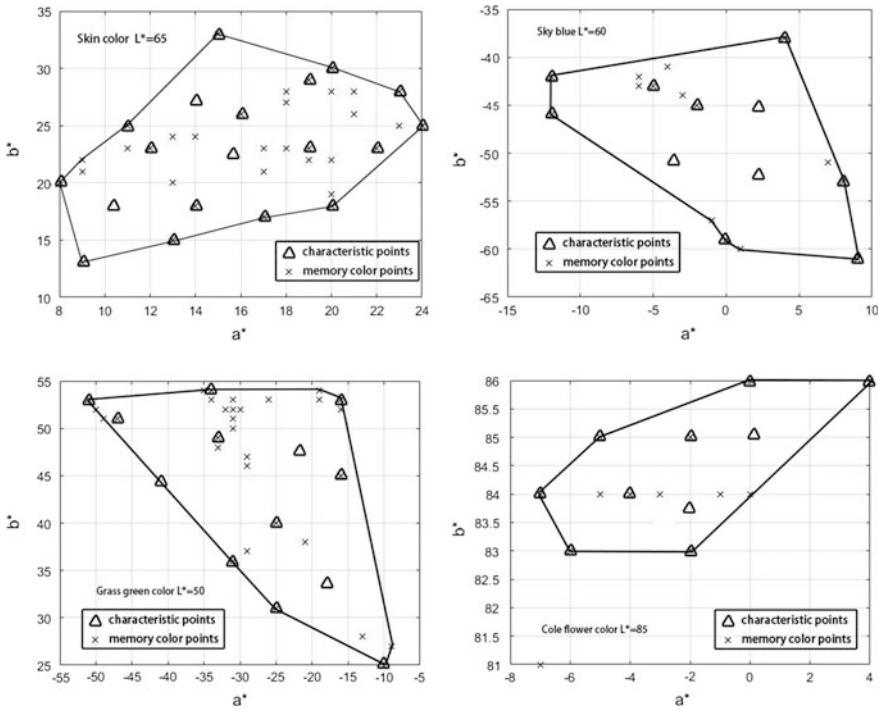

Fig. 4 The instance of the selection of typical memory color characteristic color

green color characteristic color lump and 15 chroma values of cole flower yellow characteristic color lump, so the assessment for color lump and color code of the typical memory color is generated.

(b) Select 10 pieces of portrait image, 11 pieces of sky landscape image, 9 pieces of grassland landscape image and 9 pieces of rape flower image with the corresponding memory color characteristic color codes to compose the test pattern, modify the L*, C_{ab}*, h_{ab}* values (the changed maximum range of portrait skin chroma is among the $h_{ab}* \pm 12$, $C_{ab}-6$ and $C_{ab}* + 14$, $L* \pm 10$; the changed maximum range of portrait sky blue chroma is between the $h_{ab}*-18$ and $h_{ab}* + 8$, $C_{ab}*-12$ and $C_{ab}* + 20$, $L* \pm 14$; the changed maximum range of green grass chroma is between the $h_{ab}*-2$ and $h_{ab}* + 10$, $C_{ab}*-18$ and $C_{ab}* + 20$, $L*-2$ and $L* + 12$; the changed maximum range of rape flower chroma is between the $h_{ab}*-1$ and $h_{ab}* + 4$, $C_{ab}*-12$ and $C_{ab}* + 14$, $L*-10$ and $L* + 8$) of test pattern image by the electronic image of test pattern in the maximum range of single dimensionality and equivalent gradient, which can be used for simulating all kinds of output situation of color cast.

(c) Use the Epson Stylus pro 7800 and Epson photo quality ink-jet printing paper, print several output modified test patterns by using the color management technology (the chroma values of all kinds of the color targets of memory color all in the range of printer output color area).

(d) The visual evaluation experiment [5] carries out the observation on the measuring platform which takes D65 standard white light as the lighting light and 2300 lx as illuminance, 10 observers whom have the normal eyesight vision and color vision and have a certain color knowledge base, in a series of samples with the marked serial numbers, the observers separately select the optimal specimen page of color objective vision from the changed equivalent gradient with the homogeneous brightness, chroma and hue, and the visual acceptable maximum colour cast specimen page, then record successively the serial numbers of the optimal specimen pages and the visual acceptable specimen pages, the experiment should be repeated three times, after complete the observing experiment, carry out the statistics of the serial numbers of the experiment record, under three dimensionality of L*, C_{ab}* and h_{ab}*, the corresponding test pattern specimen pages of the optimal objective visual color quality of all kinds of memory color test pattern and the visual acceptable color cast limit are ensured.

(e) Carrying out the measurement of the L*, C_{ab}* and h_{ab}* chroma values of the characteristic color code on the test pattern sample pieces of the optimal and acceptable color cast limit of the vision of all kinds of memory color subjective visual color quality under the D65 and 2° by using the i1-iSis colorimeter, the measurement should be carried out three times, and reserve successively the results of three data average value.

(f) Making the ascending order for the chroma values L* of the corresponding color code and color lump of the confirmed subjective visual color quality optimal specimen pages under L* dimensionality of all kinds of memory color, record their serial number order of the corresponding color lump in the color code, draw the L* optimal reference curves of all typical memory color; then draw the L* upper limit changed curves and lower limit changed curves of all typical memory color for the chroma value L* of the corresponding color code and color lump of the confirmed acceptable color cast limit sample pieces of all kinds of memory color under the L* dimensionality according to the above serial number order, as shown in Fig. 5.

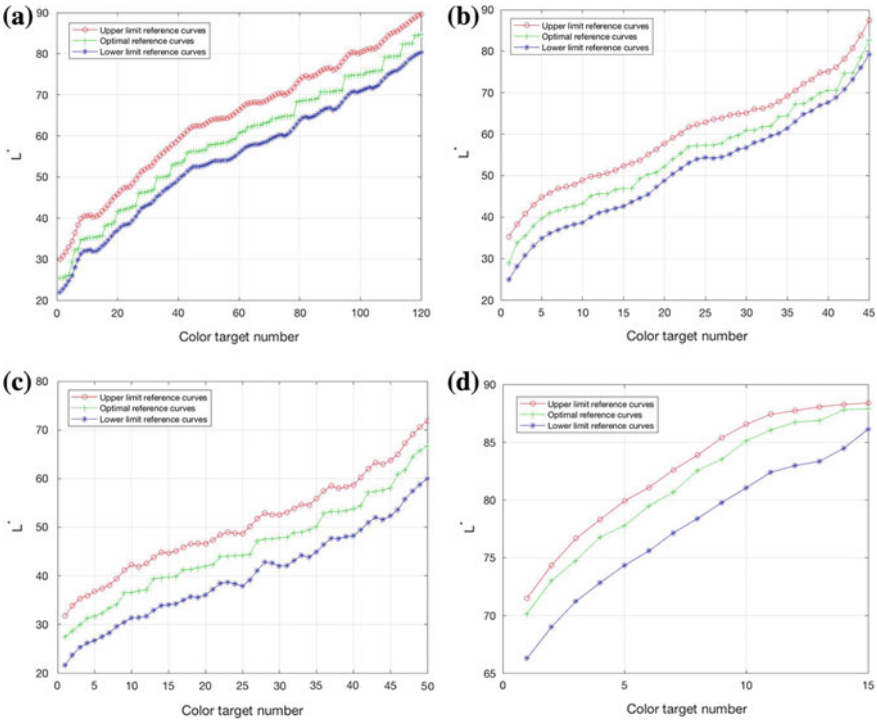

Fig. 5 The reference curves of all kinds of typical memory color brightness

According to the above same method, separately carry out the similar treatment for C_{ab}* and h_{ab}*, so the curves are obtained as shown in Figs. 6 and 7.

Taking the L*, C_{ab}*, h_{ab}* optimal reference curves, upper limit reference curves and lower limit reference curves of all kinds of typical memory color as the compared scale of the color quality evaluation, which can be used for the compared evaluation of the color quality of digital hardcopy output.

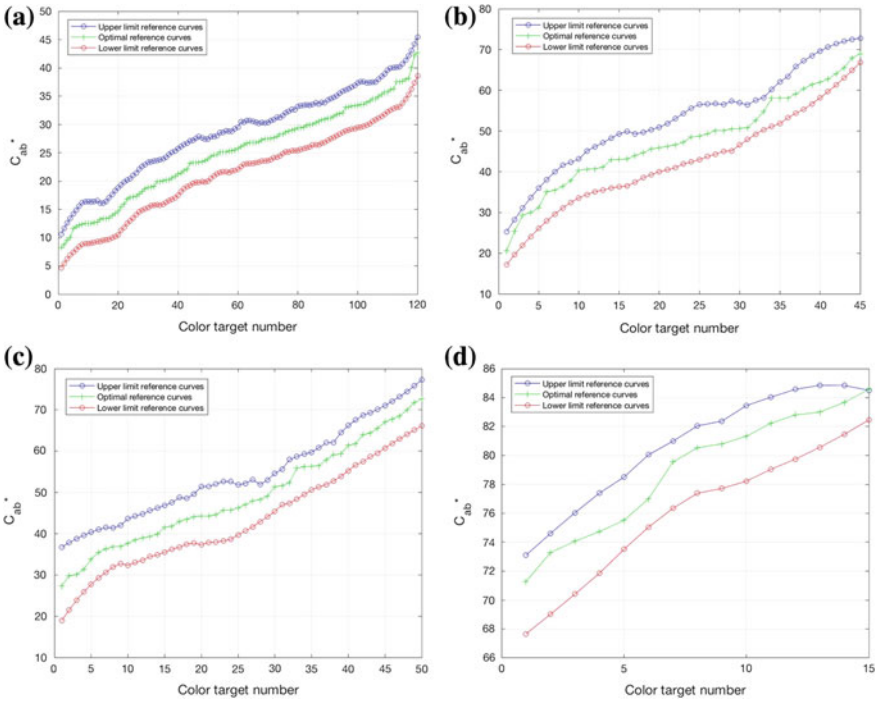

Fig. 6 The reference curves of all kinds of typical memory color chroma

2.3 Method of the Compared Evaluation of Color Quality

Make the actual measurement of the chroma value of the color targets of all kinds of typical memory color, draw separately the L*, C_{ab}*, h_{ab}* curves, according to the serial numbers of the color lump of the corresponding curves, and carry out the analysis of the confirmed reference curves of the corresponding experiments. Through the compared analysis of curve, evaluate the color quality of hardcopy output from the three aspects of representation of lightness, chroma and hue. When the chroma value curve of the color targets is closed to the corresponding optimal reference curve, it is shown that the color expression and quality of the typical memory color exports is better; when the chroma value curve of the color targets is far away from the corresponding optimal reference curve, but it still in the range of two upper limit and lower limit reference curves, it is shown that the color expression and quality of the typical memory color exports can be accepted; when the chroma value curve of the color targets is far away from the corresponding optimal reference curve, and it is not in the range of two upper limit and lower limit reference curves, then the color expression and quality of the typical memory color exports cannot be accepted.

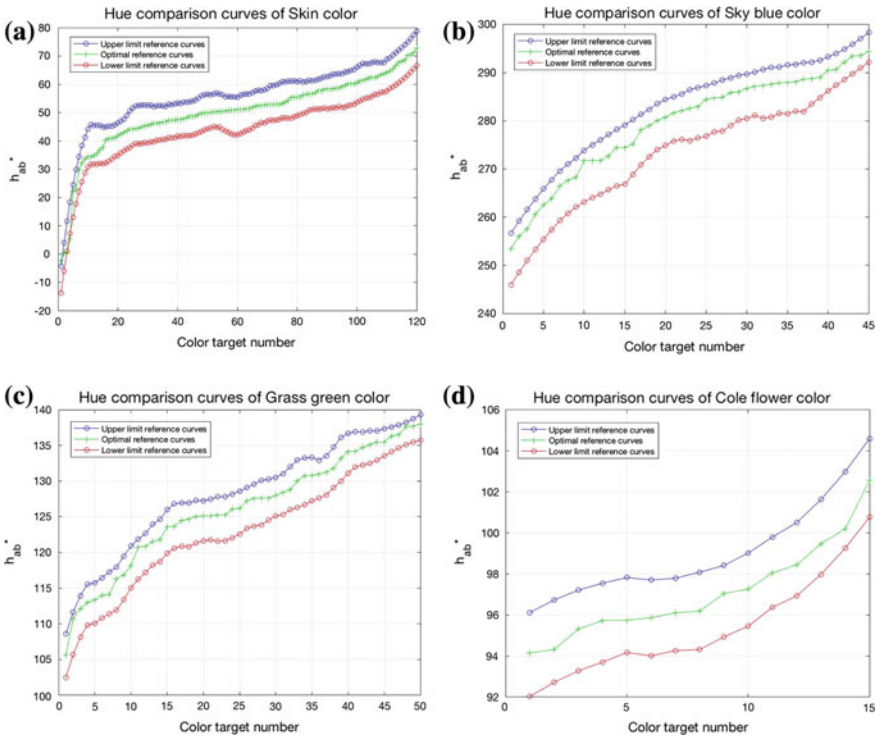

Fig. 7 The reference curves of all kinds of typical memory color hue angle **a** skin color **b** sky blue color **c** grass green color **d** cole flower color

3 Conclusions

Take the memory color as the key of the color quality of digital hardcopy output, the characteristic color targets which can reflect the chroma characteristics of each typical memory color is extracted from a mass of sRGB images with the memory color, through the subjective vision experiments, the best and acceptable chroma values of the corresponding color targets of each typical memory color sample and color expression are ensured under three dimensionalities of L*, C_{ab}*, h_{ab}* and the corresponding optimal reference curve, the upper limit reference curve and the lower limit reference curve are drawn as the compared scales, through the measurement of color targets, color lump and chroma of the actual output, the comparison of standard scale curve, the color quality of hardcopy output sRGB images is evaluated from three aspects of lightness, chroma and hue. This assessment method is objective, fast and convenient and other characteristics, especially its color evaluation is more targeted, which can avoid the difference, instability and in-concreteness of the objective evaluation.

References

1. Yao H (2007) The problems in the matching of proofing and printing. Pr China 2:78–80
2. Huang XQ, Shi JS, Yang J, Yao JC (2007) Study on color image quality evaluation by MSE and PSNR based on color difference. Acta Optica Sinica 36(8):295–298
3. Liu R, Wang Q, Dai J (2014) Research of the digital proofing color quality evaluation method. Packag Eng 35(1):120–123
4. (2013) A new handheld spectrophotometer-X-rite eXact. Printing Quality & Standardization, 2013(1), 4
5. Hui-hui S, Xiu-ping Z, Zhan-jun Si (2008) Research on image quality of glossy inkjet paper based on subjective evaluation. Packag Eng 29(5):39–42

The Experimental Research on Color Gamut Transformation Method Based on Different Types of Images

Peipei Ran, Wenjie Yang, Zhongyue Da, Zhen Liu, Ruili He and Min Huang

Abstract Different color devices can display different color range and the image color passed in different devices can not accurately reproduce too. In order to minimize these differences, the gamut mapping techniques are required. The theories of gamut are basis of the paper and five types of images are mapped, the converted image are evaluated and analyzed to finalize appropriate color gamut mapping method. The experimental results will have a significant meaning for color reproduction and color management.

Keywords Color gamut · Color gamut mapping method · Rendering intent

1 Introduction

In the transmission of cross-media color, color gamut mapping must reach a certain satisfaction and accuracy [1]. There are more research on gamut mapping including two main methods: mapping point by point and space mapping. Based on the principle of Retinex theory, Mc Cann [2] proposed an iterative color gamut mapping algorithm. The method can have better effect in speed and image quality, but there is a little difficult in reproducing for tone and level of images. Kurt Muenger, Yuanhong Zhu and Lianfa Si proposed the method of "Compressing the color gamut with the mark method" [3], which can compress color which beyond the color gamut into color gamut of the target device, this method almost have no influence in color and gray scale.

Perceptual, Saturation, Relative Colorimetric and Absolute Colorimetric are the four rendering intents in International Color Consortium [4]. These are part of color gamut mapping. The paper referring to the experiment is a part of total experiment

P. Ran (✉) · W. Yang · Z. Da · R. He · M. Huang
School of Printing and Packing Engineering, Beijing Institute of Graphic Communication, Beijing, China

Z. Liu
School of Engineering, Qufu Normal University, Rizhao, Shandong, China

P. Zhao et al. (eds.), *Applied Sciences in Graphic Communication and Packaging*, Lecture Notes in Electrical Engineering 477,
https://doi.org/10.1007/978-981-10-7629-9_20

that through it we can make a conclusion: the bright and dark images are suitable for reproduction by relative colorimetric, and the gray and skin images are suitable for reproduction by saturation, but the memory color image is suitable for reproduction by absolute colorimetric.

2 Experiment

2.1 Tested Images

The quality of tested images will influence the experimental results, because this is the key to ensure the reliability of experimental results.

Therefore, the images which have obvious characteristics and rich in contents and details are the best choice to evaluate the features of color gamut mapping method. As Fig. 1, from left to right is respectively gray image, dark image, skin image which are selected from ISO400 standard test images and bright image, memory color image which are selected from network pictures according to their characteristics. Their mapping images are obtained through changing arguments of the color setting in Photoshop.

2.2 Observer

The observers' knowledge about color science, photography and quality inspection will have a significant impact on the experimental results. So we select ten students who have normal visual and printing knowledge. Informed consent is obtained from all individual participants included in the study.

2.3 Process of Experiments

Experiments are conducted in a dark room. The liquid crystal display NEC and spectral radiation meter PR655 are chosen in the experiment. The stability of

Fig. 1 Five experimental images

display will have an impact on the experimental results, so time stability and space uniformity should be tested in the first.

2.3.1 Time Stability of Display and Results Analysis

Time stability of display [5] is defined by the changes of color information since starting up. The smaller the change is, the better the stability of display. Measure the white block showing on the display every 2 min in 3 h from the start of opening the monitor. During the measurement, the distance between the spectral radiation meter PR655 and the center of display is 45 cm. After the measurement, the average values of XYZ in the last 3 sets are defined as the standard value, then the Lab color difference of each measured value with standard value are calculated, the changes of color difference with time is as shown in Fig. 2.

It can be concluded from Fig. 2 that the color difference of each measured value with standard value is small and below 0.3, the color difference is unstable in 90 min, and gradually tends to 0 after 120 min. Therefore, we should start the display for 2 h before observation experiment.

2.3.2 Space Uniformity of Display and Results Analysis

The space uniformity of display [6] is defined by the changes of color information of pixel between different positions in the display when the RGB values of each pixel are equal. The smaller the change is, the better the space uniformity of display. The screen is divided into nine positions from left to right and from top to bottom. First, the display is started for 2 h, and then the screen color is set to red, and the spectral radiation meter PR655 is used to measure the center point of each position from 45 cm. The Lab values of center point in screen is defined as standard value because the image is usually set in the center of display when it is observed, then the Lab color difference of other measured values with standard value is calculated as shown in Table 1.

It can be concluded from Table 1 that the color difference of each positions with center is below 3, the space uniformity of display is fine and image is set in different positions have little impact on results of observation experiment.

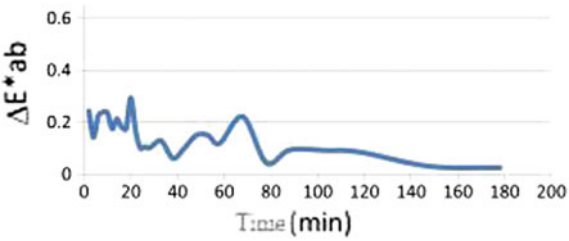

Fig. 2 The changes of color difference with time

Table 1 The color difference in different positions

Tested positions	1	2	3	4	6	7	8	9
ΔE	1.72	0.45	0.77	0.91	1.74	0.90	0.06	2.14

2.3.3 Observation Experiment

Visual evaluation experiments are conducted in a dark room. The original images and 4 color gamut mapping images are showed on the screen at the same time, which are as Fig. 3. The middle position is the original image, and the upper left, upper right, lower left and lower right are respectively the images of perceptual, saturation, relative colorimetric and absolute colorimetric. The background of display is gray.

The visual direction of observers is perpendicular to the original image when starting visual evaluation experiments. First, the display is started for 2 h. Then the observers are organized to carry on the visual evaluation experiment. Finally the observers give scores for each images based on the effect of reproduction and color consistency. If the difference is small, the images are judged from the details, color, contrast and edge performance, and then the images are divided into different levels which are as shown in Table 2.

Fig. 3 Experimental example

Table 2 The basis for visual evaluation

Levels	Basis of the classification	Scores
1	The effect of reproduction for whole images and details is good	4
2	The effect of reproduction for whole images is acceptable but details are fuzzy	3
3	The images are more brighter or darker than original image	2
4	The level of images is loss and effect is poor	1

3 Experimental Results

3.1 Analysis of Observer Accuracy

The average of observer's scores are compared with scores of the accuracy for color gamut conversion method which are given by every observer for each type image, then the root of mean square error are calculated to represent observer's accuracy. Calculation formula is:

$$R_{MSE} = \sum_{i=1}^{N} (x_i - \bar{x})^2 / N \tag{1}$$

x_i represents the scores of a certain color gamut conversion method given by each observer for one type image, $\bar{x}$ represents the average scores given by all observers for a certain color gamut conversion method. The smaller the value of R_{MSE} is, the smaller the deviation of mean and observer's score.

The root of mean square error of 4 color gamut conversion methods given by 10 observers for every type image is range in 0.45–1.18 which are in the acceptable range, so the data of visual evaluation experiment is effective.

3.2 Analysis of Experimental Data

The evaluation results of color gamut conversion method can be defined by the average score given by a certain observer and the number of supporters for each color gamut conversion method. Calculation formula is:

$$\overline{C} = \sum_{i=1}^{4} N_i C_i / \sum_{i=1}^{4} N_i \tag{2}$$

N_i represents the number of observers whose scores are consistent for the image obtained by a certain color gamut conversion method, C_i represents the scores of images. The average score of each color gamut conversion method is calculated as shown in Table 3.

The number of supporters for each color gamut transformation method is as shown in Fig. 4.

Table 3 The valuation results

	Perceptual	Saturation	Relative colorimetric	Absolute colorimetric
Bright image	2.2	1.6	3.6	2.3
Gray image	3	2.4	2.1	1.3
Dark image	2.1	1.9	3.3	2.7
Skin image	1.7	3.6	3.3	1.4
Memory color image	1.7	3.3	1.4	3.6

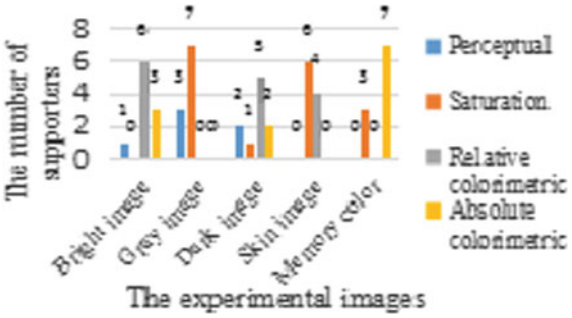

Fig. 4 Data statistics of observers (Color figure online)

3.3 Analysis of Experimental Results

It can be concluded from Table 3 and Fig. 4 that the favorable color gamut conversion method is different for images of different types according to features of images.

For bright image, most observers judge the details of images and support the relative colorimetric. For gray image, most observers support the saturation, it can be seen from the details of the image obtained by saturation is better for color reproduction of the original image. For dark image, the image transformed by relative colorimetric is true and nature; half of observers support the method. For skin image, the image obtained by saturation is similar to original image in skin color and details of figures, more than half of observers support the method. Memory color image is a special kind of image compared by observers with the color in memory, so in the process of color reproduction, these images have higher requirement for accuracy of color reproduction. From the analysis of data, image obtained by the absolute colorimetric is more nature, true and similar to color in memory of observers.

4 Conclusions

In the process of evaluation, we should follow the standards from color gamut conversion method in International Color Consortium. The results of experiment indicate that in order to ensure the accuracy of image reproduction, the appropriate

color gamut conversion method is chosen for images of different types according to features of images in application. Perceptual and relative colorimetric are better to reflect the characteristics of images which emphasize on performance of hue and levels such as figures and landscapes. The image which emphasizes color rendering such as commercial advertisement is suitable for saturation, and absolute colorimetric is usually chosen by images that need to be accurately reproduced.

Acknowledgements The study is supported by the National Key Scientific Instrument and Equipment Development Project (No. 2013YQ140517).

References

1. Morovic J, Luo MR (1998) The pleasantness and accuracy of gamut mapping algorithms. In: ICPS conference proceedings, pp 39–43
2. Mc Can J (1999) Lessons learned from mondrians applied to real images and color gamuts. In: Proceedings of IS &T/SID 7th color imaging, pp 380–393
3. Muenger K, Zhu Y, Si L (2002) Compress the color gamut with the marker method. J Wuhan Univ Inf Sci Ed 27(3):321–326
4. ICC (2005) ICC Profile Specification 4.1: The file format of ICC Profile [EB/OL]. (2005-09-01) [2005-09-21]. http://www.color.org
5. Xu H (2005) Color information engineering. Zhejiang University Press, Hangzhou
6. Hu Y, Zhang X (2011) Test method for performance of display for soft proofing. Printing Mag 3:45–48

Part II
Image Processing Technology

A Novel Blind JPEG Image Quality Assessment Based on Blockiness and the Low Frequency Feature in DCT Domain

Wei Wang, Yuanlin Zheng, Kaiyang Liao, Li Liu and Zhisen Tang

Abstract Blind image quality assessment metrics play an important role in the field of image processing. Blind image quality assessment methods, which are specific to a given type of distortion, are very popular for different image processing applications. JPEG compression is one of the most common image compression methods. In this paper, a support vector regression approach is adopted to assess the quality of JPEG compressed images without reference image. At first, the low frequency feature in DCT domain and the blockiness feature are calculated to present the distortion information of an image. Second, the JPEG dataset is divided into training and testing set randomly. The training set is used to build the SVR model, and the testing set is used to predict the quality score. Finally, combining with MOS or DMOS, the quality score is predicted by SVR model. Extensive experiments on LIVE database demonstrate that the proposed method outperforms the state-of-art methods both on predict accuracy and computational complexity.

Keywords Blind image quality assessment · JPEG compression
Support vector regression

1 Introduction

Image quality assessment plays an important role in the field of computer vision and image processing. According to the degree of reference information needed for IQA, the objective IQA metrics can be classified into full-reference(FR) [1, 2], reduced-reference (RR) [3, 4] and no-reference (NR) methods. With the development of objective IQA methods, no-reference methods had drawn widespread

W. Wang · Y. Zheng (✉) · K. Liao · L. Liu · Z. Tang
Faculty of Printing, Packaging Engineering and Digital Media Technology,
Xi'an University of Technology, Xi'an, China
e-mail: zhengyuanlin@xaut.edu.cn

Y. Zheng
Shaanxi Provincial Key Laboratory of Printing and Packaging Engineering, Xi'an, China

P. Zhao et al. (eds.), *Applied Sciences in Graphic Communication and Packaging*, Lecture Notes in Electrical Engineering 477,
https://doi.org/10.1007/978-981-10-7629-9_21

attention especially when it is difficult to obtain reference image. In addition, specific distortion type NR-IQA methods are very popular for different image processing applications. And JPEG is one of the most popular and widely used images. Therefore, this paper mainly focuses on studying the NR-IQA method for JPEG-compressed image.

During past decades, a lot of NR-IQA methods have been proposed. Bovik et al. proposed BLINDS [5] and BLINDS-II [6] metrics based on DCT domain to evaluate image quality. Zhan and Zhang [7] proposed a NR-IQA method for JPEG image, which obtains the quality score by considering the luminance changes and the blocking artifacts from all non-overlapping 8×8 blocks in one JPEG image. In Ref. [8], image quality is obtained by counting the number of DCT coefficients with each block, and then using the quality relevance map to weight the counts. In [9], a new two-step framework named BIQI for NR-IQA based on natural scene statistics (NSS) is proposed. The DIIVINE [10] is proposed based on the assumption that the statistical propertied of natural scenes are altered in the presence of distortion.

The rest of this paper is organized as follows. In Sect. 2, the proposed method is presented in detail. Section 3 shows the experimental results. Finally we conclude in Sect. 4.

2 Proposed Method

In JPEG compression, the image is firstly divided into many non-overlapping 8×8 blocks, as an input of two-dimensional discrete cosine transform (DCT). Therefore, the blockiness and DCT coefficients feature are important for JPEG compressed image. In this paper, the blockiness and low frequency feature in DCT domain are adapted to present image distortion information. Then, SVR is adapted to predict image quality score. Figure 1 is the flowchart of the proposed method.

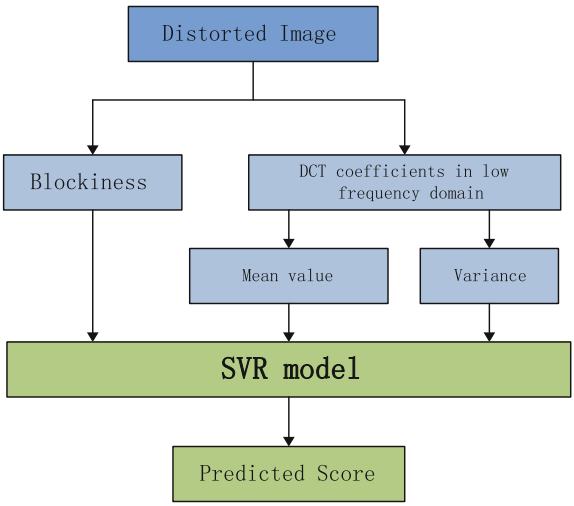

Fig. 1 The flowchart of the proposed method

2.1 Blockiness Feature

The blockiness can be considered as discontinuities among the boundaries of contiguous blocks. In order to measure the blockiness of one block, the average of the amount of discontinuities along four boundaries of the block is calculated to present the blockiness. In this paper, the blockiness is obtained as Ref. [7].

At first, let I and T denote an image and a block size of $m \times n$ respectively, and the first pixel of T is located at $I(\mathrm{x}, \mathrm{y})$. The difference between the boundaries gradients and the mirrored external surroundings gradients outside the boundaries is calculated to present the discontinuities along four boundaries of the block T. The discontinuities along the four boundaries of T are calculated as:

$$D_{v1} = \frac{1}{n}\sum_{j=y}^{y+n-1}(\mathrm{G}_h(x-1),j) - \frac{1}{\lfloor m/2 \rfloor * 2}\cdot \sum_{i\in 0<|\mathrm{i}-x+1|\le \lfloor m/2 \rfloor}(G_h(i,j)) \quad (1)$$

where $\lfloor a \rfloor$ denotes the largest integer smaller than a. The calculation of D_{h1}, D_{v2} and D_{h2} are similar to D_{v1}. D_{vi} and $D_{hi}(i \in (1,2))$ are vertical and horizontal difference respectively. And the gradient is defined as:

$$G_h(i,j) = |I(i,j+1) - I(i,j)| \quad (2)$$

The blockiness B of T is obtained by:

$$B = D_{v1} + D_{v2} + D_{h1} + D_{h2} \quad (3)$$

A higher value of B manifest more evident blockiness.

2.2 Low Frequency Feature in DCT Domain

The discrete cosine transform is a commonly method in JPEG compression. Many researches demonstrated that DCT coefficients are important for presenting image distortion information. And the low frequency features in DCT domain are sensitive to human visual system. In this paper, the mean and variance of low frequency feature in DCT domain are calculated to be the import of SVR model. The two-dimensional discrete cosine transform is defined as:

$$F(u,v) = \frac{2}{\sqrt{MN}}c(u)\mathrm{c}(v)\sum_{x=0}^{M-1}\sum_{y=0}^{N-1}f(x,y)\cos\frac{(2x+1)u\pi}{2M}\cos\frac{(2y+1)v\pi}{2N} \quad (4)$$

where $x, u = 0, 1, 2, \ldots, M-1$; $y, v = 0, 1, 2, \ldots, \mathrm{N}-1$;

$$c(u) = c(v) = \begin{cases} \frac{1}{\sqrt{2}}, & u = 0, v = 0 \\ 1, & \text{otherwise} \end{cases} \tag{5}$$

Let ω be a spatial frequency value in cycles per degree for (u, v)th DCT coefficient, $\omega = \delta \cdot \sqrt{u^2 + v^2}$. δ is a constant and is determined by a visual angle per pixel. Therefore, $t(\omega)$ is the magnitude of a normalized DCT coefficient at ω, and is defined as

$$t(\omega) = (\varepsilon + |c(\omega)^{\lambda}|)/\mathrm{Q} \tag{6}$$

where Q is a normalization factor to make $t(\omega)$ as a probability value over ω, and $c(\omega)$ is the DCT coefficient value at ω. ε is a small constant value. λ is an adjustment parameter to fit measured results. In addition, the DCT coefficients of low frequency domain are extracted to present the frequency feature. The mean and variance of $t(\omega)$ is defined as follows respectively:

$$\bar{t} = \frac{1}{n}\sum_{i}^{n} t_i(\omega), \quad S = \sqrt{\frac{1}{n}\sum_{i}^{n} (t_i - \bar{t})^2} \tag{7}$$

where n is the number of $t(\omega)$. Therefore, the mean value $\bar{t}$ and the variance of DCT coefficients S in low frequency domain, are calculated to present the DCT coefficient feature of an image. In addition, $\bar{t}$ and S are used for the import of SVR model.

2.3 Support Vector Regression

Vapnik brought up support vector regression based on statistical learning theory. Because of its perfect theoretical framework and good practical application effect, SVR has been widely used in image processing. LIB-SVM is a package of SVM and can be modified to suit users. In this paper, the LIB-SVM, $\varepsilon{-}SVR$ and RBF kernel function are chosen to establish the SVR model. The regression equation of $\varepsilon{-}SVR$ is defined as:

$$f(x) = \sum_{i=1}^{n} (\alpha_i - \alpha_i^*)\mathrm{K}(x_i, x) + \mathrm{b} \tag{8}$$

where α_i and α_i^* are Lagrangian coefficients of certain samples. $K(\mathrm{x}_i, \mathrm{x})$ is the RBF kernel function. Particle Swarm Optimization (PSO) is adopted to search for the best parameters of SVR. The blockiness feature B, the DCT coefficients feature $\bar{t}$ and S are used for the import of SVR model.

SVM model requires a training procedure to calibrate the regression. Hence, in this paper, the dataset is divided into two randomly chosen subsets 80% for training and the rest 20% for testing. Because the training sample set and testing set of SVR model are selected randomly, the experimental results might vary in each time. To eliminate the randomness, experimental results represented in all Tables within this paper are the median of the performance across 1000 times.

3 Experimental Results

We operated the proposed method on LIVE database. The performance is evaluated by the consistency between objective predicting score and the difference of subjective mean opinion score (DMOS). To provide a complete evaluation of each IQA methods, two commonly used performance metrics are employed. These two performance metrics are the Spearman rank-order correlation coefficient (SROCC) and Pearson linear correlation coefficient (PLCC). Before calculating these criterions, a five-parameter logistic function for nonlinear mapping as suggested by Video Quality Experts Group (VQEG), is conducted between the subjective and objective scores:

$$f(x) = \beta_1 \left(\frac{1}{2} - \frac{1}{1 + e^{\beta_2 (x - \beta_3)}}\right) + \beta_4 x + \beta_5 \tag{9}$$

where β_i, $i = 1, 2, 3, 4, 5$ are the parameters determined by least square fitting to the actual MOS or DMOS value. x denotes the objective score and $f(x)$ denotes the predicted subjective MOS or DMOS score. The Matlab function "nlinfit" is used to find the best values of parameters.

Table 1 provides the comparison between the proposed algorithm and various NR-IQA methods for JPEG images on the JPEG subset of the LIVE database. Both of SROCC and PLCC of the proposed are higher than other methods. It shows that the proposed algorithm maintains a high consistency with the subjective quality ratings.

Table 1 Comparison of the proposed method versus various NR IQA method on the JPEG subset of the live database

	Ref. [10]	Ref. [11]	Ref. [12]	Ref. [13]	Ref. [14]	Proposed
SROCC	0.910	0.904	0.904	0.902	0.911	0.914
PLCC	0.921	0.932	0.940	0.923	0.928	0.949

4 Conclusions

In this paper, a novel blind JPEG image quality assessment method is proposed, which is based on low frequency feature in DCT domain and blockiness. The SVR is adapted to predict the quality score. Comparing with state-of-art FR and NR IQA methods, the proposed method shows good performance in predicting accuracy. Experimental results demonstrated that the proposed method performs highly consistent with human visual perception.

Acknowledgements This study is funded by Shaanxi Provincial Key Laboratory of project-Printing image quality assessment based on human visual features (13JS082).

References

1. Zhang L, Zhang L, Mou X, Zhang D (2011) FSIM: a feature similarity index for image quality assessment. IEEE Trans Image Process 20:2378–2386
2. Gao F, Yu J (2016) Biologically inspired image quality assessment. Signal Process 124:210–219
3. Wang S, Gu K, Zhang X, Lin W, Ma S, Gao W (2016) Reduced-reference quality assessment of screen content images. IEEE Trans Circuits Syst Video Technol 1–1
4. Wang Z, Xu K, Yan S (2015) Reduced-reference image quality assessment in modified reorganized DCT domain. In: Proceedings of 2015 IEEE international conference on computer and communications (ICCC), pp 161–165
5. Saad MA, Bovik AC, Charrier C (2010) A DCT statistics-based blind image quality index. IEEE Signal Process Lett 17:583–586
6. Saad MA, Bovik AC, Charrier C (2012) Blind image quality assessment: a natural scene statistics approach in the DCT domain. IEEE Trans Image Process 21:3339–3352
7. Zhan Y, Zhang R (2017) No-reference JPEG image quality assessment based on blockiness and luminance change. IEEE Signal Process Lett 1–1
8. Golestaneh SA, Chandler DM (2014) No-reference quality assessment of JPEG images via a quality relevance map. IEEE Signal Process Lett 21:155–158
9. Moorthy AK, Bovik AC (2010) A two-step framework for constructing blind image quality indices. IEEE Signal Process Lett 17:513–516
10. Moorthy AK, Bovik AC (2011) Blind image quality assessment: from natural scene statistics to perceptual quality. IEEE Trans Image Process 20:3350–3364
11. Pan F, Lin X, Rahardja S, Ong EP, Lin WS (2004) Measuring blocking artifacts using edge direction information [image and video coding]. In: Proceedings of 2004 IEEE international conference on multimedia and expo (ICME), vol 492, pp 1491–1494
12. Liu H, Heynderickx I (2008) A no-reference perceptual blockiness metric. In: Proceedings of 2008 IEEE international conference on acoustics, speech and signal processing, pp 865–868
13. Pan F, Lin X, Rahardja S, Lin W, Ong E, Yao S, Lu Z, Yang X (2004) A locally-adaptive algorithm for measuring blocking artifacts in images and videos. In: Proceedings of 2004 IEEE international symposium on circuits and systems, vol 923, pp III-925–928
14. Hua Z, Yiran Z, Xiang T (2008) A weighted Sobel operator-based no-reference blockiness metric. In: Proceedings of 2008 IEEE Pacific-Asia workshop on computational intelligence and industrial application, pp 1002–1006

The Modeling of 3D Color Topography Based on DEM Data for 3D Printing

Kaili Zhang, Liuxi He, Xiaochun Wang and Guangxue Chen

Abstract The simulation of the three-dimensional image could not convey the exact three-dimensional (3D) information to people in the practical application; meanwhile 3D terrain model of the physical manufacturing encountered difficulties in mold manufacturing, such as high cost, short life and other bottlenecks. The technology of 3D printing provided a solution for the manufacture of 3D topographic map. Therefore, in this paper, the NSDTF-DEM data was built by colorful 3D model to meet the needs of 3D printing. Based on the Crust algorithm, the regional reconstruction and Delaunay tetrahedral meshing were used to reconstruct the surface of DEM point cloud data. The depth map of the 3D model was obtained by the topography projection of the 3D surface. The color assignment was carried out by using the correspondence between the depth graph gray value and the number of indexed image columns, which was designed to produce the same color texture image as the depth map. This modeling method not only improved the modeling accuracy of the 3D mesh model, but also achieved higher color accuracy.

Keywords Three-dimensional printing · 3D topographic map · DEM data
Surface reconstruction · Texture mapping

1 Introduction

DEM was a 3D terrain model of ground elevation in the form of an array of ordered numerical arrays in geographic information systems [1, 2]. DEM data could be simulated by software to solve the practical problems, but the simulation of 3D images could not convey the exact 3D information to people in practical applica-

K. Zhang · X. Wang · G. Chen (✉)
State Key Laboratory of Pulp and Paper Engineering, South China University of Technology, Guangzhou, China
e-mail: chengx@scut.edu.cn

L. He
YUTO Institute, Shenzhen YUTO Packaging Technology Co., Ltd., Shenzhen, China

P. Zhao et al. (eds.), *Applied Sciences in Graphic Communication and Packaging*, Lecture Notes in Electrical Engineering 477,
https://doi.org/10.1007/978-981-10-7629-9_22

tions. Thus, there were no mass production, high cost, short life and other defects while we used traditional manufacturing mold methods to produce three-dimensional topographic map. The emergence of 3D printing technology provided a new way for creating three-dimensional topographic map exactly.

The main link between DEM data and 3D printing was the format of the source file. The most commonly used 3D print file format was a triangular mesh model, such as STL, OBJ. What's more, many scholars have studied in the 3D digital model modeling and texture mapping. As is known to all, Wu T [3] constructed each triangular plane in the STL file as a tetrahedron and added a byte space to store the color information at the end of the memory cell to form an enhanced version of STL. Pelagotti A and Del Mastio A [4] proposed an automatic texture mapping technique for image registration based on the depth map of 3D model, and realized the fully automated texture mapping, which avoided the subjective problem that might occur in the process of manual detection. Liao [5] of Hunan University used a curved surface to generate algorithm which was based on Crust graph to ensure the unchangeable shape of the original sampling surface. According to Chunli Qiu of Beijing Jiaotong University, an improved algorithm of spatial triangulation supported by the incremental grid was proposed. The dynamic ball strategy was introduced into the space segmentation, and the vertex metric function was designed in the Delaunay triangulation to solve the inconsistency between the maximum criterion of the normal vector and the maximum criterion of the minimum angle in the constraint criterion [6]. Faqiang Wang and Guohua Geng proposed a method of face texture mapping on the base of feature point constraints. Using the least squares conformance mapping parameterization required fixed vertices to complete feature point constraints [7]. Guo Y and Pan Y [8] proposed a method of constrained texture mapping which was relied on harmonic mapping, and it had the property of minimizing the energy of mapping and could obtain a formal exact solution of constraint texture mapping problem. Yong Tang and Lianjun Liu have proposed a new algorithm for hemispherical texture mapping in order to reduce the texture deformation caused by the hemispherical mapping algorithm. Using the aspect ratio of the texture region on the texture plane and hemisphere as the constraint condition could improve the texture quality [9]. Junjie Wang and Yunan Wang realized that the grid model reduced the accuracy of the original sampling points, and then they proposed a method of texture mapping directly using the point cloud data supported by the least squares principle. It could improve the efficiency of mapping and reduce the roughness of the texture, but the method was only applicable to the point cloud data where the feature points were more enough. When the feature point of the cloud data was not enough, the systematic displacement between the texture map and the point cloud model might be caused by the improper selection of the feature points [10].

Herein, this paper investigated a construction of triangular mesh model for DEM data based on crust algorithm, and the file format was saved as OBJ finally. The texture map based on the depth map was built according to the characteristics of the 3D model so that it could accomplish the construction of the color 3D topographic map model.

2 DEM Data Triangle Mesh Model Construction

2.1 Crust-Based Tetrahedral Mesh

The concept of partitioning and tetrahedral mesh segmentation was introduced based on the Crust algorithm. On the one hand, the spatial division could improve the efficiency of the algorithm because of the large amount of point cloud data in the DEM data. On the other hand, the spatial partition could limit the points to be treated in the local area, and it was easy to determine the boundary of the point cloud data.

2.1.1 Spatial Area Division

In order to find the boundary coordinates of the point cloud collection, it was the maximum and minimum coordinates of the point cloud on the three axes of X, Y, and Z. These six coordinate values could determine the hexahedral boundary of the 3D space where the point cloud data was located. This boundary was used as the convex closure of the cloud data, and then the grid closure of the point cloud data was divided (Fig. 1). The number of divided regions was determined by the size, the density and other factors of the point cloud data. These elements ensured that the ideal and efficient algorithm could be prepared. After the partition, the original large hexahedron was divided into several small hexahedrons; the eight vertices of each small auxiliary hexahedron could be used to determine the five tetrahedrons. The blue hexahedron in Fig. 1 determined the ABDE, CBDG, HDEG, FBEG, and BDEG, these five tetrahedrons.

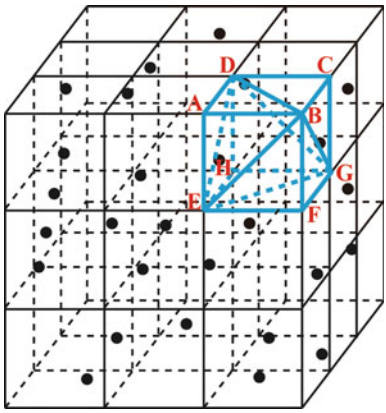

Fig. 1 Spatial grid division principle

2.1.2 Delaunay Tetrahedral Mesh

The tetrahedral mesh was the Delaunay triangulation of the 3D space point setting. The Delaunay trihedral mesh was subdivided by the point wise insertion method, which could be used to generate the optimized Delaunay grid and approximated the original sampling boundary.

The 3D space point was set as $S = \{p_i : i = 0, 1, 2, \ldots, n\}$, which was based on the properties of Delaunay triangulation, Delaunay tetrahedral mesh had the following three properties:

(1) Uniqueness: the result of Delaunay tetrahedron was unique if there were no five or more points.
(2) Certainty: if the tetrahedron of all tetrahedron in the external ball did not contain other point cloud, the division was Delaunay tetrahedron.
(3) The Delaunay cavity of point p: the Delaunay cavity of point p was a set of all non-Delaunay tetrahedra relative to the insertion point p, the finding method was as follows:

   (A) In S, the tetrahedron where the insertion point p located was searched firstly, and then the other adjacent tetrahedrons to the tetrahedron would be found. If there were non-Delaunay tetrahedra in the adjacent tetrahedron on which was relative to p, the adjacent tetrahedron would be discovered until no non-Delaunay tetrahedron could be found in S.
   (B) While all of the non-Delaunay tetrahedral collections was searched, only the outer faces of all tetrahedra containing point p were retained and all the inner faces would be deleted.

2.1.3 Extraction and Filtration

When generating the surface mesh, all tetrahedrons were eliminated to connect the eight points of the original point cloud convex closure. The rest was the triangular mesh surface formed by the point cloud data. In the end, crossing and overlapping triangles might appear, so the Voronoi filtering and normal filtering would be used to get by employing the Crust principle. DEM 3D surface model was shown in Fig. 2.

2.2 Format Storage of Triangular Mesh Model

The triangular mesh model for 3D printing must be a closed model; otherwise a hierarchical file error might take place when the model was hierarchized. DEM data surface modeling was the terrain surface of the triangular mesh model, not the non-closed model. Materialise Magics software provided a direct method for closed

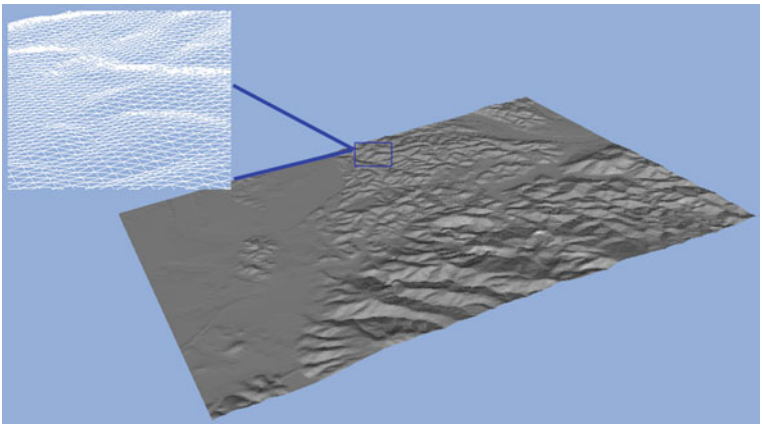

Fig. 2 DEM 3D surface model

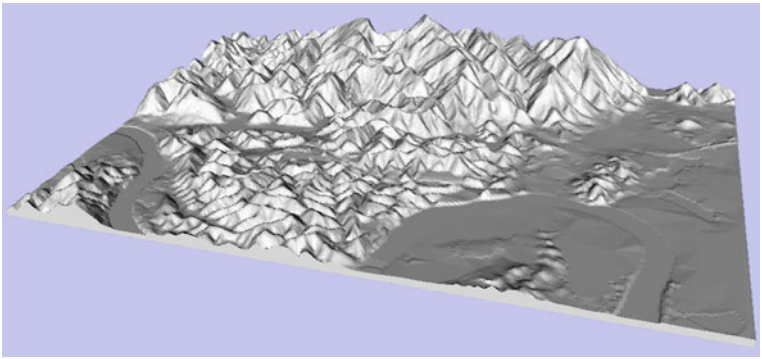

Fig. 3 Entity 3D topographic map model

modeling of 3D models, the Offset tool, the Extrude Stretch tool, and the Cut/punch cutting tool, which could be used to construct a 3D model of the surface as a solid 3D model (Fig. 3). The file was saved as OBJ format lastly.

3 DEM Texture Map of 3D Topographic Map

3.1 Depth Map of 3D Model

The depth map of the 3D model was referred to the projection of the 3D model. The DEM data recorded the elevation data of the surface sampling points. Each sampling point corresponded to only one elevation data. In other words, the 3D

terrain surface obtained by DEM data modeling was only different in high and low and there was no difference in x-y direction of the cave. Then, the depth map of the 3D terrain surface of the DEM could contain all the sampling points in the 3D terrain surface. It could satisfy the one-to-one correspondence between the depth image and the 3D terrain surface sampling point. Therefore, the upper surface of the DEM 3D terrain model was extracted firstly, and then it made a depth map of the top surface.

3.1.1 DEM 3D Surface Extraction

The DEM three-dimensional surface was extracted according to the normal vector of the triangular plane. As is shown in Fig. 4, the normal vectors for the front, back, left, and right vertical faces of DEM terrain model had only four cases, namely (1, 0, 0), (−1, 0, 0), (0, 1, 0), (0, −1, 0). The bottom face was a horizontal plane, and its normal vector was (0, 0, −1). While the top face was the ups the terrain surface, there existed no vertical surface and no faces with normal vector of (0, 0, −1). Therefore, the triangles with normal vector of (1, 0, 0), (−1, 0, 0), (0, 1, 0), (0, −1, 0) and (0, 0, −1) could be deleted through the ergodic calculating of the normal vector. There would remain the top face of DEM terrain model, which was the 3D terrain surface of DEM.

3.1.2 3D Surface Depth Map Generation

The depth graph acquisition of the 3D model determined the correspondence between the two-dimensional image pixels and the 3D model vertices. This process would make a projection on the 3D terrain surface of DEM, and then a two-dimensional image matrix was projected onto the X-Y plane. The row information and column information of each pixel in the matrix corresponded to the x and y coordinates of each vertex of the DEM 3D surface respectively. The gray value of the pixel was the elevation value of each vertex of the DEM 3D surface. In fact, this process was the DEM 3D surface and expressed as ARCINFO GRID data body format contrarily. The elevation value of the three dimensional surface vertex

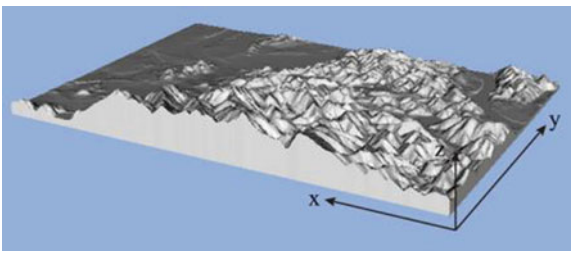

Fig. 4 DEM 3D terrain model coordinate map

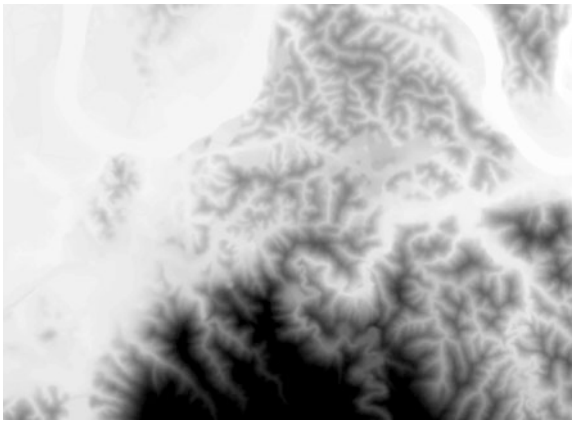

Fig. 5 Depth of DEM 3D terrain surface

of DEM was mapped to the gray value in the range of 0–255 and calculated following the formula (1). It finally got the depth map (Fig. 5).

$$g_{x,y} = 255\frac{h_{x,y}}{H} \tag{1}$$

The gray value of the x rows and y columns in the depth graph was the elevation value at the x and y coordinated in the 3D terrain surface, which represented the maximum value of the vertex elevation and the value of the 3D terrain surface.

3.2 Texture Map Generation

DEM 3D terrain surface depth map was a plane grayscale. The gray value in the figure was the location of the pixel corresponded to the height of the vertex in the 3D surface. The goal of the DEM 3D model texture map was to render the color according to the terrain elevation level. The warm color was set to the pixels with larger gray scale values, and the cool color with the smaller gray scale would get a color texture image.

Firstly, a picture with "Green-Yellow-Red" gradient bar was to be drew by Photoshop software with a 1×256 pixel size. This picture was called "index image".

Then, the matrix M_{xy} was obtained by reading the depth image M, and three matrices $R_{Mx,y}$, $G_{Mx,y}$, and $B_{Mx,y}$ with the same size as M_{xy} were to be created. The three component matrices of R, G, and B of the index image I, namely $R_{I1,n}$, $G_{I1,n}$, $B_{I1,n}$ (n = 1,2,…,256) would be acquired. The value was obtained according to the column value n of $R_{I1,n}$, $G_{I1,n}$, $B_{I1,n}$ with each gray value g_{xy} of M_{xy} plus 1. Then the RGB component values would be assigned to the n column of $R_{I1,n}$, $G_{I1,n}$, $B_{I1,n}$ to the elements of g_{xy} in M_{xy} respectively. The assignment formula was shown in

formula (2). The color texture image T could be gained from assigning $R_{Mx,y}$, $G_{Mx,y}$, $B_{Mx,y}$ as the RGB component values to T. As shown in Fig. 6, the contour line color of texture image was set based on gradient color of index image.

$$\begin{cases} T(:;:;1) = R_{M_{x,y}} = R_{I_{1,n}} \\ T(:;:;2) = G_{M_{x,y}} = G_{I_{1,n}}, \\ T(:;:;3) = \mathrm{B}_{M_{x,y}} = B_{I_{1,n}} \end{cases} \quad (n = g_{x,y} + 1) \tag{2}$$

3.3 DEM Texture Mapping

According to the depth map of the 3D terrain surface of the inverse transformation, this could be achieved by 3D terrain surface texture map.

(1) To extract the upper surface of the DEM 3D terrain model, the texture coordinated "vt (u, v)" were added to the vertices which was contained in the upper surface of the OBJ file. The triangular faces of the "vertex" were to be modified to "vertex/texture" coordinates in the form of triangular faces [11].
(2) After the texture image was generated, it was saved in the specified position, and the physical storage path of the texture image was loaded in the map_Kd attribute location in the MTL file [12, 13].

When the texture map was finished, the results of the OBJ and MTL files were to be parsed with OpenGL, as shown in Fig. 7.

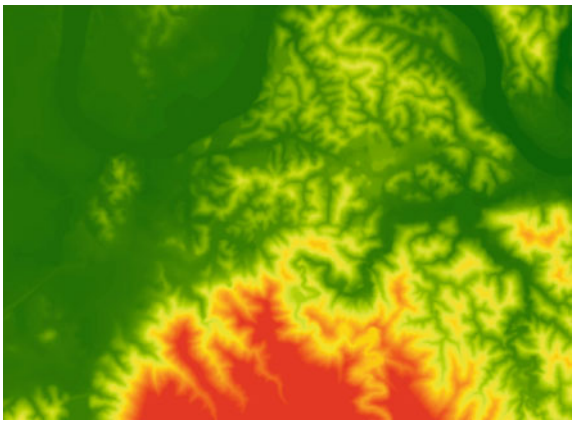

Fig. 6 Texture image (color figure online)

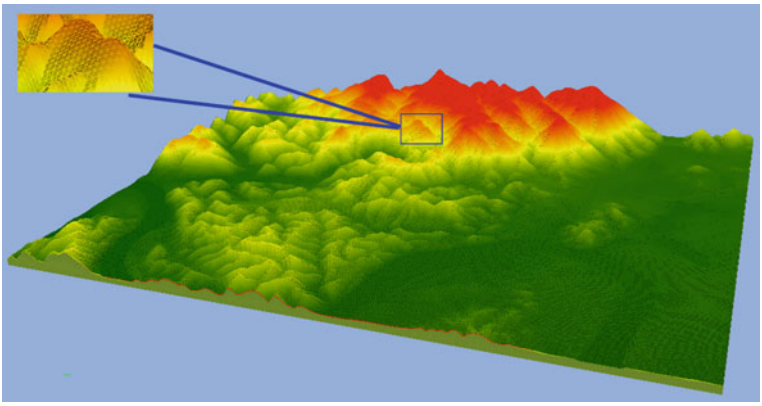

Fig. 7 DEM color 3D terrain model

4 Conclusions

Based on the Crust algorithm, the concept of spatial region division and tetrahedral mesh segmentation was investigated in this paper. The new algorithm not only improved the efficiency, but also increased the data of the point cloud data surface. Reconstruction effectively solved the problem of edge adhesion for non-closed models. With such support from the OpenGL interface, the depth map of the 3D surface was obtained by the overhead projection. Then, the texture image was generated according to the corresponding relationship between the gray scale value of the depth map and the number of the index graph. Finally, the texture map of the 3D topographic map was realized by modifying the OBJ and MTL files. Through the color 3D printing could make the DEM 3D terrain data into a visible and tangible practical model. It could accomplish kinds of function of information, just as simulation, load, transmission and understanding. What's more, the modeling of 3D color topography based on DEM data for 3D printing can play very important roles in the military exercise, sand table Manufacturing, teaching demonstration and other practical applications.

Acknowledgements This research was financially supported by the Guangdong Provincial Science and Technology Project (2016070220045 and 2017B090901064) and the Key Laboratory of Pulp and Paper Engineering Funding Project (2016c01) of South China University of Technology.

References

1. Zhang J (2015) Establishment and application of digital elevation model. Modern Surveying Mapp S1:213–214
2. Li Z, Li M, Du X (2008) Experiments on DSM to DEM in flat area. J Surveying Mapp Geogr 2:29–31

3. Wu T, Cheung EHM (2006) Enhanced STL. Int J Adv Manuf Technol 29(11–12):1143–1150
4. Pelagotti A, Del Mastio A, Uccheddu F et al (2009) Automated multispectral texture mapping of 3D models. In: Proceedings of signal processing conference, European. IEEE, pp 1215–1219
5. Liao H. Study on algorithm of surface mesh reconstruction based on crust graphs. J Hunan Univ Sci Technol
6. Qiu C (2014) Study on surface cloud based surface reconstruction technology. Beijing Jiaotong University
7. Wang F, Geng G, Li K et al (2012) Face texture mapping based on feature point constraints. J Comput Appl 09:3509–3511
8. Guo Y, Pan Y, Cui X et al (2005) Constrained texture mapping method based on harmonic mapping. J Comput Aided Design Graphography 07:1457–1462
9. Tang Y, L Liu, Lv M (2007) Hemispherical texture mapping algorithm based on long and wide equal constraints. J Syst Simul 18:4209–4211
10. Wang J, Wang YN, Cao Q (2011) Point cloud data direct mapping method. Modern Surveying Mapp 05:22–24
11. Chen L, Ding J, Li S (2002) Texture mapping of complex surfaces based on OpenGL. Comput Dev 02:57–60
12. Wang Z (2015) Mass texture image storage management and index research. Beijing University of Architecture
13. Zhu H, Gao C, Chen H et al (2012) The research on FDTD mesh generation and visualization technology. Environ Electromagnet 282–284

High Dynamic Range Image Compression Algorithm for Reproduction

Haiwen Wang, Jie Li, Pengfei Wang, Jiting Wang and Honglin Wang

Abstract High dynamic range image possesses characteristics of wide tone, rich color and detail information, providing better reproduction information. Expound first on principle and features of three high dynamic range image compression algorithms, and the image quality is evaluated by HDR-VDP method. The results indicate that tonal homogenization histogram method can enlarge image tone and contrast, but it causes distortion of color and detail information; Local color adaptive algorithm can maintain better tonal features and detail information, which is compliant for printing output; Algorithm based on iCAM compression can ensure better visual features of human, but the loss of image tones is serious. The comparison of the above three kinds of image compression algorithms provide a better technical approach and method reference for high fidelity reproduction of high dynamic range images.

Keywords High dynamic range image · Image compression algorithm
High-fidelity reproduction · HDR · iCAM

H. Wang (✉) · P. Wang · J. Wang
School of Biological and Chemical Engineering, Zhejiang University of Science and Technology, Hangzhou, Zhejiang, China

H. Wang · P. Wang · J. Wang
School of Light Industry, Zhejiang University of Science and Technology, Hangzhou, Zhejiang, China

J. Li
School of Information Engineering, Quzhou College of Technology, Hangzhou, Zhejiang, China

H. Wang
Zhejiang Minong Century Group, Hangzhou, Zhejiang, China

P. Zhao et al. (eds.), *Applied Sciences in Graphic Communication and Packaging*, Lecture Notes in Electrical Engineering 477,
https://doi.org/10.1007/978-981-10-7629-9_23

1 Introduction

High dynamic range image (HDR for short) can show more tonal levels, color range and image details [1], hence it is of great significance to high fidelity visualization and high fidelity printing. In order to achieve high fidelity reproduction of high dynamic range image, the key problem is to design a scientific and efficient high dynamic range image compression algorithm, ensuring that it basically doesn't cause distortions of image tones, colors and details. Current high dynamic range image compression algorithm for reproduction can be divided into three classes: global compression algorithm, local compression algorithm and hybrid compression algorithm [2–4]. The most representative image compression algorithms are tonal homogenization histogram method, local color adaption method and image color appearance model (iCAM for short) compression algorithm.

Tonal homogenization histogram method often generates contrast distortion. At present, linear sealing method is mainly adopted to improve overall result of image compression [5, 6]. Not considering actual dynamic range of original image, local color adaptation method results in lack of perception of accuracy [7]. With compression algorithm based on the iCAM, prediction of constant perception hue is good, and image attributes are independent. Defect is lack of efficiency [8, 9]. Therefore, in order to research on high dynamic range image compression algorithm for high fidelity reproduction, the paper respectively chooses tonal homogenization histogram method, local color adaptation method and compression algorithm based on iCAM to experiment. The result of compression algorithm is evaluated by using perceptual accuracy evaluation method (subjective evaluation method) and HDR-VDP quantification model method (objective evaluation method), so as to provide a technical and methodological reference for development and selection of image compression algorithm to meet quality requirements of high fidelity reproduction.

2 High Dynamic Range Image Compression Algorithms

2.1 Tonal Homogenization Histogram Method

Tonal homogenization histogram method is a process that normalizes each grey level in the histogram, and calculates each kind of gray value of accumulative distribution, thus obtaining a corresponding gray value mapping table, finally determining every pixel in original image [4]. The basic principle is: first, use Formula (1) to calculate brightness value of each pixel, construct brightness histogram of HDR image; then, use Formula (2) to perform equalization operation; and compress dynamic range of image; finally use Formula (4) to recover gray-scale images from equalization back to compressed chromatic image.

$$L = 0.299R + 0.578G + 0.144B \tag{1}$$

$$E_b(c) = \frac{[c - 0.5(L_{\max} + L_{\min})]^2}{L^2} + \lambda \frac{\left[\sum_{x=L_{\min}}^{c} h(x) - 0.5N\right]^2}{N^2} \tag{2}$$

Among them, L is brightness, N is the total amount of pixels, λ is a variable coefficient, used to adjust the effect of output image.

$$c = \arg\{\min[E_b(x)]\} \tag{3}$$

Among them, arg is the abbreviation of elements, that is, the final assignment value c of minimum x value of $E_b(x)$.

$$R_{out} = \left(\frac{R_{in}}{L_{in}}\right)^{\gamma} \cdot L_{out},\ G_{out} = \left(\frac{R_{in}}{L_{in}}\right)^{\gamma} \cdot L_{out},\ B_{out} = \left(\frac{R_{in}}{L_{in}}\right)^{\gamma} \cdot L_{out} \tag{4}$$

Among them, the value range of index γ is [0.4, 0.6].

2.2 Local Color Adaptation Method

Local color adaptation method is a compression algorithm which simulates photography [9], first use the Formula (5) to calculate average logarithmic value of whole image brightness, then use Formula (6) to normalize pixels, and finally map pixel value of image to [0, 1].

$$L_{avg} = \exp\left[\frac{1}{N}\sum \log(\delta + L_W)\right] \tag{5}$$

Among them, δ = 0.0001, N is total quantity of image pixels, Lw is brightness value of pixels, and its value taking method is identical as Formula (1).

$$L_d = \frac{L_{avg}(1 + \frac{L_{avg}}{L_{white}^2})}{1 + L_{avg}} \tag{6}$$

Among them, the L_{white} is brightness value that is mapped to white dots, which is image pixel brightness value after target transformation.

2.3 Compression Algorithm Based on iCAM

First the input data of high dynamic range image is transformed into device-related RGB data, then converted to device-independent CIEXYZ standard color space which can perform chromatic adaption, as Formulas (7) and (8).

$$\begin{bmatrix} R \\ G \\ B \end{bmatrix} = M_{CAT02} \cdot \begin{bmatrix} X \\ Y \\ Z \end{bmatrix}, \quad M_{CAT02} = \begin{bmatrix} 0.7328 & 0.4296 & -0.1624 \\ -0.7036 & 1.6975 & 0.0061 \\ 0.0030 & 0.0136 & 0.9834 \end{bmatrix} \tag{7}$$

$$D = 0.3F\left[1 - (\frac{1}{3.6})e^{\frac{-(L_A-42)}{92}}\right] \tag{8}$$

Among them, D is the adapted factor, F is the environmental parameter, R, G, B is the input color tristimulus value, M_{CAT02} is the chromatic adaptation matrix.

And then is the performing chromatic adaptation transformation, achieving by transforming local adaptation and global white spots from high dynamic range scene. And convert RGB signals after chromatic adaptation to IPT contradiction space, as Formulas (9)–(13).

$$R_C = \left[(R_{D65}\frac{D}{R_W}) + (1 - D)\right] \cdot R \tag{9}$$

Among them, G_c, B_c is in same way, R_c, G_c, B_c is cones respond to tristimulus values after chromatic adaptation transformation.

$$\begin{bmatrix} X_{D65} \\ Y_{D65} \\ Z_{D65} \end{bmatrix} = M_{CAT02}^{-1} \begin{bmatrix} R_C \\ G_C \\ B_C \end{bmatrix} \tag{10}$$

$$\begin{bmatrix} L \\ M \\ S \end{bmatrix} = \begin{bmatrix} 0.4002 & 0.7075 & -0.0807 \\ -0.2280 & 1.1500 & 0.0612 \\ 0.0 & 0.0 & 0.9184 \end{bmatrix} \cdot \begin{bmatrix} X_{D65} \\ Y_{D65} \\ Z_{D65} \end{bmatrix} \tag{11}$$

Among them, L, M and S are the nonlinear switching signal, $L' = L^{0.43F_L}, L \geq 0$; $L' = -|L|^{0.43F_L}, L \leq 0$, M', S' is the same.

$$F_L = 0.2k^{0.4}(5L_A) + 0.1(1 - k^4)^2(5L_A)^{1/3} \tag{12}$$

Among them, $k = 1/(5L_A + 1)$, F_L is brightness level adaptive factor.

$$\begin{bmatrix} I \\ P \\ T \end{bmatrix} = \begin{bmatrix} 0.4000 & 0.4000 & 0.2000 \\ 4.4550 & -4.8510 & 0.3960 \\ 0.8056 & 0.3572 & -1.1628 \end{bmatrix} \cdot \begin{bmatrix} L' \\ M' \\ S' \end{bmatrix} \tag{13}$$

Among them, I, P, T is transformed image display values.

3 HDR-VDP Image Quality Evaluation Method

According to the original image information, the objective evaluation can be divided into full-reference image quality assessment, reduced-reference image quality assessment and blind image quality assessment [10]. Among them, the full-reference image quality assessment evaluate by means of difference between standard image and distorted image, which possesses high accuracy; Reduced-reference image quality assessment uses part of the original image information to evaluate quality of compressed image. Blind image quality assessment is an evaluation method which doesn't require any original image information and can directly compress image.

The high dynamic range images evaluation, HDR-VDP (High Dynamic Range Image-Variable Data Printing) model, is applicable to the quality requirements of high-fidelity reproduction. It is a modification to the original VDP model, the evaluation of image quality is mainly based on the human eyes' perceptual difference prediction ability in the range of perceptual luminance range. The principle of the evaluation method is shown in Fig. 1.

4 Test Results and Analysis

4.1 Test Results

The compression effect of the high dynamic range image is tested by using tonal homogenization histogram method, local color adaptive algorithm and iCAM compression algorithm respectively. Among them, the high dynamic range image

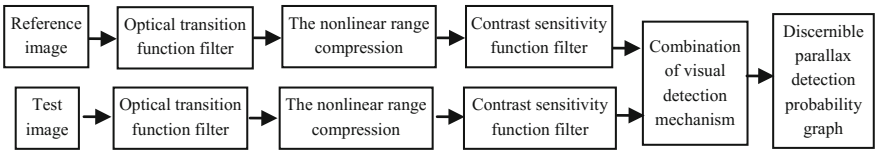

Fig. 1 Principle of HDR-VDP image quality assessment method

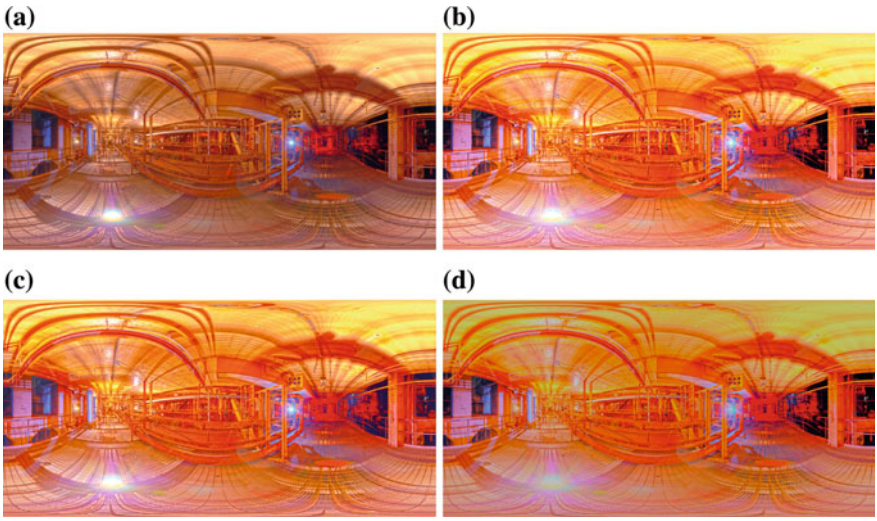

Fig. 2 Treatment effects (Factory Catwalk)

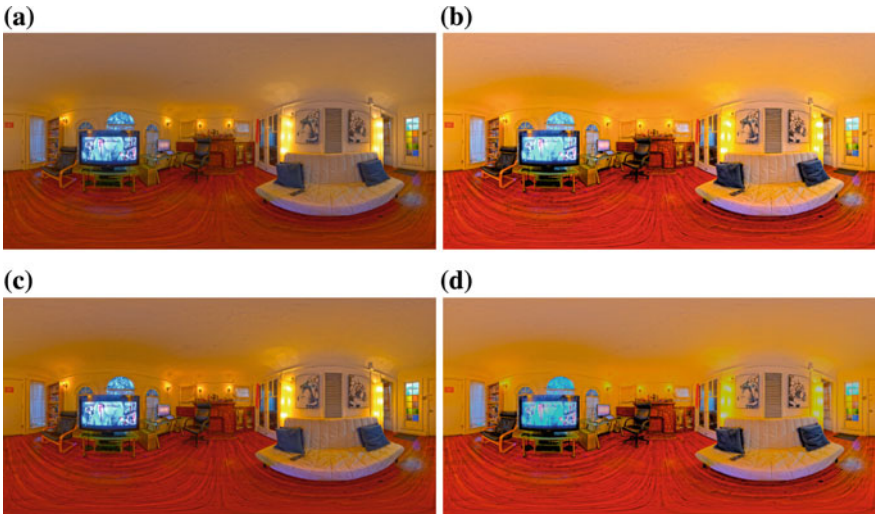

Fig. 3 Treatment effects (Alex's Apartment)

uses HDR format. (It selects two representative scenes, the factory and apartment, to test) After three algorithm compression processing, image saves in JPEG format. The specific results are shown in Figs. 2 and 3 (a is the original images, b is the colors homogenization histogram method images, c is local color adaptive algorithm images and d is the iCAM algorithm images).

4.2 Result Analysis

4.2.1 Colors Homogenization Histogram Method

The method is simple, image tone is stretched, pixels distribute equally, and contrast is enhanced. But the image details are lost and therefore not available for printing output. It can be used for the field which is undemanding to image color and detail, mainly highlight image tone and color brilliance.

4.2.2 Local Color Adaptive Algorithm

This method is not hard and can better keep the overall tone characteristics and image details. Image contrast is obvious, which is more suitable for printing output. However, without considering accuracy of image color perception, it does not apply to high fidelity display and cross-media representation.

4.2.3 Compression Algorithm Based on iCAM

This method is quite complex. The image tone range is narrow, lost much details, image contrast is weakened, so the printing output is the worst. But iCAM algorithm has the characteristics that fit human visual system, and can predict image color appearance, thus providing a new technical way for high-fidelity display and cross-media reappearance.

5 Conclusions

The core problem of high dynamic range image high-fidelity reproduction is to design and select a scientific and effective image compression algorithm. Among those algorithms, color homogenization histogram method can enlarge the image tone, which is suitable for fields which is undemanding to image tone and color fidelity such as advertising design and product display, etc.; Local color adaptive algorithm can keep image tone characteristics and details well, which is suitable for printing output; Compression algorithm based on iCAM considers the human's visual characteristics, which provides a good technical way for high fidelity display and cross-media representation. The future research will consider adaptive color appearance model compression algorithm with human visual characteristics to achieve comprehensive harmonization of image tone, color and details information and efficiency, so as to meet the technical requirements of high fidelity reproduction.

Acknowledgements This work is funded by application research project of Zhejiang Province public technology (2016C31080), key technology innovation special project of Zhejiang Province (2015-422), postdoctoral fund of Anhui Province (2016B125) and interdisciplinary research project of Zhejiang University of Science and Technology (2015JC06Y).

References

1. Li J, Wang H, Wan X (2014) High dynamic range image display technique based on image color appearance model. Packag Eng 35(5):112–115
2. Wang D (2011) A research of HDR image tone compression technology based on modified iCAM. Master thesis, Nanjing Forestry University, Nanjing, China
3. Man W et al (2007) A survey of HDR range compression technology. J Commun Univ China Sci Technol 14(4):66–72
4. Liu Z, Yang D, Zhu M (2011) Comparison of HDR image compression algorithms. Imaging Sci Photochem 29(1):32–44
5. Zhang S (2011) Research on high dynamic range compressing algorithm. Master thesis, Xidian University, Xi'an, China
6. Duan J, Qiu G (2004) Fast tone mapping for high dynamic range images. In: Proceedings of the 17th international conference on pattern recognition, pp 847–850
7. Qiu G, Duan J (2005) An optimal tone reproduction curve operator for the display high dynamic range images. In: Proceedings-IEEE international symposium on circuits and systems, pp 6276–6279
8. Fairchild MD (2005) Color appearance models. Wiley, UK
9. Wan X et al (2009) Color vision based high dynamic image rendering algorithm. China Printing Packag Study 1(1):53–59
10. Zhu M (2011) The research on high-fidelity reproduction of high dynamic range images. PhD thesis, Nanjing Forestry University, Nanjing, China
11. Cao Y (2013) High dynamic range image compression method research and the realization of the reader. Master thesis, Hunan University, Wuhan, China

Research on Image Segmentation of Flexographic Plate Based on OTSU Algorithm

Yuhui Guo, Wangjian Qiu and Qiang Wang

Abstract This paper uses the improved OTSU algorithm to process the image of dot on flexographic plate and gets the best threshold which can segment the image of dot on flexographic plate accurately. The results prove that the improved OTSU algorithm can obtain the better binarization image of dot, which realizes a high accurate segmentation of the image that the dot area percentage below 10% and deletes the noise in the image. Users calculate the ratio of dot on flexographic plate area by means of the binarization image of dot. The ratio helps people control the quality of dot and error compensation, and makes the prints better.

Keywords Flexography · Printing plate · OTSU · Image segmentation

1 Introduction

With the flexo CTP of China has showed a good development in last 10 years [1], the demand of detection equipment is getting higher and higher which can help people get the parameters of dot and control the quality of prints [2, 3]. But compared to offset, the dot of flexographic plate has a high transparence, 3D structure, slope edge and the dot irregular changes [4, 5]. What's worse, there are few study on the dot image of flexographic plate, the detection technology and equipment of the dot of flexographic plate is very difficult and expensive. It's not conducive to the enterprises to control the quality of flexo-prints.

This paper focuses on the dot of flexographic plate, to study the complicated dot reorganization and poor image segmentation. It uses the improved OTSU algorithm

Y. Guo (✉) · W. Qiu (✉) · Q. Wang
School of Digital Media and Art Design, Hangzhou Dianzi University, Hangzhou, Zhejiang, China
e-mail: guoyuhui@hdu.edu.cn

W. Qiu
e-mail: 141220003@hdu.edu.cn

P. Zhao et al. (eds.), *Applied Sciences in Graphic Communication and Packaging*, Lecture Notes in Electrical Engineering 477,
https://doi.org/10.1007/978-981-10-7629-9_24

to get the best threshold [6] that segments the dot image of flexographic plate precisely and will be helpful in calculating the ratio of flexographic plate dot area.

2 OTSU Algorithm

The ideal of OTSU algorithm is in literatures [7]: The size of dot image is $M * N$, the gray value is L, the range of dot image gray scale is $0–L - 1$, the number of pixels with the gray value of i is n_i. The total pixels is $M * N$, so the probability of the gray value of n_i is $Pi = n_i/(M * N)$. According to the gray scale divides the dot image into two parts, A and B, which uses the threshold.

The threshold range for part A is $0–t$, the part B is $t + 1–L - 1$. The probability of two parts is expressed as:

$$\omega_0 = \sum_{i=0}^{t} P_i, \quad \omega_1 = \sum_{i=t+1}^{L-1} P_i \tag{1}$$

The average gray value of two parts is expressed as:

$$\mu_0 = \sum_{i=0}^{t} (i * P_i)/\omega_0 \tag{2}$$

$$\mu_1 = \sum_{i=t+1}^{L-1} (i * P_i)/\omega_1 \tag{3}$$

The variance of two parts expressed as:

$$\sigma_0^2 = \sum_{i=0}^{t} [(i - \mu_0)^2 * P_i/\omega_0], \quad \sigma_1^2 = \sum_{i=t+1}^{L-1} [(i - \mu_1)^2 * P_i/\omega_1] \tag{4}$$

The interclass variance between part A and B is:

$$\mathrm{D} = \omega_0 * \omega_1(\mu_1 - \mu_0)^2 \tag{5}$$

The threshold is the optimal segmentation threshold when the interclass variance D is the largest. Setting (i, j) at the gray value is $f(i, j)$, the original dot gray-scale image binarization process is:

$$f(x, y) = \begin{cases} 0, & f(i,j) < t \\ 255, & f(i,j) > t \end{cases} \tag{6}$$

Through the study and understanding of the OTSU algorithm, the OTSU to segment is used and the dot image of the flexographic printing plate is binarized. This paper selects dot area that 5, 10, 50, 90% of the flexographic printing plate image as an example, the results of segmented image shown as Fig. 1.

In the segmentation of binarized the image of dot on flexographic plate, Although there is a small amount of noise, the segmentation effect are clear in 50 and 90% of the dot, which can distinguish between the dot area and the base area. Because the dot area and the base area is clear so that the OTSU algorithm can segment them easily. However, in 5 and 10% of the dot area percentage, the segmentation effect is poor, which can't distinguish between the dot area and the base area and have a lot of noise. It will have a bad influence on calculating the ratio of flexographic plate dot area. So the original algorithm is not satisfactory, it is necessary to improve and optimize the OTSU to meet the requirements of image segmentation of flexible plate.

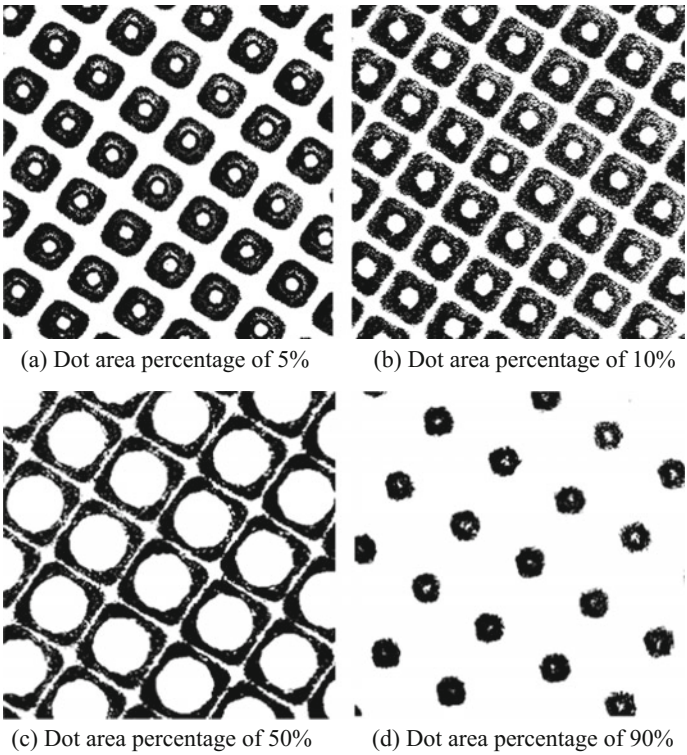

(a) Dot area percentage of 5% (b) Dot area percentage of 10%

(c) Dot area percentage of 50% (d) Dot area percentage of 90%

Fig. 1 The original OTSU algorithm segmentation effect

3 Improved OTSU Algorithm

3.1 Threshold Analysis

The basic tenet of OTSU algorithm is to determine the gray value of the entire image [8, 9]. According to the image of the gray values, the image is divided into two parts,Which are the background and the target, and then use the gray-scale relationship to select the threshold, find the grayscale variance on both sides of the threshold area. If the between-cluster variance between the background and the target is greater that means the background and target of the image are different. When the partial target is divided into the background or the partial background is divided into the target error, it will make these two parts become smaller. After traversing the entire gray scale value, the gray value of the selected maximum variance is the required image segmentation threshold.

In view of Fig. 2, in 50% of the flexographic plate dot area percentage, the selected threshold is the trough of the gradation histogram. In 5% of the flexographic plate dot area percentage, it is difficult to find the appropriate threshold in the gradation histogram when uses the OTSU where the troughs are not obvious. As a result, the effect is bad, and have a lot of noise in binarization process. It means the threshold selected is not the best image segmentation threshold when the original OTSU algorithm is used to binarize the flexographic plate dot image.

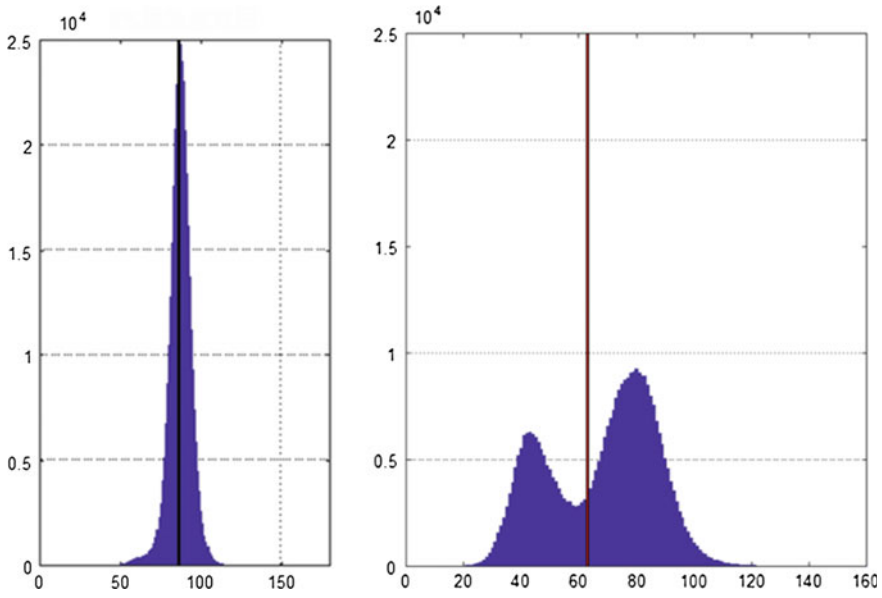

(a) Dot area percentage of 5% (b) Dot area percentage of 50%

Fig. 2 5 and 50% of the dot area percentage of the gradation histogram

3.2 *Improvement of OTSU Algorithm*

Based on the original OTSU algorithm, it can achieve good segmentation effect when the dot area percentage is more than 10% in the flexographic plate. In the gradation histogram, there are no obvious troughs and crests when the dot area percentage is below 10% in the flexographic plate. So it can't get a satisfactory image segmentation effect when use the original OTSU algorithm on the flexible plate dot image segmentation to determine the threshold, which will have segmentation error and affect the calculation of the dot area percentage.

Through the study, we find the binarized image have lots of noise and the dot shape is not clear enough when the dot area percentage below 10%. In order to eliminate the noise in the image and preserve the original information of the dot, this paper improves the threshold segmentation algorithm based on OTSU. The idea is to corrode the image of dot on flexographic plate, which the dot area percentage below 10%. It can eliminate the noise in the dot image and segment the dot image elements [10]. Then, the dots of image on flexographic plate are segmented through the idea of dynamic threshold segmentation and get the best segmentation threshold. At last, the image is binarized with the best threshold. The process shown in Fig. 3.

The steps of improved algorithm based on OTSU are as follows:

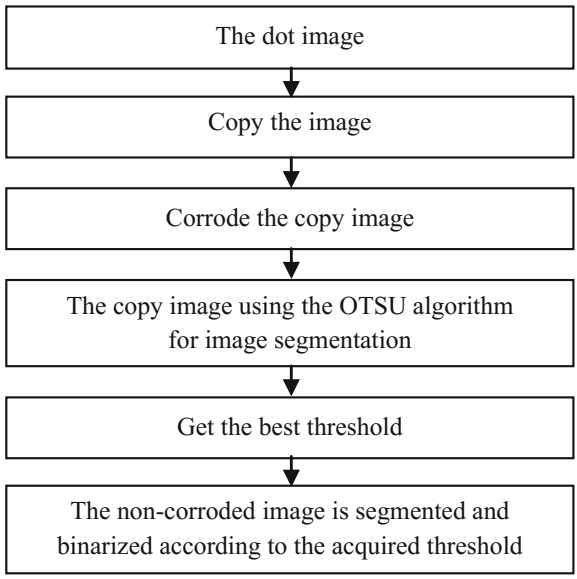

Fig. 3 The process of improved OTSU algorithm

(1) Corroding the backup dot image, this eliminates the noise and segments the independent dots. And the corroded image is taken as the input parameter of the OTSU.
(2) Calculating the best segmentation threshold after the corrosion of the dot image through the OTSU algorithm.
(3) The non-corroded dot gray scale image is segmented and binarized using the best segmentation threshold.

4 Results and Analysis

According to the threshold obtained from the improved OTSU algorithm, the rate of different area of the dot image is segmented with the threshold. The improved binarized image is shown in Fig. 4.

To better reflect the effect of the improved algorithm, this paper takes the 5, 10, 50, 90% of the dot area percentage, for example. The binarized image results are shown in Fig. 5.

The flexographic plates with different percentages are segmented, and the thresholds are shown in Fig. 6.

The results show that the improved OTSU algorithm not only successfully segments the dot image below 10%, but also improves the segmentation effect of the dot image above 10%. Therefore, the improved algorithm is effective in segmenting the percentage of different dot areas of images in flexographic plate, which can eliminate the noise generated in the threshold segmentation, and segment the dot area and the background area without affecting the target area image. It is proved that the improved OTSU algorithm can effectively segment the dot images.

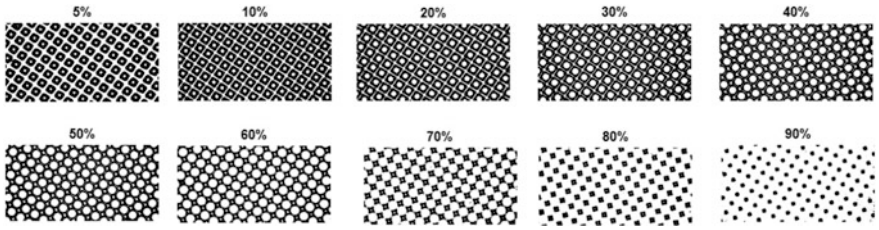

Fig. 4 The segmentation results of different dot area percentage by improved OTSU algorithm

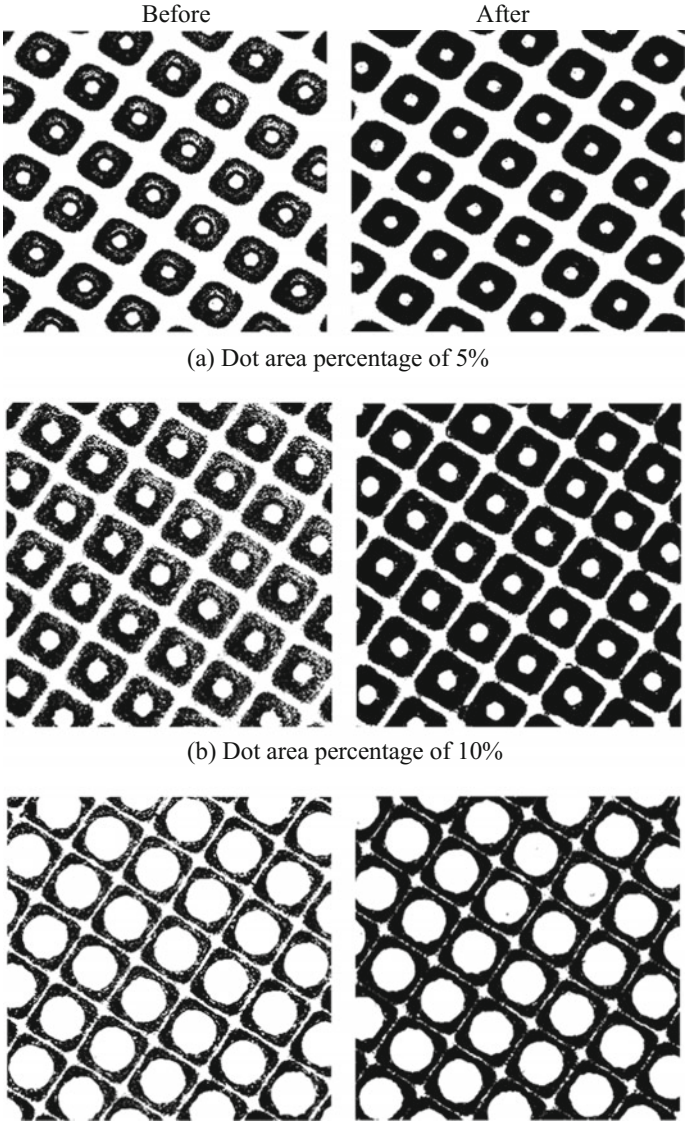

(a) Dot area percentage of 5%

(b) Dot area percentage of 10%

(c) Dot area percentage of 50%

Fig. 5 Comparison of threshold segmentation of original and improved OTSU algorithm

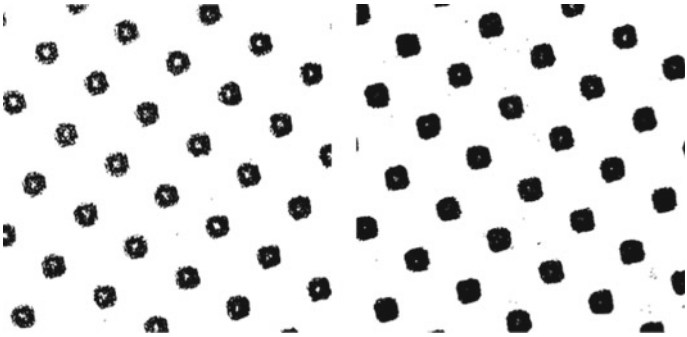

(d) Dot area percentage of 90%

Fig. 5 (continued)

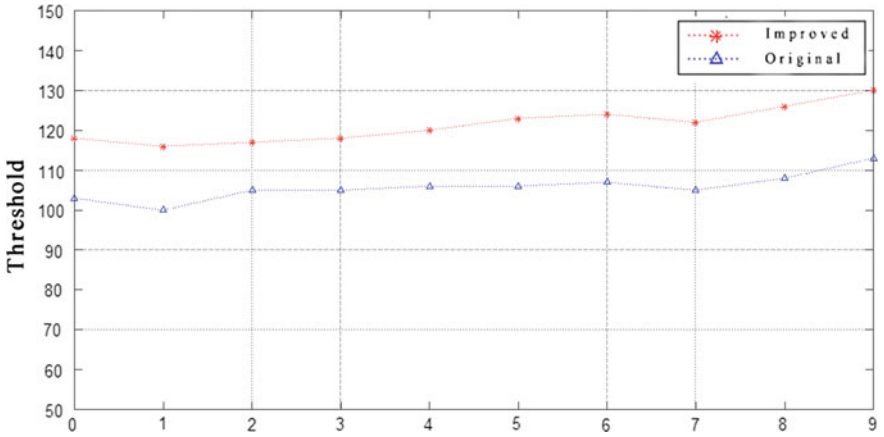

Fig. 6 Threshold comparison of original and improved OTSU algorithm under different dot area percentage

5 Conclusions

In this paper, according to the problem of the image segmentation of dot on flexographic plate, the OTSU method is used to segment the dot image of flexographic plate. For the image threshold segmentation effect is poor when the dot area percentage of flexographic plate below 10%. This paper improves and optimizes the OTSU algorithm, making the dot area ratio of flexographic plate below 10% get the best segmentation threshold. It realizes a high accurate segmentation for the dot image of flexographic plate, which laid the foundation for the detection of the area rate of the flexographic plate.

Acknowledgements The authors acknowledge the support of Research on Technology Integration Standards and Specifications of Cross-media Digital Publishing (grant KYZ223613001), the Technology Innovation Team of Cross-media Digital Publishing Platform (grant ZX140206320005) and the Graduate Student Innovation Project of Development and Application of Fabric Digital Inkjet Printing Color Management (grant ZX150606320030).

References

1. Enterprise Report Network (2015) Analysis on the development trend and competitiveness of the new flexo machine market in 2016. Enterprise Report Network, Beijing
2. Gao F, Xue XL (2009) Why do we choose Flex CTP? GuangDong YinShua 2:11–12
3. Ma BZ (2005) The detection of printing plate dot area percentage. Printing Technol 5:63–64
4. Chen YC (2004) New development of flexible plate making. Print World 3:6–8
5. Shi XF (2003) Technology of flexo CTP. Guangdong YinShua 2:42–43
6. Jiang L (2004) Research on printing plate based on image segmentation. Xi'an University of Technology
7. Otsu N (1979) A threshold selection algorithm from gray-level histograms. IEEE Trans Syst Man Cybern 9:62–66
8. Chai JS, Wang Q Liu HH (2015) Threshold segmentation algorithm for printing dot microscopic image. Packing Eng 13:115–121
9. Peng YP, Ma BZ, Xu JL (2006) Comparison research of dot area measurement algorithm. Packing Eng 27:76–78
10. Yu JY, Li YM (2012) Detection of dot area coverage on the plate based on image processing. China Printing Packing Study 4:17–21

Feature Extraction and Selection by Machine Learning for Image Quality Assessment

Yehong Chen, Xiaopeng Sun and Bin Zou

Abstract In this paper, we study on image quality related feature extraction and selection for no reference Image Quality Assessment (IQA). For color images, YIQ space transformation is used for the original RGB image, to carry on the separation of brightness and chromatic information. The 2D log Gabor filters and the Prewitt operators are used to convert these channels into the Phase congruency (PC), the image gradient magnitude (GM), the gradient orientation (GO) and the relative gradient magnitude (RM), which are perception mappings from image as quality features. The final representation of an image is an HVS (human visual system) vector according to the histogram variance of perception mappings. Finally, a mapping from image HVS features to image quality score MOSs is built via an AdaBoost BP neural network on the training data. From the experiments, the quality prediction results in noisier distortion, color images shows that our HVS feature extraction and selection methods are both validated.

Keywords No reference image quality assessment · Phase congruency Oriented gradient correlation · AdaBoost BP neural network

1 Introduction

Before being presented to human consumers, images suffer from a great deal of processing, e.g., restoration, super-resolution, and so on, all of which introduce extra noise [1]. There are different methodologies [2] that can be used to evaluate the quality of an image, however, the humans subjective judgment is always

Y. Chen (✉)
Key Lab of Pulp and Paper Science and Technology, Ministry of Education, School of Printing and Packaging, Qilu University of Technology, Jinan, Shandong Province, China
e-mail: chenyh@qlu.edu.cn

X. Sun · B. Zou
School of Printing and Packaging, Qilu University of Technology, Jinan Shandong Province, China

P. Zhao et al. (eds.), *Applied Sciences in Graphic Communication and Packaging*, Lecture Notes in Electrical Engineering 477,
https://doi.org/10.1007/978-981-10-7629-9_25

deemed as the most accurate and reliable [3, 4]. Consequently, it is very important to design a proper objective computational model which can evaluate images accurately and automatically. Generally speaking, objective IQA (image quality assessment) models can be categorized into full-reference (FR), reduced-reference (RR), and NR (no reference) three kinds of approaches. In fact, there is an unquestionable need to develop metrics that closely correlate with human perception without needing the reference images.

HVS (Human visual system) features for predicting the perceptive image quality are extracted by considering key human visual sensitivity factors such as edge amplitude, edge length, natural scene statistics, and contrast masking [5, 6]. For example, well known human eye is not equally to perceive distortions in brightness (luminance) and color (chrominance) components. Meanwhile, the image gradient magnitude (GM) is computed as the feature to encode contrast information. We also seek to amend the gradient information by studying the quality relevance of the gradient orientation relative to the surround [7–9]. From recently researches, people found that at points of high phase congruency (PC) we can extract highly informative features [10] as HVS features.

In this work, the problem of color image quality estimation without requiring the reference image is reduced to learn a complex functional relationship by the machine learning method between extracted HVS features and subjective evaluated MOSs (mean opinion score). Liu et al. [11] utilize an AdaBoost back-propagation (BP) neural network to map the image features to image quality scores. The power of AdaBoost method is due to its feature selection capability. The AdaBoost BP neural network trained on HVS feature vectors of training images has been used as the metric to predict a real value as the quality prediction in this paper, and the obtained results are "compared" to the corresponding MOS values by Spearman and Kendall correlation coefficients. There are two main contributions of this paper, one is the integrated various HVS feature extraction, and the other is to weight all integrated features by AdaBoost BP for special image quality estimation. Experimental results prove that the prediction of the trained network does emulate the mean opinion score (MOS).

2 Dataset and Extraction of HVS Features

2.1 Feature Extraction

The dataset used here is a subset of the TIP 2008 dataset [4]. There are 25 original images in this dataset as the reference image. Mean Opinion Scores (MOS) of images have been obtained as a result of subjective experiments. The types of distortion used in TID2008 is 17, and 4 types of distorted images are used in this paper. There are as following, (1) Additive Gaussian noise; (2) Additive noise in

color components is more intensive than in the luminance component; (3) Spatially correlated noise, and (4) Masked noise.

2.2 Feature Extraction

Color Space Transformation We adopt the widely used YIQ color space, in which Y represents the luminance information and I and Q convey the chrominance information. The transformation from the RGB space to the YIQ space can be accomplished via a transformation matrix:

$$\begin{bmatrix} Y \\ I \\ Q \end{bmatrix} = \begin{bmatrix} 0.299 & 0.587 & 0.114 \\ 0.596 & -0.274 & -0.322 \\ 0.211 & -0.523 & 0.312 \end{bmatrix} \begin{bmatrix} R \\ G \\ B \end{bmatrix} \tag{1}$$

Our work is closest to the work of [11], however [11] only use the brightness channel image for feature extraction. Because of the change of hue and saturation sometimes does not affect the brightness component, the better performance can be expected if these three covered channels are incorporated within the IQA solution.

Phase Congruency The phase relations between the Fourier components are important to the structure perceived in images. For example, Phase Congruency holds the key to the mach bands, which is a special visual phenomena. For no reference IQA model, we can extract PC features from two scales of the image, the second scale is 0.5 sizes of the original image as self-reference for structure comparison. In this paper, we adopt the method developed by Kovesi in [7], which is widely used in literature to extract PC mapping from image channels. To compute the PC of 2D grayscale images, Log-Gabor filters constructed with arbitrary bandwidth and the bandwidth can be optimized to produce a filter with minimal spatial extent by using Gaussian as the spreading function. By modulating and convolving G2 with 2D image, we get a set of response at each point (x, y) as the local amplitude on scale n An and the local energy along orientations θ_j, $E_{\theta j}$. Then PC at (x, y) is defined as:

$$PC_{2\mathrm{D}}(x,y) = \frac{\sum_j E_{\theta_j}(x,y)}{\varepsilon + \sum_n A_n(x,y)} \tag{2}$$

ε is a small positive constant, and $PC_{2D}(x, y)$ is a real number within 0–1.

Gradient Magnitude Features PC is contrast invariant. The contrast information does affect HVS' perception of image quality, so the image gradient magnitude (GM) is also employed a role in this paper. First, we explore the estimated image gradient magnitude. In practice, the gradient operators can be expressed by convolution masks. For simplicity, the Prewitt operators are used for gradient in two

orthorhombic directions. Here, $I(i, j)$ can be one of the three channels as Y, I and Q transformed from RGB images. The gradient orientation (RO) conveys information that is complementary to that carried by the gradient magnitude, and has been used as a sensitive feature in some related research works. Likewise, the relative gradient magnitude (RM) is the another related features. Thus, three types of gradient maps are computed from Ix and Iy, and utilized to characterize the quality-dependent behavior of the image gradient over patches of size M × N, as GM, RO and RM.

Histogram Variance According to our hypothesis, changes to the statistical distributions of the gradient and relative gradient quantities caused by image distortions can be used to quantify the degree of perceived image distortion. The histogram variance can be used to characterize the corresponding distributions [11]. Given a (normalized to unit sum) histogram h(x), define the variance as $\mathrm{Var}[h] = \sum_x (h(x) - \bar{h})^2$. Where $\bar{h}$ is the sample mean of the histogram. in this paper var[h] is finally used as HVS features for IQA. For PC, GM, RO and RM, then we get a 4-dimensional feature vector. Feature = [vPC, vGM, vRO, vRM]. For no reference IQA modelling, we can extract above HVS features from two scales of the image, the second scale is 0.5 sizes of the original image as self-reference for structure comparison. Then Feature = [vPC1, vGM1, vRO1, vRM1, vPC2, vGM2, vRO2, vRM2]. For three channel image, we get 24 feature items for every RGB image as the representation vector.

3 Learning Image Quality Evaluation

After extracting the features which are expected predictive of image quality in a 24-dimensional space, we build a mapping from image features to image quality via an AdaBoost BP neural network. AdaBoost algorithm has the strong power of feature selection and can weight all extracted features by their contributions to the quality scores. Here, the BP neural network is treated as the Weak Learner element of the AdaBoost algorithm for every extracted HVS feature item. Hence, we use the designed structure of the BP neural network as two hidden layers, where the first hidden layer auto-normalizes the features by the sigmoid transfer function, and the design details can be found in the reference literature [11]. The Spearman's Rank Ordered Correlation Coefficient (SROCC) between the predicted objective quality scores and the subjective quality scores MOS were used as performance evaluation indices (Fig. 1).

4 Experiment Results

In our implementation, we used a random selection of 60% of the images in the dataset as a training set and the remaining (content-separate) 40% as the test set to build the AdaBoost BP neural network. The Spearman's Rank Ordered Correlation

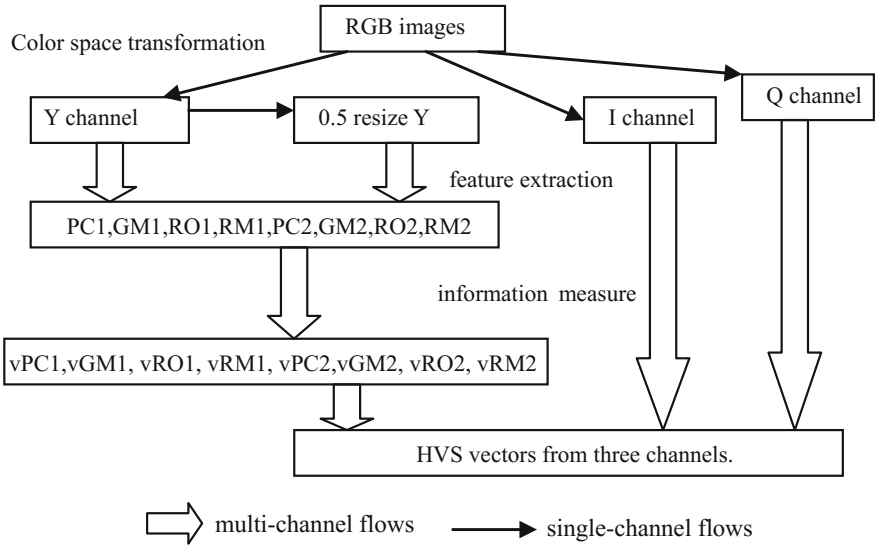

Fig. 1 Overview of feature extraction phase

Coefficient (SROCC) between the predicted objective quality scores and the subjective quality scores MOS were used as performance evaluation indices. A value close to 1 for SROCC indicate superior linear rank-order correlation. Metrics of MSE and PSNR usually are around 0.5 with MOSs by Spearman correlation. In our experiments, we first evaluated our proposed model with some other options. For example, the method built in the RGB channels or only on the brightness channel as proposed in OG-IQA.

From Table 1, it may be seen that YQI channels are more sensitive to evaluate IQA than RGB channels, however, only Y channel information is a little bit better than RGB channels. PC feature is helpful for image quality assessment when combined with gradient information. Our extracted 24 features are proving to be validated on 400 noisy distortion images. We also compare different feature/feature vectors for learning IQA model on 4 groups of noisy distortion images, every group has 100 distorted images.

In Table 2, all selected features are extracted from Y, I, Q three channels. It is proved in Table 2 that all these extracted features are closely related to noisy distortion problem, and the Adaboost BP network can combine these features together to build an enhanced IQA prediction model. In the future, we will train our model on more kinds of distorted images to build a more robust and stronger prediction model for real word IQA applications.

Table 1 By comparison between RGB channels, only brightness channel and YIQ channels for our proposed methods

Distortion type	Feature channels	SROCC
Gaussian noise	POG-CIQA	0.7856
	YIQ (without PC)	0.7663
	RGB channels	0.4263
	OG-IQA	0.4019
Noise in color components	POG-CIQA	0.6216
	YIQ (without PC)	0.6875
	RGB channels	0.5276
	OG-IQA	0.4763
Spatially correlated noise	POG-CIQA	0.7163
	YIQ (without PC)	0.6361
	RGB channels	0.2198
	OG-IQA	0.4163
Masked noise	POG-CIQA	0.5892
	YIQ (without PC)	0.5082
	RGB channels	0.4568
	OG-IQA	0.5371

Table 2 By comparison, between different feature subset according to noisy distortion type

SROCC	Group 1	Group 2	Group 3	Group 4
v_{PC1}, v_{GM1}, v_{RO1}, v_{RM1}, v_{PC2}, v_{GM2}, v_{RO2}, v_{RM2}	0.7856	0.6216	0.7163	0.5892
v_{PC1}, v_{PC2}	0.3104	0.2689	0.0013	0.3668
v_{RO1}, v_{RO2}	0.2701	0.5100	0.3929	0.4862
v_{GM1}, v_{GM2}	0.6345	0.5900	0.3169	0.6096
v_{RM1}, v_{RM2}	0.6698	0.5959	0.5965	0.3193

5 Conclusions

The performance of our proposed POG-IQA method validates the extracted features as a complementary and effective "quality-aware" source of information for conducting NR IQA. In this paper, RGB digital image quality assessment is on the basis of YIQ space transformation. Indeed, the experimental results show that POG-CIQA is highly competitive with the most popular IQA approaches OG_IQA. Going forward, we believe that the concept of the PC and relative gradient values (computed in space-time) may prove useful for the development of blind image quality models, an area that remains open.

Acknowledgements This study is supported by a foundation of Key Lab of Pulp and Paper Science and Technology, Ministry of Education (Shandong Province) in 2017–2018, China (0308250502).

References

1. Bovik A (2000) Hand book of image and video procession. Academic Press
2. Wang Z, Bovik A, Sheikh H, Simoncelli E (2004) Image quality assessment: from error visibility to structural similarity. IEEE Trans Image Proc 13(4):600–612
3. Kalpana S, Rajiv S, Alan CB, Lawrence KC (2010) Study of subjective and objective quality assessment of video. IEEE Trans Image Process 19(6): 1427–1441
4. Ponomarenko N, Ieremeiev O, Lukin V, Egiazarian K, Jin L, Astola J, Vozel B, Chehdi K, Carli M, Battisti F, Kuo CCJ (2013) Color image database TID2013: peculiarities and preliminary results. In: Proceedings of 4th European workshop on visual information processing, pp 106–111
5. Venkatesh Babua R, Sureshb S, Perkisc A (2007) No-reference JPEG-image quality assessment using GAP-RBF. Sig Process 87:1493–1503
6. Zhang X, Feng X, Wang W, Xue W (2013) Edge strength similarity for image quality assessment. IEEE Signal Process Lett 20(4):319–322
7. Kovesi P (1999) Image features from phase congruency. Videre J Comp Vis Res 1(3):1–26
8. Cheng G, Huang J, Liu Z, Cheng L (2011) Image quality assessment using natural image statistics in gradient domain. Int J Electron Commun 65(5):392–397
9. Wang Y, Jiang T, Siwei M, Gao W (2010) Image quality assessment based on local orientation distributions. In: Proceedings of 28th picture coding symposium, pp 274–277
10. Yang Y, Tu D, Cheng G (2013) Image quality assessment using histograms of oriented gradients. In: Proceedings of international conference on intelligent control information process, pp 555–559
11. Liu L, Hua Y, Zhao Q, Huang H, Bovik AC (2015) Blind image quality assessment by relative gradient statistics and AdaBoost neural network. Signal Process Image Commun. http://dx.doi.org/10.1016/j.image

Print Inverse Halftoning and Its Quality Assessment Techniques

Zhangying Jin and Enyin Fang

Abstract The technology of converting halftone image back to the continuous tone image (i.e. inverse halftoning) and method of quality assessment of inverse halftone images are studied. A general method for inverse halftoning of printed image is present in the paper. We use several filters to obtain the smoothing image and edge information of halftone image, and obtain the inverse halftone result by adding the edge information on the smoothing image. The inverse halftone results using the method presented in this paper are visually better than that of using Gaussian low pass filter or that of combining Gaussian low pass filter and median filter. The PSNR of inverse halftone result of amplitude modulation image (value 18.6134) is lower than that of other halftone images, but in fact, the inverse halftone result of amplitude modulation image is visually better. While using the new index of quality assessment D presented in this paper, D value of inverse halftone result of amplitude modulation image is significantly smaller than that of frequency modulation image (the former 5.9506, the latter 0.248), which means the tone feature of inverse halftone result of the amplitude modulation image is more consistent with the continuous image. The inverse halftone results by using the method presented in this paper is good, and the method can be applied to different types of halftone images. And, the index of quality assessment D presented in this paper is helpful to avoiding wrong judgment while PSNR is not consistent with the visual result.

Keywords Halftone image · Inverse halftoning · Image quality assessment

Z. Jin (✉) · E. Fang
Department of Printing and Packaging Engineering, Shanghai Publishing and Printing College, Shanghai, China
e-mail: 15525933@qq.com

P. Zhao et al. (eds.), *Applied Sciences in Graphic Communication and Packaging*, Lecture Notes in Electrical Engineering 477,
https://doi.org/10.1007/978-981-10-7629-9_26

1 Introduction

The digital files from reflective originals by scanning or photographing need appropriate image processing before applying to printing. However, the reflective prints such as newspapers, magazines, books, maps, etc. contain a halftone dot pattern, so the digital images from the prints may look discontinuous and sometimes even contain Moiré pattern. Image distortions or degradations caused by image processing such as sharpening, zoom, resampling, etc. may seriously affect the use of images. Therefore, effective inverse halftoning of prints is necessary for obtaining high quality digital originals, and it is also the problem concerned by many image processors.

Digital halftone technology often called digital screening technology is a kind of technology that will transfer continuous tone (contone) images into halftone images (usually binary images) which look like continuous tone. Study on inverse halftone technology began in 1990s. The so-called inverse halftoning refers to the inverse processing of halftone processing, which means restoring original contone images as real as possible [1–3].

Halftone processing is classified into three types: amplitude modulation (AM), frequency modulation (FM) and AM-FM modulation. The halftone images produced by these methods have their own characteristics, but they all get noise from halftone processing, i.e. halftone noise. In general, the halftone noise is mainly distributed in the middle and high frequency of the image, so the inverse halftone method such as low pass filtering, etc. which filter the middle and high frequency noise out occurred earliest. However, the inverse halftoning based on low pass filter usually results in image edge blurring, so a variety of algorithms based on edge preserving are proposed. These inverse halftone schemes have their own characteristics, but no one has obvious advantage. Some algorithms lose image edge and details seriously, some are high computational complexity, some need to know the error diffusion kernel, and some only can be used for a specific type of halftone images. At present, domestic related research is very scarce and only a few brands of scanners provide “De-screening” function, but it is only the most primary and the simplest low-pass filtering which often causes the edge information loss while descreening. There is also no software of inverse halftone image on the market.

This paper will give a basic method of inverse halftone processing of general prints and propose an inverse halftone method suitable for images from different halftone methods, which has low computational complexity and can maintain the edge sharpness while descreening. We also propose a new quality evaluation parameter improving the effectiveness of evaluation, which helps to avoid mistakes caused by the problem that the objective evaluation index is not consistent with the visual perception of the human eye and improve the effectiveness of quality assessment.

2 Method of Inverse Halftoning for Prints

The general method of inverse halftone process is presented in Fig. 1. The halftone image is obtained by scanning (or photographing) and removing the noise from printing and scanning; Then the screening characteristics of the halftone image is analyzed, and the inverse halftoning is processed according to the characteristics and scanning resolution. This method is presented in a general form based on the summary of a variety of inverse halftone algorithms, but the inverse halftone algorithms that needs to know the prior knowledge of the halftoning is not taken into account. It is because in general we don't know the screening way and parameters of prints while inverse halftoning. Analyzing of screening characteristics of halftone image also is needed, but we just need to distinguished the image is AM or FM screening. If it is AM, the screen line number should be analyzed out; while if it's FM, there is no need to know screening prior knowledge such as the error diffusion kernel or ordered dither matrix. In Fig. 1, the ways of analyzing screening characteristics are various, such as neural net [4–6], support vector machine (SVM) [7, 8], etc. The dashed line part in Fig. 1 is the part of inverse halftone processing. The methods of obtaining smoothing image and edge information in this part is various; such as low-pass filtering and edge extraction [9], wavelet-based method [10, 11], etc.

Although the inverse halftone processing of prints in Fig. 1 involve many research fields such as image capturing, de-noising, analysis, processing, etc., we don't discuss all of them in this paper limited by the length of paper. In this section we focus on image inverse halftoning described by the dashed line part in Fig. 1. We propose an inverse halftone algorithm with low computational complexity suitable for different screening types of images, which can maintain the edge sharpness while descreening. The flow chart of the algorithm is given in Fig. 2.

Gauss lowpass filtering can effectively remove high-frequency noise in halftone images. However, if lowpass filter threshold is not set properly, it will directly cause

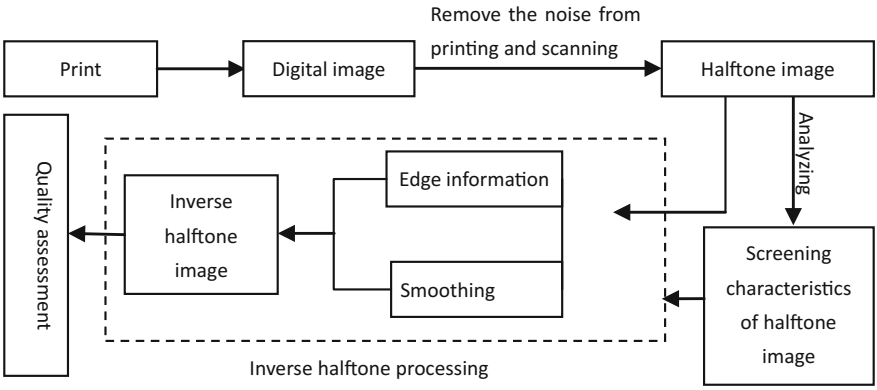

Fig. 1 General method for inverse halftoning of printed image

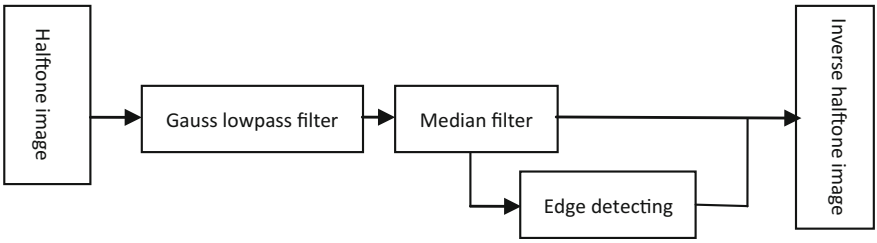

Fig. 2 Algorithm of inverse halftoning

inverse halftone image blurring severely. The frequencies of halftone images obtained by different screening methods are different, so the strength of filter should be adjusted to gain best effect and avoiding excessive blurring. The smoothing effect of median filter is better than lowpass filter if the gray level doesn't varied dramatically, and it can retain the edge information as much as possible. The image gained after Gauss lowpass and median filtering is blurring because the high frequency information of the edges and textures is damaged by lowpass filter [12]. To extract the image edge form the image after median filtering, we use Laplace operator considered all directions. Then, the image edge is added back to the image out from median filtering, and we obtain the final inverse halftone image. The contone image (not experiencing screening) used in the experiment is *lean1* shown in Fig. 3a. Figure 3b is the Gauss low-pass filtering result of the order dithered image from *lena1*, Fig. 3c is the result after Gauss low-pass filter and median filter, and Fig. 3d is the final inverse halftone image by the algorithm proposed above. The visual effect of final inverse halftone image (Fig. 3d) is better than the image (Fig. 3b) only processing by Gauss lowpass filtering or the image (Fig. 3c) by Gauss lowpass filter and median filter. It should be noted that the resolution of order dithered image using to do inverse halftone process is 5 times the contone image *lena1*, and this is consistent with the actual situation of the printing. Nowaday, the offset resolution can be higher than 3000 dpi. Even the resolution of original contone image is 300 dpi, the Offset resolution is 5 times much higher than it. Hence, if order dithered technology is applied in actual printing, the recording

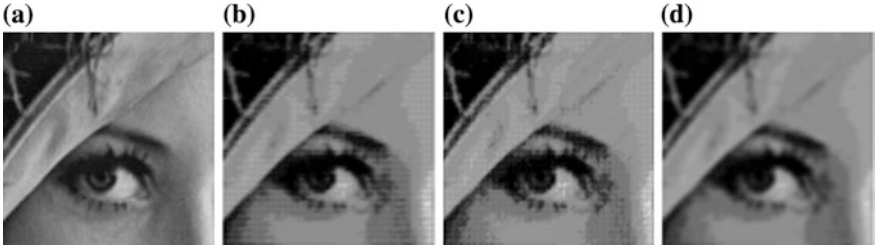

Fig. 3 Contone *lena1* image (**a**), inverse halftone image with Gauss lowpass filter (**b**), inverse halftone image with Median filter (**c**) and inverse halftone image with a method of this paper (**d**)

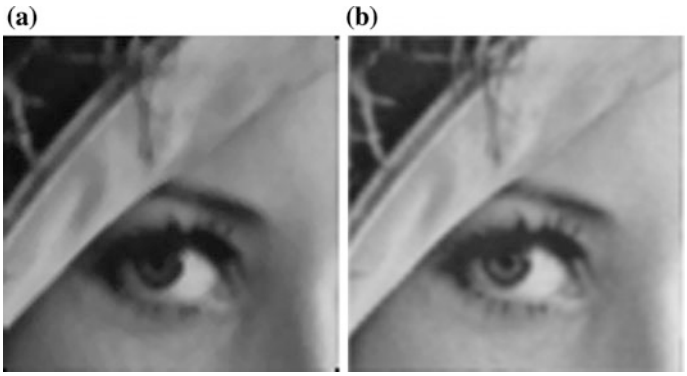

Fig. 4 Inverse halftone results of halftone images of *lena1*. **a** Inverse halftone result of error diffused halftone image. **b** Inverse halftone result of amplitude modulation halftone image

resolution will be several times the original contone image while screening in order to improve the printing quality.

The inverse halftone results of images from different screening methods are shown in Fig. 4. Figure 4a is an inverse halftone result of the error diffusion dithering image of *lena1*, and Fig. 4b is result of the FM screening image of *lena1*. Compared to Figs. 3d and 4 has a better visual effect. It's because that the information loss and additional noise level of images from different screening methods are different and the inverse halftone effects are consequently different.

3 Quality Assessment of Inverse Halftone Image

Common quality assessment methods of inverse halftone images come from the evaluation methods of image coding and video compression technology, which can be divided into two categories: subjective and objective evaluation. Subjective evaluation depends on human and is closely related to eyes, so it's easily affected by subjective factors and environmental factors, and the efficiency is low. Objective evaluation is processed by comparing the image information of the original and inverse halftone image through a certain formula with an objective and efficient advantage.

3.1 Objective Evaluation Method

The most commonly used evaluation index of all kinds of studies on inverse halftoning is the peak signal to noise ratio (PSNR), which is used as an objective

evaluation index in almost every research literature. In addition, clarity is also quite often used as an objective evaluation index.

(1) PSNR

The expression of PSNR is defined as follows [13]:

$$\mathrm{PSNR} = 10\log_{10}\left[\frac{255^2}{(1/NM)\sum_{i=1}^{N}\sum_{j=1}^{M}[F_0(i,j)-F(i,j)]^2}\right]. \quad (1)$$

The F_0 and F in the Formula (1) are the gray values of the original image and the image to be evaluated; i and j are the coordinate of the image matrix; N and M represent the length and width of the image; and 255 corresponds to the peak value of the 8-bit image. The larger the PSNR value is, the less the distortion in image reconstruction is. In the published literatures and research reports about inverse halftoning, the most frequently used index of image quality assessment is PSNR which is often used to evaluating image compression encoding and video communication system. Image compression encoding and inverse halftoning are both degraded image reconstruction problem and there are some similarities, so there is certain rationality using this index in quality assessment of inverse halftoning. However, the biggest problem with PSNR is that sometimes it may be a far cry from human vision [14, 15].

(2) Clarity

All kinds of distortions in inverse halftone image, such as edge blurring effect etc., can't be fully shown by PSNR. Lowpass filtering often causes image blur, so evaluating the clarity of image is also very important. The image gradient can well describe the edge information of the image, so we can use the gradient to define the clarity index [12]:

$$\mathrm{S} = \frac{1}{(M-1)(N-1)}\sum_{i=1}^{M-1}\sum_{j-1}^{N-1}\sqrt{\frac{[f(i,j)-f(i+1,j)]^2+[f(i,j)-f(i,j+1)]^2}{2}}. \quad (2)$$

The f in the Formula (2) is the gray value of inverse halftone image; i and j are the coordinate of the image matrix; and N and M represent the length and width of the image. The greater the value of the S, the more the tones are, and the clearer the contours are.

3.2 Objective Evaluation Results and New Quality Assessment Index

The PSNR and S values of Figs. 3b–d and 4a, b are shown in Table 1. By comparing the PSNR values of Fig. 3b–d, we can find the PNSR of the inverse halftone image from the algorithm proposed in this paper is higher than that from Gauss low-pass filter or that from Gauss low-pass filter and median filter. This also matches the visual effect.

The inverse halftone images from error diffusion dithering image and AM screening image is better by subjective evaluation. However, although the PSNR of Fig. 4a is higher than that of Fig. 3d, which matches the visual effect, the PSNR of Fig. 4b whose visual effect is better than Fig. 3d is significantly lower than that of Figs. 3d and 4a. It indicates the problem mentioned in Sect. 3.1, i.e. PSNR sometimes may be far away from human vision.

By comparing the clarity index S in Table 1, the values of Figs. 3d and 4a are close and are slightly lower than that of Fig. 4b, which matches the visual effect that the contours of Fig. 4d are clearer indeed. The reason for this phenomenon is that the amount of information remained in the AM image is usually larger than that remained in the ordered dither image and the error diffusion dithering image.

Through the above analysis we can see that the existing objective evaluation index has a certain significance, but it can't be completely consistent with the visual effect. For example, the biggest problem encountered in this article is the visual effects of Fig. 4a, b are obviously both good and even Fig. 4b is better than Fig. 4a visually, but the values of the evaluation index PSNR are contrary. If we look carefully at Fig. 4a, b, we can find the differences between them are mainly embodied in the image brightness and contrast; so it is easy to understand why the PSNR of Fig. 4a is very low. This is because the PSNR reflects mainly the difference of pixels values between original image and inverse halftone image and cannot represent whether the tone feature (such as distribution of brightness) of inverse halftone image is consistent with that of original image, so, although the tone feature of Fig. 4b is quite consistent with the original image and it could get very similar to the original image by simply adjusting the brightness and contrast. But, because the pixel values of the inverse halftone image is quite different from that of original image, it will performance poor on PSNR. However, because of the different screening algorithms, inverse halftone algorithms, different scanners (or camera), even different scanning time and other reasons in the actual work, all of these may lead to the final inverse halftone image is different from the original image in the brightness and contrast. In particular, the cases that the images

Table 1 Comparison table of PSNR for processing images

	Figure 3b	Figure 3c	Figure 3d	Figure 4a	Figure 4b
PSNR	25.1068	25.2822	26.2746	31.8875	18.6134
S	9.47	9.5279	6.4588	5.9636	7.5815

captured by scanning or photographing are brighter or darker than the original image are not rare, therefore, the cases that the visual effect is inconsistent with PSNR are not that rare.

So, this paper presents a new index D which helps to avoid mistakes caused by the problem that the objective evaluation index is not consistent with the visual perception of the human eye. The formula is as follows:

$$\mathrm{D} = ||RME_e| - RME_0|. \tag{3}$$

The RME_e is the relative standard deviation of the absolute of pixel difference between inverse halftone image and contone original image (for convenience, we will use the phrase "the pixel difference" instead of the phrase "the absolute of pixel difference between inverse halftone image and contone original image"), and the RME_0 is the relative standard deviation of contone original image. Since the discrete degree of the pixel difference is irrelevant to the plus-minus sign in front of the relative standard deviation, we only need the absolute value of RME_e. The plus-minus sign of the difference between $|RME_e|$ and RME_0 means little, so we take the absolute value of it. RME_0 can reflect the discrete degree of the original image value and has certain relationship with contrast. The larger the RME_0 is, the higher the contrast is. Most images are not high contrast such as the *lena1*, and the discrete degree is low. Therefore, when D is small, the discrete degree of the pixel difference is also not high. The values of D and C (the relative error of contrast) of Fig. 4a, b are shown in Table 2. The relative errors of contrast of the inverse halftone image and the original image are small, no matter the inverse halftone image is processed from error diffused halftone image or AM image, which means the contrast of inverse halftone image is consistent with the original image; while the D have significantly different values. The smaller the value of D is, the more similar the discrete degree of the pixel difference and that of original image are; i.e. the pixel difference and original image have similar tone feature. Specifically, although the pixel values of Fig. 4b are fairly different with the contone original image, which results in poor PSNR; the value of D is very small, which means the discrete degree of the pixel difference is consistent with original image and the pixel difference is quite uniform. So, the image (i.e. inverse halftone image) obtained by adding the pixel difference to the original image, the tone feature is still fairly consistent with original image and naturally visual effect is good. What has to be noted is that we don't define D by directly comparing the tone feature of inverse halftone image with contone original image. This is because if the visual effect of inverse halftone image is good, then the tone feature of it must be consistent with the original image. So, if we define D like this, the D values of Fig. 4a, b won't differ greatly, and it's meaningless to define such an index.

Table 2 D and relative error C of contrast for inverse halftone images

	Figure 4a	Figure 4b
D	5.9506	0.248
C	0.005%	0.01%

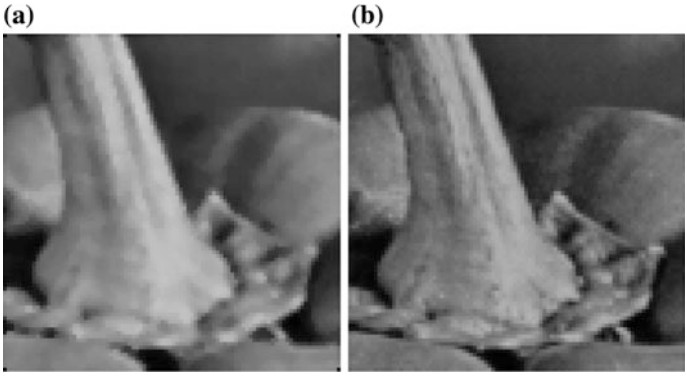

Fig. 5 Inverse halftone images of different halftone methods with the method of this paper, **a** for the inverse result of error diffused halftone image, **b** for the inverse result of amplitude modulation halftone image

Table 3 PSNR and D for inverse halftone images

	Figure 5a	Figure 5b
PSNR	28.0332	24.0896
D	10.0041	0.0363

In order to verify the D index further, the values of PSNR and D of the inverse halftone image (Fig. 5) from error diffusion dithering halftone image and AM halftone image are shown in Table 3. Although the inverse halftone image of AM halftone image (Fig. 5b) is darker than the original image, the D value is still significantly less than that of Fig. 5a. So, the D value has a good warning effect on the inaccurate evaluation of PSNR caused by the change of image brightness. Therefore, in the batch processing of inverse halftoning, if the PSNR is poor and the D value is good, do not rush to a conclusion that the inverse halftone algorithm is failed, the subjective evaluation should be processed and then a decision can be made.

4 Conclusions

In this paper, the general method of inverse halftoning for prints is presented, and an inverse halftone algorithm suitable for images from different halftone methods, which can maintain the edge sharpness while descreening is proposed. The image processed by the inverse halftone method in this paper has higher PSNR value and better visual effect than the image processed by Gauss low-pass filter. In order to avoid as much as possible the misjudgment because of the inconsistence between PSNR and visual effects, we also propose a new quality evaluation parameters contributing to avoid the problem that the objective evaluation index is not

consistent with the human eyes, which can improve the evaluation efficacy and reduce the possibility of a miscarriage.

Acknowledgements This study is funded by laboratory construction project called Green plate-making and standardization Laboratory, which is belonged to Key Laboratory of science and stander press and publication, State Administration of Press, Publication, Radio, Film and Television of the People's Republic of China.

References

1. Kong Y (2008) Researching on image inverse-halftoning and quality evaluation technologies. PhD thesis, Xidian University, Xi'An
2. Bertero M, Bocacci P (1998) Inverse problems in imaging. IOP Publishing, Bristol
3. Zhang Yuming (2007) Image engineering, the second edition. Tsinghua University Press, Beijing
4. Chang PC, Yu CS (1997) Neural net classification and lms reconstruction to halftone images. In: Proceedings of SPIE—the international society for optical engineering, vol 3309, pp 592–602
5. Du X (2009) Study on the recognition method of halftoning image classification. PhD thesis, Xi'an University of Architecture and Technology, Xi'An
6. ZhaofengLv XiaohongWang (2013) Research on color space conversion model based on saturation priority BP neural network. Packag Eng 2(3):109–112
7. Duan X, Zheng G, Chao H (2010) An adaptive real-time descreening method based on SVM and improved SUSAN Filter. In: Proceedings of 2010 IEEE international conference on ICASSP, pp 1462–1465
8. Smith SM, Michael Brady J (1997) SUSAN—a new approach to low level image processing. Int J Comput Vis 23(1):45–78
9. _Shen M, Jay Kuo CC (2001) A robust nonlinear filtering approach to inverse halftoning. J Vis Commun Image Represent 12:84–95
10. Zixiang X, Orhard M, T'Ramchandran K (1999) Inverse halftoning using wavelets. IEEE Trans Images Process 8(10):1479–1483
11. Neelamani R, Nowak R, Baran Niuk R (2002) WinHD: wavelet-based inverse halftoning via deconvolution. IEEE Trans Image Process 21(10):75–90
12. Liu S, Lu P (2012). Scanned-image discerning based on Gaussian filter. Packag Eng 33 (13):108–111
13. Jin J (2004) Visual C++ wavelet technology and engineering practice. Posts & Telecom Press, Beijing
14. Wang Z, Blvik AC, Lu L (2002) Why is image quality assessment so difficult. In: Proceedings of IEEE international conference on acoustics, speech and signal processing'02, vol 4, pp 13–17
15. Damera-Venkata N, Kite TD, Geisler WS et al (2000) Image quality assessment based on a degradation model. IEEE Trans Image Process 9(4):636–650

Status and Tendency of Augmented Expression for Paper Map

Hui Ye, Ruizhi Shi and Shenghui Li

Abstract In the wake of developments in science and technology, a variety of map products comes along. However, there are some inherent defects in the conventional paper map. For instance, it can't be changed once published; contains limited information; and its real-time performance is also poor. In addition, static rendering mode, lack of interaction and dynamic effect also slow down the development of conventional paper map. The augmented reality makes it possible to present the conventional paper map vividly, and it has wide application prospects. In this paper, the status and progress of augmented expression for paper map are reviewed which may provide reference for future related research.

Keywords Paper map · Augmented reality · Augmented expression

1 Introduction

Augmented reality (AR) is committed to combining computer generated information with the real world scene [1], it can serve as a bridge for seamless integration of digital world and the real world, provide a new way of cognition and experiencing things around for people [2]. There are so many researchers have defined AR diversely. Currently, the definitions of AR by Milgram and Azuma are widely accepted. Milgram [3] shows AR as a mixture between the real environment and virtual reality (Fig. 1). According to Azuma [4], the combination of real and virtual worlds, real-time interaction and 3D registration are the necessary factors for an AR system.

In recent years, the improving for mobile terminals in some related technology such as computer technology, image processing technology, photoelectric display

H. Ye · R. Shi (✉) · S. Li
Zhengzhou Institute of Surveying and Mapping, Zhengzhou, China
e-mail: ruizhishi@sina.com

H. Ye
e-mail: 260094480@qq.com

P. Zhao et al. (eds.), *Applied Sciences in Graphic Communication and Packaging*, Lecture Notes in Electrical Engineering 477,
https://doi.org/10.1007/978-981-10-7629-9_27

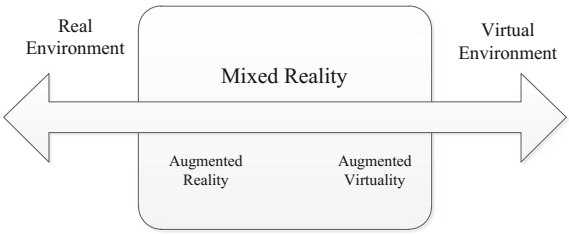

Fig. 1 Milgram's reality-virtuality continuum

technology, sensor technology and multimedia technology contributes significantly to the improvement of MAR. Besides, AR applications become more widespread because of their mobility improvements.

At present, the most famous and popular AR applications are distributed in advertising, commercial, entertainment, education, medical and mobile phone applications [5]. The AR application for paper map is expanding rapidly, the augmented expression systems for paper map depend on both fixed and mobile platform. Besides, interactive technology and tracking and registration technology that based on artificial markers and natural features still need further studies. And the research on the status of augmented expression for paper map can lead a better plan for future research work.

2 Status of Augmented Expression for Paper Map

The research of AR system stared in 1960s, and AR has become a hot research topic in many research institutes because of its extensive application prospects. A complete AR system is mainly composed of three parts: tracking and registration part, display part and real-time rendering part. As for hardware, an AR system mainly depends on head mounted display (HMD) or mobile terminals such as smart phones and PDAs. The advent of the Internet age and the improvement of hardware configuration for the mobile terminals lead to an increasingly promising future for MAR applications.

2.1 Foreign Status

After entering twenty-first Century, with the further development of AR technology, the AR application for map has begun to appear. Bobrich [6] proposed the concept of Augmented Map. His system can overlay DEM and 3D-TIN on the paper map that is bordered with four markers with the help of HMD and ARToolKit. Hedley [7] described two explorations for collaborative geographical data visualization that combining computer vision, hand and object tracking, VR

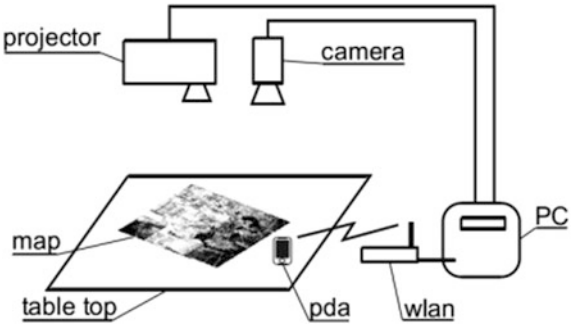

Fig. 2 Schematic overview of the system

Fig. 3 Implementation effect of the system

with AR. Teresa Romão [8] proposed an AR project for providing geo-referenced environmental information. And three main driving applications were developed to augment the reality with geo-referenced information related to water quality, temporal evolution of superficial solid structures and subsoil structure.

Reitmayr [9] developed an AR system for paper map which can project the augmented information to maps on a table top environment (Fig. 2). In addition, it supports an image browser and PDA to interact with information referenced by locations on the maps (Fig. 3).

Szchmalstieg [10] proposed that AR can be applied as a medium for cartography by explaining basic technology of AR and discussing some existing augmented map system and some Mobile AR system. Morrison [11] presented a MAR map named Map Lens that using a mobile phone with camera and GPS over a paper map (Fig. 4). He believes that the main potential of AR maps lies in their use as a collaborative tool because Map Lens was not very suitable for single use.

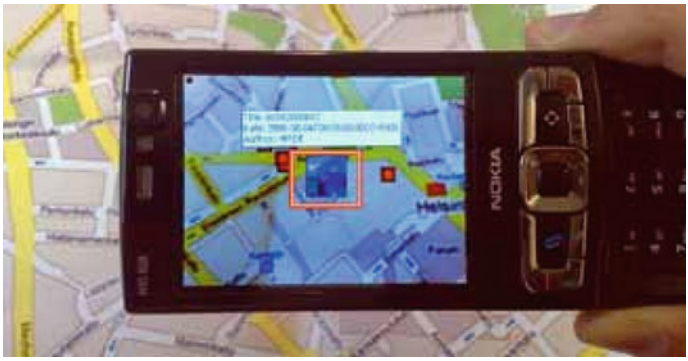

Fig. 4 MapLens overlays digital information on screen

(a) Input (b) Tagged images

Fig. 5 Display of tagged images on a map

Uchiyama [12] presented a system for combining 3D GIS data information with paper urban map. Their system can display a related picture at the captured place on the map (Fig. 5). Entered information is pictures and their locations, and the application will display these pictures on the map based on their captured place (Fig. 5b).

Paelke [13] achieved a meaningful integration by combining paper maps with a PDA (Fig. 6). Some meaningful functions such as GPS positioning, location data updating and interactive e-map functionality were integrated with paper navigation charts.

Chatain [14] introduced a spatial AR map for comparing three modalities (touch-based, object-based and spatial) for three different map functions (zoom, panning and changing the basemap) in order to identify advantages and disadvantages of each technique for a specific task.

Fig. 6 Paelke's APM system

2.2 Domestic Status

With the advent of some professional institutes for AR technology, great progresses in the technical level and application level in our country have been made. However, there are still so many things need to be done to narrow the gap with those technologically advanced countries.

Under the premise of rapid development of AR technology, how to enhance the performance of the paper map with AR technology has attracted the attention of the relevant personnel. Zhang [15] developed a prototype system using ARToolKit which can only overlay a 3D symbol on a marker. The 3D symbol in the video stream captured by camera will move and rotate when paper map is moved and rotated in front of the camera. But the marker is directly covered on the map, which affects the appearance and expression of the map. Fang [16] developed a real estate information AR system for Android phone based on Fuzhou real estate information map by using Qualcomm Vuforia SDK. And the main overlaid information includes text annotation and related video. Deng [17] combined Qualcomm Vuforia SDK and Unity 3D to develop a paper map AR system for Android phone based tourism map of Shanxi province. The main functions include layer control, data browse and spatial measurement. Wang [18] applied MAR technology to the augmented expression of city map and developed a system which can provide the latitude and longitude, the linear distance and azimuth information by combining QR codes and ARToolKit. Xu [19] proposed an adaptive processing method of

marker information by using the map identification library based on graphic feature of paper map. There are four artificial markers set at four corners of map in order to overlay the global terrain. And the partial overlay is realized by tracking and registration method based natural features. The main functions of his study include terrain overlay, partial information query.

3 Tendency of Augmented Expression for Paper Map

3.1 Hardware

As for main hardware, the AR system based on HMD will give users a sense of discomfort when use it for a long time. The great improvement of processing capacity for mobile terminals (such as smart phones) will open up a new field. And augmented paper map based on MAR system will become the mainstream of the future paper map AR system.

3.2 Key Technical

Tracking and registration are the fundamental and key factors of the augmented expression for paper map. Currently the most common method of tracking and registration is based on computer vision (Table 1). There are two types: one is based markers and another is based natural features. The method based markers are stable and fast. But the markers must be completely visible in the scene of the camera, otherwise the registration will fail. The method based on natural features uses the natural features such as feature points, feature lines, and textures to obtain the registration matrix. The algorithm of this method is usually designed by the researchers according to the requirements, and it has yet to form a unified theory. It doesn't need artificial markers but the implementation difficulty also increases greatly.

In the future, the two methods will be used in more properly ways to realize more functional application systems. The main development trend is embodied in the following aspects:

1. Cartography, the artificial markers used in AR made by invisible spectrum to lead the markers on the map "stealth" in order not to effect the expression of the map and disturb the users. When tracking and registration, using special cameras to detect and recognize.
2. According to the characteristics of the map, improving the tracking and registration algorithm based on natural features continually. At present, the algorithm has high complexity, large calculating quantity and low real-time performance. The performance improvement of the algorithm is a constant theme. And

Table 1 comparison of these studies

Author	Main hardware of system	Tracking and registration method	Interaction and function	Several users manipulate simultaneously
Joachim Bobrich	HMD, paper map	ARToolKit markers	Overlaying DEM, 3D-TIN Altering the virtual theme and modifying the appearance of a theme by makers	Yes
Nick. R. Hedley	HMD, paper map or projected map (projector and desktop)	ARToolKit markers	Overlaying terrain model, soil, hydrology and well information by makers Projecting 2D imagery Annotation of the virtual model Paddle interaction with the AR scene	Yes
Teresa Romão	HMD, laptop computer with camera	GPS	ANTS3D model editor Synthetic elements visualization in real-time	No
Gerhard Reitmayr	projector, camera, PC, PDA, table top, paper map	Computer vision method without markers	Interactive PDA and image browser to project dynamic and selective digital media	No
Morrison	Nokia mobile phone, paper map	Natural features tracking method	Overlay digital information	No
Hideaki Uchiyama	digital camera, laptop, physical map, desktop	LLAH & RANSAC (computer vision method without markers)	Overlay 3D GIS data information; Displaying a picture on the map based on its captured place	No
Paelke Volker	mobile device, paper navigation chart	ARToolKit markers	Establishing current position on chart; input waypoint; query area; query location	No
Julia Chatain	projector, RGB-camera, depth camera, table top	ARToolKit markers, color-based recognition algorithm	Touch-based, object-based and spatial interaction for zoom, panning and changing the basemap	Not mentioned
Zhang An	camera, computer, paper map	ARToolKit markers	overlaying 3D symbol; moving and rotating the paper map	No

(continued)

Table 1 (continued)

Author	Main hardware of system	Tracking and registration method	Interaction and function	Several users manipulate simultaneously
Fang Xiaojuan	Andriod phone, paper map	Qualcomm Vuforia SDK (computer vision method)	text annotation; overlaying related video	No
Deng Qiuyue	Andriod phone, paper map	Qualcomm Vuforia SDK	layer control; data browse; spatial measurement	No
Wang Zhangang	Andriod phone, paper map	QR code; ARToolKit markers	providing latitude and longitude, linear distance and azimuth information	No
Xu Wang	HMD, paper map	ARToolKit markers, natural feature-based method	overlaying terrain, querying partial information	Not mentioned

combining the depth learning, cloud technology and tracking and registration technology is an effective way to improve the algorithm.
3. Combining tracking and registration technology that using markers and that based on natural features reasonable. In order to maintain the integrity of content for paper map, the markers should be in the space of the map.

3.3 System Function

With the development of the application of AR in the paper map, a unified cartography standard and system framework based on AR will be formed in the future so that AR system for paper map will be universal.

In the interactive function, with the development of interactive technology in AR system, the ways of interaction between paper map and virtual information will be more convenient and friendly. For the same paper map, many people can operate by the mobile terminal simultaneously and choose an optional model based on personal goals and preferences. The forms of interaction will be more abundant, that is to say, the combination of command input, voice input, gestures, special tools and other forms will be more masterly and practical. The combination of interactive functions such as map rotation and translation, virtual model operation, layer selection, network connection, map software (baidu map, high moral map) connection is the inevitable trend of future AR system for paper map.

In order to improve the functionality of the system, in the virtual information content, will be created and managed in different types according to the corresponding users because different users are concerned about diverse information. For example, what the government departments concerned are mainly information related to government agencies, enterprises, institutions, and other disaster locations; what the public security departments (police and fire) concerned are mainly the information about the locations like staff-intensive, vulnerable to accidents; in daily life people mainly pay attention to the information about food, shopping, tourism, traffic. According to the type of user to customize the corresponding virtual information, both to facilitate management and enhance the availability of the system.

In the real-time capability of virtual information, an efficient data update mechanism should be established. The data related to geographic information is constantly updated, so the system must have a high update rate to meet the needs of users. The system should have the interface of the network and some special permissions to obtain some real-time information such as weather, real-time traffic conditions, and even real-time information of surveillance camera for some important locations (need be authorized by government).

4 Conclusions

In the information age, the development of traditional paper map is restricted because of its inherent defects. AR technology can inject new vitality into the application of paper map. With the advent of powerful mobile terminal, the combination of MAR and paper map has a broad application prospect. However, there are many technical problems remain to be solved. The tracking and registration algorithms whether based on markers or natural features have their own advantages and disadvantages. It is important for the future work that can not only improve the efficiency of the algorithm but also take the characteristics of paper map into account. Besides, the function of the AR system for paper map is not universal, and there is no unified system framework. And the form and content of interaction is not perfect enough that need to be further explored. In short, there are still many problems that need to be studied in the augmented expression of paper map, and we believe that a perfect system which is widely used will be established in the future.

References

1. Yao Y (2006) Studies on Implement Technology of Augmented Reality. Doctoral dissertation, Zhejiang University
2. Wu F, Zhang L (2012) A survey on development and application of augmented reality computer engineering and applications. Comput Knowl Technol 34:8319–8325
3. Milgram P, Kishino F (1994) A taxonomy of mixed reality visual display. IEICE Trans Inf Syst 77(12)
4. Azuma R (1997) A survey of augmented reality. Presence Teleoperators Virtual Environ 6 (4):355–385
5. Carmigniani J, Furht B, Anisetti M, Ceravolo P, Damiani E, Ivkovic M (2011) Augmented reality technologies, systems and applications. Multimedia Tools Appl 51(1):341–377
6. Bobrich J, Otto S (2002) Augmented maps. Int Arch Photogrammetry Remote Sens Spat Inf Sci 34(4):502–505
7. Hedley NR, Billinghurst M, Postner L et al (2002) Explorations in the use of augmented reality for geographic visualization. Presence Teleoperators Virtual Environ 11(2):119–133
8. Teresa O, Dias E, Danado J et al (2002) Augmenting reality with geo-referenced information for environmental management. In: Proceedings of ACM international symposium on advances in geographic information systems, pp 175–180
9. Reitmayr G, Eade E, Drummond T (2005) Localisation and interaction for augmented maps. In: Proceedings of IEEE and ACM international symposium on mixed and augmented reality, pp 120–129
10. Szchmalstieg D, Reitmayr G (2006) Augmented reality as a medium for cartography. Multimedia Cartogr 267–281
11. Morrison A, Oulasvirta A, Peltonen P et al (2009) Like bees around the hive: a comparative study of a mobile augmented reality map. In: Proceedings of international conference on human factors in computing systems, pp 1889–1898
12. Uchiyama H, Saito H Servières M et al (2009) AR city representation system based on map recognition using topological information. Lecture Notes in Computer Science, vol 5622, pp 128–135

13. Paelke V, Sester M (2010) Augmented paper maps: Exploring the design space of a mixed reality system. Isprs J Photogrammetry Remote Sens 65(3):256–265
14. Chatain J, Demangeat M, Brock AM et al (2015) Exploring input modalities for interacting with augmented paper maps. In: Proceedings of conference on l'interaction Homme-Machine, p 22
15. Zhang A, Zhuang J, Qingwen QI et al (2012) Visualization and interaction of augmented paper maps based on augmented reality. Trop Geogr 32(5):476–480
16. Fang X, Wu Q (2014) Paper map expression and its application based on mobile augmented reality. Microcomput Appl 7:41–43
17. Deng QY (2015) Application of augmented reality technology in paper map. Surv World 6: 1–14
18. Wang Z, Zhu X (2016) Design and implementation of mobile map augmented reality system. J Beijing Inf Sci Technol Univ
19. Xu W, Li AG (2016) Research on paper map augmented reality registration technology. J Geomatics Sci Technol 33(2):185–190

Unsupervised Image Histogram Peak Detection Based on Gaussian Mixture Model

Yingping Zheng, Zhijiang Li and Liqin Cao

Abstract Image histogram peak detection is a fundamental technique in digital image processing and relative areas. It has been found that Gaussian mixture model is an effective method to obtain the histogram peaks. However, how to set cluster centers and fit truncation data remain problems that deserve to be explored further. To solve the latter problem, this paper proposes a method consisting of data prediction, unsupervised data fitting and peaks acquisition. Extensive experiments are carried out to demonstrate the performance, and the results prove that our method can improve stability, deal with truncation data, and adaptively find histogram peaks.

Keywords Gaussian mixture model · Truncation data problem
Expectation maximization algorithm · Least squares regression

1 Introduction

Image histogram peak detection is a fundamental technique in digital image processing that can be directly and efficiently used in image segmentation, quality evaluation, enhancement, data reduction and so on.

General peak detection methods can be divided into direct method and indirect method. When using direct method, peaks can be obtained through directly discrete data analysis [1, 2]. Common indirect method consists of two steps. The first step is data fitting to obtain probability density function (PDF) [3–6]; the second step is calculation of the derivative of PDF to obtain significant peaks. It is found that indirect method is more stable, although it has some defects such as inaccurate peak positions and interference of pseudo local peaks.

Y. Zheng · Z. Li (✉) · L. Cao
School of Printing and Packaging, Wuhan University,
Wuhan, Hubei Province, China
e-mail: lizhijiang@whu.edu.cn

P. Zhao et al. (eds.), *Applied Sciences in Graphic Communication and Packaging*, Lecture Notes in Electrical Engineering 477,
https://doi.org/10.1007/978-981-10-7629-9_28

Literatures indicate that GMM can be used in data modeling [7–9]. Nevertheless, EM algorithm, which is used in GMM to obtain parameters of PDF, is sensitive to initial values; and it is difficult to fit truncation data that is in the form of partial Gaussian distribution at the edge of histogram. To solve the truncation data problem, a kind of indirect method, which consists of three steps, is proposed in this paper. The first step is estimating whether data is truncated. If true, predicting data based on least squares regression. The second step is using unsupervised improved FJ algorithm mentioned in Sect. 2 to obtain PDF. The third step is taking the derivative of PDF to obtain significant peaks. Meanwhile, Maximum Likelihood Estimation (MLE) and Expectation Maximization (EM) Algorithm [10, 11] are used to obtain PDF.

The rest of this paper is organized as follows: Section 2 proposes method to solve truncation data problem. Section 3 shows experiments and results. Section 4 states the conclusion of proposed method.

2 Proposed Method

2.1 Data Prediction

Firstly, estimating integrality of edge data. If edge data is truncated, fitting and predicting truncation data will be implemented. It is known that least square method can be used to fit and predict data. Subsequently, fitting and predicting left truncation data will be introduced as an example.

Let $D = \{(x_1, y_1), (x_2, y_2), \ldots, (x_n, y_n)\}$ be a set of left truncation data, relationship between x, y is

$$y = f(x, \vartheta) \tag{1}$$

where $\vartheta = \{\sigma, \mu\}$ represents parameters that need to be calculated.

It is assumed that D obeys Gaussian distribution, due to the usage of GMM to obtain PDF. Thus, Formula (1) can be rewritten as

$$y = \frac{1}{\sqrt{2\pi}\sigma} \mathrm{e}^{-\frac{(x-\mu)^2}{2\sigma^2}} \tag{2}$$

According to least square theory, if θ satisfies (3), it will become optimal parameter (θ^*).

$$\vartheta^* = \arg\min_{\vartheta} S \tag{3}$$

where S represents residual sum of squares (RSS)

$$S = \sum_{i=1}^{n} (y_i - f(x_i, \vartheta))^2 \tag{4}$$

Gauss-Newton method [12], which starts with an initial θ^0 for the minimum, and proceeds by iterations, is used to obtain θ^*.

$$\vartheta^{(n+1)} = \vartheta^{(n)} - (J_r^T J_r)^{-1} J_r^T (y_i - f(x_i, \vartheta^{(n)})) \tag{5}$$

where θ are column vectors, J_r is Jacobian matrix defined as

$$(J_r)_{ij} = \frac{\partial (y_i - f(x_i, \vartheta^{(n)}))}{\partial \vartheta_j} \tag{6}$$

Now applying Formulas (5) and (6) to Formula (2), we can fit and predict left truncation data to make it complete. Likewise, right truncation data can be fitted and predicted in the similar way.

2.2 Unsupervised Data Fitting Based on GMM

Thus far, following discussion is focused on full data fitting. Formula (7) shows general data fitting model.

$$f(x_i|\vartheta) = \sum_{j=1}^{K} p(\vartheta_j) p(x_i|\vartheta_j) \tag{7}$$

where $p(x_i|\vartheta_j)$ refers to any kind of probability distribution, such as Gaussian distribution, Cauchy distribution, Laplace distribution etc. It is assumed that all components obey Gaussian distribution in this paper. Meanwhile, $p(\vartheta_j)$ represents prior probability of each component satisfying the constraints below.

$$p(\vartheta_j) \geq 0 \quad and \quad \sum_{j=1}^{K} p(\vartheta_j) = 1 \tag{8}$$

Next, improved FJ algorithm proposed in [9], which is a kind of efficient improved EM algorithm, is used to obtain PDF in Formula (7). Similar to EM algorithm, it consists of E step and M step as well.

E step: Calculate $p(\vartheta_j|x_i)$ in Formula (9) based on Bayesian posterior probability theory.

$$p(\vartheta_j|x_i)^{(n+1)} = \frac{p(x_i|\vartheta_j^{(n)})p(\vartheta_j)^{(n)}}{\sum_{j=1}^{K} p\left(x_i|\vartheta_j^{(n)}\right)p(\vartheta_j)^{(n)}} \tag{9}$$

M step: Calculate parameters in Formulas (10)–(12), and obtain PDF $f(x_i|\vartheta)$ in Formula (7).

$$\mu_j^{(n+1)} = \frac{\sum_{i=1}^{N} p(x_i)p(\vartheta_j|x_i)^{(n+1)}x_i}{\sum_{i=1}^{N} p(x_i)p(\vartheta_j|x_i)^{(n+1)}} \tag{10}$$

$$\sigma_j^{(n+1)} = \sqrt{\frac{\sum_{i=1}^{N} p(x_i)p(\vartheta_j|x_i)^{(n+1)}(x_i - \mu_j^{(n+1)})^2}{\sum_{i=1}^{N} p(x_i)p(\vartheta_j|x_i)^{(n+1)}}} \tag{11}$$

$$p(\vartheta_j)^{(n+1)} = \frac{\sum_{i=1}^{N} p(x_i)p(\vartheta_j|x_i)^{(n+1)}}{\sum_{i=1}^{N} p(x_i)} \tag{12}$$

According to MLE, E step and M step need to be implemented until log-likelihood function in Formula (13) converges. If log-likelihood function converges, obtained parameters will be optimal.

$$L(\vartheta) = \log \prod_{i=1}^{N} f(x_i|\vartheta) = \sum_{i=1}^{N} \log \sum_{j=1}^{K} p(\vartheta_j)p(x_i|\vartheta_j) \tag{13}$$

Definitely, optimal parameters can be calculated when the number of components of GMM (K) is given. However, K is unknown. Thus, it is necessary to implement the process of calculating optimal K, which will make data fitting unsupervised.

Through extensive experiments, it is found that optimal K is at the range of 2–20 upon most occasions. According to least square principle, optimal K can be obtained when the RSS between fitting data $f(x|\vartheta)$ and original data y satisfying

$$K = \arg\min_{K} \{(f(x|\vartheta) - y)^2\} \tag{14}$$

Obviously, PDF can be obtained through Formulas (2) and (7). Finally, by taking a derivative of PDF, significant peaks will be obtained.

3 Experiment and Result

To demonstrate the performance of the stability of the result of peak detection and the ability to solve truncation data problem, extensive experiments were carried out.

3.1 Performance of the Stability of the Result of Peak Detection

Compared with direct method, the performance of indirect method is stability. To demonstrate the performance of it, we used direct method proposed in [2] and proposed method respectively. In Fig. 1a, we show one image from Ground Truth Database of University of Washington. Figure 1b shows the result of direct method, and Fig. 1c shows the result of indirect method. There are three peaks in Fig. 1b and seven peaks in Fig. 1c. Subjectively comparing Fig. 1b, c, we can find that four of peaks (the 3rd, 4th, 5th, and 7th peaks) in Fig. 1b are not significant.

It is known that the condition, which is used to obtain peaks in direct method, varies with image types. With image types changing, foregoing condition may not be applicable. The reason why four unimportant peaks exist is that the condition in direct method is not suit for Fig. 1a. Therefore, Fig. 1 suggests the stability of indirect method.

3.2 Performance of the Ability to Solve Truncation Data Problem

Compared with common indirect method, which does not implement data prediction, the proposed method has the ability to solve truncation data problem. To demonstrate the performance, we carried out some experiments as follows.

Step 1: Obtaining histogram data, which is truncated.

Step 2: Carrying out experiments with improved FJ algorithm [9] and proposed method respectively. Both of them are initialized with the result of k-means algorithm. Figure 2a shows one image from internet. Figure 2b, c show the different fitting results between common indirect method and proposed method when using Fig. 2a.

Step 3: Using both subjective and objective methods to judge the fitting accuracy of each method. RSS is used to measure the fitting accuracy of proposed method objectively. RSS can be calculated by (4), where y_i refers to real data, and $f(x_i, \vartheta)$ refers to calculated data. Table 1 shows the RSS value of common indirect method and proposed method based on data in Fig. 2b, c respectively.

Through Fig. 2, we find that when truncation data exist, the proposed method can obtain peaks more coincidently according to subjective analysis. Objectively analyzing the RSS in Table 1, we find that the RSS of proposed method is lower. Thus, the fitting accuracy of proposed method is better, and it can solve truncation data problem to some degree.

In our experiments, there are more than two hundred images are used, which are from USI-SIPI Image Database of University of Southern California, Ground Truth

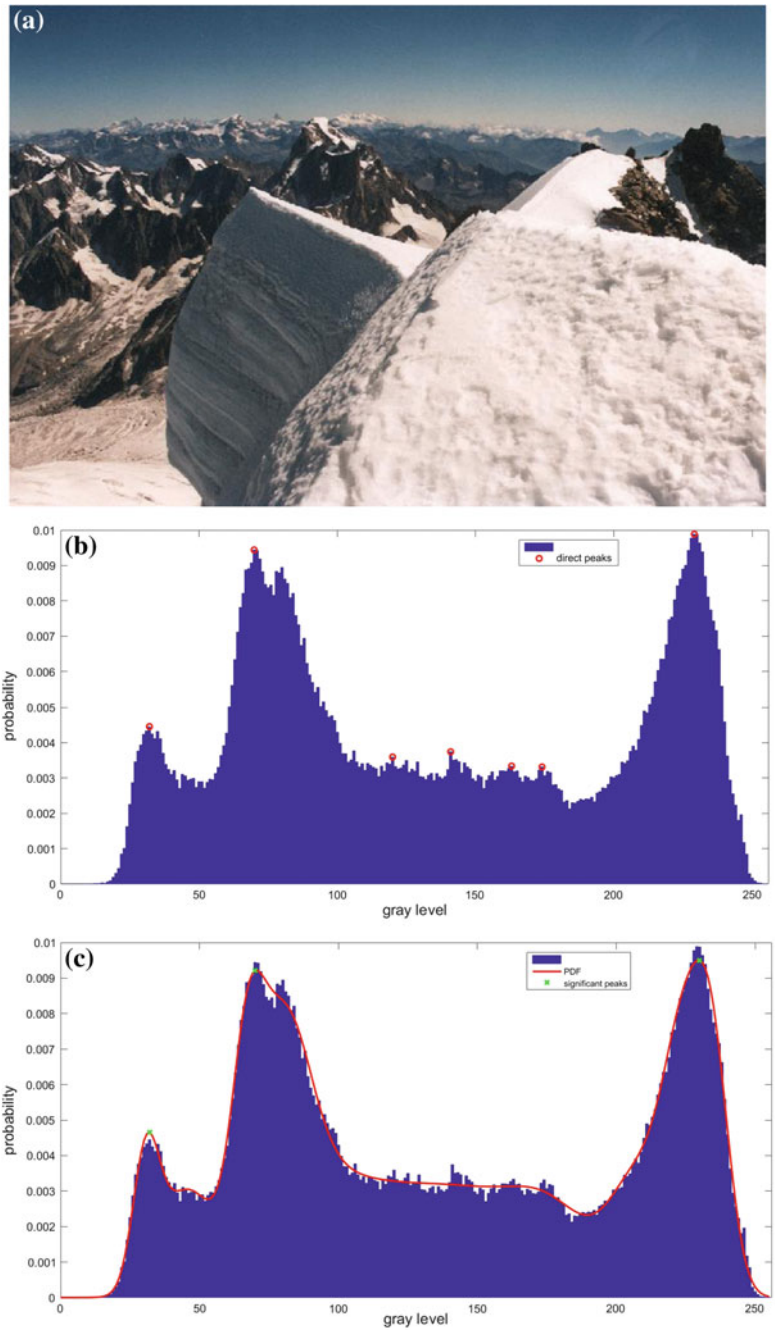

Fig. 1 The results of peak detection: **a** the original image (from Ground Truth Database of University of Washington); **b** the result of direct method; **c** the result of indirect method based on GMM

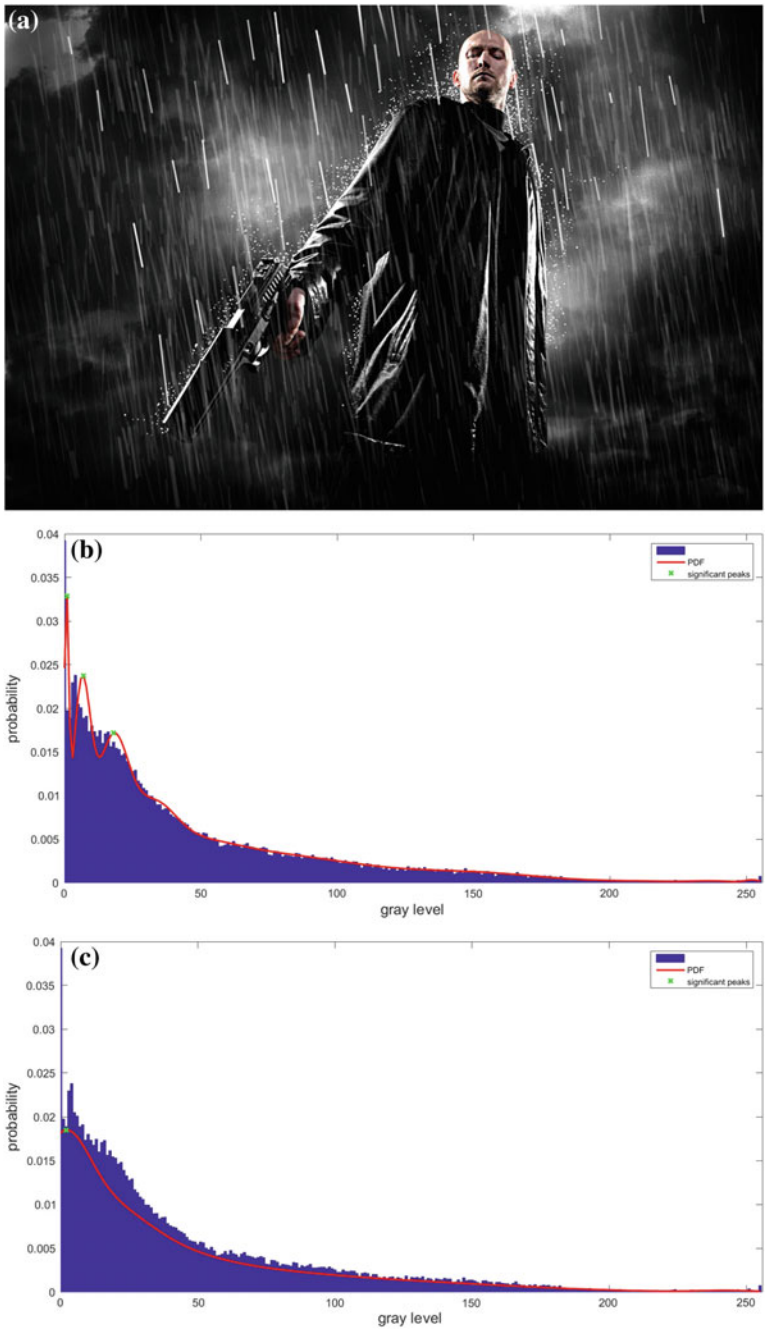

Fig. 2 Date fitting: **a** the original image (from internet); **b** common indirect method; **c** proposed method

Table 1 The RSS value of common indirect method S_1 and proposed method S_2 based on data in Fig. 2a, b respectively

S_1	S_2
5.9267×10^{-4}	1.7961×10^{-4}

Database of University of Washington and internet. The experiments find that our method is suit for a majority of images.

4 Conclusions

A method of peak detection, which consists of data prediction, unsupervised data fitting and peaks acquisition, is proposed in this paper. Experiments indicate that the proposed method is stable; and it can satisfactorily solve truncation data problem based on unsupervised data fitting. However, pseudo local peaks are still exist. We will focus on this problem in future work.

Acknowledgements This study is supported by the National Natural Science Foundation of China (65201701).

References

1. Yue XD, Miao DQ, Zhang N, Cao LB, Wu Q (2012) Multiscale roughness measure for color image segmentation. Inf Sci 216(24):93–112
2. Sastry SS, Mallika K, Rao BGS, Tiong HS, Lakshminarayana S (2012) Liquid crystal textural analysis based on histogram homogeneity and peak detection algorithm. Liq Cryst 39(4): 415–418
3. Boukharouba S, Rebordao JM, Wendel PL (1984) An amplitude segmentation method based on the distribution function of an image. Comput Vis Graph Image Process 29(1):47–59
4. Elguebaly T, Bouguila N (2011) Bayesian learning of finite generalized gaussian mixture models on images. Sig Process 91(4):801–820
5. Azam M, Bouguila N (2015) Unsupervised keyword spotting using bounded generalized Gaussian mixture model with ICA. In: IEEE global conference on signal and information processing, pp 1150–1154
6. Nguyen TM, Wu QMJ, Zhang H (2014) Bounded generalized Gaussian mixture model. Pattern Recogn 47(9):3132–3142
7. Figueiredo MAT, Jain AK (2002) Unsupervised learning of finite mixture models. IEEE Trans Pattern Anal Mach Intell 24(3):381–396
8. Elguebaly T, Bouguila N (2011) Infinite generalized Gaussian mixture modeling and applications. In: Proceedings of image analysis and recognition international conference, vol 6753, pp 201–210
9. Chen Y, Zhu M, Liu J, Li Z (2015) Automatic low light level image enhancement using Gaussian mixture modeling. Chin J Liq Cryst Disp 30(2):300–309

10. Yang M-S, Lai C-Y, Lin C-Y (2012) A robust EM clustering algorithm for Gaussian mixture models. Pattern Recogn 45(11):3950–3961
11. Redner RA, Walker HF (1982) Mixture densities, maximum likelihood and the EM algorithm. SIAM Review 26(2):195–239
12. Brillinger DR (1974) Quasi-likelihood functions, generalized linear models, and the Gauss-Newton method. Biometrika 61(3):439–447

Image Retrieval Based on the Multi-index and Combination of Several Features

Ziwei Tang, Kaiyang Liao, Yuanlin Zheng, Wei Wang, Mengying Liu and Hui Yuan

Abstract Local interest points serve as elementary building blocks in many image retrieval algorithms, and most of them exploit the local volume features using a Bag of Feature (BOF) model. However, the model ignores seriously valuable information about the global features in image and the distribution of the interest points. In this paper, we combine the sift feature and a global color feature. Then, we propose an improved strategy based on the BOF model. Finally, we embed the binary of the sift and color feature in the BOF model. Convincing experimental results on several datasets demonstrate that our proposed method approaches to the state-of-the-art level in image retrieval.

Keywords Image retrieval · BOF index model · Similarity search

1 Introduction

In the past decade, many models or algorithms about image retrieval have been applied. The best-known is the bag-of-features (BOF) model. The BOF is traceable to the text retrieval. The BOF is used in image retrieval firstly in Sivic's method [1]. While using the BOF model, the local interest points should be detected with the special descriptors, such as sifts, surf and so on. At this point, quantize them to the visual words with the pre-trained the codebook. According to this, the inverted index can be structured and weighted by term frequency–inverse document frequency.

The traditional BOF is limited by the single local descriptor without other efficient information. So this paper is to deal with this problem. The BOF has been updated to 2D with corresponding features. In addition, a global feature has been used with localized process.

Z. Tang · K. Liao (✉) · Y. Zheng · W. Wang · M. Liu · H. Yuan
Faculty of Printing, Packaging Engineering and Digital Media Technology, Xi'an University of Technology, Xi'an 710048, China
e-mail: liaokaiyang@xaut.edu.cn

P. Zhao et al. (eds.), *Applied Sciences in Graphic Communication and Packaging*, Lecture Notes in Electrical Engineering 477,
https://doi.org/10.1007/978-981-10-7629-9_29

2 Proposed Approach

This paper focuses on improving the recall and precision of image retrieval and the BOF model combining with the local descriptor and localized global descriptor.

2.1 Construct Sift-Color Multi-index

This part considers the 2D multi-indexing. The two dimensions correspond to the sift [2] and color feature.

2.1.1 Color Feature

Extract our color feature includes following steps.

Color Space. Similar to most color descriptors, we use the CIE Lab color space, in which our color descriptor is represented, and sRGB color space for transition.

Color Codebook. Our method needs a color dictionary $C = \{c_1, c_2, \ldots, c_k\}$, which is defined as k different color words and similar to the method proposed by Wengert [3]. The color dictionary is learned from the natural image. Considering some special color, the clustering includes the following procedures.

(1) Choose half number of images from the flicker 25K image dataset randomly.
(2) Resize the whole images to 256 * 256 pixels. So that an image can be split into 256 blocks, and each blocks has 16 * 16 pixels in sRGB color space.
(3) In each block, find the most occurring color in sRGB color space, and then convert the color in sRGB color space into the color in CIE Lab color space. Therefore, each block can be represented by a color, and an image can be represented by 256 colors.
(4) At the same time, the cluster resource (256 * 12,500) is prepared. The k-means algorithm is applied, and refers the color histogram's data; the size of codebook is 64, 256 or 512, which can be chosen. Considering the memory cost, the smaller means better.

Extract Color Feature. Color feature is extracted around a 16 * 16 pixels area of sift interest point. This area should be calculated as the color feature. Extraction is similarity to produce the color codebook. In the area around the sift interest point, find the most occurring color in sRGB color space, and then convert the color in sRGB color space into the color in CIE Lab color space. After that, quantize the colors extracting around the sift interest point to the color codebook, and produce the color visual word for each area.

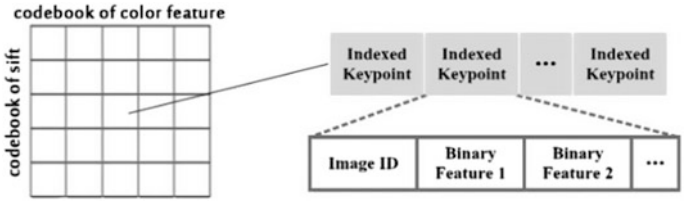

Fig. 1 Structure of multi-index

2.1.2 Structure of Multi-index

From the above, sift and color feature have been prepared. Upon this basis, multi-index can be constituted by sift and color feature shown as Fig. 1.

At this point, for a given query image, the sift and color feature are extracted firstly, and then quantize them in independent ways. Combine sift visual word and color visual word into a pair of visual words *word* (u, v) (u and v mean the position in their own quantization). Be similar to the common BOF adopted by Jegou [4], Rankis evaluated by score function f, following as:

$$f(\mathrm{x},\mathrm{y}) = (\mathrm{idf}(\mathrm{q}(\mathrm{y})))^2 \delta_{q(\mathrm{y}),q(\mathrm{x})} \tag{1}$$

where $q(x)$ is the feature in querying image and $q(y)$ is the feature in corresponding image. $\delta_{q(\mathrm{y}),q(\mathrm{x})}$, $q(x)$ and $q(y)$ are quantized to the same visual word, it is 1. Specially, $idf(u, v)$ is defined as:

$$idf(\mathrm{u},\mathrm{v}) = \log_{10}(\frac{N}{n_{u,v}}) \tag{2}$$

where N is the number of the images in dataset and $n_{u,v}$ is the number of members in the *word*(u, v).

Moreover, the l_2-*norm* is to calculate the frequency normalization in each image, computed as following:

$$\|I\|_2 = (\sum_u \sum_v tf_{u,v}^2)^{\frac{1}{2}} \tag{3}$$

2.2 *Binary Signatures*

In order to enhance the recall and precision further, some binary signatures have been employed. In a visual word, color binary and sift binary have been embedded.

Sift Binary Signature. This part explains how to produce the sift binary signature or say hamming embedding. As the process [5], for each sift vector, we can apply the corresponding codebook to perform binarization. At this point,

dissimilarity among sifts are measured by hamming distance d_{sift}. While querying, if d_{sift} is smaller than a prepared threshold κ, the score function f can be re-defined as follow:

$$f(\mathrm{d}_{sift}) = \begin{cases} idf^2 * \exp(-\frac{d_{sift}^2}{\sigma_{sift}^2}) * \delta_{q(\mathrm{y}),q(\mathrm{x})}, & if\ d_{sift} < \kappa_{sift} \\ 0, & \text{otherwise} \end{cases} \tag{4}$$

Color Binary Signature. Considering spot color may appear around the sift interest point, a special color descriptor named Color Names (CN) [6] is applied in this part. CN deals with each pixel surrounding the sift point. Each pixel is assigned to one of eleven spot colors: black, blue, brown, grey, green, orange, pink, purple, red, white and yellow. The area can be describe as a 11-bit vector $CN = (cn_1, cn_2, \ldots, cn_{10}, cn_{11})$. And CN has a binary method in [4]. Its process can be presented as follow:

$$(\mathrm{b}_i, \mathrm{b}_{i+11}) = \begin{cases} (1,1), & if\, cn_i > th_1 \\ (1,0), & if\, th_2 < cn_i \le th_2 \\ (0,0), & if\, cn_i \le th_2 \end{cases} \tag{5}$$

The 22-bits b is the result of CN binary. Threshold th_1 is the second-largest and th_2 is the fifth-largest number in 11-bits vector CN.

So the sift binary and color binary add into the score function f, and score function f updates as follow:

$$f(sift{-}\mathrm{color}) = \begin{cases} idf^2 * \exp(-\frac{d_{sift}^2}{\sigma_{sift}^2}) * \exp(-\frac{d_{cn}^2}{\sigma_{cn}^2}) * \delta_{q(\mathrm{y}),q(\mathrm{x})}, & if\ d_{sift} < \kappa_{sift} \,\&\, d_{cn} < \kappa_{cn} \\ 0, & \text{otherwise} \end{cases} \tag{6}$$

3 Experiments

3.1 Datasets and Baseline

Holidays [5]. The Holidays dataset is a set of images which mainly contains some of our personal holidays photos. The dataset contains 500 queries and 991 corresponding relevant images.

Ukbench [7]. This dataset contains 10,200 images of 2550 groups. Each of the 10,200 images is taken as the query image in turn.

This paper adopts the baseline proposed by Zheng [8]. However, the sift is extracted without affine and Root-SIFT is employed. The average IDF also been applied. AKM algorithm is implemented and produced the 20K codebook.

3.2 Parameter Selection and Results

This part includes two parts: binary signatures and multiple assignment.

Binary Signatures. In every binary signature, there are two parameters threshold κ and weighting σ. For sift binary signature, the Zheng's results are adopted [8], $\kappa = 22$ and $\sigma = 16$. The parameters for color features binary signature can be available with the following experiment.

This experiment is performed with sift combining with color feature and sift binary signature in the Holidays dataset. The result is presented as Fig. 2. Obviously, except parameter $\sigma = 2$, the other choices are very close to each other. So, the $\sigma = 3$ and $\sigma = 4$ can be chosen, whose variances are smaller than the other's by change of κ. Then, the parameter κ is available by the trend of line chart. As seen in the Fig. 2, after $\kappa = 7$, the change of mAP is negligible on each line. Therefore, the $\kappa = 7$ is the result.

Multiple Assignment. Multiple assignment (MA) can improve the recall extremely [9]. Therefore, MA is employed in the retrieval process. MA of sift and color feature are re-measured with following experiment.

This experiment is performed in the Holidays dataset and adopts the parameters $\kappa = 22, \sigma = 16$ for sift binary signature and $\kappa = 7, \sigma = 4$ for color feature binary signature. The result is presented as Fig. 3. The bigger MA of sift means the better recall. Considering precision, MA of sift is 5. The line begins decreasing while MA of color feature is 20. So, MA of color feature is 20 means the line peak.

Moreover, after ensuring the parameters, the final results are aggregated into the Table 1. All experiments below are performed with MA.

In addition, keep other parameters invariable, the experiments with $\kappa = 7, \sigma = 3$ for color feature binary signature have also been conducted. The final two mAP are 0.8225 (with Burst) and 0.8182 (without Burst) in Holidays dataset. Compare with corresponding data in Table 1, difference between them is neglected anyway.

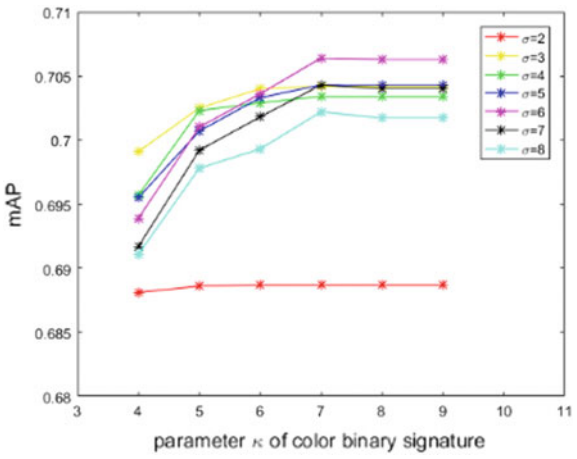

Fig. 2 Measure parameters κ and σ for color binary signature in Holidays

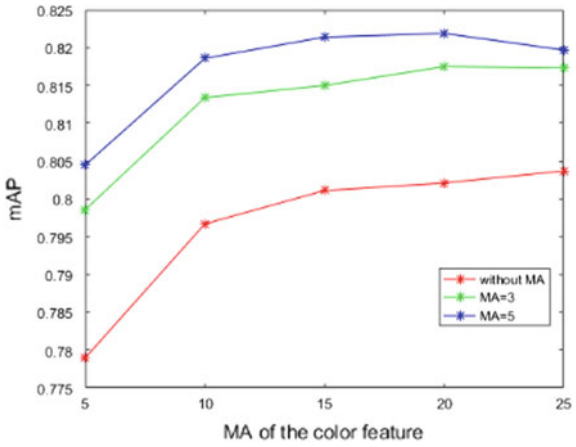

Fig. 3 Ensure the MA for sift and color feature in Holidays

Table 1 The result of several methods in Holidays and Ukbench dataset

Method	Color features	Hamming embedding	Color binary	Burst	Holidays (mAP)	Ukbench (NS)
Sift					0.5018	2.64
Sift		*			0.7641	3.30
Sift	*				0.5109	2.72
Sift	*	*	*		0.8219	3.35
Sift	*	*	*	*	0.8223	3.40

Table 2 Performance comparing with state-of-the-art methods

Method	Proposed approach	[4]	[10]	[9]
Holidays (mAP)	0.8223	0.813	0.821	0.84
Ukbench (NS)	3.40	3.42	–	3.71

3.3 Comparison with State-of-the-Arts

This part is to compare proposed approach with state-of-the-art methods. The comparison as shown in Table 2 concludes proposed approach is consistent to Jegou's method [4], but cannot beyond Zheng's method [9] with the less cost of memory.

4 Conclusions

This paper proposes a novel image retrieval method based on the multi-index and combination of several features. First, our method choose the two different types of feature, so that, the stabilization of interest point can be risen. Then, the improved multi-index is applied for better precision. Experiments demonstrate the strength of our method.

Acknowledgements This work is supported by the National Natural Science Foundation of China Project No. 61671376, 11272253 and Natural Science Foundation of Shaanxi Province No. 2016JM6022.

References

1. Sivic J (2003) Video Google: a text retrieval approach to object matching in videos. In: IEEE international conference on computer vision, vol 1472, pp 1470–1477
2. Lowe DG (2004) Distinctive image features from scale-invariant keypoints. Int J Comput Vis 60:91–110. https://doi.org/10.1023/B:VISI.0000029664.99615.94
3. Wengert C, Douze M, Jegou H (2011) Bag-of-colors for improved image search. In: Multimedia ACM multimedia, pp 1437–1440
4. Jegou H, Douze M, Schmid C (2010) Improving bag-of-features for large scale image search. Int J Comput Vis 87:316–336. https://doi.org/10.1007/s11263-009-0285-2
5. Jegou H, Douze M, Schmid C (2008) Hamming embedding and weak geometric consistency for large scale image search. In: European conference on computer vision, vol 5302, LNCS, pp 304–317
6. Khan FS, Anwer RM, Van De Weijer J, Bagdanov AD, Vanrell M, Lopez AM (2012) Color attributes for object detection. In: Proceedings of 2012 IEEE conference on computer vision and pattern recognition, pp 3306–3313
7. Nister D, Stewenius H (2006) Scalable recognition with a vocabulary tree. In: Computer vision and pattern recognition, pp 2161–2168
8. Zheng L, Wang S, Guo P, Liang H, Tian Q (2015) Tensor index for large scale image retrieval. Multimedia Syst 21:569–579
9. Zheng L, Wang S (2014) Packing and padding: coupled multi-index for accurate image retrieval. In: Computer vision and pattern recognition, pp 1947–1954
10. Qin D, Wengert C, Van Gool L (2013) Query adaptive similarity for large scale object retrieval. In: Computer vision and pattern recognition, pp 1610–1617

Research on PCB Micrograph Registration Based on FSK Method

Jie Wang, Qiang Wang, Zheng Gong and Ping Yang

Abstract To realize automatic optical visual inspection (AOI) in the high resolution image for image matching, the extraction and registration of feature points is critical. The traditional image registration algorithm is time-consuming, computationally intensive and ineffective. In this paper, an optimization algorithm based on FAST, SURF and K-Means algorithms is proposed to optimize the feature point selection and reduce the matching point pairs. The algorithm uses the FAST algorithm to extract the feature points, and then generates the SURF descriptors according to the information in the fields around the feature points, and the K-Means algorithm is used to cluster the feature points. Finally, the error matching points are eliminated by the consistency check. The experimental results show that the proposed algorithm has high speed and precision in extracting the feature points.

Keywords FAST · SURF · K-Means · Feature point · Image registration

1 Introduction

In the manufacturing of ultra-thin, small components, high-density electronic components (such as PCB), automatic optical inspection technology (AOI) has become the mainstream to replace the manual inspection,which brings new technical challenges in product quality inspection [1]. In the use of image mosaic method for high-resolution image mosaic and registration, the extraction of feature points is very essential. Zhang [2] and other scholars have evaluated the feature points of Harris, SIFT, and SURF and so on. The result shows that the SURF algorithm has the advantages of accurate parameter estimation, small computation and fast speed, but the number of matching points obtained is low. FAST algorithm

J. Wang (✉) · Q. Wang · Z. Gong · P. Yang
School of Digital Media and Art Design, Hangzhou Dianzi University, Hangzhou Zhejiang, China
e-mail: 1347150711@qq.com

P. Zhao et al. (eds.), *Applied Sciences in Graphic Communication and Packaging*, Lecture Notes in Electrical Engineering 477,
https://doi.org/10.1007/978-981-10-7629-9_30

is simple and fast and the detection time is short, which can quickly determine the feature points, but it does not show feature point description information. In order to improve the number and speed of matching points in image auto-registration, a new algorithm called of FAST-SURF-K-means (FSK algorithm) was proposed in this paper, based on the advantages of FAST algorithm and SURF algorithm K-means clustering image registration algorithm. The improvement of the number and efficiency of the feature points is obtained, which satisfies the practical application needs.

2 Related Work

2.1 FAST Feature Point Detection

FAST is the abbreviation of Features from Accelerated Segment Test [3] which is based on the image gray value around the feature point. When the candidate point has sufficient number of pixels on the adjacent circumference, the difference between the gray value of the candidate point and the pixels is greater than a given threshold, the candidate point can be set as a feature point.

2.2 SURF Feature Descriptor

SURF is an accelerated robust feature algorithm that uses haar features and integral images to improve SIFT algorithm and reduce computational complexity. The SURF descriptor generation is such a process that the vector is formed by calculating the Haar wavelet in the X and Y directions of the feature point to establish the main direction of the longest vector as its feature point and then through the Haar wavelet response of the pixel in the neighborhood of the feature point to determine the 64-dimensional eigenvector. The feature points between different images are registered according to the Euclidean distance between the two feature points.

2.3 K-Means Algorithm

K-means algorithm [4] is a distance-based clustering algorithm. When the distance is used as the evaluation index of the similarity, that is considered that the closer the two objects are, the more similar they are. K-means algorithm can be clustered with the same characteristics or based on certain rules to form different clusters; each cluster is compact inside and independent outside.

3 FSK Algorithm Implementation

In order to solve the problem off ewer features, low precision in the traditional algorithm, an optimization algorithm (FSK algorithm) is proposed according to the characteristics of microscopic image. The image samples used in this paper are pre-processed microscopic images, and the algorithm flow is shown in Fig. 1.

3.1 Feature Point Extraction

In the microscopic image registration, the process of screening feature points is extremely critical. In order to extract feature points in high efficiency and high quality, this paper firstly uses the Fast algorithm to extract a large number of feature points quickly, and then uses the SURF algorithm to carry out the vector description. Finally, the K-means algorithm is used to obtain the best registration feature point.

3.1.1 *Preliminary* Selection of Feature Point

Preliminary selection of feature point refers to the use of FAST-based feature detection to obtain possible feature points quickly. In the FAST algorithm, difference of gaussian is used to construct the scale space to extract the feature points in the image, and then the non-maximal suppression of the image is performed to calculate its response function (score function V) for each detected feature point. V is defined as the sum of the absolute deviations of point p and its surrounding 16 pixels. And then considering two adjacent feature points and compare their V values, points with lower V values will be deleted.

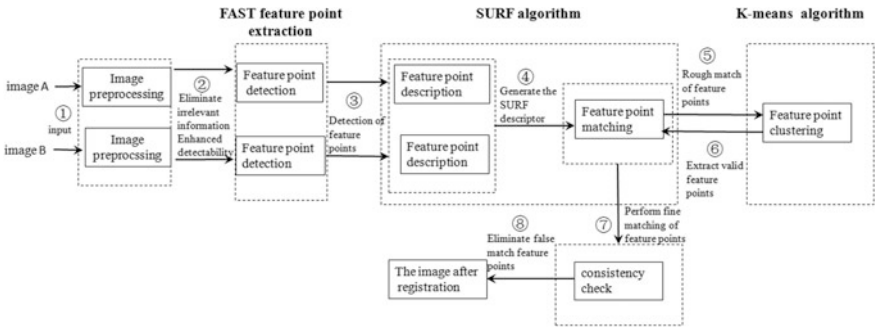

Fig. 1 Algorithm flow chart

3.1.2 Feature Vector Description

Feature vector description refers to assigning specific information which is related to the image to feature points. After obtaining the primary feature points, the vector description is carried out using the SURF feature detection. The procedure is described as follows:

(1) Making the feature point as the center and aggregating the Haar wavelet response in the neighborhood where the radius is 6s (s is the scale value of the feature point), and the Gaussian weighting coefficient is assigned according to the response value.
(2) In the neighborhood of the feature point, the sum of the horizontal Haar wavelet and the vertical Haar wavelet feature at all points in the sector is counted every 60°.
(3) Traverse the entire circular neighborhood to the maximum fan direction as the main point of the feature point.
(4) Take a 20s square box around the feature point and disassemble it into 16 sub-regions. Then aggregate the Haar wavelet characteristics of the 25-pixel horizontal and vertical directions in each sub-region.
(5) The feature point as the center of the Gaussian function for weight processing to get 4-dimensional vector descriptor V_4:

$$V4 = \left(\sum dx, \sum dy, \sum |dx|, \sum |dy|\right) \tag{1}$$

3.1.3 Screening of the Best Registration Point

In this paper, we use the high-dimensional vector to describe and store the eigenvalues of the SURF descriptor, and the feature vector is as high as 64°. This will lead to the problem that the matching time is too long. The K-means clustering algorithm is selected to reduce the number of feature points, and screen out the best registration point. The specific algorithm process as follows:

(1) Selecting the number of K feature points (A_1, A_2, A_3, …, A_k) randomly from the feature point sets of S1 and S2 as the cluster center.
(2) According to the Formula (2) obtained the distance from each feature point to the center of the cluster, divided into the different clusters:

$$A^{(i)} := \arg\min_j \left\| q^{(i)} - A_j \right\|^2 \tag{2}$$

(3) According to the formula (4), to re-calculate the cluster center for each cluster, repeat steps (2) and (3) until the cluster elements from the center point of the distance is not greater than λ.

$$A_j := \frac{\sum_{i=1}^{m} \{A^l = j\} q^l}{\sum_{i=1}^{m} \{A^i = j\}} \tag{3}$$

$$\min \sum_{i=1}^{k} \sum_{q \in A^i} dist(A^i, q)^2 \leq \lambda \tag{4}$$

(4) According to the obtained cluster center, select the square area point A_i (x, y) as the center:

$$A_i(x \pm \Delta x, y \pm \Delta y) \in Z_{(n)} \tag{5}$$

(5) Traverse all the feature points; delete all the features that are not included.

Since the K's value selection directly affects the clustering efficiency and the extraction of the effective feature points, and the number of selected clusters is not fewer than the number of real clusters, the K's value of the optimal clustering effect is 4 in this paper through a lot of experiments.

3.2 Registration of Microscopic Images

Based on the best registration point, this paper uses the operator of SURF descriptor to realize the registration of feature points. By calculating the Euclidean distance between the two feature points to determine the matching degree, the shorter the Euclidean distance is, the higher matching degree of the two feature points.

The matching algorithm is executed twice. It is divided into feature points rough matching and feature points accurate matching according to the different thresholds, The rough matching is mainly to find the overlapping area of the image, and the matching precision is low while the speed is fast. After the K-means algorithm clustering, feature points accurate matching is used to match feature points in few and high quality.

4 Experimental Results and Analysis

In this paper, we use the Olympus microscope as platform in color high-fidelity reproduction laboratory of Hangzhou Dianzi University, and two splicing experiments were carried out at 20 times magnification to verify the performance of FSK algorithm. In order to verify the extraction efficiency and registration accuracy of feature points, the following two comparative experiments are conducted:

4.1 Comparison in the Number and the Time of Extracting Feature Points

The comparison results in the number and the time of extracting the feature points among this algorithm and FAST, SURF are shown in Fig. 2 and Table 1.

As it can be seen from Fig. 2 and Table 1, compared with the traditional SURF algorithm, the FSK algorithm has taken the advantages of high extracting speed of FAST algorithm and the feature description of SURF algorithm, and it takes less time to extract more feature points by using K-means algorithm to obtain the best registration feature points.

4.2 Comparison in Stability and Registration Accuracy

In this paper, two important evaluation indexes (Rejection (Rj)) and precision (Pr) are evaluated according to the Recall and Precision evaluation criteria [5]:

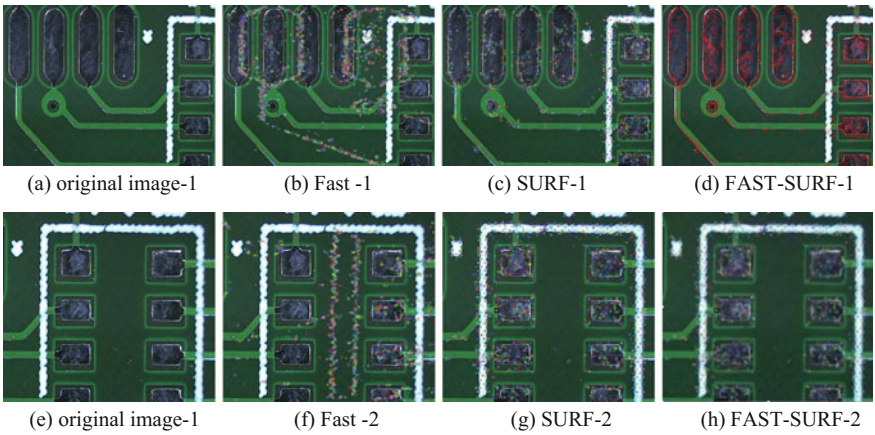

(a) original image-1 (b) Fast -1 (c) SURF-1 (d) FAST-SURF-1

(e) original image-1 (f) Fast -2 (g) SURF-2 (h) FAST-SURF-2

Fig. 2 Different algorithms extract feature points after the image

Table 1 Comparison of the number of feature points and time under different algorithms

Algorithm	Image 1		Image 2	
	Feature points	Extraction time	Feature points	Extraction time
FAST	5642	362	4986	254
SURF	1483	3589	1138	2023
FSK	2643	2942	2368	1652

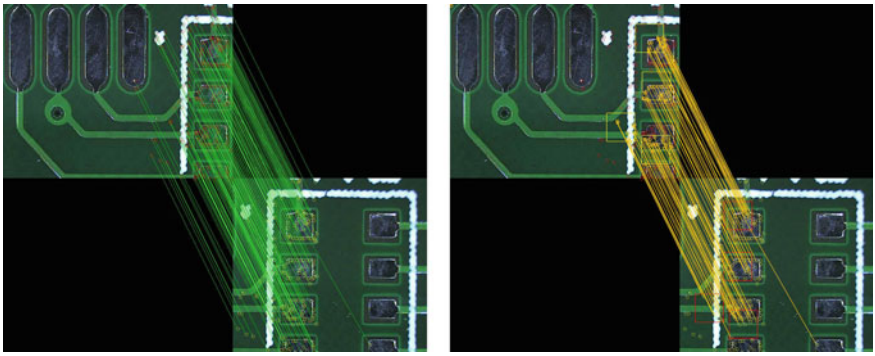

(a) SURF+RASAC (b) Ourmethed

Fig. 3 Feature point screening algorithm comparison

Table 2 Feature point screening algorithm comparison

Algorithm	SURF + RANSAC	Our method
Initial match	1036 ms	1125 ms
Final match	590 ms	306 ms
Rj	43%	73%
Pr	85.6%	97.5%
Time	2838 ms	978 ms

$$\mathrm{Rj} = \left(1 - \frac{\mathrm{TP}}{\mathrm{FP}}\right) \times 100\% \tag{6}$$

$$\mathrm{Pr} = \frac{\mathrm{TR}}{\mathrm{TP}} \times 100\% \tag{7}$$

In the formula: TP is the number of feature points matched, FP is the number of feature points to be found, and TR is the number of feature points observed by the human eye. Based on this, the algorithm compared with the SURF + RASANC algorithm in rejection rate and accuracy rate. The results are shown in Fig. 3 and Table 2.

From the data in Table 2, we can see that the algorithm is not only higher than SURF + RANSAC at the feature point rejection rate, but also higher than the contrast algorithm. Therefore, the efficiency of the algorithm is about 3 times higher than SURF algorithm to meet the real-time requirements of image stitching.

5 Conclusions

In this paper, by combining the advantages of algorithms of FAST, SURF, and K-means, FSK algorithm has solved the problems that there are not enough feature points, long matching time and low algorithm reliability in the traditional micro-image mosaic algorithm, and improved the feasibility of the algorithm effectively as well as micro-image stitching accuracy and efficiency. However, in the special cases where the image features are few and the similarity is high, the overall performance of the algorithm is still insufficient, which needs to be further optimized later.

Acknowledgements This work is funded by National Key Technology Research and Development Program of the Ministry of Science and Technology of China (2012BAH91F03).

References

1. Wu P, Dai X (2009) PCB test technology introduce. Mod Mach 04:90–93
2. Zhang C, Gong Z, Huang Y (2008) Performance evaluation and improvement of several feature point extraction algorithms. J Surveying Mapp Sci Technol 03:231–234
3. Bay H, Tuytelaars T, Van Gool L (2006) SURF: speeded up robust features. In: Proceedings of 9th European conference on computer vision, Graz, Austria, ECCV2006, pp 404–417
4. Wang Z, Liu G-Q, Chen E-H (2009) A K-means Algorithm for optimizing initial center point. Pattern Recog Artif Intell 02:299–304
5. Amin S, Hamid E (2015) Very high resolution image matching based on local features and K-Means clustering. Photogram Rec 30(150):166–186

Study on Digital Acquisition Method of High Dynamic Range Image

Weiyan Zhang, Qiang Wang, Ping Yang and Jing Cao

Abstract Based on the optimal image exposure set, the dynamic range of the image acquired by the digital camera is extended. In this paper, a high dynamic range image acquisition method is proposed to control the linear dynamic range of single segment exposure by gray scale. When letting the linear dynamic range of the gray scale's correct single exposure as a benchmark, the range of image is determined. However, the details of the image are seriously missing. To solve this problem, the whole gray scale samples are segmented with the linear part being exposed firstly, leaving high key and shadow for next exposure. The experimental results show that this method can effectively extend the dynamic range of the acquired image, while eliminating the huge image data set by the premise of acquiring the static scene, and increase the detail information of the image's shadow and high key.

Keywords High dynamic range image (HDRI) · Optimal image exposure set Segmented shooting · Dynamic range extension

1 Introduction

With the development and application of digital imaging technology, the dynamic range is extended to meet the need of human vision in many applications. Therefore, high dynamic image acquisition is becoming one of the key issues to be solved in digital image technology. In the 1950s, Gustave Le Gray proposed multi-exposure synthesis of high dynamic range imaging technology [1]. In 1995, Mann and Picard proposed the method that used different exposure images to extend the dynamic range of digital cameras [2] and other methods. A high dynamic image is synthesized using a plurality of low dynamic images by continuous exposures, which are no noise, no ghosting and eliminate defect that image

W. Zhang (✉) · Q. Wang · P. Yang · J. Cao
School of Digital Media and Art Design, Hangzhou Dianzi University, Zhejiang, China
e-mail: 347343875@qq.com

P. Zhao et al. (eds.), *Applied Sciences in Graphic Communication and Packaging*, Lecture Notes in Electrical Engineering 477,
https://doi.org/10.1007/978-981-10-7629-9_31

exposure set is redundant and so on [3]. This is becoming a research focus in high dynamic imaging field.

This paper uses conventional digital camera as an acquisition tool. A high dynamic range image acquisition method is proposed, which is to control the linear dynamic range of single segment exposure by gray scale. Through the multi-segment exposure for the highlight, middle tone and shadow of the imaging scene, it is effective to solve the problem that brought by redundant exposure bracketing image sets. By forming an optimal low dynamic range image exposure set, the dynamic range of imaging can be extended.

2 Principle of High Dynamic Range Acquisition

High dynamic range (HDR) is to compensate for the lack of dynamic range of imaging sensors, which using technology to accurately capture the relative radiation brightness of the real scene, keeping the real scene information completely and satisfying HDR images helps HVS identify the scene [4]. At present, basically there is no mature and available HDR sensor to acquire scene in high dynamic range. The digital acquisition of the scene is mainly using multi-exposure to achieve high dynamic range imaging. That is multiple LDR images are continuously shot with a single exposure device for different exposure levels on the same scene, including the image of the scene's highlight area, the image of the scene's shadow area and the image of the scene's normal area. And then combining these images into one HDR image by using the response function of the imaging device [5, 6]. Thus, accurately to obtain a valid exposure images set to fully extend the dynamic range of target image, which is a key issue of digital acquisition in high dynamic imaging.

Because the acquisition and calibration of the image device's response function is more complex. This paper uses the conventional camera to shoot the specially designed density-dot gray scale. Through calibrating the dynamic range of the correct single exposure by the digital camera, the corresponding response curve of the camera is plotted. The image's highlight areas and image's shadow areas whose details are missing is inverting. Then, respectively, partial and segmented multiple exposure sampling is performed for these two parts, to obtain an exposure image which can accurately reproduce details of the saturation area and shadow area. As shown in Figs. 1 and 2, in the premise of ensuring the image's high dynamic range, the exposure number of the exposure sequence of this study's exposure bracketing significantly reduced compared with the optimized exposure sequence of existing multiple exposure.

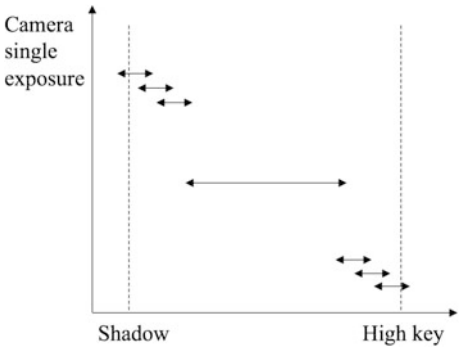

Fig. 1 Ordinary bracketing sequence

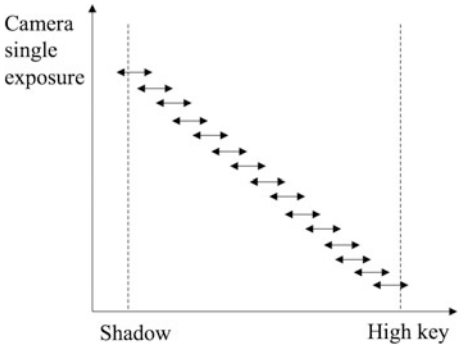

Fig. 2 Exposure sequence for this paper

3 Experiment Design and Implementation

In this study, we optimized the image exposure set for low dynamic range image acquisition and specially designed a set of gray scales to calibrating the correct exposure and HDR. Moreover, the experimental scheme of acquiring the optimal exposure set and effectively extending the dynamic range of the image is determined.

3.1 Design of Density-Dot Gray Scale

In this study, the characteristics of the whole gradation change for high dynamic range image, while taking into account the response of the camera's RGB three channels, the density-dot gray scale of the 51 grayscales is specially designed. Particular the details and the levels of the shadow area and the highlight area in the image should be emphasis on. The main parameters are as follows:

3.1.1 Maximum Value of Density

In this paper, the maximum density value is that the solid or 100% dot area coverage can reach the maximum density in the conditions of under existing printing. The greater the density value, the more details and the levels of the gray scale can be reproduced. This study uses digital inkjet printer to output and the maximum value of density after linearization sets to 2.14.

3.1.2 Interval of the Gray Scale

This paper designed a sequence of patches with gradients or gradations, which can meet the needs of the camera response curve and density measurement, as shown in Fig. 5. The gray scale of the interval of 5% dot area coverage as the standard is shot by the camera auto exposure mode to determine the interval of the gray scale, as shown in Fig. 3. Collecting the data of each gray scale and plotting the camera response curve, as shown in Fig. 4. The two response curves of the dot area coverage-gray level and the density-gray level have the same trend, which means that the two parameters can reflect the input dynamic range. According to the setup needs of tonal sequences' number, the interval in 4% is determined in 30–70% area of the gray scale, which shows the linear feature. The interval in 2% is determined in 10–30 and 70–90% areas of the gray scale and the interval in 1% is determined in 0–10 and 90–10% areas of the gray scale, which shows the non-linear features.

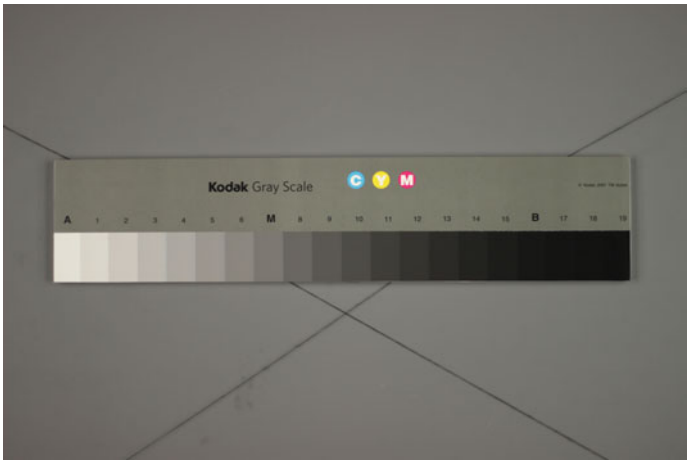

Fig. 3 Gray scale with interval of 5%

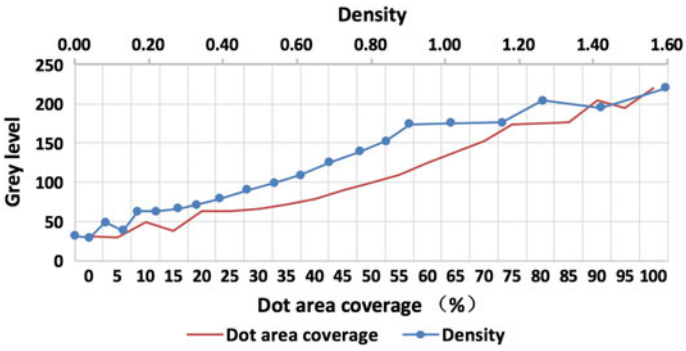

Fig. 4 Camera response curve

3.1.3 Sorting and Positioning of Gray Blocks

According to experimental conditions and camera's viewing field,the gray scale is monotonically graded and then arranged. This study wants to eliminate the phenomenon which the density value or pixel value is jump, caused by segmented and line breaking arrangement in the monotonous increase of the gray scale. The upper and lower lines of the two gray level blocks set to the same dot area coverage. Horizontal monotonically increasing and vertical monotonically increasing arrange to eliminate the phenomenon. As shown in Fig. 5.

3.1.4 Data Measurement

In the synthesis of the above parameters,the density-dot gray scale can be obtained as shown in Fig. 6. The X-rite Eye-One Pro is used to measure the density and dot values of each gray block.

Fig. 5 Gray scale's schematic diagram

0%	1	2	3	4	5	6	7	8	9	10
10	12	14	16	18	20	22	24	26	28	30
30	34	38	42	46	50	54	58	62	66	70
70	72	74	76	78	80	82	84	86	88	90
90	91	92	93	94	95	96	97	98	99	100%

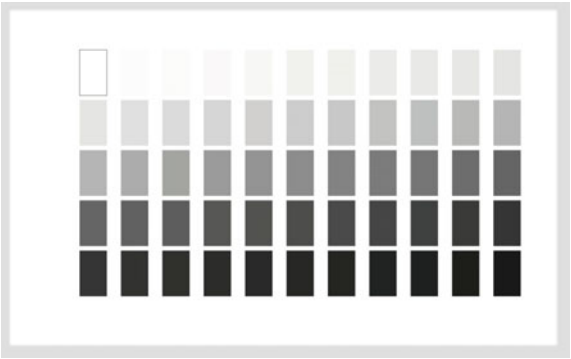

Fig. 6 Gray scale's physical diagram

3.2 Data Acquisition and Data Analysis

3.2.1 Date Collection

In this study, using the multiple exposure to get the sample image set, which has an image of the correct single exposure of the entire gray scale and an image of the partial segment exposure for the portion the information that is severely missing. The process of shoot in Fig. 7.

Whole Tone Shooting

The study wants to determine the exposure range for normal exposure, which to exposure shoot on the gray scale specifically, to screen out and determine the correct exposure parameters,and then to design the shutter speed as a single variable to adjust the exposure quantity from up and down. As shown in Fig. 8.

According to the overall distribution of gray histogram is relatively uniform as a prejudgment, to obtain a few images with normal exposure, as shown in Fig. 8.

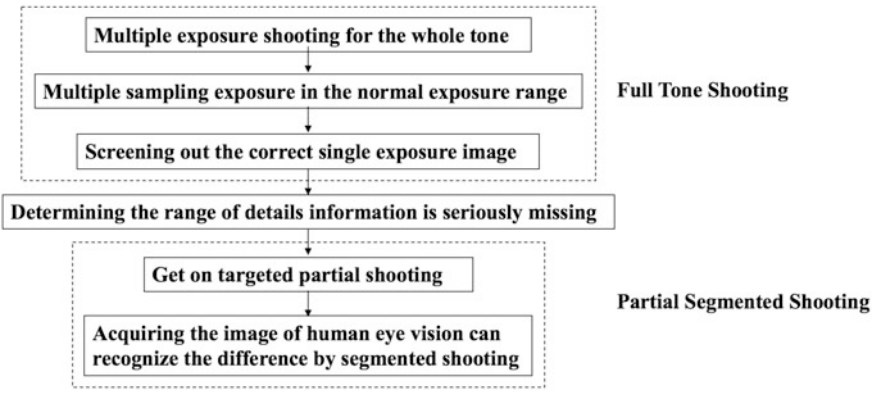

Fig. 7 Shooting flow chart

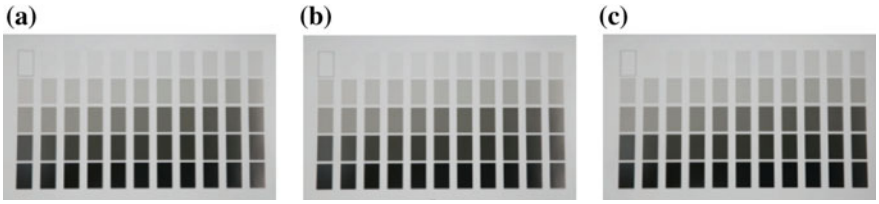

Fig. 8 Some normal exposure images with different shutter speeds

Then based on the human eye, each gray block distribution uniformity of the image is judged.

According to Fig. 8a as the correct single exposure image, using MATLAB to read the pixel values for each gray block, converting pixel values to gray levels and handling RGB three-channel data. Figure 9 shows the camera response curve of the R channel, making a second derivative to get the inflection point of the curve. So that to determine the non-linear variation range of the curve and the range of missing detail information, that is the gray block on the corresponding about 16% below and above 78% of gray scale. There are two parts of missing details information, which is necessary to increase the number of gray block from partial segmentation appropriately, in order to make up and perfect the part of partial segmented shooting in the late. In this study, the gray scale is properly cut to improve, which is easy to partial shooting for the gray scale, as shown in Fig. 10.

Partial Segmented Shooting

In order to obtain gray scale of about 16% below and above 78%, it is necessary to correctly reproduce the gray blocks' details information of the shadow area and highlight area for the real scene. In this study, graded and multiple exposure methods were used to screen out the gray level blocks, which can correctly reproduce details and levels in the highlight area of 0–15% and the shadow area of

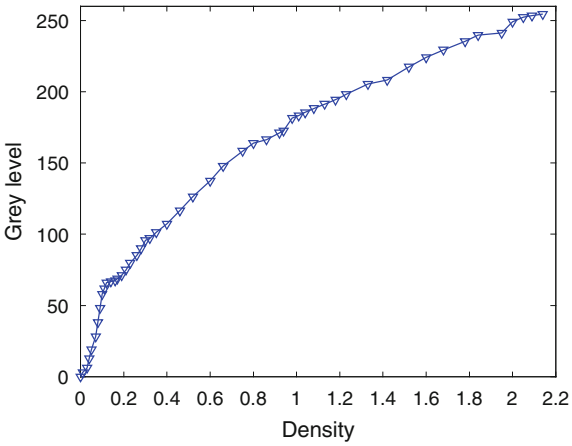

Fig. 9 Camera response curve after change

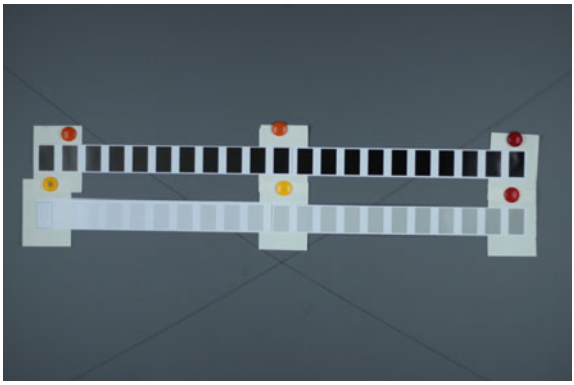

Fig. 10 Improved gray scale

78–100%. To get a partial shot image that can be interlinked and partially repeated in turn, and then to screen out the optimal image exposure set. As shown in Fig. 11.

3.2.2 Data Analysis

The study method acquires the optimal image exposure set, which has a normal single exposure image of mid tone, a segmented exposure image set of shadow and a segmented exposure image set of highlight. Using MATLAB, according to the interlinked and partially repeated gray block of gray scale in the process of integrating the optimal image exposure set, and using the function translation transformation to make the three curves are spliced and interpolated, then fitting into a curve. The curve is ensured that the darkest detail information corresponds to a gray level in 255 and the brightest detail information corresponds to a gray level in 0. Thus, obtain the HDR image, which effectively widens the dynamic range of the image, as shown in Fig. 12. Compared with the dynamic range of normal single exposure in Fig. 12, it is not difficult to find out that, in the shadow range of density

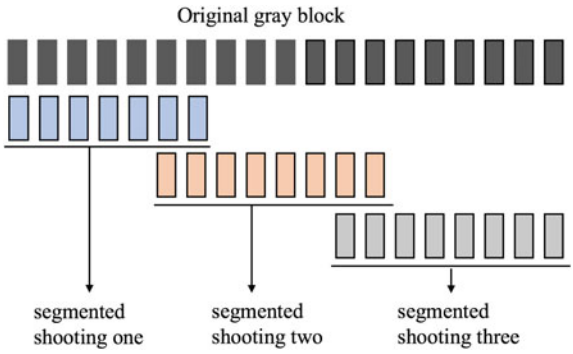

Fig. 11 Partial segmented shooting schematic diagram

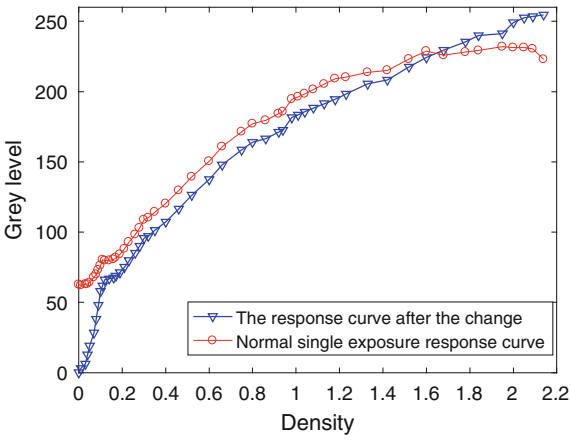

Fig. 12 Dynamic range comparison

1.1–2, the original shadow area can be distinguished by 21 gray levels, extending to 51 gray levels to describe. And in the highlight range of density 0–0.15, the original highlight area can be distinguished by 19 gray levels, extending to 79 gray levels to describe, thus details information can be well reproduced.

Experimental results show that this study acquires the optimal image exposure set, which can effectively extend the dynamic range.

4 Conclusions

The study depends on conventional digital camera as an acquisition tool, a digital acquisition method of high dynamic range image is proposed, which uses the linear dynamic range of gray scale to control single segment exposure. In the promise of ensuring synthetic image quality, this method is compared with the exposure bracketing acquisition method [1] of accurately capture scenes, which can effectively reduce the quantity of acquire images. By exposure bracketing acquisition method of accurately capture scenes, so saving storage space. Then it indirectly improves the synthetic efficiency of late high dynamic range images. The experimental result shows, in the promise of acquiring static scenes, this method can effectively solve the problem, which is the redundancy of image set by exposure bracketing, forming an optimal low dynamic image exposure set. Thus, it fully and effectively expands the dynamic range of image. It has a good theoretical guidance and engineering application value for acquiring optimal image exposure set in high dynamic range imaging.

Acknowledgements This work is funded by National Key Technology Research and Development Program of the Ministry of Science and Technology of China (2012BAH91F03).

References

1. Bai B, Liu J, Fan J (2016) Recent research in high dynamic range imaging. J Xi'an Inst Posts Telecommun 1–14. https://doi.org/10.13682/j.issn.2095-6533.2016.03.001
2. Jiang S (2015) Dynamic range extension based on multiple exposure fusion and ghost removal. Zheijang University
3. Bai B, Fan J (2015) Minimal exposure bracketing algorithm for high dynamic range imaging. J Xi'an Inst Posts Telecommun 43–47. https://doi.org/10.13682/j.issn.2095-6533.2015.05.008
4. Reinhard E, Heidrich W, Debevec P et al (2010) High dynamic range imaging: acquisition, display, and image-based lighting. Morgan Kaufmann
5. Sen P, Kalantari NK, Yaesoubi M et al (2012) Robust patch-based HDR reconstruction of dynamic scenes. ACM Trans Graph 31(6):203
6. Kalantari NK, Shech Tman E, Barnes C et al (2013) Patch-based high dynamic range video. ACM Trans Graph 32(6):202

Online Image Processing Based on Web

Zhongyue Da, Wenjie Yang, Shuai Shao, Xinggen Qian, Shun Pan, Yan Li and Bingjie Shi

Abstract In this paper, online image processing method is researched and online image processing based on server designed. First, system requirements analysis on basis of background is introduced. Then, java language, AJAX (Asynchronous JavaScript and XML) and digital image processing technology are used, and Tomcat is used as a server, Hibernate + Spring + Dorado is used as a system architecture, JavaScript and Dorado view control is used as display technology. Finally, the following three functions are implemented: (1) image upload, which is achieved by using the upload file API; (2) online image browsing, which achieves the client browser server images; (3) online image processing, including the saturation, contrast, brightness, cutting and other functions. The test results show that the system can meet the basic image processing and require very few client resources.

Keywords Image processing · Image browse · Web

1 Background

With the development of information technology, great changes have taken place in the document management [1, 2]. For example, archive file management in the government and enterprises and bill management in financial industry are undergoing information transformation. They have a lot of image that need to be browsed and processed. In the social field like QQ and Facebook, people often upload, process and browse images [3]. There is a huge demand for online image processing.

The current popular in image processing is based on client-side image processing techniques, such as image processing based on Flash or HTML5 [3]. But

Z. Da (✉) · W. Yang · S. Shao · X. Qian · S. Pan · Y. Li · B. Shi
School of Printing & Packaging Engineering, Beijing Institute of Graphic Communication, Beijing, China

P. Zhao et al. (eds.), *Applied Sciences in Graphic Communication and Packaging*, Lecture Notes in Electrical Engineering 477,
https://doi.org/10.1007/978-981-10-7629-9_32

the use of flash processing images need installing third-party plug-ins and consumes a lot of client resources [3]. And there is no consistency in browser compatibility with HTML5. If we put the image processing function on the server, the client does not need to be installed a third party plug-in and doesn't restricted by browsers [4]. Therefore, in this paper, we designed a server-based online image processing system. The system is suitable for image management and other aspects of image processing. In addition, the system can be called by other system.

2 System Requirements Analysis

The system is designed for user groups with daily image processing, but non-professional image processing [2]. The System has taken a simple and convenient interface to achieve. This design not only requires to meet the individual's basic image processing functions, but also requires a large number of image processing, which are used in archives, bills and other aspects of information management.

The specific requirements are as follows:

(1) The system can communicate with the local image, including image upload and online browsing.
(2) The system can achieve the basic properties of the image processing, such as contrast, brightness, saturation, and eraser.
(3) From an interactive perspective, the interaction of the system should be as simple as possible and reduce unnecessary cumbersome operations.

3 Test Environments

The test and development environment of the system is as shown in Table 1.

Table 1 Development environment

Demand name	Platform and tools
Hardware platform	8G memory, Inter (R) Core (TM) series processor
Development tool	Eclipse
Development language	Java, JavaScript
Compile environment	Win10 + JDK1.7
Testing environment	Chrome
Server	Tomcat
Database	MySQL

4 System Design and Implement

4.1 Overall Design

The system uses a multi-layer ORM structure (Dorado + Spring + Hibernate). This architecture is designed to facilitate expansion and development. The system implements image processing on the server side. As shown in Fig. 1, the system uses the B/S model.

4.2 System Function

According to the demand analysis, the system implements the following functions: (1) Online image browsing; (2) Image upload; (3) Online image processing. Specific process is shown in Fig. 2.

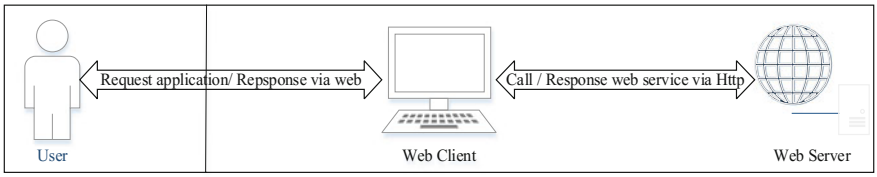

Fig. 1 Overall diagram

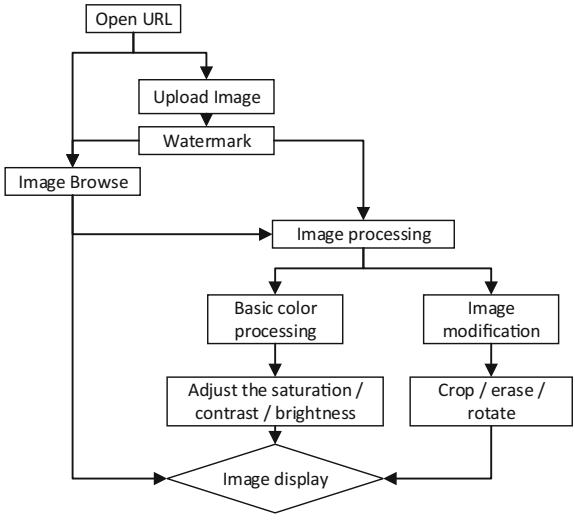

Fig. 2 Overall flow chart

Table 2 File record table

Attribute	Means	Data type	Data sources
Filename	File name	Char(40)	File
Storename	Store name	Char(40)	Systematic random
Dir	File path	Char(64)	System
Inputman	Recorder	Char(64)	System
Inputdate	Record time	Datetime	System time
Size	File size	Int	File attribute
Introduction	File introduction	Varchar	File attribute

4.3 Database Design and Implementation

In order to management the files, we designed the data record in the database. Specific field design is shown in Table 2.

4.4 Image Upload and Browse Function Implementation

4.4.1 Image Upload and Browse

To facilitate communication between users and servers, we designed the image upload and browse functions. The system uses dorado-upload control and a button on the interface to achieve user upload function. While the browser listens for click events from the button, the client will trigger upload function.

The server receives the file and saves the file to the specified folder.

In Fig. 3, the image shows the response after the click of the button. Click the button on the window that pops up to see the image selection window. Uploaded images will be added to the list on the left side of the window.

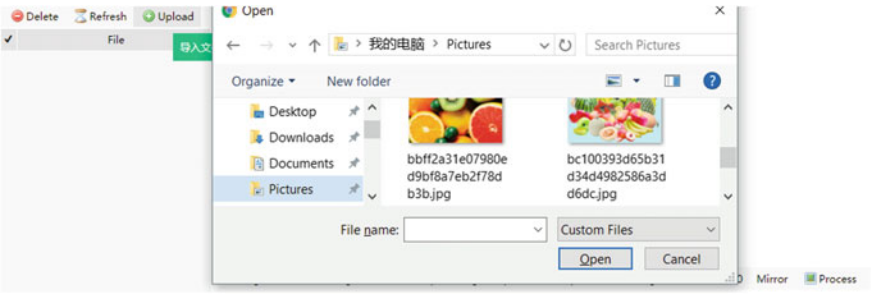

Fig. 3 File upload interface

Fig. 4 Image browsing interface

The server reads the attribute information of the file. The browser displays all the files based on the data. Users can browse images based on their needs. As shown in Fig. 4, there are three buttons and a list of image files on the left side of the window. The right sides are the original image and the image display adjustment button.

4.4.2 Implementation of Watermark

In order to protect the copyright of the image, the system designed to automatically load the watermark function. We use a light gray as the watermark color, and set transparency to 0.5f. First, the system creates a brush, and set the color, transparency and font properties and prints it to the image. On the right side of Figs. 4 and 5, watermark is in the middle of the picture, which content is "[watermark]".

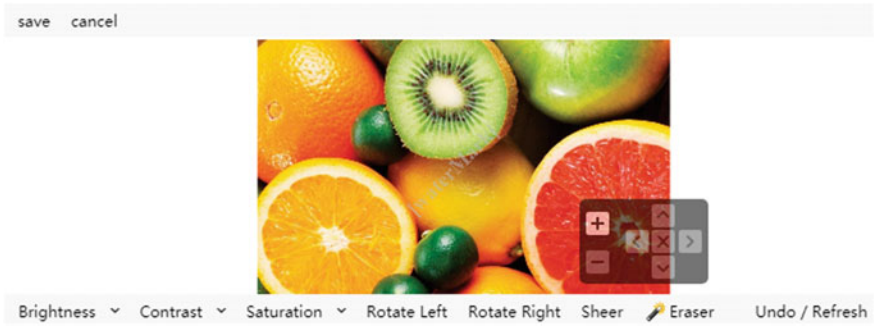

Fig. 5 Image processing interface

4.5 Online Image Processing Function Design and Implementation

4.5.1 Principle of Image Processing

On the server, the image processing is based on the color space of the pixel processing. The default color space is RGB color space. In the processing of saturation and brightness, the color space of the converted image is converted from RGB color space to HSL color space. In HSL color space, L is the brightness and S is the saturation. After the brightness and saturation processing, the image color space converted from HSL to RGB [5].

The contrast is adjusted in the RGB color space. In order to simplify the calculation, the 0.5d is taken as the average value of the image RGB.

The rotation of the image is based on the pixel position. And the principle of the eraser is to change the color of the selected area to the background color. Here is the selected area of the RGB value to white.

4.5.2 Implementation of Image Process

In order to deal with the simplicity and convenience, interface takes a different button rather than a professional processing toolbox. The client interface is laid out by container control. This interface design is relatively simple and easy to use.

On the server side, we use the Image IO class to achieve image file read and write operations and Buffered Image class to achieve the image of the property operation. For example, we use the get Sub Image method to achieve image cropping. The rotation of the image is done by using the rotate method in the Graphics2D class.

The server and the client are communicated via AJAX technology.

Figure 5, it is an image processing interface. From top to bottom, we first see the Save and Cancel buttons, which are used to determine and exit the image processing process. The middle shows pending or processed images. The bottom line is the image button. It contains brightness, contrast, rotation, sheer and other buttons.

5 Conclusions

The system realized the image upload, image online browsing and online image processing functions. After repeated testing, system consume very little client resources and does not require third party plug-ins or support for HTML5. This provides a solution for a large number of image file processing projects. However, system is greatly affected by the speed of the network. So it is suitable for use under the LAN or larger bandwidth.

Acknowledgements The study is supported by the National Key Scientific Instrument and Equipment Development Project (No.2013YQ140517).

References

1. Tang J (2016) Design and implementation of painting image management system based on web. Beijing Institute of Graphic Communication, Beijing
2. Zheng X (2015) Design and implementation of image management system based on Web. University of Chinese Academy of Science, Beijing
3. Zhu W (2013) Research on online image processing method based on HTML5 canvas technology. South China University of Technology, Guangzhou
4. Yang J, Li Y (2009) Online image processing method based on web. J Wuhan Univ Technol 31 (6):105–108
5. Burger W, Burge MJ (2009) Digital image processing java language algorithm description. Tsinghua University Press, Beijing

High Image Quality Tone Adjustment Methods for Binary Images

Jing Geng, Congjun Cao and Weiguo Wu

Abstract Graduation adjustment of a binary image is different from the grayscale image. Printing density measured value of binary image dots is regarded as the gray value of a grayscale image. In this study, based on the boundary pixel conversion around a dot, we propose the graduation adjustment scheme for image shading information. The scheme shows the effect of suppressing image blurring and folding noise.

Keywords Binary image · Graduation adjustment · Boundary pixel

1 Introduction

In the image reproduction technology, the tone, used to describe a color different from the other color characteristics, it can be the color type or shade degree.

The tone value is a measure of tone in printing technology, usually expressed by the degree and density of transmission and reflection. The dot area coverage can be used for halftone images. If the image is digital, the tone value is the gray value of the pixel.

A binary image is an image in which each pixel is not black or white, and its gray value does not have an intermediate transition. Binary images are generally used to describe text or graphics, the advantage is that they occupy less space; the disadvantage is that when the image of the characters and the scenery is represented, the binary image can only describe its outline and cannot describe the details. Use a higher gray level at this time.

J. Geng (✉) · C. Cao
Faculty of Printing, Packaging Engineering and Digital Media Technology,
Xi'an University of Technology, Xi'an, China

W. Wu
The Information Center, Xi'an Center Hospital, Xi'an, China

P. Zhao et al. (eds.), *Applied Sciences in Graphic Communication and Packaging*, Lecture Notes in Electrical Engineering 477,
https://doi.org/10.1007/978-981-10-7629-9_33

The layout of a newspaper or a printed page, similar to these binary images, has no intermediate color. Therefore, dealing with the adjustment of the image tone is difficult.

In addition, the gray value of a grayscale image is 0–255 and is divided into 256 grades. Relative to the grayscale image, the gray level of a binary image is expressed as the percentage between 0 and 100%.

The ratio of the number of black pixels in a region to the total number of pixels in the region is called the graduation adjustment of the binary image. Adjust the image density information by changing the number of black pixels in the region.

2 Previous Methods About the Graduation Adjustment for Binary Images

In the previous method [1–3], the input binary image is converted into a multi-valued image. After the conversion, the multi-valued image is adjusted according to the processing method of the multi-valued image graduation adjustment, and the processed multi-valued image is reduced to the binary image.

The problem with this method is that some of the dot density information is lost and information on the original binary image cannot be faithfully reproduced in the process of image conversion.

Another processing method is that the input binary image is divided into a predetermined block.

And the density of these blocks is increased or decreased. This treatment method, as the concentration measurement area is fixed, the concentration of the measurement region is averaged, and the degree of continuity of the associated graduation is lost in the measurement regions, thus cause problems of tone jump.

Previously, the authors proposed a contour tracking method to determine the concentration of each dot. According to the increase or decrease of the pixels of each dot profile adjust the graduation of the image.

This processing method needs to measure the concentration of each dot, thus making the calculation massive. For large images, time consumption is large, and high-speed processing has become a new topic.

3 Method of This Study

Based on previous research [4–6], this study aims to suppress image quality degradation and to improve image quality after transformation. The correlation between the block and the surrounding reference block is established.

The contours of the dots are set according to the parameters of the dotted line, the setting of the concentration measurement, and the transformation process, among others. Consequently, the early problems were improved.

3.1 Variable Concentration Detection Method

The tone adjustment process involves the display of the density information of the binary image, the existence of a variety of screen technologies, good versatility, and the concentration measurement error of a small concentration measurement block set.

To reduce the gradient error among the measurement blocks and to prevent a jump, among others, a method of calculating the correlation between the measurement block and the surrounding reference block is proposed.

In this study, the ratio of the number of black pixels in the measurement area to the number of pixels in the whole area is defined as the concentration value R.

Figure 1 illustrates eight blocks of the same size around the measurement block. The ratio of the number of black pixels of each reference block accounting for the total number of pixels of the reference block is defined as the density value *Ri* of the reference block.

According to Formula (1), the measured density r of the measurement block is calculated.

$$r = \frac{12 \times R + \sum_{i=0}^{i=7} R_i}{20} \tag{1}$$

3.2 Probability Value of the Pixel Conversion in Increasing or Decreasing the Number of Black Pixels

According to the measurement process of dot concentration mentioned above, we can see that when the measurement density r is smaller than the target density r′, the black pixels on the boundary of dot will replace white pixels until the density of the image up to the target density.

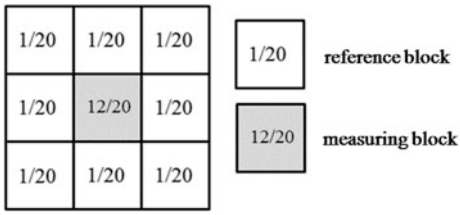

Fig. 1 Method for determination of concentration of binary image

When the dot density r is smaller than the target density r′, the white pixels on the boundary line (white pixels) of the dot are replaced with black pixels, thus raising the image density to the target density r′. Conversely, when the measurement density r is larger than the target density r′, the white pixels on the boundary of dot will replace black pixels until the density of the image down to the target density.

Therefore, obtaining the pixel conversion probability value on the contour (boundary) line is necessary. Specifically, when the measured density value r is low, the number of pixels on the boundary line is based from the difference of r and r′. The ratio of the white pixels on the boundary line is replaced by the black pixels. The transformation probability δ of the pixels is defined by Formula (2).

$$\delta = \frac{|r' - r| \times TPLS}{WPS} \quad (2)$$

(WPS : The number of white pixels on the boundary line,
$TPLS$: The total number of pixels in the area of dot).

When the measured density r is relatively high, the difference between the measured concentration r and the target density r′ is calculated. The ratio of the black pixels to the white pixels and the pixel transformation probability v are calculated from Formula (3).

$$v = \frac{|r' - r| \times TPLS}{BPS} \quad (3)$$

(BPS : The total number of black pixels on the contour line,
$TPLS$: The total number of pixels in the area of dot).

3.3 *Tone Adjustment Method Using the Probability Values of Pixel Transformations*

In this study, the binary image gradation adjustment process is performed using the pixel transformation probability value δ(v) in accordance with the contour line tracking processing so that the target density value r′ coincides with the target value.

When the dot density r is smaller than the target concentration r′, the size of the dot gradually increases, and the density of the dot increases too. The uniform random number ε (the range of values [0, 1]) is assigned to the transformation threshold κ. Then, for the detected boundary line, the calculation of $\kappa = \kappa + \delta$ is performed for each white pixel along the tracking order. When the kappa is less than 1, nothing is done. When κ is greater than 1, the corresponding white pixels are converted into black pixels, and the numbers after the decimal point of κ are discarded. The same reason is used in tracking all the white pixels on the boundary line (Fig. 2).

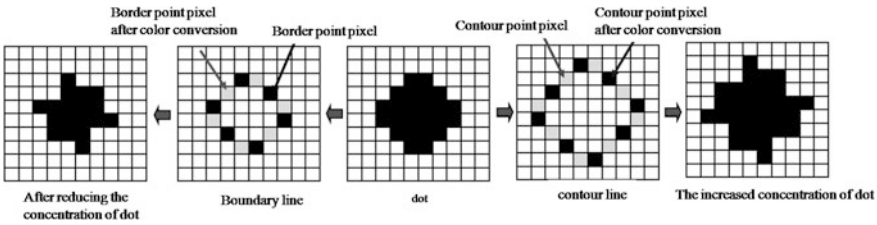

Fig. 2 Dot density conversion processing

When the dot density r is larger than the target concentration r′, the dot enlarges and the concentration is reduced. Similarly, the uniform random number ε (the range of values [0, 1]) is assigned to the transformation threshold κ. Then, for the detected boundary line, the calculation of $\kappa = \kappa + \nu$ is performed for each black pixel along the tracking order. When the κ is less than 1, nothing is done. When the κ is more than 1, the corresponding black pixels converts into white pixels, and the number after the decimal point of κ is discarded. The same reason is used to track all the black pixels on the boundary line.

The random number ε is given to the transformation threshold value. The purpose of the initial value is to track the short contours with the small pixel transformation probability δ(ν) to prevent rounding errors and suppressions in the case of density increase or decrease.

For example, the image of a certain area has the same characteristics as the dots. Following the same pattern of the processing methods, the implementation of the black pixels may increase or decrease. The increase and decrease of the black pixels may enable the possibility of a Moiré pattern. However, from the overall perspective of the image, producing Moiré fringes is difficult even when the characteristics of the closed area are the same.

From the local perspective of the image, the density of each closed area is adjusted. Rounding errors can be scattered across various parts of the image.

4 Results and Discussions

The evaluation is performed by the gradation correction processing of the image for the original image in Fig. 3, using the wavy gradation curve in Fig. 3. With the image processing method described in this paper, the original image of Fig. 4 is transformed. Compared with the previous image processing methods, the new images produced rarely produce Moiré pattern, and the quality of images has been improved.

Then, the image obtained with the standard method (Fig. 4) is evaluated against the image obtained with the proposed method, and the validation method is conducted. Figure 4 illustrates the graduation adjustment chart.

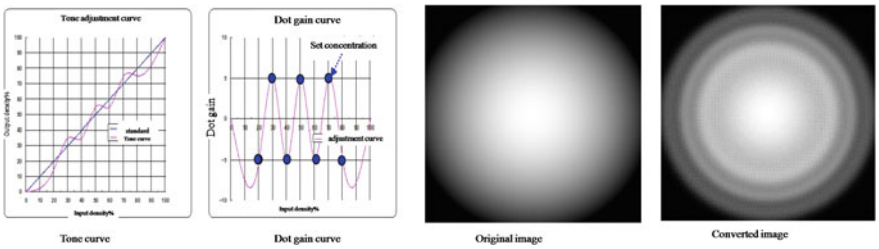

Fig. 3 Graduation evaluation image

Fig. 4 Evaluation of image: **a** density control curve, **b** density reduction portrait, **c** original image, **d** density increase portrait

Based on the original image (Fig. 4c), Fig. 4b is the result of a 10% reduction in the original image density, and Fig. 4d is the image after adding 10% of the original image density. In verifying the results, adjusting the tone of the image does not produce Moiré fringes to achieve a stunning picture quality transformation. This outcome explains the effectiveness of this study.

5 Conclusions

This paper presents a method for increasing and decreasing the edge pixel around a dot. This method realizes the tone adjustment of the binary image. Based on the distribution characteristics of edge pixels, this method makes the image clearer and suppresses the generation of image noise. In this way, the image quality of the binary image is maximally reflected.

Acknowledgements This study is funded by a Startup Foundation for Doctors of Xi'an University of Technology awarded to the first author in 2015. This work is also supported by the Key Laboratory for printing and packaging engineering scientific effort plan of Education Department of Shaanxi Provincial Government (16JS082).

References

1. Yasuo K (1997) A method of scale transformation for binary image including dithered image. Trans Instit Electron Inform Commun Eng 80(10):2723–2732
2. Yamada H (1997) A segmentation method for images containing text and halftone images. In: Proceedings of IEICE general conference, 199
3. Ken K, Naokazu A, Hiroyuki K (2012) High-quality segmentation method for binary image based on contour. J Print Sci Technol 49(1):45–52
4. Chai J, Wang Q, Liu H (2015) Threshold segmentation algorithm for printing dot microscopic image. Pack Eng 36(13):115–121
5. Zeng D, Wang Y, Lai P (2015) Binary image compression algorithm based on nine-box grid. Comput Appl Softw 32(7):259–296
6. Wang D (2015) Binary image enhancement algorithm based on space of FH neural network. Ind Control Comput 28(12):21–22

The Effect of Surface Structured Light's Phase-Shift on 3D Measurement Accuracy

Shun Pan, Dan Zhu, Yonghao Xiao, Jiong Liang, Yusheng Lian and Kun Hu

Abstract In the field of 3D vision measurement, surface structured light measurement is a new active technology, which can be widely used in the field of non-contact 3D modeling. Through the analysis of the mathematical model of the surface structured light system, a key point for the accuracy of 3D measurement is whether the spatial coordinates of pixels in encoding patterns can be accurately obtained, which is also the standard to judge the quality of coding method. Therefore, the paper adopts a coding method combining Gray code with Phase-Shift patterns. Simultaneously, a 3D vision measurement system composing a single digital camera and a single digital projector is constructed. This method is proved not only to improve the accuracy of 3D measurement, but also to be more efficient than only Gray coding method, which is apt in oil painting scanning with 3D reproduction, incomplete cultural relic's repair and construction of 3D geological model etc.

Keywords Surface structured light · Gray coding · Phase-Shift coding
3D vision measurement

1 Introduction

With the rapid development of modern computer technology and optoelectronic technology, machine vision is no longer limited to the acquisition and processing of 2D images [1]. It has been an important research direction to obtain the object's 3D data and surface topography for measurement. For surface structured light measurement, one of the most important branches, encoding technique is the key to

S. Pan · D. Zhu · Y. Xiao · J. Liang (✉) · Y. Lian (✉) · K. Hu
School of Printing & Packaging Engineering, Beijing Institute of Graphic Communication, Beijing, China
e-mail: joanlian@bigc.edu.cn

P. Zhao et al. (eds.), *Applied Sciences in Graphic Communication and Packaging*, Lecture Notes in Electrical Engineering 477,
https://doi.org/10.1007/978-981-10-7629-9_34

affect the accuracy of measurement, which has been paid much attention by researchers.

In the past decades, many scholars have taken the studies on Binary coding technology. Inokuchi [2] proposed an encoding method to replace the ordinary Binary with Gray coding because it had less fringe boundaries than that of the ordinary Binary obviously, which can effectively reduce the decoding error caused by boundary recognition error.

The projection patterns of Binary encoding are easy to be segmented, but it is often necessary to project multiple patterns for ensuring measurement accuracy, which may cause low calculating efficiency. By increasing the brightness levels of the fringe patterns, that is, using the N coding technique, proposed by Hom [3], the number of projection patterns can be reduced effectively. It achieves optimal design by finding the minimum projection patterns with the premise of satisfying certain accuracy and anti-noise performance.

The advantage of Phase-Shift coding is that it can obtain higher spatial resolution, but with the drawback that the period of projection image patterns is ambiguous to determine. Gray encoding method can accurately encode the pixels without considering the situation of the neighboring points, but it only achieves decoded projection sequence with low spatial resolution. The encoding method combining Gray with Phase-Shift proposed by Bergmann [4] is alleged to solve the ambiguity of the calculated period and to obtain higher spatial resolution, but the research in this aspect is only at the beginning.

In order to obtain the surface's complex texture information, a 3D vision measurement system based on a single digital camera and a single projector is constructed as shown in Fig. 1. Gray coding with Phase-Shift coding is adopted in it for 3D data's collection.

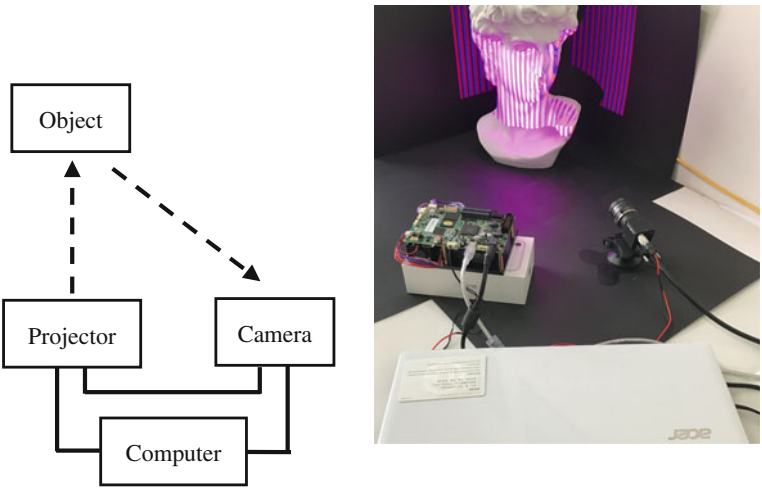

Fig. 1 The experiment system of 3D vision measurement composed of a single digital camera and a single digital projector

2 3D Measurement System of Surface Structured Light

From the projector in Fig. 1, a set of coding patterns are projected to the measured object, and then each projection pattern is captured by the camera. After the image processing system receives and preprocesses the images of the projection patterns, they are utilized to calculate the 3D coordinates of the measured object, by combination with the system parameters obtained from the step of camera and projector calibration. Finally, the 3D coordinates are reconstructed to get the 3D model of the measured object.

3 Pattern Encoding and Image Decoding

The Gray coding belongs to the temporal encoding. Normally, Gray coding method needs projection of multiple patterns, which is low efficiency. The paper adopted the coding method combining Gray with Phase-Shift, in which the Gray black and white patterns and Phase-Shift patterns are projected simultaneously. When encoding, the projective Gray and Phase Shift patterns must satisfy a relationship: the two areas must be completely matched in size; the minimum period of Gray patterns is four times of that of Phase-Shift patterns.

The code values of Gray pattern determine the length of a decoding cycle, and each decoding cycle corresponds to the space of a minimum unit of projection angle. Thus, to which unit any pixel belongs can be determined. Phase-Shift patterns are usable for the projection angles' further subdivision in each cycle. The decoding process consists of two steps: to calculate the pixels' phase and then to determine its projective angle [5–7].

3.1 Calculate the Phase of Pixels

Four Phase-Shift patterns is usually used, and 1/4 cycles shift exists between two neighboring patterns. The projective rules of Gray and Phase-Shift patterns are shown in Fig. 2. Four gray values of a pixel will be obtained, noted as I_1, I_2, I_3, I_4. The phase value φ of a pixel is calculated with Formula 1, and then added with the Gray's decoding phase in kth period. Finally, the absolute phase Ψ is obtained with Formula (2).

$$\varphi(x,y) = \arctan\frac{I_4 - I_2}{I_1 - I_3} \quad -\pi \le \varphi \le \pi \tag{1}$$

$$\Psi(x,y) = -2k\pi + \varphi(x,y) \tag{2}$$

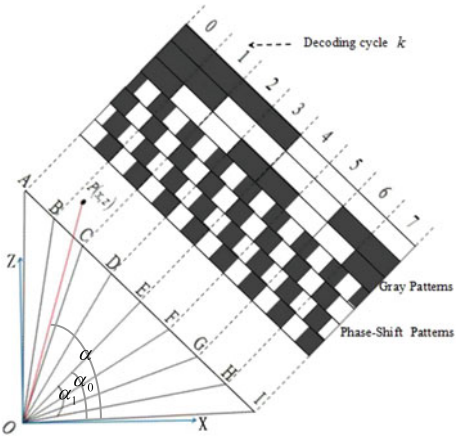

Fig. 2 The Gray and Phase-Shift patterns projection rules [8]

3.2 *Calculate the Projective Angles of Pixels*

The relationship between phase and projective angle of a pixel is shown in Fig. 2. According to the Formula (3), the absolute phase Ψ is mapped into the projective angle α.

$$\alpha = \alpha_0 + \arctan\left[\left(2^n - 1 + \frac{\Psi}{\pi}\right)\frac{\tan\alpha_1}{2^n}\right] \tag{3}$$

Note: n is the total number of Gray patterns projected.

4 Applications and Analysis

The evaluation board's points are obtained to verify the coding method's practicability. Data from Gray coding and the combining method is listed in Table 1. As shown in Fig. 3, the point cloud obtained by combining method is better than the point cloud obtained by Gray coding, and the reconstructed surface's details are more abundant.

Table 1 Data comparison between Gray coding and combining method

Instance		Points	Point's average distance (mm)	Triangle facets	Surface's details
Evaluation board (W:450 mm H:360 mm)	Gray coding	38,035	0.081	75,703	Not enough
	Gray and Phase-Shift coding	103,601	0.052	205,204	Abundant

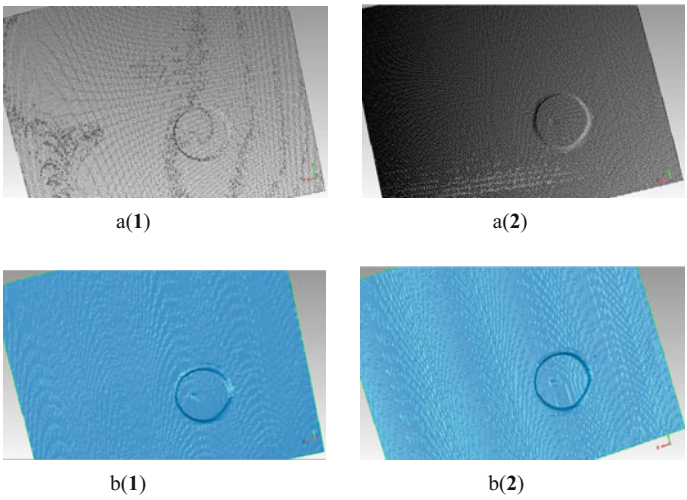

Fig. 3 Instances: evaluation board. **a**(**1**) is a point cloud obtained by Gray coding; **a**(**2**) is a point cloud obtained by combining Gray coding with Phase-Shift; **b**(**1**) and **b**(**2**) are created triangular mesh models from **a**(**1**) and **a**(**2**)

From the above analysis, it is quite obvious that combining Gray with Phase-Shift coding can obtain more details of the measured object.

5 Conclusions

The research constructed a 3D measurement system with the coding method combining Gray with Phase-Shift composed of a single digital camera and a single digital projector, which is used to scan an evaluation board. From the data analysis, the method is proved not only to improve the accuracy of 3D measurement, but also to be more efficient than Gray coding technique, which will be apt to the object with complex surface texture.

Acknowledgements This study is funded by The Practical Cultivation Plan (Scientific Research) of Beijing Municipal Commission of Education in 2016 (Grant No. 289). This work was supported by the Science and Technology Project of Beijing Educational Committee of China (Grant No. SQKM201610015005), and the Project funded by China Postdoctoral Science Foundation (Grant No. 2016M600052).

References

1. Huang (2016) Embedded structured light 3D scanning system based on DLP. Dissertation, Zhejiang University
2. Inokuchi S (1984) Range imaging system for 3-D object recognition. In: Proceedings of the 7th international conference on pattern recognition, pp 806–808
3. Hom E (1999) Toward optimal structured light patterns. Image Vision Compute, 87–97
4. Bergmann D (1995) New approach for automatic surface reconstruction with coded light. In: Proceedings of SPIE—the international society for optical engineering, pp 2–9
5. Wang (2013) Binocular three-dimension reconstruction combined with Gray coding and Phase-Shift. Comput Eng 39(5):178–182
6. Lu (2012) Key techniques for 3-D structured light photogrammetry. Comput Syst Appl 21(3): 88–89
7. Zhang (2009) Study of coding and decoding based on gray-code structure light. J Changchun Univ Sci Technol (Natural Science Edition), 636–638
8. Yin (2007) The development of 3D measurement technology based on structured light by combining Gray code with Phase-Shift. J Harbin Univ Sci Technol, 6–7

Part III
Digital Media Technology

The Research and Application of Augmented Reality in 3D Interactive Books for Children

Chunxia Dong and Zhanjun Si

Abstract This paper studies the application of augmented reality technology in children's 3D interactive books, which can bring interesting, interactive, immersive and realistic reading experience for children. First, the relevant audio, video and other materials were processed by multimedia software. And the three-dimensional models were created by 3ds Max. Then, the multimedia resources and 3D models were integrated in Unity 3D. Finally, the recognition function was realized with the help of Vuforia SDK, and the interactive functions were accomplished by writing scripts. The result was that an augmented reality mobile application based on android platform was developed as well as a book was designed. By scanning the image of the book with the mobile camera, it can present animals' three-dimensional models. Users can watch the animation by clicking the button. The application of augmented reality technology in children's books makes its expression rich and vivid. It also can achieve the purpose of edutainment. Besides, combining this technology with publishing industry can help to promote the transformation and upgrading of the publishing industry.

Keywords Augmented reality · Children's books · Three-dimensional interaction Mobile application

1 Introduction

With the advent of the new media era and the development of computer level, the dissemination way of information has changed over and over [1]. Augmented reality technology has the feature of combining virtual world and reality [2]. And because of its powerful reproduction function, novel mode of operation and the unique communication experience, it has been widely used in many fields, such as

C. Dong · Z. Si (✉)
College of Packaging & Printing Engineering,
Tianjin University of Science & Technology, Tianjin, China
e-mail: szj@tust.edu.cn

P. Zhao et al. (eds.), *Applied Sciences in Graphic Communication and Packaging*, Lecture Notes in Electrical Engineering 477,
https://doi.org/10.1007/978-981-10-7629-9_35

game entertainment, medical education, military training, industrial training, product marketing and so on [3, 4]. Augmented reality technology can integrate digital media resources into publishing, which can break traditional way of reading books, and makes up the weakness of books, such as textual, unidirectional and limitations of expression, promotes the process of digital publishing. However, the AR books are vivid and interesting, which makes children easy to understand and memory, and improves children's initiative and enthusiasm of reading [5]. In the era of new media, bending the augmented reality technology into publishing is beneficial to combine the emerging technology with publishing industry, as well as promote the digital transformation and upgrade of publishing industry [6].

2 Augmented Reality Technology

Augmented reality was based on virtual reality technology. With the help of computer graphics and visualization technology, the image which is not present in the real environment is accurately located in the real environment through the computer sensing and image recognition technology. This relies on the display device to integrate virtual objects with the real environment, and provides a real sense of new environment to users [7]. Augmented reality system is usually composed of 6 parts: image acquisition, recognition and tracking, 3D registration, virtual and real combination, display terminal, human-computer interaction [8]. The system framework was shown in Fig. 1.

At present, there are many mainstream development tools, such as AR Toolkit, Wikituted, Vuforia, Metria, HiAR, Easy AR and Void AR. AR Toolkit cannot identify the natural feature points. Metria's operation is simple, but it has single effect. Wikituted has the advantage of location-based. The domestic AR tools still have the shortcomings of low accuracy and poor applicability. Vuforia uses feature points to detect. The identifier is not limited by the complexity of the environment, and the tracking effect and the compatibility are good. This application was based on the Vuforia SDK to develop the augmented reality applications.

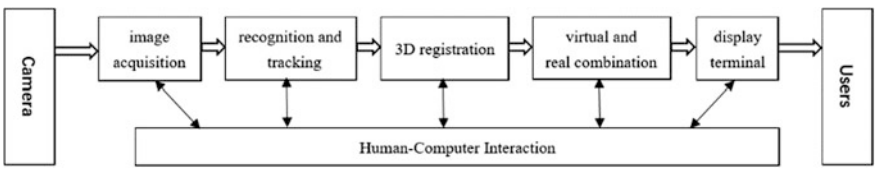

Fig. 1 The system framework of augmented reality

3 Designing and Implementation

There are two parts in the production of augmented reality book. One is the design of paper books, and the other is the development of the application program. First of all, the content and preferences were investigated around children. According to the results of survey, the content, style, printing and binding of the book were determined. In the production, the book was typesetting with the help of graphic design software. Audio, video, 3D models were edited and processed by multimedia software. Through the comparison and analysis, Vuforia SDK which has strong stability was selected. At last the application was developed by Unity 3D and Vuforia SDK. The application can realize the recognition of text. After scanning the picture, it can show the three-dimensional model. And the model can be controlled by fingers. The design ideas were shown in Fig. 2.

3.1 Make Paper Books

"Dinosaur ABC" is for children of 3–5 years old. The theme of the content was set in prehistoric large animals—dinosaurs. Many children like dinosaur, but they have

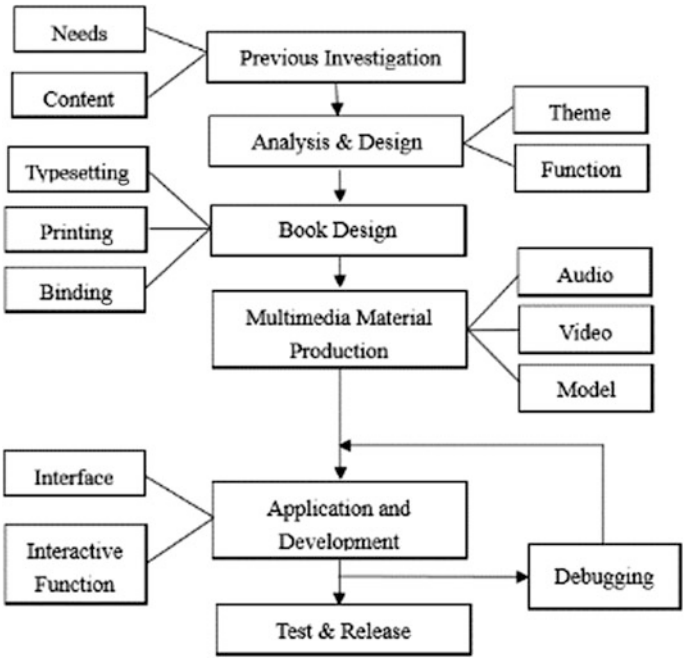

Fig. 2 Design ideas of the augmented reality book

extinct now and cannot be seen in the zoo. It is difficult for children who want to know different types of dinosaur to distinguish through two-dimensional pictures and text description.

Children's books are generally selected small and medium-sized format. The length-to-width ratio is 1–1.4. The book of "Dinosaur ABC" chose 32(184 * 130) format. The paper was selected to coated paper with 280 g, which can ensure that the paper was crisp and the whole book was not too heavy. At the same time, coating on the paper surface increased the books' stain resistance and water resistance. At Last, the two-hole loose-leaf nail binding method was taken to facilitate observation and separation.

3.2 Making Multimedia Resources and 3D Models

Audio was recorded and processed by Audition which is non-linear processing software. In this design, the dinosaur's name and introductory text was recorded. After recording, audio's noise was reduction by using "noise reduction" to ensure that the sound was clear. And the video was processed by Premiere which is the mainstream software currently. The video was cut, integrated and processed to rich their presentation. The audio and video were exported to mp3 and mp4 format that Unity supported at last.

The 3D models were mapped and optimize by 3ds Max. The texture map of dinosaur models were baked into image. Then models were returned by supporting function. Models which had many facets were converted to small amount of facets, so that the model can take up less resources and show more details. At the same time, it can reduce the system cache. At last, the "scene units into" selected "cm" while the models were exported to ensure the models' size were unified in Unity.

3.3 Recognition Function

3.3.1 Image Recognition

The function of image recognition is to match the existence identification images with the images that camera captured, and then coming out of the corresponding three-dimensional model. In order to improve the recognition accuracy, the identification images should have high contrast, high resolution and distinct outline. The application used Vuforia engine to identify and track the identification images' feature points. The more feature points, the better recognition effect. The feature of dinosaurs' recognition image is shown in Fig. 3.

In the production, the Camera that comes with system was replaced by Vuforia AR Camera. And the information was given to recognition images' in Image Target Inspector. Then the 3D model was imported into the scene. At last,

Fig. 3 Recognition of features

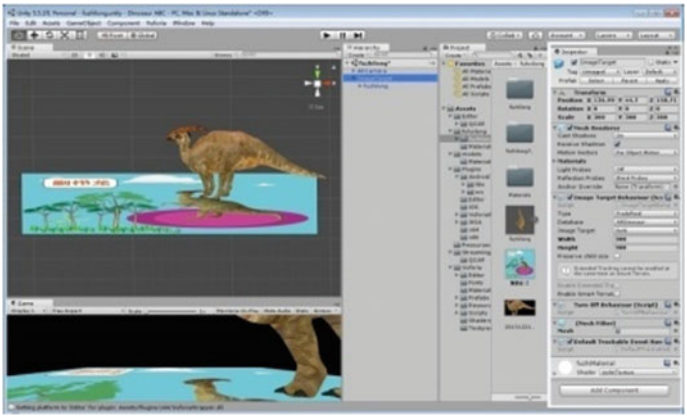

Fig. 4 Settings of image recognition

put Image Target as the parent class, and set its position rotation angle and zoom size in the scene. The interface is shown in Fig. 4.

3.3.2 Character Recognition

This function is that the audio was played after the camera scanning the text. First, calling the Image Target control and put it into the scene. Then, opening the recognition function of the image's. Next, creating an empty object as the image's child object and associating with the Image Target. At last, creating a sound control script to come true the character recognition.

Fig. 5 The recognition effect

3.3.3 Video Recognition

This function is that the video appeared at a specific location after the identification was response. First, the video was imported into Unity, and the recognition image was set for Image Target. Then, the video control was placed on the child object and the video "playback Behavior" script was loaded. In addition, video recognition also requires the main camera to load the script, so that it has the interactive effect of playing the video.

3.4 Test and Release

After implementing the interaction functions, the program files were matched in "Build Settings". The scenes were added in turn. Then, Clicking the button of "Build" to release the application. After releasing, the installation package was installed in the phone. Finally, the fluency and recognition of the system was tested. After modified, the final version was released. The final result was shown in Fig. 5.

4 Conclusions and Prospects

The augmented reality application combined with the book of "Dinosaur of ABC" can show different types of dinosaurs. It can bring multimedia and multi-dimensional interaction reading experience to children through the sounds, 3D models, animations and interactive operations. It also can improve children's interest in reading and help them understanding and remembering the habits and characteristics of dinosaurs. The traditional books combined with the augmented reality application not only can retain the reader's reading habits of traditional publications, but also expand the books' scope to three-dimensional and multi-dimensional interaction. In addition, the rich audio, video, animation and other effects also can increase books' information, sublimating its entertainment.

References

1. Sun Y (2014) The application of digital media in all media era. West China Broadcasting TV, 21(09):23
2. Xia SQ (2013) The application and realization of augmented reality technology in children's publications. Beijing University of Technology, Beijing
3. Shi AB, Zhang YZ (2016) The rise of virtual reality/augmented reality and the turning of traditional journalism. The Journalist Monthly 34(01):34–41
4. Wu F, Zhang L (2012) A survey on development and application of augmented reality. Comput Eng Appl 8(34):8319–8325
5. Tomi AB, Rambli D (2013) An interactive mobile augmented reality magical playbook: learning number with the thirsty crow. Procedia Comput Sci 25:123–130
6. Liu YH (2015) Analysis of book publishing in the new media era. J News Res 6(07):109
7. Tang Y (2013) Research of CNC machining display technology based on augmented reality. Huazhong University of Science and Technology, Wuhan
8. Gao Z (2016) Research on museum services using mobile augmented reality technology. Shenyang University of Technology, Shenyang

Research and Implementation of Autolayout and Its Third Party Framework Masonry Based on IOS Development

Chao Chen, Xin Zhen, Kangye Wang, Aibin Huang and Caifeng Liu

Abstract IOS Autolayout technology used to solve the UI visual unit or element layout, and arrangement of the problem which can be a perfect solution to adapt to different sizes of the screen, and solve the problem of vertical and horizontal screen, and make programming no longer boring, so it is widely accepted by programmers. The core of Autolayout is the constraint. Research and the implementations of Autolayout's constraints were introduced. Then, the basic properties and instructions of Masonry, which is now widely used, were introduced. Finally, through a specific interface in Wisdom Life App and comparative analysis the results of using Masonry or not, reflecting the Masonry's advantage in automatic layout.

Keywords IOS · Autolayout · Masonry · Constraint

1 Introduction

IOS is an operating system which released by Apple in January 2007, the original name for the "iPhone Runs OS X". In March 2010, Apple released the first beta development kit, renamed it "iphone OS", until June 2010, Apple will "iphone OS" renamed "IOS". With the gradual popularization of smart phones, Apple mobile phone as a leader in the smart phone industry, it is firmly occupied the leading position in the mobile phone industry, its independent development system IOS contributed.

IOS development mainstream programming language is Objective-C and Swift. Objective-C is primarily used for IOS development. Objective-C is based on the C, adding object-oriented features of the programming language. Swift is Apple's new development language released in 2014. Swift is still Object-C, but Swift greatly reduces the development threshold. The implementation language of this case is Objective-C [1].

C. Chen · X. Zhen · K. Wang · A. Huang · C. Liu (✉)
Hangzhou Dianzi University, Hangzhou, China

P. Zhao et al. (eds.), *Applied Sciences in Graphic Communication and Packaging*, Lecture Notes in Electrical Engineering 477,
https://doi.org/10.1007/978-981-10-7629-9_36

Equipment	Size	Pixels	Point
iphone\iphone3C\iphone3CS	3.5 inch	320 * 480	320 * 480
iphone4\iphone4S	3.5 inch	640 * 960	320 * 480
iphone5\iphone5C\iphone5S	4.0 inch	640 * 1136	321 * 568
iphone6\iphone6S	4.7 inch	750 * 1334	375 * 667
iphone6 plus\iphone6S plus	5.5 inch	1242 * 2208	414 * 736
ipad\ipad2	9.7 inch	768 * 1024	768 * 1024
ipad3\ipad4\ipad air	9.7 inch	1536 * 2048	768 * 1024
ipad Mini	7.9 inch	768 * 1024	768 * 1024
ipad Mini2(Mini with retina display)	7.9 inch	1536 * 2048	768 * 1024

Fig. 1 The size of each types of iPhone application

The IOS interface development mainly in the following stages:

The first stage: in the iphone1-iphone3gs era, window size fixed (320, 480), we only need to simply calculate the relative position.

The second stage: iphone4-iphone4 s era, Apple launched the retina screen, but the window size unchanged, still (320, 480).

The third stage: in the iphone5-iphone5 s era, window size into (320, 568), then autoresizingMask came in handy.

The fourth stage: in the iphone6 + era, until now, each generation of new iphone window screen size have changed, as shown in Fig. 1, Apple's screen size has a luxury family members.

With the IOS device screen size increases, for an application, it must meet the different models of different sizes of Apple devices can run. And Apple since the IOS6 launched Autolayout automatic layout technology, the perfect solution to this problem. Therefore, for IOS developers, whether it is pure code development or Xib/StoryBoard development, the use of Autolayout is imperative.

2 Autolayout Overview

2.1 Brief Introduction

Autolayout is a layout technology, dedicated to the layout of the UI interface. It is used to replace the frame layout in the face to meet the size of the screen a variety of deficiencies. Autolayout and Frame positioning, the same need to provide location and size information. Unlike Frame, however, it does not provide (x, y, width, height) these direct position data, but rather deduce the corresponding size and position by various constraints. That Frame is absolutely positioned, and Autolayout is relative positioning.

2.2 Autolayout Implementation Introduction to Masonry

There are two ways to implementation Autolayout. One is based on IB or StoryBoard implementation, the other is a pure code to achieve.

(1) AutoLayout + IB:

When the Autolayout just came out, AutoLayout + IB implementation mode has been used all the rage [2]. Apple App's development tool Xcode will support UI interface design of the automatic layout properties of the package, through the visualization of the tool operation, making the programmer in the IB on the layout, only need for each View Autolayout attributes to fill out the appropriate. The AutoLayout + IB have the advantage of being visualizable and easy to implement. However, if there is particularly large number of subviews on an interface, using AutoLayout + IB will be cumbersome and prone to Bugs. Of course, there are still many programmers still through this model to achieve part of the program UI interface layout.

(2) Pure code to achieve:

For Autolayout, the core is the most fundamental constraint. The most common constraint in IOS is NSLayoutConstraint, which is used to set the relationship between the view tree in the view tree, its size, and so on. We generally create a constraint through AutoLayout the core formula (formula 1).

$$Obj1.property1 = obj2.property2 \ * \ multiplier + constant\,value \tag{1}$$

Where obj1.property1 represents a property of the target object, obj2.property2 represents a property of the reference object, multiplier represents the magnification, and constant value represents the deviation.

However, a View generally has upper, lower, left, right, and four attributes, so when you implement the View layout by code, each View requires four such constraints. So, by NSLayoutConstraint to add constraints on the View is very cumbersome.

3 Masonry

Autolayout automatic layout technology in IOS6 has been introduced, since it is too cumbersome to add constraints through the official NSLayoutConstraint, so it has not been accepted by the majority of developers when it just came out. Until later, the emergence of third-party framework Masonry is only to completely change this embarrassing situation [3].

Masonry is a third-party automatic layout framework that encapsulates the system NSLayoutConstraint, which is provided to the developer API in a chained

```
@property (nonatomic, strong, readonly) MASConstraint *left;
@property (nonatomic, strong, readonly) MASConstraint *top;
@property (nonatomic, strong, readonly) MASConstraint *right;
@property (nonatomic, strong, readonly) MASConstraint *bottom;
@property (nonatomic, strong, readonly) MASConstraint *leading;
@property (nonatomic, strong, readonly) MASConstraint *trailing;
@property (nonatomic, strong, readonly) MASConstraint *width;
@property (nonatomic, strong, readonly) MASConstraint *height;
@property (nonatomic, strong, readonly) MASConstraint *centerX;
@property (nonatomic, strong, readonly) MASConstraint *centerY;
@property (nonatomic, strong, readonly) MASConstraint *baseline;
```

Fig. 2 Attributes of Masonry

way, concise, and highly readable. System AutoLayout support operations, Masonry support, compared to the system API function, Masonry is beyond Fig. 2.

3.1 Masonry Attribute

Masonry comes from the Autolayout package, so its attribute is equivalent to Autolayout provides the attributes, divided into two, size and location.

(1) Size: Width and Height.
(2) Location: top, bottom, left, right, leading, trailing, centerX, centerY, baseline.

The properties of Masonry are shown in Fig. 1.

3.2 Basics of Masonry API

(1) First Section

Add a constraint to mas_makeConstraints ()

Mas_remakeConstraints () removes the previous constraint and re-adds the new constraint.

Mas_updateConstraints () updates the constraint.

(2) Second Section

The equalTo () parameter is an object type, typically a view object or a coordinate system object such as mas_width.

Mas_equalTo () and the above function is the same, the parameters can pass the basic data type object, can be understood as more powerful than the above API.

Mas_makeConstraints is to add constraints to the view, there are several constraints, namely, margin, width, height, left and right lower distance, the baseline. After the addition of constraints can be amended to correct the offset (offset) correction

and multiplied By (magnification) correction. Similarly, mas_remakeConstraints () is to remove the previous constraints, re-add a new constraint. Mas_updateConstraints () is different from mas_remakeConstraints (), it does not have to clear the constraint, just change the constraint on the basis of the previous constraint.

3.3 Masonry Basic Use Steps

Step1: Create all the child View, and load it into the parent view.
Step2: Use the Masonry special Block statement to add constraints to each subview, each of which is a Block.

3.4 Masonry Use Attention

(1) You must add a view to the parent view before you can add a constraint to it. Otherwise the system will report an error that you added a constraint to a view which does not exist.
(2) The difference of using masequalTo () and equalTo (): equalTo () parameter is the object type, the general view object or mas_width such coordinate system object; mas_equalTo () and equalTo () function the same parameters can pass the basic data Type object, can be understood as more powerful than the above API.
(3) Pay attention to the method 'with' and 'and', these two method do not actually do any operation, only to read up a little fluent. For example: make.left.and. right.equalTo (self.view); and make.left.right.equalTo (self.view); are exactly the same, but obviously add 'and' method the statement is more readable.

4 Application of Msonry in Wisdom Life

Wisdom Life is an app which based on IOS platform, it uses the Objective-C language and is developed by pure code. Initially run only on the iPhone5 s (size is equalto (568, 320)) simulator, so all view sizes is set using the specific frame values. Example selects a basic view of the application for analysis.

Figure 3 is a common interface in the application, which shows the recipe for breakfast at the mountain base restaurant on Tuesday. Figure 3a, b are designed using the specific dimensions of Frame, and Fig. 3c is designed using Autolayout's third-party framework, Masonry. Figure 3a is the result of running on the iPhone5 simulator, Fig. 3b, c are the interfaces that are running on the iPhone7 emulator.

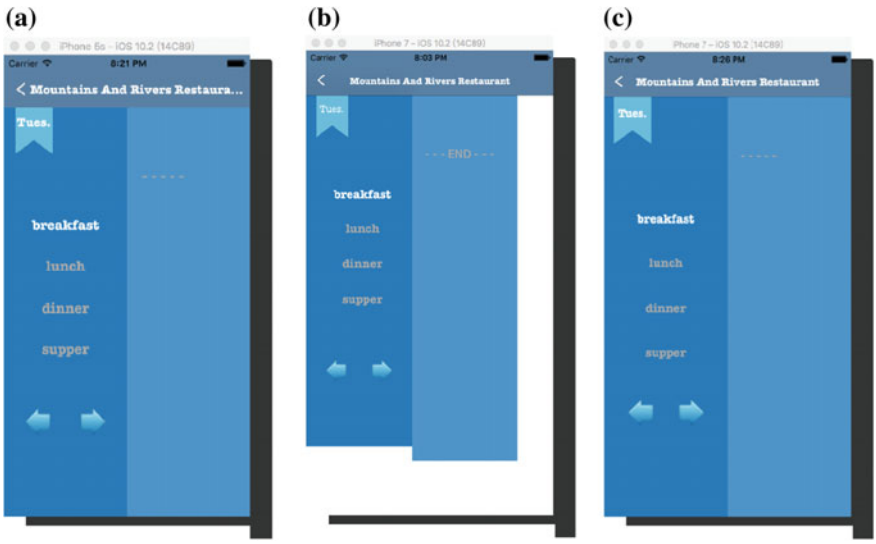

Fig. 3 One View of smart life app

As can be seen from the results shown in Fig. 3a, b, when using the frame to absolutely position the view of the view class, only on the iPhone (for example, iPhone5 s) with a screen size of (568, 320) to be perfectly displayed on the screen. If the phone screen size changes, such as running on the iPhone7, the screen border appears extra white, that is, the background color of the screen, making the interface not coordinated and unsightly.

So I view all the sub-view through the Autolayout way to re-layout, the use of Masonry statement on the interface of all sub-view were added constraints, and ultimately achieved in all iPhone devices can be perfectly fit the screen, as shown in Fig. 3c shows the final renderings of the interface on iPhone 7.

5 Conclusions

Autolayout in the current IOS development has been very mature, but just joined the ranks of IOS development programmers, Autolayout is necessary to master the core technology. This article through the wisdom of life application app example to prove the effect of Masonry, reducing the amount of cumbersome code, greatly improves the development efficiency of the app.

References

1. Chung C (2011) Pro objective-C design patterns for IOS. China Comput Commun 6:70–80
2. Erica S (2013) IOS Auto Layout Demystified. Addison-Wesley Educational Publishers Inc. (2):88–94
3. IOS Auto Layout with Masonry. https://www.infoq.com/news/2014/02/ios-auto-layout. Accessed 20 Apr 2017

The Applied Research of Mobile Augmented Reality in Prints

Shenghui Li, Ruizhi Shi and Hui Ye

Abstract In this paper, we analyzed the characteristic and principles of image cloud recognition, and build the applied process of Mobile Augmented Reality in prints combined with Mobile Augmented Reality. Based on the analysis and research of Mobile Augmented Reality and image cloud recognition's technical features, an interactive prototype system for apartment model also is developed with the help of Qualcomm AR open SDK. The conventional paper prints simply present information by physical images or text, whereas the new prototype system developed in this paper can provide more accurate and diversified information to individuals. In order to make the Mobile Augmented Reality more effective in printing industry, suggestions are provided for further implementation.

Keywords Mobile terminal · Cloud computing · Augmented reality
Image recognition

1 Introduction

The conventional prints always play a vital role in the process of information presentation, transmission and preservation. As mobile technology becomes an essential in daily life, the demands of personalized service on the rise, leading to the conventional prints cannot meet the diverse needs of people. However, the conventional prints have some distinct advantages, such as low-cost, easy saving and easy reading [1]. Thus, how to combine the advantages of mobile technology and conventional prints has become a new research direction.

S. Li · R. Shi (✉) · H. Ye
Zhengzhou Institute of Surveying and Mapping, Zhengzhou, China
e-mail: ruizhishi@sina.com

P. Zhao et al. (eds.), *Applied Sciences in Graphic Communication and Packaging*, Lecture Notes in Electrical Engineering 477,
https://doi.org/10.1007/978-981-10-7629-9_37

One of the most recent technological advances that could be used to combine the advantages of mobile technology and conventional prints is Augmented Reality (AR). Augmented Reality made possible an innovative way of information acquisition by providing additional virtual objects to the real prints [2]. In this paper, we analyzed the characteristic and principles of Mobile Augmented Reality and build the applied process of Mobile Augmented Reality in prints. Based on the applied process, we developed an interactive prototype system for apartment model with the help of Qualcomm AR open SDK.

2 Image Cloud Recognition

Compared with computer equipment, the configuration of mobile phone is lower. So the algorithm's efficiency should be taken into account firstly. Many researchers try to improve the efficiency by reducing the computational complexity of recognition algorithm [3]. However, with the development of cloud computing technology, we can put the work of image recognition in the cloud server. In this way, not only the load of the mobile phone can be alleviated greatly, but also the data updating and maintenance become more convenient [4].

Figure 1 illustrates the process of image cloud recognition. The mobile phone captures images by camera, and sends the feature information to the cloud server after image preprocessing. The cloud server implements the image feature extraction, image recognition and database access and return the recognition result to the mobile phone.

During the transmission process of image feature information between mobile phone and server, the data exchange is very little, because we just transfer the image feature information, rather than the entire image file. Hence, with the improvement of mobile network, the speed of the mobile network has already been able to meet the requirements of image cloud recognition.

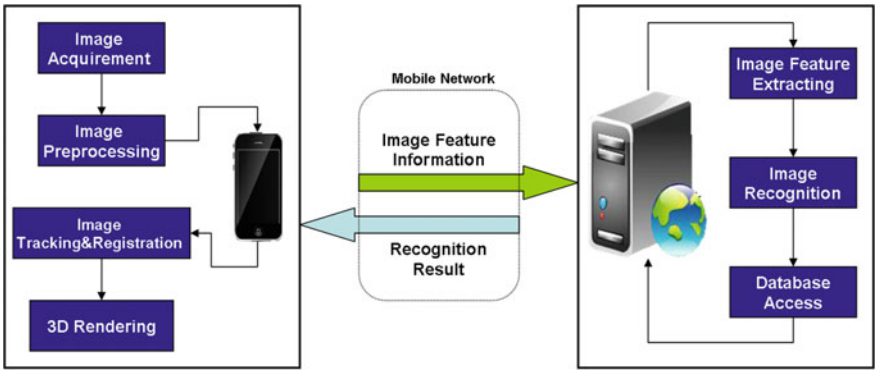

Fig. 1 Process of image cloud recognition

3 Application Analysis of Mobile Augmented Reality

Augmented reality refers to technologies that project digital materials onto real world objects. Augmented reality provides a better way for information access, which might not be satisfied by traditional approaches such as prints or handheld displays. Additionally, as the traditional augmented reality technology has been planted into mobile devices, Mobile Augmented Reality can be used in many fields, such as printing & publishing, mobile navigation and mobile game.

3.1 Applied in Printing & Publishing

In the field of printing, Mobile Augmented Reality can be used for outdoor advertising, children's books, newspapers or magazines, etc. Figure 1 shows two application examples of the Mobile Augmented Reality. As shown in Fig. 1, by combining Mobile Augmented Reality technology with conventional prints, the prints become more lively and interesting. Mobile Augmented Reality has the capability to significantly change the way in which information delivered from prints to individuals Fig. 2.

Mobile Augmented Reality recognizes and track images which printed on the prints, and process in real time [5]. According to the change of relative position between prints and mobile phone, the virtual information also is adjusted in real time, as if the virtual information indeed exists in the surrounding environment. Furthermore, by touching the screen, the user can control the virtual objects and get more information about the prints.

Fig. 2 Application of augmented reality

Table 1 Comparison of AR SDK

AR SDK	Development platform		Operating environment			Research & development cost	Performance
	Mac	Window	Android	IOS	Web		
Metaio	√	√	√	√	√	High	Better
Vuforia	√	√	√	√	×	Middle	Best
ARToolkit	√	√	√	√	×	High	Better
EasyAR	√	√	√	√	×	Low	Good

3.2 Mobile Augmented Reality Technology

Mobile Augmented Reality applications and systems should satisfy most or all of the below mentioned properties [6]:

- Sense properties about the real world.
- Process in real time.
- Output information to the user, including via visual, audio, and haptic means, often overlaid on the user's perception of the real world.
- Provide contextual information.
- Recognize and track real-world objects.
- Be mobile or wearable.

In order to create Mobile Augmented Reality applications, some of the most popular Augmented Reality Software Development Kits (AR SDK) are listed below Table 1.

Since the present study aims to use AR SDK as a development tool in the field of printing, and there are some limitations from the writer's side related to programming skills. Based on the comparison of AR SDK which listed in Table 1, the AR SDK that has been chosen is Vuforia. It provides an easy way to use environment that does not require programming skills.

3.3 Establish the Application Process of Mobile AR

Since AR is considered to be a relatively new technology, the applied research in prints is in an embryonic stage too. Therefore, based on the analysis of the applied requirement in prints and the technology characteristics of Mobile Augmented Reality, we established the application process of Mobile Augmented Reality in prints, as shown in Fig. 3.

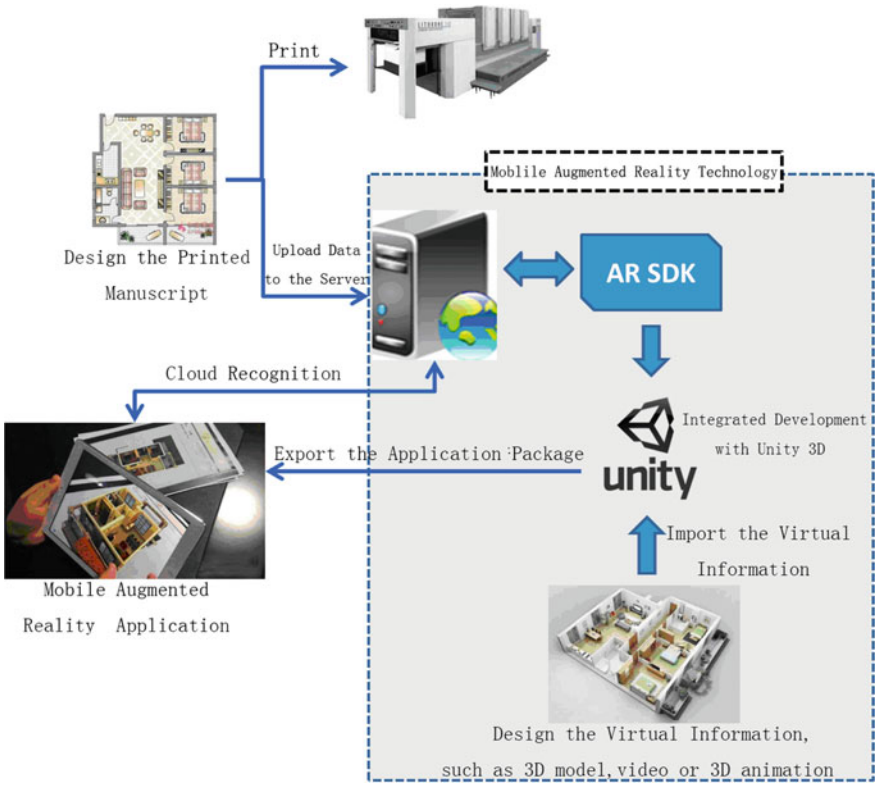

Fig. 3 Application process of mobile augmented reality

The application process includes three steps:

(1) Designing of Printed Manuscript

Because the current recognition algorithms are mostly using the geometrical characteristics of the image for image recognition and tracking, so the efficiency and robustness of the algorithms depend on the amount of feature points in the image. In order to increase the amount of image feature points, we should ensure that the printed manuscript has more geometric features. Then the manuscript could be printed and uploaded to the server respectively for image recognition.

(2) Application of Mobile Augmented Reality Technology

Mobile Augmented Reality technology is the key part of the whole process. We choose Vuforia AR SDK to create the AR content, and the choice of development programs is also an important aspect. The platform that has been chosen for creating the mobile application is Unity 3D, which enables the user to create mobile application with some basic programming skills.

(3) Deploy the Application to Mobile Phone

We develop the mobile application in Unity 3D, and set up the basic environment necessary for deploy, then build the application in a mobile phone through USB. Eventually, the augmented reality application can be executed in the mobile phone.

4 System Implementation

Based on the application process of mobile AR, we developed an interactive prototype system for apartment model. By scanning the image printed on paper, the system allows users to observe 3D apartment model from different directions. Moreover, users can control the lighting effects and housing decoration of 3D apartment model by mobile phone, so they can get more information about the apartment.

4.1 Development and Running Environment

The development tools we used in this paper include Unity 3D, Vuforia SDK 4.0 and Android SDK. Table 2 shows the details of the hardware and software involved in this paper.

Table 2 Development and running environment

Development platform			Running environment	
Hardware	Operating system	Development tools	Hardware	Android version
Personal Computer Memory:4G Processor: Core i5-750	Windows 7 Professional	Development Platform: Unity 3D 4.6.3 AR SDK: Vuforia SDK 4.0 Android SDK platform: android-23	Android-phone Memory: 3G Camera: 13-megapixel camera	Android 6.0.1

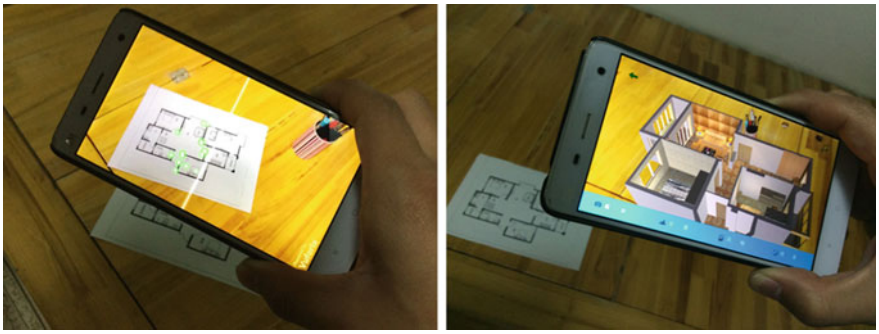

Fig. 4 Image acquisition and recognition

4.2 Operation of the Mobile Application

After the development of prototype system, we install the mobile application on the mobile device. Because the images feature information must be sent to the server for cloud recognition, so the mobile network should be kept open in the process of software running. If the recognition fails, the camera will continue to scan images, as shown in Fig. 4(Left). If the recognition is successful, a virtual 3D model will be superimposed upon the prints, as shown in Fig. 4(Right).

As shown in Fig. 5, users can observe the 3D apartment model from different direction and different distance by moving the mobile camera, so they can get more

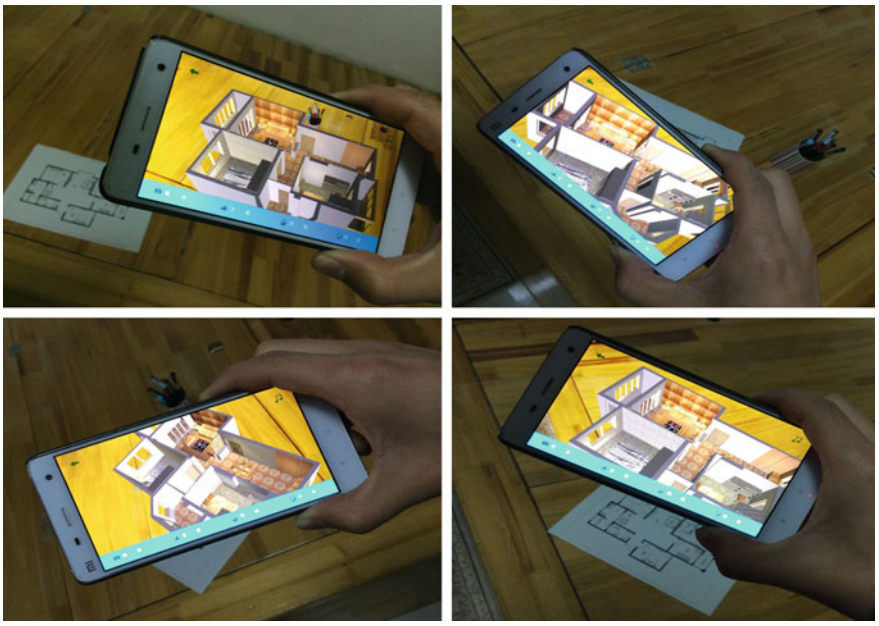

Fig. 5 3D model from different perspectives

information about the structure of real apartment, which could not get by conventional paper prints. Furthermore, users can rotate the 3D apartment model, or change the lighting effects and housing decoration to observe the apartment in a variety of decorating styles.

5 Conclusions

In this paper, based on the Mobile Augmented Reality and image cloud recognition technique, a prototype system for apartment model was developed and evaluated. Unlike the conventional paper prints which simply present information by physical images or text, the method proposed in this paper can provide a variety of information in a more accurate and faster way.

Mobile Augmented Reality is an emerging technology, which have potentially broad application in many fields. In the field of printing, application of this technology is still at an early stage. Therefore, how to further perfect the flow of application in the field of printing, establish an integrated application system, improve the computation accuracy and computation efficiency of relevant algorithms, and still need further analysis and research.

References

1. Morrison A, Mulloni A, Lemmelä S et al (2011) Collaborative use of mobile augmented reality with paper maps. Comput Graph 35(4):789–799
2. Billinghurst M, Clark A, Lee G (2015) A survey of augmented reality. Found Trends Hum-Comput Inter 8(2–3):73–272
3. Li S, Shi R (2016) The comparison of two image matching algorithms based on real-time image acquisition. In: Advanced graphic communications, packaging technology and materials, vol 369, pp 241–248. https://doi.org/10.1007/978-981-10-0072-0_31
4. Hashem IAT, Yaqoob I (2015) The rise of "big data" on cloud computing: review and open research issues. Inf Syst 47(47):98–115
5. Wagner D, Reitmayr G, Mulloni A (2010) Real-time detection and tracking for augmented reality on mobile phones. IEEE Trans Visual Comput Graph 16(3):355
6. Roesner F, Denning T, Newell BC (2014) Augmented reality: hard problems of law and policy. The workshop on usable privacy & security for wearable and domestic ubiquitous devices. ACM, pp 1283–1288

Research and Implementation of Online Training Cross-Platform Mobile Application Based on PhoneGap

Xin Zhen, Aibin Huang, Chao Chen, Kangye Wang and Caifeng Liu

Abstract At present, there are many kinds of mobile operation platforms on the market, and the application software running on each operating system is independent and incompatible, which causes the long-time development period of multi-platform application. We propose a cross-platform mobile application scheme based on the study of the current mobile application development solution. A power plant enterprise online training system was developed based on the Android platform by the cross-platform mobile application scheme. The online training cross-platform mobile application was valuable based on PhoneGap for it can improve the compatibility on different operating systems.

Keywords Mobile application · Cross-platform · PhoneGap · Web HTML5

1 Introduction

With the rapid development of the mobile Internet industry, mobile phones and other mobile devices become necessary for people's daily life [1]. Unlike desktop device, mobile device has its own features and application questions. First of all, there are various types of mobile devices, which are developed by different technology with different platform. The current iOS, Android, Black Berry, Windows Phone and other mobile operating systems accounted for most of the smart platform market share [2]. The diversity of mobile operating systems requires different programming languages and development platforms for developing one application. For example, Android applications need to use Java language development, while iOS applications need to use Objective-C language development [3]. Secondly, Mobile device has limited computing power and storage space, so that application developers should consider more efficiency and space issues of mobile applications

X. Zhen · A. Huang · C. Chen · K. Wang · C. Liu (✉)
Hangzhou Dianzi University, Hangzhou, China
e-mail: lcf88089135@126.com

P. Zhao et al. (eds.), *Applied Sciences in Graphic Communication and Packaging*, Lecture Notes in Electrical Engineering 477,
https://doi.org/10.1007/978-981-10-7629-9_38

in mobile system than applications running on computers. For example, it requires developers to consider the difference between high-end models and low-end models in the Android platform. Finally, the screen size and the resolution restriction of mobile devices is also an important issue to be considered in the actual development.

2 Mobile Application Development Solution Comparison Analysis

2.1 Native APP Development Model

Native APP development pattern is known as the traditional development mode. This development mode is developed based on the operating system of the mobile terminal, such as iOS application development using Objective-C, Android application development using Java. Native APP can not only directly access the hardware devices and various sensors of the mobile devices (such as cameras, gyroscopes, GPS, etc.), but also have the access to some of the built-in services (such as address book, photo library, media player, etc.), for online or offline use, as well as message push or local resource access etc. The imperfection of native app is related to the limitations of mobile device itself. The Native APP is developed separately for different popular platforms, which requires establishing multiple development teams, using different development techniques to implement function, and the maintenance and upgrade of the application in later period costs much [4]. To update one application on different platforms, developers have to resubmit new versions of the application to the different app stores.

2.2 Web APP Development Model

Web APP development model, refers to the Web based systems and applications, running on the high-end mobile phone network and browser, with web technology to develop specific functions of the application development model [5]. The development model has the advantages of cross-platform. So that developers do not need to focus on specific operating platform during developing, the development cycle is short, and almost has no dependence on the hardware. The applications do not need to be installed and, the update and maintenance is very convenient. One disadvantage of Web App development is that it relies heavily on the network. The data are basically all from the server, so the network status will directly affect the user experience. Besides, web app cannot access the hardware API of the mobile phone (such as camera, accelerator, location information, contacts, photo gallery, memory card, media player, etc.) so that, the application function is limited.

2.3 *Hybrid Mobile Application Development Model*

In this paper, we developed a cross-platform mobile application combined with the characteristics of Native APP and Web APP. The system implementation process used a solution which adopts an app container with a native technology application to package the website to develop cross-platform mobile applications. The hybrid mobile application development using both native and Web technology will combine the advantages of "good user interaction experience for Native APP" and "the advantages of cross-platform development for web APP".

3 Framework for Mobile Application Development Solutions

Hybrid mobile application program structure was shown in Fig. 1 (Icon to the user's most commonly used Android system and iOS system as an example). Based on the Web application, the entire site is encapsulated before to be published, and the site is packaged with native application containers to generate hybrid mobile applications. With this hybrid mobile application development model, developers can take full advantage of the existing Web mobile site, and the device API which is called by native technology only when needing the native function of devices.

Compared to mobile Web applications, hybrid mobile applications do not run directly on the device's browser, but run on the Web View provided by the Platform SDK. Web View is a component for embedding Web pages, which is equivalent to a simplified browser, with the ability to display Web pages and perform JavaScript. It is called UI Web View in the iOS platform, while called Web view in the Android platform.

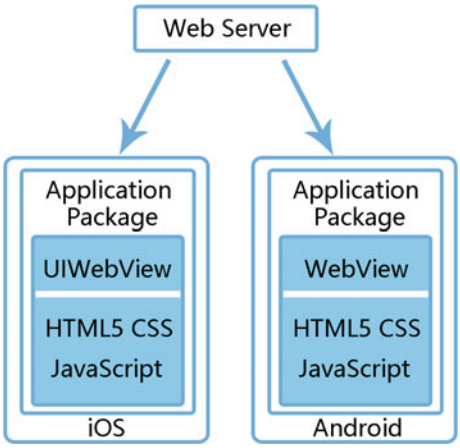

Fig. 1 The scheme of the hybrid mobile application

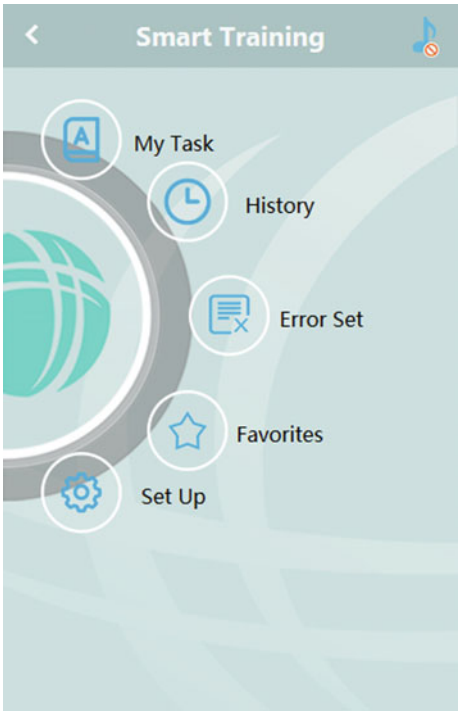

Fig. 2 Application index

Based on the solution talked above, we make use of the existing mobile application development framework PhoneGap. The PhoneGap framework provides a series of API calls in JavaScript code for developers, which allows users to access the local application of mobile devices, API and application libraries through the Web technology. Using PhoneGap framework can generate cross platform mobile applications quickly and efficiently. At run time, files written using Web Technology (html/javascript/css) will be packaged as a similar "image files" in the form, and then publish it to the platform to be run, such as IOS's IPA, Android's apk.

4 Implementation of Online Training Cross-Platform Mobile Application Based on PhoneGap

4.1 System Requirements Analysis

The online training system is a stylish and flexible way for study exams. In this work, we developed a set of cross-platform mobile application online training system for a hydropower station. Due to working characteristic of the hydropower

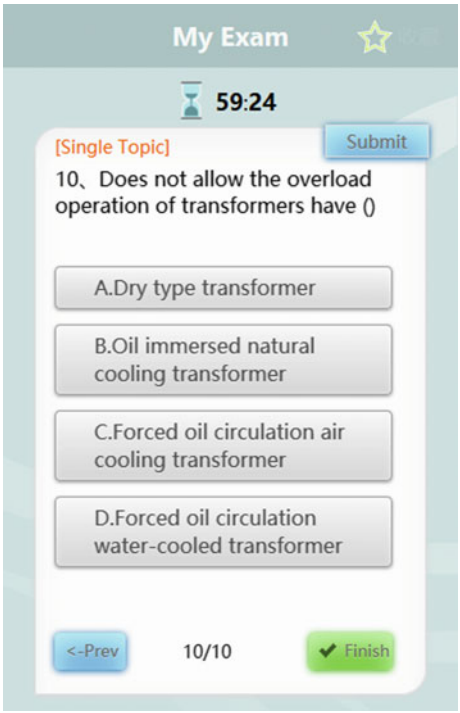

Fig. 3 Answer details page

station, the network state is not always good which requires the application to has off-line function and the employees have various types of mobile phone. Besides, the company expects to invest less and do a rapid development of the training applications. In this case, a cross-platform on-line training application achieved by PhoneGap cross-platform framework is the best solution to meet the business needs.

4.2 System Development Environment and Platform

The system development and simulation environment setup consists of the following steps:

(1) Installed Java environments. It should be configured by the system environment variables after download and installation.
(2) Download and install the node js.
(3) The SDK installation. Using PhoneGap framework to develop applications, application corresponds to the mobile device must be installed on development environment SDK.

(4) Install the PhoneGap. Enter cmd, Executive life: “NPM install-g Cordova”, download and install the PhoneGap.
(5) Database was installed. The system uses SQL SERVER as the database management system. Download and install, administrators should pay attention to security and password settings.
(6) Building PHP environment. PHP is a general-purpose open source scripting language. Syntax absorbed the C language, and Java and Perl features conducive to learning, using broad, mainly applicable to Web development areas.

4.3 Key Technologies

It used document processing technology on API of the mobile phone in system development processes. When user is viewing one document, system uploads this document from specific SD card cache folder. If system is failing to upload the document, a new sub thread will be created to download the document and save it to the specific local cache folder. After successfully uploading this document, system will choose corresponding ways to open the document based on its suffix. The key code is as shown below:

```
/ **
* Depending on the file type, and returns a different intent,
and then use that are specific to open target file
* /
@ Suppress Lint (“Default Locale”)
public static Intent open File (String file Path) {
File file = new File (file Path) ;
If ( (file = = null) | | ! file. exists( ) | | file. Is Directory( ) )
return null;
String end = file.get Name ().substring (file.get Name().last Index Of
(“.”) + 1, file.get Name().length()).to Lower Case ();
if(end.equals(“ppt”) ){
        return get Ppt File Intent (file Path);
} else if ( end.equals(“doc”) ){
        return get Word File Intent (file Path);
}else if( end.equals(“pdf”) ){
        return get Pdf File Intent (file Path);
}else{
        return get All Intent (file Path);
}
        ……
}
```

4.4 System Test

Online training system enables employees to participate in the exam, questionnaire and access to training documents online. The screenshots of specific implementation interface were shown in Figs. 2 and 3. From the system test results, the system runs well in Android platform, and the interface is smooth and clear, data processing is stable, and can completely meet the appearance and performance requirements of the users. By converting the SDK within PhoneGap to corresponding SDK, this system can be adopted in iOS system, test results show that the system is running smoothly. Therefore, this research scheme satisfies the needs of cross-platform mobile development.

5 Conclusions

Based on the research of the existing mobile platform development scheme and the latest mobile development technology, we proposed a cross-platform mobile application scheme, which includes the application of native technology to the website to generate mobile applications with cross-platform characteristics. An online training system was design and implementation based on Android platform by PhoneGap cross-platform framework. The cross platform application of online training system was valuable for mobile internet application.

References

1. Gao XH (2011) Mobile internet overview. China Comput Commun 6:130–140
2. Perez S (2015) Report: google play's app store and developer community grew faster than apple's in 2014. http://techcrunch.com/2015/01/13/google-plays-app-store-and-developer-community-grew-faster-than-apples-in-2014/
3. Li BH (2012) Android-based phonegap platform research and the expansion of the media platform across mobile platforms. South China University of Technology, Guangzhou
4. Gu CL (2014) APP application development model. Silicon Valley 5:35–36
5. Meng F, Cong ZC, Huang ZX, He Z (2013) Research on cross-platform development of mobile internet application. Mob Commun 13:60–63

The Research and Application of WebGL Technology on Color Experiment Learning Platform

Donghan Zhang, Zhanjun Si and Jiaojiao Zhang

Abstract The goal of this paper is to develop the digital color experimental learning website by using a variety of technologies so as to assist teachers in color experiment teaching and learning. The color test is not easy to achieve in real life, so we collected data and creating color model, color rendering by using 3ds max, making experimental study of color site layout design of a web site with HTML5 and CSS3. Using Three.js 3D model make files into the web page, released the final color experiment learning website. The design of Color Science Learning Websites with virtual display module of the website can show the user simulation experiment model and color phenomenon. The paper concludes that the application of the WebGL technology in the virtual display of color experimental model can provide teachers and students a teaching and learning platform. Besides, this application can also spread to the internet school and the virtual education.

Keywords Color model · Virtual display · Max 3DS modeling · VRP

1 Introduction

Printing color science is the basic course of printing reproduction. Understanding the color characteristics, color system and mastering the method of calculating the color is essential to the understanding of the principle of color reproduction and learning printing technology [1]. At present, China's printing industry education lags behind and the printing color courses are mainly based on classroom lectures in most of the colleges and universities [2]. Although with the popularity of multi-media teaching, students can see the process of demonstration presented by the pictures, animation, video, etc. [3]. These forms are mainly two-dimensional,which is not vivid enough to show the knowledge and easily causes the blind spot [4].

D. Zhang · Z. Si (✉) · J. Zhang
College of Packaging and Printing Engineering, Tianjin University of Science and Technology, Tianjin, China
e-mail: szj@tust.edu.cn

P. Zhao et al. (eds.), *Applied Sciences in Graphic Communication and Packaging*, Lecture Notes in Electrical Engineering 477,
https://doi.org/10.1007/978-981-10-7629-9_39

Therefore, the establishments of color experiment platform based on WebGL technology, in three dimensions to show the abstract color model, can be a useful complement to traditional teaching, and can effectively improve the quality of teaching.

2 WebGL Technology

WebGL's full name is Web-based Graphics Language, which provides the use of JavaScript and GPU interaction method. It is the 3D graphical standards.

The advent of WebGL is a perfect solution to the two problems of 3D animation interaction in web pages: First, WebGL can achieve the interactive 3D animation rendering process directly through the HTML script without the help of any third-party browser plug-ins; Second, WebGL takes advantage of the graphical hardware acceleration of the computer's underlying graphics for rendering, which is achieved through a standard, unified, cross-platform OpenGL interface. With the development of computer technology, the application area of WebGL technology is becoming wider. At present, the main game-developing engines on the market include Unity, Egret, Cocos2D, etc. Using the technology of Mozilla's Asm.js, all these platforms provide the technology support of WebGL, making WebGL's game-developing function have a more professional engine and can make the games more brilliant. The WebGL-based web interaction has been widely used in many fields.

3 The Design of Color Experiment Learning Website

3.1 Design Ideas

Through the comparison survey, this paper combines the powerful modeling tools like 3ds Max and other software through WebGL technology, to study the application of the WebGL technology in color experiment learning platform. Figure 1 shows the designing framework of this paper. The design is mainly produced by 3ds Max color model, using HTML5 and CSS3 for web design, with WebGL technology to embed 3D model files into the page, and finally using the script to generate and run the test.

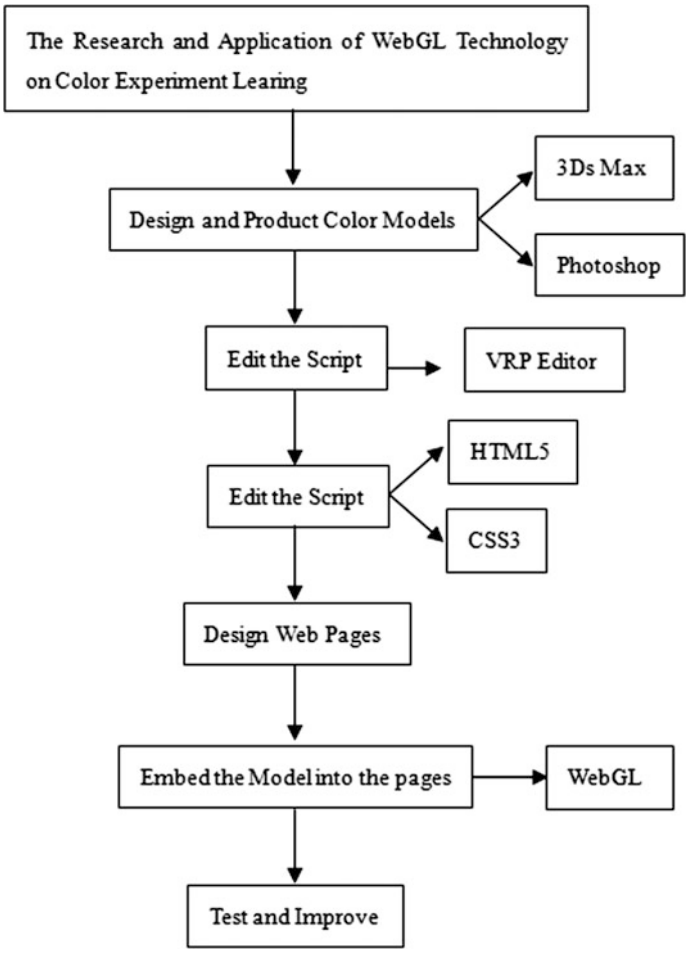

Fig. 1 Flow chart

3.2 Production Software and Development Environment

Production software: Photoshop CC; 3ds max 2013; VRP2010; Modeling environment: Windows7, Intel (R) Core (TM)i3CPU, 2G memory, 32-bit operating system.

4 Production Process and Main Points

4.1 Experimental Design

This paper studies the application of virtual reality technology in color experiment. we select ten color experiments that are not easy to realize in ten real life, including Light dispersion experiment, Blackbody Demonstration and Blackbody Radiation at Different Temperatures, Three-color and four-color theory, CIE 1931 chromaticity diagram, CIE 1976 L*a*b*color space, Three-dimensional Munsell color system, Printer color management, network of superposition and side by side color, shade color method, and color reduction method. Firstly, we carefully design the color experiment, and then use 3D MAX software to create a virtual model, and then release it on the site after being rendered and compiled with WebGL model. Finally, Use the virtual reality technology to simulate the color experiment in color science.

4.2 Establishment of the Color Model

4.2.1 Blackbody Radiation

Firstly, open 3ds max 2013, and then use the graphical tools to make a shell and inner shell, and then give the material to the black background, the base, the temperature control, the bold shell, the black shell, and the radiation light model. Finally, add four floodlights at the appropriate location in the scene, and build the model as shown in the figure below (Fig. 2). After the rendering is finished, complete the script editing so as to finish the experimental process of the bold and black body (Fig. 3).

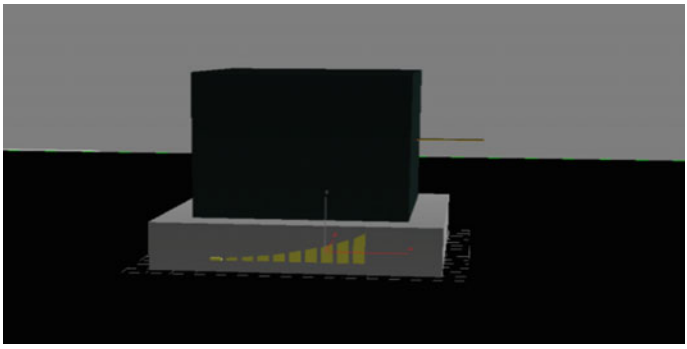

Fig. 2 3d max built in the model

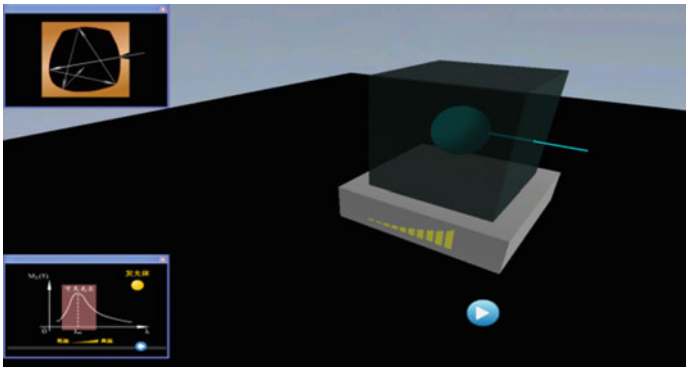

Fig. 3 Blackbody demonstration with blackbody radiation

4.2.2 Munsell Color System

Model with a geometric tool and draw the Munsell color's three-dimensional central axis and other color patches (Fig. 4). After the model is built, the color of the material is given by the "color selector". Click the "Assign Material to Selected Object" button in the Material Editor to assign the cylinder to the corresponding color (Fig. 5).

4.3 Virtual Display Platforms Production

The overall layout of the virtual color experiment learning platform is mainly designed by HTML5 and CSS3 (Fig. 6). It is mainly composed of the toolbars of experimental display, course record and notes, practical and the problems part, etc.

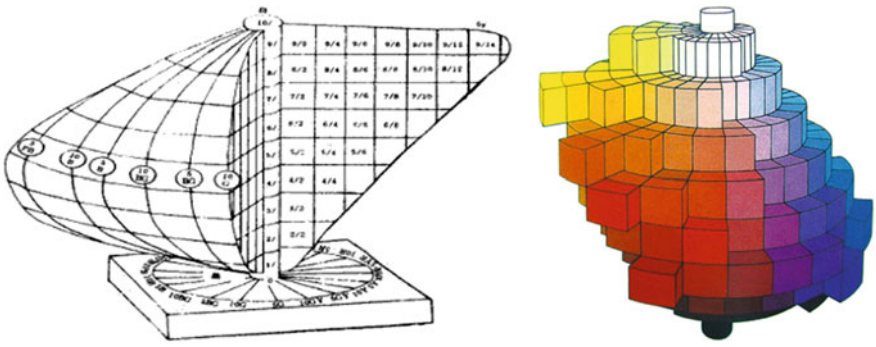

Fig. 4 Munsell color stereoscopic diagram

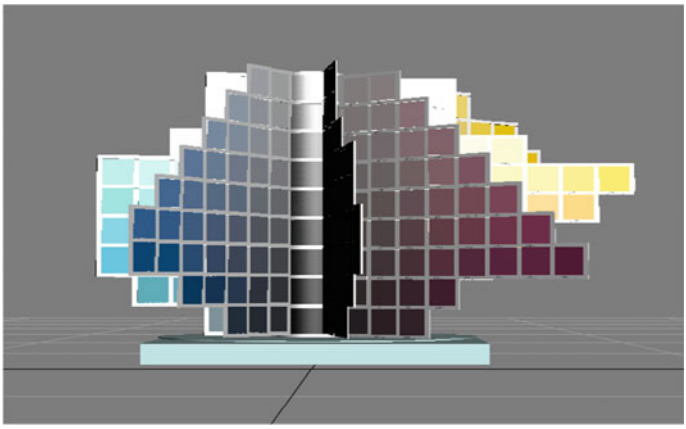

Fig. 5 Built the color of the three-dimensional model

Fig. 6 Virtual display platform

5 Conclusions

The characteristics of the virtual reality technology that it can simulate the reality but stays beyond the reality can help it watch the hardly observed part that exists in reality but is not related with the application and even causes disturbs during the application of color experiments. Therefore, it can improve the quality of the experiments or observations and is featured with rich resources, personal learning, and close interaction. In addition, with respect to the fact that the communication between teachers and students is ineffective in many printing institutions, this platform can help teachers to share the learning resources more effectively and can motivate the students as well.

References

1. Liu H (2012) Color science and technology. China Light Industry Press, Beijing
2. Zhao HY, Qian R, Li XD (2011) Research on simulated operation software of printing machine. Packag Eng 32(11):103–107
3. Li WX, Si ZJ, Zhang Y (2014) Design and implementation of digital printer virtual demonstration system. Packag Eng 07:114–118
4. Chou B (2013) The research of graphics and image processing technology in HTML5. Forestry University, Beijing

Analysis and Implementation of Message Pushing Technology Based on Third Party Platform

Kangye Wang, Caifeng Liu, Xin Zhen, Chao Chen and Aibin Huang

Abstract It was very important to solve the problem of message conveniently, economically, stably and safely pushing to mobile devices based on Android platform. The manuscript discussed the advantages and disadvantages of traditional Pull and Push methods such as simple polling, SMS service, persistent connection and long polling technology. The push methods about C2DM, MQTT and XMPP based on Android platform were discussed too. Finally, a third-party platform was achieved to push the message service. The push system was examined to verify that the push service easy to operate, cost savings, less occupation of resources, higher efficiency. It hints that the message pushing technology based on third party platform may be a superior technology to solve the problems of message pushing.

Keywords Push message · Android · C# · Third-party platform

1 Introduction

With the development of mobile Internet and intelligent terminals, a higher requirement was put forward to mobile client APP. It mainly lies in mobility and timeliness. Mobility, requiring low power consumption, low rate conditions of message transmission. Timeliness required pushing message to the mobile terminal equipment within a specified time.

It's a key technology of pushing information to app on the mobile terminal equipment within a specified time. Here we discussed some kinds of methods to solve the problem of pushing information to app on the mobile terminal equipment and finally we find a better way to deal with it.

K. Wang · C. Liu (✉) · X. Zhen · C. Chen · A. Huang
Hangzhou Dianzi University, Hangzhou, China

P. Zhao et al. (eds.), *Applied Sciences in Graphic Communication and Packaging*, Lecture Notes in Electrical Engineering 477,
https://doi.org/10.1007/978-981-10-7629-9_40

2 Traditional Message Pushing Technology

To get message which not regularly updating on the server, usually in two ways: ① *Pull*, Namely, client access server at intervals to see if there is updated message; ② *Push*, Server automatically push the latest message to the client when it has new message. Pull and Push technology mainly include the following four types [1–4].

2.1 Simple Polling

Simple polling technology requires the client application to connect to the server regularly, and to check whether a new message arrived. Essentially it is *pull* technology. It is important to choose an appropriate polling interval, which may causes messages delay if it is too long and consumes a lot of network bandwidth and battery power if it is too short. This method is generally applicable to the occasion that real-time requirement is not high.

2.2 SMS Service

SMS technology to send binary message to mobile client, mobile client intercept such text message, analyze the data of the SMS PDU to understand the intention of the server, and then take the appropriate actions. It is a typical *Push* technology. But it costs so high to pay the cost to the mobile corporation. For example, it needs to pay Y 2700 per month to the mobile corporation if it costs Y 0.06 per message and it has 500 users and three messages to be sent each day.

2.3 Persistent Connection

It requires the establishment of a long-term connection between the client and server, as long as the server has a message to send, it can be completed by pushing the message. This method can achieve timely and real-time pushing messages, but it needs to maintain long-term connection with the server, not only consume the power of mobile terminals, but also easier to consume server resources. Be careful to use this method, server overloads and occupies for a long time may cause system breakdown.

2.4 Long Polling

Long polling is also known as persistent polling. The client initiates the request, which is pending until timeout, exception, or server needs to process the response, and then server returns a response. After client received the response, it requested server once again, and server processes the response. This method solves the problem of poor real-time performance of simple polling, and the problem of persistent connection consuming server resources. But it still consumes the power of terminal client because each time after receiving the data the client needs to connect to server. If the transmission of data is relatively small, the establishment of the connection time will become the main matter for much costs and the effective utilization rate is low.

In summary, there is a series of problems of the traditional message pushing technology, such as power consumption, data flow consumption, high cost and unstable server system.

In fact, the Android operating system in the case of high memory occupy will usually kill services automatically, that is messaging service running on the mobile terminal is likely to be killed by the system. Therefore, regardless of the server resource consumption and power consumption issues, *persistent connection* and *long polling* and other traditional message pushing technology are still not suitable for Android platform.

At present, some corporations developed the following message pushing technology specifically for Android platform.

3 Message Pushing Technology Based on Android Platform

3.1 Google's Official C2DM Cloud Push Technology

The main default of this technology is that C2DM needs to rely on Google's official C2DM server [5]. Due to the impact of the network environment, for domestic network users, may not be able to successfully achieve the message pushing.

3.2 IBM's Message Pushing Technology Based on MQTT Protocol

MQTT is a lightweight, proxy based *publish/subscribe* message transfer protocol [6]. The protocol is simple, compact, scalable, provincial flow, electricity saving and it has been applied to the enterprise field. The technology is not suitable for small enterprise

of pushing message service to mobile terminal based on Android platform for that it was difficult to achieve and high cost of deploying hardware.

3.3 Push Technology Based on IETF Standardized XMPP Protocol

The technology is not yet mature enough, the main problems exist:

(1) Mobile client will never receive message after a long time;
(2) Message once pushed out from server, whether or not pushed onto the mobile client, no longer manage it [7];
(3) Performance is not stable enough.

In order to solve the problem that employees are tired of ordering meals due to their busy work when the author completes the *intelligent ordering meal system* for the enterprise, the service of *order reminder pushing* was required to be added to the mobile app without increasing the cost, and app is possible to receive the push message in time and to light the screen and display the information in the form of a pop-up box while vibrating. At the same time, the background program can push message every day, pushing time may often be modified, and manual operation as little as possible.

The author analyzed the traditional technology of message pushing, C2DM, MQTT and XMPP, and finally tried to use a third-party platform in China to push *ordering meal reminder* message automatically to the employees' mobile app, and achieved project requirements eventurally.

4 Implementation of Message Pushing Based on Third-Party Platform

The following describes the process of the implementation of message pushing based on a domestic third-party platform named GeTui.

4.1 Implementation on Server-Side

The platform provides software development kits for background software based on Java, Python, C/C++, C#, and other mobile devices based on Android and iOS system, and message can be pushed directly through the Web page. This paper mainly uses the C# and Android SDK.

Fig. 1 The appid, appsecret, appkey and mastersecret were assigned on the web page

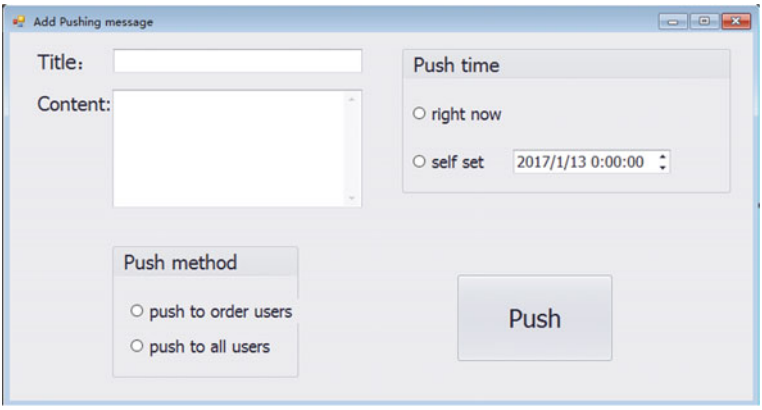

Fig. 2 Operating page on the background program

(1) Creating an app that requires message pushing service on the website, the unique appid, appsecret, appkey and the corresponding server-side mastersecret will be assigned.
(2) Configuring the app's appsecret, appkey, mastersecret and other necessary information in the background software.
(3) Push message Regularly (Fig. 1).

On the server-side to establish a regular query database task, it could access to the database to get the already set up pushing time. Because the third party platform provides timed message pushing service, the task can be sent to the third party platform by SDK, the follow-up work will be completed by it (Fig. 2).

4.2 Implementation on Android-Platform

(1) Import jar file to the project
Add some services, such as accessing to the third-party server and registering the current device's ID service, receiving pushed message service, and can freely access to the data processing, such as display message in the dialog or in the notification bar.

(2) Configure the Android Manifest.xml file
Need to configure some permission like vibration, notification bar display, background start and other permissions. The most important thing is to configure the SDK core services, these services ensure that app can receive the normal pushing message.

(3) Configure the gradle file
Mainly configured are appid, appkey and appsecret.

(4) Display message on pop-up window
The app is not able to display message on pop-up window when screen is locked or app is running in background, so here use an activity simulation pop-up window.

Need to set the properties of the Activity:

```
win.addFlags(WindowManager.LayoutParams.FLAG_SHOW_WHEN_LOCKED
|WindowManager.LayoutParams.FLAG_DISMISS_KEYGUARD
|WindowManager.LayoutParams.FLAG_KEEP_SCREEN_ON
|WindowManager.LayoutParams.FLAG_TURN_SCREEN_ON);
```

Here we use WakeLock to let the Activity wake up the screen and display the message when the screen is closed or locked (Fig. 3).

(5) Keep app service running in background [8]
OnStartCommand method returns START_STICKY, so that if the service process is killed by the system after running onStartCommand, service will try to re-create. Use startForeground to put the service in the foreground state, to improve the process priority and reduce the probability of being killed by the system in low memory. However, above several ways can not achieve the same result for different kinds of Android system, need for fine-tuning of different ROM. The proper way to keep app service running in background is adding app to the list of ROM protected applications, improve the priority of the service, and can not clear out the app from the background.

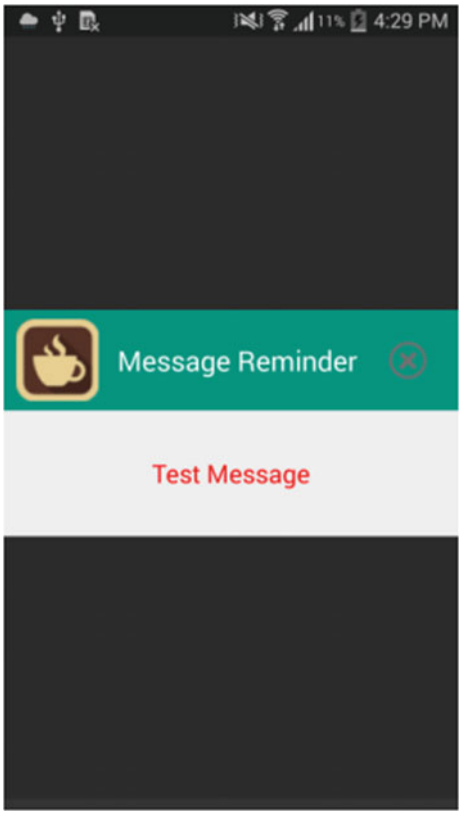

Fig. 3 Message displayed on the phone

5 Conclusions

Although it has some defaults of the third party android platform message pushing system such as the information delivery rate constrained by the system, time delay of network effects and other issues, it is totally free, and the delivery rates of pushing message were higher than 80% after several times of testing and it suggested that the message pushing system based on the third party android platform was superior for that it has many advantages such as simple operation, cost savings, less resources consumption, high efficiency utilization. It hints that it the message pushing system based on the third party android platform may be a superior technology to solve the problems of message pushing.

References

1. Hua C, Hu M (2008) Analysis and simulation to push scheme and pull scheme. Opt Commun Technol 57–59
2. Smiljanic A (2008) Rate and delay guarantees provided by clos packet switches with load balancing. IEEE/ACM Trans Networking 170–181
3. Thompson T (2008) The Android mobile phone platform. World Softw Dev 40–47
4. Zhang CX, Zhang W, Dong ZM (2011) Aspects ofmobilepush technology. Mobile Commun 21–27
5. C2DM (Android Cloud to Device Messaging). https://en.wikipedia.org/wiki/c2dm
6. MQTT (Message Queuing Telemetry Transport). https://www.ibm.com/support/knowledgecenter/en/SS9D84_1.0.0/com.ibm.mm.tc.doc/tc10140_.htm
7. XMPP (Extensible Messaging and Presence Protocol). https://xmpp.org/
8. Keep app service alive in background. http://stackoverflow.com/questions/3856767/android-keeping-a-background-service-alive-preventing-process-death

Design and Implement of a Social-Publishing App Based on iOS Platform

Yuchen Ye and Hongyan Zhao

Abstract Social-Publishing App is a community where users can post their stories, articles or any user-generated content through a mobile app. Through this, every user can write their own works and share them with like-mended readers through social networks. One function of the software allows users to participate into the book creation process, as well as communication activities, such as common, annotation, fellow works or writer, etc. This article will introduce the app's function and the software utilized in the development of the app. The Social-Publishing app was developed on Mac system using Xcode tools, Object-C programming language, and SQLite database. The app's interactive prototype was created through Axure, according to the user's reading habits. The UI complements control all the buttons and respond immediately to the user's click and touch gestures.

Keywords Social-Publishing · Axure · Object-C · SQLite · UI complements

1 Introduction

The last few years have been quite challenging for the traditional publishing industry. As social media tools and social networking platforms improve and adapt to promote various works, especially user-generated content, they offer new ways of entertainment. A new type of publishing was born: social-publishing [1]. As such, the traditional relationship between reader and author has evolved. Readers are willing to write their own works and share these through their various social network accounts. In other words, the social networking community has become the media between readers and writers; and through the community, users can launch the experience and inspiration to fans and friends. Therefore, the app can motivate the user to create all kinds of works.

Y. Ye · H. Zhao (✉)
College of Packaging and Printing Engineering, Tianjin University of Science and Technology, Tianjin, China
e-mail: zhaohongyan800@tust.edu.cn

P. Zhao et al. (eds.), *Applied Sciences in Graphic Communication and Packaging*, Lecture Notes in Electrical Engineering 477,
https://doi.org/10.1007/978-981-10-7629-9_41

With the development and improvement of tools, specifically desktop tools designed to facilitate the process of making a prototype, designers can easily create the app's interface and architectural structure.

2 Software Structure and Function Analysis

For this project, the iOS system was chosen to support the platform because of its popularity and flexibility. It has the largest software market and is the most widely used software on smartphones.

According to the demand of users, the social-publishing app combined 'reading' and 'social' elements together. Users can read, write and share their works on the platform. It comprises five views: home, library, publishing, forum and me. To implement the software on the iOS system, UI complements (such as UIButton and UIViewController) were used to control all buttons in this system.

Supplementary data associated with this article can be found in the online version at [2] (Fig. 1):

(1) Register and log in: New users can create a new account by associating or linking with other social networking software; for example, WeChat, Weibo, QQ, etc.
(2) Friend's works: App recommend the works written by friends.
(3) New book's recommendations: The most frequently visited stories will appear on the "Hot List" on home pages.
(4) Publishing: The platform aims to help authors build a "Personal zone" for communicating.

A prototype social-publishing platform was designed and developed for displaying the "Home" page. The "Home" page is the first screen to greet users. It comprises four parts: continue reading. Friends' works, #topic and most popular. All the works was selected in the library and recommend works that are related to the user's reading and social habits (Fig. 2).

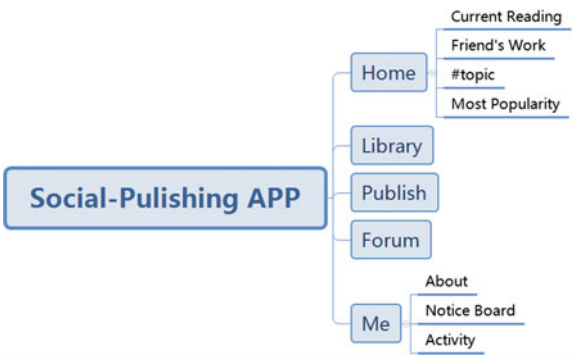

Fig. 1 Structure of software

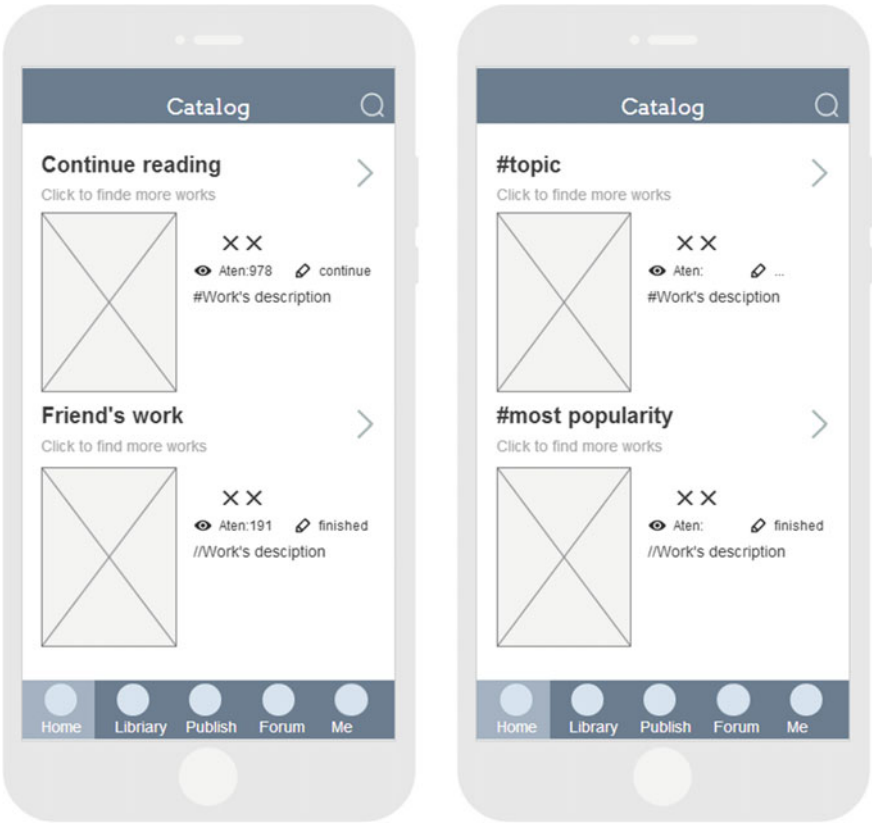

Fig. 2 Home page

3 Relative Technology

The following details the process of creating a new internet product: user's demand analysis, product sketch, low fidelity prototype, high fidelity prototype, design instruction, and project development.

After organizing the interactive needs by users, the interactive interface was made in Axure. The foreground app software design is based on Object-C language, in the Xcode compiler platform application SQLite, which is Apple's own data inventory information and Core Data technology.

3.1 User's Interactive Interface Prototype

Axure (Rapid Prototyping) was desktop software designed to facilitate the creation of prototypes (software, webpages, other digital contents) for mobile devices [3]. By using the tools provided by Axure (template, widgets, inline frame, dynamic panel), designer can efficiently produce an interactive prototype for programming development engineers. According to the interactive prototype, the developer can better understand the users; reading habits and demand.

Axure share is a tools base on Axure software for sharing the prototype online. It is supported on iPhone, iPad, and Android mobile devices.

We designed the interface of "Publishing" screen based on Axure and its tools. The prototype version shows the process that users create a new work (Fig. 3).

3.2 iOS Developing Environment and Object-C Language

The social-publishing app was developed with Object language and Xcode development environment on the iOS system. The main programming language used by Apple's iOS operating system is Object-C, which is an extension of C language [4]. Especially for coding for logic program. Xcode is integrated development environment (IDE) for developing software on macOS. Xcode generated Object-C original code program files. The files usually have .m (implementation), .s (interface) and .h file name extensions. Apps can be designed, with coding and

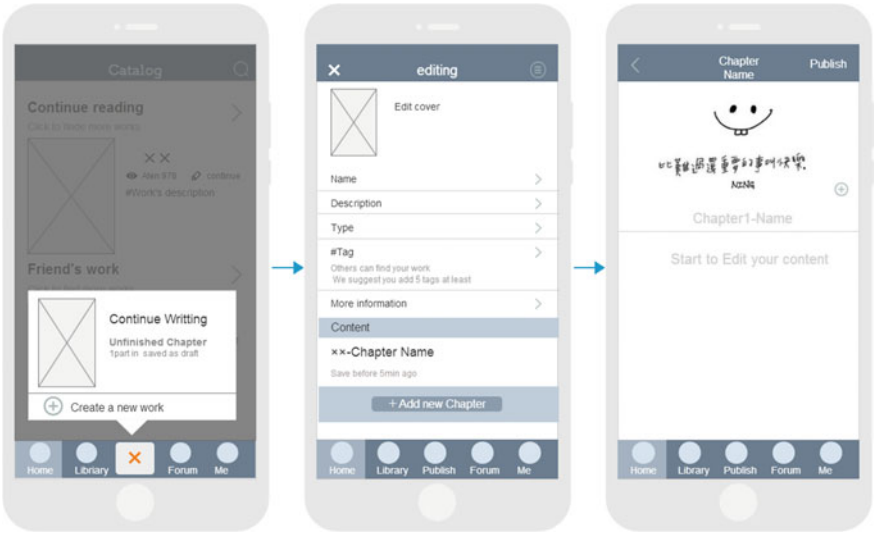

Fig. 3 The process of "Publish" (create a new work)

textflighting on Xcode environment by integrating .s, .h and .c files; thus, generating the project.

3.3 SQLite Database and Core Data Frame

For this project's system, we elected to include SQLite database with Core Data frame [5]. SQLite is an in-process library that provides a self-contained, server-less and transactional database, which is perfectly suited to mobile devices, especially Apple and Android phones. It solves the problem to use little memory by using a small code footprint. Core data is an object graph on iOS operating system. These provide the object lifecycle and object graph management. Through core data technology, data can be transformed into an object and generate the data model.

The database includes users' basic information, book contents, and some address in local. Information is exchanged with the server via mobile data (Tables 1 and 2).

Table 1 The information collection on "users"

Name	Type	Description
User_id	Integer	Primary key, Not full
Name	Text	Can not change
Password	Text	Not full
Email	Text	
Heading	Text	Address of picture
What's up	Text	Sentence and emotion
Works	Integer	Work's number
Reading list	Integer	
Fans	Integer	Fans' number

Table 2 The information collection on "works"

Name	Type	Description
Work_id	Integer	Primary key, Not full
User_id	Integer	Foreign key
Cover	Text	Address of picture
Title	Text	
Description	Text	Sentence and emotion
Category	Integer	Foreign key
Tag	Text	No more than 3 words
Chapter	Text	
Fans	Integer	Work following

4 Conclusions

This article introduced and discussed the process and technology used in implementing a social-publishing app. The system was developed by Object-C language and Xcode programming software. In the future, however, as users increase, the serer will be under great pressure; therefore, we will continue to focus on optimizing the server-side code and providing a better experience to our users.

Acknowledgements This study is funded by College Students Innovative and Entrepreneurial Training Program of China (201610057097).

References

1. Zhou M, Zhang J (2015) From minority to mass-the evolution and challenge of social-publishing. Science-Technology & Publication. https://doi.org/10.16510/j.cnki.kjycb.2015.09.029
2. iOS-UI Complements (2015) http://www.cocoachina.com/ios/20151110/14067.html
3. Chen Y (2015) A prototype collaborative develop system based on axure rapid prototyping. South China Univ Technol 06
4. Zhou YY (1991) The design philosophy and implementation principle of objective-language. Comput Eng Appl 02
5. Tang M, Song J (2008) The mechanism and application of SQLite. Comput Knowl Technol 04:600–603

The Research of Application of 720° Panoramic Roaming Technology in Indoor Display

Jiaojiao Zhang, Zhanjun Si and Donghan Zhang

Abstract Object 720° panoramic roaming technology has been widely used in outdoor panoramic roaming production, but the research on indoor panoramic production is few. This paper aimed to study the application and prospect of 720° panoramic roaming technology in indoor display. Method First, take pictures at "Yin Yuejia Cultural and Art Center". Next, splice the plane panoramas in PTGui. Then modify the flat panoramas in the photoshop. Adjust the hue and saturation to ensure the same effect among the panoramas. Finally, create the panoramic effect in the 720 platform. The result was that a good interactive indoor panoramic roaming was completed. Conclusion 720° panoramic roaming technology has the advantages of all-round, real scene and other strong points. It has broad prospects in indoor panorama display and thus this research makes a lot of sense.

Keywords 720° panoramic roaming · 720 platform · Indoor display

1 Introduction

At present, there are many third-party technologies to display panoramic images at home and abroad, such as VRML, X3D, Java, QuickTime, Flash, etc. [1]. These methods require language basis and also browser plug-ins, and they can't be released across platforms, either [2]. Panorama effect can also be achieved through VRP, Unity3D, Virtools, Pano2VR and other software. But VRP, Unity3D, and Virtools are all based on three-dimensional modeling. They need a long production cycle and higher technical requirement, and the software simulation operation is more complex. While 720° panoramic roaming technology is based on HTML5 language. It develops rapidly and becomes a new popular visual technology around the world [3]. It can achieve the effect of "one development, multi-platform

J. Zhang · Z. Si (✉) · D. Zhang
College of Packaging and Printing Engineering, Tianjin University of Science and Technology, Tianjin, China
e-mail: Szj@tust.edu.cn

P. Zhao et al. (eds.), *Applied Sciences in Graphic Communication and Packaging*, Lecture Notes in Electrical Engineering 477,
https://doi.org/10.1007/978-981-10-7629-9_42

applications". It doesn't need to install additional plug-ins and has uniform standards [4]. At present, 720° panoramic roaming technology has been widely used in outdoor panoramic roaming production, but indoor panoramic production and research is few. In this study, indoor panoramic roaming display of "Yin Yuejia Cultural and Art Center" was completed by 720° panoramic roaming technology. It was found that the 720 technology had a huge advantage and prospect in indoor display and in this sense, and this study may contribute to the development of 720° panoramic roaming technology.

2 Development Environments and Software

Development environment: windows 7 system.

Software: fisheye camera, PTGui, photoshop and 720 platform. Take pictures with fisheye camera to ensure the realism and high definition. Then use PTGui to stitch panoramas. Next, modify the panoramas in the photoshop. At the last, make panoramic effects in the 720 platform.

3 Ideas and Framework

First of all, do some homework on "Yin Yuejia Cultural and Art Center". There were totally ten points, including hall, corridor, percussion classroom, piano classroom, etc. Then use a fisheye camera to shoot each point. Put the tripod in the center of each point and shoot six photos on each point. Each group of pictures needed to be taken under the same camera parameters. Then stitch in the PTGui and each two pictures needed to be added 5–10 control points to ensure the accuracy. Generate panoramas and export them in jpg format. Name each panorama and save them in a folder for later use. Then process panoramas in photoshop. It was necessary to deduct people and tripods in the pictures, and adjust the hue and saturation to ensure each point has the same effect. Finally, make panoramic effects in 720 platform to achieve its powerful interactive features.

4 Designing and Implementation

4.1 Collection and Shooting of Pictures

Collecting and capturing pictures was critical in the whole process. The quality of the picture directly affected the realism and fidelity of the final work. The best collection program was based on continuous exploration and practice. First,

shooting time should be in the morning from Monday to Friday to ensure the quiet shooting environment, because there was no student in class this time. Then, all the curtains should be pulled and all the lights should be opened to ensure the lighting effect. At last, the shooting method was very important, and each point had the same one. Specifically, put the fisheye camera on the tripod and adjust it to a moderate height on the center of the indoor space. Adjust the camera's shooting parameters, including exposure, focusing distance and white balance conditions and take a photo for trial to find the best shooting parameters. Fix tripod and shoot. Taking 4 pictures in the horizontal direction, turn the camera, then take one on the ceiling, and take one on the floor. It should be noted that the shooting people should squat down to avoid entering the lens when shooting the ceiling. Through the above collecting program, a set of high-definition scene graph was gathered. They were materials for later production and research.

4.2 Splicing and Processing of Panoramas

4.2.1 Splicing of Panoramas

PTGui is a user interface of Helmut Dersch's Panorama tool. It can create a dazzling panorama picture quickly and easily. After the picture is imported, a panorama image can be generated automatically with appropriate lens parameters [5].

The splicing and integration of pictures were completed in the PTGui. Firstly, select the panorama model. The splicing and display technology of panorama are closely related. Based on different ways of display, the resulting panoramic image can be divided into spherical panorama, cube panorama and columnar panorama [6]. The spherical panorama model uses a non-uniform pattern of sampling. It has wide field of view to support the observer with any angle to observe the surrounding scene and can achieve a true 360° viewing without dead angle. The spherical panoramic image is consistent with the human eye structure and adapts to the habit of observing the environment. Therefore, this study used spherical panoramic model for its strongest sense of reality [7]. Secondly, the control points should be added reasonably to achieve a better seamless splicing. According to the experiment and research, it was concluded that the number of control points should be 15–20 for the best stitching effect.

4.2.2 Processing of Flat Panoramas

The process of shooting was influenced by the time, environment and other factors. It was impossible to completely restore the real scene, so the post-adjustment was needed to ensure the realism and fidelity. This was mainly finished in Photoshop. First, modify the dislocated, stitch the ineffective points and deduct people and tripods. Then adjust the hue and saturation to ensure the same effect

among all the panoramas. As shown in Fig. 1, the flat panoramic effect of hall and Fig. 2, the flat panoramic effect of percussion classroom.

4.3 Realization and Research of Panorama Roaming Effect

The design criteria for interactive design and production of panoramic roaming were as follows:

(1) All the panorama images must have the size of 2:1 or 1:1 for the better browsing effect.
(2) The hot spot should be set reasonably. Hot spots can be switched from one to another. It meant that the users can move from one scene to another freely. There should not be dead angles.
(3) The selected music should be consistent with the scene atmosphere.
(4) Links can be added by writing HTML5 languages. There cannot be syntax errors.
(5) HTML5 project files can be exported for secondary development to achieve more features and better effects.

All the materials of the study were from the real scene, so it was very realistic and had strong human-computer interaction [8]. At the same time, It had other advantages of smooth playback, plasticity and available network promotion. Its prospects are broad and it has great value of research [9].

Fig. 1 The flat panoramic effect of hall

Fig. 2 The flat panoramic effect of percussion classroom

5 Conclusions

In this study, indoor panoramic roaming display of "Yin Yuejia Cultural and Art Center" was completed by 720° panoramic roaming technology with detailed production process. 720° panoramic roaming technology has a high degree of realism. It has a powerful human-computer interaction, smooth playback and has a strong security features. It provides a good tool and platform for the indoor panoramic display and has broad prospects and great research significance.

References

1. Li H (2012) The realization of campus 360 degree panoramic display technology. Technol Inf 18:211–212
2. Dong CX, Si ZJ (2017) Application of panorama technique in campus panorama roaming. Comput Eng Appl Technol 4(13):210–211
3. Wang J (2014) Demonstration of ground subsidence monitoring system based on 3D panorama technology. Shanghai Land Resour 2:98–100
4. Dong CX, Si ZJ (2017) Application of panorama technique in campus panorama roaming. Comput Eng Appl Technol 4(13):210–211
5. Yu D (2013) Design and realization of panorama virtual our system in Nanjing Xianlin University City. Nanjing Normal University
6. Liu HN (2013) Research on panorama roaming technology based on HTML5. Zhengzhou University

7. Ji QS (2015) Design and research of panorama roaming system production platform based on HTML5. Lanzhou Jiaotong University
8. Zhao HX (2015) 3D panoramas based on the Google Chrome kernel. Shandong Normal University
9. Huang XB (2012) Design and implementation of landscape online roaming based on panoramic technology. Shanghai Jiaotong University

Design and Development of Mobile Interactive Picture Books

Jing Zhao, Lei Guo, Shirong Zheng, Shuming Li and Jiahong Zhu

Abstract The objective of this essay is to provide a design project for a mobile interactive picture book that features Chinese short stories and to develop a mobile application of interactive picture books by using Unity 3D. The author attempts to discuss the design solution and development process of the mobile interactive picture book compatible with children's cognitive characteristics by weighing up the pros and cons of interactive designs of mobile picture books both at home and abroad. In conclusion, by recognizing the importance of current mobile interactive media in children's early education, the author puts forward the concept that education is in line with recreation, featuring seeing, hearing, entertaining and thinking combined together, and designs and develops the mobile interactive picture book from the perspectives of content, interactive approach and interface design so as to make the childhood education more interesting and boost the interaction between parents and children. Also, the author aims to feasible way of spreading and inheriting traditional Chinese culture.

Keywords Mobile terminal · Picture books · Interactive design
Development of mobile application

1 Introduction

Mobile picture books are electronic publications, which break the limitation of traditional two-dimensional reading and mark a transition from printed media to digital media. Recent years have witnessed a great breakthrough in network and

J. Zhao (✉) · L. Guo · S. Zheng · J. Zhu
Faculty of Art and Design, Zhongshan Institute, University of Electronic Science and Technology of China, Zhongshan, Guangdong Province, China
e-mail: 13531897885@163.com

S. Li
Faculty of Computer Engineering, Zhongshan Institute, University of Electronic Science and Technology of China, Zhongshan, Guangdong, China

P. Zhao et al. (eds.), *Applied Sciences in Graphic Communication and Packaging*, Lecture Notes in Electrical Engineering 477,
https://doi.org/10.1007/978-981-10-7629-9_43

digital technology. Young adults prefer using electronics to read, including smart phones, kindles and iPads [1]. Interactive design in electronic picture books highlights the features of screen and makes full use of modern technology to evoke children's multi-sensory feelings in full measure and provide a multi-dimensional reading experience for them. Also, it awakens parents to the convenience brought by technological development in parent-child reading and boosts the interaction between parents and children. Compared with traditional printed books, interactivity is the prior advantage of mobile picture books. The emotionalized interactive design compatible with children's cognition is easy to understand, providing timely feedback and gameplay. It provides children with a wonderful experience which will gradually turn into knowledge and abilities with the passage of time and finally will benefit children with joys and happiness [2].

2 Major Design Points of Mobile Interactive Picture Books

2.1 Reasonable Layout of Picture Books

The difficulty degree and pages of picture books should agree with the reading habit of children of different ages due to the maximal length of reading for children. Generally, when parents are reading with their children, they are expected to let children see pictures first and then explain the words for them, so as to provide room for children to imagine. For interactive picture books, time used for seeing pictures, telling stories and listening to audio put together shall not exceed one maximal length of reading for children.

2.2 Importance of Text-Image Relation

As a kind of independent book, picture books emphasize the inner relation between image and text instead of the simple combination of "image plus text". In picture books, pictures are no longer merely supplementary to text, but a story-teller the same as text. Children's understanding of the outside world comes from an overall feeling, rather than detailed analysis. That's the reason why some famous picture books are picture-oriented without a single Chinese character, which makes telling story a challenging job for parents. In order to make the parent-child reading interesting, the design of a picture book not only enables each picture to speak, but pays attention to narrative relations among different pictures and strikes a proper balance between image and text so as to make them complementary to each other and bring out the best of a picture book [3]. By doing so, children can instinctively

immerse themselves into the world created by the picture book and listen to the story naturally.

2.3 Reasonable Layout of Visual Elements

Mobile picture books offer various ways of reading, such as parent-child reading, children reading and listening to audio by themselves, adults reading for children, and etc. Children are the target audience of mobile picture books. That's the reason why many designs, including the proportion of pictures to text, the number of words, the size of illustrations, fonts, font size and color combinations, are expected to be in harmony with children's reading habits and visual characteristics [4].

2.4 Importance of Multi-dimensional Experience

Since kids are barely literate and cannot read independently, parents should help their kids to read and explain to them. That is to say, text in picture books is not written for kids to read, but for them to "listen to". When kids are reading with their parents, they are not just hearing a story of other people, but are also connected with the character in the story and put themselves in the character's place. With multi-dimensional experience of seeing, hearing, entertaining and thinking, children can fully participate in the reading [5]. Meanwhile, with audio included, kids can listen to a certain story for several times, each of which is a brand new experience for them. By doing so, children can be aware of the beauty of the classics and the order in picture books and have a better understanding of the overall artistic conception of the picture book [6].

3 Development of the Mobile Interactive Picture Book Series Ten-Minutes Reading

3.1 Design of the Picture Book Series and Layout of the Contents

Ten-minutes Reading series we designed is a mobile interactive picture book, which has many series with different kinds of stories. The first series begins with traditional Chinese short stories. The first story is *The Story of Huangxiang*.

In light of the cognitive characteristics of pre-school and school-age children, we aim to tell each story of a series in ten certain pages. When waiting for a bus or in a

queue, children can casually read a whole story in a short time and learn things little by little.

Due to the limited space for each story, editors are required to clarify the whole story in ten pages regardless of the length of the story. Editors need to properly arrange the storyline and the content of each page in terms of the plot and the demand of expressing emotion.

Noticeably, children need to accomplish each task in sequence before they can move on and unlock the next task. That is to say, children cannot read the second story until they finish the first story. By doing so, children can develop the habit of systematic reading (Fig. 1).

3.2 Design Features and Methods of the Characters, Scenes and Interfaces of the Picture Book

Design features and methods of characters' appearances.

Taking into account of the image designs of different picture books, we find that many picture books, be they traditional printed picture books or electronic picture books in vogue, can be classified into the following two types in terms of painting style. The first type adopts Q-version (Cute-version). Such two to three-heads tall (a height measurement that uses the length of a head as a unit) images take up a larger area of the picture book. The second one is the healing style featuring normal-sized characters and cheerful tones, making people feel comfortable and peaceful at first sight. Since most neighboring children interviewed and surveyed say they love the Cute-version, we follow their preference and design characters into three-heads tall. Later we find that three-heads tall characters are much cuter than many adult characters of six-heads tall. Such design is more acceptable to children readers and preferred by parents who choose picture books for their children. Also, we think characters of Q-version bear a closer resemblance to children.

Fig. 1 Unlock stories in the form of game clearance

As for the design of the scene, we take *The Story of Huangxiang* as an example. Firstly, we have to figure out when the story took place and characters' background information. Then we draw a preliminary sketch of the surroundings and the characters based on their personalities. One of the scenes depicts Huangxiang helping his mother take medicine. Since the story took place in Han Dynasty, some furniture such as bed and pillows in the scene should bear the features of Han Dynasty. Therefore, by consulting different sources and referring to different types of bed, we finally choose the most suitable items and make them more adaptable to the scene by making a few minor adjustments.

As for the design of UI (User Interface), we choose the icons and interactive elements that match the content of the story, so as to increase fun in children's reading. Such elements include titles of different stories on the interface of game level, planks on stories' homepages with themes on them and guideposts with options on them. All these are designed to match the story's content and the painting style (Fig. 2). Also, we design larger-sized icons and buttons such as Backspace, Set and Next Page, and place them in conspicuous positions, so that children can precisely touch them and operate the system smoothly (Fig. 3).

3.3 Interactive Design of the Picture Book and Applying Unity 3D in the Design

Take the interactive design of *The Story of Huangxiang* as an example. The second picture is designed to depict Huangxiang holding a bowl of medicine and helping his mother to take medicine. There are three choices of items in Huangxiang's hands, which are a bowl of medicine, a bowl of wine, and a bowl of water. When children touch each of items, they can hear the pronunciations of water, medicine and wine. Children need to move the correct item towards the mother's mouth. Only if the correct answer is chosen can they continue the game, or the image will freeze (Fig. 4). Such design is aimed at increasing interactivity. Children can

Fig. 2 Interactive interface design of the picture book

Fig. 3 Design of icons and interactive elements in the interface

Fig. 4 Interactive design in the picture book

develop their ability to recognize and operate while thinking independently in this process. It also aims to make the reading more interesting, since children will easily lose interests if they keep turning pages.

The gist to operate this in Unity 3D:

The first step is to make objects move with the mouse. First we use start coroutine function to start coroutine. Then we transfer objects' coordinates from the World Coordinate transform position to the Screen Coordinate screen space (to obtain the Z-axis of the Screen Coordinate). Next, we calculate the distance between different objects by using the formula offset = transform position-the mouse's Screen To World Point (After transferring the mouse's coordinate from the Screen Coordinate to the World Coordinate, the Z-axis of the mouse's world coordinate is consistent with that of the object. Through direct subtract, we can obtain the offset). Then we hold down the button of the mouse and set cur-screenspace to record the X-axis and Y-axis of the mouse's Screen Coordinate (Z-axis remains to be the target object), and turn it into the World Coordinate. Finally, plus the offset calculated before and assign the final result to transform position. Add the statement yield return new wait for fixed update to make objects move with the mouse.

The second step is to set a trigger that will be activated when an object is moved to a certain place. Here we set up a trigger. First, we need to create the basic settings by adding respectively two same box collider 2D components to the attributes of the background image and another object that needs moving, and ticking one of Is Trigger. Next, we need to add a rigid body 2D between the two objects and turn the gravity into 0. Then we enter the unity's own code block on trigger Enter 2D and add a statement to this function. Through the previous settings, we can know whether an object has been successfully moved to certain places from the tag in objects' attributes.

4 Conclusions

Reading mobile interactive picture books is not just equal to simply reading stories on mobile platforms, but also a multi-dimensional interaction that is easy to understand and provides timely feedback and strong gameplay. Such interaction is designed in terms of children's cognitive characteristics, reading habits and visual features. It contains meticulously selected stories and cares about the balanced relation between image and text, and emotional needs of children, making reading an interesting thing. For the design of interactive picture books, good stories are basic, it also needs the supports of technology and interaction, so as to strengthen the multi-dimensional experience of seeing, hearing, entertaining and thinking during the reading, and increase fun in it. With mobile devices popularized in users of different ages, the domestic market of electronic picture books is destined to have a bright prospect. Interactive electronic picture books are attracting more and more children's attention with distinctive advantages. Such picture books makes childhood education more interesting, boosts the interaction between parents and children, and provides a feasible way of spreading and inheriting traditional Chinese culture.

Acknowledgements This study is supported by 2016 Key Platform and Scientific Research Projects of Guangdong Provincial Education Department (Education and Scientific Research Projects) (No. 2016GXJK195), 2015 Key Platform and Scientific Research Projects of Guangdong Provincial Education Department (Youth Innovative Talent Project) (No. 416YCQ06), and 2016 Quality Engineering Project of UESTC, Zhongshan Institute (No. JY201628). This work is also supported by a Zhongshan City Science and Technology Plan Project (No. 2017B1132), 2017 Innovative Entrepreneurship Education Curriculum Construction Project of Guangdong Province (No. S-CXCYKC201701) and 2014 Research Project of Department of Education of Guangdong Province (Education and Scientific Research Projects) (No. W-JYY201401).

References

1. Aliagas C, Margallo AM (2017) Children's responses to the interactivity of storybook apps in family shared reading events involving the iPad. Literacy 51(1):44–52
2. Barr R (2013) Memory constraints on infant learning from picture books, television, and touchscreens. Child Dev Perspect 7(4):205–210
3. Yang ML (2012) Research on design of human computer interaction interface for children's learning game. Packag Eng 33(22):45–48
4. Xiao H (2012) Discussion on the visual design principle of multi-sense human-computer interface. Packag Eng 33(8):35–37
5. Ma MY, Wei CC (2016) A comparative study of children's concentration performance on picture books: age, gender, and media forms. Interact Learn Environ 24(8):1922–1937
6. Lin RL (2011) A study of mixed media art creation for children's picture books. Adv Mater Res 213:172–176

Printing Media's New Blue Ocean—From Customized Web-to-Print to Me-Commerce Cloud Printing

Chi-Feng Cheng, Yung-Cheng Hsieh and Ming-Chw Wei

Abstract The Web-to-Print platform offers print service providers a brand new sales channel. The channel enables providers to expand customers from business entities to end users via Internet; meanwhile, through this channel, providers can cast off price competition of being standardized and increase product value via personalization and customization. By adopting highly automatic production, print service providers can establish efficient business procedure in developing new customer and good customer service; also, providers can reduce labor cost and improve performance. Nevertheless, the Web-to-Print is not only a new platform but also a new business ecosystem. The keynote for traditional print industry to lead the Web-to-Print is to consolidate business flow and to transform company culture. The Internet marketing's education and implementation become crucial for Web-to-Print providers to develop business. Web-to-Print providers will eventually design customized product by satisfying Me-Commerce along with 3D printing technology being refined. On Me-Commerce platform, the print service will be completed from two-dimensional to three-dimensional, from graphic as flat to unique and unmatched as a whole. With the growing of subscribers, the Big Data application will be an important tool to reinforce Web-to-Print's ecosystem and Me-Commerce platform. In the era of Internet, either Web-to-Print or Me-Commerce is important for print service provider's competitiveness and development.

Keywords Web-to-Print · Business ecosystem · Me-Commerce
Big data · 3D printing

C.-F. Cheng · Y.-C. Hsieh (✉)
College of Communications, National Taiwan University of Arts,
New Taipei City, Taiwan R.O.C.
e-mail: ych@ntua.edu.tw

M.-C. Wei
Graduate School of Creative Industry Deign, National Taiwan University of Arts,
New Taipei City, Taiwan R.O.C.

P. Zhao et al. (eds.), *Applied Sciences in Graphic Communication and Packaging*, Lecture Notes in Electrical Engineering 477,
https://doi.org/10.1007/978-981-10-7629-9_44

1 Introduction

Web-to-Print, W2P, or Printing E-Commerce is the commercial activity combining related printing services via virtual web channels such as Website, Cloud, Mobile Application and Virtual Reality. It is not only a technique or platform linking customers and professional service providers, but also a series of integrated system of marketing, promotion, payment, production, quality control, distribution and customer service. Through Information Technology application, print service providers can retrieve purchase orders from all over the world without limitation, and to extend their market from business entity to private individuals. In addition, the highly automatic solution of W2P offers providers an opportunity to reduce their labor cost.

W2P is not only a new access for business expansion, but also an important strategy for company transformation from "offline" to "online", and from physical to virtual. In terms of value creation, such as Information Sharing, Cost Saving, Operation Efficiency Improvement and Customer Service Satisfaction, etc., Web-to-print systems enable printers to construct a better business ecosystem among customers, designers and service providers than conventional printing systems. Meanwhile, W2P creates a new economy system to enlarge customer database and shift to Me-Commerce gradually. Me-Commerce possesses great potentials to develop a brand new market value, and offers massive appeal for those existing W2P service providers and potential E-Commerce market entrants. This study explores W2P's current development, system structure, and Me-Commerce development trend.

2 Discussions

The W2P market is mainly led by digital printing technology. In recent years, W2P makes enormous improvements on cost, speed and quality, and is gradually competitive with traditional printing technique. On the other hand, the digital printing technology progresses rapidly that fastens W2P's market share in the industry. According to the "Web-to-Print, A Global Strategic Business Report" of Global Industry Analytics (GIA) in August 2016 [1], the global W2P sales revenue will increase from USD800 million in 2017 up to USD1300 million in 2022 with over 10% growth. In regions, Europe is the largest market and Asia-Pacific is the highest performance area with over 12% growth. In fact, in Asia-Pacific, the actual growth percentage is higher than the report's estimate since most of the W2P service providers are not listed in the study [2].

The W2P development is like the other digital businesses in the market that only a few companies are fast growing because of being early entrants or best service [3], such as U-Printing, VistaPrint, Zazzle, Cafepress, Fedex Office and Pixum in Europe and North America, and Gain How Printing, BlueCo Printing, Youprint in

Taiwan. Reviewing from the past business experience in Taiwan, the W2P providers are non-traditional printing service providers in small scale in the beginning, later on mid-sized printing companies join the market, hence the W2P market share grows rapidly over 50% in short period. In China, there are many W2P companies, such as Yifutu, EP365 and EasyPrint, basically providing only standard paper-printed related product, but not highly customized products, such as personal gifts for special events, tailored made product for family members including pets. This is different from customization service provided in Europe and North America.

For creating higher revenue, W2P's products are mainly customized to increase value, but on contrarily, the traditional printing company's products are mainly standardized to decrease cost [4, 5]. There are four advantages in W2P: (1) Large customer base: customers can be reached all over the world via internet and direct mail; (2) Long business hours: the highly automatic printing solution enables customers to design product, place order, edit, and request delivery on line without limited operation hours; (3) Good customer relationship: it is efficient to manage customer relationship by providing low cost and various service upon customer's request through email or social media; (4) Different personal service: customers are able to share, edit, and preview their own design virtually on website. The W2P printing solution is well developed in Europe and North America, therefore, a printing service provider can design the software in-house or outsource professional software companies.

3 Subjects

The purpose of this research was to study the ecosystem, process and flow constructed by Web-to-Print and the future tendency of Web-To-Print.

4 Research Method and Approach

This research findings and conclusion was derived from content analyses from some vital web-to-print websites, including www.gainhow.tw/, www.blueco.com.tw/, www.youprint.com.tw/, www.yifutu.com/, www.ep365.com/, www.98ep.com/, www.zazzle.com/, www.uprinting.com/, www.vistaprint.com/, www.cafepress.com/, www.fedex.com/us/office/, and int.pixum.com/ , etc.

5 Data Analysis

5.1 Business Ecosystem

W2P platform establishes a business ecosystem among customers, print service providers, designers and personalized products (Fig. 1). W2P customers are divided into two majorities: private users and small to mid-sized companies. Normally, these types of customer's printing and design knowledge are limited, order quantity is small and uncertain, demanding is personal and variable. Concerning customer's knowledge is limited in printing and design, W2P platform offers easy-to-use interface for design, editing, preview and order placement online.

Meanwhile, various platforms including PC, mobile phone, internet TV and tablet can be connected though Cloud to Print which gives customers better mobility and flexibility [6]. W2P customer source are existing customer from traditional printing and new customer from website. Website is an important resource to expand customer base and website marketing is an important tool to attract new customers continuously. Website marketing strategy includes social media, website blogger, keyword search engine, webpage banner, and movie promotion. It is a major challenge for traditional printing industry on how to use these new marketing strategies.

In China and Taiwan, most conventional printers emphasize their physical facilities and in-house services rather than diverse product with creative design. In contrast, in Europe and North America, W2P's printing is not only limited on paper goods, such as book, business card, greeting card and calendar, but also on different materials, such as fabrics (clothing, bag, purse), metals (cellphone case, tablet cover), plastic (pen, plate), or ceramic (mug). Moreover, if the market demand is higher than a W2P service provider's own capacity, the service provider can alternatively use outsourced contractor maintaining lower capital expenditures and

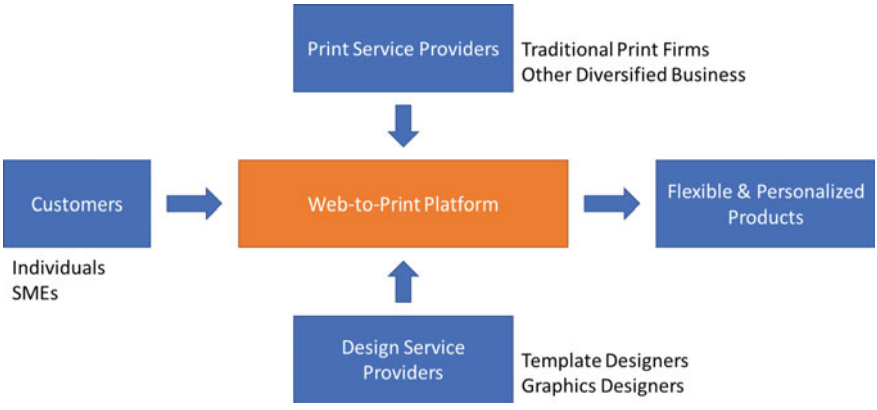

Fig. 1 Customized Web-to-Print ecosystem platform

higher financial leverage. In fact, some of major W2P printers with large production scale take third party orders on line to enlarge their profit.

On a W2P platform, it comes with basic layout and template for customers, and it integrates customer's uploaded image for further personalization. To satisfy more customization demand, W2P service providers usually present various layout, template, highly resolution image or pattern from third party in which another trade market is created for customer to pay per use or free use, and for professional to design per request. Moreover, variable and famous pictures of Exclusive Intellectual property rights, such as cartoon characters from the Disney and masterpiece from the Louvre, are available on the website that enriches customization more ample and diversified.

There are abundant personalized products from customized W2P platform, including paper printing, stationary, 3C accessary, fabrics, interior decoration, and furniture. These personalized products can be sold for personal use, as well as for business trading on the platform. Designers or W2P service providers can sell their customized merchandize to individuals or other business sectors through the website. Therefore, in the business ecosystem, customers, designers, and printing service providers are multivariate and multidirectional on the platform (See Fig. 1).

5.2 Physical Structure of W2P Platform

On a W2P platform, highly automation enables conventional printers to process an order from acquiring customer to tracking delivery on website without extra labor and time cost. In addition, the system consolidates information flow, capital flow, trading flow and distribution flow: information flow manages customer/subscriber login, product search and data comparison; capital flow is in charge of payment method, online billing and supplier's online payment; trading flow resolves customer relationship and order processing; distribution flow regards to both internal and external logistics and raw material delivery. By integrating W2P's digitalized system and business flows, printing service providers can save on cost and time, on the other hand, improve effectiveness and customization flexibility. A typical W2P platform contains eight online systems and order transfer interface (Fig. 2). The eight online systems are: online member login, design and edit online/offline, online preview, online estimate, online order process, online payment, online tracking and online customer service (Live Chat) [4, 7].

"Online member login" offers registered member with user-friendly webpage to manage personal account information. "Online/offline design and edit" makes customer's personal design is viewable and easy to upload file offline. "Online preview" visualizes personal design before order placement. Therefore, the importance of online preview is to insure product quality and customer satisfaction on color reproduction and image quality. "Online order process" is purchase, tracking, cancellation, refund policy and return of goods. "Online payment" deals with various payment options, invoice and refund. "Online tracking" enables

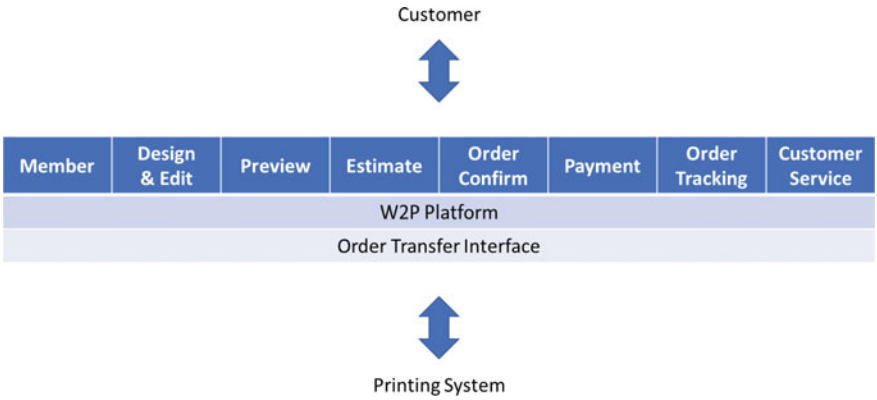

Fig. 2 A typical W2P system structure. *Source* Modified from [2]

customer tracking order update. "Online customer service" is a twenty-four hours interaction channel in replying customer's request and questions, including, online representative, email, live chat and message board.

On W2P platforms, the order transfer interface is another important feature that throws order confirmation into production. This interface shifts website's online image into manufacture system. Therefore, this interface's efficiency involves with how the printing system is digitalized and how the production procedure is effective in back-end. The growing customization demand normally requires multiple procedures, that if the higher the printing and production system is digitalized and integrated, the better the manufacture efficiency and product quality is improved. However, it costs larger capital investment. If the printing system is in lower integration, the labor cost is higher in manual operation; meanwhile, it is difficult to control production efficiency and product quality. Therefore, the capital investment on a W2P front-end platform as well as digital system in back-end is both competitive advantages in W2P industry.

5.3 Me-Commerce Platform

The robust 3D-Printing technology and Industrial 4.0 leaps printing solution with fully automatic and robotic, and benefits customized printing in lower cost and less time consuming. With the new generation production technology, merchandises on a customized W2P are often in tailor-made from top to bottom including printing material, which is so-called "Me-Commerce" on Forbes Magazine 2012. On Me-Commerce platform, one purchase order involves diverse service providers from 3D printing provider to industrial 4.0 intellectual manufactures. Designer's artwork becomes comprehensively from flat graphic to 3D-dimensional.

Because of increasing subscriber and improving data management on Me-Commerce, the Big Data is used for trading analysis as well as marketing strategy. Through Big Data, information is sharable and accessed on Me-Commerce, which allows all the printing service providers to obtain productive information regarding designer's service type and manufacture's product category. By means of Big Data application, every participant on the platform is closely connected and widely influenced, and the platform's advantage is competitively. If a traditional printing company wants to transform from W2P to Me-Commerce, the company's production procedure needs to be fully automated and customer base needs to be continuously expanded. Due to Me-Commerce requires many technology in cross fields, printing service providers can choose self-development or strategic alliance in order to shift to 3D printing and Industrial 4.0 intellectual production; they can work with other Me-Commerce providers by developing their own system investment or outsourcing. It is an important task to develop a user-friendly and highly visualized interface for a customized W2P business transform to 3D printing.

6 Discoveries and Recommendation

W2P is a new business development and growing opportunity for printing service providers. However, the W2P and Me-Commerce clouding is not only a new sales channel and a new business model, but also a new transformation. In internet era, all the commercial activities are trying to catch one's eyeball with faster, better and more capable service. Therefore, if printing service providers want to be in Me-Commerce cloud printing market, the must-do homework is to maximize targeted internet marketing to catch users' eyes, personalization and creativity sharing. The development trend of Me-Commerce cloud printing includes, but not limited to the followings: built-in (imbedded) online design/editing/proofing, diverse tailored-made product and merchandise, licensed images/design for free download, designed content sharing service for customers, free unlimited cloud storage space, prompt customer service response at every time, anywhere and anytime, absolutely satisfaction guaranteed (24-h online), offering design software for free download, customers using that software to design/edit their own product and place the order, consignment service provided for designers, and Apps for mobile devices or tablets. It is a good opportunity for conventional printers to activate a new generation of their business with the adoption of Me-Commerce cloud printing. Me-Commerce cloud printing also brings in a new impact on business flow, business culture and thoughts to the printing industry and only the ones who embrace the opportunities can be the next tycoon.

References

1. Global Industry Analytics Research Report (2016). Web-To-Print-a global strategic business report
2. Hsieh YC, Lin HS (2011) A study of the functionalities and workflow for Web-to-Print platform. Adv Mater Res 174:151–154
3. Na F (2011) The starting of cloud printing. Retrieved 19 Mar 2017 from http://blog.xuite.net/cathy.shiau/twblog/132577610-%E9%9B%B2%E7%AB%AF%E5%8D%B0%E5%88%B7%E8%B5%B7%E6%AD%A5
4. Lin HS (2010) Development difficulties and needs of Web-to-Print. Master thesis, National Taiwan University of Arts
5. Liu YJ (2012) The study of business model of Taiwan Web-to-Print printing. J Cagst 28 (2):493–502
6. Hartley S (2012) The rise of "Me-Commerce" Forbes Magazine. Retrieved on 19 Mar 2017 from https://www.forbes.com/sites/scotthartley/2012/08/17/the-rise-of-me-commerce/#37578cdc638d
7. Liu N, Cao C (2016) The design of network printing function model. Adv Graph Commun Packag Technol Mater 369:423–431
8. Top Ten Website Review. 2017 Best online printing service review. Retrieved 19 Mar 2017 from http://www.toptenreviews.com/services/internet/best-online-printing-services/

Part IV
Printing Engineering Technology

Inkjet Etching Silver Nanowire Film for Multi-touch Sensors

Zhiqiang Gao, Biyu Yuan and Cheng Sun

Abstract The paper studies how to fabricate multi-touch sensors with ink etching silver nanowire film. With PET film covered with silver nano wire as conductive material layer and diluted nitric acid as etching ink, people can produce a conductive grid with multi-touch screen by the technology of piezoelectric ink-jet printing. The stability of volume and the accuracy of the ink droplets are improved when the pulse of the waveform and printing strategies are adjusted. Then a double-sided capacitor film is produced of which the width of etching line is 65 μm. And the resistance is about 11 kΩ when the length of the grid is 20 cm.

Keywords Ink jet · Etching · Touch sensor · Silver nanowire

1 Introduction

Touch sensors are becoming more and more popular between devices and users, but the supplies market is almost entirely dependent on indium tin oxide (ITO) materials. ITO is expensive not only because indium is rare metal but also because the deposition of high quality and large area conductive film require higher temperature conditions. So many other transparent conductive materials have been produced as alternatives. Many research groups have demonstrated that the silver nanowire film has the property of transmittance of 90% and RS can achieve 50 Ω/□ [1]. These characteristics can meet the requirements of ITO in the present manufacturing of touch sensors. In this study, the conductive network was prepared with the help of ink-jet printing by etching the silver nanowire with acid [2, 3]. The etching process does not affect the conductive fibers on the other side which assures

Z. Gao · B. Yuan
Packaging and Printing Engineering College, Tianjin University of Science and Technology, Tianjin, China

C. Sun (✉)
Tianjin Vocational Institute, Tianjin, China
e-mail: chengsun55@sina.com

P. Zhao et al. (eds.), *Applied Sciences in Graphic Communication and Packaging*, Lecture Notes in Electrical Engineering 477,
https://doi.org/10.1007/978-981-10-7629-9_45

the flexibility of the double-sided conductive network. So that the number of layers required for the multi-touch capacitive screen is reduced and the thickness of the product in the end is reduced as well.

In fact, the accuracy of etching through laser is much higher than that of ink-jet printing. So the ways to use ink-jet printing need to be improved by precisely controlling the quality of the etching solution and improving the accuracy of the droplets placement to meet the requirements of the conductive network. The strategy of ink-jet printing is particularly important in this study [4].

The process of ink jet-printing for the purpose of graphic reproduction will rasterize the image to dots, then fills the dots through the printing head. If a nozzle is clogged, then the process of ink-jet printing scanning will appear in the starved area and lost points. Therefore, multi-scanning and plug-in printing methods are used to weaken the influence of the abnormal nozzles. In the process of ink-jet printing, we will focus on the realization of function. In order to fabricate a silver nanowire conductive film as substitute for ITO, we study ink-jet etching effects on the linearity and conductivity of conductive network, the accuracy of ink droplets effects on open circuit and short circuit.

2 Experiments

2.1 Nanowire Film Deposition

The silver nanowire was prepared by wet reduction of silver nitrate with an average diameter of 20 nm and an average length of 15 μm. The silver nanowire was sonicated by ice bath and diluted in an isopropanol solution at concentration of 0.2 mg/ml. And an aqueous solution of isopropyl alcohol with a mass fraction of 10–15 wt% is obtained. Through the spraying method, the dilution sprays of silver nanowire will be in the washed, leached PET surface. PET film was placed in an vacuum oven at 90 °C for 30 min. After the removal, using the plastic wrap to cover the coating surface and apply the same coating and drying on the other side. Changing the number of sprays obtain film with different transmittance and surface resistance, using a spectrophotometer to test the transmittance and a four-point probe tester for sheet resistance.

2.2 Inkjet Etching Strategy Test

Ink-jet printing strategy is mainly about the waveform development and the sequence of ink-jet printing, the purpose is to enhance the accuracy of the amount of the droplets. The ink drop observation system is used for waveform development to obtain the optimum pulse width and to get ink droplets with faster speed and smaller volume.

High-precision sports platform (NT221-116A, Nanothink) is used as an ink-jet printing platform, which is a X-Y two-dimensional motion system, positioning accuracy ± 3 μm, repeated positioning accuracy ± 5 μm. Three kinds of jetting methods were designed: (a) sequential injection which means that the ink dots forming the vertical lines were sequentially jetted by several nozzles; (b) random injection which means that the ink dots forming the vertical lines were randomly assigned to several nozzles; (c) short continuous jetting which means that the vertical line is divided into micron-level lines, each line assigned to a single nozzle, then these lines combine with each other into a vertical line.

3 Results and Discussion

3.1 Performance of Nanowire Film

Figure 1 is silver nanowire film with different coating times under the observation of electron microscope transmission. It can be seen that the density of the silver nanowire can be controlled by the times of spraying. With different spraying times, the dispersion state of the silver nanowire is good, there is no circumstance of local accumulation. Figure 1a is silver nano wire coating which is sprayed three times, Fig. 1b is 6 times. As we expected, the purpose of spraying for three times is to obtain a higher transmittance, and the 6 times one is to obtain the higher visual haze because of the opacification, resulting in light scattering. The Fig. 1b shows a lot of bright nodes, which is due to the process in the oven, silver nano wire overlaps area which appears in the mutual melting and bridging. This bridge is conducive to increase the continuity of the electronic resistance and to reduce resistance, but it is not conducive to light transmittance.

Figure 2 is a diagram which shows the relationship between silver nano wire coating square resistance and light transmittance. The visible light band was selected as the transmittance test range. The relationship between square resistance

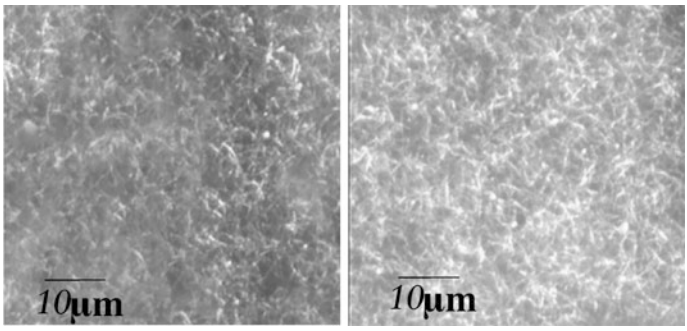

Fig. 1 Silver nanowire film

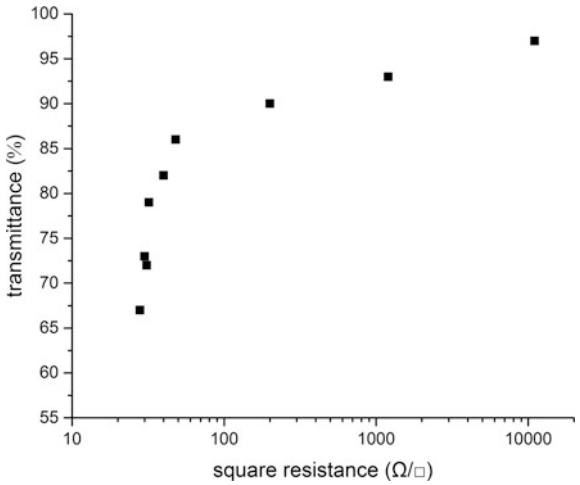

Fig. 2 Square resistance of silver nano wire films of various densities

and light transmittance is that with more spraying, the resistance and the light transmittance will be lower which should be sprayed more than 4 times in order to meet the requirement of light transmittance of 86%, square resistance of 48 Ω/□ of the touch screen light transmission.

3.2 Drive Waveform Development

Figure 3 shows the volume and velocity of the etching ink droplets under the affection of pulse width over time by the observation system. The droplet separation is considered as a satellite dot. The satellite will play in the non-target area, greatly affecting the straightness of the etching line. Therefore, the pulse width which raise the satellite point is excluded, and only if the pulse width area is away from the satellite between 1.664 and 2.496 μs, can it be scanned and observed.

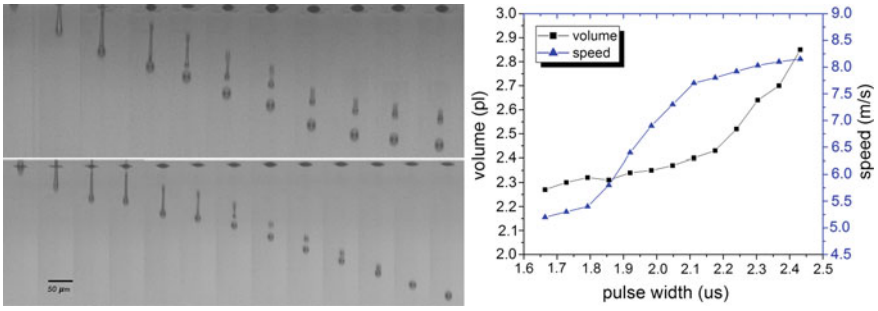

Fig. 3 Effect of pulse width on droplets

It can be seen that when the pulse width is 2.112, the droplet velocity is fast and the droplet volume is small. Therefore, it is suitable for ink-jet printing when the pulse width is 2.112 μs, with ink droplet volume is 2.4 pl and droplet speed is 7.7 m/s.

3.3 *Performance of Silver Nanowire Network*

Figure 4 were conductive grid printed through jetting methods a, b and c. It can be seen that the edge under method is neat, but the width is about 88 μm. The edge under method b is zigzag and the width was different, range from 50 to 75 μm; the edge and width under method c is uniform and the width is about 65 μm. According to the experimental ink-jet printing characteristics, the conclusion is that the method is more accurate method but there is an enlarged situation. The method b has the most obvious deviation and fluctuation. The method c is accurate and hardly expanded (Fig. 5).

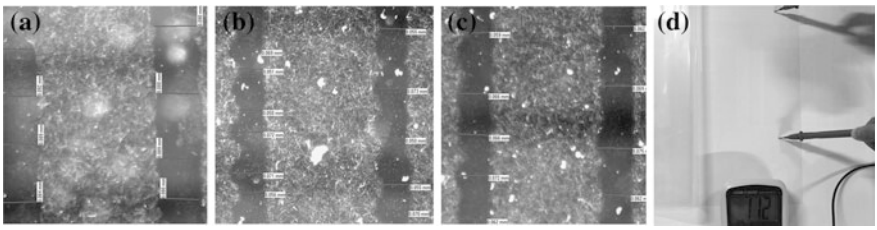

Fig. 4 Droplets volume and velocity with Pulses. **a–c** Refer to method a–c, **d** resistance test

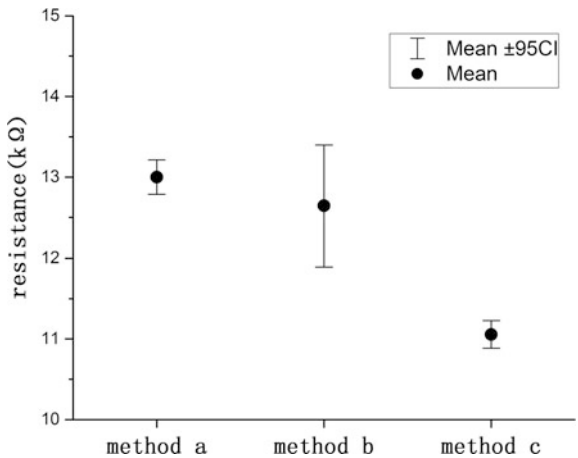

Fig. 5 Droplets volume and velocity with Pulses

The main cause of the difference is the residual vibration in the piezoelectric nozzle. A pulse waveform is applied to the nozzle, and the ink droplets fly out from the nozzle, then the residual vibrations inside the nozzle lasts for several or tens of microseconds. If the next pulse is applied before the pressure wave is dissipated, the flight pattern of the next droplet will be different from the preceding droplet. Method c assures a continuous firing in a short time then the trigger frequency is fixed, the residual vibration is the same to each droplet, the flight speed is relatively stable.

A conductive grid with a length of 20 cm was used as standard to test the average resistance. Through method a, the average resistance of 13 kΩ is obtained. Under method b, the etching width is narrow, but the resistance is large and fluctuated apparently which mainly because the film resistance depends much more on the material's own conductivity and plane characteristics. Plane characteristics include length, width and line edge uniformity and other characteristics which the uniformity of edge will seriously affect the load current, resulting in instability. The resistance in method c keeps stable at about 11 kΩ. The conductive thin film network in this study was used for capacitive multi-touch sensor, grid uniformity and conductivity to affect capacitance characteristics. Method c is better than other methods.

4 Conclusions

In this article, the flexible double-sided silver nanowire network film can be made by the inkjet etching method, with the light transmittance 86% and the square resistance 48 Ω. The width of etching line is uniform about 65 μm. The resistance of conductive grid with a length of 20 cm is about 11 kΩ on average. Silver nanowire network film obtained through this method can realize the fabrication of flexible touch sensor with large area. Double-sided conductive network features also help reduce thickness of the screen and cost.

References

1. Khaligh HH, Liew K, Han Y et al (2015) Silver nanowire transparent electrodes for liquid crystal-based smart windows. Sol Energy Mater Sol Cells 132:337–341
2. Scardaci V, Coull R, Lyons PE et al (2011) Spray deposition of highly transparent, low-resistance networks of silver nanowires over large areas. Small 7(18):2621–2628
3. Langley D, Giusti G, Mayousse C et al (2013) Flexible transparent conductive materials based on silver nanowire networks: a review. Nanotechnology 24(45):452001
4. Calvert P (2001) Inkjet printing for materials and devices. Chem Mater 13:3299

Applications Analysis of Paper-Based Color 3D Printing in the Map Industry

Xingyan Yan, Jiangping Yuan and Guangxue Chen

Abstract To provide business cases and creative ideas for paper-based color 3D printing applied into the map industry, two map categories including military derivative map market and civilian derivative map market were introduced and analyzed with lots of famous applications. According to the statistic results, the 3D map printed by various 3D printing processes will be attributed to a promising 3D printing application market in China. At last, three flexible business modes were also offered with detail cases and usage development guides based on paper-based color 3D printing process.

Keywords 3D printing · Map industry · 3D map · Business analysis
Case study

1 Introduction

3D printing was known as one of three most revolutionary technology among recent years. And it was also applied into different industries in China with developed modern cases. Currently, most researchers were paid much attention on printing precision, printing speed and printing materials, all of these were just focused on the manufacturing view, which maybe lead to less 3D printing industrialization cases. In our opinion, the development period of 3D printing can divided into three phases: precision era, color era and intelligence era, which were easier to understand industrialization of 3D printing technologies. In the era of color 3D printing, different color 3D printing based on various substrates were developed, such as popular paper-based color 3D printing [1], powder-based color 3D printing

X. Yan · G. Chen (✉)
State Key Laboratory of Pulp and Paper Engineering,
South China University of Technology, Guangdong, China
e-mail: chengx@scut.edu.cn

J. Yuan
Color 3D Printing R&D Center, Yuncheng University, Shanxi, China

P. Zhao et al. (eds.), *Applied Sciences in Graphic Communication and Packaging*, Lecture Notes in Electrical Engineering 477,
https://doi.org/10.1007/978-981-10-7629-9_46

[2], plastic-based color 3D printing [3] and others. For a new view about 3D printing in 3D map industry, it is urged for creative principles and feasible business modes to guide 3D printing service provider.

From the online survey about 3D map production and application, it is indicated that military derivative map market and civilian derivative map market had been the most important part of 3D map market printed by 3D printing processes [4, 5]. What's more, there is a big change from the functional aspects to cultural aspects of 3D printed applications in 3D map industry industrialization color 3D printing.

2 Color 3D Printing Application Status in the Map Industry

According to the Chinese geographic information industry, the map industry was subdivided into military map industry and civilian map industry [6]. The National Surveying and Mapping Geographic Information Bureau counted that the total output value of geographic information industry was expected to reach 436 billion RMB in 2016, with 20.1% growth year by year, and listed enterprises exceeded 200, which indicated that the domestic map industry with rapid development.

In the military map industry, military 3D map is the most important form of 3D map applications. For military 3D map, in terms of application patterns, the functionality was more concerned for the 3D map, such as presentation capabilities of physical production flexibility, potential cost economy, low-carbon potential and intelligent convergence. Due to the thickness advantage of the 3D map, the integration of intelligent was provided enough physical space, which provided a technical direction for the exploration of low-cost intelligent 3D map. It was more successful in the Lanzhou Military Region, the derivative application market about the gift and civilian of Lanzhou urban 3D topographic map model was explored by the paper-based color printing technology.

The following three types of business enterprises were recommended to business layout: flat graphic map printing enterprises, cultural and creative operation of enterprises, as well as possessed 3D design capabilities businesses. When it comes to this business, the cultural military 3D maps need to consider two key issues for better printing level when performing color 3D printing and custom production: 3D modeling accuracy of remote sensing data and the color reproduction accuracy of 3D printing. Although ICC-specific verification was configured from the printing process based on specific paper-based 3D printers, it was necessary to develop an overall optimization process to simplify acquisition of high-precision color models from existing prints result.

Civilian map industry had occupied the most share of the market capacity, the industry total value of civilian map derived application also exceeded 400 billion RMB which also contained the contribution of the 3D physical map [7]. For example, the "travel life—explore the map" series of 2D-paper tourism map was

developed by TopdoT, which has achieved 2 million RMB sales per year, as showed Fig. 1, which benefited from its good interpretation for the current popular "experiential economy" experience and the essence of service.

Regarding the civilian 3D map in aspect of Application mode, functional applications and cultural applications shared half in the civil market, which was mainly for the derivative application market. A single application of functional applications not only can be developed by enterprises, such as 3D print pen holder as shown in Fig. 2. A cultural application of a single product also can be developed, such as the United States well-known geographical and cultural products site which named Landprint.com products, as shown in Fig. 3. The functional applications and cultural applications both are regarded as composite products can be developed, such as IP game line 3D map scene.

In the process of civilian 3D map derivative application development, the mainstream sub-derivative application market has formed like the real estate 3D map, 3D blinder map, 3D real scene map, 3D tourismmaps, 3D home decoration map and so on. In the real estate 3D map application, city subway route map re-design and publicity souvenirs was developed, such as full-color block building 3D map model, shown in Fig. 4. In the form of 3D blinder map application, point-line-strip type 3D maps can be developed, such as the Japanese Geographic Information Space Agency is developing a navigation software, which not only allowing users to download data from the internet and the 3D blinder local map was prepared by using 3D printing technology, as shown in Fig. 5. Moreover, the overall real miniature 3D navigation map was also developed by domestic company, as shown in Fig. 6.

Fig. 1 The best-selling paper map

Fig. 2 3D print pen holder

Fig. 3 3D print topographic map

Fig. 4 Paper-based color 3D print real estate 3D map

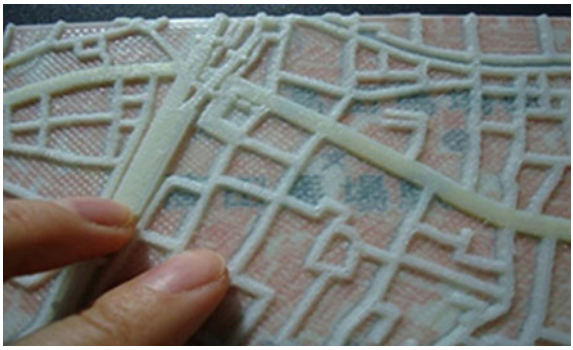

Fig. 5 Line-type blind 3D map

Fig. 6 Panoramic miniature blind 3D map

3 Color 3D Printing Business Analysis in Civilian 3D Map Applications

The civilian map industry, as the user market is vast and huge, is similar to the user object of traditional map printing industry, so the analysis from the business development standpoint will help the printers to carry out new business expansion. The business form can be divided into three types of business including stable style business, marketing style business and symbiosis style business. Three core indices including target market, business planning and exploring strategy were analyzed to guide interested investors for 3D service providers.

Stable style business means the business style behaved the stable application market, and then its target market shows a good continuity. This type of business development can be located as the dominant business in the most market segments of civilian 3D print map application, and it was performed more obviously in the real estate 3D map application market, 3D blinder map application market and real scene 3D map application market.

Marketing style business is a class of the business that tempt and grasp the initiative customers as well as the stronger marketing design ability and planning execution capacity were required. Development of marketing style business should be focused on celebration and sports events to print various derivative products and services based on traditional map elements. Thus, a professional marketing planning team will be a good preparation for this target market. For the enterprise lacking of powerful marketing planning team, it can also cooperate with other social network brands to promote market prospect with integrated planning solutions.

Symbiosis style business, this total market scale has been rising rapidly in recent years. During the business exploitation, it is required new entrants to pay more attention on daily activity venues which the customer can usually stay longer time, such as coffee shops, restaurants and bookstores and other places. Taking Starbucks for example, customers can not only taste unique drinks and enjoy the elegant environment in the store, and you can also buy customized gifts. Since 2012, to accommodate the Chinese customer market, Starbucks had established the brand customized Gift Center program.

4 Conclusions

3D map market is the fastest growing target market in the map industry, which benefited from the color 3D printing technology, especially for paper-based color 3D printing process. From the survey about various sub-application categories of 3D map market, it can be found that the business scale of 3D map printing had been up to be an important and huge sub-map market. The 3D map products had been developed from the functional applications to cultural applications with rich cases. The proposed three defined business style including stable style business, marketing style business and symbiosis style business can provide enough ideas and judgments for interested investors and managers.

Acknowledgements This research was financially supported by the Guangdong Provincial Science and Technology Project(2013B090600060 and 2017B090901064), and the Applied Basic Research Program of Foundation of Yuncheng University (Grant No.CY-2016012).

References

1. Ramdzan AN et al (2016) Development of a microfluidic paper-based analytical device for the determination of salivary aldehydes. Anal Chim Acta 919:47–54
2. Zhang Z et al (2017) 3D-printed poly(epsilon-caprolactone) scaffold augmented with mesenchymalstem cells for total meniscal substitution. Am J Sports Med. https://doi.org/10.1177/0363546517691513
3. Xun Y (2017) Sparse 3D directional vertices vs continuous 3D curves: efficient 3D surface matching and its application for single model face recognition. Pattern Recogn 65:296–306

4. Wang H, Chen G, Zhang W (2014) 3D printing of topographic map based on UV ink-jet printer. Appl Mech Mater 309–312
5. Guerin S, Lempereur C, Brevet P (2012) 3D temperature mapping of turboshaft components using thermal paints and color recognition. Proc SPIE
6. Alkawaz MH et al (2014) Realistic facial expression of virtual human based on color, sweat, and tears effects. Sci World J 367013
7. Osman RB, Alharbi N, Wismeijer D (2017) Build angle: soesit influence the accuracy of 3D-Printed dental restorations using digital light-processing technology. Int J Prosthodont 30 (2):182–188

Influences of Paper on 3D Printing Quality in UV Ink-jet Printer

Liuxi He, Guangxue Chen, Minghui He and Junfei Tian

Abstract The paper intended to research the influences of paper in UV ink-jet printer, mainly including the height and glossiness. Results proved that infiltrations had all appeared between three selected substrates of paper, on which the paper roughness and bulkiness had a linear effect. And the infiltration on the first layer of ink was bigger than those on other layers of ink. It is too stable to not be changed by the paper that the infiltrations between two layers of ink. As we knew, paper roughness and bulkiness would reduce the glossiness. There existed ink sticks on the third layer of ink and more, even some ink holes when the infiltrations were too big because of the substrate of paper had a bigger roughness and bulkiness. Therefore, the substrates used for UV ink-jet 3D printing should have a property of tight and smooth, and the first layer of ink must not be calculated in the whole height of model, so that the printing result would be satisfied.

Keywords UV Ink-jet · Thickness · Roughness · Infiltration · Glossiness

1 Introduction

1980s, stratifying 3D model with computer software, then stacking the molding material by producing it layer by layer to create the 3D model that was needed ultimately, the concept of 3D printing was proposed [1, 2]. There were many kinds of molding materials which could be used for 3D printing, but the solid model could not get rich color and high accuracy. So, it was urgent to find a new material

L. He · G. Chen (✉) · M. He · J. Tian
State Key Laboratory of Pulp and Paper Engineering,
South China University of Technology, Guangzhou, China
e-mail: chengx@scut.edu.cn

M. He
e-mail: 839475230@qq.com

L. He
Shenzhen YUTO Packaging Technology Co., Ltd., Shenzhen, China

P. Zhao et al. (eds.), *Applied Sciences in Graphic Communication and Packaging*, Lecture Notes in Electrical Engineering 477,
https://doi.org/10.1007/978-981-10-7629-9_47

to improve properties of 3D model. UV ink was a chemical substance that could rapidly form to be a stable layer of ink when UV light irradiated, and the ink layer had high glossiness and bright color, substantially without solvents volatilizing [3, 4]. Because of these characteristics and properties, UV ink was selected by us to be a kind of 3D printing material.

In recent years, many researchers have conducted experiments of 3D printing technology based on light curing material, which made UV ink-jet 3D printing possible. A 3D printer with adhesive powder as materials was developed [5]. A light cure 3D printer used photosensitive resin to produce 3D model was developed by 3D systems [6–8]. In China, Doctor Li had successfully developed a 3D printer with adhesive material [9]. Wang Jian from Nanjing University of Science and Technology applied light-cure 3D printing technology in the study on manufacturing chemical chip [10]. Wang Huanmei had successfully produced a 3D topographic map by UV ink-jet printer [11]. However, for UV ink-jet 3D printing, there also needed further improvement. Based on the results of previous researches, this paper took paper as substrate, and conducted experiment to analyze the influences of paper on 3D printing.

2 Experiments

2.1 Substrates

Three kinds of paper (a#, b# and c#) were selected to be the substrate, they had different properties, which were shown in Table 1. The paper tightness whose reciprocal was bulkiness could be calculated by basic weight and paper thickness.

2.2 Instruments

Mimaki UJF-3042 UV ink-jet printer; Novo-Gloss TM glossiness gauge; Labthink CHY-C2 thickness gauge; Illustrator CS6.

Table 1 Values of paper properties

Paper	Roughness [um]	Basic weight [g/m^2]	Thickness [um]	Tightness [kg/m^3]	Bulk [(kg/m^3)$^{-1}$]
a#	0.97	230.7	236.4	957.66	0.00104
b#	1.03	157	132.2	1187.59	0.00084
c#	3.31	165.6	174.9	946.83	0.00106

2.3 Test Chart

Use Illustrator CS6 to design a black test chart, which would be printed with once, twice, triple, four times, twelve times, and twenty times (shown in Fig. 1).

2.4 Procedure

The black test chart shown in Fig. 1 would be printed with white ink to the surface of a#, b# and c# by Mimaki ink-jet printer. The thicknesses of printed samples would be measured and recorded by thickness gauge, and every value would be measured 10 times to calculate the average value. The glossiness would also be measured and recorded by glossiness gauge, and 75° measuring angle would be used.

3 Results and Discussion

3.1 Thickness Results

The samples contained models with one layer, two layers, three layers, four layers, twelve layers, and twenty layers of ink. The average thickness in each sample was calculated based on the calculation of sample thickness and paper thickness. The thickness and layer numbers of samples were shown in Fig. 2.

In Fig. 2, it could be seen that the first segment slopes of six samples were relatively small, which illustrated that the thickness of first layer of ink was relatively small. The phenomenon was caused by the infiltration between paper and ink, as we know, ink printed on the surface of paper would wet the paper along the capillaries of paper, while the infiltration between two layers of ink was relatively small. The thickness values of the first layer of ink on a#, b#, and c# samples were 9.2, 9.9 and 8.2 μm. Because of the smaller tightness and similar roughness, infiltration on #a sample was larger than the infiltration on #b sample. Because the bigger roughness and similar tightness, the infiltration on c# sample was larger than the infiltration on a# sample.

If the results of the first layer of ink was removed, the growth trends of ink thickness on all samples were all nearly linear growth. Use the thickness values of

Fig. 1 Black test chart with different printing times

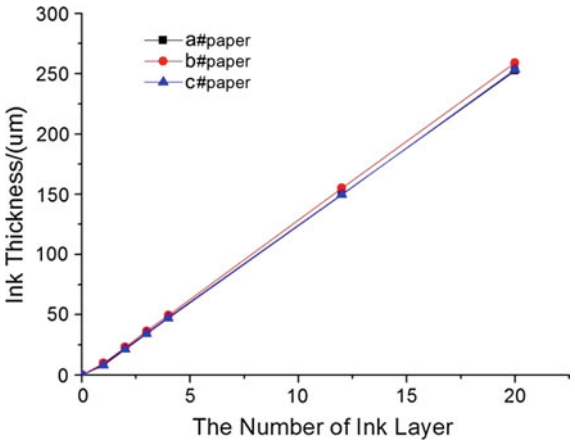

Fig. 2 The thickness and the layer numbers of samples

two layers, three layers, four layers, twelve layers, and twenty layers of ink to minus the thickness values of one layers of ink, the relationship between ink thickness values and the numbers of ink layers could be fitted out, as was shown in Eqs. 1–3.

$$y_1 = 12.7974x_1 + 0.0389 \tag{1}$$

$$y_2 = 13.1163x_2 + 0.3226 \tag{2}$$

$$y_3 = 12.8894x_3 + 0.0966 \tag{3}$$

In the upper equations, the coefficients were 1, 0.99998, and 0.99999, these three values explained that the relationship between ink thickness values and the numbers of ink layer were linear growth, in other words, the infiltration between ink layers would not affect the growth trend. Do not take the first layer of ink into consideration, the average ink thicknesses on a#, b#, and c# samples were calculated to be 12.80, 13.12, and 12.91 μm, these values illustrated the thickness of this UV white ink used in this experiment was almost 12.94 μm, the thickness values would be important for the height of solid model.

3.2 Glossiness Results

The glossiness values of one layer, two layers, three layers, four layers, twelve layers, and twenty layers of ink on a#, b#, and c# samples were shown in Tables 2, 3, and 4. In the tables, the zero layer of ink meant there was no ink on the surface of paper. Figure 3 showed the relationships between ink glossiness values and the numbers of ink layer.

In Fig. 3, on a# and b# samples, the glossiness values of the first layer of ink was smaller than the values of paper, and the glossiness values of the second layer of ink

Table 2 The glossiness values of a# sample

The number of ink layer	Zero	One	Two	Three	Four	Twelve	Twenty
Glossiness [GS]	69.9	64.9	71.8	64.2	59.6	47.2	42.8

Table 3 The glossiness values of b# sample

The number of ink layer	Zero	One	Two	Three	Four	Twelve	Twenty
Glossiness [GS]	70.3	66.2	73.7	65.9	61.8	48.1	43.3

Table 4 The glossiness values of c# sample

The number of ink layer	Zero	One	Two	Three	Four	Twelve	Twenty
Glossiness [GS]	43.4	49.1	52.5	48.4	45.9	33.5	31.4

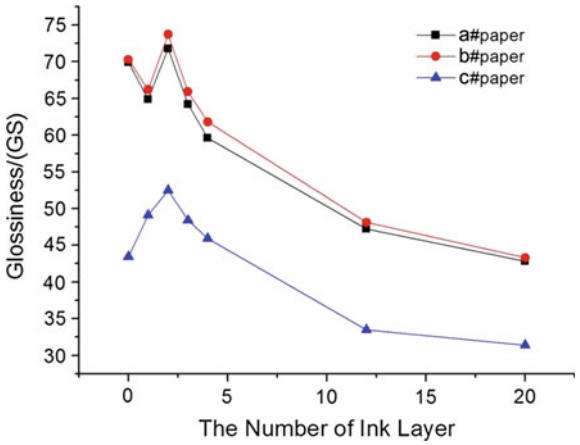

Fig. 3 The glossiness and the layer numbers of samples

was bigger than the values of the first layer of ink, while the glossiness values of the first and the second layers of ink were both increased on c# sample. Because of the bigger roughness, there existed larger infiltrations on a# and b# samples, which roughened the surface of the first layer of ink. However, on c# sample, the smaller roughness increased the glossiness values of the first layer of ink. From the thickness results, it could be known that the infiltration between ink layers was much smaller than that occurred between ink layer and paper, so that the glossiness values of the second layers of ink all had increased.

From Fig. 3, it was obviously shown that the glossiness values of three samples in every number of ink layer could be ordered as the data size: b# > a# > c#. Because the bigger tightness and similar roughness, the infiltration on b# would be less than the infiltration on a#. Because the smaller roughness and similar tightness,

the infiltration on a# would be less than the infiltration on c#. Thus, it could be seen that the kind of paper would have a big effect on the glossiness value of ink layer.

Still in Fig. 3, the glossiness values had an overall downward trend on three samples, and the decline degree gradually decreased when the numbers of ink layers increased. This phenomenon could be explained through the index values from Table 1, because there had ink sticks when ink-jet printer printed ink on the surface of sample layer by layer. As was shown in Fig. 4, the printing head of ink-jet printer would print ink along the X axis, and then move a certain range that was equal to the diameter of nozzle to repeatedly print. In this process, the latter printed ink could overlay the former printed ink to some extend, because it could have a bigger capacity when ink was jetted by nozzle. It would not be clearly when the numbers of ink layer were few, but it would be obviously with the accumulation of values. The ink sticks on samples would reduce the glossiness values of ink player, so that the values began to drop from two layers. It was also need to be known that ink was liquid so that it would have a dynamic balancing with the numbers of ink layer increased, so that the decline degree of glossiness values gradually decreased.

In Fig. 5, it could be seen that there were many ink holes on c# samples of twelve layers to twenty layers. Because the roughness of c# was 3.31, the biggest value in three kinds of paper. The ink holes not only reduced the glossiness value of ink layer, but also affected the appearance of solid model. This problem needed some further precious experiments to discover the solution.

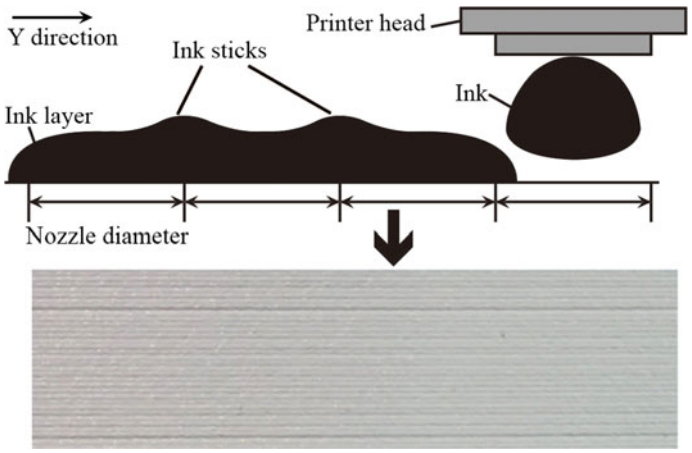

Fig. 4 Ink sticks on samples

Fig. 5 Ink holes on c# sample

4 Conclusions

The infiltration between the first layer of ink and paper must have a big influence on the solid model for UV ink-jet 3D printing. So, we can print a uniform layer of ink on the surface of paper before the 3D model is be produced, and this height of layer will not be calculated in the whole height of solid model. In this way, the error of the first layer of ink can be solved.

In addition, as the substrate of 3D printing, paper should have tight structure and smooth surface, so that the infiltration between ink and paper will be controlled within a certain range, which could improve the ink sticks and ink holes on the surface of solid model. Moreover, some further mechanical measurements and precise experiments should be done to establish a strict operating standards for UV ink-jet 3D printing technology.

Acknowledgements This work was financially supported by Cuangdong science and technology plan project (2017B090901064: 3D color paper-based printer and its application in the field of literature and atr), Chinese National Natural Science Foundation of China (21404042), State Key Laboratory of Pulp and Paper Engineering Project (2016C01, 2016C02), and the Science and Technology Planning Project in Guangzhou (2016070220045).

References

1. Guo ZH, Wang QJ, Guo YH (2013) 3D printing technology and social manufacturing. J Baoji Univ Arts Sci 33:64–70
2. Bassoli E, Gatto A, Iuliano L et al (2007) 3D printing technique applied to rapid casting. Rapid Prototyping J 13:148–155
3. Stowe RW (2006) Alternative UV radiometry and process verification for UV ink jet printing. Nip Digit Fab Conf 6:50–60
4. Siegel SB (2004) UV curing for ink jet printer. US, US20040164325

5. Yang XL, Zhou TR (2009) Three dimensional printing prototyping rapidly technology and its application. J Zhejiang Univ Sci Technol 3:186–189
6. Ladd C, So JH, Muth J et al (2013) 3D printing of free standing liquid metal microstructures. Adv Mater 25:5081–5085
7. Lipson H, Kurman M (2013) Fabricated: the new world of 3D printing. The new world of 3D printing. Wiley, Canada
8. Campbell TA, Ivanova OS (2013) 3D printing of multifunctional nanocomposites. Nano Today 8:119–120
9. Li XY, Zhang S, Yu DG (2007) Application of uniform design method in research of three dimensional printing's powder. J Univ Shanghai Sci Technol 2:183–188
10. Wang J (2006) Research on rapid prototyping technology of chemical chip. Nanjing University of Science and Technology, Nanjing
11. Wang HM, Chen GX (2014) 3D printing of topographic map based on UV inks. Packag J 6:48–56

Research on Process Parameters of Screen Printed RFID Tags

Junhui Fang, Youci Liang, Ruojing Wang and Yunfei Zhong

Abstract RFID is an automatic identification technology. The screen-printed RFID tag is gradually applied broadly in logistics management, anti-counterfeiting and many other fields according to its uniqueness. Based on the principle of RFID tag and its antenna performance, this paper conducted a comparative RFID analysis on both traditional and new silk printing ways. The result of this research demonstrated that the process of silk-screen printing RFID is simpler and therefore has a significant cost advantage. Antennas of different structures and sizes were designed in this paper and the factors influencing the performance of antennas were analyzed. As for experiment, three factors influencing the performance of antennas were considered: mesh count, squeegee angle and the curing conditions of conductive ink (such as drying time and drying temperature). The screening experiment and analysis results illustrated that it is most conducive to RFID printing and the performance of conductive ink screen printed reaches its peak when the mesh of the silk screen is above 200 mesh/inch, squeegee angle is around 55°–75°, dying temperature is 100 °C in 10–15 min. From above processes, a most conductive ink screen printed performance can be fulfilled.

Keywords Screen printing · RFID · Antenna · Anti-counterfeiting
Vaccine and drugs · Process parameters

1 Introduction

Radio Frequency Identification technology is called RFID for short, using radio frequency signal through space coupling (magnetic field or electromagnetic field) to transmit information without contact as well as to achieve automatic recognition through the contact information [1]. Each RFID electronic tag corresponds to an ID

J. Fang · Y. Liang · R. Wang · Y. Zhong (✉)
School of Packaging and Materials Engineering, Hunan University of Technology, Hunan, China
e-mail: yfzhong@hut.edu.cn

P. Zhao et al. (eds.), *Applied Sciences in Graphic Communication and Packaging*, Lecture Notes in Electrical Engineering 477,
https://doi.org/10.1007/978-981-10-7629-9_48

number which is wrote to the storage in the process of label production. Because writing information cannot be modified once it's written, [2] so that the electronic tag is unique. RFID as an advanced automatic identification data acquisition technology, has been successfully applied to manufacturing, logistics management, and public security, anti-counterfeiting and other various areas [3]. Screen printing has the unique advantages of thick ink layer, strong covering power, and small printing pressure and so on. Producing the RFID tag by screen printing will reduce the complexity of the production, which is one of the most potential and most feasible process to achieve low cost, miniaturization, high precision and high production, [4, 5] provides more possibility for the application of tags [6]. The performance tests of RFID including tag testing, reader testing, system testing, etc. [7] however, in the process of screen printing RFID tag, the special demand on printing precision, ink thickness, uniformity and so on are required. In this paper, we designed experiments and analysis for several process parameters of the screen printing RFID tags to get optimal performance of conductive ink, screen printing of passive UHF antenna.

2 The RFID Tag Antenna Performance Requirements

A basic RFID system consists of three parts: the tag, the reader and the antenna. The antenna is used to transmit the RF signal [8] between the tag and the reader, the performance of the RFID tag affected by the screen printing is reflected in the main electrical performance of the antenna, the curvature has little effect on the tag antenna performance when the passive UHF RFID tag is printed on the plane and the convex surface. The proper tag performance [9] should be guaranteed in the initial label design process, the quality of antenna of screen printing tag is mainly measured by calculating its gain and radiation efficiency.

3 Experimental Design and Results Analysis of the Effect of Screening Process Parameter

Because of the uncontrollability of parameters, high cost and poor quality stability of RFID tag printing, [10] this paper designed a different tag antenna according to different needs based on the above. By comparing the electrical performances of passive tags with different structure sizes, we obtained the optimal results. Passive UHF tag structures are varied, the experiment selected three passive UHF antenna structures are shown in Fig. 1, the structure A is mainly used in ticket security, the main application of structural B for the vaccine drug security, structure C mainly used in high-grade alcohol security.

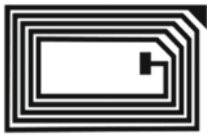

(a) antenna structure A

(b) antenna structure B

(c) antenna structure C

Fig. 1 The antenna structure for experiment

Table 1 The antenna structure and size for experiment

Antenna number		Label size (mm)	Line width (mm)
Structure A	1	78 × 47	2
	2	78 × 47	2
	3	78 × 47	1.5
	4	60 × 31	1.5
	5	60 × 31	1
Structure B	6	71 × 21	1.2
	7	71 × 21	1
	8	51 × 15	1
	9	51 × 15	0.5
Structure C	10	51 × 41	4
	11	51 × 41	2

Three different structures of the electronic label size and line width were designed, and the coefficients are shown in Table 1.

3.1 Effect of Mesh Number on Antenna Quality

Mesh number refers to the number of mesh per square centimeter, the mesh size and the wire diameter will determine the screen precision, the choice of screen material will directly affect the quality of printed materials.

3.1.1 Experimental Design

(1) Experimental apparatus and materials:
Manual flat screen printing machine, pointed scraping plate (hardness of Shore 55°), universal meter, double-sided glossy coated paper (weight 150 g), 'Sunflower' 8000 °C conductive silver paste (polyurethane 30%; fluorine ketone 10%; silver powder 55%; agent 5%), pneumatic stretching machine,

hollow aluminum frame (A3), polyester mesh, diazo sensitive adhesive, scraper, slow drying water.

(2) Experimental requirements:
Using mesh width of 100, 120, 200, 300 mesh/inch polyester meshes, stretching tension of 2.1 N/mm, drying temperature of 45 °C, exposure time of 35 s, blade angle set to 60°, the screen distance is adjusted to 2 mm.

3.1.2 Analysis and Evaluation of Experimental Results

The experiment printed different structure of the passive UHF electronic tags by screen plate with different mesh, repeat experiment three times while keeping other conditions consistent. Using a universal meter to test the resistance value of each antenna at both ends after the samples are naturally dried, record the data and calculate the average value of the input resistance and draw the Fig. 2a.

It can be seen from Fig. 2a, under the same conditions, resistance change of structural A and structural B are greater than the structure C. When the mesh number is less than 200 mesh/inch, the printed antenna will appear rough boundary, the edge of the line ink layer is not uniform, conductive ink film size expanded, ink spread and other phenomena, when the mesh is more than 200 mesh/inch, the passive ultra-high frequency antenna line edge has high printing smoothness, high printing accuracy, ink adhesion uniformity, which meet the printing quality requirements of the screen printing antenna.

3.2 *Effect of Scraping Parameters on Antenna Quality*

In the process of high-speed printing antenna, adequate and appropriate amount of conductive ink should be ensured to transfer from the screen mesh of small cells to the substrate (coated paper), forming a image which has clear edge of the print and uniform ink layer.

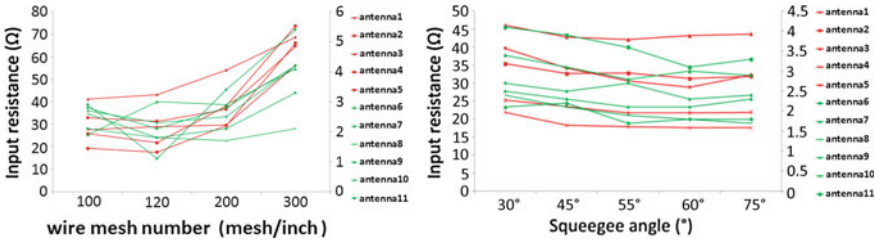

(a) Wire mesh number (b) Angle of scraping printing

Fig. 2 The influence of wire mesh number and the angle of scraping printing of input resistance (the red line corresponds to the right data axis) (Color figure online)

3.2.1 Experimental Design

(1) Experimental apparatus and materials:
Same as 3.1.1, pointed scraping plate (hardness of Shore 70°).
(2) Experimental requirements:
Using a 300 mesh/inch polyester screen, stretching tension of 2.1 N/mm, drying temperature of 45 °C, exposure time of 35 s, scraper angle of 60°, screen distance of 2 mm, respectively, 30°, 45°, 55°, 60°, 75° scraping angle printing antenna.

3.2.2 Analysis and Evaluation of Experimental Results

Repeat the process, record the data. As shown in Fig. 2b, when the angle of the scraper changes, the structure A is less affected by the angle of the scraper, and the input resistance of the structure B and the structure C fluctuate greatly.

We are using a manual flat screen printing machine so omit some of the error data. In actual production applications, the various parameters of the scraper in the screen printing are mutually constrained such as the scraping pressure and the scraping angle, and the greater the scraping angle of the scraper, the greater the force acting on the screen in the vertical direction (this experiment only selected a factor of the scraper angle). It can be seen from Fig. 2b: within a certain range, the printing angle is increased, the amount of leakage ink is reduced, the passive UHF antenna input resistance is reduced as well, screen printing label passive UHF antenna scratch angle is appropriate of 55°–75°.

3.3 Effect of Ink Curing Conditions on Antenna Quality Experiment

3.3.1 Experimental Design

(1) Experimental apparatus and materials:
Same as 3.2.1, oven (air conditioning, XMTD digital modifier).
(2) Experimental requirements:
Using a 300 mesh/inch polyester screen, stretching tension of 2.1 N/mm, drying temperature of 45 °C, exposure time of 35 s, scraper angle of 60°, screen distance of 2 mm, with 60° printing angle printing multiple proofs, proofs of natural dry for half an hour after the random selection of two parts proofs, the randomly selected samples were dried at 40, 50, 60, 70, 80, 90, 100, 110 and 120 °C for 15 min while the randomly selected samples were dried at 90 °C under hot air conditions in 5, 10, 15, 20 min.

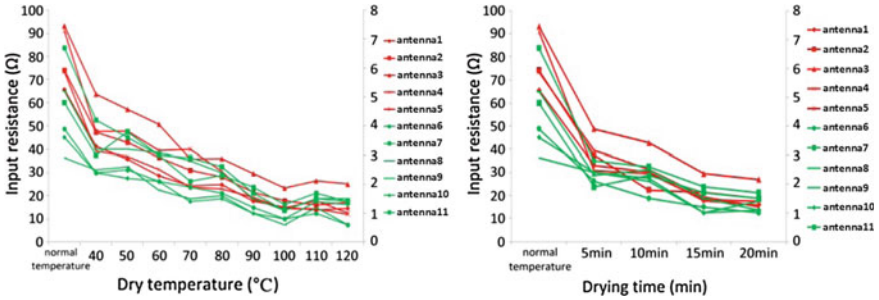

(a) Drying temperature (b) Drying time

Fig. 3 The influence of drying temperature on the input resistance and drying time on the input resistance (the red line corresponds to the right data axis) (Color figure online)

3.3.2 Analysis and Evaluation of Experimental Results

Repeat the process, record the data and calculate the average of the input resistance. Draw the line graph is shown in Fig. 3.

As shown in Fig. 3, keeping the other conditions consistent, with the increase of time, the antenna input resistance tends to be flat after the decline. In the actual production, the temperature of the drying product should be in a reasonable range and the substrate and energy-saving aspects should take into account. This experiment shows that when the most conducive performance of passive UHF antenna can be got when the drying temperature is at 100 °C. In terms of energy, to take drying time 10–15 min is appropriate.

4 Conclusions

From the printing point of view, the choice of substrate, the choice of the number of head, screen printing scraper speed (printing speed), scraper and screen printing angle (scraping angel), the pressure applied to the screen plate, the viscosity of the conductive ink, the curing temperature of the conductive ink, and the curing time [11] have effects on the quality of the passive UHF antenna printed on the screen.

The experimental results show that: ① In a certain range, the printing quality of screen printing UHF tag is closely related to the resolution (mesh number) of screen. The low ink transfer rate of the high wire mesh screen will result in the thin link film thickness of each UHF tag, the smaller the size of the ink film, and the better surface and inner quality than the low wire mesh. ② The change of the printing angle will affect the quality of the passive UHF antenna, but relatively speaking, the blade angle and other factors of the scraper influence each other mutually, this paper suggests that take 55°–75° is appropriate in the actual operation process. ③ In the ink curing conditions, drying temperature and drying time

increases, the antenna performance has improved. This paper suggests that the drying temperature is 90 °C, the drying time is 10–15 min.

In the actual screen printing, the screen mesh selection should take into account the antenna width, thickness, length, clearance and conductive silver paste performance. Drying temperature and drying time selection need to take into account the energy consumption. RFID tag antenna be printed by screen printing method has many advantages such as a simple operation, high production efficiency, green, label printing materials, wide and rich features [12], silk screen process must be strict in all aspects of the parameters, continue to trial and optimize, so as to obtain printing quality breakthrough [13] as well as to bring a broader prospect in the application of RFID tags.

Acknowledgements Project is supported by Natural Science Foundation of Hunan Province (Grant No. 2016JJ6034), Training Project of Hunan Industrial Application of Higher Education Institutions (Grant No. 15CY003), Hunan Province Higher Education Institutions Demonstration Base of Production, Education and Research (Grant No. 2014-117).

References

1. Tang BL (2007) Manufacture technology of antenna for RFID. Printed Circ Inf 15(06):24–27
2. Wang Y (2010) Introduction to the RFID technology. GuangdongYingshua 32(5):42–45
3. Zuo L, He YG, Li B, Zhu YQ, Fang GF (2012) Analysis and improvement for UHF RFID reading region in real environments. Acta Phys Sin 80(24):222–228
4. Rao K, Lam S, Nikitin P (2011) UHF RFID tag for metal containers. In: Microwave conference proceedings. IEEE Xplore, pp 179–182
5. Ni WH, Zhang YX (2010) Research on the mathematical model for industrial screen printing. Packag Eng 32(15):102–105
6. Vivek S, Paul CC, Daniel H (2006) All Printed RFID tags: materials, devices, and circuit implications. In: Proceedings of the 19th international conference on VLSI design
7. Hou ZHG, He YG, Li B, Tu K, Zhu YQ (2010) Measurement of the passive UHF RFID tags, performance based on software-defined radio. Acta Phys Sin 78(08):5606–5612
8. Huang T, Zou XC, Zheng Y, Wang JQ, Mao CH (2005) Optimization of 13.56 MHz RFID system performance. Comput Digital Eng 33(05):15–17
9. Sari LM, Toni B, Leena U (2011) Characterization of UHF RFID tags fabricated directly on convex surfaces by pad printing. Int J Adv Manuf Technol 53:577–591
10. Liu CF, Liu SN, Wang ZY (2008) Study on mathematical model of the quality of printing process of passive RFID'Antenna. Packag Eng 30(11):46–47
11. Li XL, Guo YF (2004) Shallow theory of anti-counterfeiting technology in packaging and printing. Guangdong Packag 4:1–3
12. Zhong YF, Liu AP, Chen L (2007) RFID tag anti-counterfeit it of packaging by screen printing. Packag Eng 29(12):60–63
13. Zhang YC, Li F (2012) Study of screen printing process of RFID tag antenna. Packag Eng 34 (13):120–122

Study on the Registration Testing of Color Digital Printing Machine

Enyin Fang, Shengwei Yang, Lingjun Kong and Jinghuan Ge

Abstract The paper designs a kind of testing chart for registration detection which has a property of strong adaptability and expansibility. After scanning the testing charts output by different color digital printing machines, the corresponding digital samples are obtained and identified by Image-quality software. Through subjective and objective analysis based on the data of the digital samples, a method is proposed to evaluate the accuracy of registration of the color digital printing machine. The experiment shows that it cannot only be used to effectively judge registration of different color, but also can conclude which registration accuracy coming from different color digital printing machines is better. It is proved that this method can be used to evaluate the accuracy of color digital printing machine quickly and successfully; it has certain practice guiding sense for development and application of registration measurement technology.

Keywords Color digital printing machine · Registration testing
Interest area · Testing chart

The registration of the printing is process that the separated images are transfer to the required position on the substrate according to the color sequence, and finally obtained the copy image having the same level, tone with the original image. Based on the quality requirements of the printing, it is called an accuracy registration that the outline of the each separated image is completely overlapped in the same image position. However, in the actual printing process, there are many factors that affect the accuracy of registration. If the deviation of registration is occurred during the process, it will produce substandard products, which have these properties such as blur, ghost and other phenomena, reducing the quality of printed matter and resulting in serious waste. Therefore, the accuracy of registration is one of the

E. Fang (✉) · S. Yang · L. Kong · J. Ge
Department of Printing and Packaging Engineering, Shanghai Publishing and Printing College, Shanghai, China
e-mail: fensarying@163.com

P. Zhao et al. (eds.), *Applied Sciences in Graphic Communication and Packaging*, Lecture Notes in Electrical Engineering 477,
https://doi.org/10.1007/978-981-10-7629-9_49

important factors to measure the quality of printing products in multicolor printing [1].

With the development and popularization of digital printing, the detection and evaluation of the quality of digital printing has become the focus of the industry, and also the basis of the quality of digital printing [2]. At present, the methods of adjusting the registration is detected by hand or on-machine, which basically can meet the general needs, but for output of the high-end products, if the company know the machine registration itself very well before they receive the job, rather than relying on operation manual to answer the customer, so they can make the choices even more apposite, and the same time, reputation of an enterprise can be improved. In order to better understand the performance of the equipment itself, these papers analyze the characteristics and similarities of existing registration detection sample, and then do some researches on the registration testing of color digital printing machine by designed registration sample based on analyzing the relationship between the mechanical properties and accuracy.

1 Methods of Registration Testing

In the color printing process, people usually use "location marker" to measure the registration. As shown in Fig. 1a, by detecting the registration marks on the same side edge distance d and d′, and the relative deflection angle of two cross line to get the registration error data.

In addition, according to the different test items and printing methods, people often design different color detection methods to solve the problem. Figure 1b is a cross detection icon that is used to evaluate the accuracy of registration, according to the degree how the green (C), magenta (M), yellow (Y) and black (K) color icon blended together, which have a principle that a good printing matter have a good registration appearance without any form of color edge using this method; when the color edge is emerged, it indicates that registration of the printing matter have some problems. The more dislocation is, the worse the registration become. This method can only be applied to the visual judgment and is not suitable for the quantitative detection of machine. Figure 1c is the "Union Jack" icon, this icon is formed by 4 separated printing color lines to avoid the overlap of the colors. The method can

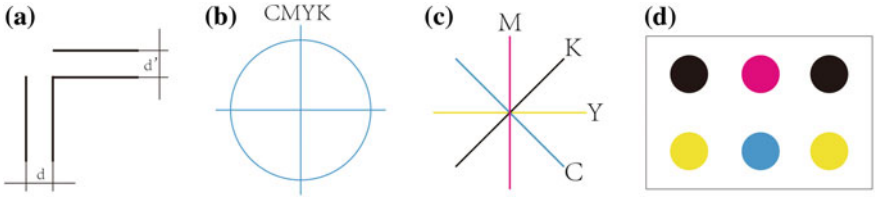

Fig. 1 Schematic diagram of registration test (Color figure online)

evaluate the accuracy of the registration through calculating the position and tilt angle of each color line. Although the design of this method use "Union Jack" instead of "crossing" to separate printing colors compared with the Fig. 1b, it is hard to ensure the robustness and accuracy of the algorithm, because the image acquisition and processing is very difficult to guarantee the printing color pixel is not lost, Fig. 1d is the "Circular" detection icon, the icon is made of monochrome, which fundamentally solve the problem of pixel overlap and easily get the digital image because the circular have no azimuth requirement. But the subsequent processing is more complex. First, we should distinguish the "Union Jack" and transfer them into bitmap in the registration data collection, then measure the center distance among them, which would be compared with standard distance to evaluate the accuracy of the registration. Based on discussion the testing icon above, we design a detection sample, which can be easily recognized and obtained by measuring equipment, to evaluate the accuracy of registration of digital printing machine itself.

2 Measuring Instruments and Software

Currently, density meter and spectrophotometer are often used to measure and evaluate the quality of lines [3]. Digital cameras and scanners can transfer the lines testing graph into a digital image using high sampling frequency, which can then be combined with image processing technology to measure and analyze the printing line. Therefore, we use quality detection system of digital printing based on CCD image capture technology to complete the experiment [4–7]. According to the ISO13660, the instrument should have following properties. First, the resolution is of not less than 600DPI; second, the pixel of the image capture device should be described by 8-bit depth. In this experiment, we choose EPSON GTX970 scanner as our image capture device, which have capacities mentioned above. The software called Image-quality can be used to analyze and evaluate the quality of digital lines testing graph, which is pre-installed on the computer with window system, after space calibration and density calibration, scanner can be used to get digital marks by Image-quality software, then we can detect and analyze the quality of the registration of printing. All these operations and data obtained are in the following environment: clean and tidy, dustproof worktop, temperature (23 ± 5) °C, relative humidity (50 ± 10)%, which are accord with GB/T 33259-2016, named Quality requirements and test methods for digital printing.

3 Selection of Interest Areas and Design of Testing Chart

3.1 Selection of Interest Area

Considering scanning, analysis time and accuracy of measurement, we use scanner with a sampling frequency 600DPI to obtain the digital testing chart through scanning the original, which is printed by the color digital printing machines. The digital testing chart was selected by Image-quality software to measure the area of interest. There are three types of interest areas. First, the measuring interest area absolutely contain the whole testing line including the line end, the second, we called relative inclusion, which is not including the line end. Third, only contain one side of line end (type 3 contains two cases), as shown in Fig. 2. Taking into account the design of registration testing chart, we chose type 2 as the principle to obtain measurement data of the line [8].

3.2 Design of Registration Testing Chart

The normal registration testing chart is made of process color, due to the positioning error of color digital printing machine, the sets "cross" registration line is not entirely consistent, in addition, because of mutual interference between sets of alignment, people are not easy to detect the selection of interest area. In order to measure registration of the color digital printing, also taking into account the Spatial details of the digital printing machine in the registration, we design the registration testing unit as shown in Fig. 3a. Black is considered as the baseline, cyan, magenta and yellow lines are necessary to be included as the independent objects instead of overprint.

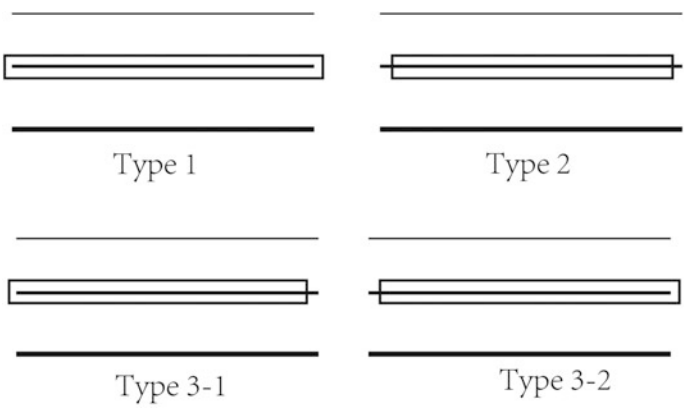

Fig. 2 Types of interest areas

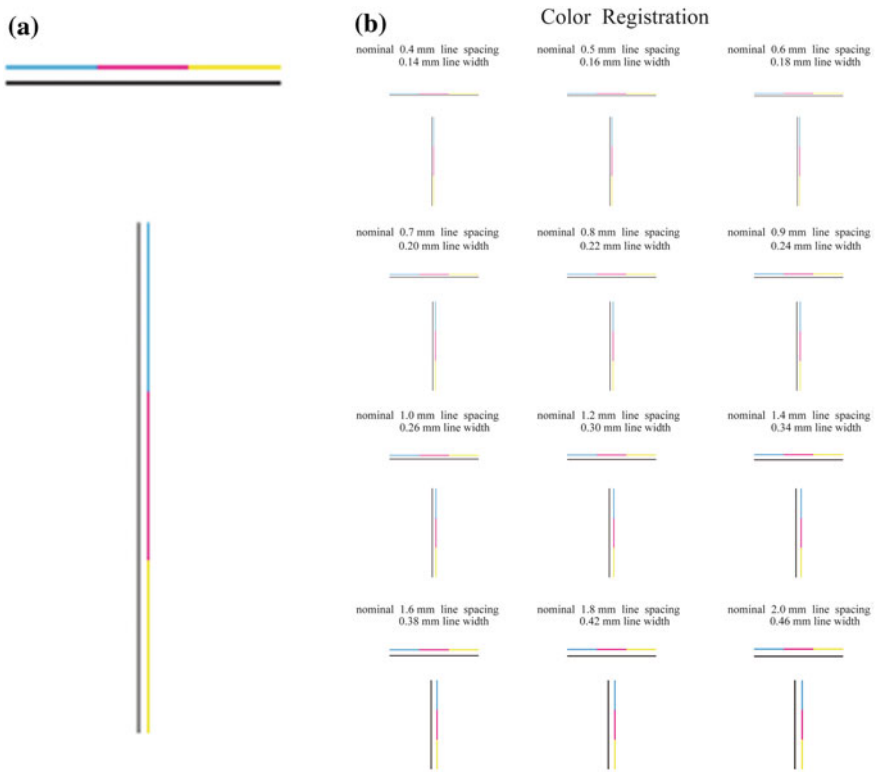

Fig. 3 The registration testing chart (Color figure online)

The registration testing chart consists of horizontal and vertical lines, as shown in Fig. 3b, considering the output precision of the color digital printing, so the line width of the registration testing chart is designed into two kinds of steps, the first, line is from 0.14 mm up to 0.24 mm by the step width 0.02 mm, the second, line is from 0.26 mm up to 0.46 mm by the step width 0.04 mm. Similarly, the distance between the green, magenta, yellow test line objects to the black baseline line is also designed into two kinds of steps. First, line distance is from 0.4 mm up to 0.9 mm in accordance with the step size 0.1 mm. Second, line distance is from 1.0 mm up to 2.0 mm in accordance with the step size 0.2 mm. The testing chart is formed by 12 horizontal and vertical testing units and produced by the Illustrator, CMYK mode, which is consistent with the actual production situation. Respectively output by A, B two kinds of Xerographic digital printing, the testing charts is printed on 80 g/m^2 uncoated paper and 157 g/m^2 coated paper which are from the same company. Then use the scanner with a sampling frequency 600DPI to obtain the digital testing chart. Through the software called Image-quality, which is a commercial image quality analysis system, we can measure the distance between the green, magenta, yellow, each color test line object to the black baseline line.

4 Result Analysis of Measurement

Due to the registration error detected by the above method is not real error, so the accuracy and reliability of detection results should be compared with the design value to evaluate the method. The interest area in this paper is a rectangular box which size is 5 mm by 2 mm; the type of interest area can not contain the end of line. Considering the measurement error of Image-quality software, each group of data should be measured for five times and get the average value, and then compared with the theoretical design value. The relative average error of the results is shown in Fig. 4.

Subjective evaluation: According the Fig. 4, we can conclude that although A and B two kinds of color digital printing machine belong to different equipment manufacturers, but the regularities of the performance are roughly the same: first of all, with line width and line distance increasing, the registration precision is obviously enhanced and the value of the registration error is the decreased; secondly, as for the uncoated paper, yellow registration precision in the transverse direction along the short side of the paper is lower than the magenta and cyan, but is higher in the vertical direction along the long side of the paper; in addition, as for the coated paper, yellow registration precision in the two direction is higher than the magenta and cyan.

Objective evaluation: In order to evaluate the accuracy of A and B two kinds of color digital printing machine more intuitively, we use to represent the average value, which is sum of the absolute errors between the measured value and the standard value. The unit is millimeter. Setting YC, CC, MC as the measurement registration value of yellow, cyan, magenta and Yb, Cb, Mb as the standard registration value of the yellow, cyan, magenta. The value of YC, CC, MC, Yb, Cb and Mb are the average data of five times results. The formula is shown in Table 1. The K is the number of sampling points, according to Fig. 3, each color has 12 sampling points, and so the value of K is 12.

$$\partial = \frac{\frac{1}{k}\sum_{n=1}^{k}\left(Y_c^n - Y_b^n\right) + \frac{1}{k}\sum_{n=1}^{k}\left(C_c^n - C_b^n\right) + \frac{1}{k}\sum_{n=1}^{k}\left(M_c^n - M_b^n\right)}{3} \tag{1}$$

Table 1 is the result calculated according to formula (1). The following conclusions can be drawn by contrast. First of all, the average horizontal alignment accuracy of the type A color digital printing machine is lower than the vertical, the average horizontal alignment accuracy of the type B color digital printing machine is higher than the vertical; Secondly, the average registration accuracy of the type A color digital printing machine is higher than the type B color digital printing machine.

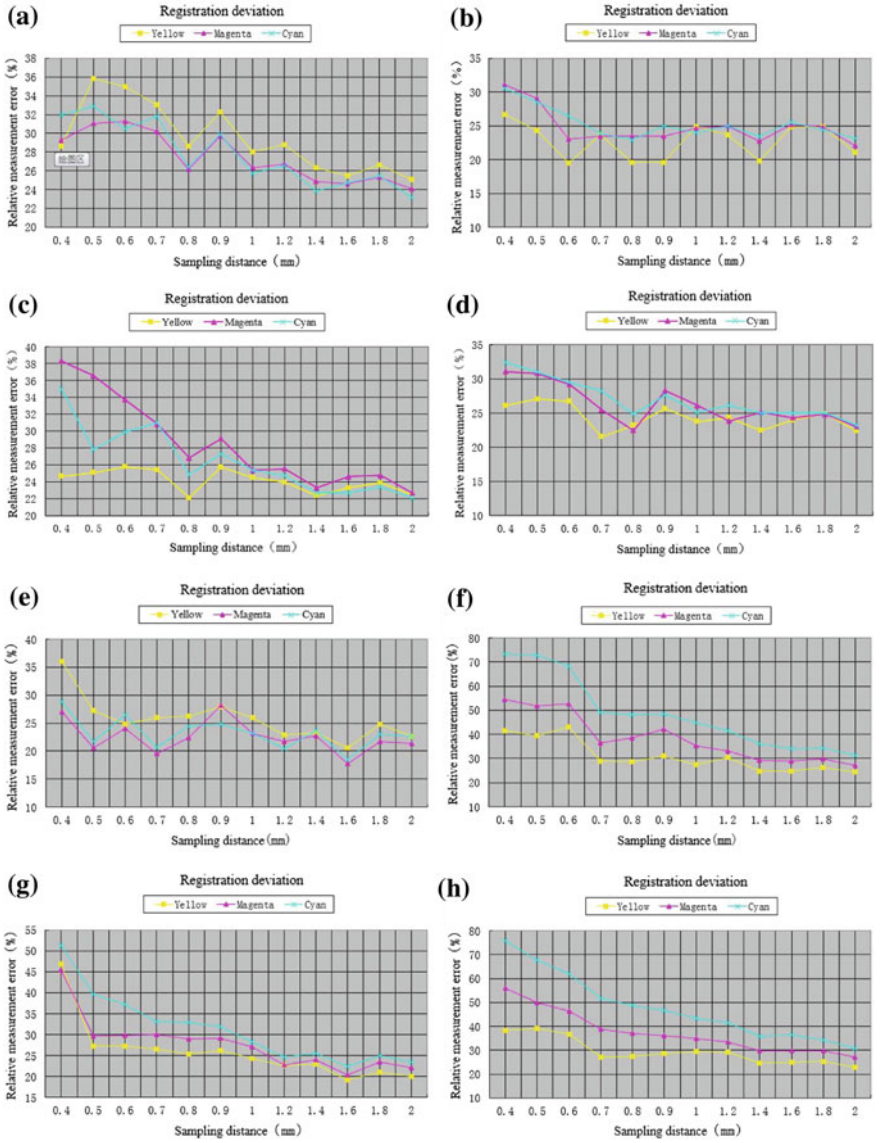

Fig. 4 Error analysis diagram of registration **a** horizontal registration error of the type A, 80 g/m^2 uncoated paper; **b** vertical registration error of the type A, 80 g/m^2 uncoated paper; **c** horizontal registration error of the type A, 157 g/m^2 coated paper; **d** vertical registration error of the type A, 157 g/m^2 coated paper; **e** horizontal registration error of the type B, 80 g/m^2 uncoated paper; **f** vertical registration error of the type B, 80 g/m^2 uncoated paper; **g** horizontal registration error of the type B, 157 g/m^2 coated paper; **h** vertical registration error of the type B, 157 g/m^2 coated paper (Color figure online)

Table 1 The comparison of the assessment and the design value

	Type A color digital printing machine		Type B color digital printing machine	
	Average horizontal registration error ∂ of the C, M, Y	Average vertical registration error ∂ of the C, M, Y	Average horizontal registration error ∂ of the C, M, Y	Average vertical registration error ∂ of the C, M, Y
80 g/m^2 uncoated paper	0.2602	0.2562	0.2777	0.3776
157 g/m^2 coated paper	0.2690	0.2689	0.2939	0.3707

5 Conclusions

At present, the common methods of registration detection are generally used for subjective judgment or online detection, which is lack of understanding of the accuracy of the equipment itself. This paper discusses the characteristics of common registration detection samples and design a registration testing chart, which can be used to evaluate the accuracy of color digital printing machine itself, at the same time, this registration testing chart that has a wide applicability and scalability can be modified according to different registration accuracy of the different equipment; in addition, through the experimental data, not only can we effectively judge which color has the best registration, but also can conclude which registration accuracy coming from different color digital printing machine is better. It is of certain guiding significance that if we can use this method in practice. There are some limitations of this experiment, after scanning the registration testing chart, the noise produced during the scanning should be eliminated by median filter and Gauss filter to improve the accuracy of data and provide the better image to the subsequent processing. In addition, the grain of the uncoated paper should be considered as a factor which can affect the results of measurement.

Acknowledgements This study is funded by laboratory construction project called Green plate-making and standardization Laboratory, which is belonged to Key Laboratory of science and stander press and publication, State Administration of Press, Publication, Radio, Film and Television of the People's Republic of China.

References

1. He F, Zhou JY (2013) Research on the registration of lithography. Printing Qual Stand 11:34–36
2. Jin ZY, Zheng L, Guan WJ (2012) Line quality analysis and evaluation of digital printing based on ISO13660. Packing Eng 15(33):97–103

3. Zheng L, Jin ZY (2011) Quality analysis of xerographic printing based on CCD. Packing Eng 32(7):112–116
4. Kong LJ, Liu Z, Jiang ZM (2010) CCD based digital print quality measurement and analysis techniques. Packag Eng 31(2):92–95
5. Briggs J, Ahklein C, TSE MK (1999) Applications of ISO-13660, a new international standard for objective print quality evaluation. Jpn Hardcopy'99 Imaging Soc Jpn (7):1–5
6. Dhopade A (2008) Image quality assessment according to ISO 13660 ad 19751. IPA Digital Print Forum 43–50
7. Chen YJ, Zhang E (2005) Research on-line defect detection system for printed-matter based on image processing. Packag Eng 26(6):64–65
8. Yao HG (2011) Proposed test regulation to edge quality of lines. China Printing Packag Study 3(5):28–33

The Solutions to the Quality Defects of Inkjet Printing

Xuemei Li, Shiyong Luo, Shaoguo Li, Yan Zhao, Gang Deng and Guorong Cao

Abstract Inkjet printing technology has advantages of energy saving and environmental protection, as well as personalized on-demand printing. Inkjet digital printing is a pressure free printing method, its quality defects is different from other printing method,such as offset printing and gravure printing. The analysis shows that the main types of inkjet digital printing defects include color rendition, paper flatness, graphic edge sharpness, back sticks, dirty ink dots and white lines. By analyzing the specific characteristics of the above inkjet printing quality defects, the possible causes and the solutions to the quality defects of inkjet printing are given.

Keywords Inkjet printing · Quality defects · Reasons · Penetration and spread Causes and solutions

1 Introduction

Digital inkjet printing is a kind of pressure free printing method that all kinds of figure and text information are processed by computer. The micro ink droplets are obtained from the nozzle to the printing material [1]. Because of using water-based ink, there is no emissions of waste water and VOCs in the printing process. In addition, it has the characteristics of personalized on-demand printing, variable data printing, small amounts and lots of batches, zero inventory, forever version without break and rapid response [2]. At present, inkjet printing is suitable for social development trend that is known as increased reading of paper media. It had been

X. Li · S. Luo (✉) · G. Cao
Beijing Key Laboratory of Printing and Packaging Materials and Technology, Beijing Institute of Graphic Communication, Beijing, China
e-mail: luoshiyong@bigc.edu.cn

S. Li · G. Deng
Shaoxing Hucais Group Output Center, Shaoxing, China

Y. Zhao
LUSTER Light Tech Group, Beijing, China

P. Zhao et al. (eds.), *Applied Sciences in Graphic Communication and Packaging*, Lecture Notes in Electrical Engineering 477,
https://doi.org/10.1007/978-981-10-7629-9_50

widely applied in various journals, books, advertising, personalized packaging and other fields. The main direction of the study is generally to improve testing and analysis of the quality of paper or inkjet printing quality. Relatively speaking, there are few evaluation systems, which introduce quality defects of inkjet printing and the appropriate possible solutions. Therefore, in order to get high quality reproduction of the original image of the print and provide a corresponding solution to solve the actual operation of inkjet printing quality defects, the article is intended to provide assistance for inkjet printing.

2 Experiments

Experimental materials: Defect samples of digital inkjet printing are from Shaoxing hucais group output center.

Experimental instruments: Digital camera (Sony-nex5T); con-focal laser microscopy (VK-X200K Kean).

Experimental instruments were used to observe microscopic structure of the quality defects on digital inkjet printing samples. The causes and solutions of the quality defects in inkjet printing are concluded by the above observation results and the actual inkjet printing process.

3 Results and Discussion

The main quality defects of inkjet digital printing are as follows:

3.1 Color Rendition

Figure 1 is partial magnification of poor color reduction and good reduction with con-focal microscope. On the poor color rendition sample, as indicated by the left photo: too large lateral spreading of the four color ink spots, the uneven arrangement of the infiltration, the exudation of the interface, and the irregular edges of the printed text.

At present, speed of roller digital printing is as high as 180 m/min. After jetted on the surface of the paper, the micro ink droplets are longitudinal seepage and lateral spreading that depend on capillary action of the paper coating [3]. If speed of the longitudinal seepage and lateral spreading are slow, the ink droplet drying would be difficulty and the ink adhesion on the paper become worse [4]. Therefore, the key to improve the quality of digital ink printing is to precisely control the longitudinal diffusion and lateral spreading of the micro ink droplets on the surface of the paper.

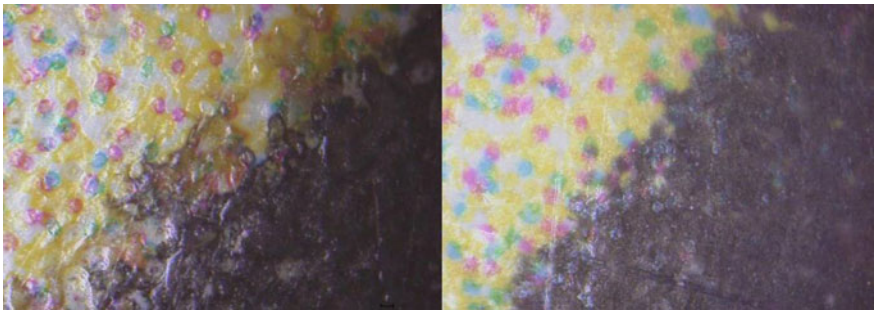

Fig. 1 Contrast photos between poor and good color rendition

3.2 Paper Flatness Defects

The reason of "Lotus leaf edges" defect: if printed matter has large image area, color image need to use CMYK color ink and one or two special color ink that make overlay overprint. In the image area, paper absorbs much more water than other regions, causing the paper to curl and create a "lotus leaf" defect (Fig. 2).

Solution: The inkjet drying process should intelligently adjusted, which to increase the amount of dry air or temperature on large image area. Then the degree of drying of paper tends to be consistent; a set of pressure roller should attach to the production line after drying of printing process, which can flatten the paper; maybe we can use UV or UV-LED curing ink in printing to reduce the "lotus leaf" quality defects.

3.3 Edge Sharpness Defects

Edge Sharpness sample, which printing dot at the edge of the black ink and green ink dot doped with each other is not present independent dot distribution.

A large number of spreading printing dot give rise to edge sharpness defects. The main reasons for the edge defects include:

(1) The arrangement of the nozzle is unreasonable. When the ink droplet size of the nozzle is constant, the arrangement interval of the single row nozzle should increase. Only in this way, this is lower than the original resolution ratio [5].

Fig. 2 "Lotus leaf edges" defect

(2) Imaging suitability between ink and materials is exceedingly necessary. Surface pore size and porosity of the paper, as well as paper coating surface will affect the path that the flow of ink to the paper, which is not completely straight down but can also spread to the surrounding at the same time, which also makes the record points generated at the edge fuzzy phenomenon [6]. Ultimately, all of those causes affect the accuracy of the color reproduction.
(3) The paper high roughness, low density of ink layer, the poor reproduction off small dot and breezing of imprinting, which will cause branches expand and deform.

Aiming at the problem of "burr", we can take the following methods:

(1) In order to improve the precision of the image and improve the printing speed, we adopt cross arrangement of two or more columns to replace the single nozzle.
(2) Select the coated paper with appropriate ink absorbing properties to reduce "burr" defect on the edge of the imprinting.
(3) Select coated paper with smooth surface, which can reduce the apparent contact angle and increase penetration rate.

3.4 Back Stick

On account of using water-based ink, low pigment content, high water content, slow drying, which lead to ink is not completely dry and it can be applied to the backside under pressure.

Causes:

(1) The absorbency of paper is poor, which affects the vertical permeability and horizontal absorption of ink dot. Moreover, adhesive force of the ink is not forming, which prone to "pulverization phenomenon" and not easy to dry, causing the smearing on the back.
(2) In the printing process, the lower water content of the paper will lead to electrostatic adsorption phenomenon, which result in difficulty delivering paper, and then lead to printing paste back.

Solution:

(1) Choose paper with good coating layer and appropriate ink absorption.
(2) Before printing, the paper should be put in the place where the temperature (12 + 3) °C higher than printing workshop and relative humidity (15 + 5)% higher than normal. The printing paper should be suspended for 2 h, and then piled up in paper carrying table where temperature and humidity are same as the printing workshop. Generally speaking, In order to make water content of the paper reached the theoretical value that is (5.5 + 0.5)%, the paper need to place more than 10 h.

Fig. 3 Ink on the surface of the printing sheet

3.5 Dirty Ink Dots

In addition the incompletely dry of water-based ink lead to back stick, there is a series of satellite droplets around the main ink drops [7], and flying marks of satellite style ink droplets will be left behind on the paper (Fig. 3).

Dirty mainly due to ink viscoelasticity in the inkjet printing process [8]; the second, oversizing of flow amount of ink make that penetration and spread of the ink on the paper cannot get the balance.

In order to solve the problem of Ink dot on the paper surface, it can be used to add high molecular polymer to ink that can effectively inhibit the number and size of the satellite droplets; adjust the nozzle volume.

3.6 White Lines

The main reason is that the printing nozzle on the printing lever is not cleaned in time, which will lead to the dried and solidified ink. The end result is that the nozzle is blocked. The solution is to regularly check the print head on the printing bar and wash the printing spray in time.

4 Conclusions

Compared with other printing methods, the printing quality defects such as color rendition, paper flatness, graphic edge sharpness, back sticks, dirty ink dots and white lines are especially serious in inkjet printing. To reduce the quality defects of inkjet printing, in addition to precisely control process parameters, it is important to build a layer of functional coating on the surface of the paper, which could accurately regulate the relative amount between penetration and spread of single droplet ink.

Acknowledgements This study is funded by the Key Science and Technology Project of Beijing Municipal Education Commission (KZ201610015015),the National Key Scientific Instrument and Equipment Development Project (NO. 2013YQ140517),the support of the teaching engineering team (construction) (22150116006/017) and the printing and packaging research project of cultivating innovative talents in (22150116007/055).

References

1. Pu JL (2005) Ink jet technology and applications. Printing Today 1:2–8
2. Gao C, Huang SX, Chen L (2004) Progress in droplet spray technology. Chin J Inorg Mater 19 (4):714–722
3. Zhang Y (2015) Research on optimization and evaluation of ink jet printing. Paper. Nanjing Forestry University, Nanjing
4. Liu GD (2014) Study on the mechanism of self-imbibition behavior and theoretical modeling of paper coating materials. Shanxi University of Science and Technology, Shanxi
5. Shi LQ (2005) Key factors affecting the quality of inkjet printing. Packag Eng 26(4):46
6. Zheng L, Jin ZY, Cheng PF (2012) Analysis of ink jet expansion on the surface of paper. Packag Eng 33(23):114–115
7. Chen JF, Tang ZN, Li JF (2012) Study on the spreading mechanism of droplet on inkjet printing paper. Packag Eng 33(23):131–132
8. Guo J (2015) Study on the effect of rheological properties on the ink jet printing process. Jiangnan University, Wuxi

Flexography Printed Pattern Based on Nano-Copper Conductive Ink

Yi Fang, Zetao Li, Rumeng Yao, Aixin Tang, Tingting Zhang, Yaling Li, Yanfang Xu, Li Yang and Luhai Li

Abstract This work demonstrates a simple printed electronics process to obtain the copper pattern by flexography. The nano-copper suspension was synthesized by liquid chemical reduction method. The conductive ink was prepared with nano-copper and glycerol. The copper pattern was printed by a flexo graphic printability tester and then dried in an oven at 80 °C. The copper in square pattern exhibits better conductivity than that in hexagon, because of the higher surface line density. The confocal laser scanning microscope (CLSM) indicates that the heights of the copper patterns are different in relation to printing direction and shape. The morphologies of the two kinds of the copper pattern were fine. This process could apply to the poly (ethylene terephthalate) (PET) substrate and is easily operated. The printed copper pattern would be used for transparent electrode, printed circuit board, antenna and flexible displays.

Keywords Flexography Printed pattern · Nano-Copper Conductive ink

1 Introduction

Printed electronics has obtained great progress in the recent years. Printed electronics is a promising technology for the flexible, light and low cost electronic devices, leading to the development of efficient and environmental fabrication [1]. Researchers are focused on the developments of simple, green, large area and

Y. Fang (✉) · Y. Li · L. Li
Beijing Engineering Research Center of Printed Electronics, Beijing Institute of Graphic Communication, 102600 Beijing, China
e-mail: fangyi@bigc.edu.cn

Z. Li · R. Yao · A. Tang · T. Zhang · Y. Xu · L. Yang
School of Printing and Packaging Engineering, Beijing Institute of Graphic Communication, 102600 Beijing, China

P. Zhao et al. (eds.), *Applied Sciences in Graphic Communication and Packaging*, Lecture Notes in Electrical Engineering 477,
https://doi.org/10.1007/978-981-10-7629-9_51

flexible printed electronics process. Conductive ink plays an important role in the printed electronics. Recently, nano-silver inks are usually used to fabricate conductive structures such as circuits, transparent electrode or functional layers in devices [2]. However, high cost and scarcity of silver limit large-scale applications [3]. Copper is a good alternative metal since the electrical conductivity of copper is high and the price of copper is much lower. The nano-copper ink can also be applied on a variety of substrates by flexography, gravure, screen or inkjet technology [4]. Flexography printing technology which has fast printing speed and good printability will have wide range of applications in the field of printed electronics industry [5, 6]. The advantages of nano-copper ink would be greatly beneficial for the reduction of the production cost. The printing products of nano-copper ink may include transparent electrode, printed circuit board, antenna and flexible displays [7–9].

This work represents a simple approach to print with copper ink by flexography. This method is compatible on the PET substrate. The conductive ink can be easily prepared with nano-copper suspension and glycerol. The copper pattern can be dried at only 80 °C. The copper pattern of square has a better conductivity than the hexagon pattern. The CLSM reveals that the heights of the pattern are determined by the printing direction and shapes. The morphologies of the two shapes of copper pattern were fine. The method obtained printed copper layers with high conductive on PET film and can be applied to large-scale production.

2 Experiments

The nano-copper ink was prepared in our laboratory which is specific for flexography. The dry solid content is 70 wt%. The solvent is glycerol and water (Fig. 1a). The ink and the synthesizing process use poly-vinylpyrrolidone (PVP) as the dispersant and protective agent for stabilization. The PET film was purchased from China Lucky Group Corporation. Prior to print, the substrates were cleaned with ethanol, then blown dried with high purity nitrogen. An IGT-F1 Printability tester was used in the printing process (Fig. 1b). The flexo-plates were purchased from a plate manufacturer. The flexo-plates were patterned with long strips. The square or hexagon patterns are on the strips. The line space of the square and hexagon shapes on the flexo-plates is 300 μm. The line width of the square and hexagon shapes on the flexo-plates is 20 μm (Fig. 1c). The printing pressure is 150 N. The printing velocity is 0.3 m/s. The obtained copper patterns were dried in a hot oven under 80 °C. The printed copper patterns were analyzed by the CLSM. The conductivity of the printed copper patterns is measured with the 4-point probes resistivity measurement system (RTS-9, Four Probes Tech).

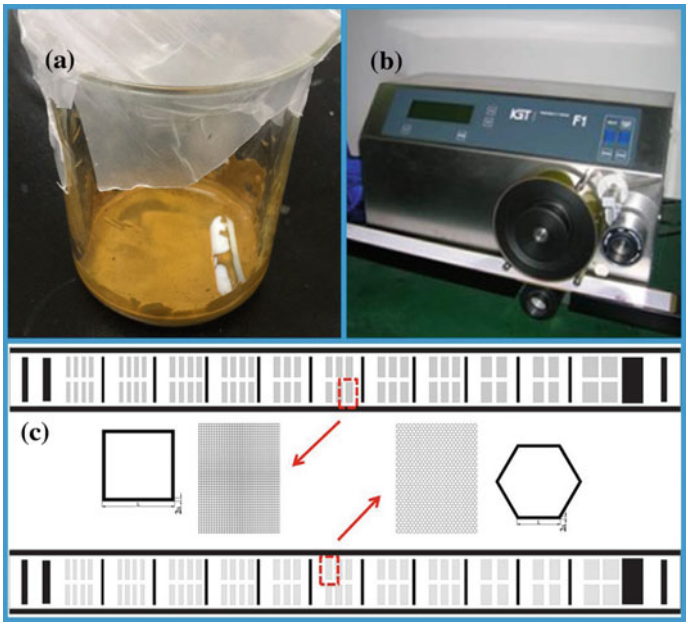

Fig. 1 The nano-copper conductive ink (**a**), the IGT-F1 printability tester (**b**) and the designed flexographic plates of square and hexagon (**c**)

3 Results and Discussion

The printing quality of the printed copper pattern of square and hexagon is fine, as shown in Fig. 1. The yellow grid patterns are evident under a black background. The copper pattern exhibits the clear metallic luster. The edge of the pattern is very neat. The dried copper ink gathered at the overlap of the printed lines by the CLSM analyzing. It is found that the copper ink gathered more on the square pattern. This is due to the mechanism of the flexographic plates. The width of the printed lines is about 40 μm, because of the dot gain effect. The level of width could still meet the requirements of device application, although the width of the lines was doubled (Fig. 2).

The heights of the lines of the hexagon pattern are 3.12 μm (Fig. 3a) and 1.02 μm (Fig. 3b) depending on orientations of the lines. The heights of the lines of the square pattern are 3.66 μm (Fig. 3c) and 9.51 μm (Fig. 3d), respectively. The height difference is due to the printing direction. The characteristics of the flexible plate of the flexography exhibit a noticeable degree of plate squash and ink squash, particularly on the non-absorbent substrates (such as PET substrate). This caused the similar effect on the square pattern and hexagon pattern. The height difference of the lines on different printing directions is about three times.

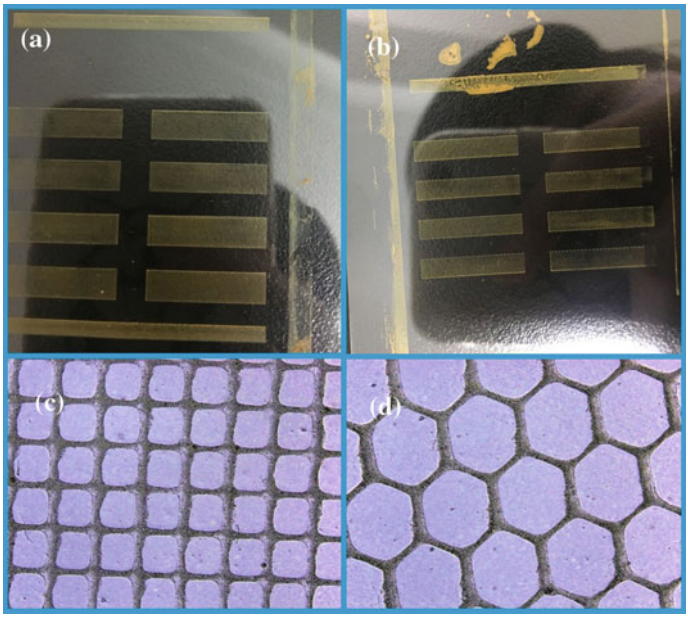

Fig. 2 Pictures of the printed copper pattern (**a**: square, **b**: hexagon) and the CLSM pictures of the printed copper pattern (**c**: square, **d**: hexagon)

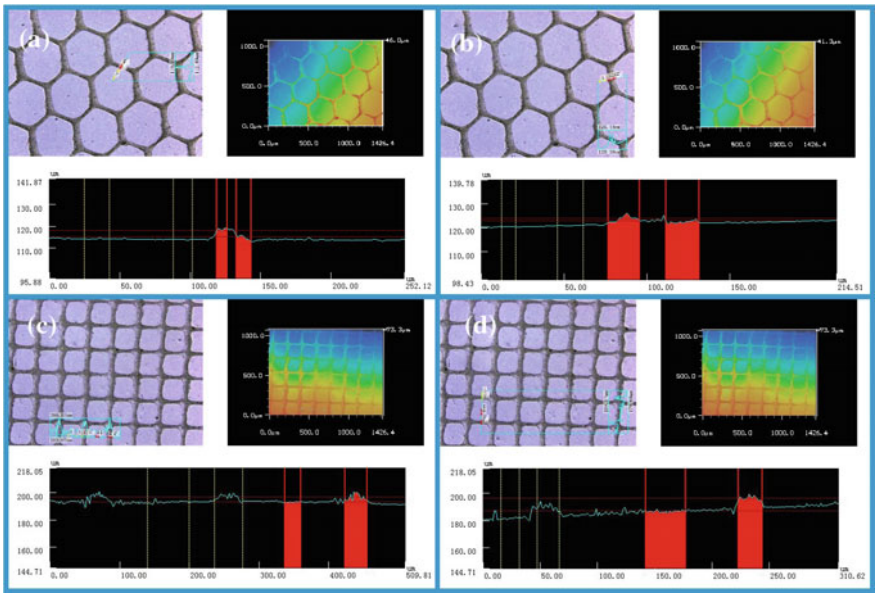

Fig. 3 The morphological analysis of copper pattern by CLSM (**a**, **b**: different position of square pattern; **c**, **d**: different position of hexagon pattern)

The conductivity of the all of the printed copper patterns reaches the level of 0.1 kΩ/γ. The square pattern has the lowest surface resistance which is to 90 Ω/γ, since the greater surface lines density of square pattern, whereas the hexagon pattern is to 230 Ω/γ. The PET film limits the copper pattern's conductivity as the PET film has a low melting point. The surface resistance of copper pattern could be much lower if the nano-copper particles were sintered at a higher temperature on polyimide or glass substrates. The printed pattern has the potential to be used as the electrode of the optoelectronics devices.

4 Conclusions

The flexographic conductive ink was prepared with nano-copper suspension and glycerol. The square and hexagon copper patterns were obtained by flexography printing. The morphology of the printed copper pattern of square and hexagon are fine. The CLSM analysis indicates that the height of pattern's line is influenced by the printing direction. The lowest surface resistance of the copper pattern is 90 Ω/γ. The approach realizes a low cost production method of high conductive film on PET substrates and has potential to be utilized in electronics industry. The printed copper patterns of square and hexagon may be used for transparent electrode, printed circuit board, antenna and flexible displays.

Acknowledgements This work has been financially supported by the Beijing Municipal Commission of Education Foundation for Ability Construction of Scientific and Technological Innovation Service (4190117017), Key Project of Beijing Institute of Graphic Communication (Ea201501), the National Natural Science Foundation of China (NSFC) through the projects: printing dynamics for high-definition printed electronics (61474144), Cross training plan for high level talents in Beijing colleges and Universities (2017), 2017 Cultivation and development of innovation base (Z171100002217032), Beijing Municipal of Education 2011 Collaborative Innovation Center, Printed Electronics Technology & Engineering Discipline Construction (III) (grant number 21090116001).

References

1. Aleeva Y, Pignataro B (2014) Recent advances in upscalable wet methods and ink formulations for printed electronics. J Mater Chem C 2:6436–6453
2. Allen M, Leppaniemi J, Vilkman M, Alastalo A, Mattila T (2010) Substrate-facilitated nanoparticle sintering and component interconnection procedure. Nanotechnol 21:475204
3. De Gans B, Duineveld P, Schubert U (2004) Inkjet printing of polymers: state ofthe art and future developments. Adv Mater 16:203–213
4. Allen M, Lee C, Ahn B, Kololuoma T, Shin K, Ko S (2011) R2R gravure and inkjet printed RF resonant tag. Microelectron Eng 88:3293–3299
5. Hübler A, Bystrik T (2011) Printed, paper photovoltaic cells. Adv Energy Mater 1:1018–1022
6. Vena A, Perret E, Tedjini S, Tourtollet G, Delattre A (2013) Design of chipless RFID tags printed on paper by flexography. IEEE Trans Antennas Propag 61:12

7. Tsai C, Chang WC, Chen GL, Chung CH, Liang JX, Ma WY, Yang T (2015) A study of the preparation and propertiesof antioxidativecopper inks with high electrical conductivity. Nanoscale Res Lett 10:357–363
8. Kaltenbrunner M, Sekitani T, Reeder J, Yokota T, Kuribara K, Tokuhara T et al (2013) An ultra-lightweight design for imperceptible plastic electronics. Nat 499:458–463
9. Chen Y, Au J, Kazlas P, Ritenour A, Gates H, McCreay M (2013) Flexible active-matrixelectronic ink display. Nat 423:136

Analysis and Research on Several Mainstreams Printing Digital Workflow

Chao Peng and Guangxue Chen

Abstract In this study, we report on the quality and characterization of printing brochure, which was treated by founder ElecRoc and Cleo Prinergy digital workflow respectively. The color of brochure showed improved printing quality and work efficiency with the using of digital printing workflow, which is convenient, easy and low energy-consuming tool to control and manage printing process. The printing brochure were analyzed by Spectrophotometer and their image definition and dot features were investigated. It was found that the printing brochure with digital work flow can be completed within 24 h, moreover with less mistake, but normal process will take at least 72 h. Also the color characterization of the brochure is more close to the original.

Keywords Digital printing · Digital workflow · Founder ElecRoc Prinergy

1 Introduction

With the global high speed into the digital era of the Internet economy and transformation and upgrading of traditional printing industry, the printing technology is developing towards digitization and networking, it has become the trend of future development of the printing industry. The application of digital technology in the printing process is changing the production, management and operation mode of the printing industry. The so-called "digital workflow", that is, to the digital production control information will be treated as before printing, printing and postpress three points process integration into an integral system, make the transmission of graphic information is complete and accurate digital, and eventually processed into printed products [1]. Digital workflow incorporate a variety of

C. Peng · G. Chen (✉)
School of Light Industry Science and Engineering, South China University of Technology, Guangzhou, China
e-mail: chengx@scut.edu.cn

P. Zhao et al. (eds.), *Applied Sciences in Graphic Communication and Packaging*, Lecture Notes in Electrical Engineering 477,
https://doi.org/10.1007/978-981-10-7629-9_52

control information of pre-printing processing, printing, postpress finishing into computer management, Integrating entire printing process by printing digital workflow [2].

Much work so far has focused on printing digital workflow. Meng [3] has introduced problems and current solutions of printing digital workflow, and their technical parameters and market prices are analyzed and compared with each other. Ji [4] compared the features technically and economically between several mainstream printing digital workflow, exhibits the superiority of printing digital workflow application in printing and packaging industry. Although much research pay attention to the impact of printing digital workflow, but little attention is paid to the printing quality and efficiency of digital printing process.

In this study, we also test and evaluate the printing quality evaluation parameters of brochures for understanding deeply the details of digital process.

2 Analysis of Print Quality Parameters

In color printing, parameters that affect the quality of printed matter include solid density, relative contrast, ink trapping rate [3].

2.1 Solid Density

Print solid density is density of the total coverage of the ink layer on the printed material, which is measured using a reflectance densitometer. Through field tricolor ink density measurement and calculation, the actual analysis of aqueous ink tricolor of error. The printing solid density and color, and the dot covering rate are the most important factors influencing printing quality of magazine. It's not only influenced by ink thickness, but also by paper surface structure. Generally speaking, the thicker the ink layer, the greater the density and the smoother the paper, the greater the density [5].

2.2 Relative Contrast

Both halftone dot accretion and relative contrast are the important parameters of printing quality control system based on density. The relative contrast value refers to as K, is the ratio of the difference with the solid density and dot density and solid density, which is seen by the human eye color difference. It can determine the expansion of the dot. More over it is a very important parameter for not only controlling proofing or printing, but also controlling the image index of the darkened parts. The formula is as follows:

$$k = 1 - Dr/Dv \tag{1}$$

where D_R represents the integrated density of the dot area between the halftone to dark tones on printed matter and Dv the solid density. At home and abroad, the printing industry choose 75% or 80% round dot as the density reading block to calculate the K value. Because this area is the largest part of the round dot, and the contrast to solid field is decreased, resulting hierarchical variation more easily. This site copy quality can reflect the print tone and contrast level from the middle to the dark [6].

3 Experimental

3.1 Preparation of Brochure

At first, text, graphics, image material are collected which brochures required. Then the layout of the brochure is designed by Adobe Photoshop and finally set up the type by using the Adobe InDesign software.

3.2 Design of Brochure Digital Printing Workflow

See Figs. 1, 2 and 3.

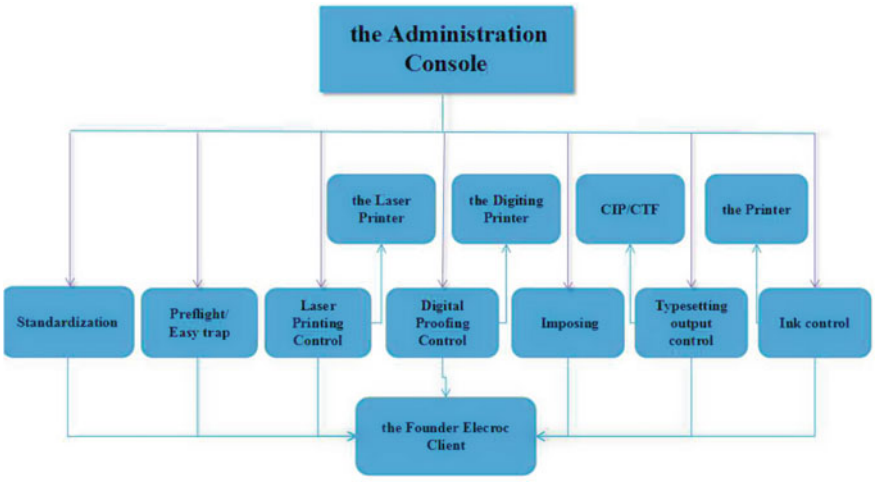

Fig. 1 The detail of the founder ElecRoc

Fig. 2 The parts detail of the brochure

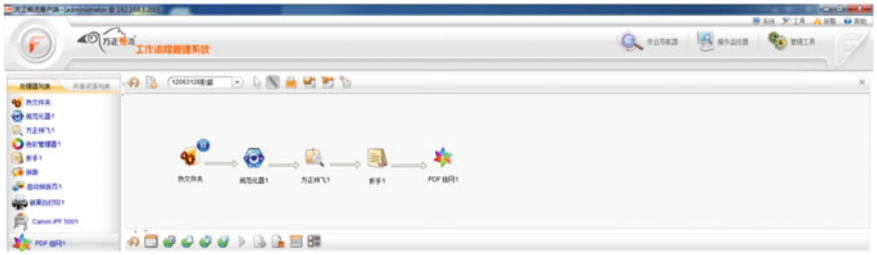

Fig. 3 The working interface of the founder ElecRoc

3.3 Test of Printing Quality Parameters

Test block were sampled at the same position in the three brochures, and the quality parameters of the prints were tested by using the X-Rite528 type densitometer.

4 Results and Discussion

4.1 Test Results

4.1.1 Field Density

The average values of the solid density test data for each sample are shown in Table 1.

Table 1 Solid density

D_0	D_E	D_P
1.42	1.60	1.58

Table 2 Relative contrast value

K_0	K_E	K_P
0.50	0.71	0.78

Table 3 Comparison of the time required

E_0	E_E	E_P
72 h	22.3 h	23 h

4.1.2 Relative Contrast

The average values of the test data for each sample are shown in Table 2.

4.1.3 Efficiency

The average values of the test data for each sample are shown in Table 3.

4.2 Results and Analysis

The digital workflow greatly improves the quality of the finished product. After Creo Prinergy coping with the brochure, the prints contrast value is 0.78, K value is greater, indicating the smaller dot density and solid density ratio and the greater the printing contrast. Conversely, the smaller the K value, the more serious the dot gain and the smaller the printing contrast. Contrasting the length of time required, it is clear that the digital process software greatly improves the efficiency of print out, saving production costs. The founder ElecRoc, basing Internet open architecture and browser interface, can be operated on any platform and any internet terminal by users with standard Internet PC/MAC. It saves a lot of equipment and maintenance personnel expenses. Moreover work can be successfully for remote submission, remote proofing and remote management, and it lays a solid foundation for the realization of remote output and network online service. The Cleo's Prinergy workflow shows a high degree of flexibility, which provides effective control methods, outstanding performance, overall coordination and stability for prepress operations. From a technical point of view, they have tended to perfect, and have their own characteristic, both emphasize openness, compatibility and operability [7].

5 Conclusions

Through the design and comparison of digital process, testing with printing quality control parameters, the paper not only further clarify the application status of the digital process, making us to get a more profound understanding, but also provide certain data reference for future digital printing process.

Acknowledgements This research was financially supported by the State Key Laboratory of Pulp and Paper Engineering Project (2016c01) and Science and Technology Program of Guangzhou (201607020045).

References

1. Huang C (2008) Realization of digital printing workflow. Guangdong Printing 1:21–23
2. Wang CC, Liu Y (2006) Realization of printing digital workflow. Screen Printing 4:37–39
3. Meng XZ (2008) Digital printing workflow. Printing Ind (3):98–102
4. Ji YQ (2004) Technology comparison of several mainstream digital process systems. Print World 7:20–22
5. Wang CX, Zhou SS (2004) Detection and control of printing quality. Print World 7:29–31
6. Sun ZQ, Zhang Z (1996) The theory and technology of intelligent control. Control Decis 11 (1):1–8
7. Leng CF (2009) CTP printing quality control parameter testing and analysis. Packag Eng 30 (5):9–10

Study on the Effect of PVA Aqueous Solution on Water Quality

Meiqi Yang, Guorong Cao, Dongli Li and Xinting Wang

Abstract Polyvinyl alcohol (PVA), polymer material, with excellent polymer properties and water solubility, it is widely used in the field of hydrographics transfer printing, textile, pesticide and washing and packaging. In this paper, infrared spectroscopy and various parameters of PVA and reference water samples were tested, such as pH, dissolved oxygen, anionic surface activity of aqueous solution, PVA aqueous solution and so on. The effect of PVA film on water quality was studied. The research results showed that by infrared spectroscopy, there were a large number of hydroxyl groups and possible residual ester groups in PVA. The pH, color, dissolved oxygen, total phosphorus, ammonia nitrogen, sulfide, total E. coli and suspended matter in the PVA aqueous solution satisfied the requirements required in the standard values.

Keywords PVA · Aqueous solution · Infrared spectroscopy · Water quality

1 Introduction

Polyvinyl alcohol (PVA) is a kind of excellent performance, widely used general purpose and functional polymer material, which has a polyhydroxy strong hydrogen bond molecular structure and a single –C–C–key backbone, the structural formula is:

$$-[-CH_2-\underset{\displaystyle OH}{\underset{|}{CH}}-]_n-$$

With the characteristics of polyhydroxy strong hydrogen bonds, PVA is a synthetic water-soluble polymer material [1], which is widely used in the field of water transfer, textile, pesticide and washing and packaging. At present, the application and research of PVA are mostly based on its aqueous solution, and PVA

M. Yang · G. Cao (✉) · D. Li · X. Wang
School of Printing and Packaging Engineering, Beijing Institute of Graphic Communication, Xinghua Avenue (Band Two), Daxing, Beijing 102600, China
e-mail: caoguorong@bigc.edu.cn

P. Zhao et al. (eds.), *Applied Sciences in Graphic Communication and Packaging*, Lecture Notes in Electrical Engineering 477,
https://doi.org/10.1007/978-981-10-7629-9_53

in the water solubility of the excellent decision determines its product quality, price, consumer experience and environment-friendly factors. At present, in order to shorten the drying time, improve the industrial production efficiency and productivity effect, the development of excellent performance of PVA is more extensive, but the impact of aqueous solution of PVA on water quality has not been reported. Therefore, the paper studies the composition of PVA aqueous solution, compares and analyzes the effect of PVA aqueous solution on water quality, which is of great significance to the market application of PVA water solubility.

2 Experiments

2.1 Analysis of PVA Films by Infrared Spectroscopy (IR)

Based on PVA film and infrared spectroscopy (FTIR-8400S), the IR spectra of PVA films were measured by liquid film method, and the PVA film was analyzed.

2.1.1 Sample Preparation

PVA film and water were prepared into 1% concentration of PVA aqueous solution, Make the potassium bromide tablet in the appropriate environment, and coat the appropriate amount of PVA aqueous solution evenly on potassium bromide tablet, then, put it into the infrared spectrometer for testing.

2.1.2 Infrared Spectra Analysis

The infrared spectrum usually refers to the absorption spectrum between wavelengths of 2 $\sim$ 25 μm, which can be applied to the determination of molecular structure of compounds, identification of unknown materials and analysis of mixture composition [2]. PVA is obtained by polymerization of polyvinyl acetate, so that the molecular structure of the polyhydroxy and residual carbonyl groups makes it have a long absorption wavelength in the infrared spectrum. In addition, the additives added during the PVA sample production process may have an effect on the infrared absorption of PVA. The infrared spectra of PVA is shown in Fig. 1.

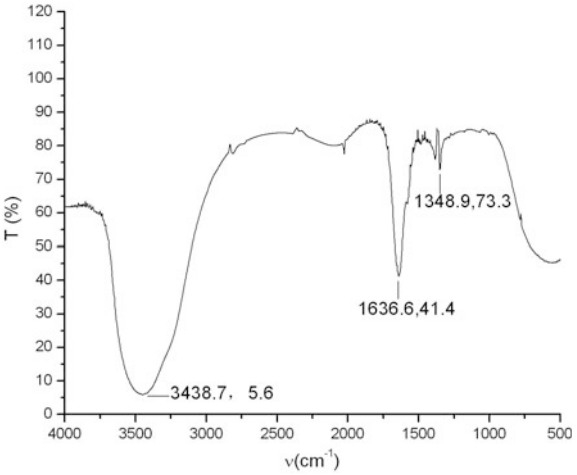

Fig. 1 Infrared spectra of PVA

2.2 Determination of PVA Aqueous Solution

Based on PVA film and deionized water, PVA aqueous solution was prepared by quantitative dilution method. The aqueous solution of PVA was compared with the material composition in deionized water samples of the same environment. In order to exclude interference from PVA detection in water samples. According to GB 8978–1996 *the Discharge Standard for Integrated Wastewater*, GB 3838–2002 *the Environmental Quality Standards for Surface Water* and GB 3544–2008 *the Discharge Standard for Pulp and Paper Industry Pollutant*, take comparative analysis of PVA aqueous solution on water quality.

2.2.1 Sample Preparation

Homemade 10L deionized water, 5L as a component to detect standard water samples, stand-by.

Weigh 50 g PVA film, cut into small sample and dissolve them into the remaining 5 L deionized water, with 70–100 r/min speed stirring to prepare into a 1% concentration of PVA aqueous solution, stand-by.

2.2.2 Testing Items and Methods

The test items include pH, chroma, turbidity (NTU), dissolved oxygen, dissolved total solids/filter residue, total phosphorus (calculated as P), total nitrogen (calculated as N), ammonia nitrogen (calculated as N), total organic carbon, total alkalinity ($CaCO_3$), chemical oxygen demand (CODCr), anionic surfactants, sulfides, total coliforms, suspended solids. The above methods were as followings seen in Table 1.

Table 1 The comparison of PVA aqueous solution test items and the corresponding standard

Sequence numbers	Pollutant	Deionized water	PVA aqueous solution	The Integrated Wastewater Discharge Standard[1]	The environmental quality standards for surface water[2]	The pulp and paper industry pollutant discharge standard[3]	Testing methods
1	pH	7.12	6.08	6 ~ 9	6 ~ 9	6 ~ 9	Glass electrode method
2	Chroma (dilution ratio)	<1	2	80	–	50	Dilution multiple method
3	Turbidity (ntu)	<0.5	11.2	–	–	–	Turbidity meter method
4	Dissolved oxygen (mg/L)	8.2	3.4	–	3	–	Iodometric method
5	Dissolved total solids/ filter residue (mg/L)	33	172	–	–	–	Gravimetric method(105 ° C)
6	Total phosphorus (mg/L)	<0.01	<0.01	–	0.3	0.8	Ammonium molybdate spectrophotometry
7	Total nitrogen (mg/L)	1.46	20.5	–	1.5	15	UV spectrophotometer
8	Ammonia nitrogen (mg/L)	<0.01	<0.01	50	1.5	12	Salicylic acid spectrophotometry
9	Total organic carbon (mg/L)	0.5	1.06×10^4	–	–	–	Combustion oxidation Infrared cabsorption method
10	Total alkalinity (mg/L)	12.4	76.0	–	–	–	Acid and alkali indicator titration method
11	Chemical oxygen demand (mg/L)	<10	3.43×10^4	200	30	100	Potassium citrate method
12	Anionic surfactants (mg/L)	<0.05	2.33	10	0.3	–	Methylene blue spectrophotometry
13	Sulfides (mg/L)	<0.005	<0.005	1.0	0.5	–	Methylene blue spectrophotometry
14	Total coliforms (mpn/ 100 ml)s	<2	<2	103	2 × 104	–	Multi-tube fermentation method

Note

[1]In accordance with the second category of pollutants the maximum allowable emission concentration of secondary standards of the Discharge Standard for Integrated Wastewater

[2]Basic items Standard limits Class IV of surface water environmental quality standards in the Environmental Quality Standards for Surface Water

[3]New corporate pollutant emission limits, the type of production is the pulp business in the Discharge Standard for Pulp and Paper Industry Pollutant

3 Result and Analysis

3.1 Analysis of PVA Films by Infrared Spectroscopy (IR)

Figure 1 shows the infrared spectra of PVA. The presence of strong and broad absorption peaks in the 3400 $\sim$ 3500 cm^{-1} region indicates the presence of a large number of –OH hydroxyl groups in PVA. The presence of absorption peak at 1636 cm^{-1} can be presumed to ester base carbonyl peak. The reason may be the experiment with PVA by polyethylene (vinegar) vinyl ester in the presence of alkaline catalyst or acidic catalyst hydrolysis derived [3]. So there will be ester residues on the polyvinyl alcohol.

PVA polyhydroxy strong hydrogen bond characteristics can be confirmed by infrared spectroscopy, intermolecular and intramolecular polyhydroxy strong hydrogen bonds will hinder its dissolution in water. At the same time, from the infrared spectrum can be inferred PVA aqueous solution in the presence of residual carboxylate. The presence of carboxylate can reduce the intermolecular and intramolecular hydrogen bonds, and thus improve the solubility of PVA in water. This will be of great significance to study the effect of PVA aqueous solution on water quality and improve the efficiency of PVA industry.

3.2 Analysis of the Test Results of PVA Aqueous Solution

Table 1 shows that a number of test items of PVA aqueous solution are in line with a number of related national standards, which provide a scientific basis for the development of PVA new market applications [4].

The detection value of anionic surfactants accorded with the Discharge Standard for Integrated Wastewater and did not meet the Environmental Quality Standards for Surface Water. This result may be affected by the addition of additives in PVA products. It may be supposed to make some further research for PVA product formulations or the treatment to reduce the surface activity of PVA aqueous solution.

PVA material has the characteristic that a high face activity, which leads to produce a large number of bubbles after dissolving in water with mixing. The test results can be compared to show that the chemical oxygen demand detection value is far beyond the above three national standards.

4 Conclusions

The influence of PVA aqueous solution on water quality was analyzed in the paper. The results showed that the PVA aqueous solution was analyzed by infrared spectroscopy, and there were a large number of hydroxyl groups and possible residual ester groups in PVA. The pH, color, dissolved oxygen, total phosphorus, ammonia nitrogen, sulfide, total E. coli and suspended matter in the aqueous solution were lower than the national standard values. The total nitrogen, anionic surfactants and chemical oxygen demand did not satisfy the relevant national standards. Therefore, the article provides a reference for the study of the natural environment degradation ability of PVA aqueous solution and the recycle of slurry containing PVA components.

Acknowledgements The authors gratefully thank the support from the teaching engineering team (construction) (22150116006/017) and the printing and packaging research project of cultivating innovative talents in (22150116007/055) Beijing-Tianjin-Hebei universities. We are here with best thanks.

References

1. Lei CT, Pan XY, Yao GH Wang, L., Zhou G, Wang Q, Li L, Chen N (2011) Research progress of water-soluble polyvinyl alcohol. Plas Ind 02:39–02
2. Deng QY, Liu L, Deng HM (2005) Spectrum analysis tutorial. Sci Press
3. Cui HL (2012) The relationship between FTIR spectra of PVA film and its heat preservation capability. Spectrosc Spectral Anal 32(1):96–98
4. Yang T (2015) Using water-soluble PVA bag packaging is solutions for the harm of pesticide packaging. Plast Packag 25(3):22–25

Part V
Packaging Engineering Technology

Evaluation on Cushioning Packaging System of Laptop During Drop Based on ABAQUS

Gaimei Zhang, Xiaoli Song, Yue Shi, Fan Su and Yue Cao

Abstract The main reason is vibration and shock in the circulation for the damage of packaging product in the logistics process. The impact is one of the main factors, which causes product damage and packaging failure. To prevent the damage, drop test of packaging system must be carried on. However, this detect is generally destructive for products and so much samples are consumed. In this paper, the models of laptop and its cushioning packaging system are built, and the drop analysis of the system is developed based on ABAQUS software. The stress of the laptop during drop is simulated. Comparing the laptop without cushion and the packaging system using the cushion, the results show that the stress is different for two types, and the stress of laptop without the cushion is bigger than the other.

Keywords Finite element method · Drop simulation analysis · Stress Cushion

1 Introduction

Packaging and its content are affected by various environmental factors such as impact and vibration, so the damage occurs unavoidably during transport [1]. The impact is one of the main factors causing product damage and packaging failure, it causes the product damage due to its accelerate more than promise of brittle value, meanwhile the physical damage of product mostly is suffered from impact in the circulation [2]. The physical test for product and its packaging are done generally to study the process of package damage and product failure, but it is usually destructive and is not easy to control, meanwhile the high cost and consumption are needed, [3]. Effective method solving this problem is to simulate the process based on finite element method. The drop properties of product were studied using ANSYS by some scholars [4–6].

G. Zhang (✉) · X. Song · Y. Shi · F. Su · Y. Cao
Beijing Institute of Graphic Communication, Beijing, China
e-mail: zhang_gaimei@163.com

P. Zhao et al. (eds.), *Applied Sciences in Graphic Communication and Packaging*, Lecture Notes in Electrical Engineering 477,
https://doi.org/10.1007/978-981-10-7629-9_54

In this paper, the construction of packaging cushion for laptop was designed, and the models of laptop using and not using cushion were built, and the stress of laptop is analyzed based on the finite element software ABAQUS [7–10]. The stress was analyzed for different types including not using and using cushion. The results show that the stress and deformation of the laptop without the packaging cushion is bigger than the other, and the stress changes with time for same node.

2 Modeling of Laptop Including Using and Not Using Cushion

Using ABAQUS the laptop is simplified as a cube with 400 mm length, with 300 mm width and with 10 mm thickness, as shown in Fig. 1. The cushion of Expanded Polystyrene (EPS) was designed to protect the laptop. The parameters of material can be seen in Table 1 and the EPS is plastic strain. The element length is respectively 10 mm for the rectangle, the interaction between the laptop and the cushion is with the tie coupling. The models of laptop after meshing not using and using cushion are shown in Fig. 2.

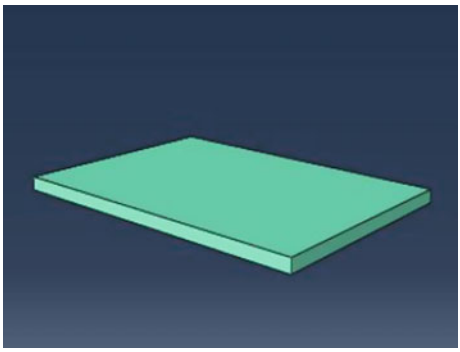

Fig. 1 The simplified model of laptop

Table 1 Material parameters

Part name	Elastic modulus (GPa)	Passion's ratio	Density (kg/m^3)	Yield strength (MPa)
Laptop	2.6	0.38	1140	80
EPS	5.5×10^{-4}	0.3	20	0.176

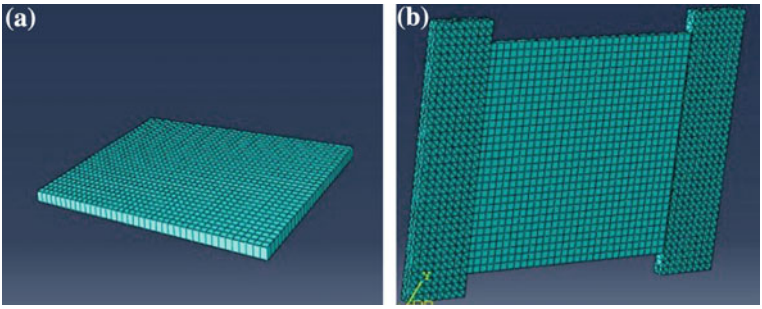

Fig. 2 The model of laptop after mesh not using (**a**) and using (**b**) cushion

3 Simulation Analysis of Laptop During Drop

The stress of the laptop is analyzed, and the curve of accelerate and distribution of stress were obtained for with and without cushion.

3.1 Acceleration Curves Analysis

The acceleration curves are showed in Fig. 3a and b respectively for the laptop not using and using cushion during drop. The maximum acceleration can be found as 9401.1 and 500.9 m/s^2 without and with cushion, which can showed the cushion absorb the impact energy and protect the laptop.

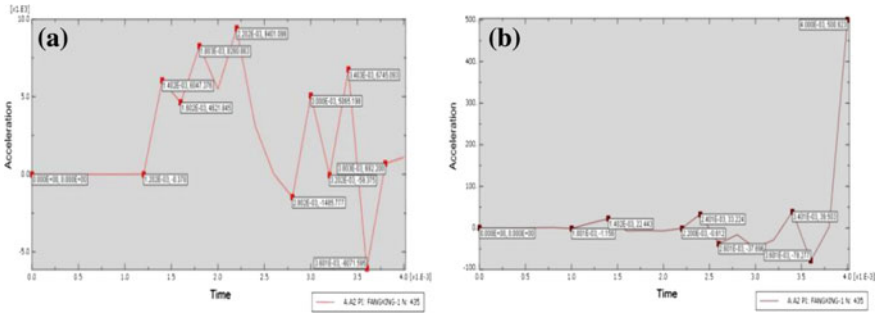

Fig. 3 Curves of accelerate of laptop not using (**a**) and using cushion (**b**)

3.2 *Stress Analysis*

3.2.1 Distribution of Stress for Laptop

Figure 4 shows the stress nephogram during the drop process for the laptop not using cushion pad. Figure 4a and d are the stress picture before and after impact, Fig. 4b and c are the stress picture during impact. The maximum stress is respectively 1.14 Pa, 18.8, 24.0 and 1.08 MPa. The results show the maximum stress is at the corner of laptop.

Figure 5 shows clearly the stress nephogram of packaging system including the laptop and cushion pad during the drop process. Figure 5a is the stage beginning the impact, Fig. 5b is the process of impact and Fig. 5c is the rebounding stage. It can be seen that the maximum stress is 0.2592 MPa at the angle of contact with the plane during the falling, and it is bigger than the yield strength with 0.176 MPa [11], so the plastic deformation occurred for EPS. It is consistent with the stress picture, which can reflect the real situation.

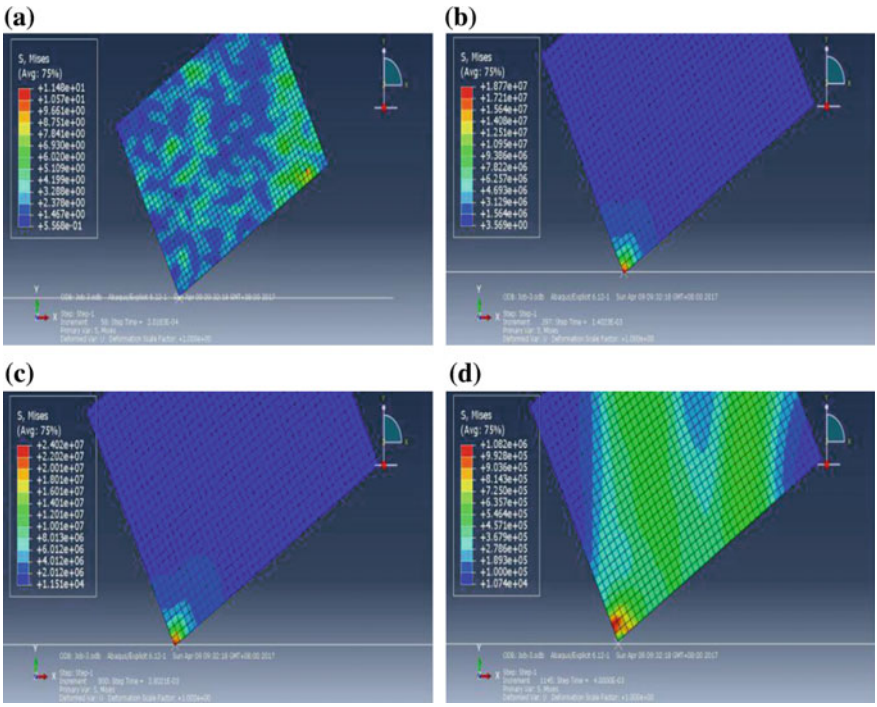

Fig. 4 Distribution of stress of laptop for different time not using cushion

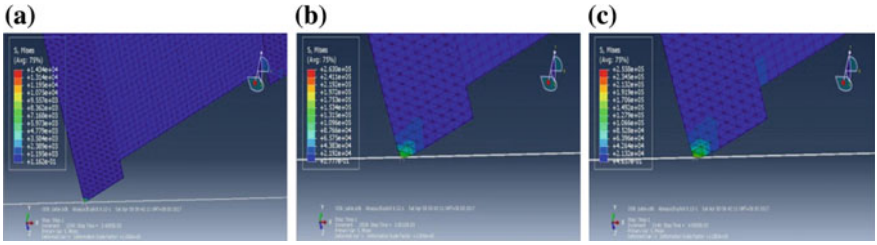

Fig. 5 Distribution of stress of laptop for different time using cushion

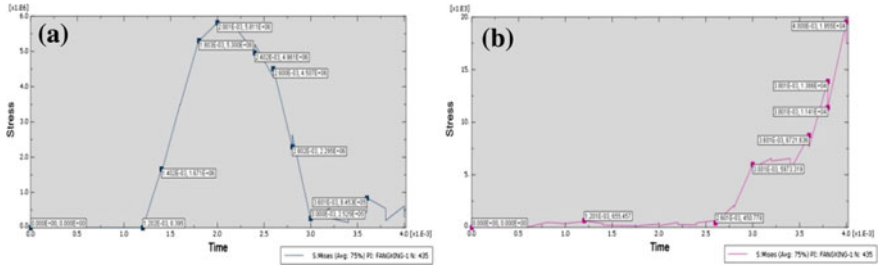

Fig. 6 The stress of the laptop changing with time for not using (**a**) and using cushion (**b**)

3.2.2 Stress Changing with Time

Figure 6a and b show the stress of same location of laptop changing with time during the drop not using and using cushion. It can be found that using the cushion the impact is delayed and the maximum stress is reduced to 0.01955 MPa from 5.811 MPa, which is much smaller than the yield strength with 80 MPa, so the cushion can protect the laptop.

4 Conclusions

The finite element model of the laptop using and not using cushion are built based on the ABAQUS. The drop simulation analysis is carried out, dynamic response of laptop are obtained. It can be found from the simulation results of the respond stress, stress of the laptop are decreased using the EPS cushion pad. Compared with the traditional cushioning packaging design method, finite element simulation can effectively shorten the test period and save manpower and material resources.

Acknowledgements This research was supported by the National Natural Science Foundation of China (No.51305038) and general research projects of Beijing Institute of Graphic Communication (Eb201701).

References

1. Peng GX (2006) Logistics and transport packaging design. Printing Ind Press, Beijing
2. Xiaogang LI (2012) Random vibration frequency domain analysis of transport packaging system. Packag Eng 33(15):50–54
3. Huming D, Feng S, Fei X et.al (2009) A survey of road roughness study. J Vibr Shock 28 (9):95–101
4. Zhang B (2014) Free fall test simulation analysis and research based on laptop. Suzhou Univ, Suzhou
5. Song RH, Zhang ZG (2009) Simulation on laptop package dropping by using ANSYS software. J Zhejiang Univ (Sci Tech) 21(4):332–335
6. Xianxiang C (2013) Computer simulation on drop tests of packaging and optimization of cushion foams structure. Shandong Univ, Jinan
7. Yiping S, Yurong Z (2006) Detailed examples of the finite element analysis based on abaqus. Chin Mach Press, Beijing
8. Zhuo Z, Xiao-chuan Y, Jianhui L et al (2009) Finite element analysis and application based on abaqus. Tsinghua Univ Press, Beijing
9. Zhang J et.al (2014) Abaqus finite element analysis from entry to master. Chin mach Press, Beijing
10. Zhang G, Song X, Zhao X et al (2017) modal analysis on laptop and its pakaging system based on finite element method. Lect Notes Electr Eng 417:627–633
11. Zhang S, Qian Y (2012) Simulation analysis of vibration characteristics of induction cooker package. 33(23):56–59

Analysis of the Use Principle of Fabric Materials in Packaging Design

Jianhua Wang, Kongpeng Shi and Shanshan Gao

Abstract Under the background of disposal packaging waste is the challenge faced by all the countries; the green packaging has become the development trend of packaging design. This paper elaborated the theme of the modern packaging design, analyzed the advantages of various kinds of cloth materials and the differences in artistic feeling, studied the use and design principles of fabric materials, and widened the application scope of fabric materials in green packaging design which can not only reduced the environmental pressure, but also strengthened the awareness of environmental protection which accelerated the development of green packaging design.

Keywords Cloth material · Packaging design · Environment friendly

1 Introduction

In the era of environmental protection, in stead of innovative, artistic and practical, people pay more attention to environmental protection and energy saving of the packaging [1, 2]. Green packaging has attracted a great deal of interests from researchers all over the word because of their merits that they can not only reduce environmental pollution, promoting ecological balance, but also recycling, meanwhile, the discarded packaging materials are more likely to degrade or corrupt

J. Wang (✉)
Printing Process Integrated Laboratory, Guilin University of Technology, Guilin, Guangxi, China
e-mail: jianhua222@163.com

J. Wang · K. Shi
Art Design Virtual Simulation Experimental Teaching Center, Guilin University of Technology, Guilin, Guangxi, China

S. Gao
College of Chemical Engineering, Qing Dao University of Science and Technology, Qingdao, Shandong, China

P. Zhao et al. (eds.), *Applied Sciences in Graphic Communication and Packaging*, Lecture Notes in Electrical Engineering 477,
https://doi.org/10.1007/978-981-10-7629-9_55

which can also improve environment in the framework of sustainable development [2]. From the perspective of human health, green packaging is harmless to our body that we no longer worry about the various hazards and diseases caused by petroleum based plastic packaging on our environment and our bodies [3]. Therefore, the biomass of environmental protection materials are gradually developed and utilized by researchers. As one of the biomass materials, fabric materials have unique advantages both in terms of economic benefits and environmental benefits. Moreover, for fabric materials, the price is acceptable and the species are very abundant and, above all, they are pollution-free, nuisance-free from the production to the end of life.

2 Fabric Materials and Their Characteristics

Cloth refers to plant cotton, hemp and cotton type chemical fiber woven fabric by the spinning process. Divided according to its raw materials, fabric materials can be divided into cotton, chemical fabric, linen, silk and non-woven fabrics. The raw materials and weaving process differences cause cloth performance difference, as well as make their application areas difference. See Table 1 for details.

Most of the raw materials for the cloth packaging come from natural biomass materials, such as cotton, hemp, plant fiber etc. [4, 5]. They have good biocompatibility, eco-friendly, recycling and abundant in nature, and provide a reliable protection for the development of cloth materials. Compared with other packaging materials, cloth packaging materials have an unmatched advantage in Table 2.

From Table 2, we can know that cloth materials have better performance than plastic and metal packaging materials except moisture resistance. However, the problem of plasticity and cost are the most important problem in the field of cloth materials, which are also the first consideration in packaging design [6]. The flexibility of cloth material make it has superior plasticity, also make designers complete the modeling and reproduction in a short time, greatly lessened the design period [1, 3]. Moreover, cloth material is one of the abundant resources and eco-friendly that not only in line with the principles of green design, but also broaden the application range in packaging.

3 Principles of Using Cloth Materials in Packaging Design

3.1 Choose Cloth Materials Correctly

Choosing cloth materials correctly is the precondition of packaging design. Cloth materials are different from other materials, especially in waterproof performance and flame retardant, which limit their application [7]. Hence, it is very important for

Table 1 Advantages and disadvantages of various types of cloth materials comparison

Types of cloth	Advantages	Disadvantages	Art sense	Packaging application
Cotton	Good moisture absorption, excellent air permeability	Easy shrink, easy wrinkle	Beautiful and generous	Cloth packaging bags
Chemical fabric	Colorful, soft, anti-crease	Poor wear resistance, poor hot resistance, poor moisture absorption, poor air permeability	Soft	Cloth, bags and suitcases, canvas, military goods packaging
Linen	High strength, good moisture absorption, good air permeability, good antiseptic and antibacterial property	Easy wrinkle, poor stability	Rough, hard	Fashion handbag, hardware packaging bags, eco-packaging
Silk	Anti-ultraviolet, dust absorption, good heat-resistant, good moisture absorption	Poor color fastness, easy shrink, easy wrinkle, easy fade	Soft, bright-colored and beautiful, noble	High-grade cosmetics, wine packaging, tea packaging
Non-woven fabrics	Good moisture absorption, good air permeability	Poor strength, easy cracking	Lightness, soft	Medical equipment packaging, wall cloth, industrial coated cloth

Table 2 Performance comparison of various types of packaging materials

Packaging materials	Moisture resistance	Firmness	Plasticity	Cost
Cloth	Poor	Good	Excellent	Low
Paper	Poor	Poor	Good	Low
Plastic	Excellent	Ordinary	Excellent	Low
Metal	Poor	Excellent	Poor	Expensive
Glass	Excellent	Poor	Poor	Ordinary

designers to accurately master the properties of various cloth materials. And then, they can select cloth materials correctly according to packing requirements and properties of inner packing, avoiding the wasting of cloth and the increasing of production costs.

Fig. 1 The package of Lipton tea

Such as the package design of Lipton tea in Fig. 1, it broke the traditional package of large bags and used small bags with quantitative packaging, which adopted non-woven fabric materials to control the moisture balance and guard against moist and mildew effectively. The excellent permeability of non-woven fabric had a good barrier effect to separate tea and water in the process of making tea, which provided convenience to the fast-food style life of office workers. Moreover, it had a good deal of discarded tea after drinking, so as to avoid dumping randomly which effectively prevented the pipeline block and reduced the workload of cleaning staff.

3.2 Appropriate Materials

Moderation principle has always been considered as the design principle followed by the design industry in the development of green environmental protection, for the packaging design application of eco-friendly cloth materials is no exception. This requires designers use the material rationally to design the inner packaging in order to meet the packaging function. Suit packing design, complex packing design and excessive package of ordinary commodities used by high-quality cloth materials should be limited because this measures will put up the price of commodities, mislead consumers and destruct the market rules.

For example, Fig. 2 presents the lightweight laundry baskets. Designers used ordinary fabrics and polyester materials in combination cleverly to produce barrel-like laundry baskets which not had too much modification but a simple three-dimensional visual impact. Moreover, it could compress into a cake to save space when it is not in use.

3.3 Humanized Design

In accordance with the packaging function of the internal materials to choose cloth materials, the design should not only consider the appropriate materials, but also consider the application of artistic aesthetics and human-computer interaction

Fig. 2 The laundry basket

concept [8]. Although cloth materials are the most common materials, long-term use of which can cause visual fatigue. Thus, we should consider our sensory system in packaging design, such as how to use light technology and color to dilute the visual fatigue. Furthermore, according to the differentiation of consumer groups, we pay more attention to the user's personal experience in design by coordinating our somatic sensation, muscle physiology ability, the angular movement, rotary motion, circular motion and range of the movement of the human body and the applicable range and properties of the packaging material to achieve user centered human-computer interaction. For instance, Fig. 3 shows the cloth supermarket shopping bag, which has a wide but not narrow cloth belt. It is mainly because of the narrow cloth belt always made hand or shoulder feel uncomfortable in the case of more items. The reason is the smaller force area and the larger force of unit area, so that slowed down the limb blood circulation speed lead to hand and other bodies have a feeling of pain and numbness. The use of wide cloth belt increased the force area and reduced the force of unit area, which relieved the stimulus of the human nerve endings by the gravity.

3.4 Post Processing Technology

As the preliminary design of cloth packaging is rough and the aesthetic feeling is poor, it is difficult to meet the demand of consumers under the current trend of society and fierce market competition. So it needs further modification to meet the market demand. It requires designers to avoid complex structural design and select

Fig. 3 The cloth supermarket shopping bag

proper materials. If designers only pursue preliminary design appearance and detachment processing technology, it will be designed in odd shape and cannot be processed after processing which is often referred to a failed design [9].

4 Conclusions

Cloth packaging materials gradually recognized and loved by people, because the materials are environmentally friendly, renewable and rich in raw materials. In order to further expand the application scope of cloth materials, reduce the use of plastic products and the pressure of environment and resource, the designers have the obligation to strengthen the application of cloth materials in the field of packaging design, designing intelligent, beautiful and generous environmental packaging.

Acknowledgements This study is supported by the Guangxi Higher Education Undergraduate Teaching Reform Project of China (No. 2017JGB262).

References

1. Dai HM, Dai PY (2014) The basic characteristics and the development trend of ecological packaging materials. Packag J 1–9. https://doi.org/10.3969/j.issn.1674-7100.2014.03.001
2. Huang GX (2015) Application and development of green materials packaging design. Chin Packag Ind 50–52. https://doi.org/10.14047/j.cnki.cpi.2015.09.019
3. Fu N, Zhao XY (2016) Research progress of green package. Plastics Sci Technol 88–92. https://doi.org/10.15925/j.cnki.issn1005-3360.2016.02.017
4. Chen XL (2012) Cloth art packaging design and material structure and the relationship of the process. Art Res 10–12. https://doi.org/10.13944/j.cnki.ysyj.2012.02.004

5. Zhu DJ (2017) Effects of gauge length and strain rate on tensile behaviour of jute yarn. Acta Materiae Compositae Sinica 446–455. https://doi.org/10.13801/j.cnki.fhclxb.20160406.001
6. Wu XX (2017) The structure and properties of superfine wool and its dyeing property with plant dyes. Wool Text J 12–16. https://doi.org/10.19333/j.mfkj.2016001020205
7. Zhao W (2017) Study on the wear ability of blended fabrics of cotton, modal and bamboo fiber. Synth Mater Aging Appl 22–27. https://doi.org/10.16584/j.cnki.issn1671-5381.2017.01.006
8. Zhao JH (2006) Ergonomics. Higher Education Press, Beijing
9. Pan SN (2011) Packaging technology. Printing Industry Press, Beijing

Sustainable Development Mode of Express Packaging Based on Green Concept

Mi Zhang, Li Yang and Ping Deng

Abstract With the rapid development of Internet technology, online shopping has become an important part of daily life. It makes life more convenient and also promotes the development of express business. However, the environmental pollution problem caused by the express packaging has become more and more serious. Relying on this situation, the paper studies an innovative sustainable development mode of express packaging based on green concept. Firstly, the outstanding problems of express packaging are analyzed, from the aspects of packaging materials, packaging design, packaging methods and packaging handling. Then the solutions are proposed from the point of view of the government, enterprise and consumer, to build a three-party cooperation mode of express packaging. And it should implement the green concept in the whole life of this mode, in order to reduce the resource waste and environmental pollution.

Keywords Sustainable development · Express packaging · Green concept

1 Introduction

With the rapid development of Internet technology, online shopping has become an important part of daily life. It not only makes life more convenient but also promotes the development of express business. It is reported that the volume of express business has achieved more than 30 billion in 2016. And also the annual growth rate is more than 50% for six consecutive years. Meanwhile it also produces a large number of express packaging. According to the statistics, the express industry in

M. Zhang (✉) · L. Yang
School of Packing and Printing Engineering, Tianjin University of Science & Technology, Tianjin, China
e-mail: zhangmi@tust.edu.cn

P. Deng
School of Economics and Management, Chongqing Jiaotong University, Chongqing, China

P. Zhao et al. (eds.), *Applied Sciences in Graphic Communication and Packaging*, Lecture Notes in Electrical Engineering 477,
https://doi.org/10.1007/978-981-10-7629-9_56

China use about 12 billion plastic bags, 14 billion packaging boxes and 24 billion meters sealing tapes in 2016 [1]. And most of these packages cannot be effectively recycled and are difficult to be degraded, which causes million tons of packaging waste. The resulted problems of resource waster and environmental pollution are becoming increasingly serious. Relying on this situation, the paper analyzed the problems of express packaging development, and put forward to a sustainable development mode to implement the green concept in the full lifecycle of express packaging.

2 State of Art

2.1 Main Research About Green Express Packaging

Now, the research on the sustainable development of express packaging mainly concentrates upon the green packaging materials, the innovation of packaging design and the recycling mechanism of express packaging.

About green packaging materials and design concept, Gu analyzed the decision-making system of green packaging and established a tree drawing system of green packaging structure [2]. Xu et al. [3] focused on the specific application mode of green concept for commodity packaging. In addition, some multinational companies have begun to focus on innovative biological packaging materials, such as sugarcane, wheat, etc. Williams focused on the food packaging and developed a model to calculate the environmental balance factor between food losses and more packaging material [4]. Chen focused on the innovation design of express packaging and discussed some methods through typical examples. It put forward to the main theme of express packaging including simplicity, reduction, humane and facilitation [5].

For the recycling mode of express packaging, Yang et al. [6] presented the difficulties in the process of establishing express packaging recycling system, such as lack of national policies and regulations, disparity of technical level and weak environmental awareness. Gan et al. carried on the research about the recycling mode of express packaging in university campus from the concept of circular economy. According to the different radiation range of the recovery point, they put forward to a recovery mode including the participation of students, express companies and schools [7]. He et al. present the progress in recycling of plastic packaging wastes (PPW). It classified the decomposition technology of PPW, and also gave some suggestions on recycling approaches of PPW [8]. Zhang et al. [9] put forward to some management strategies for express packaging recycle from the perspective of government and enterprise.

2.2 Current Problems of Express Packaging Development

In summary, the research and application about the sustainable development mode of express package in our country is still at the initial stage, especially in the field of specific recovery method and strategy. The current problems mainly focus on the following aspects.

(1) **Excessive form of Express Packaging**. In order to strengthen the protection of commodity, many businesses or express companies choose two or even multiple packaging, or add buffer materials ceaselessly and wrapping tape repeatedly. This form not only affects the appearance and opening of the packaging, but also increased the number of packaging waste, resulting in a waste of resources and environmental pollution (see Fig. 1).
(2) **Lack of Uniform Express Packaging Standards**. As the express packaging is highly personalized, many express companies have their own internal operations for packaging standard. It not only affects the rapid transferring of express packaging between different transport modes and equipments, but also makes against recovering and reusing of resources. Although the standardization of logistics packaging in China has made some achievements, such as the application of turnover boxes, pallets and containers, there is a lack of specific standards for the express packaging size, packaging structure and internal filling materials.
(3) **Lack of Effective Recovery Mechanism of Express Packaging**. At present, only a few of express enterprises and electronic commerce platform have implemented recycling strategies, but the current effect is not satisfactory, for example the plan of "environmental protection, carton recycling" organized by the ecommerce platform "Yihaodian", and the work of recycling packaging cartons carried out by "Sfbest". However, due to the lack of specific policy support, the incomplete recovery system, the weak environmental awareness of consumers, and the unsound recycling channels, these projects has stopped. It causes a difficult situation in the implementation of express packaging recycling. According to statistics, the recycling rate of express carton in China is less than 20% in contrast to more than 50% in U.S.A.

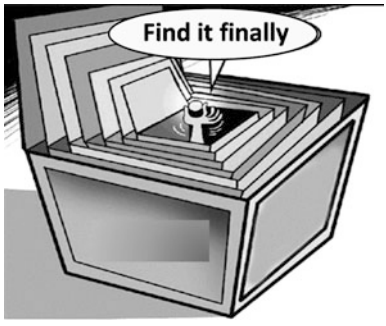

Fig. 1 Excessive form of express packaging

(4) **Relevant Laws and Regulations are Imperfect**. Compared with developed countries, the laws and regulations related to logistics packaging, especially to express packaging are imperfect and need to be completed. The relevant provisions mainly exist in other kinds of laws and regulations. There is lack of independent, complete regulations related to express packaging and the handling of related wastes. In addition, the government has the responsibility to strengthen supervision to implement laws and regulations about express packaging.

3 Sustainable Development Mode of Express Packaging

3.1 Framework of the Sustainable Development Mode

In order to solve the above problems and promote the application of green packaging, the sustainable development mode of express packaging needs the coordination of government, enterprise and consumer. It should implement the green concept in the whole supply chain of express packaging including green packaging materials, simple packaging method, green packaging production, and green packaging transportation. In addition, it is necessary to prolong the lifecycle of the express package through a reasonable and effective recycling mechanism (see Fig. 2). All stages are interrelated and interdependent each other to build a collaborative system with the characteristics of reverse logistics.

3.2 Strategy of the Sustainable Development Mode

In the implementation process of the sustainable development mode of express packaging (see Fig. 3), the government has the obligation to educate and guide the environmental awareness of consumers. At the same time, it has the responsibility to encourage enterprises to practice the green packaging concept. Meanwhile, the enterprise should focus on the research of green packaging materials and the design of simple packaging method. In addition, the green production process and the application of standardization should be strengthened. As the final user and handler of the express package, the consumer should constantly improve the concept of

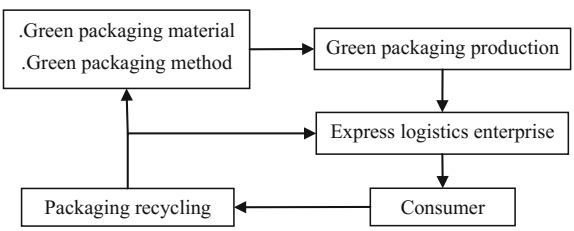

Fig. 2 Green concept in the whole lifecycle of express packaging

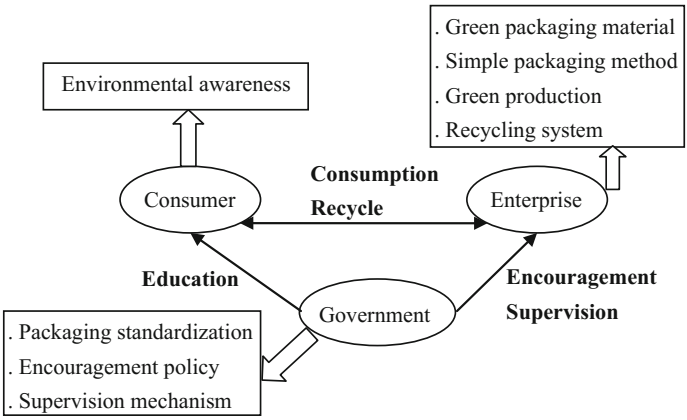

Fig. 3 The sustainable development mode of express packaging

environmental protection, understand the recycling policies of express packaging, be familiar with the recycling channels, handle the different packaging waste based on the classification, and then reduce resource waste and environmental pollution.

(1) **The Government Party**. In the whole mode, the government should play a leading role. On the one hand, it can learn advanced experiences of developed countries to make reasonable policies and regulations. On the other hand, it can promote packaging enterprises to implement the green concept in the development of raw materials and packaging products. Specific measures are as follows.

   a. Improve the laws and regulations related to green express packaging as soon as possible and also strengthen the supervision of enterprises. In addition, some social organizations can also make industry rules to encourage the implementation of green concept in express packaging enterprises.
   b. Make the unified standard on express packaging, involving the basic packaging module, the using of packaging materials and the design of packaging structure, etc., so as to lay the foundation for the effective recovery of express packaging.
   c. Implement the examination and authorization for the green express packaging, and then encourage related enterprises to develop and use the authorized green packaging products by making the reward and punishment mechanism. For example, it can reduce certain taxes for enterprises which meet green standards, otherwise collect certain fines.
   d. Encourage social organizations to establish a professional centralized recycling center and waste classification handling system. Then the express packaging can be returned to different places after the unified recycling, classification, processing or decomposition. It can reduce the resources waste and prolong the lifecycle of express packaging.

(2) **The Enterprise Party**. As the main implementation party of the sustainable development mode, all related enterprises should carry out the green concept from the perspective of supply chain. They should follow the principle of lightweight, recyclable and biodegradable to promote the development of green packaging. Specific measures include the following:

a. Actively develop and use green packaging materials, such as the mushroom, honeycomb packaging materials (see Fig. 4) and other renewable, degradable, even edible materials. This is the basic guarantee for the sustainable development of express packaging.
b. Simplify express packaging and reduce packaging costs. On the premise of meeting the basic function of express packaging, it should minimize the consumption of raw materials as much as possible, promote a concise packaging form, reduce the stages of packaging and printing technology, and then practice the low-carbon concept.
c. Make innovative packaging structure to reduce the consumption of non-degradable packaging materials such as tape. It should use the green packaging structure with the characteristics of rapid shaping and easy disassembly, such as the packaging "YISIDE" and the integrative carton (see Fig. 5).
d. Establish a complete express packaging recycling system. It can carry out the online recovery through the development and application of express packaging recycling APP, so as to achieve the transparency of the recovery chain and improve the recycling efficiency [10]. At the same time, express companies should implement some preferential policies to attract consumers to recycle packaging actively, for example the point redemption system and sending a gift or discount to ones who return packages.
e. Apply the information technology and use the green logo for express packaging (see Fig. 6). For example, it can apply the barcode technology and data management technology to identify the recovery ration, but also can establish a completed recycling logistics business platform to achieve effective recovery of express packaging.

Fig. 4 Mushroom and honeycomb packaging materials

Fig. 5 Innovative design of express packaging

Fig. 6 Green logo of express packaging

(3) **The Consumer Party**. As the key link of effective recovery for express packaging, consumers should raise awareness of environmental protection, understand the recycling information and related channels of express packaging, and then return actively the express packaging to the recycling sites. It is also possible to strengthen environmental publicity through the establishment of spontaneous community recycling points. In addition, consumers should supervise the green process of relevant enterprises, so as to form a good social atmosphere and reduce the environmental pollution of the express packaging.

4 Conclusion

With the development of e-commerce, the business volume of express industry shows a trend of increasing year by year. It also causes a large number of express packaging wastes, which put pressure on social resources and environment. Based

on this situation, the paper mainly analyzed the outstanding problems of express packaging development. Then it built a three-party cooperation sustainable development mode for express packaging, where the government is the leading party, the enterprise is the main party and the consumer is the key party. Then it put forward the corresponding strategies in order to ensure the implementation of green concept in the whole lifecycle of express packaging. In the future, the greenization, intelligent, standardization of express packaging will become urgent problems to be solved. The study will also focus on the establishment of an effective express packaging recycling system.

Acknowledgements This study is funded by a project of National Social Science Foundation of China (No. 16CJL054).

References

1. http://www.chinawuliu.com.cn/zixun/201703/14/319728.shtml. Accessed 20 Mar 2017
2. Gu H (2002) Description of green packaging. Packag Eng 23(5):78–80
3. Xu L, Li M (2016) The embodiment and application of green design concept in packaging design. Packag Eng 18:203–206
4. Williams H (2011) Food packaging for sustainable development. Karlstad University
5. Chen Y (2014) Innovation design on express packaging in the concept of sustainable development. Packag Eng 35(24):10–12, 26
6. Yang Y, Zhang Q, Bo F, Ge D (2011) Discuss on low-carbon operational strategies of express enterprise. Logistics Sci-Tech 08:70–72
7. Gan J, Jiang Y, He Y (2015) Study on the selection of express packaging recycling mode in university campus from the perspective of circular economy. Manager' J 09:219
8. He Q, Huang C, Chang H, Nie L (2013) Progress in recycling of plastic packaging wastes. Adv Mater Res 660:90–96
9. Zhang G, Zhao Z (2010) Green packaging management of logistics enterprises. In: Proceeding of 3rd international conference on power electronics and intelligent transportation system, pp 151–154
10. Yi Z, Zijing L (2016) Application study of express package recycling APP in college students online shopping. Value Eng 06:184–186

Study on the Life Cycle Assessment of Folding Carton

Mengting Li, Guorong Cao, Lizheng Zhang and Yabo Fu

Abstract According to the theory of life cycle assessment, the paper presents a life cycle assessment of folding carton products. It identifies the scope of the study, establishes a life cycle model of folding carton and analyzes the input and output data list of production engineering. The results show that the impact of folding carton production process on the environment mainly comes from the process of offset printing and silk screen and propose an improved method to reduce the pollution to the environment.

Keywords Folding carton · Life cycle assessment (LCA) · Environmental impact

1 Introduction

Folding carton is widely used in product packaging because of its low processing cost, convenient storage and transportation, suitability for various printing methods, easiness of sell and display [1]. In recent years, with the improvement of environmental protection requirements, people pay more attention to the consumption of resources and energy in the carton production, as well as the impact of wastewater, waste gas and solid waste produced by the production process on the environment. The paper takes the production process of a folding carton as the object of study. Its environmental impact was analyzed quantitatively by life cycle assessment (LCA), thus providing a basis for the optimization of folding carton process [2].

M. Li · G. Cao (✉) · L. Zhang · Y. Fu
School of Printing and Packaging Engineering, Beijing Institute of Graphic Communication, Beijing, China
e-mail: caoguorong@bigc.edu.cn

P. Zhao et al. (eds.), *Applied Sciences in Graphic Communication and Packaging*, Lecture Notes in Electrical Engineering 477,
https://doi.org/10.1007/978-981-10-7629-9_57

2 Production Process of Folding Carton

Flow chart of a folding carton production is shown in Fig. 1. The base paper is put into the slitting machine and cut according to certain specifications. Then the finished paper is sent into the offset press to print graphic according to the requirement of the product, and is gilded to become the semi-finished product 1. The semi-finished product 2 is obtained by screen printing, and the semi-finished product 3 is obtained by the second screen printing. The concave and convex mould is used to carry out concave convex processing, so that the plastic deformation of the printed material is produced, and the surface is artistically polished, and the semi-finished product 4 is obtained. The printed board is slotted and impressed by the die-cutting machine. Finally it is packed and stored. The production process of folding carton consumes water, electricity, paper, ink and other auxiliary materials. While the printed product is obtained, waste water, waste gas and solid waste are discharged to the outside environment, including ink, solvent evaporation, waste dampening solution, and leftover material produced in the production process. The input and output factors of these printing systems involve the consumption of resources and energy and the discharge of pollutants and wastes, which lead to differing impacts on the environment.

3 Method of LCA

According to the LCA technical framework established by the IS014040 series standard, the LCA evaluation of the folding carton production process includes the following process: the research scope and objectives are determined, and the system boundaries and functional units are obtained; inventory analysis is implemented, that is, every production process input and output data of the folding carton is quantifiably analyzed to get system list data; impact assessment is conducted, which means that, the list of data is quantifiably evaluated according to characteristics and environmental impact type indicators. Finally, the results are explained and the improvement suggestions are obtained, thus providing the basis for the optimization of the folding carton process.

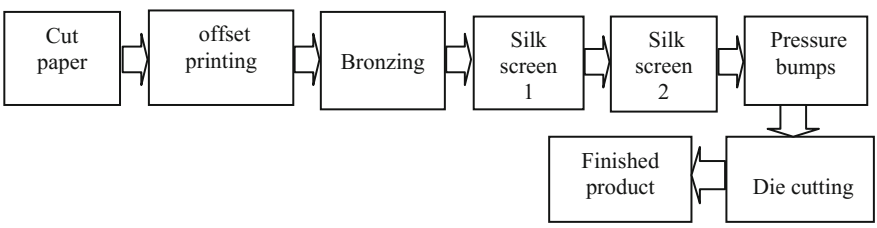

Fig. 1 Flow chart of folding carton production

The research is studied by SimaPro software, which can automatically generate charts and simplify the life cycle assessment process. Besides when the software is used, the input and output data can be quantified and analyzed, the types of environmental impact are compared and analyzed more intuitively. And the evaluation process and results of each link can be expressed in the manner of system flow which is more convenient and quick. SimaPro uses the average data in the European Union ELCD database, which is the basic database of the European Union. The database provides basic data support for the product during the use phase. The EPD evaluation method is used to analyze the data. And EPD is a type III environmental mark specified by ISO14025, which is a third-party verification of product quality and environmental performance double excellent data expression.

4 LCA Evaluation

4.1 Determination of Target and Scope

Through the life cycle evaluation of the folding process of a folding carton of a certain enterprise, the quantitative description of the resources, energy use and environmental discharge of the printed materials in the process of obtaining, printing and recycling of raw materials is carried out and the relevant analysis is used, for the enterprise to provide the scientific basis of product ecological identification and technological improvement. Functional unit is the production of 1000 kg folding cartons. The system boundary is the whole process of producing from the cardboard supply to the finished carton, as shown in Fig. 2. Within the boundaries of the system, most of the waste related parts in the output are recyclable waste materials and the waste materials can be used as raw materials for power generation, so the process of recycling does not take into account the impact of emissions. The waste ink produced in the printing process and the solid particles produced by the manufacturing process of the carton are very small and the composition is uncertain, so the influence is negligible [3]. The use and maintenance are not considered, and the mode of transportation is varied, not considered in detail. The study assumes that the mode of transportation is road transport, and the geographic scope of the study is confined to china. In the study, the process data of folding carton production and processing are obtained through a practical investigation of an enterprise.

4.2 List Analysis and Impact Assessment

According to the investigation of the actual production data of a folding carton enterprise, the data list of input (material consumption and energy consumption) in

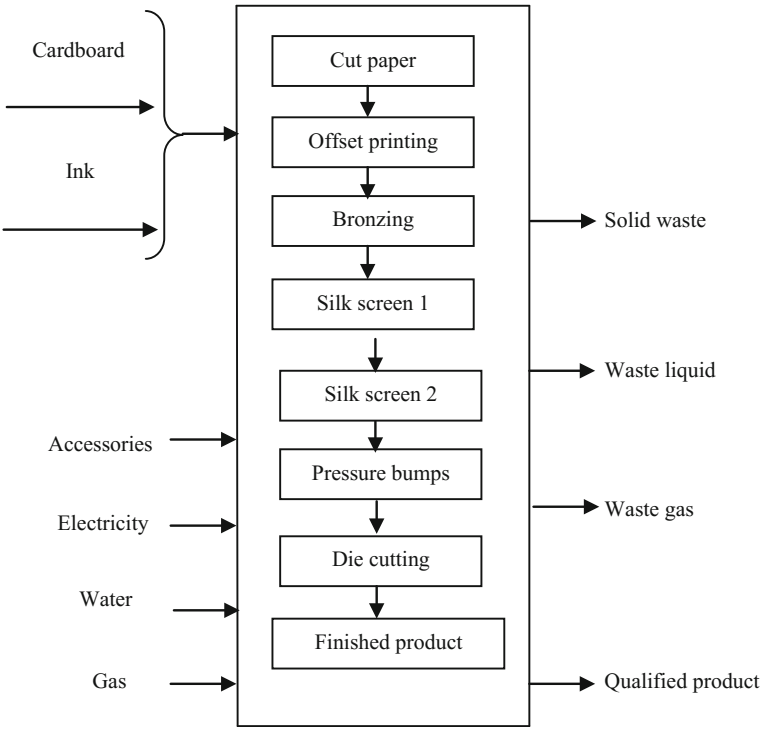

Fig. 2 System boundary of life cycle assessment of folding carton

each function unit folding carton production process is shown in Table 1, and the data list of output in each function unit folding carton production process is shown in Table 2.

For the more obvious effect of the inventory analysis, the process is analyzed without the substrate and ink. There are results as shown in Figs. 3, 4, and 5.

4.3 Results and Analysis

The results of the inventory analysis and impact assessment show that the main environmental impacts of the process flow in the folding carton production process are fossil energy consumption, acidification, eutrophication and global warming. The consumption of fossil fuels is due to the consumption of coal and electricity in the process of carton production. Acidification and global warming are mainly due to the consumption of electricity, heat energy and the emission of harmful gases in the carton production process. The emissions of these harmful gases aggravate the global greenhouse effect, and more importantly, they affect people's health. The

Table 1 Inventory of inputs for 1000 kg folding carton production

Category	Name	Quantity (kg)	Technology	Quantity (kg)
	Cardboard	955.66		
	Ink	44.34		
	Ethanol	3.67		
Raw material	PE protective film	1.80		
	Ethyl acetate	0.52		
			Offset printing	533.71
	Water	2203.58	Silk screen	1214.39
			Pressure bumps	455.48
			Cut paper	4.75
Energy	Electricity (kWh kg^{-1})	20.25	Offset printing	8.39
			Silk screen	4.59
			Finished product	5.74

Table 2 Inventory of outputs for 1000 kg folding carton production

Name	Quantity (kg)	Technology	Quantity (kg)
		Cut paper	34.10
Solid waste	50.90	Bronzing	11.71
		Silk screen	2.80
Corner of the remaining material	28.54	Cut paper	23.54
Waste cloth	3.98	Cut paper	3.34

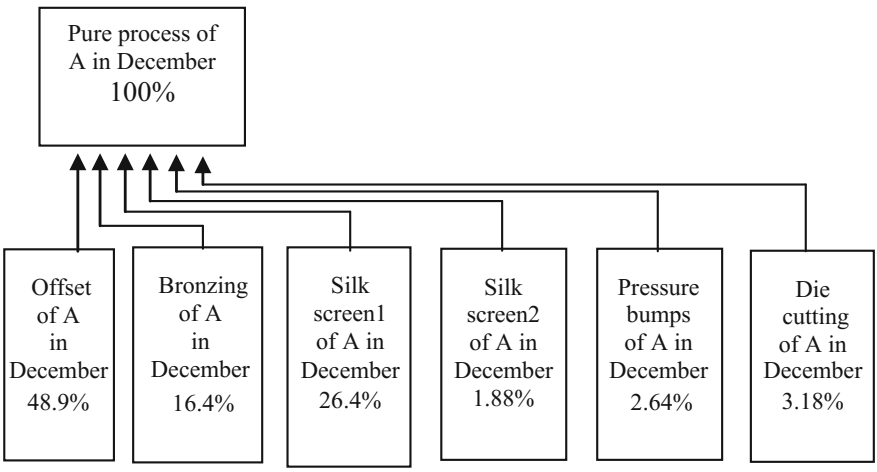

Fig. 3 Mesh structure of flow chart of folding carton production

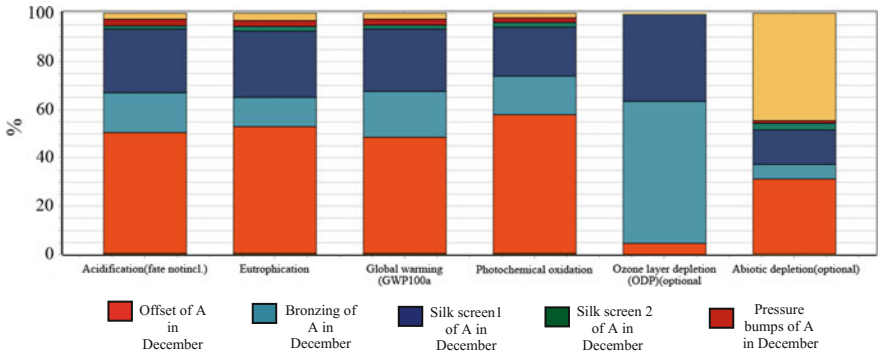

Fig. 4 Impact assessment characterization of flow chart of folding carton production

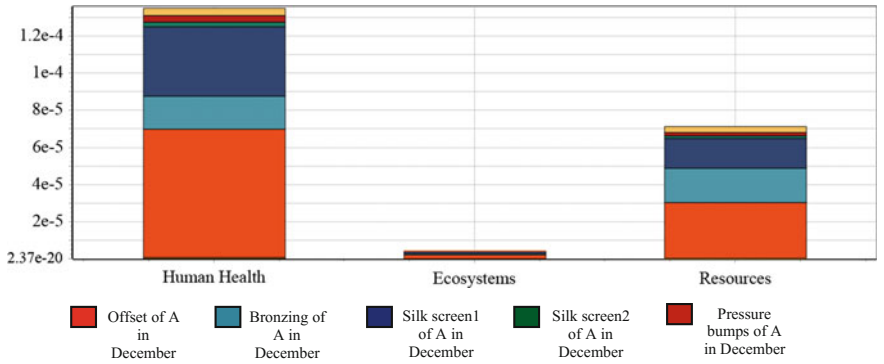

Fig. 5 Standardization of impact assessment of flow chart of folding carton production

reason for the eutrophication is that a large amount of cleaning water is needed to clean the printing press during the process of offset printing and silk screen printing, and the cleaning water with ink is discharged without treatment, resulting in the eutrophication of the water.

In the production process of folding cartons, offset printing accounts for the largest proportion of the entire processing technology, about 48.9%, so the impact of offset printing on the environment is also the largest, followed by silk-screen printing and bronzing. The environmental impact of offset printing and screen printing is mainly acidification, eutrophication, global warming. In the offset printing process, some harmful gases are emitted, such as carbon oxides, sulfides and aldehydes, which cause acidification and global warming. Ink on the printing press needs to be regularly cleaned, so waste water contains pigments, resins and ethanol. And then the waste water is discharged and results in eutrophication. Bronzing process causes more serious damage to the ozone layer, mainly due to that the etching produces fluoride, hydrogen chloride and nitrogen oxides. And these

gases are discharged into the atmosphere, which results in the destruction of the ozone layer. Die cutting technology consumes more fossil energy, followed by offset printing and screen printing, because they consume a lot of electricity.

4.4 Suggestions for Improvement

It is should be that the printing ink used for offset printing and screen printing is improved. Using some more environmentally friendly ink could reduce the generation of harmful gases, so as to reduce the pollution of environment and the harm to the human health. The water which is used to clean the ink tank and ink roller should discharge after treatment and the number of cleaning should be reduced appropriately. And then the waste water emissions and pollution of water can be reduced. Using the new electric heating system not only improves the quality of bronzing, but also enhances the work efficiency. Besides, It improves the operating environment, eliminates the risk of high temperature thermal oil leakage and reduces the pollution of environment [4].

In the analysis of the three major effects of folding carton production process on human health, ecological system and natural environment, the impact on human health is the most serious. For example, aldehydes pollutants not only pollute the atmosphere, but also do great harm to human health. So it is necessary to take reasonable consideration of gas recovery and emission control. In the process of production and processing, workers need to take some protective measures, such as wearing gas masks and dealing with pollution sources timely, and pay attention to personal safety and health.

5 Conclusions

According to life cycle assessment theory (LCA), the life cycle assessment of folding carton products in an enterprise is carried out. And the input and output data list of the production process is analyzed. Then the environmental impact types of folding carton production and the quantitative indexes of environmental impact are obtained, among which the printing process has the largest impact on the environment. Based on the analysis of the causes of environmental impact, some suggestions for improving the production process of folding carton are put forward, so as to optimize the production process and reduce environmental pollution. Because of the insufficiency of relevant basic data in our country, the average data in JEMAI-LCA Pro database is adopted in the analysis and calculation of this research, which has certain influence on the accuracy of the numerical results.

Acknowledgements The authors gratefully thank the support from the teaching engineering team (construction) (22150116006/017) and the printing and packaging research project of cultivating innovative talents in (22150116007/055) Beijing-Tianjin-Hebei universities. We are here with best thanks.

References

1. Hong Y (2003) Application of gam technology in post-processing of carton. Printing World 49–50
2. Ren X, Huo L (2010) Case study on life cycle assessment of corrugated box production. Packag Eng 31(5):54–57
3. Liu J, Yang Q, Han X (2008) Study on environmental impact assessment of corrugated box life cycle. Environ Sci Res 21(6):105–109
4. Guo S, Liu B, Gao H (2005) Technical improvement and application of new bronzing rolling plate. China New Technol Prod 54–54

Study on the Cushion Performance of the Cushion Material Composed of EPE and Corrugated Paperboard

Xiaoli Song, Gaimei Zhang, Jiandong Lu, Lizheng Zhang and Shuo Zhang

Abstract This paper analyzes the static compression performance of the cushion material which is composed of EPE and corrugated paperboard. The cushion coefficient and the stress-strain curve are investigated under different thickness of EPE and different corrugated paperboard. The results show that the static cushion coefficient is not proportional to the strain with the increased height of corrugated paperboard. When $\varepsilon < 58\%$, the static cushion coefficient of the cushion material which is composed of A corrugated paperboard and EPE is smaller. The cushion performance is better than the one composed of AB corrugated paperboard and EPE. When $\varepsilon \geq 58\%$, the static cushion coefficient of the cushion material which is composed of AB corrugated paperboard and EPE is smallest. And the static cushion performance is best. With the increase in EPE thickness, the static cushion coefficient is not proportional to the thickness. The increase in thickness does not necessarily improve the cushion performance of the cushion material.

Keywords Cushion material · EPE · Corrugated paperboard

1 Introduction

During the process of transportation and handling, the packaging products will inevitably suffer from mechanical shock, vibration and other impacts. If the packaging is not good enough, it is easy to cause damage to the product and cause huge economic losses to businesses. The cushion material can absorb the energy generated by the impact, so it can effectively protect the goods to avoid the damage [1–3]. Therefore, the cushion material is widely used in today's packaging. At present, EPE (Expandable Polyethylene), EPS (Expanded Polystyrene), corrugated paperboard, honeycomb board and other cushion materials are widely used in packaging. However, the cushion mechanism and performance of different cushion

X. Song (✉) · G. Zhang · J. Lu · L. Zhang · S. Zhang
School of Printing and Packaging Engineering, Beijing Institute of Graphic Communication, Beijing, China
e-mail: songxiao109@163.com

P. Zhao et al. (eds.), *Applied Sciences in Graphic Communication and Packaging*, Lecture Notes in Electrical Engineering 477,
https://doi.org/10.1007/978-981-10-7629-9_58

materials are different. For example, the cushion performance of honeycomb paperboard is mainly reflected in the compression failure stage of honeycomb core structure, that is, the elastic-plastic stage and plastic collapse stage. At this stage, the yield platform is long, the cushion coefficient is small, and the impact energy is very absorbent. EPE is the high foam product produced by extrusion of LDPE as the main raw material. So the quality of EPE is very small and the elasticity of EPE is high. And EPE has very good absorbability under the small load. EPE is more suitable for anti-vibration materials. Corrugated paperboard has good cushion performance under slight load. But it is difficult to predict what kind of the impact or vibration will be in the transportation and handling. Cushion interval of single material is always limited [4–7]. Therefore, to better apply the cushion material, constantly promote and improve the design of cushion packaging, reduce the economic losses caused by vibration, shock and other impacts through the process of mobilization, this paper mainly tests the stress-strain of the cushion material composed of EPE and corrugated paperboard, draws the static cushion coefficient-strain curve and analyzes the influence of the thickness of corrugated paperboard and EPE on the cushion performance of the cushion material.

2 Experiment

2.1 Sample

The density of EPE is 18.869 kg/m^3. The size of EPE is 100 mm × 100 mm and the thickness is 20, 30, 40 and 50 mm. A, E and AB corrugated paperboard are taken respectively. The density of AB corrugated paperboard's face paper and inside paper is 220 g/m^2. The density of core paper is 170 g/m^2. The size of AB corrugated paperboard is 100 mm × 100 mm × 7.4 mm. The density of A and E corrugated paperboard's face paper is 220 g/m^2, and the density of core paper is 150 g/m^2. The sizes of A and E corrugated paperboard are 100 mm × 100 mm 4.7 mm and 100 mm × 100 mm × 3 mm. All the experimental samples were pretreated according to GB4857.2. The environmental conditions are as follows: temperature in 23 °C, relative humidity of 55%, and treated for more than 24 h.

2.2 Equipment

Microcomputer control electronic universal testing machine is used.

2.3 Method

(1) EPE and corrugated cardboard are combined in a certain form, which is shown in Fig. 1.

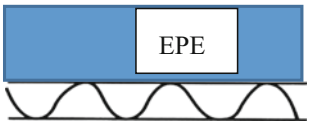

Fig. 1 The combination picture of EPE and corrugated paperboard

(2) The static compression test was based on GB/T 8168-2008 Static Compression Test Method for Packaging Buffer Material [8]. The compression speed of 12 mm/min is used. Finally, the stress-strain curve is recorded.
(3) Applying the data to calculate the static cushion coefficient, draw the static buffer coefficient-strain curve.

3 Results and Analysis

3.1 Static Compression Performance of EPE with Thickness of 40 mm

Test the static compression performance of EPE with thickness of 40 mm and obtain the stress-strain curve of EPE, which is shown in Fig. 2.

It can be discovered from Fig. 2 that in the compression process, EPE is mainly divided into linear elastic stage, yield stage and dense stage. When $\varepsilon \leq 6.520\%$, EPE is in the linear elastic phase, which mainly absorb energy by the elastic deformation of the material, and the energy absorbed occupies only a small part of the total. At this stage, its cushion performance is limited. When $6.520\% < \varepsilon$ 29.520%, EPE is in the yield stage, which is the most important stage of energy absorption, and the energy absorbed occupies for most of the total energy absorption. When the material is just compressed to the end of the platform area, the maximum dynamic strain is the corresponding strain at the end of the platform area.

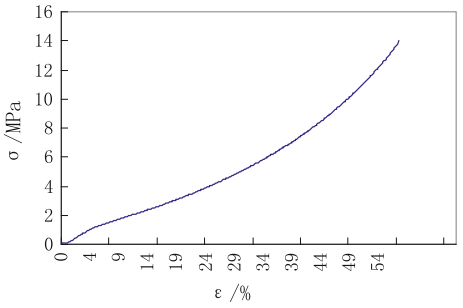

Fig. 2 The stress-strain curve of EPE with thickness of 40 mm

Table 1 The table of stress, strain value and strain increment

Strain ε (cm/cm)	Strain increment Δε (cm/cm)	Stress σ (N/cm^2)	Stress increment Δσ (N/cm^2)	Energy increment ΔE (N cm cm^3)	Energy E (N cm cm^3)	Cushion coefficient C
0.200	0.100	3.194	3.104	0.252	0.348	9.173
0.300	0.100	4.940	1.746	0.407	0.755	6.544
0.400	0.100	7.225	2.286	0.608	1.363	5.301
0.500	0.100	10.375	3.150	0.880	2.243	4.626
0.520	0.020	11.156	0.781	0.215	2.458	4.538
0.540	0.020	12.002	0.846	0.232	2.690	4.462
0.550	0.010	12.450	0.448	0.122	2.812	4.427
0.560	0.010	12.920	0.470	0.127	2.939	4.396
0.570	0.01	13.409	0.490	0.132	3.071	4.367
0.577	0.007	13.746	0.336	0.090	3.160	4.349
0.580	0.003	13.990	0.245	0.044	3.205	4.365

When most of the cell body is yield damage, the material enters into the dense area. In the compression process, the greater the internal damage to the material, the higher the utilization rate of it, and the more energy absorbed, with better cushion performance.

According to the measured data, calculate the cushion coefficient C, including the following procedures: ① measure and record the strain ε and incremental Δε; ② measure and record the strain σ and its incremental Δσ; ③ calculate the deformation energy increment ΔE and its cumulative value E in each pressure section; ④ calculate the ratio σ/E, which is the cushion coefficient C, where the energy increment ΔE is equal to each strain increment Δε, with the integral area under the curve; the energy increment can be calculated by Eq. (1) [9, 10].

$$\Delta En = \frac{\Delta\varepsilon \cdot \Delta\sigma + \Delta\varepsilon \cdot \sigma n - 1}{2} \tag{1}$$

According to the calculation results, as shown in Table 1, take C as the ordinate, ε as the abscissa, draw EPE static cushion coefficient-strain (C-ε) curve, as shown in Fig. 3.

It can be discovered from Fig. 3 and Table 1 that when ε = 57.680%, the static cushion coefficient is the smallest, indicating that the cushion material absorbs the most energy and has the best cushioning properties.

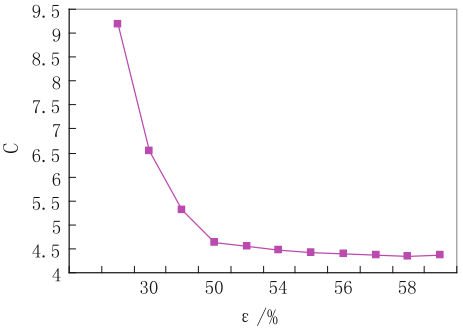

Fig. 3 The static cushion coefficient-strain curve of EPE with thickness of 40 mm

3.2 *The Impact of the Type of Corrugated Paperboard on the Buffer Performance*

The thickness of EPE is 40 mm, but the type of corrugated paperboard take respectively A, E and AB in this experiment. Finally the stress-strain curves are gained, which are shown in Fig. 4.

It can be discovered from Fig. 4 that compression process is divided into viscoelastic stage, yield stage, collapse stage and dense stage. In viscoelastic stage and yield stage, the three curves are basically overlap, indicating that EPE plays a major role in this stage. As the experiment continues, the energy is gradually passed to the corrugated paperboard. The sharp decline of strain appears in the curve, indicating that when the corrugated paperboard was crushed, it entered into the plastic collapse stage. With the corrugated paperboard crushed, the pressure will rise sharply, and the cushion material went into the dense stage. However, AB corrugated paperboard have the sharp decline in pressure for two times in the compression process. The first strain drop is greater than the second drop, indicating that the first crush is A and the second crushed is B.

According to the test results, calculate the buffer coefficient (C), take C as the ordinate, ε as the abscissa, and draw the static buffer coefficient-strain (C-ε) curve, as shown in Fig. 5.

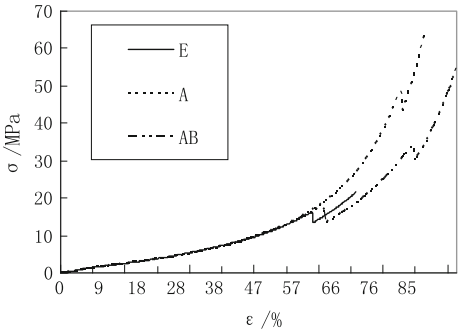

Fig. 4 The stress-strain curve of the cushion material composed of EPE with thickness of 40 mm and different type of corrugated paperboard

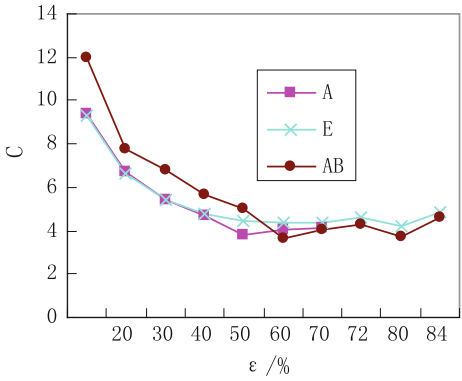

Fig. 5 The stress-strain curve of the cushion material composed of EPE with thickness of 40 mm and corrugated paperboard

It can be discovered from Fig. 5 that when $\varepsilon \leq 40.4\%$, the curve of the cushion material composed of A corrugated paperboard and EPE overlaps with the one composed of E corrugated paperboard and EPE. The cushion coefficient is the smallest, indicating its absorption is more. The cushion coefficient and the cushion performance of the cushion material composed of A Corrugated cardboard and EPE is smaller than that composed of A corrugated paperboard and EPE; when ε 58%, the cushion material composed of AB corrugated paperboard and EPE has the smallest cushion coefficient and the best cushion performance.

3.3 Impact of EPE's Thickness on the Cushion Performance

AB corrugated paperboard is chosen in this experiment, EPE with thicknesses of 20, 30, 40 and 50 mm are selected. Finally the stress-strain curves are gained, which are shown in Fig. 6.

It can be discovered from Fig. 6 that the first occurrence of plastic collapse stage of corrugated paperboard are basically in about 55% of its deformation, the second occurrence are basically in about 75% of its deformation, therefore the thickness of EPE does not have much impact on the plastic collapse stage.

According to the stress and strain data, calculate the cushion coefficient C, and draw the static cushion coefficient-strain curve, as shown in Fig. 7.

It can be indicated from Fig. 7 that the cushion performance of the cushion material is not directly proportional to the thickness of EPE. When $\varepsilon \leq 50.070\%$ and the thicknesses of EPE are 20, 30 and 50 mm, the curves are almost overlapped. The three structures have small cushion coefficient, better cushion performance, which are better than the cushion material composed of EPE with thickness of 40 mm and AB corrugated paperboard; when $50.070\% < \varepsilon \leq 64.430\%$, the cushion material composed of 20 mm and AB corrugated paperboard has the smallest cushion coefficient and the best cushion performance. When

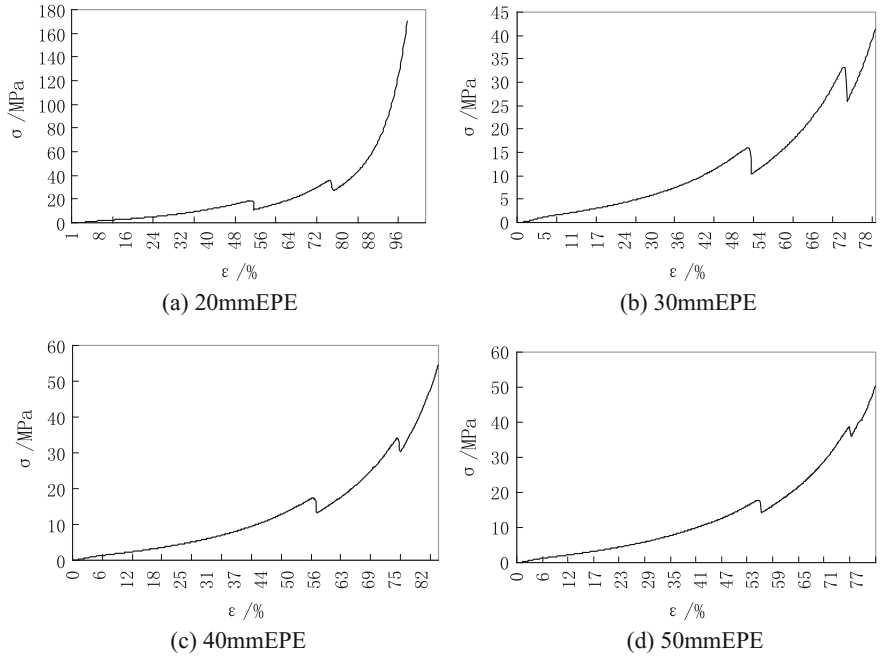

Fig. 6 The stress-strain curve of different thickness of the cushion material composed of EPE and AB corrugated paperboard

Fig. 7 The stress-strain curve of different thickness of the cushion material composed of EPE and AB corrugated paperboard

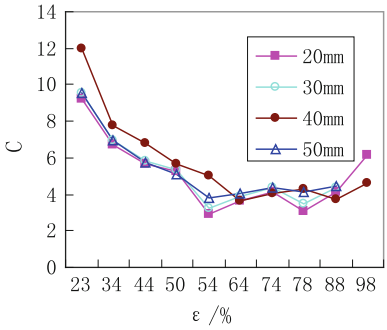

64.43% < ε ≤ 74.400% and the thicknesses of EPE are 20 and 40 mm, the curves are overlapped. They have the smallest cushion coefficient and the best cushion performance. When 74.400% < ε < 88.030%, the cushion material composed of EPE with thickness of 20 mm and AB corrugated paperboard has the best cushion performance and the smallest cushion coefficient; when ε ≥ 88.03%, the cushion material composed of 40 mm and AB corrugated paperboard has the best cushion performance and the smallest coefficient.

4 Conclusions

Comparing the results, the conclusion can be obtained:

(1) The static cushion coefficient is not proportional to the strain with the increased height of corrugated paperboard. When $\varepsilon < 58\%$, the cushion material composed of A corrugated paperboard and EPE has the smaller cushion coefficient and its cushion performance is better than the one composed of AB corrugated paperboard and EPE. When $\varepsilon \geq 58\%$, the static cushion coefficient of the cushion material which is composed of AB corrugated paperboard and EPE is smallest. And the static cushion performance is best.
(2) With the increase in EPE thickness, the static cushion coefficient is not proportional to the thickness. The increase in thickness does not necessarily improve the cushion performance of the cushion material.

Acknowledgements The project is supported by the general research projects of Beijing Institute of Graphic Communication (Eb201701), the National Natural Science Foundation of China (51305038) and Bei Yin talent selection and development project of Beijing Institute of Graphics Communication (Byyc201316-016).

References

1. Liu Y, Zhang Y (2011) Dropping simulation and design improvement of a washing machine based on fe analysis. J Vib Shock 30(2):164–166
2. Song T, Liu Y, Zhu R (2006) Structure optimization design of cushion packaging based on dynamic property test and orthogonal design. Packag Eng 27(5):56–63
3. Zhang G, Wu J, Guo F (2011) Drop analysis of pop can based on ANSYS/LS-DYNA. Packag Eng 32(5):4–5
4. Liu J (2014) Analysis method and research progress in cushioning performance of cushion. Packag Eng 35(7):149–155
5. Li-juan W, Jiang S (2006) Dynamic compression buffer performance of three kinds of common cushioning materials. China Water Transp 6(11):62–64
6. Fang T (2013) Study on cushioning properties of cushioning packaging materials. Tianjin University of Science and Technology, Tianjin
7. Zheng H, Wu J, Cao G (2008) Analysis of impact energy absorption and vibration transfer rate of polyethylene foam plastics. Packag Eng 29(3):30–32
8. GB/T 8168-2008, Static Compression for Package Cushioning Materials Experiment Method
9. Peng G (2006) Logistics and transport packaging design. Printing Industry Press, Beijing, 1–64
10. Zhang G (2001) Study on the buffering property of the honeycomb board. Packag Eng 22 (5):7–9

Study on Damage Analysis and Random Vibration Detection of Transportation Goods

Hanyue Zhang and Xueqiong Feng

Abstract In the process of the actual product transportation, the enterprise usually to improve the vehicle turnover efficiency through the goods stacking form, reduce business costs. But because of the complexity of transport packaging system stacking itself, so that in the transportation process often falls, damage and even destroyed, resulting in unnecessary losses. In view of this, the paper based on the transport packaging dynamics as the starting point, first analyzes the typical factors influencing the dynamic characteristics of multilayer transport packages, and choose the stacking height and road roughness as the focus of the later analysis and the research object, focuses on the influence of random vibration on the safety of the goods and give the optimization scheme. Secondly, this paper introduces the virtual prototyping technology in the engineering field, through the simulation of ADAMS software to different stack height and road surface under the action of dynamic response characteristics, through the analysis of each layer of the transport package of each kind of vibration acceleration response curve under the experimental conditions, and obtains the influence law of pile dynamic code height and pavement roughness.

Keywords Transportation · Stacking · Random vibration · Dynamics ADAMS

1 Introduction

In recent years, with the rapid development of e-commerce in China, the modern logistics industry is booming. A large increase in the transport of goods in the economic interests of the stimulus, in order to improve transport efficiency, reduce business costs, in the transit of goods stacking method is usually used to store goods. This method can improve the transportation efficiency and improve the

H. Zhang · X. Feng (✉)
Tianjin University of Science and Technology, Tianjin, China
e-mail: 2352616969@qq.com

P. Zhao et al. (eds.), *Applied Sciences in Graphic Communication and Packaging*, Lecture Notes in Electrical Engineering 477,
https://doi.org/10.1007/978-981-10-7629-9_59

quality of service to a certain extent. But it must be noted that the stacking and transportation layers have great influence on the overall performance of the transport package, in the transport process caused a lot of goods falling, damaged or even destroyed, resulting in unnecessary losses. Therefore, the study on random vibration of cargo stacking during its transport is very important, to improve the problems caused by the damaged goods in transit through the research.

As early as the middle of twentieth Century, foreign countries began to study the dynamic characteristics of transportation packaging system. Lee et al. [1] using the finite element software ANSYS to simulate the impact and vibration of the package in the actual engineering, and finally obtained the peak acceleration of the product. Bernad et al. [2] studied the transport multilayer stacking package's deformation characteristics in the external mechanical excitation. Then he found the dynamics of the transport package is influenced by two factors, namely, external excitation and system characteristics. Some achievements have been made in this field in China. Du [3] focuses on the analysis of the effect of stacking height, stacking sequence, road excitation and packaging material factors on the transport package dynamics, obtained certain dynamics response law. Wang [4] applied dynamic analysis method to analyze the forced vibration mode and law of two degree of freedom system, and deduced the acceleration state response equation generated on the inner and outer package. At the same time, the use of software for simulation analysis of vehicle dynamics has been widely used in various fields of research, [5–7].

2 Analysis on the Main Factors Influencing the Dynamic Characteristics of Goods Stacking

At present, the research on the mechanical properties of stacking cargo mainly concentrates on both static and dynamic aspects. Static analysis is a variety of mechanical characteristics of stacking goods showing in the static state, such as goods force, material creep properties, compressive degree of goods. The dynamic analysis is to study the dynamic response characteristics such as displacement, velocity, acceleration and so on in the process of the complex movement of goods, such as cargo lifting, transportation and distribution [2]. Therefore, this paper analyzes the dynamic characteristics of freight transportation.

2.1 Temperature and Humidity Factors

In the course of transportation, the closed box after a long time of light, friction, and many other factors often occur in the outsourcing parts, internal buffer material or commodity surface temperature and humidity changes [8]. When the temperature and humidity changes, the whole packaging system on its own material, more or

less has some physical or chemical changes, which changes its original performance. Such as rubber and plastics in low temperature brittleness increases, in vibration and impact is easy to damage; some metals and paper products, because it is easy to absorb moisture in the air, and with the chemical reaction, accelerated corrosion, aging or deformation.

2.2 Light Factors

The impact of light on the transport of goods is mainly reflected in the infrared and ultraviolet. The infrared ray can cause the carrier and the package to produce the thermal effect, rising the object temperature, speeding up its physical and the chemical change, thus affecting the goods package to its protection function. The ultraviolet radiation on the object will produce a stronger blessing, especially for the materials with the most sensitive wavelengths, such as cartons, plastics, rubber, UV will accelerate the aging and corrosion of these substances.

2.3 Stress Factors

In the course of transportation, the goods will be subjected to external pressure due to shock and vibration. But the package has the maximum capacity of its own. When the external pressure is greater than the maximum force, the package will make its original deformation protection ability decreasing or even lost, resulting in damage to the goods. Generally speaking, the pressure of transport package includes two kinds of static pressure and dynamic pressure.

2.3.1 Static Pressure

Stacking in the carriage of goods, goods of goods by the upper lower pressure, this pressure is the static pressure, including deformation and creep. The static pressure is equal to the total weight of all cargo on the upper deck. So the bottom of the cargo by the static pressure is the largest. The static pressure at the bottom of the cargo can be calculated by the formula (1).

$$P = k\frac{H - \mathrm{h}}{h}W \tag{1}$$

P represents the lowest packing pressure (kg). H represents the stacking height (cm). h represents the height of the bottom package (cm). W represents the quality of the underlying package (cm). k represents the stacking environment degradation coefficient.

Therefore, the static strength of transport of goods is in line with the standard, the stacking height factors must be considered. In general, the height of the warehouse stack is 3–4 m, automobile transportation during the stacking height of not more than 2.5 m, the train stacking is not more than 3 m, ocean liner warehouse stacking is not more than 7 m [9].

2.3.2 Dynamic Pressure

Dynamic pressure refers to the pressure deformation in the external force of goods during transportation, for example, formed by the upper air collision force and extrusion pressure to force the floor [10]. In fact, the damage caused by dynamic pressure is far greater than the static pressure. Therefore, the bottom of the cargo is not only the largest static pressure, but also bear greater pressure.

2.4 Vibration and Shock

2.4.1 Vibration

The reason why the goods are subjected to actual transportation is complex, in large part because of the mechanical load given by the outside world. The excitation of the road roughness, the vibration of the vehicle itself and the impact of the vibration and impact of the goods on the goods are particularly prominent. According to the relevant information, when the vehicle at the speed of 30 km/h through the 6 cm pavement protrusions, acceleration can reach 12.9–24.1 km/h. In the domestic three grade road, the random vibration acceleration is 5–10 g, the maximum can reach 35 g [11].

Brittleness is defined as the maximum acceleration of a product that cannot be sustained by physical or functional damage, usually expressed as a multiple of the

Table 1 Japan's "industrial packaging technical data" recommended crisp value

Brittleness (g)	Product type
<10	Large electronic computers, large transformers
10–20	Precision measuring instrument, electronic copying machine
21–40	Large electronic tube, precision display, camera
41–60	Large recorder, color TV set, clock
61–90	Camera, sound device, radio recorder, desktop computer, thermos bottle, glass bottle, egg
91–120	Typewriter, refrigerator, radio, beer bottle
>120	Ceramic ware, mechanical product, calculator

acceleration of gravity *g*. Table 1 is recommended by Japan's *industrial packaging technical data* product fragility. It is best to take the lower limit.

2.4.2 Impact

The car in the process of transportation through the bulge on the road, or due to start, speed, steering, braking, can make the vehicle speed mutation. So it is inevitable to make the goods and cars or adjacent cargo collision. If loose goods stacking, and even cause the goods fall so that the goods or packages damaged by shock. The impact will cause the body to bear a large external force in a moment, resulting in considerable acceleration. The magnitude of the impact acceleration is mainly related to the driving speed, the weight of the goods, the road conditions, the load and the fixed mode.

To sum up, there are many factors that cause the damage of the goods in transit, but the analysis is mainly about the influence of the pressure and the vibration and impact on the safety of the goods [12]. The main factors that influence the pressure acting on the goods is the goods of the stacking height and vehicle; vibration and shock is mainly affected by factors such as mutation acceleration and velocity of the vehicle, and the vehicle road is a certain relationship [13]. Therefore, in this article, the types of goods of different stacking height and road freight are the research key point for studying transport safety.

3 Modeling

Many experts and scholars establish the existing transport packaging system model by using MATLAB, ADAMS, ANSYS and other software. The simulation results show that the vibration response value and acceleration of the stacked goods are obtained by simulation test, and the dynamic law of the multilayer stacker is summarized. Using this method to study is more efficient, fast and convenient to analysis the kinetics of transport packaging stacking in goods in circulation. So as to provide a more general analytical method and model are for researchers in related fields. We use the ADAMS software to establish the truck and road model, simulation of different stacking height and different road excitation, which used to analyze the dynamics characteristics of the goods, in order to improve the safety of transport of goods.

3.1 Introduction to ADAMS Software

ADAMS (Automatic Dynamic Analysis of Mechanical System), is a virtual prototyping analysis software developed by MDI company. The complete set of

analysis tools enable engineers to build a mechanical system "virtual prototyping", analyzing its performance, a better understanding of the mechanical system motion; comparing various design schemes, accurately predicting of the variation of the load, calculating the trajectory, velocity and acceleration etc. [14].

3.2 Vehicle Modeling

Select the ADAMS/Car module [15], the establishment of the vehicle model, as shown in Fig. 1.

3.3 Road Modeling

Considering that this study is the safety of transport vehicles in different road conditions of the goods, in order to improve the efficiency and accuracy of the simulation, it focuses on some characteristics of potentially dangerous road simulation [1]. In this paper, the characteristics of the road simulation scene mainly have the following three.

3.3.1 Barrier Road

There may be a large obstacle in the road. The simulation scene is shown in Fig. 2.

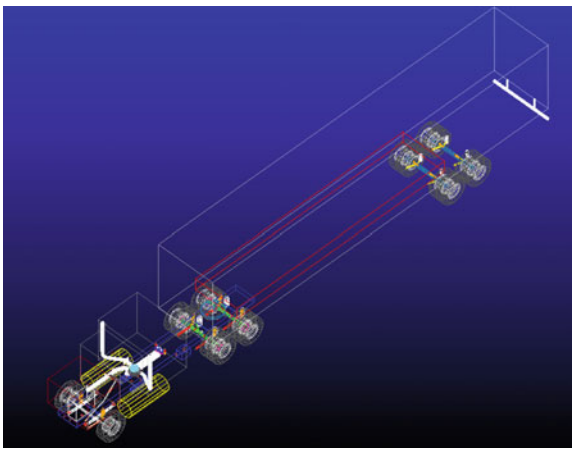

Fig. 1 Truck model

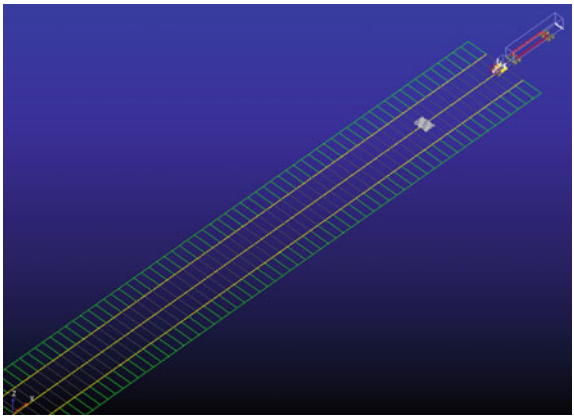

Fig. 2 Obstacle roads

3.3.2 Up and Down Road

The upper and lower slope of the road will have an impact on the vehicle. The simulation scene is shown in Fig. 3.

3.3.3 Uneven Road

Due to the use of the highway or the maintenance of the reasons for the uneven road surface will often occur, as shown in Fig. 4.

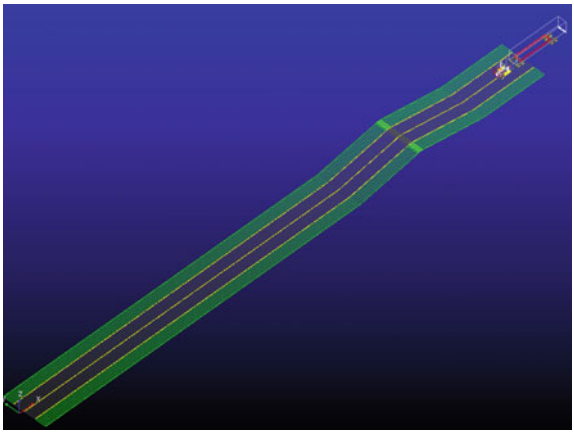

Fig. 3 Up and down road

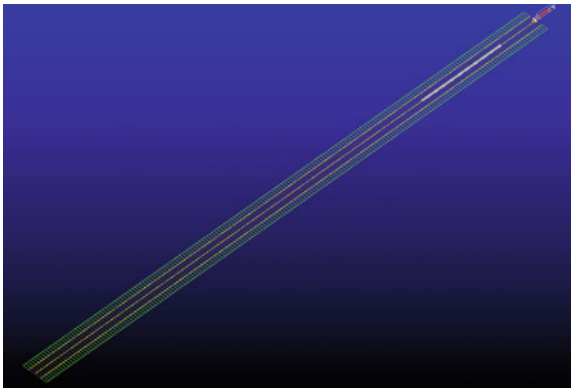

Fig. 4 Uneven road

3.4 Cargo Stacking Modeling

Considering the extremely complex dynamics of the stacking of goods, the following assumptions are made on the modeling of the stacked goods:

(1) Ignore the specific shape and volume of each package (outer packing material, inner material, buffer material), which will be regarded as a cuboid of equal volume;
(2) Each cargo stacking are regarded as rigid body, not considering the deformation characteristics;
(3) The transport of goods is only affected by the vertical force, regardless of any other direction of force and torque;
(4) The external mechanical excitation at the bottom of the freight train is the vertical force at the bottom of the rear compartment.

To wine (4 bottles/box, weigh about 2 kg) for example, after calculation, covered with a layer of the car is about 144 boxes, weighing about 300 kg, about 40 cm high, and so on. Use ADAMS as an example to establish cuboid model.

4 Simulations

4.1 Simulation Study on Dynamic Characteristics of Different Road Freight

The simulation is based on the case of the vehicle loading a layer of goods, respectively, with the speed of 60 km/h, through different roads, to measure the vibration acceleration of goods. As shown in Figs. 5, 6 and 7, respectively, the vibration acceleration (g) of vehicle through the barrier Road, the up and down road and the uneven road.

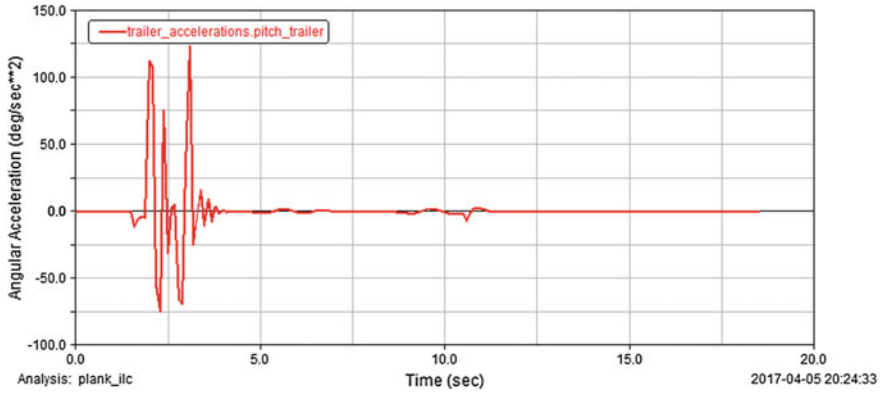

Fig. 5 Obstacle road acceleration

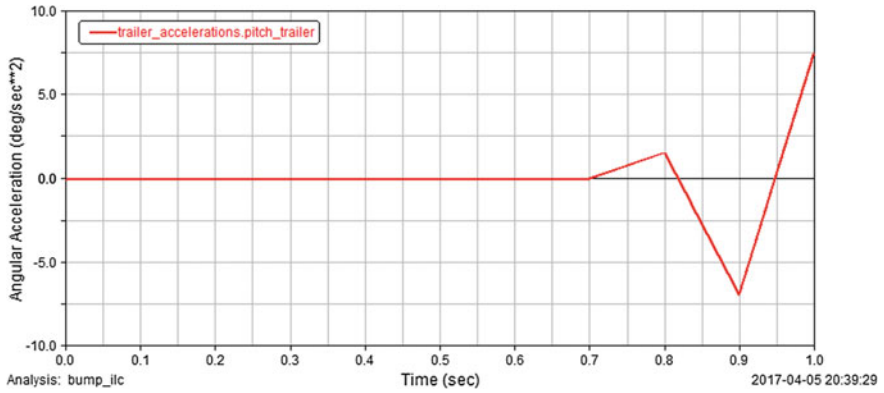

Fig. 6 Up and down road acceleration

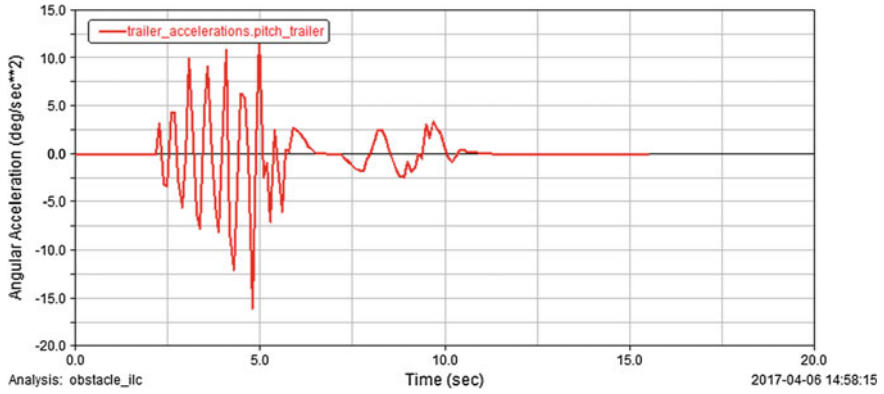

Fig. 7 Uneven road acceleration

It can be seen from the figure that the vibration acceleration of the vehicle is up to 10 g when the road is up and down road and obstacle road, in line with the safe transport of goods. Only through the obstacles road, vibration acceleration unexpectedly reached the highest 120 g. From Table 1 known, a lot of goods to be damaged, this situation is to avoid. So the analysis shows that the road is relatively large obstacles to the most serious damage to the goods. If there is no special protection in the case of vehicle transport, be sure to avoid driving on large obstructions.

4.2 *Different Stacking Height of Goods Dynamics Simulation Research of Pressure*

This simulation is based on a vehicle traveling at a 60 km/h speed on a normal B grade road surface (surface friction coefficient for dry pavement friction coefficient 0.6), the vibration acceleration of the cargo measured in the case of one layer, two layers and three layers respectively. As shown in Figs. 8, 9 and 10, respectively, the vehicle is loaded in a layer (40 cm high), two layers (80 cm high) and three layers of goods under the measured vibration acceleration (g).

It can be seen from the figure, when the number of stacking layers is one layer and two layers, the vibration acceleration is not obvious, the maximum for about 30 g. From Table 1 shows some measuring instruments, precision electronic instrument fragility reaching this value, most of the goods are in a safe range. But when the goods stacking layer is three, the maximum vibration acceleration reaching 100 g, most of the goods are damaged in this case. Therefore, some fragile goods in the absence of special protection under the stacking height are not suitable for more than two.

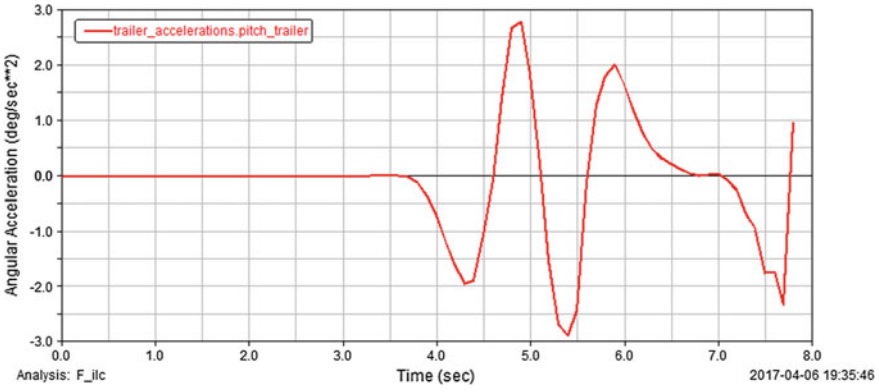

Fig. 8 One layer acceleration (40 cm high)

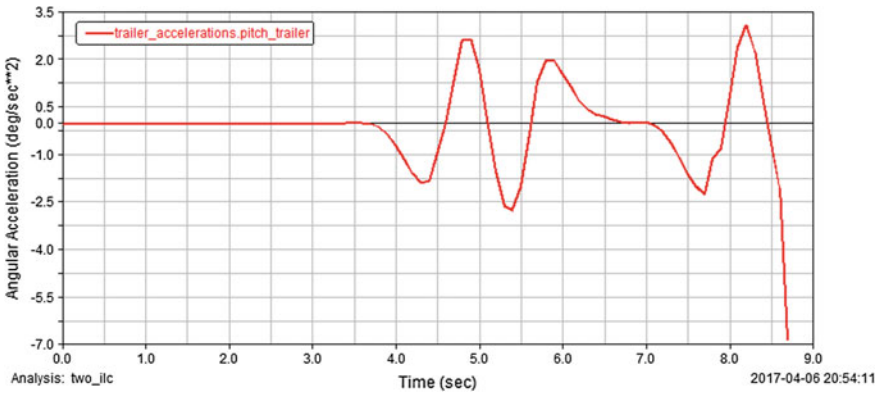

Fig. 9 Two layer acceleration (80 cm high)

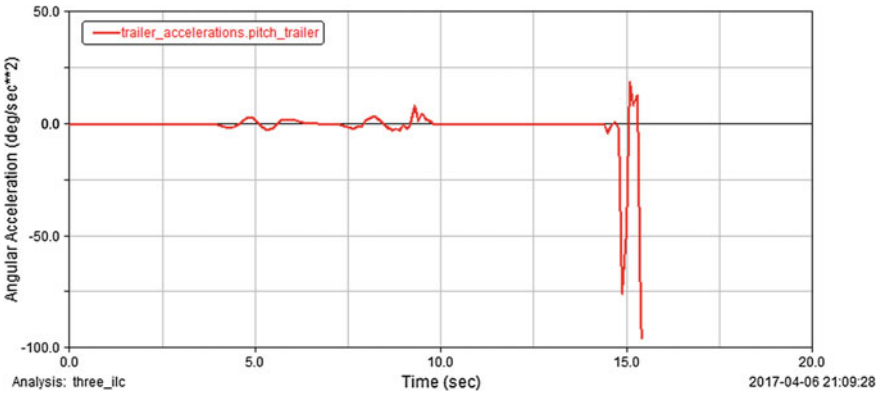

Fig. 10 Three layer acceleration (120 cm high)

5 Optimization Suggestions

The fourth part through the simulation analysis, it is the pure light of goods stacking is extremely unsafe during transportation. Therefore, this paper puts forward an improved scheme to improve the transportation quality. The insecurity in the carriage of goods is mainly due to the displacement and acceleration of the goods in all directions of transport. Therefore, as long as the reduction of these displacements and acceleration can improve the quality of transport of goods, we can fix the way through the goods to achieve this purpose. It can be between the goods and goods with airbag to fix the goods to prevent the transport of the shaking. It is also possible to reduce the pressure between the upper layer and the lower layer by adding a separator between the cargo layer and the layer. It also can film a number

of goods or a bundle of goods, that is to play a fixed role, but also played a cushion packaging effect.

6 Conclusions

This paper uses the ADAMS dynamics simulation software to study the different road model and the cargo vibration condition of stack height. The analysis shows that the larger obstacle on the road has the most obvious impact on the safety of the cargo. The stacking height of the fragile material is not suitable for stacking height without any special security. However, it can be achieved by means of fixing the goods.

The innovation of this paper is to apply the mechanical dynamics software to the logistics to analyze the vibration of the goods in transit, and study the influence of different roads on the goods. In this paper, there are still many defects, such as ignoring the goods and the goods of the lateral force; Vehicles, roads and transport goods being assumed to be rigid. These factors have a certain impact on the vibration situation of goods, can be more in-depth study in the future research.

References

1. Lee YS, Ryu CH, Kim HS (2005) A study on the free drop impact of a cask using commercial FEA codes. Nucl Eng Des 234:2119–2226
2. Bernad C, Laspalas A, Gonzalez D et al (2013) Dynamic study of stacked packaging units by operational model analysis. Packag Technol Sci 23(3):121–133
3. Du H (2015) Dynamic characteristics simulation of different forms of transport packages based on stacking. Southeast University, Nanjing
4. Wang L (2011) Study on dynamic characteristics of road dangerous goods packaging. Southwest Jiao Tong University
5. Pan Z (2012) A study on abnormal wear of tires based on ADAMS simulation. Chang'an University
6. Chen S (2011) A study of modeling, simulation and parameter matching of minibus ride comfort. Jilin University
7. Xu M (2013) Ride comfort simulation analysis and optimization of rigid flexible coupling vehicle model based on ADAMS. Hefei Polytechnic University
8. Wu Y (2014) Cargo damage analysis and random vibration detection and data processing technology. Hebei University of Technology
9. Zhou H (2012) Simulation research on vehicle safety driving speed based on vehicle road condition. Chongqing Jiaotong University
10. Fang H (2008) Study on mechanical characteristics and package design of cushion packaging for ceramic arts and crafts. Northeast Forestry University
11. Weigel TG, White MS (2012) The effect of pallet connection stiffness, deck stiffness and static load level on the resonant response of pallet decks to vibration frequencies occurring in the distribution environment. Packing Technol Sci 12(2):47–55
12. Xue F (2014) Design of drop impact test system and research on EPE cushioning vibration isolation performance. Taiyuan University of Science and Technology

13. Li H (2013) Review of research on dynamic characteristics of ammunition highway transportation. Packag Eng 115–119
14. Zhang L, Song N, Liu P (2017) Simulation and evaluation of vehicle modeling and handling stability based on ADAMS-Car. J Qingdao Technol Univ 38(1):114–118
15. Chen S (2013) Study on vehicle vibration smoothness of small forest fire engine. Beijing Forestry University

Progress in Technology of Fresh-Keeping Packaging

Chenyang Liu and Lijiang Huo

Abstract This paper introduces the present situation and main forms off resh-keeping packaging in China, and summarizes the main characteristics and application prospect of traditional fresh-keeping packaging, modified atmosphere packaging and active fresh-keeping packaging respectively. The active fresh-keeping packaging for the most promising applications is expounded in detail. The problems existing in the development process are summarized and analyzed. Finally, the future development of the fresh-keeping packaging is also discussed.

Keywords Traditional fresh-keeping packaging · Modified atmosphere packaging Active fresh-keeping packaging

1 Introduction

Fresh-keeping packaging is a new type of packaging technology. It can keep the freshness of all kinds of food and protect the products from the impact, such as biological, microbial and environmental factors in the storage and transportation process. The packaging method can maintain the original flavor of food in color, aroma, taste and other aspects, and increase the shelf life of food. With the gradual improvement of people's living standards and the level of consumption, the requirements on foods, fruits and vegetables for people are higher and higher. The traditional fresh-keeping packaging technology has been unable to meet the needs. Therefore, modified atmosphere packaging, active packaging, etc. come into being.

C. Liu · L. Huo (✉)
Light Industry and Chemical Engineering Institute, Dalian Polytechnic University, Liaoning, China
e-mail: lijianghuo@163.com

P. Zhao et al. (eds.), *Applied Sciences in Graphic Communication and Packaging*, Lecture Notes in Electrical Engineering 477,
https://doi.org/10.1007/978-981-10-7629-9_60

2 Traditional Fresh-Keeping Packaging

The main forms of the traditional fresh-keeping packaging are: preservative preservation, frozen preservation, high temperature sterilization preservation, vacuum packaging, and so on.

Preservatives play a role in preservation by interfering with microbial enzymes, destroying its normal metabolism and inhibiting its activity. In general, we use the refrigeration equipment for refrigerated preservation. The mature temperature of the refrigerated preservation: 5–15 °C, mainly used for transportation, frozen food (mainly for chocolate, seafood and other high-grade food); 0–10 °C, mainly used for biological products transportation; 0–20 °C, mainly used for constant temperature preservation of food transportation. Frozen preservation can extend the shelflife of the food, but it affects the taste of food. The high temperature sterilization preservation technology includes two ways: The first method is high temperature sterilization, which is suitable for the disinfection of canned food. The usual temperature is 120 °C, the time is 30 min, sometimes 60 min, sometimes even 90 min. Many families store tomatoes in this way when tomatoes are sold on a large scale in the summer. The second method is pasteurization. It takes 30 min to heat food in 60–65 °C. In generally, it can kill pathogenic microorganisms to achieve the purpose of prevention. Recently, the high temperature instant pasteurization method is often used and takes 30 s or 1 min to heat food in 80–90 °C. The method can be used for disinfection of milk, soy sauce, beverages, and so on. The food can be preserved at room temperature. But to some extent, the appearance and taste of food is affected. Vacuum packaging is mainly through the reduction of oxygen content within the package, to prevent the deterioration of the packaging of food spoilage, so as to maintain the color and flavor of food, and extend the shelf life [1–3].

Traditional fresh-keeping packaging has its unique application, but with the development of the times and technology, it has been unable to meet the packaging of some new products. For example, frozen packaging is the most effective way for quick-frozen dumplings. Ham sausage with vacuum packaging can fully show its color, arouse the desire of consumers to buy.

3 Modified Atmosphere Packaging

The modified atmosphere packaging is internationally known as MAP or CAP. Its principle is that mixing CO_2, O_2, N_2, etc. in a certain proportion and then pouring it into the food packaging, so as to replace the original air in the package [4, 5]. The CO_2 has a potent inhibitory effect on bacteria, fungi and enzymes, and has a toxic effect on aerobic bacteria. The elevated concentration of CO_2 has obvious inhibition and killing effect on mold and aerobic bacteria. O_2 plays a role in preservation of mixed gases. The appropriate concentration of O_2 can maintain the respiration of

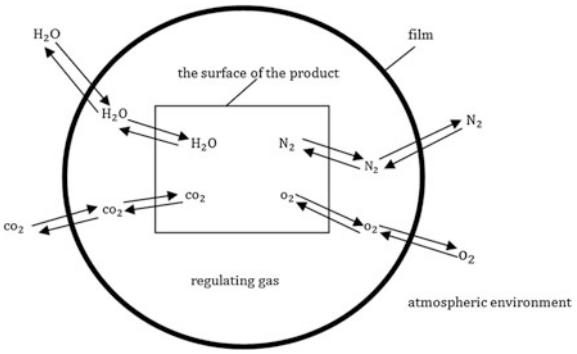

Fig.1 Schematic diagram of MAP

plants and animals, to ensure freshness. N_2 can't inhibit the multiplying of microorganisms, but also harmless to the food. However, it can be used as filling gas because of its weak chemical properties. It can reduce the number of residual oxygen in the package, and make the packaging full and beautiful to the eye [6–8] (Fig. 1).

The successful application of modified atmosphere packaging depends on the following basic process elements:

(1) Selection of gas composition in packaging and determination of packaging storage temperature
(2) Selection of high barrier packaging materials and sealing of packaging containers
(3) Packaging method and packaging machinery selection

The effect of different proportions of gas on the preservation of food is different. Therefore, different foods use different proportions of mixed gas to replace, so as to ensure the freshness of food requirements [9].

Compared with traditional fresh-keeping packaging, modified atmosphere packaging has the following advantages:

(1) The method can have a longer shelf life and maintain better flavor for foods without heating or freezing, with or without chemical preservatives
(2) Simple process and low cost
(3) No side-effects on the human body while ensuring freshness of the product.

4 Active Fresh-Keeping Packaging

The active fresh-keeping packaging is an active packaging system that combines the deoxidizer, the antibacterial agent, the odor (rot taste), the water and the CO_2 control agent with the packing materials. This system could extend the shelf life of

foods, effectively maintain the nutrition and flavor of food. And it can also improve the safety and quality of food. The typical active packaging systems has are as follows [10, 11]:

4.1 Oxygen Removed Active Fresh-Keeping Packaging

Oxygen is easy to have oxidation with protein, vitamins, oils and fats in food. It makes not only the loss of nutrients in food, but also easily leads to bacterial growth. In addition, water and oxides during oxidation process can easily lead to the breeding and reproduction of bacteria to accelerate the deterioration of food spoilage. Traditional packaging generally uses vacuum to remove oxygen. But still a lot of oxygen can't be removed. Usually, we need deoxidizer to absorb excess oxygen, it is generally placed in a gas bag with good gas permeability, and then placed in the food packaging bag for sealing [12]. Because the iron deoxidizer has the advantages of high safety, low raw material cost, easy access, good deoxidation effect, etc., it was vigorously promoted in the market.

4.2 Active Packaging System for Controlling CO_2 Content

Fresh fruits and vegetables tend to produce CO_2.It can inhibit microbial growth. However, high concentration of CO_2 can make fruits and vegetables into the glycolysis stage, accelerate the decay of fruits and vegetables. Therefore, the generation and removal of CO_2 is the focus of active system research. Active Packaging System for Controlling CO_2 content includes the generation and removal of CO_2 system [13]. The common form of CO_2 is the inclusion of CO_2 releaser in the form of packets added to product packaging or directly into films, to form a composite packaging film with CO_2 releasing function. The common removal forms are to add $Ca(OH)_2$, NaOH, KOH, CaO, and to reduce the content of CO_2 in the system of fruits and vegetables.

4.3 Active Packaging System for Ethylene Removal System

Fresh fruits and vegetables would produce ethylene gas in the package. The release of ethylene gas to a certain extent will cause deterioration of food. In order to extend the shelf life of fruits and vegetables, the accumulation of ethylene gas should be reduced as far as possible. Generally, highly permeable packaging materials are used to maximum send out the ethylene produced by fruits and vegetables [14], or the package is coated with ethylene removal agent film or directly coated ethylene

removal agent. Currently on the market there are generally used silica gel including ethylene removing agent containing Potassium Permanganate, palladium containing active carbon ethylene removing agent, inorganic porous mineral ethylene removing agent [15].

Up to now, active packaging hasn't been widely used in China. But it has been widely used in Europe and the United States, and has the highest popularity in Japan. Under the situation that people pay more and more attention to food safety, active packaging systems will get a wider range of applications and developments in the food industry.

5 Conclusions

As consumers pay more attention to food safety and environmental awareness, as well as the extension of the supply chain and shelf life and food safety requirements, active food packaging will have a broader market space. But at the same time, there are still many problems which are needed to be improved in the future. For instance, the complexity of the active packaging technology and a high degree of specialization make the product cost higher. Consumers have lower awareness of active and intelligent packaging. Many components of the active packaging make packaging with a certain smell and color, and this affects its business. The lack of perfect laws and regulations, appropriate assessment methods and clear regulatory measures, need to be improved and verified in practice. Nevertheless, these can't stop the development of active packaging, active packaging system is a revolutionary change in packaging industry, and has broad application prospects.

References

1. Cui S (2007) Fresh-keeping packaging for fruits and vegetables. Packag Eng
2. Fan K, Wang ZL, Cao ML (2014) The fresh-keeping technology for food. Packag Eng
3. Li J (2010) Research progress of fresh-keeping technique for fresh food. J Chin Inst Food Sci Technol
4. Huang J, Han C, Jiang H (2007) Applications of modified atmosphere packaging technology. Packag Eng 28(1):44–48
5. Yang K (2015) Applications of modified atmosphere packaging technology. Plastics Paper Box (14)
6. Zhang L, Ning L, Huang J (2008) The modified atmosphere packing for fresh fruits and vegetables. J Hunan Univ Technol
7. Lee L, Arul J, Lencki R et al (2010) A review on modified atmosphere packaging and preservation of fresh fruits and vegetables: physiological basis and practical aspects—Part I. Packag Technol Sci 8(6):315–331
8. Charles F, Sanchez J, Gontard N (2010) Active modified atmosphere packaging of fresh fruits and vegetables: modeling with tomatoes and oxygen absorber. J Food Sci 68(5):1736–1742

9. Pluta A, Ziarno M, Kruk M (2005) Impact of modified atmosphere packing on the quality of grated Mozzarella cheese. Polish J Food Nutr Sci
10. Vermeiren L, Devlieghere F, Beest MV et al (1999) Developments in the active packaging of foods. Trends Food Sci Technol 10(3):77–86
11. Sirocchi V (2014) Development a new active packaging system for fresh food through the studies of chemical and biological markers
12. Adur AM, Marano GA, Volpe RA et al (2000) Oxygen-scavenging filled polymerblend for food packaging applications. At Be ChCy De DkEs Fi Fr Gb Gr Ie It Lu Mc Nl Pt Se
13. Gao Y (2006) The active packaging system. Packag Eng (5):306–306
14. Du F, Sun B et al (2014) Progress in active and intelligent packaging technology in food industry. Packag Eng (1):135–140
15. Zagory D (1995) Ethylene-removing packaging. Active food packaging. Springer US, pp 38–54

Research and Application Progress on Food Active MAP Packaging

Pengfei Guo, Yabo Fu, Xiaowen Liu, Dongli Li and Wencai Xu

Abstract With the development of food packaging, active modified atmosphere packaging (MAP) has become a hot topic in recent years. Unlike traditional inert packaging, active MAP packaging can be designed to interact with the surrounding environment. This paper provides an overview of the various active MAP packaging, including oxygen scavenging packaging, carbon dioxide scavenging/generating packaging, ethylene scavenging packaging, humidity controlled packaging, antibacterial packaging and spontaneous modified atmosphere packaging, and sums up the research progress as well as the problems on food packaging safety in recent years. Active MAP packaging is the current focus but also will be the future direction of food packaging technology.

Keywords Active packaging · MAP · Food preservation · Shelf life

1 Introduction

Packaging is defined as enclosing food to protect it from tampering or contamination from physical, chemical and biological sources. Food packaging prevents food from being attacked by oxygen, water vapor and microbial contamination during storage and transportation. In recent years, with the consumer attention to the safety of food packaging, people put forward higher requirements on the food packaging safety, preservation and practical aspects under the premise of the three major functions of the traditional packaging. Active packaging and modified

P. Guo · Y. Fu (✉) · X. Liu · D. Li · W. Xu
Beijing Key Laboratory of Printing & Packaging Materials and Technology, Beijing Institute of Graphic Communication, Beijing, China
e-mail: fuyabo@126.com

W. Xu
Institute of Packaging and Printing Engineering, Tianjin University of Science and Technology, Tianjin, China

P. Zhao et al. (eds.), *Applied Sciences in Graphic Communication and Packaging*, Lecture Notes in Electrical Engineering 477,
https://doi.org/10.1007/978-981-10-7629-9_61

atmosphere packaging have shown excellent results in slowing the rate of food quality degradation, extending food shelf life and improving product value.

This paper introduces the research status and application of the research on the active MAP packaging in recent years, and introduces the research achievements of the team of the Beijing Institute of Graphic communication.

2 Active MAP Packaging

Active packaging, also known as AP packaging, is a packaging technology to extend the shelf life of packaged food, and maintain or improve the quality of food [1]. The principle is to add a variety of absorbent and release agent in the bag to remove excess CO_2, ethylene and water, and add the appropriate O_2. So that the environment of bag can be maintained suitable for fresh food storage and preservation, then the purpose of food preservation can be achieved. Modified atmosphere packaging, also known as MAP, is a technology by changing the atmosphere inside the packaging, so that food is storage in an atmosphere different from air components, and shelf life can be extended [2]. AP packaging is usually combined with MAP packaging to achieve better freshness.

2.1 Present Situation and Application Prospect

In recent years, the active packaging has been actively introduced as an innovation concept into the food package. At present, the application of active MAP packaging on the market accounted for the vast majority of intelligent packaging products. Active packaging defines maintaining food condition in a way that covers various aspects that influence the shelf life of packaged foods, including physiological processes (e.g., respiration of fresh fruit and vegetables), chemical processes (e.g., lipid oxidation), physical processes (e.g., staling of bread, dehydration), microbiological aspects (e.g., spoilage by microorganisms), and infestation (e.g., by insects) [3].

Active MAP packaging is mainly used for preservation of fresh fruits and vegetables, meat and other food. Foreign research and application of AP and MAP theory (Packaging temperature and humidity, gas changes and other models of the establishment) is very extensive, including fruits and vegetables, livestock and poultry meat and other types of aquatic products. There are few studies about theory and many researches on its application in China. It mainly focuses on exploring the suitable packaging gas components and selecting packaging materials [4]. In general, the Active MAP packaging is in the later start and slower development stage in China.

2.2 Research Progress on Active MAP Packaging

2.2.1 Oxygen Scavenging Packaging

For meat, milk and other oxygen sensitive food, corruption is mainly due to the oxidation and mold, bacteria, yeast and other microorganisms. Oxidation on food of oils and fats is the result of direct effects of oxygen and microbial [5]. So the oxygen adsorbed packaging materials, or deoxidizer sealed into the packaging, can remove the headspace oxygen of the packaging, and reduce the oxygen content of the package to 0.01%, achieving a state with no oxygen and a better preservation effect [6].

In recent years, many scholars conducted a lot of research, and made a lot of achievement. Gómez-Estaca et al. [7] added antioxidant butylated hydroxytoluene (BHT) or butylated hydroxyanisole (BHA) to the polyethylene film of the packaging material to delay the rate of fat oxidation in the meat. Huiye Duan [8] prepared a multi-layer composite oxygen scavenging film for food packaging, and blended the oxygen-absorbing resin into LDPE (low-density polyethylene) as an oxygen-absorbing layer. When the moisture in the food contacted with the packaging material, the moisture coming from the inner layer contact with the oxygen-absorbing layer, and the oxygen-absorbing resin is activated and reacts with the oxygen. Test showed that it can be completely absorbed that the dissolved oxygen and heatspace oxygen in the food on 7–10 days, maintaining a low concentration rate of oxygen in the package.

2.2.2 Carbon Dioxide Scavenging/Generating Packaging

(1) Carbon Dioxide Scavenging Packaging

Fresh foods such as fruits, vegetables and meat needed to be stored in high concentration CO_2 to inhibit the growth of microorganisms on food surface and the respiration of fruits and vegetables, which is very important to maintain the quality of food and extend the shelf life. Its main form is to add CO_2 release agent in the form of packets into the product packaging or directly into the film to form a composite packaging film with CO_2 release function.

Verifrais invented by France SARL Codimer Company for fresh meat preservation. A mixture of sulfite deoxidizer and sodium bicarbonate can simultaneously act as a deoxygenation and produce carbon dioxide [9]. Schirmer et al. [10] mixed CO_2 and citric acid, acetic acid, cinnamaldehyde for salmon storage and achieved good results.

(2) Carbon Dioxide Generating Packaging

For fruit, excessive CO_2 will promote fruit anaerobic respiration, reduce fruit quality, but also promote the growth and reproduction of anaerobic bacteria.

Reducing the concentration of CO_2 can be achieved by means of physical adsorption, such as the use of zeolite or activated carbon. and the NaOH, Mg $(OH)_2$ to produce carbonates with CO_2. It also can be achieved by a combination of physical adsorption and chemical reactions to reduce CO_2 in packaging materials.

Aday et al. [11] used sodium carbonate, sodium carbonate, sodium chloride and bentonite to make EMCO carbon dioxide adsorbents and studied the effect of EMCO on the quality of strawberries in active packaging. The results showed that the ratio of EMCO was 50% sodium carbonate, 20% sodium carbonate, 14% sodium chloride and 16% bentonite, which could delay the sugar metabolism of strawberry, effectively maintain the quality of strawberry and extend its shelf life to 4 week.

2.2.3 Ethylene Scavenging Packaging

This packaging is mainly used for the preservation of fruits and vegetables to absorb the ethylene produced during its ripening process, reduce the rate of respiration and extend the shelf life. Commonly ethylene removal methods include: the use of high permeability packaging materials to exclude internal gas maximum; or a small bag with the ethylene remover are put in the packaging.

Substances that have the effect of removing ethylene include potassium permanganate, zeolite, cristobalite, and partial carbonates, which are packaged with pouch with high permeability to ethylene. Substrates with active surfaces can also be physically adsorbed on ethylene. Bailén et al. [12] showed that palladium powder with 1% mass fraction was added to activated carbon which have a good adsorption effect on ethylene. Ethylene adsorption function film made by film with ethylene removal agent can achieve the ethylene removal effect. In recent years, it has been successfully studied that the fine particles of zeolite clay are dispersed in the packaging film to adsorb ethylene, but it affects the light transmittance of the package and does not completely achieve the purpose of adsorbing ethylene in the package [13].

2.2.4 Humidity Controlled Packaging

Humidity controlled packaging is mainly used for two major categories of food packaging, dry and fragile food and fresh food. The former, such as biscuits will be damp softened in the high water activity conditions; the latter will produce condensate in the storage and transportation process due to the respiration. If the condensate water condenses on the surface of the food, it causes the water-soluble nutrients in the food to dissolve and brew a large number of microorganisms biscuits, dried fruit, beef and other products in China are through a separate packaging of desiccant to reduce the humidity inside the package. In contrast, there are processes that add desiccant directly to aluminum foil composites or bags in foreign countries(Such as SuperDryFoil™ packaging from Baltimore Innovations,

UK, DesiMax® SLF packaging from Multisorb Technologies, USA, Activ-Blister® packaging from CSP Technologies, USA) [14]. Mahajan et al. [15] developed a desiccant consisting of sorbitol, bentonite and $CaCl_2$, with a mass ratio of 5:11:4, which had a low moisture absorption and a strong water holding capacity that can be used for the preservation of fresh fruits and vegetables.

2.2.5 Antibacterial Packaging

Antibacterial packaging has attracted much attention because of its convenience and effectiveness. The antibacterial agent is mixed with one or several polymer packaging materials to make it antibacterial. Antibacterial agents are added to the packaging in a variety of ways: adding an antimicrobial substance directly to the polymer; applying an antimicrobial substance to the surface of the polymer; immobilizing the antimicrobial substance on the surface of the polymer by chemical bonds; and using certain polymers having antibacterial activity.

Antibacterial materials have a very wide range of applications in the field of food packaging. Deng et al. [16] using thyme essential oil antibacterial coating film packaging fresh lettuce, through experiments to explore the inhibition effect on fresh lettuce rotten bacteria. The results showed that it could inhibit the respiration intensity, microbial growth and polyphenol oxidase activity of fresh lettuce, reduce the loss of VC during storage and maintain the good sensory quality of lettuce. Xu et al. [17] developed a controllable film for the release of LF by the addition of an antifungal function of loofah fiber extract (LF), and studied the antibacterial properties and biodegradability of the film. The results show that the higher the concentration of LF in the cast film, the higher the concentration of tannins and glycosides in the film, and the stronger the inhibitory effect on the microorganisms. When the LF/MCC addition is 20%, the antibacterial activity of the membrane was increased by 61.5%.

2.2.6 Spontaneous Modified Atmosphere Packaging

The principle of spontaneous modified atmosphere packaging is to use of fresh cut fruit and vegetable their own breathing and the selective permeability of plastic film packaging [18]. Liu et al. [19] used the multi-functional atmosphere packaging bags made of nano-modified film material, laboratory independent research and development, to keep litchi fresh. The results showed that litchi in the exposed group had a browning within 1–2 days, and lost the commercial value. The sample of the modified bag group can still maintain good quality on the 4–5 days of the experiment, indicating that the spontaneous modified atmosphere packaging can extend the shelf life of fresh litchi at room temperature.

3 Current Problems and Trends

Active MAP packaging plays an important role in maintaining food quality, ensuring food safety and helping consumers to access effective messages. The main problems at present include: the complexity and professionalism of the technology make the product cost higher, it is difficult to meet the market requirements; Consumers have a lower level of cognition, resulting in lower acceptance of their efficacy and safety; Packaging has a certain smell and color and affect its commercial as many ingredients are added to the packaging; There is no sound regulations, appropriate assessment methods and clear regulatory measures.

Active MAP packaging still have many problems such as efficacy, safety and reliability currently. With the development of technology and the continuous improvement of consumer awareness, active packaging and modified atmosphere packaging will be an important component of product packaging part, will also lead the packaging industry to further increase the profitability of technological progress. Future trends include: Natural active ingredients are used in active packaging, which can be in direct contact with food and make consumers easy to accept in food safety; Combined with active packaging and modified atmosphere packaging, it reflects the intelligence and initiative of packaging, prolongs the shelf life of food and improves the quality of food, meanwhile, it can independently judge the freshness of the product being packed; For the atmosphere packaging, it has been found that Ar and N_2O can also be used for food preservation, but needed more in-depth study.

4 Conclusions

Food packaging is changing developing in the direction of informatization, functional and environmental protection. Active MAP packaging technology has the similar characteristics of intelligent, healthy and environmental protection, and occupies a significant position in food packaging. As consumers focus on food quality and safety, active MAP packaging will play a more important role in future food packaging. In addition, active MAP packaging also has the issues of safety, and the economy, which will be the key point of the future research.

Acknowledgements This work was supported by the National Key Scientific Instrument and Equipment Development Project (No. 2013YQ140517), National Key R&D Program (No. 2016YFC0204202), and the Coordinative Innovation Project of Beijing Municipal Commission of Education (No. 04190117019).

References

1. De Kruijf N, Van Beest M, Rijk R, Sipiläinen-Malm T, Paseiro Losada P, De Meulenaer B (2002). Active and intelligent packaging: applications and regulatory aspects. Food Addit Contam 19 Suppl(sup1):144
2. Sandhya (2010) Modified atmosphere packaging of fresh produce: current status and future needs. LWT Food Sci Technol 43(3):381–392
3. Bodbodak S, Rafiee Z (2016) 3–recent trends in active packaging in fruits and vegetables. Eco-Friendly Technol Postharvest Produce Qual 77–125
4. Cheng S, Fuhua W, Fenghua B et al (2017) Research status of modified atmosphere packaging technologies for fresh food in China. Packag Food Mach 35(1)
5. Li J, Zhang L (2010) The quality impact studies of different packaging methods on cake. Packag Food Mach 28(2):17–20
6. Murat O, John DF (2005) Active food packaging technologies. Crit Rev Food Sci Nutr 44 (3):185–93
7. Gómez-Estaca J, López-De-Dicastillo C, Hernández-Muñoz P, Catalá R, Gavara R (2014) Advances in antioxidant active food packaging. Trends Food Sci Technol 35(1):42–51
8. Huiye D (2013) Research on preparation and properties of oxygen scavenging packaging film based on gallic acid. Doctoral dissertation, Beijing Institute of Graphic Communication
9. Suppakul P, Miltz J, Sonneveld K, Bigger SW (2003) Active packaging technologies with an emphasis on antimicrobial packaging and its applications. J Food Sci 68(2):408–420
10. Schirmer BC, Heiberg R, Eie T, Møretrø T, Maugesten T, Carlehøg M et al (2009) A novel packaging method with a dissolving CO 2 headspace combined with organic acids prolongs the shelf life of fresh salmon. Int J Food Microbiol 133(1):154–160
11. Aday MS, Caner C, Rahvali F (2011) Effect of oxygen and carbon dioxide absorbers on strawberry quality. Postharvest Biol Technol 62(2):179–187
12. Bailén G, Guillén F, Castillo S, Zapata PJ, Serrano M, Valero D et al (2007) Use of a palladium catalyst to improve the capacity of activated carbon to absorb ethylene and its effect on tomato ripening 5(4):579–586
13. García-García I, Taboada-Rodríguez A, López-Gomez A, Marín-Iniesta F (2013) Active packaging of cardboard to extend the shelf life of tomatoes. Food Bioprocess Technol 6 (3):754–761
14. Dobrucka R, Cierpiszewski R (2014) Active and intelligent packaging food - research and development - a review. Polish J Food Nutr Sci 64(1):7–15
15. Mahajan PV, Rodrigues FAS, Motel A, Leonhard A (2008) Development of a moisture absorber for packaging of fresh mushrooms (agaricus bisporous). Postharvest Biol Technol 48 (3):408–414
16. Deng W, Jiang W, Chen A, Lan W, Xiaoxia X, Chen M (2016) Effect of thyme essential oil antibacterial coating films on physicochemical quality and microorganisms of fresh-cut lettuce during its shelf life. Food Ferment Ind 42(7):247–253
17. Wencai X, Liu P, Li D et al (2015) Preparation and properties of biodegradable and controllable bacteriostatic functional film. Packag Eng 11:1–4
18. Wenda X (1999) Fresh fruits and vegetables modified packaging. Food Ind 3:35–38
19. Liu H, Wencai X, Li D, Chang H (2016) On the application of multi function integrated MAP in litchi preservation at room temperature. J Beijing Inst Graphic Commun 24(6):17–21

Experimental Study on Fresh-Keeping Packaging of Rice Antistaling Agent

Xue Gong, Jiang Chang and Zhihui Sun

Abstract Regarding the main problems in the process of China's rice storage, with commercially available Northeast Wuchang rice as a test material, the in-depth study of the relationship between different packing types and rice preservation has been conducted by focusing on physical and chemical properties of rice. The accelerated high temperature experiments were carried out for rice packaging by using general packaging, vacuum packaging, chitosan packaging, bamboo charcoal packaging, vacuum plus chitosan packaging, and vacuum plus bamboo charcoal packaging. The rice moisture content, fatty acid content, reducing sugar content and protein content were measured every 7 days to investigate the influence of fresh-keeping packaging on rice nutritional quality. According to the experimental results, vacuum plus bamboo charcoal packaging is conducive to the preservation of rice and the fresh-keeping effect is obvious. The water content was reduced by 0.21%, the content of fatty acid was increased by 7.2 mg, the content of reducing sugar was increased by 0.15% and the content of protein was reduced by about 0.91%.

Keywords Rice · Fresh-keeping packaging · Preservative · Quality

X. Gong (✉) · J. Chang
Light Industry College, Harbin University of Commerce,
Harbin, Hei Longjiang, China
e-mail: gongxue@hrbcu.edu.cn

J. Chang
e-mail: kahn82@163.com

Z. Sun
Dean's Office, Harbin University of Commerce,
Harbin, Hei Longjiang, China
e-mail: sunzhihui1962@163.com

P. Zhao et al. (eds.), *Applied Sciences in Graphic Communication and Packaging*, Lecture Notes in Electrical Engineering 477,
https://doi.org/10.1007/978-981-10-7629-9_62

1 Introduction

China is a major consumer of rice and its annual demand is relatively large. In some developed countries, rice is generally stored in the form of brown rice, and when used in the process of milled rice, brown rice due to the protection of the shell is relatively easy to save. However, in the domestic China, rice most often are stored in the form of rice, when the rice is processed into rice, rice hull itself lost protection, organization structure, endosperm exposed [1, 2], making it particularly poor storage stability. In the process of rice refining, enzyme activation, contact with the outside air, accelerated the physiological and chemical reaction, which accelerated the deterioration rate of rice mildew. After a period of time, increased free fatty acids in rice endosperm, cell membrane composed of starch hardening will occur, in addition to these chemical reactions, the organizational structure of rice will thus change, these changes will lead to changes in the appearance of rice cooking and taste, are prone to pests and aging, mildew and other problems [3].

With the development of society, people are no longer concerned about the problem of food and clothing, but how to improve the quality of life. Rice as the main food of most residents, the quality has received widespread attention. How to maintain the nutrition and taste quality of rice during storage, i.e., keeping rice fresh has become a major problem of packaging in rice industry [4].

2 Experimental Preparation

2.1 Experimental Materials

Experimental object: commercially available Northeast Wuchang rice. Packaging material: 0.125 mm PA/PE composite film. Preservative agent: chitosan, bamboo charcoal.

2.2 Experimental Materials and Instruments

Main equipment: DQB—700 N air conditioning and packaging machine; constant temperature box; digital constant temperature water bath HH-4; electrothermal constant temperature drying box type 202; Kjeldahl apparatus.

2.3 Sample Packaging

Weighing 100 g of rice for each bag, followed by heating sealing, one packaging was obtained. For chitosan or bamboo charcoal involved packaging, a small

packaging bag with 0.3 g of chitosan or bamboo charcoal was sealed inside the packaging. For vacuum packaging, the PA/PE packaging bag was vacuum pumped by DQB—700 N air breathing packaging machine.

3 Experimental Results and Analysis

3.1 Initial Value of Rice Quality

The initial values of each index are shown in Table 1.

3.2 Experimental Results and Analysis

After the treatment of packaging, rice is placed at 45° under the constant temperature box, once every 7 days to determine the main components of the experiment. 5 experiments were conducted for a total of 35 days. The changes of the composition of the different packaging methods were compared with the storage time.

3.2.1 Effects of Different Packaging Methods on Water Content of Rice

The variation of rice moisture content is related to the environmental temperature, humidity and other factors. The relative humidity of different fresh keeping bags is not the same, and the water content of rice is not the same [5]. The relationship between water content of rice with different packaging methods with time is shown in Fig. 1.

As can be seen from Fig. 1, packing different moisture content are reduced to some extent, general packaging dropped 1.08%; vacuum packaging fell 0.41%; chitosan packaging decreased 0.73%; bamboo charcoal decreased 0.37% packaging; vacuum packaging of chitosan decreased by 0.26%; bamboo charcoal decreased 0.21% vacuum packaging. The combination of vacuum and bamboo charcoal two packaging methods is more conducive to the preservation of rice.

Table 1 Initial value of rice quality

Index	Water content (%)	Fattyacid content (mg KOH/100 g)	Reducing sugar content (%)	Protein content (%)	Viscosity (m pa s)
Rice	15.58	6.66	0.11	7.43	12.2

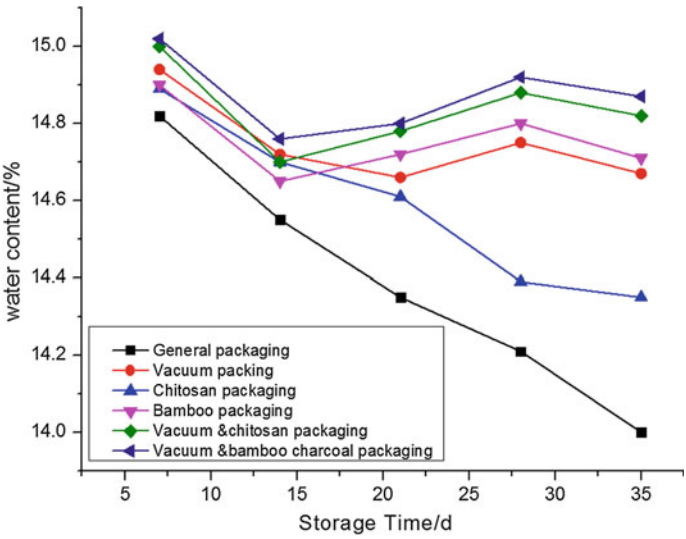

Fig. 1 Curves of water content in rice with different packaging methods

3.2.2 Effects of Different Packaging Methods on the Content of Fatty Acids in Rice

In the process of storage, fat is more easily hydrolyzed than protein, and the rate of lipid oxidation increases with the increase of storage time and temperature [6]. The relationship between the content of fatty acid in rice with different packaging methods with time is shown in Fig. 2.

From Fig. 2, the fatty acid value of rice increased with the storage time. The fatty acid content of the vacuum packed rice increased slowly, the growth of 7.20 mg, the line graph can be seen: the fatty acid content of each package in the experiment of rice is lower than the suitable storage rice quality control index (30 mg KOH/100 g).

3.2.3 Effects of Different Packaging Methods on Reducing Sugar Content in Rice

Rice contains a small part of low molecular sugars, which contain a free reducing group, the non-reductive sucrose hydrolysis of fructose and glucose, reducing sugar content will increase. According to the relationship between reducing sugar content and storage time, the deterioration of rice quality was also evaluated. The change of reducing sugar content in rice with different packaging methods with time is shown in Fig. 3.

As can be seen from Fig. 3, using different packaging methods of rice the reducing sugar content increased, reducing sugar content and water content in the

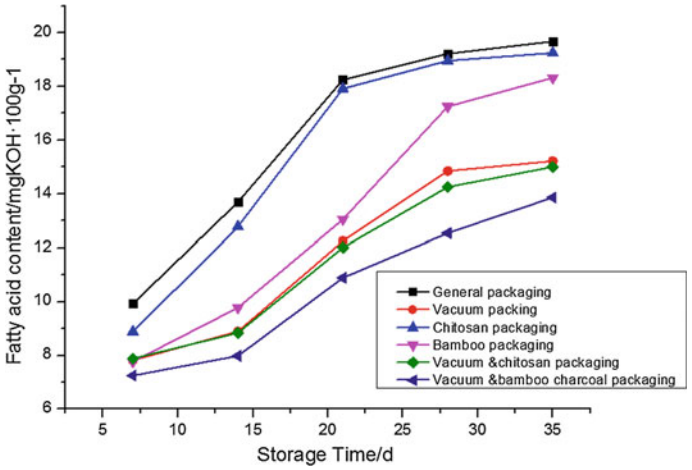

Fig. 2 Curves of fatty acid content in rice with different packaging methods

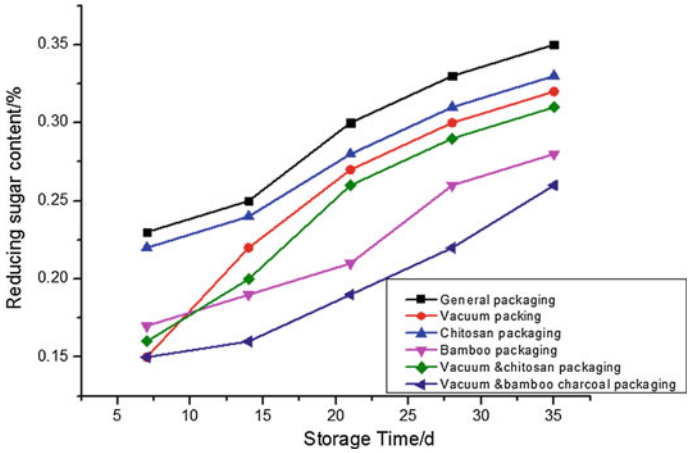

Fig. 3 Curves of reducing sugar content in rice with different packaging method

packing bag also has a certain relation with bamboo charcoal packaging rice the reducing sugar content was slightly higher than that of the vacuum packaging of the bamboo rice, but lower than other forms of packaging, in addition of bamboo charcoal the packing bag, the bag in the water can be controlled very well, the reducing sugar content of rice increased low, 0.17%; change of vacuum packaged rice also can reducing sugar content of rice has played a certain role, its value is far below the national standard value of 0.58%.

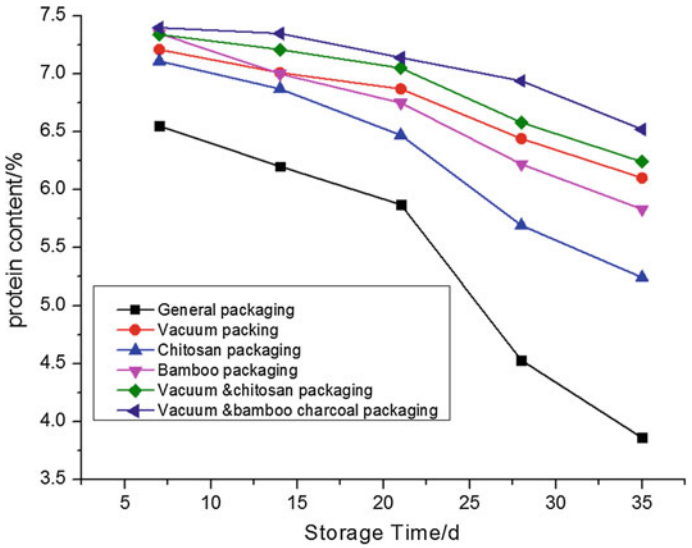

Fig. 4 Curves of protein content in rice with different packaging methods

3.2.4 Effects of Different Packaging Methods on Protein Content in Rice

The vast majority of rice starch, only the tip of the embryo contains a small amount of protein, but in the process of rice milling is very easy to get rid of the protein, a meter is about 0.8%. The protein content of rice with different packaging methods varies with time, as shown in Fig. 4.

It can be seen from Fig. 4, the protein content of different package of rice are reduced, decreased protein content of common packing of rice protein content rate decreased relatively quickly, other packaging of rice is relatively close, so in the process of rice storage protein content. This is unavoidable, should pay more attention to the rice, rice milling technology aspects should be improved, which retains more protein.

4 Conclusions

The effect of vacuum bamboo charcoal packaging is relatively good, vacuum bamboo charcoal packaging is conducive to the preservation of rice, the effect is obvious. The water content was reduced by 0.21%, the content of fatty acid was increased by 7.2 mg, the content of reducing sugar was increased by 0.15% and the content of protein was reduced by about 0.91%. Experiments show that the vacuum packaging and preservative packaging of rice has certain effect, for water, vacuum,

bamboo charcoal, chitosan is conducive to maintaining the rice moisture, the fatty acid, the vacuum can better inhibit the increase in reducing sugar, as long as the bag without much water, growth the rate is very low, for the protein, in order to save more protein, suggestions for improving the rice milling technology in rice, leaving more rice embryo.

Acknowledgements National Science and Technology Support Programme Project (2016YFD0400301); Harbin University of Commerce research team support program (2016TD005).

References

1. Pan J (2004) Rice storage technology research. Northwest Agriculture and Forestry University
2. Wang Z, Zhao S, He X (2000) Progress in research and application of preservation technology of rice. Food Process Mach (10):35–36
3. Zheng X (2004) Current situation of rice quality in China and the latest technology for food preservation. Food Process Food Mach (4):10–12
4. Xu X, Wang W et al (2005) Study on vacuum packaging technology of rice based on circulation environment. Packag Eng 26(2):85–87
5. Wang Y, Zhang L (2006) Effect of different barrier packaging materials on rice storage quality. China Packag 26(06):57–61
6. Pan J, Li X et al (2007) Development of multifunctional rice fresh-keeping film. Shanghai Agricu Sci Technol 1:20–21

Modified Atmosphere Packaging and Postharvest Treatments on Mango Preservation: A Review

Xiaowen Liu, Yabo Fu, Pengfei Guo and Wencai Xu

Abstract This review provides various methods of postharvest treatment and modified atmosphere packaging (MAP) of mango fruit preservation. On the one hand, significant amount of postharvest storage research has been done in this area to improve shelf life and quality of fruit, especially, pulsed light, irradiation, hot water, bio-control agents, malicacid dipping and 1-MCP treatment. On the other hand, modified atmosphere technology has extensive application prospect in mango fruit preservation. Some comparison and effects of these techniques have been mentioned and recommended in this paper. The post-harvest treatments in combination with MAP could be used to inhibit browning, decay, and deterioration of mangoes.

Keywords Postharvest treatment · Modified atmosphere packaging
Mango · Preservation

1 Introduction

Fresh mango is susceptible to disease organisms because of increased respiration rate after harvesting. However, due to the application of conventional technology for the transfer of the produce and an irregular storage period more than 30% is wasted [1].

Several mango postharvest handle have been developed for controlling disease and insects and for protection. Low temperature handling and storage are the most important physical methods of postharvest management. For example, air cooling, hydro-cooling, vacuum cooling, hypobaric storage [2], high-pressure-shift freezing (HPSF) and other techniques are used to extend mango shelf life.

X. Liu · Y. Fu (✉) · P. Guo · W. Xu
Beijing Key Laboratory of Printing and Packaging Materials and Technology,
Beijing Institute of Graphic Communication, Beijing, China
e-mail: fuyabo@126.com

P. Zhao et al. (eds.), *Applied Sciences in Graphic Communication and Packaging*, Lecture Notes in Electrical Engineering 477,
https://doi.org/10.1007/978-981-10-7629-9_63

Modified atmosphere packaging (MAP) can alleviate fruit undesirable quality as well as improve shelf life. It has a wide use in improving the appearance of food, reducing waste and extending the shelf life [3]. The atmosphere generated by MAP delays ripening of certain subtropical-tropical fruits, including mango. The main factors that maintain mango quality in various films are increased CO_2 and decreased O_2 levels [4]. It can retard the biochemical activities and extend the shelf life of fresh produce.

In this paper, various postharvest treatments and modified atmosphere packaging methods have been discussed along with the technologies used. In view of the existing literature, there is little research on the combination of the advanced postharvest treatment and MAP packaging. It is suggested that postharvest treatments combined with MAP in the future, to extend the mango preservation effect.

2 Postharvest Treatments

There are many ways to deal with post-harvest mango, for example, pulsed light, irradiation, hot water, bio-control agents, malicacid dipping and 1-MCP treatments.

2.1 Pulsed Light Treatment

Inactivation of mango slices was higher as pulse number increased in pulsed light treatment [5]. A flash lamp system composing eight lamps which has a total fluence of 8 J cm^{-2} was implemented in pulsed light treatment [6]. Pulsed light treatment maintained the firmness, the colour of fresh mangoes.

2.2 Irradiation

Irradiation causes the ion loss on the surface of the material. Radiation may induce stress in postharvest fruits, which is a protective mechanism. However, fruit tissue can deploy a range of protection mechanisms, such as antioxidants, at reasonable radiation doses [7]. Radiation can also minimize the colonization of fruit with pathogens due to con tamination, insect infestation, postharvest disease, as well as delay ripening. The three most commonly used are UV-C, X- and gammarays [8].

Ultraviolet (UV) is non-ionizing and is frequently used for post harvest management of fruit. X- and gammarays: These are especially effective for killing parasitic microbes, fungi and insects. Mangos cv 'Haden' were exposed to UV-C irradiation energy levels of 2.46 and 4.93 kJ m^{-2} and they can store 18 days at 25 °C [9]. UV-C treatment maintained better overall appearance and increased shelf life of fruit.

2.3 Hot Water Treatment

Metabolic processes such as respiration and ripening are very susceptible to temperature. Heat treatments are widely used in many countries for specific pest disinfection and decay control in mango [10]. It is advisable to carry out hot water treatment within 24 h after harvest. Philippines mango flotation in 10% salt solution was practiced and if the fruit floats, hot water treatment is delayed [11]. Exposing fruit to higher temperatures(37–42 °C) before freezing could delay maturation and enhance resistance to pathogens [12]. Therefore it is one method to reduce chilling injury.

2.4 Biocontrol Agents

Biological control using microbial antagonist could be used on its own. Combination with synthetic fungicides is one approach to reduce fungi injury [13].

2.5 Malic Acid Dipping Treatment

Organic acids (acetic, lactic, citric, malic) have be used as food additives and preservatives for preventing food deterioration and extending shelf life [14].

2.6 1-MCP Treatment

1-MCP application suppressed ethylene production and respiration rate, delayed loss of fruit firmness and reduced the activities of enzymes in 'Kensington Pride' mango [15]. It reduces many of the changes associated with maturation such as respiration rates and color change.

3 Methods for Mango MAP

The application of MAP technology can extend the storage life of food while maintaining overall quality. MAP with CO_2 and lower O_2 can retard ripening by inhibiting ethylene production and delaying metabolism.

Pesis et al. [4] were the first who tried to increase 'Kensington' mango shelf life by using MAP. The gas composition in perforated polyethylene (PE) bags was 8.9% CO_2 and 15.2% O_2, and that in sealed PE bags 14.8% CO_2 and 1.8% O_2.

They concluded that storage of mangoes in PE bags at 20 °C could cause development of abnormal peel.

Sanginga [16] suggested that a reducing O_2 concentration of around 3–5% and an elevating CO_2 concentration of 5–10% are a successful atmosphere system for mango fruit. Mature green mango (cv. Tommy Atkins and Kent) in MAP with CO_2 composition of over 10% results in fading color. Although higher concentration of CO_2 (above 10%) can prevent the incidence of diseases, CO_2 concentration must not result in any quality defects such as skin fading or fruit softening.

Lalel et al. [17] recommended that storage of mangoes in 1.5% or 2% O_2 in combination with 8% CO_2 extend the shelf life with satisfied quality.

A MAP containing with 3% O_2 and 10% CO_2 had a low incidence of anthrax in 'Tommy Atkins' mangoes, and the effect of MAP still controlled anthrax when it were moved from cold storage to room temperature [18].

The total soluble phenols and antioxidant capacity of intact mature mangoes(cv. Tommy Atkin) were not significantly affected in MAP(21% O_2, 97% N_2; 3% O_2, 97% N_2; and 3% O_2, 10% CO_2, 87% N_2) [19].

González-Aguilar et al. [20] used 4-hexylresorcino(HR) + D-isoascorbic acid (ER), and D-isoascorbic acid (ER) + potassium sorbate(KS) treatments to protect mangoes. Oxygen levels decreased ceaselessly in these treatments until concentrations of 4–5% O_2 were reached, whereas CO_2 levels increased more rapidly in control group and stabilized after 6 days. These treatments did not affect significantly the changes in organic acids and sugar content of slices during the 14 days of storage at 10 °C. Combinations of several browning inhibitors were more effective than those applied individually. HR + ER + KS treatment in combination with MAP could prolong storage life of mangoes for 7 days at 10 °C.

Pesis et al. [4] designed a MAP (5% CO_2 and 10% O_2) in polyethylene or Xtend TM film to reduce the chilling injury and reported that most effective reduction in chilling injury was found in 'Tommy Atkins and Keitt' mangoes which were packed in Xtend TM film in 4 weeks.

In 10% CO_2, 4% O_2, 86% N_2 MAP of green mango showed low activity values in microbial populations such as fungi and yeasts. After processing, fruit carry its native microbial flora, and may have about 104–105 colony forming units per gram (cfu/g). Normally, once these levels are increased to 107–108 cfu/g, it will be spoiled [21]. It can presented the best L and b values that showed a pleasing appearance and a fresh texture for 10% CO_2, 4% O_2, 86% N_2 gas mixture in 25 days at 5 °C.

Chitosan coated, sliced mango fruit showed slower attenuation and lower water loss. Combination of antimicrobial agents and MAP reduced browning and deterioration of mango stored at 10 °C [22].

It is important that the MAP will only slow the natural deterioration of the product without improving the quality of the product. It is ordinarily believed that the use of penetrable membranes will result in the spoilage of fruits prior to the production of toxins. MAP should use materials that do not cause hypoxia in the packaging environment when stored at the appropriate temperature.

A MAP with successful control of both product respiration and ethylene production and sensory can lead to fruit with high sensory quality. However, MAP is not an effective controller for preventing microbial growth, but a single prevention strategy. Isolation technology may be an effective way to ensure food safety. Therefore, there should be more research about other treatments combined with MAP.

4 Conclusions

It is a reasonable way to decrease the loss of post-harvest and prolong the storage life of mango after controlling disease and infection. Advanced post-harvest treatment in combination with MAP could be applied to inhibit browning, decay and deterioration of mangoes. For optimum MAP performance, the mechanical properties of films must be balanced with their chemical properties for ease of use by consumers. Mathematical modeling and prediction tools provide significant help for obtaining the best gas transmission rate for a variety of packaging materials. In general, inconsistent temperature conditions can cause fruit respiration and increasing of transpiration rate, which increase microbiologic population and deteriorate MAP environment. Therefore, strict cold chain mechanisms need to be maintained more consistently throughout the transport process. In the future, we can integrate MAP system with microbial data and then obtain online evaluation system. Besides, it is believed that more materials would be developed for the packaging of mango preservation in the future, to better meet the requirements of MAP gas composition.

Acknowledgements This work was supported by the National Key Scientific Instrument and Equipment Development Project (No. 2013YQ140517), National Key R&D Program (No. 2016YFC0204202) and Coordinative Innovation Project of Beijing Municipal Commission of Education.

References

1. Baloch MK, Bibi F (2012) Effect of harvesting and storage conditions on the post harvest quality and shelf life of mango (*Mangifera indica* L.) fruit. S Afr J Bot 83:109–116
2. Tefera A, Seyoum T, Woldetsadik K (2007) Effect of disinfection, packaging, and storage environment on the shelf life of mango. Biosys Eng 96(2):201–212
3. Day BPF, Gorris LGM (1992) Modified atmosphere packaging of fresh produce on the West European market. Int Food Manuf 44:35–37
4. Pesis E, Aharoni D, Aharon Z et al (2000) Modified atmosphere and modified humidity packaging alleviates chilling injury symptoms in mango fruit. Postharvest Biol Technol 19 (1):93–101

5. Salinas-Roca B, Soliva-Fortuny R, Welti-Chanes J et al (2016) Combined effect of pulsed light, edible coating and malic acid dipping to improve fresh-cut mango safety and quality. Food Control 66:190–197
6. Charles F, Vidal V, Olive F et al (2013) Pulsed light treatment as new method to maintain physical and nutritional quality of fresh-cut mangoes. Innov Food Sci Emerg Technol 18:190–195
7. Beckles DM (2012) Factors affecting the postharvest soluble solids and sugar content of tomato (*Solanum lycopersicum* L.) fruit. Postharvest Biol Technol 63(1):129–140
8. Bower C (2007) Postharvest handling, storage, and treatment of fresh market berries. Food Sci Technol N Y Marcel Dekker 168:261
9. González-Aguilar GA, Zavaleta-Gatica R, Tiznado-Hernández ME (2007) Improving postharvest quality of mango 'Haden' by UV-C treatment. Postharvest Biol Technol 45(1):108–116
10. Sivakumar D, Fallik E (2013) Influence of heat treatments on quality retention of fresh and fresh-cut produce. Food Rev Int 29(3):294–320
11. Aveno JL, Orden MEM (2004) Hot water treatment of mango: a study of four export corporations in the Philippines. KMITL Sci Technol J 4:1685–2044
12. Ozkan IA, Akbudak B, Akbudak N (2007) Microwave drying characteristics of spinach. J Food Eng 78(2):577–583
13. El Ghaouth A, Wilson CL, Wisniewski M et al (2002) Biological control of postharvest diseases of citrus fruits. Marcel Dekker, New York, pp 289–312
14. Ricke SC (2003) Perspectives on the use of organic acids and short chain fatty acids as antimicrobials. Poult Sci 82:632–639
15. Razzaq K, Singh Z, Khan AS et al (2016) Role of 1-MCP in regulating 'Kensington Pride' mango fruit softening and ripening. Plant Growth Regul 78(3):401–411
16. Sanginga PC (2009) Innovation Africa: enriching farmers' livelihoods. Earthscan
17. Lalel HJD, Singh Z, Tan SC (2003) Aroma volatiles production during fruit ripening of 'Kensington Pride' mango. Postharvest Biol Technol 27(3):323–336
18. Kim Y, Brecht JK, Talcott ST (2007) Antioxidant phytochemical and fruit quality changes in mango (*Mangifera indica* L.) following hot water immersion and controlled atmosphere storage. Food Chem 105(4):1327–1334
19. Kim K, Ng K, Rugg-Gunn PJ et al (2007) Recombination signatures distinguish embryonic stem cells derived by parthenogenesis and somatic cell nuclear transfer. Cell Stem Cell 1(3):346–352
20. González-Aguilar GA, Wang CY, Buta JG (2000) Maintaining quality of fresh-cut mangoes using antibrowning agents and modified atmosphere packaging. J Agric Food Chem 48(9):4204–4208
21. Martínez-Ferrer M, Harper C, Pérez-Muntoz F et al (2002) Modified atmosphere packaging of minimally processed mango and pineapple fruits. J Food Sci 67(9):3365–3371
22. Chien PJ, Sheu F, Yang FH (2007) Effects of edible chitosan coating on quality and shelf life of sliced mango fruit. J Food Eng 78(1):225–229

Study on Shelf Life Prediction of Edible Oil in BOPP/VMPET/CPP Flexible Packaging

Yayun Liu, Qifeng Chen and Guangxue Chen

Abstract This experiment explores changes of peroxide value and acid value of the edible oil that is over-wrapped with BOPP/VMPET/CPP composite film and then stored at 35 °C, 50% RH, and predicts the shelf life of edible oil under this condition by means of dynamics equation. At the same time, the barrier property of the film was evaluated by measuring the initial permeability and moisture permeability of the film and the tensile properties at different time periods. Research shows that peroxide value and acid value in the edible oil increase with time linearly, tensile properties of the soft package decreased gradually with time. Under the experimental conditions, the oil packed in BOPP/VMPET/CPP composite film had a shelf life of about 70 days, far below that of polyester plastic bottle packaging in the market for sale, so the application of flexible packaging in edible oil still need to explore.

Keywords Edible oil · Peroxide value · Acid value · Shelf life
Tensile property

1 Introduction

Oil plays an important role in increasing the color, aroma and taste of food, and it is also one of the indispensable nutrition sources. Oil is easy to rancidity during storage, not only cause deterioration of taste, smell and health quality index, but also caused some changes in color and transparency. Peroxide generated by the reaction of oil and oxygen in the air is the primary product by the effect of oxidation of lipids, it is highly active, can be quickly decomposed into aldehydes, ketones and oxides, resulting in deterioration of oil [1]. In general, a slight increase of peroxide value and acid value will not cause harm to human health, but if the acid value and

Y. Liu · Q. Chen · G. Chen (✉)
State Key Laboratory of Pulp and Paper Engineering, South China University of Technology, Guangzhou, Guangdong, China
e-mail: chengx@scut.edu.cn

P. Zhao et al. (eds.), *Applied Sciences in Graphic Communication and Packaging*, Lecture Notes in Electrical Engineering 477,
https://doi.org/10.1007/978-981-10-7629-9_64

peroxide value is too high, the body will lead to gastrointestinal discomfort, diarrhea and liver damage, long-term consumption can cause a lot of diseases. So we usually take the acid value and peroxide value as important health indicators to detect and control.

Shelf life refers to the term of quality guarantee of pre-packed food under the storage conditions as stated on its labels [2]. In food engineering, chemical reaction kinetics is used as the basic theoretical model to establish the food quality function to predict the shelf life of food [3]. The shelf life of food is usually affected by four factors: chemical composition, processing method, packaging and storage conditions. These four factors have been included in hazard analysis and critical control points [4]. Currently, the main packaging forms of edible oil on the market is glass bottle, polyester plastic bottle and flexible packaging, the glass bottle has good oxygen barrier and gas barrier, which can effectively prolong the shelf life of edible oil, but at the same time there are deficiencies such as frangibility and high cost. Polyester plastic bottles have become a mainstream packaging form because the raw materials are widely available and the processing is simple, but it's too costly for small-capacity edible oil. The latest development packaging is flexible packaging, which not only has a lower cost, but also has a more convenient processing and transportation, shows a broad development prospect for small-capacity edible oil. Based on the above background, the shelf life of edible oil was studied under the condition of flexible packaging to provide a certain guidance and reference for the actual production and sales.

2 Materials and Methods

2.1 Materials and Reagents

BOPP/VMPET/CPP composite film, edible oil, distilled water, chloroform-acetic acid, saturated solution of potassium iodide, phenolphthalein, starch indicator, 0.002 mol/L standard solution of sodium thiosulfate, 0.02 mol/L potassium hydroxide standard solution.

2.2 Instruments and Equipment

Instruments and Equipment: VAC-V2 air permeability tester, XLW intelligent electronic tensile machine, TSY-T1 moisture permeability tester.

2.3 Experimental Method

2.3.1 Accelerated Oxidation Storage of Edible Oils

In the circulation of edible oil, the highest temperature is generally 35 °C, in order to test the feasibility of using flexible packaging in the worst circulation environment and shorten the experimental cycle, we put the number of composite film bagged edible oil in the constant temperature and humidity drying box (35 °C, 50% RH) for accelerated oxidation test, take three bagged edible oil samples for parallel experiment at regular intervals to determine the tensile properties of packaging bag of edible oil, and the content of peroxide value and acid value in edible oil.

2.3.2 Experimental Determination of Peroxide Value and Acid Value

According to GB5009.37 "*Method for analysis of hygienic standard of edible vegetable oil*", determine peroxide value and acid value by iodimetry and KOH titration respectively, take three bagged edible oil samples for parallel experiment at regular intervals, and average the results.

2.3.3 BOPP/VMPET/CPP Packaging Performance Test

Take the initial BOPP/VMPET/CPP packing bag, air permeability is determined by differential pressure according to the GB/T1038 2000 standard; moisture permeability is determined by cup methodon according to the GB/T1037-1988 standard; the initial tensile properties is determined by XLW intelligent electronic tensile machine. After the experiment begin, take three bags of edible oil at regular intervals, wipe the bag clean and cut into 150 mm long, 20 mm wide strips to determine the tensile properties on an electronic tensile machine after finished the determination of acid value and peroxide value.

3 Results and Analysis

3.1 Barrier Properties of Film

The air permeability and moisture permeability of the packaging could affect the content of gas and moisture in the package, which further affects the shelf life of food. In the moisture permeability and air permeability experiment, the initial oxygen permeability of the composite membrane is 1.9 cm^3/m^2 d · 0.1 MPa, the initial moisture permeability is 2.67 g/m^2 d, we can see that the visible barrier

properties of the composite membrane is very good, this is because the polyester aluminized coating contained in the composite film has good barrier property [5].

3.2 Changes of Peroxide Value and Acid Value in Edible Oil

The changes of acid value and peroxide value content in edible oil during the storage could be shown in Figs. 1 and 2 respectively.

It can be seen from Figs. 1 and 2, in the process of storage, the content of peroxide value and acid value in the edible oil increased with time gradually, the oxidative rancidity follow the first order chemical reaction kinetics model, the equation is as follows:

$$P^t = P^0 \bullet e^{kt} \tag{1}$$

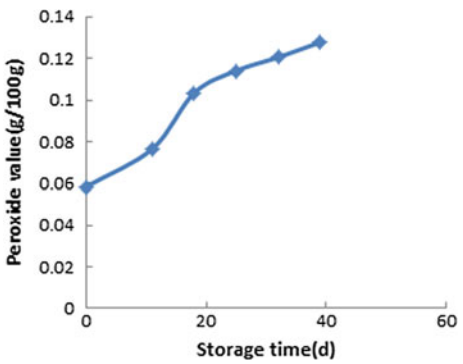

Fig. 1 The peroxide value of edible oil in different time periods

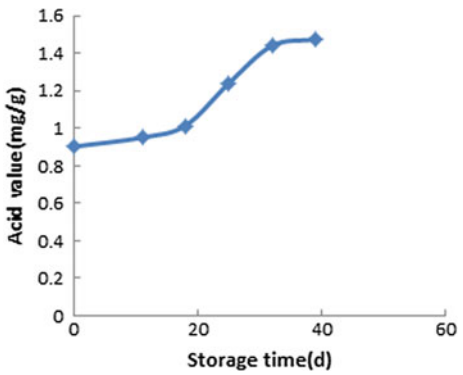

Fig. 2 The acid value of edible oil in different time periods

Table 1 Rancidity rate equation of edible oil on accelerated oxidation conditions

	Regression equation	Regression coefficient
Peroxide value	$P_t = 0.0584e^{0.0206t}$	0.9185
Acid value	$P_t = 0.9028e^{0.0145t}$	0.9239

where, P^t—the peroxide value or acid value of edible oil at regular intervals; P^0—initial peroxide value or acid value of edible oil; k—the rate constant of peroxide value or acid value in edible oil; t—storage days of edible oil.

Take the data in Figs. 1 and 2 into the formula (1) for linear regression, we can calculate the generation rate of peroxide value and acid value in edible oil wrapped with BOPP/VMPET/CPP is 0.0206 and 0.0145 respectively at 35 °C, 50% RH, the regression equation and regression coefficient are shown in Table 1, as we can see, the two regression coefficient is greater than 0.9, indicating a good linear relationship between the two, the two indexes of peroxide value and acid value can well response quality changes of edible oil.

The hygienic standard of edible vegetable oil in China (GB/T5009.37-2003) stipulates that the peroxide value of edible vegetable oil should not exceed 0.25 mg/g, and the acid value should not exceed 4.0 mg/g. According to the critical value, the above kinetic equation can be used to calculate the shelf life of edible oil: t(POV) = 70 days, t(AV) = 102 days. Because the critical value of the above two indexes must be satisfied, the smaller value of the two can be obtained, finally we could get the storage time of edible oil is about 70 days. The oil shelf life is short and the analysis of the main reasons are as follows:

(1) The composite film we used has a lower oxygen barrier and moisture resistance than the polyester plastic bottles, so the shelf life has been reduced compared to the oil in the market.
(2) As a result of the accelerated oxidation of 35 °C experimental conditions, the oxidation reaction of peroxide value and acid value accelerated.
(3) In this experiment, the three side seal is used in the process of packaging edible oil, artificial operation cannot grasp the appropriate heat sealing time, so the heat sealing effect is not good, which results in the decrease of the actual oxygen resistance and the short shelf life of edible oil.

3.3 Tensile Properties of Film

The tensile strength and elongation at break of BOPP, VMPET, CPP differ greatly, so in the tensile test, some composite films were broken in succession or broken at the bayonet, the available data is limited, resulting in deviation of tensile data [6]. On the whole, however, the tensile stress and elongation at break of the composites

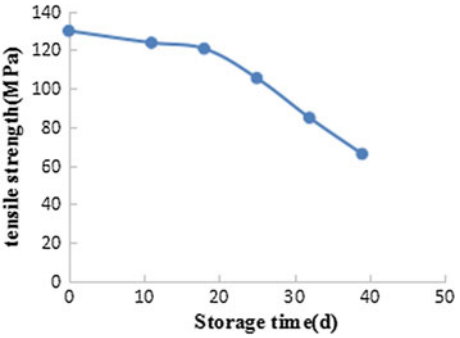

Fig. 3 The tensile strength of edible oil in different time periods

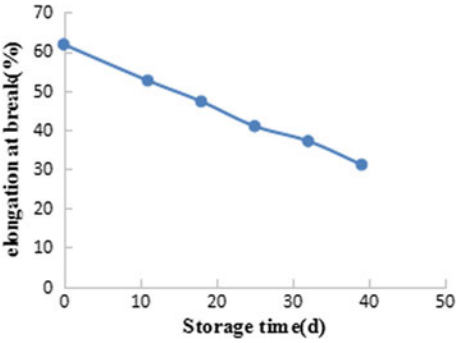

Fig. 4 The elongation at break of edible oil in different time periods

decrease with the increase of time, which indicates that the tensile properties of the composite films become worse, as shown in Figs. 3 and 4.

Analysis of the following factors:

(1) As viscoelastic materials, there is a great relationship between the mechanical relaxation process of plastics and temperature, when the temperature rise, thermal motion of polymer chain segments increased and relaxation process accelerated, the deformation and low strength will be shown in the process of drawing [6]. The first test was carried out at room temperature, the samples were then placed in an environment with a temperature of 35° and a humidity of 50%, the relaxation process of the composite film was accelerated under this condition.

(2) Both sides of the film are fully exposed to oil, the film will dissolve and swell in oil, the degree of dissolution and swelling is also related to the structure and properties of oil. As a result, the physical and chemical properties of the film will be changed to a certain extent, which results in the change of tensile properties.

(3) Plastic in the atmosphere will gradually aging during storage, the aging strength will decline with time.

4 Conclusions

The shelf life is critical to the safety of consumers, through the study of food shelf life, we can not only predict the shelf life of food, but also find out the key factors through the study of the key factors that affect the quality of food to provide a theoretical basis for prolonging the shelf life of food [7]. Through the experiment, it was found that the linear degree of content of peroxide value and acid value in edible oil and time is very high, indicating the two indexes of oxidation and acid value can be used as an important characterization of edible oil quality changes. And with the change of time, the peroxide value and acid content gradually increased, the tensile properties of thin films gradually decreased. From the predicted results of the shelf life, we can see the shelf life of edible oil over-wrapped with BOPP/VMPET/CPP composite film is short at 35 °C, 50% RH, so it is necessary to take more in-depth study to seek a kind of edible oil soft packaging with stronger barrier.

Acknowledgements This research was financially supported by the Guangdong Provincial Science and Technology Project (2016070220045) and the State Key Experimental Funding Project (2016c01).

References

1. Zhi H, Han Y (2004) Studies on shelf life of oil food. China Packag Ind 11:67–68
2. Kilcast D, Subramaniam P (2000) The stability and shelf-life of food. Wood Head Publishing Limited
3. Juan Li, Liping Zhang, Zhang Lei J (2009) Study of shelf life prediction model of food packaging based on kinetics theory. Packag Eng 12:118–120
4. Labuza TP (1980) Temperature/enthalpy/entropy compensation in food reactions. Food Technol 34(2):67
5. Liu Z, Wan F, Liu Y, Li H (2012) Study on permeability of plastics with different materials for food packaging. Packag Food Mach 06:26–28
6. Mahendrasingam A, Blundell DJ, Parton M et al. (2005). Time resolved study of oriented crystallization of poly(1acticacid) during rapid tensile deformation. Polymer **46**(16):6009–6015
7. Yu X, Che X, Zhang L (2011) Prediction shelf life of food—a review. Food Res Dev 3:84–87

Study on Migration Model of Phthalic Acid Esters Plasticizer in Different Kinds of Plastic Bottle Packaging Materials

Yan Zhang, Yueyue Qi and Qingbao Wei

Abstract With the social development and the scientific progress, more and more plastic products have been used as packaging materials, especially the plastic bottles widely used in food package. With the plasticizers used in different kinds of plastic bottle packaging materials PE, PET, and PVC as study objects, the migrations of plasticizers into food simulants were studied by univariate analysis (food simultant kind, temperature and time) in this paper. Meanwhile, the migration model of phthalic acid esters in different plastic bottle packaging materials was established on the basis of Fick diffusion, and finally the migration of phthalic acid esters plasticizer into the food simulant was stimulated numerically by means of MATLAB software to forecast the migration rule and quantity of phthalic acid ester plasticizer.

Keywords Plastic bottle · Phthalic acid esters · Migration model

1 Introduction

During the manufacture of plastic bottles, some additives are often added to improve the processing performance, such as anti-oxygen, plasticizer [1] and heat stabilizer. Such micromolecule additives may move into the food when the food package contacts with the food, and thus affect the food quality and safety. Therefore, we shall check if any component of chemical additive can move into the food, and test if the migration quantity reaches the level endangering the human health. Recently, the scientists have established the corresponding mathematical

Y. Zhang · Y. Qi · Q. Wei (✉)
Henan University of Animal Husbandry and Economy, Zhengzhou, China
e-mail: zzmzwqb@163.com

Y. Zhang
Zhengzhou Sanquan Foods Co., Ltd, Zhengzhou, China
e-mail: yanzhang12@yeah.net

P. Zhao et al. (eds.), *Applied Sciences in Graphic Communication and Packaging*, Lecture Notes in Electrical Engineering 477,
https://doi.org/10.1007/978-981-10-7629-9_65

model to forecast and evaluate the migration action and quantity of additives, to avoid the heavy transfer tests and simplify the safety study of food plastic bottles.

In this paper, the migration action of plasticizer into the food simulant was studied by univariate analysis (kind, temperature and time of food simulant), and finally the migration of phthalic acid esters plasticizer into the food simulant was stimulated numerically by means of MATLAB software to forecast the migration rule and quantity of phthalic acid ester plasticizer, and make comparison.

2 Mathematical Model

Figure 1 illustrates the transmission between polymer and food. In most cases, diffusions are unstable, i.e. the concentration of polymer at one point varies with time. The second Fick diffusion law can describe the migration process from polymer to food simulant, as the following Eq. (1) [2]:

$$\frac{\partial C_p}{\partial_t} = D_p \frac{\partial^2 C_p}{\partial x^2} \tag{1}$$

where, C_P(mg/kg) indicates the concentration of migration component in packaging material at time t(s) and position x(cm); D_P(cm^2/s) indicates the diffusion coefficient of migration component in packaging material.

In order to simplify the process, we usually use the following assumptions [3]:

(i) The migration components are distributed evenly in the foodcontact material; The food contact material has no swelling;
(ii) The migration occurs just between the food contact material and the food without any diffusion into air or other medium;
(iii) The diffusion speed of migration component in food is much faster than that in the food contact material;
(iv) The diffusion coefficient is always a constant at any moment of diffusion process.

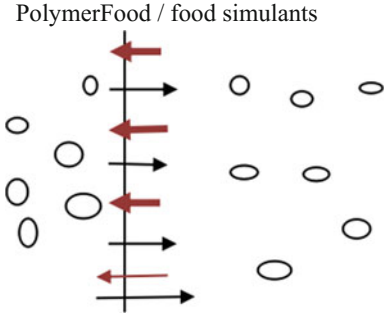

Fig. 1 Diffusion process of polymers

2.1 Mathematical Model of Diffusion

The polymer material can be classified into infinite package and finite package in accordance with its size; the volume of food simulant can be classified into infinite food and finite food. In this paper, the migration of finite polymer in the finite food volume is analyzed [4].

Through simplifying Eq. (1), the ratio Eq. (2)—Piringer model of the quantity of additives migrating from the material into the food from time 0 to t and the migration quantity at the moment of migration balance is calculated by Fourier series [5].

$$\frac{M_{F,t}}{M_{F,\infty}} = 1 - \sum_{n=1}^{\infty} \frac{2\alpha(1+\alpha)}{1+\alpha+\alpha^2 q_n^2} \exp\left(-\frac{Dq_n^2}{L^2}t\right) \tag{2}$$

where, $M_{F,t}$ indicates the migration quantity of migration component moving from the macromolecule food contact material to the food at a moment; $M_{F,\infty}$ indicates the migration quantity of migration component moving from the macromolecule food contact material to the food at the moment of balance; L indicates the thickness of macromolecule food contact material; D indicates the diffusion coefficient of migration component in the food; α indicates the mass ratio of migration component in food and in the film at the moment of balance, which is a physical quantity related with the balance constant. q_n is the nonzero positive root in the equation $\tan q_n = -\alpha q_n$.

$$\alpha = \frac{V_F}{V_P K_P} \tag{3}$$

VF indicates the volume of food; V_P indicates the volume of food packaging material; parameter K_P indicates equilibrium constant.

$$K_P = \frac{C_{P,\infty}}{C_{F,\infty}} \tag{4}$$

$C_{F,\infty}$ indicates the concentration of migration component in the food at the end of migration; $C_{P,\infty}$ indicates the concentration of migration component in the material at the end of migration.

For the short-time migration, Eq. (2) is simplified to:

$$\frac{M_{F,t}}{M_{F,\infty}} = \frac{2}{L}\left(D\frac{t}{\pi}\right)^{1/2} \tag{5}$$

With the migration test data, the diffusion coefficient D can be calculated through Eq. (5).

3 Migration of Phthalic Acid Esters in Different Food Simulants

3.1 Migration of DBP in Different Food Simulants

Phthalic acid esters are contained in all PE, PET and PVC materials which are common in our life. The dibutyl phthalate (DBP) among the phthalic acid esters is selected as the study object, whose molecular formula is $C_{16}H_{22}O_4$, and molecular weight is 278.34 g/moL.

The migration rules in different food simulants of DBP used in three kinds of plastic bottles (yogurt bottle, mineral water bottle and edible oil bottle), and the influence of temperature and time on migration during this process were studied. During this test, the following food simulants were selected: acetic acid solution with volume content of 4%, distilled water and n-hexane.

3.1.1 Raw Materials

The plastic bottle manufactured by a yogurt plant is marked as "A", is milk white, and has a volume of 250 mL, a surface area of about 1.95 dm^2, a wall thickness of 0.010 cm, and a plastic density of about 0.97 g/cm^3 (calculated as per the wall thickness). The weight of packaging material in contact with food is 12 g, and the weight of contained food is 300 kg.

The selected plastic bottle manufactured by a drinking water plant is marked as "B", is light blue and transparent, and has a volume of 350 mL, a surface area of about 2.50 dm^2, a wall thickness of 0.012 cm, and a plastic density of about 1.40 g/cm^3 (calculated as per the wall thickness). The weight of packaging material is 16 g, and the weight of contained mineral water is about 350 g.

The plastic bottle manufactured by an edible oil plant is marked as "C", is colorless and transparent, and has a volume of 1000 mL, a surface area of about 5.2 dm^2, a wall thickness of 0.040 cm, and a plastic density of about 1.48 g/cm^3 (calculated as per the wall thickness). The weight of packaging material is 40 g, and the weight of contained edible oil is 950 g.

3.1.2 Simulation Test Conditions

(1) The stimulated storage temperature of yogurt is 5 and 10 °C, the simulated storage time is from 1 to 20 days, and the simulating agent is the acetic acid solution with volume content of 4%.
(2) The stimulated storage temperature of drinking water is 15 and 35 °C, the simulated storage time is from 1 to 20 days, and the simulating agent is the distilled water.

(3) The stimulated storage temperature of edible oils 20, 30 and 40 °C, the simulated storage time is from 1 to 80 days, and the simulating agent is the n-hexane.

4 Migration Result and Discussion

4.1 Migration Result of Yogurt Test

The DBP content was detected by the national standard GB/T21911. It was 2.03 μg/dm^2. With the aforementioned migration model, known conditions and Eq. (5), the calculated diffusion coefficient of DBP in the high-density polyethylene was 2.2 × 10^{-11} cm^2/s.

With $M_{F,t} = 0.129t^{1/2}$ at 10 °C and $M_{F,t} = 0.067t^{1/2}$ at 5 °C, the migration curve was drawn, as shown in Fig. 2. It can be seen that at the same storage temperature, the migration quantity of DBP from packaging material to acetic acid aqueous solution increases as time goes on, and finally tends to balance. Upon the same storage time, the higher the storage temperature is, the more the migration quantity is. For example on the 18th storage day, the migration quantity is almost 0.24 μg/dm^2 at 5 °C, but nearly 0.55 μg/dm^2 at 10 °C.

4.2 Migration Result of Drinking Water Test

The DBP content in unit area was 2.16 μg/dm^2. With the aforementioned migration model, known conditions and Eq. (5), the calculated diffusion coefficient of DBP at 15 and 35 °C was 2.51 × 10^{-12} and 2.82 × 10^{-11} cm^2/s respectively. With

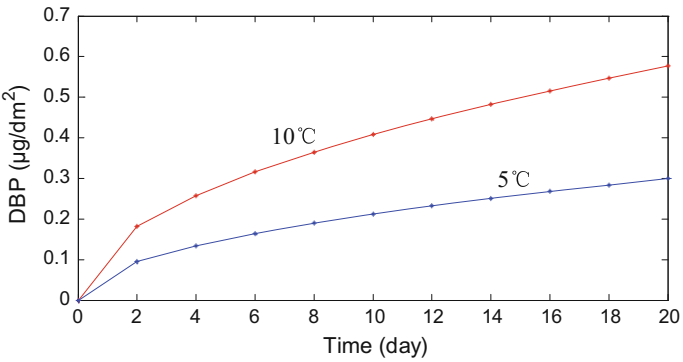

Fig. 2 Packing DBP moving toward acetic acid aqueous solution

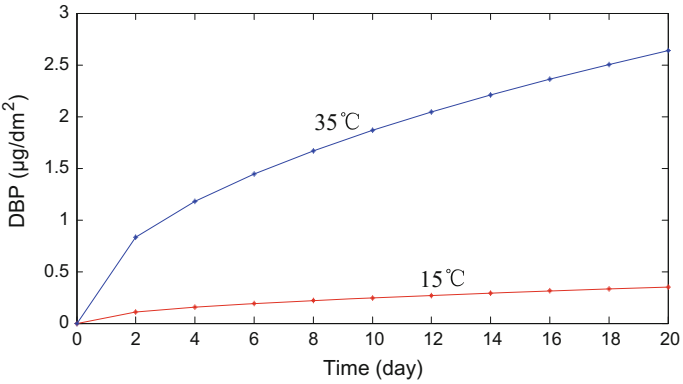

Fig. 3 Packing DBP moving toward distilled water

$M_{F,t} = 0.078t^{1/2}$ at 15 °C and $M_{F,t} = 0.590t^{1/2}$ at 35 °C, the migration diagram of DBP from PET to distilled water was drawn (Fig. 3).

The test proves that if the drinking water is stored for a long period at a temperature, DPB in the package may enter the distilled water via migration; the higher temperature will affect the migration rate, for example on the 20th day, the migration rate of DBP at 35 °C is eight times of that at 15 °C.

4.3 Migration Result of Edible Oil Test

The DBP content in unit area was 286 μg/dm^2. With the aforementioned migration model and known conditions, the calculated diffusion coefficient of DBP at 20 and 30 °C was 2.98×10^{-12}, 3.26×10^{-11} and 4.08×10^{-11} cm^2/s respectively. Under the given conditions, the edible oil packaging material contacted the food simulant (n-hexane) for a period; afterwards, the test data were recorded as per the suitable time interval, and the migration content equation was estimated. With $M_{F,t} = 2.84t^{1/2}$ at 20 °C, $M_{F,t} = 23.09t^{1/2}$ at 30 °C and $M_{F,t} = 42.10t^{1/2}$ at 40 °C, the migration curve was drawn, as shown in the following picture.

From Fig. 4, the migration quantity of DBP from PVC to n-hexane increases as time goes on, and gradually tends to balance. The test proves that after a long-period storage at a temperature, DBP in package enters the edible oil via migration so it is recommended to select the small package of edible oil, and keep the edible oil at the room temperature and far away from the heat source such as stove.

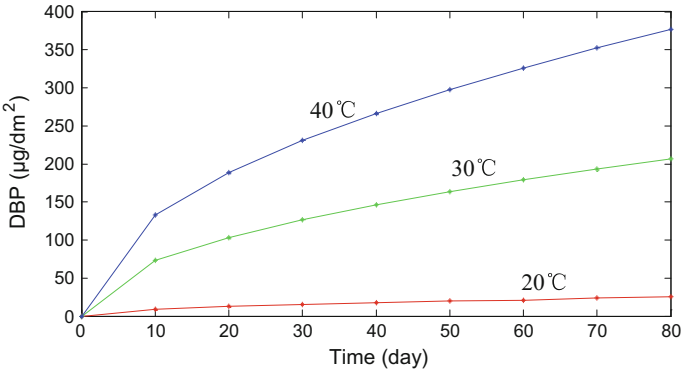

Fig. 4 Trends in the migration of DBP to n-hexane in packaging

5 Conclusions

After long-period storage at a temperature, DBP in package can enter the product via migration. Temperature has obvious influence on the DBP stability. At the low temperature, DBP has a higher stability; after the temperature rises, the plasticizer in every simulant becomes unstable at the high temperature. The influence of temperature change during the yogurt test is higher than other two test.

The migrations of plasticizer DBP in acid, waterborne and lipoid food simulant liquids are compared and analyzed. The migration ratio in lipoid food simulant liquid is highest, and the migration is most obvious. The influence of high temperature and high fat on the migration of DBP is highest. The higher the temperature is, the higher the migration content is so it is recommended to store the temperature at the room temperature, and keep the product away from heat source such as stove.

References

1. Leda-Coltro JBP, Afonso da Costa P et al (2014) Migration of conventional and new plasticizers from PVC films into food simulants: a comparative study. Food Control 44 (10):118–129
2. Brandsch J, Mercea P et al (2002) Migration modelling as a tool for quality assurance of food packaging. Food Addit Contam 19(1):29–41
3. Oriella-Gennari SA, Magali-Monteiro A (2012) GC-FID method to determine styrene in polystyreneglasses. Food Anal Method 6(5):1411–1420
4. Albert-Guart MW, Mezquid A, Lacorte S et al (2013) Migration of plasticisers from Tritan™ and polycarbonate bottles and toxicological evaluation. Food Chem 141(3):373–380
5. Grob K (2008) The future of simulants in compliance testing regarding the migration from food contact materials into food. Food Control 19(3):263–268

Application of Barcode Technology in Warehouse Management of Printing and Packaging Enterprises

Chongchong Jia, Junyan Huang, Qinghua Gao and Shilei Luo

Abstract In order to study the application of barcode technology in warehouse management of printing and packaging enterprises, an overview of barcode technology and feature is briefly stated, the significance and effect of the barcode technology applied in warehouse management of printing and packaging enterprises are analyzed, and the composition of barcode warehouse management system and its specific application in raw material warehouse management of printing and packaging enterprises are described. Thus it is concluded that the barcode warehouse management system not only highly improves the level of inventory management and reduces the labor intensity, but also decreases the total storage cost and improves inventory management efficiency with its application in warehouse management of printing and packaging enterprises. Simple, safe, quick and efficient barcode warehouse management system is becoming more proficient, and it will play an increasingly significant role in the warehouse management of printing and packaging enterprises.

Keywords Barcode technology · Printing and packaging enterprises
Warehouse management · Application

1 Introduction

China's printing and packaging enterprises are usually small and medium-sized, the warehouse management of various raw materials and auxiliary materials and finished goods includes multiple aspects in the daily management. Meanwhile it is a complex and important management process with high added-value. But in today's information age,

C. Jia · J. Huang (✉) · Q. Gao · S. Luo
School of Light Industry and Chemical Engineering,
Dalian Polytechnic University, Dalian, Liaoning, China
e-mail: 643217963@qq.com; huangjunyan@126.com

S. Luo
Dalian Huacheng Printing Co., Ltd, Dalian, China

P. Zhao et al. (eds.), *Applied Sciences in Graphic Communication and Packaging*, Lecture Notes in Electrical Engineering 477,
https://doi.org/10.1007/978-981-10-7629-9_66

many printing and packaging enterprises still do not get rid of the traditional management style, especially many enterprises' warehouse management still remain the manual operation method, by which all data of warehousing-in or warehousing-out are entered, verified and determined by warehouse manager one by one. This kind of warehouse management style can directly lead to the possibility of errors caused by human factors, and the high pressure and high risk of management [1], which seriously affects the efficiency of warehouse management, increases the cost of warehouse management and restricts sustainable development of printing and packaging enterprises [2].

The meaning and function of barcode technology were analyzed and its implementation and application method in the warehouse management of printing and packaging enterprises were summed up in this paper. After the actual application, the warehouse management of printing and packaging enterprises has realized digitization and informatization so that the warehouse material management becomes more timely, more accurate and more efficient, which greatly improves the warehouse material management level of printing and packaging enterprises, reduces the labor intensity and inventory costs, and improves the modern management level and market competitiveness of enterprises.

2 Meaning of Applying Barcode Technology in Warehouse Management of Printing and Packaging Enterprises

The barcode technology is an automatic identification technology based on computer technology, and it is designed for the automatic scanning of information [3, 4]. Using barcode technology can collect vast information quickly and accurately, thus it is suited to logistics management system which has higher requirements for collecting information massively and high-speed. Meanwhile, it is also a technological base which can realize the automation and real-time management of material purchase, arrival, warehouse-in, storage, custody, warehouse-out and query [5].

Especially, if printing and packaging enterprises could not accept the model of modern warehouse management with the increasing fierceness of market competition, they would be eliminated in the fierce market competition. So the use of barcode technology is very important.

The barcode technology plays an important role in warehouse management of printing and packaging enterprises.

(1) Coding material and printing barcode labels not only track material but also help the enterprises get ready for material in time and enhance productivity [6], and the funds will be used reasonably. Meanwhile, if we use uniform material coding which is based on the industrial standards, we will not get into trouble because of the chaotic material management.
(2) Printing the barcode labels which not only track material but also establish complete material files for material.

(3) We can stock, sell and store material by using barcode technology so that we can reduce the inventory cost effectively.
(4) We can establish an inspection records about the quality of the material and product, and make the quality inspection reports by identification of product. And it is closely related to purchase and indent, so that we can establish an assessment system for suppliers.

3 Application of Barcode Technology in Warehouse Management of Printing and Packaging Enterprises

3.1 Barcode Warehouse Management System of Printing and Packaging Material

The barcode warehouse management system of printing and packaging material is a management system which can manage warehouse by using barcode automatic identification technology. The whole system includes database server, client software, wireless network, PDA and barcode label printer. Taking material management in printing and packaging enterprises for example, its system operation process is shown in Fig. 1.

3.2 Application of Barcode Warehouse Management System in Warehouse Management of Printing and Packaging Material

3.2.1 System Management

Only the administrators have permission to manage the system, and the system assigns authority according to account groups. Usually, the system establishes many accounts and makes them belong to different account groups. Every account possesses the permission which belong to its location. Assigning the permissions to user group is shown in Fig. 2. Besides, the system can also add new users and carry out user management.

3.2.2 Basic Data Management

Some basic data, such as ordinary data, unit of measurement, warehouse data, location data, picking data, material data, finished goods data, supplier's files, customer's files and production workshop's data can be increased, deleted and compiled in the system. The page of material information management is shown in Fig. 3.

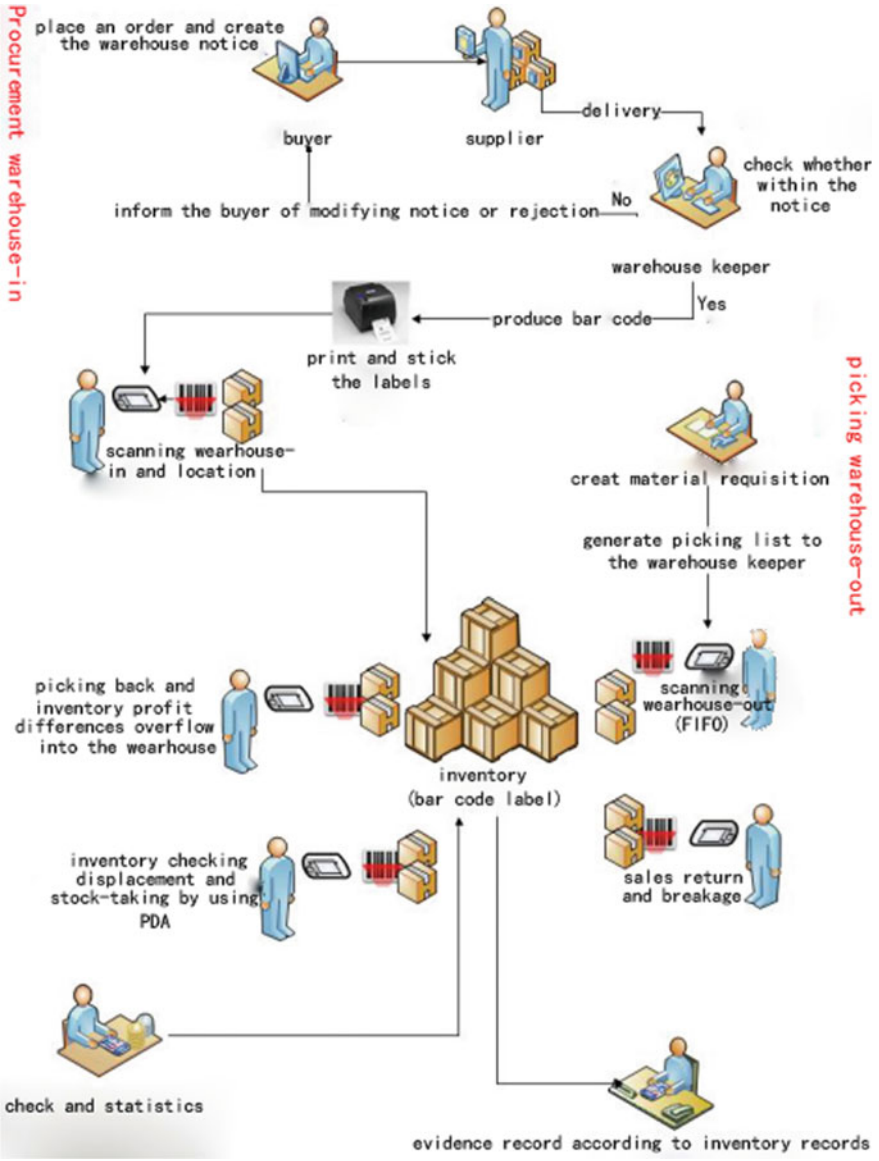

Fig. 1 The operation process of barcode warehouse management system of printing and packaging material

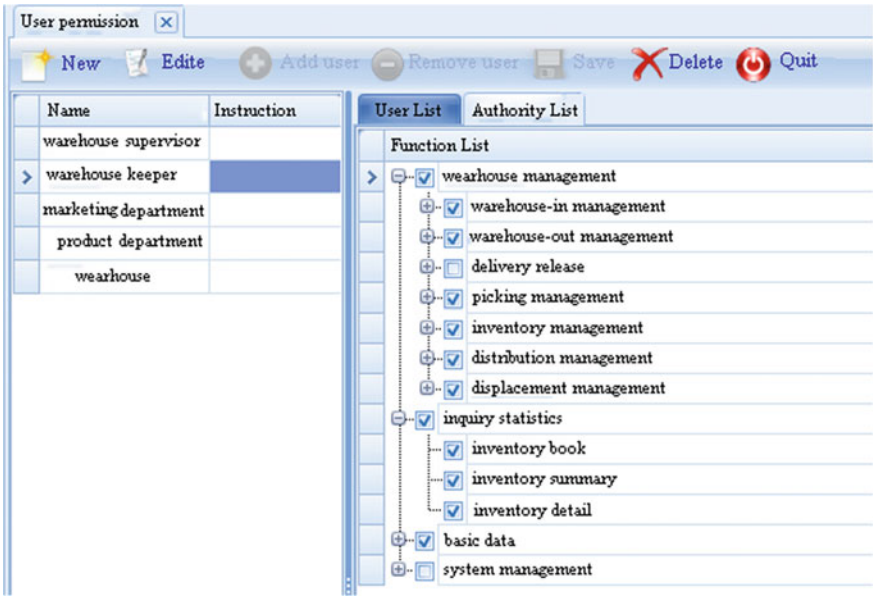

Fig. 2 Assigning the permissions to user group

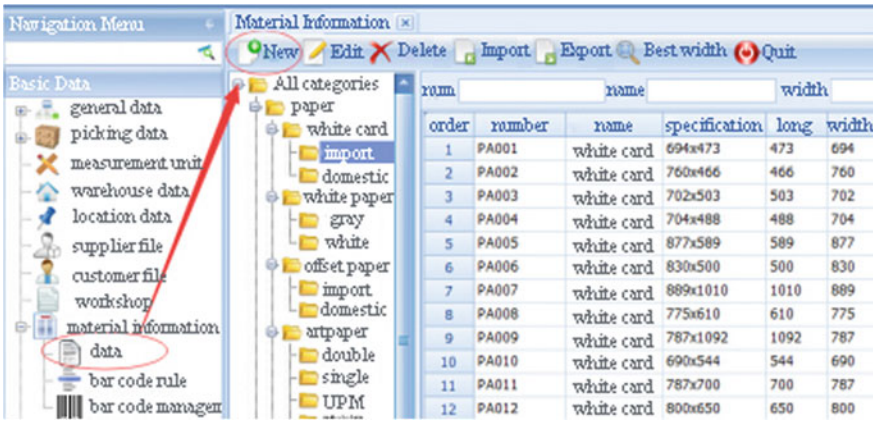

Fig. 3 Material information management

3.2.3 Generating Barcode and Printing Labels

Generating barcode and printing labels are original works for the only identification of material in barcode system. And we have to operate carefully and avoid making mistakes in material data and information, such as supplier batch number, production batch, packing specification, suppliers' name, raw material production date

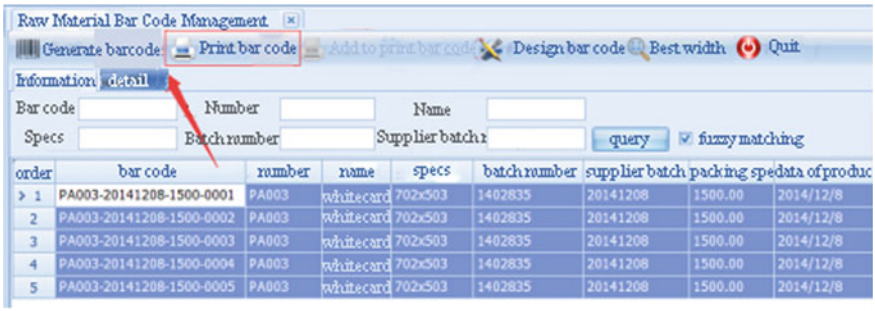

Fig. 4 Generating barcode and printing labels

and so on. The labels after being printed are stuck on location where can scan easily and the raw material after being scanned is stored. The page of generating barcode and printing barcode labels is shown in Fig. 4.

3.2.4 Inventory Management

The inventory management is a main functional module, such as warehouse-in management, warehouse-out management, evidence record, displacement, inventorying and so on.

Warehouse-in management includes raw material storage (purchase), picking back into storage, storage overflow. Firstly, we can generate and print barcode for the purchased raw material. Secondly, we need to stick the labels. Finally, we can put raw material into storage according to the warehouse notice. The warehouse warrant is closely related to the warehouse notice. The material without the notice will not be allowed to put into storage and the PDA will also warn in time. The page of warehouse-in management is shown in Fig. 5.

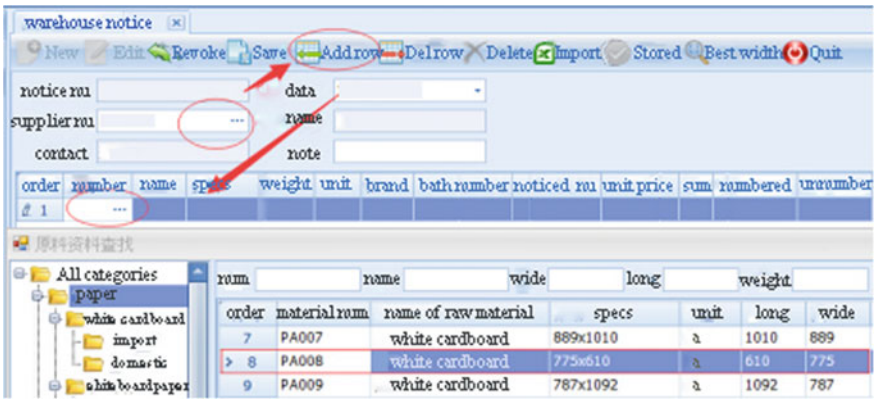

Fig. 5 Warehouse-in management

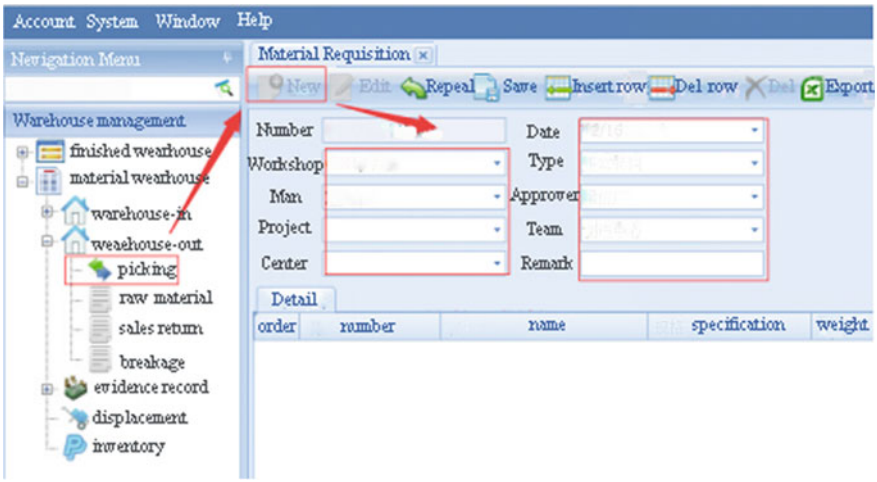

Fig. 6 Warehouse-out management

Warehouse-out management includes picking out-of storage, sales return, breakage, especially the picking out-of storage. We can make the raw material out-of storage by scanning according to the material requisition. The goods without material requisition will not be allowed to put out storage and the PDA will also warn in time. The page of warehouse-out management is shown in Fig. 6.

Displacement management is a shifting operation which can move the goods from one warehouse to another in the barcode system. Firstly, we should increase the displacement lists in the inventory management system. Next, we need to seek corresponding displacement number to scan after saving. Finally, we need to affirm that whether the data and physical objects are fitted after the displacement and finish displacement operation.

When the data and physical objects are discrepant, we need to use inventorying management system after running a longer period of time. The way of inventorying is that we can click the lists by the computer client software firstly, and next we can scan corresponding barcode by PDA. Finally, we can know the profit and loss situation so as to make effective measures. The page of inventorying management is shown in Fig. 7.

Inventory checking can inspect the data and physical objects for uniformity and the operation is run only by PDA.

3.2.5 Inquiry Statistics

The inquiry statistics includes shelf life warning, inventory warning, inventory checking, warehouse-in details, warehouse-out details, inventory daily report,

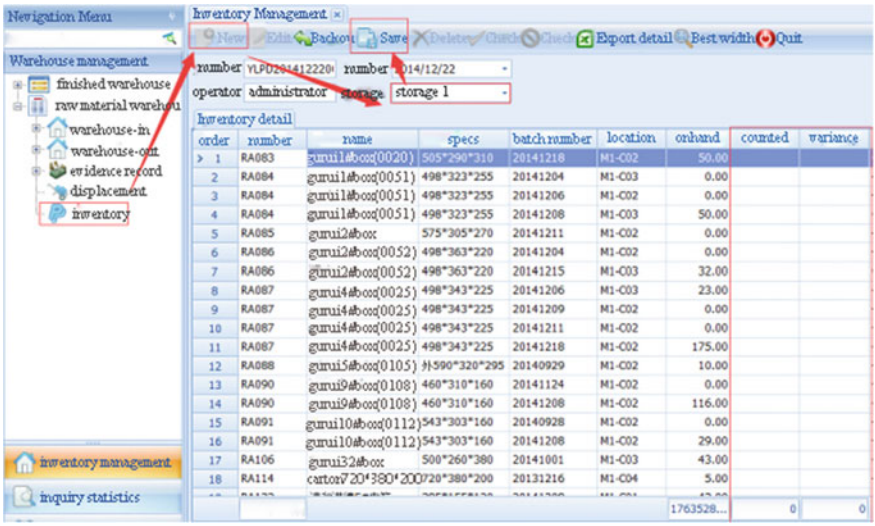

Fig. 7 Inventorying management

non-voucher statement, non-payment statement and total arrears statement. Most statements can be exported in Excel tables formats.

4 Conclusions

The barcode technology has many advantages such as easiness, convenience, collecting information quickly and largely, reliability, flexibility and freedom. And it has penetrated into all sectors of production management and circulation, and the application of barcode technology is maturing gradually in warehouse management of printing and packaging enterprises. We firmly believe that if the enterprises adopt the technology in warehouse management according to their own situation, they will achieved good results and remarkable economic benefits.

References

1. Chen J (2008) Exploring the applicationof bar codetechnologyin inventory management system. Railw Purch Logist J 7:30–31
2. Zheng X, Yu X (2013) The application of wireless bar code scanning technology in small and medium enterprise warehouse management. Mod Econom Inf 3:55–56
3. Xue H (2015) Problems and countermeasures in the application of bar code technology in warehouse management. Chin Market **37**:26–27
4. Wang S, Shen Y (2015) The application of bar code technology. Chin Market 45:59–61

5. Wang G (2014) The application of bar code scanning technology in material warehouseman agement. Chin Foreign Entrep **17**:227
6. He X (2015) The introduction of the application of bar code technology in logisticsenterprises in China. Great Eastern **12**:210

Part VI
Mechanical Engineering and Numerical Control Technology

Fault Diagnosis in Printing Press Roller Bearing Based on Spectrum Kurtosis and Improved EEMD

Jialing Zhang, Jimei Wu, Yan Wang, Kaikai Li, Li'e Ma and Fan Zhao

Abstract According to the problem of the poor rolling bearing signal under the high background noise of the high-speed printing press, the fault diagnosis method is proposed, which is combined with Ensemble Empirical Mode Decomposition (EEMD) and spectrum kurtosis (SK). Due to the traditional EEMD has the defect of directly rejecting the high-frequency section impact fault signal, this paper adopts the three principles of EEMD noise reduction to carry on the improvement processing. The fault vibration signal of rolling bearing was decomposed into several intrinsic mode functions (IMF) under different characteristic scales with EEMD. The false signal of IMF is removed by the three principles of noise reduction to construct a new fault signal. In this paper, the bandwidth and central frequency of band-pass filter are selected by SK method and the envelope spectrum of the filtered signal is analyzed. The result shows that the combination of improved EEMD and SK method are effective than the method of conventional EEMD and envelope analysis. It promotes fault recognition rate of printing press bearings.

Keywords Spectrum kurtosis · Ensemble empirical mode decomposition Rolling bearing · Fault diagnosis

J. Zhang · J. Wu (✉) · K. Li · L. Ma · F. Zhao
Faculty of Printing, Packaging Engineering and Digital Media Technology, Xi'an University of Technology, Xi'an, China
e-mail: wujimei@xaut.edu.cn

Y. Wang (✉)
Faculty of Civil Engineering and Architecture, Xi'an University of Technology, Xi'an, China
e-mail: wangyan@xaut.edu.cn

P. Zhao et al. (eds.), *Applied Sciences in Graphic Communication and Packaging*, Lecture Notes in Electrical Engineering 477,
https://doi.org/10.1007/978-981-10-7629-9_67

1 Introduction

The Rolling bearing is an important part of the packaging equipment, but it is easy to damage. When the bearing has pitting corrosion, abrasion, corrosion and other surface damage, the damage will be aggravated rapidly, which will seriously affect the operation of the machine and the quality of finished products [1]. Therefore, the analysis of the bearing vibration signal is widely concerned in the state monitoring and fault diagnosis.

When the rolling bearing is fault, the vibration signal is non-stationary and nonlinear. The ability to extract fault characteristics from vibration signals is the key to mechanical fault diagnosis. Huang [2] proposed the method of a time-frequency analysis Ensemble Empirical Mode (EMD). But one of the most prominent problems is endpoint effect and pattern of aliasing [3]. Wu and Huang [4] proposed Ensemble Empirical Mode Decomposition (EEMD) method. Cheng [5] introduced EEMD and local Hilbert energy spectrum into rolling bearing fault diagnosis. Noise reduction of EMD based on cross-correlation and kurtosis criteria is used to preprocess sampled signals in document [6], and the high-frequency resonance components are highlighted. On this basis a method of mutual information was proposed to eliminate false components in document [7]. Wu et al. [8] mentioned that EEMD, relative analysis and kurtosis are used to extract the fault feature.

Spectral Kurtosis (SK) first proposed by Dwyer makes up power spectrum method to extract signal detection and transient component faults. Wu et al. [9] proposed a hybrid method based on the EEMD.SK and improved morphological filtering method to improve bearing diagnosis. In this paper, the fault diagnosis method that combined with improved EEMD and SK is proposed.

2 Improved EEMD Method

2.1 EEMD Decomposition Principle

The EEMD decomposition is based on the EMD algorithm, the Gaussian white noise is added to the signal in order that the signal components are automatically mapped to the scale plane associated with background white noise [10]. The EEMD decomposition process is listed as follows:

Step 1: According to the standard deviation of signal to set the number of integration and add the white noise amplitude.

Step 2: To add white noise signal is decomposed by EMD. The intrinsic mode functions (IMFs) are decomposed into several characteristic time dimensions and the residual component.

Step 3: Repeat Step 1–2 M times. Add a random normal distribution of the white noise-added signal sequence every time.

$$x_i(t) = \sum_{j=1}^{K} c_{ij}(t) + r_i(t) \tag{1}$$

where $x_i(t)$ indicates the ith white noise-added signal, $c_{ij}(t)$ indicates the ith added Gaussian white noise to decompose the jth IMF, $r_i(t)$ indicates residual component.

Step 4: The overall decomposition of the IMF obtained by the average operation to get the final signal.

$$x(t) = \sum_{j=1}^{K} c_j(t) + r(t) \tag{2}$$

where $c_j(t)$ represents the IMF component of signal is decomposed by EEMD.

2.2 Three Principles of Noise Reduction

Mutual information is used to measure the similarity of two random signals. The larger mutual information of two random signals provided, the greater amount of information provided by each other. Kurtosis is a dimensionless parameter, which is sensitive to impulsive signals. When the rolling bearing is faultless, the kurtosis index value is approximately equal to three [11]. The correlation coefficient is used to judge the decomposed IMF original signal and determine the authenticity of the IMF.

3 Spectral Kurtosis

The Spectral Kurtosis (SK) can be used to measure a process at particular frequency on the probability density function of peak value [12]. The $Y(t)$ is assumed to be a non-stationary signal and respondent system of a strictly white noise $X(t)$ with varying time system $h(t, s)$. Wold-Cramer decomposition of non-stationary signal $Y(t)$ is as follow:

$$Y(t) = \int_{-\infty}^{+\infty} e^{j2\pi fi} H(t, f; \varpi) dX(f) \tag{3}$$

where $H(t,f;\varpi)$ represents frequency f in the process of complex envelop, mainly determined by the output results ϖ, and $dX(f)$ represents the spectral process of the signal $X(t)$. Spectral kurtosis is defined as:

$$K_Y(f) \stackrel{\Delta}{=} \frac{C_{4Y}(f)}{S_{2Y}^2(f)} = \frac{S_{4Y}(f)}{S_{2Y}^2(f)} - 2, \quad f \neq 0 \tag{4}$$

4 Analysis of Bearing Failure of Offset Press

4.1 Experimental Setup and Data Acquisition

In this experiment, the vibration signals are collected from GUANGHUA650 offset printing press roller in Shaanxi Province, printing and packaging engineering key laboratory. The failure of this test is the bearing cage damage. The test bench consists of LMS Vibration test system, GUANGHUA650 offset printing press and PCB333B30 accelerometer. The vibration testing system and faulty bearings are shown in Figs. 1 and 2. The accelerometer is mounted on inking roller bearing outer ring. The parameter of bearing is given in Table 1. The ball pass frequency on

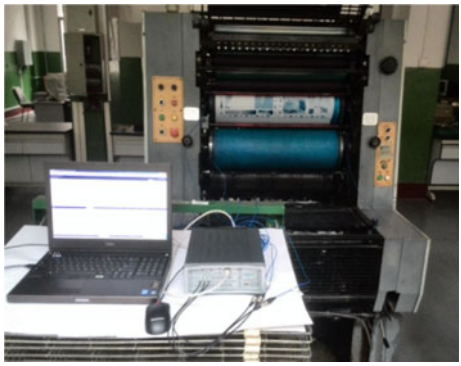

Fig. 1 Vibration testing system

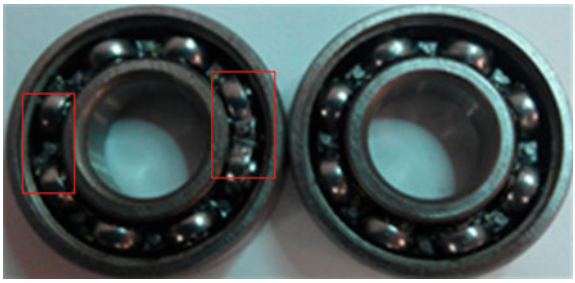

Fig. 2 The tested bearing

Table 1 The parameter of the tested bearing

Parameter	Value
Bearing specs	NSK 6001Z
Inner race diameter	12 mm
Outer race diameter	28 mm
Shaft rotation speed	7200r/h

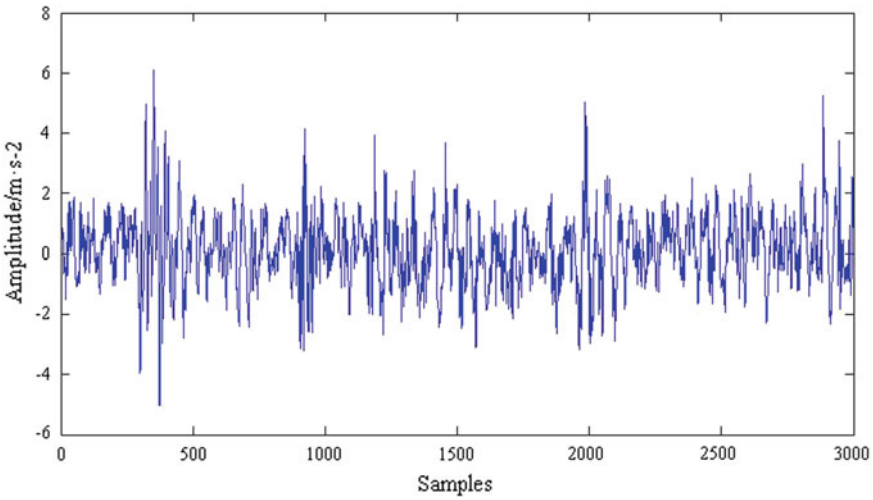

Fig. 3 Original vibration signal

the outer race, ball pass frequency on the inner race and cage frequency are respectively 6.4, 9.6, 0.8 Hz.

4.2 Ensemble Empirical Mode Decomposition

The raw vibration signals of faulty bearings are shown in Fig. 3. The fault of the rolling bearing in the picture cannot be identified. The pulse associated with the function of the fault bearing is almost masked by noise. The EEMD method is adopted to decompose the vibration signal; the result is given in Fig. 4.

The three principles of noise reduction index are shown in Table 2. The correlation coefficients and mutual information values larger are chosen based on analysis of the three principles of noise reduction. Thus, the IMF1–IMF4 are selected to get the new composite signal. The time domain waveform of the composite signal is shown in Fig. 5.

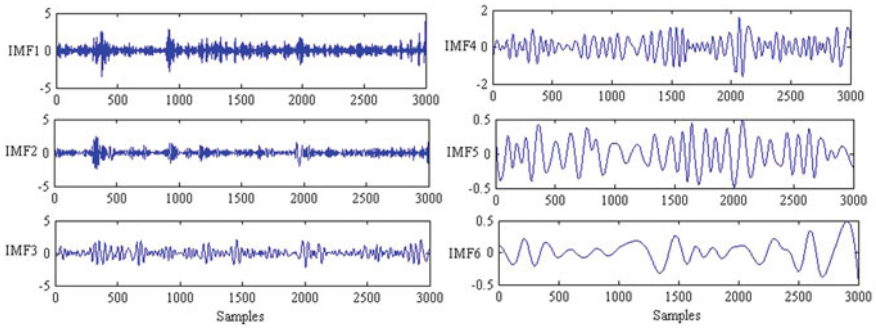

Fig. 4 The first six IMFs

Table 2 The correlation coefficient, kurtosis and mutual information value of the first six IMFs

IMFs	IMF1	IMF2	IMF3	IMF4	IMF5	IMF6
Correlation coefficient	1.2590	1.4236	1.8802	1.8500	1.0827	1.9280
Kurtosis	8.7432	7.0298	3.6081	3.0757	2.2711	2.1610
Mutual information	0.4785	0.4407	0.6198	0.4378	0.1548	0.1148

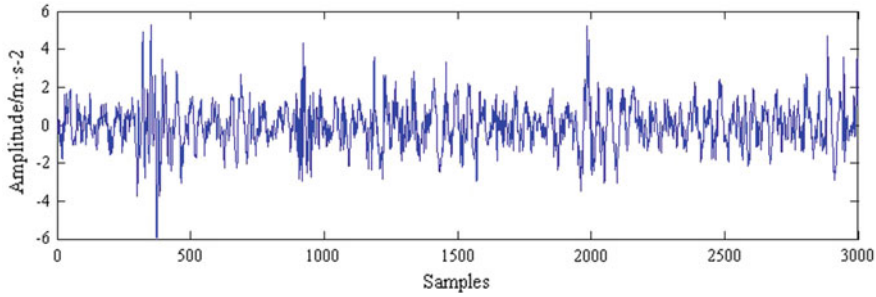

Fig. 5 Synthetic signal

4.3 Spectrum Kurtosis Analysis

The optimal band-pass filter based on spectral kurtosis is used to filter the composite signal. The Fast kurtosis is shown in Fig. 6. It is found that the maximum kurtosis value of the synthesized signal is 32.2, the optimal bandpass filter center frequency is 950 Hz. The bandwidth of the composite signal is filtered to get the envelope spectrum. The envelope spectrum is shown in Fig. 7.

The frequency of 0.782 Hz and multiplication frequency (1.580 Hz and 2.563 Hz) can be found in the envelope spectrum, the amplitude is gradually decreased at the frequency of the fault frequency. By comparing the characteristic frequency of the rolling bearing fault, the cage failure frequency is 0.8 Hz.

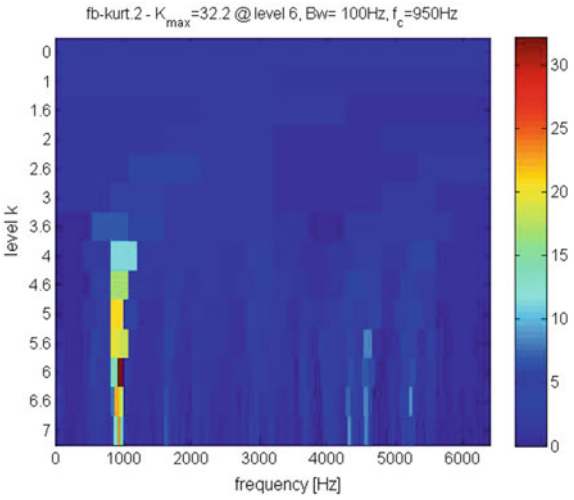

Fig. 6 Fast spectral kurtosis

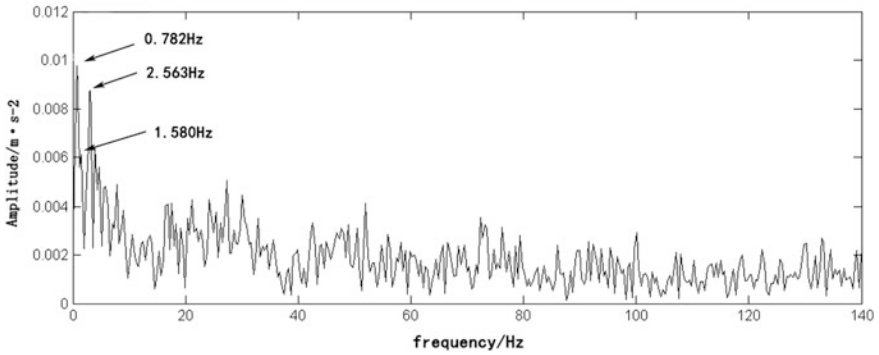

Fig. 7 The envelope spectrum

Therefore, it is possible to diagnose the bearing's cage failure, the validity of the method in the actual.

5 Conclusions

In this paper, the fault signal is extracted from lots of background noises by the method which is combined with the improved ensemble empirical mode decomposition (EEMD) and spectral kurtosis (SK). The results show that:

(1) The improved EEMD and the spectral kurtosis method improve the false component of EMD and the bandwidth of the empirical selection filter. It can accurately determine the fault impact component and effectively extract the true component of the fault signal. The combination of two methods play the respective advantages;
(2) The failure of the bearing failure cage is analyzed by this method. It can accurately extract the characteristic frequency, the modulation characteristic frequency and the sidebands. It is easy to be applied in the actual working conditions meanwhile it can effectively improve the fault recognition rate of printing press bearings.

Acknowledgements The author gratefully acknowledges the support of the National Natural Science Foundation of China (No. 61671376, 11272253 and 11202159). This work is also supported by the Natural Science Foundation of Shaanxi (Grant No. 2016JM5023).

References

1. Zhang X, Li CL et al (2016) Application and extension of empirical mode decomposition in fault diagnosis for rolling bearings. Bearing 6:59–62
2. Huang NE, Shen Z, Long SR et al (1998) The empirical mode decomposition and the Hilbert spectrum for nonlinear and non-stationary time series analysis. Proced R Soc Lond Ser A 454 (1971):903–995
3. Ma WP, Zhang JH et al (2015) Applications of improved empirical mode decomposition in machinery fault diagnosis. J Vibrat Measure Diagnosis 35(4):637–644
4. Wu ZH, Huang NE (2009) Ensemble empirical mode decomposition: a noise-assisted data analysis method. Adv Adapt Anal 1(1):1–41
5. Cheng JS, Yu DJ et al (2008) Application of frequency family separation method based upon EMD and local Hibert energy spectrum method to gear fault diagnosis. Mech Mach Theory 43(6):712–723
6. Su WS, Wang FT et al (2010) Application of EMD denoising and spectral kurtosis in early fault diagnosis of rolling element bearings. J Vibrat Shock 29(3):18–21
7. Jing SX, Yang X et al (2016) Fault feature extraction of rolling bearing based on improved EMD and spectrum kurtosis. Mech Transmiss 40(4):125–128
8. Wu GH, Ding JM et al (2016) The EEMD-RA-KU method on diagnosis of bearing fault. J Mech Strength 38(6):1167–1172
9. Wu XT, Yang M et al (2015) Bearing fault diagnosis using EEMD and improved morphological filtering method based on kurtosis criterion. J Vibrat Shock 34(2):38–44
10. Singh Jaskaran, Darpe AK et al (2017) Bearing damage assessment using Jensen-Rényi divergence based on EEMD. Mech Syst Signal Process 87:307–339
11. Hu AJ, Ma WL et al (2012) Rolling bearing fault feature extraction method based on ensemble empirical mode decomposition and kurtosis criterion. Proc CSEE 32(11):106–111
12. Wang YX, Xiang JW et al (2016) Spectral kurtosis for fault detection, diagnosis and prognostics of rotating machines: a review with applications. Mech Syst Signal Process 66:679–698

Modeling of the Robot of Sleeve Installation for Printing Machine

Xinpei Li, Shaozhong Cao, Hongfeng Xiang, Zhengjie Jin and Mingdao Wang

Abstract Due to the low efficiency in the installation of the bearing sleeves for the printing machines and the great damages to the operators in the installation process, a robot of sleeve installation for printing machine is proposed. For the robot, the precise measurement and accurate model are the basis of completing assembly. Firstly we resolve the inverse solutions by the kinematics of 6-DOF parallel platform (Jiang et al. in Proc Inst Mech Eng 8, 2015, [1]) to obtain the Jacobian matrix between the thrust of rods and generalized force. Secondly, the kinetic equation among thrust rods, the platform position and speed is established by Lagrange equation (Sirouspour and Salcudean in Trans Robot Autom 17:173–182, [2]). Finally, the strategy of using probe-into measure tooling is put forward, which establishes the relative pose relations among the readings of probe-into measure tooling, platform and the through-holes. Thus, eventually, we can obtain the relationship between the readings of probe-into measure tooling and the thrust of rods, laying a foundation for the accurate controlling of robot based on probe-into measure tool.

Keywords Printer precision assembly robot · 6-DOF platform
Inverse kinematics · Lagrange · Probe-into measuring tooling

1 Introduction

Bearing sleeve installation of large printing machine is quiet difficult assembly operation in the whole printing industry. The weight of the printing machine sleeve is up to more than 40 kg; the precision in the installation process requirements

X. Li (✉) · S. Cao (✉) · H. Xiang · Z. Jin · M. Wang
Beijing Key Laboratory of Signal and Information Processing for High-End Printing Equipment, Beijing Institute of Graphic Communication, Beijing, China
e-mail: 1247741680@qq.com

S. Cao
e-mail: caoshaozhong@bigc.edu.cn

P. Zhao et al. (eds.), *Applied Sciences in Graphic Communication and Packaging*, Lecture Notes in Electrical Engineering 477,
https://doi.org/10.1007/978-981-10-7629-9_68

Fig. 1 Robot of sleeve installation for printing machine

5 μm or less; the sleeve passes must be in frozen state where the temperature is less than subzero 30 °C and installed within 10 min. At present, bearing sleeve installation of large printing machine can only rely on manual installation. Although workers work hard, the actual assembly accuracy cannot meet the requirements of assembly accuracy and it does great damage to workers. So it is necessary to realize the intelligent assembly of the printing machine sleeve. As a kind of high-precision and micro-motion platform, the 6-DOF parallel platform [3, 4] has many advantages such as stable structure, no under-drive operation and no accumulation of joint error. Therefore, based on the 6-DOF parallel platform, a Robot of Sleeve Installation for Printing Machine has been proposed, the robot is as shown in Fig. 1.

The Robot of Sleeve Installation for Printing Machine is mainly composed of 6-DOF parallel platform, a probe-into measuring tool and a control console, etc. The probe-into measuring tool is one of the key technologies to realize the precise installation of the printing machine sleeve. And its diameter is slightly smaller than the through-hole in the printing machine. The probe-into measuring tool is equipped with two sets of position-sensors, each of which has three position-sensors symmetrically distributed on the circular surface for measuring the distance to the through-hole, as shown in Fig. 2.

The process of assembly work is as follows:

(1) Install the probe-into measuring tool in the 6-DOF parallel platform at the origin position;
(2) The 6-DOF parallel platform is used to move for the probe-in measuring tool getting to the general position of the through hole by inputting the height of the

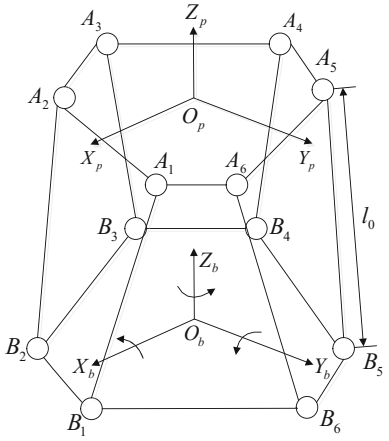

Fig. 2 Schematic diagram of a 6-DOF parallel platform

through-hole of the wall panel, and then insert the probe-into measuring tool into the printing machine body assembly hole by rough measurement;

(3) We can get six readings by the probe-in measuring tool, then feedback to the control system, which control the motion of 6-DOF parallel platform according to the data obtained, making the axis of the probe-in measuring tool is aligned with the axis of the through-hole in the printing machine. Then the control system records and saves the location of the platform at this moment;

(4) Move the 6-DOF parallel platform to start position, remove the probe-into measuring tool and mount the frozen sleeve on the 6-DOF parallel platform. Then control the robot to move to the position of the computer memory. Thus the printing press sleeve installation is successfully completed.

To realize installation process, it is necessary to carry out the precise calibration, modeling and control of the robot. In the paper, main job is modeling for the Robot of Sleeve Installation for Printing Machine, including kinematics, dynamics modeling of 6-DOF parallel platform and probe-in measuring tool modeling.

2 Kinematic and Dynamic Modeling of the 6-DOF Parallel Platform of the Robot of Sleeve Installation for Printing

In order to solve the spatial position relation of the 6-DOF parallel platform, the static and dynamic coordinate systems are established represented by $O_b - X_bY_bZ_b$ and $O_p - X_pY_pZ_p$.

Figure 2 A1–A6—The upper joint of the six rods; B1–B6—The lower joint of the six rods; A1B1–A6B6—The every rod; l_0—The initial length between the upper and lower joint of the rod.

The position of the rods on moving platform is denoted by point matrix $\boldsymbol{A}$, where $\boldsymbol{A}_i(i = 1, 2, \ldots 6)$ represent the upper joint of the six rods in the $O_p - X_pY_pZ_p$. And matrix $\boldsymbol{B}$ represent the position of the lower joint of the six rods in the $O_b - X_bY_bZ_b$.

For convenience, three successive Euler angles [6] are defined as follows: First rotate about the base X axis by the angle α. Next rotate about the base Y axis by the angle β. Finally rotate about the mobile Z axis by the angle γ. In this case, the homogeneous orientation matrix (T) of the platform is given by:

$$\boldsymbol{T} = \begin{bmatrix} c\beta c\gamma & -c\alpha s\gamma + s\alpha s\beta c\gamma & s\alpha s\gamma + c\alpha s\beta c\gamma & x_0 \\ c\beta s\gamma & c\alpha c\gamma + s\alpha s\beta s\gamma & -s\alpha c\gamma + c\alpha s\beta s\gamma & y_0 \\ -s\beta & s\alpha c\beta & c\alpha c\beta & z_0 \\ 0 & 0 & 0 & 1 \end{bmatrix} \tag{1}$$

where $c\beta$ and $s\beta$ represent $cos\beta$ and $sin\beta$ in the pager.

The position of the rods on the moving platform is denoted by point matrix G after moving in the $O_b - X_bY_bZ_b$, $\boldsymbol{G} = [g_{ij}]_{4\times 6} = \boldsymbol{T} \cdot \boldsymbol{A}$. The generalized vector coordinates describing the position and orientation of the platform are defined as $\boldsymbol{q} = [\,x \quad y \quad z \quad \alpha \quad \beta \quad \gamma\,]^T$.

The length between the upper and lower joint of the rod after the platform moving is given by

$$l_i = \sqrt{\sum_{k=1}^{3} (g_{ki} - b_{ki})^2} \quad (i = 1, 2, \ldots, 6) \tag{2}$$

The relation between flex quantity $\dot{l}$ and $\dot{\boldsymbol{q}}$ is given by:

$$\dot{l} = \boldsymbol{J}\dot{\boldsymbol{q}} \tag{3}$$

where $\boldsymbol{J}$ is Jacobian matrix of the robot between the velocity and acceleration if $\boldsymbol{q}$ is invertible matrix. By inverse solution, we know:

$$\dot{\boldsymbol{q}} = \boldsymbol{J}^{-1}\boldsymbol{v} \tag{4}$$

We resolve the inverse solutions by the kinematics of 6-DOF parallel platform to obtain the Jacobian matrix between the thrust of rods and generalized force:

$$\boldsymbol{F} = \boldsymbol{J}^T\boldsymbol{\tau} \tag{5}$$

We get the dynamic equation by Lagrange:

$$\boldsymbol{M}(\boldsymbol{q})\ddot{\boldsymbol{q}} + C(\boldsymbol{q}, \dot{\boldsymbol{q}})\dot{\boldsymbol{q}} + G(\boldsymbol{q}) = \boldsymbol{J}^T\boldsymbol{\tau} \tag{6}$$

3 The Using Strategy and Modeling of the Probe-in Measuring Tool

3.1 Using Strategy of the Probe-in Measuring Tool

When the probe is inserted into the body through-hole after rough measurement, establish the relationship between the current position and the target position of the 6-DOF parallel platform by the readings of probe-in measuring tool. Control the robot to move for making sure the central axis of the probe-in measuring tool and through-hole in the printing machine completely coincident. The moving strategy for probe-in measuring tool is as follows.

Firstly, fix a point represented N in the probe-in measuring tool that is the intersection of the central axis line and the front plane of the tool shown in the picture 3. Next adjust the 6-DOF parallel platform to make center axes between probe-in measuring tool and through-hole in the printing machine parallel. Finally, control the 6-DOF platform to translate for coincidence.

3.2 Modeling of the Probe-in Measuring Tool

The structure of the probe-into measuring tool is shown in Fig. 3.

In order to establish the relationship between the probe-in measuring tool and the 6-DOF parallel platform, create a new coordinate system $O - xyz$: the center line of the probe-in measuring tool is z axis, the position of the over upper position-sensors is x axis, the y axis is established according to the right hand rule. The position of the six position-sensors is shown in Fig. 4.

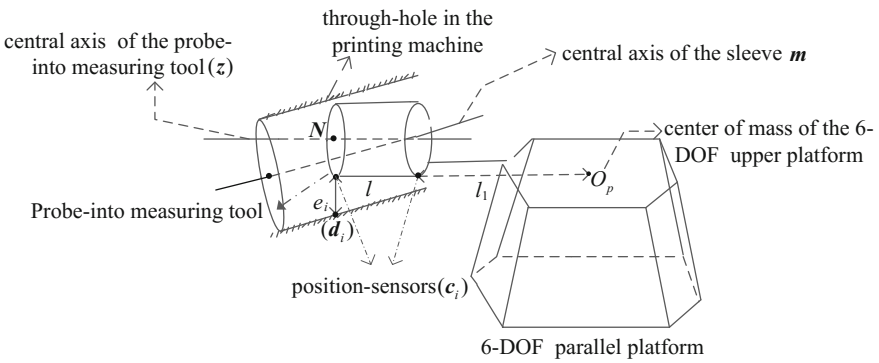

Fig. 3 Main view of probe-in measuring tool of the robot of sleeve installation for printing machine

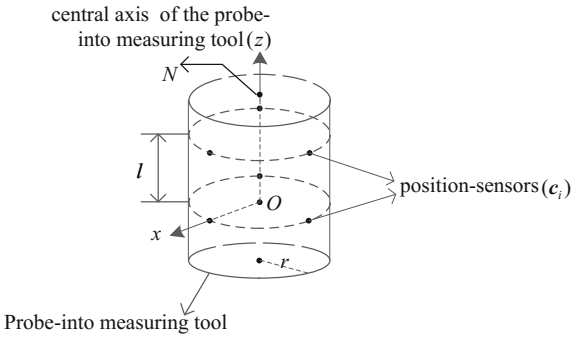

Fig. 4 Schematic diagram of the measurement platform

Where r is the radius of the probe-in measuring tool, l is the length between the two sets of position-sensors, l_1 is the length between the extremes of the probe-in measuring tool and center of mass of the 6-DOF upper platform, l_2 is the length between the bottom of the probe-in measuring tool and the 6-DOF upper platform, $\boldsymbol{c}_i (i = 1, 2, 3, 4, 5, 6)$ are the position of the position-sensors, e_i are the readings through the position-sensors, $\boldsymbol{d}_i$ are the position of the position-sensors hitting the inner wall of the sleeve.

And we can easily obtain the position of the position-sensors in the new coordinate system $O - xyz$ through geometric data mentioned above given by:

$$\begin{aligned}
&\boldsymbol{c}_1 = \left(-\frac{1}{2}r, \frac{\sqrt{3}}{2}r, 0\right), \quad \boldsymbol{c}_2 = \left(-\frac{1}{2}r, -\frac{\sqrt{3}}{2}r, 0\right) \\
&\boldsymbol{c}_3 = (r, 0, 0) \quad \boldsymbol{c}_4 = \left(-\frac{1}{2}r, \frac{\sqrt{3}}{2}r, l\right) \\
&\boldsymbol{c}_5 = \left(-\frac{1}{2}r, -\frac{\sqrt{3}}{2}r, l\right), \quad \boldsymbol{c}_6 = (r, 0, l)
\end{aligned} \tag{7}$$

According to geometric relationship of the mechanical structure, we obtain the position of the position-sensors hitting the inner wall of the sleeve. Calculation is given by:

$$\begin{aligned}
&\boldsymbol{d}_1 = \left(-\frac{1}{2}r - \frac{1}{2}e_{11}, \frac{\sqrt{3}}{2}r + \frac{\sqrt{3}}{2}e_{12}, 0\right), \quad \boldsymbol{d}_2 = \left(-\frac{1}{2}r - \frac{1}{2}e_{21}, -\frac{\sqrt{3}}{2}r - \frac{\sqrt{3}}{2}e_{22}, 0\right), \\
&\boldsymbol{d}_3 = (r + e_{31}, 0, 0), \quad \boldsymbol{d}_4 = \left(-\frac{1}{2}r - \frac{1}{2}e_{41}, \frac{\sqrt{3}}{2}r + \frac{\sqrt{3}}{2}e_{42}, l\right) \\
&\boldsymbol{d}_5 = \left(-\frac{1}{2}r - \frac{1}{2}e_{51}, -\frac{\sqrt{3}}{2}r - \frac{\sqrt{3}}{2}e_{52}, l\right), \quad \boldsymbol{d}_6 = (r + e_{61}, 0, l)
\end{aligned} \tag{8}$$

The center coordinates $\boldsymbol{M}_1$ and $\boldsymbol{M}_2$ can be obtained by the position of the position-sensors hitting the inner wall of the sleeve.

$$\boldsymbol{M}_1 = \frac{\boldsymbol{d}_1 + \boldsymbol{d}_2 + \boldsymbol{d}_3}{3}, \quad \boldsymbol{M}_2 = \frac{\boldsymbol{d}_4 + \boldsymbol{d}_5 + \boldsymbol{d}_6}{3} \tag{9}$$

And $\boldsymbol{m} = \boldsymbol{M}_1 - \boldsymbol{M}_2$, where $\boldsymbol{m} = (m_x, m_y, m_z)$ is the unit vector of central axis of the sleeve. The calculation is given by:

$$\begin{aligned} m_x &= \frac{1}{6}(2e_{61} - 2e_{31} + e_{11} - e_{41} + e_{21} - e_{51}), \\ m_y &= \frac{\sqrt{3}}{6}(e_{42} - e_{12} + e_{22} - e_{52}), \\ m_z &= l \end{aligned} \tag{10}$$

With the origin O as a fixed point, make a straight line that length is l parallel to the sleeve. $\boldsymbol{C} = (x_c, y_c, z_c)$ is the endpoint of the line segment. Because of the line segment being parallel and a fixed length, we know $|\boldsymbol{C}|^2 = x_c^2 + y_c^2 + z_c^2 = l^2$, $\frac{x_c}{m_x} = \frac{y_c}{m_y} = \frac{z_c}{m_z} = \lambda$, we can calculate λ and $\boldsymbol{C}$ given by

$$\begin{aligned} \lambda &= \frac{l}{\sqrt{m_x^2 + m_y^2 + m_z^2}}, \mathbf{C} \\ &= \left(\frac{lm_x}{\sqrt{m_x^2 + m_y^2 + m_z^2}}, \frac{lm_y}{\sqrt{m_x^2 + m_y^2 + m_z^2}}, \frac{l^2}{\sqrt{m_x^2 + m_y^2 + m_z^2}} \right) \end{aligned} \tag{11}$$

The homogeneous orientation matrix ($\boldsymbol{R}_1$) between the platform's coordinate system and the probe-in measuring tool' coordinate system is given by

$$\boldsymbol{R}_1 = \begin{bmatrix} 0 & -\frac{\sqrt{2}}{2} & \frac{\sqrt{2}}{2} \\ 0 & \frac{\sqrt{2}}{2} & \frac{\sqrt{2}}{2} \\ 1 & 0 & 0 \end{bmatrix} \tag{12}$$

$\boldsymbol{C}'^T = \boldsymbol{R}_1 \boldsymbol{C}^T$, $\boldsymbol{n}'^T = \boldsymbol{R}_1 \boldsymbol{n}^T$ and $\boldsymbol{C}'^T = \boldsymbol{R}\boldsymbol{n}'^T$, where $\boldsymbol{C}'^T$ represents the position $\boldsymbol{C}^T$ in the upper platform coordinate system, $\boldsymbol{n} = (0, 0, l)$ is the unit vector of central axis of the probe-in measuring tool, $\boldsymbol{R}$ represents the homogeneous orientation of the platform. So the relationship between (α, β, γ) and e_i is given by:

$$\begin{cases} x = (1 - c\beta c\gamma)(l_1 + r) + l_2(s\alpha s\gamma + c\alpha s\beta c\gamma - 1) \\ y = (1 - c\beta s\gamma)(l_1 + r) + l_2(-s\alpha s\gamma + c\alpha s\beta s\gamma - 1) \\ z = (1 + s\beta)(l_1 + r) + l_2(c\alpha s\beta - 1) \end{cases} \tag{13}$$

So far, it has been known that the axis of the probe-in measuring tool is rotated to the axis of the through-hole in the printing machine with a fixed point making them parallel. Then, as long as the platform up and down or left and right translations, can be two axes coincide to realize precise installation. Finally, after coinciding the relationship between (x, y, z) and the six readings is given by:

$$\begin{cases} x = (1 - c\beta c\gamma)(l_1 + r) + (s\alpha s\gamma + c\alpha s\beta c\gamma - 1)l_2 + x_c - m_x \\ y = (1 - c\beta s\gamma)(l_1 + r) + (-s\alpha s\gamma + c\alpha s\beta s\gamma - 1)l_2 + y_c - m_y \\ z = (1 + s\beta)(l_1 + r) + (c\alpha s\beta - 1)l_2 + z_c - m_z \end{cases} \tag{14}$$

We know how to adjust the movement of the 6-DOF platform by the computer calculating through Eqs. (13) and (14).

4 Conclusions

In the paper, the Robot of Sleeve Installation for Printing Machine has been modeled, including 6-DOF platform modeling, the probe-in measuring tool modeling and dynamic modeling. Based on the position inverse solution, the Jacobi matrix between the force of the rod and the generalized force on the upper platform is obtained. After that, the dynamic model of 6-DOF is established by Lagrange equation, and the dynamic equations of the position and velocity of the supporting rod were obtained. What's more, the paper puts forward the strategy of the using probe-in measuring tool, sets up the model and obtains the relationship between the platform and the relative position of the through-hole in the printing machine by the readings of the probe-in measuring tool. The relationship between the probe reading and the propulsion force is obtained, which will lay the foundation for the precise control based on the probe-in measuring tool, and will be also the basis for the precision assembly of the sleeve of the printing press. This project not only can be applied to the installation of the sleeve of the printing machine, but also has a wide range of application value in the field of precision assembly, precision operation, surgical treatment, and so on.

Acknowledgements This paper was supported by "National Key Scientific Apparatus Development of Special Item" (2013YQ140517), "Nonlinear Dynamics model and Analysis of Gear Systems for Offset Press" (No. 61472461) and "Graduate School of electronics and communication engineering master's degree joint training" (21090117006).

References

1. Jiang S, Lou F, Sun F, Yang Z et al (2015) Modeling and control of a high-precision tendon-based magnetic resonance imaging-compatible surgical robot. Proc Inst Mech Eng 8
2. Sirouspour MR, Salcudean SE (2001) Nonlinear control of hydraulic robots. IEEE Trans Robot Autom 17(2):173–182
3. Li L (2008) Research on forward kinematics and control method of 6-DOF parallel platform. Harbin Technical University
4. Huang L (2011) Modeling and simulation for robot. Zhejiang University
5. Qazani MRC, Pedrammehr S, Rahmani A et al (2014) Kinematic analysis and workspace determination of hexarot-a novel 6-DOF parallel manipulator with a rotation-symmetric arm system. Robotica
6. Kurazume R, Oshima S, Nagakura S et al (2016) Automatic large-scale three dimensional modeling using cooperative multiple robots. Comput Vis Image Understand
7. Jiang S, Lou J, Sun F et al (2015) Modeling and control of a high-precision tendon-based magnetic resonance imaging–compatible surgical robot. J Syst Control Eng 229(8):711–727
8. Kavacan E, Kayacan E, Racoon H et al (2012) Adaptive neuro-fuzzy control of a spherical rolling robot sing sliding-mod-control-theory-based online learning algorithm. IEEE Trans Syst Man Cybernet-Part B: Cybernet 99:1–10
9. Zhao W, Sun H, Jia Q et al (2013) Mechanical analysis of the jumping motion of a spherical robot. Sensors and Transducers, Orlando, FL, United States, 21(SPEC.5):42–47
10. Kurazume R, Oshima S,Nagakura S et al (2016) Automatic large-scale three dimensional modeling using cooperative multiple robots. Comput Vis Image Understand (5):8–12

Study on the Mechanical Performance Optimization of FDM Built Parts

Kaikai Li, Linlin Liu, Jimei Wu, Meng Li and Shenghui Yong

Abstract With the development and application of additive manufacturing technology, the mechanical properties of parts have become more important. The functional parts with complex shape have become an urgent need in manufacturing industries. The performance of FDM built parts exhibit high dependence on process parameters, and it can be improved by setting suitable parameters. Hence, the work focuses on extensive study to understand the effect of four important parameters such as fill density, layout angle, filling shape and layer thickness on the tensile stress of orthogonal test specimen. The results show that the important parameters affecting the mechanical properties of parts are the filling density and filling shape, and the process parameters of tensile strength are optimized. The optimization of process by range analysis gives the maximum tensile strength and the optimum value of filling density, layout angle, filling shape and layer thickness as 50%, 0°, Honeycomb shape and 0.15 mm respectively. In this paper, the optimization of process parameters can effectively improve the mechanical properties of FDM built parts.

Keywords Orthogonal test specimen · Mechanical property · Fused deposition modeling · Parameter optimization

1 Introduction

Additive manufacturing technology is also called 3D printing technology [1]. Fused deposition modeling (FDM) is gaining distinct advantage in manufacturing industries because it has flexibility and ability to build complex parts. However, the forming quality of FDM process is not optimistic, and it is easy to appear the phenomenon of low surface precision, warpage, collapse and lack of strength.

K. Li · L. Liu (✉) · J. Wu · M. Li · S. Yong
Faculty of Printing, Packaging Engineering and Digital
Media Technology, Xi' an University of Technology, Xi'an, China
e-mail: liulinlin1978@qq.com

P. Zhao et al. (eds.), *Applied Sciences in Graphic Communication and Packaging*, Lecture Notes in Electrical Engineering 477,
https://doi.org/10.1007/978-981-10-7629-9_69

Domestic and foreign scholars improved the quality of FDM process by study a large number of experiments deeply. For example, Yong He [2] improved the influence of the molding precision and efficiency by optimizing the filling path in the deposition. Sood et al. [3] studied the influence of process parameters on the dimensional accuracy using Taguchi method and artificial neural networks (ANN).

Zhang [4] analyzed the influence of processing parameters on the precision of parts fabricated by FDM technology based on a series of performed experiments. Processing parameters of FDM in terms of wire-width compensation, extrusion velocity, filing velocity, and layer thickness are chosen as the control factors.

In the field of material processing, the definition of the model geometry in the macro and meso has a profound impact on the manufacturing process and molding quality[5]. The STL file contains the model information, which can reflect the macro geometry of the model. The engineer can arrange the manufacturing process according to the macro geometry of the model, and determine the manufacturing direction to ensure the integrity and loyalty of the geometry [6]. At the macroscopic scale, the STL file will be redefined and the geometry model will be divided into several layers by slicing technology. Mechanical property of FDM processed component depend on four important control factors such as layout angle, filling density, filling shape, layer thickness [7]. The influence of each factor on the quality of the part forming is different [8]. In this paper, the mapping relationship between the process parameters and the mechanical properties of the parts will be established, and the orthogonal experimental optimization scheme will be established. The optimal parameter combination is obtained to improve the mechanical performance.

2 Key Parameters

As an additive manufacturing (AM) technology, based on the principle of digital model-discretion-accumulation, fused deposition modeling (FDM) allow for quick and clean development of prototypes and functional components. In this process, the material is heated and melted in the nozzle. Nozzle extrudes the molten material along with sectional profile of part. The material is rapidly cured and bonded with other material in surrounding. Strength of FDM processed component primarily depend on four important control factors. They are defined as follows:

Layout Angle. Build orientation refers to the way in which the part is oriented on the build platform with respect to X, Y, Z axes, as shown in Fig. 1. X and Y-axis are considered parallel to build platform and Z-axis is along the direction of part build [9].

Filling Density. Filling density is the percentage of the volume of the filler material in the part in overall volume of the material. Figure 2a shows the filling density of ten percent, Fig. 2b shows the filling density of thirty percent.

Filling Shape. Molten material along with designated geometry is extruded from nozzle.

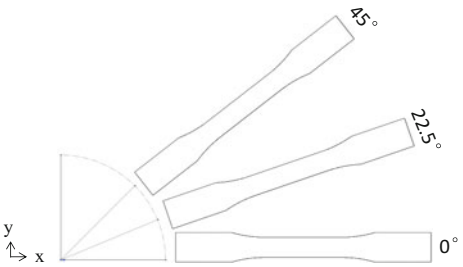

Fig. 1 Layout angle diagram

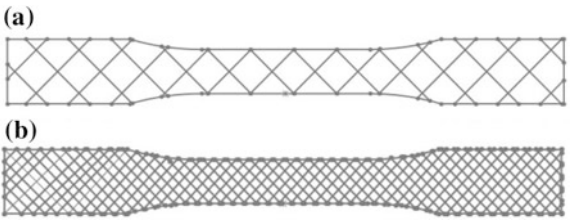

Fig. 2 Sketch map of filling density

Layer Thickness. It is a thickness of layer deposited by nozzle and depends upon the type of nozzle used.

3 Experimental Design

Orthogonal experimental design is a method of multi factor and multi level, it is based on the orthogonality of the selected points from the comprehensive test conducted experiments. And it is an efficient, rapid and economical design method that has the representative points with characteristics of uniform, neat comparable. The specific level is shown in Table 1.

As shown in Fig. 3, in this paper three-dimensional model of parts is established and saved as STL file. Then the data information of each layer generates the corresponding control code to control the operation of the printer. According to the orthogonal design, nine groups of experimental data were obtained. Each group had five samples, and a total of forty-five samples were obtained.

Table 1 Main factors and levels

Level	Factor			
	(A) Filling density [%]	(B) Layout angle [°]	(C) Filling shape	(D) Layer thickness [mm]
1	10	0	Grid	0.1
2	30	22.5	Honeycomb	0.15
3	50	45	Triangle	0.2

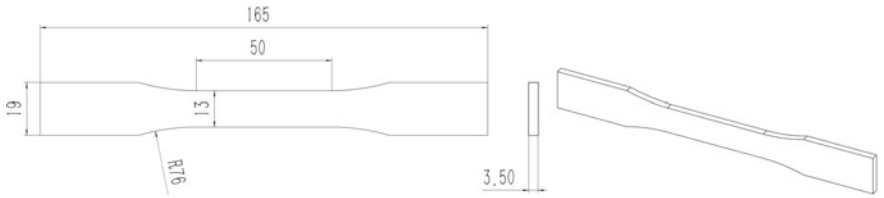

Fig. 3 Schematic diagram of 3D model

4 Results and Analysis

As shown in Fig. 4, nine groups of experimental samples were prepared according to the orthogonal test table. The maximum load and elongation of the sample were obtained because parts of the cross section are specific structure. Maximum load and elongation were obtained. The experimental data of the models is shown in Table 2 (Fig. 5).

In this paper, the influence of different factors on the tensile strength and expansion quantity is obtained. As shown in Figs. 6 and 7. The three points shown in each plot of the four control factors represent the average value of experimental data while such a factor was set at different levels (M_i from low to high), respectively.

Influence of Filling Density. The effect of filling density on tensile strength and elongation is significant, with the increase of filling density, the tensile strength is greatly increased and the amount of expansion is greatly reduced. When the filling density is continuously increased, the material strength of parts is improved in total because of the material volume of parts inside increased. On the other hand, due to the force of interaction between materials, material deformation ability is limited and the elongation of part is decreased.

Fig. 4 Experimental model

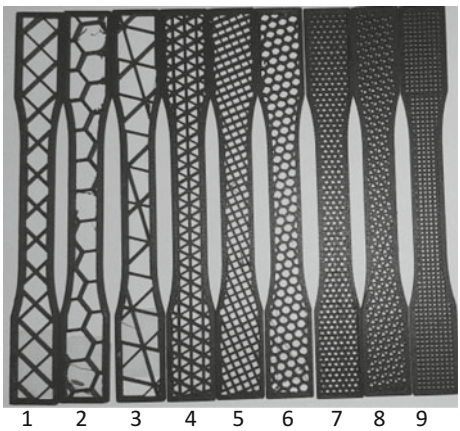

Table 2 Experimental data

Run	Factor				Maximum tension (N)	Maximum elongation (mm)
	A	B	C	D		
1	1	1	1	1	605.0	3.698
2	1	2	2	2	565.0	4.822
3	1	3	3	3	555.0	3.097
4	2	1	3	2	672.5	3.341
5	2	2	1	3	630.0	3.454
6	2	3	2	1	755.0	3.542
7	3	1	2	3	992.5	3.901
8	3	2	3	1	812.5	2.961
9	3	3	1	2	945.0	2.685

Fig. 5 Tensile test

Influence of Layout Angle. The tensile strength of the parts at 22.5° is the lowest and the elongation is the largest. Because there is an angle between the path of material and the stretching direction and the material is affected by the tensile and the bending moment at the same time. As shown in Fig. 4, the parts 5 has good ductility with a parallelogram shape interior.

Influence of Filling Shape. The tensile strength and elongation of honeycomb structure is the best, the honeycomb structure with suitable advantage has been the object of the scholars.

Influence of Layer Thickness. The influence of layer thickness on tensile strength and elongation is not significant. The tensile strength and elongation of parts with the layer thickness of 0.15 mm are the best because of its continuous

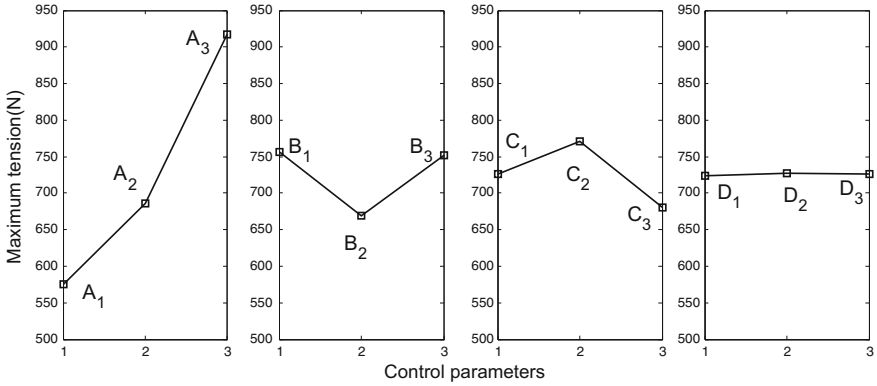

Fig. 6 Effect of different factors on tensile strength

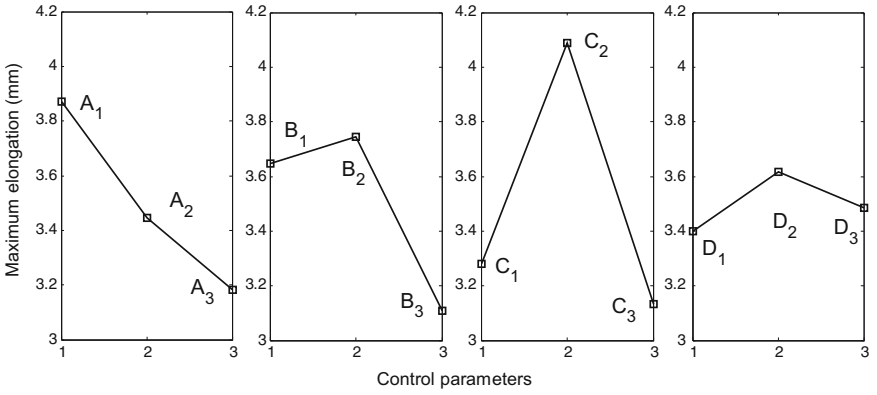

Fig. 7 Effect of different factors on expansion

material properties and the bonding force between the layer and the layer is better than the layer thickness of 0.2 mm.

5 Conclusions

In this paper, the parameters of preprocess which affect the mechanical properties of FDM parts are described. An orthogonal test scheme is established to obtain the tensile strength and elongation of the parts. The optimal parameter combination is obtained by data processed. The conclusions are as follows:

The optimization of process by range analysis gives the maximum tensile strength and the optimum value of filling density, layout angle, filling shape and Layer thickness as 50%, 0°, Honeycomb shape and 0.15 mm respectively.

The optimization of process by range analysis gives the maximum elongation and the optimum value of filling density, layout angle, filling shape and Layer thickness as 10%, 22.5°, Honeycomb shape and 0.15 mm respectively.

Acknowledgements The author gratefully acknowledges the support of the National Natural Science Foundation of China (Grant No. 11272253), Key Laboratory Science Foundation of Department of Education of Shaanxi Province (16JS083), and Foundation of Bureau of Science and Technology of Beilin District (GX1620).

References

1. Kai CC, Fai LK, Chu-Sing L (2003) Rapid prototyping: principles and applications in manufacturing. World Scientific Publishing Co, Inc
2. Jin Y, He Y, Fu J, Gan W, Lin Z (2014) Optimization of tool-path generation for material extrusion-based additive manufacturing technology. Addit Manuf 1–4:32–47. https://doi.org/10.1016/j.addma.2014.08.004
3. Sood AK, Ohdar R, Mahapatra S (2009) Improving dimensional accuracy of fused deposition modelling processed part using grey Taguchi method. Mater Des 30(10):4243–4252. https://doi.org/10.1016/j.matdes.2009.04.030
4. Zhang J, Peng A (2012) Processing parameter optimization of FDM based on robust design. Trans Nanjing Univ Aeronaut Astronaut 29(1). https://doi.org/10.16356/j.1005-1120.2012.01.006
5. Yang J, Xu L, Li C, Wang J, Yin Y (2013) Research of process parameters optimization of molding quality based on FDM. J Nanjing Normal Univ (engineering and technology edition) 13(2). https://doi.org/10.3969/j.issn.1672-1292.2013.02.001
6. Liu L, Wan C, Li K (2015) CFD simulation and structure optimization on hot-air drying oven of gravure printing machine. Int J Heat Technol 33197–202. https://doi.org/10.18280/ijht.330426
7. Mohamed OA, Masood SH, Bhowmik JL (2015) Optimization of fused deposition modeling process parameters for dimensional accuracy using i-optimality criterion. Measurement 81 (11):174–196. https://doi.org/10.1016/j.measurement.2015.12.011
8. Liu L, Li K, Lu F (2016) Dynamic simulation modeling of inking system based on elastohydrodynamic lubrication. Int J Heat Technol 34(1):124–128. https://doi.org/10.18280/ijht.340118
9. Liu L, Wan C, Li K, Wu J (2016) Research on warpage deformation mechanism & control method of fused deposition parts. Lect Notes Electr Eng 417:729–737. https://doi.org/10.1007/978-981-10-3530-2_91

Design of an Extrusion Painting Test Device with Preheating and Self-cleaning

Bo Gao, Xiaogui Zhang and Wencai Xu

Abstract At present, some traditional and digital printing methods are used in electronic printing technology. But it is inconvenient in making one experiment in laboratory. So a kind of extrusion painting test device is designed, used for special printing objects of line pattern. This paper analyzed the working principle of extrusion painting test device, designed 2D motion system of extrusion painting head. The motion system is controlled on Arduino control panel. The extrusion painting head has the function of preheating and self-cleaning. The workbench integrates heating and drying functions. The device is used for the study of electronic ink 2D planar painting technology and relevant properties.

Keywords Extrusion painting · Printed electronics · Experimental device

1 Introduction

The manufacture of printed electronics is based on a variety of mature and similar printing technology, and uses printing methods painting on the corresponding functional layers. It has been applied in many ways [1–6]. In the laboratory, the traditional printing technology are generally used, such as lithograph, letterpress, gravure, silk-screen printing. New digital ink jet printing is used too.

Under laboratory conditions, the electronic ink is limited in weight, and the residue on the printing equipment wastes some of the electronic ink. The painting thickness controlled by printing methods is relatively stable, and its range of change

B. Gao (✉) · W. Xu
School of Printing and Packaging Engineering, Beijing Institute of Graphic Communication, Beijing, China
e-mail: gaobo@bigc.edu.cn

X. Zhang
School of Mechanical and Electrical Engineering, Beijing Institute of Graphic, Communication, Beijing, China

P. Zhao et al. (eds.), *Applied Sciences in Graphic Communication and Packaging*, Lecture Notes in Electrical Engineering 477,
https://doi.org/10.1007/978-981-10-7629-9_70

is limited. Traditional lithography, embossing, gravure printing and screen printing require plate making. Digital inkjet printing will cause a blockage in the inkjet head.

The design adopts an extrusion nozzle to squeeze filiform, for controlling extrusion nozzle moving path to achieve the desired shape of graffiti. That is another way to achieve some line pattern painting under laboratory conditions. Graffiti shape can be arbitrarily changed; Extrusion painting can change the thickness. On the same device, extrusion painting can be carried out on different substrate materials. It has some advantages to the line type of one piece making in the laboratory.

2 Working Principle and Design Requirements of the Experimental Device

Figure 1 is the Schematic diagram of the working principle of extrusion painting device. To make it simple, the extrusion painted nozzle is as a pen for writing on the substrate. To realize this process, the following conditions is required.

Extrusion painting nozzle is the basis of painting. Electronic ink is squeezed by extrusion painting nozzle to paint on the surface of the material.

Extrusion painting nozzle is painting as the requirements of the pattern, that is, the extrusion painting nozzle could move in accordance with a track, the track is on 2D planer.

When the extrusion painting nozzle moves along a certain track, it requires for certain extrusion output, which means to maintain constant pressure on the supply of extrusion painting nozzle.

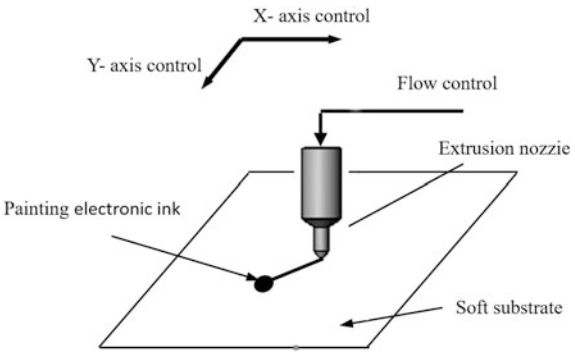

Fig. 1 Schematic diagram of extrusion painting

3 Design of the Overall Structure of the Experimental Device

The extrusion painting device is designed according to the above requirements. The device can be mainly divided into the following sections: the motion part in 2D plane, the table part with drying function, the extrusion nozzle part with automatic cleaning and preheating function, control part and auxiliary parts, etc. The overall structure of the device is shown in Fig. 2.

The moving part in 2D plane is composed of linear motion units moving in two directions, the repeated positioning accuracy of each linear motion unit is ±0.01 mm, the positioning accuracy is 0.2 mm, which are arranged in the form of a portal frame and crossed vertically in space. Through the control of the two linear motion units, the extrusion nozzle can be dislodged in a plane direction of XY axis in 2D, which is relative to the worktable. On this account the desired shape is painted on the base material.

The table part with drying function comprise a working table, a heating plate, a heat insulating plate and a supporting plate for the heating plate, which are fixed on the X axis direction moving unit as a component. The heat insulation plate separates

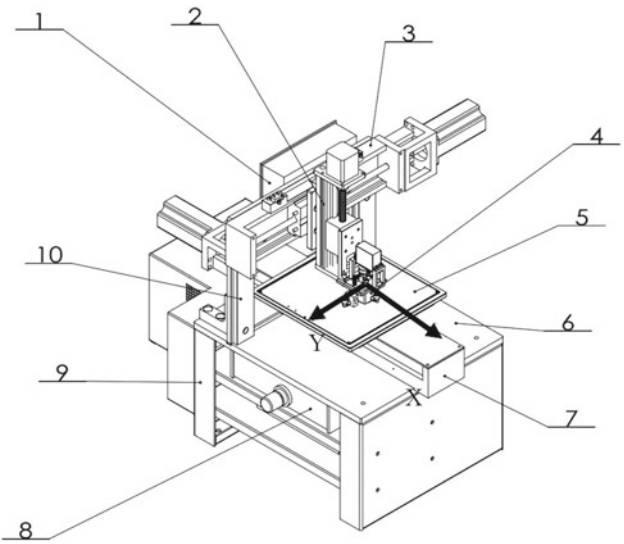

1-Control panel 2-Z linear motion unit 3-Y linear motion unit 4-Extrusion painting assembly 5-Workbench 6-Frame bedplate 7-X linear motion unit 8- Pressure regulator 9- Frame 10- Longmen frame

Fig. 2 Overall structure of extrusion platform

the working table from the body of the device to prevent the heat from escaping through the body.

Electronic ink painted on substrate surface needs to be preheated through the ink extrusion part and then further heated and dried on the worktable, to make sure the shape of the painted electronic ink can be dried in time and set quickly.

The device adopts the method of pressure extrusion, and the auxiliary part is mainly to provide constant pressure electronic ink for ink extrusion.

The ink extrusion part and control part with self-cleaning and preheating function is the key part of extrusion painting, which will be introduced in the following content.

4 Design of Extrusion Nozzle for Experimental Device

The ink extrusion part is fixed on the linear motion unit on the Z axis direction of that controls the lift of ink extrusion part relative to the working table, as shown in Fig. 2. The linear motion unit on the Z axis direction is installed on the one on the Y axis.

The ink extrusion actual part is shown in Fig. 3, and the inner section is shown in Fig. 4.

The ink extrusion part is composed of an ink extrusion component, a mounting plate and a supporting plate. The ink extrusion component is composed of a valve body, a valve core, an extrusion nozzle, a heating body, a motor, an air inlet interface and an ink inlet interface. The ink extrusion component is arranged on the supporting plate through a guide column and is pressed by a spring. Thus, the ink extrusion component can be floated up and down to avoid the accidental collision and damage between the ink extrusion nozzle and the working table.

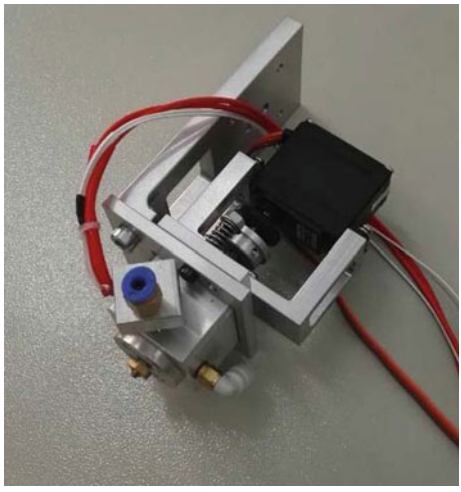

Fig. 3 Ink extrusion actual parts

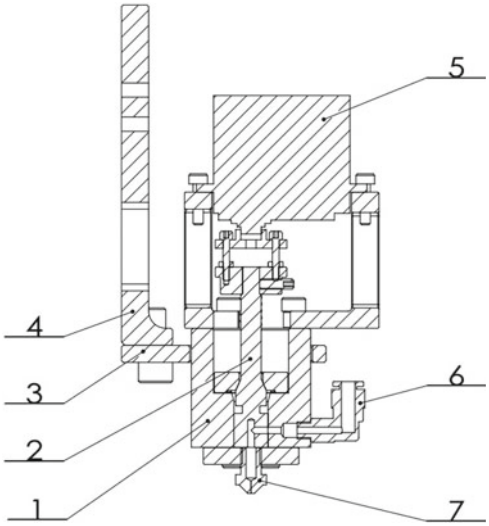

1- valve body 2- valve core 3- Pallet 4- Mounting plate 5- Electric motor 6- Inlet connector 7- Extrusion nozzle

Fig. 4 Section plan of ink extrusion

The principle of preheating and self-cleaning of the electronic ink for the ink extrusion component is as follow.

The outer surface of the valve body is provided with two through holes which are separated 90° apart on the same horizontal plane. The two through holes are respectively connected with a right angle connecting head, one of which connects to compressed air and the other one connect to electronic ink. The ink-distributing valve core is provided with a sealing ring on the upper part to prevent the leakage of the electronic ink. It is driven by the motor to convert the extrusion painting and cleaning.

The heating element contains heating element, which preheat through the electronic ink. After preheating, it improves the liquidity of the electronic ink, and it also prepares for drying. The preheating makes it no more affected by the environmental temperature, which also is in favor of the stability of the painting process.

When the work is finished, the ink-distributing valve core is connected to the compressed air inlet for removing the residual ink in the painting nozzle, avoiding blocking exports from drying residues in export of electronic ink. At the same time, close the imports of electronic ink to ensure that the ink in the channel cannot contact with the outside to prevent the oxidation of electronic ink.

The diameter of the extrusion nozzle for experiment is 0.2, 0.3 and 0.4 mm, the control range of preheating temperature is from room temperature to 40 °C.

5 Design of Control System

Basing on the requirements of the previous analysis, an integrated control panel with AVR processor based on the Mega2560 is selected, which is designed for the 3D printer, engraving machine, laser cutting machine and other CNC processing.

Due to the adoption of integrated design, the control panel is easy to install and debug. It also uses the common Arduino IDE as the development software to make it simple for firmware upgrade and parameter configuration [7, 8].

The control panel can be controlled by a personal computer through USB communication to control the 2D movement of the extrusion nozzle relative to the working table. It needs the motion instructions if it follows the required path motion, that is, G code files.

G code file is an intermediate format file that each line of the code in the document can be understood by the command board. These commands, also known as the G-code commands, are the most important command interaction channels between the control panel and the computer.

The CAD model is discretized along a certain direction (such as Z axis direction) into a series of 2D level (called as layered or sliced) to obtain a series of 2D plane information (section information) [9]. The G-code files can be obtained by layering.

During the processing of modeling or layering, the information of the painting path of the extrusion nozzle can be obtained by setting the layered result which contains only one layer.

It is chosen Repetier-Host as the control software, which is integrated with two slicing programs. Repetier-Host software is features-rich and user-friendly that helps users to manually debug, slice model, position parts and to control machine operations and so on.

Use the SolidWorks to establish a quadrilateral pattern, the outline dimensions are shown in Fig. 5, to save it as a slicing program which is accepted by STL format. Then import the SolidWorks output of the STL file into the Repetier-Host, through the embedded slice program analysis to get the G code file.

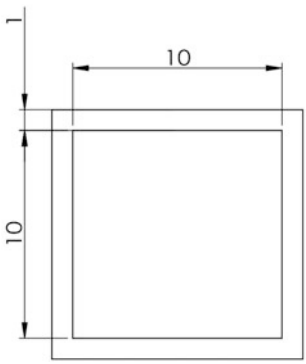

Fig. 5 Dimensions of the painted shapes

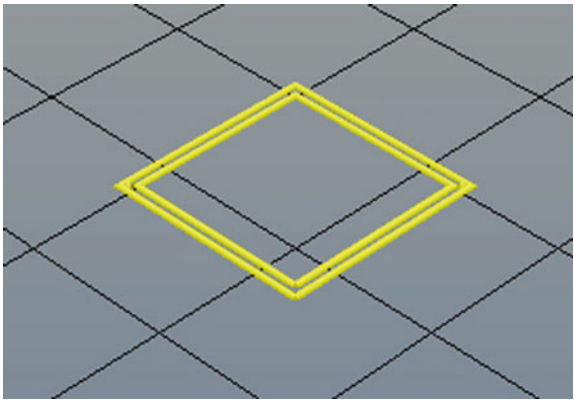

Fig. 6 Trajectory simulation of painting

Corresponding to the painting shape of Fig. 5, the simulation result with the above G code file is shown in Fig. 6.

From the generation of G-code file, put forward the motion control G-code command for two lines inside and outside of the outline as follows:

G0 F9000 X94.20 Y94.20
G1 F2400
G1 F1800 X105.80 Y94.20
G1 X105.80 Y105.80
G1 X94.20 Y105.80
G1 X94.20 Y94.20
G0 F9000 X94.80 Y94.80
G1 F1800 X94.80 Y105.20
G1 X105.20 Y105.20
G1 X105.20 Y94.80
G1 X94.80 Y94.80

6 Conclusions

In this paper, a kind of device for extrusion painting is designed, which can be applied to paint line patterns in the 2D plane of electronic ink.

The design of the ink extrusion part contains preheating and self-cleaning function. The electronic ink is preheated to improve the fluidity and prepare for drying. When the work is finished, the valve core is rotated and the ink in the closed channel cannot contacted with the outside air to prevent the oxidation of electronic ink. At the same time, the compressed air is used to automatically remove the residual ink in the painting nozzle to prevent blockage.

The working table is designed with the function of heating and drying as to the shape of the electronic ink painting can be dried in time and shaped rapidly.

Acknowledgements This work was Supported by the National Key Scientific Instrument and Equipment Development Project (NO. 2013YQ140517). The work was also supported by Institute Level Key Projects Funded by Beijing Institute of Graphic Communication, under grant E-a-2013-18 and E-a-2014-14.

References

1. Zhang X (2014) Paper batteries and printed electronics. Mater China 33:186–188
2. Guan J, Cheng D, Shen X, Yu Z (2010) Electrode modification research of organic solar cell. Electron Packag (10):38–43
3. Lv X (2012) Novel pressure sensor for electronic skin. PhD thesis, Donghua University, Shanghai, China
4. Park SK, Kim YH, Han JI (2009) High-resolution patterned nanoparticulate ag electrodes toward all printed organic thin film transistors. Org Electron 10(6):1102–1108
5. Mahajan A, Frisbie CD, Francis LF (2013) Optimization of aerosol jet printing for high-resolution, high-aspect ratio silver lines. ACS Appl Mater Interfaces 5(11):4856–4864
6. Kelley TW, Baude PF, Gerlach C et al (2004) Recent progress in organic electronics: materials, devices, and processes. Chem Mater 16(23):4413–4422
7. Founder studio (2015) Rumba main control board. https://www.ifmy.net. Accessed 21 Apr 2017
8. RepRap (2017) https://reprap.org/wiki/RUMBA. Accessed 21 Apr 2017
9. Zhao C (2009) The design and implementation of 3D printer layered software. Thesis, Dongnan University. 20090401

Part VII
Paper and Related Technology

Analysis and Measurement of the Imbibition Characteristic of Paper Based in the *y*-Direction

Guodong Liu, Sijia Fu, Meiyun Zhang and Yue Wang

Abstract The transport of print fluids into the paper including *x*, *y* and *z*-directions is directly dependent on the imbibition characteristic of paper, and some common printing problems, such as print mottle, colour unevenness, and colour bleeding, are considered highly relevant with printing liquid uptake performance of paper. As the measurement of print fluid imbibition into the paper oriented in *z*-direction is extremely difficult in reality as the paper is too thin to be measured. However, the imbibition along the *x* and *y*-directions respectively, is a more practical solution since the wicking amount can be more easily measured. Therefore, in this paper we resort to imbibition measurement along the *y*-direction of paper to analysis imbibition dynamic of paper, imbibition mechanism oriented to *y*-direction, and further explore the possibility of replacing the *z*-direction imbibition of paper using *y*-direction imbibition. Considered the structural changes for samples, uncoated papers were filled to differing levels of 0, 0.75, 1.25 and 1.5% by weight using the technique of surface filling, to form a transition from the differential equivalent capillary radius. The imbibition characteristics of the paper then were measured with an accurate gravimetric balance system. Considering the classical imbibition dynamics of Lucas-Washburn, inertial and Bosanquet imbibition models for a common porous media, the measured imbibition performance was characterised with square root time ($\sqrt{t}$) and time (t), respectively. Therefore, the imbibition behaviour of papers was expressed using these two classical timescales and the analysed results are shown that the imbibition performance of uncoated unfilled paper oriented in the *y*-direction follows neither the classical Lucas-Washburn imbibition nor the Bosanquet imbibition, but associating with the surface wicking

G. Liu (✉) · S. Fu · M. Zhang
College of Bioresources Chemical and Materials Engineering,
Shaanxi University of Science and Technology, Xi'an 710021, China
e-mail: Lgdmax587@aliyun.com

G. Liu
Department of Bioproducts and Biosystems, School of Chemical Engineering,
Aalto University, Aalto 00076, Finland

Y. Wang
Department of Culture Media, Shaanxi Youth Vocational College, Xi'an 710068, China

P. Zhao et al. (eds.), *Applied Sciences in Graphic Communication and Packaging*, Lecture Notes in Electrical Engineering 477,
https://doi.org/10.1007/978-981-10-7629-9_71

occurs rather via a surface film flow along the paper fibres leaving large voids initially empty. However, by adding more filler into paper, the imbibition dynamic can be reverted to Bosanquet imbibition model since the filler load in the surface layer of the paper, the imbibition dynamic is seen to revert to the Bosanquet imbibition model since the filler disrupts the fibre wicking arising from the reduction in permeability and the filling effect into the large voids, thus forming new finer pores by particle packing and aggregation. These findings enable a controlled design of imbibition properties when modifying the pore structure using high surface filled paper.

Keywords Inertial imbibition · Lucas-Washburn imbibition · Bosanquet imbibition · *y*-direction imbibition · Wicking characteristics

1 Introduction

The transport of print fluids into either uncoated paper or into the coating materials coated onto the surface of paper is directly dependent on the imbibition characteristic of materials. During the interaction of printing inks with the surface layer of coated paper, the ink colorant pigments remain at the surface creating the desired print image. The image then coheres and adheres (fixed) by cross-linking resin as the ink vehicle, making up the liquid phase, either becomes evaporated or undergoes capillary-driven imbibition into the paper, or both. Alternatively, if the colorant is a dye, it enters the paper surface in conjunction with the ink vehicle and undergoes adsorption onto the pore walls internally at the paper surface. Many of the common problems in print quality, such as print mottle, colour unevenness, and colour bleeding are highly relevant with the imbibition properties of the paper, some of which relate to lateral wicking in the x and y-directions, especially for uncoated paper. It is, thus, a major concerned area for the technologist in the paper or print industry to control the interactions of pore network of paper and coated layer with print liquid. Therefore, the imbibition mechanism and the factors affecting on absorption process for print fluids, has become huge concern in the industrial application in past decades. The traditional, classical and long-accepted pore filling Lucas-Washburn (L-W) model [1] is frequently employed to characterise the imbibition performance along the z-direction of paper or coated layer of paper, but practical imbibition in complex pore network media frequently shows some deviations from the L-W model, which cannot meet the observed requirements of modern printing. Issues such as high printing quality demand a more representative model to satisfy the demand for accurate colour reproduction conversion, transport and handling. In the L-W imbibition mechanism, a single equivalent capillary tube is considered to describe the capillary dynamic balance between wetting force and viscous drag, and imbibition length inside the capillary is in directly proportional to root time ($\sqrt{t}$) of imbibition process, which is derived in respect to the viscosity and surface tension of print fluid, and the radius of assumed

equivalent capillary tube, not, however, involving an important parameter of the fluid, its density. It means obviously that the L-W imbibition regime does not consider any inertial effect during the imbibition process. However, Quéré [2] captured an image of the inertial plug flow in the equivalent capillary tube using a high-speed camera and elaborated the inertial effect for spontaneous imbibition by proposing the inertial plug flow model. Thus, the inertial regime is not related to the viscosity of a fluid but rather to its density and, as a result, is directly proportional to imbibition time and not in accordance with the classical L-W root time. In addition, combining the inertial force with the viscous role, the Bosanquet imbibition model [3] was proposed to emphasise the contributory role of the inertial force during the imbibition process. Despite the attractiveness of the Bosanquet model it has not been adopted widely. This is possibly due to Bosanquet's own dismissal of the concept in respect to the application to a single classical capillary experiment of the time, as he explained that the inertial effect would not last long enough to be important in a practical measurement [4]. As a result, the impact of inertia was considered by many to be negligible so long as the imbibition was occurring in a single capillary or bundle of capillaries. However, it is now understood that this assumption overlooks the acceleration and deceleration at the wetting front as it progresses through a geometrically complex porous network [5]. Gane et al. [6] more recently drew attention to the cumulative effect of inertia, and derived an expression, termed network complexity, exemplifying the concept using the fine coating structure of printing paper. Schoelkopf et al. [7] provided experimental observation of deviation from the L-W imbibition model into paper coatings and claimed it was due to the omission of the role played by inertia. Liu et al. [8] went on to consider the complete timescale range of imbibition for the same selected coating material, namely ground calcium carbonate (GCC), confirming the Bosanquet model as being applicable to a pore network layer. The key finding is that it describes the faster inertial uptake at the start of imbibition and, later in time, reverts to the slower imbibition rate controlled by the L-W model, indicating the transfer from plug flow to viscous laminar flow behaviour.

Although some evidences of the above-mentioned studies have successfully shown a working model for coating materials on paper, there are no direct experimental cases to show these parallel deviations for uncoated paper imbibition due to the difficulties of performing a measurement in the z-direction, since the paper is too thin to be easily measured. Methods have been developed, however, to measure the liquid permeability under external pressure of such papers by forming a stack. However, if the paper sheets are stacked together sufficiently to reach a practicable thickness for the test, one cannot guarantee to remove the air trapped between paper layers adequately, which is not an appropriate method to answer the question regarding free liquid imbibition rather than pressurised permeability. It, thus, has been frequently assumed to abide by a traditional L-W regime. According to this hypothesis, however, there is a fundamental problem, since both L-W and Bosanquet models assume pore filling while the imbibition progresses into those pores involved in the capillary activity, whereas the large pores and cavities in uncoated fibrous paper rarely can be considered as capillaries, except where fibres

meet and join together. This is particularly the case when considering lateral wicking in paper. Therefore, we set out to measure the imbibition characteristic of paper along the y-direction by means of a highly accurate balance system to present the wicking performance of paper as well as to explore the possibility of replacing the large voids in the paper with a more differential network of voids and finer pores using the technique of surface filling, where a low solids content slurry (or slip) of pigment particles is applied to the paper surface using a film press. Analysing the resulting effect on wicking enables a semi-quantitative understanding of how the papermaker can resolve some of the print quality problems, such as colour bleeding etc. associated with the lateral wicking characteristics of paper.

2 Paper Samples Preparation and the Measurement Method of Imbibition Using a Gravimetric System

The samples chosen were uncoated offset paper manufactured from TMP/CTMP furnish throughout, basis weight 80 g m^{-2}. To generate different equivalent capillary radii in a range of samples, the paper was surface filled with fine ground calcium (fGCC, Omya International AG, Baslerstrasse 42, CH-4665 Oftringen, Switzerland). Application levels of 0, 0.75, 1.25 and 1.5% by weight were applied by a typical film press/surface size press [9]. The paper samples filled with GCC particles eventually were cut into strips of 20 mm × 30 mm to be tested on the gravimetric imbibition apparatus, as shown in Fig. 1. The rate of liquid imbibition was measured using an automated microbalance (Mettler Toledo AX504), having a capacity of 10 measurements per second under a controlled precision of 0.1 mg. The apparatus and samples in this study were maintained at ambient lab temperature and humidity: 23.0 ± 1.5°C and 50% RH. The chamber designed around the balance is to shield from external air movement. The sample was lowered towards the fluid slowly, and the liquid-paper contact was recorded at the point when the

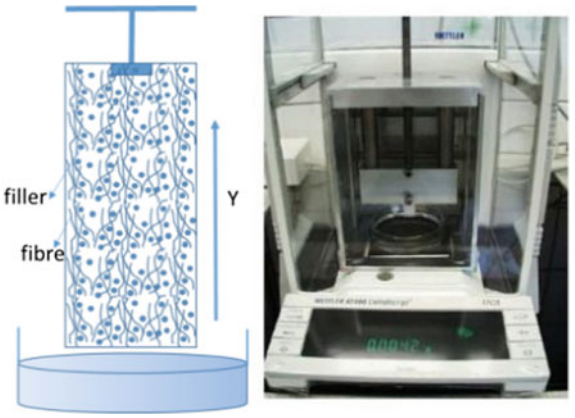

Fig. 1 Gravimetric wetting and imbibition apparatus [10]

Table 1 The physical properties of printing liquid hexadecane

Printing liquid	Viscosity (Pa s)	Density (kg m^{-3})	Surface tension (N m^{-1})	Contact angle (°)
Hexadecane	0.003	773	0.030	0

liquid jumped up to contact the sample. The imbibition rate finally is averaged after five measurements.

As a pure alkane, hexadecane, representing a purely dispersive organic liquid, and so typifying mineral oil properties typically found as a main ingredient in printing inks, is frequently used as a non-reactive wetting liquid for imbibition experimentation. Hexadecane (Dow Chemical Company, Midland, Michigan 48674, USA), therefore, is employed as the example fluid in this study. The physical parameters of the print liquid are listed in Table 1.

3 Results and Analysis of Imbibition Performance in Paper

For the paper samples filled with GCC particles, the more the filling into the paper, the more the voids in the fibrous paper become filled. Thus, the radius of an equivalent capillary tube (R) as a function of filler loading, will progressively change, such that $R_{1.5} < R_{1.25} < R_{0.75} < R_0$, where the subscript refers to the surface applied filler level. The imbibition characteristic of each sample shows a classical root time during the first absorption measurement, as an exemplified in Fig. 2. The initial specific imbibition is re-plotted for a clearer observation, as seen in Fig. 3. The averaged imbibition rate after five measurements is presented then in Table 2.

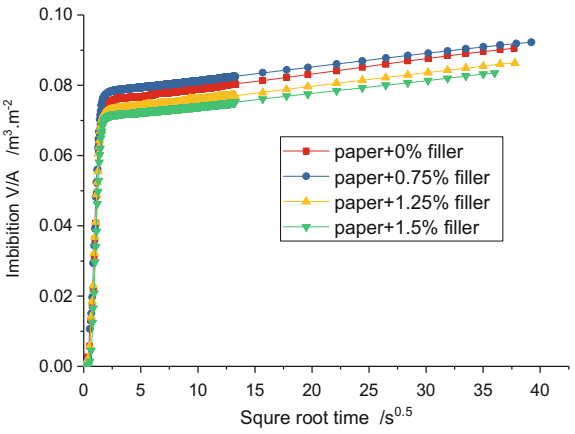

Fig. 2 The whole imbibition with square root timescale

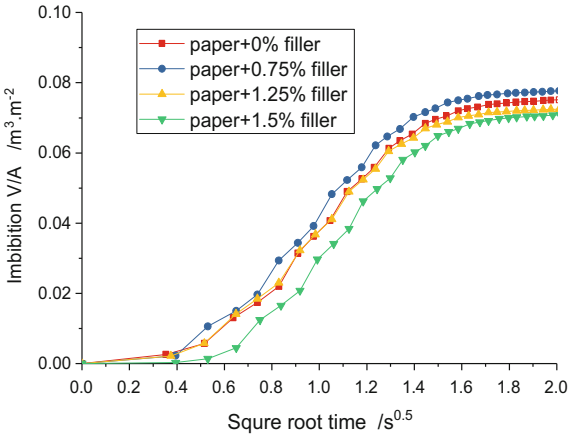

Fig. 3 The initial imbibition with square root timescale

Table 2 The imbibition rate with root time regime and time regime

Samples	Initial imbibition rate with square root time regime ($\sqrt{t}$) (m $s^{-0.5}$)	Long-time imbibition rate with square root time regime ($\sqrt{t}$) (m $s^{-0.5}$)	Initial imbibition rate with linear time regime (t) (m s^{-1})
Paper + 0%	7.448×10^{-2}	3.994×10^{-4}	3.768×10^{-2}
Paper + 0.75%	7.648×10^{-2}	4.084×10^{-4}	3.864×10^{-2}
Paper + 1.25%	7.060×10^{-2}	3.808×10^{-4}	3.564×10^{-2}
Paper + 1.5%	7.192×10^{-2}	3.598×10^{-4}	3.650×10^{-2}

In Fig. 2, the whole imbibition into paper samples with root time is seen to be similar to the imbibition behaviour of coating materials [4], which is divided into two linear parts where the initial imbibition rate is distinctly faster than the subsequent longer timescale imbibition. The initial fast imbibition ends at around 1.96 s (equal to a 1.4 $s^{0.5}$ in root time) and the later imbibition becomes slower than before. As the dry time of print matter in practical production is far longer than 1.96 s, we need to consider these two stages of imbibition for the real imbibition process on printed matter.

If we now represent the pore filling regime expressed as being related to the different capillary tube radii according to these two different stages, we see that the ordering does not follow the expected radius size (R) described earlier. Since the equivalent radius of all samples is decreased in turn as a function of filler loading, the imbibition rate thus should be reduced correspondingly if the L-W model is considered to apply, but at the initial stage of pigment filling the imbibition rate is not dropping continuously but rather increasing when filler is increased at 0.75%, but then reduced at 1.25% and increased again at 1.5%, as shown in the first

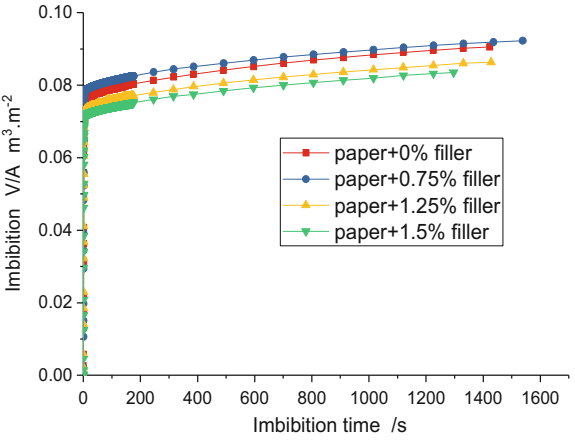

Fig. 4 The whole imbibition with time

column of Table 2. For the long-time imbibition in the middle column of Table 2, the circumstance is quite similar, i.e. increased at 0.75%, and then reduced at 1.25%, and finally a further drop at 1.5% filler loading. Comparing the imbibition rate change trends of initial imbibition (the first column in Table 2) with subsequent long time imbibition (the middle column), it is obvious to observe that the filler added into the paper has changed the structure of the paper samples. As suggested, the less filler-containing samples, such as at 0 and 0.75%, show a huge difference compared with higher filler loading samples i.e. the 1.25 and 1.5% compositions.

Since applying fine calcium carbonate in coating materials for paper products have been shown to follow a Bosanquet imbibition described by an inertial regime at the initial stage with linear time, and eventually returning to a classical L-W regime over longer timescale [4, 5]. Therefore, it is necessary to consider the Bosanquet imbibition also for these paper wicking data as shown in Fig. 4. In terms of Bosanquet imbibition, the imbibition characteristics at the initial stage are thus shown for greater clarity in Fig. 5. The averaged imbibition rate is also summarized for each sample in the last column of Table 2 at the initial imbibition stage. It indeed has a linear relationship as imbibition time increases as shown in Fig. 5. For the samples with less filler, such as filler amount 0 and 0.75%, it looks reasonable that the imbibition rate is increasing from 3.768×10^{-2} to 3.864×10^{-2} as expected with this model with reducing radius of the capillaries, and so the imbibition rate is inversely proportional to the typical equivalent radius. However, as expected there is a contradiction to this relationship occurring in the long-time imbibition as shown in the middle column of Table 2 from 3.994×10^{-4} to 4.084×10^{-4}. Thus, the imbibition rate should be dropping on the long timescale owing to reverting to the L-W expression eventually as pore radius decreases. We see that the situations are quite distinct when more filler is added into the paper, such as at 1.25 and 1.5%, as the equivalent capillary tube is reduced, the initial imbibition is increased from 3.564×10^{-2} to 3.65×10^{-2} as seen in the Table 2. On the contrary, the imbibition rate for these two samples is thus decreased arising

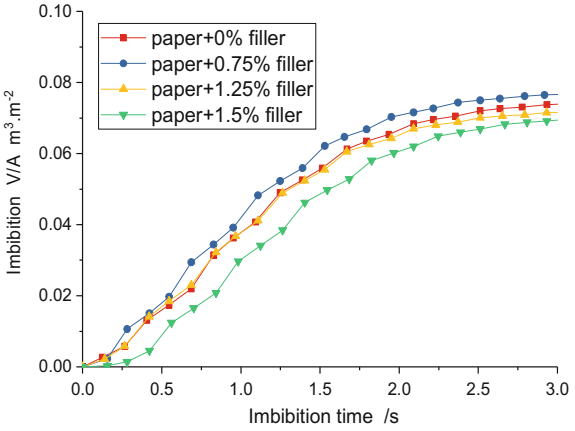

Fig. 5 The whole imbibition with time

from a return to L-W imbibition from the 3.808×10^{-4} to 3.598×10^{-4} as seen in the middle column of the Table 2. The effect of more filler in the paper results in the large pores inside the paper becoming progressively filled with GCC particles, whilst further fine pores are generated due to packing or aggregation of the filler particles. As fine pores can provide rapid absorption under inertial plug flow at short times, and inertia retards absorption into large pores, the behaviour becomes totally predictable when more filler is added. Therefore, once more filler is added inside the paper, so the role of the finer pores increases and the imbibition behaviour oriented in the *y*-direction is found to parallel with those of previous studies of coating materials in the *z*-direction. We can use the imbibition characteristic along the *y*-direction to replace the *z*-direction imbibition of paper provided filler level is sufficiently raised. However, for paper with less filler or without any filler, the imbibition regime in the *y*-direction neither follows the classical L-W imbibition nor the Bosanquet imbibition, but is following the fibre surface wicking effect, which cannot be captured using porosimetric pore sizing techniques. In the case of more filler added, the small filler particles form surface features on the fibres, which together disrupt the fibre film flow, such that the imbibition then reverts to the initial fast imbibition dominated by inertial dynamic in fine pores and the later L-W dynamic imbibition controlled by the viscous dynamic, which can be described sufficiently with the complete Bosanquet expression for the imbibition in these cases.

It should be noted that the filler levels used in this work are very low compared to wet end filler addition, but the specific application method means that the filler particles are dispersed homogeneously in the fibre mat, and so the effect is greater than in wet end filling where the filler particles reside mainly at the fibre joints due to capillary drying and filler adsorption effects.

4 Conclusions

In this paper, we measured the imbibition characteristic and discussed an imbibition wicking dynamic of paper. We employed a highly accurate gravimetric balance system to measure the imbibition process of paper. According to the widely used classical Lucas-Washburn, inertial and Bosanquet imbibition models for porous media, the imbibition dynamic of paper was respectively characterised with root timescale and linear time. We found that the imbibition performance of uncoated unfilled, or only lightly filler, paper oriented in the *y*-direction follows neither by the classical Lucas-Washburn nor the comprehensive Bosanquet description. Since both these descriptions rely on pore filling, we must conclude the wicking in paper follows a likely surface wetting dynamic along the fibres inside the paper. Interestingly, when more filler is added into the paper using the surface filling technique, the imbibition dynamic reverts to the Bosanquet imbibition model due to the filler acting to fill-in the paper voids and creates finer pores which then fill, and thus the particles disrupt the fibre surface wicking. Therefore, once more filler is added into the paper, especially for highly filled papers, the imbibition dynamic for printing liquid will mainly follow the Bosanquet mechanism, meaning a fast imbibition at the initial stages, dominated by the inertial dynamic, and reverting to a Lucas-Washburn imbibition, eventually over longer timescales. Using this description and technique of surface filling could supply some theoretical basis for modifying the imbibition behaviour of paper, especially for highly surface filled paper.

Acknowledgements The authors acknowledge the Scientific Research Project (51402180) supported by NSFC, Natural Science Basic Research Plan in Shaanxi Province of China (Program No. 2016JQ3033) and the Scientific Research Foundation for the Returned Overseas Chinese Scholars of Shaanxi province ([2014]1059, No. 35). Thanks are given to Cathy Ridgway of Omya International AG for paper filled samples preparation and to Prof. Patrick Gane of Aalto University for helpful discussions.

References

1. Washburn EW (1921) The dynamics of fluid flow. J Phys Rev 17:273–283
2. Quéré D (1997) Inertial capillarity. Europhys Lett 39(5):533–538
3. Bosanquet CH (1923) On the flow of liquids into capillary tubes. Philos Mag 6(45):525–531
4. Liu G, Zhang M, Ridgway C, Gane PAC (2014) Pore wall rugosity: the role of extended wetting contact line length during spontaneous liquid imbibition in porous media. Colloid Surf A Physicochem Eng Aspects 443:286–295
5. Liu G, Zhang X, Zhang M, Gane P (2016) Revealing the components at work in classical liquid imbibition models: inertial, Bosanquet and Viscous Lucas-Washburn applied to printing. In: Zhao P, Ouyang Y, Xu M, Yang L, Ouyang Y (eds) Advanced graphic communications and media technologies. PPMT 2016. Lecture Notes in Electrical Engineering, vol 417, pp 987–995

6. Gane PAC, Ridgway CJ, Schoelkopf J (2004) Absorption rate and volume dependency on the complexity of porous network structures. Transp Porous Med 54(1):79–106
7. Schoelkopf J, Gane PAC, Ridgway CJ, Matthews GP (2000) Influence of inertia on liquid absorption into paper coating structures. Nordic Pulp Paper Res J 15(5):422–430
8. Liu G, Zhang M, Ridgway C, Gane PAC (2014) Spontaneous inertial imbibition in porous media using a fractal representation of pore wall rugosity. Transp Porous Med 104(1): 231–251
9. Laufmann M, Gisella U (2011) Surface filling of wood-free paper with natural ground calcium carbonate. Appita J 64(5):403–407, 411
10. Ridgway CJ, Gane PAC (2002) Controlling the absorption dynamic of water-based ink into porous pigmented coating structures to enhance print performance. Nord Pulp Pap Res J 17 (2):119–129

$SiO_x/TiO_y/C_zH_t$ Composite Coatings Prepared by Magnetron Co-sputtering on Substrate Paper

Zhuang Liu, Lin Zhu, Hanlin Yang, Jiang Chang and Wenping Cao

Abstract $SiO_x/TiO_y/C_zH_t$ composite coatings were deposited on papers by magnetron co-sputtering. Influences of RF power on structures and properties of coatings were investigated. The result from SEM applied to investigate the microstructure showed that coatings could be prepared with good capillary structure as suitable input powers, which helped to get a good printability for papers. Raman test results showed that different input power ratios could be applied to deposit coatings with modifiable inorganic and organic components.

Keywords Composite coatings · Magnetron sputtering · Paper

1 Introduction

Paper as the carrier of information, its printability is extremely important in the expression of information transmission process. The coating technique on the surface of the paper is the main way to improve its printability, which can improve the surface structure, optical properties, smoothness and ink absorption performance of the paper. Conventional coating techniques are mostly carried out by means of artificial or mechanical methods, with appropriate rheological properties on the surface of the paper. Coating materials are often more complex ingredients with a lot of pollutants in the traditional coating process, and they are not easy to control to distribute uniformly [1, 2]. More importantly, the larger size of the coating materials results the lower resolution and unclear reproduction of the image information. In this paper, using vacuum magnetron sputtering method rather than the existing paper coating modification methods to deposit $SiO_x/TiO_y/C_zH_t$ composite coatings on the paper surface to improve the paper surface performance and its printability. The coatings were synthesized using RF sputtering tri-target method. C_zH_t component of composite coatings was mainly produced by sputtering

Z. Liu (✉) · L. Zhu · H. Yang · J. Chang · W. Cao
School of Light Industry, Harbin University of Commerce, Heilongjiang, China
e-mail: hitprint@163.com

P. Zhao et al. (eds.), *Applied Sciences in Graphic Communication and Packaging*, Lecture Notes in Electrical Engineering 477,
https://doi.org/10.1007/978-981-10-7629-9_72

a polymer target, dicyclopentadiene dioxide cured with maleic anhydride (DCPD/MA), which was one of the three targets. The segments are bombarded out due to incident particles effect on the polymer target, which could react and re-deposited on the surface of the substrates.

Researches exploited polymer target in sputtering system date back to 1970s [3]. Polytetrafluoroethylene (PTFE) was frequently used to prepare functional films and coatings [3]. Biederman group studied and verified the feasibility of polyethylene (PE) and polypropylene (PP) as polymer targets [4, 5]. Researchers combined polymer targets and inorganic targets to prepare composite films with complicated structures and components, such as SiO_2/PTFE, SiO_2/PI and SiO_2/DCPD/MA targets [6–8]. These investigates have proved that the method of magnetron co-sputtering polymer/inorganic targets is an effective and promising way to prepare composite films and coatings.

2 Experimental

2.1 Composite Coatings Deposition

A self-equipped coating system (Fig. 1) was used to prepare composite samples on paper substrates. The device can prepare sample area size up to 210 mm × 297 mm on a rotatable samples holder. The rotate rate is adjustable from zero to 5000 circles per hour. Three circular targets in size of 150 mm diameter were established in the vacuum chamber. During the deposition, we kept the distance between the targets and paper substrates as a constant 120 mm. SiO_2 and TiO_2 targets are purity

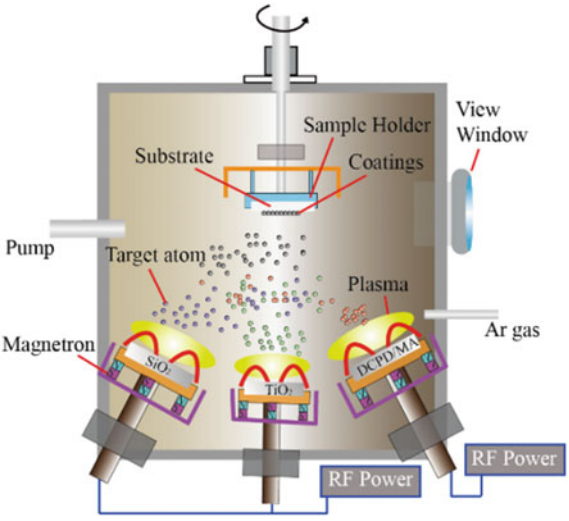

Fig. 1 The schematic representation of RF magnetron co-sputtering

of 99.999%. Polymer target DCPD/MA was prepared by our lab. Argon in purity of 99.999% was used for sputtering gas. The base pressure in vacuum chamber was 10^{-4} Pa prior to sputtering, and the working pressure adjusted by the argon flux. In this work, argon flow rate was 50 sccm (standard cc per min) and 0.1 Pa working pressure was gained. For DCPD/MA target, RF sputtering power was set to 100 W, and for SiO_2 and TiO_2 targets varied from 50 to 250 W. 80 g/m^2 uncoated papers were put 24 h at temperature 25°C and RH 65% before sputtering. During the preparation process, efficient cooling of the substrate was a key factor due to chemical properties of substrate papers.

2.2 Characterization Techniques

The chemical properties of the coatings were characterized using a Raman spectroscopy (XploRA PLUS, HORIBA Scientific) with a resolution of 1/cm.

The composite coating $SiO_x/TiO_y/C_zH_t$ morphology of samples was studied by scanning electron microscopy (SEM, FEI Sirion, Philips, the Netherlands) using an accelerating voltage between 20 kV.

The oil contact angle measurement was performed using an apparatus produced by employing the conventional oil droplet method. There was a syringe needle with a 0.5 mm internal diameter fixed on the apparatus. An oil drop was injected from the needle onto the central area of the sample during the examination. Contact time from 0.1 to 60 s passed after the dropping of the water, pictures were taken by a CCD camera and stored them to the computer, and then the angles were measured and calculated using a software. The average angle values were averaged from three different positions.

3 Results and Discussion

The Raman absorption bands of $SiO_x/TiO_y/C_zH_t$ composite coatings were identified in Fig. 2. The films had a complex chemical structure changed with different input powers. The peak of wavenumber 520 cm^{-1} owed to –Si–O– components [9]. The peak of 145 cm^{-1} displayed anatase TiO_2 vibration feature [10]. The peaks in the region of 360–450 cm^{-1} are complicated to distinguish their attribution materials. They can be thought as the combination of TiO_2 rutile phase, O–Si–O signal of SiO_2 in the parallel polarization mode and C–C vibration [9, 10]. The intensity of peaks varied with input powers on tri-target.

The morphologies of $SiO_x/TiO_y/C_zH_t$ coatings were investigated by SEM, which were shown in Fig. 3 to reveal their microstructure. SEM images of the composite coatings formed at different RF power exhibited obvious differences.

The white particles on the images represent the SiO_x/TiO_y component of the coatings are not continuous phase as higher power input the inorganic targets (Fig. 3d, e). As lower RF power input the inorganic targets (Fig. 3a, b), continuous

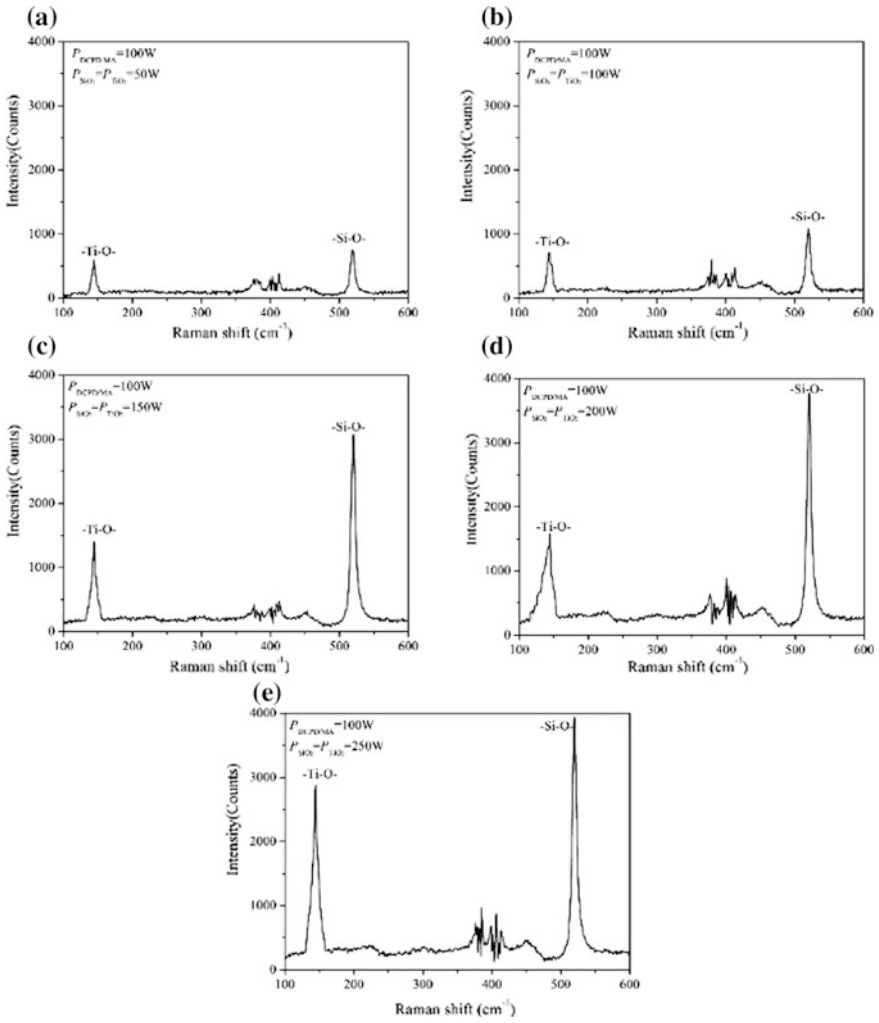

Fig. 2 Raman spectra of the coatings deposited at different RF power

C_zH_t matrix produced on substrate paper. As input power on targets SiO_2 and TiO_2 was 150 W (Fig. 3c), SEM image indicate that SiO_x/TiO_y is embedded in a continuous C_zH_t phase. These results were in accordance with Raman results. As the SiO_x/TiO_y component in the composite coatings increased and the C_zH_t component decreased, the smoothness of the coatings got worse. It is worth noting that a suitable power ratio input on targets SiO_2/TiO_2 and DCPD/MA will produce an optimization of organic-inorganic component, which results in an important capillary structure for achieving better ink absorption properties.

In this paper, the absorption properties of the coatings on the ink were characterized by the absorbency of the No. 6 adjusting oil. Figure 4 showed SiO_x/TiO_y/

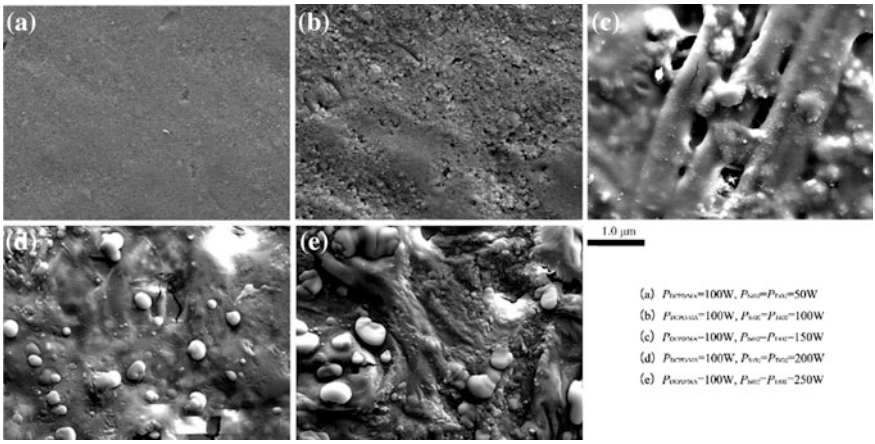

Fig. 3 SEM images of the coatings deposited at different RF power

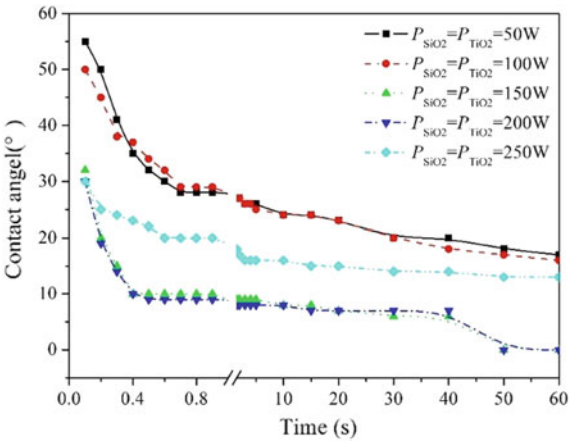

Fig. 4 Contact angles of the coatings deposited at different RF power

C_zH_t coatings deposited at different power absorption abilities. Those coatings prepared at the power on SiO_2 and TiO_2 of 150 W had a good capillary structure, which cause good instantaneous absorption to the oil, that is, the dynamic ink absorption of the ink is good. The oil absorption in a short time is advantageous for the reproduction of the image clarity during the printing process. Instantly absorb the material of the ink component, the pigment can be retained in the paper quickly in imprinting process, which is helpful for printing image details reproduction, that is, the small dots are not lost easily. As sputtering power is too high, SiO_x/TiO_y particles are too large, which causes poorer capillary structures and worse ink absorption. As sputtering power is too low, there are more high molecular components, which results in the poor ink absorption due to the inherent characteristics of materials. Thus, appropriate sputtering power delicate the inorganic particles into

the staggered fibers to improve the smoothness of the paper and ink absorption and then can have a good ability to reproduce the image.

4 Conclusions

The method of RF magnetron co-sputtering to prepare the $SiO_x/TiO_y/C_zH_t$ coatings on the surface of paper substrate is feasible through this experiment. A composite coating with a suitable pore structure can be prepared by adjusting the sputtering power ratio to improve the print adaptability of papers.

Acknowledgements This research was supported by the Natural Science Foundation of Heilongjiang Province (Grant No. E201356), the Natural Science Foundation for Young Scholars of Heilongjiang Province (Grant No. QC2012C008) and the National Science Foundation for Young Scholars of China (Grant No. 51302054).

References

1. Wu YM, Duan HD, Yu YQ, Zhang CG (2001) Preparation and performance in paper coating of silicone-modified styrene–butyl acrylate copolymer latex. J Appl Polym Sci 79(2):333–336
2. Lee YK, Kim SG, Won JM, Kim YH (2015) Application technology of environmental-friendly starch-based biobinder and synthesized binder in order to substitute SB latex for paper coating (1)—application of substitute binder for pre-coating layer. J Korea Tech Assoc Pulp Paper Ind 47(5):134–140
3. Biederman H, Stelmashuk V, Kholodkov I, Choukourov A, Slavínská D (2003) RF sputtering of hydrocarbon polymers and their derivatives. Surf Coat Technol 174–175:27–32
4. Stelmashuk V, Biederman H, Slavínská D, Trchová M, Hlidek P (2004) RF magnetron sputtering of polypropylene. Vacuum 75:207–215
5. Kousal J, Hanus TJ, Choukourov A, Hlídek P, Biederman H, Slavínská D, Zemek J (2005) RF magnetron sputtering and evaporation of polyisobutylene and low density polyethylene. Surf Coat Technol 200:472–475
6. Drabik M, Kousal J, Pihosh Y, Choukourov A, Biederman H, Slavinska D, Mackova A, Boldyreva A, Pesicka J (2007) Composite SiO_x/hydrocarbon plasma polymer films prepared by RF magnetron sputtering of SiO_2 and polyimide. Vacuum 81:920–927
7. Pihosh Y, Biederman H, Slavinska D, Kousal J, Choukourova A, Trchová M, Mackova A, Boldyryeva A (2006) Composite SiO_x/fluorocarbon plasma polymer films prepared by r.f. magnetron sputtering of SiO_2 and PTFE. Vacuum 81:38–44
8. Liu Z, Sun ZH, Ma XX, Yang CL (2013) Characterization of composite SiO_x/polymer barrier films. Packag Technol Sci 26:70–79
9. Choudhury S, Sasikala R, Saxena V, Aswal DK, Bhattacharya D (2012) A new route for the fabrication of an ultrathin film of a PdO–TiO_2 composite Photocatalyst. Dalton Trans 41:12090–12095
10. Mélinon P, Kéghélian P, Prével B, Dupuis V, Perez A (1998) Structural, vibrational, and optical properties of silicon cluster assembled films. J Chem Phys 108(11):4607–4613

Study on Phthalates Plasticizers Detection of Food Paper Packaging

Xiaomin Li, Lijiang Huo and Chenyang Liu

Abstract Qualitative and quantitative analysis on phthalate plasticizes (DEHP, DIBP and DBP) of 24 kinds of common food paper packaging were carried out. The study determined the plasticizers using four kinds of organic extraction reagent named n-hexane, ethyl acetate, anhydrous ethanol, and acetone by the Ultrasonic extraction and the gas chromatograph-mass spectrometer technology. The best temperature, time and the way of the extraction of these four different reagent were obtained. Through experiments and analysis, the best extraction reagent of the plasticizers remained in the food paper packaging is ethyl acetate and the best way to extract targets is the combination of ultrasonic oscillation 30 min with vortex 3 min. For the extraction using ethyl acetate, the best temperature of the ultrasonic operation is 25 °C, and the time of the optimum ultrasonic extraction is 90 min. The plasticizers were detected in all of the 24 kinds of food paper packaging samples by the method. The content of DEHP, DBP and DIBP were 0.33497–211.02104, 0.34484–519.9099, 0.20224–37.67883 mg/kg respectively. The result shows that the method is comparatively simple, fast and quantitative accuracy. But the safety of the food paper packaging should be concerned deeply.

Keywords Food paper packaging · Phthalate plasticizers · Gas chromatography-mass spectrometry · Detection of plasticizers

1 Introduction

The phenomenon of toxic and hazardous substances remained in paper packaging materials which migrate into food and harm to human health has gradually been concerned [1–5]. Plasticizer vestigital within common food paper packaging in China was determined in this study. The Ultrasonic extraction and the gas

X. Li · L. Huo (✉) · C. Liu
School of Light Industry and Chemical Engineering, Dalian Polytechnic University, Liaoning, China
e-mail: lijianghuo@163.com

P. Zhao et al. (eds.), *Applied Sciences in Graphic Communication and Packaging*, Lecture Notes in Electrical Engineering 477,
https://doi.org/10.1007/978-981-10-7629-9_73

chromatograph-mass spectrometer technology were used in the analysis process. It aims at obtaining a detection method can be used in practice effectively. Meanwhile, the safety of current food paper packaging in China was explored.

2 Experiment Materials and Method

2.1 Experiment Materials

24 kinds of common food paper packaging were involved and their parameters can be seen in Table 1. Laboratory reagent used in the study was shown in Table 2.

Table 1 Experimental materials

No.	Name	Weight (g/m^2)	Thickness (mm)	Handling
1	Cola cup	2.4498	0.370	Coated with PE and printed
2	Soy-milk cup	2.9957	0.365	Coated with PE and printed
3	Moon-cake carton	3.0404	0.472	Coated with PE and printed
4	Popcorn carton	3.1551	0.415	Coated with PE and printed
6	Cake carton bottom	10.1235	2.906	Printed
7	Cake paper tray	0.5186	0.142	Non printed
8	Instant noodle bowl	5.1326	0.712	Coated with PE and printed
9	Bean vermicelli bowl	5.1352	0.745	Coated with PE and printed
10	Instant noodle bowl	4.8921	0.700	Coated with PE and printed
11	Instant noodle bowl	4.9882	0.677	Coated with PE and printed
12	White ground paper	0.5595	0.066	Non printed
13	White ground paper	0.2526	0.034	Non printed
14	Hamburg packaging paper	0.3442	0.039	Coated wax and printed
15	French fries packaging paper	0.4226	0.064	Printed
16	Flour yeast paper bag	0.8201	0.093	Coated wax and printed
17	French fries paper bag	0.4558	0.056	Printed
18	Self-raising flour bag	0.8271	0.104	Printed
19	Black white stripe bag	0.8268	0.099	Printed
20	Cake paper tray	0.5186	0.142	Printed
21	White lining paper	0.3651	0.034	Coated wax and non printed
22	White paper board	2.6408	0.344	Non printed
23	Hamburg packaging paper	0.2767	0.033	Coated wax and printed
24	White tea bag without heat-sealing	0.1535	0.047	Non printed

Table 2 Laboratory reagent

Reagent	Class rating	Production firm
N-hexane	HPLC	Tianjin Kemiou Chemical Reagent Co.Ltd., China
Ethyl acetate	HPLC	Tianjin Kemiou Chemical Reagent Co.Ltd., China
Anhydrous ethanol	HPLC	Tianjin Kemiou Chemical Reagent Co.Ltd., China
Acetone	HPLC	Tianjin Kemiou Chemical Reagent Co.Ltd., China
Reomol mixed standard solution	1000 μg/mL	Accu Standard, USA

2.2 Experiment Method

2.2.1 Gas Chromatography-Mass Spectrometry Conditions

Gas Chromatography Conditions. Dchromatographic column was B-5MS quartz capillary column (ID 0.32 mm), introduction port temperature was 265 °C, high-purity helium gas (purity ≥ 99.9999%), constant flow speed was 1.5 mL/min, splitless injecting samples, connecting line temperature was 290 °C, sample introduction volume was 1 μL [6–10].

Mass Spectrometry Conditions. Interface temperature was 285 °C, ion source temperature was 230 °C, selected ion monitoring (SIM), onization energy was 70 eV, reagent latency was 3.5 min, NIST MS Search 2.0 [6–10].

2.2.2 Preparation of Standard Solution and Phthalates Plasticizers Detection

Standard solution (0.5 μg/mL consistency) were prepared by using n-hexane, ethyl acetate, anhydrous ethanol and acetone respectively. Reomol mixed standard solution (25 μL) was taken and diluted progressively in 50 ml bottle and put into refrigerator (0–5 °C temperature). The content of DEHP, DBP and DIBP within the 24 kinds of food paper packaging samples were detected though gas chromatography-mass spectrometry system [6, 7, 11].

3 Results and Discussion

The best temperature and time of the detection by using n-hexane, ethyl acetate, anhydrous ethanol and acetone respectively were obtained, as shown in Table 3.

Meanwhile, the experiments shown that ethyl acetate was the best one of the reagent for extracting the total amount of the phthalate plasticizers within the samples. The best way to extract targets was the combination of ultrasonic oscillation 30 min with vortex 3 min. The DEHP, DIBP and DBP were found in all of

Table 3 The best temperature and time of the detection by using different reagent

Reagent	Best temperature (°C)	Best time (min)
N-hexane	20	120
Ethyl acetate	25	90
Anhydrous ethanol	25	120
Acetone	30	60

Table 4 Three kinds of PAEs plasticizers content in samples (unit: mg/kg)

No.	DEHP	DBP	DIBP	Total amount
1	1.31219	5.1174	1.35369	7.78328
2	1.4226	3.72147	2.32023	7.4643
3	0.45663	0.70983	37.67883	38.84529
4	18.97869	1.21108	0.20224	20.39201
5	0.89589	1.13723	4.38	6.41312
6	1.16149	2.52241	14.20924	17.89314
7	2.14248	5.73347	1.05514	8.93109
8	1.61894	3.44476	6.21859	11.28229
9	2.70719	33.24118	1.16434	37.11271
10	2.42801	3.04015	9.89969	15.36785
11	0.33497	0.90755	7.94291	9.18543
12	1.7099	2.34653	4.38812	8.44455
13	3.84462	4.34891	2.23827	10.4318
14	1.31257	0.77119	1.84597	3.92973
15	1.77703	17.87645	1.70174	21.35522
16	3.13133	3.79194	2.19823	9.1215
17	35.36632	2.98378	2.60054	40.95064
18	211.02104	1.12713	2.67092	214.8191
19	17.03446	1.36996	2.2344	20.63882
20	4.71188	519.9099	2.18515	526.8069
21	0.54555	0.34484	2.77204	3.66243
22	1.8702	1.19505	3.52356	6.58881
23	1.65027	2.12864	2.12864	6.27555
24	1.24501	0.74152	2.68613	4.67266

the 24 kinds of food packaging paper samples. The content of them are 0.33497–211.02104, 0.34484–519.9099, 0.20224–37.67883 mg/kg respectively, as shown in Table 4. The results also shown that the total amount of the DEHP, DBP and DIBP within the samples are different. The difference was gigantic.

Among the rest, No. 7, 12, 13, 21, 22, 24 samples without PE coating and printing, their DEHP, DBP and DIBP content are 1.24501–3.84462, 0.74152–5.73347 and 1.05514–4.38812 mg/kg respectively, lower than that of the others with coating or printing. That is to say that handling processes including printing,

PE coating, wax coating and adhesion can bring the phthalates plasticizers into the food paper packaging. Even the handling led to very high content of the phthalate plasticizers impacting food paper packaging, such as No. 20 sample etc. Especially, the overrun content of DBP is easy to migrate into food contained in the packaging.

4 Conclusions

The phthalates plasticizers within food paper packaging can be detected quantitatively by Ultrasonic extraction and the gas chromatograph-mass spectrometer technology. The best extraction reagent for carrying out the detection is ethyl acetate and the best condition to extract the targets is the combination of ultrasonic oscillation 30 min with vortex 3 min. Also, it is shown that the phenomenon of phthalates plasticizers remained in food paper packaging existed widely. The potential impact brought by the food paper packaging products in current markets and perhaps harm to customers should be concerned deeply.

References

1. Yue Q (2011) Study on potential harm and migration of paper packaging material. Environ Prot Energy Save 4(42):61–63
2. Yang C (2012) Study on printing ink migration with AAS and GC-MS for paper packaging material. Packag Eng 33(11):18–20
3. Yamaguchi Y, Fujita Y, Kuroda K, Endo G (2004) Chemical analysis and genotoxico logical safety assessment of paper and paper board used for food packaging. Food Chem 42:1323–1337
4. Gottfried Z (2001) Odorous compounds in paperboard as influenced by recycled material and storage. Packag Technol Sci 14:13l–136
5. Wang X, Lin X, Ke H et al (2007) Study progress on pollution and alate plasticizers. Environ Health 24(9):736–738
6. Wang C, Yang Z, Rong X et al (2013) Detection of plasticizers within costing paper with Ultrasonic extraction-gas chromatograph-mass spectrometer. Technol Prog 3:19–21
7. Liu Z, Huang H, Liu J et al (2010) Detection of Phthalates plasticizers within tipping paper and packaging paper with isopropanol extraction-gas chromatograph. Anal Instrum 2:30–35
8. Zhang L, Rong H, X Yu et al (2012) Detection of Phthalates plasticizers within plant fibre food packaging material with Gas chromatograph method. China Sanitary Inspection J 22 (3):450–452
9. Wang C, Mai J et al (2013) Detection of Phthalates plasticizers within costing paper with microwave-assisted extraction-gas chromatograph-mass spectrometer/selected ion monitoring (SIM). Fujian Anal Determ 22(4):1–7
10. Song YS, Park HJ, Komolprasert V (2000) Analytical procedure for quantifying five compounds suspected as possible contaminants in recycled paper/paperboard for food packaging. J Agric Food Chem 48(12):5856–5859
11. Yang Y, Xie Y, Tian F et al (2013) Migration detection of Phthalate plasticizers within common food and packaging material. Colour Spectr 31(7):674–678

Research on Properties of the Edible Chinese Cabbage Paper Packing

Danting Li, Jiang Chang and Xue Gong

Abstract This paper was based on Chinese cabbage, characterizations were performed to determine the properties of Vegetable fiber. Both Vegetable paper formula and process parameters were studied. It was researched the effect of the additive amount of the starch, binder and plasticizer on the properties of Chinese cabbage paper by the experiment of single factor. By optimizing the test, it was researched and developed of the new vegetable paper. It was obtained the optimum process parameters of making vegetable papers for produce the edible vegetable paper packaging material that had a better performance and suitable to food packaging, and the reliable data for the large-scale production of vegetable papers were provided. It was shown that the new materials can be used in food packaging and even could be directly used as instant food. The use of edible Chinese cabbage packing not only can reduce the environmental pollution, but also can enhance the sense of beauty of the food.

Keywords Vegetable paper · Fiber · Edible packing

1 Introduction

In recent years, with the enhancement of environmental protection consciousness, biodegradable polymeric materials has been paid more and more attention, edible packaging film is a focus of research [1]. Many research studies have been carried out on this topic. As the popular edible film, vegetable paper is quite an ideal food packaging materials [2]. It has a higher nutritional value and can be used as carrier material, pigment, flavor of food nutrition fortifier, antioxidant and antimicrobial agents. It can be eaten together with the food, so it don't have pollution to food and environment. It can be convenient for single packaging; and has moisture barrier property that can delay the migration and diffusion the water and oil, food and other

D. Li (✉) · J. Chang · X. Gong
Light Industry College, Harbin University of Commerce, Heilongjiang, China
e-mail: ldtjing@sina.com

P. Zhao et al. (eds.), *Applied Sciences in Graphic Communication and Packaging*, Lecture Notes in Electrical Engineering 477,
https://doi.org/10.1007/978-981-10-7629-9_74

components. It has the permeability and anti permeability to avoid evaporation of the flavor substances in food. It has good physical and mechanical properties to protect the packaging [3]. The quality and shelf life of products has improved by vegetable paper [4]. It conforms to the concept of a pollution-free development.

2 Experimental Researches

It has a great impact on the types and proportions of starch, binder and plasticizer, during the preparation of the Chinese cabbage paper packaging.

2.1 Effect of Starch on Properties of Chinese Cabbage Paper

Starch can improve the fluidity of pulped Chinese cabbage and the strength of Chinese cabbage paper. Figure 1 is shown the effect of starch on tensile strength and elongation of Chinese cabbage paper. Experimental results show that the tensile strength are increased and the elongation are firstly increased and then decreased with the starch viscosity increasing. The maximal elongation occurs when the starch viscosity is 3.0%.

2.2 Effect of Binder on Properties of Chinese Cabbage Paper

The binder can make the structure of Chinese cabbage paper packaging material more compact and uniform. Furthermore the binder can improve the strength and

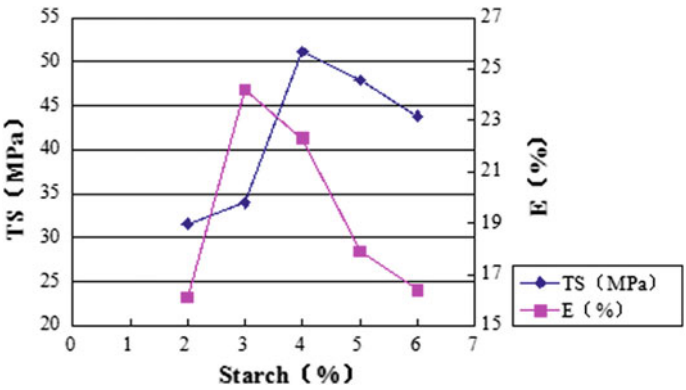

Fig. 1 Effect of starch on tensile strength and elongation of Chinese cabbage paper

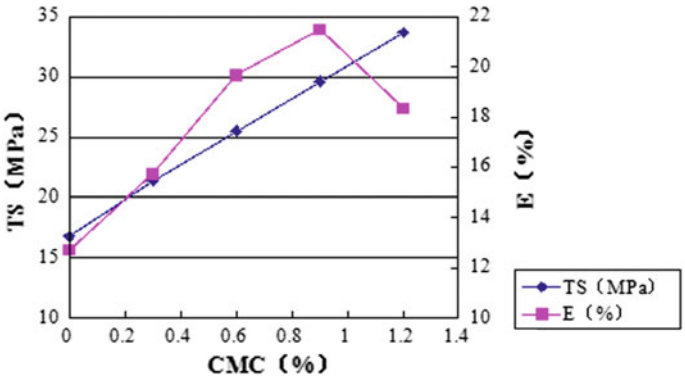

Fig. 2 Effect of CMC on tensile strength and elongation of Chinese cabbage paper

toughness of Chinese cabbage paper. Addition of binder can make chelation between macro-molecular chain in the fiber which has a great influence on the properties of the Chinese cabbage paper [5].

2.2.1 Effect of CMC on Properties of Chinese Cabbage Paper

CMC (Carboxyl Methyl Cellulose) is the highly viscous solution. The effect of CMC on tensile strength and elongation of the Chinese cabbage paper is shown in Fig. 2.

The results show that the tensile strength is increased and the elongation are firstly increased and then decreased with the CMC increasing. The maximal tensile rate occurs when the CMC is 0.9%.

2.2.2 Effect of Sodium Alginate on Properties of Chinese Cabbage Paper

Sodium Alginate is a natural polysaccharide which is extracted from seaweed in carbohydrates. The property is not only concluded the stability, solubility, viscosity and security performance, but also has a concentrated solution, gel formation and film forming ability. Sodium alginate is widely used in the food industry. Americans call it “wonderful food additive” to the Japanese as “longevity food additives”. Figure 3 shows the effect of sodium alginate on tensile strength and elongation of Chinese cabbage paper.

Daily rations are adjusted accordingly. When the content is below 0.9%, the tensile strength and the elongation are increased with the addition of sodium alginate. When the content is above 0.9%, the tensile strength and the elongation are decreased with the addition of sodium alginate.

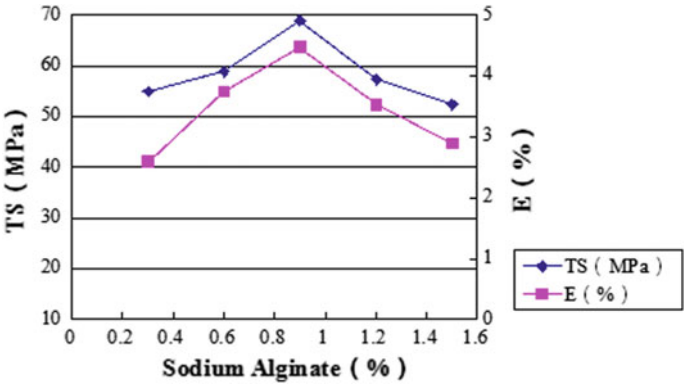

Fig. 3 Effect of sodium alginate on tensile strength and elongation of Chinese cabbage paper

2.3 *Effect of Sorbitol on Properties of Chinese Cabbage Paper*

Sorbitol is a white water-soluble crystalline alcohol with a sweet taste. During the processing of Chinese cabbage paper Sorbitol can decrease the interaction between the fibers and the structure rigidity, then increase the ductility, and improve the glossiness and elasticity.

The graph (Fig. 4) is shown that the tensile strength of Chinese cabbage paper is decreased with Sorbitol increase. Because of the sorbitol has reduced the force between the fiber molecules. The elongation of Chinese cabbage paper is decreased while content. With the increase of Sorbitol content, the elongation first increase and then decrease, the max Sorbitol content is about 8%.

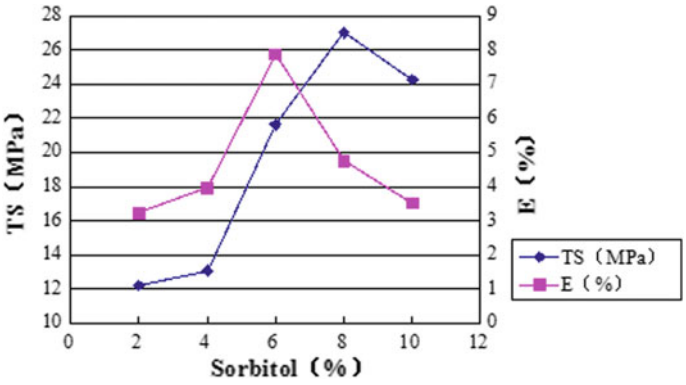

Fig. 4 Effect of sorbitol on tensile strength and elongation of Chinese cabbage paper

3 Conclusions

By the experiment, the best medium formula is got, that is starch 3%, CMC 0.9%, sodium alginate 0.9% and sorbitol 8%. This thesis gets the optimum parameters related to producing cabbage paper with a series of experiments, and It can provide theoretical basis and technical assistance for edible Chinese Cabbage paper industry.

References

1. Luo X (2009) Progress in the research of the eatable packaging film at home and abroad. China Packag 19(5):102–103
2. Jr Bentley DJ (2010) Edible packaging: round 2. Film Foil Converter 76(9):12
3. Garcia MA, Martino MN, Zaritzky NE (2010) Lipid addition to improve barrier Properties of edible starch-based films and coating. J Food Sci 65(6):941–947
4. Perez-Gago MB, Krochta JM (2009) Water vapor permeability of whey protein emulsion as affected by PH. J Food Sci 64(4):695–698
5. Xu K, Cai Z, Zhang Y (2010) The study on the processing method of vegetable paper and key factors. Packag Food Mach 21(1):8–10
6. Zeng F, Wu J (2006) Effects of plasticizer on the structure and properties of cellulose membrane. Packag Eng 27(1):16–17

Research on the Preparation and Properties of Water Resistant and Oil Resistant Paper Tableware Made by Bagasse Brown Pulp

Li Liu, Yichao Lei and Guangxue Chen

Abstract Water-resistant and oil-resistant paper tableware has broad application prospects. The mechanism of water resistance and oil resistance properties of paper and the determination of oil resistance properties were introduced. The water/oil resisted paper was made of bagasse brown pulp by beating and adding oil-resistant agent, water-resistant agent and retention aid. The effects of water repellent, oil repellent and other factors on the oil and water repellency of paper tableware ware studied. The analytical and experimental results showed that the paper preparation using method proposed in this paper has a good performance in oil resistant agent of 2%, water resistant agent of 5%, retention agent of 0.02%, beating revolution of 1200 r respectively.

Keywords Bagasse brown pulp · Paper tableware · Oil resistance
Water resistance

1 Introduction

The "white pollution" brought by disposable tableware is becoming increasingly serious [1–3]. The ecological environment on which human beings depend is destroyed. In view of the serious damage to the environment and human health caused by the traditional non-environmentally friendly foam plastic packaging containers, a cheap and environmentally friendly plastic tableware substitutes has become an inevitable trend of social development [4]. "Paper on behalf of plastic" [5, 6], not only can take full advantage of the plant fiber raw materials in natural environment, but also paper tableware can be degraded. Therefore, it is the most effective alternative to foam plastic tableware. Pulp-molded tableware is prepared by adding functional chemicals (such as oil-resistant agent, water resistant agent,

L. Liu · Y. Lei (✉) · G. Chen
State Key Laboratory of Pulp and Paper Engineering, South China University of Technology, Guangzhou, China
e-mail: ppyclei@scut.edu.cn

P. Zhao et al. (eds.), *Applied Sciences in Graphic Communication and Packaging*, Lecture Notes in Electrical Engineering 477,
https://doi.org/10.1007/978-981-10-7629-9_75

retention agent, etc), vacuum suction molding, heating, drying and cutting with straw pulp as raw material [7]. This kind of tableware presents beautiful appearance and excellent properties such as oil resistance, water resistance, permeability, great toughness and strength. It is healthy, recyclable, and soon natural degradation. In United States and Europe, they have higher standard to packaging paper for food and the chlorine bleached pulp is not allowed at all whereas the more safer way, such as using chlorine-free bleach, is frequently advocated in the industrial application. We advocated bagasse brown pulp in the production of pulp molded tableware, which makes the tableware safer and environmentally friendly.

2 Experiments

Compared with plastic film, as the fiber structure is loose which easily cause the penetration of grease into paper arising from the capillary absorption. In addition the surface of the fiber contains a large number of hydroxyl, resulting in a higher surface energy, strong lipophilic, so no oil treatment of paper tableware has strong oil absorption. The water resistant agent and oil resistant agent usually refers to a series of additives that can reduce the surface tension of paper. For the food packaged, we have to face a reality problem, such as liquids including the soup, oil and liquid seasoning, so we will add some water resistant agent and oil resistant agent in the production of the paper tableware in order to achieve the purpose of preventing leakage of soup oil. In addition, appropriate other additives (such as retention aids, enhancers, etc.) should be added to meet requirements.

2.1 Section of Experiment

2.1.1 Materials of the Experiment

Bagasse brown pulp from a pulp factory in Guangxi with pulp moisture content of 9.39%, pulp freeness of 645 ml, small fiber content of 34.65%, kappa value of 12.27; Castor oil (chemical pure, Tianjin Yongda Chemical Reagent Co., Ltd.); toluene (chemical pure, Guangzhou Chemical Reagent Factory), n-Heptane (chemical pure, Tianjin 100 World Chemical Co., Ltd.), Oil resistant agent (solid content 23.48%); Water resistant agent (solid content 21.76%); Cationic Polyacrylamide (solid powder).

2.1.2 Method of the Experiment

The dry pulp board was disintegrated based on the standard method and adjusted the pulp consistency to 10%. After beating in the PFI mill, oil resistant agent, water resistant agent and retention aid solution as additives added into the pulp according

to the proportion and order. Then 80 g/m^2 weight of handsheets was prepared through a standard handsheet former. After drying, the experiment was ended.

2.1.3 Detection of the Experiment

The Cobb value of the paper was measured according to GB/T 1540-2002 using the Cobb Absorption Tester. The oil resistant value of paper and paperboard was measured by TAPPI 559 pm-96 "Grease resistance test for paper and paperboard" test [8]. 12 grades of test solution are prepared from a series of different proportions of castor oil, toluene and n-heptane. The lowest oil resistant level is 1, the highest oil resistant level is 12.

2.2 Analysis of Experiment Results

2.2.1 Effect of the Amount of Oil Resistant Agent on the Oil Resistance Property of the Sample

The positive charge had been interacted with the negatively charged fiber when the positively charged cationic oil resistant agent combined with the fiber. The oil-based orientation outward forming an oil film has low surface tension on the fiber surface to prevent the penetration of oil (Fig. 1).

For safety reasons, the oil resistant value of packaging paper for food should be 5–8 level [9]. So considering the production cost and performance of paper, the initial choice of oil resistant agent is 1–2.5%.

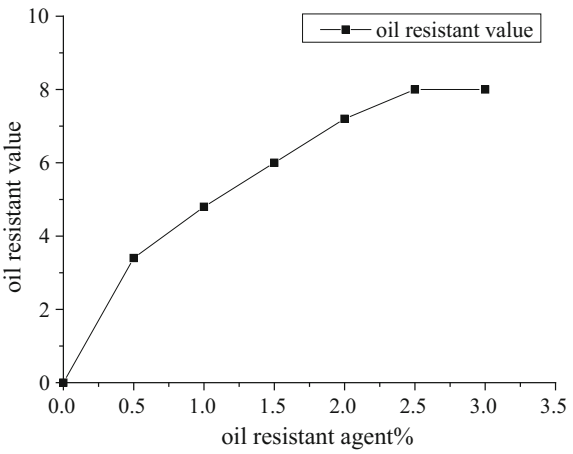

Fig. 1 The curve of the relationship between oil resistant agent and the oil resistant value

2.2.2 Effect of the Amount of Water Resistant Agent on the Water Resistance Property

Cationic water resistant agent with a positive charge can be adsorbed in the fiber with negative charge by electrostatic force. This bought the form of the hydrophobic membrane on the fiber, which give the sample water resistant property.

It can be seen from Fig. 2 that considering the economic cost and performance requirements, the initial choice of water resistant agent is 5–7%.

2.2.3 Composite Effect of Water and Oil Resistant Agent on Water and Oil Resistant Properties

The water resistant agent and the oil resistant agent used in the experiment are all cationic additives, which are adsorbed on the fiber surface by the combination of the positive charge and the negative charge. This formed a water and oil resistant film on the fiber surface. But adding the two additives successively will inevitably lead to competitive response. So it is important to consider the choice of appropriate addition process and study each other's the mutual influence.

It can be seen from Fig. 3 that if you add a certain amount of water resistant agent after adding anti-oil agent, which can improve the oil resistance of paper.

It can be seen from Fig. 4 that the amount of oil resistant agent has an effect on the water resistance of paper. When the oil resistant agent is 2.5%, the paper achieves the best excellent properties.

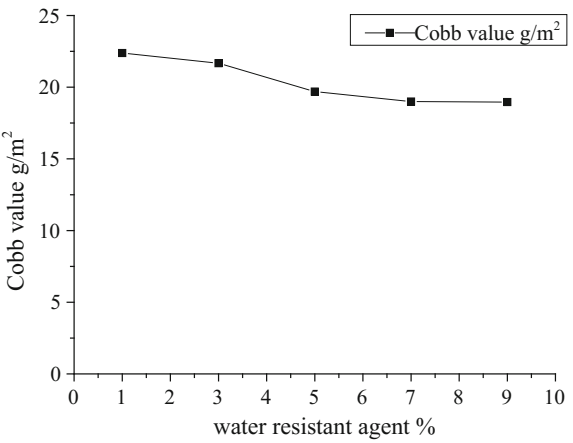

Fig. 2 The curve of the relationship between water resistant agent and the Cobb value

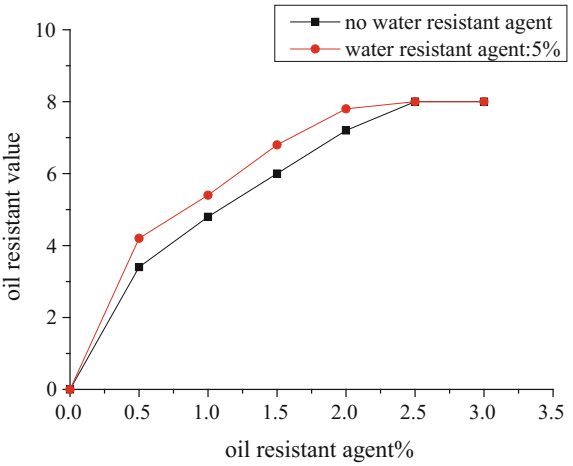

Fig. 3 The effect of water resistant agent on oil resistance

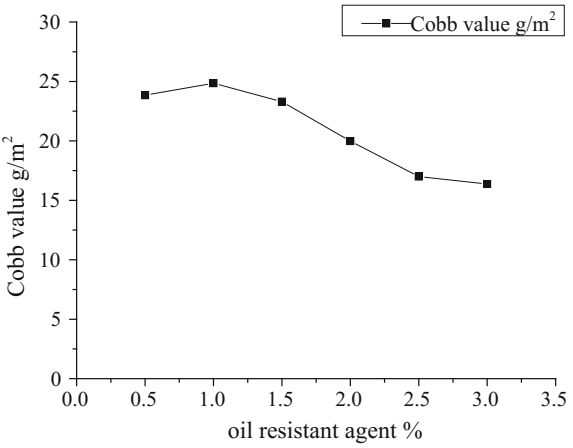

Fig. 4 The effect of oil resistant agent on water resistance

2.2.4 Orthogonal Test

Based on the orthogonal test of four factors and three levels, orthogonal experiment was designed by means of orthogonal assistant software. The factors include beating revolution, oil resistant, water resistant agent and retention agent respectively. According to the results of the single factor test of the beating degree [10], the three levels selected in this paper are shown in Tables 1, 2, 3, and 4.

Considering the oil resistant value, Cobb value, finally determine the best conditions for paper: beating revolution of 1200 r, oil-resistant agent of 2%, water resistant agent of 5%, retention agent of 0.02%.

Table 1 The level of factors table

Level	(A) Beating revolution (r)	(B) Oil-resistant agent (%)	(C) Water resistant agent (%)	(D) Retention agent (%)
1	0	1	3	0
2	1200	2	5	0.02
3	3000	3	7	0.04

Table 2 The orthogonal experiment results

Number	A	B	C	D	Oil resistant value	Cobb value (g/m^2)
1	1	1	1	1	4	19.77
2	1	2	2	2	8	15.36
3	1	3	3	3	7	22.61
4	2	1	2	3	5	15.24
5	2	2	3	1	7	16.52
6	2	3	1	2	8	16.08
7	3	1	3	2	4	19.55
8	3	2	1	3	6	17.6
9	3	3	2	1	6	15.94

Table 3 Oil resistant value factor table of orthogonal experiment

Index		A	B	C	D
Oil resistant value	k1	6.333	4.333	6.000	5.667
	k2	6.667	7.000	6.333	6.667
	k3	5.333	7.000	6.000	6.000
	R	1.334	2.667	0.333	1.000
	Factors order	BADC			
	Excellent	$B_2A_2D_2C_2$ or B_3A_2 D_2C_2			

Table 4 Cobb value factor table of orthogonal experiment

Index		A	B	C	D
Cobb value (g/m^2)	k1	19.247	18.187	17.817	17.410
	k2	15.947	16.493	15.513	16.997
	k3	17.697	18.210	19.560	18.483
	R	3.300	1.717	4.047	1.486
	Factors order	CABD			
	Excellent	$C_2A_2B_2D_2$			

3 Conclusions

(1) The water/oil resisted paper was prepared with the method proposed in this paper. It shows that the excellent properties of water resistant and oil-resistant can be guaranteed by means of setting a proper beating revolution and adding some chemicals such as, oil resistant agent, water resistant agent and retention aid.
(2) The paper has good oil resistance when the chemical dosage was oil resistant agent of 2%, water resistant agent of 5%, retention agent of 0.02%, beating revolution of 1200 r respectively by orthogonal test.

Acknowledgements This research was financially supported by the Guangdong Provincial Science and Technology Project (2016070220045) and the Key Laboratory of Pulp and Paper Engineering Funding Project (2016c01).

References

1. Guo D, Chen Y (2007) Study on the present situation and prospect analysis of disposable degradable tableware. Resour Conserv Environ Prot 23(2):40–41
2. Yang C, Bao J (2002) The development of disposable tableware and the realization of large–scale production measures. Environ Pollut Control 24(6):329–331
3. Lin F, Yang K (2004) Comparison of life cycle assessment of two disposable plastic lunch boxes. J East China Norm Univ 4:122–129
4. Hao X (2008) Biodegradable composition for the preparation of tableware, drink container, mulching film and package and method for preparing the same. United States Patent 7402618
5. Cheng P, Wang Q (2006) Study and development trend of paper packaging materials. China Packag 6(6):39–42
6. Yang T (2008) The development trend of paper packaging materials. Today's Print (1):42–44
7. Xin C (1997) Talking about "Pulp molding". China Packag 1
8. 2012TAPPI Grease resistance test for paper and paperboard
9. Li D, Liu J (2003) The mechanism and application of fluorine-based anti-oil agent. Papermak Chem 22(5):51–57
10. Liu L, Lei Y (2016) Research on the preparation and properties of water resistant and oil resistant paper made by bagasse brown pulp. Pap Sci Technol 6:28–30

Effect of Filler on the Hue of Ink-jet Base Paper

Zhencai Qu and Shiwei Liu

Abstract Filler is an important part of the production of ink-jet paper, adding filler in the pulp can not only improve the hue of ink-jet paper, but also can effectively reduce costs. The effects of pulp ratio, filler type and dosage on the hue of ink-jet paper were studied by adding titanium dioxide, ground calcium carbonate, kaolin and talcum powder. The results showed that when the ratio of softwood kraft pulp to hardwood kraft pulp was 3:7, the titanium dioxide was filled with the amount of 3% (relative to absolute dry pulp), the ink-jet base paper can get a better hue, its L = 94.26, a* Value = +0.25, b* Value = −0.19. The addition of filler in the pulp can significantly improve the hue of ink-jet base paper, which can provide a certain technical guidance for the further production and research in ink-jet paper.

Keywords Filler · Ink-jet base paper · Hue

1 Introduction

With the continuous development of ink-jet technology, ink-jet printing on the requirements of the paper is also getting higher and higher. The ink-jet paper with high-quality requires a better optical performance, and the optical performance depends not only on the whiteness of ink-jet paper, the hue of the base paper also plays a significant role in the coating of the ink-jet paper, the whiteness of the printing and the color reproduction [1]. In order to obtain the ink-jet paper with high quality, the hue of the base paper must be studied to be corrected in the production of the base paper [2]. In the paper-making process, in addition to the pulp itself hue, the use of dyes and fillers plays a decisive role in the hue of the paper. Previously, the paper industry improved the hue of the paper by adding a fluorescent whitening agent, but the fluorescent whitening agent contained carcinogenic substances and

Z. Qu (✉) · S. Liu
College of Packaging and Printing Engineering, Henan University of Animal Husbandry and Economy, Henan, China
e-mail: quzhencai@126.com

P. Zhao et al. (eds.), *Applied Sciences in Graphic Communication and Packaging*, Lecture Notes in Electrical Engineering 477,
https://doi.org/10.1007/978-981-10-7629-9_76

made its application severely restricted. Fillers commonly used in paper are titanium dioxide, calcium carbonate, kaolin, talcum power, etc., they are safe and have a high whiteness and light reflection coefficient. When adding the fillers into the pulp, it can not only save the costs, but also improve the physical properties of paper and optical properties [3]. However, different fillers have different shapes and structures, and the impact on the ink-jet base paper is also different. The influence of pulp ratio, filler type and its amount on the hue of the ink-jet paper was studied in this paper, and the optimum conditions for the use of filler in ink-jet base paper were determined.

2 Experiment

2.1 Experimental Apparatus

Materials: Softwood kraft pulp (beating degree 40–42°SR), Hardwood kraft pulp (beating degree 40–42°SR), UPM Co., Ltd.; Titanium dioxide, Ground calcium carbonate, Kaolin, Talcum power, AR, 6.5 μm, Guangzhou Bangyou Chemical Technology Co., Ltd.

Equipment: Kaiser Sheet Former BB/BBS Broker, Germany ERNST HAAGE Co., Ltd.; ZY-DJ-23 Valley beater, Zhongyi Instrument Equipment Co., Ltd.; HD-802 pulp beating degree tester, Haida detection equipment Co., Ltd.; YZ-800 vertical press, Chuangshengyuan filter press factory; SP60 spectrophotometer, X-Rite (Shanghai) color equipment trading Co., Ltd.

2.2 Experiment Procedures

(1) Preparation of the pulp [4]. The soaked pulp was beaten with a valley beater, and the beating degree was tested by the HD-802 pulp beating tester. When the beating degree was 40–42°SR, the beating was finished, then the pulp was put into the drying vessel to balance the water and its moisture content was tested after 48 h.

(2) Preparation of paper sheets [5]. The prepared pulp and the metered water were added into the standard pulp dissociator for untwining (3000 rpm), the concentration of the pulp was diluted to 0.4%, the filler was added into the pulp, continuously stirred it until the filler and the pulp was mixed evenly. Water was added into the storage tank to about 3L, the prepared pulp was put into it, then 2 L water was continued to add in it. The mixture was stirred for 5 s, then the water was sucked out with a vacuum pump, and the wet paper was formed. A blanket was placed on the wet paper sheet and rolled back with a roll for 3 s, then the wet paper was put into the dryer, dried for 6 min with a vacuum of 0.08 MPa [6].

2.3 Results Test

SP60 spectrophotometer was used to measure L, a* Value and b* Value of the different pulp ratio, filler types and dosage, and finally the best filling condition were determined.

3 Results and Discussion

3.1 Effect of Pulp Ratio on the Hue of Paper

The types and ratio of the pulp are the primary factor in determining the hue of the base paper. The effect of the pulp ratio on the hue of the base paper was shown in Figs. 1 and 2.

As shown from Fig. 1, with the proportion of softwood kraft pulp increasing, the brightness of the paper became gradually larger. This phenomenon could be explained by the characteristics of the pulp, as the fiber of the softwood kraft pulp was fine and neat, with less mixed cells, and thus it had a higher brightness, while the fiber of the hardwood kraft pulp was short, with high levels of mixed cells, then the brightness of the paper was affected. When the ratio of softwood kraft pulp to hardwood kraft pulp was 3:7, the brightness of the paper was enhanced slowly, as the two kinds of pulp was intertwined seriously, so the brightness change was small.

As shown in Figs. 2 and 3, with the proportion of softwood kraft pulp increasing, a* Value was greater than 0, and it remained basically unchanged, which indicated that the color of the paper was slightly reddish. While b* Value was gradually decreased, and it was less than 0, which indicated the color of the paper was gradually bluish. When the ratio of softwood kraft pulp to hardwood kraft pulp was 3:7, a* Value and b* Value were small, it was conducive to obtain a pure hue of the paper.

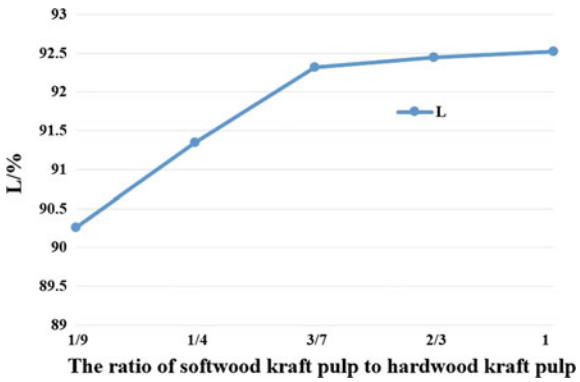

Fig. 1 The effect of pulp ratio on the L (Color figure online)

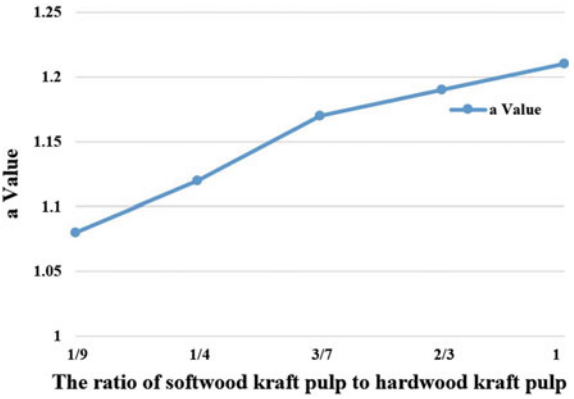

Fig. 2 The effect of pulp ratio on the a* Value (Color figure online)

3.2 *Effect of Filler Type and Dosage on the Hue of Paper*

When the ratio of softwood kraft pulp to hardwood kraft pulp was 3:7, the influence of filler types and their amount on the hue of the ink-jet paper were shown in Figs. 4, 5 and 6.

As shown in Fig. 4, with the addition of filler, the whiteness of the paper had a significant increase, during the four kinds of fillers, the addition of titanium dioxide can obtain the highest brightness in the paper, when the filling content was 3%, the paper brightness got up to 94.26%. The effect of the filler on the brightness of the paper was titanium dioxide > talcum powder > calcium carbonate > kaolin, as in the four kinds of fillers, titanium dioxide had the highest whiteness and the refraction index was up to 2.5, and thus it can get a higher brightness. Talcum powder had the whiteness between 90 and 96.8%, which was obviously higher than that of calcium carbonate and kaolin. The whiteness of kaolin was the lowest, it just got up to only 80–86%, so the filling effect was not obvious.

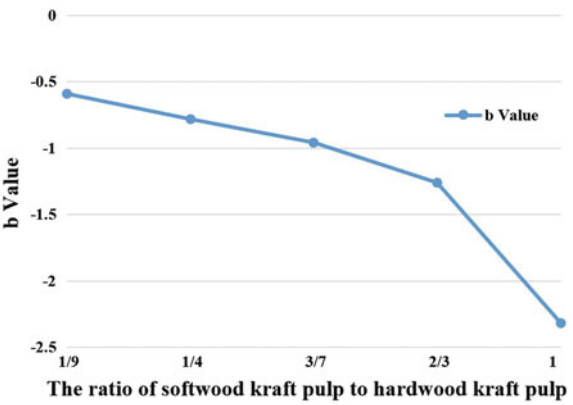

Fig. 3 The effect of pulp ratio on the b* Value (Color figure online)

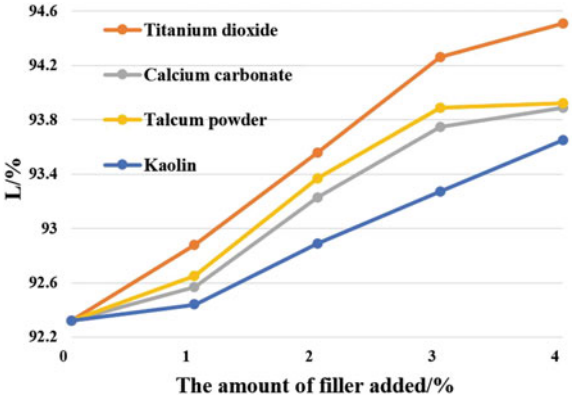

Fig. 4 The effect of different fillers on L (Color figure online)

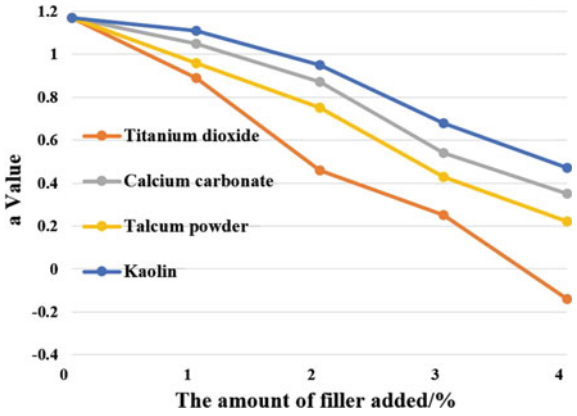

Fig. 5 The effect of different fillers on a* Value (Color figure online)

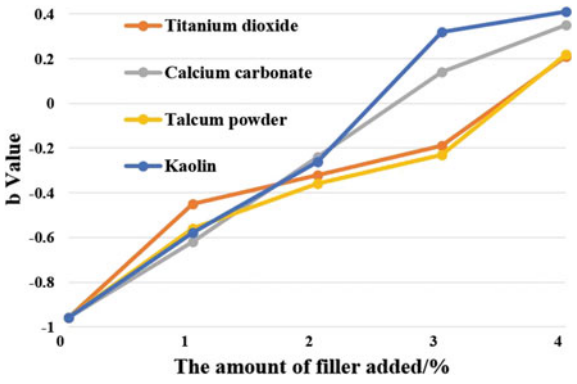

Fig. 6 The effect of different fillers on b* Value (Color figure online)

As was shown in Fig. 5, with the filler content increasing, a* Value became smaller, it meant the color of the paper was changed from red to green, when the content of titanium dioxide was 3%, a* Value = +0.25, which was close to 0.

From the Fig. 6, with the filler content increasing, b* Value became bigger, it meant the hue of the paper was gradually changed from blue to yellow. When the content of titanium dioxide was 3%, b* Value = −0.19, which indicated the hue was partial green, it was useful for the printing process.

4 Conclusions

The hue of the pulp itself played a decisive role in the hue of the base paper. When the softwood kraft pulp was mixed with the hardwood kraft pulp for paper-making, it can not only provide the strength of ink-jet paper performance, but also to meet the requirements of rapid ink absorption. Experiments show that when the ratio was 3:7, a pure hue ink-jet base paper can be obtained. The filler can improve the hue of the sheet, the study showed that titanium dioxide had a significant role in improving the brightness of ink-jet paper sheet, when the amount of filler added was 3%, the best effect can be gained.

Acknowledgements This work is funded by scientific and technological project of Henan province (122102210169 and 142102210441).

References

1. Qu ZC, Chen GX, Li HK (2011) Effect of solid VBL on the hue and whiteness of high-gloss color ink-jet base paper. Pulp Paper Ind 32(22):40–42
2. Chen HS (2012) Effect of solid VBL and talcum powder on the hue and whiteness of ink-jet base paper. China Pulp Paper Ind 33(16):45–48
3. Wu J, Niu MH, Ping QW, Li N, Shi HQ, Zhang J (2015) Characteristics of shell powder and the effect of its application as filler on paper properties. China Pulp Paper 34(12):7–10
4. Qu ZC, Chen GX, Tang BL, Wen SS (2011) Effect of paper surface characteristics on dot gain in ink-jet printing. Adv Mater Res 174:227–230
5. Qu ZC, Chen GX, Tang BL, Wen SS (2011) Study on model of dot gain in ink-jet printing. Adv Mater Res 236–238:1405–1409
6. Qu ZC, Liu SW, Wei QB, Zhang Y (2016) Research on the performance of screen printing line in water conductive ink. Lecture Notes in Electrical Engineering, vol 369, pp 477–482

Study on Ink-jet Printability of Surface Coated Rich Mineral Paper

Yunzhi Chen, Xuehua Ren, Zhengjian Zhang and Yi Sun

Abstract Rich mineral paper has been applied in many fields. The effects of coating using precipitated silica mixed with colloidal silica on the ink-jet printability of the rich mineral paper were investigated as the physical properties and printing performance were taken into comprehensive consideration. The results showed that precipitated silica had better adsorption of ink than colloidal silica and the two composites were better than the single one. When the ratio of pigment to glue was 100:20, precipitated silica was 70 parts, colloidal silica was 30 parts, PVA-1799 was 10 parts, latex was 10 parts and the coating weight was 8 g/m^2. The color density C, M, Y, K of formula 2 was increased by 83.8, 66.2, 51.9 and 73.7% respectively and the smoothness was improved by 100% compared to the base paper. The smoothness of formula 2 was improved by 232% and color density C, M, Y, K was increased by 44.3, 0.9, 51.9 and 23.4% respectively compared to the color ink-jet paper with base weight of 128 g/m^2.

Keywords Rich mineral paper · Printability · Surface treatment
Ink-jet printing

1 Introduction

Rich mineral paper, mainly composed of two raw materials containing 80 wt% Grinding Calcite Carbonate (GCC) and 15 wt% Polypropylene (PP) or polyethylene (PE) [1], has the features of waterproof, moisture-proof, anti-corrosion, pest control, antifreeze, fire-retardant, non-toxic etc. The new material has broad application prospects in packaging, sticker and inkjet printing etc. [2, 3]. Studies showed that the important parameters of coating were pore size, pore number, net structure and chemical types [4, 5]. The surface of rich mineral paper does not have

Y. Chen · X. Ren · Z. Zhang (✉) · Y. Sun
College of Packaging and Printing Engineering, Tianjin University of Science and Technology, Tianjin, China
e-mail: zhangzj@tust.edu.cn

P. Zhao et al. (eds.), *Applied Sciences in Graphic Communication and Packaging*, Lecture Notes in Electrical Engineering 477,
https://doi.org/10.1007/978-981-10-7629-9_77

the similar porous structure of the paper. If the surface is not treated, the ink absorption will be extremely poor [6]. In order to improve the printability, the surface coating treatment was applied in this research.

2 Experimental Materials, Equipments and Methods

2.1 Experimental Materials and Equipments

The rich mineral paper, obtained from Liaoning Shenyang Longxing New Environmental Protection Material Co. Ltd., was used as received. The precipitated silica and the colloidal silica were supplied respectively by Shouguang Hengtai Chemical Co., Ltd., Shanxi Tianyi Nano Co. Ltd. The PVA-1799 and the white latex were provided respectively by Sinopec Group Sichuan Vinylon Factory and Tianjin Tengu Decoration Chemical Co., Ltd. The dispersion, the CMC and the defoamer were offered respectively by Zhongshan Coron Fine Chemical Co., Ltd., Jinan Yuantong Chemical Co., Ltd. and Dongguan Yi Li'an Chemical Technology Co., Ltd. The equipments used in this study were showed in the Table 1.

2.2 Experimental Methods

The coating formulations showed in Table 2. The pigments were dispersed and the adhesives were formulated before coating. The different parameters were selected to enable 8 g/m^2 of the coating weight to be applied. After calendaring, the samples were printed on the inkjet printer and analysed by subjective and objective evaluations. Then, the samples were kept in a conditioning room specified in TAPPI T 402 om 93. The gloss and smoothness were measured.

Table 1 Laboratory equipments

Equipment name	Model	Manufacturer
Coater	CU5-200	Germany Sumet-Messtechnik company
Calendar	CA5\200	Germany Sumet-Messtechnik company
Gloss meter	Novo-gloss	UK RHOPOINT company
Smoothness meter	DCP-PHY10K	Sichuan Changjiang Papermaking Equipment Co., Ltd.
Color Inkjet Printer	WF-7610	Japan Seiko Epson Corporation
Density meter	X-Rite 518	American X-Rite Instrument Company
Digital microscope	GE-5	Shenzhen Hampshire Detection Instrument Co., Ltd.

Table 2 Coating formulations

Coating formulations		1	2	3	4	5
Pigment	Precipitated silica (20 wt%)	100	70	50	30	0
	Colloidal silica (17 wt%)	0	30	50	70	100
Adhesive	PVA-1799(10 wt%)	10				
	White latex (24 wt%)	10				
Additive	PDADMAC	1				
	CMC	0.5				
	Defoamer	1				

3 Results and Discussion

3.1 Comparison of Physical Properties of Paper

As we all know, the gloss and the smoothness have a great effect on the reproduction of the inkjet printing images. The smoothness and the gloss of the surface of rich mineral paper were improved by coating, as shown in Fig. 1. In the coating of formula 2, the smoothness was improved by 100% compared to the base paper and 232% compared to the color inkjet paper. The fine particles of coating filled the surface pores of the base paper and the particle of colloidal silica was relatively smooth so that the smoothness of the paper was improved significantly. The uneven surface of the base paper acquired the high gloss of paper by calendaring. The precipitated silica and the colloidal silica were not gloss materials resulting in the gloss was not high, but the gloss improved greatly compared to the base paper and the color inkjet paper.

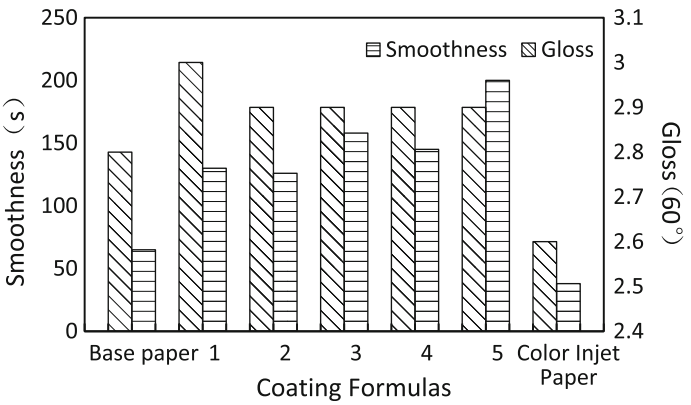

Fig. 1 The physical properties of coated rich mineral paper

3.2 *Printing Performance Analysis of Coated Paper*

The color density value of the experiment was taken from the solid color density. The color density C, M, Y, K of the coated papers using the two pigments were better than the single one, as shown in Fig. 2. The color density C, M, Y, K of the formula 2 was increased by 83.8, 66.2, 51.9 and 73.7% respectively compared to the base paper. At the same time, it was also increased by 44.3, 0.9, 51.9 and 23.4% respectively compared to the color inkjet paper. The color density of the formula 2 was the optimal. Due to the larger specific surface area, the ink adsorption of precipitated silica was better than colloidal silica. When the formula 2 was applied, the synergistic effect of the two kinds of pigments was obtained, and the ink adsorption was better than other formulas.

The text (4pt), the degree of bleed and the ink dots roundness were presented respectively in the following pictures as Figs. 3, 4 and 5. Patriot Digital Observing

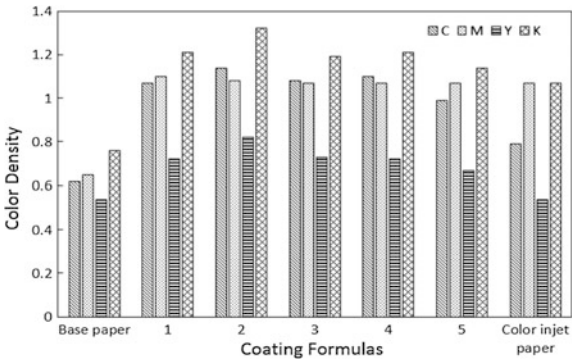

Fig. 2 Comparison of color density of prints

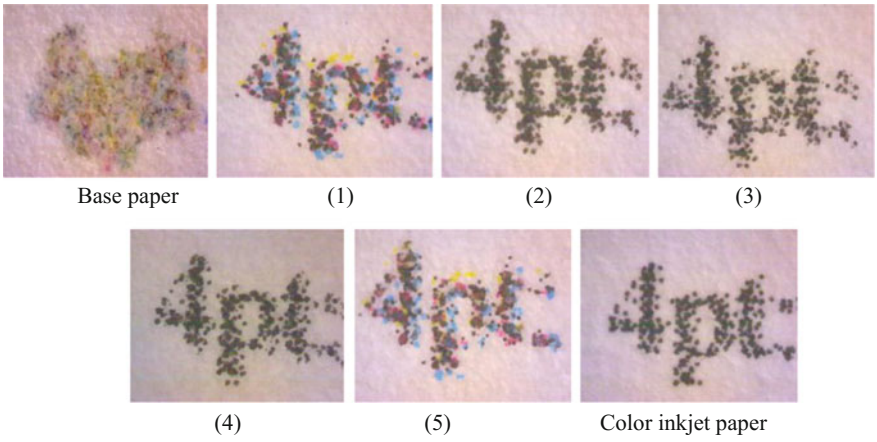

Fig. 3 The microscopic pictures of text

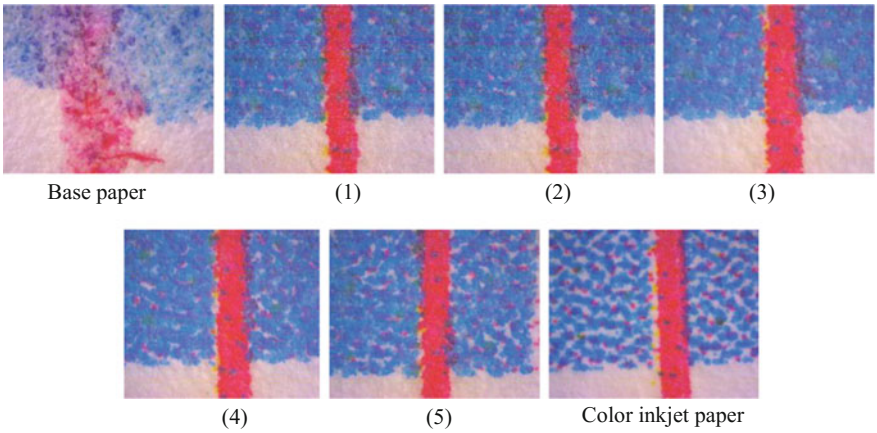

Fig. 4 The microscopic pictures of bleeding

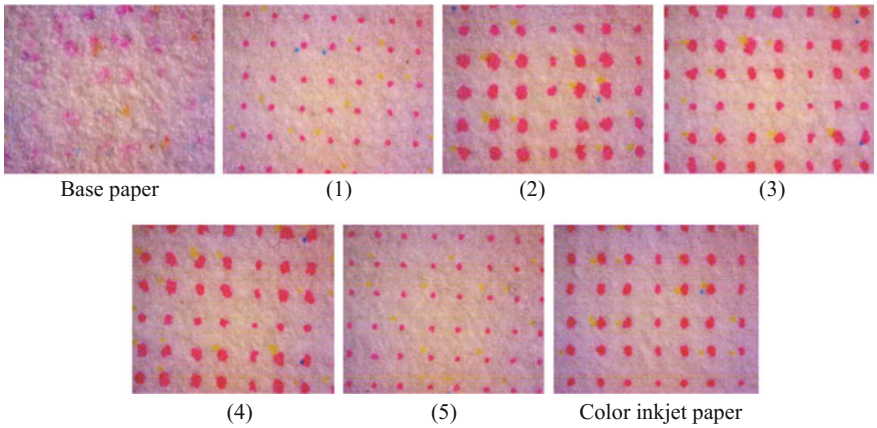

Fig. 5 The microscopic pictures of ink dots roundness

King was used to enlarge the specified portion of samples by 180 times. The text (4p), the degree of bleeding and the dot (1 pixel) were subjectively evaluated by comparing the four levels of excellent, good, medium and poor.

The coating of SiO_2 provided paper with excellent print performance due to the performance of the pigment and the coating network structure. The first reason was that the particle size of precipitated silica was smaller than that of the colloidal silica, and thus had a higher specific surface area leading to the stronger adsorption capacity to the ink. The second reason was that the fixing ink performance of the coated surface was better. The text (4pt) for the formula 2 was more distinct. Because the pigments used to retain the ink point was good. The degrees of bleed of the coated papers were reduced obviously compared to the base paper. Because of

the higher specific surface area contributed to the stronger adsorption capacity of the ink instead of surface diffusion. The single pigment of ink roundness was bad, while the other groups were good. Because the color of the single pigment coating and the color ink-jet paper were lighter than the mixed pigment coatings, which indicated that the larger coating pores let the more ink to retain in the pores of the paper rather than leaving more ink on the surface.

4 Conclusion

The results have shown that the formula 2 was better than other formulas in comprehensive performance. Therefore, the best coating conditions were as follows: the ratio of pigment to glue was 100:20, precipitated silica as the pigment was 70 parts, colloidal silica as the pigment was 30 parts, PVA-1799 as adhesive was 10 parts, white latex as adhesive was 10 parts and the coating weight of rich mineral paper was 8 g/m^2. The color density C, M, Y, K of coated rich mineral paper using the formula 2 was increased obviously and the smoothness was improved significantly compared to the base paper and the color inkjet paper. The printability also improved greatly.

Acknowledgements This study was funded by Tianjin Research Program of Application Foundation and Advanced Technology (Grant Nos. 15JCQNJC42300) in 2015.

References

1. Kong LF (2014) A coating solution for the surface of green rich mineral paper. China, CN 102675989
2. Qian J (2010) Characteristics of rich mineral paper and its application. Printing Technol 15: 38–39
3. Li YF et al.(2010) Present situation and development prospect of synthetic paper. Shanghai Plast 04
4. Wang L, Li XC, Zhu M (2012) Micropore inkjet paper manufacturing process. China's Paper Ind 3:59–62
5. Dong JL (2013) Preparation of dispersions for the preparation of high gloss water proof paper. Image Technol 25(6):54–56
6. Wan MB, Lan J, Gong L et al (2012) Study on printing adaptability of coated modified synthetic paper. Guangdong Printing 06:51

Experimental Study on the Ink Jet Printing Quality Improvement of Ordinary Printing Paper with Polyvinyl Alcohol

Jiang Chang, Xue Gong, Junhao Pang, Yu Wang, Jinyuan Tu, Haoran Wu and Zihui Liu

Abstract At present, the quality of ink-jet printing depends to a great extent on the surface quality of the printing material. The commonly used high gloss paper and coated paper have excellent color rendering results, but the cost is higher, which affects the further application of ink-jet printing. Therefore, the low cost ordinary printing paper is used as the base paper, and the surface of the base paper is coated with polyvinyl alcohol solution to improve the surface quality of the base paper. Preparation of test specimens for color strength condition of different coating solution concentration and coating were tested and compared with the base paper, color intensity was the standard color is obviously improved; printing characteristic curve of the samples were tested and analyzed, compared the change trend of density in the actual printing process of the various. It is found that the printing quality can be improved obviously by adopting the above process.

Keywords Polyvinyl alcohol · Ink-jet printing · Printing paper

1 Instruction

Paper is widely used as the main printing material, but the structure and performance of paper are different. Because of the different production process, The coated papers are used for ink-jet printing with high gloss and smoothness which has good color and high color gamut space and small gray level, but the cost of this kind of paper is relatively high. Ordinary printing paper, although the cost is low, but because of the smoothness and gloss of the paper surface and stronger paper absorbency, the ink diffusion is serious and ink jet printing quality is poor.

So far the research on the quality of ink-jet printing in China mainly focuses on the distribution ratio and optimization of the surface coating of coated paper [1]; effect of paper structure on ink jet printing quality [2] and Ink jet printing quality

J. Chang (✉) · X. Gong · J. Pang · Y. Wang · J. Tu · H. Wu · Z. Liu
Light Industry College, Harbin University of Commerce, Harbin, Heilongjiang, China
e-mail: kahn82@163.com

P. Zhao et al. (eds.), *Applied Sciences in Graphic Communication and Packaging*, Lecture Notes in Electrical Engineering 477,
https://doi.org/10.1007/978-981-10-7629-9_78

evaluation method [3, 4]. Few researches have been done on the quality improvement of ordinary printing paper.

Therefore, it is possible to improve the printing quality of ordinary printing paper by exploring proper raw materials and process methods, which can not only improve the printing quality of ordinary printing paper but also reduce the overall cost of ink-jet printing.

2 Experiment

2.1 Test Drugs and Equipment

The drugs used in this experiment are shown in Table 1:

The main instruments used in the test are shown in Table 2:

2.2 Test Flow

The experimental flow shown in Fig. 1:

Test process: (1) The polyvinyl alcohol is prepared into 5, 10, 15, 20 and 25% solution by mass ratio. (2) The starch and calcium carbonate are mixed at a mass ratio of 1:1, and the mixture is added to the polyvinyl alcohol solution at different concentrations. (3) The surface of the treated ordinary printing paper was cleaned. (4) Wire rod coater was used to select different concentration of mixed solution, and the coating amount of 5 and 10 g was coated evenly on the surface of the

Table 1 Experimental chemicals

Drug name	Molecular formula	Molecular weight
Calcium carbonate	$CaCO_3$	100
Starch	$(C_6H_{10}O_5)_n$	162n
Polyvinyl alcohol	$(C_2H_4O)_n$	44n

Table 2 Instruments used in experiments

Instrument name	Instrument type
Electronic balance	JY502
Wire rod coater	HH-4
Spectrophotometer	SpectroEye
Densitometer	D1181C
Multifunctional stirrer	HJ-5
EPSON color printer	R230

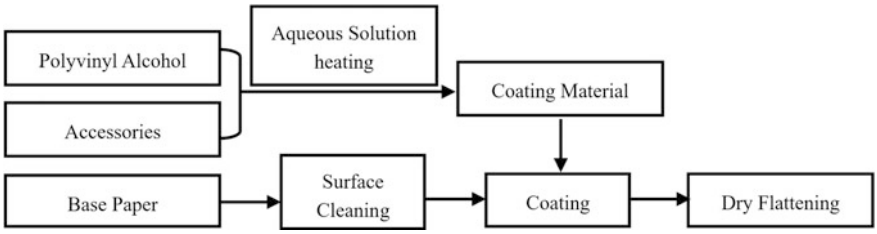

Fig. 1 Experimental process of ordinary printing paper surface treatment

printing paper. (5) The samples were dried and pressed after coating. (6) EPSON color integrated printer was used to print the pre-designed standard color blocks on the surface of sample. (7) The Ink density and spectral reflectance of base paper and coated samples were measured by spectrophotometer.

3 Analysis and Discussion

3.1 The Effect of Different Concentration of Polyvinyl Alcohol on Color Intensity of Printed Color

Polyvinyl alcohol solutions of 5, 10, 15, 20 and 25% were applied on the surface of the sample with the same coating amount of 5 g, the otherwise designed standard color was printed by ink-jet printer, the maximum intensity in the three density were recorded and drawn which tested by spectrophotometer, as shown in Fig. 2:

From the above data trends shows that with the increase of the concentration of PVA coating solution, green (C), (M), yellow (Y), red (R), green (G) and blue (B) color intensity and 6 color paper compared to uncoated were significantly

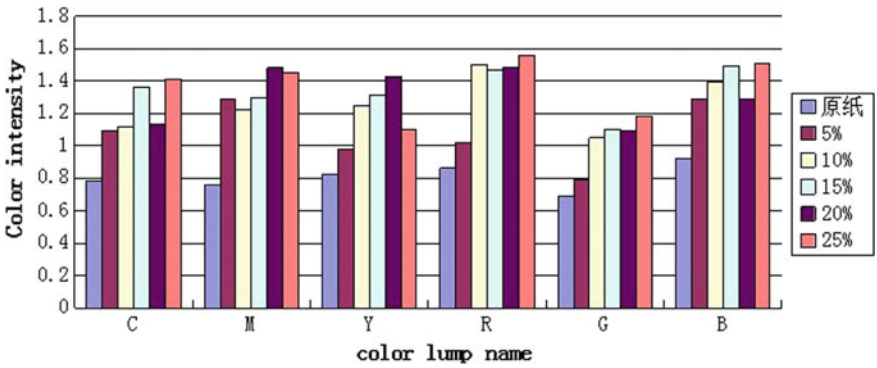

Fig. 2 Influence of color intensity with different concentration of polyvinyl alcohol (Color figure online)

improved, but the growth trend of color strength gradually slow down. The surface quality of ink-jet printing can effectively improved because of the good film-forming properties of polyvinyl alcohol solution, the higher coating concentration the stronger color intensity. The concentration of the coating solution is not the higher the better indicated that the growth trend of follow-up data is gradually slowing down, meanwhile too high concentration will cause waste of raw materials.

3.2 *Effect of Different Coating Amount on Color Intensity of Printing Color*

The color intensity of the samples which was coated with 5 and 10 g coating amount with 25% polyvinyl alcohol solution that on the basis of the previous samples were measured and calculated, the result is shown in Fig. 3:

As you can see from the diagram, with the increase of coating amount, the color intensity of each color block has been improved compared with the original paper. However, the growth of the amount of 10 g coating was not large compared with the amount of 5 g coating. The reason is that the uniform smooth surface film layer formed by polyvinyl alcohol coating improves the quality of ink jet printing of the ordinary printing paper, the improvement of ink efficiency and the improvement of orange performance are related to the smoothness and glossiness of the film, but not to the thickness of the film.

3.3 *Sample Printing Characteristic Curve*

The base paper was coated by 5 g coating amount with the 25% polyvinyl alcohol solution, four color of Cyan (C), M (yellow), Y (yellow) and black (Bk) density

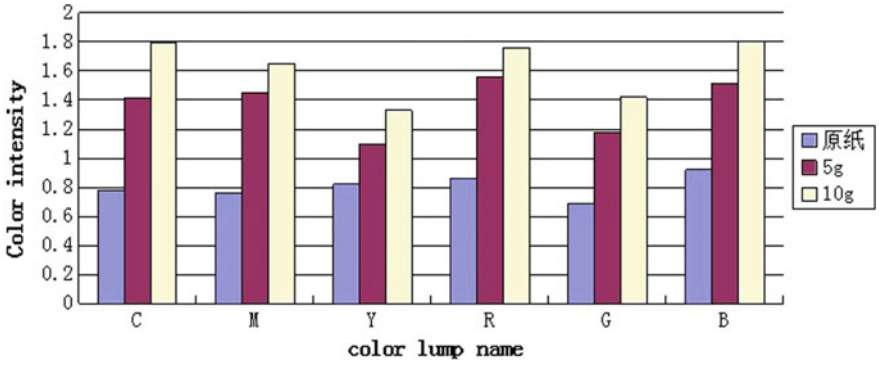

Fig. 3 Influence of color intensity with different coating weight of polyvinyl alcohol (Color figure online)

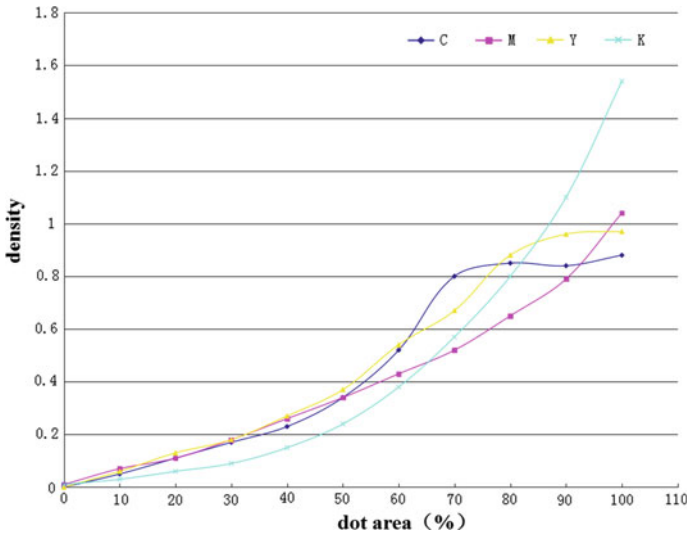

Fig. 4 Printing characteristic curve of samples (Color figure online)

ladder color block was printed on the surface by ink-jet printer. The printing characteristic curve of the sample was drawn after the density of each color block tested which was shown as Fig. 4.

As can be seen from Fig. 4, the density of color block increases with the increase of dot area, the change of the front section of curve is slow, the density varies of cyan, magenta and yellow basically on one line and black block density is relatively lower than them. The density suddenly increases rapidly, in which the change of green, yellow and black blocks is very obvious, the change of black block is most remarkable, and the density change of color block is not obvious compared to the other three colors after the dot area rate reached 60%; when the dot area ratio reached 80%, the density of green and yellow blocks tended to change obviously, while the products and black blocks continued to rise; the black block density is highest when the dot area rate is 100%.

4 Conclusion

(1) The surface coating of PVA solution can effectively improve the ink jet printing quality of ordinary printing paper. The color strength of the sample increases with the increase of the concentration of the coating solution; the improvement of color intensity by the coating capacity increased was weakened when the coating reaches a certain amount.

(2) The printing characteristic curve of test print showed that the density of color block increases with the increase of dot area, and the trend of density growth varies in different range.

Acknowledgements Harbin University of Commerce research team support program (2016TD005), Project of Education Department of Heilongjiang province (12541207), Innovative and Entrepreneurial Training Program for College Students (201610240013).

References

1. Zhang Y, Chen J, Cao Y (2015) The effect of the ratio of adhesive on the diffusion and diffusion of ink in ink jet printing paper. Chin J Papermaking 30(1):32–35
2. Liu F (2014) Analysis of the influence of paper and ink on the quality of digital ink jet printing. Printing Technol 2(2):57–58
3. Xu J (2013) Application of grey relational analysis in quality evaluation of paper inkjet printing. Paper Sci Technol 32(2):67–72
4. Wu J (2012) Analysis technology and quality evaluation method of ink-jet printing materials. Chem Adhes 35(3):57–60

Part VIII
Ink and Related Technology

Synthesis of Acrylate Copolymer Emulsion in the Presence of Macromolecule Emulsifier

Shuhan Jin, Xiaoyu Li and Haiqiao Wang

Abstract Acrylic emulsion is the most widely used binder in water-based inks due to its low price, safety, resource and energy saving, and environmentally friendly. How to improve the properties of the acrylic emulsion to meet the needs of the practical application has always been an important research topic in this field. In this contribution, a series of acrylate copolymer emulsions were synthetized using binary composite emulsifiers consisting of a macromolecular emulsifier and a regular emulsifier by pre-emulsification technology. Then the effects of regular emulsifier types, neutralizing degree and the dosage of macromolecular emulsifier on properties of the emulsion such as particle size, adhesive force and thermal stability were investigated, which would provide an important guidance for the broad readerships.

Keywords Acrylic resin · Macromolecule emulsifier · Binder · Adhesive force Thermal resistance stability

1 Introduction

In recent years, as the air pollution and environmental protection has drawn more and more attention, the traditional packaging and printing industry which has a high VOC emission is facing tremendous pressure to transform, therefore the position of flexible printing and water-based ink gradually increased. As a water-based ink binder, acrylic resin was favored by printing industry because of its simple synthesis, high molecular weight and excellent weather resistance, oil resistance and high glossiness [1]. However, there are still some disadvantages for the conventional acrylic resin, such as insufficient adhesion on non-absorbent substrates, slow drying speed, high film-forming temperature, poor water resistance and poor stain

S. Jin · X. Li · H. Wang (✉)
Key Laboratory of Carbon Fiber and Functional Polymers, Ministry of Education, Beijing University of Chemical Technology, Beijing, China
e-mail: wanghaiqiao@mail.buct.edu.cn

P. Zhao et al. (eds.), *Applied Sciences in Graphic Communication and Packaging*, Lecture Notes in Electrical Engineering 477,
https://doi.org/10.1007/978-981-10-7629-9_79

resistance of prepared water-based inks, so the modification of acrylic resin is urgent.

The use of macromolecules as emulsifiers in conventional emulsion polymerization is an effective means for obtaining water-based polymer dispersions with improved colloidal properties. Macromolecular emulsifiers play important roles as steric stabilizers in emulsion polymerizations, where hydrophobic moieties are attached onto the polymer particles, while hydrophilic moieties stretch out in the water phase to provide stability to the dispersion [2]. The addition of macromolecular emulsifiers is expected to bring many advantages, such as Newtonian rheological behavior, excellent freeze-thaw properties and stability, good pigment dispersion, good wetting properties, ease of printing machine cleaning, and good rewet characteristics [3]. In order to prove these advantages, many researchers did a lot of work on macromolecule emulsifier. For example, Doug et al. [4] studied the preparation of PBA emulsion in the presence of polystyrene/a-methyl phenylene/AA copolymer emulsifier. Satoshi et al. [5] investigated the kinetic process of styrene emulsion polymerization with MMA/methacrylic acid copolymer as the emulsifier.

Despite the commercial importance of macromolecular emulsifier, few systematic studies on researching the effects of macromolecular emulsifier to the properties of emulsions using on water-based ink have been reported. In this paper, a series of acrylate copolymer emulsions were synthesized using a binary composite emulsifier system consisting of a macromolecular emulsifier and another kind of regular emulsifier by pre-emulsification technology. And the effects of the regular emulsifier types, neutralizing degree and the dosage of macromolecular emulsifier on properties such as particle size, adhesive force and thermal resistance stability of water-based ink were studied.

2 Experimental

2.1 Materials

Butylacrylate (BA), 2-Ethylhexyl acrylate (EHA) and Styrene (St) were technical grade. Acrylic acid was provided by Tianjin Fuchen Chemical Reagents Factory and was analytical reagent (AR). Dodecyl mercaptan was chemically pure (CP) and provided by Sinopharm Chemical Reagent Co. Ltd. Sodium persulfate (SPS) was purchased from Beijing Chemical Works and used as the initiator. Macromolecular emulsifier and regular emulsifiers were used as received. Deionized water was applied for the polymerization processes.

2.2 Emulsion Preparation

The acrylic emulsions were synthesized by pre-emulsification technology. Macromolecular emulsifier was neutralized with right amount of neutralizing agent in order to obtain a 25 wt% macromolecular emulsifier aqueous solution. A 2L 4-necked round-bottom flask was equipped with a reflux condenser, a thermometer, a nitrogen inlet and a stirrer. The reactor flask, charged with deionized water, macromolecular emulsifier aqueous solution, regular emulsifier, buffer agent and a part of mixed monomers, was immersed in a water bath at 82 °C. It was stirred at 300 rpm for 15 min. Then half of the initiator was added into the flask in 10 min under nitrogen atmosphere to initiate the polymerization. After the reaction system turned into light blue, let the reaction run further for half an hour at 82 °C. Then, another half of the initiator and the remainder part of monomers were added to the flask in 1.5 h. After the addition was finished, the reaction was maintained for 3 h at 82 °C. Finally, it was cooled to room temperature, filtered through a 200 mesh filter cloth and neutralized to pH 9.0–9.3 by AMP-95.

2.3 Characteristic

(1) Particle size: The particle size was determined by dynamic light scattering using a zetasizer Nano-ZS. The reported results are average of 3 runs.
(2) Adhesive force: An appropriate type of rod coating was selected to coat emulsion or ink films on PET. A 3 M tape with appropriate length was pasted on the emulsion or ink film and was peeled off quickly. According to the degree of ink film was damaged, from completely peeled off or not, divided adhesive force into 5 to 0 level. The interval for each level is 0.5.
(3) Thermal resistance stability of inks: 50 g emulsion was placed into a beaker under stirring using high mixing machine at the speed of 1500 rpm. Then, equal color paste was mixed into the emulsion, and was stirred for half an hour. Then the pre-set ink was put into 50 °C oven for 48 h. The viscosity of the ink before and after 48 h was measured by Zahn Cup (measurement should be conducted in the case of no bubble in the ink and at room temperature).

3 Results and Discussion

3.1 The Effect of the Regular Emulsifier Types on the Properties of the Emulsions

Anionic and nonionic emulsifiers were usually used together on emulsion polymerization in order to obtain a smaller particle size and stable emulsion. In our experiment, several emulsifiers including SDS, nonionic emulsifiers F-45 and X-30 were selected to match with molecular emulsifier for preparing the latex by emulsion copolymerization. The fundamental properties of the obtained emulsions are shown in Table 1.

It can be seen from Table 1 that different emulsifiers have a significant effect on the appearance, particle size and adhesion of the emulsions. SDS is an anionic emulsifier, and has excellent ability to reduce particle size. X-30 has excellent emulsification, dispersion, wetting, permeability. But neither of the two emulsifiers can help enhancing the adhesive, whereas F-45 has obvious positive effect on enhancing the adhesive, that's because, compared with other two surfactants it shows a faster wetting time and a smaller contact angle on the plastic surface. So based on improving adhesion property, F-45 will be a better choice.

3.2 Effect of the Neutralizing Degree on the Properties of the Emulsions

The macromolecular emulsifier solution with different neutralizing degrees from 90 to 130% were used on emulsion polymerization to investigate the effect on the properties of emulsions in this work. The properties, such as particle sizes of emulsions and adhesion, viscosity and stability of corresponding water-based inks were shown in Table 2.

It can be seen that with the increase of the neutralizing degree of the macromolecular emulsifier, the particle sizes of the emulsions increased, and the viscosity of the inks in 50 °C after 48 h increased, which means the thermal resistance stability of the relative inks became worse. That's because the electrolyte concentration in the emulsion increased and the ionic strength in the aqueous phase improved with the increase of the neutralizing degree. Thus lots of electrolyte ions

Table 1 The fundamental properties of the emulsions with different emulsifier

	Emulsifier	Outward appearance	Particle size (nm)	Adhesive force
A	No emulsifier	Creamy white, a little foam	78.97	1.5
B	SDS	Creamy white, little foam	70.10	2
C	F-45	Creamy white, lots of foam	76.68	0.5
D	X-30	Creamy white, a little foam	76.29	2

Table 2 The fundamental properties of the emulsions prepared by macromolecular emulsifier with different neutralizing degrees

	Neutralizing degree (%)	Particle size (nm)	Zeta potential (mV)	Adhesive force	Ink viscosity	Ink viscosity after 48 h in 50 °C
A	90	73.27	−57.3	0.5	51.42	64.35
B	100	76.68	−55.5	0.5	46.63	64.09
C	110	78.93	−52.5	0.5	39.48	63.91
D	120	84.99	−52.3	0.5	41.39	61.29
E	130	91.30	−52.2	0.5	34.37	59.22

were adsorbed on the surface of the latex particles, and the double layers around latex particles were oppressed, so that zeta potential was declined, which would lead to the aggregation of the particles and raise of the particle sizes. Consideration of the applied condition of water-ink, the neutralizing degree of 100% is better.

3.3 Effect of Dosage of Macromolecular Emulsifier on Properties of the Emulsions

The effect of macromolecular emulsifier dosages was investigated. Here, the latexes was prepared by emulsion copolymerization using the dosage of macromolecule emulsifier of 25, 30, 35, 38 copies respectively (insufficient or overmuch dosage of macromolecular emulsifier will lead to instability). The fundamental properties of the obtained emulsions are shown in Table 3. The results are that, with the increase of the dosages of the macromolecule emulsifier, the viscosity, particle sizes and the particle size distributions of emulsions decreases. That's because the emulsification effect got better with the increase of the dosage of macromolecular emulsifier, and more solubilized micelles were formed, leading to smaller particle sizes and narrower particle size distributions. But too much emulsifiers would lead to poorer water resistance, higher cost and other negative effects for the emulsions, so the appropriate dosage is 35%.

Table 3 The fundamental properties of the emulsions prepared with different dosage of macromolecular emulsifier

	Dosage of macromolecule emulsifier	Outward appearance	Particle size (nm)	PDI
A	25	No liquidity	323.7	0.625
B	30	A little bit viscous	94.72	0.326
C	35	Good liquidity	76.68	0.127
D	38	Good liquidity	74.27	0.198

4 Conclusions

The polyacrylate emulsions using binary composite emulsifiers consisting of a macromolecular emulsifier and a regular emulsifier were prepared, and the effects of the regular emulsifier types, neutralizing degree and the dosage of macromolecular emulsifier on the properties such as particle size, adhesive force and thermal resistance stability of the emulsions and relative pre-set inks were studied. Compared with other regular surfactants, F-45 can obviously enhance the adhesive because of its faster wetting time and smaller contact angle on the plastic surface. With the increase of the neutralizing degree of the macromolecule emulsifier, the particle sizes of the emulsions increased, and thermal resistance stability of the inks gone worse. 100% is the best neutralizing degree under comprehensive consideration. When the dosage of the macromolecular emulsifier is 35 copies, the emulsion obtained possesses the best performance.

References

1. Zubitur M, Asua JM (2001) Factors affecting kinetics and coagulum formation during the emulsion copolymerization of styrene/butyl acrylate. Polymer 42(14):5979–5985
2. Carra S, Sliepcevich A, Canevarolo A, Carra S (2005) Garfting and adsorption of poly(vinyl) alcohol in vinyl acetate emulsion polymerization. Polymer 46:1379–1384
3. Amaral MD, Jose MA (2004) Synthesis of High Solid-Content Latex Using Alkali-Soluble Resin As Sole Surfactant. Macromol Rapid Commun 25:1883–1888
4. Lee DY, Park YJ, Khew MC et al (2000) Mechanistic study on latex film formation in the presence of alkali-soluble resin using atomic force microscopy. Macromol Symp 151(1): 479–485
5. Kato S, Suzuki K, Nomura M (2005) Kinetic investigation of styrene emulsion polymerization with surface-active polyelectrolytes as emulsifier, 1 Kinetic study. Eur Polym 33:1–15

Preparation and Characterization of Polyacrylate Emulsion

Chengfang Wang and Fuqiang Chu

Abstract In this paper, polyacrylate emulsion was prepared by using methyl methacrylate (MMA) and butyl acrylate (BA) as polymerization monomer and acrylic acid (AA) as functional monomer via seed pre-emulsification method. The effects of emulsifier dosage, rotated speed and temperature on the properties of acrylate emulsion were studied. The results showed that the optimum condition was as follows: the emulsifier content was 3%, the pre-emulsification speed was about 480 r/min, the polymerization speed was 250 r/min, the pre-emulsification temperature was about 35 °C, and the reaction temperature was about 80 °C.

Keywords Emulsion polymerization · Emulsifier · Acrylate · Emulsion

1 Introduction

In recent years, as a widely used emulsion, acrylate emulsion has played a pivotal role both in industry and daily product. However, with the improvement of people's requirements and the progress of science and technology, the traditional acrylate emulsion has got into the bottleneck period, so a variety of studies about acrylate emulsion have been carried out and achieved certain results, such as silicone modified polyacrylate, which has a good water resistance, heat resistance and so on [1]. As the polyacrylate emulsion has excellent light resistance, acid and alkali resistance, corrosion resistance, it has been widely used in coatings, adhesives, etc. [2]. The process of emulsion polymerization has experienced many stages. And the process is constantly updated, the performance of the emulsion is also be improved.

In this paper, the acrylate emulsion was prepared by the method of seed emulsion polymerization, and an acrylate emulsion with solid content of about 40% was synthesized. The effects of emulsifier, rotated speed and temperature on the solid content and stability of polyacrylate emulsion were discussed.

C. Wang · F. Chu (✉)
College of Printing and Packaging Engineering, Qilu University of Technology, Jinan, China
e-mail: fqchu@126.com

P. Zhao et al. (eds.), *Applied Sciences in Graphic Communication and Packaging*, Lecture Notes in Electrical Engineering 477,
https://doi.org/10.1007/978-981-10-7629-9_80

2 Experimental

2.1 Materials

Materials: Methyl methacrylate (MMA), Acrylic acid (AA) and Butyl acrylate (BA) were purchased from Tianjin Chemical Reagents Plant of China. Sodium dodecyl sulfate (SDS), potassium persulfate (KPS) and alkylphnol ethoxylate (OP-10) were supplied from Tianjin Guangcheng Chemical Reagent Co. Ltd., China. Sodium bicarbonate ($NaHCO_3$) were obtained from Tianjin Daming Chemical Reagent Factory. Ammonia were purchased from Laiyang City Kant Chemical Co. Ltd., China.

2.2 Preparation of Polyacrylate Emulsion

2.2.1 Preparation of Stable Pre-emulsion

Firstly, partially distilled water, the mixed emulsifier and the KPS were added into a 250 ml of four-necked flask, and the system was heated to a certain temperature. Then the mixed monomer was added into the four-necked flask in a certain period of time under high-speed stirring. Finally, when the mixed monomer was finished, the system was continued to stir for a period of time to get a stable pre-emulsion, spare.

2.2.2 Core-Shell Polymerization

Firstly, the remaining mixed emulsifier, distilled water, KPS and $NaHCO_3$ were added into a 250 ml four-necked flask with the thermometer, condenser. Then nitrogen was passed for five minutes. Secondly, the appropriate amount of pre-emulsion was added into the four-necked flask at 80 °C. After one hour, blue or light blue seed emulsion was got. The remaining pre-emulsion was then added dropwise over 3 h, refluxed for a time, then cooled to room temperature while stirring. The pH value was maintained in the desired range with addition of $NaHCO_3$. Finally, the polyacrylate emulsion was obtained.

3 Results and Discussions

The monomer ratio was constantly controlled to MMA/BA/AA = 15/30/1, the results and discussions were as follows:

3.1 Effect of Emulsifier Contents on Properties of Emulsion

From Table 1, we could see that when the emulsifier contention was 3%, the stability and performance of emulsion were the best, the emulsion solid content was the highest and the gel rate was the lowest. The reasons were as follows: the smaller the emulsifier was the less the number of micelles was, the less the latex particles relatively absorbed on the surface of the emulsifier was [3]. And with the growth of latex particles, emulsifier could not be wrapped and then there would be a lot of gel. On the contrary, monomer droplets would be small, so the stability of pre-emulsion was good, but it should not be too large, or a large number of foam would generated, which would affect the coating products.

3.2 Effect of Pre-emulsification Speed on Emulsion Properties

It can be seen from Table 2 that rotating speed had a certain impact on the stability and performance of the emulsion. When the rotation speed was 450–500 r/min, the stability and performance of emulsion were the best, the solid content was higher and the gel rate was lower. If there was no agitation, the small monomer droplets would tend to coalesce into large droplets, resulting in the stratification of the pre-emulsion. In the appropriate range, the higher the stirring speed was, the better the properties of pre-emulsification was. But if the rotating speed was too fast, the monomer droplets would disperse too through, the surface free energy would be higher than before, the monomer could only through increase droplets to automatically reduce the surface free energy, which would cause the system instability.

Table 1 Effect of emulgator contents on performance of emulsion

Emulsifier (%)	Emulsion appearance	W (Solid content) (%)	W (Gel rate) (%)	Stability
1	White, blue light, layered	Very low	Gels	Bad
2	Milky white, blue light	40.03	2.9	Bad
3	Milky white, blue light	40.89	2.6	Good
4	White, blue light, bubbles	40.67	2.9	Good
5	White, blue light, bubbles	40.36	2.8	Bad

Table 2 Effect of pre-emulsification speed on emulsion properties

Rotating speed (r/min)	Emulsion appearance	W (Solid content) (%)	W (Gel rate) (%)	Stability
300	White, blue light	39.05	4.5	Bad
400	Milky white, blue light	39.67	3.9	Bad
450	Milky white, blue light	40.76	2.3	Good
500	Milky white, blue light	40.56	2.1	Good
550	White, blue light	40.03	3.2	Bad

3.3 Effect of Speed on Emulsion Properties

It could be seen from Table 3 that when the rotated speed was 250 r/min, the emulsion polymerization stability and emulsion performance were the best, and the gel rate was low. At the beginning, the high agitation rate would make the monomer droplets become very small, which would reduce the number of micelles of the system. At the same time, too high stirring rate would make the oxygen get into the system to prevent aggregation [4]. In addition, the emulsifier adsorbed on the surface of the latex particles would be off with the high stirring rate, the stability of the emulsion system would be affected.

3.4 Effect of Pre-emulsification Temperature on Emulsion Properties

As seen from Table 4, when the temperature was 35 °C, the emulsion polymerization stability and emulsion performance was the best, the solid emulsion content was the highest, gel rate was low. The temperature of the mixed monomer and the distilled water was related to the ambient temperature. If the lower ambient

Table 3 Effect of speed on emulsion properties

Roating speed (r/min)	Emulsion appearance	W (Solid content) (%)	W (Gel rate) (%)	Stability
150	White with blue light	39.12	2.6	Bad
200	Milky white, blue light	39.56	1.9	Good
250	Milky white, blue light	40.12	1.7	Best
300	White with blue light	40.05	2.3	Good

Table 4 Effect of pre-emulsification temperature on emulsion properties

Temperature (°C)	Emulsion appearance	W (Solid content) (%)	W (Gel rate) (%)	Stability
25	Milky white, blue light	39.23	3.1	Bad
30	Milky white, blue light	40.02	2.4	Good
35	Milky white, blue light	40.14	1.9	Great
40	White, blue light	40.01	2.0	Good

temperature was, the longer the time to prepare stable pre-emulsion was. On the contrary, the shorter the time to prepare pre-emulsification was. In addition, the solubility of the emulsifier in water, the speed of micelle aggregation of emulsifier molecules were both affected [5]. Therefore, the effective way to obtain a stable pre-emulsion in a relatively short period of time was to properly improve the temperature.

3.5 Effect of Emulsification Temperature on Emulsion Properties

From Table 5 it could be seen that when the temperature was about 80 °C, the emulsion polymerization stability and emulsion performance were the best. According to theory of emulsion polymerization, the higher the reaction temperature was, the faster the reaction rate was, the lower the molecular weight of the polymer was. In the experiment, it was found that when the reaction temperature was higher than 90 °C, a large amount of gel was formed and the reaction was too severe, which would make the polymerization reaction can not be carried out. In the later stage of the reaction, the initiator concentration was low, the temperature was increased to about 85 °C, which was beneficial to increase the polymerization rate and the residual monomer content was reduced so that the conversion rate was improved.

Table 5 Effect of emulsification Temperature on emulsion properties

Temperature (°C)	Emulsion appearance	W (Solid content) (%)	W (Gel rate) (%)	Stability
70	White, blue light	39.04	3.2	Bad
75	Milky white, blue light	39.89	2.6	Good
80	White, blue light	40.06	1.9	Best
90	White, more gel	39.12	4.3	Bad

4 Conclusions

The results showed that when the monomer ratio was MMA/BA/AA = 15/30/1, the optimized condition was as follows: the emulsifier content was 3%, the pre-emulsification stirrer was about 480 r/min, the agitator was 250 r/min, the pre-emulsification temperature was about 35 °C, and the reaction temperature was about 80 °C.

References

1. Huang K, Liu Y, Wu D (2014) Synthesis and characterization of polyacrylate modified by polysiloxane latexes and films. Prog Org Coat 77(11):1774–1779
2. Lovell PA, El-Aasser MS (1997) Emulsion polymerization and emulsion polymer. Wiley
3. Liu BL, Zhang BT, Cao SS et al (2008) Preparation of the stable core–shell latex particles containing organic-siloxane in the shell. Prog Org Coat 61(1):21–27
4. Cheng YK, Xiang ZK, Yuan Q et al (2001) Morphological prediction and its application to the synthesis of polyacrylate/polysiloxane core/shell latex particles. J Appl Polym Sci 80 (12):2251–2258
5. Chaudhuri RG, Paria S (2012) Core/shell nanoparticles: classes, properties, synthesis mechanisms, characterization and applications. Chem Rev 112(4):2373

Synthesis and Characterization of Acrylic Resin Applied for UV-Curing Conductive Ink

Ting Mi, Qifeng Chen, Yong Hu, Yu Yang and Guangxue Chen

Abstract With the rapid development of electronic technology, printable electronics guides the development direction of the miniaturization of electronic products, flexibility, environmental protection to electronic equipment. As the key material of printable electronics, it's practical significance for the development of conductive ink. In general, current conductive ink has some problems such as high sintering temperature and poor adhesion. In order to improve the poor adhesion of conductive ink layer, easy to deinking and other bad mechanical phenomena, this paper prepared acrylic UV curing resin. Water-soluble light-cured acrylic resin with double-bond functional groups was obtained through the reaction of different acrylic monomers with isocyanate. And the influence of reaction conditions on the acrylic resin was analyzed. At last, acrylic resin with an average molecular weight of 7800 was prepared under the condition of 50% solvent, 3% initiator, 2% the dosage of chain transfer agent, the reaction time is 5 h. And the characterization of the isocyanate modified acrylic resin was discussed through Fourier transform infrared spectrometer (FTIR), differential scanning calorimetry (DSC) etc.

Keywords Conductive ink · Acrylic resin · Copolymerization
Isocyanate

T. Mi · Y. Yang
South China University of Technology, Guangzhou, China

Q. Chen · G. Chen (✉)
State Key Laboratory of Pulp and Paper Engineering, National Engineering Research Center of Papermaking and Pollution Control, South China University of Technology, Guangzhou, China
e-mail: chengx@scut.edu.cn

Y. Hu
Jinniu District Chengdu Environmental Monitoring Station, Chengdu, Sichuan, China

P. Zhao et al. (eds.), *Applied Sciences in Graphic Communication and Packaging*, Lecture Notes in Electrical Engineering 477,
https://doi.org/10.1007/978-981-10-7629-9_81

1 Introduction

As with traditional inks, conductive inks are made up of two basic components, pigments (made of nano silver) and bonded materials. The affinity of the linker and the pigment (i.e., the wetting ability of the binder to the surface of the pigment particles) determines the dispersion uniformity and dispersion stability of the pigments [1]. After the completion of printing, the link material plays a connection between the role in the pigments and pigments, pigments and printing materials. Printing ink gloss, water resistance, flexibility, adhesion, resistance and printing performance are basically related to the resin [2].

The acrylic resin refers to a copolymer obtained by polymerization of a homopolymer produced by radical polymerization or polymerization with another monomer containing a double bond [3]. Polyacrylate Acrylic resin is an important type of photocurable prepolymer. Most of its main chain is polyacrylate or methacrylate [4]. By introducing monomer with functional groups such as acrylic acid in the polymerization process, further reacting the photoactive groups with the prepolymer to obtain the polyacrylate acrylate resin. Acrylic acrylic resin forms the main chain by the C-C single bond, its molecular chain flexibility is good, and the absorption of UV light is not strong, with strong anti-UV light [5]. Changing the side chain groups gives a resin having a different glass transition temperature, and the side chain can also increase the gloss of the resin.

As the water-soluble polyacrylate acrylic resin with more hydrophilic groups, the surface can increase, reducing the ability to spread, affecting the subsequent inkjet ink printing performance. There are many studies on the viscosity reduction of polyacrylic acid ester acrylic resin [6], but they are often started from raw materials, and there are few products for modification. The reaction of isocyanate groups with hydroxyl groups is a fundamental and important chemical reaction in the synthesis of polyurethanes [7].

2 Experimental

2.1 Chemicals and Materials

Chemicals. Methyl methacrylate (MMA) ($C_5H_8O_2$, Tianjin Zhiyuan Co., LTD, AR grade), Butyl acrylate (BA) ($C_7H_{12}O_2$, Tianjin Zhiyuan Co., LTD, AR grade), Acrylic acid (AA) ($C_3H_4O_2$, Tianjin Zhiyuan Co., LTD, AR grade), Isooctyl acrylate (2-EHA) ($C_{11}H_{20}O_2$, Shanghai Aladdin Biochemical Technology Co., LTD, AR grade), Hydroxypropyl methacrylate (HPMA) ($C_7H_{12}O_3$, Japan Mitsubishi Co., LTD, technical grade), Hydroxyethyl methacrylate (HEMA) ($C_6H_{10}O_3$, American Sharma Co., LTD, technical grade), Isophorone diisocyanate (IPDI) ($C_{12}H_{18}N_2O_2$, Shanghai Aladdin Biochemical Technology Co., LTD, AR grade), Dibutyltin dilaurate (DBTDL) ($C_{32}H_{64}O_4Sn$, Shanghai Aladdin

Biochemical Technology Co., LTD, AR grade), Ethyl acetate ($C_4H_8O_2$, Daomao Chemical Co., LTD, AR grade).

Materials. DF-102S magnetic stirrer, IY5002 balance, TENSOR27 infrared spectrometry(FTIR), Q200 differential scanning calorimetry(DSC), UV-curing machine, QFZ-II adhesion tester, DHG-9140A hot air oven.

2.2 Experimental Procedure

2.2.1 Synthesis of Acrylic Copolymer

The reaction was carried out in a four-necked flask, which was connected to a condenser for condensing the reflux reaction solution. The reaction was continued with nitrogen protection to prevent the oxygen blocking effect. The amount of acrylic acid and acrylic acid monomer (methyl methacrylate, butyl acrylate, isooctyl acrylate, hydroxyethyl methacrylate), 2/3 formulation of initiator AIBN, 50% formulation of acetic acid ester and the amount of dodecyl mercaptan mixed evenly, the mixture was called solution A, 2/3 formulation of the initiator AIBN dissolved in 20 mL ethyl acetate, the mixture was called solution B.

A 50% formulation of ethyl acetate and 10% homogeneous solution A were added to the four-necked flask and slowly heated to 72 °C. After 30 min of reaction, the remaining 90% solution A was uniformly added to the four-necked flask at a rate of 1 drop/s. After 1.5 h, then the mixed solution B was added dropwise at the same speed, and the reaction was carried out for 3 h after completion of the addition, a colorless transparent resin was obtained, which was a hydroxyacrylate copolymer PAC, the PAC oligomer was cooled below 60 °C, and then triethylamine (TEA) was added with stirring to effect a salt-forming reaction to obtain a water-soluble acrylate copolymer WPAC.

2.2.2 Synthesis of Isocyanate Modified Acrylic Resin

The dextrose-based amount of isophorone diisocyanate was added to the four-necked flask, and the temperature was raised to 50 °C gradually. While stirring, the dextrose-based amount of hydroxyethyl methacrylate was added dropwise. After the dropwise addition, the reaction was continued at 60–65 °C for 2 h. After cooling to 50 °C, dibutyltin dilaurate was added, and WPAC was bubbled with nitrogen was also added while stirring, and the reaction was carried out at 55 °C for 2.5 h after completion of the dropwise addition. Finally, the addition of the inhibitor H-TEMPO obtained isocyanate-modified WPAC.

3 Results and Discussion

3.1 Effect of Reaction Conditions on Synthetic Resin

3.1.1 Effect of Reaction Time on Monomer Conversion

Experiments were carried out by equidistant interval sampling and the solid content determination of the product was used to calculate the monomer conversion. The results of the final test are shown in Fig. 1. Within 1 h of the initial reaction, the conversion of the monomer was very small and the polymerization reaction proceeded slowly. After 5 h of reaction, the monomer conversion rate can be as high as 89% or more, and the polymerization reaction was completed basically. Therefore, the effective reaction time was 5 h.

3.1.2 Effect of Initiator Amounts

Figure 2 shows that the molecular weight of the prepolymer WPCA tended to decrease with the increase of the amount of initiator AIBN, and the number of free radicals in the system increased with the increase of AIBN dosage. The presence of more free radicals makes the free radicals chained and chained more frequently, resulting in a smaller molecular weight of the prepolymer and a decrease in the molecular weight distribution of the polymer. According to the requirements of the polymer performance, the choice of AIBN dosage was the quality ratio of 3%.

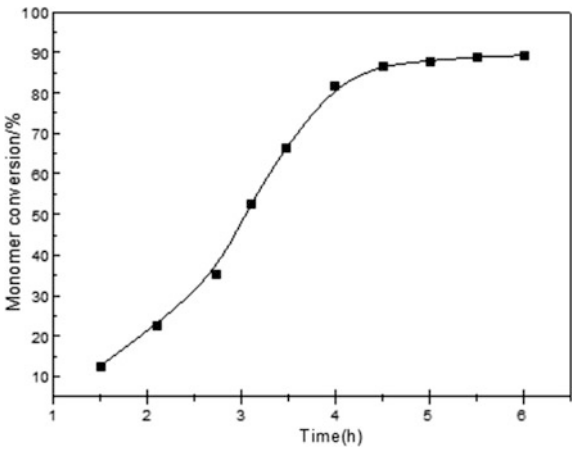

Fig. 1 The acrylate monomers conversion versus reaction time

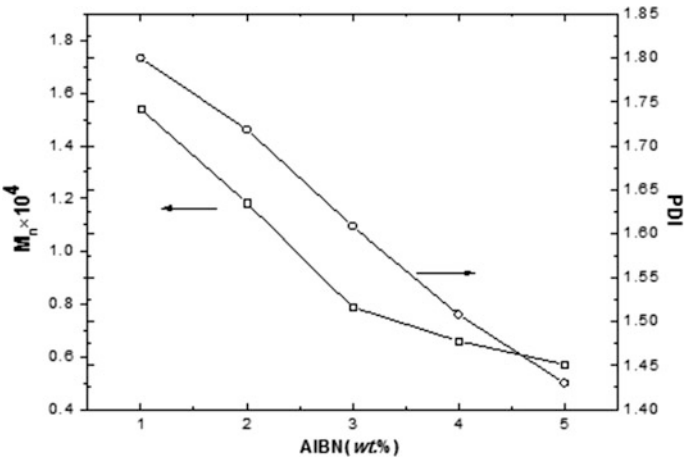

Fig. 2 Influence of initiator amounts on molecular weight and distribution of the polymer

3.2 Characterization of Isocyanate Modified PCA

3.2.1 FTIR

The structure of isocyanate modified acrylic resin was further analyzed by FTIR. As shown in Fig. 3, 3383 and 1539 cm^{-1} are characteristic peaks of –NH and 1706 cm^{-1} is the ester bond characteristic peak in carbamate to produce a large number of urethane bonds, 2950 cm^{-1} is C-H stretching vibration. There was no absorption peak at 2265 cm^{-1} in the modified resin, which proved that the –NCO group had reacted completely. The absorption vibration of = CH_2 appeared at 1720

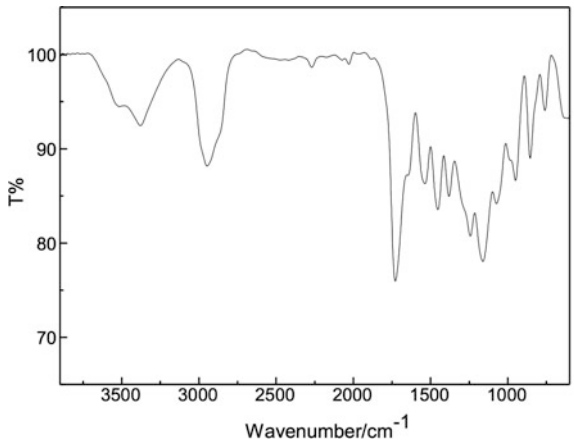

Fig. 3 FTIR spectra of isocyanate modified PCA

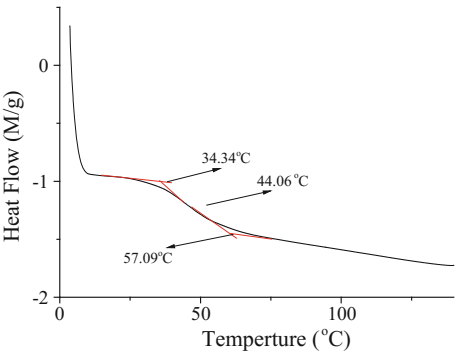

Fig. 4 DSC trace of isocyanate modified PCA

and 810 cm^{-1}, which proved that the double bond was bonded to PCA on the side chain.

3.2.2 DSC

Figure 4 shows that the glass transition temperature Tg measured by the polyacrylate after modification with isocyanate, the Tg value was 34.34 °C, which was higher than the calculated value of FOX formula slightly. Mainly due to the introduction of polar groups on the side chain to increase the intermolecular force, so that the glass transition temperature of the polymer is improved.

4 Conclusions

This paper mainly discussed the synthesis and characterization of acrylic UV-curing resin, and the resin synthesis factors were discussed.

(1) The use of acrylic groups with different functional groups copolymerization under catalysis, the introduction of soft monomers in the copolymer to give resin adhesive properties, hard monomer to give resin cohesion, functional monomer to give special functional groups.
(2) The effects of solvent dosage, reaction time, amount of initiator and amount of chain transfer agent on resin synthesis were discussed.
(3) The modified resin was characterized by FTIR, DSC, and so on.

Acknowledgements This research was financially supported by the Guangdong Provincial Science and Technology Project (2016070220045), the Key Laboratory of Pulp and Paper Engineering Funding Project (No. 2016C01 and 2016C02), and the Fundamental Research Funds for the Central Universities (No. D2154620).

References

1. Li WJ, Zhou GD, Li BG (2016) Preparation and performance of uv-curing waterborne dry film photoresist based on acrylic resins. Imaging Sci Photochem 34:172–180
2. Wei XF (2010) UV Ink and its application technology. Chin J Printing Packag 06:1–8
3. Wu LM (2000) Design of modern paint formulation. Beijing Chemical Industry Press, Beijing
4. Zhou Y (2015) Synthesis and Properties of acrylated polyacrylates. Xiangtan University
5. Ou XW, Nie J, He Y (2010) Preparation and Properties of a low molecular weight polyacrylate acrylic resin with carboxyl groups. J Image Sci Photochem 03:182–192
6. Liu XL, Liu X (2010) Study of the Synthesis of water-borne acrylic resin for printing ink. Mod Paint Finish 13:32–35
7. Wang F, Hu JQ, Tu WP (2010) Synthesis and UV-curing kinetics of epoxy acrylate modified by isocyanate. J Chem Eng Chin Uni 02:233–238

Synthesis of Novel Hyperbranched Polyurethane Acrylate Based on Pentaerythritol

Yuxiu Wang, Guangxue Chen, Minghui He and Qifeng Chen

Abstract Three generations of hyperbranched polyester polyol were synthesized by the reactions from pentaerythritol (PE) and 2,2-dihydroxy-methyl-propionic acid (DMPA) by melt polycondensation technique. They were characterized by 1H NMR, 13C NMR and the results indicated that each had a high degree of branching. Then HBPE-3 was end-caped by urethane acrylate (UA) synthesized from isophorone diisocyanate and (IPDI) and hydroxyethyl methacrylate (HEMA) to obtain a novel hyperbranched polyurethane acrylate (HPUA). The structure of it was characterized by FTIR, DSC and TG techniques. The results showed low glass transition temperature (Tg) and good thermal stability. Tg of HBPE-3 was 56.13 °C, HPUA-3 was a kind of semi-crystalline material, its Tg was 35.56 °C, cold crystallization temperature (Tc) 110.92 °C and melting temperature (Tm) 134.74 °C. The introduction of a large number of unsaturated units to the end portion can provide new ideas for the development of new UV-curable materials.

Keywords Hyperbranched polyester polyol · Urethane acrylate
NMR · DSC

1 Introduction

Polyesteris generally obtained through grafting an unsaturated group to the circumference of polyfunctional dendritic core. As it has high functionality, spherical symmetry three-dimensional structure without intra-and intermolecular entanglement. It not only has high activity, low viscosity, and also be easy to make the modification with functional groups on the surface depending on the purposes.

Y. Wang · G. Chen (✉) · M. He · Q. Chen
State Key Laboratory of Pulp and Paper Engineering,
South China University of Technology, Guangzhou, China
e-mail: chengx@scut.edu.cn

Y. Wang
e-mail: 839475230@qq.com

P. Zhao et al. (eds.), *Applied Sciences in Graphic Communication and Packaging*, Lecture Notes in Electrical Engineering 477,
https://doi.org/10.1007/978-981-10-7629-9_82

It has greater advantages than the linear polymers and dendritic polymers in the application and can be used in coatings, binders, carriers, surfactants and so on [1].

The general method used to synthesize the hyperbranched polymers is the polycondensation of ABx monomers and By ($y \geq 2$) core molecules. This involves no purification steps and facilitates large scale production, but recent studies have found that when using high functionality monomers, one-step synthesis of the product will cause gelation phenomenon. To solve this problem, quasi-one-step method develops. ABx monomer was slowly added during the reaction and by monomer was added as a central core in the initial stage. This method not only can control the molecular weight of the product, reduce the dispersibility, also can give the product a higher degree of branching [2]. Shi Wenfang etc. [3], successfully synthesized the hydroxyl-terminated hyperbranched polyurethane with lower dispersion and controllable molecular weight by quasi-one-step method.

Hyperbranched polyester molecule consists large quantities of easily modified terminal group. Hyperbranched polyester can be controlled by location of functional groups and the number of them. The introduction of new features, enhanced synergies between different characteristics can realize applications of hyperbranched polyester in different fields [4].

In this paper, hyperbranched polyester containing different number of hydroxyl terminus was synthesized by quasi-one-step method polycondensation based on PE as the core and DMPA as the arm. While using homemade UA to modify polyesters of its end group, characterize them with FT-IR, 1H NMR, 13C NMR, DSC and Tg to explore the performance of the new product.

2 Experiments

2.1 Experimental Materials and Equipments

Pentaerythritol (PE), AR, Tianjin Kermel Chemical Reagent Co. 2,2-bis (hydroxymethyl) propionic acid (DMPA), chemically pure, Shanghai Aladdin Reagent Company. P-toluenesulfonic acid (p-TSA), AR, Guangdong Province Chemicals Engineering Research and Development Center. Isophorone diisocyanate (IPDI), chemically pure, Bayer company. Hydroxyethyl methacrylate (HEMA), chemically pure, Shanghai Aladdin reagent Company. Acetone Thermostated oil bath pot, DF101S, Guangzhou Yuhua instrument Co. Flask, global G-17, Guangzhou Branch Fine Bose Equipment Magneton. Thermometer Condenser Nitrogen bottle. Fourier transform infrared spectrometer, Spectrum 2000 USA PERKIN ELMER. NMR, Differential Scanning Calorimetry DSC, Q2000, USA Instron. TGA Q500TGA, USA TA Co.

2.2 Synthesis of Hyperbranched Polyester Polyols(HBPE)

PE (1.362 g, 0.01 mol), DMPA (5.365 g, 0.04 mol) and p-toluenesulfonic acid (0.01 g) were introduced into the three-necked flask equipped with a thermometer, a magneton, a condenser and anitrogeninlet. DMPA was gradually added. Place the flask in a thermostated oil bath pot. Keep the reaction at 142 °C with nitrogen gas. 20 min later materials melted. After one hour, stop nitrogen gas and seal the flask. To continue the reaction under reduced pressure of 0.06 MPa, thereby removing the water generated during the reaction. The product of the first generation hyperbranched polyester polyol was marked as HBPE-1. Gradually added double DMPA and double p-TSA and keep the reaction under the same conditions for 2 h to get the second generation HBPE-2. The third generation HBPE-3 was got in the same way.

2.3 Synthesis of Hyperbranched Polyurethane Acrylate (HPUA)

The HPUA was synthesized via a two-step procedure. In the first step UA was obtained by the reaction of an equimolar amount of IPDI and HEMA. IPDI (6.6 g, 0.03 mol), DBTDL (0.03 g), and hydroquinone (0.02 g) were introduced into a three-necked flask equipped with a thermometer, a magneton, a condenser and a nitrogen inlet. The reaction mixture was dissolved in acetone and HEMA (3.90 g, 0.03 mol) was dropped into the flask at room temperature. After the complete addition of HEMA, the reaction was maintained at 40 °C until the content of isocyanate reached the theoretical value 13.8%. In the second step, UA was reacted with HBPE-3 with the ratio of 32:1 at 70 °C. The mixture was refluxed until the peak at 2261 cm^{-1} for –NCO group in FTIR spectrum disappeared. Then the solvent was evaporated and the product was dried in a vacuum to give slightly yellow to clear HPUA.

3 Results and Discussion

3.1 FT-IR

Three generations of HBPE were characterized by FT-IR. Results were shown in Fig. 1. Hyperbranched polyesters that include different numbers of terminal hydroxyl have a similar structure peak. Peak of –OH is at 3398 cm^{-1} and a large number of hydroxyl groups exist. C-H aliphatic stretching vibrations of CH_2 and CH_3 were at 2889–2947 cm^{-1}. Peak of C = O is at 1732 cm^{-1}. Symmetric and asymmetric stretching vibration absorption peaks are at 1132 and 1045 cm^{-1}. Three

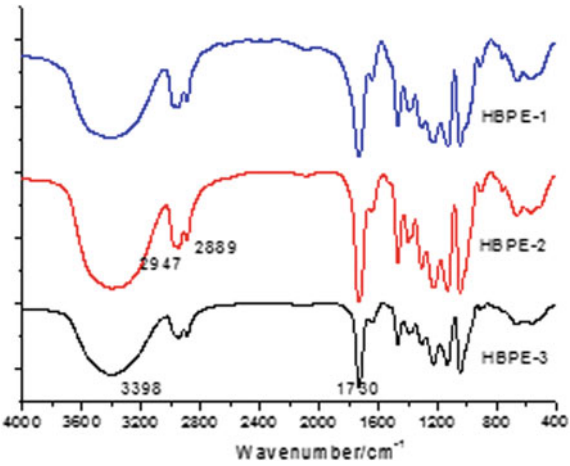

Fig. 1 FT-IR of three generations of HBPE

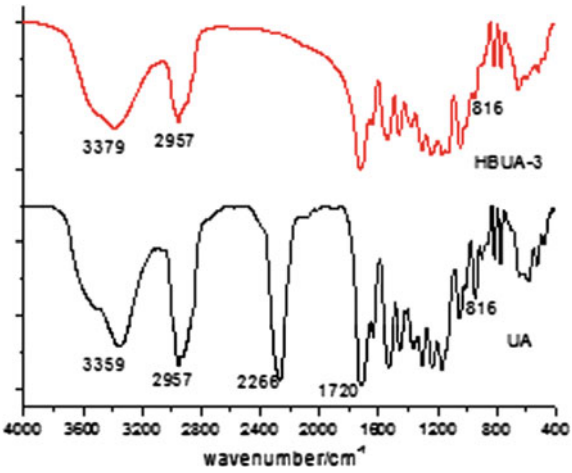

Fig. 2 FT-IR of HPUA-3 and UA

peaks above proved the existence of an ester group. Carbonyl peak of DMPA at 1689 cm^{-1} had basically disappeared which meant the esterification reaction been completed. Figure 2 shows that UA has peaks of –NCO group at 2266 cm^{-1}, HPUA-3 dose not, which indicates the completed reaction of –NCO groups.

3.2 13C NMR and 1H NMR

The degree of branching of the hyperbranched polymer marks the proximity of the hyperbranched structure with the dendritic polymer molecule and be of the key

Fig. 3 1H NMR of HBPE-1

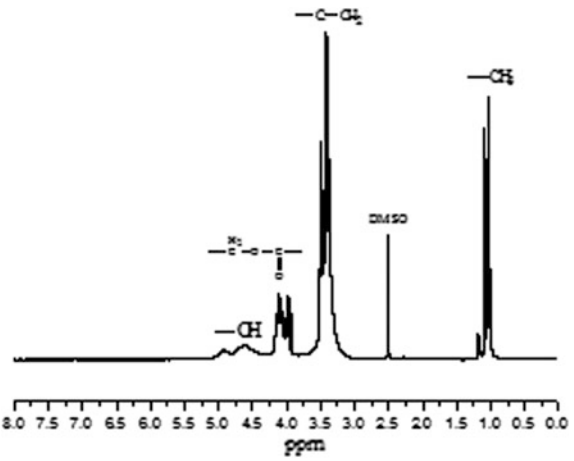

parameter to characterize the shape of the hyperbranched polymer. The DB value of dendrimer molecule is 1. There is only one type of repeating unit, while the hyperbranched polymer is composed of terminal (T), linear (L) and dendritic (D) units. DB values are generally less than 1, and the higher the value DB, the closer to the structure of dendrimer, the better the solubility and the lower the melt viscosity. It was reported that the DB of hyperbranched polyester polyol is more than 0.4–0.5 and is usually determined by 13C NMR spectroscopy [5]. Figures 3 and 4 show the 1H NMR and 13C NMR of HBPE-1. By the integral calculation, D = 1.00, L = 9.52, T = 12.17. Calculated according to the DB formula proposed by Frechet (1), the result was 0.46. It proved a low viscosity. The DB of HBPE-2 and HBPE-3 were got in the same way and they were 0.47, 0.45.

$$DB = (D + T)/(D + T + L) \tag{1}$$

3.3 TGA

TGA was done to study thermal stability of HBPE-3 and HPUA-3 at a heating rate of 10 °C/min. As can be seen from Fig. 5, both products have shown good thermal stability. HBPE-3 began to decompose at a temperature of 238 °C and the decomposition rate was maximized at 310.77 °C. The end of the decomposition temperature was 350 °C. HPUA-3 started the decomposition at 214 °C which slightly decreased compared with HBPE-3 and the decomposition rate reaches the maximum at 309.77 °C. The end of the decomposition temperature was 450 °C which was significantly higher than HBPE-3. Since UA modified HBPE, linear ester linkages of small molecules were introduced to the branched terminus. Differences in molecular structure resulted that the thermal motion of the chain had

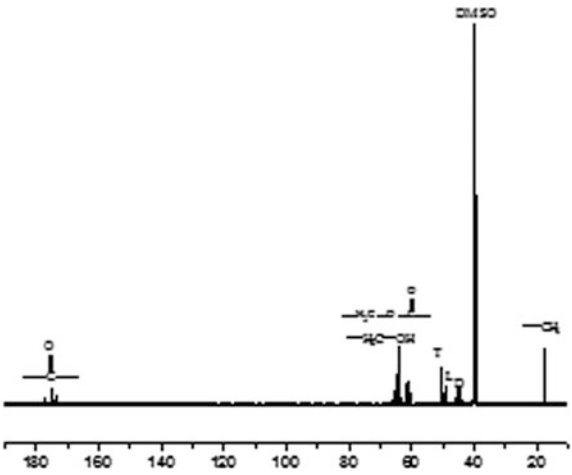

Fig. 4 13C NMR of HBPE-1

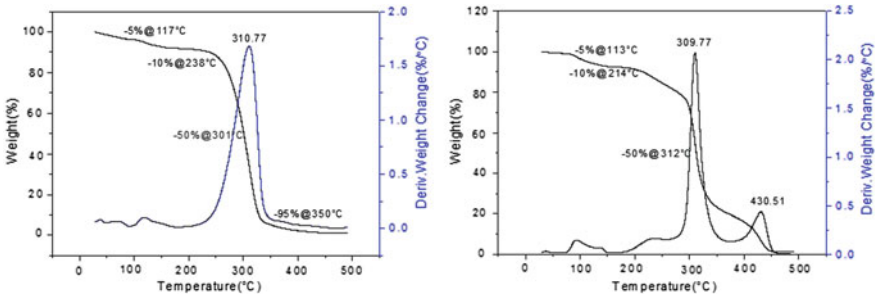

Fig. 5 Tg of HBPE-3 and HPUA-3

undergone significant changes. The Tg curve showed two stages. Chain ester-based segment pyrolyzed at 280–350 °C, urethane acrylate segment at 400–450 °C. HPUA-3 exhibited similar thermogravimetric characteristics as HBPE-3. The initial decomposition temperature drops slightly while the end of the decomposition temperature rose slightly.

3.4 DSC

DSC results of HBPE-3 and HPUA-3 were shown in Fig. 6. The highlybranched three dimensional structures and a large number of end groups make Hyperbranched polymers exhibit amorphous characteristics. The increase of ester groups in hyperbranched polyester branching units contribute the hardness of the

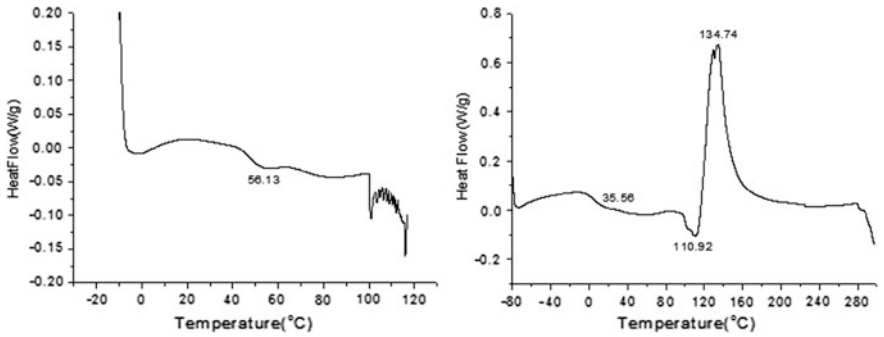

Fig. 6 DSC of HBPE-3 and HPUA-3

polyester, so that the polyester will give a higher Tg while the linear chain of urethane acrylate make a polyester more flexible, significantly decreases the Tg. The glass transition temperature Tg of HBPE-3 was 56.13 °C, HPUA-3 was a semi-crystalline material, its Tg was 35.56 °C. Curves inflect a little which means slightly endothermic. Its cold crystallization temperature Tc was 110.92 °C, higher than Tg, then the segment can move into the lattice and be exothermic. The melting temperature Tm was 134.74 °C which can make the crystalline melt.

4 Conclusions

Three generations of hyperbranched polyester polyol were synthesized by melt polycondensation technique. HBPE-3 was end-caped by homemade UA to give a novel HPUA-3. It was characterized by FT-IR, DSC and TG. The results showed low glass transition temperature and good thermal stability. Since the introduction of unsaturated units to the end portion of HPUA-3, it can be applied into the UV curable system. Initiate the reaction between substances with an unsaturated double bond by the photo initiator in the UV light of appropriate wavelength and intensity, forming a three-dimensional cross-linked network structure. Then it would be used in coatings, inks, adhesives and other fields.

Acknowledgements This work was financially supported by Chinese National Natural Science Foundation of China (21404042), State Key Laboratory of Pulp and Paper Engineering Project (2016C01,2016C02), and the Science and Technology Planning Project in Guangzhou (2016070220045).

References

1. Benthem RAV (2000) Novel hyperbranched resins for coating applications. Prog Org Coat 40:203–214
2. Yates CR, Hayes W (2004) Synthesis and applications of hyperbranched polymers. Eur Polymer J 40:1257–1281
3. Kou HG, Shi WF (2000) Study of photopolymerization characteristics of hyperbranched methacrylated poly(amine-ester)s. J Polymer Sci 5:554–558
4. Zhang LY (2011) The preparation of dendritic hyperbranched maleate resin and its application in uv-curable coating. In: Machinery, materials science and energy engineering (ICMMSEE 2015), pp 403–416
5. Sabani S, Onen AH, Gungor A (2012) Preparation of hyperbranched polyesterpolyol-based urethaneacrylates and applications on UV-curable wood coatings. Technol Res 9:703–716

The Study on the Photopolymerization Reaction of UV-LED Inkjet Ink

Beiqing Huang, Yiran Li, Wan Zhang and Xianfu Wei

Abstract The study on the photopolymerization reaction of UV-LED inkjet ink is very significant in order to improve the curing speed. The effects of the type and content of photoinitiator, the content of pigment and the intensity of light source on the curing speed of yellow UV-LED inkjet ink were studied by the combinative test method between touch method and real-time infrared spectroscopy. Meanwhile, the optimal proportion of photoinitiator was determined by formula experiment, and then, the content of pigment was obtained by combining the color density of ink. The results showed the absorptivity of photoinitiator to the light source of UV-LED and the quantum yield of active species impact seriously the curing speed of ink. The effect of the content of photoinitiator on the reaction speed of photopolymerization exhibited the tendency is fast increase firstly, and then, stabilization, slight decrease finally. The reaction speed of photopolymerization improved with the increase of the intensity of light source. The curing speed of ink decreased with the increase of the content of pigment, and the optimal content was 2–3% under guaranteeing the appropriate color density. The curing speed of yellow UV-LED inkjet ink was the best of all by using photoinitiators ITX, 910 and 819 (the mass ratio is 38:34:29).

Keywords UV-LED inkjet ink · Photopolymerization reaction
Curing speed

1 Introduction

UV-LED light source with energy conservation, environmental protection, high efficient emission, long lifetime, less heat release and low radiant energy exhibits more advantages than traditional light source [1]. As one of the fast development of

B. Huang (✉) · Y. Li · W. Zhang · X. Wei
School of Printing and Packaging Engineering, Beijing Institute of Graphic Communication, Beijing, China
e-mail: 384573464@qq.com

P. Zhao et al. (eds.), *Applied Sciences in Graphic Communication and Packaging*, Lecture Notes in Electrical Engineering 477,
https://doi.org/10.1007/978-981-10-7629-9_83

digital printing method, inkjet printing with excellent development prospect can obtain the high quality and environmental prints and be suitable for various substrates [2]. Curing speed is the key property of UV-LED inkjet ink, which can decide printing efficiency. Moreover, one of the main factors which can affect the curing speed is photoinitiator, and then, are the content of pigment and the intensity of light source. The analysis of the effects of these factors on photopolymerization reaction and curing speed can improve the curing speed of UV-LED inkjet ink.

2 Experiments

2.1 Experimental Materials

Photoinitiator: Easepi ITX, Irgacure 615, Irgacure 910, Irgacure 184, Irgacure 819, Irgacure TPO (Insight High Technology Co., Ltd.); Pigment: benzidine yellow PY-180 (Clariant International Ltd.).

2.2 Experimental Instrument

1. Constant temperature magnetic stirrer (Jiangsu Changzhou Ronghua Instrument Manufacture Co., Ltd.)
2. JJ-I mechanical stirrer (Changzhou Guohua Instrument Co., Ltd.)
3. GJ-2S high speed grinding machine (Qingdao HaiTongDa Special Purpose Instrument Co., Ltd.)
4. UPL3-5410 UV-LED curing machine [UVATA (Shanghai) precision photoelectric Co., Ltd.]: power: 3 W/cm^2, wavelength: 365 nm
5. Nicolet iS50 FTIR Analytical Spectrometer (Thermo Fisher Scientific (China) Co. Ltd.)
6. X-rite X-528 spectrodensiotometer (X-Rite Incorporated Company)

2.3 Experimental Method

2.3.1 Preparation of UV-LED Inkjet Ink

Firstly, the monomers and dispersants were mixed in beaker and placed on constant temperature magnetic stirrer for 5 min, the pigment was then added and the mixture was placed on mechanical stirrer for 30 min; secondly, the mixture was poured into grinding machine with zirconium bead for 60–180 min, the color paste were obtained, when pigment was wetted enough in binder; thirdly, according the

formula, the color paste, prepolymer, monomer, photoinitiator and additive were mixed on mechanical stirrer for 30 min; finally, the ink was obtained by filtration.

2.3.2 Curing Speed Test

The ink was coated on PET by hand screw (12 μm) to obtain proof under room temperature. And then the proof was cured by UV-LED curing machine with the different speed of conveyor belt and fixed power of light source. The curing speed was the speed of conveyor belt, when the curing time of both ink's surface and inner was least of all.

2.3.3 Photopolymerization Reaction Test

The curing process of UV-LED inkjet ink was real-time monitoring by using real-time infrared spectroscopy. On the other hand, the change of C=C double bond was real-time monitoring following the time variation, and then, the percent conversion and speed rate curves of polymerization were obtained [3, 4]. Firstly, the test platform of real-time infrared was constructed on FTIR Analytical Spectrometer, as shown in Fig. 1. Secondly, ink sample was coated on KBr tablet and placed on test platform which can be irradiated by UV light. The photopolymerization process was real-time monitoring by infrared spectroscopy. In other words, the change of peak area on the characteristic absorption peak of C=C double bond at 828–793 cm^{-1} was real-time monitoring. Finally, according the programme OMNIC7.1, the percent conversion of double bond can be obtained by Eq. (1).

$$DC\% = (A_0 - A_t)/A_0 \times 100\% \tag{1}$$

In this Eq. (1), A0 and At represented the peak area of the infrared characteristic absorption peak of double bond before and after curing respectively, DC% represented the last percent conversion of double bond in acrylic acid.

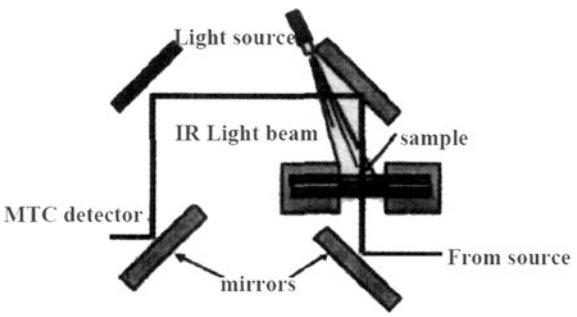

Fig. 1 The test platform of real-time infrared

2.3.4 The Color Density Test of Ink

The ink was coated on PET by hand screw (12 μm) to obtain proof under room temperature and the proof was cured by UV-LED curing machine. And then the color density of ink layer was tested by spectrodensiotometer and the final value of color density was obtained by calculating the average value of five data tested on the five different places of ink layer.

3 Results and Discussion

3.1 The Effect of Photoinitiator on the Photopolymerization Reaction of UV-LED Inkjet Ink

Photoinitiator is one of the critical components of the photocuring system, which concerns whether the cross-linking polymerization reaction between prepolymer and reactive diluent can be initiated under optical radiation and plays a decisive role in photocuring speed [5]. UV-LED light source is a single wavelength light source, which has more requirements to the absorption peak of photoinitiator. Thus, the correct choice of photoinitiator is very significant on ink's curing process [6]. In addition, the content of photoinitiator impacts the rate of photopolymerization reaction largely.

3.1.1 Effect of the Type of Photoinitiator on the Curing Speed of UV-LED Inkjet Ink

The ink samples were prepared by using different photoinitiators ITX, TPO, 910, 819, 615, 184 under fixing the other components of constant yellow UV-LED inkjet ink. The curing speeds of ink samples were measured, as shown in Fig. 2.

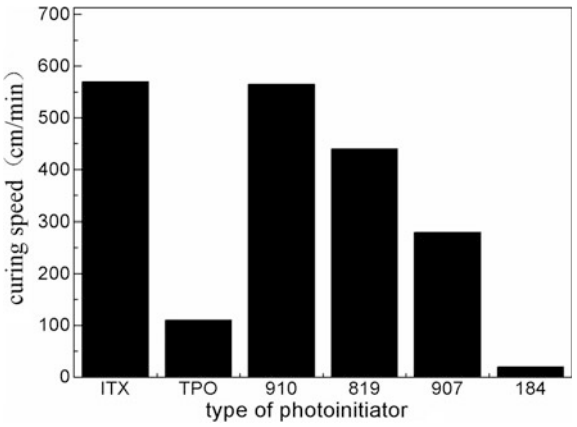

Fig. 2 The curing speed of yellow UV-LED inkjet ink prepared by different photoinitiators

Figure 2 shows the curing speeds of inks prepared by different photoinitiators are different and the initiated speed of ITX and 910 is the fastest of all, 184 and TPO is the slowest of all, and 819 and 907 is between two parts. The reason is UV-LED light source only emits single wavelength 365 nm UV light and the optical absorption efficiency and quantum yield of active species of different photoinitiators are different under near this single wavelength 365 nm. Photoinitiators ITX, 910, 819 and TPO all have absorption peaks near 365 nm. In particular, photoinitiator 910 has the more strong absorption peak near 365 nm than others due to two initiated methods (Cracking, Hydrogen abstraction). The main initiated method of photoinitiator 910 is Cracking, which can generate two free radicals alkyl and benzoyl to initiate efficiently the system of UV-LED inkjet ink. ITX is a common photoinitiator with hydrogen abstraction, which has also the strong absorption peak near 365 nm. Because the photolytic product of ITX is α-amino alkyl radical with high initiated activity and quantum yield of active species, which has fast curing speed. The curing speed of 819 is far faster than TPO owing to the high absorption intensity (the absorption peak: 370 nm for 819, 379 nm for TPO) and more number of free radicals. The photolytic product of 819 and TPO are trimethylbenzoyl and diphenylphosphinyl free radicals respectively and the former has one more free radical than the latter. The curing speed of 907 and 184 are slower than 819 owing to low molar extinction coefficient to light source at 365 nm. The molar extinction coefficient of 907 is lower one order of magnitudes than 819 and 184 is lower one order of magnitudes than 907.

3.1.2 Effect of Recombined Photoinitiators on the Curing Speed of UV-LED Inkjet Ink

The curing speed of ink can be improved efficiently by using recombined photoinitiators which can absorb sufficiently UV light from light source. Photoinitiators ITX, 910 and 819 were selected according to the effect of different photoinitiators on the curing speed of yellow UV-LED inkjet ink and the properties of different photoinitiators. The optimal proportion of recombined photoinitiators with the fastest curing speed was obtained by formula experiment. The yellow UV-LED inkjet inks were prepared according to seven different formulas designed by simplex center of gravity with three factors and three levels. The curing speeds of ink samples were tested and showed in Table 1.

The regression equation between the normative variable designed by simplex center of gravity with three factors and three levels and test indexes was shown in Eq. (2).

$$y = \sum_{i=1}^{3} b_i x_i + \sum_{i<j} b_{ij} x_i x_j + b_{123} x_1 x_2 x_3 \tag{2}$$

Table 1 The formula experiment and results of photoinitiators of yellow UV-LED inkjet ink

No.	X1 (ITX)	X2 (910)	X3 (819)	Curing speed (cm/min)
1	1	0	0	570
2	0	1	0	565
3	0	0	1	440
4	1/2	1/2	0	700
5	1/2	0	1/2	640
6	0	1/2	1/2	570
7	1/3	1/3	1/3	880

The regression coefficient can be obtained by the data of curing speed in Table 2 and Eq. (2), and then the regression Eq. (3) between curing speed y and variable can be constructed.

$$y = 315x_1 + 660x_2 + 120x_3 + 1210x_1x_2 + 3130x_1x_3 - 760x_2x_3 + 9105x_1x_2x_3 \quad (3)$$

In Eq. (3), y represents the curing speed. The maximum of regression equation was 884.93, when X1 = 0.38, X2 = 0.34, X3 = 0.29 by programming solver. On the other hand, when the mass ratio was ITX:910:819 = 38:34:29, the curing speed of ink was the highest of all. The curing speed of yellow UV-LED inkjet ink prepared by this mass ratio is 890 cm/min, which was in accordance with the prediction of regression equation and superior to the curing speed of inks prepared by single photoinitiator.

3.1.3 Effect of the Content of Photoinitiators on the Photopolymerization Reaction of UV-LED Inkjet Ink

The ink samples were prepared by changing different contents of photoinitiator under fixing the other components of yellow UV-LED inkjet ink. The conversion rates of double bond in the process of photopolymerization reaction were tested and shown in Fig. 3. From Fig. 3, the conversion rates of double bond of UV-LED inkjet inks prepared by different contents of photoinitiator exhibit rapid increase in the shorter time firstly, and then, slow increase and small change with the time change. Thus, the final conversion rate is the conversion rates of double bond under the light source for about 200 s. Meanwhile, the effect of the content of photoinitiators on the final conversion rates of double bond of UV-LED inkjet ink can be obtained and shown in Fig. 4.

Figures 3 and 4 show the speed of photopolymerization reaction and the conversion rate of double bond of UV-LED ink increase following the increase of the content of photoinitiator, when the content of photoinitiator is 2–7%. When the content of photoinitiator is 4%, the conversion rate of ink is 29% after curing for 200 s. However, when the content of photoinitiator is 7%, it is only need more than 10 s to up to conversion rate 50% and the final conversion rate of bouble bond

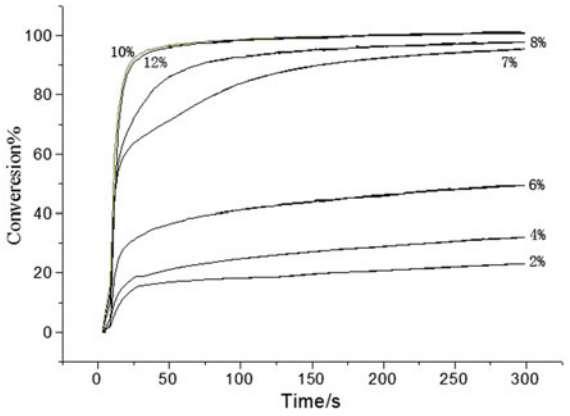

Fig. 3 The effect of the content of photoinitiators on the conversion rate of double bond in the process of photopolymerization reaction

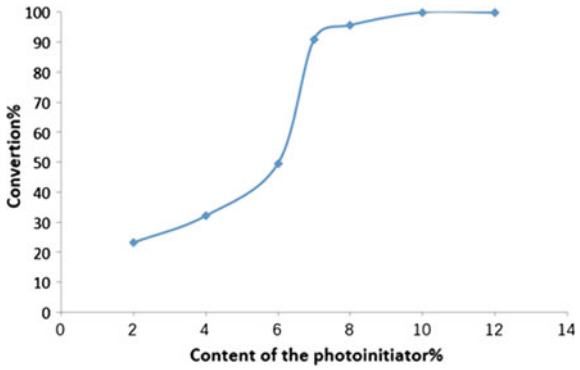

Fig. 4 The effect of the content of photoinitiator on the final conversion rates of double bond of UV-LED inkjet ink

is 93%. When the content of photoinitiator is 7–10%, the speed of photopolymerization reaction and conversion rate also increase with the increase of the content of photoinitiator but very slow. When the content of photoinitiator is in the range 10–12%, the speed of photopolymerization reaction and conversion rate all decrease slightly with the increase of the content of photoinitiator. Both the speed of photopolymerization reaction and the conversion rate of double bond with the content of photoinitiator for 10% are fast slightly the ink prepared by the content of photoinitiator 12%. This is because photoinitiator can generate more active free radicals with the increase of content of photoinitiator within a certain range, which promotes the more prepolymer and monomers to participate in polymerization reaction. It is can be seen in Fig. 4, when the content of photoinitiator exceeds 7% and the conversion rate of double bond is more than 92%, the chance of polymerization reaction joined by prepolymer and monomers decreases and the speed of polymerization reaction changes to slow. Moreover, when the content of photoinitiator is overmuch, the too many active free radicals are generated, which can lead to the decrease of the curing speed of ink and conversion rate of double bond

because active free radicals are easy to side reaction in high concentration, for example, coupling termination.

Therefore, the optimal content of photoinitiator is 7–10% in order to obtain the high curing speed of yellow UV-LED inkjet ink.

3.2 *The Effect of the Content of Pigment on the Photopolymerization Reaction of UV-LED Inkjet Ink*

Pigment is one of the essential components in ink system, which can decide the color of ink and printing quality. The content of pigment is familiar with the color density of ink, which also impacts the curing speed of UV-LED inkjet ink at the same time. The ink samples were prepared by changing different contents of pigment under fixing the other components of yellow UV-LED inkjet ink. The curing speeds and color densities of ink samples were measured and shown in Fig. 5. The conversion rates of double bond in the process of photopolymerization reaction were tested and shown in Fig. 6. Meanwhile, the effect of the content of pigment on the final conversion rate of double bond of UV-LED inkjet ink can be obtained and shown in Fig. 7.

Figures 5, 6 and 7 exhibit the curing speed and conversion rate of double bond are decrease with the increase of the content of pigment. When the content is 6%, the conversion rate of double bond is 41.9% under the UV light for 90 s, however, the conversion rate of double bond of ink prepared by the content of pigment for 1% can up to 73.36% under the UV light for 90 s, which is higher than the content

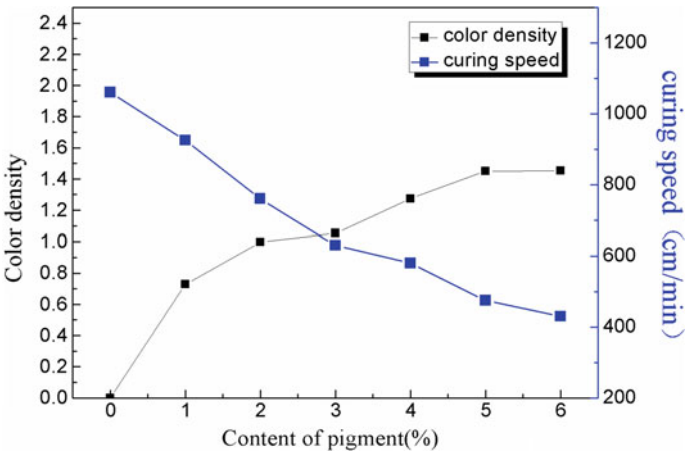

Fig. 5 The effect of the content of pigment on the curing speed and color density of yellow UV-LED inkjet ink

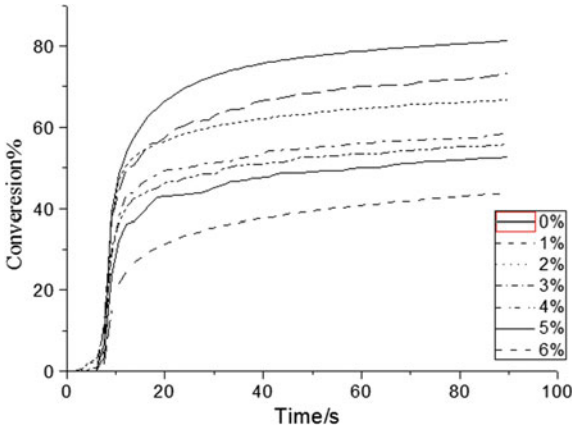

Fig. 6 The variation of the conversion rates of double bond of yellow UV-LED inkjet ink prepared by different content of pigment in the process of polymerization reaction

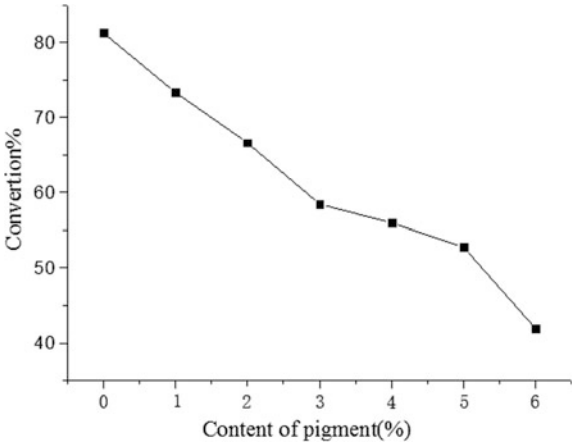

Fig. 7 The effect of the content of pigment on the final conversion rate of double bond of yellow UV-LED inkjet ink

of pigment for 6%. The reason is pigment has an absorptivity to UV light, which can decrease the light absorbed by photoinitiator. Thus, the free radicals generated by photoinitiator decrease, the curing speed changes to slow and the conversion rate decreases.

Figure 5 also shows the color density of ink increases gradually, and it is because the light absorption of ink increases with the increase of the content of pigment.

The optimal content of pigment is 2–3% in order to guarantee the color density of ink is about 1.

3.3 *The Effect of the Intensity of Light Source on the Photopolymerization Reaction of UV-LED Inkjet Ink*

The intensity of light source decides the light absorption of photoinitiator and the number of active free radicals generated by photoinitiator. Thus, the effect of the intensity of light source on the curing speed of ink is significant. The conversion rate of double bond in the process of photopolymerization reaction was measured, as shown in Fig. 8. Meanwhile, the effect of the intensity of light source on the final conversion rate of double bond of UV-LED inkjet ink can be obtained and shown in Fig. 9.

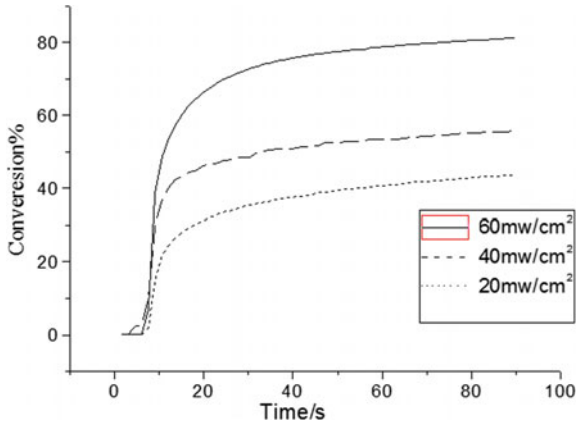

Fig. 8 The conversion rate of double bond of yellow UV-LED inkjet ink under different intensities of light in the process of photopolymerization reaction

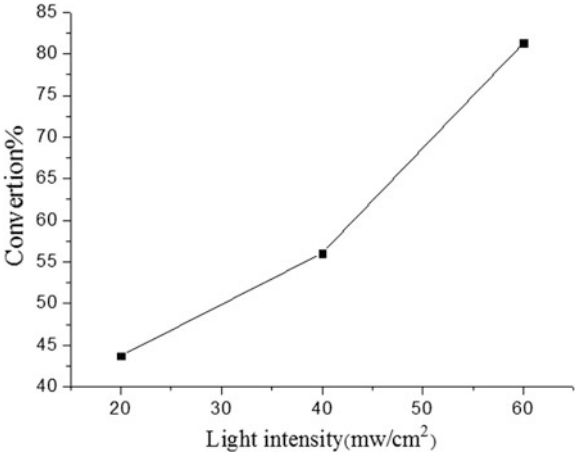

Fig. 9 The effect of different intensities of light on the final conversion rate of double bond

From Fig. 8, the conversion rate of bouble bond and the speed of photopolymerization reaction of UV-LED inkjet ink increase following the increase of the light intensity. Ink can finish the photopolymerization reaction in a shorter time and have a higher conversion rate of double bond. When the light intensity is 20 mW/cm^2, the final conversion rate of polymerization is 43.7% and the need time is 100 s, and when the light intensity is 60 mW/cm^2, the final conversion rate of polymerization is 81.3%, which is higher than former and only need 10 s to obtain conversion rate of polymerization for 43.7%. The reason is the enlargement of light intensity can make the photoinitiator to absorb enough energy in more shorter time and the more numbers of free radicals generated in this system can initiate rapidly monomers and prepolymers to polymerizate. Therefore, the increase of light intensity not only improves the speed of photopolymerization reaction, but also enhances the final conversion rate of double bond.

4 Conclusions

Through the above analysis, the following conclusion can be obtained under this experimental condition.

1. The absorptivity of photoinitiator to UV-LED light source and the quantum yield of active species impact the curing speed of ink largely. For single photoinitiator, the curing speeds of ink samples prepared by photoinitiators ITX and 910 are the highest of all. For recombined photoinitiators, the curing speed of ink sample prepared by photoinitiators ITX, 910 and 819 with the mass ratio ITX: 910: 819 = 38:34:29 is the highest of all.
2. The effect of the content of photoinitiators on the photopolymerization reaction of UV-LED inkjet ink exhibits rapid increase firstly, and then, stability, and slight decrease finally.
3. The speed of photopolymerization reaction is slower and the color density is higher with the increase of the content of pigment. The optimal content of pigment is 2–3% under guaranteeing the basic color density of ink.
4. The speed of photopolymerization reaction of UV-LED inkjet ink is higher following the more high light intensity.

Acknowledgements This work is supported by BIGC Project (Grant no. 04190117001/008).

References

1. Gao J (compile) (2012) UV-LED curable. Printing Field (02)
2. Ji D (2010) The LED in the application and development trend of UV printing. Printing Field (5)
3. Gao X, Lie J (2006) Method of real-time infrared detection is uv polymerization kinetics of bisphenol a epoxy resin. Inf Rec Mater 05,7(5)
4. Wei Jie, Jin Yangzhi (2013) UV-curable coatings. Chemical Industry Press, Beijing
5. Jin Yangzhi (2010) Light curing material performance and application manual. Chemical Industry Press, Beijing
6. Yi Q, Huang B, Wei X (2013) The UV Printing ink light initiator—LED and light matching. J Beijing Inst Printing 12, 21(6)

Development of Water-Based UV Inks Based on Wood-Based Panel Printing

Xinya Du, Qifeng Chen and Guangxue Chen

Abstract In this paper, we explore different wetting dispersant (BYK190, BYK193, BYK198), wetting dispersant dosage and the effect of different milling time on the UV printing ink. By studying its curing time, particle size as the performance index, calculate the configuration to meet the requirements of production, and search the superior performance of UV ink formula. First, the red, yellow, blue, and black pigment use four different BYK dispersant (BYK190, BYK193, BYK198) (Yang in Printing Technol 21(7):79–81, 2014, [1]) for grinding in 2, 4, 6, and 8 h to take on curing time, particle size. They respectively were determined to find out the different types of ink the best condition to the production of wetting dispersant type and the best milling time. Finally, to explore the best wetting dispersant dosage, adding dispersant dosage is 0.2, 0.4, 0.6, 0.8 and 1%, and then to make particle size, curing time, etc., so as to find the most superior performance meeting the requirements of production and the best water-borne UV ink formula.

Keywords Water-based UV inks · Wetting dispersant · Particle size

1 Introduction

Water-based UV inks are mainly a kind of new environmentally friendly ink [2], which is composed of prepolymer (water curing resins), photo initiators, pigments, amines, water, cosolvents and other additives. UV ink as a new environmentally friendly ink has been highly valued with energy saving, high production efficiency, excellent printing performance, low investment in equipment. Water-based UV ink is a new research direction of UV ink [3]. At the same time, the rapid development

X. Du · Q. Chen · G. Chen (✉)
South China University of Technology, Guangzhou, China
e-mail: chengx@scut.edu.cn

X. Du
e-mail: 984039239@qq.com

P. Zhao et al. (eds.), *Applied Sciences in Graphic Communication and Packaging*, Lecture Notes in Electrical Engineering 477,
https://doi.org/10.1007/978-981-10-7629-9_84

of ink technology has also promoted the rapid development of its application field. It makes it is possible for water-based UV ink to be printed on the surface of wood-based panel. Water-based UV ink in food, medicine, packaging, decoration, tobacco and alcohol, newspapers and other media is an indispensable raw material [4]. It has get involved in all aspects of our daily life.

Water-based UV inks combine the characteristics and advantages of traditional UV inks and water-based materials, which use UV irradiation curing technology to dilute water as a diluent. It is because water-based UV ink combines the advantage of both, in the past 10 years getting faster development. According to the composition and the different means of water dispersion, light-cured water-based ink is divided into four generations. The first generation of light-cured water-based ink external emulsification; Second-generation light-cured water-based ink non-ionic self-emulsification is poor; Three generations of light cured water-based ink mixed with water-dispersed resin solution; The fourth generation of light-cured water-based ink ion-based self-emulsification [5].

With the traditional oily UV ink, water-based UV inks have the following advantages [6]: (a) Green environment-friendly materials. (b) Conducive to business cost savings. (c) To maintain the machine. (d) To simplify the amount of work tasks. (e) Printing equality and stability. (f) High safety factor. (g) Network clear and fine. (h) Overprint effect is good. Water-based UV inks compared with the traditional ink in the performance have been greatly improved, especially in the green and reducing the side effects of the human body. However, water-based UV ink as a new ink, also have its own limitations: (a) Drying process more cumbersome. (b) High storage environment requirements. (c) High scrap rate. (d) The process is complex. (e) High prices [7].

Water-based UV inks as a modern printing ink market, a new type of environmentally friendly ink, with significant development and research value, water-based UV inks as environmentally friendly ink representative, is the future of printing ink research in the field of important direction and research hot spots in the wood-based panel decoration. On one hand, to expand the use of water-based UV inks field, on the other hand it also helps to improve the quality of wood surface printing. Therefore, by the exploration of the stability and adhesion of water-based UV inks, it can be controlling the technical process of the dispersion stability of water-based UV inks and improve adhesion in the surface of the wood. It can great improve printing quality in the wood surface. It will contribute to the development of water-based UV inks in wood-based panel printing technology and the efficient of using inks in wood surface printing [8–10].

2 Experimental Materials

Black, yellow, blue, red, four-color pigments, anhydrous ethanol, deionized water, urethane resin; photo initiators (9450, 42,272, 9641 diacetone and 2-hydroxy-Phenylacetone); 1619 mixture (TEGO 815 N, polyether-modified silicone

mixture used as silicone surfactant); 805 mixture (LIQUID SURFACE CEREADDITIVE, 2-amino-2-methyl–propanol, 2-methyl-2-2-methylamino-1-propanol); 063 mixture [DEHYDRAN1293, hydroxyl-terminated; Ethoxypropoxylated-dimethyl 2-butoxyethanol, ethylene glycol monobutyl ether butyl fluffin]; 2411 mixture TAFIGELPUR40; 2-[2-(2-butoxyethoxy) ethoxy] Ethanol; Ethylene glycol butyl ether; Defoamer, wetting and dispersing agent (BYK190, BYK193, BYK198).

2.1 Experimental Apparatus

Spectrophotometer; Printability tester (F1 Netherlands); Magneticstirrer (ZKAC-MAGHS7); Solidify IGT (UN50013-0001); Viscosimeter (CAP2000+; USA); Marvin Instruments; Scraper fineness meter.

2.2 Preparation of Water-Based UV Inks

According to searching paper to determine the formulation of the water-based UV ink, polyurethane resin: deionized water: anhydrous alcohol: pigment: other additives = 6: 2: 0.3: 1: 0.7. First, polyurethane resin, deionized water, anhydrous alcohol, etc. added to the grinding flask, the first pre-grinding and mixing half an hour, the speed set to 4000 r/min. Grinding the beginning of the grinding cup in the outer layer of plastic wrap. And then connecting to a good condensing device, and then stirring speed of 4000 r/min grinding for 8 h, each 2 h to stop the machine for about 15 min, taking a certain amount of ink into the opaque black plastic box as samples, and then the ink particle size, curing time, color density, etc. make measurements and analysis for the subsequent data analysis.

There are three kinds of variables in this work, respectively, the effect of grinding time on water-based UV inks. Through a large number of experimental operation to determine the blue, red, yellow, black four kinds of pigments the best wetting and dispersing agent.

According to the above order to explore the impact of water-based UV inks variables.

2.3 Water-Based UV Inks Formulations of the Proportion of Each Component

The proportions of the components and their proportions of waterborne UV are shown in Table 1.

Table 1 Water-based UV inks raw material proportion of each branch office

Name of pharmacy	The proportion (%)
Polyurethane resin	60
Deionized water	20
Water free alcohol	3
Pigment	10
Photo initiator	2
1619 mixture	0.25
805 mixture	0.25
3063 mixture	0.20
2411 mixture	2
Ethylene glycol butyl ether	2
Defoamer	0.10
Wetting and dispersing agent	0.20

3 Results and Discussion

Through the study, we know that wetting and dispersing agent, mainly the surfactant, plays an important role in the paint grinding process. It can reduce the liquid surface tension between the liquid and the solids, improve ink dispersion efficiency that shortening the ink grinding time to improve production efficiency. In order to investigate the effect of different wetting and dispersing agents on the particle size of different colors, we choose three different wetting and dispersing agent, BYK190, BYK193 and BYK198 (Table 2; Figs. 1, 2, 3 and 4).

Through the data analysis we can know that blue ink using wetting agent BYK190 effect will be better. Magenta water-based UV ink configuration using wetting agent BYK198 configuration of the ink is better. Yellow water-based UV

Table 2 To explore different dispersant type experimental particle size data table

	Yellow				Black			
	Particle (size/μm)				Particle (size/μm)			
Wetting dispersant type	2H	4H	6H	8H	2H	4H	6H	8H
BYK190	1.31	0.88	0.78	0.69	2.53	1.47	1.20	1.02
BYK193	1.24	0.92	0.73	0.64	2.74	1.61	1.38	1.20
BYK198	1.14	0.74	0.59	0.52	2.44	1.93	1.11	1.00
	Blue				Red			
	Particle (size/μm)				Particle (size/μm)			
Wetting dispersant type	2H	4H	6H	8H	2H	4H	6H	8H
BYK190	3.04	2.20	1.39	1.15	1.68	1.65	1.33	0.53
BYK193	1.78	1.22	1.24	1.44	0.76	0.56	0.56	0.65
BYK198	9.70	7.58	4.57	1.27	0.83	0.57	0.53	0.51

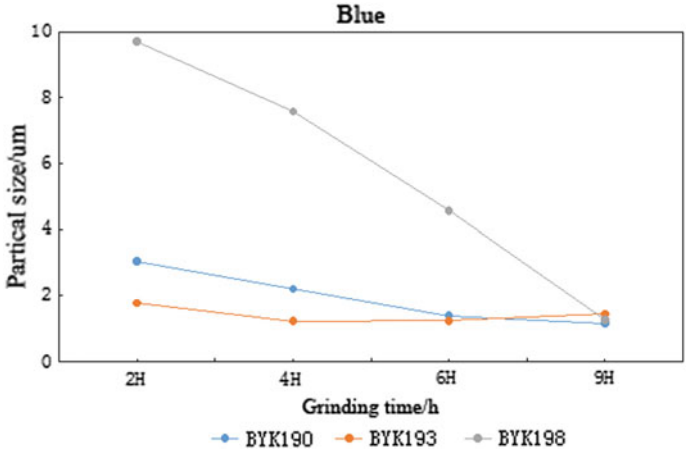

Fig. 1 Blue ink particle size variation

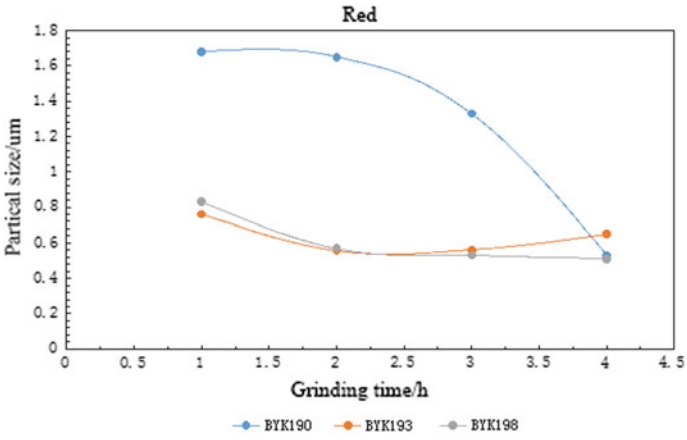

Fig. 2 Red ink particle size variation

ink configuration using BYK198 is better. It is better to use the wetting agent BYK190 on the configuration of the black waterborne UV ink.

3.1 Effect of Wetting and Dispersing Agent on the Stability of Waterborne UV Inks

The stability of the ink during storage (particle size change) is also very important. The degree of change in the particle size of the aqueous UV ink was observed to determine the stability of the ink (Tables 3, 4, 5 and 6; Figs. 5, 6, 7 and 8).

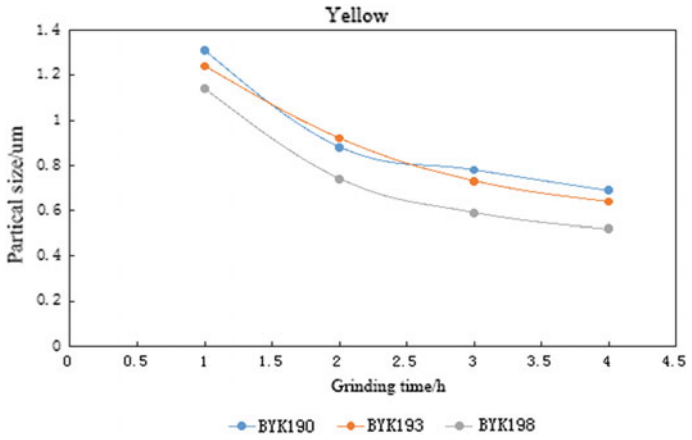

Fig. 3 Yellow ink particle size variation

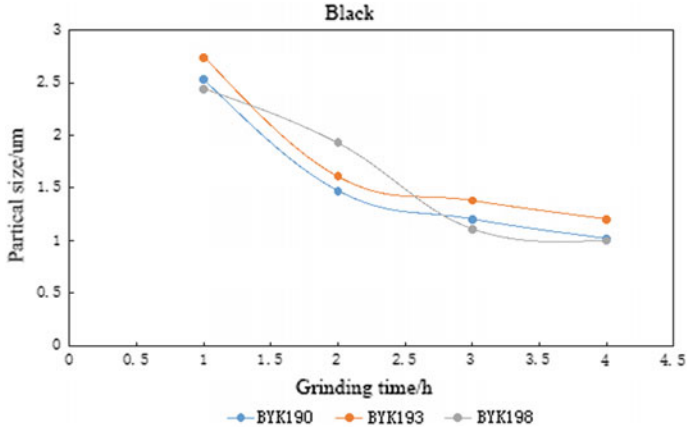

Fig. 4 Black ink particle size variation

3.2 Effect of Wetting and Dispersing Agent on the Particle Size of the Ink

After exploring the best wetting and dispersing agents for each color of water-based UV inks, we also explore the optimum amount of the best wetting and dispersing agent (Table 7; Fig. 9).

Table 3 Blue ink particle size change after storage

Blue			
Wetting dispersant type	Particle (size/μm)		
	1 day	7 days	14 days
BYK190	1.15	0.95	0.94
BYK193	1.44	1.98	1.41
BYK198	1.27	2.26	2.45

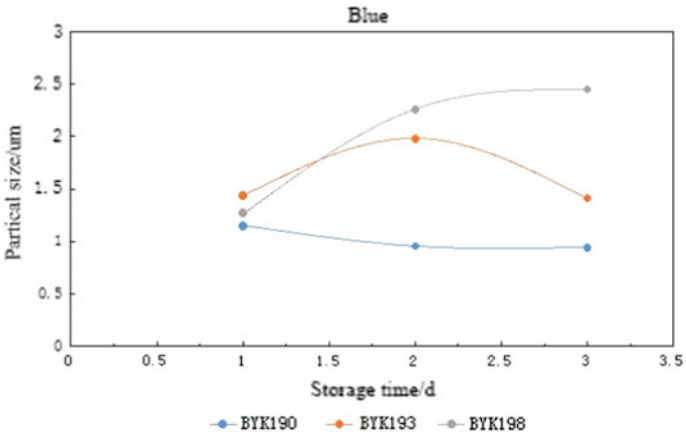

Fig. 5 Blue ink particle size variation after storage

Table 4 Red ink particle size change after storage

Red			
Wetting dispersant type	Particle (size/μm)		
	1 day	7 days	14 days
BYK190	0.53	0.50	0.49
BYK193	0.65	0.48	0.58
BYK198	0.51	0.48	0.48

3.3 Effect of Curing Time on Color Density

We found that the overall color density of yellow and curing time is not related to the red and black water-based UV inks curing time longer these two ink printing after the color density worse; blue water UV ink color density change is not obvious, which Color density is the strongest blue and black color of these two pigments the deepest effect, the worst is yellow (Table 8; Fig. 10).

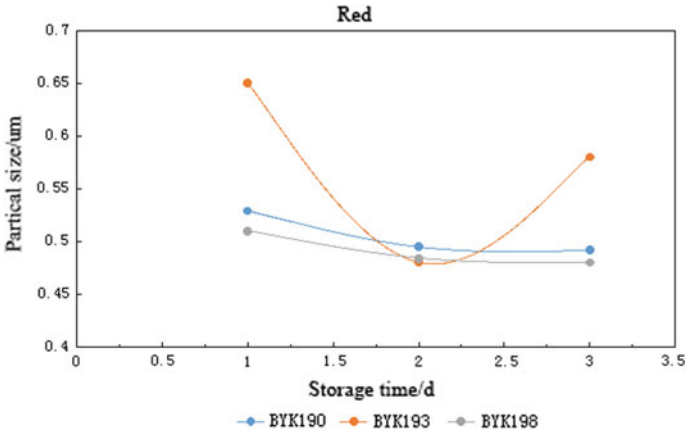

Fig. 6 Red ink particle size variation after storage

Table 5 Yellow ink particle size change after storage

Yellow			
Wetting dispersant type	Particle (size/μm)		
	1 day	7 days	14 days
BYK190	0.69	0.68	0.69
BYK193	0.64	0.66	0.65
BYK198	0.52	0.51	0.50

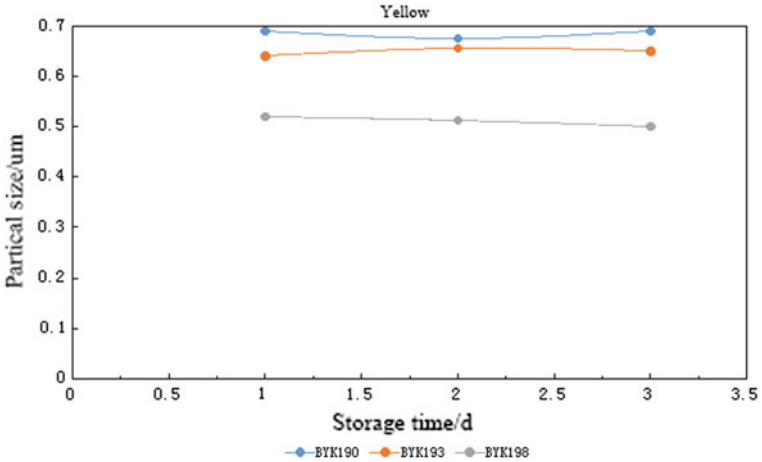

Fig. 7 Yellow ink particle size variation after storage

Table 6 Black ink particle size change after storage

Black			
Wetting dispersant type	Particle (size/μm)		
	1 day	7 days	14 days
BYK190	1.02	0.87	0.99
BYK193	1.20	0.85	1.02
BYK198	1.00	1.02	1.01

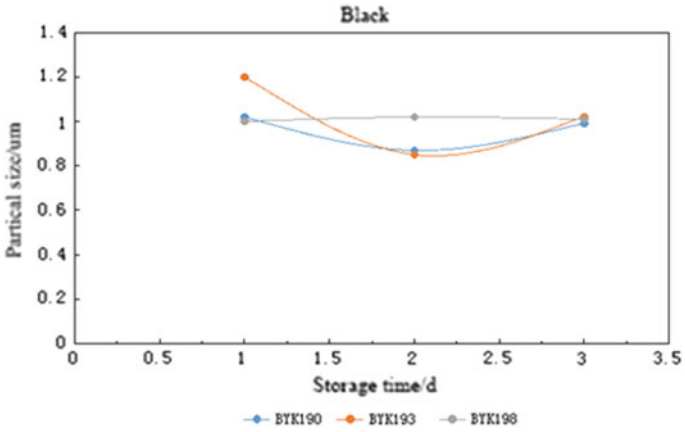

Fig. 8 Black ink particle size variation after storage

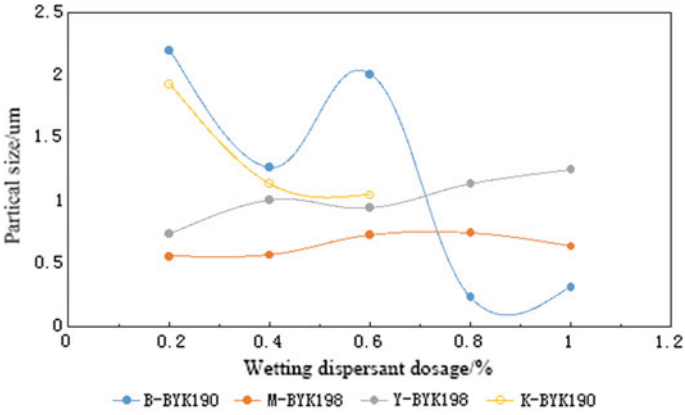

Fig. 9 Particle size under different wetting dispersant dosage

Table 7 Black ink particle size change table after storage

Wetting dispersant type	Particle (size/μm)				
	The proportion				
	0.20%	0.40%	0.60%	0.80%	1.00%
B-BYK190	2.20	1.27	2.01	0.24	0.32
R-BYK198	0.56	0.57	0.73	0.75	0.64
Y-BYK198	0.74	1.01	0.95	1.14	1.25
K-BYK190	1.93	1.14	1.05		

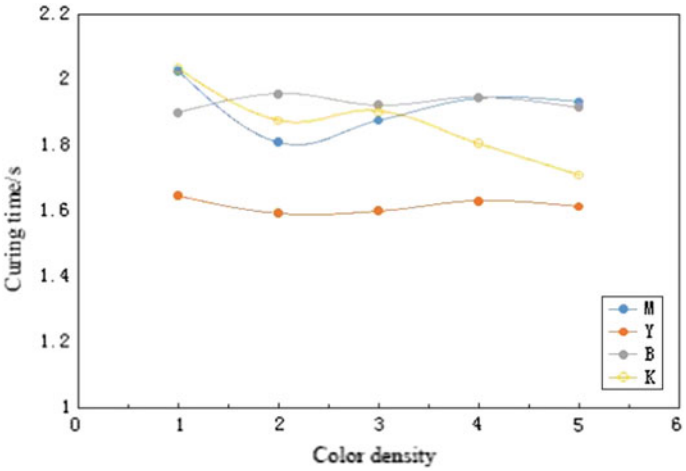

Fig. 10 Different curing time corresponding color density figure

4 Conclusions

The aim of this study is to explore the particle size and stability of water-based UV ink. The optimum wetting and dispersing agent, the optimum wetting and dispersing agent dosage and the grinding time are obtained by comparing with different variables of different color of water-based UV ink. So that can obtain different colors of water-based UV ink of the particle size range and the stability of the experimental products, and then according to the color density of ink and other printing performance indicators. There is an objective and impartial evaluation to the ink, to get the best water-based UV inks formulations and operating options.

Table 8 Curing time on the influence of color density

Curing time (s)	Color density			Average
5 (red)	2.03	2.01	2.04	2.03
6	1.82	1.80	1.81	1.81
7	1.87	1.86	1.90	1.88
8	2.00	1.92	1.91	1.94
9	1.94	1.92	1.94	1.93
5 (yellow)	1.62	1.65	1.67	1.65
6	1.60	1.60	1.58	1.59
7	1.61	1.58	1.61	1.60
8	1.62	1.63	1.64	1.63
9	1.63	1.60	1.61	1.61
5 (blue)	1.94	1.89	1.87	1.90
6	1.99	1.98	1.90	1.96
7	1.98	1.90	1.89	1.92
8	1.94	1.97	1.93	1.95
9	1.95	1.88	1.92	1.92
5 (black)	2.00	2.03	2.07	2.03
6	1.85	1.86	1.92	1.88
7	1.87	1.92	1.92	1.90
8	1.79	1.88	1.75	1.81
9	1.80	1.67	1.66	1.71

In this work, we explored the optimal wetting and dispersing agent for different color inks and their dosage, and obtained the best grinding time and the best curing time. Through the study of this paper, we can target on different colors of pigment adding to the corresponding species and components of the wetting and dispersing agent, in order to get more suitable for printing ink. In particular, we obtain the curing time based on the optimum color density, which can be used for printing on different print media. In fact, it also makes more possibilities for the printing on wood-based panel mentioned in this article.

Acknowledgements This work was supported by the independent research project of Key Laboratory of Pulp and Paper, South China University of Technology (Nos. 2016C01), the Science and Technology Project of Guangdong Province (No. 201607020045).

References

1. Yang H (2014) China's packaging and printing ink market strong development]. Printing Technol 21(7):79–81
2. Jia Y (2007) Water-based UV ink. Screen Printing 11:32–34
3. Liu Xin, Zhai Yuyue, Ren Ye (2014) The invention of a new type of water-based UV ink. Printing Technol 05:50–52

4. Wang S (2006) Water-based UV inks. Screen Printing 9:32–33
5. Song Q (2007). Analysis of water-based UV ink. Printed World 10(22):42–44
6. Nan Jingsheng (2014) Printing ink market situation analysis. Today's Printing 2(3):44–47
7. Yu J (2015) Concerned about the development of environmentally friendly water-based ink technology. China Printing 8(7):66–69
8. Liu X, Xie D, Wu J et al (2008) Synthesis of waterborne acrylic resin modified by water—based ink. Packag Eng 29(7):31–33
9. Chen Y, Yang J, Zeng Z (2003) Radiation curing materials and their applications. Chemical Industry Press, Beijing
10. Zhang K, Li T, Zhang T et al (2013) Adhesion improvement of uv-curable ink using silane coupling agent onto glass substrate. J Adhes Sci Technol 27(12):1499–1510

Coloring of Aluminum Powder Based on Double-Layer Coated Waterborne Silver Ink

Zhengneng Wu, Shisheng Zhou, Wenlong Zhao, Bin Du, Yan Zhang, Shangjie Jiang and Bin Deng

Abstract In this paper, the double-layer coated colored aluminum powder was created by sol-gel and in situ polymerization methods, considered the addition order of the phthalocyanine blue. One is coloring when monolayer coated, the other is coloring when double coated, respectively. To analyze the effects of color and corrosion resistance on the two-layer coated aluminum powder, SEM and EDS analysis were used, and the results showed that double coated coloring is the best. The optimum reaction conditions were set as follows: MMA, 0.35 g, temperature, 85 °C, reaction time, 4 h, phthalocyanine blue, 3.0 g.

Keywords Aluminium powder · Double coated · Coloring · Corrosion inhibition efficiency

Silver paste ink is abstracted from the metal aluminum pigments, resins, solvents, additives and other materials, with high gloss [1]. The color carrier and coloring agent of aluminum pigment have lively chemical properties, and the hydrogenation reaction is very rapidly when touching air [2–7]. Since the particularity of metallic aluminum pigment in silver paste ink, two kinds of double color coated aluminum powder were created by two methods.

1 Experimental

(1) Method 1: coloring when single layer coating and then double-coating; solution A: 2 ml TEOS was mixed with 30 ml absolute ethanol, solution B: 3 ml VTES, 3 ml aqueous ammonia, 10 ml deionized water and 30 ml absolute ethanol. 2 g aluminum pigment, 1.5 g phthalocyanine blue pigment, 50 ml absolute ethanol,

Z. Wu (✉) · S. Zhou · W. Zhao · B. Du · Y. Zhang · S. Jiang · B. Deng
Faculty of Printing, Packing Engineering and Digital Medial Technology, XUT, Xi'an, Shaanxi, China
e-mail: 1368691812@qq.com

P. Zhao et al. (eds.), *Applied Sciences in Graphic Communication and Packaging*, Lecture Notes in Electrical Engineering 477,
https://doi.org/10.1007/978-981-10-7629-9_85

solutions A and B were added, stirred for 1 h under nitrogen to get a single layer of coated aluminum powder. Xylene and butyl acetate were mixed with mono-layer coated aluminum powder, MMA and MA were mixed, BPO and 10 ml butyl acetate, vacuum drying at 50 °C for 24 h, get double-coated aluminum powder.

(2) Method 2: coloring when double-layer coating; 2 g aluminum pigment, 50 ml absolute ethanol, solutions A and B were added, stirred for 1 h under nitrogen get a single layer of coated aluminum powder. Mono-layer coated aluminum powder, phthalocyanine blue pigment, 60 ml mixed solvent MMA and MA were mixed, BPO and 10 ml butyl acetate, vacuum drying at 50 °C for 24 h, get double-coated aluminum powder.

2 Experiment Analysis

2.1 Analysis of Orthogonal Experimental Design

Coloring when coated on a single layer (Table 1).

Table 1 Optimization of preparation of double-layer coated color aluminum powder

Factor	Temperature (°C)	MMA (g)	Time (h)	Gloss (GU)	Corrosion inhibition efficiency (%)
Maximum gloss	80	0.20	4	51.98	73.2
Maximum corrosion inhibition efficiency	85	0.35	6	50.72	97.6
Optimizing experiment	85	0.35	4	51.44	92.3

Coloring when double-layer coating (Table 2).

Table 2 Optimization of preparation of double-layer coated color aluminum powder

Factor	Temperature (°C)	MMA (g)	Phthalocyanine blue	Time (h)	Gloss (GU)	Corrosion inhibition efficiency (%)
Maximum gloss	90	0.35	1.5	4	59.84	90.0
Maximum corrosion inhibition efficiency	85	0.35	1.0	6	58.38	98.5
Optimizing experiment	85	0.35	3.0	4	55.36	92.1
	85	0.35	3.0	6	53.56	97.5

2.2 Scanning Electron Microscopy (SEM) Analysis

In the experiment of method 1, 5000 times the electron microscope (a) and 2000 times the electron microscope (b) of the modified aluminum powder selected according to the maximum degree of gloss, 5000 times the electron microscope (c) of the modified aluminum powder according to the corrosion inhibition efficiency and 2000 times the electron microscope (d), according to the maximum choice of modified aluminum powder 5000 times the electron microscope (e) and 2000 times the electron microscope picture (f) for comparison, as shown in Fig. 1. In the experiment of method 2, (a)–(f) are the same as the selection in the method 1, and the second group of modified aluminum powder 5000 times the electron microscope (g) and 2000 times the electron microscope (h), as shown in Fig. 2.

In the experiment of method 1, we can see that the edge of the modified aluminum powder has a translucent film, indicating that the polyacrylate was coated. (a) the edge of the modified aluminum powder is smoother, but the coating is not dense; (c) the edge of the modified aluminum powder is slightly burr and the coating is dense; (d) the surface of the modified aluminum powder is smooth, no burr, the effect is better. (b) the distribution of phthalocyanine blue particles on the modified aluminum powder surface is not uniform and the agglomeration phenomenon; (d) group of modified aluminum phthalocyanine blue and aluminum powder sheet stacked together, and the distribution of uniform.

In the experiment of method 2, also, you can see the edge of modified aluminum powder has a layer of translucent membrane, indicating that polyacrylate was coated. (a) group modified aluminum powder surface is phthalocyanine blue

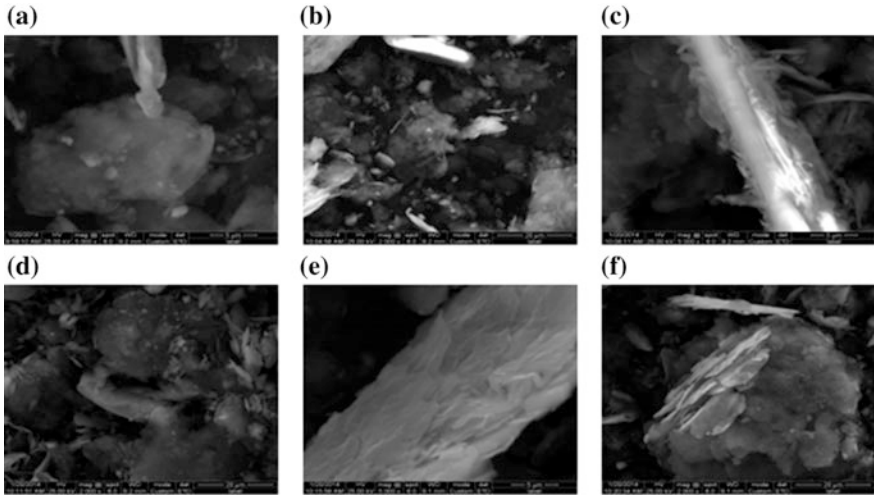

Fig. 1 SEM images of the modified aluminum powder obtained by coloring the mono-layer coating

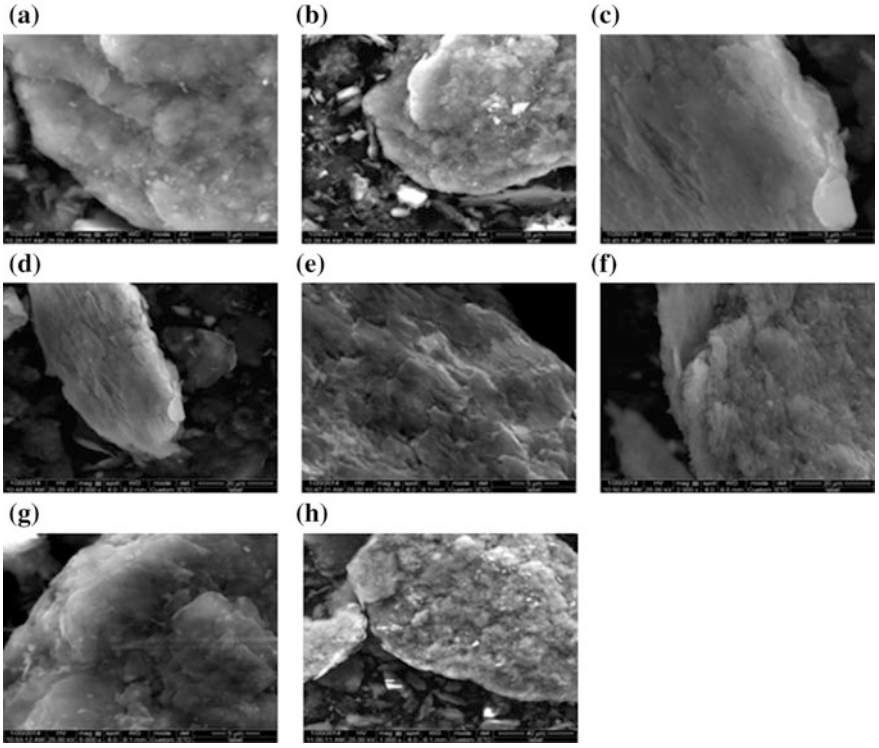

Fig. 2 SEM of the modified aluminum powder obtained by coloring the double-layer coating

pigment particles, coating is more dense; (f) group of modified aluminum powder without agglomeration phenomenon; (h) group modified aluminum surface (f) group is smooth, there is a small amount of agglomeration phenomenon, so that the first group based on the maximum choice of modified aluminum powder coated was better.

2.3 X-ray Energy Dispersive Spectrometer (EDS) Analysis

The EDS analysis spectrum of the modified aluminum powder (a) was selected according to the principle of maximum range in method 1 and the first group of modified aluminum powder (b) was selected according to the principle of maximum range in method 2, as shown in Fig. 3. The newly emerging characteristic peak Cu is caused by the Cu element contained in the phthalocyanine blue pigment. And the content of the aluminum element in the EDS spectrum of the double-layer coating is decreased, indicating that the surface of the aluminum powder colored by the double-layer coating is denser.

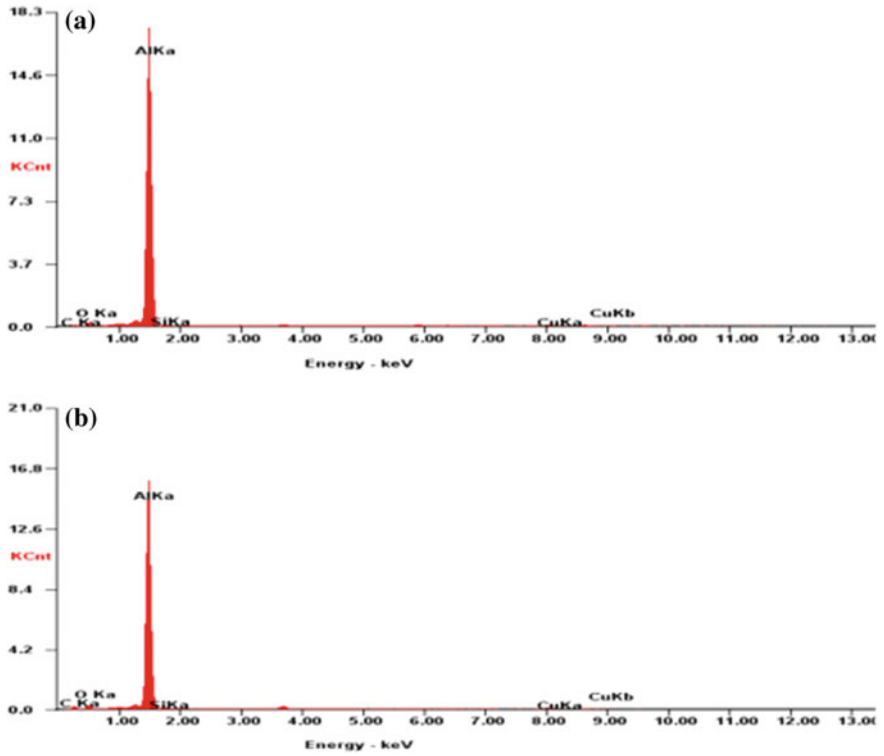

Fig. 3 EDS analysis of modified aluminum powder obtained by two coloring methods

2.4 Color Difference Analysis

The color difference of the double-layer coated aluminum powder when coloring at the time of double-layer coating is generally higher than that of the double-layer coated aluminum powder coloring when coated in a single layer, and both are larger than 6. Color difference of coloring when double-layer coated aluminum powder was bigger, the human eye can be easily identified.

2.5 Gloss and Corrosion Resistance Analysis

The gloss and corrosion inhibition efficiency of the nine groups of experiments and the tenth group of the maximum range in method 1 experiment, the gloss and corrosion inhibition efficiency of the nine groups of experiments and the tenth and eleventh group of the maximum range in method 2 experiment.

In method 1, the sixth group of experiment has the greatest degree of gloss, but the corrosion efficiency is not good; the fifth group of experiment has the largest corrosion efficiency, the thickness is also good. The tenth group of experiment, the maximum range group, the gloss is smaller than the sixth group, bigger than the fifth group, and the corrosion efficiency is slightly lower than the fifth group.

In method 2, the sixth group has the highest gloss, but the corrosion efficiency is not good; the fifth group has the greatest corrosion inhibition efficiency and good gloss. The maximum range of the two groups, the tenth group of gloss is higher than the eleventh, slightly smaller than the sixth group, but the corrosion efficiency is smaller than the eleventh, bigger than the sixth group.

Organic pigments phthalocyanine blue has strong coloring but poor hydrophilicity, after ultrasonic dispersion the settlement rate decreased significantly. The optimum conditions for the preparation of double-coated colored aluminum powder are: the amount of MMA is 0.35 g, the temperature is 85 °C, the time is 4 h, and the phthalocyanine blue is 3.0 g.

3 Conclusions

(1) In this chapter, two-layer coated aluminum powder was created by two methods: sol-gel method and in situ polymerization methods.
(2) TEOS and VTES occurred hydrolysis and polycondensation reactions during the experiment, accompanied by generation of a dense coating on aluminum powder's surface. The presence of pigment particles was found in several groups of SEM selected in SEM, which means that the pigment deposited in the aluminum surface. By the EDS detection that the presence of aluminum powder Cu and C elements, showed that the pigment deposited in the aluminum surface, respectively.
(3) The gloss and corrosion inhibition efficiency of the double-layer coated aluminum powder were slightly lower than those of the double-coated aluminum powder, but both can fulfill requirements.
(4) Above all, the results show that the optimum reaction conditions are as follows: MMA was 0.35 g, temperature was 85 °C, reaction time was 4 h, phthalocyanine blue was 3.0 g.

Acknowledgements This study is supported by Scientific Research Program of Key Laboratory Funded by Shaanxi Education Department (14JS067).

References

1. Howe KS, Clark ER, Bowen J, Kendall K (2013) A novel water-based cathode ink formulation. Int J Hydrogen Energy 3(38):1731–1736
2. Robert T (2015) "Green ink in all colors"—printing ink from renewable resources. Prog Org Coat 78:287–292
3. Noonpui S, Thiravetyan P, Nakbanpote W, Netpradit S (2010) Color removal from water-based ink wastewater by bagasse fly ash, sawdust fly ash and activated carbon. Chem Eng J 2 (162):503–508
4. Żołek-Tryznowska Z, Izdebska J, Tryznowski M (2015) Branched polyglycerols as performance additives for water-based flexographic printing inks. Prog Org Coat 78:334–339
5. Emregül KC, Aksüt AA (2003) The effect of sodium molybdate on the pitting corrosion of aluminum. Corros Sci 45(11):2415–2433
6. Putilova IN, Balezin SA, Barannik VP (1960) Metallic corrosion inhibitors. Pergamon Press, p 125
7. Becaria AM, Chiarutini L (1999) The inhibitive action of metacryloxypropylmethoxysilane (MAOS) on aluminum corrosion in NaCl solution. Corros Sci 41(5):885–889

Preparation of Low Temperature Expandable Microspheres and Its Application in Foaming Ink

Meijuan Cao, Zhicheng Sun, Guangwen Bin, Qing Xia, Luhai Li, Jianhua Li and Hongjuan Li

Abstract The thermally expandable microspheres were prepared through suspension polymerization methods with acrylonitrile (AN), methyl methacrylate (MMA) and methyl acrylate (MA) as monomers. In addition, the research on the morphology and thermal performance of microspheres showed that the expandable microspheres had a higher expansion ratio and the initial expansion temperature was fairly low. The physical foaming ink was prepared using microspheres with a certain proportion. The ink was transferred to three kinds of printing substrates including non-woven fabric, coated paper and aluminum foil paper by screen printing. As well, several effective factors were investigated, such as the relationship between printing substrates and foaming heights, the foaming height variation with the temperature, and the color characteristics before or after ink foaming. Through the above research, the three-dimensional printing products with high saturation color effects on the flexible substrate are obtained.

Keywords Thermally expandable microspheres · Preparation · Foaming ink Screen printing

M. Cao · Z. Sun (✉) · G. Bin · Q. Xia · L. Li
School of Printing and Packaging Engineering, Beijing Engineering Research Center of Printed Electronics, Beijing Institute of Graphic Communication, Beijing, China
e-mail: sunzhicheng@bigc.edu.cn

M. Cao
Beijing Key Laboratory for Microanalytical Methods and Instrumentation, Department of Chemistry, Tsinghua University, Beijing 100084, China

J. Li (✉) · H. Li
Hebei Provincial Engineering Technology Research Center of Coal-Based Chemicals and Materials, Tangshan 063018, China
e-mail: ecljh@kailuan.com.cn

P. Zhao et al. (eds.), *Applied Sciences in Graphic Communication and Packaging*, Lecture Notes in Electrical Engineering 477,
https://doi.org/10.1007/978-981-10-7629-9_86

1 Introduction

The thermally expandable microspheres are the main functional components of the physical foaming printing ink, which has the characteristics of light weight, low toxicity and friendly environment. The thermoplastic polymers are the shell of thermally expandable microspheres, and the low-boiling organic solvents are usually coated as the core materials inside the thermally expandable microspheres. When the microcapsules were heated, the capsule core (low-boiling organic solvent) rapidly vaporized under the role of internal pressure, and the wall materials began to expand. The volume of microspheres increased and the density decreased from the original 1100 to 30 kg/m^{-3}. In general, the diameter of microspheres after heating increases several times and the volume increases fairly one hundred times contrasting with the original microspheres. Meanwhile, the morphologies of microcapsules after expansion are relatively stable, keeping their shapes after cooling [1–4]. Due to the unique characteristics, the thermally expandable microspheres have been widely used in the field of light industry, especially in wall paper, printing ink [5], stereoscopic printing and micro fluid [6–8].

Physical foaming printing ink was usually transferred to the substrates such as papers, plastics, leathers, textiles and began heating, and then, the foam printing design pictures will be showed with embossed graphics after natural cooling. This is a kind of novel printing way, without relying on the concave-convex embossing and carving gravure printing [9]. The composition of physical foaming printing ink [10–12] is: 60% of acrylic ester and other resin copolymer, 20% of foam microsphere, 5% of urea, 10% of paste, 5% of other ingredients. Through the stability of post-processing microspheres foaming printing, a embroidery or flocking artistic effect can be presented [13]. Though foaming printing, the three-dimensional effect can be got, but the foam control precision demand is higher [14]. Therefore, it is obviously important to analyze the characteristics of foaming ink.

2 Experiments

2.1 Experimental Materials

Unless otherwise noted, the reagents were obtained from commercial suppliers and were used without further purification. Acrylonitrile (AN); Methyl methacrylate (MMA); Azodiisobutyronitrile (AIBN); Methyl acrylate (MA); 1, 4-butanediol dimethyl acrylic (BDDMA); N-hexane; Sodium hydroxide; Sodium dodecyl sulfate; Aluminum foil paper; Non-woven fabrics.

2.2 Instruments and Equipments

High speed disperser, XHF-D; Thermal expansion instrument, DIL 402 PC, German; Thermogravimetric analyzer, TG209C, German; Scanning electron microscope, SU8020, Japan; Laser confocal microscope, VHX-5000, Japan; Electric heating plate, PB-3; Silk screen version and 100 mesh; Screen printing machines, OS-500.

2.3 Preparation of Thermally Expandable Microspheres

The preparation of oil phase: the monomer acrylonitrile (14 g), methyl methacrylate (4 g), methacrylate (2 g), initiator azodiisobutyronitrile (0.43 g), crosslinking agent (0.04 g) and foaming agent n-hexane (5.12 g) were added into the flask and mixed with magnetic stirring.

The preparation of aqueous phase: NaOH (2.5 g) and distilled water (45 g) were added into the flask and mixed fully for use. Moreover, $MgCl_2{\cdot}6\ H_2O$ (6 g) and distilled water (45 g) was added into another flask and mixed fully for use. After being both dissolved completely, the NaOH solution was added into the three flask, and a certain amount of sodium dodecyl sulfate was added with mechanical agitation for a period of time. After that, $MgCl_2{\cdot}6\ H_2O$ solution was added at a certain speed with a funnel and stirred with higher speed, forming the relatively stable magnesium hydroxide particles dispersion. Finally, sodium chloride, sodium nitrite and anhydrous ethanol were added into the flask and stirred well to get the reaction system of water phase.

The water phase and oil phase were mixed and homogenized, making the oil phase dispersed in water phase and fully dispersed. The temperature of reaction was 65 °C and the mechanical stirring speed was 150–400 rpm. After reaction, the materials were washed, filtered and dried. Accordingly, the final physical foaming microcapsules were obtained.

2.4 Preparation of the Foam Printing Ink and Printing Applications

The foaming printing ink was obtained through mixing printed protoplasmic (50%), water-based acrylic resin (25%), water (5%) and paste (9%), foaming microcapsule (10%), defoaming agent (0.2%) and flattering agent configuration (0.8%) in a certain proportion.

Take high temperature resistant experiments with the coated paper, aluminum foil paper, non-woven fabric, screening substrate which can withstand certain high temperature, foaming printing inks in the three different substrate by screen printing

press, 50 °C pre heating in the oven for 10 min, heating with heating plate 150 °C for 1 min, test the steric effect of the sample.

2.5 Analysis Test

Using TG curve to analysis microspheres foaming agent cubed out (that is, the quality percentage of the total quality of microspheres foaming agent), microspheres foaming agent starting weightlessness temperature, the temperature of the foaming agent completely volatilization, etc.

DSC curve by the German resistance chi technology company of DSC measurement 214, using the DSC curve analysis of the glass transition temperature of the polymer shell.

Thermal expansion curve (DIL) by thermal expansion measurement instrument, starting with the analysis of curve precise microspheres foaming temperature Tstart, maximum foaming temperature Tmax and expansion rate of dL/d0, and record data analysis.

Scanning electron microscope is used to observe the surface morphology of microspheres with a laser confocal microscope all of the surface topography. The thickness of the thickness gauge is used to test. Chroma value determination is done by X-ray rite spectrophotometer.

3 Results and Discussion

3.1 Morphology Analysis of Thermally Expandable Microspheres

As shown in Fig. 1, microsphere expansion before shape for dry shell microspheres of nuclear structure, particle size distribution is relatively uniform, after expansion diameter, shape is ball, diameter ratio of 4–5 times before and after the expansion, expansion ratio is bigger, can be applied to the preparation of the foam printing ink.

3.2 Thermal Analysis of Microcapsules

Microspheres for thermal expansion, thermo-gravimetric analysis and differential thermal analysis, and respectively get DIL, TG and DSC curve, as shown in Figs. 2 and 3, the thermal analysis curves shows that polymer shell of the glass transition temperature (TG) is about 70 °C, after the glass transition temperature is reached, polymer shell began to soften, cubed out 17.5% of the foaming agent and

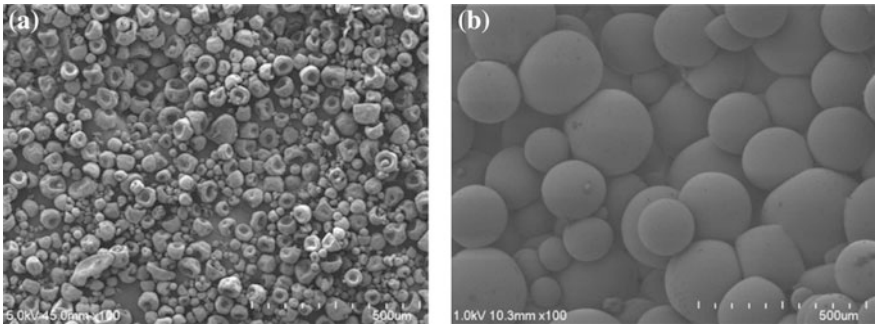

Fig. 1 SEM of microspheres **a** unexpanded, **b** expanded

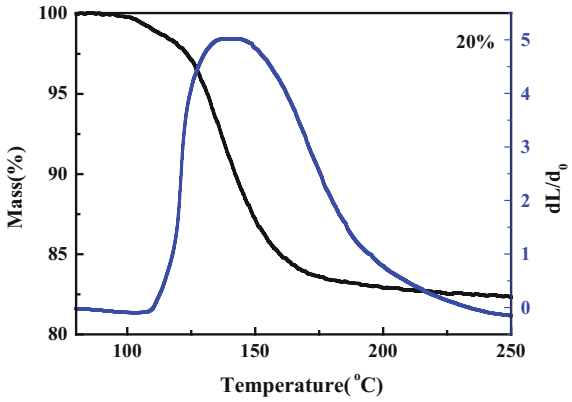

Fig. 2 Dilatometer (DIL) and TG curve of microspheres

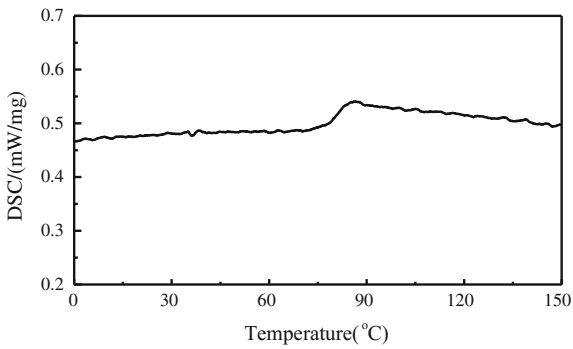

Fig. 3 DSC curve of microspheres

microspheres, the ball inside the pressure is less than the outside pressure, will not be enough to make microsphere expansion, when the temperature is 108.3 °C, the microspheres began to expand, Inflation reached maximum when the temperature is 141.8 °C. In addition, with the increase of temperature of larger diameter and volume expansion gradually, the morphology of microspheres by the expansion of dry shrinkage shape into full ball state. When microsphere volume expansion to the largest, continue to raise the temperature, leading to polymer shell is weak, the gas easily within the microspheres through the escape capsule wall, when the temperature exceeds 200 °C, shell polymer adhesion and gradually broken down slowly.

3.3 Relationship Between Foam Height and Base Material Surface Printing Ink

As can be seen from Fig. 4, microspheres was transferred to the substrate, after 150 °C heating processing microspheres began foaming, diameter is significantly larger, ink thickness is increased, the vivid image of 3 d printing is achieved. Relative to the aluminum foil paper and coated paper two substrates, non-woven

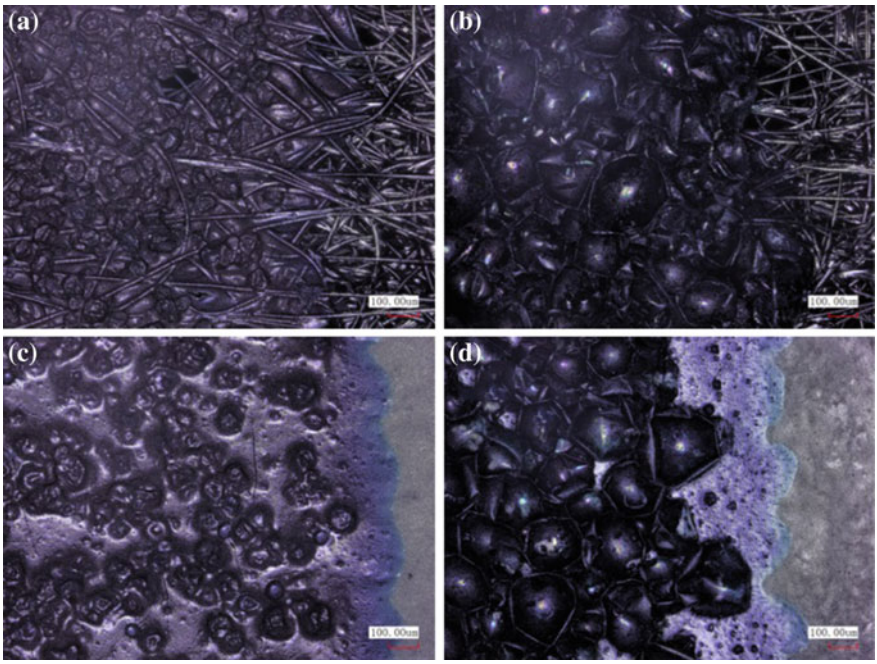

Fig. 4 Morphology of ink with different temperature

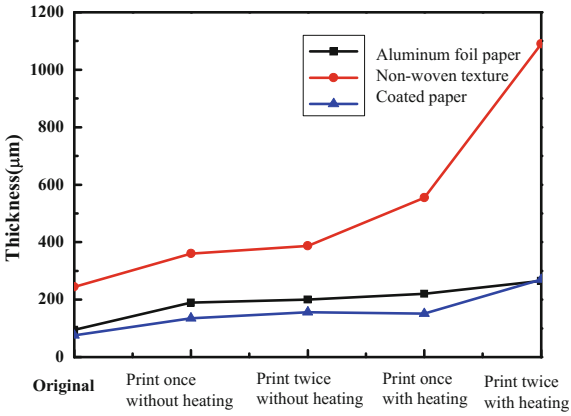

Fig. 5 The thickness curve of foaming ink printed on different printing materials

fabric texture surface is rough and porosity is large, which lead to the uniformity of the foam printing ink and graphic sex is affected by a certain effect.

In addition, the extension of the foam printing to a variety of substrates such as paper, cloth, leather, after dealing with the same condition of heating, we found the phenomenon that due to different morphology and surface properties of base material itself different on the surface of the substrate ink foaming body height is not the same. Second, non-uniform size and foam expansion ratio also can make ink foaming body height fluctuation, so at the time of preparation foam ink, choose the same or choose preparation of microspheres particle size and foam expansion ratio similar microspheres as foaming agent of foam ink, ruled out as much as possible because of the expansion of the foaming ratio in different thickness error caused by different. As can be seen from the Fig. 5, non-woven is significantly better than the thickness of the foam before and after foam aluminum foil paper and coated paper, and the thickness of the foamed body after two overprint than the thickness of the foam increased evidently. Especially when using non-woven fabric printing, foam steric effect is more apparent, mainly because of non-woven own fiber gap is big, uneven surface texture, absorb ink into the hole, so the ink foaming body height increased, while the coated paper and aluminum foil surface is smooth, instead of foam height is less. The above data can be drawn into a foaming temperature, height of the curve as shown in Fig. 5.

3.4 The Relationship Between Print Foam Height and the Foaming Temperature

As shown in Fig. 6, the foam heights of aluminum foil printing samples change with the foaming temperature. Each point on the curve are repeatedly measured average on the basis of the statistical results. The main purpose is to reduce the error caused by a single measurement, increase data reliability and repeatability.

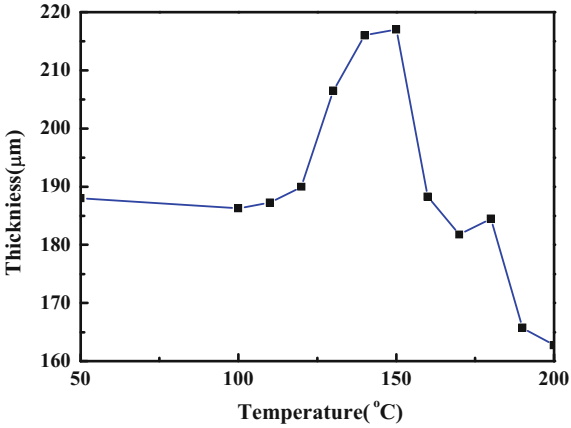

Fig. 6 Foam height of aluminum foil printing samples under 50–200 °C

The starting temperature of foaming is about 100 °C, when the temperature is below 150 °C, with the increase of temperature, organic solvent evaporation in microspheres in pressure, prompting wall of micro balloon expansion and the volume increases, the height of the microspheres foaming body increases with the rise of temperature. When the temperature rose to 150 °C, the microsphere expansion to the limit and foam height reached the highest, the temperature is the largest foaming temperature at this time. If the temperature continues to rise, micro balloon wall will become weak; there will be a part of the core material of organic solvent through the escape capsule wall and microspheres, results in the decrease of microsphere internal pressure. Under the action of atmospheric pressure on the world and the microspheres can appear the phenomenon of volume, instead foam height decreased. When the temperature higher than 170 °C, the core material all escape and microspheres polymer starts to break down, which cause foaming height decreased. Therefore, the height of the foam can be manipulated by adjusting temperature; in general, the best expansion foam temperature should be controlled between 120 and 160 °C. In three different kinds of foam printing ink printed on the base material, the influence of foaming temperature on foaming body height is obvious, and the trend of change is same.

3.5 Color Characteristics of Foaming Printing Ink

Measuring the shade of the foam before and after values and L*, a*, b* value by Spectrophotometer, as shown in Table 1, foaming samples after saturation decreases besides the black sample. M, C, and BK dark colored sample lightness value increases. While Y, Ag, G of light colored sample lightness value decreases a little, the change is little. In addition, the green colored sample of chromaticity value mapped on the CIE1931 chromaticity scale map, as shown in Fig. 7,

Table 1 Chrominance value of the sample before and after expansion

Sample	L*	a*	b*	C	ΔE
M-before	41.28	59.41	33.08	68.00	11.19
M-after	45.78	52.45	25.57	58.35	
C-before	35.29	5.42	−45.09	45.42	16.66
C-after	44.75	−0.67	−32.81	32.82	
BK-before	24.56	−0.003	−0.90	0.90	9.64
BK-after	34.19	−0.19	−1.23	1.25	
Y-before	81.08	9.71	87.33	87.86	20.87
Y-after	79.97	7.19	66.63	67.02	
Ag-before	90.13	0.74	−2.97	3.06	2.68
Ag-after	88.74	0.006	−0.79	1.02	
G-before	91.04	1.67	−2.29	2.87	1.33
G-after	90.62	0.93	−1.26	1.57	

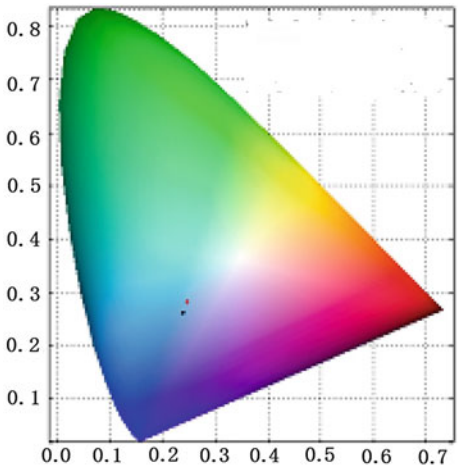

Fig. 7 CIE1931 chromaticity scale diagram of cyan sample (color figure online)

the shade of the same quality sample before and after the foaming basically are in the same line, which shows that both the same color or change little.

By color difference formula $\Delta E = \sqrt{(\Delta L^*)^2 + (\Delta a^*)^2 + (\Delta b^*)^2}$, It is generally believed that visual color difference is strong when the color difference between 6 and 12, and when the color difference is greater than 12, which is very strong [15]. Therefore, in addition to Ag, G, the color difference of foam before and after is very strong.

4 Conclusions

The low temperature expandable microspheres are prepared by the method of suspension polymerization microcapsule. The diameter of foam expands to 4–5 times, and the inflation rate is higher. The starting temperature of microspheres is 108.3 °C, while it turns to 141.8 °C as expansion reaches to the maximum. Using screen printing process, the preparation of the physical foaming type printing ink made up by the thermally expandable microspheres prepared according to certain proportion. The screen printing is on three kinds of non-woven fabrics, coated paper, aluminum foil paper printing substrate, and the surface of printing non-woven fabric is rougher than other two kinds of substrates. Its porosity is large and the height of the foaming body is bigger, and the thickness of the foam after two foaming lather has changed significantly. The best expansion foam temperature should be controlled between 120 and 160 °C. The color difference of Ink foaming is bigger from a very intense visual color to the reduced black saturation value. The dark colored sample lightness value increases, and the lightness value changes very little or even the light colored sample basically remain unchanged.

Acknowledgements This work was supported by the National Natural Science Foundation of China (Grant No. 21646013, 21776021, 21206171), the Project of Natural Science Foundation of Beijing (Grant No. 2152012), the Young Elite Teacher Project and BIGC Key Project (Grant No. Ea201701, Ea201603), Cross training plan for high level talents in Beijing (2017), 2011 Collaborative Innovation Center of Green Printing & Publishing Technology (CGPT). Beijing Postdoctoral Research Funds Grant No. (2016-ZZ-53), Initial funding for the Doctoral Program of BIGC.

References

1. Fredlund J (2011) Short of thermo expandable microspheres. Master of science thesis Sundsvall, Sweden
2. Hou ZS, Kan CY (2014) Preparation and the properties of thermoexpandable polymeric microspheres. Chin Chem Lett 25(9):1279–1281
3. Jonsson M, Nordin O, Kron AL et al (2010) The thermally expandable microspheres with excellent expansion characteristics at high temperature. J Appl Polym Sci 117(1):384–392
4. Fujino M, Taniguchi T, Kawaguchi Y et al (2013) The mathematical models and numerical simulations of a thermally expandable microballoon for plastic foaming. Chem Eng Sci 104:220–227
5. Urbas R, Elesini Us (2015) Color differences and perceptive properties of prints made with microcapsules. J Graph Eng Des 6(1):15
6. Jeong JW, McCall JG, Shin G et al (2015) The wireless optofluidic systems for programmable in vivo pharmacology and sights on. J Cell 162(3):662–674
7. Banea MD, da Silva LFM, Carbas RJC et al (2014) The mechanical and thermal characterization of a structural polyurethane adhesive modified with thermally expandable particles. Int J Adhes Adhes 54:191–199
8. Banea MD, Da Silva LFM, Carbas RJC (2015) Debonding on command of adhesive joints for the automotive industry. Int J Adhes Adhes 59:14–20

9. Ji C (2004) The characteristics of the foam printing ink and troubleshooting. Printing Today 11:68–69
10. Jia J, Yang L-Z, Kun M (2001) Practical silk screen printing technology. Chemical Industry Press, Beijing
11. Liu J (1994) Foam ink. J Screen Printing 1:20–23
12. Zhou Z (2006) Printing ink. Chemical Industry Press, Beijing
13. Huang T (1994) Foaming printing ink features. Chin Printing 12(4):34–38
14. Chen SY, Sun ZC, Li LH et al (2017) Preparation and characterization of conducting polymer-coated thermally expandable microspheres. Chin Chem Lett 28(3):658–662
15. Lu X-G, Huang L-G, Cao G-H (2001) Packaging color science. The Printing Industry Press, Beijing

The Study on Color Reproduction of Fluorescent Inkjet Ink

Lili Wang, Wan Zhang, Beiqing Huang, Xianfu Wei, Xiaotong Xiong and Lu Zhang

Abstract At present, the fluorescent ink has been widely used in security printing and packaging, as well as the interior. However, in view of the fluorescent ink color control is still lack of perfect standard, even for basic information collection of fluorescent ink color piece have no standard test method, which hindered the development of fluorescent ink. In early, we have realized the fluorescent ink jet ink printing output. The paper makes a further study on the printing methods and color test methods of fluorescent inkjet ink. First, we design different ladder color patch and print proof, choose RF-5301PC and PR-655 for color block information acquisition and compare the test precision. Using self-developed dot coordinate software and dot trapping software (Photoshop) respectively print proofs, and analyze color reproduction ability of the two kinds. Finally, we explore the influence of different substrates on the color reproduction range of fluorescent ink. The experimental results show that the PR-655 is more accurate than the RF-5301PC. Since the ink layer for inkjet printing is thin, the dot trapping and dot coordinate have little difference with the same amount of ink output. The performance parameters of the paper have a significant effect on the color reproduction of the UV fluorescent inkjet ink.

Keywords Fluorescent inkjet ink · Dot trapping · Dot coordinate Substrates

1 Introduction

UV fluorescent ink is a kind of special ink which absorb in the ultraviolet wavelength range (320–380 nm) and reemit light in part of the visible wavelength range (380–780 nm) [1, 2]. It not only has merits such as simple implementation, low

L. Wang · W. Zhang · B. Huang · X. Wei (✉) · X. Xiong · L. Zhang
School of Printing and Packaging Engineering, Beijing Institute of Graphic Communication, Daxing, China
e-mail: weixianfu@bigc.edu.cn

P. Zhao et al. (eds.), *Applied Sciences in Graphic Communication and Packaging*, Lecture Notes in Electrical Engineering 477,
https://doi.org/10.1007/978-981-10-7629-9_87

cost, good concealment, colorful and convenient testing, but also can enhance artistic effect of print and improve the additional value [3]. Currently, the fluorescent ink is mainly used screen printing, gravure and flexible printing and other traditional printing methods [4], but only limited to some simple graphic printing, not form a perfect control system in the color reproduction. UV fluorescent inkjet ink is one of the most widely used digital anti-counterfeiting technology. Different from ordinary color ink, the principle of fluorescent ink is colored additive method, the color saturation is higher, but there is no standard color control method for fluorescent ink.

In order to study the color test method and printing effect of UV fluorescent inkjet ink print proofs, we design different ladder patch, and choose RF-5301P and PR-655 for color piece information acquisition and compare the test precision by color difference. Using self-developed dot coordinate software and dot trapping software (Photoshop) respectively print proofs, and analyze color reproduction ability of the two kinds. Finally, we explore the influence of different substrates on the color reproduction range of fluorescent ink.

2 Experiments

2.1 Equipment and Materials

See Tables 1 and 2.

Table 1 Experimental materials

Name	Weight (g/m^2)	Color	Format	Fluorescent agent
Munken	100	Beige	A4	No
Dowling	100	Off-white	A4	No
Offset paper	80	White	B3	Yes
coated paper	100	White	A4	Yes

Ink: R, G, B UV fluorescent inkjet ink (Japanese corporation SO-KEN)

Table 2 Experimental equipments

Name	Type	Manufacturer
Inkjet printers	Epson Stylus Pro 7600	Epson
Fluorescence spectrometer	RF-5301PC	Shimadzu, Japan
Standard color light source lamp box	JudgeII	Guangzhou Li Po Laboratory Testing Instrument Co., Ltd.
Spectral radiometer	PR-655	Photo Research, Inc.

2.2 The Preparation of Test Proofs

In the Photoshop software RGB mode, draw 21 color patches whose dot percentage from 0 to 100% (size 1.5 cm × 2.0 cm). Set the resolution is 720 dpi, line number is 150 lpi, round dot, bitmap mode. Use Epson7600 to print inkjet proofs.

2.3 Comparison of Acquisition Methods About Color Block Information

PR-655 can directly measure the $L_1a_1b_1$ value of the color block, RF-5301PC measure the spectral curve of each color block. According to Eq. 1, the product of the spectral data with the standard observer's chrominance data is integrated, converting to XYZ value, and then converted to $L_2a_2b_2$ value according to Eq. 2. In Eq. 1, Φ(λ) is the spectral curve data measured by RF-5301PC, x(λ), y(λ), z(λ) are CIE standard colorimetric observer data. In Eq. 2, Xn, Yn, Zn are the three stimuli of the CIE standard illuminator irradiated on the complete diffuse scatterer, representing the color of the illumination light source. The standard Lab value is converted by the RGB value in photoshop. Then compare the color difference between $L_1a_1b_1$ ($L_2a_2b_2$) and standard Lab to compare the test precision.

$$\begin{aligned} X &= k\sum_{\lambda}\phi(\lambda)\bar{x}(\lambda)\Delta\lambda \\ Y &= k\sum_{\lambda}\phi(\lambda)\bar{y}(\lambda)\Delta\lambda \\ Z &= k\sum_{\lambda}\phi(\lambda)\bar{z}(\lambda)\Delta\lambda \end{aligned} \tag{1}$$

$$\begin{cases} L_2 = 116(Y/Y_N)^{\frac{1}{3}} - 16 \\ a_2 = 500[(X/X_N)^{\frac{1}{3}} - (Y/Y_N)^{\frac{1}{3}}] \\ b_2 = 200[(Y/Y_N)^{\frac{1}{3}} - (Z/Z_N)^{\frac{1}{3}}] \end{cases} \tag{2}$$

$$\begin{aligned} \Delta E_1 &= \sqrt{(L_1 - L)^2 + (a_1 - a)^2 + (b_1 - b)^2} \\ \Delta E_2 &= \sqrt{(L_2 - L)^2 + (a_2 - a)^2 + (b_2 - b)^2} \end{aligned} \tag{3}$$

2.4 The Comparison of Dot Trapping and Dot Coordinate

For the same color patch, dot trapping can achieve 100% output; dot coordinate can achieve only 33% output for each color. In order to compare the effect of them on

the luminous intensity of the ink, we compare the fluorescent intensity of 100% dot coordinate and 33% dot trapping. Because the two pieces of color output the same amount of ink.

3 Results and Discussion

3.1 The Comparison of Acquisition Methods About Color Block Information

First, we design different ladder color patch and print proof using Epson7600, as shown in Fig. 1. From left to right are R, G, B, RGB three-color superposition (W). Each of the color patches in Fig. 1 is collected using RF-5301PC and PR-655. And then calculate the color difference of RGB three-color superposition (W) through the comparison with the standard color block according to Sect. 2.4. The results are shown in Fig. 2.

As can be seen from Fig. 2, RF-5301PC has a smaller color difference for lower dot percent, while PR-655 has smaller color difference for higher dot percent. In other words, RF-5301PC applies to the color information collection of dark tone part, PR-655 applies to the color information collection of middle tone and

Fig. 1 Fluorescent inkjet ink print proofs (Color figure online)

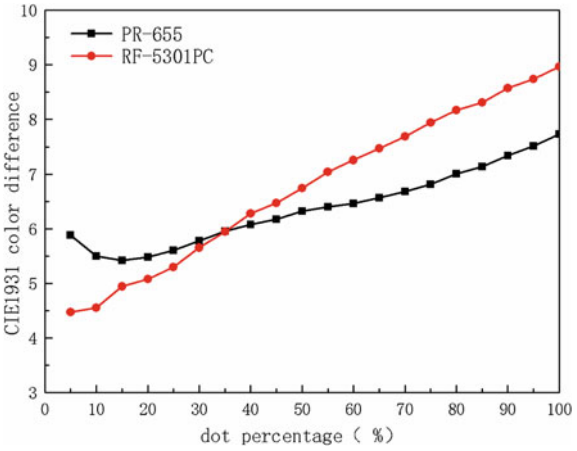

Fig. 2 Comparison of color difference between the two methods (Color figure online)

highlight part. From the overall consideration, for the collection of fluorescent ink color information, the test of PR-655 is more accurate.

3.2 The Comparison of Dot Trapping and Dot Coordinate

Dot trapping and dot coordinate are two different ways to generate color [5]. For ordinary color ink, the principle of dot trapping is the dot selectively absorbs the incident white light, and the color formed through the colored light emitted by the substrate [6]. The principle of dot coordinate is the dot selectively absorbs the incident white light, and the remaining shades were mixed by coloring [7]. For fluorescent ink, dot trapping and dot coordinate are the direct additive color shade. That is to say, if we use the dot trapping, light emitted from the lower layer of the ink must penetrate the upper layer of the ink to be reflected, the upper ink may affect the intensity of the lower ink excited. And dot coordinate can avoid this defect. In order to compare the effect of dot arrangement on the color characteristics of UV fluorescent inkjet ink, we developed a software which can achieved dot coordinate. And then compare the color reproduction abilities with dot trapping, as shown in Figs. 3 and 4.

It can be seen from Fig. 3, for the peak, the maximum emission wavelengths of RGB three-color fluorescent ink are 616, 524, 448 nm for dot trapping; the maximum emission wavelengths of RGB three-color fluorescent ink are 616, 524, 436 nm for dot coordinate. The blue ink has a slight blue shift for dot coordinate. For wave width, two curves are almost overlap. Therefore, the two kinds have little effect for color reproduction. From Fig. 4 we can see that for any dot percentage, the fluorescence intensity: G > B > R. The fluorescence intensity of the green ink is significantly increased with the increase of dot percentage, the discernible brightness level is wide and the range of reproduction is wide. The color reproduction

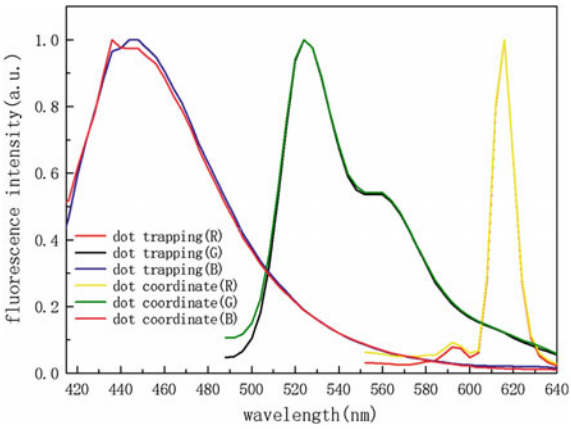

Fig. 3 Three—color fluorescence intensity of dot trapping and dot coordinate (Color figure online)

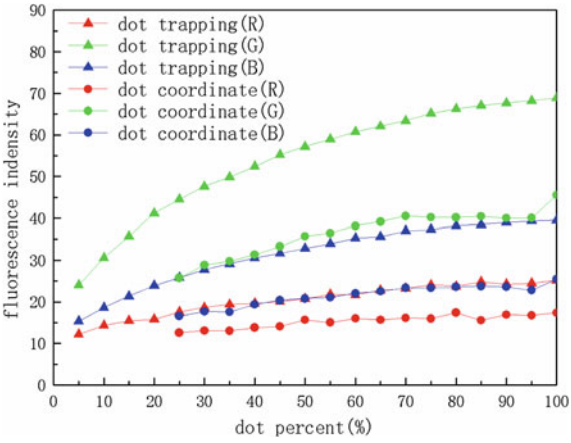

Fig. 4 The relationship between the dot percentage and the fluorescence intensity of dot trapping and dot coordinate (Color figure online)

ability of three-color fluorescent inkjet ink is significantly different. As can be seen from Fig. 4, the fluorescent intensity of 100% dot coordinate and 33% dot trapping is very close.

In contrast to the dot coordinate, the upper layer of ink will affect the luminous intensity of the underlying ink in dot trapping, but this has a great relationship with the thickness of the ink layer of the upper layer. As can be seen from the data in Fig. 4, since the ink layer for inkjet printing is thin, the dot trapping and dot coordinate have little difference with the same amount of ink output.

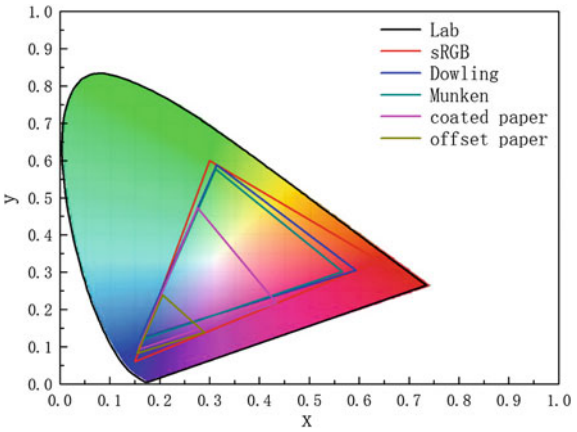

Fig. 5 The color gamut of different substrate (Color figure online)

3.3 The Comparison of Printing Effect for Different Substrates

The difference in paper is one of the important factors contributing to the color difference [8], In particular, the optical properties such as brightness and gloss of the paper have an important effect on color reproduction and color characterization profiles [9]. Therefore, it is of great importance to seek some paper performance parameters that match the fluorescent inkjet ink and to be able to predict the color reproduction capability of the prints [10]. In order to compare the influence of the paper performance parameters on the color reproduction range of the fluorescent inkjet ink, we choose two kinds of non-fluorescent paper (Dowling and Munken) and two kinds of paper containing fluorescent agents (coated paper and offset paper) for color gamut comparison. Select 100% R, G, and B blocks in Fig. 3, measure their x, y color coordinates, and plot the color gamut.

As can be seen from Fig. 5, the color gamut of different substrate: Dowling > Munken > coated paper > offset paper. The color gamut of Dowling and Munken is close to the color gamut of sRGB; the color gamut of the coated paper and the offset paper is much smaller than the color gamut of the two non-fluorescent paper. Therefore, the fluorescent agent has a great influence on the color reproduction of the ultraviolet fluorescent inkjet ink. As the Dowling with high gloss and the coated paper with smooth surface, we should choose substrate without fluorescent agent, high gloss, smooth surface for fluorescent ink color reproduction.

4 Conclusions

1. RF-5301PC applies to the color information collection of dark tone part, PR-655 applies to the color information collection of middle tone and highlight part. From the overall consideration, for the collection of fluorescent ink color information, the test of PR-655 is more accurate.
2. Different dot arrangement has a great impact on the color reproduction ability of UV fluorescent inkjet ink. In view of the luminous mechanism of fluorescent ink, three-color fluorescent inkjet ink will not affect each other with the method of dot coordinate. In contrast to the dot coordinate, the upper layer of ink will affect the luminous intensity of the underlying ink in dot trapping, but this has a great relationship with the thickness of the ink layer of the upper layer. Since the ink layer for inkjet printing is thin, the dot trapping and dot coordinate have little difference with the same amount of ink output.
3. The performance parameters of the paper have a significant effect on the color reproduction of the UV fluorescent inkjet ink. We should choose substrate without fluorescent agent, high gloss, smooth surface for fluorescent ink color reproduction.

Acknowledgements This work is supported by BIGC Project (Nos. 20190116002/043, 04190117001/019).

References

1. Hersch RD, Donzé P, Chosson S (2007) Color images visible under UV light. ACM Trans Graphi 26(3)
2. Li Z (2009) The common application of several kinds of anti fake ink in anti fake technology. Guang Dong Yin Shua 1:45–47
3. Dehai W, Ling J (2001) UV curable materials-theory and applications. The Science Publishing Company, Beijing, p 138
4. Qi C (2005) Application of fluorescent ink in screen printing. Screen Printing 8:18–21
5. Wang Q, Zhou X, Zhang L et al (2011) Research on differences of color reproduction based on dots distribution state. Packag Eng 7:89–111
6. Wyble DR, Berns RS (2000) A Critical review of spectral models applied to binary color printing. J Color Res Appl 25:14–19
7. Wyszecki G, Stiles WS (1982) Color science, 2nd edn. Wiley
8. Ying L (2010) Effect of paper surface characteristics on printing color reproduction. Packag Eng 7:25–28
9. Liu X, Liu Z (2007) Effect of paper performance on color reproduction and color management. Tianjin Papermaking 3:32–36
10. Sun Z (2009) Statistical analysis of the effect of paper performance on print color reproduction. Packag Eng 12:83–87

Extraction of Natural Pigment from Purple Potato in Preparation of Edible Ink

Guhong Liu, Qifeng Chen and Guangxue Chen

Abstract Natural pigment is safe and non-toxic, and the pigment in purple potatoes is bright in color, which is a good material to produce edible ink. This paper reported a green method of extracting the pigment of purple potatoes and produced edible ink with it. The optimum condition of extracting pigment was obtained by varying ethanol concentrations, feed liquid ratios, extraction times and temperatures. The obtained pigment was characterized by spectrophotometer. The result showed that the edible ink was in good color on paper, biscuits and bread and the light could make it fade in a short time.

Keywords Green printing · Purple potato · Natural pigment · Edible ink

1 Introduction

With the development of economy, environmental protection and health has aroused great concern around the world. Due to the solvents of traditional solvent-based inks usually comprised by alcohols, gasoline, xylene, toluene, kerosene, aromatic compounds, etc [1]. Therefore, it is inevitable that the traditional ink contained volatile organic compounds (VOC) which damaged human body, polluted the environment when used in drugs, food and other packaging printings [2]. Edible ink with non-toxic, bright colors, edible and other characteristics has become preferred choose in a food and pharmaceutical packaging.

As a special ink, edible ink not only has the same corresponding printability as ordinary ink, but edible. The connecting material is made up of general oil (such as soybean oil) and addictions. The carrier of pigment is sucrose or maltose, while distilled water as solvent [3]. Su et al. [4] prepared edible ink using distilled water, monascus red, sucrose, xanthan gum, soybean oil. However, as for current printing technology, edible ink is unpopular in printing industry [5]. Therefore, it is the

G. Liu · Q. Chen · G. Chen (✉)
South China University of Technology, Guangzhou, China
e-mail: chengx@scut.edu.cn

P. Zhao et al. (eds.), *Applied Sciences in Graphic Communication and Packaging*, Lecture Notes in Electrical Engineering 477,
https://doi.org/10.1007/978-981-10-7629-9_88

prime mission to choosing a material in better color for preparation of edible ink with lower cost.

Natural pigment is a kind of pigment which is directly extracted from the plants and microorganisms. Natural pigment is not only harmless to body and some pigments are benefit to health because of trace elements. There are lots of methods to obtain natural pigment. While, organic solvent extraction is the simplest one. This method used ethanol, methanol, acetone and other organic solvents to soak the plant. Then, the soaking solution was concentrated to extract the pigment.

In this study, the raw material for extraction is purple potato, which contains purple potato pigment belonging to anthocyanin, a type of natural pigment with bright color and able to be dissolved in water. Purple potato pigment is used to prepare edible ink generally [6, 7]. This research focuses on the optimum condition of extraction and measure the quality of the edible ink made from the pigment.

2 Experiments

2.1 Experimental Instruments and Materials

Purple potatoes and sucrose were purchased from food market. Citric acid, xanthan gum and anhydrous ethanol were provided by Zhongxuan Biochemical Co., Ltd (Zibo, China). Soybean oil were purchased from Bauhinia Ink Co., Ltd. Ultrasonic cleaning machine (SB-5200DTN) for cleaning purple potato surface stains was provided by Xinzhi Biotechnology Co., Ltd (Ningbo, China). Spectrophotometer (X-Rite 528) was purchased from Jiaen Printing Equipment Co., Ltd (Shanghai, China).

2.2 Methods

Non-destructive, fresh purple potato was crushed with a juicer. The slurry was immersed in anhydrous ethanol at 50 °C for a period of time. Then ultrasonic oscillation was started in a certain temperature. After centrifugation, a portion of the filter was diluted 50 times with distilled water and placed in a cuvette to measure the absorbance with a two-beam UV spectrophotometer at 282 nm. The other part was adjusted to pH 3.0 with citric acid to gain pigment extract, and then placed in 4 °C refrigerator. The light stability experimental was carried out. 10 ml pigment extract and 20 g sucrose were added in a 100 ml beaker and stirred in a certain temperature until it was completely dissolved. After xanthan gum dissolved fully in it, 20 g soybean oil slowly added it to make fully emulsified. Finally, the configuration of the ink set aside for 60 min, the preparation was completed.

3 Results and Discussion

3.1 *Effects of Different Reaction Conditions on Absorbance of Pigment Extraction*

Add the solution by the feed liquid ratios of 1:4 (g/ml) separately into those 100 ml beakers with pH 2, 30, 50, 60, 80, 90% of ethanol solvent. Ultrasonic dispersion under 50 °C. Effect of concentration of ethanol solvent on absorbance of purple potato extract measured by dual beam UV photometer is shown as Fig. 1a. It is shown by Fig. 1a that with the increase of ethanol concentration from 30 to 80%, the absorbance of solvent is increasing as well, so the highest absorbance of pigment extract appeared when the concentration of ethanol concentration was 80%. Therefore, the best ethanol concentration is 80%.

Add the solution by the feed liquid ratio of 1:2, 1:4, 1:6, 1:8, 1:10 (g/ml) separately into those 100 ml beakers with pH 2, 80% ethanol solvent. Ultrasonic dispersion was carried out under 50 °C for 1 h. Effect of concentration of extraction solution on absorbance of purple potato extract measured by dual beam UV photometer is shown as Fig. 1b. It is shown by Fig. 1b that with the increase of the feed liquid ratio, the absorbance of obtained pigment extraction was decreased. Therefore, the best feed liquid ratio is 1:2.

Add the solution by the ratio of 1:2 (g/ml) separately into those 100 ml beakers with pH 2, 80% of ethanol extraction solvent. Ultrasonic dispersion under 50 °C for 0.5, 1, 1.5, 2, 2.5 h respectively. Effect of extraction time on absorbance of pigment extraction measured by dual beam UV photometer is shown as Fig. 1c. It is showed by Fig. 1c that the absorbance is the highest when the extraction time is 2 h.

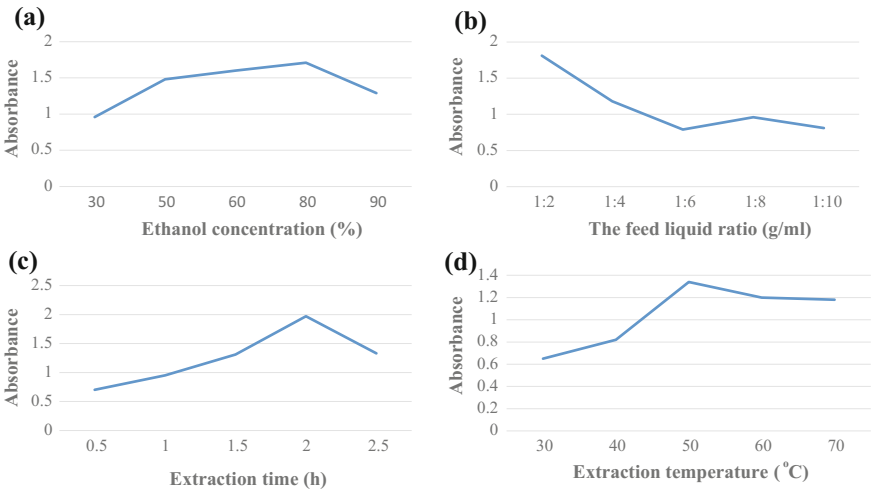

Fig. 1 Effects of different reaction conditions on absorbance of pigment extraction. **a** Ethanol concentrations. **b** Feed liquid ratios. **c** Extraction times. **d** Extraction temperatures

Add the solution by the ratio of 1:2 (g/ml) separately into those 100 ml beakers with pH 2, 80% of ethanol extraction solvent. Ultrasonic dispersion worked for 2 h under 30, 40, 50, 60, 70 °C separately. Effect of extraction temperature on absorbance of pigment extraction is shown as Fig. 1d. It is showed by Fig. 1d that the absorbance is the highest when the temperature was 50 °C. Therefore, the best temperature of extraction was 50 °C. It is known from the results above that the efficiency of extraction is the highest when the ethanol concentration was 80%, the feed liquid ratio was 1:2, the extraction time was 2 h, and the extraction temperature was 50 °C.

3.2 *Color Effect of Ink on Different Printing Substrates*

It is shown by Fig. 2 that the effect of color on biscuits and bread was good and the color was basically not changed after drying

As it can be seen from Table 1, when the obtained edible ink was printed in 80 g double offset paper by screen printing, the color effect on the paper is good and the color differences were all small met the requirements of fine printing ($\Delta E < 2.0$). And as time goes by, the color effect is more stable.

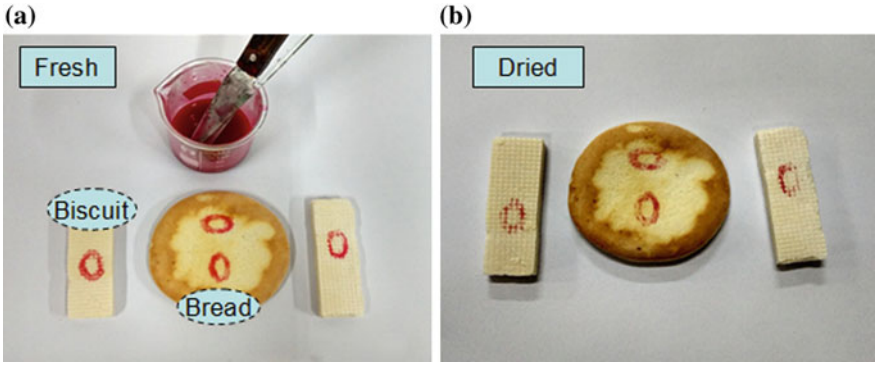

Fig. 2 The color effect of prints when printed biscuits and bread. **a** before drying. **b** dried (Color figure online)

Table 1 The color difference (ΔE) of ink when printed in 80 g double offset paper under different illumination time

Lighting/h	0	0.5	1	1.5
L	73.47	72.25	73.21	72.58
A	2.35	2.24	2.23	2.18
B	1.75	1.76	1.83	1.72
ΔE	/	1.225	0.297	0.243

4 Conclusions

This research mainly focused on the extraction of purple potato pigment, the preparation of edible ink and the test of the quality of ink. In this study, the purple pigment extract has high absorbance and good color rendering. The optimum conditions for extracting purple potato pigment was found when the ethanol concentration was 80% with pH 2, the extraction time was 2 h, the optimum feed liquid ratio was 1:2, and the optimum extraction temperature was 50 °C. Moreover, the obtained edible ink has excellent color effect in different substrates.

Acknowledgements This paper was supported by the Key Laboratory of Pulp and Paper Engineering Project (2016C01, 2016C02), and the Science and Technology Planning Project in Guangzhou (2016070220045).

References

1. Li G (2011) Analysis on the development of edible ink. Sci Technol Winds 13:209
2. Zhao X, Zhao Y (2009) Preparation and analysis of edible ink and its performance. Packag Eng 30(6):32–33, 62
3. Fang Y, Zhu K, Yao R et al (2013) Research and application of edible ink in food packaging printing. Food Ferment Technol 49(1):85–90
4. Su Y, Zhao X (2009) Preparation of edible ink and its rheological study. Tianjin: Tianjin Univ Sci Technol
5. Cheng J (2013) Research status and trend of edible ink printing. Printing Qual Stand (3):11–13
6 Zhu M, Yao Y, Han X et al (2009) Study on extraction and stability of purple sweet potato pigment. Anhui Agric Sci (36):7885–7887 + 7913
7 Wang S, Deng Z, Cao S (2004) Research progress of purple potato pigment. Cereals Oils Sci Technol 02:45–46

The Preparation and Characterization of Water-Based Pigment Paste

Xitong Mao, Xiulan Xin, Baocai Xu, Bin Li, Shukai Huang and Peng Wang

Abstract The different water-based pigment paste was prepared using copper phthalocyanine blue pigment and dispersion resin, the influences of different pre-dispersion speed on dispersion of pigment paste were also investigated. And the characterization of the different pastes was investigated by rheology behavior, dynamic light scattering (DLS) and scanning electron microscopy (SEM) respectively. The results showed that the results measured by dynamic light scattering the best dispersion of the pigment paste was made when the pre-dispersion speed at 1000 rpm. But the results evaluated by rheology behavior showed that the best dispersion was when the pre-dispersion speed at 1500 rpm. Then the additional technique such as scanning electron microscopy was employed for proofing of pigment pastes. The SEM images of different samples are compared, and it is found that when the pre-dispersion speed at 1500 rpm, the pigment paste samples with good dispersion. Based on the results from different assessment methods, the pigment paste with best dispersion were prepared when pre-dispersion speed at 1500 rpm.

Keywords Water-based pigment paste · Dispersion resin · Dispersion Pre-dispersion speed

1 Introduction

Statutory regulations have forced paint users to make increasing use of more environment-friendly coating systems, which is why water-based coatings are particularly attractive and important. To achieve the optimum visual and economic benefits of a pigment, the dispersion process is critical; the degree to which the pigment particles are dispersed is indeed a major factor in the quality and stability

X. Mao · X. Xin (✉) · B. Xu · B. Li · S. Huang · P. Wang
School of Food and Chemical Engineering, Beijing Technology and Business University, Beijing, China
e-mail: xinxl2007@126.com

P. Zhao et al. (eds.), *Applied Sciences in Graphic Communication and Packaging*, Lecture Notes in Electrical Engineering 477,
https://doi.org/10.1007/978-981-10-7629-9_89

of the finished paint products [1]. For the pigment particle distribution has an effect on the rheology and how stable a system against pigment settling. And also the pigment particle distribution has an effect on the color strength, transparency and gloss in the final film [2].

Many researchers have studied the dispersion of color paste with different methods, such as transmission electron microscopy (TEM), scanning electron microscopy (SEM), atomic force microscopy (AFM), and ultraviolet-visible (UV-vis) spectroscopy [3].

In this paper, in order to study the some different command methods to assess the pigment dispersion within a system, the water-based pigment paste were prepared with five different pre-dispersion speed. The flow behavior, dynamic light scattering (DLS) and scanning electron microscopy (SEM) measurements were used to assess the effect of the dispersant concentration on the pigment particle dispersion.

2 Experimental

2.1 Materials

The dispersion resin SR 639 used in this paper were supplied by DIRANSA SAN LUIS SA (Argentina), the dispersion resin should be aminated before further used. The organic pigment (commercial C.I. name: Pigment Phthalocyanine Blue PB 15:3) was obtained from Meilida Pigment Industry CO. Ltd, its chemical structure and SEM image were shown in Fig. 1. The defoamer was supplied by the BYK, and the ammonia was courtesy of Chinese Medicine Group Chemical Reagent Co. Ltd (AR).

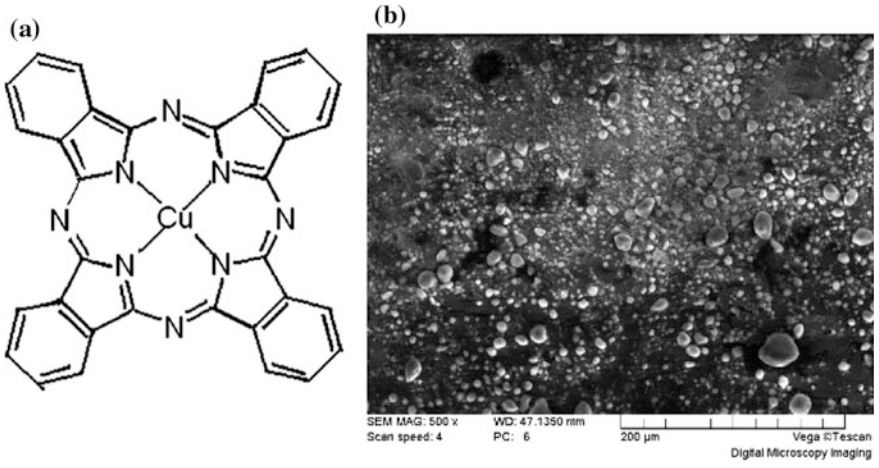

Fig. 1 Chemical structure: (**a**) and particle size (**b**) of pigment phthalocyanine blue (PB 15:3)

2.2 Amination of Dispersion Resins

The amination reaction was carried out between the dispersion resin and amine agents before experiments in this paper. First, the distilled water was prepared in the in a three-necked flask equipped with a reflux condenser, a mechanical stirrer and heated with the water bath. Then, the dispersion resin and ammonia were added into the flask slowly at 40 °C. Finally, the mixed system were heated to 60 °C for 120 min. Thus, the liquid resin was obtained. And the liquid resin needed to place more than 24 h before further using.

2.3 Preparation of the Pigment Paste

The pigment paste was made by disperser machines. Into a clean breaker, an exact amount of distilled water, and defoamer were added and stirred for 20 min. Then the different pre-dispersion speeds (500, 700, 1000, 1500 and 2000 rpm, respectively) were made after pigment phthalocyanine blue was added into the clean breaker for 30 min. Finally, the bead was added into the system before the pigment paste was ground thoroughly for 150 min. The pigment pastes needed to stable 24 h before further assessments.

2.4 Characterization

The rheological behavior of the pigment pastes were investigated using a Haake Mars Rheometer (Thermo Fisher Scientific, USA) with a plate to plate geometry (gap 0.38 mm) with a controlled applied shear rate increasing from 0.01 to 100 s^{-1} and the temperature was kept at 25 °C. The degree of fineness of pigment pastes was measured by Hegman Gauge as JJG 905-2010. The particle distribution of pigment paste was estimated from SEM micrograph. The average particle size of pigment paste was measured by Dynamic Light Scattering (DLS) using a Zetasizer Nano Series.

3 Results and Discussion

3.1 Rheology Behavior of Different Pre-dispersion Speed

The viscosity vs shear rate plots for the pigment pastes of different pre-dispersion speed are given in Fig. 2. The pre-dispersion speed has a noticeable effect on the rheological behavior curve. When the speed at 500 and 700 rpm, the pigment pastes

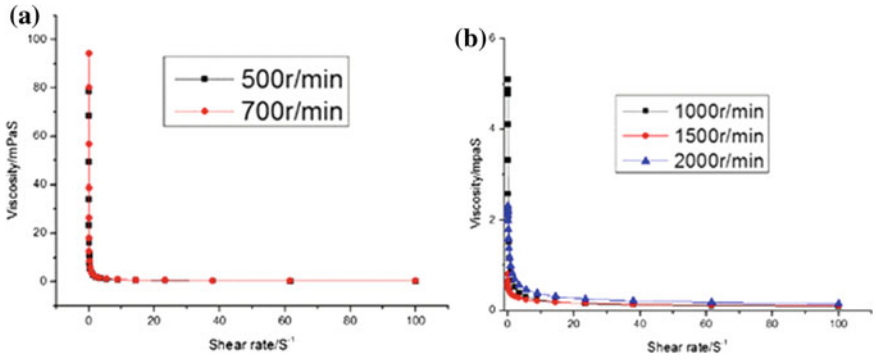

Fig. 2 Rheological behavior curve of investigated pigment pastes

exhibited shear-thinning flow behavior at very low shear ratio, but at higher shear rates (higher than 10 s^{-1}) this can be considered as a Newtonian flow behavior. In the contrary, the flow behavior of pigment pastes exhibited ideal viscous (Newtonian) flow behavior when the pre-dispersion speed at 1000, 1500 and 2000 rpm. According to the literature which reported before, the viscosity of a coating colloidal dispersion strongly depends on the interactions between the particles; therefore the lower the viscosity is, the lower are the interactions, and the better is the given pre-dispersion speed [4, 5]. Figure 2 shows that the viscosity of the pigment paste in different pre-dispersion speed from low to high is 1500, 2000, 1000, 500 and 700 rpm. Therefore, the dispersion of the pigment paste should be in same order with the viscosity.

3.2 Particle Size of Different Pre-dispersion Speed

The particle sizes volume distribution of pigment pastes are listed in Fig. 3. As shown in the Fig. 3, the size first decrease and then increase along with the increase of pre-dispersion speed. The results demonstrate that the particle size distribution of the pigment pastes at 700 and 1500 rpm are double-peak distribution, while it is unimodal distribution when the pre-dispersion speed at 500, 1000 and 2000 rpm. In addition, it indicated that the best particle size distribution of the pigment paste is when the pre-dispersion speed at 1000 rpm, then its order from small to large is 700, 1500, 500 and 2000 rpm.

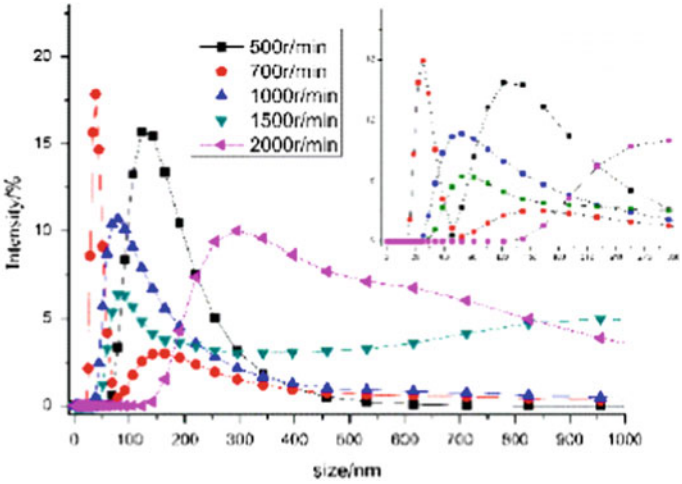

Fig. 3 The effect of pre-dispersion speed on particle size

3.3 SEM Images of Different Pre-dispersion Speed

Then the quality of dispersion was further confirmed using SEM. In Fig. 4, the SEM images of different samples are compared. As shown, these can be clearly distinguished that the particles of pigment showing the smallest diameter when the pre-dispersion speed at 1500 rpm. The larger particle size measured in the sample when the pre-dispersion speed at 700 rpm, may be the reason caused by the fact that it is double-peak distribution in particle size measured by dynamic light scattering. The presence of the agglomerates and aggregates can be seen in the micrographs when the pre-dispersion speed at 500 rpm.

4 Conclusions

Five different pigment pastes were prepared with different pre-dispersion speed. And three methods were measured to assess the dispersion of the different samples.

(1) The results showed that the good dispersion of the pigment paste was made when the pre-dispersion speed at 1500 rpm.
(2) The SEM image method that has been described gives quantified information concerning the particle size distribution and the degree of the pigment dispersion in the system. And this result is in close relation to the result from dynamic light scattering.

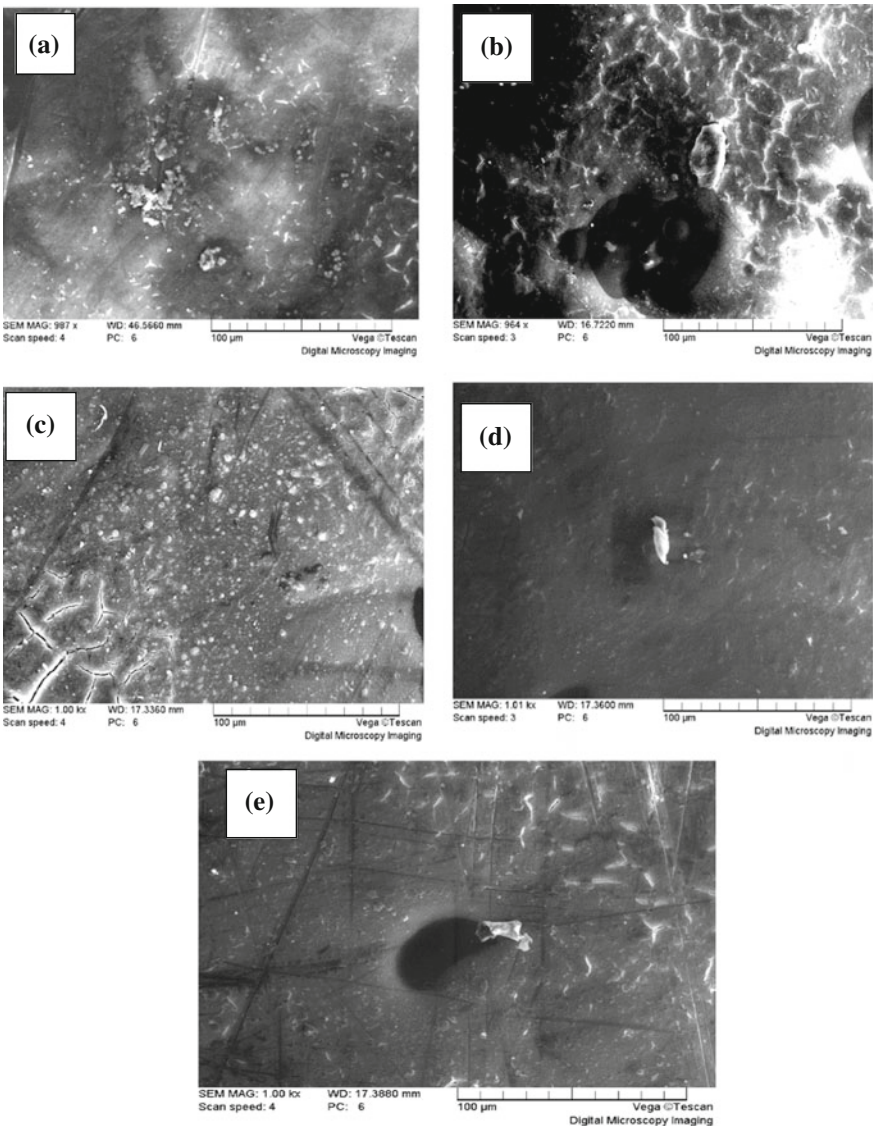

Fig. 4 SEM images of pigment paste of different pre-dispersion speed samples. **a** 500 rpm. **b** 700 rpm. **c** 1000 rpm. **d** 1500 rpm. **e** 2000 rpm

Acknowledgements This work is supported by the National Nature Science and Foundation of China (21376008) and the Young Teachers' Scientific Research Foundation of Beijing Technology & Business University (QNJJ2015-13)

References

1. Saeed F, Gayle EM, Daniel F, Peter S (2010) Stabilisation of titania pigment particles with anionic polymeric dispersants. Powder Technol 202:143–150
2. Antti M, Alexey Z, Sirkka-L et al (2012) Optimization of the grinding parameters in the production of the colorant paste. Powder Technol 217:216–222
3. Van S, Velamakanni B, Adkins R (2001) Comparison of methods to assess pigment dispersion. J Coat Technol 73:61–70
4. Moloney V, Parris D, Edirisinghe MJ (1995) Rheology of zirconia suspensions in a nonpolar organic medium. J Am Chem Soc 783:225–3232
5. Marco P, Llorens J (2009) Surface charge and rheological properties of raw porcelain gres suspension with acrylic copolymers bearing carboxylic groups. J Eur Ceram Soc 29:559–564

The Effect of Grinding Conditions on Disperse Particle Size of Ultrafine Organic Pigment Water-Based Dispersion System

Qichao Hou, Mengmeng Liang, Zhenguo Wang, Ruping Liu and Luhai Li

Abstract In recent years, with the gradual emphasis on environmental protection, more and more extensive attention has been paid to the water-based ink in the market. The dispersion of organic pigments has been a key part of the research of water-based pigment inks. In the use of organic pigments, the pigment must be effectively dispersed, so that it has a fine and uniform particle size distribution and finally forming a stable dispersion system. The dispersion effect of the pigment is determined by many factors. In this paper, the effect of grinding speed, grinding time and the mass ratio between grinding medium and ink slurry on the dispensability of organic pigment yellow 100 was studied mainly from the viewpoint of the grinding process conditions. It is found that the particle size of the pigment decreases first and then increases with the increase of the grinding speed. When the rotational speed is 3100–3200 r/min, the average particle size reaches the minimum of 278 nm. Besides, the particle size of the pigment decreases first and then hold steady with the increase of the grinding time. When the grinding time is 1 h, the average particle size is the smallest. Furthermore, the particle size of the pigment decreases first and then increases with the increase of the mass ratio between grinding medium and base ink. When the mass ratio is 2, the particle size is the smallest and the dispersion effect is the best.

Keywords Dispersion · Water-based ink · Grinding

1 Introduction

Pigments are usually dispersed in the system with the form of particles [1–3]. Generally, the pigment with particle size less than 1 um is called ultrafine pigment [4]. Compared with ordinary pigments, ultrafine pigments possess excellent

Q. Hou · M. Liang · Z. Wang · R. Liu · L. Li (✉)
Beijing Engineering Research Center of Printed Electronics, Beijing Institute of Graphic Communication, Beijing, China
e-mail: liluhai@bigc.edu.cn

P. Zhao et al. (eds.), *Applied Sciences in Graphic Communication and Packaging*, Lecture Notes in Electrical Engineering 477,
https://doi.org/10.1007/978-981-10-7629-9_90

properties, such as greater surface area, higher color strength, more vivid colors and better gloss. In order to give full play to the advantages of various aspects of the pigment, it is necessary to disperse the pigment particles in the medium with a fine, uniform and stable state. It requires that the pigment can be sufficiently refined to reach a stable dispersion effect via the physical or chemical method before being used. Besides, ultrafine pulverization method is usually used to prepare ultrafine organic pigments in the production process. This method mainly used the mechanical force to grind and cut the organic pigment particles. So that the pigment particles can be fully refined and distributed in the media uniformly, and finally forming a non-flocculating, non-precipitated stable dispersion system [5–7]. On the other hand, ultrafine pulverization is not only a simple physical pulverization process, sometimes accompanied by chemical changes. Therefore, the factor that affect the efficiency of crushing is quite complex. For example, the initial velocity of the particles, the properties and content of the various additives and the various parameters of the crushing machinery will affect the final crushing effect.

In this paper, we respectively use the zirconia beads and high-speed sand mill as the grinding medium and grinding equipment, investigate the effect of grinding time, rotational speed and grinding media ratio on the particle size distribution of ultrafine organic pigment yellow 100. The optimum dispersion process for this pigment was found finally in our experiment.

2 Experimental

2.1 Preparation of Ultrafine Organic Pigment Yellow 100 Waterborne Dispersion System

Firstly, the dispersant (Croda, Hypermer KD24, UK) was dissolved and dispersed to pigment yellow 100 with a certain ratio on an electric mixer (IKA, RW20 digital, Germany) for 30 min. Secondly, it was added with a quantitative defoaming agents and then grinding in a sand mill (Qingdao Senxin, GJ-3S, China). Thirdly, the water-based dispersion system after grinding was added with 0.5 mol/L NaOH solution and processed on an electromagnetic stirrer for 30 min. Next, the pH of the dispersion system is adjusted to about 9. Finally, the ultrafine organic pigment water-based dispersion system formulation shown in Table 1.

Table 1 Formula of ultrafine organic pigment yellow 100 waterborne dispersion system

Component	Pigment	Deionized water	Dispersant	Defoamer	NaOH
content	5%	92%	0.50%	0.50%	2%

2.2 *Effect of Grinding Speed on Pigment Dispersion*

In the paint grinding process, the grinding speed has a very large impact on the grinding effect of the pigment and the particle size of the finished product. When the diameter of the zirconium beads is 0.3–0.4 mm, the grinding time is 1 h, the mass ratio between the zirconium bead and base ink is 2, the relation between the dispensability of the pigment and grinding speed was plotted in Fig. 1.

It can be seen from Fig. 1 that the particle size of the pigment decreases first and then increases with the increase of the grinding speed. When the grinding speed is 3100–3200 r/min, the particle size of the pigment is the smallest. The dispersion of the pigment is the process of pulverizing the aggregate and the agglomerates into native particles [8]. Where, the aggregates are particles composed of multiple crystal units, with a strong van der Waals force between the particles. Besides, the agglomerates are the combination of aggregates and native particles. Pigment aggregates were broken and dispersed into native particles only in the case of being gained enough energy. The higher the grinding speed is, the greater the shear force generated, the more energy the pigment particles gained in the unit time. Therefore, when the grinding speed is lower than 3000 r/min, the particle size gradually decreases with the increase of the rotational speed. However, when the pigment particle size gradually decreases, the particle surface attraction (polarity, hydrogen bond) gradually increases, so that the particles gather together [9]. Furthermore, when the grinding speed is further increased, the shearing force is so large that the dispersant coated on the surface of the pigment is peeled off. It makes the dispersion effect of the pigment particles to become worse, and thus the particle size of the

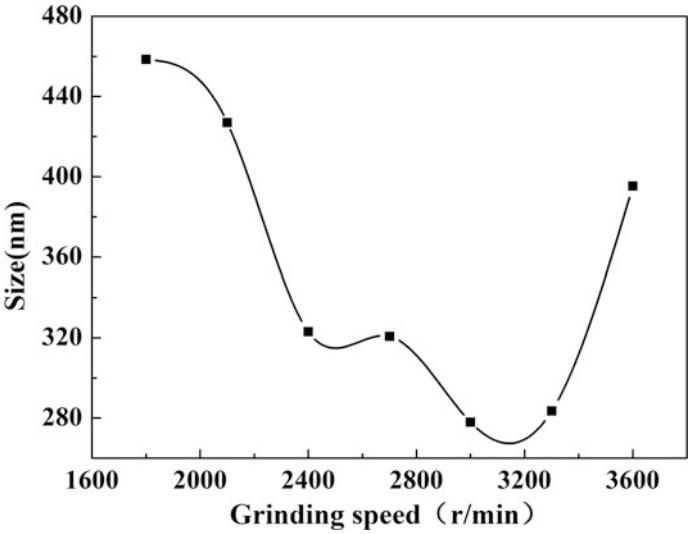

Fig. 1 Effect of grinding speed on particle size of ultrafine organic pigments dispersion

Table 2 Effect of grinding time on particle size of ultrafine organic pigments dispersion

Grinding time (min)	Size (nm)
30	417.5
60	278
90	289
120	294
150	283
180	289

pigment becomes larger. Therefore, when the grinding speed is higher than 3100 r/min, the particle size gradually increases with the increase of the rotational speed.

2.3 *Effect of Grinding Time on Pigment Dispersion*

When the grinding speed is 3100–3200 r/min, the diameter of zirconium beads are 0.3–0.4 mm and the mass ratio between the zirconium bead and base ink is 2, the relation between the dispersibility of the pigment and grinding time was plotted in Table 2.

We can see from Table 2 that the particle size of the pigment decreases gradually with the increase of the grinding time. When the grinding time is about 60 min and the particle size reaches the minim. On the other hand, the particle size is almost no longer changed after the grinding time is larger than 60 min. The dispersion and aggregation of the pigment is a dynamic process, in which, the energy obtained by the pigment increased with the increase of the grinding time. It makes the pigment particles to be dispersed, and thus the particle size is gradually reduced. However, the decrease of the particle size of the pigment leads to the increase of the surface area, the surface energy, the attracting of the pigment particles under the action of van der Waals force, and the tendency of the particles to accumulate automatically. When the effect of the dispersion and aggregation of the pigment tends to be balance, the particle size of the pigment remains substantially unchanged. The table shows that when the particle size is about 280 nm after grinding for 60 min, the dispersion and aggregation are balanced.

2.4 *Effect of Grinding Media Ratio on Pigment Dispersion*

The mass ratio between the grinding medium and base ink has a direct effect on the grinding efficiency. When the diameter of zirconium beads are 0.3–0.4 mm, the grinding speed is 3100–3200 r/min, and the grinding time is 1 h, the relation between the dispersibility of the pigment and the mass ratio between the grinding medium and base ink was plotted in Fig. 2.

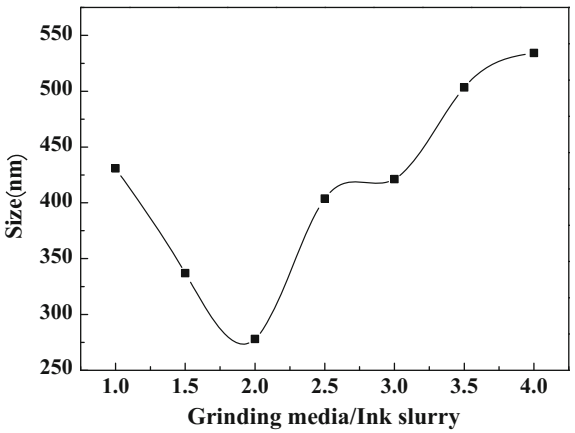

Fig. 2 Effect of grinding media/ink slurry on particle size of ultrafine organic pigments dispersion

Figure 2 shows that the particle size of the pigment decreases first and then increases as the mass ratio between the grinding medium and ink slurry increases, and the pigment particle size is the smallest when the mass ratio between the grinding medium and ink slurry is 2. This is because the greater the mass ratio is, the more the amount of grinding media have, the greater the contact frequency between the grinding media obtained, the greater the shear force generated, the more energy the pigment particles gained in the unit time, the smaller the particle size is. However, when the mass ratio between the grinding medium and ink slurry exceeds a certain limit, the phenomenon of "bead grinding bead" occurs, it makes the grinding efficiency to be lowered. Therefore, when the mass ratio between the grinding medium and ink slurry is 2, the particle size of pigment is the smallest and the ratio is most suitable.

3 Results and Discussion

The dispersion effect of the pigment is determined by many factors. In this paper, the effect of grinding speed, grinding time and the mass ratio between grinding medium and ink slurry on the dispersibility of organic pigment yellow 100 was studied. Firstly, we demonstrate that the particle size of the pigment decreases first and then increases with the increase of the grinding speed. When the rotational speed is 3100–3200 r/min, the particle size reaches the minimum of 278 nm. Then, the particle size of the pigment decreases first and then holds steady with the increase of the grinding time was also demonstrated. The minimum particle size occurs in the case of the grinding time reaching 1 h. Furthermore, we demonstrate that the particle size of the pigment decreases first and then increases with the increase of the mass ratio between grinding medium and ink slurry. When the mass ratio is 2, the particle size is the smallest and the dispersion effect is the best.

Acknowledgements This work was supported by the National Natural Science Foundation of China (61501039), the Beijing Natural Science Foundation (2162017), the Beijing Research Grant (No.Z15110000915071), the support of Beijing Municipal Education Commission (No. SQKM201710015005), the Initial funding for the Doctoral Program of BIGC (27170116005/040), and the Elite Program of BIGC (04190117004/010). The Collaborative Innovation Center 04190117029/002, the Discipline Construction 04190117013, the Discipline Construction of Printed Electronic Technology and Engineering Advantage 21090117001, and financial support for Innovative Teams of Printed Electronic Materials and Technologies.

References

1. Chen H, Liu L, Li G, Jiang J (1998) Application of pigment dispersion and hyperdispersant. Printing Dyeing 24(8):50–53
2. Hays BG (1984) Amer Ink Maker 62(6):28
3. Athey RD (1984) Mod Paint Coat 74(1):31
4. Shen Z, Zhao Z, Wang G (2004) Colloid and surface chemistry. Chemical Industry Press, 3rd edn. Beijing, pp 24–25
5. Wang L, Liang X, Liu Z, Zhang Y (1997) Dispersion of organic pigments in waterborne coatings. Dyestuff Ind 34(5):1–8
6. Wicks JR (2001) Pigment Dispersion. J Coat Technol 21(9):145–153
7. Daescu C (1998) Dispersibility of organic pigments. Dyes Pigm 38(1–3):173–180
8. Ren J, Shen J, Lu S (2003) Particle dispersion science and technology. Chemical Industry Press, Beijing, pp 144–166
9. Chun Z, Zhen M (2014) Organic pigment technology. China Petrochemical Press, Beijing, pp 319–320

Research of Wax Additives in the Water-Based Ink for Flexographic Printing

Yun Ouyang, Weiguang Feng, Zhiyong Sun, Xiaoli Liu, Shuangyang Li, Pengfei Zhao, Wei Lv, Xue Gao and Jingjing Zhang

Abstract Effect of three types of wax additives in the water-based ink is discussed, which are wax emulsion, micro-wax dispersions and wax dispersions. Softening point and particle size of wax are mainly studied on the ink's performances, such as gloss, friction resistance and rub resistance. The result shows that ink added WE3 which is micro-wax dispersions has good performance, and has best performance on the BOPP film while added 3 wt%.

Keywords Wax additives · Water-based ink for flexographic printing Gloss · Friction resistance · Rub resistance

1 Introduction

In order to meet the requirements of high-speed printing of CI flexo press and rubbing requirements of soft packaging products, water-based ink should have excellent performances in resistance of friction, rubbing etc. Besides choosing the appropriate water-based resin, using rational wax additives is one of the key factors [1].

Y. Ouyang · Z. Sun (✉) · X. Liu · P. Zhao · X. Gao
Key Laboratory of Printing Environmental Protection Technology, Beijing Key Laboratory of Packaging and Printing New Technology, China Academy of Printing Technology, Beijing, China
e-mail: Sunzhiyong@keyin.cn

W. Feng · J. Zhang
Xi'an Space Engine Factory, Xi'an Aerospace-Huayang Mechanical & Electrical Equipment Co., LTD, Xi'an, China

S. Li
School of Food and Chemical Engineering, Beijing Technology and Business University, Beijing, China

W. Lv
Shenzhen Jinjia Group Co., Ltd., Shenzhen, China

P. Zhao et al. (eds.), *Applied Sciences in Graphic Communication and Packaging*, Lecture Notes in Electrical Engineering 477,
https://doi.org/10.1007/978-981-10-7629-9_91

This paper mainly studies how different kinds of wax additives used in water-based ink for flexographic printing effect the performance of print.

2 Experiments

2.1 Raw Materials

Pigment: cyan color paste C3.

Resin: acrylic film-forming resins R1 and R2, assisted resin R3 and R4.

Additives: wetting agent W1, defoamer F2, wax emulsions WE1, WE2, WE3, WE4, WE5 and WE6.

Printing substrate: BOPP film.

The reference formula is shown in Table 1.

2.2 Test Methods

2.2.1 Friction Resistance Test

According to the national standard GB/T17497-2012 Flexible printing packaging products (Plastic and metal foil), use MCJ-01A to test.

Friction resistance = $D/D_0 \times 100\%$

D_0—average density value before friction;

D—average density value after friction.

2.2.2 Rub Resistance Test

Clamp the test print using thumb and index finger, and knead 10 times to the opposite direction without stretching the print. The test is distinguished five levels. "5" is best that ink layer without any damage, and "1" is that layer is completely destroyed.

Table 1 The reference formula of table printing water-based ink

Raw materials	Manufacturers	Amount (wt%)
Water-based resin	Import	45.45–48.3
Color paste	Domestic	45.45–48.3
H_2O	Made in laboratory	2–5
Wetting agent	TEGO	0.1–0.3
pH modifier	Domestic	0.1–0.3
Defoamer	TEGO	0.2–0.5
Wax	Domestic/import	1–3

2.2.3 Water Resistance Test

Put the print in the water 40 h, and then test the decoloration, scratch resistance of the print. Assessment method is as rub resistance test.

3 Results and Discussion

3.1 Preliminary Test of Water-Based Wax Additives

According to different particle size, emulsified wax is classified wax emulsion, micro-wax dispersions and wax dispersions. Select six water-based wax additions which are all polyethylene wax to do experiments. It is mainly studied effects of different wax additives with the same content on the performances of ink, such as adhesion, friction resistance, rub resistance, water resistance and gloss. Basic performances index of the six wax additives are shown in Table 2, and their effect on the ink performances is shown in Table 3.

Integrated the data of Table 2, we can conclude as follows:

(1) Wax dispersions: inks adding WE1 and WE2 are improved the resistance of friction and rub of the coating, but they have a great influence on the gloss of the ink, which may be related to the large particle size of the waxes.
(2) Micro-wax dispersions: rub, friction and water resistance of the ink is improved significantly.
(3) Wax emulsion: WE5 and WE6 have high melting point, but their particle size is so small that their ability to resist the friction is relatively weak, that can't meet the requirements of printing.

Integrated above data, adding appropriate wax dispersion can improve friction resistance of the ink greatly. Because of its irregular particles and wide particle size distribution, wax particles form a heterogeneous and microscopically uneven surface on the ink film. The light waves produce a strong scattering effect, and reduces gloss of ink [2], which can be reduced that affects print quality. Due to particles of

Table 2 Basic performance index of water-based wax additives

Type	Company	No.	Particle size (μm)	Melting point (°C)	Solid content (%)
Wax dispersions	BASF	WE1	4	132	40
	Yijiu	WE2	6–8	120–125	40 ± 1
Micro-wax dispersions	Unkel	WE3	1.0–1.4	128	50 ± 1
	Yijiu	WE4	0.5–1	120–125	40 ± 1
Wax emulsion	Yijiu	WE5	≤0.1	137	42 ± 1
	Unkel	WE6	≤0.1	125	42 ± 1

Table 3 Wax additives (3 wt%) on performances of ink

No.	Adhesion	Friction resistance (%)	Rub resistance	Gloss (%)	Water resistance
No wax	5	0	2	76.47	1
WE1	5	97.6	5	71.77	5
WE2	4	97.9	5	65.8	5
WE3	5	97.7	5	82.2	5
WE4	3	90.58	5	79.0	3
WE5	5	42.3	2	82.3	2
WE6	4	65.23	2	80.8	2

Notes While adhesion/water resistance is 5, it indicates the best; while 1, it indicates the worst

micro-wax dispersion has spherical structure, they have little effect on the gloss of print, and it can improve friction and rub resistance of the ink if adding appropriate dosage. Particles of wax emulsion are sphere that they could not reduce the gloss of the ink, but because of their small size, it has little effect on improving friction resistance.

3.2 Effect of Wax Additives on Ink Performances

Because of speciality of plastic soft package such as food and hygiene products, besides high requirements of adhesion, leveling and gloss, there are high requirements for friction resistance and rubbing resistance. Adding appropriate wax additive into the ink can improve these performances. According to the influence of wax additives on the ink adhesion and gloss of Sect. 3.1, select WE1, WE3 and WE5 which have better performances in the ink to do gradient experiments. This chapter is mainly studied the influence of wax on friction resistance, rub resistance and gloss of the ink.

3.2.1 Effect of Different Wax Additives on the Friction and Rub Resistance

Integrated Table 4 and Fig. 1, after adding WE1, WE3 and WE5, friction and rub resistance are improved to different degree.

(1) While WE1 is added 1 wt%, the ink has significant improvement in friction resistance, and while added 2 wt%, the ink has the best performances of friction and rubbing resistance. It is chiefly because large particles in the WE1 play a vital role in the ability of exterior force resistance that can destroy the ink film. And these large wax particles can prevent further extension and deterioration of scratches which should protect the coating.

Table 4 Effect of wax additives on the friction and rub resistance

WAX	Performances/amount (wt%)	0	1	2	3	4	5
WE1	Friction resistance	30.1	80.2	97.4	97.6	97.2	97.3
	Rub resistance	2	4	5	5	5	5
WE3	Friction resistance	30.1	50.4	78.9	97.7	97	97.4
	Rub resistance	2	3	4	5	5	5
WE5	Friction resistance	30.1	35.1	39.4	42.3	50.7	67.5
	Rub resistance	2	2	2	2	2	3

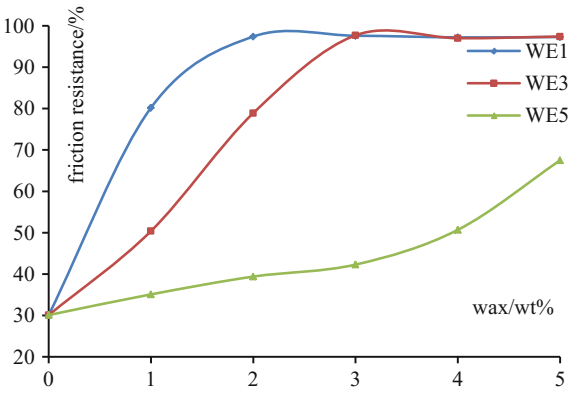

Fig. 1 Effect of wax additives on the friction resistance

(2) Due to the particle size of WE3 is less than WE1's, while WE3 is added 3 wt%, ink's performances could achieve optimal such as friction and rub resistance, and added its amount, performances of the ink can't improve. It may be that spherical wax particles that arranged on the surface of the ink layer have an effect on friction resistance. While added its amount, space between wax particles on the surface of the ink layer reduces, that is the surface area dominated by wax particles increased, which makes ink layer surface friction resistance decline. If WE3 is continued to increase, wax particles on the surface of the ink layer are arranged closely, and new particles are unable to enter so that they can only be arranged within the coating, which has little effect on friction coefficient of the layer [3]. Figure 2 is print's rub resistance while amount of WE3 is 0, 1, 2 and 3 wt% respectively.

(3) WE5 is nanoscale additive. Due to its particle size is too small, there is no obvious improvement on the ink's friction and rubbing resistance.

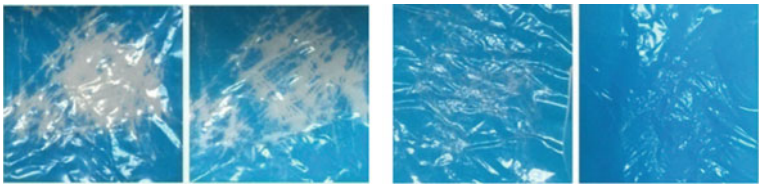

Fig. 2 Pictures of print's rub resistance while adding different amount of WE3

3.2.2 Effect of Different Wax Additives on Ink Gloss

While Wax additive added into the water-based ink, the wax particles approximate dispersed uniformly in the system. From Fig. 3, due to different particle size and distribution of the three types of wax additives which are wax emulsion, micro-wax dispersions and wax dispersions, the light will produce different degrees of diffuse reflection, and this will affect gloss of printing. From the data of Table 5 and Fig. 4, effect of different wax additives on ink gloss can be got. The influence of WE1 to the printing gloss is very great, that is mainly related to its large particle size and maldistribution. The gloss of ink film has certain improvement after adding WE3

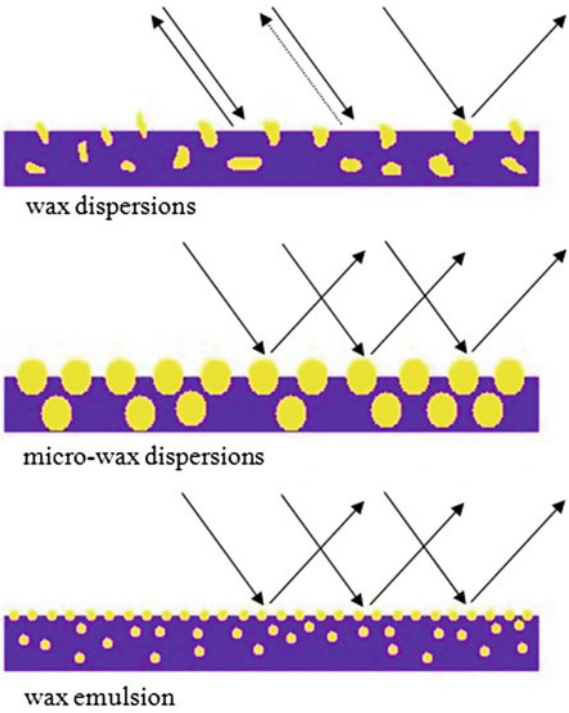

Fig. 3 Distribution and reflection of different kinds of wax additives in ink

Table 5 Effect of different wax additives on ink gloss

Addition (%)	0	1	2	3	4	5
WE1	76.47	75.63	73.13	71.77	69.23	67.0
WE3	76.47	77.3	79.5	82.2	79.5	78.8
WE5	76.47	78.2	80.1	82.3	84.6	83.9

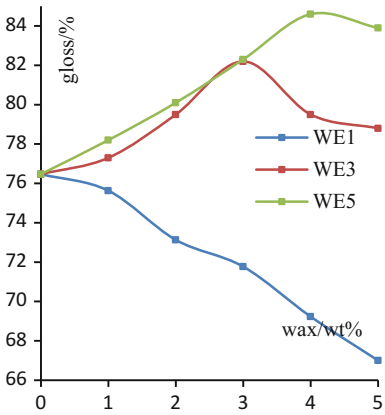

Fig. 4 Effect of different wax additives on ink gloss

and WE5, and amount of them is 3 and 4 wt% respectively, gloss of ink film is best. While increase their dosage could reduce the gloss. It may be because that some silicone additives float on the surface of ink layer which makes the coating uneven and decrease the gloss of the print [4]. Adding the two wax additives can make up these minor defects and increase the gloss. If dosage of them exceeds a certain amount, excess wax particles store inside the ink layer. At the same times, low content of large particle size of wax particles also affect the gloss of coating.

4 Conclusions

As an important table printing ink composition, wax additives can not only improve the resistance of friction and rub, but also affect the gloss of ink film. The results of experiments indicate that while addition of WE3 is 3 wt%, performances of the above mentioned are best. So select WE3 as anti-abrasion additives of water-based ink.

Acknowledgements This study is funded by Science and Technology Plan of Beijing (Z171100002417025), press and publication reform development project library (0020131646) and culture industry development foundation of China, and cross training plan for high level talents in Beijing colleges and universities: deepening project of undergraduate research training program.

References

1. Scholz W, Gilsbach M, Kapp B, Fitting U (2004) Application of wax additives in waterborne parquet floor lacquer and printing ink. Shanghai Coat 42(5):19–23
2. Zhang J (2008) Wax emulsion in water-based glazing oil. Petrol Refinery Eng 12:37–40
3. Yang W (2012) Application of wax products in the water-based coating materials, vol 21. 1994–2015 China Academic Journal Electronic Publishing House, pp 203–204
4. Zhang S (2012) Application of wax additives in waterborne wood coatings, vol 19. 1994–2012 China Academic Journal Electronic Publishing House, pp 33–38

Research of Cigarette Packaging Printing Ink Without Phthalate Plasticizer

Yun Gong, Shubao Zhou, Heng Xu, Jinghuan Ge, Lin Jin and Jie Pan

Abstract Since the forbidden of phthalate plasticizer, the folding quality of the printed products was sharply decreased. In this article, with the addition of food grade of plasticizer,the folding quality of printed products was enhanced,but the toughness was insufficient and the cost was high. On the other hand, using thermoplastic resin as the main body of the ink, the folding quality was greatly improved, but the tack is higher and difficult to dry in the process of printing. Combined two methods together is a suitable solution that the cigarette packaging printing ink meet the standards of tobacco, printing and packaging industry was successfully obtained, as well the folding quality and critical ink performance was similar to the phthalate plasticizer printing ink, without obvious cost increase.

Keywords Phthalate plasticizer · ATBC · Polyurethane · Ink

1 Introduction

Phthalic acid esters is now the most widely used plasticizer in ink to enhance toughness and folding quality, such as DOP (DEHP, di(2-ethylhexyl) phthalate,), DINP (diisononyl phthalate), DIDP(di-iso-decylphthalate), BBP (benzyl butyl Phthalate), DBP (din-butyl phthalate) and so on. DOP is one of the most common and most widely used varieties in industry because it is tasteless, colorless and liquid. However, many studies have shown that, the phthalic acid esters plasticizer are carcinogenic and teratogenic, will increases the risk of cardiovascular disease on human health [1–3]. Since plasticizer scandal, non-phthalate plasticizer industry is

Y. Gong · S. Zhou · H. Xu · J. Ge · L. Jin · J. Pan (✉)
Department of Printing and Packing, Shanghai Publishing and Printing College, Shanghai, China
e-mail: sppcpj@qq.com

Y. Gong
e-mail: 331391649@qq.com

P. Zhao et al. (eds.), *Applied Sciences in Graphic Communication and Packaging*, Lecture Notes in Electrical Engineering 477,
https://doi.org/10.1007/978-981-10-7629-9_92

fast developed by the government support in order to reduce the plasticizer pollution.

Strict censorship and restrictions on the use of plasticizers are formulated by countries in the world. Now, the phthalic acid esters materials are placed on the list of maybe illegal to add non-food substances in food and easy to abuse of food additives [4].

As a special food, the use of phthalic acid esters in cigarette packaging are restrictly required. For the 17 kind of phthalic acid esters, the single content should be less than 30 ppm, and the total content should be less than 100 ppm [5]. In order to protect consumers & environment and improve the quality of the cigarette, the application of phthalate plasticizer was forbidden in cigarette packaging printing ink. However, the folding quality of the printed matter was sharply decreased without the phthalate plasticizer.

This article involves two solutions based on the soft packaging ink in the king of lotus. On the one hand, food grade of plasticizers were used as substitutes of phthalate plasticizer, such as ESO (Ethyl hexyl ester Of epoxidized soybean Oil), DIHCN (Cyclohexane 1, 2-dicarboxylic acid two different nonyl ester), ATBC (acetyl tributyl citrate) [6, 7]. On the other hand, the folding quality of the body ink was enhanced with the addition of thermoplastic resin.

2 Experiment

2.1 Preparation of Ink

Due to the low folding quality of the 60 g/m^2 transfer paper in the king of lotus cigarette, plasticizer such as DOP, DBP were added in the ink formulations to enhance the folding quality of ink. In the ink formulation, the proportion of DOP is 5% as shown in Table 1.

Table 1 Ink formulation

Ingredient	Proportion (%)
Nitrocellulose	15
Dispersant	1
Pigment	10
N-propyl ester	30.3
Ethanol	5
Acetic ether	10
n-Propyl alcohol	8
Propylene glycol monomethyl ether	5
35% polyurethane	10
Plasticizer	5.7

New green plasticizer, such as ESO (Ethyl hexyl ester of epoxidized soybean oil), DIHCN (Cyclohexane 1, 2-dicarboxylic acid two different nonyl esters), ATBC (acetyl tributyl citrate), were added to replace plasticizer DOP and DBP as alternative plasticizer.

2.2 Print Processes

The king of lotus cigarette with blue soft package were printed by 60 g/m^2 transfer paper, ink was transferred onto paper by gravure printing and screen printing with colorful thread, the specific processed by die-cutting was shown in Table 2.

2.3 Test Condition

Folding test was operated on the MIT folding strength testing machine, samples were prepared into 15 × 150 mm and fixed at both end. Hanging load weight is 500 g × 3 to withstand a certain tension and maintain the level of state for the sample. The sample was reciprocating bend 90° at a speed of 360 times/min and until broken. The test results were detected by computer counter.

Drying test was operated on the ZGY automatic drying tester and referenced the QB562 standard which is used for ink dry test method. The 100 g pressure wheel was turned 120 rounds at a speed of 2 mm/round. The drying times was measured through scratches on the backing paper.

Viscosity was test by the 2# Zahn Cup. Tack test was operated on the Tachmaster-92 machine with the speed of copper roll is 1200 rpm.

Table 2 Processes of ink transfer onto paper

Substrate materials	Gravure printing						Screen printing
	First color	Second color	Third color	Fourth color	Fifth color	Sixth color	Seventh color
Transfer paper	Barcode white	Blue	Red	Yellow	Pearlescent	Over print	Colorful thread

3 Results and Discussion

3.1 The Selection of Replaced Plasticizer

The addition of restricted plasticizer DOP is 5% in the original formula. Now, the same addition of replaced plasticizer were added into the substrate ink. After printing and folding 10 times, the test results were shown in Table 3.

After 10 times folding, there was no obvious crease on the samples with DOP and ATBC, but slight crease appeared on the samples with ESO and DIHCN.

After 20 times folding, slight crease appeared on the samples with DOP and ATBC, and sharp creases appeared on the samples with ESO and DIHCN. After 30 times folding, sharp creases were shown up on the samples with DOP and ATBC, and broken/threadbare were shown up on the samples with ESO and DIHCN in Fig. 1. The folding test results indicate that ATBC as replaced plasticizer have the same effect with original phthalate plasticizer DOP on strengthening the folding performance of the ink.

As shown in Fig. 2, the breaking times of the samples with ATBC is higher than samples with DOP and ATBC, but lower than samples with DOP. This suggests that ATBC as replaced plasticizer have the closest effect with original phthalate plasticizer DOP on strengthening the folding performance of the ink.

Table 3 Folding results with different replaced plasticizer

Name / Folding time	5% original plasticizer	5% ESO	5% DIHCN	5% ATBC
10	No crease	Slight crease	Slight crease	Slight crease
20	Slight crease	Sharp creases	Sharp creases	Slight crease
30	Sharp creases	Broken	Threadbare	Sharp creases

Fig. 1 Broken/crease after folding

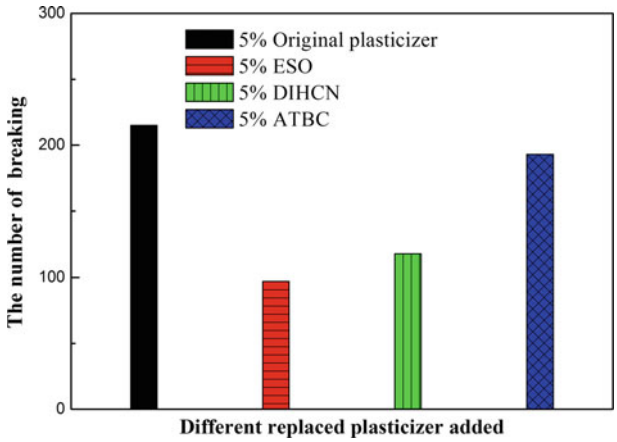

Fig. 2 The number of breaking times in the samples printed by ink with different replaced plasticizer added

3.2 *The Influence of Concentration on the Folding Performance*

To enhance the folding performance of the ink with ATBC, different concentration of ATBC were added in the ink. Samples with higher concentration show better folding performance in Table 4. The breaking times in Fig. 3 shown that, the increase of concentration of ATBC cause the breaking times increase, but, the two increases are not linear relationship samples with 7% ATBC show the best performance in consideration of the breaking times and concentration.

3.3 *Optimization of the Resin*

Plasticizers as additives, have limitations on improving the ink folding performance. Environmental friendly plasticizer such as ATBC can't reach to the effect of DOP now. To achieve the effect of DOP and meet cigarette packaging requirements, ink resin structure were adjusted.

Table 4 Folding results with different concentration of ATBC

Addition / Folding time	5%	7%	9%	11%
10	No obvious crease	No obvious crease	No obvious crease	No obvious crease
20	Slight crease	Slight crease	No obvious crease	No obvious crease
30	Sharp creases	No obvious crease	No obvious crease	No obvious crease

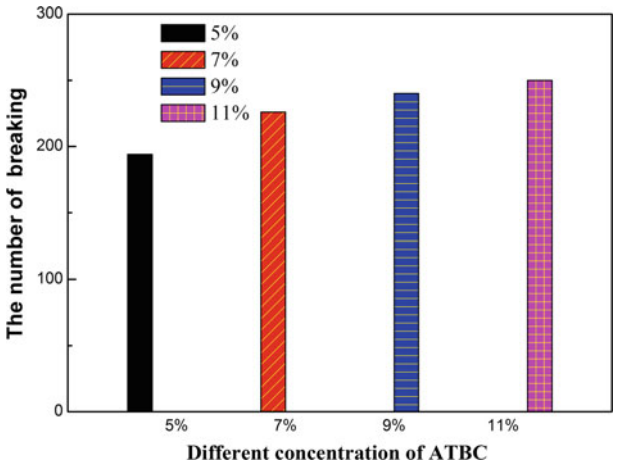

Fig. 3 The number of breaking times for the samples printed by ink with different concentration of ATBC on the same paper

In the original ink formulation, nitrocellulose is the main body in the ink because of its excellent film-forming performance, quickly drying, anti-sticky and etc., has advantages in solvent ink compared with acrylic resin and other resins [8]. However, nitrocellulose also has its obvious shortcomings, it is poor flexibility and the nitrocellulose resin film is very fragile. These shortcomings are not important in cigarette packaging because DOP can recover it. Once DOP was replaced, the resin structures should be optimized to overcome the shortcomings of nitrocellulose and modified resin flexibility.

Nitrocellulose resin has a wide range of compatibility with polyurethane resin in alcohol ester solvent system, polyurethane resin added as modified resin to increase the tack of the ink [9, 10].

U-391, U-324 and 3588A were selected to modified the resin because there large use in the other ink. Now, the same addition of modified resin were added into the substrate ink. The drying time was shown in Fig. 4.

The time of drying in original ink with DOP is 20 s. Compared with other ink in Fig. 4, ink with U-391 is the fastest drying, and when the addition up to 20%, the drying is closed to the original ink with DOP. Considering the drying time, U-391 is the best modified resin.

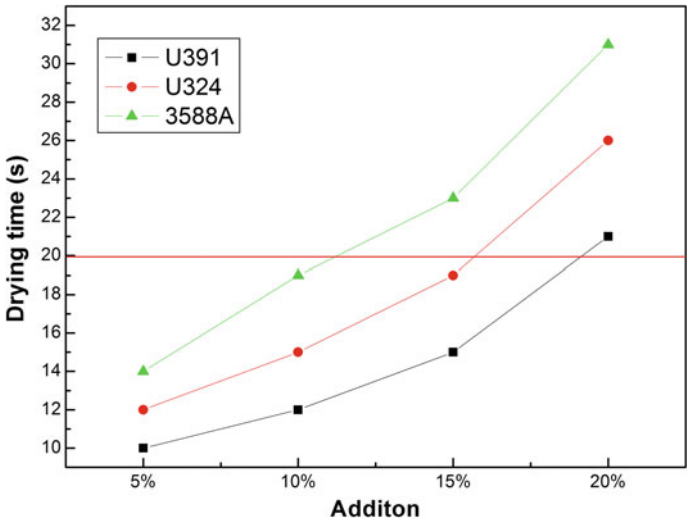

Fig. 4 Drying time of samples with different addition of polyurethane modified resin

3.4 Comprehensive Optimization

Both ATBC and polyurethane separately added can appropriately increase the flexibility of ink. Once add together, the performance of the ink will be different.

In the test, the value of original ink with DOP is about 10, when tack value is higher than 10, the ink will be too sticky to print. Form Fig. 5, when the addition of

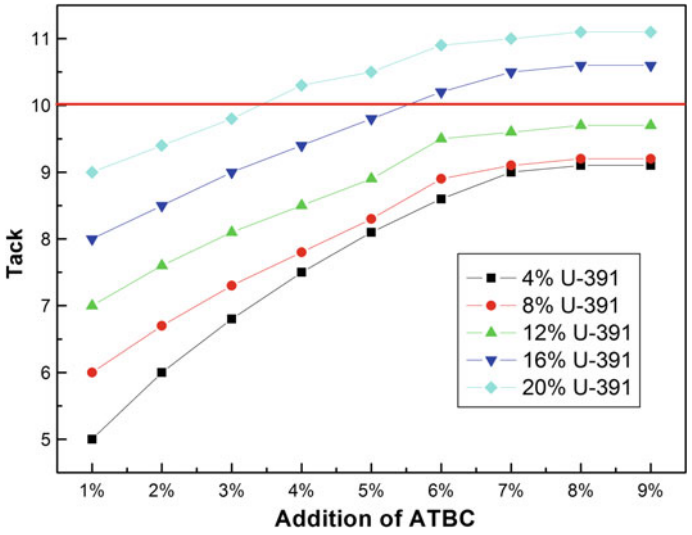

Fig. 5 Tack of samples with different addition of ATBC and U-391

ATBC is 6% and U-391 is 16%, the folding resistance of the ink can reach 10, which is considered to be the best effect.

4 Conclusions

In summary, on one hand, ATBC was used as plasticizer to replace DOP, on the other hand, the polyurethane modified resin U-391 was added to enhance the compatibility and flexibility. Through the addition of replaced plasticizer ATBC and the polyurethane modified resin, similar final effect with the DOP addition was achieved.

Acknowledgements This study is sported by "Chenguang Program" of Shanghai Municipal Education Commission and Shanghai Education Development Foundation (14CGB15) and lab of green platemaking and standardization for flexographic printing.

References

1. Shailaja S, Venkata Mohan S, Rama Krishna M, Sarm PN (2008) Degradation of di-ethylhexyl phthalate (DEHP) in bioslurry phase reactor and identification of metabolites by HPLC and MS. Int Biodeterior Biodegradation 62:143–152
2. Fierens T, Servaes K, Van Holderbeke M et al (2012) Analysis of phthalates in food products and packaging materials sold on the Belgian market. Food Chem Toxicol 50:2575–258
3. Bernard L, Decaudin B, Lecoeur M et al (2014) Analytical methods for the determination of DEHP plasticizer alternatives present in medical devices: a review. Talanta 129:39–54
4. Zhu Z-G (2016) Shallow Syria food flexible packaging composite membrane application and development of polyurethane adhesive. Plast Packag 26(4):32–56
5. Zhao J, Xu F-X, Meng S (2013) Plasticizer in food and its detection technology. Food Ferment Ind 39(6):141–145. https://doi.org/10.13995/j.cnki.11-1802/ts.2013.06.032
6. Hassouna F, Raquez J-M, Addiego F et al (2012) New development on plasticized poly (lactide): chemical grafting of citrate on PLA by reactive extrusion. Eur Polymer J 48:404–415
7. Gao S, Wang Z-W, Hu C-Y, Wu Y-M (2014) Migration of plasticizers from paper packaging inks to milk powder. Food Sci 35(1):18–21
8. Ge Y-L, Pan M-M, An Z (2016) The research status of the connection material for waterborne ink. Guangdong Chem Ind 16(43):278–279
9. Jiang J, Ruan J-H (2012) Synthesis of polyurethanes with different molecular weight and its impact on the ink properties. Chin Print Packag Study 6(04):33–36
10. Mekewi MA, Ramadan AM, ElDarse FM et al (2017) Preparation and characterization of polyurethane plasticizer for flexible packaging applications: natural oils affirmed access. Egypt J Petrol 26:9–15

Preparation of X-ray Developing Screen Printing Ink

Yonghao Xiao, Jia Yan, Kun Hu, Shun Pan, Caixia Du, Xi Li, Yen Wei and Luhai Li

Abstract Recently, the incidence of cardiovascular disease, which is mainly represented by myocardial infarction and cerebral infarction, is increasing, the corresponding surgical also showed an upward trend. Only X-ray irradiation could not accurately determine the location of the three-dimensional position of the patient, which would cause some difficulties in the efficiency of surgery and the implants continued positioning. Screen printing with a wide range of applications, ink layer coverage, cheap, easy to control the characteristics of technology, can be widely used in various fields. This experiment focuses on the development of an ink using for screen printing which could be developed under X-ray. And this ink could be applied for medical measurement tape, so as to improve the accuracy and efficiency of the operation.

Keywords Screen printing · Ink · X-ray development · Measurement tape

1 Introduction

In recent years, vascular disease is slowly approaching the first place in the cause of human death, the most common of which is myocardial infarction and cerebral infarction [1–3]. In the light of vascular disease, the corresponding surgical treatment methods have been developed, including: stent implantation, in situ bypass grafting, venous filter implantation, preoperative balloon angioplasty and so on [4, 5]. In order to understand the vascular placement of these devices, the procedure is

Y. Xiao · J. Yan · K. Hu (✉) · S. Pan · C. Du · X. Li · Y. Wei · L. Li
Beijing Institute of Graphic Communication, Institute of Printing and Packaging and Beijing Engineering Research Center of Printed Electronics, Beijing, China
e-mail: kunhu@139.com

Y. Xiao
Tsinghua Redbud Innovation Institute Baodi Tianjin, Tianjin, China

K. Hu
Collage of Biological Science and Engineering, Fuzhou University, Fujian, China

P. Zhao et al. (eds.), *Applied Sciences in Graphic Communication and Packaging*, Lecture Notes in Electrical Engineering 477,
https://doi.org/10.1007/978-981-10-7629-9_93

commonly used in the process of angiography. Because the X-ray cannot penetrate the developer, vascular lesions and equipment into the situation could be seen easily. Despite this, the human body's blood vessels are intricate, and the X-rays only provide a planar map, so it is difficult to find the lesion site and increase the difficulty of the surgery [6–9].

X-ray development medical measurement tape is a one-time radiation imaging aid that is effective in X-ray diagnostic testing, and it can locate and measure the target site or lesion site, improving the accuracy and efficiency of diagnosis and treatment [10]. Through pasting a number of measurement tape in the surface of human body could quickly help doctors find the lesion site surgery. Usually, the measurement tape has five layers. The first layer is the protective layer, the second layer is the measurement layer, the third layer is the non-woven layer of chitosan fiber material, the fourth layer is the medical pressure sensitive adhesive layer, and the fifth layer is the anti-stick paper layer.

The using of screen printing will reduce the costs in large-scale production, while screen printing ensures the thickness of the printed pattern providing a good development effect under the X-ray machine [11, 12]. The ink prepared in this experiment is a key component of this developing tape.

2 Materials and Methods

2.1 Materials and Machines

Acrylic resin was purchased from D. BASF. Aqueous red and blue color paste was purchased from KuiXiang, XiaMen. Sodium dodecyl benzene sulfonate was purchased from Tianjin Guangfu Fine Chemical Research Institute. Barium sulfate powder was purchased from Quagga Trading (Beijing) CO., Ltd. Deionized water was homemade. Ammonia and ethanol were purchased from Beijing Chemical Works. All chemical reagents are chemically pure.

2.2 Methods

The acrylic resin is placed in a beaker and stirred by a magnetic stirrer. Then, a certain amount of deionized water, barium sulfate, surfactant, pigment, ammonia and ethanol are added in ordered after each half an hour. After mixed to form a uniform ink, it can be used in screen machine. Finally, kinds of proofs will be observing under the CT machine.

According to the literature research and expert consultation, there are four groups of ink composition:

(a) 2# ink: 30% acrylic resin + 40% barium sulfate + others;
(b) 3# ink: 30% acrylic resin + 45% barium sulfate + others;
(c) 4# ink: 33.6% acrylic resin + 45.5% barium sulfate + others;
(d) A ink: 35% acrylic resin + 47% barium sulfate + others.

3 Results and Discussion

Stability contains mechanical stability and storage stability. For the mechanical stability test, 1 ml of water-based ink is held in the centrifuge tube, inside the high-speed centrifuge with the speed of 3000 r/min centrifugal 30 min, observing the state of water-based ink changes. The stability of the storage test, the water-based ink is at room temperature for 6 months to observe the state changes. And the result shows that all kinds of these four ink have the phenomenon of stratified. 3# ink layer very serious and 2# ink is better than 3#. 4# and A ink also have this phenomenon, which shows that these four ink didn't have a good mechanical stability. At room temperature after a month, 2# and 3# ink have the phenomenon of layering and sedimentation, 4# and A ink no significant stratification and settlement, indicating 4# and A ink storage stability is better than 2# and 3# ink.

As Fig. 1 shown above, particle size is carried out with reference to GB/T 11175-2002. 2# ink appeared two peaks, indicating uniform particle size distribution, poor dispersion of particles in the ink, 100 μm peak may indicate the emergence of nano-barium sulfate powder agglomeration phenomenon, 3# ink also

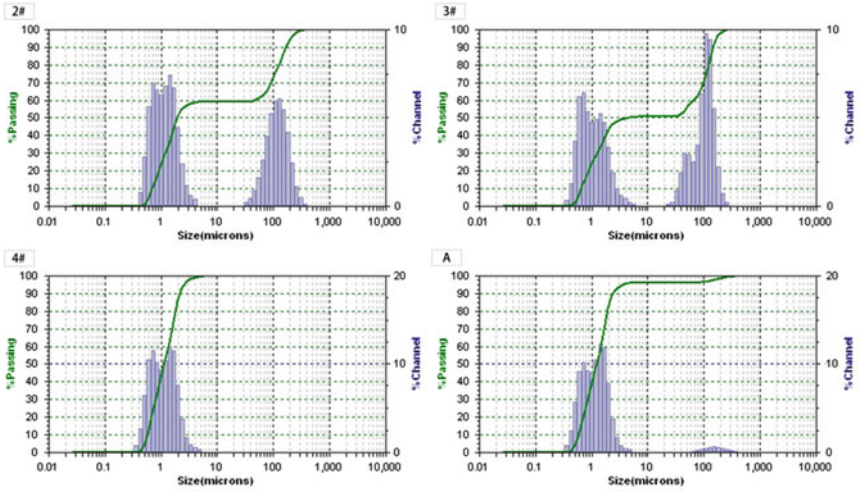

Fig. 1 Particle size of four kinds of ink

appeared two peaks, decentralized is not good as well. Even worse than 2# ink. 4# and A ink only appeared a single peak, indicating that the ink particle size uniform. As well the particle is dispersed evenly, and mostly concentrated in about 2.5 and 3.56 μm.

Because acrylic resin is an important carrier material, barium sulfate powder was dispersed in the acrylic resin under the playing of stirring. The content of acrylic resin determines the dispersion effect of barium sulfate powder, which is the main reason for the phenomenon of precipitation and agglomeration of 2 ink and 3 ink. According to Pan Zhengfeng's literature, the proportion of carrier material and barium sulfate is about 4 ml/g.

Rheology is an important property of all kinds of ink. Generally speaking, the rheology of screen printing ink is from 4 to 10 Pa s. Figure below shows the result of these four kinds of ink.

It can be seen from the Fig. 2 that the ink is a fractured type with a yield value and the apparent viscosity decreases with the increase of the shear rate. With the increase of the rest time, the apparent viscosity increases gradually. 2# ink with the shear rate of viscosity changes in the value of instability, the final viscosity value tends to stabilize the value of 0.01 Pa s, viscosity is too small. 3# ink with the shear rate of viscosity changes in continuous and stable change, the final viscosity value tends to stabilize the value of 0.5 Pa s. 4# ink have the same change rules as 3# ink, and the final viscosity value tends to stabilize the value of 0.5 Pa s. However, from the details of the changes in the Fig. 2 observed, rheology of the 4# ink is better than 3# ink. And compared with above three kinds of ink, A ink with the shear rate of viscosity changes in continuous and stable, and its final viscosity value tends to stabilize the value of 6 Pa s, viscosity significantly improved.

As well, the tests of surface tension are used for test these four kinds of ink. Table 1 shows the results of these four kinds of ink.

Screen printing ink has the request of pH, which pH is always during 8.0 and 9.5. The pH of 2# ink, 3# ink, 4# ink, and A ink are respectively 7.5, 8.3, 8.5 and 8.6 (Table 2).

At last, the ink is printed with the screen printing plate of 200 mesh and then observing the surface smoothness of the printed. Also the printed matter was test using X-ray machine. 2# ink appears disconnection phenomenon, 3# ink is not clear, 4# ink and A ink can be better display in the X-ray. The following figure shows the effect of the four inks under X-ray. As the same time, the leveling property and adhesion of the ink using the subjective evaluation and 3 M tape are checked and find that 4# ink has good leveling property and adhesion. Because the character are used arial 14 pt with no bold, the number is not clear under the X-ray (Fig. 3).

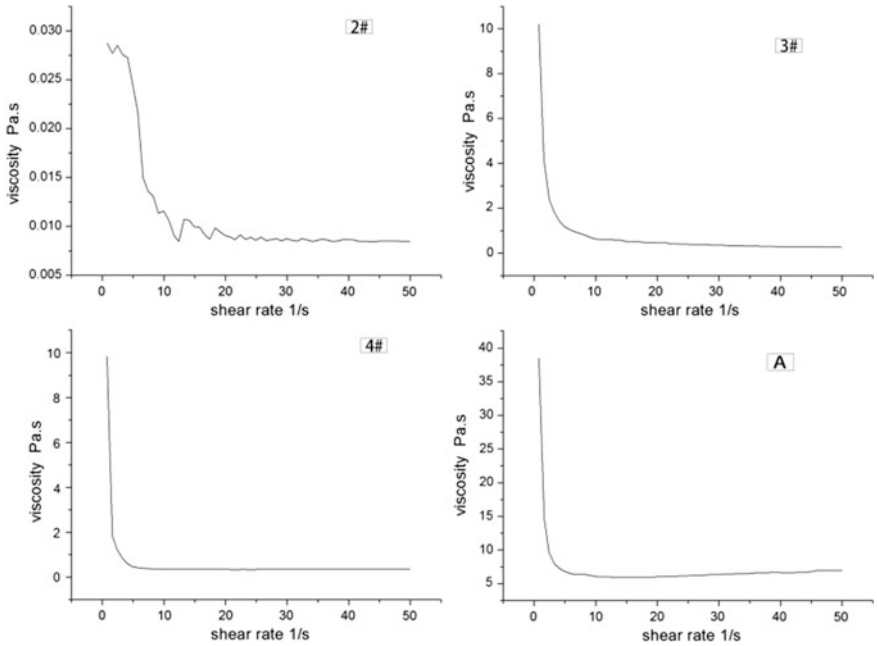

Fig. 2 The ink's viscosity with the change of shear rate

Table 1 Main machines

Name	Model	Company
Magnetic stirrer	98-2	Shanghai Sile Instrument Co., Ltd.
Electronic balance	BSA224S	Sartorius
Screen machine	SWS-JH-4560	Samwo International Group
Pure water meter	MIcra + LA753	ELGA
CT machine	–	–

Table 2 Surface tension of these four kinds of ink

Ink	Surface tension (mN/m)			
	1st surface tension	2nd surface tension	3rd surface tension	Average surface tension
2#	27.69	20.1	23.13	23.64
3#	35.2	33.92	31.56	33.56
4#	24.09	21.85	20.94	22.29
A	15.1	8.83	6.9	10.28

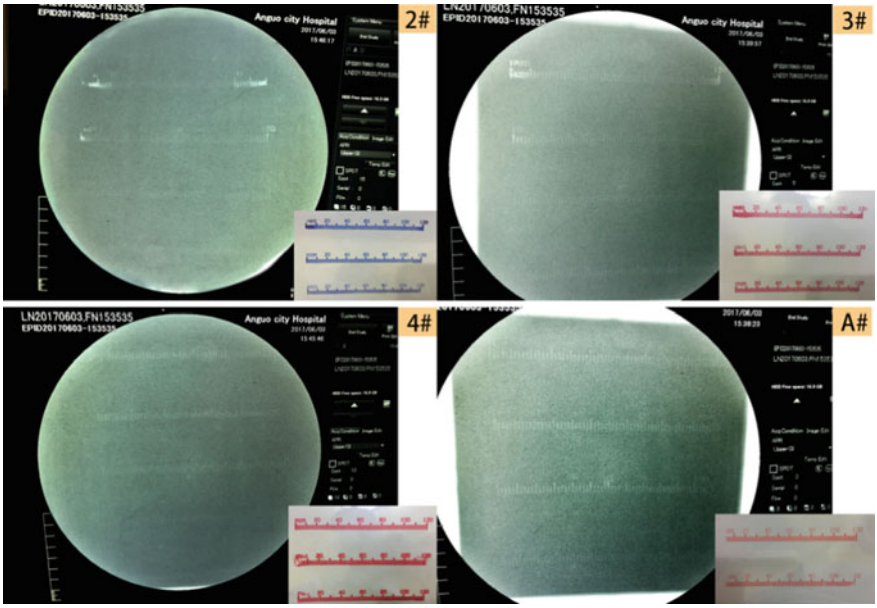

Fig. 3 Four kinds of ink in the X-ray development effect

4 Conclusions

Based on these tests, the preparation of these inks could be used for making the measurement tape, which could be developed in the X-ray. However, medical measurement tape has five kinds of layers. Substrate layer, adhesive layer, protective layer and so on. All of the others should also be matched up with the ink. And these all kind of ink will dry in a very shot minutes, maybe it is also a problem in large-scale printing in the factories.

Acknowledgements This study is funded by University scientific research project—3D Printing mineralized collagen-based child mandible (No. 20190116002/037), Students research—Medical X-ray imaging measurement tape prepared by screen printing (No. 22150116005/074). Beijing Municipal Collaborative Innovation Research Program (04190117029/002). High level crossing training plan of Beijing high school—Construction of small—caliber artificial blood vessels with cells. And thanks for the help of Tsinghua Redbud Innovation Institute Baodi Tianjin.

References

1. Erkinjuntti T, Inzitari D, Pantoni L et al (2000) Research criteria for subcortical vascular dementia in clinical trials. J Neural Transm Suppl 59(59):23
2. Critchley J, Liu J, Zhao D et al (2004) Explaining the increase in coronary heart disease mortality in Beijing between 1984 and 1999. Circulation 110(10):1236–1244

3. Bhatia LC, Naik RH (2013) Clinical profile of acute myocardial infarction in elderly patients. J Cardiovasc Dis Res 4(2):107–111
4. Yamagami T, Yoshimatsu R, Matsumoto T et al (2008) Prophylactic implantation of inferior vena cava filter during endovascular therapies for deep venous thrombosis of the lower extremity: is it necessary? Acta Radiol 49(4):391–397
5. Yan Dijk LC, Van UH, Laméris JS et al (1997) Residual arteriovenous fistulae after "closed" in situ bypass grafting: an overrated. Eur J Vasc Endovasc Surg 13(5):439–442
6. Lou XF, Mei J (2006) Modified lead oxide-gelatin injection technique for angiography. Chin J Clin Anat 24(3):4
7. Tang M, Yin Z, Morris SF (2008) A pilot study on three-dimensional visualization of perforator flaps by using angiography in cadavers. Plast Reconstr Surg 122(2):429
8. Desena D (2001) X-ray labeling tape: US, US6198807
9. Hai-Chun LU (2004) Study on properties of medical self-crosslinking acrylic pressure-sensitive adhesive. China Adhesives 13(4):12–13
10. Lemaitre GW, Lemaitre GD (2001) Single-use radiological imaging aid: US, US6333970
11. Pemberton RM, Pittson R, Biddle N et al (2009) Fabrication of microband glucose biosensors using a screen-printing water-based carbon ink and their application in serum analysis. Biosens Bioelectron 24(5):1246–1252
12. Menoud A, Veya P, Sa SH (2003) Water-based screen printing ink

Ultraviolet Curing Kinetics of Epoxy Resin in UV-Curing Reaction Photopolymerization with Real-Time Fourier Transform Infrared Spectroscopy

Lu Zhang, Xianfu Wei, Beiqing Huang, Lili Wang and Xiaotong Xiong

Abstract The photo-induced curing kinetics of cationic UV curing of epoxy resin were investigated with real-time Fourier transform infrared (RT/FT-IR) spectroscopy with an optical fiber ultraviolet curing system. The consumption of epoxy group as a function of time was obtained by monitoring of the oxirane absorbance in the 795–824 cm^{-1} region. A spiro orthocarbonate expanding monomer 3,9-diethyl-3,9-dihydroxymethyl-1,5,7,11-tetraoxa-spiro[5.5]undecane was added to UV curing molding material of 3D printing in different mounts. As a result, when the content of the expanded monomer is increased from 0.5 to 2.0 wt%, conversion rate increased from the original 95–98%, when the amount of expanded monomer is 0.5%, the relative reaction rate of the system achieve the highest.

Keywords Expanding monomer · Epoxy resin · Ultraviolet curing kinetics

1 Introduction

In the photo-curing polymerization, some compounds that undergo cationic ring-opening polymerization can undergo volume expansion at the time of polymerization, and these compounds are commonly referred to as swelling monomers. Expanded monomer and epoxy resin in photo-curing system can be copolymerized under ultraviolet light irradiation.

The real time FT-IR (RT/FT-IR) technique has been recognized as a very vital tool to quantitatively study the curing parameters such as the effects of initiator (or catalyst) type and concentration, accelerator, stabilizer, irradiation wavelength,

L. Zhang (✉) · X. Wei · B. Huang · L. Wang · X. Xiong
Beijing Institute of Graphic Communication, Beijing, China
e-mail: 634698575@qq.com

X. Wei
e-mail: weixianfu@bigc.edu.cn

B. Huang
e-mail: huangpeiqing@bigc.edu.cn

P. Zhao et al. (eds.), *Applied Sciences in Graphic Communication and Packaging*, Lecture Notes in Electrical Engineering 477,
https://doi.org/10.1007/978-981-10-7629-9_94

temperature, and curing environments [1]. With a good quantitative effect, the response time is short, the experimental equipment is simple [2–4]. In this paper, we used real-time infrared spectroscopy to study the effect of 3,9-diethyl-3,9-dihydroxymethyl-1,5,7,11-tetraoxa-spiro[5.5]undecane on photopolymerization kinetics of 3D printed photo curable materials. The effects of different monomers on the photopolymerization kinetics of the system were investigated.

2 Experiments

2.1 Materials and Reagents

3,9-diethyl-3,9-dihydroxymethyl-1,5,7,11-tetraoxa-spiro[5.5]undecane(Shenzhen Pulisigao molding materials Co., Ltd.); Prepolymer: bisphenol A epoxy resin (E44, Shandong Tianmao Chemical), Hyperbranched polyester acrylate prepolymer (V400, Cytec Industries), Hyperbranched polyester acrylate (V100, Cytec Industries); Reactive monomer: 3,4-Epoxycyclohexylmethyl 3,4-Epoxycyclohexane Carboxylate (TTA21, Jiangsu Tai Teer Chemical); Bis ((3,4-epoxycyclohexyl) methyl) adipate (TTA26, Jiangsu Tai Teer Chemical); hoxyethoxy acrylate (EOEOEA, Changxing chemical Taiwan); 1,6-hexanediol diacrylate (HDDA, Changxing chemical Taiwan); Photoinitiator: Thiophenyl—oxygen ring nitrogen acetone (907 Tianjin long day chemistry); Mixed triarylsulfonium hexafluorophosphate sulfate (PAG 201, Changzhou powerful electronic); Mixed triarylsulfonium hexafluorophosphate (PAG202, Changzhou powerful electronic).

2.2 Equipments

Real-time Fourier Transform Infrared Spectrometer (KBr Beam splitter, MCT/A detector, Spectra were collected at a resolution of 4 cm^{-1} and at the rate of 2 spectra/s.) Thermo Fisher Nicolet FT-IR is 50. The experimental setup is shown in Fig. 1. UV light source UV curing system, (OmniCure®S1000, 100 W Mercury lamp, equipped with 5 mm quartz fiber, 320–500 nm filter); UV-A UV irradiance meter, (Beijing Normal University photoelectric instrument factory) (Fig. 2).

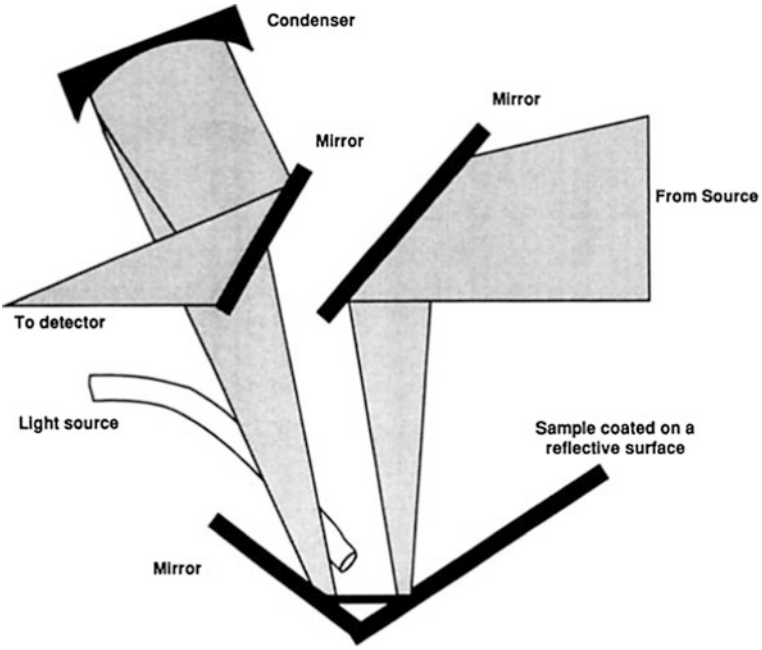

Fig. 1 Versatile reflection attachment schematic illustration of optics in a RT/FT-IR sample chamber using a Harrick

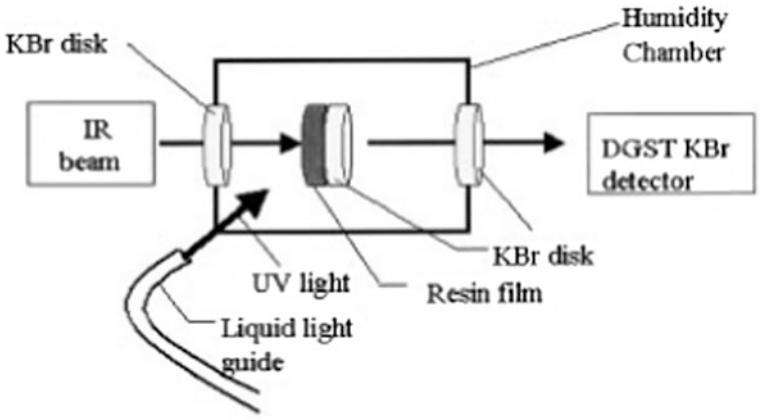

Fig. 2 Real-time FTIR experimental setup

2.3 Characterization and Testing

2.3.1 Infrared Characterization

A wave number of 1220 cm^{-1} can be seen in Fig. 3, the monomer having a obvious spiro ring group characteristic absorption peaks, in the wave number 3400 cm^{-1} appears near the hydroxyl absorption peak width.

2.3.2 Photopolymerization Kinetics Test

The mass fraction of 0.5, 1, 1.5, 2% expansion monomer is added to the light curing material basic formulation (see Table 1) respectively and stirred with a glass rod into the expansion monomer was completely dissolved. At the same time a blank test was prepared.

Experimental method: The prepared liquid was coated on a KBr wafer, cover another KBr chip above, The thickness of the sample film was controlled by placing different thicknesses of aluminum foil between the two KBr wafers as spacers, the sample is fixed on a special fixture, the fiber is 5 cm from the sample, the light intensity is fixed at 40 mw/cm^2. The change of the absorption peak area at 795–824 cm^{-1} was monitored by RT-FTIR at 365 nm wavelength with ultraviolet light irradiation.

The infrared spectrum of the expanded monomer before and after irradiation is shown in Fig. 4. As can be seen from the Fig. 4, the absorption peak of epoxy group at 810 cm^{-1} changed obviously after irradiation indicating that during the irradiation process, the epoxy compound undergoes an open loop reaction.

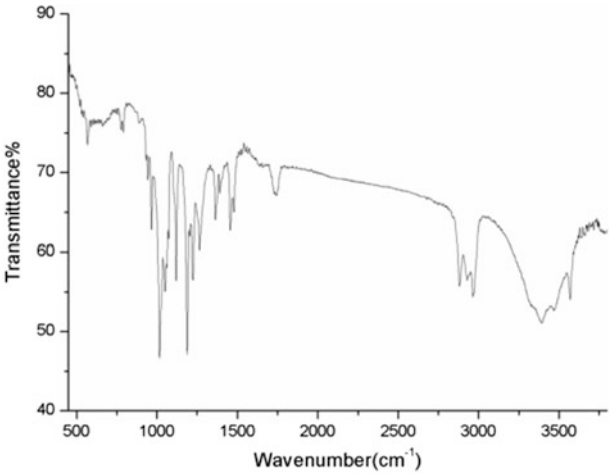

Fig. 3 IR spectrum of the expanding monomer

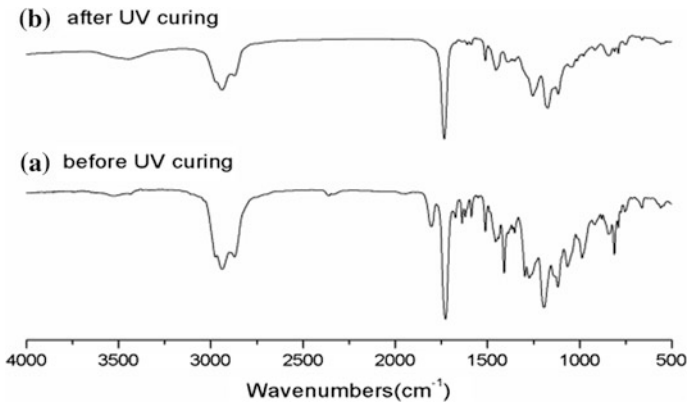

Fig. 4 IR spectrum of **a** before and **b** after UV curing

3 Results and Discussion

The results of photo-curing kinetics of the addition of different contents of the expanded monomer in the photo-curable material are shown in the Fig. 5.

As can be seen from the Fig. 5, when the content of the expanded monomer is increased from 0.5 to 2.0 wt%, conversion rate increased from the original 95–98%, when the amount of expanded monomer is 0.5%, the relative reaction rate of the system achieve the highest. Since the expanded monomer and the epoxy resin 3,4-epoxycyclohexylmethyl 3,4-epoxycyclohexyl carboxylate in the photo-curing system can be copolymerized under ultraviolet light irradiation. With the addition of the monomer in the system, the polymerization conversion rate gradually increased, when the monomer was added continuously, the reaction rate did not increase significantly. When a small amount of swelling monomer is added to the photo-curing system, the overall enthalpy of the system increases, the conversion of the epoxy group can be increased; but when the expansion of the monomer added too much to make the proportion of epoxy resin is too low, even if the conversion rate per unit mass increases, the exothermic enthalpy of the whole system is still reduced, that is, the overall degree of response to reduce [5].

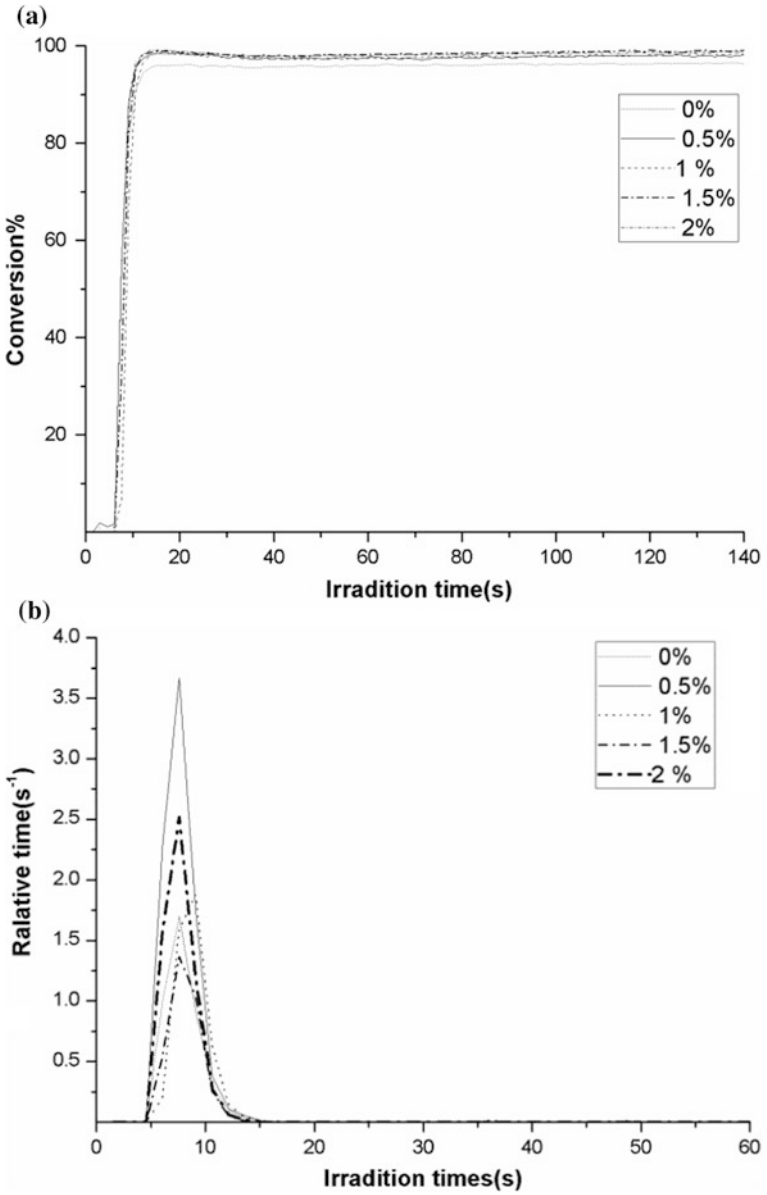

Fig. 5 **a** conversion-time **b** relative rate-time curves

4 Conclusions

By the experiment, we conclusion that when the content of the expanded monomer is increased from 0.5 to 2.0 wt%, conversion rate increased from the original 95 to 98%, when the amount of expanded monomer is 0.5%, the relative reaction rate of the system achieve the highest.

References

1. Yang DB (1993) Kinetic studies of photopolymerization using real time FT-IR spectroscopy. J Polym Sci Part A: Polym Chem 31(1):199–208
2. Scherzer T, Decker U (1999) Real-time FTIR-ART spectroscopy to study the kinetics of ultrafast photopolymerization reactions induced by monochromatic UV light. Vib Spectrosc 19:385–398
3. Decker C, Moussa K (1989) Real time kinetic study of lase induced polymerizarition. Macromolecules 22:4455–4461
4. Lee TY, Roper TM, Jonson ES (2003) The kinetics of vinacrylate photopolymerization. Polymer 2003(44):2859–2865
5. Chen X, Wang L, Huang P, Shi J (2005) Synthesis of a spiro-cyclic carbonate ester expanded monomer and its heat curing with epoxy resin. J Nanjing Univ Technol 2

The Adhesive for the Production of High Strength Composite Corrugated Board

Qinghua Gao, Junyan Huang and Huizhong Zhang

Abstract To study the adhesive effects on the strength of core paper of high strength composite corrugated board, cassava starch adhesive, water glass binder, CP-88, polyvinyl alcohol and polyvinyl acetate adhesive were prepared for adhesive of composite core paper. The comparative performance tests were conducted including the edgewise/flat crush resistance. Environmental-friendly modified water glass binder adhesive was more suitable for composite core paper.

Keywords High strength composite corrugated board · Core paper
Five adhesive · Edgewise crush resistance · Flat crush resistance

1 Introduction

Corrugated box stood out from the packaging and the transportation aspect accompanying development of the economy and environmental friendly consciousness in China. It had a simple production process and easy to recycle and was a packaging structure with softness and strength. High strength composite corrugated board came up with diversified shipping packages styles and various forms. One was made by high weight basic paper, usually was odd number layer, such as five or seven layers. The other was a rising product [1, 2]. It seemed to notice any difference with the same thickness corrugated board, but superior performance was featured especially the edgewise crush resistance and puncturing resistance [3]. Double core paper was the kernel technology of even number

Q. Gao · J. Huang (✉)
Dalian Polytechnic University, Dalian, Liaoning, China
e-mail: huangjunyan@126.com

Q. Gao
e-mail: 13516053085@163.com

H. Zhang
Tat Seng Packaging (Suzhou) Co., Ltd, Suzhou, Jiangsu, China
e-mail: 13706216515@163.com

P. Zhao et al. (eds.), *Applied Sciences in Graphic Communication and Packaging*, Lecture Notes in Electrical Engineering 477,
https://doi.org/10.1007/978-981-10-7629-9_95

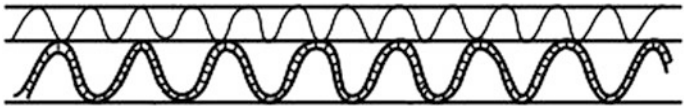

Fig. 1 High strength composite corrugated board

corrugated board that appeared between face paper and medium paper, so its strength performance was highly increased [4]. As shown in Fig. 1. The most common even number corrugated board was four, six, eight layers. To some extent, it could replaced wooden box in transport package. Eight layer high strength composite corrugated board could weight 500 kg and quality issues could stand very possible test to export Europe, data had showed [5].

The adhesive selection of high strength corrugated board was crucial. To choose ideal, affordable and suitable adhesive for composite core paper, the main content of the article was shown below. Cassava starch adhesive, water glass binder, CP-88, polyvinyl alcohol [6] and polyvinyl acetate adhesive were used in core paper and then tested strength performance to decide on the best solution. Because this article focused on practical application, so we mainly tested the edgewise/flat crush resistance [7] that were the most important performance of corrugated board.

2 Experiments

2.1 Main Material

High strength composite corrugated board (six layer); Cassava starch adhesive, it was prepared from starch, water by a certain proportion of 1:3. Water glass binder. CP-88 adhesive, it was prepared from CP-88, starch by a certain proportion of 1:30. Polyvinyl alcohol adhesive, it was prepared from 220 type polyvinyl alcohol, water by a certain proportion of 1:10. Polyvinyl acetate adhesive.

2.2 Test Apparatus

The edgewise/flat crush resistance strength tester, The thickness testing instrument.

2.3 Performance Test

Different adhesive corrugated board that was made by Germany BHS equipment must be set aside for 24 h under the condition of constant temperature, constant humidity [8].

The edgewise crush resistance were executed according to GB6546-1998 [9]. The flat crush resistance were executed according to GB/T22874-2008 [10].

We divided the experiment into two parts, every part included two test performances, every adhesive and every performance tested ten groups. Because cassava starch adhesive was the most common one for corrugated board production line, so every adhesive test performance was compared with cassava starch adhesive.

The first group: the corrugated board were made by cassava starch adhesive, water glass binder and CP-88 adhesive. Test projects contained the edgewise/flat crush resistance.

The second group: the corrugated board were made by cassava starch adhesive, polyvinyl alcohol adhesive and polyvinyl acetate adhesive. Test projects contained the edgewise/flat crush resistance.

3 Results and Discussion

3.1 The First Group Experiment and Performance Analysis of Edgewise Crush Resistance

The first group experiment and performance analysis of edgewise crush resistance was shown in Fig. 2. Three curves tendency were almost the same. The corrugated board edgewise crush resistance of cassava starch adhesive was lower than other kinds. The average value were 814.04, 890.11, 864.15 N/m. The edgewise crush resistance of water glass binder was increased 9.34% better than cassava starch adhesive. The fourth data was relatively small, reached 710.4 N/m. During the practical process, a lot of factors could decide the result, such as speed, temperature and so on. Fast or low speed could led to poor or false sticking, so temperature control was crucial. Environmental-friendly modified water glass binder adhesive had a perfect performance in purely strength terms, but the flat crush resistance was needed to take into account.

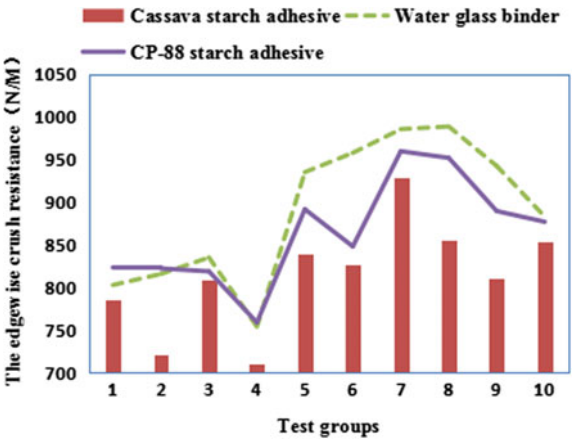

Fig. 2 The first group experiment and performance analysis of edgewise crush resistance

3.2 *The First Group Experiment and Performance Analysis of Flat Crush Resistance*

The first group experiment and performance analysis of flat crush resistance was shown in Fig. 3. As the figure shown, although the edgewise crush resistance test result of water glass binder adhesive was good, its flat crush resistance did not have the obvious advantages. The common cassava starch adhesive stood out. CP-88 adhesive even appeared small fluctuations.

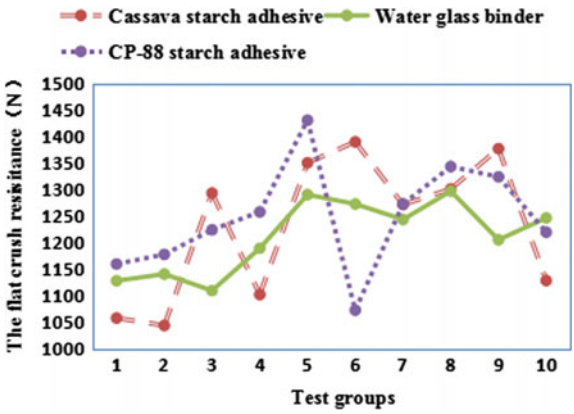

Fig. 3 The first group experiment and performance analysis of flat crush resistance

3.3 The Second Group Experiment and Performance Analysis of Edgewise Crush Resistance

The second group experiment and performance analysis of edgewise crush resistance was shown in Fig. 4. The conclusions drawn that polyvinyl alcohol and polyvinyl acetate adhesive curves tendency were very close and significantly outperformed cassava starch adhesive. But their test curves had a large fluctuates, cassava starch adhesive test curve remained relatively stable. During the practical process, polyvinyl alcohol adhesive must be immediately used after preparation, otherwise, problems arose, such as coagulation, cohesion and so on. Besides, temperature had great effects on it. In the process of preparation, bubbles were difficult to erase, so it could cause the corrugated board false viscosity in actual production and affect the strength of the corrugated board.

3.4 The Second Group Experiment and Performance Analysis of Flat Crush Resistance

The second group experiment and performance analysis of flat crush resistance was shown in Fig. 5. As seen in figure, the flat crush resistance curves of polyvinyl alcohol and polyvinyl acetate adhesive corrugated board had a large fluctuates possibly because of coagulation, cohesion or bubbles. The average value were 1372.94 N/32.2 cm^2, 1221.26 N/32.2 cm^2, 1287.89 N/32.2 cm^2. The flat crush resistance of cassava starch adhesive was increased 151.68 better than the polyvinyl alcohol adhesive and 85.05 better than the polyvinyl acetate adhesive.

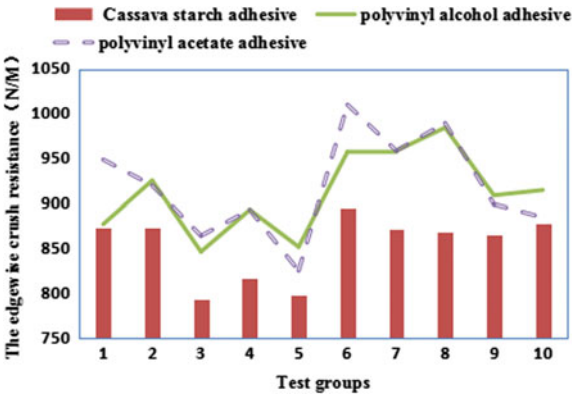

Fig. 4 The second group experiment and performance analysis of edgewise crush resistance

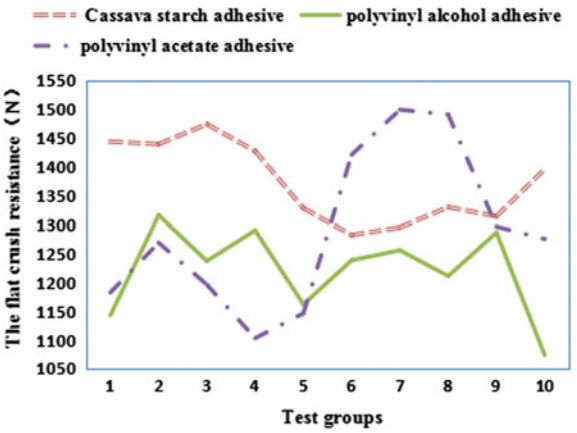

Fig. 5 The second group experiment performance analysis of flat crush resistance

3.5 *Comprehensive Analysis of Five Adhesive Corrugated Board Performance*

The edgewise crush resistance, flat crush resistance, edgewise crush resistance average value, flat crush resistance average value of five adhesive corrugated board respectively were shown in Figs. 6, 7, 8, and 9. Taken together, the edgewise/flat crush resistance of cassava starch adhesive corrugated board remained relatively stable, but it was lower than the other four adhesives. The edgewise crush resistance of polyvinyl alcohol and polyvinyl acetate adhesive corrugated board kept higher and changed slightly, but their flat crush resistance changed relatively greatly. Due to the limitation of production process conditions, it was difficult to invest in mass production. The edgewise crush resistance of CP-88 adhesive corrugated board remained stable, however, its flat crush resistance fluctuated greatly which led to the strength performance was not guaranteed. The edgewise crush

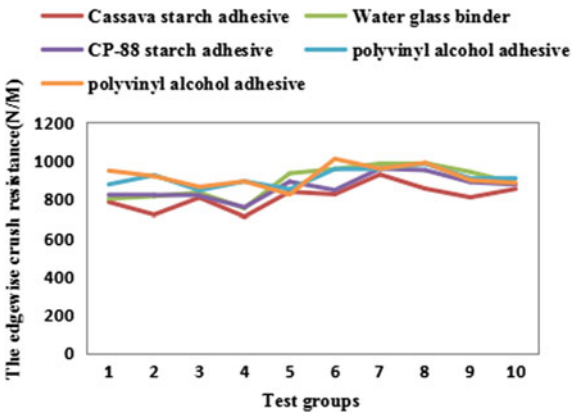

Fig. 6 Comparison results for edgewise crush resistance of five adhesives corrugated board

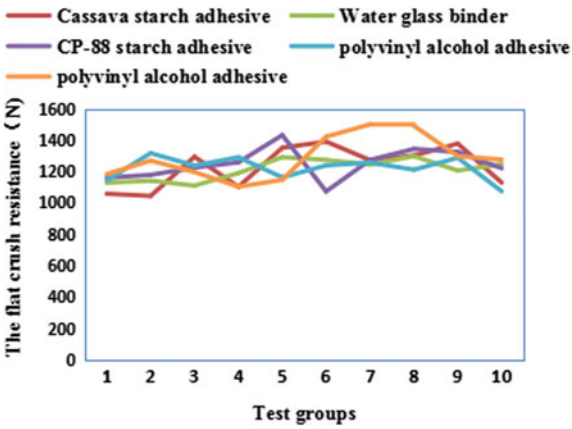

Fig. 7 Comparison results for flat crush resistance of five adhesives corrugated board

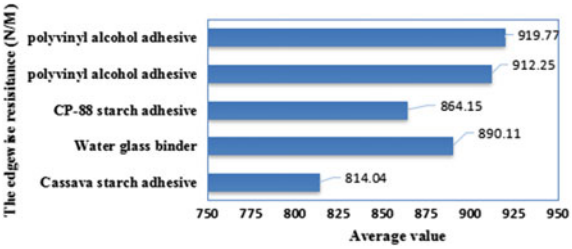

Fig. 8 The edgewise crush resistance average value of five adhesives corrugated board

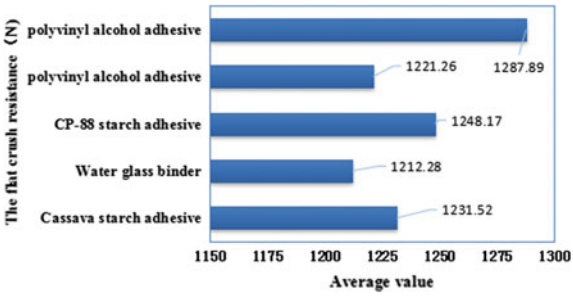

Fig. 9 The flat crush resistance average value of five adhesives corrugated board

resistance of water glass binder adhesive corrugated board was relatively superior, although, its flat crush resistance was lower than other four adhesive. However, whether edgewise crush resistance or flat crush resistance all remained stable, which could provide a strong guarantee of performance. Water glass binder adhesive had good fluidity, low processing cost, environment friendly way and was suitable for mass production.

4 Conclusions

By comparing edgewise/flat crush resistance of five adhesive corrugated board and considering cost, actual production, environmental factors and so on, excellent performance environmental-friendly modified water glass binder adhesive was more suitable for core paper adhesive of high strength composite corrugated board.

References

1. Zhao R (2006) The advantage of four layer composite corrugated paper. World Print 11:8–9
2. Zeng R, Zhong Z, Shi Y (2002) Study on performance and economic benefit of 2A four layer composite corrugated board. Chin Packag Ind 96:35–36
3. Lv X, Zhang Y, Guo X (2007) Discussion on the 4 layer manufacturing process of composite corrugated board. Packag Eng 28:3–4
4. Guo J, Liu G (2005) Novel corrugated board (double arch) study on properties of composite structure. Packag Eng 26:52–53
5. Zhang H (2010) Development and application of six plyer heavy duty corrugated board. Chin Packag Ind 8:28–29
6. An M (2005) Properties of several kinds of adhesive and its application in the packaging of comparison. Packag Food Mach 23:42–44
7. Hahn EK, Carisson LA, Westerlind BS (1992) Edge-compression fixture for buckling studies of corrugated board panels. Exp Mech 32:252–258
8. Zhang C (2005) BHS corrugated board production line and production practice of technology application. Master diss. Dalian Polytechnic University
9. GB 6546-1998 (1998) Corrugated fibreboard-determination of edgewise crush resistance
10. GB/T 22874-2008 (2008) Single-faced and single-wall corrugated fibreboard—determination of flat crush resistance

Part IX
Film and Related Material Technology

Structure-Colored Polymer Film Fabricated by Surface Immobilizing Amorphous Photonic Crystals

Yanan Liu, Yaping Yan, Jinmei Zhu, Shengliu Wang, Yun Ouyang and Lianying Liu

Abstract Amorphous photonic crystals display isotropic photonic band gaps and angle-independent non-iridescent, structural color, which leads to increasing interest and promising applications in image display, laser light, environment-friendly ink/coating, etc. However, previous amorphous photonic crystals usually exhibit low strength, and their structure is easily destroyed. Thus, their unique optical properties cannot be fully exhibited. Herein, amorphous photonic crystals of core (polystyrene-PSt) and shell (poly (4-methacryloyloxybenzophenone)-PMABP) structured microspheres are formed. Using polymer films (PET, PP, PMMA and PE) coated with poly (4-(methacryloxy) benzophenone-*co*-*N*-Isopropyl acrylamide) as substrates, the amorphous photonic crystals are immobilized under UV-irradiation. Adding cross-linker of ethoxylated trimethylolpropane triacrylate (ETPTA) in microsphere dispersion, transparent and flexible free-standing films of photonic crystals are fabricated. Angle-independent structural colors are observed and tuned by varying microsphere concentration in dispersions and content of cross-linker.

Keywords Amorphous photonic crystals · Structural color · Polymer film

Y. Liu (✉) · Y. Ouyang
Beijing Key Laboratory of Packaging and Printing New Technology, Key Laboratory of Printing Environment Protection Technology, China Academy of Printing Technology, No. 2 Cuiwei Road, Haidian District, Beijing, China
e-mail: liuyanan@keyin.cn

J. Zhu
Shijiazhuang University of Applied Technology, No. 12 Changxing Road, Zhongshan West Street, Shijiazhuang City, Hebei Province, China

Y. Yan · L. Liu (✉)
Beijing University of Chemical Technology, No. 15 Beisanhuan East Road, Chaoyang District, Beijing, China
e-mail: lyliu@mail.buct.edu.cn

S. Wang
Beijing LiTuoDa Sci-Technology Co.Ltd, Beijing, China

P. Zhao et al. (eds.), *Applied Sciences in Graphic Communication and Packaging*, Lecture Notes in Electrical Engineering 477,
https://doi.org/10.1007/978-981-10-7629-9_96

1 Introduction

Structural color is usually generated by periodic or amorphous photonic nanostructure, which can control the transportation of light [1]. Compared with periodic photonic crystals, amorphous photonic crystals possess only short-range order that leads to many unusual electronic, mechanical, and lattice dynamical properties [2]. The photonic pseudo-gap or photonic band gaps in amorphous photonic crystals are direction-independent because light is scattered evenly in all directions. Therefore, the structural color is independent of the viewing angle, and amorphous photonic crystals potentially used in cosmetics, paint products, printings and fabrics for their high brightness and saturation, color-fastness and environmental friendliness [3].

However, most amorphous photonic crystals hardly have strong mechanical strength because there is nearly no interaction between the particles and the substrates. Thus, it limits the application of amorphous photonic crystals.

Here, in order to interconnect the microspheres consist of polystyrene core and poly (4-methacryloyloxybenzophenone) shell and immobilize amorphous photonic crystals on polymer films (PET, PP, PMMA and PE), poly(BPMA-NIPAM), which is photoactive and hydrophilic, was synthesized. With the aid of photosensitive BP groups, surface hydrophilicity of polymer films was increased, and active sites were introduced under UV-irradiation. Therefore, it is favorable for spreading and immobilizing of microsphere dispersion on the surface of polymer films. Further, amorphous photonic crystal films with high mechanical strength were prepared by adding photoinitiator and cross-linker into microsphere dispersion. The hydrophobic poly (St-MABP) microspheres dispersed in a photo-curable monomer (ethoxylated trimethylolpropane triacrylate-ETPTA) formed amorphous arrays through shear-induced assembly, and UV-induced polymerization enabled the rapid solidification of the amorphous arrays.

2 Experimental Sections

2.1 Preparation of Core-Shell Particles

Briefly, styrene (St, 2.5 ml), Azobis(isobutyronitrile) (AIBN, 2%), Sodium p-styrenesulfonate (NaSS, 2%), methanol and deionized water were added to a 100 mL three-neck round-bottom flask equipped with a reflux condenser and a mechanical stirrer. The flask was then immersed in a water bath. The mixture was stirred at a speed of 200 rpm. The polymerization was started at 75 °C. After 180 min, 4-(methacryloxy) benzophenone (MABP, 4%) dissolved in St (20%) was added dropwise. The polymerization was conducted for 400 min. Final particles were separated by centrifugation washed with MeOH for several times, and dried overnight at 25 °C in a vacuum oven. All the proportions are based on weight of initial St [4].

2.2 Immobilizing Amorphous Photonic Crystals on Polymer Films

Firstly, amorphous photonic crystals assembled by core-shell microspheres (poly (St-MABP)) were prepared on the quartz by the method of spin coating. Secondly, polymer film (PET, PP, PMMA and PE) coated with poly (BPMA-*co*-NIPAM) was covered by the quartz, and microspheres contacted the polymer films possibly. Finally, with the aid of photosensitive benzophenone (BP) groups of microspheres, amorphous photonic crystals were immobilized on the surface of polymer films by hydrogen abstraction and coupling reaction under UV-irradiation.

2.3 Preparation of Free-Standing Film

Photoinitiator and cross-linker (ETPTA) were added into microsphere dispersion (5% particles were dispersed in mixture of water and methanol). The microspheres formed amorphous arrays through shear-induced assembly. Then the particles assembled were transferred to the surface of polymer film and flattened by the quartz. UV-induced polymerization enabled the rapid solidification of the amorphous arrays under UV lamp.

2.4 Characterization

Morphology of particles was observed using scanning electron microscope (SEM, Hitachi S-4700, at 20 kV accelerating voltage). Optical photos of polymer films and free-standing films were obtained by using digital camera.

3 Results and Discussion

3.1 Immobilizing Amorphous Photonic Crystals on Polymer Films

In order to interconnect the core (polystyrene-PSt) and shell (poly (4-methacryloyloxybenzophenone)-PMABP) structured microspheres and immobilize amorphous photonic crystals on polymer films (PET, PP, PMMA and PE), poly (BPMA-NIPAM) was synthesized, which is photoactive and hydrophilic. With the aid of photosensitive BP groups, surface hydrophilic of polymer film was increased, and active sites were introduced by hydrogen abstraction and coupling reaction under UV-irradiation [5, 6]. Therefore, it was favorable for spreading and

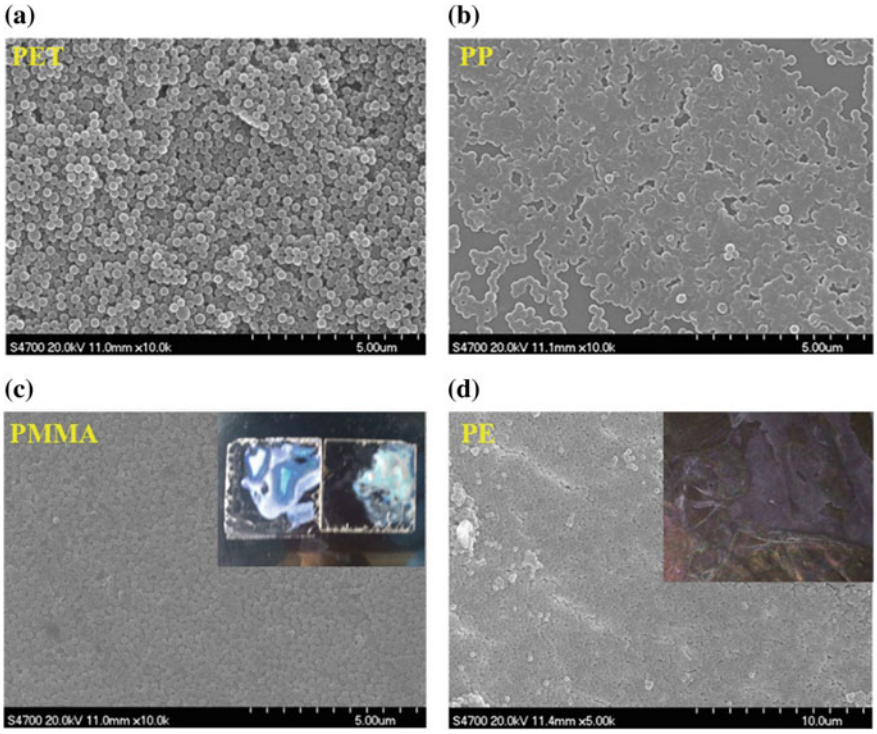

Fig. 1 SEM images of PET (**a**), PP (**b**), PMMA (**c**) and PE (**d**) surface grafted the amorphous photonic crystal. The inserted are optical photos of polymer films grafted the amorphous photonic crystal

immobilizing of microsphere dispersion on the surface of polymer films. As shown in Fig. 1, polymer films immobilized amorphous photonic crystals display single structural color.

3.2 Preparation of Free-Standing Film

When photoinitiator and cross-linker ETPTA (5%) were added in microsphere dispersion, amorphous photonic crystals separated from the polymer film, and transparent and flexible free-standing polymer film was fabricated. With the increase of cross-linker content, the space between particles became large, and the photograph of free-standing film displayed a distinct angle-independent non-iridescent structural color (Fig. 2a, b). From SEM images of free-standing amorphous photonic crystal polymer film, the particles are assembled disordered. And multiple diffraction rings were obtained by 2D fast Fourier transform-spatial information. These results indicated that the free-standing films showed

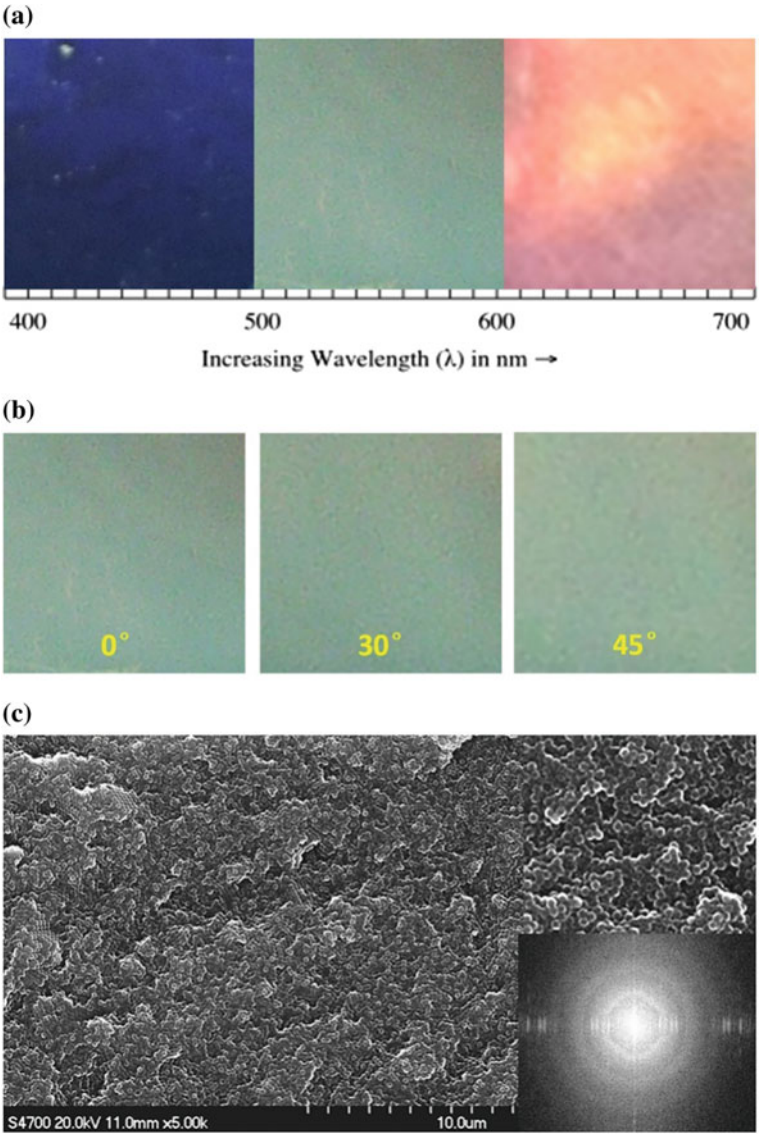

Fig. 2 **a** Optical photos of free-standing amorphous photonic crystal polymer film with different content cross-linker (5, 8, and 10%, based on weight of dispersion); **b** Optical photos of free-standing amorphous photonic crystal polymer film under different angles of view with 8% ETPTA; **c** SEM images of free-standing amorphous photonic crystal polymer film with 8% ETPTA (The inserted is multiple diffraction rings obtained by 2D fast Fourier transform-spatial)

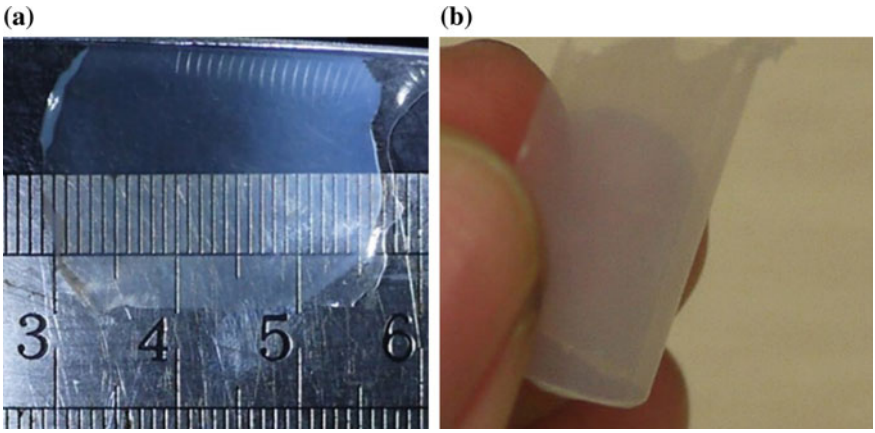

Fig. 3 Free-standing amorphous photonic crystal polymer film with good transparency and flexibility

angle-independent structural color (Fig. 2c) [7]. Moreover, free-standing films exhibit unique transparency and flexibility because of adding transparent and high molecular weight ETPTA (Fig. 3).

4 Conclusions

We have demonstrated that using polymer films (PET, PP, PMMA and PE) coated with poly (BPMA-NIPAM) as substrates, the amorphous photonic crystals of core (PSt)-shell (PMABP) structured microspheres are immobilized under UV-irradiation. Further, when cross-linker ETPTA was added into microsphere dispersion, transparent and flexible free-standing films with angle-independent structural color can be prepared. The structural color of free-standing films can be tuned by cross-linker content.

Acknowledgment The authors acknowledge funding from Science and Technology Plan of Beijing(Z171100002417025).

References

1. Zhao Y, Xie Z, Gu H, Zhu C, Gu Z (2012) Bio-inspired variable structural color materials. Chem Soc Rev 41:3297–3317
2. Shi L, Zhang Y, Dong B, Zhan T, Liu X, Zi J (2013) Amorphous photonic crystals with only short-range order. Adv Mater 25:5314–5320

3. Takeoka Y, Yoshioka S, Takano A, Arai S, Khanin N, Nishihara H, Teshima M, Ohtsuka Y, Seki T (2013) Production of colored pigments with amorphous arrays of black and white colloidal particles. Angew Chem Int Ed 52:7261–7265
4. Liu YN, Ma YH, Liu LY, Yang WT (2015) Facile synthesis of core-shell/hollow anisotropic particles via control of cross-linking during one-pot dispersion polymerization. J Colloid Interface Sci 445:268–276
5. Liu YN, Liu W, Ma YH, Liu LY, Yang WT (2015) Direct one-pot synthesis of chemically anisotropic particles with tunable morphology, dimensions, and surface roughness. Langmuir 31:925–936
6. Deng JP, Wang LF, Liu LY, Yang WT (2009) Developments, new applications of UV-induced surface graft polymerizations. Prog Polym Sci 34:156–193
7. Magkiriadou S, Park JG, Kim YS, Manoharan VN (2012) Disordered packings of core-shell particles with angle-independent structural colors. Opt Mater 2:1343–1352

Effect of Antimicrobial Packaging Film Coated with Ajowan and Cinnamon Essential Oil on Shelf Life of Fresh Chilled Pork

Wei Huang, Jianqing Wang, Haiyan Song, Qian Zhang and Guangfa Liu

Abstract This work was aimed to explore the effect of antimicrobial packaging film coated with ajowan and cinnamon essential oil (EO) on shelf life of fresh chilled pork. Antimicrobial compound solution was prepared with ajowan EO, cinnamon EO, polyvinyl alcohol, glycerol, corn starch and distilled water according to a certain proportion, and it was coated on the corona-treated PP/EVA film to prepare antimicrobial films. The fresh pork was divided into 5 groups and packaged in bags which was made of films as follow, the blank PP/EVA film was used as the control group, and the antimicrobial films contain combination EO with concentration of 0.4, 0.8, 1.2 and 1.6% were recorded as BF1, BF2, BF3 and BF4 group respectively, and all groups were stored at 4 °C. The total viable count (TVC), total volatile basic nitrogen (TVB-N), pH, TBARS value and sensory quality of pork were tested for evaluating the effect of antimicrobial packaging film on quality of pork. The results showed that BF4 antimicrobial film could reduce the increase of TVC, TVB-N, pH and TBARS value of pork significantly ($P < 0.05$), and the BF4 film was superior to other kinds of antimicrobial film on maintaining the sensory quality of fresh pork. In conclusion, the fresh chilled pork packed in BF4 film presented the best quality and its shelf life was extended for 4 days.

Keywords Ajowan essential oil · Cinnamon essential oil · Antimicrobial packaging film · Fresh chilled pork · Shelf life

W. Huang (✉) · J. Wang · H. Song · Q. Zhang · G. Liu
China Light Industry Key Laboratory of Food Packaging Materials and Technology, Tianjin University of Science & Technology, Tianjin, China
e-mail: huangwei@packagetest.net

G. Liu
e-mail: liuguangfa@tust.edu.cn

W. Huang
China Packaging Research & Test Center, Tianjin, China

P. Zhao et al. (eds.), *Applied Sciences in Graphic Communication and Packaging*, Lecture Notes in Electrical Engineering 477,
https://doi.org/10.1007/978-981-10-7629-9_97

1 Introduction

Pork is popular with Chinese consumers, and 54,870,000 tones pork were consumed in China in 2015 [1]. However, fresh chilled pork has only few days of shelf life in general, which is attributed to the quick growth of spoilage microorganisms and the lipid oxidation [2]. In recent years, some studies have found that many essential oils (EOs) from natural plants have significant antimicrobial activity against food spoilage microorganisms [3], and many essential oils have been studied for their effectiveness in food safety and preservation applications [2, 4].

Ajowan is mainly grown in India and Xinjiang Hotan region in China, which is mainly used as a cooking spice and as herbal medicine. Cinnamon is widely used as a spice and Chinese medicine in China. Some studies have shown that ajowan essential oil (EO) and cinnamon EO have good inhibit effect on food-borne pathogens [5, 6]. In this work, antimicrobial packaging films were prepared by coating antimicrobial compound solution contain ajowan EO and cinnamon EO on corona-treated PP/EVA film. The objective was to explore the effect of antimicrobial packaging film on shelf life of fresh chilled pork.

2 Materials and Methods

2.1 Materials

Ajowan EO extracted by steam distillation (46.22% of thymol, 19.03% of p-cymene, 22.41% of γ-terpinene, 3.23% of β-pinene, and 2.15% of eugeno). Cinnamon EO (83.09% of cinnamaldehyde, 1.58% of cinnamic acid, Ji'an Luyuan natural perfume oil refinery, Ji'an, China). Bromocresol green, ethylenediamine tetraacetic acid, were purchased from Tianjin Chemical reagents Co., Ltd. Thiobarbituric acid was purchased from Shanghai Kefeng Industry Co., Ltd. Magnesium oxide was purchased from Sinopharm Group Chemical Reagent Co., Ltd. The above reagents are of analytical grade. PP/EVA film was purchased from Wenzhou Quanlian packaging materials Co., Ltd. PVA 1788 was purchased from Shanxi Sanwei Group Co., Ltd.

2.2 Preparation of Antimicrobial Film

In previous experiments, the antimicrobial activity of ajowan EO, cinnamon EO, and combination EO of ajowan and cinnamon (the volume ratio were 2:1, 1:1, and 1:2 respectively) against 4 kinds of food-borne pathogens of Escherichia coli, Staphylococcus aureus, Bacillus subtilis, Salmonella were tested by the agar disk diffusion method described by Han [6], and the results showed that the inhibition

zone diameters of the three kinds of combination EO with different volume ratio were larger than that of the ajowan EO and cinnamon EO, in which the difference was not significant ($P > 0.05$). In order to obtain a wider antimicrobial activity, combination EO of ajowan and cinnamon with the volume ratio of 1: 1 was used to prepare antimicrobial packaging film. In order to prepared the antimicrobial coating solution, 6.0% PVA (w/v) was slowly dissolved in distilled water at 90 °C and stirring for 90 min, followed by adding 1% corn starch (w/v), 3.5% glycerol (v/v), and a series of concentrations (0.4, 0.8, 1.2, 1.6, 2.0%)of combination EO of ajowan and cinnamon with the ratio of 1:1 at 60 °C in order and stirring for 10 min, then treated with ultrasonic of 600 W for 60 min under the condition of polyethylene film for sealing, and standing for about 12 h to remove the bubbles. The antimicrobial coating solution was coated on corona-treated PP/EVA film by the coating machine of CU5/200 (Germany). Parameters of coating machine were as follow, rod pressure was 1 N, roller pressure was 1 N, coating speed was 6 m/min, heating temperature was 60 °C, and heating time was 180 s. In order to obtain better coating effect, the second coating was carried out according to the preceding coating process parameters. The antimicrobial film were marked as BF1, BF2, BF3, BF4, BF5, which contain combination EO with concentration of 0.4, 0.8, 1.2, 1.6, 2.0% respectively.

2.3 Sample Preparation

Fresh pork was purchased from an agricultural market in Tianjin, which was freshly slaughtered by market staff and was not involve ethical aspects issues. Pork samples approximately 200 g were cut using sterile knives in a sterile cutting table, which were divided into five groups stochastically. The control group pork samples (marked as CK) were packed with 10×18 cm^2 bags made of PP/EVA film without coating. The other groups were packed in 10×18 cm^2 bags made of BF1 to BF4 films. BF5 film was not selected for fresh-keeping experiment because its antimicrobial activity against food-borne bacteria such as E. coli was not significantly improved ($P > 0.05$) compared with BF4 film, this reason could be attributed to excessive oil result in an increase of viscosity of antimicrobial coating solution and lead to the amount of the antimicrobial coating solution reduced. All packaged pork samples were stored in freezer at a temperature of 4 °C, and their qualities were monitored on the 0th, 2nd, 4th, 6th, 8th, 10th, 12th, and 14th day.

2.4 Microbiological Analysis

The total viable count (TVC) was measured according to the Chinese national standard GB 4789.2-2016 with slight modification. In brief, 10 g pork meat was cut from the center of each sample, and then was crushed and homogenized in 100 ml

sterile saline for 1 min using a sterile homogenizer. Then the homogenized samples mixture were diluted 10^3–10^6 times, and the serial dilutions were spread on nutrient agar plate and incubated at 37 °C, and the TVC were counted after 48 h, which were expressed as lg CFU/g pork.

2.5 Measurements of pH

The pH of pork samples were measured according to the Chinese standard GB 5009.237-2016. Duplicate 10 g samples were crushed and homogenized in 100 ml distilled water for 1 min and the homogeneous mixture was filtered with double gauze. After 30 min, the pH value of the pork filtrate was tested using a PHS-25 pH tester (Shanghai Precision Science Instrument Co., Ltd, Shanghai, China).

2.6 Measurements of TVB-N

The total volatile basic nitrogen content (TVB-N) of pork sample was tested by the semimicro-quantitative nitrogent method according to GB 5009.228-2016 (Chinese standard).

2.7 Measurements of TBARS

The TBARS of pork samples was measured according to Shirong Huang's methods [7], which was expressed as mg malondialdehyde (MDA)/kg meat.

2.8 Sensory Evaluation

Sensory evaluation of pork samples was carried out by six selected postgraduate students (3 males and 3 females, ranging from 20 to 40). Sensory qualities of each sample was evaluated on the 0th, 2nd, 4th, 6th, 8th, 10th, 12th, and 14th day, mainly on color, odor, and overall acceptable indicators. The evaluation standard for sensory score was as follows: excellent sensory, score of 9; very good sensory, score of 8; good sensory, score of 7; acceptable sensory, score of 6; unacceptable sensory, score of < 6;

2.9 Statistical Analysis

The figures of experimental data were drawn with Excel 2007, and the significance analysis was carried out by using ANOVA in SPSS 17.0 software. The difference was considered significant when the value of P was less than 0.05.

3 Results and Discussion

3.1 Changes in TVC

The total viable count (TVC) is a key indicator to evaluate the degree of fresh meat rot, which is directly related to the quality of meat. It is generally believed that the TVC of fresh pork is less than 4.0 lg CFU/g, and its max acceptable TVC is 7.0 lg CFU/g [8]. The TVC of control and treated pork samples during refrigerated storage of 4 °C were shown in Fig. 1. The initial TVC of control pork (marked as CK) was approximately 3.2 lg CFU/g, and increased to 7.5 lg CFU/g after 8 days storage, which already exceeded the maximum acceptable limit (7.0 lg CFU/g). Similar to the control sample, the TVC of BF1 samples increased rapidly, and the value reached to 7.0 lg CFU/g on the 8th days. However, the increase rate of TVC in BF2, BF3 and BF4 sample was obviously lower than control and BF1 ($P < 0.05$). The TVC in the samples of control, BF1, BF2, BF3, and BF4 group were 8, 7.7, 7.2, 6.4 and 5.8 l g CFU/g respectively on the 10th days of storage, which showed a significant reduction in the TVC of pork with the increase in the concentration of essential oil in the antimicrobial film ($P < 0.05$). This phenomenon is due to the different concentrations of EOs in the 4 kinds of antimicrobial packaging film.

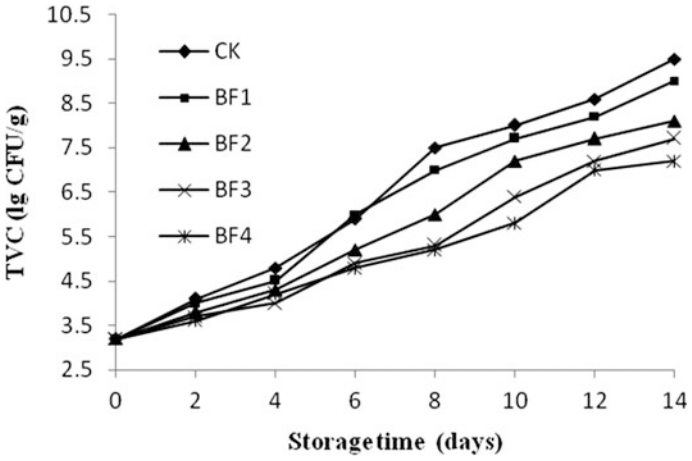

Fig. 1 Changes in TCV of fresh pork with different treatments during storage at 4 °C

The concentrations of EOs in BF1 and BF2 antimicrobial film was too low to inhibit the spoilage microorganisms growth in pork, BF3 and BF4 antimicrobial film released more ajowan EO and cinnamon EO, which could effectively inhibit the reproduction of microorganisms. Furthermore, the TVC in sample with the packaging of BF4 antimicrobial film was lowest in all samples because its higher concentrations of EO compared with the other antimicrobial films. A similar effect on the TVC of pork during storage has been also reported on other antimicrobial agents, such as chitosan nanoparticles added with cinnamon EO [9].

3.2 Changes in PH

The effect of different packaging film on the pH values of pork during storage at 4 °C was shown in Fig. 2. The initial pH value of all the pork samples was about 6.12, and the pH of all the fresh pork samples increased gradually during the storage period, the rise of pH was due to the growth of spoilage bacteria leading to the accumulation of alkaline components, this phenomenon can be confirmed by the increase in TVB-N (Fig. 3). However, the pH values of different antimicrobial films treatment groups were various. The pH of the pork in the control group increased most rapidly, and the pH reached 6.67 on the 6th day of storage. The pH value of the BF2, BF3 and BF4 samples was lower than the pH of the control sample. In addition, the pH value of BF4 group was significantly lower than the pH of BF1, BF2 and BF3 pork ($P < 0.05$). The treatment of BF4 was best efficacy for inhibiting the increase of pH in fresh chilled pork, and the pH of pork of BF4 was 6.71 at the 12th day, which was significantly lower than the pH in control pork of 7.0

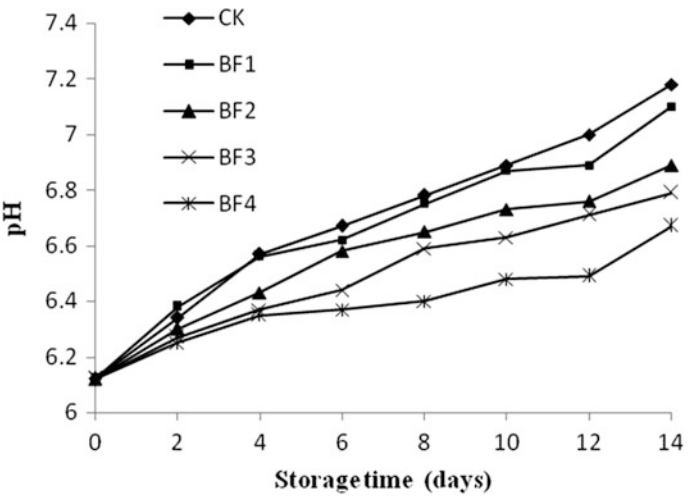

Fig. 2 Changes in pH of fresh pork with different treatments during storage at 4 °C

($P < 0.05$). This reason should attribute to ajowan EO and cinnamon EO effectively inhibiting the growth of microorganism to reduce its production of metabolized basic nitrogen compounds [2], and the higher pH in pork of CK, BF1, BF2 and BF3 may attribute to the higher TVC, compared to BF4 sample after 12 days storage. And this conclusion also consistent with Hu et al. [9] and Rahman's [10] reports, such as chitosan cinnamon essential oil nanoparticles, electrolyzed water and calcium lactate could inhibit the rise of pH in pork.

3.3 Changes in TVB-N

Total volatile basic nitrogen (TVB-N) refers to substances such as ammonia and amines produced by the decomposition of protein in animal foods due to the effects of various enzymes and microorganisms, which is an important indicator of meat spoilage [11]. As shown in Fig. 3, the TVB-N values of pork increased gradually during storage at 4 °C. TVB-N values in control sample increased from the initial value of 7.9–13.1 mg/100 g at the 4th day, and this value continues to rise to 17.5 mg/100 g at the 6th day, which exceeded the limit value of 15 mg/100 g in GB2707-2016 (national standard of China). TVB-N of BF1 and BF2 sample reached to 17.0 and 15.0 mg/100 g at the 6th day respectively, which had also exceeded or reached the limit value in national standard of China, whereas TVB-N value of BF3 and BF4 sample was 12.3 and 11.2 mg/100 g respectively. The TVB-N value of BF4 sample was significantly much lower than BF3, BF2, BF1 and control samples ($P < 0.05$), which was only 14.5 mg/100 g on the 8th day. The order of TVB-N value of pork packaged with different antimicrobial films at the 10th day as follow, BF4 (15.9 mg/100 g) < BF3 (21.3 mg/100 g) < BF2

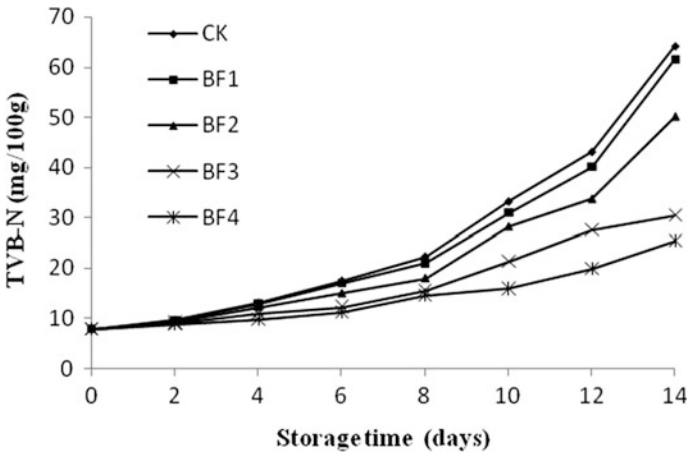

Fig. 3 Changes in TVB-N of fresh pork with different treatments during storage at 4 °C

(28.2 mg/100 g) < BF1 (31.0 mg/100 g) < CK (33.2 mg/100 g). The results of TVB-N was consistent with the above data of TVC (Fig. 1), and this is because TVB-N might be produced by the activity of endogenous enzymes and spoilage bacteria [12], and the increased TVB-N value could account for the rising pH values (Fig. 2). The results showed that BF4 antimicrobial packaging film could effectively reduce the increase of volatile nitrogen content in pork under the condition of 4 °C. Considering the TVB-N as indicator of the shelf life for fresh pork, the addition of 1.6% concentration of combination EO of ajowan and cinnamon was better than other samples, and the shelf life of fresh pork was prolonged to 8 days compared with the control pork of 4 days.

3.4 Changes in TBARS

Lipid oxidation is an important factors leading to the deterioration of fresh meat, and TBARS is used to evaluate the freshness of fresh meat and the degree of lipid oxidation [13], which is expressed as mg malondialdehyde (MDA)/kg meat. Hasty suggested that the TBARS value of fresh pork ranging from 0.202 to 0.664 [14]. Changes in TBARS of pork during storage at 4 °C were shown in Fig. 4. The TBARS values in each group of pork samples were gradually increased with the prolongation of storage period. The initial TBARS value of pork was 0.31 mg MDA/kg indicated that the lipid oxidation of pork is relatively low. The TBARS value of the control sample increased most rapidly, which was 0.31 mg MDA/kg on the 0th days, and increased to 1.18 mg MDA/kg at the 8th day, showing that lipid oxidation became more serious. Compared with the control sample, the increase of TBARS value in BF1, BF2, BF3 and BF4 samples were inhibited in some degree, and the TBARS value of the BF4 sample remained the lowest value during the

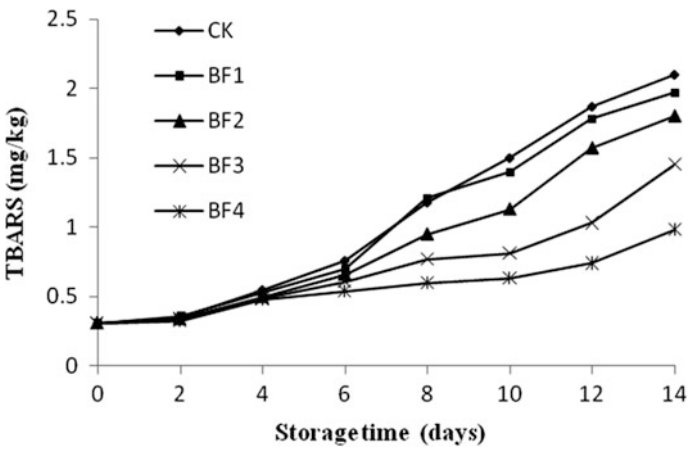

Fig. 4 Changes in TBARS value of fresh pork with different treatments during storage at 4 °C

storage. On the 8th day of storage, the TBARS value in control, BF1, BF2, BF3, BF4 samples were 1.18, 1.21, 0.95, 0.77 and 0.6 mg MDA/kg respectively. The increase of TBARS value of pork could attribute to the accumulation of lipid oxidation [15]. The results showed that the BF4 film could effectively reduce the lipid oxidation of fresh pork, this might be related to thymol and cinnamaldehyde in EO that mainly contributed to the antioxidant activity [16, 17].

3.5 Changes in Sensory

As shown in Fig. 5, sensory score of every pork samples properties decreased gradually with increase of storage time. The obvious spoilage of the control sample occurred at the 4th day, whereas the pork sample of BF1, BF2 and BF3 were spoiled on the 4th, 8th, and 8th day respectively. The best sensory score was observed in BF4 sample pork, and its sensory score was 6.0 at the 10th day, which was significantly better than the control pork sample ($P < 0.05$) and the other pork samples in antimicrobial films of BF1, BF2 and BF3. The reason for this phenomenon could be attributed to the addition of ajowan EO and cinnamon EO in the BF4 antimicrobial film effectively inhibited the growth and reproduction of spoilage microorganisms in pork, while the concentration of essential oil in the other three kinds of films (BF1, BF2 and BF3) were too low to inhibit spoilage microorganisms in pork. Hu et al. [9] also has reported similar extended shelf life for chilled pork by chitosan nanoparticles loaded with cinnamon essential oil in their previous studies.

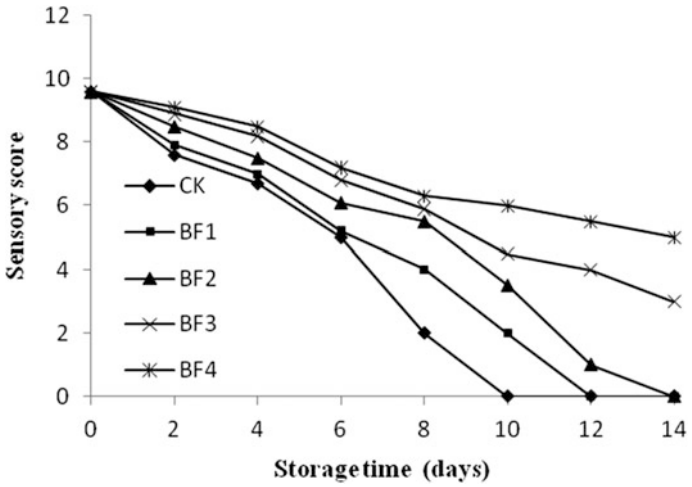

Fig. 5 Changes in sensory score of fresh pork with different treatments during storage at 4 °C

4 Conclusions

Pork sample stored in package bags made of antimicrobial films presented better quality than the control sample. The antimicrobial film of BF4 had significantly ($P < 0.05$) reduce the increase of TVC, TVB-N, pH value and TBARS value of pork, and the BF4 film was superior to other kinds of antimicrobial film on maintaining the sensory quality of fresh pork. In conclusion, the fresh chilled pork in BF4 film presented the best quality in all samples, and its shelf life was extended for 4 days. This work indicated that antimicrobial films in combination with ajowan EO and cinnamon EO could effectively prolong the shelf and increase the quality of fresh chilled pork. However, further studies need to carry out such as testing the release rate of antimicrobial agents.

Acknowledgements This work was supported by the "13th Five-Year" scientific research and innovation team of Tianjin University of Science & Technology (green food packaging and intelligent packaging) and the "12th Five-Year" National Science and Technology Support Project of People's Republic of China (Grant No.2015BAD16B05-02).

References

1. Wang K, Ye K, Zhu Y et al (2015) Prevalence, antimicrobial resistance and genetic diversity of Listeria monocytogenes isolated from chilled pork in Nanjing, China. LWT-Food Sci Technol 64(2):905–910
2. Cao Y, Gu W, Zhang J et al (2013) Effects of chitosan, aqueous extract of ginger, onion and garlic on quality and shelf life of stewed pork during refrigerated storage. Food Chem 141:1655–1660
3. de Carvalho RJ, de Souza GT, Honório VG et al (2015) Comparative inhibitory effects of Thymus vulgaris L. essential oilagainst Staphylococcus aureus, Listeria monocytogenes and mesophilicstarter co-culture in cheese-mimicking models. Food Microbiol 52:59–65
4. Paparella A, Mazzarrino G, Chaves-Lopez C et al (2016) Chitosan boosts the antimicrobial activity of Origanum vulgar essential oil in modified atmosphere packaged pork. Food Microbiol 59:23–31
5. Kedia A, Prakash B, Mishra PK et al (2015) Trachyspermum ammi L. essential oil as plant based preservative in food system. Ind Crops Prod 69:104–109
6. Han C, Wang J, Li Y et al (2013) In vitro antimicrobial activity and effect on e.coli integrity of cinnamon essential oil and rhubarb ethanol extract. Food Sci Technol Res 19:1155–1163
7. Huang S, Liu B, Ge D et al (2017) Effect of combined treatment with supercritical CO_2 and rosemary onmicrobiological and physicochemical properties of ground pork stored at 4 °C. Meat Sci 125:114–120
8. Tang X, Sun X, Wu VCH et al (2013) Predicting shelf-life of chilled pork sold in China. Food Control 32:334–340
9. Hu J, Wang X, Xiao Z et al (2015) Effect of chitosan nanoparticles loaded with cinnamon essential oil on the quality of chilled pork. LWT-Food Sci Technol 63:519–526
10. Rahman SME, Wang J, Oh DH (2013) Synergistic effect of low concentration electrolyzed water and calcium lactate to ensure microbial safety, shelf life and sensory quality of fresh pork. Food Control 30(1):176–183
11. Fan WJ, Sun JX, Chen YC et al (2009) Effects of chitosan coating on quality and shelf life of silver carp during frozen storge. Food Chem 115:66–70

12. Ruiz-Capillas C, Moral A (2005) Sensory and biochemical aspects of quality of whole bigeye tuna (Thunnusobesus) during bulk storage in controlled atmospheres. Food Chem 89(3): 347–354
13. Qin YY, Yang JY, Lu HB et al (2013) Effect of chitosan film incorporated with tea polyphenol on quality and shelf life of pork meat patties. Int J Biol Macromol 61:312–316
14. Hasty JL, Van Heugten E, See MT et al (2002) Effect of vitamin E on improving fresh pork quality in Berkshire- and Hampshire-sired pigs. J Anim Sci 80(12):3230–3237
15. Chouliara E, Karatapanis A, Sawaidis IN et al (2007) Combined effect of oregano essential oil and modified atmosphere packaging on shelf-life extension of fresh chicken breast meat, stored at 4 °C. Food Microbiol 24(6):607–617
16. Ramos M, Jiménez A, Peltzer M et al (2014) Development of novel nano-bio composite antioxidant films based on poly (lactic acid) and thymol for active packaging. Food Chem 162:149–155
17. Uchi H, Yasumatsu M, Morino-Koga S et al (2017) Inhibition of aryl hydrocarbon receptor signaling and induction of NRF2-mediated antioxidant activity by cinnamaldehyde in human keratinocytes. J Dermatol Sci 85:36–43

Study of the Influence of Preparation Conditions of γ-PGA Ester as a Food Packaging Material on the Biodegradation Performance

Wei Xiao, Zhihui Sun, Jia Liu and Jing Dong

Abstract As people enhance consciousness on food safety and environmental protection, the research of food packaging materials has been widely noted. Non-degradable disposable food packaging plastics as the most common food packaging materials have some disadvantage such as harmful substances migration, air pollution and waste of land resources. γ-PGA ester is a new kind of food packaging materials which attracted the attention of the researchers due to its non-toxic and biodegradable. This study analyzed the influence of preparation conditions of γ-PGA ester as a food packaging material on the biodegradation performance through the orthogonal experiment methods which provide references for the related researchers.

Keywords γ-PGA ester · Food packaging materials · Biodegradable

1 Introduction

Food is a great demand of FMCG which also produced a big proportion of packaging waste after eating. Most of the food packaging waste is made of plastic which is widely used because of its low cost and good performance [1]. But the processing of plastic food packaging waste is mainly based on landfill and incineration at present which could pollute the environment and waste the land resources seriously. In addition, the problem of food safety from the migration of harmful substances in the food packaging materials is also very prominent. So the development of food packaging materials with the characters of degradable, safe and non-toxic is

W. Xiao (✉)
College of Food Engineering and Packaging Science and Engineering Technology Laboratory, Harbin Commercial University, Harbin, China
e-mail: xiaoweianny@126.com

Z. Sun · J. Liu · J. Dong
Packaging Science and Engineering Technology Laboratory, Harbin Commercial University, Harbin, China

P. Zhao et al. (eds.), *Applied Sciences in Graphic Communication and Packaging*, Lecture Notes in Electrical Engineering 477,
https://doi.org/10.1007/978-981-10-7629-9_98

becoming a hot research spot. Such as the γ-PGA (γ-Poly Glutamic Acid) which is a poly amino acid material is nontoxic and biodegradable. But the γ-PGA cannot satisfy the requirements of the moisture barrier properties of food packaging materials because it has a large number of carboxyl [2]. Although esterification modification for the γ-PGA could improve the water resistance, the biodegradability will be affected by the modification conditions [3]. The influence of preparation conditions of γ-PGA ester as a food packaging material on the biodegradation performance was analyzed by the orthogonal experiment method in this research.

2 Experiments

2.1 Experiment Reagent and Instrument

The experiment reagents: γ-PGA, DMSO, hydrogen chloride, DMF, $NaHCO_3$, DBN, anhydrous ethanol, THF. All of the reagents are analytically pure. The experimental apparatus: threeneck flask, centrifuge tube, measuring cylinder, separatory funnel, the evaporating dish, pipette, etc. The experimental equipment: magnetic stirrer, drying oven, water bath pot, airing chamber, centrifuge, electronic balance, etc.

2.2 Methods

2.2.1 Modified of γ-PGA

γ-PGA and DMSO were put into the three neck flask heated to melt before the $NaHCO_3$ was joined. Then continuous reaction completely after bromine ethane was slowly drops into the mixture. The mixture was put into the cold hydrochloric acid aqueous solution which with the pH was 2 after the mixture was cooled to the room temperature to get the white sediment blob. The residue reagent of the sediment was soak washed with anhydrous ethanol and distilled water many times repeatedly, and the high purity product was get after vacuum drying. The modified equation of γ-PGA was shown in Fig. 1.

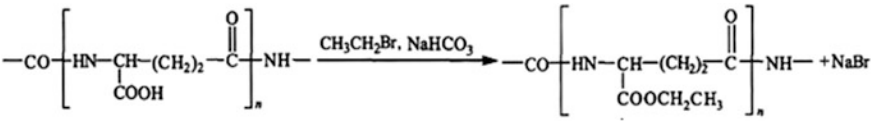

Fig. 1 Modified equation of γ-PGA

2.2.2 Preparation of the Film

Tape-casting technology was adopted in this experiment because it has the advantage of good quality, controllable and uniformity of the thickness of the film. The γ-PGA ester was heated until dissolved to paste in a small amount of DMSO, and a small amount of THF was added to increase the volume. The paste was put on the smooth glass plate, and was drying in the 80 °C. At last, the glass plate was put below 0 °C for hours after the solvent was evaporated completely and the surface was non-viscous to get the smooth and elastic film.

2.2.3 Biodegradability of the Film

Biodegradable materials will be decomposed into water and CO_2 in the soil, and the quality is reduce with the air evaporation [4]. But the degradation rate can be affected by the character of the material itself that the biodegradability of products are different because of the different preparation conditions. The effect of biodegradability of modified γ-PGA from three factors that were the reaction temperature, reaction solvent and reaction time was researched by orthogonal experiment method to get the best preparation reaction conditions of the biodegradable materials [5]. There were three factors and three grades in the experiment, so L9 (3^4) orthogonal table was selected as shown in Tables 1 and 2.

Table 1 Processing Factors and Grades

Grade	Factors		
	Temperature (°C)	Reaction time (h)	Solvent
1	50	40	DMSO
2	55	45	DMF
3	60	50	NMP

Table 2 Experiment project (L9 (3^4) orthogonal table)

Number	Factors		
	Temperature (°C)	Reaction time (h)	Solvent
1	1	1	1
2	1	2	2
3	1	3	3
4	2	1	3
5	2	2	1
6	2	3	2
7	3	1	2
8	3	2	3
9	3	3	1

Nine groups modified products which were prepared with different conditions were selected according to the orthogonal experiment table. Each group product was embedded in a certain quality of fresh soil sample box respectively, and the samples were weigh after the experimental period of 28 days. The degradation rate formula was shown in formula 1.

$$degradation\ rate = \frac{original\ quality - residual\ quality}{original\ quality} \times 100\% \quad (1)$$

3 Results and Discussion

The degradation rate could reach more than 28% in each group of product from modified that can be seen from the test results as shown in Table 3 which also showed the good biodegradable properties. Especially the products from the sixth experiment group have the best degradation rate which reached 50.33% in 28 days. The influence degree of the three factors on the degradation rate could be concluded through the range analysis of the orthogonal experiment result. The influence of temperature on the degradation rate was the most notable factor that can be seen from Table 3, the second notable factor was the reaction time, but the influence of different solvents was the least significant factor.

Table 3 Test results: residual mass

Number	Factors				
	Temperature (°C)	Reaction time (h)	Solvent		Degradation rate (%)
1	1	1	1	1	28.67
2	1	2	2	2	32.00
3	1	3	3	3	33.00
4	2	1	2	3	46.00
5	2	2	3	1	47.67
6	2	3	1	2	50.33
7	3	1	3	2	37.67
8	3	2	1	3	39.00
9	3	3	2	1	41.67
K_1	93.67	112.34	118.00	118.01	
K_2	144.00	118.67	119.67	120.00	
K_3	118.34	125.00	118.34	118.00	
R	50.33	12.66	1.67	2.00	

4 Conclusions

γ-PGA ester is a new kind of biodegradable material which was still less used as the packaging material at present which mainly due to its higher costs of the raw material, the relative research is less and immature. Orthogonal experiment was used to find out the optimal production conditions which can reduce the cost of research. In order to get a good biodegradable γ-PGA ester, the preparation conditions can be chosen as follow through the analysis of this study: the temperature was 55 °C, the reaction time was 55 h, and the solvent was DMSO. The result of the research could provide certain reference to the further study and marketing of the γ-PGA ester.

Acknowledgements This study is funded by Natural Science Foundation of Heilongjiang Province, China (NO. E2016049).

References

1. Ashiuchi M (2014) Microbial production and chemical transformation of poly-γ-glutamate. Microb Biotechnol 6:664–674
2. Wei X, Wang F, Sun Z (2016) Reviewed of esterification technology of γ-poly glutamic acid as the biodegradable food packaging material. Sci Technol Food Ind 37:383–386
3. de Cesaro A, da Silva SB, da Silva VZ (2014) Physico-chemical and rheological characterization of poly-gamma-glutamic acid produced by a new strain of *Bacillus subtilis*. Eur Polym 57:91–98
4. Fabra MJ, Castro-Mayorga JL, Randazzo W (2016) Efficacy of cinnamaldehyde against enteric viruses and its activity after incorporation into biodegradable multilayer systems of interest in food packaging. Food Environ Virol 8:125–132
5. Sanyang ML, Sapuan SM (2015) Development of expert system for biobased polymer material selection: food packaging application. J Food Sci Technol 52:6445–6454

Development of New Plastic Packaging Film for Food Packaging

Hui Liu, Wencai Xu and Dongli Li

Abstract In view of the problems existing in the field of food packaging safety in China, this paper introduces the research progress of new plastic packaging films for food packaging in recent years. The research results have important practical significance for promoting the function of food packaging and the effective application of new plastic flexible packaging film in the whole process of food production, circulation and consumption in china.

Keywords Food packaging · Flexible packaging · Film

1 Introduction

In plastic packaging materials, the use of thin film materials accounted for about 46% of the total amount of plastic packaging materials, plastics have been widely used in the production of the neighborhood, which accounted for the largest proportion of food packaging. Food flexible packaging material has advantages of lightweight, moisture resistance, resistance, easy processing and low cost, so the food packaging plastic flexible packaging film has good development prospects. However, in the process of production and use of flexible packaging film for food packaging, there are many problems in the quality of the material, including the poor health indicators and the poor physical and mechanical properties of the products. Therefore, domestic and foreign research institutions have been committed to the development of new food packaging film, some of the important practical value of the advent of plastic film for the continuous development of food packaging has made a contribution.

H. Liu (✉) · W. Xu · D. Li
Beijing Key Laboratory of Printing and Packaging Materials and Technology, Beijing Institute of Graphic Communication, Beijing, China
e-mail: 1170044657@qq.com

P. Zhao et al. (eds.), *Applied Sciences in Graphic Communication and Packaging*, Lecture Notes in Electrical Engineering 477,
https://doi.org/10.1007/978-981-10-7629-9_99

In this paper, the most representative functional food packaging films are reviewed, which include five kinds of high barrier film, new pearl film, edible film, degradable film and biodegradable film.

2 Novel Food Flexible Packaging Film

2.1 High Barrier Film

The main function of high barrier film were preventing oxygen, water vapor and other gases into the interior of the package, avoiding oxidation or deterioration of the packaging items, and preventing air from getting in. It was mainly used in meat processing products, agricultural products, seafood products, pickles and other packaging products. It has a very wide range of applications and were closely related to people's lives.

Li Jianxue and others used p-phthalic acid, m-phthalic acid, polyol and CIS 9,12-eighteen carbon two enol, and then the high resistance water vapor PET copolyester film was prepared. The water vapor permeability of the prepared PET film was 1.0 g/(m^2 24 h), which was lower than that of pure PET film [1]. Zhejiang Chengxin packing material Co., Ltd. researched high barrier coating which was based on the theory of gas barrier, and through the introduction of a variety of chemical monomers with oxygen shielding function. Acrylate polymers with special molecular structure and functional group were obtained by modification. At the same time, the using of nano technology enhanced the barrier properties and stability of polymer, and optimized its coating on the film substrate and processing performance. The new type of barrier polymer BARILAYR (acrylic polymer) using in the coating was oxygen barrier material, which has the advantages of green environmental protection and high barrier performance [2].

Li Hua used the plasma to prepare high barrier packaging film and to prepare silicon oxide, alumina and diamond as the barrier layer of PET, PI, PP and PE. The PET film (12 μm) had improved the barrier properties to nearly 70 times [3]. In early 1990s, China had finally realized the industrialization of PVDC film production, and PVDC casing film was produced by co-extrusion of PVDC film and other films. It was a kind of packing material with good comprehensive barrier property. It could effectively block the oxygen, water vapor, carbon dioxide and other gases, extend the shelf life of the product, but also has good chemical stability, mechanical workability, thermal shrinkage, oil resistance and so on. PVDC film not only as casing film used to pack all kinds of ham sausage and other food products, but also widely used in packaging of fresh fish, meat, tea, vegetables and other fresh foods. In addition, in the packaging of pharmaceuticals, electronic products, handicrafts and military goods moisture also showed that its uniqueness and superiority. Therefore, as a new type of high-tech packaging materials, PVDC film had been widely concerned [4].

2.2 New Pearlized BOPP

Opaque BOPP pearl film with pearl luster, low density, excellent flatness, good gas barrier and high visible light covering power, was widely used in the package of fruit, ice cream, candy, soap, and other high-end gifts. At the same time, it was a good base for printing. The main component of BOPP pearl masterbatch was $CaCO_3$. Because of the low adhesion of masterbatch to PP, it can form a uniform hole. When the light entered the hole, the interference light of multi level formed the pearl effect [5, 6].

At present, the domestic and international production of pearlescent film generally used three layers of extrusion process, the structure of the film was ABC (single sided heat sealing type) or ABA (double sided heat seal type). The disadvantage of this film was that the pearl masterbatch and whitening masterbatch added in the core layer and greatly weakened the pearl effect of the film. Based on the research of Luoyang Petrochemical Co., Ltd., they made some improvement on the formula of the master batch of the film and got five layers of extruding polypropylene film. Because the Pearl masterbatch and whitening masterbatch were added in the core layer and sub surface, the film structure was ABCBD (single side heat sealing type) or ABCBA (double sided heat seal type) [7].

2.3 Edible Film

Edible film is a kind of green packaging material. It was a kind of edible film with specific function, which was made up of biological macromolecules.

Potato starch was main raw material, potato acetate starch, carboxymethyl cellulose sodium and potassium aluminum sulfate was additive. The preparation conditions of modified potato starch film and the effect of additives on the film properties were studied. The results showed that the tensile strength, elongation and water vapor permeability of the modified starch film were significantly higher than that of the original starch film [8]. The effects of different plasticizers on the properties of cassava starch edible films were studied. Glycerol, sorbitol and gelatin were used as plasticizers. Increasing the content of gelatin can improve the moisture permeability, and using sorbitol as plasticizer, the tensile strength and elongation at break were better than glycerol [9]. Study on the application of corn alcohol soluble protein and soy protein isolate composite polyethylene film in olive oil packaging. The results showed that the composite film of the oxygen transmission rate was significantly lower than that of low density polyethylene, the film can reduce the degree of oxidation of olive oil [10]. In University of Wisconsin, the different ratio of protein, fatty acid and polysaccharide were combined together to make edible film. The larger the fatty acid molecules, the better the water resistance. Due to the

different types of protein and polysaccharide, the permeability, water resistance, transparency and strength of edible films were different, which could provide different food packaging [11, 12].

2.4 Degradable Film

Degradable film not only has the function of traditional plastic film, but also can be degraded in the natural environment by the microorganisms in soil and water, or by the action of ultraviolet rays in sunlight. The utility model solved the recycling problem of the plastic packaging film which was not easy to be degraded, and could also protect the natural environment.

By using epichlorohydrin modified starch, LLDPE and LDPE blending extrusion and then joining EPDM as compatibilizer could improve the mechanical properties of degradable film. Instead of common mode with rotary die head could increase the content of starch film. The degradable films with uniform starch content of 70% and thickness of 0.012 mm were prepared [13]. Luffa extract (LF), micro crystalline cellulose (MCC), polyvinyl alcohol (PVA) and ethylene vinyl acetate copolymer (EVA) were melting blend in different proportion. Biodegradable films with controlled release of antimicrobial agents were prepared. When the concentration of LF in the casting film was higher, the concentration of tannins and glycosides was higher and the inhibitory effect on the microorganisms was stronger. When the amount of LF/MCC was 20%, compared with the control group, the antibacterial property of the cast film was increased by 61.5%, and under the condition of compost, 44.8% of the film could degrade after 20 days [14].

2.5 Water Soluble Film

Water soluble film is a new type of green packaging material, which has the characteristics of complete degradation, safe and convenient using. As a new kind of packaging material, polyethylene film had attracted much attention from researchers at home and abroad for its good physical properties such as water solubility and transparency. PVA could be degraded by microorganisms, microbial degradation of PVA had became a research hotspot in the field of environmental science.

In order to study the degradation of PVA water soluble packaging film, the degradation of PVA was studied in aqueous solution and then the membrane was prepared according to the best degradation of PVA [15]. Polyvinyl alcohol was used as the main raw material by Chen Zhizhou, and the water soluble gel with solid content of 15–18% was prepared by adding reinforcing agent, plasticizer, emulsifier and film removing agent. By single factor test and orthogonal test of water soluble polyvinyl alcohol film, the preparation and process conditions were

studied. The results showed that when the concentration of PVA was 11%, soluble starch was 1%, glycerol 4%, Twain 80 was 1%, silicone oil was 0.8%, and drying 20 min at 80–90 °C, water soluble film with better performance was obtained [16].

3 Summary

The continuous development of new food flexible packaging film provided the impetus for the development of food packaging. It was a hot spot in the field of food packaging both at home and abroad, and also an important profit growth point in the packaging industry in the future. The improvement of living standards, the extend of the product logistics supply chain and consumers paying more attention on food quality and safety provided a broad market space for the future application of new food flexible packaging film. Although our country started later than developed countries in this area, it developed rapidly. If the packaging industry can seize the opportunity, and constantly improve the cost of product packaging, quality, reliability and security, will be able to make a difference in the packaging industry technology upgrades. If the packaging industry can seize the opportunity and constantly improve the cost-effective, quality, reliability and safety of product packaging, packaging technology upgrading will certainly have a good role in promoting the packaging industry.

Acknowledgements This work was financially supported by the National major scientific instruments and equipment development—Development and application of micro scale high speed visual quality inspection (2013YQ140517).

References

1. Li J, Luo C, Hu J, Zhang S (2013) Study on the preparation of high barrier water vapor PET copolyester film. Insulat Mater 46(5):17–20
2. Shu X, Zhou H (2015) New type of high resistance oxygen packaging film. Plast Packag 25(6):22–25
3. Li H, Yang L, Chen Q (2015) High barrier film fabrication technology knock on the door of barrier packaging. Print Ind 5:87–88
4. Cheng X (2012) Processing and application of high barrier PVDC materials. PVC 40(10): 22–26
5. Zhou J, Zhao Y, Mai J (2005) BOPP pearlescent film and its production process. Plast Ind 33 (3):242–244
6. Shi W, Gao X (2009) Study on the production technology of BOPP wide line pearl film. Plast Packag 19(4):27–30
7. Cao Y (2009) Development and application of five layer extrusion BOPP film. Henan Chem Ind 5:21–23
8. Ma B, Yu H, Tang H et al (2008) Modified potato starch film. J Grain Oil Process 10:101–104

9. Fakhoury FM, Martelli SM, Bertan LC et al (2012) Edible films made from blends of manioc starch and gelatin T influence of different types of plasticizer and different levels of macromolecules on their properties. LWT Food Sci Technol 49(1):149–154
10. Cho SY, Lee SY, Rhee C (2010) Edible oxygen barrier bilayer film pouches from corn zein and soy protein isolate for olive oil packaging. LWT-Food Sci Technol 43:1234–1239
11. Yi CL, Yu Z (2015) Research progress of edible packaging films. Packag Food Mach 33(4):50–55
12. Yin S (2014) Advances in the application of edible films in animal food. China Brew 33(8):29–32
13. Tang Y, Xu L, Yu L et al (2013) Study on the preparation and properties of starch based biodegradable films. China Plast 6:70–74
14. Xu W, Liu P, Liao R et al (2015) Study on the preparation and properties of biodegradable antibacterial film. Packag Eng 36(11):1–9
15. Yi X (2015) Study on biodegradability of polyvinyl alcohol water soluble packaging film. Hunan University of Technology
16. Chen Z, Mou JL, Wang L et al (2008) Study on production process of polyvinyl alcohol water soluble film. J Agric Eng 24(7):247–250

Preparation and Characterization of Salicylic Acid/Polylactic Acid Composite Packaging Materials

Xing Yin, Cheng Sun, Mingyue Tian and Yuan Wang

Abstract Salicylic acid (SA) is widely used in postharvest storage of fruits and vegetables. It was added to the polylactic acid (PLA) film. And then the antibacterial rate, mechanical properties, moisture permeability of the composite packaging materials were tested. The crystallization properties and morphology were measured by X ray diffraction and scanning electron microscopy. The results showed that when the mass fraction of SA was 6%, the antibacterial rate against Escherichia coli reached to 97.63%, the water vapor permeability coefficient was 11.4×10^{-14} g cm/(cm^2 s Pa). With the mass fraction of SA increased, the tensile strength decreased, the breaking elongation increased obviously. The comprehensive performance of the composite packaging material was improved.

Keywords Poly lactic acid · Salicylic acid · Composite packaging material Fresh-keeping packaging

1 Introduction

Food is susceptible to microbial invasion and then rot. Antibacterial packaging materials can kill or inhibit microbial growth to extend its shelf life [1, 2].

Polylactic acid (PLA) is a kind of renewable polymer material, which has sufficient source and can be degraded naturally [3–7]. So it is called environmental friendly polymer material.

X. Yin (✉) · C. Sun
Packaging and Printing Engineering College, Tianjin University of Science and Technology, Tianjin, China
e-mail: yvette8030@163.com

X. Yin · M. Tian · Y. Wang
Packaging and Printing Engineering College, Tianjin Vocational Institute, Tianjin, China

P. Zhao et al. (eds.), *Applied Sciences in Graphic Communication and Packaging*, Lecture Notes in Electrical Engineering 477,
https://doi.org/10.1007/978-981-10-7629-9_100

Salicylic acid (SA) is the white powder and soluble in organic solvents such as alcohols, ketone and ethers. It is extracted from willow bark and widely used in postharvest storage of fruit and vegetables [8–10].

SA was dissolved in PLA solution and then the film was scraped out. The antibacterial rate, mechanical properties and moisture permeability of the composite packaging material were tested. The crystallization properties and morphology were measured by scanning electron microscopy (SEM) and X ray diffraction (XRD). The best proportion of antibacterial agent was obtained according to the antibacterial effect.

2 Materials and the Method

2.1 Materials

PLA, the United States NatureWorks. SA, methylene chloride, anhydrous ethanol, sodium chloride and Twain 80, Tianjin wind boat chemical reagents Limited. Escherichia coli and Staphylococcus aureus, College of Biological Engineering, Tianjin University of Science and Technology. Agar powder, beef extract and peptone, Beijing Aoboxing Biotechnology Co., Ltd.

2.2 Composite Packaging Material Preparation

PLA and SA were put into the oven at 30 °C before the experiment. First, the SA was dissolved in a little anhydrous ethanol. And then it was poured into the CH_2Cl_2. Finally, PLA was added until all of them dissolved. In order to ensure the uniformity of the film, the automatic film scraping machine was used with a fixed speed. The composite film was placed in the oven at 40 °C in order to CH_2Cl_2 was removed completely. The composite packaging film was obtained. The antibacterial rate was measured to obtain the best proportion of SA/PLA composite packaging film. The mass fraction of SA was 2, 4, 6, 8 and 10% respectively.

2.3 Properties of Composite Packaging Material

2.3.1 Test of Antibacterial Rate

The bacterial liquid was sucked on to the antibacterial film, and then it was covered by PE film and the bacteria were cultured. After 24 h, the antibacterial film and the covering film were repeatedly washed with 20 ml eluent, and 100 μL bacterial liquid was inoculated on the nutrient agar. The viable bacteria were counted after 24 h.

2.3.2 Test of Tensile Property

The Sample of composite packaging film was cut as the size of 15 mm × 150 mm. And it was measured with universal tensile testing machine at the tensile speed 50 mm/min. Each proportion sample was tested for 10 times (deviation range ± 5%).

2.3.3 Test of Water Vapor Permeability

The sample was cut with an area of 33.18 cm^2. The water vapor permeability of the sample was measured at 38 °C, RH90%. Each proportion sample was tested for 5 times (deviation range ± 5%).

2.3.4 SEM Analysis

The sample was sprayed first, and then the plane and section morphology were scanned by electron microscopy (Hitachi, S4800, scanning voltage 10 kV).

2.3.5 Wide Angle X Ray Diffraction (XRD) Analysis

The crystalline performance was measured by Rigaku D/max 2500 PC type X-ray diffractometer (Japanese science). The accelerating voltage was 40 kV, current intensity was 200 mA, scanning angle was from 5° to 50°, and scanning rate was 5°/min.

3 Results and Discussion

3.1 Antibacterial Properties of SA/PLA Composite Packaging Materials

According to Fig. 1, SA/PLA composite packaging material had an obvious bacterial effect on Staphylococcus aureus and Escherichia coli. And the antibacterial effect increased as the content of SA increased. Antibacterial effect on Escherichia coli was better than Staphylococcus aureus. When the mass fraction of SA was 6%, the bacterial rate against Escherichia coli reached to 97.63%. Because of SA could destroy the microbial fimbriae, flagella and biofilm in the period of its formation and activity.

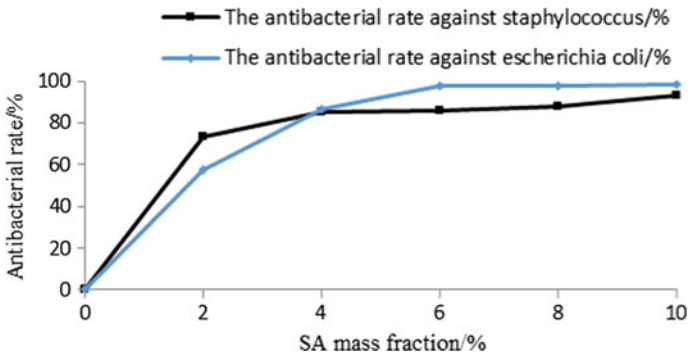

Fig. 1 Effect of SA content of the composite packaging material against staphylococcus aureus rate and escherichia coli rate

3.2 Tensile Properties of SA/PLA Composite Packaging Materials

When the mass fraction of SA was 0, 2, 4, 6, 8, 10%, the average thickness of the film was 64.58 ± 0.14, 75 ± 0.12, 75.01 ± 0.65, 78.74 ± 0.73, 78.74 ± 0.9 and 83.07 ± 0.96 μm. According to Fig. 2, the tensile strength of the composite packaging material decreased with the content of SA increased. When the mass fraction of SA was 2, 4, 6, 8 and 10%, the tensile strength decreased to 31.43, 23.26, 18.99, 15.44 and 14.54 MPa respectively. Because of with the increase of SA, the structure of PLA was destroyed, and the tensile strength of antibacterial film decreased.

The breaking elongation of the composite packaging materials increased with the increase of the content of SA. When the mass fraction of SA reached 10%, the breaking elongation reached to 256%. When the mass fraction of salicylic acid was 2, 4, 6 and 8%, the breaking elongation were 6, 34, 83 and 253% respectively. The toughening effect of composite packaging materials added with SA was obvious. The interaction between the carbonyl in PLA with the hydroxyl in the SA generated.

Fig. 2 Effect of SA content on tensile property of SA/PLA composite packaging material

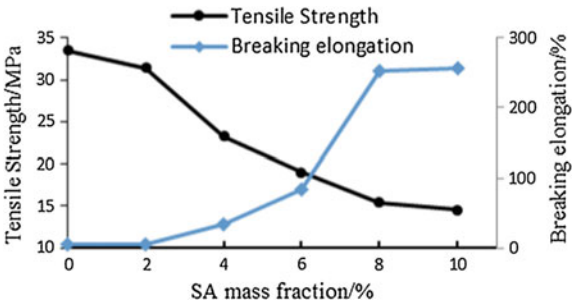

3.3 Water Vapor Permeability of SA/PLA Composite Packaging Materials

The water vapor permeability coefficient of SA/PLA composite packaging material was shown in Fig. 3. The water vapor permeability coefficient decreased first and then increased as the content of SA increased. When the mass fraction of SA reached 2%, the water vapor permeability coefficient was least that was 6.76×10^{-14}g cm/(cm^2 s Pa). Because SA penetrated into the amorphous region of PLA and the water vapor permeability decreased. However, when the mass fraction of SA was more than 2%, the SA permeated into the crystalline region of PLA. The structure of the bacterial film destroyed, which led to water vapor permeation increase [11]. The water vapor permeability coefficient of 6%SA/PLA composite packaging material was 11.4×10^{-14} g cm/(cm^2 s Pa).

3.4 XRD Analysis of SA/PLA Composite Packaging Materials

Figure 4 showed the XRD spectrum of PLA film and 6%SA/PLA composite packaging material. The characteristic peak of pure PLA was $2\theta = 16.6°$, and it showed that the crystallinity of pure PLA used in laboratory was poor. When 2θ were 10.9°, 15.3°, 17.2°, they were characteristic diffraction peaks of SA [12, 13], which didn't appeared in the XRD spectrum of 6%SA/PLA composite packaging material. At the same time, the peak height of 6%SA/PLA composite packaging material increased at $2\theta = 16.6°$, which indicated that SA increased the crystallinity of PLA.

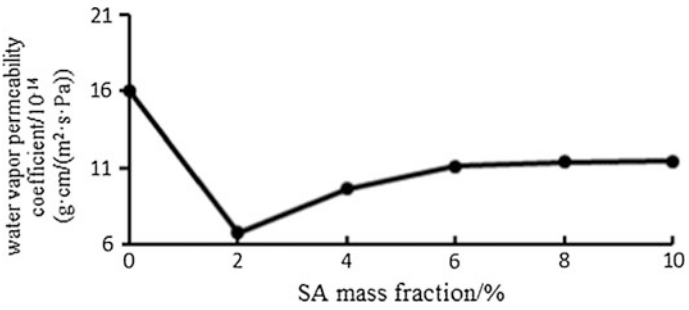

Fig. 3 Effect of SA content on the water vapor permeability coefficient of SA/PLA composite packaging material

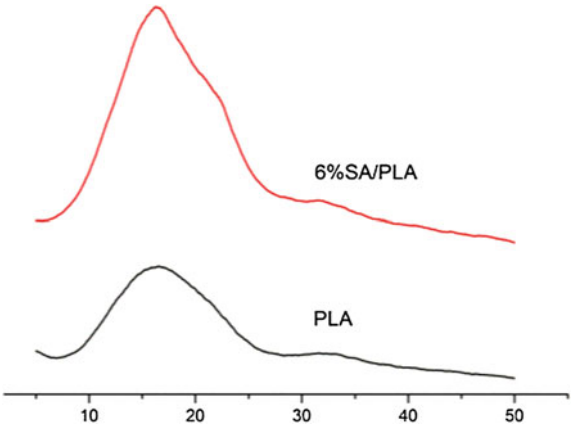

Fig. 4 XRD spectra

3.5 *Morphology of SA/PLA Composite Packaging Materials*

Figure 5a was the plane SEM photo of pure PLA film. The surface structure of pure PLA was relatively smooth. Figure 5b was the plane SEM photo of 6%SA/PLA composite packaging material. Compared Fig. 5a with b, it showed that the compatibility between SA and PLA was good.

Figure 6 were section SEM photos of PLA and 6%SA/PLA composite packaging materials. According to Fig. 6a, the pure PLA film has a layered structure and was easy to break. According to Fig. 6b, the section photo of 6%SA/PLA composite packaging film was relatively smooth, but there were long strip pores in it.

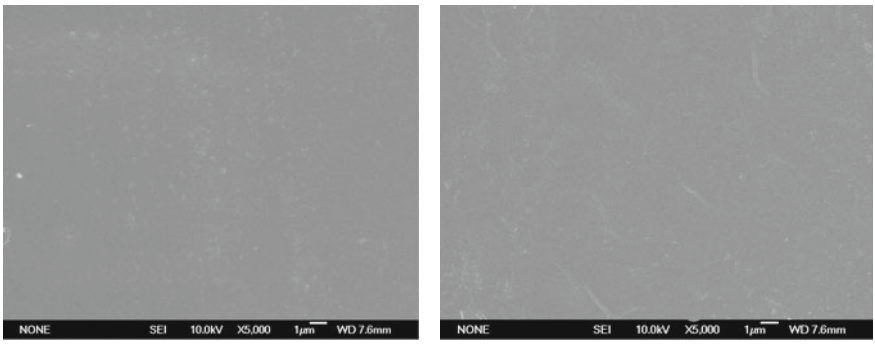

(a) Pure PLA (b) 6%SA/PLA antibacterial film

Fig. 5 Plane SEM photos of PLA and 6%SA/PLA composite packaging material

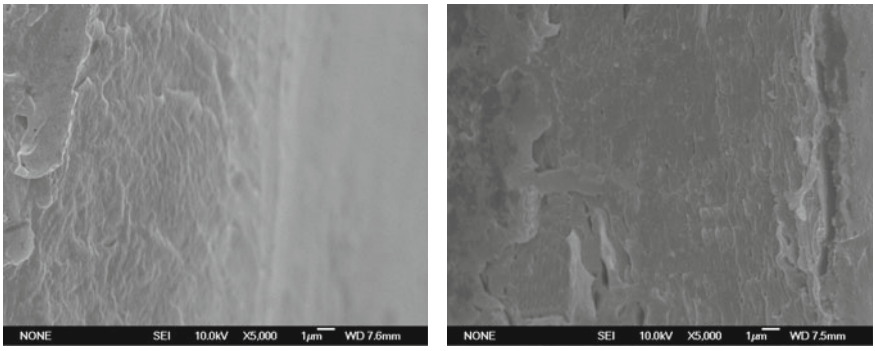

(a) Pure PLA (b) 6%SA/PLA antibacterial film

Fig. 6 Section SEM photos of PLA and 6%SA/PLA composite packaging material

4 Conclusion

(1) (1)The SA/PLA composite packaging material had significant antibacterial effect on Escherichia coli and Staphylococcus aureus. When the mass fraction of SA was 6%, the antibacterial rate against Escherichia coli reached to 97.63%.
(2) As the increase of the mass fraction of SA, the tensile strength decreased but breaking elongation increased obviously. And water vapor permeability coefficient first increased and then decreased. The water vapor permeability coefficient of 6%SA/PLA antibacterial film was 11.4×10^{-14} g cm/(cm^2 s Pa).
(3) The characteristic peak of pure PLA was $2\theta = 16.6°$, the peak height of 6%SA/PLA composite packaging material increased as the SA was added. According to the plane and section SEM photo, it showed that the compatibility between SA and PLA was good.

References

1. Xuehong L, Jinzheng Y, Xueming X (2008) Research and application progress of antimicrobial food packaging technology. J Food Res Dev 29(10):115–119
2. Xingjun H, Yan L (2010) Classification application and prospect of intelligent packaging. J Print Ind 03:24–27
3. Ashish D, Binulal N, Anitha A (2010) Preparation of poly(lactic acid)/chitosan nanoparticles for anti-HIV drug delivery applications. J Carbohydr Polym 79:114–124
4. Juan L (2010) Research on the preparation and properties of high performance poly(lactic acid) composites. MA thesis, Changchun Jilin University, Changchun, China
5. Xing Y, Cheng S, Zhiqiang G, Li X (2017) Preparation and properties of nano zinc oxide/poly lactic acid antibacterial packaging films. J Lect Notes Electr Eng. https://doi.org/10.1007/978-981-10-3530-2_126

6. Arias A, Heuzey MC, Huneault MA, Ausias G, Bendahou A (2015) Enhanced dispersion of cellulose nanocrystals in melt-processed polylactide-based nanocomposites. J Cell 22(1): 483–498
7. Guodong F, Chunmei Zh (2014) Research progress on application of polylactic acid in medical field. Sci Technol Rev 28(19):103–107
8. Shujuan W, Ming Ch, Jinyin Ch (2012) "Suichuan kumquat" effect of salicylic acid on postharvest physiology and storage effect. J Fruit Sci 29(6):1110–1114
9. Guoxing Zh, Chunle Zh, Hao H (2006) Inhibition and antibacterial action of salicylic acid. J Xiamen Univ Nat Sci Ed 46:19–20
10. Mohamadreza A, Morteza SA (2010) Impact of salicylic acid on post-harvest physiology of horticultural crops. J Food Sci Technol 21:502–509
11. Shuaifeng H, Yong Zh, Fuxin Y (2016) Preparation and properties of antibacterial films of sorbic acid-LDPE. J Packag Eng 05:15–19
12. Changlong Ch, Yanwei W, Xiaolong L, Xiuqin Y, Xiang Y (2015) Study on crystallization behavior of PLA/PEG composites. J Plast Technol 02:38–41
13. Xuan L, Mingchun L, Meihua X, Mengmeng Ch (2012) Preparation and properties of salicylic acid chitosan/PVA blend membrane. J Polym Mater Sci Eng 12:122–125

Study on Packaging Properties of Biomass Materials Made by Bagasse Pith

Zhiyu Ma and Yanna Lv

Abstract The thermoplastic starch (TPS)-based biomass packaging materials with different amounts of bagasse pith (BP) (0, 5, 10, 15, 20 and 25% relative to oven dry starch) were prepared by melting blend methods, and the effects of BP contents on the packaging properties were investigated. Results of Fourier Transform Infrared (FTIR) illustrated that the intermolecular hydrogen bondings forms in BP and TPS. TPS could restrain starch retro gradation with increasing BP content. The tensile strength, flexural strength and flexural modulus increased with increasing BP content, while elastic modulus increased first and then decreased, and the maximum value was achieved by TPS/BP with 20 wt% BP content. The different effects on water absorption of TPS/BP were observed at 43 and 100% RH. The surface morphology of tensile fracture and flexural fracture analyzed by scanning electron microscopy (SEM) revealed strong facial interactions in BP and TPS with increasing BP content.

Keywords Bagasse pith · Biomass packaging material · Thermoplastic starch Packaging properties

1 Introduction

In recent years, with the strengthening of people's awareness of ecological crisis, resource and environmental problems caused by waste plastic packaging has become a global issue of concern. So the development of renewable, recyclable, sustainable utilization of biomass packing material is worth the attention of the environmental pollution control. In terms of quantity, biomass resource is the only alternative to fossil resources for a class of renewable resources. It is estimated that the world total biomass stock is about 1.7 trillion tons and the annual biomass

Z. Ma · Y. Lv (✉)
School of Light Industry and Chemical Engineering, Dalian Polytechnic University, Dalian, China
e-mail: lvyn@dlpu.edu.cn

P. Zhao et al. (eds.), *Applied Sciences in Graphic Communication and Packaging*, Lecture Notes in Electrical Engineering 477,
https://doi.org/10.1007/978-981-10-7629-9_101

produced is about 170 billion tons, which are enough to support the survival and development of human beings [1].

Agricultural and forestry waste is one of good biomass resources. If not effectively utilized, it would cause waste of resources and environmental pollution problems. Bagasse pith is one kind of waste materials of sugar and paper industry, which is mainly used for heating and power generation, but its actual combustion heat value is lower [2]. In order to improve the utilization value and economic value of bagasse pith, composite materials (TPS/BP) were prepared using bagasse pith (BP) and thermoplastic starch (TPS) in this experiment. The effects of BP content on the mechanical properties and water resistance of the composites were studied, and the mechanism of BP enhanced TPS was analyzed by FTIR and scanning electron microscopy.

2 Experimental

2.1 Material

Corn starch procured from Changchun Dacheng Corn Development Co., Ltd. Bagasse pith (BP) were over by 40 standard inspection sieve, which procured from Jiangmen Sugarcane Chemical Factory (Group) Limited by Share Ltd. Glycerol, urea and stearic acid were purchased from Tianjin Baishi Chemical Co., Ltd., which were analytical grade.

2.2 Instruments and Equipment

Torque rheometer PolyLab QC (Thermo Fisher Scientific), press vulcanizer 50T (Guangzhou Feili Rubber Equipment Co., Ltd.), microcomputer control electronic universal testing machine CMT4204 (Shenzhen Xinsansi Material Detection Co Ltd.), fourier transform infrared spectrometer Vecto3 (German Bruker Co., Ltd.) and scanning electron microscope S-3700N (Hitachi Limited) we used in this study.

2.3 Sample Preparation

The corn starch, glycerin/urea (mass ratio 1:1) and lubricant were added to the high speed mixer at room temperature for 10 min, and then put them into the bag to seal the placement of 24 h. Then the bagasse pith (0, 5, 10, 15, 20 and 25% relative to oven dry starch) was mixed with other raw materials according to the proportion of the raw starch and added to the torque rheometer to prepare the thermoplastic starch

(TPS)-based biomass packaging composite materials with bagasse pith (BP). The composites were heat pressed at a temperature of 130 °C using vulcanizer at a pressure of about 3 MPa for 5 min. Then the composites were cold pressed to room temperature to prepare standard test strip.

2.4 Performance Testing

Tensile property were tested according to the GB/T 1040.2–2006 with tensile speed of 50 mm/min and ambient temperature of (23 + 2) °C.

Hygroscopicity: The TPS/BP samples were placed in the oven and dried at 105 °C for 10 h, which is flowed by weighing the dry weights. And the samples were placed in a sealed container filled with distilled water at (25 ± 2) °C conditions, which is flowed by weighing the wet weights every 6 d. The water absorption of the samples was calculated according to formula (1).

$$\text{Water absorption} = \frac{W_2 - W_1}{W_1} \times 100\% \quad (1)$$

Formula 1 W_1 is the dry weight of the sample and W_2 is the wet weight of the sample.

3 Results and Discussion

3.1 Infrared Spectroscopy Analysis

The TPS/BP composites with different BP content were characterized by FT-IR spectra, and the results show in Fig. 1. The absorption peak at 3332 cm^{-1} is caused by –OH stretching vibration in TPS. And the absorption peak moved to lower frequencies 3323 and 3273 cm^{-1} respectively in TPS/BP composite, it is indicated that intermolecular hydrogen bonds are formed between BP and TPS matrix. The study of Dean et al. [3] shows that the formation of hydrogen bond makes the electron cloud density averaged, so that the frequency of stretching vibration is reduced. It is worth noting that the C–O stretching vibration wave number of the C–O–H group in TPS reduces from 1149 to 1145 cm^{-1} in the TPS/BP, indicating that the C–O–H group in TPS can form a hydrogen bond with BP.

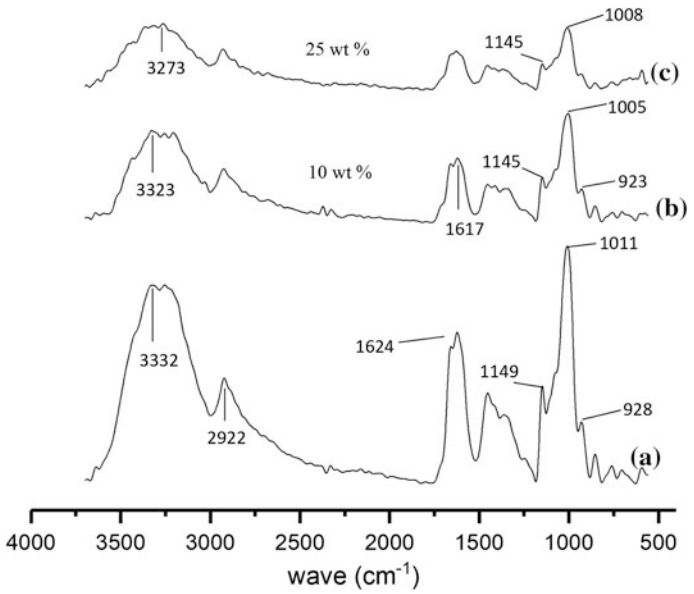

Fig. 1 FT-IR spectra of TPS/BP composites at different bagasse pith loading, **a** 0; **b** 10; **c** 25

3.2 Mechanical Properties of TPS/BP Composites

Figure 2 shows the effect of BP content on the tensile properties of TPS/BP composites. The tensile strength and tensile modulus of TPS/BP composites are significantly improved compared with TPS without BP, and this result is consistent with the literatures [4]. This is mainly because the similar chemical structure of cellulose in BP and starch can produce a strong binding force between the interface of starch and bagasse pith.

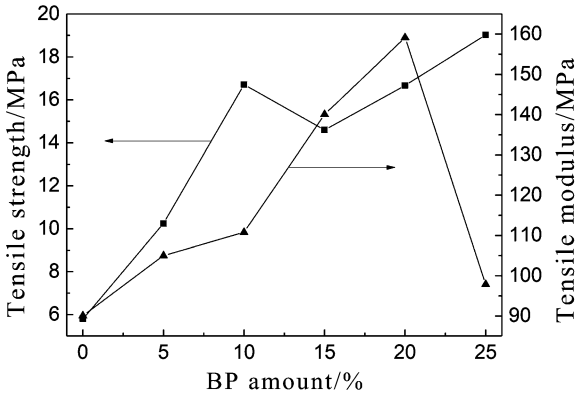

Fig. 2 Tensile strength and elastic modulus of TPS with various bagasse pith amount

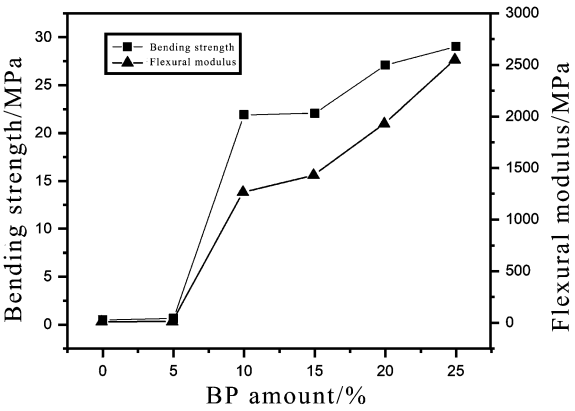

Fig. 3 Flexural strength and flexural modulus of TPS with various bagasse pith amount

According to Fig. 2, the tensile modulus of TPS/BP composites increases with the increase of BP content, and then decreases. When the BP content reaches to 20%, the elastic modulus of TPS/BP reaches the maximum of 159.13 MPa. This is because the tensile elastic modulus reflects the mechanical properties of the composites under small deformation conditions [5]. The dispersed phase BP does not slip in the matrix, so that the tensile modulus of the composites is less affected by the interfacial bond strength. BP contains more parenchyma cells, the length is short, the strength is poor. When the BP content of TPS/BP is too much, the poor performance of the composite material has a great impact on the performance of the TPS-BP interface.

The flexural behavior of TPS/BP in different BP content is shown in Fig. 3. The flexural strength and flexural modulus of BP/TPS increase with the increase of BP content. In the TPS/BP composite, the BP is equally distributed in TPS matrix. Under the action of bending stress, BP and TPS are in the form of flexural deformation jointly. With the increase of the number of BP in the TPS matrix, the interfacial effect between BP and TPS is enhanced (Fig. 1). When the BP content is 25 wt%, the flexural strength of BP/TPS increases by 57% compared with TPS.

Compared with the tensile, bending fracture can crack on the surface of the material. The damage capability of the stress on the interface between TPS and BP is different, so that the positive effect of the good interface bonding on the composite material is more than the negative effect of the insufficient performance of BP. Therefore, in Fig. 3, the flexural modulus of BP/TPS containing 25 wt% BP increases by 228% compared with that of TPS/BP containing 5 wt% BP.

3.3 Moisture Absorption Properties of TPS/BP Composites

Figures 4 and 5 show the moisture absorption rates of TPS with different BP content at RH = 43 and 100%. In the RH = 43% environment, the moisture

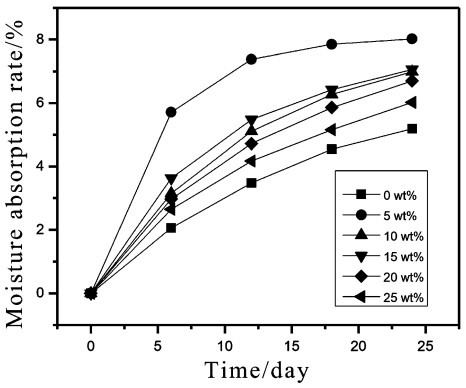

Fig. 4 The relation of water absorption of TPS/BP with different bagasse pith amount at RH = 43%

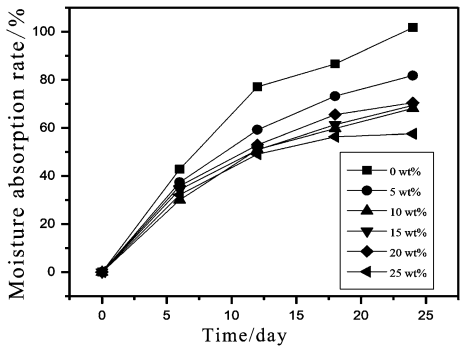

Fig. 5 The relation of water absorption of TPS/BP with different bagasse pith amount at RH = 100%

absorption rate of TPS and BP/TPS increase rapidly with time, and then increase slowly. In 24 days, the moisture absorption rate of TPS was always lower than TPS/BP, while the moisture absorption rate of TPS/BP decreased with the increase of BP content. It is probably because there are a lot of parenchyma cells in BP, these cells have the characteristics of short length, thin wall and large cavity. These cells have a strong moisture absorption ability and their moisture absorption ability is higher than that of TPS matrix. The study results show that the dried BP is soaked in the container with water, and the water is absorbed immediately, the moisture content can reach more than 80% in a short time [6]. So the addition of BP increases the moisture absorption rate of packaging materials.

The moisture absorption rate of RH = 43% and RH = 100% was tested, and it is found that plant fibers can effectively inhibit the moisture absorption of starch based materials. Compared with plant fiber, the bagasse pith cell has large cavity, thin wall, and large surface area, so that it has a strong moisture absorption ability. BP has stronger hydrophilicity compared with the TPS. Therefore, in the low relative humidity environment, TPS/BP shows a different moisture absorption law with plant fiber reinforced thermoplastic starch materials. On the other hand, compared with eucalyptus pulp fibers and kenaf stalk core fiber reinforced thermoplastic starch [7],

the bagasse pith reinforced thermoplastic starch has better moisture resistance under the same ambient humidity (RH = 100%) condition. It maybe because the larger specific surface area of the bagasse pith cell makes it more compatible with the interface of the TPS matrix, the strong adhesion between them makes the free volume of the starch molecular chain to shrink, and it hinders the penetration of water molecules [8].

According to Fig. 5, the addition of BP decreases the water absorption of TPS/BP under the condition of relative humidity 100%. With the increase of BP content, the moisture absorption rate of TPS/BP decreased gradually. This maybe because in the case of the TPS matrix and BP are fully absorbent, the interfacial properties between the two TPS/BP occupy a dominant position. Due to the similar chemical structure of TPS and BP, it's easy to form intermolecular hydrogen bond formation (Fig. 1). It makes good interfacial bonding property, and it hinders the diffusion of water molecules to some extent. Moreover, the hindering effect is enhanced with the increase of BP content and the formation of hydrogen bonds.

3.4 Micro Morphology Analysis

The SEM diagram (Fig. 6a) of the TPS section shows that the starch particles are plasticized to form a continuous interface. The surface of BP is rough and the surface area was large, which is favorable for the formation of a good interface bonding between BP and TPS matrix. Figure 6b–d are the tensile and bending section of the TPS/BP with different BP content after a magnification of 500 times.

As can be seen from Fig. 6, starch particles have been plasticized to form a continuous interface (Fig. 6a), and the rough surface and the large surface area of BP are conducive to the formation of a good interface between BP and TPS matrix. When 10% BP was added to TPS, BP was embedded in TPS, and no interfacial gaps were observed. The parenchyma cell structure of BP is locally dispersed, and the surface is coated with flaky plasticized starch (Fig. 6b), indicating that BP and TPS compatibility between the better. With the increase of BP content, the bonding effect with TPS is more prominent. Therefore, the parenchyma parenchyma cells of BP are seriously deformed, the cell cross section is uneven, and the interface is

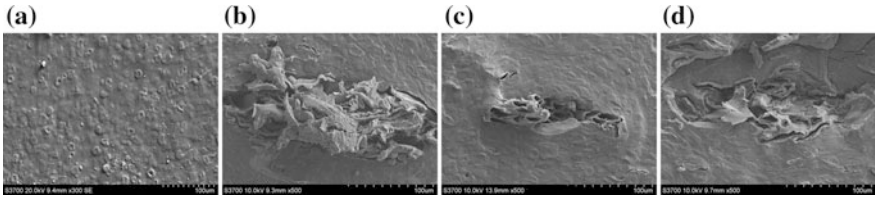

Fig. 6 SEM micrographs of TPS, 50× (**a**), tensile fracture of TPS/BP composite at 10 wt% loading, 500× (**b**), at 25 wt% loading, 500× (**c**), and flexural fracture of TPS/BP composite at 10 wt% loading,m 500× (**d**)

smoother (Fig. 6c). The good interfacial property of TPS/BP dues to the presence of hydrogen bonds between BP and TPS matrix [8] and the large surface area of BP's parenchyma cells.

4 Conclusions

(1) With the increase of BP content, the tensile strength, flexural strength and flexural modulus of TPS/BP composites increase gradually, while the elongation at break decreases obviously.
(2) The effect of BP content on the moisture absorption of TPS/BP composite packaging materials is related to the relative humidity of the environment. At low relative humidity (RH = 43%), the addition of BP leads to an increase in the moisture absorption rate of TPS, and the addition of BP can reduce the moisture absorption of TPS at high relative humidity (RH = 100%).
(3) Infrared spectrum analysis shows that the intermolecular hydrogen bonds are formed between BP and TPS matrix, which is the basic reason that BP enhanced TPS. SEM analysis shows that there is no interface gap between BP and TPS, and there is good compatibility between them.

Acknowledgements This study is funded by the Doctoral Scientific Research Foundation of LiaoNing Province (201601279).

References

1. Yan Q, Wang A, Wang J et al (2009) Evaluation of global biomass resources. Chin Agric Bull 25(18):466–470
2. Yang L (1989) Utilization of bagasse pith energy. Can Sugar Ind 2:60–61
3. Dean KM, Do MD, Petinakis E et al (2008) Key interactions in biodegradable thermoplastic starch/poly(vinyl alcohol)/montmorillonite micro-and nanocomposites. Compos Sci Technol 68(6):1453–1462
4. Dias AB, Müller CMO, Larotonda FDS et al (2011) Mechanical and barrier properties of composite films based on rice flour and cellulose fibers. LWT Food Sci Technol 44(2):535–542
5. Jizhao Liang (2012) Theory of strengthening and toughening of polymer composites. South China University of Technology Press, Guangzhou, p 11
6. Guo S (2001) Talk about the use of bagasse particleboard production must depithing. Forestry Constr 5:17–19
7. Sarifuddin N, Ismail H, Ahmad Z (2012) Effect of fiber loading on properties of thermoplastic sago starch/kenaf core fiber biocomposites. BioResources 7(3):4294–4306
8. Zhang Y, Han JH (2006) Plasticization of pea starch films with monosaccharides and polyols. J Food Sci 71(6):253–261

Large-Scale Fabrication of Ordered Monolayer Self-assembly of Polystyrene Submicron Spheres

Xiuyan Li, Zhe Li, Fenlan Xu, Yan Yan, Wei Wang, Luhai Li, Ruping Liu and Zhou Li

Abstract Fabrication of ordered array and its applications have emerged as a critical tool for micro-structure, with which generally apply in sensing, wastewater detecting, and field emission. This review focuses on the fabrication of ordered patterned array polystyrene (PS) submicron particles monolayer as well as its effect factors. Substantial progress in the two dimensional (2D) regular patterned array has made by developing variety of method. One effective method of fabricating PS submicron spheres with full regular patterned, aligned monolayer ordered array is discussed in this paper and SEM was used to characterize the performance of the monolayer. This approach opens the simplicity and convenience of creating patterned two-dimensional nanostructure. Its greatest advantage is that suitable for large particle size spheres, Finally, the development tendency and prospect of in theses research areas are outlined.

Keywords Polystyrenes microspheres · Micro-structure · Ordered pattern Self-assembly

1 Introduction

Recently, as an assembled micro-structure, the ordered microsphere array is of great importance in biosensor [1], wastewater detecting [2], solar cell [3] and other microstructure device [4]. Polystyrenes (PS) microspheres are a generally organic material of two dimensional (2D) regular patterned array, which is applied as previous substrate of single-layer microsphere film preparing microstructure [1–5].

X. Li · F. Xu · Y. Yan · W. Wang · L. Li · R. Liu (✉)
Beijing Institute of Graphic Communication, Beijing, China
e-mail: liuruping@bigc.edu.cn

Z. Li · Z. Li (✉)
Beijing Institute of Nanoenergy and Nanosystems, Chinese Academy of Sciences, National Center for Nanoscience and Technology (NCNST), Beijing, China
e-mail: zli@binn.cas.cn

P. Zhao et al. (eds.), *Applied Sciences in Graphic Communication and Packaging*, Lecture Notes in Electrical Engineering 477,
https://doi.org/10.1007/978-981-10-7629-9_102

Besides its spatiality of the ball cavity structure, it is of utmost importance to deposit this material as thin film in a way that represents a general applicability for 2D materials. There are many methods to grow the thin film of PS spheres such as gravity deposition [1], langmuir-blodgett assembled methods [4, 5], micro-propulsive injection methods [6]. Due to the large diameter spheres have over big quality and over fast deposition velocity, the currently methods unable to realize orderly arrangement in the large diameter spheres [7].

This paper will briefly describe an effective method that used for self-assemble of regular patterned, aligned monolayer film of PS microspheres [5]. This method opens the simpleness of fabricating patterned 2D microstructures which have many advantages. For example, it can satisfy the large diameter spheres arrangement and realize large-area array, save time and materials and raise the efficiency. The scanning electron microscope was used to characterize the performance of the monolayer.

2 Experiment

2.1 Raw Materials and Preparation

Monodispersed polystyrenes (PS) spheres (2, 6 μm, 2.5%) were purchased from J&K Chemical. First, a centrifuge separated the polystyrenes spheres from the suspension liquid, concentrating them in order to suitable proportion (10%). For this, PS solutions dissolved in ethyl alcohol (the proportion of PS spheres and ethyl alcohol was 1:2). Then the diluted solution was for 5 min strong ultrasonic oscillated in order to make sure its dispersion. For substrate, we used the ITO glasses, which were separated into 1 cm × 1.5 cm. In order to increasing the hydrophobicity of ITO glasses surface, surface modification was needed. The glasses substrates were cleaned and immersed in sodium dodecyl sulfate (SDS) for 24 h.

2.2 Fabrication of Ordered PS Spheres Film

Our fabrication approach firstly used 200 μL the PS spheres suspension being slowly dropped into the surface of the substrate and gently shaked the substrate so that it was spread evenly on the surface. Secondly, the substrate with the PS sphere suspension was slowing immersed into the deionized water with a certain angle of 15°. Then, to form a better thin monolayer of PS spheres, waiting for the PS sphere spreaded out the surface of water when after one or two drops of 1% peregal was dropwise added to the water. This moment, we would found that the PS spheres was pushed aside because peregal change the tension of the surface and it obtained the full regular patterned, aligned monolayer thin film. Next, we need to make the thin

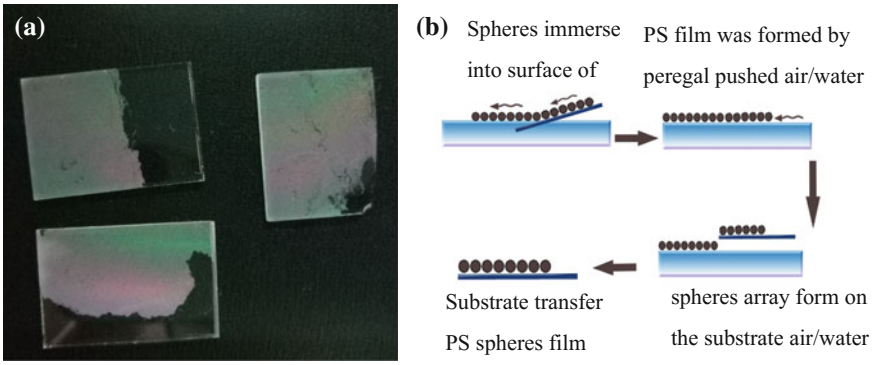

Fig. 1 **a** An optical image of the self-assembled monolayer structure on the ITO substrate. **b** The processing of fabrication of PS spheres array

film transfer from surface to substrate. The substrate slowly immerse into water where without PS spheres and then horizontally lifted substrate where PS spheres arrayed of monolayer [8]. Waiting for dry of PS spheres film, We can see that the substrate appear white PS film. This is because the diameter of PS spheres is at micron level, which produce diffracting light outside the wide of visible light [9]. Figure 1a presents an optical image of the monolayer structure formed by this method. Figure 1b presents the processing of fabrication of PS spheres array.

3 The Results and Discussion

3.1 Effect of the Substrate of Hydrophilic Treatment

Before the experiment started, the ITO glasses were washed according to the standard cleaning method. For this, the substrates were respectively ultrasonic cleaned about 30 min by acetone, ethyl alcohol and deionized water to remove grease stains and small particles. Due to the surface of pure ITO glasses substrates possess low surface free energy, it shows hydrophobicity [10] which is adverse to preparation the ordered monolayer of PS nanospheres. In order to increase the hydrophilia and surface energy of ITO glasses surface, the ITO glasses were immersed in SDS about 24 h [11] to increase the hydrophilia of the surface.

3.2 Influencing Factors of Film Forming Properties

In order to self-assembly grow regular patterned, aligned monolayer film of PS spheres, we need to control various kinds of influencing factors of film forming

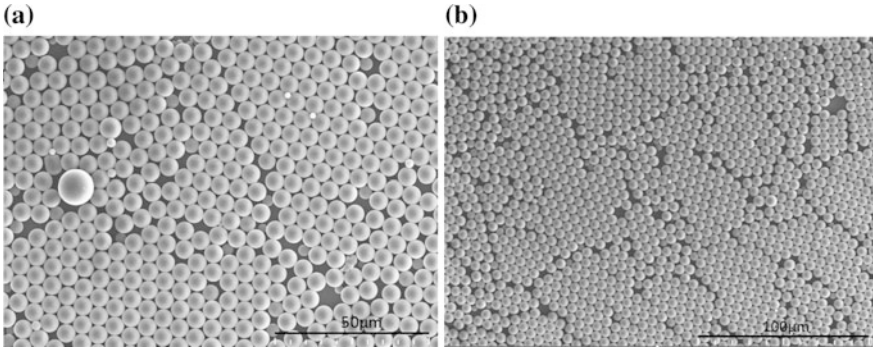

Fig. 2 The SEM images of different types of PS array defects. **a**, **b** The diameter of PS spheres is 6 μm

stability. The first one, the cleanliness and the hydrophobic of substrates and uniformity of diameter of PS spheres would influence the completeness of film and the adhesive force of PS spheres such as point defect (Fig. 2a). And with the increase of diameter of spheres, the homogeneity of diameter gradually change terrible, which could be demonstrate by Fig. 2. Secondly, for experimentation, monolayer film is very weakness and any physical vibration, especially, in the process of transferring the spheres to substrate and drying the spheres film on substrate, that would affect the completeness of film such as line imperfection (Fig. 2b).

3.3 Ratio of Ethanol and Deionized Water

In order to make PS spheres at the air/water surfaces immersed into liquid of a small number, we choose the mixture of ethanol and water as the diffusant [12]. The ratio of ethanol and deionized water of PS spheres suspension was an important element of fabrication the PS spheres array. With the increase of ethanol concentration, the order of PS spheres array presented more perfect. Some of PS spheres sedimentate into solution and film-forming performance was poor (Fig. 3a). This reason was surface density of PS spheres suspension greater than deionized water [12–15]. For another, when ethanol concentration was excessive, PS spheres array would appear some lacuna with the volatilization of ethanol [15]. Thus, for all above reasons, we choice difference ratio of ethanol and deionized water with difference diameters. Figure 3a shows the SEM images of the a full ordered structure of 2 μm with the ratio of ethanol and deionized water is 1:2, Fig. 3b shows the SEM images of the a full ordered structure of 6 μm with the ratio of ethanol and deionized water is 3:5.

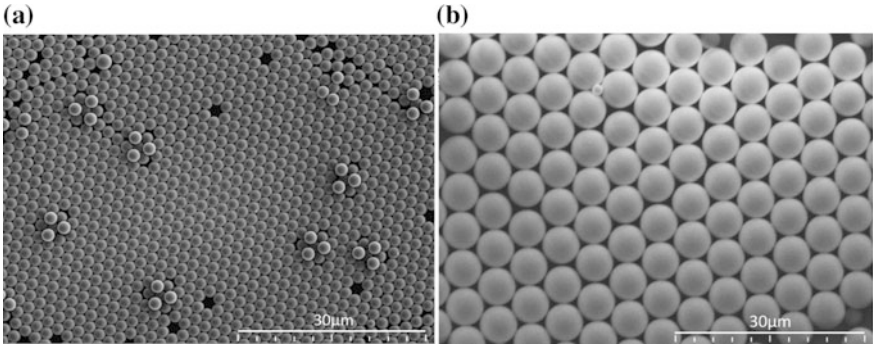

Fig. 3 **a** The SEM images of suspensions with 1:2 of 2 μm PS spheres. **b** The SEM images of suspensions with 3:5 of 6 μm PS spheres

4 Conclusions

The strategy of fabrication of fairly ordered PS spheres film appears to be quite general and applicable to many microstructure. It is based on readily available precursors and simply operation. Although there are many influence factors to obtain large-area arrangements, the fairly ordered structures meet requirements of preparative microstructure [16]. This method uses a simple fabrication technique to control the alignment, size, shape, and periodic of self-organized PS spheres monolayer patterns with feature sizes down to several micrometer and over surface area of square centimeters. Due to the various property of PS spheres, they can be template to direct the self-assembly of functional monolayer and microstructures, which can be used as biosensors, wastewater detecting and other biofunctionalized structures and systems [16–20].

Acknowledgements This work was supported by the National Natural Science Foundation of China (61501039), the Beijing Natural Science Foundation (2162017), the Beijing Research Grant (No. Z15110000915071), the support of Beijing Municipal Education Commission (No. KM2017 10015005), the Initial funding for the Doctoral Program of BIGC (27170116005/040), the Beijing Collaborative Innovation for Green Printing and Publication (04190117029/002), and the Elite Program of BIGC (04190117004/010).

References

1. Xiaolei C, Fan C (2010) Fabrication of zinc oxide microcavities array and its applications. Jiang su Univ Res 45(1):1–6
2. Liwei L, Xiuyu W, Chuanxi X, Yao L (2015) Recent advances in biological detection with magnetic nanoparticles as a useful tool. Sci China Chem 58(5):793–809

3. Yan J, Binbin Y, Jie L, Zhihua L, Jiankun S, Xinhua Z, Jinsong H, Weiguo S, Lijun W (2015) Boosting the open circuit voltage and dill factor of QDSSCs using hierarchically assembled ITO@Cu2S nanowire array counter electrodes. Nano Lett 15(5):3088–3095
4. Harneet K, Sandeep Y, Avanish K, Nidhi S, Ved VA, Ritu S (2016) Large area fabrication of semiconducting phosphorene by Langmuir-Blodgett assembly. Nature 6:34095. doi:https://doi.org/10.1038/srep34095
5. Xudong W, Christopher JS, Zhong LW (2004) Large-scale hexagonal-patterned growth of aligned ZnO nanorods for nao-optoelectronics and nanosensor arrays. ACS Nano 4(3):423–426
6. Pingqi G, Jian H, Suqiong Z, Xi Y, Sizhong L, Jiang S, Dan W, Tianbo Y, Jichun Y, Yi C (2015) Large-area nanosphere self-assembly by a micro-propulsive injection method for high throughput periodic surface nanotexturing. ACS Lett. https://doi.org/10.1021/acs.nanolett.5b01202
7. Yuanyuan W, Dan G (2010) The fabrication of PP-nanoparticles monolayer and measurement of elastic properties. China Surf Eng 23(2):86–90
8. Zhipeng H, Hui F, Jing Z (2007) Fabrication of silicon nanowire arrays with controlled biometer, length, and density. Adv Mater 19:744–748
9. Qilin X (2012) Preparation of monodisperse micron sized plystyrene microspheres and its self-assembly. Harbin Institute of Technology, Herbin Institute of Technology
10. Jingli X (2011) Preparation and application of hydrophobic film on class surface. Guangzhou Chem Ind 39(22):49–51
11. Koay Seong C, Salmah H (2014) Agrowaste-based composites from cocoa pod husk and polypropylene: Effect of filler content and chemical treatment. J Thermoplast Mater, pp 1–20. doi:https://doi.org/10.1177/0892705714563125
12. Zhiyong Z, Shuang L, Wendou Z, Minji L, Huaiyu Z (2005) Nanosphere lithography technique. Langmuir 9(36):1312–1314
13. Robert A, John HC, Dieter N, Vesselin NP (2000) Compression and structure of monolayers of charged latex particles at air/water and octane/water interfaces. Langmuir 16(4):1969–1979
14. Robert G, DiMauro AJ, Paul VB (2006) Slow vertical deposition of colloidal crystals: a Langmuir-Blodgett process. Langmuir 22(15):6507–6513
15. Xiaolei C, Tng L, Xueying W, Fan Y (2010) Fabrication micro electrode arrays and its electrochemistry. Langmuir 24(2):52–55
16. Xiaodong C, Steven L, Minchael H, Nan L, Harald F, Lifeng C (2007) Langmuir-Blodgett patterning: bottom-up way to build macrostructures over large areas. Acc Chem Res 40:393–401
17. Tetsu T, Hirohiko T, Yusuke O, Shoichiro Y, Tadashi W (1991) Bifunctional Langmuir-Blodgett film for enzyme immobilization and amperometric biosensor sensitization. Thin Solid Films 202:145–150
18. Fan Y, Kafi AKM, Hoon-Kyu S, Young-Soo K (2006) A novel amperometric hydrogen peroxide biosensor based on immobilization of hemoglobin in linoleic acid monolayer by Langmuir-Blodgett technique. SCI Direct 284–285:125–129
19. Hui H, Sanjun H, Liping G, Jiaxing L (2006) The preparation of monodisperse polystyrene latex particle and its two dimensional self-assembly of colloidal crystal. Mater Protect 39(10):26–29
20. Chongping S, Junkang L, Zhongbin N, Mingqing C, Shirong L (2012) Preparation of self-assembled polystyrene spheric colloid crystals by a solvent evaporation method. Appl Chem 29(6):639–642

Effect of Different Heat Treatment Methods on the Morphology and Electrical Conductivity of Ag Nanoparticle Films

Zhenguo Wang, Fenlan Xu, Qichao Hou, Wei Yang, Woye Zhang, Lixin Mo and Luhai Li

Abstract In order to study the effect of different heat treatment methods on the morphology and electrical conductivity of Ag nanoparticle films, the morphology and conductivity evolution of the conductive films during the heat-treatment process in an oven and on a hot plate are investigated. We found that the films heat-treated on an oven had big differences between the surface microstructural and the cross section microstructural. When the interior of the silver nanoparticle film has been significantly melted, the surface particles have not yet begun to melt. It was discovered that the surface Ag NPs of the films are lower the temperature began to melt heat-treated on a hot plate than heat-treated in an oven and the films heat-treated on the hot plate can reduce the post-treatment temperature compared with the heat treatment in the oven. Because the thermal conductivity of steel and glass is much greater than that of air, and the temperature of the films rises sharply heat-treated on the hot plate, contributing to the sintering of the Ag nanoparticle films.

Keywords Heat treatment methods · Silver nanoparticle · Printed electronics

1 Introduction

Recently, interest has grown in printed electronics because printing methods can replace the traditional silicon-based techniques, which are time consuming and involve many processing steps. Printing offers the potential for flexible, low-cost, large-area electronics for photovoltaics [1], transistors [2], displays [3], radio-frequency identification (RFID) tags [4], batteries [5], Flexible transparent

Z. Wang · F. Xu · Q. Hou · W. Yang · W. Zhang · L. Mo (✉) · L. Li (✉)
Beijing Engineering Research Center of Printed Electronics,
Beijing Institute of Graphic Communication, Beijing, China
e-mail: molixin@bigc.edu.cn

L. Li
e-mail: liluhai@bigc.edu.cn

P. Zhao et al. (eds.), *Applied Sciences in Graphic Communication and Packaging*, Lecture Notes in Electrical Engineering 477,
https://doi.org/10.1007/978-981-10-7629-9_103

conductive film [6]. Metallic conducting tracks of low resistance must be achieved at temperatures sufficiently lower so as to be compatible with organic electronics on plastic substrates.

Regarding the post-treatment method of the nano-silver conductive ink, lots of research has been done. For example, Grouchko et al. [7] used polyacrylic acid sodium as a stabilizer for silver nanoparticles, Cl^- ions as a destabilizing agent, and by chemical sintering method to achieve sintering at room temperature. The other post-treatment methods include laser [8], IR, plasma [9], and microwaves [10]. Although many results have been achieved, these processes also have caused expensive equipment or high energy consumption or complex processes or incomplete sintering.

In this report we present a new approach for low temperature sintering of Ag NPs films using the post-treatment of heat transfer medium with high thermal conductivity. The morphology and conductivity evolution of the conductive films during the heat-treatment in an oven or on a hot plate are investigated.

2 Experimental

2.1 Materials

Silver nitrate ($AgNO_3$) and acetone were purchased from Beijing Chemical Works. Hydrazine hydrate ($H_4N_2{\cdot}H_2O$), polyvinylpyrrolidone (PVP, MW = 58,000), ethylene glycol, ethylene glycol monobutyl ether and n-octanol were purchased from Tianjin Guangfu Fine Chemical Research Institute. Deionized water was used in all of the experiments.

2.2 Synthesis of Silver NPs

The fully aqueous mono-phase system contained silver nitrate as the silver source, hydrazine hydrate ($H_4N_2{\cdot}H_2O$) as the reducing reagent, PVP as the capping molecule and deionized water as the medium. The silver NPs was prepared by double column method. Weight 7.51 g PVP dissolved in 300 g deionized water, recorded as A liquid, set the experimental device, the beaker was placed in ice water cooling, and then started the mixer to the speed of 350 r/min; Weight 35 g silver nitrate dissolved in 35 g deionized water, denoted as B solution; Weight 15.35 g hydrazine hydrate dissolved in 17.80 g deionized water, recorded as C solution; When the temperature of A liquid to 6 °C, B liquid and C liquid is passed into the A liquid at 2 r/min speed with a peristaltic pump. When the feed is complete, continue stirring for 1 h. Then, acetone was added to the NP dispersion and the dispersion was stirred for 3 min at 500 rpm, and then Stranded still for 20 min. When Ag NPs

were sink at the bottom of the beaker, the upper liquid was drained. This purification process was repeated 4 times to purify Ag NPs.

2.3 Preparation of Conductive Inks and Patterns of Ag NPs

The conductive inks of Ag NPs were prepared by re-dispersing the purified Ag NPs in ethylene glycol and ethylene glycol monobutyl ether. The weight concentration of the Ag NPs in all conductive inks was adjusted to 55 wt%. A 20 mm × 20 mm pattern was fabricated by spin coating the Ag conductive ink onto a glass substrate. The patterns were dried at different temperatures in the range of 60–150 °C in an oven or on a hot plate for 10 min.

2.4 Characterization and Measurements

The particle size distribution of Ag NPs was analyzed using zeta sizer nano series (Nano-ZS, MALVERN instruments). The morphology of Ag NPs was analyzed using a scanning electron microscope (SEM, HITACHI SU-8020, 10 kV). The amount of PVP remaining on the surface of the obtained Ag NPs was determined using a thermogravimetry analyzer (TGA, NETZSCH TG-209F3). TGA measurement was operated using air at a flow rate of 50 cm^3 min^{-1} and at a heating rate of 10 °C min^{-1} from room temperature to 600 °C. The sheet resistance of the obtained Ag pattern was measured using a four-point probe equipment (Guangzhou four probe technology Corporation RTS-9). The sheet resistance of a Ag pattern was calculated from the average of those measured from five different areas of the pattern. Scanning electron microscope was used to observe the morphology and take the cross section images of the obtained Ag patterns. The resistivity of a Ag pattern was calculated from the measured sheet resistance and thickness of the pattern.

3 Results and Discussion

3.1 Properties of the PVP-Coated Silver NP

Figure 1 show the particle size distribution and a SEM image of PVP-coated silver NPs. As shown in Fig. 1a, the SEM image of the sample shows that the silver NPs could be well dispersed in solvents and demonstrates a particle size in the range of 60–350 nm. Figure 1b shows that all of the particle sizes of the silver NPs are in the range of 20–500 nm and the mean size is 148.1 nm.

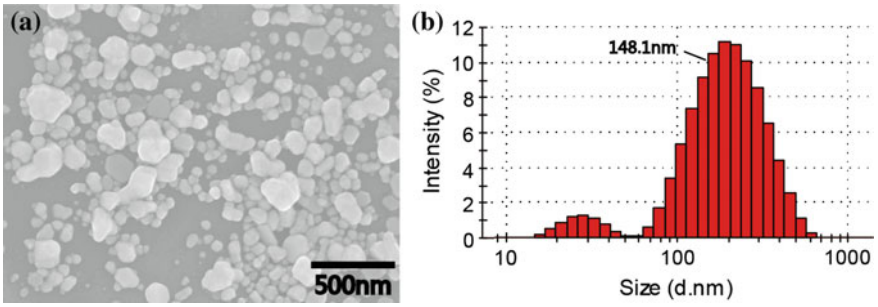

Fig. 1 **a** SEM image of synthesized silver NPs and **b** particle size distribution of silver NPs

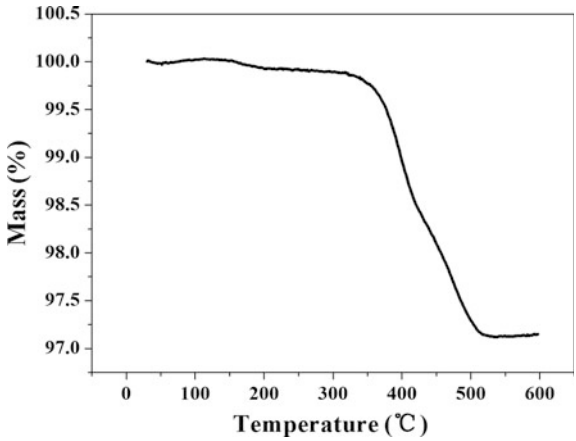

Fig. 2 TGA curve of silver NPs

The thermal analysis results obtained for the PVP-coated silver NPs are presented in Fig. 2. The sample shows a continuous weight loss from 300 to 550 °C, with a cumulative weight loss of 2.76%, which is attributed to the desorption of the PVP the surface of the silver NPs.

3.2 Effect of Different Heat Treatment Methods on the Morphology of Ag Nanoparticle Films

The surface microstructural evolution of the Ag films during the heat-treatment at temperatures ranging from 60 to 150 °C in an oven or on a hot plate for 10 min is shown in Fig. 3. As shown in Fig. 3b, the films heat-treated on a hot plate at 90 °C and the surface Ag NPs of the films began to melt. As shown in Fig. 3h, the films heat-treated on an oven at 150 °C and the surface Ag NPs of the films began

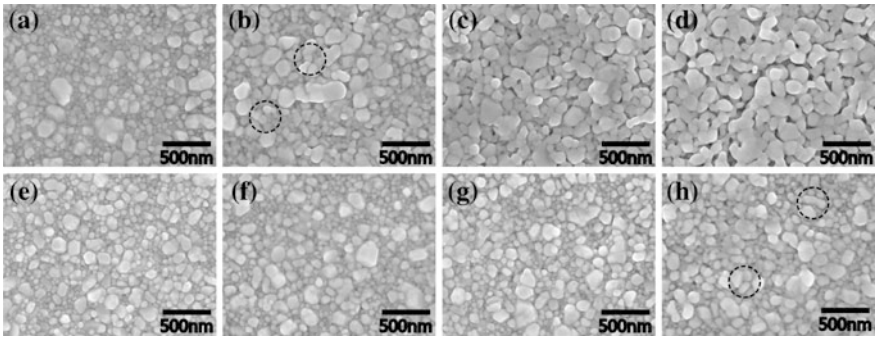

Fig. 3 SEM images for surface microstructural variations of the Ag nanoparticle films as a function of heat-treatment temperatures. The films heat-treated on a hot plate at **a** 60, **b** 90, **c** 120, and **d** 150 °C; the films heat-treated in an oven at **e** 60, **f** 90, **g** 120, and **h** 150 °C

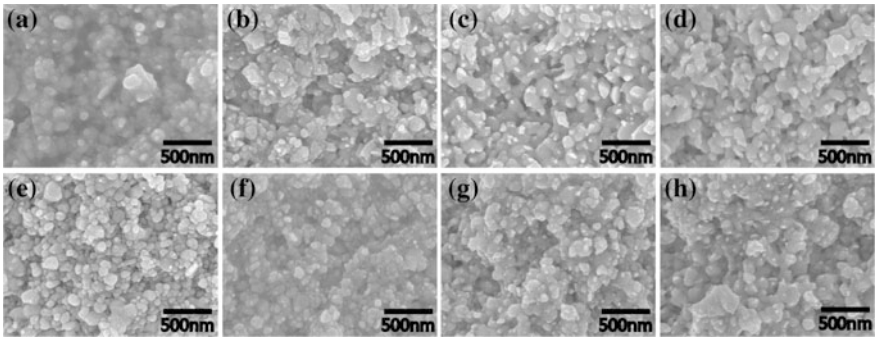

Fig. 4 SEM images for cross section microstructural variations of the Ag nanoparticle films as a function of heat-treatment temperatures. The films heat-treated on a hot plate at **a** 60, **b** 90, **c** 120, and **d** 150 °C; the films heat-treated in an oven at **e** 60, **f** 90, **g** 120, and **h** 150 °C

to melt. This suggests that the surface Ag NPs of the films are lower the temperature began to melt heat-treated on a hot plate than heat-treated in an oven.

The cross section microstructural evolution of the Ag films during the heat-treatment at temperatures ranging from 60 to 150 °C in an oven or on a hot plate for 10 min is shown in Fig. 4. As shown in Fig. 4b, the films heat-treated on a hot plate at 90 °C and the cross section Ag NPs of the films showed no apparent particle shape. As shown in Fig. 4g, the films heat-treated on an oven at 120 °C and the cross section Ag NPs of the films showed no apparent particle shape. It should be noted that the films heat-treated on an oven had big differences between the surface microstructural and the cross section microstructural.

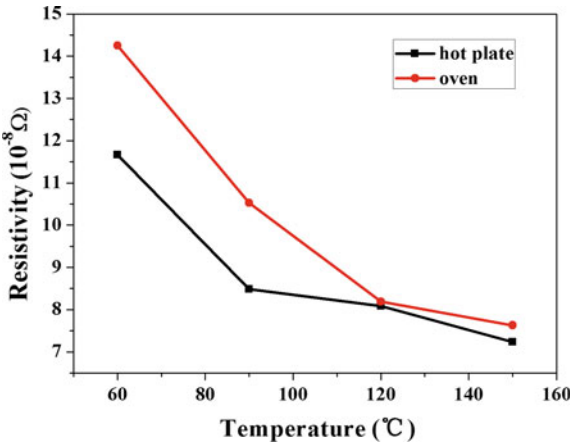

Fig. 5 Resistivity variation of the Ag conductive films composed of two different heat treatments as a function of heat-treatment temperature

3.3 Effect of Different Heat Treatment Methods on the Electrical Conductivity of Ag Nanoparticle Films

The Resistivity evolution of the Ag films during the heat-treatment at temperatures ranging from 60 to 150 °C is shown in Fig. 5. The Resistivity decreased with increasing the heat-treatment temperature. As shown in Fig. 4, it is due to inter-particle neck growth. The granular Ag films becomes relatively conductive with a resistivity of about 8.3 μΩ cm at 90 °C on a hot plate while it was at 120 °C in an oven. This indicates that the films heat-treated on the hot plate can reduce the post-treatment temperature compared with the heat treatment in the oven. This difference is largely due to the difference in heat transfer between the two. The thermal conductivity of steel (18.45 W/m K)and glass (1.09 W/m K) is much greater than that of air (0.024 W/m K). This indicates that the temperature of the films rises sharply heat-treated on the hot plate, contributing to the sintering of the Ag nanoparticle films.

4 Conclusions

In summary, we present a new approach for low temperature sintering of Ag NPs films using the post-treatment of heat transfer medium with high thermal conductivity. The morphology and conductivity evolution of the conductive films during the heat-treatment in an oven or on a hot plate are investigated. We found that the films heat-treated on an oven had big differences between the surface microstructural and the cross section microstructural. When the interior of the silver nanoparticle film has been significantly melted, the surface particles have not yet begun to melt. It was discovered that the surface Ag NPs of the films are lower the

temperature began to melt heat-treated on a hot plate than heat-treated in an oven and the films heat-treated on the hot plate can reduce the post-treatment temperature compared with the heat treatment in the oven. Because the thermal conductivity of steel and glass is much greater than that of air, and the temperature of the films rises sharply heat-treated on the hot plate, contributing to the sintering of the Ag nanoparticle films.

Acknowledgements This work has been financed by 2017 Innovation base cultivation and development project of Beijing Science and Technology Committee (Z171100002217032), Beijing university talents cross training plan (Shipei plan), 2017 Innovation entrepreneurship training program, 2017 Outstanding young scholars (CIT&TCD201704051).

References

1. Hoth CN, Choulis SA, Schilinsky P, Brabec CJ (2007) High photovoltaic performance of inkjet printed polymer: fullerene blends. Adv Mater 19:3973
2. Okimoto H, Takenobu T, Yanagi K, Miyata Y, Shimotani H, Kataura H, Iwasa Y (2010) Tunable carbon nanotube thin-film transistors produced exclusively via inkjet printing. Adv Mater 22:3981
3. Comiskey B, Albert JD, Yoshizawa H, Jacobson J (1998) An electrophoretic ink for all—printed reflective electronic displays. Nature 394:253
4. Dragoman M, Flahaut E, Dragoman D, Ahmad Al M, Plana R (2009) Writing simple RF electronic devices on paper with carbon nanotube ink. Nanotechnology 20(37):375203
5. Poizot P, Laruelle S, Grugeon S, Dupont L, Tarascon JM (2000) Nano-sized transition-metal oxides as negative-electrode materials for lithium-ion batteries. Nature 407:496–499
6. He W, Ye C (2015) Flexible transparent conductive films on the basis of ag nanowires: design and applications: a review. J Mater Sci Technol 31:581
7. Grouchko M, Kamyshny A, Mihailescu CF, Anghel DF, Magdassi S (2011) Conductive inks with a "built-in" mechanism that enables sintering at room temperature. ACS Nano 5(4): 3354–3359
8. Hong S, Yeo J, Kim G, Kim D, Lee H, Kwon J, Lee H, Lee P, Ko SH (2013) Nonvacuum, maskless fabrication of a flexible metal grid transparent conductor by low-temperature selective laser sintering of nanoparticle ink. ACS Nano 7:5024
9. Reinhold I, Hendriks CE, Eckardt R, Kranenburg JM, Perelaer J, Baumann RR, Schubert US (2009) Argon plasma sintering of inkjet printed silver tracks on polymer substrates. J Mater Chem 19:3384
10. Perelaer J, Jani R, Grouchko M, Kamyshny A, Magdassi S, Schubert US (2012) Plasma and microwave flash sintering of a tailored silver nanoparticle ink, yielding 60% bulk conductivity on cost-effective polymer foils. Adv Mater 24:3993

Effects of Several Surfactants on Surface Tension of PVA Hot-Melt Adhesive Tape

Xinting Wang, Guorong Cao, Dongli Li and Meiqi Yang

Abstract Most of current packaging tape are made of non-degradable BOPP film, subsequently rendering carton recycled lose commercial value and causing a great hazard on the living environment. PVA film is known as a type of environmentally friendly material because of its excellent characteristics, e.g. water solubility and degradability. Since PVA film has strong polarity, it is necessary to coat surfactants to reduce the surface tension. In the paper, Span20, Span60, Span80 and Tween60 were coated on the other side of PVA hot-melt adhesive tape by hand. The surface tension was measured under different placement time. It measured the 180° peel strength of PVA hot-melt adhesive tape coated with surfactants in comparison to PVA hot-melt adhesive tape without surfactants and BOPP tape so that appropriate surfactants were chosen. The results show that the surfactants can reduce surface tension of the other side of PVA hot-melt adhesive tape. However, only the mass ratio of Span60 and C_2H_6O is between 1:5 and 1:10, the 180° peel strength of PVA hot-melt adhesive tape is the best. PVA hot-melt adhesive tape with other surfactants is stuck together when the tape is crimped or its peel strength is too small.

Keywords PVA hot-melt adhesive tape · Surfactants · Surface tension

1 Introduction

With the development of e-commerce, the express industry has made our lives fast and convenient, however, its packaging waste also affects people's surroundings. The courier package can fill with nearly 200,000 football fields each year, and only packing tape can be around the equator several hundred laps [1]. On the market, most of packing tape substrate is BOPP film which has advantages of high tensile strength and good transparency [2], but its non-degradability causes great harm to

X. Wang · G. Cao (✉) · D. Li · M. Yang
Beijing Key Laboratory of Printing & Packaging Materials and Technology,
Beijing Institute of Graphic Communication, Beijing, China
e-mail: caoguorong@bigc.edu.cn

P. Zhao et al. (eds.), *Applied Sciences in Graphic Communication and Packaging*, Lecture Notes in Electrical Engineering 477,
https://doi.org/10.1007/978-981-10-7629-9_104

the environment. So it is a general trend to replace BOPP tape with biodegradable tape. PVA film has the features of high tensile strength, good transparency and high elongation at break, which is consistent with the requirements of the tape substrate [3]. And one of the most important advantages is the water-soluble characteristic that is conducive to recycle carton. When the adhesive is coated on one side of PVA film, it is necessary to coat a surfactant on the other side because of the lager polarity of PVA film. Span series and Tween60 were selected in the paper.

Span is the trade name of the sorbitan fatty acid ester emulsifier. Due to the difference in the structure and quantity of the fatty acid chain, the Span type emulsifier has a series of different brands of industrial products. Span emulsifier hydrophobic group is the fatty acid ester chain and hydrophilic group is sorbitan. Because Span contains multiple hydroxyl groups, its interface activity is larger. The esterification degree of Span molecule has a significant effect on the interfacial activity. The higher the degree of esterification, the less the number of free hydroxyl groups in the molecular structure, so the HLB value is lower and the lipophilicity is enhanced. Tween is the trade name of the epoxyethylene sorbitan fatty acid ester emulsifier, which is a product of the addition polymerization of Span and a different amount of ethylene oxide. Due to the addition reaction of ethylene oxide and hydroxyl and polyoxyethylene structure embedded in the ester bond in the Tween molecules, it makes Tween hydrophilic greatly improved. For the O/W interface, under the same conditions, interface activity of Tween is much larger than Span's [4]. The PVA film has a feature of high hydrophilicity, so the hydrophilic groups of Span and Tween extend toward the surface of the film. The lipophilic groups expand into the air. Because of the interfacial adsorption, Span and Tween reduce the PVA film Surface tension [5]. At the same time, the performance prevents film's adsorption of water vapor at a certain extent.

In the experiment, the surface tension and 180° peel strength of the Span series and Tween60 coated on PVA hot-melt adhesive tape was measured. And it made a contrast with PVA hot-melt tape without surfactants and BOPP tape in order to choose right surfactants.

2 Experiment

2.1 Experimental Apparatus and Reagents

Apparatus: Surface tension test pen (dyne test pen), Shanghai Li Chang Electronic Technology Development Co., Ltd. Magnetic stirrers, Shanghai Hao Zhuang Instrument Co., Ltd. INSTRON-5565A high and low temperature electronic tensile testing machine, Instron (Shanghai) Test Equipment Trading Co., Ltd.

Reagents: Span20, Span60, Span80, Tween60, C_2H_6O. Different proportions of samples are as follows: The mass ratio of Span20 and C_2H_6O is 1:10, 1:15, 1:20, 1:30, respectively. The mass ratio of Span60 and C_2H_6O is 1:5, 1:8, 1:10, 1:15,

1:20, 1:25 respectively. The mass ratio of Span80 and C_2H_6O is 1:10, 1:15, 1:20, respectively. The mass ratio of Tween60 and C_2H_6O is 1:10, 1:20, 1:25, respectively.

2.2 Determination of Surface Tension

Use dyne test pen draw a line on the surface of PVA film perpendicularly and observe whether it shrinks and condensates into water droplets. If there is contraction of water droplets, experiment need exchange lower level of the value of the pen until no contraction. In the end, experiment determines the surface tension of the object [6].

2.3 Measurement of 180° Peel Strength

A piece of adhesive tape is attached to a stainless steel plate which is fixed on a fixture of the tensile testing machine. The other fixture clamps the free end of the adhesive tape which is at an angle of 180° with the stainless steel plate and pulls the adhesive tape at the specified ratio. The peel force is measured by the force required to peel off the adhesive tape from the stainless steel plate and converts to peel strength [7]. The 180° peel strength is the most important factor of the adhesive properties of the adhesive product [8].

3 Experimental Results and Analysis

3.1 Effects of Surfactants on Surface Tension of Film

Span20, Span60, Span80 and Tween60 were selected in the paper. Span20 and Tween60 are paste liquid. Span60 is powdery. Span80 is liquid. As can be seen from the table below, when surfactants were coated on PVA film, surface tension reduced to between 30 and 32. Therefore, the type of surfactant does not have much effect on the decrease of surface tension. Different mass ratio of the same kind of surfactant is nothing to do with the decrease of surface tension. For example, when the mass ratio of Span20 and C_2H_6O varied from 1:10, 1:15, 1:20 to 1:30, surface tension had little changed. At the same time, we could also draw a conclusion from the change of mass ratio of Span60, Span80 and Tween60 (Table 1).

Table 1 The relationship between types of surfactants, mass ratio, different placement time of film and surface tension

Surface tension value	Placement time of film			
Mass ratio	60 °C for 2 h	After drying for 2 days	After drying for 6 days	After drying for 8 days
Span20:C_2H_6O = 1:10	30–32	30–32	30–32	30–32
Span20:C_2H_6O = 1:15	30–32	30–32	30–32	30–32
Span20:C_2H_6O = 1:20	30–32	30–32	30–32	30–32
Span20:C_2H_6O = 1:30	30–32	30–32	30–32	30–32
Span60:C_2H_6O = 1:5	30	30	30	30
Span60:C_2H_6O = 1:8	30	30	30	30
Span60:C_2H_6O = 1:10	30	30	30	30
Span60:C_2H_6O = 1:15	30–32	30–32	30–32	30–32
Span60:C_2H_6O = 1:20	30–32	30–32	30–32	30–32
Span60:C_2H_6O = 1:25	30–32	30–32	30–32	30–32
Span80:C_2H_6O = 1:10	30–32	30–32	30–32	30–32
Span80:C_2H_6O = 1:15	30–32	30–32	30–32	30–32
Span80:C_2H_6O = 1:20	30–32	30–32	30–32	30–32
Tween60:C_2H_6O = 1:10	30–32	30–32	30–32	30–32
Tween60:C_2H_6O = 1:20	30–32	30–32	30–32	30–32
Tween60:C_2H_6O = 1:25	30–32	30–32	30–32	30–32

3.2 Effects of Film Placement Time on Surface Tension

As the table above, when Span20, Span60, Span80 and Tween60 were coated on the surface of PVA film respectively, the time of placement had little effect on the decrease of surface tension of PVA film. And the placement time of PVA film coated with different mass ratio of surfactants also did not have much to do with the decrease of the surface tension.

3.3 Effects of Surfactants on 180° Peel Strength of PVA Hot-Melt Adhesive Tape

It can be seen from the figure that the 180° peel strength of PVA hot-melt adhesive tape without surfactants was the largest, and when the Span60 was coated, the 180° peel strength was reduced. Although the peel strength of PVA hot-melt adhesive tape with Span60 was reduced, it was still larger than BOPP tape. In the experiment, other types of surfactants or mass ratio caused the adhesive surface of PVA hot-melt tape to stick to the other side or peel strength is too low to stick other objects, so they could not meet the requirements of the tape. When the mass ratio of Span60 and C_2H_6O was between 1:5 and 1:10, the effect was the best (Fig. 1).

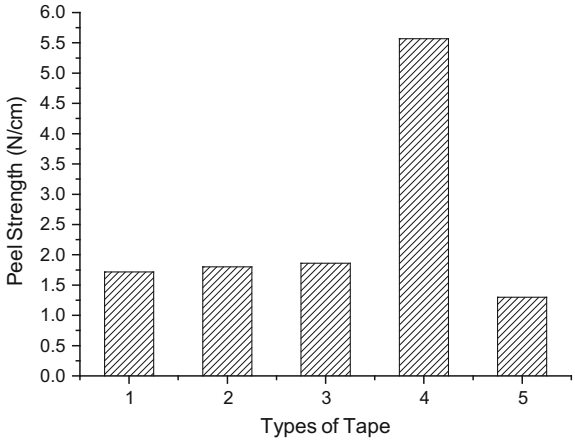

Fig. 1 The 180° peel strength of different mass ratio of surfactants coated on PVA hot-melt tape. 1—the mass ratio of Span60 and C_2H_6O is 1:5 2—the mass ratio of Span60 and C_2H_6O is 1:8 3—the mass ratio of Span60 and C_2H_6O is 1:10 4—PVA hot-melt adhesive tape without surfactants 5—BOPP tape

4 Conclusions

In the paper, different kinds of surfactants were coated on one side of PVA film, and different mass ratio of the solution was prepared. Experiment tested relationship with surfactant category, concentration, the placement time of PVA film and surface tension. At the same time, the 180° peel strength was measured. Experimental results show that surfactants used in the test can reduce the surface tension of the other side of the PVA hot-melt adhesive tape. The type of surfactant, mass ratio and placement time has little effect on the decrease of surface tension of PVA film. But only when the mass ratio of Span60 and C_2H_6O is between 1:5 and 1:10, PVA film hot-melt adhesive tape meets the requirement of packing tape by 180° peel strength testing. There are still many problems to be solved, it is need to further research on the PVA hot-melt adhesive tape.

Acknowledgements This project is supported by the support of the teaching engineering team (construction) (22150116006/017) and the printing and packaging research project of cultivating innovative talents in (22150116007/055) Beijing-Tianjin-Hebei universities and the National Key Scientific Instrument and Equipment Development Project (NO. 2013YQ140517). We are here with best thanks.

References

1. Chen C, Liang A (2016) Million tons of express packaging "garbage" to where? Party member (Hebei), vol 08, pp 40–41
2. Gu L (2008) Study on the effect of BOPP pressure-sensitive adhesive tape and adhesive thickness on adhesion properties. Jiangnan University
3. Li L, Wang Q, Wang R (2004) Research on structure and properties of polyvinyl alcohol tensile films. J Sichuan Univ (Engineering Science Edition) (05):44–48
4. Peng S, Zhang G, Chen Z, Cheng S (1998) Composition, performance, characterization and application of Span and Tween. Surfactant Ind 01:12–16
5. Xiao J, Zhao Z (2005) Application principle of surfactants. Chemical Industry Press, Beijing
6. Wang Q (2008) The method of testing the surface tension of the dyne pen. Plast Packag 05: 49–50
7. Standardization Administration of China (2014) Measurement of peel adhesion properties for adhesive tape. China Standard Press, Beijing
8. Zeng X, Duan W (2002) Studies on the factors affecting the 180° peel strength of pressure sensitive tape. Chem Adhes 03:103–104

Part X
Novel Functional Material Technology

Effects of Different Zeolites on Poly (L-Lactide) Thermal Degradation

Yuhua Hao and Zhen Huang

Abstract A comparison study has been made on thermal degradation of poly (L-lactide) (PLLA) to investigate the influences of two different zeolites filled through thermogravimetric analysis. Non-isothermal degradation measurements are conducted at a N_2 flow rate of 30 ml/min along with a constant heating rate of 5–30 K/min. The thermal degradation features of PLLA/zeolite composites are compared in terms of some specific degradation temperatures. With the selected kinetic method, the activation energy E_a values of two different zeolite-filled composites have been calculated. Calculation results indicated that the zeolite addition has rendered PLLA more thermally stable, requiring higher E_a values for thermal degradation. ZSM-5 zeolite has shown higher effect on PLLA thermal properties than Hβ zeolite.

Keywords Poly(L-lactide) · Zeolites · Thermogravimetric analysis
Multi-heating rates · Kinetic analysis

1 Introduction

Currently, bio-based polymer has received ever-increasing attention because of its biodegradable nature and satisfactory mechanical strength [1–4]. Poly(L-lactide) (PLLA) and its peers have been so far taken to be as a very important biopolymer and it may be able to replace in the coming future those less degradable polymers. For the purpose of better producing desired products or handling waste disposal through thermal treatment, PLLA should have enough thermal stability to avoid any thermal degradation for subsequent applications. As such, many researchers have conducted thermal stability studies of PLLA in recent years by means of non-isothermal methods, and carried out kinetic analyses with various

Y. Hao · Z. Huang (✉)
Department of Packaging Engineering, Tianjin University of Commerce, Tianjin, China
e-mail: huangzhen50@yahoo.com

P. Zhao et al. (eds.), *Applied Sciences in Graphic Communication and Packaging*, Lecture Notes in Electrical Engineering 477,
https://doi.org/10.1007/978-981-10-7629-9_105

temperature-integral methods and reaction mechanism functions [4–8]. Zeolites are well-known to be very common inorganic fillers or catalysts for many applications, and their effects on thermal decomposition of PLLA have been recently studied [6–8]. In this work, the effects of two zeolites on thermal degradation features of PLLA are compared and the activation energies of PLLA/zeolite composites are also calculated for such comparison purpose.

2 Experimental Section

2.1 Materials

Original PLLA pellets was obtained from Jinan Daigang Co., Ltd., China while dehydrated ZSM-5 zeolite and Hβ zeolite were both purchased from the Catalyst Plant of Nankai University, Tianjin, China. $CHCl_3$ (analytical grade, >99%) was obtained from Tianjin Kaitong Chemical Reagent Co. Ltd., China.

2.2 Sample Preparation

The zeolite-introduced PLLA samples were prepared by quickly weighing and dispersing a desired amount of zeolite powder into $CHCl_3$ in a flask under agitation for 30 min, followed by adding a small amount of polymer and stirring for 1 h. The left polymer was introduced into the flask and continuously stirred for 2 h and the resultant suspension was spread out onto a clean glass in a fume hood and flatted with a casting knife for better evaporating $CHCl_3$. The dry sample was then heated at 120 °C in an oven for 1 h and immediately kept in the desiccator before use. The samples at a zeolite loading of 10 and 20 wt% were denoted as Z-PLA-10 and Z-PLA-20 for ZSM-5 zeolite, and H-PLA-10 and H-PLA-20 for Hβ zeolite, respectively.

2.3 Sample Characterization

Powder X-ray diffraction (XRD) analysis was conducted on a Shimadzu XRD-6000 spectrometer with Cu Kα radiation (1.5406 Å). The samples were scanned from 5 to 50° in steps of 0.02° at each point. Thermogravimetric analysis (TGA) experiments of PLLA/zeolite samples with different zeolite loadings were performed on a Shimadzu DTG-60 analyzer. For each run, approximately 8 mg of the sample was heated up to 750 K at a constant heating rate of 5, 10, 15, 20 or 30 K/min in a nitrogen atmosphere at a flow rate of 30 ml/min.

3 Results and Discussion

3.1 X-ray Diffraction Analysis Results

Figure 1 shows X-ray diffraction patterns of Hβ zeolite, ZSM-5 zeolite, pure PLLA, H-PLA-10 and Z-PLA-10 samples. As evidenced by the XRD results, the zeolites used release a number of much stronger and sharper characteristic peaks, which are typical of the BEA and MFI zeolite topologies, respectively, and identical to those reported in the literature [9]. The very high peak intensity confirms that two zeolites used both have high crystallinity with negligible amorphous silica. Likewise, pure PLLA shows one very narrow and extremely stronger peak at $2\theta = 16.76$, indicative of the crystalline nature of PLLA material. After incorporating either Hβ zeolite or ZSM-5 zeolite into the PLLA, no effects are found on the microscopic crystal structure of both zeolite and PLLA, as evidenced by the presence of characteristic peaks of both PLLA and zeolite for the H-PLA-10 and Z-PLA-10 samples. But the peak intensity of PLLA polymer is seen to drop a little and the presence of amorphous phase can also be found from XRD spectra. Thus, it can be deduced that the degree of crystallinity might have decreased more or less due to the presence of zeolite powers in the polymer matrix.

3.2 Thermal Features of PLLA/Zeolite Composites

TGA curves of PLLA and its four zeolite composite samples obtained at a heating rate of 10 K/min are presented in Fig. 2. As clearly seen, the total mass loss at the end of thermal decomposition is almost 90 and 80% for the 10 and 20 wt% zeolite

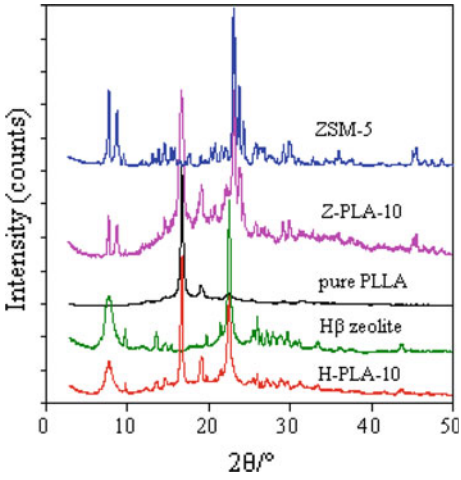

Fig. 1 XRD results obtained for Hβ zeolite, ZSM-5 zeolite, pure PLLA, H-PLA-10 and Z-PLA-10 samples

loading samples, respectively. For pure PLLA, it will be completely burnt off. This result is unsurprising since the added inorganic zeolites were not undergone thermal decomposition. It can be seen that two PLLA/Hβ zeolite composites start to thermally decompose at lower temperatures than its pure PLLA sample but after around 590 K they tend to degrade more slowly than PLLA. As for ZSM-5 zeolite, the two samples tend to undergo thermal degradation at very higher temperatures than pure PLLA, indicative of improved thermal stability.

For better examining the effect of zeolite on the thermal stability of PLLA, Table 1 lists the temperatures of 5% mass conversion (T_5), 20% mass conversion (T_{20}), maximum decomposition rate (T_p) and 70% mass conversion (T_{70}) of the PLLA and its four zeolite composites obtained at 10 K/min. These specific temperatures are abstracted from experimental TG curves shown in Fig. 2. The incorporation of Hβ zeolite into PLLA has decreased its T_5 of 566.67 to 556.67 and 522.04 K for the H-PLA-10 and H-PLA-20 samples, respectively. Similarly, T_{20} temperature of PLLA is seen to decline from 584.22 to 579.29 K for the H-PLA-20 sample. These data tend to suggest that the introduced Hβ zeolite has rendered the thermal stability of PLLA decrease, becoming less thermally stable. That is to say, the PLLA/Hβ zeolite composites may have thermally decomposed at lower temperatures than PLLA. Very interestingly, PLLA has lower T_p and T_{70} than its Hβ zeolite composite counterparts. As shown in Table 1, the T_p and T_{70} values are 608.01, 637.68 and 637.28 K, 606.12, 639.90 and 630.10 K, respectively, for the PLLA, H-PLA-10 and H-PLA-20 samples. These results indicate that the addition of Hβ zeolite may have made later thermal degradation stage of PLLA more complex. On the other hand, the Z-PLA-10 and Z-PLA-20 samples have clearly reflected higher specific temperature values than pure PLLA sample, as shown in Table 1. These results suggest that the incorporation of ZSM-5 zeolite into PLLA has led to higher thermal stability. But this enhancement tends to drop down when more ZSM-5 zeolite is used as Z-PLA-10 has higher T_5, T_{20}, T_p and T_{70} than Z-PLA-20. These interesting results suggest that the effect of zeolite on thermal degradation of PLLA is much more complicated than expected and further study is required to understand these thermal decomposition features.

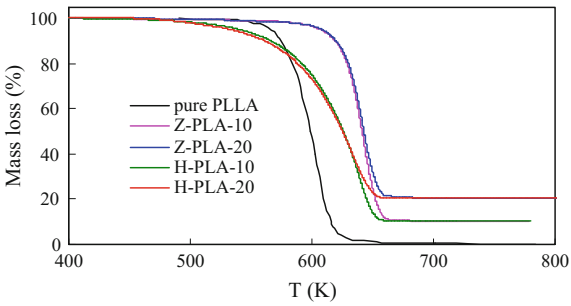

Fig. 2 TGA curves of the PLLA and its four zeolite composite samples obtained at the heating rate of 10 K/min

Table 1 Several temperatures of PLLA samples at 10 K/min

Sample	T_5(K)	T_{20}(K)	T_p(K)	T_{70}(K)
PLLA	566.67	584.22	608.01	606.12
Z-PLA-10	605.27	627.75	643.93	645.43
Z-PLA-20	603.57	626.96	643.05	644.84
Z-PLA-10	556.67	603.94	637.68	639.90
H-PLA-20	522.04	579.29	637.28	630.10

3.3 *Kinetic Analysis of PLLA Thermal Degradation*

Apart from experimental results, kinetic analysis of a set of TGA curves may provide deep understanding of the ongoing degradation process under investigation. Generally, this can be only achieved by a full knowledge of the accurate kinetic triplet, namely, the activation energy (E_a), the pre-exponential factor (ln$A$), and the kinetic conversion function, $f(\alpha)$. According to ICTAC Kinetics Committee suggestions for performing kinetic computations on thermal analysis data, a model-free isoconversional method proposed by Starink [10], denoted as the Starink method and given below, can be more accurate to estimate E_a than those reported in our earlier works [5–7].

$$\ln\left[q/T_{\alpha}^{1.92}\right] = \text{constant} - 1.0008E_{\alpha}/RT_{\alpha} \tag{1}$$

where q is the constant heating rate (K/min), T_α is the absolute temperature (K) at a given conversion level α, and R is the universal gas constant (8.314 J/mol K).

According to the calculation procedure described previously [5–7], the kinetic calculation and analysis with the Starink method have been carried out, resulting in a series of linear plots of $\ln(q/T^{1.92})$ versus $1/T$ over the whole conversion range of 0.05–0.95 for three PLLA samples. Following Eq. 1, the activation energy E_a can be calculated from the slope of the linear line for each conversion level.

The plots of E_a versus α of PLLA, Z-PLA-10, Z-PLA-20, H-PLA-10 and H-PLA-20 are graphically shown in Fig. 3. These E_a values given here are similar to those estimated by using the other methods [5–7], indicating that these model-free isoconversional methods are generally comparable to each other and it is hard to say which method is the best one. Clearly, it can be found from Fig. 3 that the activation energy E_a values of the four PLLA composites are all higher those of pure PLLA over all the entire conversion range. That is to say, the zeolite incorporation has increased the activation energy of its thermal decomposition reaction, which means the zeolite addition has made PLLA more thermally stable than its pure counterpart. However, Yuzay et al. [8] have reported that zeolite 4A and Chabazite have reduced the activation energy for PLLA and rendered it more readily to undergo thermal degradation. From Fig. 3, it can be found that ZSM-5 zeolite has resulted in higher E_a values than the other Hβ zeolite, indicating that the former zeolite has rendered PLLA more thermally stable than the latter one. A further examination shows that for both zeolites, lower zeolite content leads to

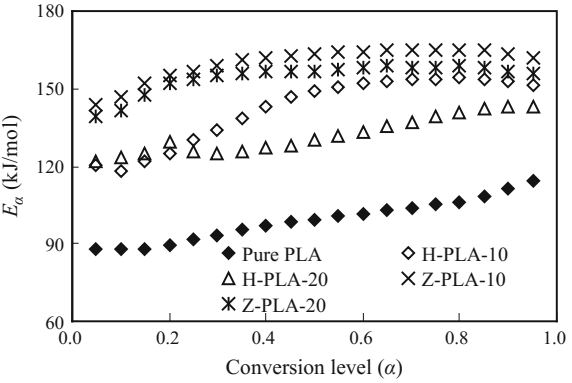

Fig. 3 The dependence of E_a on conversion level α of PLLA, Z-PLA-10, Z-PLA-20, H-PLA-10 and H-PLA-20 samples calculated by using the Starink method

higher E_a values, indicating that adding much more amount of Hβ zeolite or ZSM-5 zeolite is not good for improving thermal stability of PLLA polymer matrix.

4 Conclusions

The effects of two different zeolites on thermal degradation of poly(L-lactide) are investigated in this work. XRD results confirm that microscopic crystal structures of both zeolite and PLLA are kept very well after the zeolite introduction. TGA results reflect that the thermal stability of PLLA has been deteriorated the Hβ zeolite addition but outstandingly enhanced by the filled ZSM-5 zeolite. The Starink method has been selected to calculate the activation energy E_a values for PLLA and its four zeolite composites. Calculated results show that the zeolite addition has greatly increased the activation energy of thermal degradation as compared to pure PLLA and low zeolite content seems to lead to higher E_a values.

Acknowledgements The authors would like to thank National Students' Innovation and Entrepreneurship Training Program (No. 201510069032) and Tianjin University of Commerce (TJUC–2017-001) for funding this project.

References

1. Ansary RH, Awang MB, Rahman MM (2014) Biodegradable poly(D, L-lactic-co-glycolic acid)-based micro/nanoparticles for sustained release of protein drugs—a review. Trop J Pharm Res 13:1179–1190
2. Tawakkal ISMA, Cran MJ, Miltz J, Bigger SW (2014) A review of poly(lactic acid)-based materials for antimicrobial packaging. J Food Sci 79:R1477–1490
3. Ahmed J, Varshney SK (2011) Polylactides-chemistry, properties and green packaging technology: a review. Int J Food Prop 14:37–58

4. Zhou Q, Xanthos M (2009) Nanosize and microsize clay effects on the kinetics of the thermal degradation of polylactides. Polym Degrad Stab 94:327–338
5. Huang Z, Ye QQ, Teng LJ (2015) A comparison study on thermal decomposition behavior of poly(L-lactide) with different kinetic methods. J Therm Anal Calorim 119:2015–2027
6. Ye QQ, Huang Z, Hao YH, Wang JW, Yang XY, Fan XY (2016) Kinetic study of thermal degradation of poly(L-lactide) filled with β-zeolite. J Therm Anal Calorim 124:1471–1484
7. Hao YH, Huang Z, Wang JW, Yang XY, Fan XY, Li YI, Peng YW (2016) Improved thermal stability of poly(L-lactide) with the incorporation of zeolite ZSM-5. Polym Testing 49:46–56
8. Isinay EY, Rafael A, Herlinda SV, Susan S (2010) Effects of synthetic and natural zeolites on morphology and thermal degradation of poly(lactic acid) composites. Polym Degrad Stab 95:1769–1777
9. Breck DW (1964) Zeolite molecular sieves. Wiley, New York
10. Starink MJ (2003) The determination of activation energy from linear heating rate experiments: a comparison of the accuracy of isoconversion methods. Thermochim Acta 404:163–176

Utilization of Smart Nanomaterials for Fruit Fresh Keeping

Zuguang Shen, Guangxue Chen, Linjin Chen, Linyi Chen and Zhaohui Yu

Abstract This research reported the fresh-keeping effectivity of smart nanomaterials for bananas and kiwis. The fresh-keeping gas, 1-methylcyclopropene (1-MCP), was loaded in self-assembled nano microballoon of cyclodextrin. The amount of 1-MCP in the nano microballoon was detected by TG, and the amount of 1-MCP was up to 2 wt%. 1-MCP released much faster when the microballons were dealt with water than in the air, and it needed about 8 days for the complete release of 1-MCP in water, while it only released 0.3% under 74% air humidity after 25 days. The nano microballoons were added into printing ink uniformly, and then printed on the surface of cartons. The medium-well fruit without any treatment for fresh keeping was picked from orchard, and the fresh-keeping measure was conducted in daily environment. The storage time of kiwis in common carton was about 6 days, while the time can be prolonged to 23 days in fresh-keeping carton. And the storage time of bananas in fresh-keeping box was 5 times to that in common box, where the bananas can be stored for 5 days.

Keywords Fresh-keeping · 1-MCP · Microballons · Printing · Carton

1 Introduction

Consumption of fruit with good quality might decrease the development risk of chronic diseases in human body and provide benefits for body health [1, 2]. However, the loss of nutritional ingredients in fruit always occurs because of its

Z. Shen · G. Chen (✉) · L. Chen · Z. Yu
Shenzhen YUTO Packaging Technology Co. Ltd., Shenzhen, China
e-mail: chengx@scut.edu.cn

G. Chen
State Key Laboratory of Pulp and Paper Engineering,
South China University of Technology, Guangzhou, China

L. Chen
School of Materials Science and Engineering,
Wuhan Institute of Technology, Wuhan, China

P. Zhao et al. (eds.), *Applied Sciences in Graphic Communication and Packaging*, Lecture Notes in Electrical Engineering 477,
https://doi.org/10.1007/978-981-10-7629-9_106

decay and physiological changes, which could be induced by the microbial infection during the storage time [3, 4]. Meanwhile, the decay of fruit would decrease the farmers' income, even disorganize the rule of fruit market. Thus, a great quantity of researchers concentrate on studies of prolonging the storage time of fruit.

Nowadays, there are lots of methods for increasing storage time of fruit, including low temperature, controlled atmosphere and antibacterial. Hai et al. [5] utilized PE cling bag built-ethylene absorbent and storage at 3 °C, and litchi storage period could be extended to 18 days. Cheng et al. [6] studied the preservation of Hami-melon dealt with low temperature, the storage time was up to 30 days, and it could obviously delay the debasement of quality and keep it better nutrition and appearance qualities. Chen [7] had studied that the rate of good pear was still up to 95–98% after 240 days under the controlled atmosphere. Qi et al. [8] had studied the rate of musty fruit was reduced by 67% points 22 days after harvesting under the treatment of controlled atmosphere. Yang et al. [9] utilized antibacterial to prolong the storage time of fruit, and there was less loss of fruit nutrition after 18 days. Ren et al. [10] found out that coptis chinensis ethanol extracts can inhibit the microbial infection during the storage and prolong the storage time of oranges. Although the above methods can increase the storage time of fruit, the technologies of low temperature and controlled atmosphere will increase cost and waste energy, and they are not convenient for transportation. The antibacterial technology can inhibit the microbial infection, but the antibacterial may exist on the surface of fruit and might be harmful to health. Meanwhile, antibacterial technology can't prolong the ripen time of fruit. Thus, a simple, cheap, and effective method for fresh-keeping fruit is the direction which scientists research.

In this study, a simple, cheap, and effective method was used for fresh-keeping fruit. The microballons loaded with 1-MCP were dispersed on the surface of cartons, and bananas and kiwis were utilized for fresh-keeping measure in daily environment. Meanwhile, the amount of 1-MCP in microballons and release rate of 1-MCP in microballons wetted by water and under air atmosphere were detected.

2 Experiment Section

2.1 Materials and Equipment

Bananas, started to turn ripe and picked from an orchard; Kiwis, medium well, picked from an orchard freshly; fresh-keeping agent, including 1-MCP, cyclodextrin; cartons, produced from corrugated paper; transparent film, used to airtight carton and observe the change of fruit. Gas flowmeter (D08-1F) was purchased from Beijing Sevenstar Electronics Co., Ltd.

2.2 Characterization

The amount of 1-MCP in the microballons was detected by thermogravimetric analyzer (Daojing, Japan), the flow rate of N_2 was 50 mL/min, and the temperature was increased to 600 °C by 20 °C/min.

The release rate of 1-MCP in air and water was measured by gas chromatograph (GC-2010 plus), equipped with a flame ionization detector and a quartz capillary column (30 m × 0.25 mm × 0.25 μm). The temperatures of sample injector and detector were both 150 °C, and the temperature of capillary column maintained 50 °C for 10 min. The split ratio of N_2 was 10, and the flow rate was 1.5 mL/min. 5 mL sample was injected every time, and isobutene calibrating gas was as reference substance to calculate the amount of 1-MCP.

2.3 Fruit Fresh-Keeping Measure

The tests were divided into six groups listed as b-1, b-2, d-1, d-2, w-1, and w-2 (Table 1). 4.5 g microballons were added into printing ink uniformly, and then printed on the surface of carton. The cartons were sealed by transparent film to be observed the change of fruit during the measure easily. All the fruit was fresh, similar size, and maturity. The fresh-keeping experiment was conducted in daily environment.

3 Results and Discussion

The thermal analysis result was shown in Fig. 1, and there were three weightlessness peaks. One was located before 110 °C, due to the water evaporating from the microballons. Another one was between 180 and 210 °C, because of the release of 1-MCP. The third one was located after 320 °C, on account of decomposition of cyclodextrin. According to the amount of loss from ordinate, the weight of 1-MCP was about 2% in microballons.

Figure 2a showed the spectrum of isobutene in gas chromatograph, and the retention time was 1.551 min. Interestingly, the retention time was 1.605 min in Fig. 2b, where the relative error was less than 5%. Thus, it can be verified that the gas released from the fresh-keeping agent in Fig. 2b was 1-MCP. Figure 2c

Table 1 The different measure conditions for fruit fresh keeping

Number	b-1	b-2	d-1	d-2	w-1	w-2
Condition	Blank air holes	Blank airtight	Dry air holes	Dry airtight	Wet air holes	Wet airtight

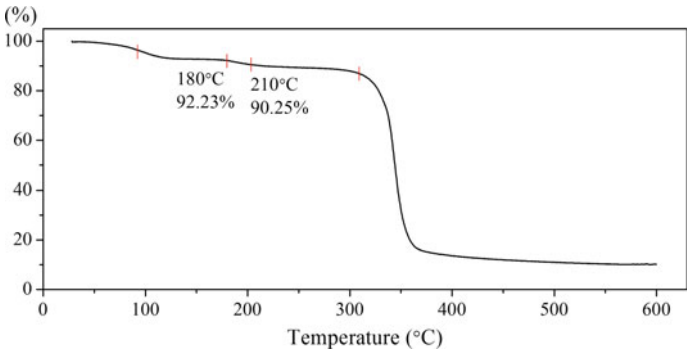

Fig. 1 The thermal analysis result of 1-MCP

depicted the standard curve of isobutene about the area and corresponding concentration. Isobutene was prepared as 25, 50, 75, 100 × 10^{-6} mol/mol with gas flowmeter, and the corresponding peak area was calculated by the spectrum of gas chromatograph. The equation of linear regression between peak area and concentration can be described as y = 19.476x + 634.5, R^2 = 0.9959. A certain quality of microballons in an enclosed bottle were wetted sufficiently, and suction of the gas was injected into capillary column after 10, 30, 60, 120, 240, 360 min, respectively. The release amount and its ratio to mass was recorded in Table 2, and the release rate of 1-MCP was described in Fig. 2d. The linear equation of release rate before 30 min can be summarized as y = 0.008x + 0.3535, R^2 = 1, while from 30 to 120 min, it can be summarized as y = 0.0012x + 0.552, R^2 = 0.9839, and from 120 to 360 min, it can be summarized as y = 0.0002x + 0.6632, R^2 = 0.9359. Thus, it needs 8 days at least to release 2% 1-MCP completely, which can be utilized to extend the mature period. For the release rate of 1-MCP in air atmosphere, isobutene was prepared as 1, 2, 3, 4 × 10^{-6} mol/mol with gas flowmeter, and the equation of linear regression between peak area and concentration can be described as y = 320.3x−62.5, R^2 = 0.9902 (Fig. 2e). Suction of the gas was injected into capillary column after 5, 8, 15, 18, 25 days under 74% air humidity, respectively. The release amount and its ratio to mass was recorded in Table 3, and 1-MCP was released only 0.3% after 25 days. The release rate of 1-MCP under 74% air humidity was illustrated in Fig. 2f, where the regression equation was y = $-2E-6x^2$ + 0.0002x + 0.0028, R^2 = 0.9926.

The result of fresh-keeping experiment for bananas was shown in Fig. 3. The blank ones both ripened after 5 days, but the storage time was prolonged when the microballons were printed on the surface of cartons. For the dry nano microballons, the bananas in airtight carton can be stored for 23 days, and just 13 days in the carton with air holes. When the microballons were wetted, the bananas in airtight carton can be stored for 28 days, and 19 days in the carton with air holes. Therefore, the microballons can prolonged the storage time, and the effect of storage in airtight place was better than that in ventilated place.

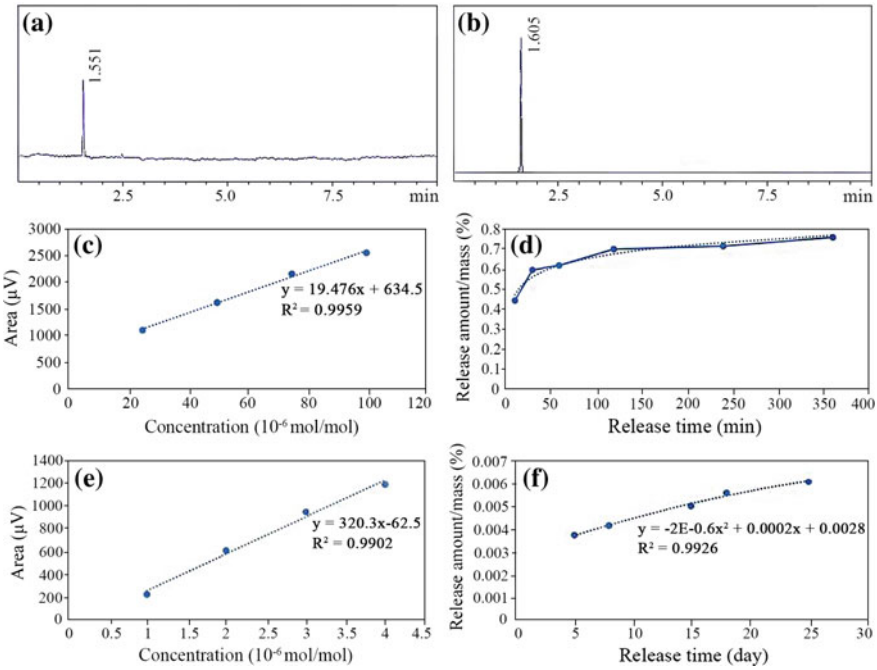

Fig. 2 The spectrum **a** of isobutene in gas chromatograph; **b** of 1-MCP in gas chromatograph; **c** of isobutene between the peak area and concentration; **d** of 1-MCP between the release amount/mass and release time in water; **e** of isobutene between the peak area and concentration; **f** of 1-MCP between the release amount/mass and release time under 74% air humidity

Table 2 The release amount and its ratio to mass of 1-MCP in water

Time (min)	Peak area	Release amount (μg)	Release amount/mass (%)
10	30,694	26.03811	0.433
30	41,699	35.57246	0.592
60	43,151	36.83813	0.614
120	48,769	41.6478	0.694
240	49,854	42.7174	0.712
360	52,739	45.2214	0.754

Table 3 The release amount and its ratio to mass of 1-MCP under 74% air humidity

Time (day)	Peak area	Release amount (μg)	Release amount/mass (%)
5	556	1.86024	0.00372
8	617	2.06928	0.00414
15	739	2.49906	0.00500
18	824	2.78435	0.00557
25	901	3.03428	0.00607

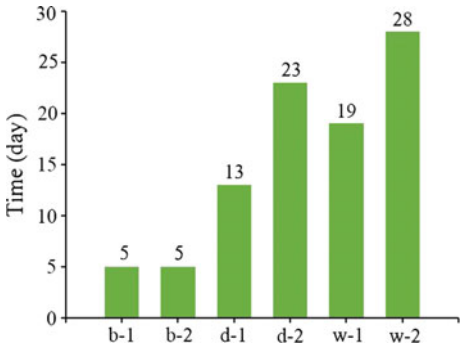

Fig. 3 The result of fresh-keeping experiment for bananas

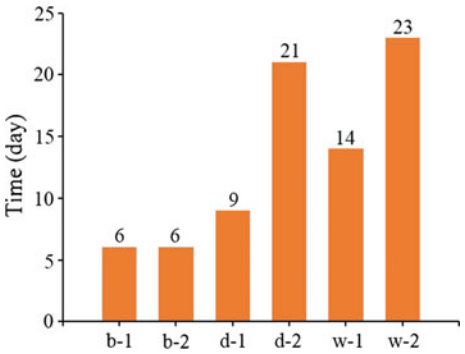

Fig. 4 The result of fresh-keeping experiment for kiwis

The result of fresh-keeping experiment for kiwis was shown in Fig. 4. The kiwis could be stored for 9 days in the carton with air holes printed by dry microballons, and 21 days in airtight carton, while it only took 6 days in blank. Kiwis can be stored for 14 and 23 days in cartons printed wet microballons with and without air holes, respectively. Thus, the microballons can prolonged the storage time, and the effect of storage with wet microballons was better than that with dry microballons under the same condition.

4 Conclusions

In this work, the nano microballons loaded 2 wt% 1-MCP, which was utilized to prolong the storage time of fruit. It needed 8 days for 1-MCP in microballons to release completely under wetting condition, which was much faster than that under air condition. The storage time of kiwis in fresh-keeping carton was 4 times to that in common carton, and the fresh-keeping carton can prolong 5 times for the storage of bananas. Moreover, the fresh-keeping effect of microballons in airtight place was

better than that in ventilated place, and wet microballons was better than dry microballons under the same condition.

Acknowledgements This work was financially supported by Research and Development of Smart Fresh-keeping Packaging Materials of Slow Release Microcapsule (JSGG201508141108 53356), the Special Funds of Strategic Emerging Industry and Future Industrial Development in Shenzhen, belonging to Engineering Laboratory of Nano Smart Coating Materials (No. 2016.939), which was the second supporting plan in 2016, the State Key Laboratory of Pulp and Paper Engineering Project (2016C01), and the Science and Technology Planning Project in Guangzhou (201607020045), which was the Key Special Project of Scientific Research.

References

1. Krikorian R, Boespflug EL, Fleck DE, Stein AL, Wightman JD, Shidler MD, Sadat-Hossieny S (2012) Concord grape juice supplementation and neurocognitive function in human aging. J Agric Food Chem 60(23):5736–5742
2. Guerra ICD, de Oliveira PDL, Santos MMF, Lúcio ASSC, Tavares JF, Barbosa-Filho JM, Madruga MS, de Souza EL (2016) The effects of composite coatings containing chitosan and Mentha (piperita L. or x villosa Huds) essential oil on postharvest mold occurrence and quality of table grape cv. Isabella. Innovative Food Sci Emerg Technol 34:112–121
3. Xing Y, Xu Q, Che Z, Li X, Li W (2011) Effects of chitosan-oil coating on blue mold disease and quality attributes of jujube fruits. Food Funct 2(8):466–474
4. Xing Y (2015) Effect of chitosan coating with cinnamon oil on the quality and physiological attributes of China jujube fruits. Biomed Res Int 2015(2):1–10
5. Hai JP, He SX (2013) Fresh-keeping on litchi by polyethylene bags and ethylene absorbent at low-temperature. Food Sci Technol 3:020
6. Qiuhua C, Lan X, Haihong W, Yongjin Q, Haifeng G, Chunying J (2010) Research of preservation and low temperature on the changes of fruit quality in storage of Hami-melon. Innovational Ed Farm Prod Process, 8:010
7. Guo-gang CHEN (2004) Technology of controlled atmosphere storage and fresh-keeping of fragrant pear of Kuerle. Storage Process 1:019
8. Qi XJ, Liang SM, Zhou LQ (2003) Study on effects of small controlled-atmosphere environment on keeping bayberry fruits fresh. Acta Agriculturae Zhejiangensis 15(4): 237–240
9. Yang C, Li C, Zhou Y, Zheng Y, Sheng S, Ding J et al (2016) Determination of main active substances in fresh mulberry fruits after fresh-keeping treatment with chitosan-g-caffeic acid derivative. Science of Sericulture
10. Ren Y, Liu C, He J, Wang S, Zhang L (2012) Fresh-keeping and antibacterial technology of citrus fruits based on ethanol extracts from Chinese herbs. Nongye Jixie Xuebao (Transactions of the Chinese Society of Agricultural Machinery) 43(5):122–129

Synthesis and Mesophases Study on 2-Hexylhexanoate-3,6,7,10,11-Pentabutoxytriphenylene

Huanzhi Yang, Zhenghu Zhang, Wanying Zhang, Xingtian Hao, Feng Hong, Chunxiu Zhang and Jialing Pu

Abstract The target product 2-hexylhexanoate-3,6,7,10,11-pentabutoxytriphenylene based molecules was synthesized and characterized. Several known experimental techniques had been used to determine the chemical structure, physical mesophase behavior of the compounds, by FT-IR spectroscopy, ^{1}H-NMR, differential scanning calorimetry (DSC) and polarizing optical microscopy (POM). By π-π stacking and dipole-dipole interaction, this compound can self-organize into columnar structures, providing useful information to organic optoelectronic applications.

Keywords Triphenylene · Discotic liquid crystalline · Columnar phase

1 Introduction

Discotic liquid crystals have becoming the focus of numerous investigations in the characterization and the optoelectronic property study, since 1977. Discotic liquid crystals consist of two important parts: the molecular center is a discoid nucleus with several flexible chains on its periphery [1]. Discotic liquid crystals display liquid-crystalline properties which can self-organize into columnar phase. Discotic liquid crystals conduct important organic semiconductors which have been involved in the operation of organic optoelectronic devices, charge transfer processes and energy transfer in several fields including organic light-emitting diodes (OLEDs), organic solar cells, organic lasers and organic field-effect transistors (OFETs) [2–4].

The synthesization and purification of triphenylene derivatives can be combined conveniently. Those derivatives self-spontaneous organization property result in higher order degree of spatial structure thermal and photochemical stability [5]. With the polarizing optical microscopy (POM) which can observe the evolution of the liquid crystal phase, and differential scanning calorimeter (DSC) which can

H. Yang · Z. Zhang · W. Zhang · X. Hao · F. Hong · C. Zhang (✉) · J. Pu
Beijing Institute of Graphic Communication, Beijing, China
e-mail: zhangchunxiu@bigc.edu.cn

P. Zhao et al. (eds.), *Applied Sciences in Graphic Communication and Packaging*, Lecture Notes in Electrical Engineering 477,
https://doi.org/10.1007/978-981-10-7629-9_107

accurately record the phase transition temperature and the corresponding enthalpy change, they can support to determine the liquid crystal phase in combination.

2 Experimental

All analytic reagents (Beijing Chemical Reagents Co.) which weren't specified were used in the synthesis. The chemical structure was characterized by measuring on a FTIR-8400 and Brucker DMX-300,300 MHz NMR spectrometer. Optical and thermal properties were observed by using Netzsch differential scanning calorimeter (DSC) and Lecia polarizing optical microscope (POM).

2.1 Synthsis of 2-Hexylhexanoate-3,6,7,10,11-Pentabutoxy-Triphenylene

A classical synthetic route was presented which was shown in Fig. 1.

According to the Williamson reaction, catechol, anhydrous K_2CO_3 was dissolved in acetone, and 10 min later, bromo-n-pentane was added into a round-bottomed flask and heated under argon for 16 h. The mixture was subjected to distillation under reduced

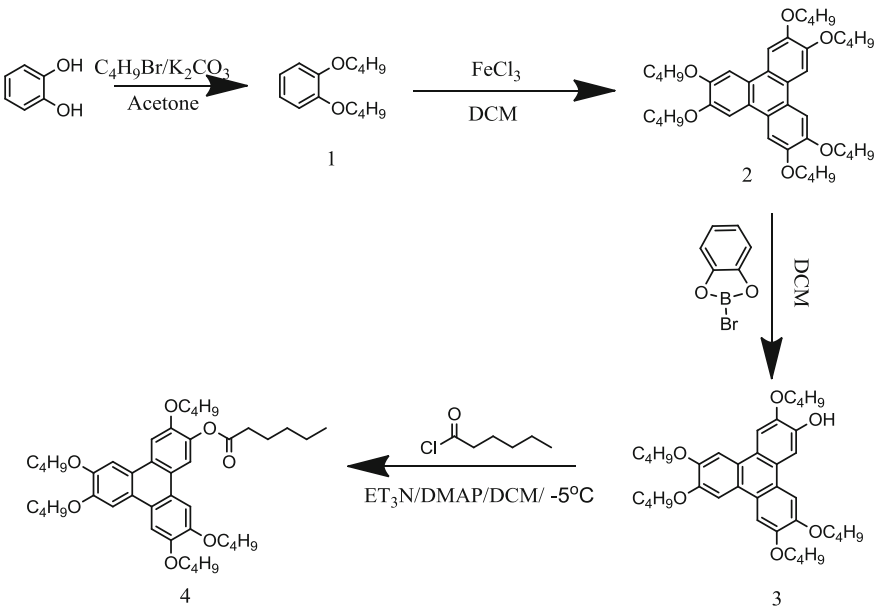

Fig. 1 Synthetic route of compound 4

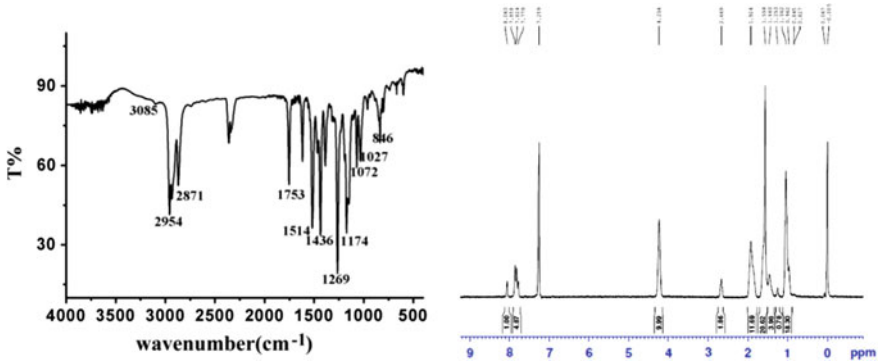

Fig. 2 IR (left) and ^{1}H-NMR spectra (right) of compound 4

pressure to obtain compound 1. Then, compound 1 was dissolved in dichloromethane, and anhydrous iron (III) chloride was added to carry out the trimerization reaction to synthesize 2,3,6,7,10,11-pentabutoxytriphenylene (compound 2) [6]. The process of preparing 2-hydroxyl-3,6,7,10,11-pentabutoxytriphenylene (compound 3) was realized by selective ether cleavages with B-bromocate-cholborane. 2-hydroxy-3,6,7,10,11-pentabutoxytripheylene, 4-dimethylaminopyridine, anhydrous dichloromethane was added to a three-necked flask and magnetically stirred at −5 °C (low temperature constant temperature mixing bath). Under the nitrogen atmosphere, triethylamine and hexanoyl chloride were injected by medical syringe to carry out the esterification reaction to obtain the product. The product was washed three times with sodium hydroxide solution and saturated sodium chloride solution, respectively. This product was purified by column chromatography with 3/1(v/v) CH_2Cl_2/petroleum ether as the eluent, which yields 52.5%.

2.2 Characterization

Through using polarizing optical microscope (POM) and differential scanning calorimeter (DSC), thermal and optical properties of the product can been clearly observed. The ramp rate was 10 °C min^{-1} in both POM and DSC. The temperature range is 0–180 °C and differential scanning calorimeter (DSC) calculated the phase change enthalpy.

3 Results and Discussion

3.1 FT-IR and ^{1}H-NMR

FT-IR (KBr): $V_{max}(cm^{-1})$: 3085 (–CH=CH_2); 2954, 2871 (–CH3/–CH_2); 1753 (–C=O); 1269 (–C–O); 1616 (–C=C–); ^{1}H-NMR: δH (300 MHz, $CDCl_3$): 7.779–8.063 (m, 6H), 4.234 (s, 10H), 2.669 (s, 2H), 1.924 (s, 10H), 1.460–1.558 (m, 16H), 0.827–1.042 (m, 18H). They are shown in Fig. 2.

3.2 DSC

As we can see in the DSC thermogram (Fig. 3), the compound 4 had an endothermic transition (23.29 J/g) at 175.9 °C. During second heating run, the compound transformed to a non-birefringent isotropic phase at around 175.9 °C which was the clearing point. There was a exothermic transition (23.35 J/g) at 172.3 °C cooled (10 °C/min) to room temperature and the liquid crystal texture characteristic was maintained until room temperature during the cooling process.

3.3 POM

Compound 4 had no crystalline phase and was birefringent at room temperature. It showed a typical texture in Fig. 4, when the liquid sample was cooled from 176 °C to room temperature. Until cooled to 150 °C, the texture of compound 4 had already formed and maintained its appearance to room temperature. The compound showed a classical columnar phase texture characteristic by POM.

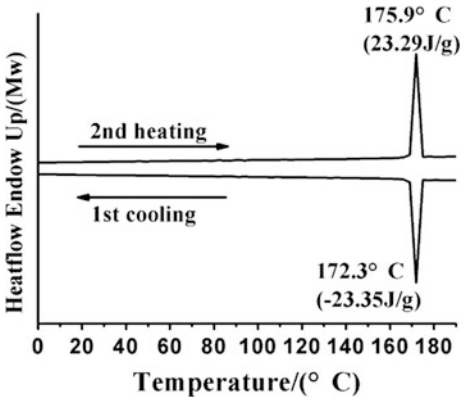

Fig. 3 DSC thermogram of compound 4

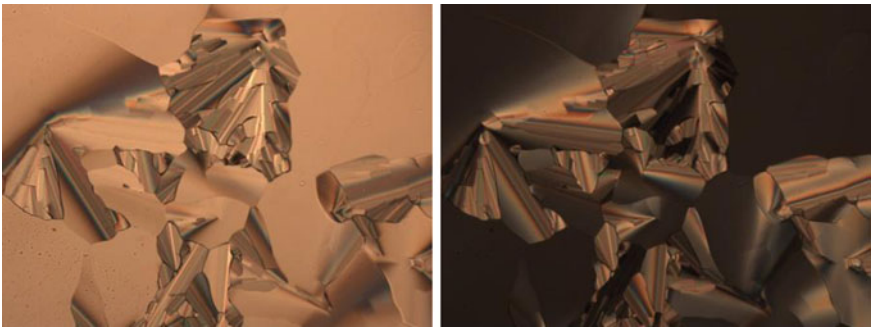

Fig. 4 Textures observed at 150 °C at different angle 0° (left) and 45° (right)

4 Conclusions

The result, the compound 2-hexylhexanoate-3,6,7,10,11-pentabutoxytriphenylene based triphenylene was prepared and fully characterized. The chemical structure was confirmed by measuring on the ^{1}H-NMR and FT-IR spectrum. The target compound's columnar phase texture was observed by POM, combining with the test results of DSC. This compound exhibited good liquid crystal columnar phase properties and liquid crystal range, which provides a basis for the subsequent synthesis organic semiconductors devices. It had also been proved that the introduction of easter group into discotic liquid crystals could suppress the crystallization, broad the mesophase range, increase the clearing temperature and stabilize columnar phase.

Acknowledgements This study is funded by the Beijing Municipal Education Commission Project under Grant (No. KM 201210015008, 21090116007, and 04190117001/002).

References

1. Chandrasekhar S, Sadashiva BK, Suresh KA (1977) Liquid crystals of disc-like molecules. Pramana 9:471–480
2. Bredas JL, Beljonne D, Coropceanu V, Cornil J (2004) Charge-transfer and energy-transfer processes in π-conjugated oligomers and polymers: a molecular picture. Chem Rev 104: 4971–5004

3. Veldman D, Meskers SCJ, Janssen RAJ (2009) The energy of charge-transfer states in electron donor-acceptor blends: insight into the energy losses in organic solar cells. Adv Func Mater 19:1939–1948
4. Uoyama H, Goushi K, Shizu K, Nomura H, Adachi C (2012) Highly efficient organic light-emitting diodes from delayed fluorescence. Nature 492:234–238
5. Funahashi M, Hanna J (2000) High ambipolar carrier mobility in self-organizing terthiophene derivative. Appl Phys Lett 76:2574–2576
6. Boden N, Borner RC, Bushby RJ, Cammidge AN, Jesudason MV (1993) The synthesis of triphentlene-based discotic mesogens new and improved routes. Liq Cryst 15(6):851–858

Synthesis and Property Study of 2-Undecenoic Acid Ester-3,6,7, 10,11-Penta-Pentyloxytri-Phenylene

Zhenhu Zhang, Huanzhi Yang, Wanying Zhang, Chunxiu Zhang, Xingtian Hao and Jialing Pu

Abstract A kind of new triphenylene-based liquid crystal 2-undecenoate-3,6,7,10, 11-pentapentyloxytri-phenylene containing carbon-carbon double bonds was synthesized by esterification. The structure of the compounds was determined via ^{1}HNMR and FT-IR spectroscopy. The thermal properties of the compound were studied in depth by differential scanning calorimeter (DSC) which showed a wide mesophase temperature from 113.8 °C to room temperature. The optical properties of the compound had also been studied by polarized light microscopy (POM) which showed a typical pyramid texture of the columnar phase. The derivative is expected to be used as polymerized monomers for the preparation of liquid crystal polymers via reversible addition chain transfer (RAFT) polymerization.

Keywords Discoid liquid crystal · Triphenylene · Texture

1 Introduction

The discotic liquid crystals of benzenediate was first discovered in 1977 by Chandrasekhar et al. [1] Triphenylene is mainly composed of disc-like core and peripheral flexible side chains which makes it and its derivative has liquid crystal performance. Due to the mechanical properties of triphenylene, it can be realized as columnar liquid crystal phase by self-assembly. Triphenylene can exhibit columnar liquid crystal phase and conductivity, so that it and its derivative will have a good development prospects when applied in photoelectric materials, information recording materials, solar cells and OLEDs [1–5]. Compared with triphenylene, its derivatives have a lot of optimized properties, such as low melting point, a variety of structures, good chemical stability and especially simple procedures of synthesis and purification.

Z. Zhang · H. Yang · W. Zhang · C. Zhang (✉) · X. Hao · J. Pu
Beijing Institute of Graphic Communication, Beijing, China
e-mail: zhangchunxiu@bigc.edu.cn

P. Zhao et al. (eds.), *Applied Sciences in Graphic Communication and Packaging*, Lecture Notes in Electrical Engineering 477,
https://doi.org/10.1007/978-981-10-7629-9_108

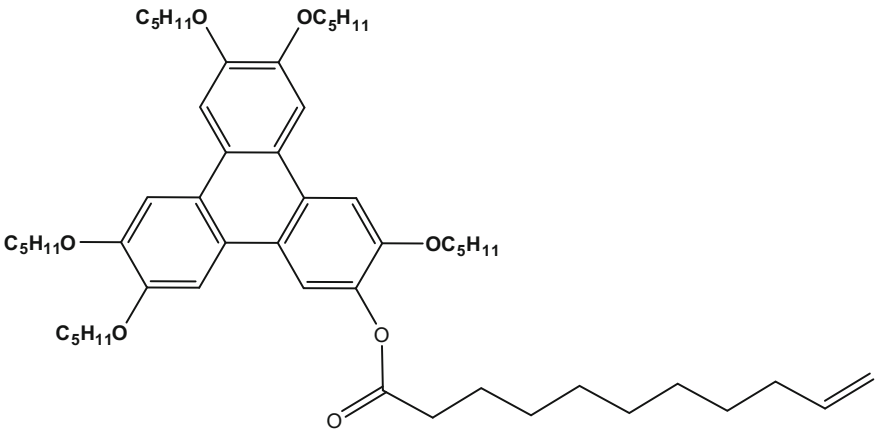

Fig. 1 Chemical structure of 2-undecenoic acid ester-3,6,7,10,11-penta-pentyloxytriphenylene

In this paper, the synthesis process and properties of the new discotic liquid crystal compound 2-undecenoate-3,6,7,10,11-pentaoxytitrishenylene were studied. This compound has many advantages among which it can change into polymers by means of the reversible addition chain transfer (RAFT) polymerization [2]. Such as it has a carbon-carbon double bond for the polymer to provide a structural basis and the presence of eight methylene groups between benzophenone and carbon-carbon double bonds can reduce the effect of steric hindrance at the time of polymerization. The structure of this compound was determined via ^{1}HNMR and FT-IR. The structure of the triphenylene derivative is shown in Fig. 1.

2 Experimental

The chemical reagents which used in the synthesis of the compounds are analytical (Beijing Chemical Reagent Company). The structure of the discotic liquid crystal derivative was judged to pass Brucker DMX-300,300 MHz NMR spectrometer and FTIR-8400. The thermal properties of this compound were studied by Netzsch differential scanning calorimeter (DSC 2010) and the optical properties were studied through Lamia polarized optical microscope (POM).

2.1 Synthesis of 2-Undecenoic Acid Ester-3,6,7,10,11-Penta-Pentyloxytriphenylene

The compound 4 was prepared via the procedure shown in Fig. 2.

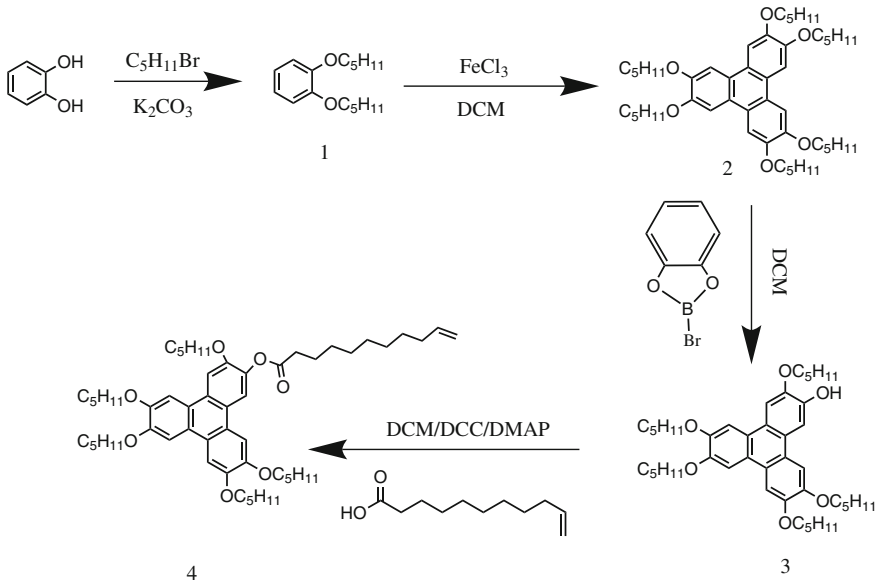

Fig. 2 Synthesized route of compound 4

The synthesis of the target compound is mainly based on the literature [2–5]. The synthesis of 1-methoxy-2-(pentyloxy)benzene (compound 1) was synthesized through Williamson reaction principle. Then, according to the mechanism of Scholl reaction, compound 1 was catalyzed by iron trichloride and trimerized to give 2,3,6,7,10,11-hexamethoxy triphenylene [6]. In order to get 2-hydroxyl-3,6,7,10, 11-penta-pentoxytriphenylene (compound 3), the B-type bromate-cholesterol was selected because it has slightly lower of the activity than boron tribromide. The ether bond is cleaved and the hydroxyl group is produced using the acidity of the catalyst [3]. I chosed 2-hydroxy-3,6,7,10,11-penta-Pentyloxytriphenylene (2 g, 2.9 mmol), DMAP (0.102 g), DCC (0.733 g, 3.5 mmol) and dichloromethane (80 ml) that were added to a 250 ml three-necked flask. When stirred about 10–15 min, 10 g Undecylenic acid (0.6552 g, 3.48 mmol) was added dropwise there to and then the reaction was heated to 40° of reflux in an oil bath. After completion of the reaction, the product was washed with water and an alkaline solution. Through dried, purified by chromatography and recrystallized from ethanol, the yield of compound 4 was 86.5%.

FT-IR (KBr): Vmax (cm^{-1}): 1746 cm^{-1}(C = O, str); 1622 cm^{-1}(C = C, str); 1509 cm^{-1}(C–H, str); 1145 cm^{-1}(C–O–C, str); 925 cm^{-1}(Ar–H, w).

^{1}H-NMR (300 MHz, $CDCl_3$) δ8.06 (s,1H), 7.78–7.86 (t, 5H), 5.79–5.88 (q, 1H), 4.93–5.04 (q, 2H), 4.20–4.24 (t, 10H), 2.65–2.70 (t, 2H), 1.84–1.97 m, 10H), 0.89–2.08 (m, 51H) (Fig. 3).

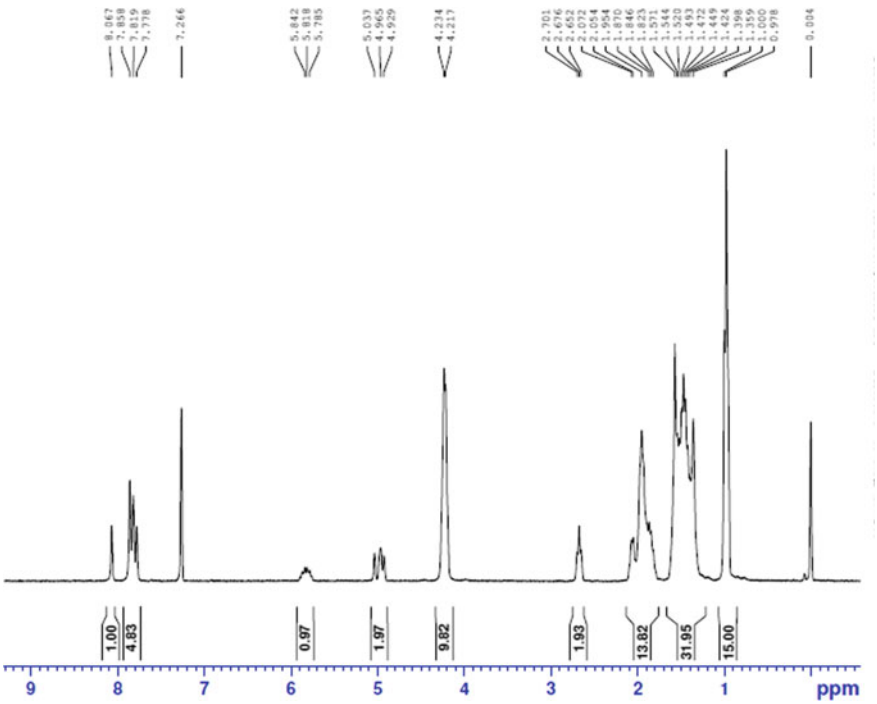

Fig. 3 ^{1}H-NMR spectra of compound 4

2.2 Characteristics of Liquid Crystal

The optical texture of liquid crystal was studied by polarized light microscope with controlled temperature. The synthesized compound was placed under a polarizing microscope and heated from room temperature to 185 °C at a rate of 10 °C/min and then dropped to room temperature at a rate of 10 °C/min. During the cooling process, the change of the texture was observed by polarizing microscope. The compound was measured by DSC for more accurate phase transition temperatures and specific enthalpy values.

3 Results and Discussion

3.1 POM

Compound 4 was slowly cooled from 185 °C to room temperature, and we can observe the classical pyramidal texture by means of polarizing microscope in this

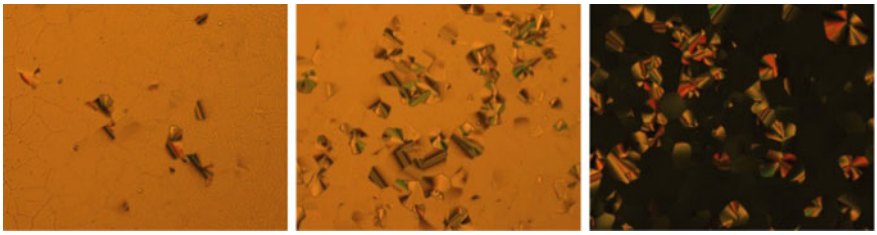

Fig. 4 Under POM, the liquid crystal texture of Compound 4 was observed at 107 °C (left), 100 °C (center) and room temperature (right) during cooling process

process. The compound was maintained at birefringence until room temperature and the crystalline phase was not observed at the POM. Its texture was shown in Fig. 4.

3.2 DSC

As shown in Fig. 5, we only observe done endothermic peak at the 113.8 °C during heating process from room temperature to 185 °C. Combined with polarizing microscope we can see that the compound got into isotropic at this time. In the cooling process, the compound was only observed one exothermic peak at 109.8 °C, and began from Isotropic get into liquid crystal state. The endothermic

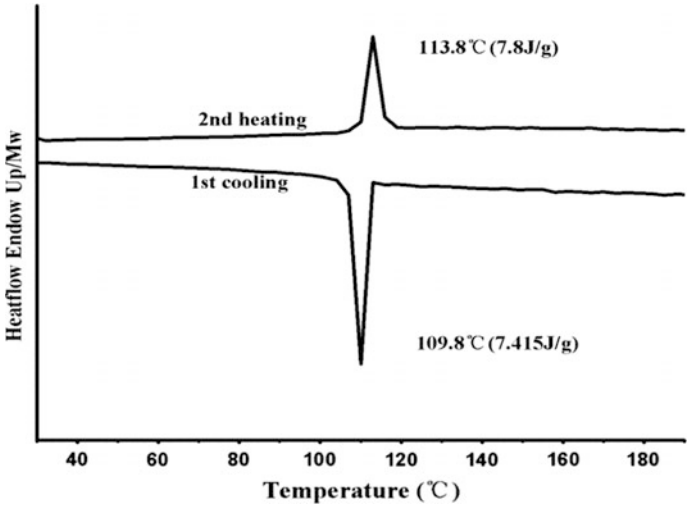

Fig. 5 DSC thermogram of compound 4

heat and release process described throughout the DSC in good agreement with the phase transition observed by the polarizing microscope. The DSC curve of Compound 4 is shown in Fig. 5.

4 Conclusions

In this study, 2-undecenoic acid ester-3,6,7,10,11-pentapentyloxytriphenylene contained multiple flexible spacers between triphenylene and double bonds were successfully synthesized and characterized. The structures of the compounds were determined by ^{1}HNMR and FT-IR spectra. Liquid crystal properties of the compounds were characterized by POM and DSC. Compound 4 exhibits columnar mesophase between room temperature and 109.8 °C, which showed a wide liquid crystalline mesophase and then lied the foundations for more optoelectronic material. This derivative is a typical disk-like liquid crystal phase and it can serve as a monomer for forming polymers which establish the foundation of research about discotic polymers.

Acknowledgements The work of this article has been supported by the Beijing Municipal Education Commission Project under Grant (No. KM 201210015008, 21090116007 and 04190117001/002).

References

1. Chandrasekhar S, Sadashiva BK, Suresh KA (1977) Liquid crystals of disc-like molecules. Pramana 7:471–480
2. Mu B, Wu B, Pan S et al (2015) Hierarchical self-organization and uniaxial alignment of well synthesized side-chain discotic liquid crystalline polymers. Macromolecules 48(8):2388–2398
3. Kumar S, Manickam M (1998) Synthesis of functionalized triphenylenes by selective ether cleavage with B-bromocateholborane. Synthesis 8:1119–1122
4. Bushby RJ, Lozman OR (2002) Discotic liquid crystals 25 years on. Curr Opin Colloid Interface Sci 7:342–354
5. Kumar S (2004) Recent developments in the chemistry of triphenylene-based discotic liquid crystals. Liq Cryst 31(8):1037–1059
6. Boden N, Borner RC, Bushby RJ, Cammidge AN, Jesudason MV (1993) Thesynthesis of triphentlene-based discotic mesogens new and improved routes. Liq Cryst 15(6):851–858

Study on Conductivity of the Composites of Polyaniline/Nano-Cellulose

Zhiwei Zhang and Fuqiang Chu

Abstract In this paper, polyaniline was synthesized by chemical oxidation under acidic conditions using ammonium persulfate as oxidant. And then, the polyaniline was doped with a certain concentration of protonic acid to make it conductive. Finally, Nano-Cellulose and polyaniline were combined to obtain composite products with good composite effect and good electrical conductivity. The results shown that the conductivity of the conductive polyaniline was 9.98 S/cm under the optimum experimental condition (reaction temperature was 0 °C, the amount of material APS:AN was 1:1, Hcl concentration was 2 mol/L). The best compound effect was that Nano-Cellulose and polyaniline were mixed by in situ polymerization and ultrasonic treatment of the combined effect and the composite ratio was 3:2.

Keywords Polyaniline · Dope · Conductivity · Nano-Cellulose

1 Introduction

Polyaniline is a typical conductive polymer. Compared with other conjugated macromolecules, conductive polyaniline has attracted much attention because of its simple preparation method, low raw material price, good electrical conductivity and good stability [1]. Polyaniline is widely used in electrochemical catalysis, electrochromic, corrosion protection, sensors and the rest, and polyaniline is the most promising one of the conductive polymer [2]. But its coral-like molecular structure determines the insoluble, has become a bottleneck restricting its development and application. Solving its insoluble is the prerequisite for the application of polyaniline.

Z. Zhang · F. Chu (✉)
College of Printing and Packaging Engineering,
Qilu University of Technology, Shandong, China
e-mail: fqchu@126.com

P. Zhao et al. (eds.), *Applied Sciences in Graphic Communication and Packaging*, Lecture Notes in Electrical Engineering 477,
https://doi.org/10.1007/978-981-10-7629-9_109

At present, the preparation method of polyaniline has been studied mainly by chemical synthesis and electrochemical synthesis [3]. Chemical synthesis method is the reaction of aniline monomer under the action of an acidic medium and an oxidizing agent to produce polyaniline. As the chemical synthesis process is relatively simple and the conditions are easier to achieve, this method is the main preparation of polyaniline [4]. Electrochemical synthesis method is the use of a certain principle of the original battery, containing aniline monomer in the electrolyte solution, so the original cell structure is formed, making the anode aniline monomer oxidation polymerization reaction, which polymerization into polyaniline powder. Although the electrochemical synthetic products with high purity, excellent performance, but only for laboratory synthesis, industrial production is more waste.

Nano-Cellulose comes mainly from wood, cotton, linen, plants and other agricultural products, that is very rich in natural reserves of renewable resources [5]. Due to its excellent physical and chemical properties, unique organizational structure, the depletion of energy and resources in recent years, Nano-Cellulose has become a new research field [6].

This paper studied the preparation of polyaniline by chemical oxidation with ammonium persulfate as oxidant under acidic conditions [7]. And then, the polyaniline was doped with a certain concentration of protonic acid to make it conductive. To study the composite condition and the composite ratio, Nano-Cellulose and polyaniline were combined, and the conductivity was measured.

2 Experimental

2.1 Materials and Instruments

Materials: Aniline (AN), AR, Damao Chemical Reagent Factory, Tianjin. Hydrochloric acid (Hcl), 36% AR, Fine Chemical Factory, Economic and Technological Development Zone, Laiyang. Ammonium persulfate (APS), AR, Damao Chemical Reagent Factory, Tianjin. Nano-Cellulose, 0.86%, Homemade.

Instruments: Precision power booster, JJ-1, Beijing Yingxun Zhiyuan Technology Co. Ltd. Four probe tester, RTS-8, Guangzhou, China. Electric blast oven, 101-3B, Tianjin Taisite Instrument Co. Ltd. Ultrasonic signal generator, BILON-500, Shanghai BINLON Instrument Co. Ltd.

2.2 Composite Method

The conductive polyaniline was prepared by chemical oxidation method. And then, the reaction of polyaniline and Nano-Cellulose was studied. The composite conditions and the composite ratio were discussed. Finally, the conductivity of the composite product was discussed.

2.2.1 Preparation of Conductive Polyaniline by Chemical Oxidation

(1) Polymerization
50 ml of 2 mol/L hydrochloric acid solution was added to a four-necked flask and a certain amount of aniline solution was added. The reaction was placed in an ice-water bath and stirring was continued for 30 min. A certain concentration of ammonium persulfate solution was dropped into a four-necked flask, and the dropping speed was controlled and addition was completed in 50 min. To maintain a certain reaction temperature, stirring until after the completion of 2 h. The reaction was over. The resulting solution was subjected to suction filtration, repeatedly washed with deionized water to the filtrate, and the water was drained.
(2) Doping Reaction
The powder thus obtained was mixed with a solution of 2 mol/L hydrochloric acid, and the stirring was continued for 2 h in a closed system. After the doping reaction was completed, the mixture was subjected to suction filtration, repeatedly washed with deionized water to the filtrate, and the product was dried. To obtain conductive polyaniline powder, the mixture was transferred to a culture dish and placed in an oven at 65 °C for 24 h.
(3) Measurement of Conductivity of Polyaniline
The already dry polyaniline powder was treated with YP-2 table press for tableting as much as possible, and the sheet thickness was about 0.5 mm. The conductivity of the sheet was analyzed by the RTS-8 four-probe instrument, and the average was measured several times.

2.2.2 Polymerization of Polyaniline with Nano-Cellulose

(1) Composite Method of Polyaniline with Nano-Cellulose
Method 1:
The freeze-dried Nano-Cellulose and the prepared polyaniline were placed in a small beaker, and the appropriate amount of deionized water was added. Under certain ultrasonic conditions, the reaction was over. After freeze-drying, the composite product was obtained.

Method 2:
In the preparation of conductive polyaniline process, the amount of freeze-dried Nano-Cellulose was added. So Nano-Cellulose involved in the formation of polyaniline process. After the doping reaction, the composite product was obtained by freeze drying.
Method 3:
In the preparation of conductive polyaniline process, the amount of freeze-dried Nano-Cellulose was added. So Nano-Cellulose involved in the formation of polyaniline process. After the doping reaction, the appropriate amount of deionized water was added. Under certain ultrasonic conditions, the reaction was over. After freeze-drying, the composite product was obtained.

(2) Composite Ratio of Polyaniline and Nano-Cellulose
After the experiment of three composite methods was completed, the conductivity of each product of the three composite methods was measured and the experiment scheme with the highest conductivity was determined.

(3) Measurement of Conductivity of Composite Products
The already dry composite products powder was treated with YP-2 table press for tableting as much as possible, and the sheet thickness was about 0.5 mm. The conductivity of the sheet was analyzed by the RTS-8 four-probe instrument, and the average was measured several times.

3 Results and Discussion

3.1 Effect of Composite Method on Conductivity of Products

Method 1: The ratio of polyaniline to Nano-Cellulose was 1:1 and the ultrasonic frequency was 300 W.

Method 2: According to yield of polyaniline preparation process, the mass ratio of polyaniline to Nano-Cellulose was 1:1.

Method 3: According to yield of polyaniline preparation process, the mass ratio of polyaniline to Nano-Cellulose was 1:1, and the ultrasonic frequency was 300 W.

As shown in the following Table 1.

From the above table, it can be seen that it was the highest conductivity that the composite product of polyaniline and Nano-Cellulose was obtained by the Method

Table 1 Effect of composite method on conductivity of composite products

Number	Approach	The conductivity of composite products (S/cm)
1	Ultrasonic treatment	0.25
2	In situ polymerization	0.54
3	In situ polymerization and ultrasonic treatment	0.83

3, and the conductivity of product can reach 0.83 S/cm. Because the Method 3 used the in situ polymerization more than Method 1, which was more advantage. During the reaction, the aniline monomer was continuously polymerized to form polyaniline, and the Nano-Cellulose are adsorbed and wound. Method 3 used ultrasonic treatment more than Method 2. A certain time of ultrasonic treatment make the dispersion of Nano-Cellulose in the reaction system more uniform. The polyaniline produced by the reaction can be more uniformly adsorbed on the Nano-Cellulose molecule, so that the composite product has better conductive effect.

3.2 *Effect of Composite Ratio on Conductivity of Composite Product*

By three experiments, the composite scheme was determined. In the preparation of conductive polyaniline process, the amount of freeze-dried Nano-Cellulose was added. So Nano-Cellulose involved in the formation of polyaniline process. After the doping reaction of the composite product, the appropriate amount of deionized water was added. Under certain ultrasonic conditions, the reaction was over. After freeze-drying, the composite product was obtained. In order to investigate the effect of the composite ratio on the conductivity of the composite product, the composite ratio of polyaniline and Nano-Cellulose was changed under the condition was kept constant, and the conductivity of the product was measured several times.

The results are shown in the following Table 2.

As shown in the above table, the mass fraction of polyaniline was divided into 10 gradients from 10 to 100%. Take the experiment product without polyaniline as the contrast group. The experiment product without polyaniline did not measure the

Table 2 Effect of composite ratio on conductivity of composite product

Number	The mass fraction of polyaniline (%)	The mass fraction of Nano-Cellulose (%)	The conductivity of composite products (S/cm)
1	0	100	–
2	10	90	0.01
3	20	80	0.10
4	30	70	0.47
5	40	60	0.65
6	50	50	0.79
7	60	40	0.96
8	70	30	1.65
9	80	20	3.56
10	90	10	6.34
11	100	0	9.98

conductivity, indicating that the Nano-Cellulose were nonconductive, or due to the conductivity was too low without effective data. The conductivity of the composite product increases with the increase of the mass fraction of polyaniline.

The composite product was dispersed in deionized water, stirred with a glass rod and placed in a petri dish. The composite product was dried in an oven at 65 °C to observe the film forming properties. Experiment shown when the content of polyaniline was about 40% in the composite product, the composite product could be formed into a brittle film. This is because the Nano-Cellulose content was too low, and the composite product cannot be effectively connected to form a conductive film.

4 Conclusions

In the experiment, conductive polyaniline was prepared by chemical oxidation method using ammonium persulfate as oxidant and hydrochloric acid as dopant. The prepared products had suitable molecular mass and good conductivity, and the conductivity of polyaniline synthesized was 9.98 S/cm under the best experimental conditions. The Nano-Cellulose was combined with polyaniline to obtain the best composite condition. When the polyaniline was prepared under the most suitable conditions, the amount of freeze-dried Nano-Cellulose was added. When the composite ratio of polyaniline to Nano-Cellulose was controlled to be 2:3, the composite product has the highest conductivity and can be formed into a film, and the conductivity was 0.65 S/cm.

The purposeof this experiment was to apply the composite product of Nano-Cellulose and polyaniline to conductive ink, which was used as conductive substrate such as circuit board, membrane switch and flexible electrode. However, taking into account the poor performance of the composite product film, the composite product needs to epoxy resin and other materials with better film forming performance. So that it has certain conductivity, while achieving the required conductivity of the conductive film.

References

1. Tian YF, Tan FR (2014) Preparation and characterization of anthracenecarboxylicacid doped polyaniline thin films. Chin J Polym Sci 32(8):1060–1067
2. Sapurina IY, Frolov VI, Stejskal J (2003) A conducting composite of polyaniline and wood. Russ J Appl Chem 76(5):835–839
3. Chen Y, Kang ET, Neoh KQ et al (2001) Intrinsic redox states of polyaniline studied by high-resolution X-ray photoelectron spectroscopy. Colloid Polym Sci 279(1):73–76
4. Nechtschein M, Tsujioka SI et al (1987) Polyaniline formation reaction and structure. Synth Met 18:341–346
5. Gray DG, Roman M (2006) ACS symposium series-cellulose nanocomposites 938:26–32

6. Li W, Wang R, Liu S (2011) Nanocrtstalline cellulose prepared from softwood kraft pulp via ultrasonic-assisted acid hydrolysis. BioResources 6(4):4271
7. Yuxin LIU, Fuqiang CHU (2015) Preparation of conductive polyaniline by chemical oxidation reaction. J Qilu Univ Technol 01:36–39

Preparation of Superhydrophobic Al Alloy for Metal Packaging and Study on Its Corrosion Resistance

Ting Mi, Qifeng Chen, Xiaohong Pan, Zheng Li and Guangxue Chen

Abstract At present, the studies of stability about aluminum alloy superhydrophobic surfaces are incomplete, the preparation process is required to simplify and the production cost is needed to reduce, it is difficult to obtained with durable microstructure and durable low surface energy materials on superhydrophobic surfaces simultaneously. The chemical and electrochemical methods are intended to construct rough surfaces on aluminum alloy in the paper. We have studied about superhydrophobic stability, the roughness, rough structure, micro-nanostructure arrangement and chemical composition in material surfaces by test equipments, in order to obtain an optimal model of rough structure on aluminium alloy surface. In this study, aluminum alloys with different surface roughness were prepared, then put the same surface coating materials on the aluminum alloy substrates, the corrosion resistance of different surface roughness on aluminum alloys were discussed. The results show that surface roughness increased can improve the corrosion resistance of aluminum alloy in weak acid, weak alkaline and salt solutions. When the contact angle is greater than 150°, the corrosion resistance of aluminum alloys has been improved greatly.

Keywords Superhydrophobic · Aluminum alloy · Stability · Corrosion resistance

T. Mi
South China University of Technology, Guangzhou, China

Q. Chen · G. Chen (✉)
State Key Laboratory of Pulp and Paper Engineering, National Engineering Research Center of Papermaking and Pollution Control, South China University of Technology, Guangzhou, China
e-mail: chengx@scut.edu.cn

X. Pan · Z. Li
Jinniu District Chengdu Environmental Monitoring Station, Chengdu, Sichuan, China

P. Zhao et al. (eds.), *Applied Sciences in Graphic Communication and Packaging*, Lecture Notes in Electrical Engineering 477,
https://doi.org/10.1007/978-981-10-7629-9_110

1 Introduction

The preparation method of the super-hydrophobic surface is divided into two parts: the rough micro-nano structure is constructed on the surface of the material, and the surface of the micro-nanometer structure is covered with low surface energy. As the reduction of surface free energy is easy to achieve technically, therefore, super-hydrophobic surface preparation technology is the key to the construction of the appropriate surface microstructure. At present, the literature has been reported on a number of super-hydrophobic surface preparation technology, from which the processing technology used and the formation of microstructure on the surface of two aspects to consider the current roughened surface methods are: silicon mold replication technique [1], a two-step process of photolithography and electrochemical deposition [2], electrochemical and nano-imprint electrochemical deposition technology [3], chemical deposition method in the glass, copper mesh, epoxy resin substrate [4], sol-gel method [5].

This study shows that the preparation of super-hydrophobic surface on the metal matrix can improve the protection ability of the metal greatly. Therefore, the preparation of the super-hydrophobic surface of the metal is very active in recent years, and the preparation of the super-hydrophobic surface of the aluminum alloy is one of the hotspots in this field [6]. Wettability refers to the phenomenon that the solid interface changes from a solid-gas interface to a solid-liquid interface. The wettability of the surface of the material is determined by the nature and stacking of the surface atoms or atomic groups, irrespective of the nature and arrangement of the atoms or molecules within it [7]. In this paper, the size of the contact angle is used to characterize the wettability of the surface of the material.

2 Experiment Section

2.1 Chemicals and Materials

Chemicals. Stearic acid (Octadecanoic acid) (Tianjin Ke Miou Chemical Reagent Co., Ltd, AR grade), sulfuric acid (H_2SO_4) (Changsha Huiyuan Chemical Reagent Co., Ltd, AR grade), hydrochloric acid (HCl) (Changsha Huiyuan Chemical Reagent Co., Ltd, AR grade), Sodium hydroxide (NaOH) (Changsha Huiyuan Chemical Reagent Co., Ltd, AR grade), Sodium chloride (NaCl) (Tianjin Yongda Chemical Reagent Co., Ltd, AR grade), oxalic acid (Tianjin Ke Miou Chemical Reagent Co., Ltd, AR grade), Aluminum, aluminum and manganese alloy (Al-1.23, Mn-0.51, Fe-0.14, Si-0.08, Cu-0.05, Zn-Mg-0.008) (Changsha Huiyuan Chemical Reagent Co., Ltd, AR grade), Deionized water (homemade).

Materials. Data Physics OCA 20 contact angle measuring instrument, SK1200H CNC ultrasonic cleaning instrument, AL104-IC balance, DZF-6050

vacuum oven, Leica DM 2500P polarizing microscope, IM6ex electrochemical test system, beaker, measuring cylinder, glass rods and so on.

2.2 Experimental Procedure

2.2.1 Preparation of Aluminum Alloy with Different Surface Roughness

At first, the surface of the smooth aluminum alloy plate cut into a size of 2 cm 2 cm × 1 mm small pieces, were marked as A, B, C, D, E.

Secondly, the sample A soaked in anhydrous ethanol, cleaned by the ultrasonic for 15 min, cleaned with deionized water, and dried, and then immersed the sample in the mass fraction of 1% stearic acid ethanol solution for 30 min, removed at room temperature for 24 h, and dried naturally, the contact angle of 116.1° aluminum alloy surface was prepared.

Sample B was polished with 380 mesh sandpaper homogeneously, washed with deionized water and dried. Then the sample was immersed in a 1% solution of stearic acid in ethanol solution for 30 min, removed at room temperature for 24 h, and dried naturally, the contact angle of 128.7° was prepared.

Sample C was polished with 600 mesh sandpaper homogeneously, washed with deionized water and dried. Then the sample was immersed in a 1% solution of stearic acid in ethanol solution for 30 min, removed at room temperature for 24 h, and dried naturally, the contact angle of 136.7° was prepared.

Sample D was polished with 1200 mesh sandpaper evenly, then soaked in anhydrous ethanol, cleaned by the ultrasonic for 15 min, cleaned with deionized water, and dried, and then the sample was immersed in a 1% solution of stearic acid ethanol solution for 30 min, removed at room temperature for 24 h, and dried naturally, the contact angle of 146.5° aluminum alloy surface was prepared.

Sample E was treated in an anodic roughening treatment, washed with deionized water and dried, and the sample was immersed in a 1% solution of stearic acid in ethanol solution for 30 min, removed at room temperature for 24 h, and dried naturally, the contact angle of 153.7° was prepared.

2.2.2 Immersion Test of Aluminum Alloy Samples

Firstly, prepare HCl solution with pH value of 4 and NaOH solution with pH value of 11. Then removed the five samples in samples A, B, C, D, E respectively, with analytical balance were measured their quality, found the average. Immerse the samples in the HCl solution of pH 4 respectively. Removed the sample every 2 days, washed with deionized water, and dried, and used the analytical balance to measure their mass, found the average, and then determined the percentage change in sample mass. Then the sample were numbered and soaked in NaOH solution of

pH 11. Finally, removed the sample every 2 days, washed with deionized water, and dried, and used the analytical balance to measure their mass, found the average, and then determined the percentage change in sample mass.

3 Effect of Different Roughness of Aluminum Alloy on Corrosion Resistance

3.1 Electrochemical Impedance Spectroscopy

Figure 2 shows the electrochemical impedance spectra of aluminum alloy samples with different surface roughness in 3.5% NaCl solution. Figure 1 is the equivalent circuit diagram. The equivalent circuit diagram of the electrochemical impedance of the aluminum alloy sample was a relatively simple resistor in parallel with the capacitor, which represents that in this case the sample's AC impedance spectrum is only a time constant, C_{dl} represents the electric double layer capacitance, R_s

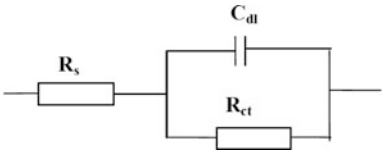

Fig. 1 Equivalent circuits of different surface wettability samples

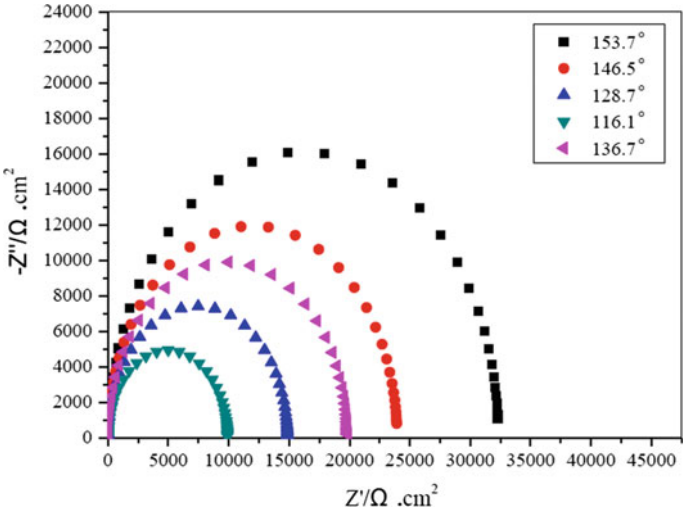

Fig. 2 Electrochemical impedance spectra of different samples in 3.5% NaCl solution

represents the solution resistance, and R_{ct} represents the transfer resistance. It can be seen from Fig. 2 that the radius of the semicircle of the curve in the Nyquist graph increased with the increase of the contact angle of the aluminum alloy. Since the radius of the curve in the Nyquist graph represents the impedance of the sample surface in the corrosive medium, that is corrosion resistance, so we can see that with the sample surface contact angle increased, aluminum alloy samples in NaCl solution charge transfer impedance increased gradually, which is beneficial to improve the corrosion resistance of aluminum alloy.

3.2 *Weight Loss Method*

The corrosion resistance of the samples was measured by weight loss method by immersing the aluminum alloy samples in a hydrochloric acid solution at pH 4 and a solution of sodium hydroxide solution at pH 11. The experimental results are shown in Figs. 3 and 4. With the aluminum alloy surface contact angle increased, in the same time, the smaller the quality of aluminum, the sample of contact angle of 153.7° had the smallest change. Experiments show that the surface contact angle of aluminum alloy increased, which was beneficial to improve the corrosion of weak alkali and alkali of aluminum alloy. When the aluminum sheet was immersed in a solution of pH = 1–14, the sample was a sheet of aluminum sheet which began to react and began to emit bubbles and had a fast bubble rate, but with a contact angle of 153.7°, It takes about 5 min to start the reaction, and the reaction rate was slow, so it can be seen that the super-hydrophobic surface was improved to improve the corrosion resistance of the material. But in the pH = 1 and 14 solution in the aluminum alloy sample reaction quickly, only soak for 1 h was corroded seriously, easy to determine the aluminum surface wetting changes could not make the aluminum alloy can be resistant to strong acid and alkali corrosion.

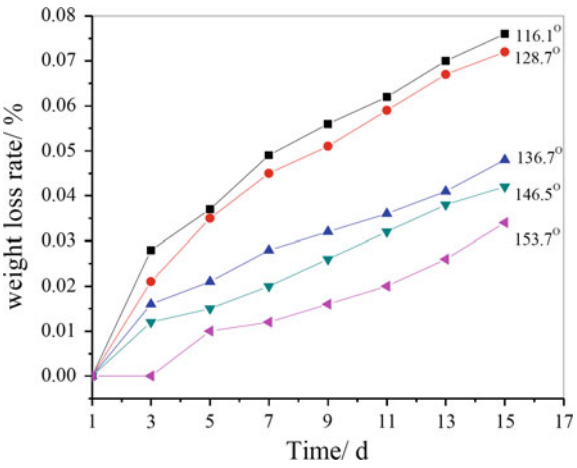

Fig. 3 Weight loss rate of different surface wettability samples in PH = 4 HCl solution

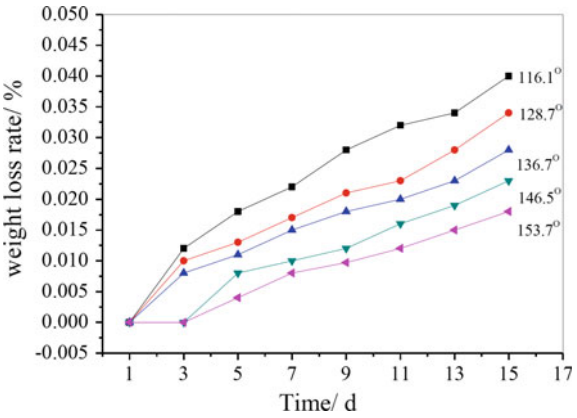

Fig. 4 Weight loss rate of different surface wettability samples in PH = 11 NaOH solution

4 Conclusions

(1) By forming different roughness on the surface of aluminum alloy, after the stearic acid coating, different contact angles were obtained on the surface of aluminum alloy.
(2) The increase of the contact angle of the aluminum alloy was beneficial to improve the corrosion resistance of the aluminum alloy.
(3) The increase of the contact angle of the aluminum alloy can improve the corrosion resistance of the aluminum alloy in the weak acid and weak alkali environment by the immersion experiment in different pH solution, but the corrosion resistance in the strong acid and alkali environment was poor.

Acknowledgements This research was financially supported by the Guangdong Provincial Science and Technology Project (2016070220045), the Key Laboratory of Pulp and Paper Engineering Funding Project (2016C01), the State Key Lab of Pulp and Paper Engineering, South China University of Technology (No. 2016C02), and the Fundamental Research Funds for the Central Universities (No. D2154620).

References

1. Furstner R, Barthlott W, Neinhuis C (2005) Wetting and self-cleaning properties of artificial superhydrophobic surfaces. Langmuir 21:956–961
2. Whitley M, Newton M, McHale G (2012) The self assembly of superhydrophobic copper thiolate films on copper in thiol solutions. Zeitschrift Fur Physikalische Chemie-Int J Res Phys Chem Chem Phy 226:187–200
3. Wang MF, Raghunathan N, Ziaie B (2007) A nonlithographic top-down electrochemical approach for creating hierarchical (micro–nano) superhydrophobic silicon surfaces. Langmuir 23:2300–2303
4. Ming W, Wu D, Benthem R et al (2005) Superhydrophobic films from raspberry-like particles. Nano Lett 5:2298–2301

5. Mahadik SA, Kavale MS, Mukherjee SK, Rao AV (2010) Transparent superhydrophobic silica coatings on glass by sol–gel method. Appl Surf Sci 2:333–339
6. Che YH (2014) Study on fabrication of superhydrophobic aluminum-alloy surface and properties of corrosion resistance and anti-icing
7. Tian J, Xu JF (1997) Hysteresis study of some fluorine polymer. Polym Mater Sci Eng 5:9–13

Application of Cellulose-Based Solid Acid in Absorption of Heavy Metal Ions from Printing Waste Water

Feiyun Li, Binshou Wang, Zhiqiang Pang, Zhe Wang and Cuihua Dong

Abstract Traditional printing (lithography, gravure, letterpress, PCB etc.) produce a large of industrial wastewater from washing printing plate, rubber cloth and circuit boards corrosion. These waste water mainly contain copper ion and silver ions, which is difficult to process under acid condition. Taking effective methods to remove the metal ions in waste water has become a hotspot in research. In this paper, cellulose-based solid acid (CCSA) was prepared using microcrystalline cellulose and 98% concentrated sulfuric acid as raw materials. The characterization of CCSA was first analyzed by acid strength and Fourier-transform infrared spectrometer (FTIR). Infrared spectrogram display that sulfonic group was successfully connected on cellulose-base. Acid value measurement indicates that the total acidic group of CCSA decline from 1.87 to 1.02 mmol/g with carbonization temperature rise. Subsequently, effects of carbonization temperature on adsorption performance to Cu^{2+} and Ag^{+} were investigated. The result shows that carbonization temperature at 400 °C reach best absorptivity of 80 mg/g (Cu^{2+}) and 247 mg/g (Ag^{+}) respectively. However, with carbonization temperature rise to 600 °C absorption quantity was just 66 mg/g (Cu^{2+}) and 158 mg/g (Ag^{+}) respectively.

Keywords Solid acid · Adsorbent · Heavy metal ions

F. Li · B. Wang · Z. Pang · Z. Wang · C. Dong (✉)
College of Printing and Packaging Engineering, Qilu University of Technology, Shandong, China
e-mail: 43981312@qq.com

F. Li
e-mail: wwwlifeiyun@163.com

F. Li · B. Wang · Z. Pang · Z. Wang · C. Dong
Key Laboratory of Pulp and Paper Science and Technology, Nanjing Forestry University, Nanjing, China

P. Zhao et al. (eds.), *Applied Sciences in Graphic Communication and Packaging*, Lecture Notes in Electrical Engineering 477,
https://doi.org/10.1007/978-981-10-7629-9_111

1 Introduction

In recent years, the water pollution caused by heavy metals has become an serious environmental problem [1], as copper ion is one of most toxic heavy metals. Exceed copper is harmed to human body [2], especially for liver and kidneys [3]. While this organs appear problem, human body metabolism cannot maintain and appear various diseases, such as liver cirrhosis, liver ascites even more serious. Silver is one of the trace elements for body tissues, trace amounts of silver is harmless to human body. But, WHO rules that the silver safe line is 0.05 ppm and drinking water limitation is 0.05 mg/l.

People who live in the era of electronic and information cannot leave the circuit board and print production, which will generate vast heavy metal pollutants and high concentration organic wastewater. This wastewater contain heavy metal ion can't direct emissions not in conformity with the national emission standard as heavy metal ions is depredated by environmental hardly. Disturbing, it is difficult to handle using the general method when metal ion concentration is low. How to effectively remove copper and silver has also become one of the attentions for government and researchers. A variety of processing methods are explored by scientific researcher, such as ion exchange method [4], precipitation method [5], electrolytic method [6], membrane filtration method [7], electro dialysis method [8], etc. However, these methods involve in some disadvantage with complex preparation technology, large energy input, high economic cost, and only for high concentration metal ions solution. Therefore, it is difficult to wildly produce and promote.

Absorption method with efficient, no harmful by-products and repeated usage is widely attention in wastewater treatment. At present, the activated carbon that possess strong absorption ability and have been high degree of commercialized can be used as adsorbent [9]. But, the cost of production is higher and refer to high-end technology of activation and carbonization. These unfavorable factors lead to activated carbon difficult to large-scale use on removing heavy metals in wastewater. Carbon-based solid acid not only has good absorption performance for high specific surface area and acid value, also easy to prepare and cheap, which features make the adsorbent is hope to use widely. The specie of carbon-based solid acid is numerous, different raw materials and preparation method produce different specific surface area and acid value. Carbonization-sulfated method is commonly used in preparation carbon-based solid acids, which mainly use cellulose as raw material.

2 Experimental

2.1 Materials and Equipment

Silver nitrate ($AgNO_3$), AR, was supplied by Tianjin Kemiou Chemical Reagent Co., Ltd. Microcrystalline cellulose purchase in anhui sunvo medicinal auxiliary co., LTD. 98% of sulfuric acid bought in the national medicine group chemical reagent co., LTD. Muffle furnace take in Shanghai TongKe electric equipment co., LTD. Copper sulfate ($CuSO_4$) purchased in Tianjin Guang Cheng chemical reagent co.

2.2 Synthesis of CCSA

Microcrystalline cellulose contact with concentrated sulfuric acid will be carbonized and prepared low acid value solid acid. So, the microcrystalline cellulose is need to incompletely carbonize, and then using sulfuric acid sulfating. Cellulose heated in isolated of oxygen will be decomposed, mainly production is polycyclic aromatic compounds. The aromatic compounds can generate solid acid in concentrated sulfuric acid under the condition of heating.

(1) In completion carbonization

The microcrystalline cellulose conducted in ceramic cup, which put into the muffle furnace under different temperature (400, 450, 500, 600 °C) for 5 h and get four kinds of carbon-based (black powder) sample. The sample was cooldown to room temperature and place into the beaker, taking dilute hydrochloric acid to dissolve ash content. Therewith, using buchner funnel separate solid until filtrate present neutral. Finally black powder was vacuum-dried at 60 °C for 12 h.

CCSA preparation principle:

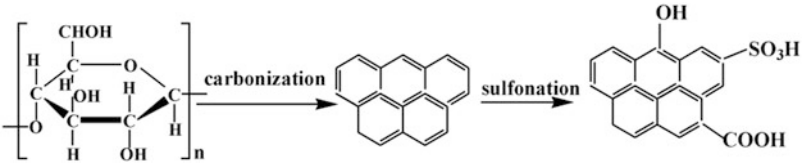

(2) Concentrated sulfuric acid sulfating

Incompletely black carbide powder 2 g, sulfuric acid (98 wt%) 15 g was placed into 50 ml flask under 150 °C stirred 6 h (800 rpm). Then mixture was cooldown to room temperature and use distilled water attenuation. Buchner funnel was used to separate solid until the filtrate was neutral. The solid material place in drying over under 60 °C dried 12 h. Finally, this kind of absorbent is placed in a sealed bag and name CCSA.

2.3 Acid Value Measurement

The total acid content of CCSA is low, which high concentrations NaOH solution titration may be production large error. So, about 0.1 mol/L standard NaOH solution was configured according to standard configuration method. Prior, samples were put into 50 ml without carbon dioxide distilled water and contain 2 h. Then, drip two drops phenolphthalein and use standard NaOH solution titration until the solution turned red, record the consumption volume of NaOH solution. Finally, conduct a blank experiment and record the consumption volume.

$$\mathrm{C}(H^+) = \frac{c(v_1 - v_2)}{m}$$

The C(H^+) is the number of hydrogen ion per gram CCSA, "c" is the concentration of NaOH solution, "v_1" is solid acid consumption NaOH solution volume, "v_2" is blank experiment consumption NaOH solution volume.

2.4 FTIR Analysis

The IR Prestige-21 infrared spectrum was used to analyze the functional groups in the samples obtained by KBr pellet technique. Samples were ground and mixed with KBr and pressed in an evacuated die under suitable pressure. The spectra were collected for 32 scans within wavenumber from 400 to 4000 cm^{-1} at 2 cm^{-1} resolution.

2.5 Cu^{2+} Adsorption

20 mg of anhydrous copper sulfate and 200 mg CCSA was added in 100 ml distilled water, which aqueous solution pH was adjusted on 4, then stirred 2 h at 800 rpm. Therewith, sample transfer to centrifuge and reserve clarifying liquid, which Cu^{2+} concentration detected by atomic emission spectrometer (PE Instruments by ICP-AES and engage Optima dv 2000).

$$\mathrm{Qe} = (\mathrm{C}_0 - \mathrm{C}_e)\ \mathrm{V/m}$$

The Qe is per gram CCSA absorption Cu^{2+} mass, C_0 and C_e is Cu^{2+} concentration of initial and after absorption solution, V is the volume of solution, m is absorbent mass.

2.6 Ag^+ Adsorption

200 mg CCSA and silver nitrate solution was added into 250 ml conical flask, which aqueous solution pH was adjusted on 4, then stirred 2 h at 800 rpm. Therewith, using centrifuge separate supernatant fluid solids, preserving clear liquid, which Ag^+ concentration detected by atomic emission spectrometer (PE Instruments by icp-aes and engage Optima dv 2000)

$$Qe = (C_0 - C_e)\ V/m$$

The Qe is per gram CCSA absorption Cu^{2+} mass, C_0 and C_e is Cu^{2+} concentration of initial and after absorption solution, V is the volume of solution, m is absorbent mass.

Metal ions adsorption metal ions (M^{n+}) principle:

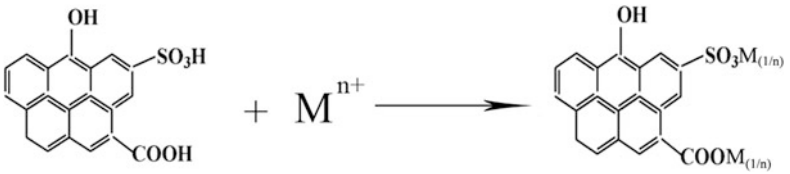

3 Results and Discussion

3.1 FTIR Analysis

Figure 1 is CCSA infrared spectrogram. Band in 1220 cm^{-1} and 1058 cm^{-1} (O=S=O and $–SO_3H$ characteristic peak), peak at 1391 cm^{-1} (phenolic hydroxyl stretching), peak at 1686 cm^{-1} (–COOH stretching) associated with CCSA were observed. It shows that CCSA solid acid contain three groups possess ion exchange performance, the main absorption groups are carboxylic and sulfonic group.

3.2 Acid Strength Analysis

The acid value of different CCSA showed in Table 1, which is inversely proportional to the temperature, from 1.87 to 1.02 mmol/g. The FTIR result indicate that the sulfonation of cellulose carbonized at ≤ 873 K results in amorphous carbon composed of small carbon sheets with phenolic OH, COOH groups in addition to SO_3H groups. The vibrating peaks strength of $–SO_3H$ decline in 400–600 °C prove that the number of acidic groups on CCSA was decline, which is why CCSA acid value fall.

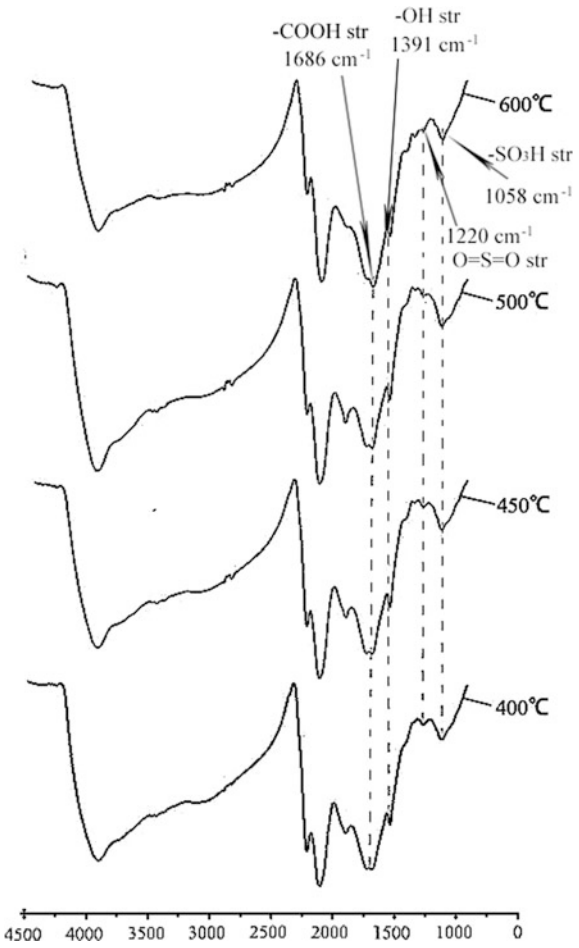

Fig. 1 CCSA infra-red spectrogram

Table 1 CCSA under different carbonization temperatures acid value

CCSA	Carbonization temperature			
	400 °C	450 °C	500 °C	600 °C
Acid number	1.87 mmol/g	1.49 mmol/g	1.11 mmol/g	1.02 mmol/g

3.3 Absorption Resulting

Figure 2 shows that CCSA has better absorption ability of Cu^{2+} and Ag^{+}, and the absorption quantity decreased when increase carbonization temperature. As for Cu^{2+} and Ag^{+}, carbonization temperature at 400 °C reached supreme absorption of

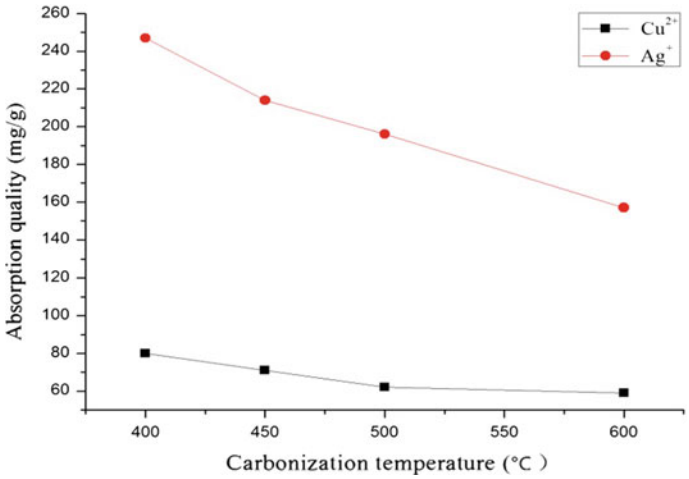

Fig. 2 CCSA adsorption quantity for different ions

80 and 247 mg/g, carbonization temperature raise to 600 °C absorption quantity only 66 mg/g and 158 mg/g. The CCSA absorb quantity of Cu^{2+} lower than Ag^{+} in the same carbonization temperature, which –COOH and $–SO_3H$ group form more stable structure with Ag^{+}. It found that the absorption quality of Ag^{+} under 400 °C is higher than in theory (acid valid), the reason is that the pore involve physical absorption of metal ions.

4 Conclusions

Microcrystalline cellulose and concentrated sulfuric acid as raw materials synthesize a kind of solid acid with high acid value, which preparation process is simple and inexpensive. The infrared spectrum shows that CCSA contain –COOH and $–SO_3H$ can used in absorption metal ions. The results of acid value measurement indicate that the total acidic group of CCSA is inversely proportional to the temperature, from 1.87 mmol/g down to 1.02 mmol/g. The absorption result show that the CCSA effective remove heavy metal ions in aqueous solution, which acid group react with heavy metal ions and generated more stable coordination bond [10]. However, the absorption quality of Ag^{+} under 400 °C is higher than in theory (acid valid), the reason is that the pore involve physical adsorption of metal ions.

Acknowledgements The authors grateful for the financial supports from the Natural Science Foundation of Shandong Province (ZR2015CM006), Open Fund of Jiangsu Provincial Key Lab of Pulp and Paper Science and Technology (201309) and Science Foundation of High School (J12LF09).

References

1. Malik D, Singh S, Thakur J et al (2014) Heavy metal pollution of the Yamuna River: an introspection 3(10):856–863
2. Holland MK, White IG (1988) Heavy metals and human spermatozoa III. The toxicity of copper ions for spermatozoa. Contraception 38(6):685
3. Oluyemi EA, Oyekunle JAO, Olasoji SO (2009) A comparative study of the removal of heavy metal ions from synthetic wastewaters using different adsorbents. Adsorpt Sci Technol 27 (5):493–502
4. Karim G (2013) Treatment of ion-exchange resins regeneration wastewater using reverse osmosis method for reuse. Desalination Water Treat 51(25–27):5179–5183
5. Xiong ZW (2007) Wastewater treatment project design using precipitation—SBR method. J Univ S China
6. Zhang S (2013) Tanning wastewater treatment and recycling method based on nano-catalytic electrolysis technology and membrane technology
7. Żyłła R, Sójka-Ledakowicz J, Stelmach E et al (2006) Coupling of membrane filtration with biological methods for textile wastewater treatment. Desalination 198(1):316–325
8. Akyeva SC, Berkelieva LK, Evzhanov KN (2008) Wastewater treatment of phosphate ions by the electro dialysis method. J Water Chem Technol 30(4):246–250
9. Aibe T, Shibata K (1995) Activated carbon adsorbent and applications thereof: US, US 5403548 A
10. Li L, Liu F, Jing X et al (2011) Displacement mechanism of binary competitive adsorption for aqueous divalent metal ions onto a novel IDA-chelating resin: Isotherm and kinetic modeling. Water Res 45(3):1177–1188

Research on Creep Resistance of Flexible Pressure Sensor Based on Anhydride Curing Agent

Fenlan Xu, Zhenguo Wang, Xiuyan Li, Mengmeng Liang, Ruping Liu, Wei Wang and Luhai Li

Abstract In this article, the resistance value of the flexible pressure sensor was measured at the constant temperature and pressure, and combined with anhydride curing agent, a comparative experiment was carried out to investigate the effect of anhydride curing agent on the creep resistance of flexible pressure sensor. The result of experiment showed that the epoxy resin and the anhydride proceed the crosslinking reaction after the flexible pressure sensor was added to the anhydride curing agent. The network structure was formed, the volume of the polymer was reduced, the hardness was increased, and the resistance creep performance was increased. In addition, the result of creep test showed that the content of curing agent and curing temperature had a significant influence on the creep resistance of the sensor.

Keywords Anhydride curing agent · Flexible pressure sensor · Resistance creep Curing temperature

1 Introduction

In recent years, with the progress and development of electronic information technology, flexible pressure sensor arouses a wide concern of academies and industries with its flexibility and high sensitivity. The perception of the external force is equivalent to the human skin, which can be used to simulate the electronic skin system [1]. For example, Lim et al. added a kind of organic nano clay in a biodegradable polymer, which could reduce the creep of the polymer in the molten state. The author suggested that the change of the activity of molecular chain in the

F. Xu · Z. Wang · X. Li · M. Liang · R. Liu · W. Wang (✉) · L. Li (✉)
Beijing Engineering Research Center of Printed Electronics,
Beijing Institute of Graphic Communication, Beijing, China
e-mail: 18900616029@189.cn

L. Li
e-mail: liluhai@bigc.edu.cn

P. Zhao et al. (eds.), *Applied Sciences in Graphic Communication and Packaging*, Lecture Notes in Electrical Engineering 477,
https://doi.org/10.1007/978-981-10-7629-9_112

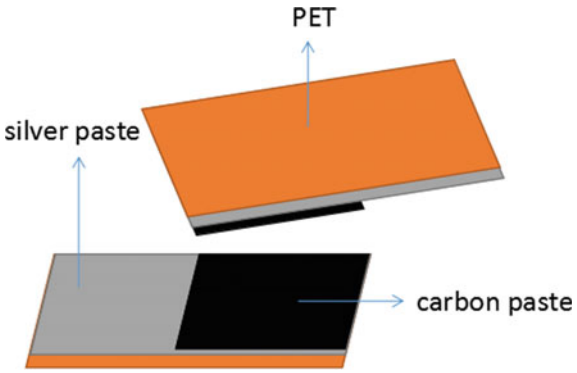

Fig. 1 Flexible pressure sensor microstructure

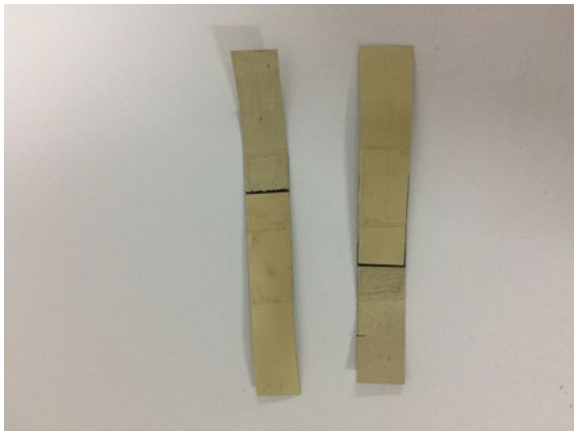

Fig. 2 Samples of homemade flexible pressure sensor

composites was closely related to creep [2]. In application, however, the sensor is viscoelastic due to the influence of the substrate material, which makes the change of the internal conductive network become more complex. It presents a strong resistance creep phenomenon, which reduces the accuracy of the sensor and limits its widespread use [3]. In order to improve its dimensional stability and increase its value, it is necessary to take measures to improve its creep resistance. The connecting material of the flexible pressure sensor is epoxy resin and the curing agent is cis-1, 2, 3, 6-Tetrahydrophthalic anhydride curing agent in our experiment. The basic principle was that the epoxy groups in epoxy resin reacted with acetic anhydride and the anhydride was opened, then the addition polymerization was carried out to form the polymer. The result of the reaction was that the relative volume decreased, the hardness increased, and the creep resistance increased (Figs. 1 and 2).

2 Creep Test

2.1 Raw Materials and Equipment

The raw materials required for the experiment include PET thin film substrate material and conductive silver paste as electrode. In the process of preparing carbon slurry, the epoxy resin was used as the connecting material, ethylene glycol butyl ether acetate was used as binder and conductive materials were conductive carbon nanoparticles. In addition, the functional additives were dispersants, additives, leveling agent and cis-1, 2, 3, 6-Tetrahydrophthalic anhydride.

The instruments used in the experiment were heat collection type constant temperature heating magnetic stirrer, three roll mill, vacuum drying box, intelligent gas sensitivity analysis system, pressure rotating test stand, beaker, glass rod and so on.

2.2 Experimental Preparation

The experiment was divided into the following steps:

(1) The preparation of carbon paste was very critical. Firstly, the epoxy resin was added to the ethylene glycol butyl ether acetate solvent for heating and magnetic stirring until completely dissolved. Then to add dispersant, additives, carbon nanoparticles and leveling agent. Continuing stirring until the carbon nanoparticles were evenly dispersed. Finally, the carbon slurry was obtained.
(2) The carbon slurry was divided into two batches: ① conducting three roller grinding directly; ② adding anhydride curing agent at first (In order to make the curing agent be dispersed evenly, the carbon slurry could be processed at 50–60 °C for 2–3 h after the mechanical stirring was carried out), and then conducting three roll grinding. We needed to adjust roller gap to 8 um, speed of 300 r/min and perform five experiments for each batch.
(3) The carbon paste was printed on the substrate PET film with conductive silver paste, which was made by using a wire rod with diameter of 50 um, and then to conduct drying curing in the vacuum blower drying box. Meanwhile, to set the curing temperature as 120 °C and time for 2 h to get samples.
(4) Cut and set the sample size as 10 mm * 40 mm, and then seal carbon paste face to face with adhesive tape and air extraction. A simple flexible pressure sensor was obtained and the creep properties of the resistance could be measured.

2.3 Creep Test

The definition of creep in teaching materials is that the deformation of the material increases with time going under certain temperature and constant pressure. In our experiment, we researched the creep resistance of the flexible pressure sensor. That was, under certain temperature and constant pressure, the resistance of the sensor fluctuated with time going. Due to the long time load of the epoxy resin, obvious creep occurred, which would affect the dimensional stability of the sensor [4], so how to reduce the creep and cut down the creep rate of the epoxy resin matrix is one of the most important problems in the application of flexible pressure sensor [5]. We conducted a set of contrast tests: Making the flexible pressure sensors by using carbon paste without curing agent and curing agent as raw material, and then testing the resistance value and getting the resistance creep by calculating the resistance change rate. We knew that there were many kinds of curing agents which could be used as epoxy resins by consulting relevant literature, but the effect of anhydride curing agent was relatively great. Therefore, we added anhydride curing agent in the two groups of carbon paste, and the other group of carbon slurry was not added to form a set of comparative experiments. The creep test results were shown in Fig. 3.

It should be noted that: in order to get rid of the influence of external factors on the experimental data, the creep experiment required the experimental platform to provide constant pressure, and the test time was set as 15 min.

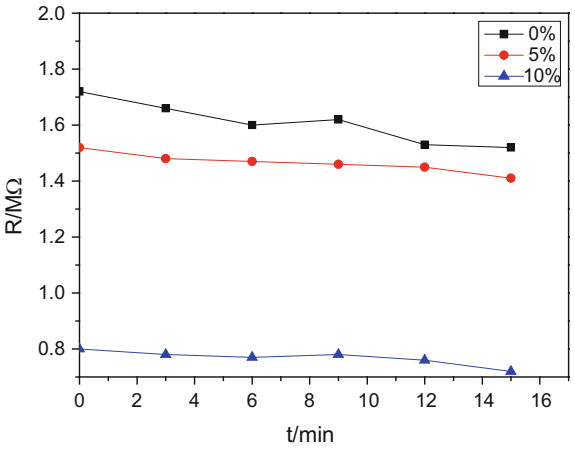

Fig. 3 Resistance curve adding different amounts of curing agent with time going

3 Results Analysis

3.1 *Effect of Curing Agent Content on Creep Resistance of Sensor*

Under the condition of constant pressure 20 N, the three groups of experiments (no curing agent, adding 5% curing agent, plus the 10% curing agent) were respectively subjected to pressure loading test, and the resistance responses of the sensor were tested. Figure 3 showed the variation of the resistance of the three groups with time going. The resistance change rate $\Delta = -\Delta R/R_0$, ΔR is the change of resistance and R_0 is the initial resistance, which can be obtained in Fig. 4. From the graph we could concluded that the sensor with 10% curing agent had the lowest resistance change rate, which was below 10%. As for the control group, the resistance change rate of the sensor without curing agent was the largest. In order to explore the reaction mechanism, we conducted a hardness test for sensors at a same time, and the hardness was increased by about 12%. On the one hand, the epoxy groups in epoxy resin reacted with acetic anhydride and the anhydride was opened, and then the addition polymerization was carried out to form the polymer. The results were that the relative volume decreased, the hardness increased, and the resistance change rate decreased. On the other hand, the epoxy group did not participate in the reaction because of the deficiency of curing agent, so only a part of the cross-linking reaction joining in, and the resistance change rate was situated between the two.

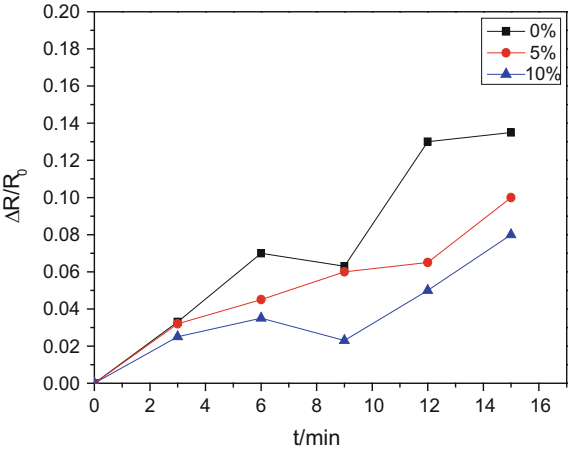

Fig. 4 Resistance rate of change curve adding different amounts of curing agent with time going

3.2 *Effect of Curing Temperature on Creep Resistance of Sensor*

The two samples with different curing agent content were respectively treated with the curing temperature of 100 and 120 °C/2 h, and then were tested at room temperature and constant pressure with 20 N. Figure 5 showed the variation of the resistance values of these two groups with time going. And we could knew that the higher the curing temperature was, the smaller the resistance change rate was, and the smaller the resistance creep was by the Fig. 6. The curing temperature did not reach, the crosslinking reaction did not occur. However, the increase of the conductivity of the particles in the slurry reduced the conductivity of the particles and the addition of particles also increased the density and hardness.

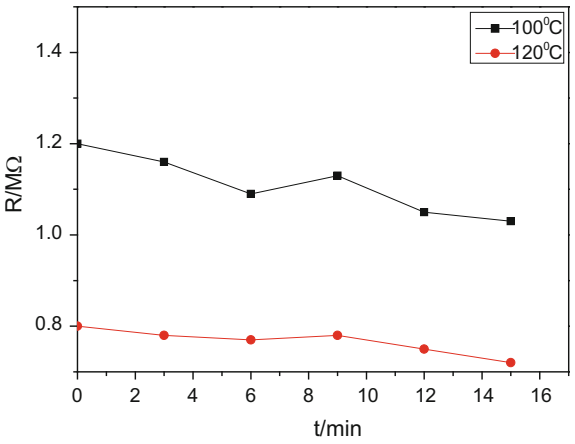

Fig. 5 Resistance rate of change curve in different curing temperature with time going

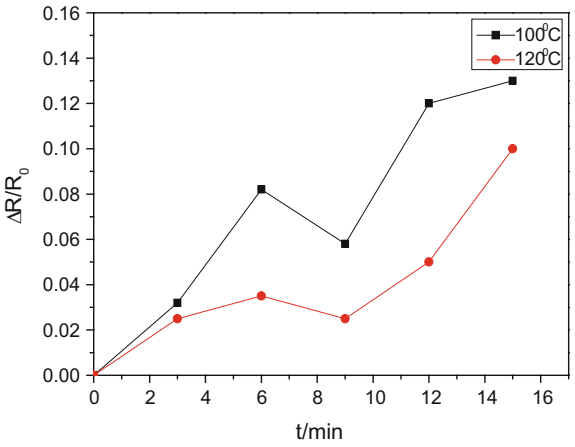

Fig. 6 Resistance curve in different curing temperature with time going

4 Theoretical Analyze

The resistance value reflects the change of the conductive network inside the sensor, and the creep resistance is divided into two stages: The resistance of the sensor decreases rapidly while loading, as the conductive network is formed by the connection of the carbon paste to form a conductive path. Another one is that the molecular chains in carbon paste under pressure are not fully compliant with stress compression, but they may cause shrinkage, bending, rotation, stretching, etc. and lead to the internal conductive network changes, reflecting the resistance creep phenomenon [6]. So the resistance creep phase, resistance value fluctuates up and down in a small range.

From the resistance change rate $\Delta = -R/R_0$, we can see that the smaller the resistance change rate, the better the resistance creep. As the curing agent is solid particles, it can't be completely uniform distribution after the anhydride curing agent is mixed with carbon paste based on the theory of conducting electricity. But there will always be a part of the reaction to form a conductive network interconnection, which provides the flow of electrons to make carbon slurry conduct electricity [7].

5 Conclusions

(1) We concluded that the creep resistance of the flexible pressure sensor with anhydride curing agent was improved by observing the variation of resistance with time increasing at constant temperature and pressure.
(2) The more the curing agent added in the carbon paste, the more the cross-linking reaction between the curing agent and the epoxy resin in carbon slurry, and the greater the rigidity of the formation. As a result, the greater the hardness of the sensor, the smaller the creep resistance.
(3) Try to set the curing temperature of the sample as high as possible based on the heat resistance of the PET film, and the creep resistance of the sensor would be better.

Acknowledgements This work is supported by the Million class brain chip project, the National Natural Science Foundation of China (61501039), the Beijing Research Grant (No. Z15110000915071), the support of Beijing Municipal Education Commission (No. SQKM201710015005), the Initial funding for the Doctoral Program of BIGC (27170116005/040), the Elite Program of BIGC (04190117004/010), the Collaborative Innovation Center 04190117029/002, the Discipline Construction 04190117013, the Discipline Construction of Printed Electronic Technology and Engineering Advantage 21090117001, and financial support for Innovative Teams of Printed Electronic Materials and Technologies.

References

1. Hou YQ, Mo LX, Li QB (2014) Effect of silver nanowire electrode microstructure on the sensitivity of flexible pressure sensor. Inf Recording Mater 15(5):13–18
2. Jia Y (2012) Preparation and creep behavior of carbon nanotubes/thermoplastic polymer composites. University of Science & Technology China, Hefei, China
3. Liu PF, Zhao QL (2013) Progress in creep behavior of resin matrix composites. FRP/Compos Mater 3:109–116
4. Zhang J, Zhang YX, Yang J (2015) Study on creep behavior of epoxy resin adhesive at room temperature and humidity. J Mech Strength 37(2):237–242
5. Xue F, Sheng L, Tan F (2010) Study on methods of improving creep resistance of epoxy resin. Compos Mater Innovation Sustain Dev 680–683
6. Wu CJ, Wang LH (2013) Research on time dependence of resistance for multiple outputs viscoelastic pressure sensitive component under constant pressure. Northeastern University, Shenyang, China
7. Zhang Z, Jia Y, Gao Y, Yang JL (2011) Progress in research on creep properties of polymer nanocomposites. Adv Mech 41(3):267–271

Thiol-ene Michael Addition Reaction Under Phototriggered Base Proliferation

Xiaoyuan Guan, Guangxue Chen, Rui Guo, Zhaohui Yu and Minghui He

Abstract Free radical reaction of thiol-ene photo click reaction is not ideal click chemistry type, there is monomer homopolymerization and low monomer conversion existing, as well as uncontrollable, it is difficult to obtain the target product. In this paper, the phototriggered base proliferation and UV photopolymerization were introduced into thiol-ene reaction. We synthesized photobase generator 2-(2-nitrophenyl) propyl oxycarbonyl-hexylamine (NPPOC-HA) and amine amplifier. NPPOC-HA has UV absorption above 300 nm, and photolysis products are amine and styrene, no free radical produced. Next, we used phototriggered amine proliferation initiated via UV light to control the thiol-ene click reaction, reducing side effects. RTIR was adopted to monitor infrared absorption peaks change of –SH and –C=C, integrating peak area to verify the equal proportion reaction of thiol-ene. UV phototriggered base proliferation reaction, which integrated the safety and strong penetrating ability of UV photopolymerization as well as Domino free radical photopolymerization based on phototriggered base proliferation reaction, is expected to expand the application of thiol-ene Michael addition reaction.

Keywords Photo click reaction · Thiol-ene reaction · UV photopolymerization

1 Introduction

In recent years, the click chemistry has attracted more and more attention of researchers, and received extensive studies. The thiol-ene reaction, as one of the most widely implemented click reactions in polymer science, has all characteristics of the click chemistry, such as non-toxicity, high yield, strong stereo

X. Guan · G. Chen (✉) · R. Guo · Z. Yu
Shenzhen YUTO Packaging Technology Co. Ltd., Shenzhen, China
e-mail: chengx@scut.edu.cn

G. Chen · M. He
State Key Laboratory of Pulp and Paper Engineering,
South China University of Technology, Guangzhou, China

P. Zhao et al. (eds.), *Applied Sciences in Graphic Communication and Packaging*, Lecture Notes in Electrical Engineering 477,
https://doi.org/10.1007/978-981-10-7629-9_113

selectivity, simple reaction conditions and the rapid reaction rate [1–3], furthermore, it is being utilized in dendrimer synthesis, polymer network formation and bioconjugation as well as polymer functionalization [4, 5]. Generally, the thiol-ene reaction can proceed via two pathways including free radical and catalytic initiation mechanism, within free radical reaction, the thiyl radical across C=C bond yields an intermediate carbon-centered radical, which can not only undergo the desired chain transfer reaction but also add another radical across C=C bond, the radical can propagate, resulting in oligomers/polymer as contaminants in the final product [6], so it is difficult to obtain ideal target product by this way. Besides, the thiol-ene reaction is readily catalyzed through either a base- and nucleophile-pathway [7, 8].

Unfortunately, though several of these reactions can proceed via photo-click, also have characteristics of click chemistry [9], many of these "click" reactions lack the control afforded by light initiation, so several researchers have come up with a scheme where utilize photocaged amine [10], the amine will be released upon UV irradiation to catalyze the thiol-ene addition of thiol and acrylate, which can allow on-demand initiation of a specific reaction, so this study broadens its applications. However, when the reaction is applied in UV-curing materials, it is difficult for the UV to enter inner of materials because of the strong absorption, scattering and reflection to UV, which causes material internal curing incomplete and curing efficiency is low, especially used in the materials with a certain thickness. Therefore, there is a need and challenge for developing new methods to solve the problem.

In this paper, we intend to introduce the phototriggered base proliferation and UV photopolymerization into thiol-ene reaction, which is expected to play an important role to improve the UV-initiated efficiency. We synthesized photobase generator (NPPOC-HA) and amine amplifier. NPPOC-HA has UV absorption above 300 nm, and photolysis products are amine and styrene, no free radical produced [11], which will be released upon UV irradiation to catalyze the addition of thiol and acrylate. Furthermore, amine amplifier has an autocatalytic decomposition when triggered by an amine, which will cause the increase of active substances hexylamine and thus accelerate photo-click reaction [12]. Besides, hexylamine as a primary amine, has strong nucleophilicity and can make the thiol and double bond proceed rapid Michael-addition reaction [13]. UV phototriggered base proliferation reaction, which integrated safety and strong penetrating ability of UV photopolymerization as well as Domino free radical photopolymerization based on phototriggered base proliferation reaction, is expected to expand application of thiol-ene click reaction.

2 Experiments

2.1 Materials and Equipments

Hexylamine (HA, 98%, Aladdin-reagent), 2-(2-Nitrophenyl)propyl chloroformate (NPPOC-Cl, 95%, Sigma-Aldrich), 9-fluorenylmethyl chloroformate (Fmoc-Cl, 98%, Shanghai Darui Finechem), dichloromethane (CH_2Cl_2, Guangzhou Chemical Reagent Factory), β-mercaptoethanol (ME, >98%, Jian Yang Biotechnology), Ethyl mercaptoacetate (EM, 98%, Aladdin-reagent), Acrylic acid (AA, Tianjin Fu Chen Chemical Reagent Factory), and Butyl acrylate (BA, 99%, Aladdin reagent) were used as received. All other chemicals used were of analytical grade and used without further purification.

Ultraviolet lamp (360 nm); Fourier transmission infrared spectroscopy (FT-IR, Tensor 27 Bruker) was used to character the structure of prepolymer over wavenumber range of 400–4000 cm^{-1}; the NMR spectra was obtained at room temperature by Superconducting Fourier Transform Nuclear Magnetic Resonance Spectrome (AVANCE III HD 400); Real-time Fourier transform infrared Perkin Elmer Lambda 750 UV-Visible spectrophotometer; UV light intensity meter (UV Meter 2000); 325 nm-Longpass Filter.

2.2 Preparation of 2-(2-Nitrophenyl)Propyl Oxycarbonyl Hexylamine (NPPOC-HA)

2-(2-Nitrophenyl)propyl chloroformate (6 mmol, 1.4619 g) was dissolved in CH_2Cl_2 (60 mL), and then added dropwise to a solution of hexylamine (12.6 mmol, 1.2749 g) in CH_2Cl_2 (30 mL). After that, the mixture was stirred under cooling for 20 min and at room temperature for 5 h. Finally, the solution was washed thrice successively with water, a 5% HCl aqueous solution, and a saturated NaCl solution, dried over anhydrous $MgSO_4$, and evaporated to obtain a light yellow liquid as the product. Yield: 75.1%.

2.3 Preparation of 9-Fluorenylmethoxycarbonyl-Hexylamine (Fmoc-HA)

Fmoc-Cl (15.44 mmol, 4.0310 g) was dissolved in CH_2Cl_2 (100 mL) under cooling, and then hexylamine (30.8 mmol, 3.1220 g) in CH_2Cl_2 (40 mL) was slowly added to an ice cooled solution of Fmoc-Cl in CH_2Cl_2, after that the mixture was stirred under cooling for 20 min and at room temperature for 1.5 h. Finally, the solution was washed thrice successively with water, a 5% HCl aqueous solution,

Table 1 Test formula of thiol-ene Michael addition reaction

Number	Ethyl-mercaptoacetate (g)	β-Me (g)	PBG (g)	AP (g)	AA (g)	BA (g)
1	0.240	–	0.012	0.033	0.144	–
2	0.240	–	0.012	0.033	–	0.256
3	–	0.156	0.012	0.033	0.144	–
4	–	0.156	0.012	0.033	–	0.256

and a saturated NaCl solution, dried over anhydrous $MgSO_4$, and evaporated to obtain a white crystalline as the product. Yield: 85%.

Test samples were prepared according to formula in Table 1, resulting mixtures were uniformly smeared onto KBr crystals in a horizontal transmission apparatus, next reactions were initiated by UV source with a irradiation intensity of 50 mW/cm^2, a longpass filter (325 nm-Longpass) was used to filter out UV light below 300 nm, which prevented production of thiol free radicals.

3 Results and Discussion

3.1 Characterization of NPPOC-HA

As shown in Fig. 1, a new peak at 3339 cm^{-1} corresponding to the stretching vibration peak of –NH was observed, which indicated the formation of –NH, meanwhile, the absorption peak of stretching vibration of –C=O and –C–N at 1712 and 1247 cm^{-1} appeared, besides, the vibration peak of –NHCO at 1530 cm^{-1}

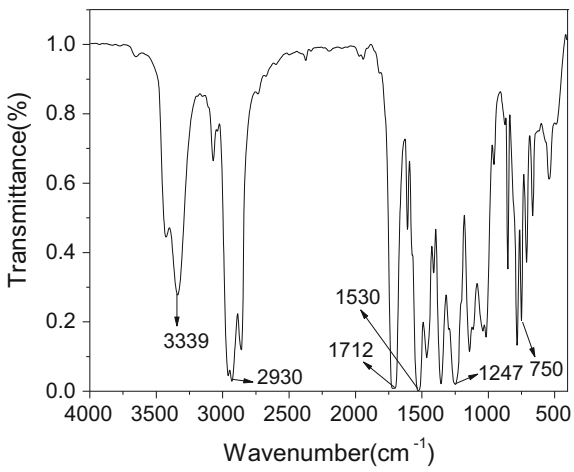

Fig. 1 FTIR spectrum of NPPOC-HA

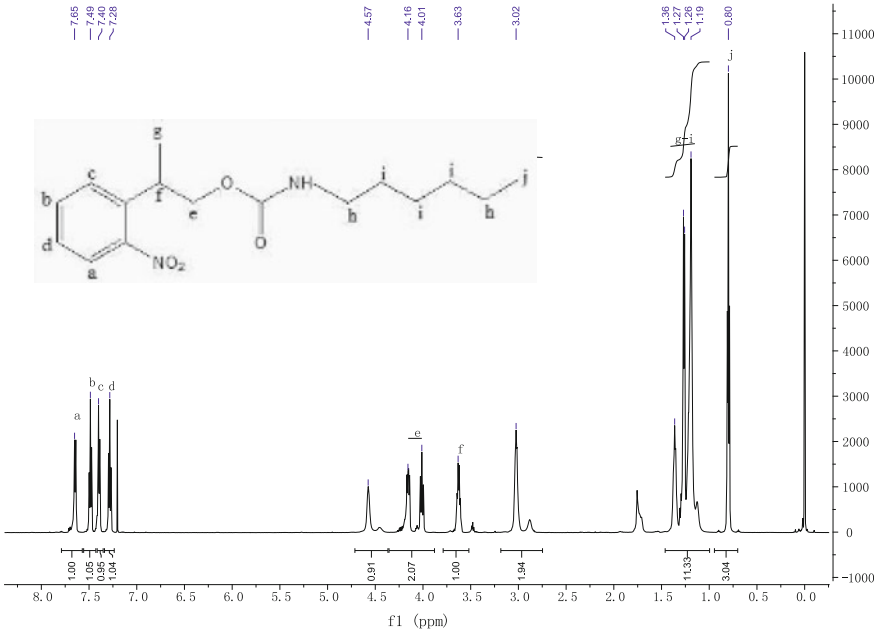

Fig. 2 ^{1}H-NMR spectrum of NPPOC-HA

appeared, indicating amine bond (–CO–NH) generated, 750 cm^{-1} is the twisting vibration of –C–H in benzene, all of which indicated that NPPOC-HA was synthesized successfully.

The ^{1}H-NMR spectrum of NPPOC-HA was measured as shown in Fig. 2, δ = 7.65 (1H, d, H-a), 7.49 (1H, t, H-b), 7.40 (1H, d, H-c), 7.28 (1H, t, H-d), 4.01-4.16 (2H, m, H-e), 3.63 (1H, t, H-f), 1.19-1.36 (13H, t, H-g-i), 0.80 (3H, t, H-h).

3.2 Characterization of Fmoc-HA

As can be seen from Fig. 3, the stretching vibration peak of –NH at 3340 cm^{-1}, and the vibration peak of –NHCO at 1540 cm^{-1} were monitored by FTIR, furthermore, the absorption peak of stretching vibration at 1269 cm^{-1} (–C–N) appeared, besides vibration peak at 3035 cm^{-1} (C–H) and 1447 cm^{-1} (C–C) in Fluorene, as well as the absorption peak at 1690 cm^{-1} (–C=O) were monitored, whose facts showed Fmoc-HA was obtained. And the formyl wavenumber is 1780 cm^{-1} in Fmoc-HA,

but the absorption peak of –C=O decreased in Fig. 3, which indicated generating ammonia ester structure, it is because when carbonyl exists in different chemical environment before and after reaction, change of chemical bond makes force constant change, so that the stretching vibration frequency decreases.

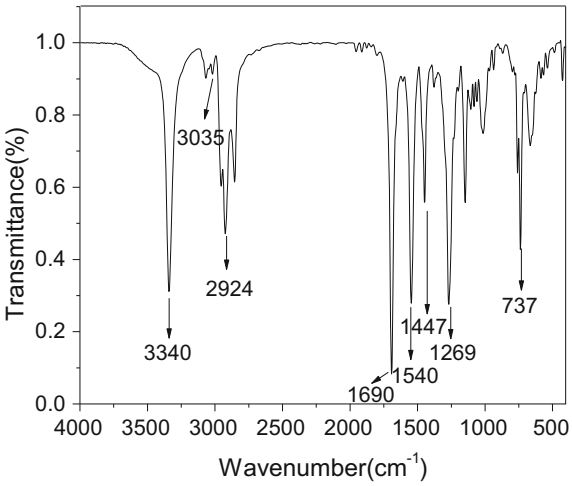

Fig. 3 FTIR spectrum of Fmoc-HA

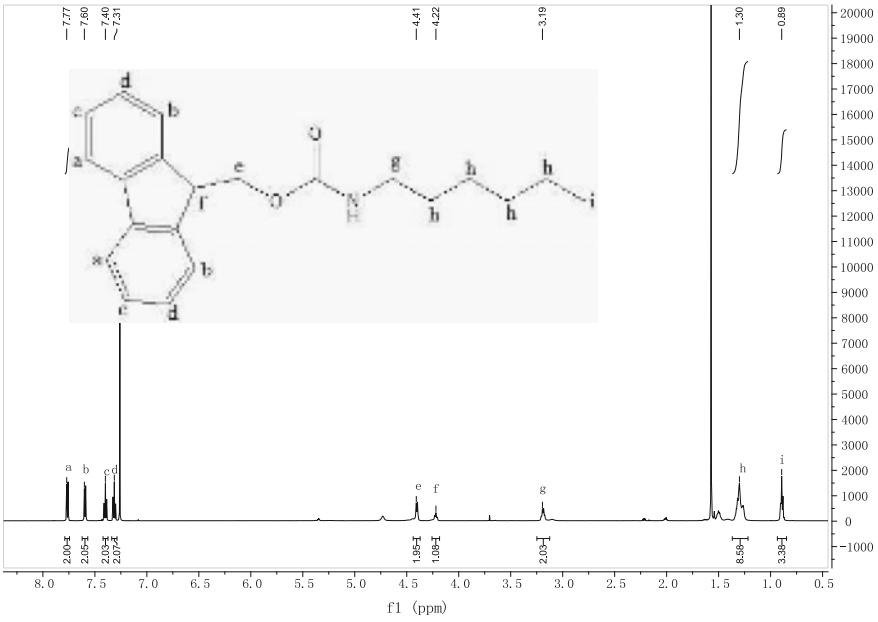

Fig. 4 ^{1}H-NMR spectrum of Fmoc-HA

The ^{1}H-NMR spectrum of Fmoc-HA was measured at room temperature as shown in Fig. 4, δ = 7.77 (2H, d, H-a), 7.60 (2H, d, H-b), 7.40 (2H, t, H-c), 7.31 (2H, t, H-d), 4.41 (2H, d, H-e), 4.22 (1H, t, H-f), 3.19 (2H, m, H-g), 1.30 (8H, m, H-h), 0.89 (3H, t, H-i).

3.3 *Michael Addition Reaction Under Phototriggered Base Proliferation*

RTIR spectroscopy was used to monitor the conversion of –C=C and –SH at room temperature to demonstrate the potential of photobase generator and base amplifier for thiol-Michael addition reaction; the irradiation time in this system was 0.5 min, then the UV light was turned off. As shown in Figs. 5, 6, 7 and 8, these reactions could be rapidly actuated under photo-irradiation without the presence of obvious induction periods, and the reaction continued after UV light (0.5 min) was turned off, results showed only 0.5 min irradiation instead of continuous irradiation could achieve >80% final conversion for both thiol and acrylate, furthermore, conversions of –C=C and –SH changed with equal proportion. And the reaction system of butyl acrylate and thiol was more efficient, its final conversion was 100% and the maximum initiation rate (R_{pmax}) was 200 min^{-1}, which showed higher catalytic efficiency. All of above results involved an autocatalytic decomposition of a base amplifier (BA), firstly, the NPPOC-HA was released upon UV irradiation to generate the hexylamine, then the hexylamine catalyzed base amplifier to decompose, generating more amines. Generally, a small amount of photobase generator can make the base amplifier self-catalyze to produce a series of base, photosensitivity can be greatly improved, more importantly, the hexylamine is a primary amine with

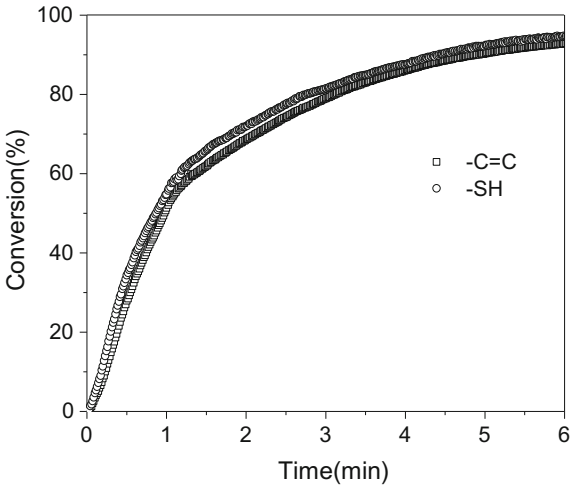

Fig. 5 The conversion of –SH in ethyl mercaptoacetate and –C=C in acrylic acid

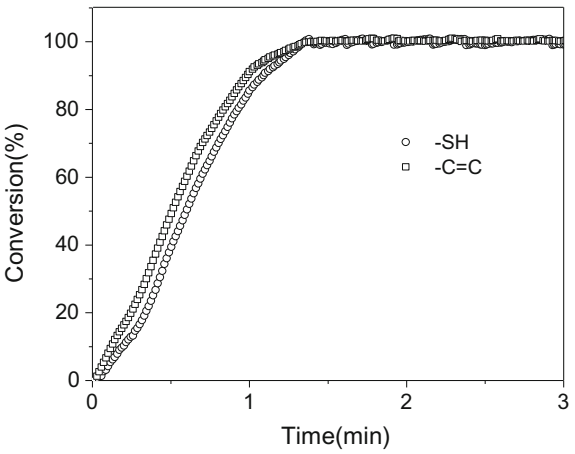

Fig. 6 The conversion of –SH in ethyl mercaptoacetate and –C=C in butyl acrylate

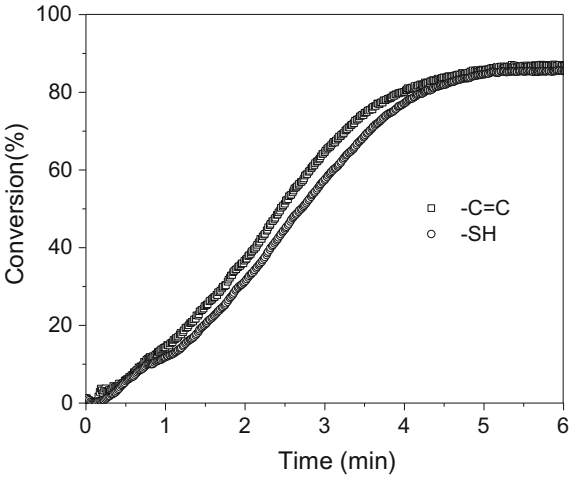

Fig. 7 The conversion of –SH in β-mercaptoethanol and –C=C in acrylic acid

a strong nucleophilicity, so when UV light is turned off after 0.5 min irradiation, reaction could continue and achieve high conversions.

This study solved the deep curing problem of materials perfectly, could be applied to photo-shield materials, and greatly improved the curing efficiency.

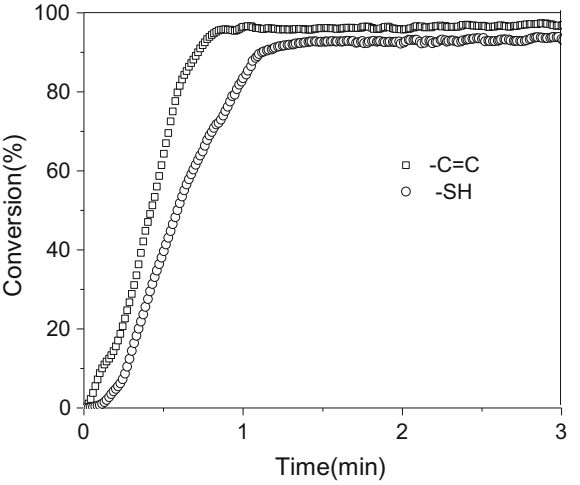

Fig. 8 The conversion of –SH in β-mercaptoethanol and –C=C in butyl acrylate

4 Conclusions

In this paper, we synthesized the photobase generator and base amplifier, characterized structure by FT-IR and ^{1}H-NMR, moreover, we studied the Michael addition reaction under phototriggered base proliferation, the results suggested that the photobase generator had photolytic efficiency, and the base amplifier could achieve self-catalysis, meanwhile the system had high photocatalytic efficiency, its final conversion could achieved >85% only needing 0.5 min irradiation instead of continuous irradiation, which offered a substantial breakthrough in the photo efficiency of amine generation and resulted in a significant improvement in photosensitivity. Furthermore, it provided a solution to the deep curing problem of materials, and expanded the application of thiol-Michael addition reaction.

Acknowledgements This work was financially supported by Construction of High Efficiency UV-LED Photopolymerization System and R&D of Environmental Friendly Ink (201607020045), the Science and Technology Planning Project in Guangzhou, and the Special Funds of Strategic Emerging Industry and Future Industrial Development in Shenzhen, belonging to Engineering Laboratory of Nano Smart Coating Materials, which was the second supporting plan in 2016,as well as State Key Laboratory of Pulp and Paper Engineering Project (2016C01).

References

1. Hoyle CE, Bowman CN (2010) Thiol-ene click chemistry. Angew Chem Int Ed 49(9):1540–1573
2. Korthals B, Morant-Minana MC, Schmid M, Mecking S (2010) Functionalization of polymer nanoparticles by thiol-ene addition. Macromolecules 43(19):8071–8078

3. Meldal M, Tornøe CW (2008) Cu-catalyzed azide−alkyne cycloaddition. Chem Rev 108 (8):2952–3015
4. Lowe AB (2010) Thiol-ene "click" reactions and recent applications in polymer and materials synthesis. Polym Chem 1(1):17–36
5. Golas PL, Matyjaszewski K (2010) Marrying click chemistry with polymerization: expanding the scope of polymeric materials. Chem Soc Rev 39(4):1338–1354
6. Xu R, Guan X, He M, Yang J (2017) Phototriggered base proliferation: a powerful 365 nm LED photoclick tool for nucleophile-initiated thiol-Michael addition reaction. RSC Adv 7 (2):914–918
7. Chan JW, Hoyle CE, Lowe AB, Bowman M (2010) Nucleophile-initiated thiol-michael reactions: effect of organocatalyst, thiol, and ene. Macromolecules 43(15):6381–6388
8. Xi W, Wang C, Kloxin CJ, Bowman CN (2012) Nitrogen-centered nucleophile catalyzed thiol-vinylsulfone addition, another thiol-ene "click" reaction. ACS Macro Lett 1(7):811–814
9. Tasdelen MA, Yagci Y (2013) Light-Induced Click Reactions. Angew Chem Int Ed 52 (23):5930–5938
10. Xi W, Krieger M, Kloxin CJ, Bowman CN (2013) A new photoclick reaction strategy: photo-induced catalysis of the thiol-Michael addition via a caged primary amine. Chem Commun 49(40):4504–4506
11. Hasan A, Stengele KP, Giegrich H, Cornwell P, Isham KR, Sachleben RA, Pfleiderer W, Foote RS (1997) Photolabile protecting groups for nucleosides: synthesis and photodeprotection rates. Tetrahedron 53(12):4247–4264
12. Yin X (2010) Study on synthesis and properties of amine proliferators. Sun Yat-sen University, Guangzhou
13. Chan JW, Yu B, Hoyle CE, Lowe AB (2008) Convergent synthesis of 3-arm star polymers from RAFT-prepared poly (N, N-diethylacrylamide) via a thiol–ene click reaction. Chem Commun 40:4959–4961

Synthesis and Characterization of Novel Benzoperylene and Coronene Derivatives

Qi Zhu, Jialing Pu and Guangxue Chen

Abstract Novel "swallow tail" N-substituted benzo[ghi]perylene monoimides (BPI) and coronene diimides (COI) have been efficiently synthesized via Diels-Alder reaction. UV–vis spectra of BPI and COI show the representative absorption bands from 300 to 500 nm, and have obviously blue shifted absorption compared to that of PET. The analysis of DSC and POM revealed the existence of hexagonal columnar of PET and COI. With "swallow tail" alkyl chains, BPI have lower melt points and COI have lower liquid crystal region.

Keywords Benzoperylene · Coronene · Diels-Alder reaction · Liquid crystals

1 Introduction

Polycyclic aromatic hydrocarbons (PAHs) are one series of interesting organic molecules because of their have particularly large π-conjugated structure [1]. Highly conjugated PAHs derivatives have previously received greatly research interest as industrial colorants [2] and molecular fluorescent probes [3]. Now, their unique electronic π-stacked structure allow their utilization in organic thin-film optoelectronic materials [4, 5]. The core size, coplanarity, and charge distribution of these molecules are considered to affect their self-assembly and charge-transport properties [6].

Q. Zhu · J. Pu · G. Chen (✉)
State Key Laboratory of Pulp and Paper Engineering, South China University of Technology, Guangzhou, China
e-mail: chengx@scut.edu.cn

Q. Zhu
e-mail: 839475230@qq.com

J. Pu
Laboratory Information Recording Materials, Beijing Institute of Graphic Communication, Beijing, China

P. Zhao et al. (eds.), *Applied Sciences in Graphic Communication and Packaging*, Lecture Notes in Electrical Engineering 477,
https://doi.org/10.1007/978-981-10-7629-9_114

Benzoperylene and coronene are the representative molecules among a variety of PAHs. Benzo[ghi]perylene (Bp) has six aromatic rings, of which five are arranged around a central ring. Coronene (Cor) is similar to Bp but with the symmetry among the six outer rings. Several attempts have been made to synthesize new Bp and Cor molecules to improve their applicability by introduction of polar groups or side chains into the molecular structure [7–9]. Introduction of electron-accepting or electron-donating groups into the π-conjugated aromatic core enables to control the charge distribution and photophysical properties [6]. Because of the presence of alkyl chains, the molecules shows greatly increased solubility in common organic solvents. Moreover, introduction of alkyl chains do not affect the electronic distribution of the molecules [10].

In this work, "swallow tail" N-substituted benzo[ghi]perylene monoimides (BPI) and coronene diimides (COI) have been designed and synthesized. Their chemical structures were confirmed by nuclear magnetic resonance spectroscopy (NMR), Fourier transform infrared spectroscopy, UV–Vis absorption spectroscopy and mass spectrometry. The thermal and liquid crystalline properties were investigated by Thermogravimetric Analysis (TG), differential scanning calorimetry (DSC), and polarizing optical microscopy (POM).

2 Experimental Sections

Target compounds was obtained from the Perylene 3,4,9,10-tetracarboxylic tetraisobutylester by the Diels-Alder reaction, and the synthetic schemes shown in Fig. 1. Two intermediate of 1 and 2, were prepared according to a reported literature [11]. The synthetic procedures of the representative compound 3 and 4 were shown in detail.

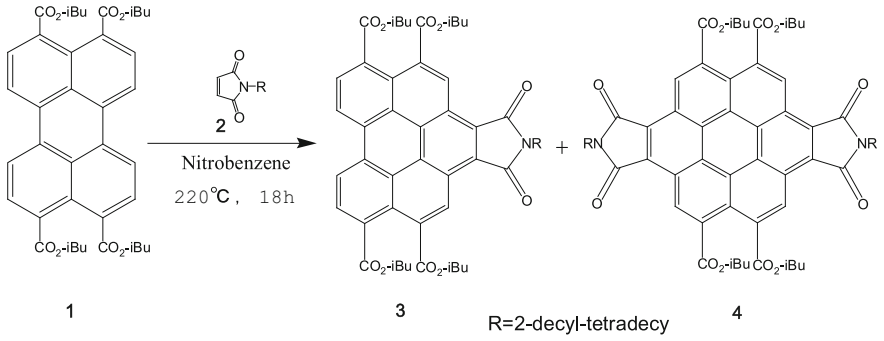

Fig. 1 The scheme of synthesis of BPIs and Cols

2.1 Synthesis of 3

Perylene 3,4,9,10-tetracarboxylic tetraisobutylester 1 (2.35 g, 3.6 mmol) and 1-(2-Decyl-tetradecy)-pyrrole-2,5-dione 2 (7.8 g, 18 mmol) in nitrobenzene (20 ml) was stirred to reflux for 10 h at 220 °C. The reaction mixture was poured into chloroform (100 ml) and separated on silica column. The nitrobenzene and other impurities were eluted with petroleum ether. The product was further purified by column chromatography on silica gel eluting with chloroform/petroleum ether (4:1). Yield: 3.35 g (3.1 mmol, 86%) as red viscous solid. ^{1}H NMR (300 MHz, $CDCl_3$, TMS): δ = 9.67 (s, 2H; ArH), 8.78 (d, 2H; ArH), 8.35 (d, 2H; ArH), 4.26 (m, 8H; CH_2O), 3.83 (d, 2H; CH_2N), 2.35 (t, 4H; CH), 2.23 (s, 2H; CH), 1.20 (m, 40H; CH_2), 1.15 (d, 24H; CH_3), 0.84 ppm (d, 12H; CH_3); ^{13}C NMR (300 MHz, $CDCl_3$ TMS): δ = 168.6 (C=O), 167.3 (C=O), 164 (CAr), 163.6 (CAr), 133.0 (CArH), 132.5 (CAr), 72.4 (CH_2O), 32.8 (CH_2N), 27.1 (CH), 23.4 (CH), 20.6 (CH_2), 14.4 (CH_3), 11.0 ppm (CH_3); MALDI-TOF MS (m/z): 1104.6 $[M + Na]^+$, Calcd for $C_{68}H_{91}NO_{10}$: 1081.66.

2.2 Synthesis of 4

Compound 1 (2.35 g, 3.6 mmol) and compound 2 (15.6 g, 36 mmol) in nitrobenzene (20 ml) was stirred to reflux for 18 h at 220 °C. The reaction mixture was poured into chloroform (100 ml) and separated on silica column. The nitrobenzene and other impurities were eluted with petroleum ether. The product was further purified by column chromatography on silica gel eluting with chloroform/petroleum ether (1:1). Yield: 1.52 g (1.0 mmol, 28%) as an orange-yellow waxy solid ^{1}H NMR (300 MHz, $CDCl_3$, TMS): δ = 10.59 (s, 4H; ArH), 4.41 (d, 8H; CH_2O), 3.93 (d, 4H; CH_2N), 2.37 (t, 4H; CH), 2.16 (s, 2H; CH_2), 1.60-1.20 (d, 80H; CH_2) 1.0-0.86 ppm (s, 32H; CH_3); ^{13}C NMR (300 MHz, $CDCl_3$ TMS): δ = 169.4 (C=O), 168.3 (C=O), 132.2 (CAr), 127.6 (CAr), 126.0 (CArH), 123.5 (CAr), 72.4 (CH_2O), 31.8 (CH_2N), 28.1 (CH), 26.4 (CH), 22.6 (CH_2), 19.4 (CH_3), 14.0 ppm (CH_3); MALDI-TOF MS (m/z): 1534.9 $[M + Na]^+$, Calcd for $C_{96}H_{138}N_2O_{12}$: 1512.03.

3 Results and Discussion

3.1 Synthesis

Comparing to the Diels-Alder reaction of perylene 3,4,9,10-tetracarboxylic tetra-isobutyl ester (PET) and N-ethyl maleimide with the p-chloranil [11], the use of nitrobenzene instead of p-chloranil make the reaction systems with lower viscosity.

The occurrence of saponification reactions of the vicinal ester groups is effectively reduced, resulting in the yield of the BPI and COI obviously improved.

3.2 FT-IR Spectra

The IR spectra of PET, BPI and COI in KBr film are shown in Fig. 2. The absorption at 2960 and 2921 cm^{-1} in the IR spectrum of PET are assigned to the Alkyl chain group C–H vibration band, similar absorption peak of BPI and COI at 2957 and 2921 cm^{-1} are also observed. In the IR spectrum of PET, a relatively strong band appeared at 1724 cm^{-1}, which are usually assigned to the carbonyl group vibration band. However, the same band is not observed from the IR spectrum of BPI and COI, but at 1705 cm^{-1} of BPI and at 1701 cm^{-1} of COI is observed. The frequency of C=O is shifted to lower position by 20 cm^{-1}, because of the presence of –CO–N–.

3.3 UV–Vis Spectra

UV–vis spectra of PET, BPI and COI in chloroform are shown in Fig. 3. The spectra of BPI and COI show the representative absorption bands from 300 to 500 nm, and have obviously blue shifted absorption compared to that of PET. The absorption of COI shows a strong peak at 357 nm, and BPI shows a strong peak at 352 nm and two weak peak at 394 and 416 nm. The existence of multiple-peak structure in spectra of BPI hints to its structural relation with PET and COI. There is

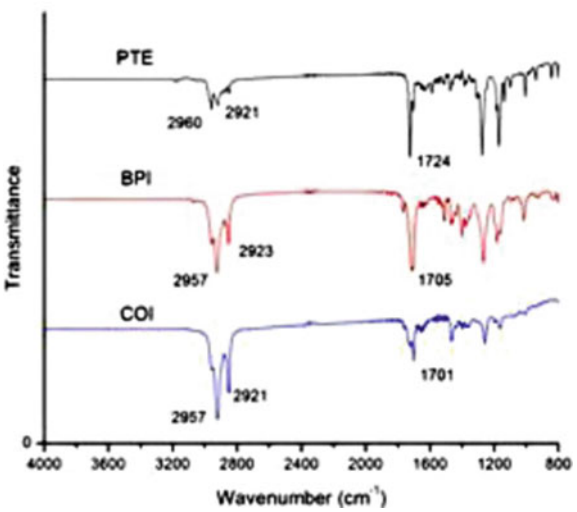

Fig. 2 IR spectra of PET, BPI and COI in KBr film

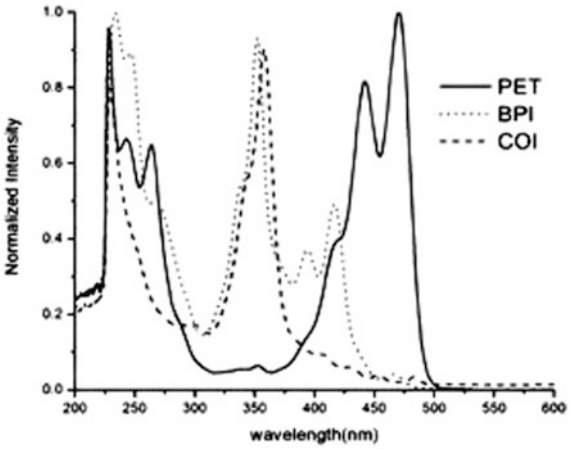

Fig. 3 UV–vis spectra of PET, BPI and COI in chloroform

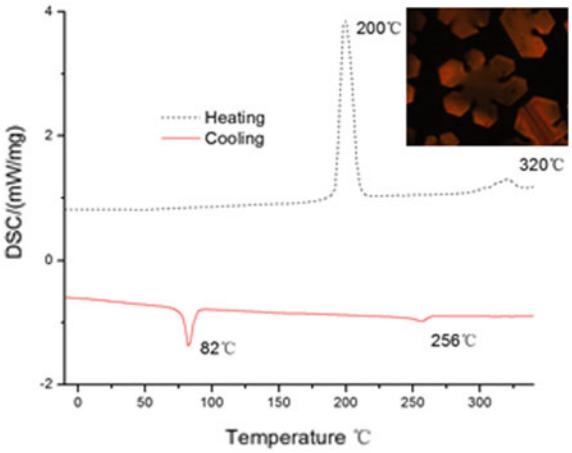

Fig. 4 DSC curves of PET. The inset shows a POM texture at 160 °C

a small red shift (5 nm) of the main absorption band, which is ascribed to the higher symmetry and the introduction of one further imide group.

3.4 Thermal Properties

TGA measurements revealed that all compounds were thermally stable up to about 330 °C with a 5% weight loss. The DSC curves of PET exhibited exothermic and endothermic peaks in heating and cooling processes in Fig. 4. A typical textures of 160 °C reveals the existence of hexagonal columnar. COI exhibited inconspicuous mesomorphic behaviors, as shown in a DSC curve in Fig. 5. The POM texture

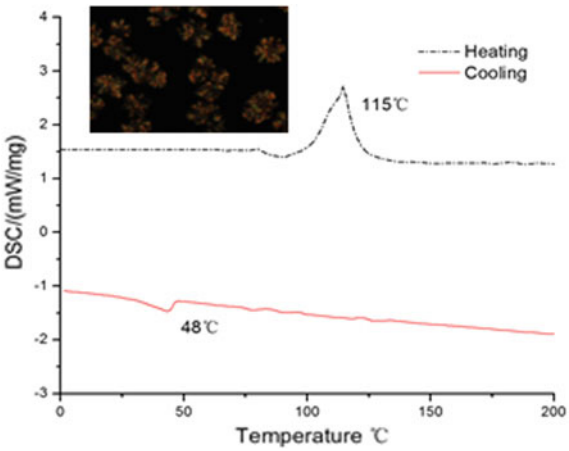

Fig. 5 DSC curves of COI. The inset shows a POM texture at 50 °C

at 50 °C presented a Fan-shaped texture indicating the formation of columnar phase. There is no evidence that BPI was found to be liquid crystal molecule, which is viscous solid at room temperature. With "swallow tail" alkyl chains, the dicotic molecule have lower melt points or liquid crystal region.

4 Conclusions

Novel "swallow tail" N-substituted benzo[ghi]perylene monoimides (BPI) and coronene diimides (COI) have been synthesized and Characterized. UV–vis spectra of BPI and COI show the representative absorption bands from 300 to 500 nm, and have obviously blue shifted absorption compared to that of PET. The analysis of DSC and POM revealed the existence of hexagonal columnar of PET and COI. With "swallow tail" alkyl chains, BPI have lower melt points and COI have lower liquid crystal region.

Acknowledgements This work was financially supported by Chinese National Natural Science Foundation of China (21404042); State Key Laboratory of Pulp and Paper Engineering Project (2016C01, 2016C02), and the Science and Technology Planning Project in Guangzhou (2016070220045).

References

1. Hasobe T, Ida K, Sakai H, Ohkubo K, Fukuzumi S (2015) Coronenetetraimide -centered cruciform pentamers containing multiporphyrin units: synthesis and sequential photoinduced energy- and electron-transfer dynamics. Chemistry 21(31):11196–11205
2. Huang C, Barlow S, Marder SR (2011) Perylene-3,4,9,10-tetracarboxylic acid diimides: synthesis, physical properties, and use in organic electronics. J Org Chem 76(8):2386–2407
3. Dubey RK, Knorr G, Westerveld N, Jager WF (2016) Fluorescent pet probes based on perylene-3,4,9,10-tetracarboxylic tetraesters. Org Biomol Chem 14(5):1564–1568
4. Wu D, Zhang H, Liang J, Ge H, Chi C, Wu J et al (2012) Functionalized coronenes: synthesis, solid structure, and properties. J Org Chem 77(24):11319–11324
5. Dijk JTMV, Hartwijk A, Bleeker AC, Lugtenburg J, Cornelisse J (1996) Gram scale synthesis of benzo[ghi]perylene and coronene†. J Org Chem 61(3):331–346
6. Ida K, Sakai H, Ohkubo K, Araki Y, Wada T, Sakanoue T et al (2014) Electron-transfer reduction properties and excited-state dynamics of benzo[ghi]peryleneimide and coroneneimide derivatives. J Phys Chem C 118(14):7710–7720
7. Hasobe T, Rabbani MG, Sandanayaka AS, Sakai H, Murakami T (2010) Synthesis and aggregate formation of triphenylene core-centered porphyrin hexamers. Chem Commun 46 (6):889–891
8. Lu J, Sun R, Chen M, Xu X, Zhang X (2012) Design, synthesis, and self-assembly of optically active perylenetetracarboxylic diimide bearing two peripheral chiral binaphthyl moieties. Mater Sci Eng C 32(7):1948–1954
9. Wasielewski MR (2009) Cheminform abstract: self-assembly strategies for integrating light harvesting and charge separation in artificial photosynthetic systems. Acc Chem Res 42 (12):1910–1921
10. Manning SJ, Bogen W, Kelly LA (2011) Synthesis, characterization, and photophysical study of fluorescent n-substituted benzo[ghi]perylene "swallow tail" monoimides. J Org Chem 76 (15):6007–6013
11. Alibert-Fouet S, Seguy I, Bobo J-F, Destruel P, Bock H (2007) Liquid-crystalline and electron-deficient coronene oligocarboxylic esters and imides by twofold benzogenic diels–alder reactions on perylenes. Chemistry 13(6):1746–1753

Preparation and Characterization of Cross-Linked Chlorinated Polystyrene Microspheres

Ruixia Duan, Jinzhou Chen, Guandong Hou and Jianxiang Ke

Abstract The research and application of polymer microspheres have developed very fast in recent years. Especially the polymer microsphere with large size has been widely applied in many fields, such as standard measurement, information, medicine, immunity, biochemistry etc. Meanwhile, cross-linked mono-disperse microspheres are of more extensive application prospect, because of their good adsorption properties, mechanical properties. The topic of this thesis, belonging to the field of polymer microspheres, is about the preparation of 30–50 μm cross-linked chlorinated polystyrene microspheres. Adopting the method between dispersion polymerization and suspension polymerization, PS, CMS as the monomers, AIBN as initiator, DVB as cross-linker, ethanol and water as the reaction medium, cross-linked chlorinated polystyrene microspheres can be prepared. Then the microspheres were detected by infrared and the morphology was observed by SEM. Through the polymerization parameters on particle size and size distribution of the study, this issue determines a recommended formula for 30–50 μm cross-linked chlorinated polystyrene microspheres.

Keywords Polystyrene microspheres · Size · Cross-linked · Chlorine

1 Introduction

Polymer microsphere is the polymer material or the polymer composite material whose diameter is in the nanometer level to the micron level. Its shape is ball or other geometry body, and the morphology can be varied. Because of its special size and structure, it plays a special and crucial role in many important fields. Different particle size and morphology of the microspheres have different functions [1].

In recent twenty years, due to the application field of polymer microspheres from the previous general industrial application development to high-technology areas,

R. Duan · J. Chen (✉) · G. Hou · J. Ke
School of Materials Science and Engineering, Zhengzhou University, Henan, China
e-mail: cjz@zzu.edu.cn

P. Zhao et al. (eds.), *Applied Sciences in Graphic Communication and Packaging*, Lecture Notes in Electrical Engineering 477,
https://doi.org/10.1007/978-981-10-7629-9_115

preparation and application research of polymer microsphere entered a new climax. Especially in the last ten years, nanospheres (tens of nm) and large microspheres had a breakthrough [2]. The studies on polymer microspheres were mainly reflected in the following two aspects: the first was to control the particle size and size distribution; the second was the study of the structure of the microspheres, mainly focused on the preparation of porous and hollow structure.

Specially, micron-sized polymer microspheres with chloromethyl groups on their surfaces are useful in a variety of applications where grafting or coupling reactions are required. The main advantage of chloromethyl groups is that it needs no activation process, unlike other functional groups, such as hydroxyl or carboxyl groups, etc. [3].

The method of preparing polymer microspheres reported by using monomer as raw material was mainly divided into emulsion polymerization, dispersion polymerization in polar and/or non-polar media, emulsion polymerization, seeded emulsion polymerization, precipitation polymerization, etc. [4–7]. Among them, suspension polymerization preparation of microspheres particle size was generally in the 100–1000 μm, while the dispersion polymerization preparation of microspheres size in the 1–10 μm in most case, microspheres between 10 and 100 μm is very hard to prepare.

Mono-disperse polystyrene microspheres with different functional groups, large specific surface area, strong adsorption, strong coagulation and surface reaction ability, has a broad application prospect in many fields [8, 9]. In this paper, controlling the size and size distribution of microspheres, the poly(-chloromethyl styrene) microspheres were modified and then pored by supercritical carbon dioxide, and the microspheres were used in drug carriers and clinical medicine. The purpose of this study is to prepare the cross-linked chlorinated polystyrene microspheres between size of 30–50 μm, which used in drug carriers and clinical medicine.

This experiment used a unique polymerization reaction between the dispersion polymerization and suspension polymerization. Mechanism of the microspheres polymerization contained three stages (showed in Fig. 1), which had the following characteristics: low cost, polymerization heat was easily removed without recovery problem, using water and ethanol as reaction medium, easily to control temperature, the particle size can control in small range and higher product purity.

2 Experiments

2.1 Main Materials and Reagents

The main materials and reagents used in the experiment are listed in Table 1. In order to ensure the smooth progress of the polymerization, it is usually necessary to remove the polymerization inhibitor by caustic washing and vacuum distillation

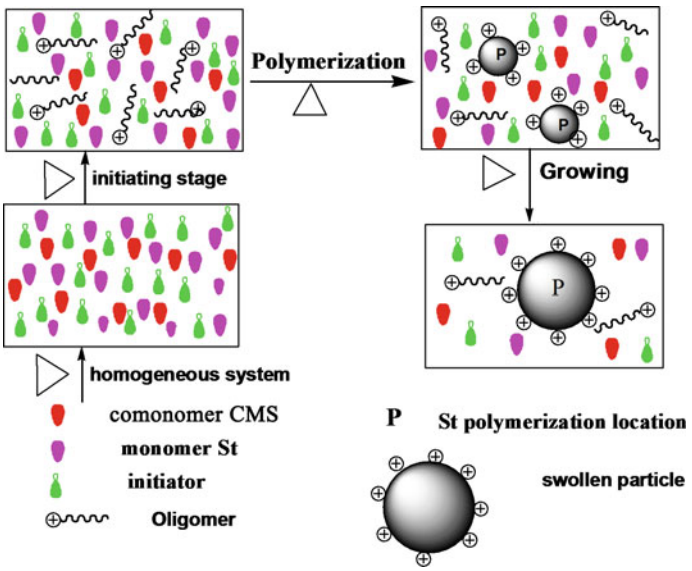

Fig. 1 Mechanism of the microspheres polymerization

Table 1 Main materials and reagents (analytically pure)

Sample	Purpose	Source
Styrene (St)	Monomer	Fengchuan Chemical, Tianjin
Chloromethyl styrene (CMS)	Monomer	Xiya Chemical, Sichuan
EtOH/H_2O	Reaction medium	Fengchuan Chemical, Tianjin
2,2-azobis (iso-butyronitrile) (AIBN)	Initiator	Kermel Chemical, Tianjin
Poly vinyl pyrrolidone (PVP)	Stabilizer	Kermel Chemical, Tianjin
Hydroxypropyl methyl cellulose(HPMC) () (HPMC)	Dispersant	Aladdin Reagent
n-Hexanol	Assistant dispersant	Xingzhi Chemical, Shanghai
Di-vinyl benzene (DVB)	Crosslinking agent	J&K Scientific Ltd., Beijing

method. The styrene, chloromethylated styrene and divinyl benzene were dealed by vacuum distillation method in the scheme. Appropriate amount of styrene, chloromethylated styrene and divinyl benzene were added into round-bottom flask for vacuum distillation, and after heating, vacuum pumping and distillation, the fractions obtained into brown bottle and preserved in a refrigerator.

2.2 Preparation of Microspheres

Firstly, the given amount of HPMC, distilled water and EtOH were joined to the three mouth flask and stirred to form homogeneous system, then the solution was sucking filtrated out impurities. Secondly, PVP was adding slowly into the solution and so did n-hexanol. Thirdly, after mixing evenly St, DVB, AIBN were joined reaction system simultaneously, reacted for 5 h with mixing rate stabilized at 450 r/min. Then CMS and DVB were put in the system to react for 7 h and crosslinked polystyrene microsphere emulsion was obtained. Finally, the emulsion was sonic oscillated for 12 h, and by centrifugal and dispersion for several times, the white microsphere powder was gained after being dried.

3 Results and Discussions

3.1 Characterization

The crosslinked polystyrene microspheres that diluted with anhydrous alcohol were observed under optical microscope (OPM), and Fig. 2 shows the morphology and particle size of microspheres.

In order to increase the surface area of microspheres, the pores were made in the surface of microspheres with CO_2. The microspheres with pores were observed by scanning electron microscope (SEM) under vacuum conditions, and the morphology photo was showed in Fig. 3. Figures 1 and 3 indicated that the microspheres Particle sizes were within the range of requirements, and they had good spherical degree.

Figure 4 showed the infra-red spectrogram graph of poly(-chloromethyl styrene) microspheres. There were strong absorption peaks of C–H bonds in 1264 cm^{-1} and

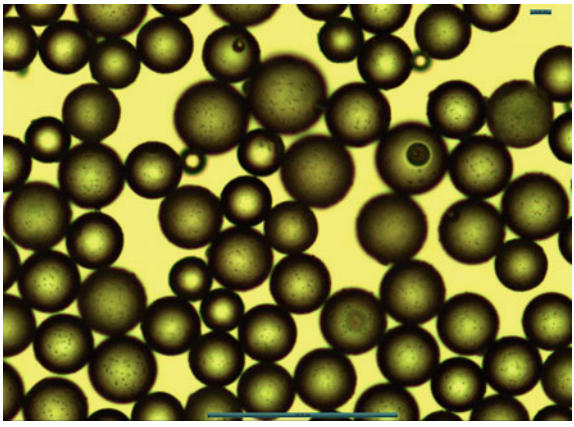

Fig. 2 The morphology of microspheres

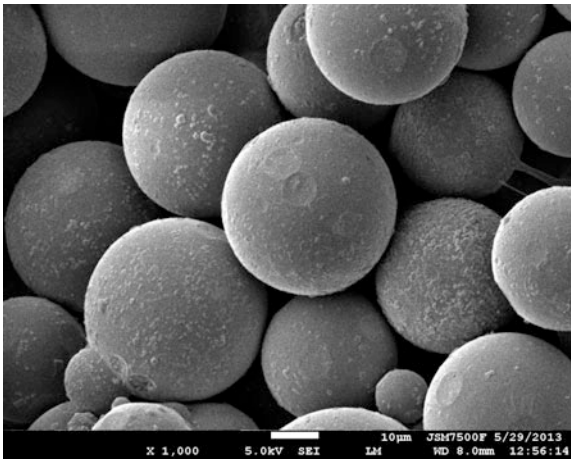

Fig. 3 SEM of microspheres with pores

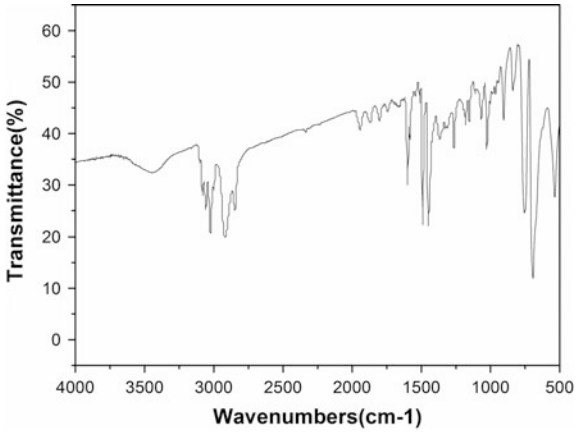

Fig. 4 Infrared spectrum graph of poly(-chloromethyl styrene) microspheres

C–H bonds in 670 cm^{-1} in the graph, which indicated there were a large amount of CH_2Cl structures in the microspheres prepared in this study. The content of chlorine in microspheres by calculated was 3.75. If you want to get poly(-chloromethyl styrene) microspheres with a higher chlorine content, you can adjust the proportion of styrene and chloromethyl styrene.

3.2 Effect of Hexanol's Amount

Figure 5 shows the morphology and size distribution of microspheres by adding different amount of Hexanol and EtOH, and the formula is showed in Table 2. As the concentration (volume ratio) of Hexanol reduced from 5 to 1.5%, the average

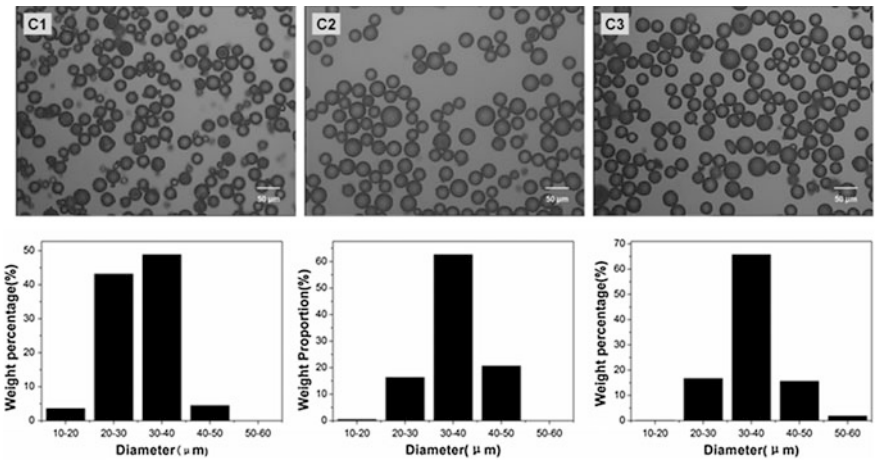

Fig. 5 The size distribution of microspheres by adding different volume ratio of Hexanol and EtOH, C1: 1/19, C2: 0.5/19.5, C3: 0.3/19.7 (Hexanol/EtOH)

Table 2 The microspheres' formula by adding different amount of Hexanol

Sample	EtOH (ml)	H_2O (ml)	Hexanol (ml)	Volume ratio of Hexanol (%)
1	19	30	1	5.0
2	19.5	30	0.5	2.5
3	19.7	30	0.3	1.5

Note The polymerization temperature was 65 °C and reaction time was 12 h

particle size of microspheres showed an increasing trend, and the ratio of microspheres between 30 and 50 μm reached the maximum value of 83% in Sample 2 when the volume ratio of Hexanol was 2.5% in Fig. 5 (C2). When the volume ratio of Hexanol was more in Sample 1, which led to a sharp decrease in the surface tension of the liquid and the formation of smaller droplets, and this will result in an increase the number of microspheres smaller than 30 μm to 47% in Fig. 5 (C1). On the contrary, when the volume ratio of Hexanol was less in Sample 3, which led to the formation of larger droplets, and this will result in an increase the number of microspheres bigger than 50 μm to 20% in Fig. 5 (C3). Therefore, it is critical to control the amount of the Hexanol accurately in the experiment.

4 Conclusions

This study prepared cross-linked poly(-chloromethyl styrene) microspheres and most of their particle size between 30 and 50 μm, which could be used to load chiral drugs. The following conclusions are drawn through the experimental study.

Firstly, it was indicated in the OPM and SEM pictures that most of the microspheres Particle sizes were within the range of requirements, and they had good spherical degree. Secondly, there were a large amount of CH_2Cl structures in the microspheres prepared in FT-IR graph and the content of chlorine was 3.75%. Thirdly, the ratio of microspheres between 30 and 50 μm reached the maximum value of 83% when the volume ratio of Hexanol was 2.5%.

References

1. Ma G, Su Z (2005) Polymer microspheres. Chemical Industry Press
2. Dai J (2006) Preparation and characterization of polystyrene functional microspheres. Jilin University
3. Kawaguchi H (2000) Functional polymer microspheres. Prog Polym Sci 25(8):1171–1210
4. Lu YY, El-Aasser MS, Vanderhoff JW (1988) Dispersion polymerization of styrene in ethanol: monomer partitioning behavior and locus of polymerization. J Polym Sci Part B Polym Phys 26:1187–1203
5. Paine AJ (1990) Dispersion polymerization of styrene in polar solvents.Ô. Solvency control of particle size from hydroxypropyl cellulose stabilized polymerizations. J Polym Sci Part A Polym Chem 28:2485–2500
6. Ugelstad J (1984) Monodisperse polymer particles and dispersions thereof: U.S. Patent 4,459,378. 1984-7-10
7. Shen S, Sudol ED, El-Aasser MS (1994) Dispersion polymerization of methyl methacrylate: mechanism of particle formation. J Polym Sci Part A Polym Chem 32(6):1087–1100
8. Tu C, Yang Y, Gao M (2008) Preparations of bifunctional polymeric beads simultaneously incorporated with fluorescent quantum dots and magnetic nanocrystals. Nanotechnology 19 (10):105601
9. Cao T (1997) Principle and application of polymer emulsion. Chemical Industry Press

Preparation of Hydrogel Material for 3D Bioprinting

Jia Yan, Yonghao Xiao, Kun Hu, Shun Pan, Yulong Wang, Baojian Zheng, Yen Wei and Luhai Li

Abstract Hydrogel is a kind of three-dimensional network polymer formed by chemical bond or physical cross-linking. It is widely used in the field of biomaterial because of its good biocompatibility. In this experiment, a gel-based composite material for 3D bioprinting was prepared using hyaluronic acid-methyl cellulose (HAMC) gel as carrier and nano-hydroxyapatite/collagen (nHAC). The effects of gel formulation on gel process were analyzed by in vitro gel test, rheological analysis, in vitro degradation and scanning electron microscopy. The results showed that HAMC with different mineralized collagen concentration could be rapidly gelatinized at 37 °C within 3 min. The rheological experiments showed that the HAMC-mineralized collagen had shear thinning properties suitable for 3D bioprinting. The results showed that the degradation rate was similar in the first 10 days, but the degradation rate was slower with the increase of mineralized collagen concentration. The porous structure and high porosity of the hydrogel were observed by scanning electron microscopy (SEM). The porous structure of the cross-linked sample was better.

Keywords Hyaluronic acid · Methyl cellulose · Mineralized collagen Hydrogels · 3D bioprinting

J. Yan · Y. Xiao · K. Hu (✉) · S. Pan · Y. Wang · B. Zheng · Y. Wei · L. Li
School of Printing and Packaging Engineering, Beijing Institute of Graphic Communication, Beijing, China
e-mail: kunhu@139.com

J. Yan · Y. Xiao · K. Hu · S. Pan · Y. Wang · B. Zheng · Y. Wei · L. Li
Beijing Engineering Research Center of Printed Electronics, Beijing Institute of Graphic Communication, Beijing, China

J. Yan
Tsinghua Redbud Innovation Institute Baodi Tianjin, Tianjin, China

K. Hu
Collage of Biological Science and Engineering, Fuzhou University, Fujian, China

P. Zhao et al. (eds.), *Applied Sciences in Graphic Communication and Packaging*, Lecture Notes in Electrical Engineering 477,
https://doi.org/10.1007/978-981-10-7629-9_116

1 Introduction

In recent years, due to the hydrogel has a good biocompatibility, biodegradability, easy molding characteristics [1, 2], in the field of biological materials called "biological ink", so many natural hydrogels and synthetic hydrogels can be used in the field of tissue engineering, but because of the low mechanical strength of hydrogels, it greatly limits its application in many fields, such as biomedical engineering, tissue engineering, etc. [3–6].

Cartilage repair is an important topic of bone tissue engineering, 3D bioprinting technology is different from the traditional construction method of tissue engineering bone, the use of computer-assisted design 3D bioprinting production of bionic tissue engineering bone structure more similar to the biological bone structure, and can be carried out Customized. According to the principle of bionics, based on the conventional synthesis of collagen-tricalcium phosphate composites, the synthesis of nano-hydroxyapatite/collagen (nHAC) has good biocompatibility and is widely used in biomaterials [7, 8]. Mineralized collagen is a bionic bone repair material with hierarchical structure designed according to the bionic thought and bionic natural bone extracellular matrix. The collagen fibers are self-assembled by collagen triple helix molecules, the collagen molecules are used as templates to prepare calcium phosphate in the liquid phase deposited onto ordered collagen fibers and self-assembled into nHAC composites with natural bone graded microstructure [9–11]. In this study, a kind of 3D bioprinting composite of gelatinous was prepared using HAMC gel as carrier and combined with nHAC according to the bionics. By optimizing the formulation and preparation process of HAMC composite gel, the biocompatibility of the material was improved, and a new composite material for 3D bioprinting was obtained.

2 Experimental

2.1 Materials

Bovine serum albumin (BSA, 98%) and Hyaluronic acid (HA, 97%) were purchased from AOBOX (China) and Macklin (China), respectively. Methyl cellulose M20 (MC), PEG-6000 and other reagents were bought from Sinopharm Chemical Reagent Co., Ltd. (China).

2.2 Preparation of Methyl Cellulose Solution

Artificial cerebrospinal fluid (aCSF) is a solution that mimics the physiological ion concentration of cerebrospinal fluid [12]. The aCSF (100 mL) solution was added

to a conical flask, heated to 90 °C in a water bath, and sodium chloride (8 g) was added to reduce the gel temperature of the sol. Weigh methylcellulose (22 g) was added to the solution and the magnetic stirring was carried out until the dispersion was uniform. Then add cold aCSF solution to a volume of 200 mL, stirring well and then remove, under the environment of ice salt bath mixing 40 min. Then, the mixture was refrigerated overnight at 4 °C.

2.3 Preparation of PEG Cross-Linked HAMC-Mineralized Collagen Composite Sol

Weigh the four groups of HA powder (0.15 g) were added to the 15 mL MC solution under mechanical stirring to make the HA powder is fully dispersed and dissolved; Weigh three groups of mineralized collagen (0.15, 0.3, 0.6 g) were added to the above three groups of MC (15 mL) solution, respectively. And then 0.5 mL of PEG-6000 (0.4 g/mL) solution was slowly added, and the pH was adjusted to about 7.4 with NaOH (1 mol/L) solution. After stirring, the mixture was allowed to stand refrigerated overnight at 4 °C.

2.4 Characterization

Since the prepared HAMC-mineralized collagen sol has a large viscosity, the gel exhibits a solid-like property. In order to verify its ability to gel in body temperature and to be used for 3D bioprinting, the sample was tested for gelation and rheology. In order to determine whether the stent formed by the gel sample was able to remain in the tissue for a long time, the in vitro degradation rate of each sample was measured. In order to realize the morphology and pore structure of the gel sample, the initial gel was lyophilized and its morphological characteristics were observed by SEM.

3 Results and Discussion

In the experiment, the gelation temperature of HAMC-mineralized collagen composite sol was preliminarily explored. As shown in Table 1, all the sol groups were gelatinized at 37 °C within 3 min, and the mineralized collagen concentration was higher, the gel time is longer. As shown in Fig. 1, can be intuitive to see the heated sol into a gel state, and that it don't flow after inversion, while the gel at 4 °C low temperature environment can change Into a liquid, it's a thermo-sensitive hydrogel and can be used as an excellent biological printing material.

Table 1 Qualitative study on gel temperature of HAMC—mineralized collagen composite sol

Mineralized collagen concentration (w/v) (%)	Observation time (s)				
	60	90	120	150	180
0	Sol	Gel			
1	Sol	Sol	Gel		
2	Sol	Sol	Sol	Gel	
4	Sol	Sol	Sol	Sol	Gel

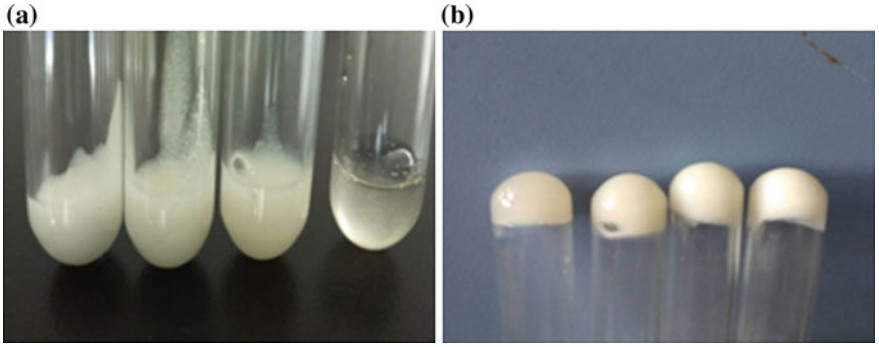

Fig. 1 Gelation test of HAMC-mineralized collagen composite sol: **a** At room temperature, **b** at 37 °C

In general, the viscosity of hydrogel is mainly determined by its molecular weight and concentration. The rheological properties of the composite gel samples are shown in Fig. 2. As the shear stress increases, the gel viscosity gradually decreased and the minimum value of four groups of sample viscosity is relatively close, the process of compound gel mobility becomes stronger, indicating that the composite gel has shear thinning characteristics, in line with the needs of 3D bioprinting. In addition, with the increase of the concentration of mineralized collagen, the viscosity of the composite gel also increased accordingly, which shows that there is stronger intermolecular interaction in the composite gel.

As shown in Fig. 3, four groups of different composite gel samples were cultured in aCSF at 37 °C to obtain the degradation of gel samples within 3 weeks. The samples were rapidly degraded in 10 days and then became slower, consistent with the experimental expectations. In addition, the greater the concentration of mineralized collagen, the degradation rate is relatively slow.

Hydrogel has been extensively studied due to its excellent properties. Figure 4 shows the SEM observations of HAMC with different concentrations of mineralized collagen, the four groups of composite gels can be clearly observed to exhibit highly porous structures at the micron scale and these pores are connected to each other. The main component of the gel-hyaluronic acid is the source of the porous structure, which forms a highly imitated environment of the actual extracellular

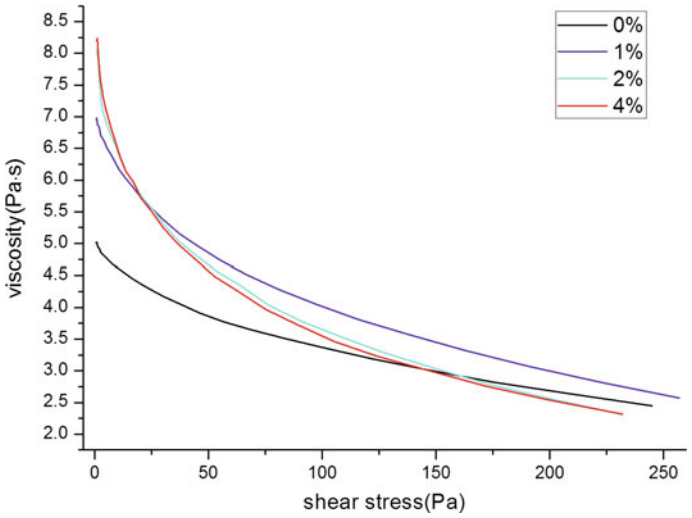

Fig. 2 Rheological properties of HAMC with different concentrations of mineralized collagen

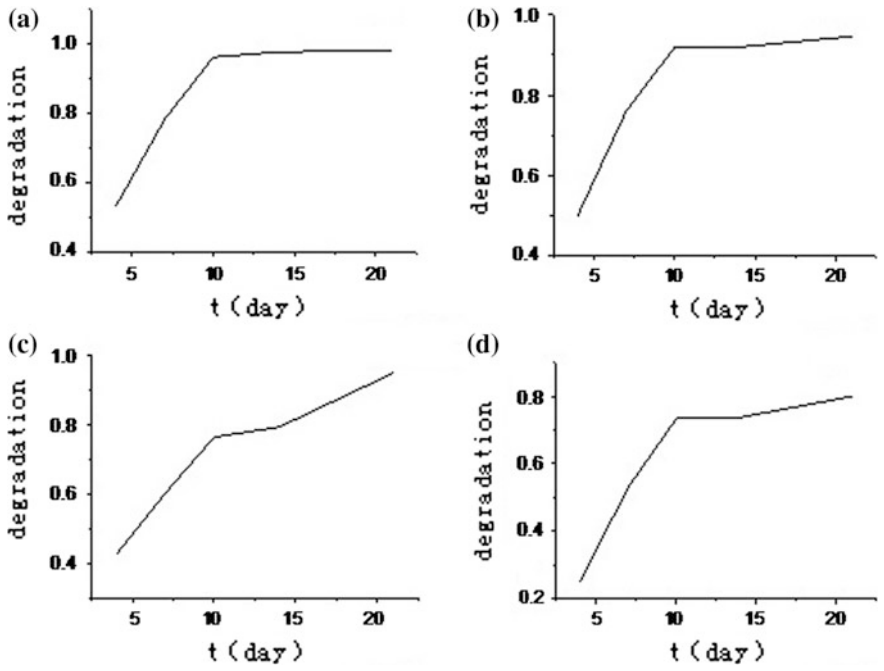

Fig. 3 In-vitro degradation curve of composite gel with different concentration of mineralized collagen: **a** 0%, **b** 1%, **c** 2%, **d** 4%

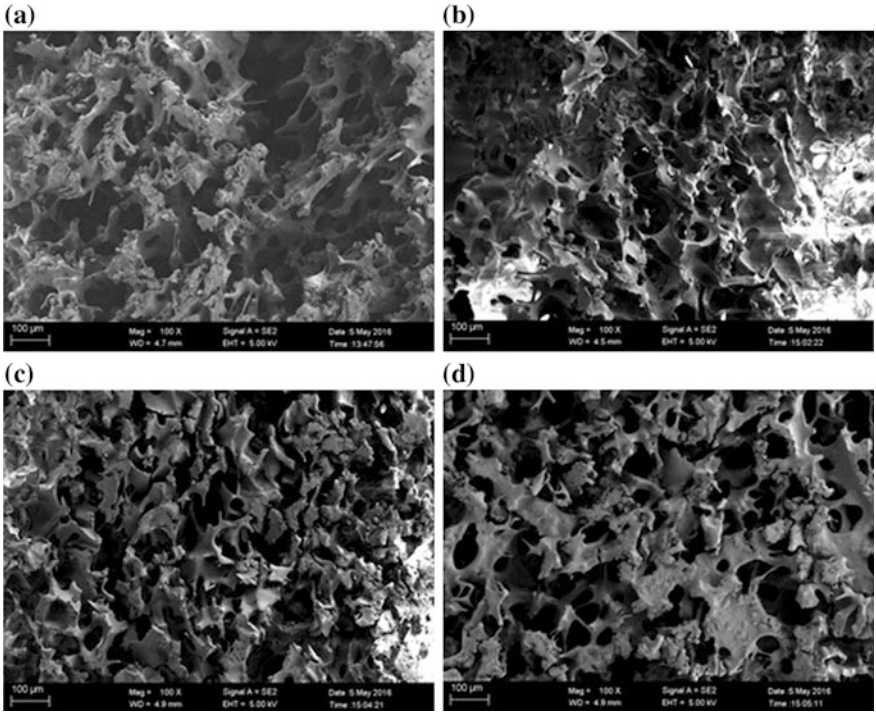

Fig. 4 SEM pictures of composite gels of different concentrations of mineralized collagen: **a** 0%, **b** 1%, **c** 2%, **d** 4%

matrix microstructure. Moreover, the porous network structure of the samples is good and uniform, and its mechanical strength is enhanced to some extent.

4 Conclusions

In this experiment, different proportions of HAMC-mineralized collagen composite gels were prepared by changing the concentration of mineralized collagen. During the gelation process, the samples could be rapidly gelatinized at 37 °C within 3 min. The rheological test results showed that the prepared hydrogels belongs to the pseudoplastic fluid, and it has the characteristics of shear thinning and can be used for 3D bioprinting. With the increase of mineralized collagen concentration, the degradation rate slows down and the SEM images show that the composite gel has a porous structure and high porosity. In order to study the application of composite gel material in tissue engineering, it is necessary to further study its biological function.

Acknowledgements This study is funded by University scientific research project-3D Printing mineralized collagen-based child mandible (Grant No. 20190116002/037), Students research-Medical X-ray imaging measurement tape prepared by screen printing (Grant No. 22150116005/074). High level crossing training plan of Beijing high school-Construction of small-caliber artificial blood vessels with cells.

References

1. Jagur-Grodzinski J (2010) Polymeric gels and hydrogels for biomedical and pharmaceutical applications. Polym Adv Technol 21(1):27–47
2. Kopecek J (2007) Hydrogel biomaterials: a smart future? Biomaterials 28(34):5185–5192
3. Sun JY, Zhao X, Illeperuma WRK (2012) Highly stretchable and tough hydrogels. Nature 489 (7414):133–136
4. Roy I (2003) Gupta M N. Smart polymeric materials: emerging biochemical applications. Chem Biol 10(12):1161–1171
5. Calvert P (2009) Hydrogels for soft machines. Adv Mater 21(7):743–756
6. Malda J, Visser J, Melchels FP et al (2013) 25th anniversary article: engineering hydrogels for biofabrication. Adv Mater 25(36):5011–5028
7. Song Q, Hu K, Cui FZ et al (2009) Effect of high temperature on morphology and structure of nano-hydroxyapatite/collagen composite. Mater Sci Forum 1360–1363 (2009)
8. Cui F, Feng Q (2004) Biomaterials science, 2nd edn. Tsinghua University Publication, China
9. Zhou H, Lee J (2011) Nanoscale hydroxyapatite particles for bone tissue engineering. Acta Biomater 7(7):2769–2781
10. Wu X, Liu S, Yeung KWK, Liu C, Yang X (2014) Biomimetic porous scaffolds for bone tissue engineering. Mater Sci Eng R Rep 80(1):1–36
11. Hench LL, Polak JM (2002) Third-generation biomedical materials. Science 295(5557): 1014–1016
12. Takeda A, Tamano H (2016) Significance of low nanomolar concentration of Zn(2+) in artificial cerebrospinal fluid. MolNeurobiol 1–6 (2016)

Study on DDSA Modified Guar Gum Used as the Retention and Drainage Did in Reconstituted Tobacco Pulp

Nan Li, Guangxue Chen, Wei Chen and Xiaofang Wan

Abstract Recently, reconstituted tobacco sheets (RTS) have played an increasingly significant role in treat and reuse tobacco waste in industry. In this paper, dodecenyl succinic anhydride (DDSA) and catalyst tetramethylammonium hydroxide (TMAH) was used to modify guar gum in ionic liquid 1-butyl-3-methylimidazolium chloride ([Bmin]Cl). The modified guar gum exhibited good retention and drainage properties in reconstituted tobacco pulp. The characterization analysis of the modified guar gum was performed using Fourier Transform infrared (FT-IR) spectroscopy. While keeping other factors the same, the effects of the shear rate, amounts of guar gum dodecenyl succinate and pH on the first-pass retention (FPR) of reconstituted tobacco pulp were evaluated. It was found that, the optimal shear rate condition is 500–750 r/min and the FPR of tobacco reconstituted pulp could reach the maximum improvement of 74% when the dosage of guar gum succinate (GGS) was 0.6 mg per g oven dry pulp. In addition, excellent retention performance could be observed between pH 7 and 8. The results of this study showed that the modified guar gum could be used as a useful retention and drainage aid in reconstituted tobacco pulp.

Keywords Dodecenyl succinic anhydride · Guar gum · Reconstituted tobacco pulp · Retention and drainage aid

N. Li · G. Chen (✉) · X. Wan
State Key Laboratory of Pulp and Paper Engineering,
South China University of Technology, Guangzhou, China
e-mail: chengx@scut.edu.cn

W. Chen
College of Engineering, Qufu Normal University, Rizhao, China

P. Zhao et al. (eds.), *Applied Sciences in Graphic Communication and Packaging*, Lecture Notes in Electrical Engineering 477,
https://doi.org/10.1007/978-981-10-7629-9_117

1 Introduction

Reconstituted tobacco sheets (RTS) are manufactured from tobacco waste material and processing by-products such as fines, dust, scrap, stems and stalks, using papermaking processes. RTS could not only reduce the risks of smoking but also meet smoker's diversified demands of various kinds of flavor cigarettes. Accordingly, it is generally recognized that RTS could be used as an important ingredient instead of tobacco leaf in cigarette producing industry. Retention and drainage aids are widely used in paper making process in an attempt to increase the rate at which water drains from the formed sheet, and to increase the amount of fines and filler retained on the sheet [1].

In this study, guar gum was modified by dodecenyl succinic anhydride in [Bmin] Cl ionic liquids in order to improve its retention and drainage properties. The modified Guar gum was characterized by FT-IR, TGA, etc. The retention and drainage properties of the modified guar gum were also evaluated. In general, this study could provide a valuable way to utilize agricultural fiber wastes.

2 Experiments

2.1 Materials

The guar gum from FoShan He Feng Biological Technology was used without further purification. Dodecenyl succinic anhydride (DDSA) was provided by Wuxi Huilong Electronic Materials Co., Ltd. Tetramethylammonium hydroxide (TMAH) were procured from Sino-pharm chemical Reagent Co., Ltd. Ionic liquid [Bmin]Cl, lab homemade. The tobacco pulp was provided by Guangdong Jinye Tobacco Company. All other chemicals used are analytical reagents.

2.2 Synthesis of Guar Gum Succinate

Guar gum was pretreated with a certain amount of TMAH to activate the hydroxyl. Afterwards, 10.00 g pretreated guar gum together with 20.00 g [Bmin]Cl Ionic liquid were added into a 250 mL beaker, 3.00 g DDSA were added drop wise into the solution, and then the reaction was carried out under N_2 atmosphere with stirring for 5 h. Thereafter, the formed product was filtered, washed thoroughly with ethanol to eliminate ionic liquid, the un-reacted anhydride, TMAH and by-products. Then the product was dried in vacuum and stored in desiccators until further use.

2.3 Characterization

The analysis of the functional groups presents of dry GG and GGS samples were made by a Fourier Transform infrared spectroscopy (Bruker Corporation, Germany). The surface wettability of the GG and the GGS was evaluated by contact angle measurement, using a Contact Angle System OCA40 Micro (Data Physics Instruments). The Dynamic Drainage Jar (DDJ) was used to test the FPR of pulp suspension. SR degrees were measured by a model ZDJ-100 SR degree tester with a 200-mesh screen (Small Experimental Machine Factory of Changchun, China)

3 Results and Discussions

GGS was synthesized by reacting GG with DDSA in the presence of TMAH as a catalyst. Succinylation of the crude GG was carried out in [Bmin]Cl ionic liquids system to esterify guar gum's O–H groups. DDSA reacts with GG to form the monoester are illustrated in Fig. 1.

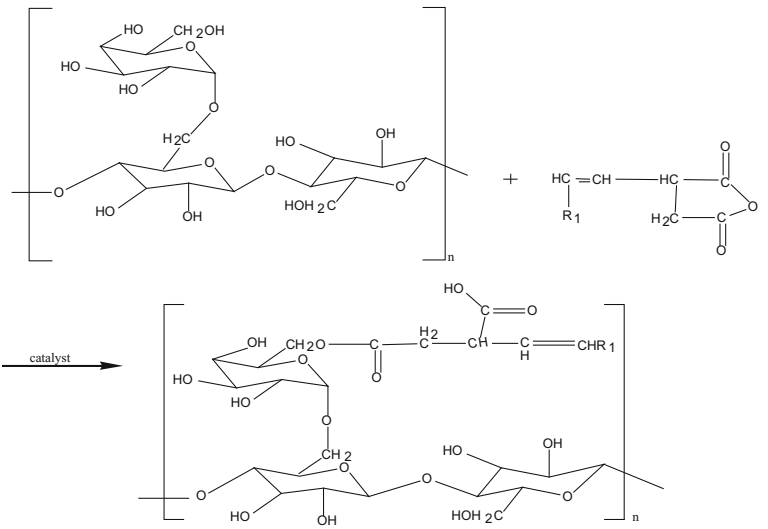

Fig. 1 Reaction of guar gum with dodecenyl succinic anhydride

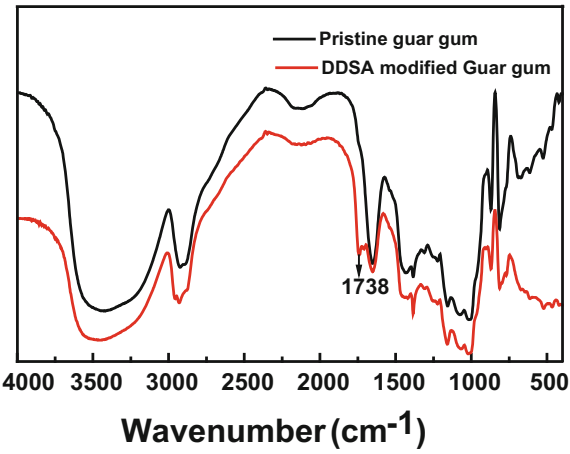

Fig. 2 FT-IR spectra of pristine guar gum and DDSA modified guar gum

3.1 FT-IR

Figure 2 depicts the infrared spectrum of native GG and GGS. The broad absorption peak at 3400 cm^{-1} can be attributed to the stretching vibrations of the hydrogen bonded hydroxyl groups (O–H) and peaks at 2919 cm^{-1} owed C–H stretching, the peaks visible in the region of 862, 810, 681 cm^{-1} are the finger print of guar gum. In case of GGS, the absorption spectrum shows an additional peak after the grafting of DDSA chains onto guar gum. This new peak was observed at 1738 cm^{-1} due to carbonyl group present in the ester linkage and confirms the formation of graft copolymers [2, 3].

3.2 Contact Angle

Figure 3 shows the contact angle (CA) change of a water droplet on GG and GGS. As shown in Fig. 3a, a water droplet could penetrate into the unmodified GG and

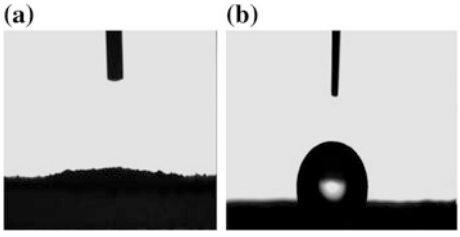

Fig. 3 TGA and DTG of pristine guar gum (spectrum a) and DDSA modified guar gum (spectrum b). **a** Water contact-angle images of the unmodified guar gum; **b** DDSA modified guar gum

the initial water contact angle of pure GG was ~0°, which consistent with the high hydrophilicity of the GG reported elsewhere [4]. The water CA of the GGS was ~111° (Fig. 3b) indicated that the graft of long alkyl carbon side chains significantly improved the water resistance of the surface. In summary, the GGS are more hydrophobic than GG indicating a superior water resistance property.

3.3 Retention and Drainage

From Fig. 4a we can conclude that the FPR of tobacco reconstituted pulp increased with increasing GGS dosage and reached the maximum improvement of 74% when the dosage of GGS was 0.6 mg per g oven dry pulp, which included an increase in retention of fines. Within a certain range, the retention of fine increased with the increase of concentration of GGS. As the addition of GGS continues increase, there were no significant improvements on the FPR of fines (Fig. 4a).

The FPR of reconstituted tobacco pulp under different shear rate of DDJ were displayed in Fig. 4b. The FPR of tobacco reconstituted pulp slightly decreased from 81 to 72% when the shear rate increased from 500 to 1200 rpm/min, and then sharply decreased to 52% with a further increase of shear rate of 2000 rpm/min

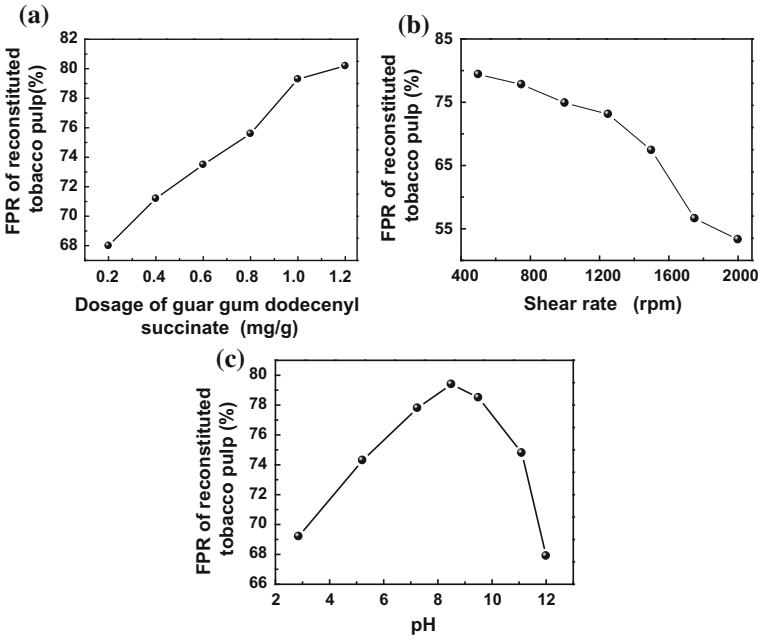

Fig. 4 Effects of the **a** dosage of guar gum dodecenyl succinate, **b** shear rate and **c** pH on FPR of reconstituted tobacco pulp

(Fig. 4b). This is because the shear affected both the flocculation rate and the breakup rate. In this experiment we also investigated the effect of pH (HCl and NaOH are used to adjust the pH value varying from 2 to 12) on FRP effect of tobacco pulp while other factors were constant. Figure 4c plots FRP of reconstituted tobacco pulp at various pH. It showed that excellent retention performance could be observed between pH 7 and 8.

4 Conclusions

The guar gum was successfully modified by DDSA in [Bmin]Cl ionic liquids. Then retention and drainage properties of reconstituted pulp suspension based on GGS or GG were studied by a dynamic drainage analyzer and a ZDJ-100 SR degree tester. It was found that GGS showed better retention efficiency than GG under different turbulent conditions. The results demonstrated that the modified guar gum could be an efficient retention and drainage aids used in the reconstituted tobacco sheet industry.

Acknowledgements The authors are extremely grateful to financial support from the Science and Technology Project of Guangzhou City in China (No. 2016070220045), State Key Laboratory of Pulp and Paper Engineering (2016 c01), State Key Laboratory of Pulp and Paper Engineering (2015TS01), Natural Science Foundation of China (No. 201404042), Shandong Natural Science Foundation (No. ZR2015PC016), Science and Technology Planning Project of Higher Education of Shandong Province (No. J14LD51), Doctoral Starting up Foundation of Qufu Normal University (No. BSQD2012058), and Science and Technology Planning Project of Qufu Normal University (No. xkj201413).

References

1. Hubbe MA (2007) Flocculation and redispersion of cellulosic fiber suspensions: a review of effects of hydrodynamic shear and polyelectrolytes. BioResources 2(2):296–331
2. Fujioka R, Tanaka Y, Yoshimura T (2009) Synthesis and properties of superabsorbent hydrogels based on guar gum and succinic anhydride. J Appl Polym Sci 114:612–616
3. Sharma R, Kaith BS, Kalia S, Pathania D, Kumar A, Sharma N, Street RM, Schauer C (2015) Biodegradable and conducting hydrogels based on Guar gum polysaccharide for antibacterial and dye removal applications. J Environ Manage 162:37–45
4. Leelamanie DAL, Karube J (2009) Effects of hydrophobic and hydrophilic organic matter on the water repellency of model sandy soils. Soil Sci Plant Nutr 55:462–467

Adhesion Improvement of Rice Straw Particleboards by Chemical Pre-treatment

Peng Luo, Chuanmin Yang, Denghui Zhao, Xiaojuan Lu and Yuanming Wang

Abstract The main objective of this study was to investigate the potential of rice straws as an alternative to wood particle to produce particleboards. As surfaces of rice straws were covered with smooth, water-repellent silica layers and wax, rice straw particleboards made with conventional water-borne resins exhibited poor mechanical properties and dimensional stability. In this study, rice straws were chemically pretreated with alkali, acid/alkali, and acid/alkali/H_2O_2, respectively. The effects of the three different chemical pretreatments on the performance of resulting particleboards were investigated. The mechanical properties of panels increased as a result of chemical pretreatment, indicating the chemical pretreatments were effective in improving performance of the rice straw particleboards. Among all chemical pretreatment processes, acid/alkali/H_2O_2 pretreatment was most effective in improving properties of the rice straw particleboards.

Keywords Rice straw · Particleboard · Pretreatment · Physical properties Mechanical properties

1 Introduction

Packaging is essential in protecting, transporting, and selling commodities. Yet packaging, which is discarded after usage, is usually one-time used. This practice not only wastes precious natural resources, but pollutes environment as well, with white pollution resulted from undegradable plastics becoming a big public hazard. It becomes an urgent subject to develop degradable packaging material. Wooden pallets and cases, which are not one-time packaging products, consume a huge amount of timbers resulting in waste of precious forest resources.

China is a big agricultural country, having plentiful agricultural straws. Agricultural straw has the same basic components, i.e., cellulose, lignin, and

P. Luo (✉) · C. Yang · D. Zhao · X. Lu · Y. Wang
College of Mechanical Engineering, Tianjin University of Commerce, Tianjin, China
e-mail: pengluo@yeah.net

P. Zhao et al. (eds.), *Applied Sciences in Graphic Communication and Packaging*, Lecture Notes in Electrical Engineering 477,
https://doi.org/10.1007/978-981-10-7629-9_118

pentosan, as wood but in different proportions, which indicates agricultural straw has potential to substitute wood for particleboard production. In order to utilize agricultural straws to make particleboard for production of pallets and cases, packaging professionals all over the world have done a lot of researches [1–3]. However, some key technologies, such as wax layers and silica existing on straw surfaces that deter bond formation between conventional urea formaldehyde (UF) and straws, have yet to be developed. Manufacture of agricultural straw particleboards with polyisocyanate resin (PMDI) leads to expensive production cost resulting in poor marketing competition. These problems hinder commercial production of straw particleboards.

Previous studies showed that a variety of chemical (acid, alkali, oxidizing agents) pretreatment techniques have been developed to remove the wax and ash contents from the surface of agricultural residues [4–7]. The chemical pretreatment can significantly improve the adhesion properties of the agricultural residue fibers [2, 3, 8]. Previous studies reported that mechanical properties and dimensional stability of the panels were improved by chemical pretreatment of agricultural residues [1, 4]. For example, Mo et al. [4] investigated the performance of particleboards made from alkali pretreated wheat straws. They reported that the overall performance of the panels made from alkali treated wheat straws was much better than that of the panels made from untreated wheat straws. Similar results were also found for particleboards made with oxalic acid pretreated rice straws and bleach pretreated wheat straws [3, 7]. But it has not been studied whether similar changes in the particleboards made from chemical pretreated rice straw bonded with UF.

Therefore, this study used acid, oxidizing agents and alkaline to pretreat rice straw, respectively, in hope of enhancing wettability of rice straw, improving adsorb, expansion and penetration of UF on rice straw.

2 Methods

2.1 Materials

Rice straw was collected from a local harvest in Shuangkou, Tianjin City, China in the fall of 2015. Rice straws were crushed thoroughly with a crusher into particles of 2 cm in length and were sieved with 1 cm mesh to remove undersize particles and impurities. Rice straw was then dried at 100 ± 2 °C to reach an average moisture content of 10%. NaOH, H_2SO_4 and H_2O_2 used in this work were purchased from Tianjin Chemicals Co., Ltd., China, which were analytically pure. Solutions with 5% NaOH or 2% H_2SO_4 or a mixture of 5% NaOH and 0.2% H_2O_2 in a proportion 1:1 solution were prepared using distilled water. Commercial UF of E1 grade was employed.

2.2 Alkali Pretreatment

The rice straws were soaked in 5% NaOH solution at a ratio of 1:6 at 50 °C for 120 min. Then, the solid residue was collected by filtration and washed extensively with tap water until neutral pH. The resultant rice straws were then oven dried at 100 ± 2 °C to reach an average moisture content of 20% [9].

2.3 Acid/Alkali Pretreatment

The acid/alkali pretreatment procedures were the same as the above alkali pretreatment, except that the rice straws were soaked in 2% H_2SO_4 solution. The residue was sequentially treated by alkali for 60 min as described above. After chemical treating, the insoluble residue was collected, washed and dried as above alkali pretreatment [9].

2.4 Acid/Alkali/H_2O_2 Pretreatment

The rice straws treated by acid/alkali were suspended in 0.05% H_2O_2 and kept at room temperature in dark for 12 h. After filtration, the residues were collected, washed and dried as above alkali pretreatment [9].

2.5 Sample Preparation

The pretreated rice straws were slowly sprayed with 8 wt% (based on the weight of the oven dried raw material) UF resin adhesive in a rotary drum mixer, respectively. After blending, the rice straw furnishes were pre-pressed into a mat in a mold. The resultant mat was then hot pressed to form composite boards using a hot press equipped with 500 mm × 500 mm metal plates. The hot press temperature, pressure and pressing time were 160 °C, 3.5 MPa and 3 min, respectively. The thickness of particleboard was controlled by stop bars which was 6 mm. Particleboards were prepared with the alkali, acid/alkali, and acid/alkali/H_2O_2 pretreated rice straws, respectively. Particleboards made with untreated rice straws were used as the control. All of the boards were manufactured with an average target density of 0.75 g/cm^3. After fabrication, the boards were conditioned at 65% relative humidity and 20 °C for 2 weeks before testing. The obtained boards were trimmed to avoid edge effects.

2.6 Testing Methods

The finished particleboard was cut into various specifications according to the GB/T 4897-2003 standard method [10].

3 Results and Discussion

Table 1 shows the mechanical properties of the particleboard composites made with chemical pretreated and unpretreated rice straws. As can be seen from the Table 1, panels produced using chemical pretreated rice straws generally showed better mechanical properties compared with the control.

Chemical pretreatment of rice straws had significant effect on the MOR of the particleboard. The results suggest that panel composites made with chemical pretreated rice straws substantially increases the bending strength. Similar results have been reported by Mo et al. in the study of particleboard manufacture from bleach pretreated wheat straw [4]. The authors stated that chemical modification of wheat straws by bleach improves the mechanical properties of composites. Rice straws pretreated by acid/alkali/H_2O_2 had the highest MOR, MOE and IB values among the four types of the specimens. The reason for the highest MOR obtained with acid/alkali/H_2O_2 pretreated rice straws could be due to efficient removal of wax or inorganic silica from the rice husk surface, resulting in the increased new reactive sites for adhesion. As a consequence, stronger bonding between particles may occur. These results show that the acid/alkali/H_2O_2 pretreatment is an efficient rice straw pretreatment technique.

In general, the MOE followed the same trend as the MOR. The boards made from chemical pretreated rice straws had greater MOE than the control (Table 1). The MOE values obtained ranged from 2584.5 to 3337.3 MPa. Chemical pretreatment of rice straws had significant influence on MOE. Particleboards made from acid/alkali/H_2O_2 pretreated rice straws showed the largest improvement in MOE, about 29.1% higher than the control. This pronounced improvement in the bending stiffness is most likely to the partial removal of wax or inorganic silica in

Table 1 Effect of pretreatment on mechanical properties of the particleboard composite[a]

Pretreatment type	MOR (MPa)	MOE (MPa)	IB (MPa)
Control	19.1(0.4)A	2584.5(2.4)A	0.41(0.04)A
Alkali pretreatment	21.4(0.7)B	2795.4(1.9)B	0.46(0.02)B
Acid/alkali pretreatment	23.7(0.3)C	3090.7(2.3)C	0.52(0.03)C
Acid/alkali/H_2O_2 pretreatment	26.7(1.9)D	3337.3(2.8)D	0.58(0.08)D

[a]Groups with the same letters in each column indicate that there is no statistical difference ($P < 0.05$) between the samples according to the Duncan's multiple range test; values in parentheses are standard deviation

rice straw particles. Mo et al. and Wang et al. reported that wheat straw treated by alkali improved bending stiffness of particleboard [4, 11]. All produced particleboards met the minimum MOE requirement of the U.S. standards for industrial uses [12].

IB values ranged from 0.41 to 0.58 MPa. The minimal requirement of internal bond strength for commercial usage, and for industrial usage are 0.4 and 0.45 MPa [12], respectively. According to the results, all particleboards produced in this work exceeded the minimum IB requirements of the U.S. Standard for commercial uses. In addition, particleboards made from chemical pretreated rice husks satisfied the IB requirements for industrial uses. The IB values of the panel composites made with chemical pretreated rice husks mixed with wood particles are much higher than those of the control. This phenomenon has been previously observed in the treatment of wheat straw by alkali and bleach [4, 11]. The improvement in IB can be attributed to improved interfacial adhesion between the particles and adhesives resulting from the partial removal of wax or inorganic silica in rice straw particles. Particleboard made from acid/alkali/H_2O_2 pretreated rice straws achieved the highest IB value. This result is consistent with the above discussion that the acid/alkali/H_2O_2 pretreatment is an efficient rice straw pretreatment technique.

Table 1 shows the percentage thickness swelling of boards. The TS values for the 2 h soaking range from 13.22 to 18.86%, and these values are increased after 24 h soaking, ranging from 26.72 to 40.51%. None of the panels produced met the maximum thickness swelling requirement of 8% stated in the U.S. Standard [12]. The TS values of the panel composites made with chemical pretreated rice straws are much lower than those of the control. Similar results have been reported by Li et al. [7] in the study of oxalic acid and steam pretreatment of rice straw for particleboard manufacture. Hemicellulose is a branched, non-crystalline polymer which has the ability to absorb water and swell. Of the different components in the cell wall, the hemicelluloses swell the most and lignin the least [13]. The improvement of dimensional stability in boards after chemical pretreatment could be mainly attributed to the partial removal of hemicellulose in rice straw particles. Another explanation for the increase is the improved bonding between the resin and particle in chemical treated panels. The panel composites made with acid/alkali/H_2O_2 pretreated rice straws show the lowest TS. These results indicate that the acid/alkali/H_2O_2 pretreatment can effectively improve absorption resistance of boards. Therefore, acid/alkali/H_2O_2 pretreatment is recommended for making rice straw particleboards.

4 Conclusions

In this study, rice straws were used to make particleboard panels. Chemical pretreatments of rice straws had a great impact on the physical and mechanical properties of the produced particleboards. The particleboards made from the chemical pretreated rice straws had significantly higher physical and mechanical

properties than the particleboards made from unpretreated rice straws. The acid/alkali/H_2O_2 pretreatment is the most efficient rice straw pretreatment technique among these three chemical pretreatment processes. The particleboards made with acid/alkali/H_2O_2 pretreated rice straws showed the highest average MOR, MOE and IB values. According to the test results, rice straw could serve as an effective particleboard raw material.

Acknowledgements The authors thank Tianjin Research Program of Application Foundation and Advanced Technology (contract number 13JCYBJC38800).

References

1. Akhtar M, Kenealy WR, Horn EG, Swaney RE, Winandy J (2008) Method of making medium density fiberboard. US Patent No. US 2008/0264588 A1
2. Wu J, Gatewood BM (1998) Bleaching of wheat straw, an alternative cellulosic (hard) fiber for potential industrial application. In: International conference and exhibition of the American association of textile colorist and chemists, pp 58–67
3. Mo X, Cheng E, Wang D, Sun XS (2003) Physical properties of medium-density wheat straw particleboard using different adhesive. Ind Crops Prod 18:47–53
4. Mo X, Hu J, Sun XS, Ratto JA (2001) Compression and tensile strength of low-density straw-protein particleboard. Ind Crops Prod 14:1–9
5. Vázquez M, Oliva M, Simón J, Luis T, Ramírez J (2007) Hydrolysis of sorghum straw using phosphoric acid: evaluation of furfural production. Biores Technol 98:3053–3060
6. Salam A, Reddy N, Yang Y (2007) Bleaching of kenaf and cornhusk fibers. Ind Eng Chem Res 46:1452–1458
7. Li X, Cai Z, Winandyc JE, Bastad AH (2011) Effect of oxalic acid and steam pretreatment on the primary properties of UF-bonded rice straw particleboards. Ind Crops Prod 33:665–669
8. Ntalos GA, Grigoriou AH (2002) Characterization and utilisation of vine prunings as a wood substitute for particleboard production. Ind Crops Prod 16:59–68
9. Zhu SD, Wu YX, Yu ZN, Wang CW, Yu FQ, Jin SW, Ding YQ, Chi RA, Liao JT, Zhang Y (2006) Comparison of three microwave/chemical pretreatment processes for enzymatic hydrolysis of rice straw. Biosyst Eng 93:279–283
10. ASTM D 1037-99 (1999) Standard methods of evaluating the properties of wood-based fiber and particle panel materials. American Society for Testing and Materials, USA
11. Wang D, Sun XS (2002) Low density particleboard from wheat straw and corn pith. Ind Crops Prod 15:43–50
12. ANSI A208.1 (1998) Particleboard. American National Standard. National Particleboard Association
13. Mosier N, Wyman C, Dale B, Elander R, Lee YY, Holtzapple M, Ladisch M (2005) Features of promising technologies for pretreatment of lignocellulosic biomass. Biores Technol 96:673–686

Preparation of Super-Hydrophobic Cotton Fabric with Crosslinkable Fluoropolymer

Yaling Ma, Congjun Cao and Chengmin Hou

Abstract Super-hydrophobic surfaces have been widely used in various fields because of its self-cleaning performance. In this study, high fluorine-containing esters and epoxy-containing esters were used to improve the hydrophobicity and durability of cotton textile substrates. The random block fluoropolymer PGMA-*r*-PDFMA was synthesized in one step by using conventional free radical polymerization of dodecafluoroheptyl methacrylate (DFMA) and glycidyl methacrylate (GMA). And then the cotton fabric was soaked in the solution of the polymer to graft the polymer to build super-hydrophobic surface. The results show that the modified cotton textile has better hydrophobic effect and the water contact angle reaches 163°.

Keywords Super-hydrophobic · Cotton fabric · Hydrophobicity
Fluoropolymer

1 Introduction

Since ancient times, the lotus has been widely praised because of its unique self-cleaning nature, and it also provides a practical way to construct super-hydrophobic surface. The surface of the plant has many protrusions that form roughness with microscale and nanoscale structures, which can help keep the air under water droplets so that the droplets remain spherical on the surface of the lotus leaves and remove dust while rolling away, this is the famous "lotus effect". Typically, the super-hydrophobic surface is defined as having a water contact angle (WCA) of greater than 150° [1–12]. At present, the preparation of super-hydrophobic surface has been made some achievements. Different wetting characteristics can be obtained through making appropriate nanoscale and micron level roughness on the surface and

Y. Ma · C. Cao (✉) · C. Hou
Faculty of Printing, Packaging Engineering and Digital Media Technology,
Xi'an University of Technology, Shaanxi, China
e-mail: caocongjun@xaut.edu.cn

P. Zhao et al. (eds.), *Applied Sciences in Graphic Communication and Packaging*, Lecture Notes in Electrical Engineering 477,
https://doi.org/10.1007/978-981-10-7629-9_119

establishing a suitable surface morphology to obtain a super-hydrophobic performance. Another theory of constructing super-hydrophobic surfaces is to use low surface energy materials for modification [2–8]. These two methods usually use silica nanoparticles (SNPs), zinc oxide, titanium dioxide and fluorocarbons, alkylamines, silicate or organosilicon compounds, respectively [2, 3, 5–7]. There are many different ways to build this special surface, including chemical vapor deposition, template methods, polymer reconfiguration, self-assembly and sol–gel processing, layer-by-layer deposition, plasma treatment, electrospinning, etc. [5, 7, 8, 13]. With some of these methods, an appropriate textured surface is constructed directly on the hydrophobic material, while others firstly create a textured surface and then coat with hydrophobic materials to form a film [8]. Xu et al. [14] reported that super-hydrophobic ZnO Nano rod array film was prepared on the cotton substrate by wet chemical method and then modified with dodecyltrimethoxysilane (DTMS). The modified cotton fabrics exhibited super-hydrophobicity with a contact angle of 161° and a roll-off angle of 9°. Abbas et al. [3] built the super-hydrophobic cotton fabric via a solution immersion process using silica nanoparticles and hexadecyltrimethoxysilane. Wu et al. [4] reported a facile fabrication approach of durable super-hydrophobic textiles by dip coating in a nanocomposite solution of fluoro-free organosilanes. Cai et al. [15] reported that 1H,1H,2H,2H-nonafluorohexyl-1-acrylate was grafted onto cotton fabric via a simultaneous irradiation induced graft polymerization technique and the fabric showed super-hydrophobicity. By γ–rays radiation-induced graft polymerization of fluorinated acrylate monomer, Deng et al. [12] fabricated a laundering-durable super-hydrophobic cotton fabric. Chang et al. [16] prepared organic super-hydrophobic films using water-repellent materials TA-N fluoroalkylate (TAN) and methyl methacrylate (MMA) copolymer and surface roughness material inorganic silica powder. Wang et al. [17] fabricated a durable and self-healing super-hydrophobic and super-oleophobic surface utilizing fluorinated-decyl polyhedral oligomeric silsesquioxane (FD–POSS) and a fluorinated alkyl silane (FAS).

Due to its excellent water repellency, self-cleaning, anti-corrosion and anti-icing properties, super-hydrophobic surfaces have caught the attention of researchers in the field of surface functional materials [18, 19]. At the same time, the potential applications of super-hydrophobic cotton fabrics in everyday life and industry, such as high-performance textiles, curtains, tablecloths and decorative fabrics, also aroused interest in functional textile [4, 20, 21]. Cotton fabric has become a very important substrate in the field of super-hydrophobic research. There are many fine fibers on the surface of the cotton fabric, which are intertwined to form a network structure. What's more, the cotton itself has a porous structure, which leads to a multilayered micrometer and nanoscale roughened structure and also provides roughness as a super-hydrophobic substrate surface should have. On the other hand, fluorocarbons were used to modify the cotton fabric to further enhance the hydrophobic properties, but adhesion of the hydrophobic coating to the fiber surface is the most crucial for the practicality of textiles. In the washing process, the fall and loss of the hydrophobic coating on the cotton fabric surface were likely to be caused by the mechanical action [3, 12, 22].

In this work, a simple approach is proposed for fabrication of durable super-hydrophobic textiles by dipping coating in a fluoride solution. A simple step in the synthesis of fluorine and epoxy group polymer is used, epoxy groups and its self-crosslinkable character are conducive to strengthening the low surface energy fluorine material and the substrate connection, polyfluorinated substances is used to get better hydrophobicity. The synthesized polymer and the resulting cotton fabric are analyzed by FTIR and SEM, the hydrophobicity is evaluated by WCA measurement.

2 Experimental

2.1 Materials

Dodecafluoroheptyl methacrylate(DFMA, 96%) was purchased from Harbin Xuejia fluorin silicon Chemical Co. Ltd, China. Glycidyl methacrylate (GMA) was obtained from Aladdin Technology Co. Ltd, Shanghai, China. Sodium Hydrogen Sulfite ($NaHSO_3$) was purchased from Xu Zhuangzi, Dongli District, Tianjin. Tetrahydrofuran (THF) was purchased from Tianjin Zhiyuan Chemical Reagent Co. Ltd, China. Azodiisobutyronitrile (AIBN) was purchased from Shanghai ShanPu Chemical Co. Ltd, China. Triethylamine was purchased from Tianjin Tianli Chemical Reagent Co. Ltd, China.

2.2 Methods

2.2.1 Synthesis of PGMA-*r*-PDFMA

GMA, DFMA, AIBN and $NaHSO_3$ were added into a flask to make a THF solution. Under the protection of nitrogen, the mixed solution is stirred at 70 °C for 50 min. Subsequently, volatilize the organic solvents and then PGMA-*r*-PDFMA was obtained, the structure diagram was shown in Fig. 1.

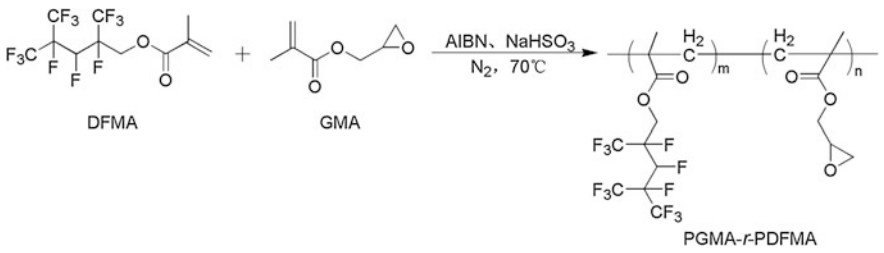

Fig. 1 Preparation of the PGMA-*r*-PDFMA

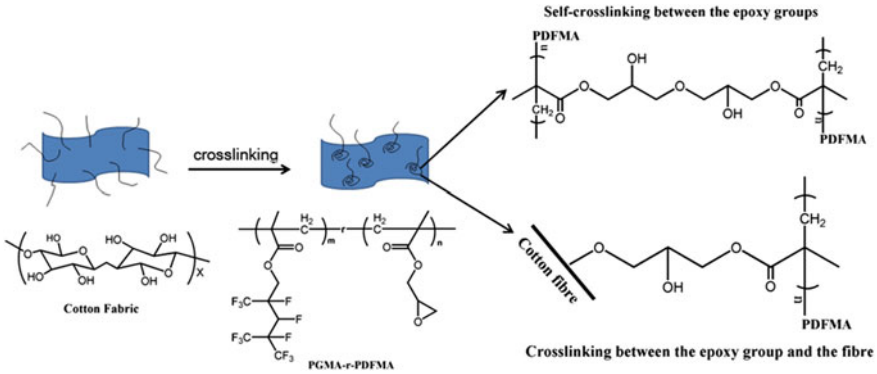

Fig. 2 The fabrication procedure of the cotton fabric modified by PGMA-*r*-PDFMA

2.2.2 Achieving Super-Hydrophobic Cotton Fabric

Cotton fabric can be casually selected. The Cotton fabric was washed by detergent and soaked in ethanol for 24 h, and then, dried at 120 °C and cut into 2.5 cm 3 cm pieces before modified. Additionally, obtained PGMA-*r*-PDFMA polymers and a few drops of triethylamine were dissolved in THF. Fabrics were stirred in 8 mg/mL polymers THF solutions at normal temperature for 8 h and dried at 120 °C for 3 h. The specific cross-linking method and assembly mechanism were shown in Fig. 2.

2.2.3 Characterization

An elemental analysis and the infrared spectra testing of the obtained PGMA-*r*-PDFMA polymer were implemented and recorded using a Fourier transform infrared spectrometer (IRPrestige21/FTIR-8400S). The polymer samples were precipitated in methanol to form powders and then compressed them into a thin disc with KBr. Different spectra were collected over the range of 0–4500 cm^{-1}. The surface morphologies of the cotton fabrics before and after treatment were examined using scanning electron microscope (Bruker FT-VERTEX 70). Fabrics samples were coated with a thin layer of gold using a sputtering machine prior to examination with SEM.

2.2.4 Measurement of Water Contact Angle

For the assessment of the super-hydrophobic character of the modified cotton fabric, the water contact angles (WCA) were measured using deionized water with a

droplet volume of 5 mL at room temperature. A contact angle instrument (Static contact angle/interfacial tension tester POWEREACHT JC2000A) was used. All the angles were determined by averaging values measured at five different points on each sample surface.

3 Results and Discussion

3.1 Fourier Transforms Infrared Spectrometer (FT-IR)

The various groups of polymers have their own specific infrared absorption peaks, so that functional groups information can be obtained by different wavelength and frequency positions of the infrared spectrum. Figure 3 was an infrared spectrum of the synthesized polymer. Each peak in the figure belonged to: The absorption peaks at 2993, 1751, 1100–1500 cm^{-1} were the stretching vibration absorption peaks of CH_2, C = O, C–F respectively; 910 cm^{-1} was the absorption peak of epoxy groups in GMA, which indicates that the prepared polymer contained some epoxy groups and ensured the chemical crosslinking of the polymer with the cotton fabric substrate. These absorption peaks further demonstrated the successful synthesis of the polymer PGMA-*r*-PDFMA.

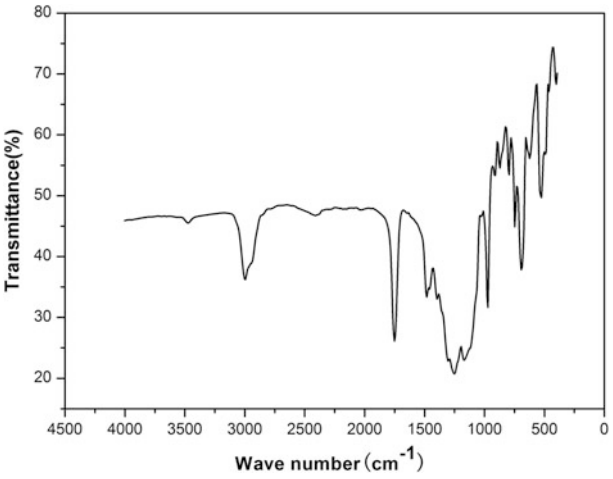

Fig. 3 The infrared image of the PGMA-*r*-PDFMA

3.2 *Film Morphology of PGMA-r-PDFMA on Cotton Substrate*

The structure or morphology of the polymer on the substrate largely determines its performance or application performance. Therefore, it is very valuable to explore its morphology on the substrate [6]. DFMA possesses low surface energy and can be absorbed on the surface of a hydrophilic substrate to form a molecular size film. Therefore, observing the modified cotton textile surface to get some information of fluorine-containing polymer on the cotton texture. And the surface morphology of the unmodified and the modified cotton fabric is shown in Fig. 4.

In Fig. 4a, it was found that the surface of the unmodified fiber interwoven was substantially smooth and showed a tight woven fabric structure. In higher magnification Fig. 4b, the surface of a single fiber also exhibited a very smooth topography, which ensures that the cotton itself has many excellent properties, such as breathability. In the lower magnification picture 4c of the modified cotton fabric, it is clear that there are other substances attached to cotton fiber surface. But the gap between the fabric fibers could be still seen clearly, which indicates the apparent appearance of the cotton clothes before and after the modification do not produce a big change and therefore do not affect the air permeability of the cotton cloth. But further observing the surface condition of a single fiber obtained by amplification

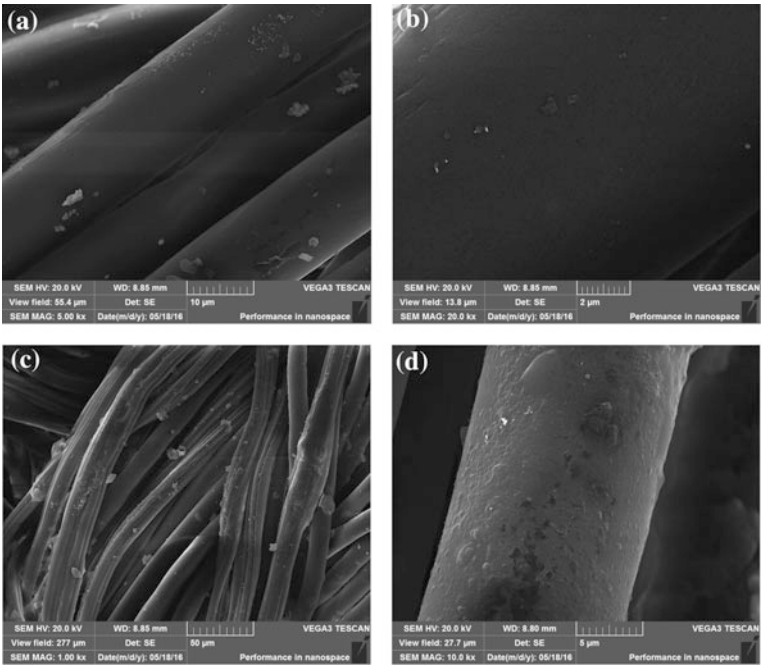

Fig. 4 SEM images of: **a** and **b** pristine cotton. **c** and **d** (PGMA-*r*-PDFMA)-coated-cotton

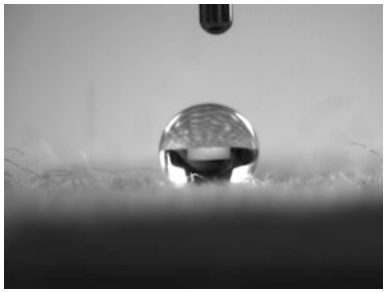

Fig. 5 The contact angle of water droplets on the surface of modified cotton textile

(Fig. 4d), a significant change could be seen. Compared with the surface of the unmodified surface, the modified one was covered with a layer of even and coarse polymer coating with a large number of tiny bulge, the contours of the fibers were clear and there was no adhesion between them.

3.3 Analysis of Super-Hydrophobic Properties of Modified Cotton

The wettability of the cotton fabrics was examined by WCA measurements. The original cotton textile surface had a large number of hydrophilic hydroxyl, and was easy to be completely wetted by water. After modified, the cotton fabric was completely different from the original one and WCA can be achieved 163° (Fig. 5), which showed that the cotton obtained super-hydrophobic performance. The high fluoride substance PGMA-*r*-PDFMA reduced the surface energy of the cotton base and introduced some hydrophobicity.

4 Conclusions

In this paper, the synthesis of cross-linkable fluorine-containing random block polymer PGMA-*r*-PDFMA and the construction of super-hydrophobic textile were mainly discussed. The functional groups of the synthesized polymers were characterized by FTIR, and the surface morphology of the cotton fabrics before and after modification was characterized by SEM. Thus the successful preparation of the polymers and super-hydrophobic fabrics was demonstrated. At the same time, the prepared super-hydrophobic textile has better hydrophobic properties and the contact angle reach 163°. The prepared super-hydrophobic cotton textile can be used as a new special printing material, the obtained polymer can also be grafted on other substrates, and the further study will be described in the later article.

References

1. Li XM, Reinhoudt D, Crego-Calama M (2007) What do we need for a superhydrophobic surface? A review on the recent progress in the preparation of superhydrophobic surfaces. Chem Soc Rev 36(8):1350–1368
2. Richard E et al (2013) A simple cost-effective and eco-friendly wet chemical process for the fabrication of superhydrophobic cotton fabrics. Appl Surf Sci 277:302–309
3. Abbas R et al (2014) Fabrication of durable and cost effective superhydrophobic cotton textiles via simple one step process. Cellulose 22(1):887–896
4. Wu L et al (2013) Mimic nature, beyond nature: facile synthesis of durable superhydrophobic textiles using organosilanes. J Mater Chem B 1(37):4756
5. Afzal SN, Daoud WA, Langford SJ (2014) Superhydrophobic and photocatalytic selfcleaning cotton. J Mater Chem A 2:18005–18011
6. An Q et al (2012) Fabrication of superhydrophobic fabric coating using microphaseseparated dodecafluoroheptyl-containing polyacrylate and nanosilica. J Appl Polym Sci
7. Xue CH et al (2010) Large-area fabrication of superhydrophobic surfaces for practical applications: an overview. Sci Technol Adv Mater 11(3):033002
8. Bravo J et al (2007) Transparent superhydrophobic films based on silica nanoparticles. Langmuir 23:7293–7298
9. He G et al (2013) Superhydrophobic hierarchically assembled films of diblock copolymer hollow nanospheres and nanotubes. ACS Appl Mater Interfaces 5(7):2378–2386
10. Abdulhussein AT et al (2016) Current trend in fabrication of complex morphologically tunable superhydrophobic nano scale surfaces. Appl Surf Sci 384:311–332
11. Erbil HY et al (2003) Transformation of a simple plastic into a superhydrophobic surface. Science 299(5611):1377–1380
12. Deng B et al (2010) Laundering durability of superhydrophobic cotton fabric. Adv Mater 22(48):5473–5477
13. Yin S et al (2011) Fabrication and surface characterization of biomimic superhydrophobic copper surface by solution-immersion and self-assembly. Appl Surf Sci 257(20):8481–8485
14. Xu B, Cai Z (2008) Fabrication of a superhydrophobic ZnO nanorod array film on cotton fabrics via a wet chemical route and hydrophobic modification. Appl Surf Sci 254(18): 5899–5904
15. Cai R et al (2012) Radiation induced graft polymerization of a fluorinated acrylate onto fabric. Radiat Phys Chem 81(9):1354–1356
16. Chang K-C et al (2007) Preparation of super-hydrophobic film with fluorinated-copolymer. J Appl Polym Sci 104(3):1646–1653
17. Wang H et al (2011) Durable, self-healing superhydrophobic and superoleophobic surfaces from fluorinated-decyl polyhedral oligomeric silsesquioxane and hydrolyzed fluorinated alkyl silane. Angew Chem Int Ed Engl 50(48):11433–11436
18. Xu B et al (2010) Preparation of superhydrophobic cotton fabrics based on SiO2 nanoparticles and ZnO nanorod arrays with subsequent hydrophobic modification. Surf Coat Technol 204(9–10):1556–1561
19. Zhang X et al (2007) Superhydrophobic surfaces: from structural control to functional application. J Mater Chem A 18:621–633
20. Zimmermann J et al (2008) A simple, one-step approach to durable and robust superhydrophobic textiles. Adv Func Mater 18(22):3662–3669
21. Song J, Rojas OJ (2013) Approaching super-hydrophobicity from cellulosic materials: A Review. Nord Pulp Pap Res J 28(2):216–238
22. Huang W et al (2011) Enhanced washing durability of hydrophobic coating on cellulose fabric using polycarboxylic acids. Appl Surf Sci 257(9):4443–4448

Research of Graphene Preparation Methods

Xiaotong Xiong, Beiqing Huang, Xianfu Wei, Lili Wang and Lu Zhang

Abstract Oxidation-reduction method and liquid-phase exfoliation method are common methods for production of graphene sheets. To explore the two kinds of preparation methods, using liquid-phase exfoliation method to product graphene sheets compare the characterization with the graphene obtained by oxidation-reduction method. On this basis, we research the graphene dispersion's stability and concentration which prepared by liquid-phase exfoliation in different organic solvents. The experiment results express that graphene prepared by liquid-phase exfoliation has better slice layer structure, molecular structure contains less defects and oxygen-containing groups, graphene layer spacing is relatively wide, thermal stability is better. The graphene concentration of the dispersion in 1-methyl-2-pyrrolidinone is as high as 0.15 mg/mL, also has a decent stability, which allows this method to easily produce films and composites for a range of applications.

Keywords Graphene · Liquid-phase exfoliation · Oxidation-reduction method Characterization comparison

1 Introduction

Graphene is the strongest and toughest material known to man, and it offers extraordinary electronic, thermal and mechanical properties, which is expected to find a variety of applications [1–3]. There are many methods for generating graphene and chemically modified graphene from graphite and derivatives of graphite, each with different advantages and disadvantages [4].

Recently, the most commonly used approach involves the oxidation of graphiteto graphene oxide (GO), followed by chemical reduction. Because each slice layer

X. Xiong (✉) · B. Huang · X. Wei · L. Wang · L. Zhang
School of Printing and Packaging Engineering, Beijing Institute of Graphic Communication, Beijing, China
e-mail: 521144884@qq.com

P. Zhao et al. (eds.), *Applied Sciences in Graphic Communication and Packaging*, Lecture Notes in Electrical Engineering 477,
https://doi.org/10.1007/978-981-10-7629-9_120

of graphite has a relatively weak Van Der Waals force between the connection, under the oxidation, each layer of graphite is denudation on the formation of monolayer graphene oxide, then reductant was added to remove oxygen containing groups on the surface of the graphene oxide, such as carboxyl, epoxy and hydroxyl, eventually we get graphene preparation [5, 6]. Oxidation-reduction method is widespread for the advantages of its low cost and easily realization. The exfoliation of graphene in a liquid phase has shown its superiority for both scaling-up and application of graphene [7]. It is believed that the liquid-phase exfoliation of graphene is potentially important for the production of conducting inks and top-down approaches to electronics. Different solvents can lead to different effects of the liquid-phase exfoliation experiment, as a result the highly polar solvents such as 1-methyl-2-pyrrolidinone (NMP) et al. have been chosen for the liquid-phase exfoliation process. The selection of these solvents was based primarily on the trial-and-error experimentation [8, 9]. Solvents that are efficient in dispersing graphene can be selected on the basis of their Hildebrand solubility parameters, Hansen solubility parameters, and surface tensions. It is known that good solvents for graphite exfoliation have surface tensions in the region of 40–50 mJ/m^2 [8, 10].

2 Experimental Details

2.1 Materials

1-methyl-2-pyrrolidinone (NMP), 1,3-dimethyl-2-imidazolidinone (DMEU), cyclohexanone (CYC), propylene carbonate (PC), expanded graphite, sulfuric acid (98%), $NaNO_3$ solution, $KMnO_4$ solution, deionized water, hydrogen peroxide, vitamin C, PH test paper. All reagents and solvents were purchased from Aldrich ChemicalInc. and used as received.

2.2 Experimental Facilities

Facilities used in the experiment was shown in Table 1.

2.3 Preparation of Graphene

2.3.1 Liquid-Phase Exfoliation

The graphite was dispersed in solvents at a concentration of 5 mg/mL, the mixture was then sonicated in a ultrasonic bath (YP-1) for 6 h. The resultant dispersion was centrifuged using a centrifuge (GYROZEN-1236MGR) at 3000 rpm for 30 min.

Table 1 Experimental facilities

Name	Type	Manufacturer
Electric blender	D2004 W	SiYue Co., LTD
Magnetic stirrer	HZ85-2	ZhongXing Co., LTD
Centrifuge	RJ-TDL-60A	RuiJiang Co., LTD
Electronic balance	BS 244S	Sartorius Co., LTD
Ultrasonic bath	YP-1	ChengGong Co., LTD
Supersonic cleaner	KQ3200DE	Kunshan Ultrasonic Co., LTD
Freeze dry	DZF-6210	bo d kang Co., LTD
Raman spectrometer	XploRA	HORIBA JobinYvon Co., LTD
FTIR spectrometer	NcoletiS 50	Sai's fly the world Co., LTD
X-ray diffractometer	D/MAX-2200PC	RIGAKU
Thermogravimetric analysis meter	SDTQ600	AT Co., LTD
Transmission electron microscopy	Tecnai G2 F20 S-TWINC	BFSSK

After centrifugation, decantation was carried out by pipetting off the top half of the dispersion, finally we dryitina freeze dry (DZF-6210) and have performance characterizations.

2.3.2 Oxidation-Reduction

According to the previous reports and the experimental research of our project group [11, 12], we use the improved Hummers of graphene oxide to prepare by vitamin C as a reducing agent. The entire reaction process keeps with 500 r/min rotating speed, this method keeps the oxidant and reducing agent with high reaction efficiency, environmental at the same time.

In this report, we use this method to prepare graphene dispersion and get performance characterizations.

3 Results and Analysis

3.1 Liquid-Phase Exfoliation Compared with Oxidation-Reduction of Graphene Characterization

3.1.1 Raman Spectroscopy Analysis

We put grapheme prepared by liquid-phase exfoliation and oxidation-reduction into the sample bottle and keep the dark environment, use raman spectrometer

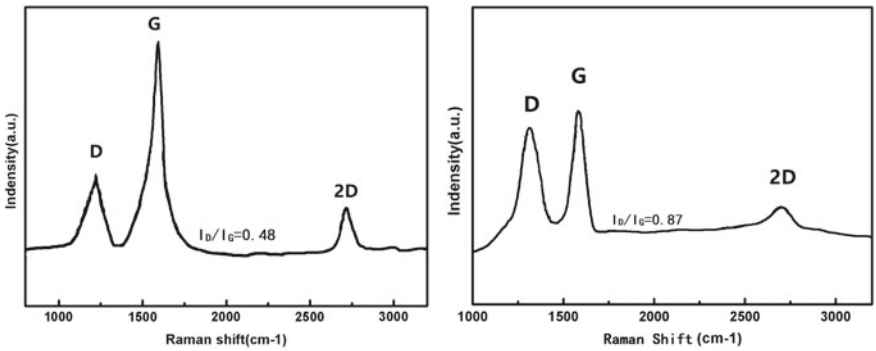

(a) liquid-phase exfoliation (b) oxidation-reduction

Fig. 1 Graphene's TEM images of different preparations

(XploRA) to scan graphene with the 532 nm excitation wavelength, results as shown in Fig. 1.

Raman spectroscopy is a fast and non-destructive method for the characterization of graphene. Raman spectroscopy results (532 nm laser excitation) confirm the graphene structure (Fig. 1). D-band ($\sim$1350 cm^{-1}), G-band ($\sim$1580 cm^{-1}), and 2D-band ($\sim$2700 cm^{-1}) appear in the Raman spectra. Relatively low D-bandintensities indicate that the graphene flakes contain few defects. These defects are predominantly located at the edges of the grapheme flakes (which are unavoidable during the preparation process), and the basal plane of the flakes are relatively defect free. The shape of the 2D-band is indicative of thin multilayer (<5 layers) [12]. The intensity ratio of D to G (I_D/I_G) is found to be 0.48 (Fig. 1a) and 0.87 (Fig. 2a), respectively, exfoliation graphene sheets much lower than chemically reduced GO further indicating high-quality.

3.1.2 Infrared Spectroscopic Analysis (FTIR)

The graphene prepared by liquid-phase exfoliation and oxidation-reduction fourier transform infrared (FTIR) spectra (Fig. 2) were recorded on a FTIR spectrometer (KBr disk method; NEXUS) at wave numbers in the range 1000–3500 cm^{-1}.

As shown in Fig. 2, The graphene prepared by liquid-phase exfoliation and oxidation-reduction have the peak at 3000–3500 cm^{-1}which is attributed to O–H stretching vibration of adsorbed water molecules. They also have a peak at 1550–1650 cm^{-1}which is graphene stretching vibration of the C = C and structural O–H groups. Besides, the graphene of oxidation-reduction has the peak 3000–3200 cm^{-1} which means the water molecule stretching vibration of–0–H, 1300 cm^{-1} is C–O stretching vibration of the peak, C = 0 ($\sim$1720 cm^{-1}) stretching vibration of the

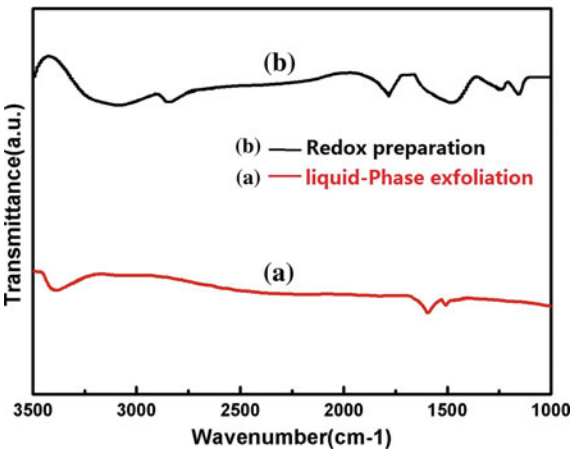

Fig. 2 Graphene's FTIR images of different preparations

peak [13]. So a lower content of edge defects of graphene obtained by liquid-phase exfoliation is confirmed by FTIR.

3.1.3 X-ray Diffraction (XRD) Characterization

XRD spectra are used to analyze the interlayer spacing determined from the diffraction peak position, X-ray diffraction (XRD) patterns were recorded on a Rigaku D/MAX-2200PC diffract to meter (35 kV, 20 m A, Japan) with Cu Ka radiation (k = 1.548 Å) at a scan rate of 2°/min, in the 2θ angles ranging from 10° to 70°. We get the XRD images as shown in Fig. 3.

In these XRD patterns, the reflection peaks of the samples (a) is gradually shifted to a lower diffraction angle compared with the pattern of the sample (b), which

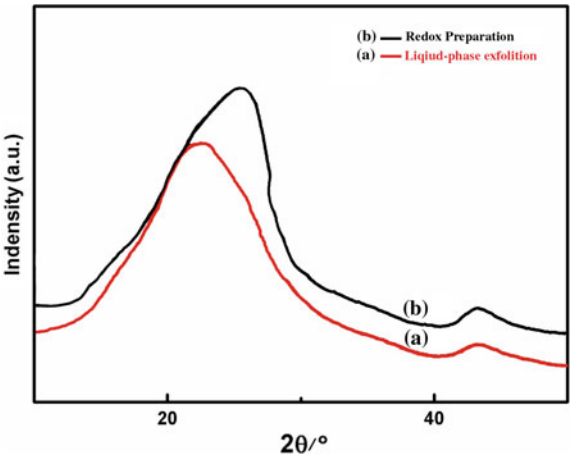

Fig. 3 Graphene's XRD images of different preparations

indicates an increase in the inter planar spacing determined from Bragg's law ($2d\sin\theta = n\lambda$) [10, 14]. The plane spacing of graphene obtained by liquid- phase exfoliation method is bigger relatively.

3.1.4 TGA Characterization

Thermogravimetric analysis is an important way to examine the stability of the material. Thermogravimetric analysis (TGA) was conducted in nitrogen atmosphere at a heating rate of 10 °C/min using a SDTQ600 TGA Thermogravimetric analyzer, as shown in Fig. 4.

TGA results reveal that graphene (Fig. 4a, b) loses weight at 450–550 °C, which is attributed to a loss of the residualoxygen-containing groups [14]. The TGA curves in Fig. 4a, b are almost identical below 500 °C. There is a difference in weight between the samples (a) and (b) at 500–550 °C, which may result from the formation of more folded and rolling structures in graphene sheets, causing more weight loss. It is most likely that more oxygen-containing groups are adsorbed on the graphene sheets of redox preparation.

3.1.5 Transmission Electron Microscope (TEM) Characterization

We obtained graphene sheets by liquid-phase exfoliation method and oxidation-reduction method, transmission electron microscope images were taken ona Tecnai G2 F20 S-TWINC with an operating voltage of 200 kV, as shown in Fig. 5.

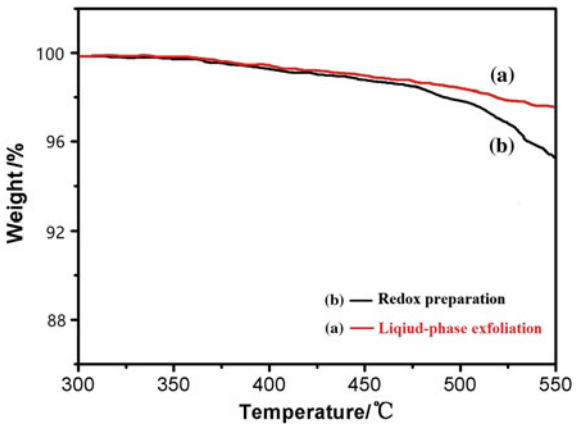

Fig. 4 Graphene's TG images of different preparations

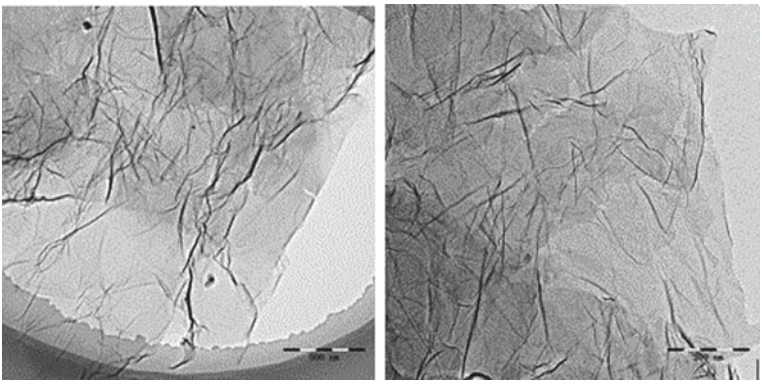

(a) liquid-phase exfoliation (b) oxidation-reduction

Fig. 5 Graphene's TEM images of different preparation

Transmission electron microscopy (TEM) study has been carried out to ascertain the degree of quality of the graphene sheets. Figure 5a and b shows the representative TEM images offew-layer graphene sheets with folded characteristics. Possibly because of the process of reaction lead to the edge of the structure defects.

3.2 Different Organic Solvents on the Exfoliation Graphene Dispersion Effect

It is known that good solvents for graphite exfoliation have surface tensionsin the region of 40–50 mJ/m^2, but different organic solvents of the preparation have different effect to the graphene dispersion, such as the dispersion's stability and concentration.

Weighing expanded graphite respectively to the same amount of organic solvents (N-methyl pyrrolidone, 1, 3-dimethyl-2-imidazoline, propylene carbonate, cyclohexanone), under the same condition, we prepare graphene dispersion through liquid-phase exfoliation method, and test the concentration of dispersions, as shown in Fig. 6. The graphene dispersions were stabled for 3 days, as shown in Fig. 7.

From these figures, Comparing with DMEU, PC and CYC, the graphene dispersion prepared by solvent NMP has the best stability, at the same time, For the solvent NMP, the grapheme concentration is $\sim$0.15 mg/mL, which is twice higher than that in the absence of CYC ($\sim$0.06 mg/mL).

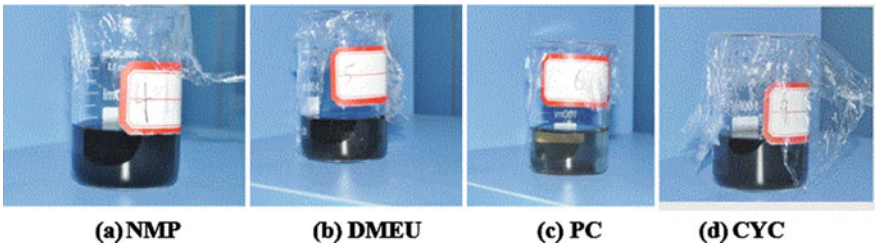

Fig. 6 Concentrations of graphene sheets dispersed in different organic solvents

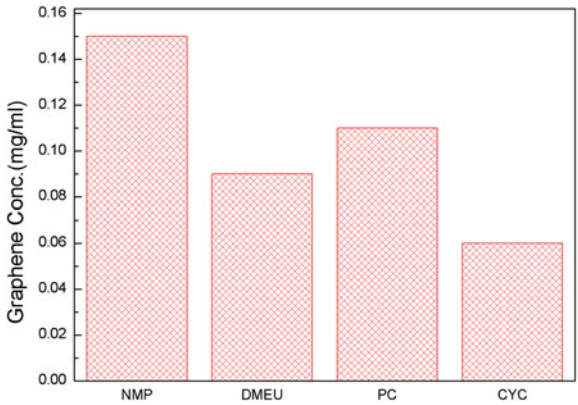

Fig. 7 Graphene dispersions in different organic solvents

4 Conclusions

We prepare the graphene by liquid-phase exfoliation and oxidation-reduction methods. The graphene prepared by liquid-phase exfoliation has better slice layer structure, molecular structure contains less defects and oxygen-containing groups, graphene layer spacing is relatively wide, thermal stability is better.

The graphene dispersion prepared by solvent NMP through liquid-phase exfoliation has the best stability, concentration is highest ($\sim$0.15 mg/mL).

References

1. Berger C, Song ZM, Li TB et al (2016) Electronic confinement and coherence in patterned epitaxial graphene. Sci 312:1191–1196
2. Cao Y, Feng J, Wu P (2010) Preparation of organically dispersible graphene nanosheet powders through a lyophilization method and their poly (lactic acid) composites. Carbon 48 (13):3834–3839
3. Yan Q, Liu Q, Wang J (2015) A simple and fast microwave assisted approach for the reduction of graphene oxide. Ceram Int

4. Wintterlin J, Bocquet M-L (2009) Graphene on metal surfaces. Surf Sci 603(10–12):1841–1852
5. Katsnelson MI (2007) Graphene: carbon in two dimensions. Mater Today 10(1–2):20–27
6. Ando Tsuneya (2014) Bilayer graphene with long-range scatterers: diamagnetism and weak-field hall effect. Physica E 58:6–15
7. Stoller MD et al (2008) Graphene-based ultracapacitors. Nano Lett 8(10):3498
8. Xu C, Yuan RS, Wang X (2014) Selective reduction of graphene oxide. New Carbon Mater 29(1):61–66
9. Mitra M, Chatterjee K, Kargupta K et al (2013) Reduction of graphene oxide through a green and metal-free approach using formic acid. Diamond Relat Mater 37:74–79
10. Park S, An J, Potts JR et al (2011) Hydrazine-reduction of graphite- and graphene oxide. Carbon 49(9):3019–3023
11. Fernandez-Merino MJ, Guardia L, Paredes JI Vitamin C is an ideal substitute for hydrazine in the reduction of graphene oxide suspensions. J Phys Chem C 114(14):6426–6432
12. Zhang Minghui, Wei Xianfu, Huang Beiqing et al (2016) Research of water-based graphene conductive screen printing ink and its property. Lect Notes Electr Eng 417:865–874
13. Ramanathan T et al (2008) Functionalized graphene sheets for polymer nanocomposites. Nat Nanotechnol 3(6):327-331
14. Zhou X, Zheng J, Wu H et al (2011) Reducing graphene oxide via hydroxylamine: a simple and efficient route to graphene. J Phys Chem C 115(24):11957–11961